生殖細胞のエピゲノムダイナミクスとその制御

領域番号：3502

平成 25-29 年度

科学研究費助成事業

（科学研究費補助金）

新学術領域研究（研究領域提案型）

研究成果報告書

平成 31 年 3 月

領域代表者　篠原隆司

京都大学大学院医学研究科遺伝医学講座

分子遺伝学分野

はしがき

新学術領域「生殖エピゲノム」を終えて

領域代表　篠原隆司

　我が国の生殖細胞の研究者人口は爆発的に増加した。私が大学生であった 90 年代前半には生殖細胞を研究している人はごく少数であったが、クローン動物やヒト ES 細胞の樹立に伴い多くの研究者がこの分野に参入した。今や多くの異なった背景を持つ研究者が生殖細胞のあらゆる段階を対象として研究を行っている。我が国で生殖細胞研究が発展するに至った礎を作ったのは中辻先生が始めた特定領域研究であることは疑いない。平成 11 年に始まった特定領域研究では学部や学会の壁を取り払われ、色々な年齢層の研究者が集まり、これまでの我が国の生殖細胞研究の中心となってきた。私が帰国して間もない頃、平成 15 年から始まった「生殖細胞の発生プロセス・再プログラム化とエピジェネティクス」に若手の計画班員として加えて頂いたことは、その後の自分の研究を進めて行く上で極めて幸運だった。年に一回の公開シンポジウムがあると、この先生に尋ねれば最先端の研究の状況が聞けるというのは出不精な自分にとっては大きな刺激であった。中辻先生の後を終了前申請で引き継いだ佐々木先生のエピゲノムネットワークでさらに研究の勢いが加速した。

　今回の新学術領域の申請した時は３回も続いた班が本当に通るのであろうかと心配ではあったが、幸いにも新領域として発足することができた。特定領域の半分のサイズになったので個々の班員と密接に接触できたと思う一方で、領域が拡大するあまりオールキャストとは行かなくなったのも事実である。領域代表というのはやってみると色々とこれまで一計画班員としては見えなかった研究の違った側面が見えてきて個人的には勉強させて頂き、楽しませても頂いた。関わった多くの先生方にこの場を借りてお礼を申し上げたい。

　急速に進むこの分野がどこに向かっていくのであろうかと興味津々である。日本が世界のトップと思い込んでいるだけではダメで教科書に記載される業績を蓄積させていかねばならない。今回の領域メンバーが生殖細胞研究の次のブレークスルーを成し遂げ、世界をリードして行くことを願ってやまない。

目次

研究組織

総括班

【研究代表者・所属・職名】 篠原隆司（京都大学医学研究科・教授） 【分担研究者・所属・職名】 伊川正人（大阪大学・微生物病研究所・教授） 【連携研究者・所属・職名】 小倉淳郎（理化学研究所バイオリソースセンター・室長） 幸田尚（東京医科歯科大学難治疾患研究所・准教授） 斎藤都暁（慶応大学医学部・助教） 相賀裕美子（国立遺伝学研究所・医学研究科・教授） 中馬新一郎（京都大学再生医科学研究所・准教授） 中村肇伸（長浜バイオ大学・准教授） 佐々木裕之（九州大学・生体防御医学研究所・教授） 東田裕一（九州大学・稲森フロンティア研究センター・教授）	【総括班における役割】 領域全体の総括、総括班の運営 事務局、遺伝子改変動物作成支援・研究情報交換窓口 顕微授精・クローン作出支援 エピゲノム解析支援 研究情報交換窓口 若手育成・集会 研究情報交換窓口・集会 広報 エピゲノム解析支援、研究情報交換窓口 広報
【研究協力者：アドバイザー・所属・職名】 石野史敏（東京医科歯科大学難治疾患研究所・所長） 斎藤通紀（京都大学医学研究科・教授） 長澤丘司（京都大学再生医科学研究所・教授） 仲野徹（大阪大学医学研究科、教授） 中辻憲夫（京都大学医学研究科・特任教授） 柳町隆造（ハワイ大学、教授）	 評価者（領域の評価、提言） 評価者（領域の評価、提言） 評価者（領域の評価、提言） 評価者（領域の評価、提言） 評価者（領域の評価、提言） 評価者（領域の評価、提言）

計画研究

研究項目 A01

　　　　相賀　裕美子　　国立遺伝学研究所・系統生物研究センター・教授
　　　　篠原　隆司　　　京都大学・医学研究科・教授
　　　　中馬　新一郎　　京都大学・再生医科学研究所・准教授

研究項目 A02

　　　　齋藤　都暁　　　国立遺伝学研究所系統生物研究センター・教授
　　　　中村　肇伸　　　長浜バイオ大学・バイオサイエンス学部・教授
　　　　伊川　正人　　　大阪大学・微生物病研究所・教授
　　　　東田　裕一　　　九州大学・稲盛フロンティア研究センター・教授

研究項目 A03

　　　　小倉　淳郎　　　独立行政法人理化学研究所・遺伝工学基盤技術室・室長
（分担　幸田　尚　　山梨大学・大学院総合研究部生命環境学域生命農学系・教授）
　　　　佐々木　裕之　　九州大学・生体防御医学研究所・教授

公募研究

平成 26-27 年度

研究項目 A01

　　　　鈴木　仁美　　　東京医科歯科大学・医歯学総合研究科・テニュアトラック助教
　　　　立花　誠　　　　徳島大学・疾患酵素学研究センター・教授
　　　　宮川　さとみ　　大阪大学・医学系研究科・特任講師
　　　　奥田　晶彦　　　埼玉医科大学・医学部・教授
　　　　山中　総一郎　　慶應義塾大学・医学部・助教
　　　　関　由行　　　　関西学院大学・理工学部・准教授
　　　　阿部　訓也　　　独立行政法人理化学研究所・疾患ゲノム動態解析技術開発チーム・チームリーダー

研究項目 A02

　　　　岡江　寛明　　　東北大学・医学系研究科・助教
　　　　谷本　啓司　　　筑波大学・生命環境科学研究科・教授
　　　　廣田　泰　　　　東京大学・医学部・助教
　　　　青木　不学　　　東京大学・新領域創成科学研究科・教授
　　　　遠藤　充浩　　　広島大学・原爆放射線医科学研究所・特任准教授

研究項目 A03

永瀬　浩喜　　　　千葉県がんセンター研究所・がん遺伝創薬研究室・研究所長

平成 28-29 年度

研究項目 A01

石津　大嗣　　　慶応義塾大学医学部・分子生物学教室・講師
栗本　一基　　　京都大学・大学院医学研究科・准教授
立花　誠　　　　徳島大学・先端酵素学研究所・教授
奥田　晶彦　　　埼玉医科大学・ゲノム医学研究センター・教授
石黒　啓一郎　　熊本大学・発生医学研究所・独立准教授
関　由行　　　　関西学院大学・理工学部・准教授
品川　敏恵　　　独立行政法人理化学研究所・石井分子遺伝学研究室・専任研究員
阿部　訓也　　　独立行政法人理化学研究所・バイオリソースセンター・チームリーダー

研究項目 A02

青木　不学　　　東京大学・大学院新領域創成科学研究科・教授
山口　新平　　　大阪大学・生命機能研究科・助教
宮本　圭　　　　近畿大学・生物理工学部・講師
北島　智也　　　独立行政法人理化学研究所・多細胞システム形成研究センター・チームリーダー

研究項目 A03

原田　哲仁　　　九州大学・生体防御医学研究所・助教

交付決定額

（単位千円）	合計	直接経費	間接経費
平成 25 年度	249,600	192,000	57,600
平成 26 年度	259,870	199,900	59,970
平成 27 年度	259,610	199,700	59,910
平成 28 年度	259,870	199,900	59,970
平成 29 年度	259,740	199,800	59,940
総計	1,288,690	991,300	297,390

研究領域の目標

　哺乳類の生殖細胞の研究は 20 世紀の半ばの報告された初期胚の培養系の確立に始まり、現代に及ぶまで急速に発展してきた。IVF 法が開発され、ついには 1978 年に試験管ベビーの誕生に至った。現在の日本では 19 人に一人はこれらの補助生殖医療により生まれている。その後、生殖細胞の研究はさらに ES 細胞の樹立や核移植技術による体細胞クローンの誕生をもたらした。これらの研究からゲノムインプリンティング機構が発見され雌雄の生殖細胞の遺伝子情報が異なる制御を受ける

図 1.　精子と卵子は異なったエピゲノムを持つ。これはどのようにして出来上がり、受精によりリプログラミングされるのか?

ことが証明されたのみならず、卵子には体細胞の核をリプログラミングする能力があることが明らかとなった。これらの発見はノーベル賞を授与され学問的に重要な発見であることが認められているが、単なる基礎研究にとどまらず、現在も我々の生活様式に広汎な影響を及ぼしており、その後も続く新しい技術課発により未来へ向けて新たな可能性を提供しつつある。

　我が国ではこれまで特定領域研究(B)「生殖細胞系列の制御機構と発生工学」(H11-14 年度、領域代表者：中辻憲夫)、「生殖細胞の発生プロセス再プログラム化とエピジェネティクス」(H15-19 年度、領域代表者：中辻憲夫)、「生殖系列の世代サイクルとエピゲノムネットワーク」(H19-24 年度、領域代表者：佐々木裕之)において生殖細胞研究者が活発に相互作用する場を提供してきた。生殖細胞増幅法の開発とその多能性細胞への転換、雌ゲノムのみをもつ胚からの産子作出、生殖細胞決定因子の同定、多能性幹細胞からの子孫作出などはこれらの特定領域の研究代表者から報告された我が国発のオリジナルな研究成果であり、日本を生殖細胞研究の世界トップレベルに押し上げた。

　特定領域研究の進展に伴い、急速に注目されるようになってきたのは生殖細胞の運命決定におけるエピジェネティック（後天的）な遺伝子制御の役割である。ヒストンのメチル化修飾研究は、2000 年に動物細胞で初めてリジンのメチル化酵素の実体が明らかにされてスタートしたが、過去 10 年において数多くのヒストンメチル化・脱メチル化酵素が次々と同定された。また DNA メチル化とヒストン修飾の連動や生殖細胞特異的な small RNA である piwi-interacting
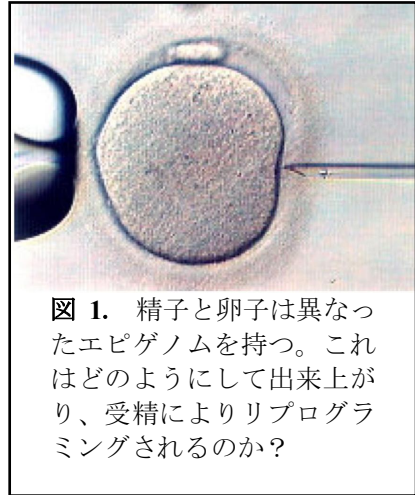
RNA（piRNA）による DNA メチル化の誘導な
ども発見され、その詳細な分子メカニズ
ムが明らかにされつつある。エピジェネ
ティクス研究は体細胞でも盛んに行わ
れるようになったが、生殖細胞は最終分
化した配偶子が全能性を持つ受精卵を経
て初期胚へと至る間やその発生過程に大
きくエピジェネティクな性質が変化する
点で体細胞と大きく異なるため、エピジ
ェネティクス研究の中心となり、その成

図 2. 本研究のねらい
エピゲノム修飾因子同定の時代から「文
法」の理解、エピゲノム操作へ

果は多くの研究者から注目されてきた。実際に生殖細胞には体細胞には存在し
ないような独自のエピジェネティック制御因子である piRNA が存在し、生殖細
胞のエピジェネティクス制御が体細胞よりも更に複雑であることを示している。
また異なったエピジェネティック因子が生殖細胞の異なる発生ステージにおい
て独自の「ネットワーク」を形成することが判明しており、その破綻は個体の発
生異常や流産、不妊症を引き起こすことから益々その研究は盛んになってきた。

　こうしたエピジェネティクス分野の発展と並行して、遺伝子の包括的発現解
析や次世代シークエンス技術も急速に進歩している。クローン個体のような極
端な異常でなくとも、生殖補助医療により生まれてきた一見「正常」だと考えら
れていた個体の一部にも、エピゲノムの異常が見られることも最近分かってき
た。さらに、これまでは生殖細胞のもつエピゲノムは受精によりリセットされ、
次世代に伝わらないとされてきたが、この常識を覆す発見もなされつつある。例
えば、親個体の生存環境の異常が生殖細胞に影響を及ぼし次世代で糖尿病や不
妊症などが引き起こされる、いわゆる Epigenetic inheritance と呼ばれる現象
はこれに相当する。数多くのエピゲノム制御因子が同定された今もこれら生殖
細胞エピゲノムのリプログラミング異常の原因は分かっていない。このため、こ
れまで行われていたエピゲノム制御因子の同定やその機能解析を超えた、時空
間軸をふまえた 4 次元的な生殖細胞エピゲノムのダイナミクスを解析する必要
が生じている。

　こうした背景から、領域代表者は生殖細胞研究の次のテーマとして 1）時間軸
に注目し、エピジェネティックネットワークが生殖系列細胞の発生過程におい
てどのように形成・維持されるのか、その分子機構の解明を明らかにする必要が
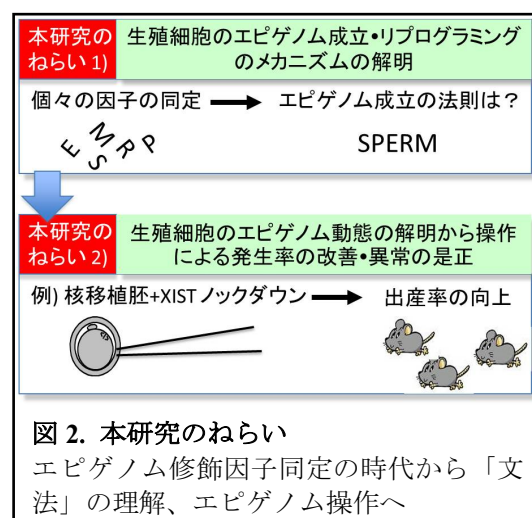
あると考えた。特に次世代シークエンサーの機能向上によりごく少数の細胞でも全ゲノムのメチル化シークエンスを決定できる現在、個々の細胞のエピゲノムの状態の解析と既に多く同定されたエピゲノム制御分子のどれが鍵分子となり、どのような「文法」に従い、生殖細胞の運命決定に影響するかを見いだすことは次の最重要課題である。

　もう一つの重要な研究目標は、2）生殖細胞のエピゲノム操作である。例えば、小倉（計画）は核移植クローンの遺伝子発現の乱れをゲノムワイドで解析し、その原因がX染色体からの遺伝子発現異常にあることを発見した（Science 2010）。さらに小倉らはX染色体の遺伝子発現制御因子であるXIST遺伝子を発現抑制することでX染色体遺伝子の発現を改善させ、核移植クローンの産仔作製率を10倍程度向上させた。この例に限らずヒト悪性腫瘍に対して DNA メチル化やヒストン修飾酵素阻害薬を用いる治療法が確立されつつある。これらの事実を鑑みると、エピゲノムの乱れによる遺伝子発現異常を外来操作により正常化・機能改善できる可能性が現実化しつつある。こうした生殖細胞のエピゲノム操作を生殖細胞のもつ可能性を引き出していくためのもう一つの重要課題として位置づけ、当領域で推進する。

　エピジェネティクス研究は今や国際的なものとなり、2010 年には国際ヒトエピゲノムコンソーシウムが発足し、ヒトエピゲノムの包括的な解析を開始した（佐々木（計画）が参加）。国際的に激しい競争の中にある当該分野において継続的に質の高い独創的な研究を続けるには、「新学術領域」として生殖細胞研究者とエピジェネティクス分野に実績のある研究者とが分野横断的に協力する必要がある。また「生殖エピゲノム」はヒト不妊症・不育症、不妊症、動物の繁殖効率改善などの生殖に関連する幅広い分野の発展に直接関連する。特にクローン動物作製や生殖補助医療のエピゲノム形成に及ぼす影響という問題の研究については学問的・社会的要請が高く、そのリスクや可能性についても実験動物を用いた更なる基礎研究を必要とする。

　本研究領域では個別研究では不可能な成果を生み出すため、近年飛躍的に高度化した生殖細胞操作技術とエピゲノム解析技術について、領域参加者に対する支援を推進する。1）佐々木（計画）・幸田（計画・分担）によるエピゲノム解析、2）小倉（計画）による顕微授精・核移植、3）伊川（計画）による遺伝子改変マウス作製支援は世界のトップレベルであり、リソースが少ない若手研究者や公募班研究者の研究推進に非常に有効であろう。

領域活動

公開班会議

第一回　2013 年 11 月 14 日（木）-15 日（金）大阪大学

第二回　2014 年 10 月 31 日（金）-11 月 1 日（土）九州大学

第三回　2015 年 2 月 17 日（水）-19 日（金）京都大学

第四回　2016 年 11 月 16 日（水）-17 日（木）三島市民文化会館

（「ステムセルエイジングから解明する疾患原理」の岩間班と合同開催）

第五回　2017 年 11 月 16 日（火）-17 日（水）つくばノバホール

若手勉強会

第一回　2014 年 7 月 16（水）-18 日（金）つくばグランドホテル（茨城県つくば市）

ベストプレゼン賞：伊藤大介（大阪大学　宮川班）、益子あかね（慶應義塾大学　齋藤班）

第二回　2015 年 7 月 22 日（水）-24 日（金）ラフォーレ修善寺（静岡県伊豆市）

ベストプレゼン賞：福田胡桃（総合研究大学院大学　相賀班）、前之原章司（九州大学　佐々木班）

第三回　2016 年 7 月 27 日（水）-29 日（金）別府　亀の井ホテル　（大分県別府市）

（「ステムセルエイジングから解明する疾患原理」の岩間班と合同開催）

ベストプレゼン賞：岸雄介（東京大学・ステムセル領域・古館班）、野田大地（大阪大学・伊川班）

第四回　2017 年 6 月 7 日（水）-9 日（金）紀州　白浜温泉　むさし（和歌山県西牟婁郡白浜町）

（「ステムセルエイジングから解明する疾患原理」の岩間班、動的クロマチン構造と機能）の胡桃坂班と合同開催）

ベストプレゼン賞：藤田理沙（早稲田大学・胡桃坂班）、京極博久（理化学研究所・北島班）、佐田亜衣子（筑波大学・佐田班）

国際シンポジウム

Epigenome dynamics and regulation in germ cells

日時：平成 28 年 2 月 17 日(水)-19 日(金)

場所：京都大学百周年時計台記念館　（京都市左京区吉田本町）

Organizers:

Takashi Shinohara (Kyoto University) (Chair)

Shinichiro Chuma (Kyoto University)

Masahito Ikawa (Osaka University)

Toshinobu Nakamura (Nagahama Institute of Bio-Science and Technology)

Atsuo Ogura (RIKEN)

Yumiko Saga (National Institute of Genetics)

Hiroyuki Sasaki (Kyushu University)

Speakers:

Robert Feil (CNRS, France)

Anne Ferguson-Smith (University of Cambridge, UK)

Gavin Kelsey (University of Cambridge, UK)

Martin M. Matzuk (Baylor College of Medicine, USA)

Alexander Meissner (Harvard University, USA)

Shoukhrat Mitalipov (Oregon Health & Science University, USA)

Donal O'Carroll (University of Edinburgh, UK)

Antoine H.F.M. Peters (FMI, Switzerland)

Fuchou Tang (Peking University, China)

Austin Smith (University of Cambridge, UK)

Azim Surani (University of Cambridge, UK)

Maria-Elena Torres-Padilla (IGBMC, France)

Monika Ward (University of Hawaii, USA)

Katsuhiko Hayashi (Kyushu University, Japan)

Tomoya Kitajima (RIKEN, Japan)

Yasuhisa Matsui (Tohoku University, Japan)

Kei Miyamoto (Kinki University, Japan)

Mitinori Saitou (kyoto University, Japan)

領域ホームページ

http://reprod-epigenome.biken.osaka-u.ac.jp/

アクセス回数

2013.08-2014.03:　延べ訪問者：1,738 人

2014.04-2015.03:　延べ訪問者：4,899 人

2015.04-2016.03:　延べ訪問者：8,371 人

2016.04-2017.03:　延べ訪問者：4,602 人

2017.04-2018.03:　延べ訪問者：2,309 人

2018.04-2018.11:　延べ訪問者：1,911 人

ピックアップトピックス一覧

2018.12.10　成果取りまとめ公開シンポジウムを開催いたしました

2018.10.01　立花班員が大阪大学教授に就任されました

2018.09.03　栗本班員が奈良県立医科大学教授に就任されました

2018.08.27　Yanagimachi 90th Birthday Symposium が開催されました

2018.04.06　幸田班員が山梨大学 大学院総合研究部教授に就任されました

2017.11.27　第 5 回領域シンポジウムを実施しました

2017.11.17　留学便り：初めての海外留学とロンドンでの生活（小倉班：畑中勇輝）

2017.11.01　中村班員が長浜バイオ大学バイオサイエンス学部アニマルバイオサイエンス学科
の教授に就任されました

2017.09.25　篠原班の論文が Stem Cell Reports に掲載されました

2017.09.20　小倉班の論文が Cell Reports に掲載されました

2017.07.04　伊川班の論文が PNAS に掲載されました

2017.06.23　相賀班の論文が Nature Communication に掲載されました

2017.06.14　3 領域合同若手勉強会 2017（クローズド形式）を実施しました

2017.05.11　北島班の論文が Developmental Cell に掲載されました

2017.05.10　小倉班の論文が Cell Reports に掲載されました

2017.05.10　小倉班の論文が EMBO Reports に掲載されました

2017.04.01　齋藤班員が国立遺伝学研究所系統生物研究センター教授に就任されました

2017.03.27 遠藤班の論文が eLIFE に掲載されました

2017.02.10 伊川班員の SSR Research Award 2017 の受賞が決まりました

2017.02.09 佐々木班員の論文が Nucleic Acids Res に掲載されました

2017.01.19 原田班員の論文が Cell Reports に掲載されました

2016.12.26 篠原班員の論文が Genes Dev に掲載されました

2016.11.24 第 4 回領域シンポジウムを実施しました

2016.11.24 優秀論文選考結果について

2016.11.22 関班員の論文が Stem Cell Reports に掲載されました

2016.10.25 篠原教授（領域代表）と伊川教授（領域事務）の両名で先端モデル動物支援
若手技術講習会（蓼科）に参加しました

2016.10.17 宮田治彦さん（伊川班）が CALAS International Award for Young Scientists を
受賞しました

2016.09.26 田中敬さん（篠原班）が JRD Outstanding Paper Award 2015 を受賞しました

2016.09.26 大我政敏さん（青木班）が JRD Outstanding Paper Award 2015 を受賞しました

2016.09.26 野田大地さん（伊川班員）が 第 109 回日本繁殖生物学会で優秀発表賞
（口頭発表部門）を受賞しました。

2016.09.23 相賀班員の論文が PLOS Biology に掲載されました

2016.09.16 佐々木班員の論文が Dev Cell に掲載されました

2016.08.10 篠原班員の論文が Stem Cell Reports に掲載されました

2016.08.09 篠原班員の論文が Dev Cell に掲載されました

2016.08.03 合同若手勉強会 2016（クローズド形式）を実施しました

2016.07.25 伊川班員の論文が Nature Communications に掲載されました

2016.07.15 齋藤班員の論文が Molecular Cell に掲載されました

2016.06.30 伊川班員の論文が Proc Natl Acad Sci U S A. に掲載されました

2016.06.20 小倉班員が第 63 回日本実験動物学会総会において安東・田嶋賞を受賞しました

2016.05.26 前之原章司さん(佐々木班員)が Cold Spring Harbor Asia で 3rd prize を受賞しま
した

2016.04.19 相賀班員の論文が Nature Communications に掲載されました

2016.04.19-2016.03.10 Domenico Iuso さん（小倉班員、国際活動支援班）が
International Symposium on the Future of Nuclear Transfer
and Nuclear Reprogramming で 優秀発表賞を受賞しました

2016.03.31 奥田班員の論文が Nature Communications に掲載されました

2016.03.14 2015 年度、優秀論文受賞者、宮田治彦さん（大阪大学　伊川班・助教）が海外発表を行いました

2016.02.24 国際シンポジウム "生殖細胞のエピゲノムダイナミクスとその制御"を実施いたしました

2015.11.30 国際活動支援班設置に伴う優秀論文選考結果について

2015.11.20 谷本班員の論文が Development に掲載されました

2015.11.13 佐々木班員が平成 27 年（秋）紫綬褒章を受賞しました PDF ファイルを開きます

2015.11.09 小倉班員の論文が Proc Natl Acad Sci U S A. に掲載されました

2015.10.02 伊川班員の論文が Science に掲載されました

2015.08.18 相賀班員の論文が Dev Cell.に掲載されました

2015.07.28 若手勉強会 2015（クローズド形式）を実施しました

2015.07.24 石井さん（篠原班）の JRD Outstanding Paper Award 2014 の受賞が決まりました

2015.07.14 青木班員の論文が EMBO J.に掲載されました

2015.07.14 阿部班員の論文が Stem Cell Reports に掲載されました

2015.05.31 中馬班員の DGD Editor-in-Chief Prize 2015 の受賞、増子さん（伊川班）の Wiley Blackwell Prize 2015 の受賞が決まりました。

2015.05.12 宮川班員の論文が Curr Biol.に掲載されました

2015.04.07 齋藤班員の科学技術分野の文部科学大臣表彰若手科学者賞受賞が決定しました。

2015.02.16 篠原班員の論文が Stem Cell Reports に掲載されました

2015.01.26 中村班員の論文が Nature Communications に掲載されました

2014.11.05 第 2 回領域シンポジウムを実施しました

2014.10.01 中村班員が長浜バイオ大学バイオサイエンス学部准教授に昇任されました

2014.09.24 篠原班員の論文が Stem Cell Reports に掲載されました

2014.09.01 遠藤班員が広島大学原爆放射線医科学研究所特任准教授に就任されました

2014.08.01 束田班員が九州大学稲盛フロンティア研究センター教授に就任されました

2014.07.23 若手勉強会 2014（クローズド形式）を実施しました

2014.06.10 篠原班員の SRF Distinguished Scientist Award 2014 の受賞が決まりました

2014.06.04 篠原班員の論文が Proc Natl Acad Sci U S A. に掲載されました

2013.11.18 第 1 回公開シンポジウム（同時開催　若手勉強会）を実施しました

2013.10.17 篠原班員の Review が Annu Rev Cell Dev Biol に掲載されました

2013.10.01 篠原班員の論文が Genes Dev に掲載されました

2013.08.14　齋藤班員の論文が Genes Dev に掲載されました

2013.08.12　篠原班員らの論文が Cell Stem Cell に掲載されました

2013.08.08　HP を開設しました

審査部会からの評価

平成 28 年 10 月 16 日に行われた、科学技術・学術審議会学術分科会科学研究費補助金審査部会生物系委員会により以下のように評価された。

A （研究領域の設定目的に照らして、期待どおりの進展が認められる）

総合所見

　本研究領域は、生殖系列細胞の形成過程におけるエピジェネティックネットワークとその制御機構を明らかにするとともに、その乱れを正常化させるエピゲノム操作法の開発を目指すもので、大きく展開されつつある研究領域をさらに推進しようとする提案である。技術支援、グループ支援がうまく機能しており、連携研究、共同研究が活発になされた結果、多数の共同研究研究成果が発表されている。今後は、新学術領域研究として研究体制を組んだことで初めて可能になる新たな発見やブレイクスルーが得られることを期待したい。

平成 30 年 10 月 1 日に行われた、科学技術・学術審議会学術分科会科学研究費補助金審査部会生物系委員会により以下のように評価された。

A （研究領域の設定目的に照らして、期待どおりの成果があった）

　本研究領域は、生殖系列のエピゲノムが発生過程において、どのように形成・維持されるのかについて時間軸を加えた 4 次元的な解析を行い、それに関与する鍵分子を制御することで生殖細胞の運命を操作することを目標としたものである。

　領域代表者による精子幹細胞のエピゲノム解析と操作、自己複製の制御因子同定などに見られるように、それぞれの研究から時空間レベルにおいて重要な成果が得られた。論文の数と質は十分なものであり、国際的な学術コミュニティへの貢献は十分に高く評価できる。特に、次世代シークエンサーを駆使したエピゲノム解析は研究領域全体の研究を加速させ、公募研究代表者をはじめとする若手研究者の支援にもつながった。計画研究と公募研究の連携も良好であり、出版された 140 報の論文のうち、研究領域内共同研究が 48 報に達したことは、適切な研究領域運営の下に共同研究が実施された結果と思われる。中間評価での指摘を受けて、関連する他の新学術領域とのシンポジウムや勉強会を開催するなど、他分野への波及を目指した活動も評価できる。

　一方で、研究領域の目標である「生殖細胞のエピゲノムダイナミクスとその制御」を明確にまとめることのできる重大な発見や、今後大きく発展することを期待させる決定的な成果にまでは到達していないと考えられることから、今後の更なる展開に期待したい。

総括班メンバーからのコメント

<中間評価>

中辻　憲夫（京都大学大学院医学研究科・特任教授）

　当該新学術領域研究の特徴は、哺乳類などの生殖系列サイクルを、個体発生過程だけでなく次世代への引き継ぎまで含めて、異分野の研究者が結集し、協働して、総合的に世界をリードする研究を進めようとしていることである。過去に大きな成功を生み出した生殖関連特定領域が、我が国の生殖系列研究を世界のトップに押し上げた実績を基盤にして、引き続き急速に発展するゲノムエピゲノムおよび生殖工学技術の進展を有効活用しながら、若手研究者を迎え入れて研究分野の持続的な発展に成功しつつあると、高く評価できる。特筆すべきは、当報告書にも強調されているように、世界最先端の生殖工学技術に熟達した研究者グループと、急速な進歩を続けるエピゲノムの包括的解析技術を保有する研究者グループが、当領域研究に分担研究者として参加しているだけでなく、若手研究者や公募研究者を含めた参加グループに積極的な技術支援と共同研究を提供していることである。これこそ、各研究者が各々優れた研究を進めるだけでなく、領域研究に参加することで初めて可能となる異分野研究者との協働を可能にすることによって、画期的な学際研究成果を生み出しつつある。領域代表者および総括班研究者による、分野と年代を超えた協働体制を構築して推進する領域運営は大きく成功しており、この生命現象の本質に迫る研究分野であると同時に、生殖医療や多能性幹細胞など社会にとっても重要な意義を有する生殖系列サイクルの研究領域において、文字通り世界をリードする研究成果が優れた論文発表などとして数多く生み出され、国際連携や社会広報にも積極的に取り組んでおり、今後も引き続き、新学術領域研究の特色を生かした優れた研究成果が期待できる。

長澤　丘司（京都大学再生医科学研究所・教授）

　本領域は、実績のある研究者で構成されており、計画研究代表者の多くが、すでに権威ある国際的学術誌上で論文を発表している。中でも、領域代表者である篠原らの研究成果が注目される。彼らは、以前樹立に成功した精子幹細胞株(GS細胞)で多能性胚性幹細胞株（ES，iPS細胞)の未分化性維持に必須のSox2蛋白質の発現が認められないことを見出し、GS細胞では、DNAメチル化酵素であるDnmt1が雄性化に必須の遺伝子Dmrt1の発現を促進することでSox2の蛋白質の翻訳を抑制していることを明らかにした。一方、GS細胞の自己複製において、活性酸素を産生する酵素(Nox1)が促進的に働くことを示し、必須のエピジェネティク制御に活性酸素が関与する可能性を示した。また、若手研究者では、立花らが転写に抑制的なメチル化ヒストン(H3K9)の脱メチル化酵素Jmjd1が精子形成特異的に必須の役割を果たすことを明らかにした研究成果が

印象的である。Jmjd1 により発現が調節される精子形成に重要な遺伝子の同定を含む研究の進展が期待される。これらの研究は、すでに論文発表に至っている。課題は、上記の研究の他に、生殖細胞での研究から他の分野にも波及効果を及ぼすようなエピジェネティクスに関する独創的な研究成果があまり見えていないことである。残された研究期間での奮闘が望まれる。総じては、優れた総括と運営のもと、研究が順調に進行していると考えられ、残りの研究期間に重要な成果が出ることが十分期待できる。

斎藤　通紀（京都大学大学院医学研究科・教授）
　本領域「生殖細胞のエピゲノムダイナミクスとその制御」は、生殖細胞の発生過程におけるエピゲノム動態の解明とその制御技術の開発を目的とし、3 つの研究項目「生殖細胞の発生から配偶子形成に至るまでのエピゲノム（A01）」「受精・初期胚におけるエピゲノム変化（A02）」「エピゲノム解析・制御技術（A03）」を設定して研究を推進中である。2013 年度に発足以来、すでに 53 報（計画班 31 報／10 名、公募班 22 報／13 名）の責任著者論文を発表しており、また領域内の共同研究、技術支援も活発で、当初の目的に向けて順調に研究が進展しつつある。A01 領域では、レチノイン酸と BMP4 による始原生殖細胞の性分化機構の解明、GS 細胞の脱分化機構・活性酸素による自己複製制御機構の解明、エピゲノム制御による遺伝子発現抑制技術の開発、ヒストン脱メチル化酵素による体細胞の性決定制御機構の解明、A02 領域では、Piwi-piRNA 複合体と相互作用する因子の同定、生殖細胞特異的 Calcineurin の精子運動能獲得過程における機能解明、PGC7 の iPS 細胞誘導過程における役割の解明、ヒト初期胚のメチル化解析、A03 領域では、顕微受精による遺伝子発現異常の解析、5hmC の 1 塩基解像度での解析法の確立、熱ショック蛋白質の piRNA 合成への関与の証明、などそれぞれの領域で顕著な成果が多数あがっている。領域代表者を中心に、若手育成や国際連携、研究成果の広報活動も適切に推進・計画されており、研究期間終了までにさらに多くの優れた研究成果が発表されると期待される。本新学術領域の環境を活かし、今後の期間における若手の一層の活躍を期待したい。

石野　史敏（東京医科歯科大学難治疾患研究所・所長）
　生殖細胞系列の研究は我が国が世界に誇る学問領域の一つである。本新学術領域は、計画班員および公募班員のそれぞれが、この良き伝統を引き継いで活発な活動を展開していると評価される。また、若手研究者育成支援にも力を注ぎ、次世代の研究者にも良い影響を与えていると評価される。この分野においては、個々の研究者の非常に高い独自性を活かした研究が幾つも産まれてきているが、それに加えて本新学術領域は、目標の一つに「異なる学問分野の研究者が連携して行う共同研究等の推進により当該研究領域の発展を目指す」ことをあげている。すでに 59 件に及ぶ共同研究が進行中であり、計画は順調に進んでいると評価できる。領域代表者のまとめにあるように、このような連携・融合研究においても、成果を世界にアピールできるよう頑張って欲しい。

本領域のような基礎的・基盤的領域の場合に求められていることは、一人一人の研究者が、時間をかけて独自性、独創性の高い研究を完成させることであろうと思われる。近年、成果をあげることが声高々に叫ばれて、得てして短期間で成果のあがるテーマに走りがちな風潮にある。成果をあげることが重要であることは間違いではないが、シニア研究層および若手研究者に充分な研究期間を保証することでそれを達成してこそ、新学術領域推進の意味があり、日本の学術研究の振興に本当に寄与することになるであろう。日本のオリジナリティーの高い科学を一般社会や世界に向かって発信するために、本領域の活動に多いに期待している。

仲野　徹（大阪大学大学院生命機能研究科長）
　『生殖細胞の発生から配偶子形成に至るまでのエピゲノム形成（A01）』、『受精・初期胚におけるエピゲノム変化（A02）』、『エピゲノム解析・制御技術（A03）』のいずれにおいても、おおよそ予定通りに研究が進捗している。

　特に、A01 では、領域代表の篠原による、multipotent GS (Germline Stem) 細胞における、DNA メチル化と細胞分化の多能性についての研究、公募班員である立花による、ヒストン修飾酵素 Jmjd1a による雄性の性決定機構の解析など、雄性生殖細胞の発生・分化において顕著な業績があげられた。ほかにも、小分子RNA である piRNA の制御機構の解析および操作法の開発（A01、A02）、インプリント領域によってインプリンティング遺伝子の発現機構（A03）など、いずれのテーマにおいても優れた研究がおこなわれ、論文として発表されている。

　領域内における共同研究は活発におこなわれており、すでに 20 報近くの論文が、班員間の共同研究として発表されている。また、エピゲノム解析、クローン動物作成、RNA シークエンス解析などの支援も活発におこなわれている。これらのことは、本新学術領域が非常に有機的に機能していることを如実に示している。

　研究は全体として順調に進捗していると考えられるが、投稿準備中や投稿中の論文が多く、論文業績としては、一部の班員を除いて十分とは言いがたい状態にある。可及的速やかに、研究成果をまとめ、ピアレビューを受け、しっかりとした論文業績として仕上げていくことが必要である。これについては、若手班員も多いことから、領域長が強いリーダーシップをもって指導することが望ましい。

＜最終評価＞

中辻　憲夫（京都大学 iCeMS 設立拠点長）
　当領域は、哺乳類の生殖という基本的な生命現象の中で、生殖系列におけるエピゲノム制御を多様な研究手法を駆使して先端的研究を行う研究者を結集して、各々の研究者の研究を推進すると同時に、学際的な共同研究を育てる役割を果たした。更に若手研究者を公募班に採択する事によって、次世代の研究者育成についても大きな成果を挙げた。領域代表者と総括班による適切で強い指導力が発揮され、参加研究者の全員が大きな研究成果を挙げた事は、発表論文の多さとレベルの高さから明瞭である。それに加えて、領域に参加した研究者には、領域研究に参加してキャリアアップに成功した班員も多く、当領域が研究者コミュニティに果たした役割は大きい。これまでも、生殖系列領域は日本の研究者達が世界をリードする研究を発展させて来た分野であり、欧米の当分野を代表する研究者からの評価も高い。日本の生命科学領域における顕著な成功例として評価される事は確実である。

長澤　丘司（大阪大学・生命機能研究科・教授）
　本領域の計画研究代表者の多くが、領域発足前の優れた研究を着実に進め、重要な成果を権威ある国際的学術誌で論文発表した。例えば、篠原は、培養精子幹細胞(GS 細胞)を用いて、DNA メチル化酵素 Dnmt1 が精子形成に必須の転写因子 Dmrt1 の発現を促進することで、多能性胚性幹細胞株の未分化性維持に必須の Sox2 の蛋白質翻訳を抑制していることを明らかにした。更に、GS 細胞の自己複製において、Myc、活性酸素が促進的に働くことを示した。また、相賀は、精子幹細胞の維持に必須の RNA 結合蛋白質 Nanos2 が、精子幹細胞の分化を進める遺伝子の mRNA を減少させることを示し、その作用の分子機構を明らかにした。斎藤は、Piwi が、トランスポゾン抑制因子 DmGTSF1 と結合してトランスポゾン活性を抑制することを見出した。公募研究でも研究が進み、例えば、立花は、セルトリ細胞の形成に必須の転写因子 Sry(Y 染色体上の雄性決定因子)の発現には、セルトリ細胞特異的に発現するメチル化ヒストン(H3K9)脱メチル化酵素 Jmjd1 が必須であることを明らかにした。この成果は特筆に価し、細胞系列決定におけるエピゲノム制御など、他の分野への波及効果が期待できる。総じて本研究領域は、優れた総括と運営のもと、研究が順調に進行し、多様で優れた研究成果が出たと考えられる。

斎藤　通紀（京都大学・医学研究科・教授）
　本研究領域では、生殖細胞の発生機構とそれに関与するエピゲノム動態、それらを制御する方法論の開発を中心とする研究が行われた。計画研究班がその中心となる研究を遂行し、公募研究班がそれを適切に補完・さらには発展させる研究を遂行した。シニア・中堅・若手研究者をバランス良く配備し、領域内における共同研究も活発で、研究期間中に、140 本の論文を発表し、そのうち 48 本が領域内共同研究という堂々たる成果を残した。計画研究班からは、精子幹細胞の

増殖における活性酸素の役割の解明、精子幹細胞の維持に関わる Nanos2 の機能解明、精子カルシニューリンの役割の解明とその阻害剤の避妊薬としての可能性の提唱、多能性幹細胞から誘導した始原生殖細胞における DNA 脱メチル化機構の解明、生殖サイクルのエピゲノム変化におけるヒストンメチル化の役割の解明、ショウジョウバエを用いた piRNA の機能制御機構の解明を含む成果が、公募研究班からは、H3K9 脱メチル化酵素 Jmj1a による性決定遺伝子 Sry の発現制御機構の解明、卵母細胞の巨大な細胞質サイズと染色体分配エラーの関係に関する研究、ヒト TS 細胞の樹立、を含む画期的な成果が発表された。総括斑評価者は主に年に一度の領域会議において領域の研究の進捗を評価、議論した。中間評価であげられた種々の指摘にも適切に対処したと評価出来、その結果、生殖細胞研究における数理解析の導入や上記のヒト TS 細胞の樹立といった顕著な業績、領域に属する若手 5 名が教授に昇進するという優れた成果をあげ、本領域の継続的な発展の礎を築いたと評価出来る。一方で、一部の班員は当初の期待通りには成果が得られなかったと言えるかもしれない。また、本研究領域を代表する研究者が集結した研究班である点を考慮すると、生殖細胞研究やエピゲノム制御に関する次の大きな方向性を明確に提示する研究は必ずしも多くはなく、その点においては今後のさらなる発展を期待したい。

石野　史敏（東京医科歯科大学・難治疾患研究所・所長）

　本新学術領域は A01：生殖細胞の発生から配偶子形成に至るまでのエピゲノム形成、A02：受精・初期胚におけるエピゲノム変化、A03：エピゲノム解析・制御技術の３つの班で研究活動が行われたが、計画班のメンバーはそれぞれ順調に業績を発展させたと評価できる。特に、篠原の「GS 細胞から Dnmt1 の発現抑制による multipotent GS 細胞を樹立成功」や、「精子幹細胞の自己複製分裂の正と負の制御因子の同定」、相賀の生殖細胞の性決定に関る「雌化因子 Stra8 と Smad4 の同定」、「精子幹細胞の維持における Nanos2 を介した mRNP 機能の必須機能の証明」、小倉の「受精時の父方ゲノムの再プログラム化にヒストン H3 アルギニン残基メチル化が必須であることの証明」、幸田の「ヒドロキシメチルシトシンの１塩基解像度での新しい解析法（Enzyme assisted Identification of Genome Modification Analysis ，EnIGMA 法）の確立」、佐々木の「始原生殖細胞におけるインプリント制御領域の脱メチル化機序の解析」、伊川の「精巣特異的 Calcineurin による精子形成の制御」などのいくつもの高い業績を上げたことが評価される。公募班にも良いメンバーを揃えているが、特に立花の「性決定遺伝子である Sry が Jmjd1a に発現制御されていることの発見」、奥田の「Max の発現抑制で GS 細胞に減数分裂初期反応の誘導」、岡江の「ヒト TS 細胞の樹立成功」、原田の「精巣特異的なヒストンバリアントである H3t 遺伝子が精子形成に必須な機能を持つことの証明」などは独自性が高い業績と評価できる。また領域全体で、領域内での共同研究による論文数の割合が計画班員平均で 25%（22/87 報）、公募班で 38%（20/53 報）となり十分な研究連携が行われたことも評価できる。

仲野　徹（大阪大学大学院・生命機能研究科・教授）

　　生殖細胞のエピゲノムダイナミクス解析とその制御を目的とした本新学術領域は、ほぼ当初の計画通りの進捗があったのみでなく、予期されていなかった進展もみせ、以下のように、十分な研究成果をあげたと判断する。

　　領域代表の篠原による、精子幹細胞のエピゲノム解析とその操作、計画班員である小倉による初期胚でのエピゲノム解析、同じく計画班員である佐々木によるインフォマティクス解析を駆使した始原生殖細胞の解析、齋藤による小分子RNA によるエピゲノム制御機構の解析などを優れた業績としてあげることができる。また、公募班員からも、北島による染色体分配エラーの解析や、岡江によるヒト TS 細胞株の樹立など、十分な業績をあげることに成功した。

　　領域内における共同研究は非常に活発で、計画班員平均で 25％、公募班では38％もの論文が連携研究による共著論文であったことは特筆すべき事項である。これは、技術支援グループによる支援のみだけでなく、領域内の連携が非常に活性化され、十分に機能したためであると考えられる。

　　問題点としては、シニアの計画研究班員に比較し、若手の業績がやや見劣りする傾向をあげることができる。ただ、そのうち 5 名が研究期間中に教授就任しており、今後の奮起に期待したい。

研究発表一覧

【発表論文】合計 406 件からの抜粋。392 報が査読あり。

研究項目 A01「生殖細胞の発生から配偶子形成に至るまでのエピゲノム形成」

計画班

A01-01 （計画・相賀　裕美子）　計１４件（査読有１４件、査読無０件）

▲Zhou, Z., Kawabe, H., Suzuki, A., Shinmyouzu, K., and *Saga, Y. (2017). NEDD4 controls spermatogonial stem cell homeosistasis by regulating messenger ribonucleoprotein complexes. Nat. Commun. *8*, 15662.

▲Kato, Y., Katsuki, T., Kokubo, H., Masuda, A., and *Saga, Y. (2016). Dazl is a target RNA suppressed by mammalian NANOS2 in sexually differentiating male germ cells. Nat. Commun. *7*, 11272.

▲Zhou, Z., Shirakawa, T., Ohbo, K., Sada, A., Wu, Q., Hasegawa, H., Saba, R., and *Saga, Y. (2015). The RNA binding protein Nanos2 organizes a post-transcriptional buffering system to retain primitive states of mouse spermatogonial stem cells. Dev. Cell *34*, 96-107.

A01-02 （計画・篠原　隆司）　計２３件（査読有２３件、査読無０件）

▲Shinohara, T., Kazuki, K., Ogonuki, N., Morimoto, H., Matoba, S., Hiramatsu, K., Honma, K., Suzuki, T., Hara, T., Ogura, A., Oshimura, M., *Kanatsu-Shinohara, M., and *Kazuki, Y. (2017). Transfer of a mouse artificial chromosome into spermatogonial stem cells generates transchromosomic mice. Stem Cell Reports *9*, 1180-1191.

▲Kanatsu-Shinohara, M., Tanaka, T., Ogonuki, N., Ogura, A., Morimoto, H., Cheng, P. F., Eisenman, R. N., Trumpp, A., and *Shinohara, T. (2016). Myc/Mycn-mediated glycolysis enhances mouse spermatogonial stem cell self-renewal. Genes Dev. *30*, 2637-2648.

▲ *Kanatsu-Shinohara, M., Naoki, H., and Shinohara, T. (2016). Nonrandom germline transmission of mouse spermatogonial stem cells. Dev. Cell *38*, 248-261.

Takashima S., Kanatsu-Shinohara, M., Tanaka, T., Morimoto, H., Inoue, K., Ogonuki, N., Jijiwa, M., Takahashi, M., Ogura, A., and *Shinohara, T. (2015). Functional differences between GDNF-dependent and FGF2-dependent mouse spermatogonial stem cell self-renewal. Stem Cell Reports *4*, 489-502.

*Kanatsu-Shinohara, M., Onoyama, I., Nakayama, K.I., and Shinohara, T. (2014). Skp1-Cullin-F-box (SCF)-type ubiquitin ligase FBXW7 negatively regulates spermatogonial stem cell self-renewal. Proc. Natl.. Acad. Sci. USA *111*, 8826-8831.

Takashima, S., Hirose, M., Ogonuki, N., Ebisuya, M., Inoue, K., Kanatsu-Shinohara, M., Tanaka, T., Nishida, E., Ogura, A., and *Shinohara, T. (2013). Regulation of pluripotency in male germline stem cells by Dmrt1. Genes Dev. *27*, 1949-1958.

Morimoto, H., Iwata, K., Ogonuki, N., Inoue, K., Ogura, A., Kanatsu-Shinohara, M., Morimoto, T., Yabe-Nishimura, C., and *Shinohara, T. (2013). ROS are required for mouse spermatogonial stem cell self-renewal. Cell Stem Cell *12*, 774-786.

A01-03 （計画・中馬　新一郎）　計９件（査読有９件、査読無０件）

▲Mochizuki, A.L., Katanaya, A., Hayashi, E., Hosokawa, M., Moribe, E., Motegi, A., Ishiai, M., Takata, M., Kondoh, G., Watanabe, H., Nakatsuji N, and *Chuma S. (2017). PARI Regulates Stalled Replication Fork Processing To Maintain Genome Stability upon Replication Stress in Mice. Mol Cell Biol. *37,* e00117-17.

公募班　（平成 28〜29 年度）

A01（公募・石津　大嗣）　計３件（査読有３件、査読無０件）

Ishizu H, Sumiyoshi T, *Siomi MC. (2017) Use of the CRISPR-Cas9 system for genome editing in cultured *Drosophila* ovarian somatic cells. Methods. *126*, 186-192.

A01（公募・栗本　一基）　計５件（査読有５件、査読無０件）

▲Mitani, T., Yabuta, Y., Ohta, H., Nakamura, T., Yamashiro, C., Yamamoto, T., *Saitou, M., and *Kurimoto, K. (2017). Principles for the regulation of multiple developmental pathways by a versatile transcriptional factor, BLIMP1. Nucleic Acids Res *45*, 12152-12169.

A01（公募・立花　誠）　計９件（査読有９件、査読無０件）

▲Kuroki, S., Nakai, Y., Maeda, R., Okashita, N., Akiyoshi, M., Yamaguchi, Y., Kitano, S., Miyachi S., Nakato, R., Ichiyanagi, K., Shirahige, K., Kimura, H., Shinkai, Y., and *Tachibana, M. (2018). Combined loss of Jmjd1a dnd Jmjd1b reveals critical roles for H3K9 demethylation in the maintenance of embryonic stem cells and early embryogenesis. Stem Cell Reports. *10*, 1340-1354.

A01（公募・奥田　晶彦）　計５件（査読有４件、査読無１件）

Suzuki, A., Hirasaki, M., Hishida, T., Wu, J., Okamura, D., Ueda, A., Nishimoto, M., Nakachi, Y., Mizuno, Y., Okazaki, Y., Matsui, Y., Izpisua Belmonte, J. C., and *Okuda, T. (2016). Loss of MAX results in meiotic entry in mouse embryonic and gremline stem cells. Nat. Commun. *7*, 11056.

A01（公募・石黒　啓一郎）　計２件（査読有２件、査読無０件）

▲Ishiguro, K., Nakatake, Y., Chikazawa-Nohtomi, N., imura, H., Akiyama, T., Oda, M., Ko, SBH., and Ko, MSH. (2017). Expression analysis of the endogenous Zscan4 locus and its coding proteins in mouse ES cells and preimplantation embryos. In Vitro Cell.Dev.Biol.-Anim. *53*, 179-190.

A01（公募・関　由行）　計２件（査読有１件、査読無０件）

▲Okashita, N., Suwa, Y., Nishimura, O., Sakashita, N., Kadota, M., Nagamatsu, G., Kawaguchi, M., Kashida, H., Nakajima, A., Tachibana, M., and *Seki, Y. (2016). PRDM14 drives Oct3/4 recruitment via active dimethylation in the transition from primed to naïve pluripotency. Stem Cell Reports *7*, 1072-1086.

A01（公募・品川　敏恵）　計１件（査読有１件、査読無０件）

Padavattan, S., Thiruselvam, V., Shinagawa, T., Hasegawa, K., Kumasaka, T., Ishii, S., and *Kumarevel, T. (2017). Structural analyses of the nucleosome complexes with human testis-specific histone variants, hTh2a and hTh2b. Biophys. Chem. *221*, 41-48.

A01（公募・阿部　訓也）　計１３件（査読有１３件、査読無０件）

▲Yanokura, M., Banno, K., Adachi, M., Aoki, D., and *Abe K. (2017). Genome-wide DNA methylation sequencing reveals miR-663a is a novel epimutation candidate in CIMP-high endometrial cancer. International Journal of Oncology *50*, 1934-1946.

公募班　（平成 26～27 年度）

A01（公募・鈴木　仁美）　計５件（査読有７件、査読無０件）

#Ren, Y., #Suzuki, H., Jagarlamudi, K., Golnoski, K., McGuire, M., Lopes, R., Pachnis, V., and Rajkovic, A. (#co-first authors) (2015). Lhx8 regulates primordial follicle activation and postnatal folliculogenesis. BMC Biol. *13*, 39.

A01（公募・立花　誠）　計５件（査読有５件、査読無０件）

Kuroki, S., Akiyoshi, M., Matsumura, Y., Miyachi, H., Mise, N., Abe, K., Ogura, A., Wilhelm, D., Koopman, P., Nozaki, M., Kanai, Y., and *Shinkai, Y, *Tachibana M. (2013). Epigenetic regulation of mouse sex determination by the histone demethylase Jmjd1a. Science *341*, 1106-1109.

A01（公募・宮川　さとみ）　計３件（査読有３件、査読無０件）

Itou, D., Shiromoto, Y., Yukiho, S.Y., Ishii, C., Nishimura, T., Ogonuki, N., Ogura, A., Hasuwa, H., Fujihara, Y., *Kuramochi-Miyagawa, S., and *Nakano, T. (2015). Induction of DNA methylation by artificial piRNA production in male germ cells. Curr Biol. *25*, 901-906.

A01（公募・奥田　晶彦）　計１０件（査読有９件、査読無１件）

Katano, M., Ema, M., Nakachi, Y., Mizuno, Y., Hirasaki, M., Suzuki, A., Ueda, A., Nishimoto, M., Takahashi, S., Okazaki, Y., and *Okuda, A. (2015). Forced expression of Nanog or Esrrb preserves the ESS status in the absence of nucleostemin expression. Stem Cells *33*, 1089-1101.

A01（公募・山中　総一郎）　計１件（査読有１件、査読無０件）

Yashiro, R., Murota, Y., Nishida, K., Yamashiro, H., Fujii, K., Ogai, A., Yamanaka, S., Negishi, L., Siomi, H., and *Siomi, MC (2018). Piwi nuclear localization and its regulatory mechanism in Drosophila ovarian somatic cells. Cell Reports in press

A01（公募・関　由行）　計１件（査読有１件、査読無０件）

Okashita, N., Sakashita, N., Ito, K., Mitsuya, A., Suwa, Y., and *Seki, Y. (2015). PRDM14 maintains pluripotency of embryonic stem cells through TET-mediated active DNA demethylation. Biochem Biophys Res Commun *466*, 138-145.

A01（公募・阿部　訓也）　計１０件（査読有１０件、査読無０件）

Sugimoto, M., Kondo, M., Koga, Y., Shiura, H., Ikeda, R., Hirose, M., Ogura, A, Murakami, A., Yoshiki, A., Chuva de Sousa Lopes, S., and *Abe, K. (2015). A simple and robust method for establishing homogeneous mouse epiblast stem cell lines by Wnt inhibition. Stem Cell Reports *4*, 744-757.

研究項目 A02 「受精・初期胚におけるエピゲノム変化」
計画班

A02-01（ 計画・齋藤　都暁）　合計５件（査読有５件、査読無１件）

Iwasaki, Y. W., Murano, K., Ishizu, H., Shibuya, A., Iyoda, Y., Siomi, M. C., *Siomi, H., and *Saito, K. (2016). Piwi modulates chromatin accessibility by regulating multiple factors including histone H1 to repress transposons. Mol. Cell *63*, 408-419.

Ohtani, H., Iwasaki, Y.W., Shibuya, A., Siomi, H., *Siomi, M.C., and *Saito, K. (2013). DmGTSF1 is necessary for Piwi–piRISC-mediated transcriptional transposon silencing in Drosophila. Genes Dev. *27*, 1656-1661.

A02-02（計画・中村　肇伸）　合計２０件（査読有１８件、査読無２件）

Furuta A, *Nakamura T. (2017). DNA hypomethylation circuit of mouse rDNA repeats in the germ cell lineage. Biochem. Biophys. Res. Commun. *490*, 429-433.

#Xu, X., #Smorag, L., #Nakamura, T., Kimura, T., Dressel, R., Fitzner, A., Tan, X., Linke, M., Zechner, U., Engel, W., and *Pantakani K. (#co-first authors) (2015). *Dppa3* expression is critical for generation of fully-reprogrammed iPS cells and maintenance of *Dlk1-Dio3* imprinting. Nat. Commun. *6*, 6008.

Funaki, S., *Nakamura, T., Nakatani, T., Umehara, H., Nakashima, H., and *Nakano, T. (2014). Inhibition of maintenance DNA methylation by Stella. Biochem. Biophys. Res. Commun. *453*, 455-460.

A02-03（計画・伊川　正人）　合計６６件（査読有６６件、査読無０件）

▲Castaneda, J. M., Hua, R, Miyata, H., Oji, A., Guo, Y., Cheng, Y., Zhou, T., Guo, X., Cui, Y, Shen, B., Wang, Z., Hu, Z., Zhou, Z., Sha, J., Prunskaite-Hyyrylainen, R., Yu, Z., Ramirez-Solis, R., *Ikawa, M., *Matzuk, M. M., and *Liu, M. (2017). TCTRE1 is a conserved component of the dynein regulatory complex and is required for motility and metabolism in mouse spermatozoa. Proc. Natl. Acad. Sci. USA. *114*, E5370-E5378.

▲Miyata, H., Castaneda, J. M., Fujihara, Y., Yu, Z. Archambeault, D. R., Isotani, A., Kiyouzmi, D., Kriseman, M. L. Mashiko, D., Matsumura, T., Matzuk, R. M. Mori, M., Noda, T. Oji, A., Okabe, M., Prunskaite-Hyyrylainen, R., Ramirez-Solis, R., Satouh, Y., Zhang, Q., *Ikawa, M., and *Matzuk, M. M. (2016). Genome engineering uncovers 54 evolutionally conserved and testis-enriched genes that are not required for male fertility in mice. Proc. Natl., Acad. Sci. USA *113*, 7704-7710.

Miyata, H., Satouh, Y., Mashiko, D., Muto, M., Nozawa, K., Shiba, K., Fujihara, Y., Isotani, A., Inaba, K., and

*Ikawa M. (2015). Sperm calcineurin inhibition prevents mouse fertility with implications for male contraceptive. Science *350*, 442-445.

Mashiko, D., Fujihara, Y., Satouh, Y., Miyata, H., Isotani, A.,and *Ikawa, M. (2013). Generation of mutant mice by pronuclear injection of circular plasmid expressing Cas9 and single guided RNA. Sci. Rep. *3*, 3355.

Hasuwa, H., Ueda, J., Ikawa, M., and *Okabe, M. (2013). MiR-200b and miR-429 Function in Mouse Ovulation and Are Essential for Female Fertility. Science *341*, 71-73.

A02-04（計画・束田　裕一）　　合計３件（査読有２件、査読無０件）

▲*Tsukada, Y., Akiyama, T., and Nakayama, K. I. (2015). Maternal TET3 is dispensable for embryonic development but is required for neonatal growth. Sci. Rep. *5*, 15876.

公募班　　（平成 **28～29** 年度）

A02（公募・青木　不学）　　合計８件（査読有８件、査読無０件）

Ooga, M., Funaya, S., Hashioka, Y., Fujii, W., Naito, K., Suzuki, M.G. and *Aoki, F. (2018). Chd9 mediates highly loosened chromatin structure in growing mouse oocytes. Biochem. Biophys. Res. Comm. *500*, 583-588.

A02（公募・山口　新平）　　合計０件

A02（公募・宮本　圭）　　合計９件（査読有９件、査読無０件）

▲*Miyamoto, K., Tajima, Y., Yoshida, K., Oikawa, M., Azuma, R., Allen, G.E., Tsujikawa, T., Tsukaguchi, T., Bradshaw, C.R., Jullien, J., Yamagata, K., Matsumoto, K., Anzai, M., Imai, H., Gurdon, J.B., and *Yamada, M. (2017). Reprogramming towards totipotency is greatly facilitated by synergistic effects of small molecules. Biol. Open *6*, 415-424.

A02（公募・北島　智也）　　合計４件（査読有３件、査読無１件）

▲Kyogoku, H., and *Kitajima, T. (2017). Large cytoplasm is linked to the error-prone nature of oocytes. Dev. Cell *41*, 287-298.

公募班　　（平成 **26～27** 年度）

A02（公募・岡江　寛明）　　合計８件（査読有５件、査読無３件）

▲*Okae, H., Toh, H., Sato, T., Hiura, H., Takahashi, S., Shirane, K., Kabayama, Y., Suyama, M., Sasaki, H., and *Arima, T. (2018). Derivation of human trophoblast stem cells. Cell Stem Cell *22*, 50-63.

A02（公募・谷本　啓司）　　合計３件（査読有３件、査読無０件）

▲Matsuzaki, H., Okamura, E., Takahashi, T., Ushiki, A., Nakamura, T., Nakano, T., Hata, K., Fukamizu, A. and *Tanimoto K. (2015) *De novo* DNA methylation through the 5′-segment of the *H19* ICR maintains its imprint during early embryogenesis. Development *142*, 3833-3844.

A02（公募・廣田　泰）　　合計４０件（査読有３１件、査読無９件）

◎Hiraoka, T., *Hirota, Y., Saito-Fujita, T., Matsuo, M., Egashira, M., Matsumoto, L., Haraguchi, H., Dey, S. K., Furukawa, K. S., Fujii, T., and Osuga, Y. (2016). STAT3 accelerates uterine epithelial regeneration in a mouse model of decellularized uterine matrix transplantation. JCI insight. *1*, e87591, 2016

A02（公募・青木　不学）　　合計８件（査読有８件、査読無０件）

Abe, K., Yamamoto, R., Franke, V., Cao, M., Suzuki, Y., Suzuki, M.G., Vlahovicek, K., *Svoboda, P, *Schultz, R.M., and *Aoki, F. (2015). The first murine zygotic transcription is promiscuous and uncoupled from splicing and 3' processing. EMBO J. *34*, 1523-153.

A02（公募・遠藤　充浩）　　合計１件（査読有１件、査読無０件）

▲Endoh, M., Endo, T. A., Shinga, J., Hayashi, K., Farcas, A., Ma, K. W., Ito, S., Sharif, J., Endoh, T., Onaga, N., Nakayama, M., Ishikura, T., Masui, O., Kessler, B. M., Suda, T., Ohara, O., Suzuki, A., Klose, R., and Koseki, H. (2017). PCGF6-PRC1 suppresses premature differentiation of mouse embryonic stem cells by regulating germ cell-related genes. Elife *6*, e21064.

研究項目 A03「エピゲノム解析・制御技術」
計画班

A03-01（計画・ 小倉　淳郎、（分担）幸田　尚）　　合計６２件（査読有６０件、査読無２件）

◎▲Hatanaka, Y.,, Tsusaka, T., Shimizu, N, Morita, K., Suzuki, T., Machida, S., Satoh, M., Honda, A., Hirose, M., Kamimura, S., Ogonuki, N., Nakamura, T., Inoue, K., Hosoi, Y., Dohmae, N., Nakano, T., Kurumizaka, H., Matsumoto, K., Shinkai, Y., and *Ogura, A. (2017). Histone H3 methylated at arginine 17 is essential for reprogramming the paternal genome in zygotes. Cell Rep. *20*, 2756-2765.

▲*Inoue, K., Hirose, M., Inoue, H., Hatanaka, Y., Honda, A., Hasegawa, A., Mochida, K., and *Ogura, A. (2017). The rodent-specific microRNA cluster within the Sfmbt2 gene is implicated and essential for placental development. Cell Rep. *19*, 949-956.

▲Hatanaka, Y., Inoue, K., Oikawa, M., Kamimura, S., Ogonuki, N., Kodama, E.N., Ohkawa, Y., Tsukada, Y., and *Ogura, A. (2015) Histone chaperone CAF-1 mediates repressive histone modifications to protect preimplantation mouse embryos from endogenous retrotransposons. Proc. Natl. Acad. Sci. U. S. A. *112,* 14641-14646.

▲*Inoue, K., Oikawa, M., Kamimura, S., Ogonuki, N., Nakamura, T., Nakano, T., Abe, K., and *Ogura, A. (2015). Trichostatin A specifically improves the aberrant expression of transcription factor genes in embryos produced by somatic cell nuclear transfer. Sci. Rep. *5*, 10127.

▲Kawasaki, Y., Kuroda, Y., Suetake, I., Tajima, S., Ishino, F., and *Kohda, T. (2016). A Novel method for the simultaneous identification of methylcytosine and hydroxymethylcytosine at a single base resolution. Nucleic Acids Res. *45*, e24.

A03-02（計画・佐々木　裕之）　　合計２０件（査読有１５件、査読無５件）

▲Maenohara, S., *Unoki, M, Toh, H., Ohishi, H., Sharif, J., Koseki, H., and *Sasaki, H. (2017). Role of UHRF1 in de novo DNA methylation in oocytes and maintenance methylation in preimplantation embryos. PLoS Genet. *13*, e1007042.

▲Inoue, K., *Ichiyanagi, K, Fukuda, K., Glinka, M., and *Sasaki, H. (2017). Switching of dominant retrotransposon silencing strategies from posttranscriptional to transcriptional mechanisms during male germ cell development in mice. PLoS Genet. *13*, e1006926.

▲Shirane, K., Kurimoto, K., Yabuta, Y., Yamaji, M., Satoh, J., Ito, S., Watanabe, A., Hayashi, K., Saitou, M., and *Sasaki, H. (2016). Global landscape and regulatory principles of DNA methylation reprogramming for germ cell specification by mouse pluripotent stem cells. Dev. Cell *39*, 87-103.

公募班　　（平成 **28～29** 年度）

A03（公募・原田　哲仁）　　合計１１件（査読有１１件、査読無０件）

▲*#Ueda, J., #Harada, A., #Urahama, T., Machida, S., Maehara, K., Hada, M., Makino, Y., Nogami, J., Horikoshi, N, Osakabe, A. Taguchi, H., Tanaka, H., Tachiwana, H, Yao, T., Yamada, M., Iwamoto, T., Isotani, A., Ikawa, M., Tachibana, T., Okada, Y., Kimura, H., Ohkawa, Y., Kurumizaka, H., and *Yamagata, K. (#co-first authors) (2017). Testis-specific histone variant H3t gene is essential for entry into spermatogenesis. Cell Rep. *18*, 593-600.

公募班　　（平成 **26～27** 年度）

A03（公募・永瀬　浩喜）　　合計２５件（査読有２２件、査読無３件）

◎Hiraoka, K., Inoue, T., Taylor, R.D., Watanabe, T., Koshikawa, N., Yoda, H., Shinohara, K., Takatori, A., Sugimoto, H., Maru, Y., Denda, T., Fujiwara, K., Balmain, A., Ozaki, T., Bando, T., Sugiyama, H., and *Nagase, H. (2015). Inhibition of KRAS codon 12 mutants using a novel DNA-alkylating pyrrole–imidazole polyamide conjugate. Nat.

Commun. *6*, 6706.

Uekusa, S., Kawashima, H., Sugito, K., Yoshizawa, S., Shinojima, Y., Igarashi, J., Ghosh, S., Wang, X., Fjiwara, K., Ikeda, T., Koshinaga, T., Soma, M., and *Nagase, H. (2014). Nr4a3, a possibile oncogenic factor for neuroblastoma associated with CpGi methylation within the third exon. Int. J. Oncol. *44*, 1669-1677.

【ホームページ】

当領域ホームページ URL　http://reprod-epigenome.biken.osaka-u.ac.jp/

【主催シンポジウム等】(主催シンポジウム合計 20 (海外 5, 国内 15 件)；ワークショップ等 16 件より抜粋)

- **2017 年：計画班**

<佐々木裕之>シンポジウム企画（企画：佐々木裕之、眞貝洋一, Robert Feil, Pierre-Antoine Defossez）：France-

Japan Epigenetics Workshop-2017, 2017, Paris, France. 2017.11. 06-08

- **2016 年：計画班**

<佐々木裕之>シンポジウム企画（企画：佐々木裕之、Genevieve Almouzni, Yang Shi, Bing Zhu）： Cold Spring

Harbor Asia Conference on Chromatin, Epigenetics & Transcription, 2017, 蘇州, 中国. 2016.05. 09-13

- **2015 年：計画班**

<小倉淳郎>ワークショップ主催: 第 1 回ゲノム編集マウスワークショップ 2015.03.17

- **2014 年：計画班**

<相賀裕美子> Organizer: The 27 the Annual Meeting of Mouse Molecular Genetics, 2014, Asilomar, CA, USA. 2014.09.29-10.03

<伊川正人>シンポジウム企画（コーディネーター：三輪佳宏, 伊川正人）：第 61 回実験動物学会総会シンポジウム「in vivo ライブイメージングによる高次生命現象の可視化と応用」2014.05.16

<伊川正人>講習会主催: 千里ライフサイエンス振興財団・技術講習会"CRISPR/Cas システム"によるマウスゲノム編集 2014.06.05

<佐々木裕之>シンポジウム企画（企画：佐々木裕之、角谷徹仁）：第 86 回日本遺伝学会 Symposium on Epigenetics: Its Role in Development, Chromosome Regulation and Genome Evolution 2014.09.17-19

- **2013 年：計画班**

<相賀裕美子> Organizer: The 26 the annual meeting of Mouse molecular Genetics, 2013, Hinxton, UK. 2013.09.18-21

<束田裕一, 佐々木裕之>シンポジウム主催（オーガナイザー：大川恭行, 束田裕一, 佐々木裕之）：The Fukuoka International Symposium on Genomics & Epigenomics 2013, –Expanding Frontiers of Genomic Science–. 2013.09.10

<束田裕一>シンポジウム企画（オーガナイザー：大川恭行, 束田裕一）：第 86 回日本生化学会大会シンポジウム「ミクロなクロマチン研究で解くマクロなエピジェネティクス研究」2013.09.11–13
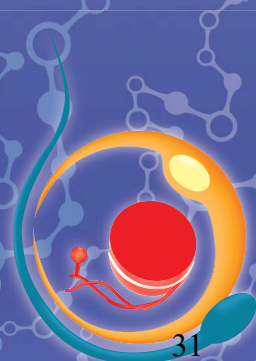
【アウトリーチ活動等】(合計 186 件より抜粋)

<篠原隆司>精子を作る幹細胞のお話 京大アカデミックデイ（京都府京都市）2013.12.21、細胞培養から見えてきた生命像・東京で学ぶ京大の知 （京都大学東京オフィス）2015.07.30

<小倉淳郎>顕微授精技術研修 (5 回、17 名)、マウス胚・精子凍結技術研修(2 回、7 名)、実験動物の発生工学の講義と発生工学実験室の案内（中学 1 回、高校生 27 回、大学 3 回、 合計 31 回）理研 BRC

ポスター集

第1回公開シンポジウム

生殖細胞のエピゲノムダイナミクスとその制御

会期	2013年 **11月14日**（木）・**15日**（金）
会場	大阪大学微生物病研究所谷口記念講堂

住所：大阪府吹田市山田丘3-1　HP：http://www.biken.osaka-u.ac.jp/access.html

11月14日（木）

18：00～19：00
　特別講演「What I learned during the past 60 years」
　ハワイ大学名誉教授　柳町隆造

19：00～
　懇親会（要予約）

11月15日（金）

12：50～13：00
　開会挨拶/領域概要説明
13：00～14：10
　精子形成
　相賀裕美子（遺伝研）、篠原隆司（京都大学）、中馬新一郎（京都大学）
14：10～14：35
　コーヒーブレイク
14：35～16：00
　卵子形成と受精
　齋藤都暁（慶応大学）、伊川正人（大阪大学）、中村肇伸（長浜バイオ大学）、束田裕一（九州大学）
16：00～16：25
　コーヒーブレイク
16：25～17：35
　エピゲノム解析
　小倉淳郎（理化学研究所）、幸田尚（東京医科歯科大学）、佐々木裕之（九州大学）
17：35～17：45
　閉会挨拶

領域代表者

篠原隆司（京都大学医学系研究科）

お問合せ
epigenome@biken.osaka-u.ac.jp

領域ホームページ
http://reprod-epigenome.biken.osaka-u.ac.jp

31

文部科学省・科学研究費補助金・新学術領域研究
第2回公開シンポジウム

領域代表者: 篠原隆司
（京都大学医学研究科）

領域ホームページ: http://reprod-epigenome.biken.osaka-u.ac.jp

生殖細胞のエピゲノムダイナミクスとその制御
Epigenome dynamics and regulation in germ cells

日時：2014年 10月31日（金）・11月1日（土）
会場：九州大学（病院キャンパス）
　　　コラボ・ステーションⅠ視聴覚ホール（２F）

住所：福岡市東区馬出３−１−１　最寄り駅：馬出九大病院前（地下鉄箱崎線），吉塚駅（JR）

10月31日（金）

13:20～13:30
　開会挨拶／領域概要説明
　　佐々木裕之
13:30～14:35
　エピゲノム解析
　　佐々木裕之・小倉淳郎・永瀬浩喜
14:55～17:15
　精子形成（1）
　　篠原隆司・相賀裕美子・中馬新一郎・
　　鈴木仁美・立花誠・奥田晶彦
17:35～18:20
　招待講演
18:30～
　懇親会（要予約）

11月1日（土）

9:30～10:30
　精子形成（2）
　　宮川さとみ・山中総一郎・関由行・阿部訓也
10:50～15:30
　卵子形成と受精
　　齋藤都暁・中村肇伸・伊川正人・束田裕一・
　　岡江寛明・谷本啓司・廣田泰・青木不学・遠藤充浩
15:30～15:35
　閉会挨拶
　　篠原隆司

招待講演
10月31日（金）
17:35～18:20

九州大学
中島欽一教授
演題：細胞外因子による神経幹細胞の
エピジェネティック制御とその影響

九州大学（病院キャンパス）マップ

コラボⅡ
コラボⅠ

図書館　駐車場
総合研究棟
病院　臨床A棟　会場（コラボⅠ）
歯学部　薬学部

馬出九大病院前駅改札
（地下鉄箱崎線）　東門

至JR吉塚駅
（1 km）

会場入り口

32

Epigenome dynamics and regulation in germ cells
Grant-in-Aid for Scientific Research on Innovative Areas,
Ministry of Education, Culture, Sports, Science and Technology, Japan

Date **Feb 17** (Wed) **- 19** (Fri), **2016**

Venue Clock Tower Centennial Hall, Kyoto University, Kyoto, Japan

Entry FREE registration
Call for poster presentation: See website for abstract submission

http://reprod-epigenome.biken.osaka-u.ac.jp/symposiums/EDRGC2016.html | **Entry**

International Symposium on
Epigenome Dynamics and Regulation in Germ Cells

Speakers:

Azim SURANI, Hans SCHÖLER,

Dónal O'CARROLL, Robert FEIL,
Anne FERGUSON-SMITH, Katsuhiko HAYASHI,
Gavin KELSEY, Tomoya KITAJIMA,
Yasuhisa MATSUI, Martin M. MATZUK,
Alexander MEISSNER, Shoukhrat MITALIPOV,
Kei MIYAMOTO, Antoine H.F.M. PETERS,
Kuniaki SAITO, Mitinori SAITOU, Austin SMITH,
Maria-Elena TORRES-PADILLA,
Yuichi TSUKADA, Monika WARD, Yi ZHANG

Speakers / Organizers:

Takashi SHINOHARA (Chair),

Shinichiro CHUMA, Masahito IKAWA,
Toshinobu NAKAMURA, Atsuo OGURA,
Yumiko SAGA, Hiroyuki SASAKI

文部科学省 新学術領域研究「生殖細胞のエピゲノムダイナミクスとその制御」国際シンポジウム

（新学術2領域共催）

第4回公開シンポジウム
生殖細胞のエピゲノムダイナミクスとその制御
ステムセルエイジングから解明する疾患原理

文部科学省・科学研究費補助金・新学術領域研究
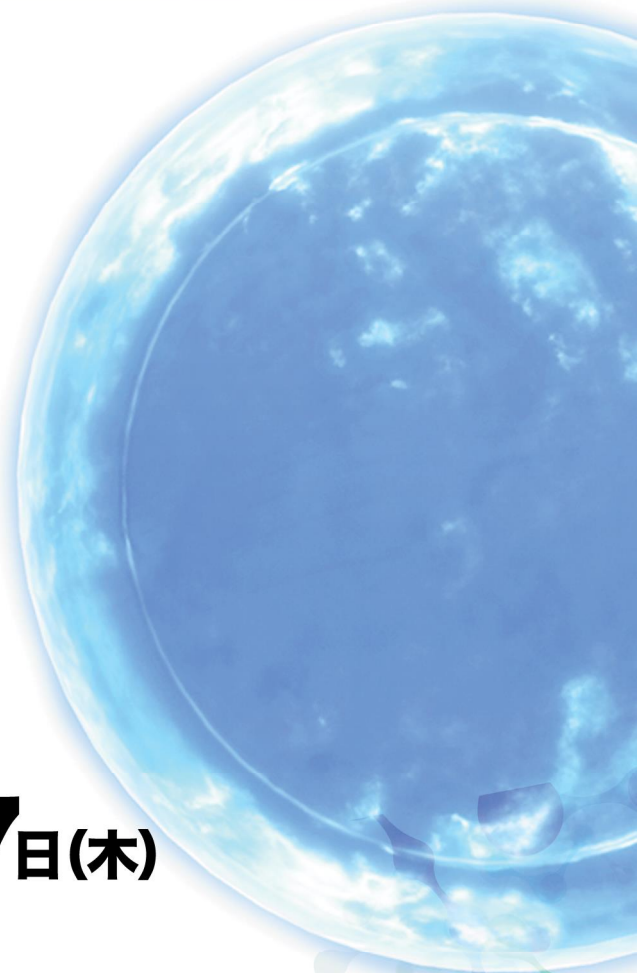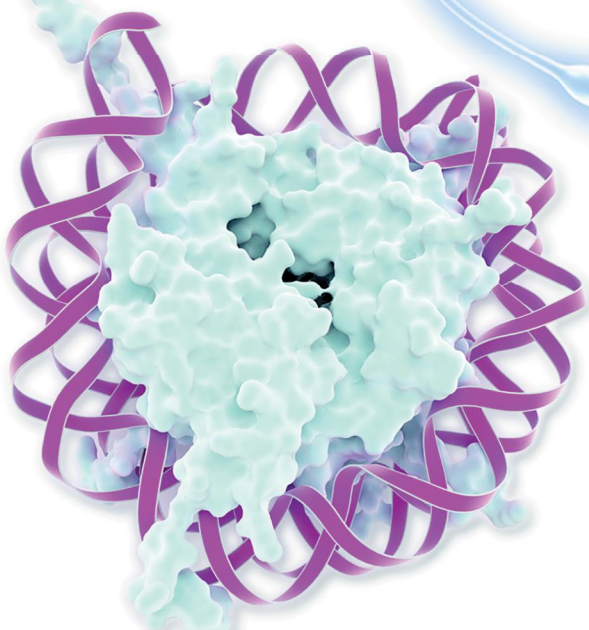
会期 2016年**11**月**16**日（水）・**17**日（木）

会場 三島市民文化会館 小ホール

住所：静岡県三島市一番町20番5号（三島駅より徒歩3分）　HP：http://www.mishima-youyouhall.com

11月16日（水）

12:50～13:00
開会挨拶

13:00～14:45
卵と初期発生
小倉 淳郎、中村 肇伸、
束田 裕一、青木 不学、
宮本 圭、北島 智也

14:45～15:00
コーヒーブレイク

15:00～16:05
生殖細胞の特性
齋藤 都暁、石津 大嗣、
奥田 晶彦、石黒 啓一郎

16:05～16:20
コーヒーブレイク

16:20～17:55
**ステムセルエイジングから
解明する疾患原理**
岩間 厚志、鍋島 陽一、
田久保 圭誉、波江野 洋、
堅田 明子

19:00～
懇親会（要予約）

11月17日（木）

9:00～10:10
PGCのエピゲノム（1）
幸田 尚、佐々木 裕之、
関 由行、阿部 訓也

10:10～10:25
コーヒーブレイク

10:25～11:25
PGCのエピゲノム（2）
山口 新平、立花 誠、
栗本 一基、原田 哲仁

11:25～13:00
昼食

13:00～14:35
精子形成とエピゲノム
相賀 裕美子、中馬 新一郎、
伊川 正人、品川 敏恵、
篠原 隆司
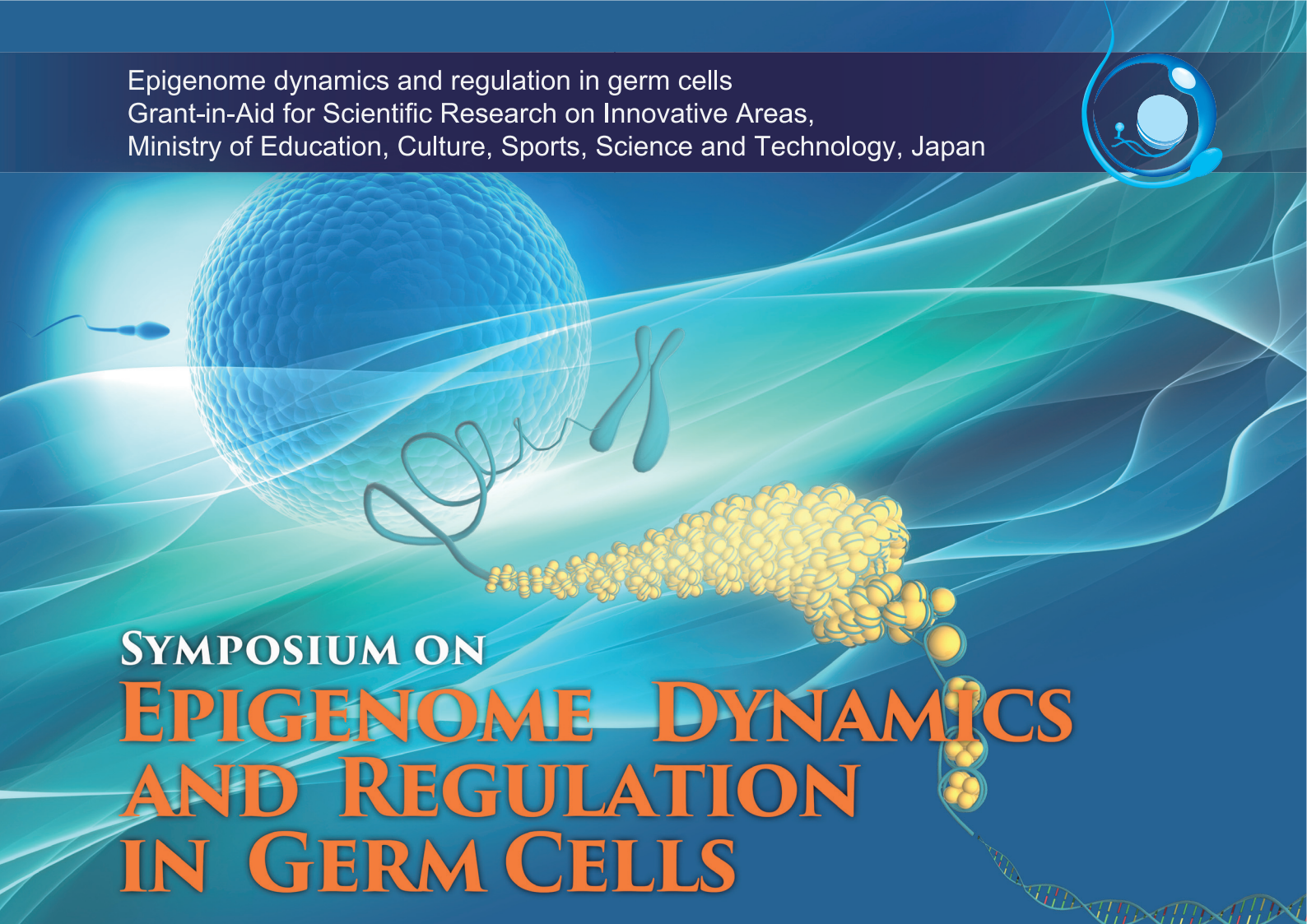
14:35～15:00
総合討論

15:00～15:10
閉会挨拶

**参加無料
事前登録歓迎**

Epigenome dynamics and regulation in germ cells
Grant-in-Aid for Scientific Research on Innovative Areas,
Ministry of Education, Culture, Sports, Science and Technology, Japan

SYMPOSIUM ON
EPIGENOME DYNAMICS AND REGULATION IN GERM CELLS

Date **Nov 21** (Tue) **- 22** (Wed), **2017**

Venue Tsukuba NOVA Hall, Tsukuba, Ibaraki, Japan
http://www.tcf.or.jp/novahall/

http://reprod-epigenome.biken.osaka-u.ac.jp/english/

Entry

* Admission FREE

Speakers:

Ryuzo YANAGIMACHI (University of Hawaii) , Dirk G. de ROOIJ (Utrecht University)

1. **Epigenome and totipotency**
   Atsuo Ogura, Yuichi Tsukada, Toshinobu Nakamura, Kei Miyamoto
2. **Epigenetic changes during fertilization and preimplantation development**
   Hiroyuki Sasaki, Masahito Ikawa, Takashi Kohda, Fugaku Aoki, Kuniya Abe
3. **Spermatogenesis, oogenesis, and meiosis**
   Takashi Shinohara, Keiichiro Ishiguro, Akihiko Okuda, Toshie Shinagawa, Tomoya Kitajima
4. **Epigenome regulatory mechanisms in germ cells**
   Yumiko Saga, Kuniaki Saito, Hirotsugu Ishizu, Akihito Harada, Makoto Tachibana
5. **Epigenetic changes during germ cell specification and development**
   Shinichiro Chuma, Kazuki Kurimoto, Yoshiyuki Seki, Shinpei Yamaguchi

Organizers:

Takashi SHINOHARA (Chair)
Atsuo OGURA

◆ 文部科学省 新学術領域研究「生殖細胞のエピゲノムダイナミクスとその制御」シンポジウム

文部科学省・科学研究費補助金・新学術領域研究

成果取りまとめ公開シンポジウム

生殖細胞のエピゲノムダイナミクスとその制御
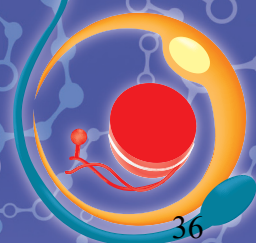
会期 2018年 **12月4日（火）・5日（水）**

会場 京都教育文化センター
住所：京都市左京区聖護院川原町4-13　HP：http://www2.odn.ne.jp/kyobun/

12月4日（火）

12:50〜13:00
開会挨拶

13:00 〜 14:30
全能性とエピゲノム
小倉 淳郎、束田 裕一、中村 肇伸、岡江 寛明、宮本 圭

14:45 〜16:10
受精・初期発生のエピゲノム変化
佐々木 裕之、伊川 正人、幸田 尚、青木 不学、阿部 訓也

16:25〜17:25
パネルディスカッション：生殖医学の倫理
発表タイトル：What an old crazy man thinks of the future of human ART
発表者：柳町 隆造　パネリスト：中辻 憲夫、阿久津 英憲、吉村 泰典

18:00〜
懇親会

12月5日（水）

9:00〜10:20
精子・卵形成と減数分裂
篠原 隆司、石黒 啓一郎、奥田 晶彦、品川 敏恵、北島 智也

10:35〜11:45
生殖細胞特有のエピゲノム制御メカニズム Ⅰ
相賀 裕美子、谷本 啓司、宮川 さとみ、齋藤 都暁

13:15〜14:15
生殖細胞特有のエピゲノム制御メカニズム Ⅱ
石津 大嗣、原田 哲仁、永瀬 浩喜、立花 誠

14:30〜15:35
PGCとエピゲノム変化
中馬 新一郎、栗本 一基、関 由行、山口 新平

15:35〜16:00
総合討論

16:00〜16:10
閉会挨拶

領域代表者

篠原隆司（京都大学医学系研究科）

お問合せ
epigenome@biken.osaka-u.ac.jp

領域ホームページ
http://reprod-epigenome.biken.osaka-u.ac.jp

36

写真集

第1回公開シンポジウム（キックオフシンポジウム）＠大阪大学
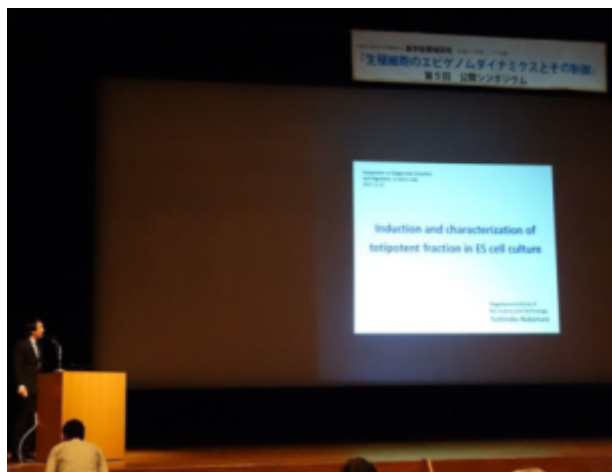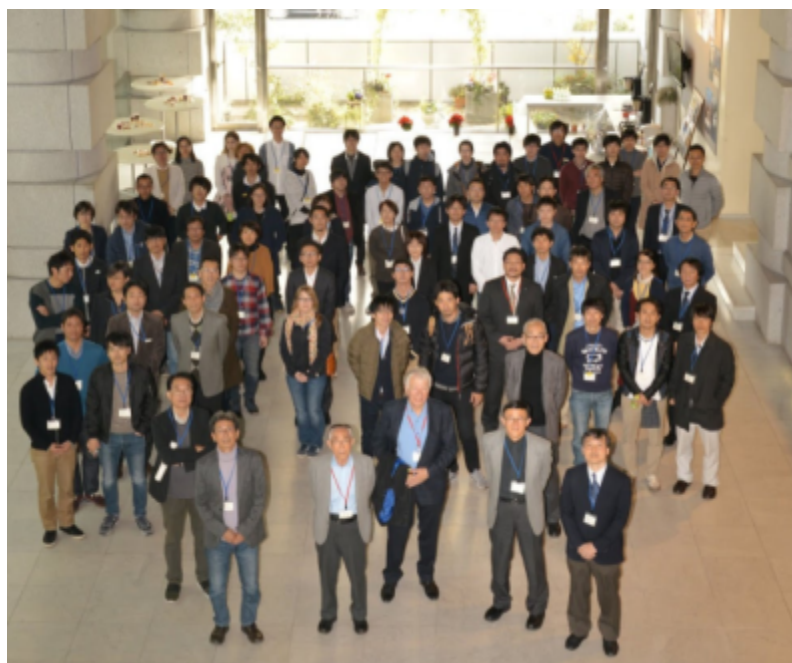2013年11月14日−15日

第2回　公開シンポジウム＠九州大学
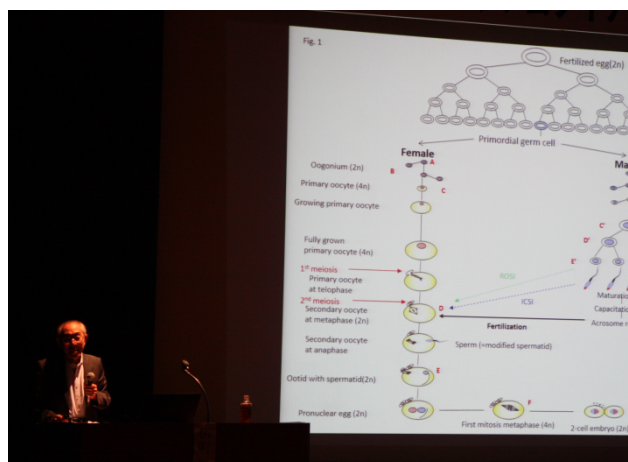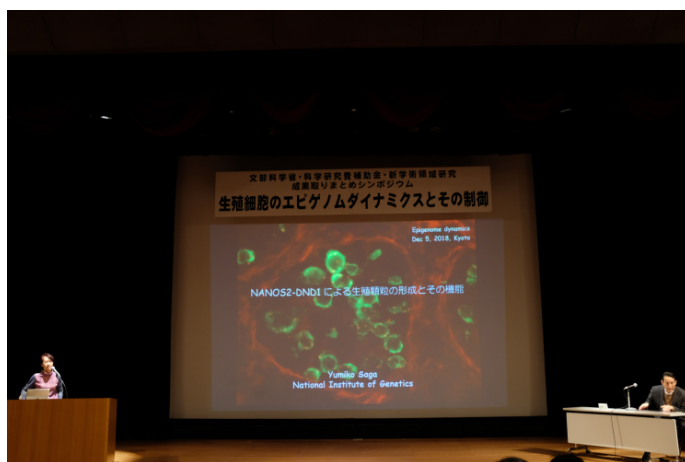2014年10月31日−11月1日

第3回公開シンポジウム（国際シンポジウム）＠京都大学
2015年2月17日−19日
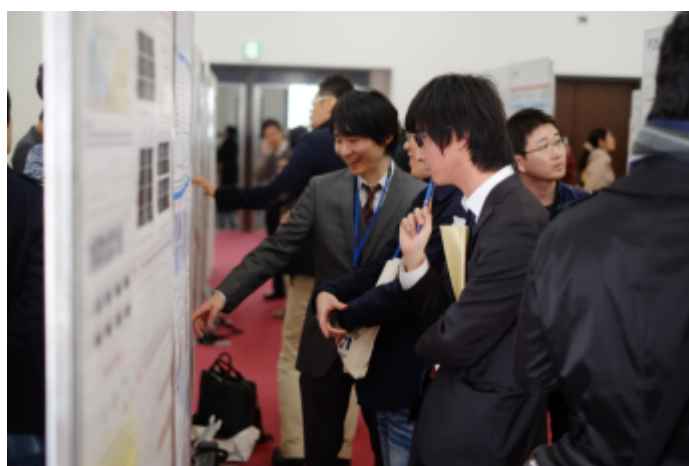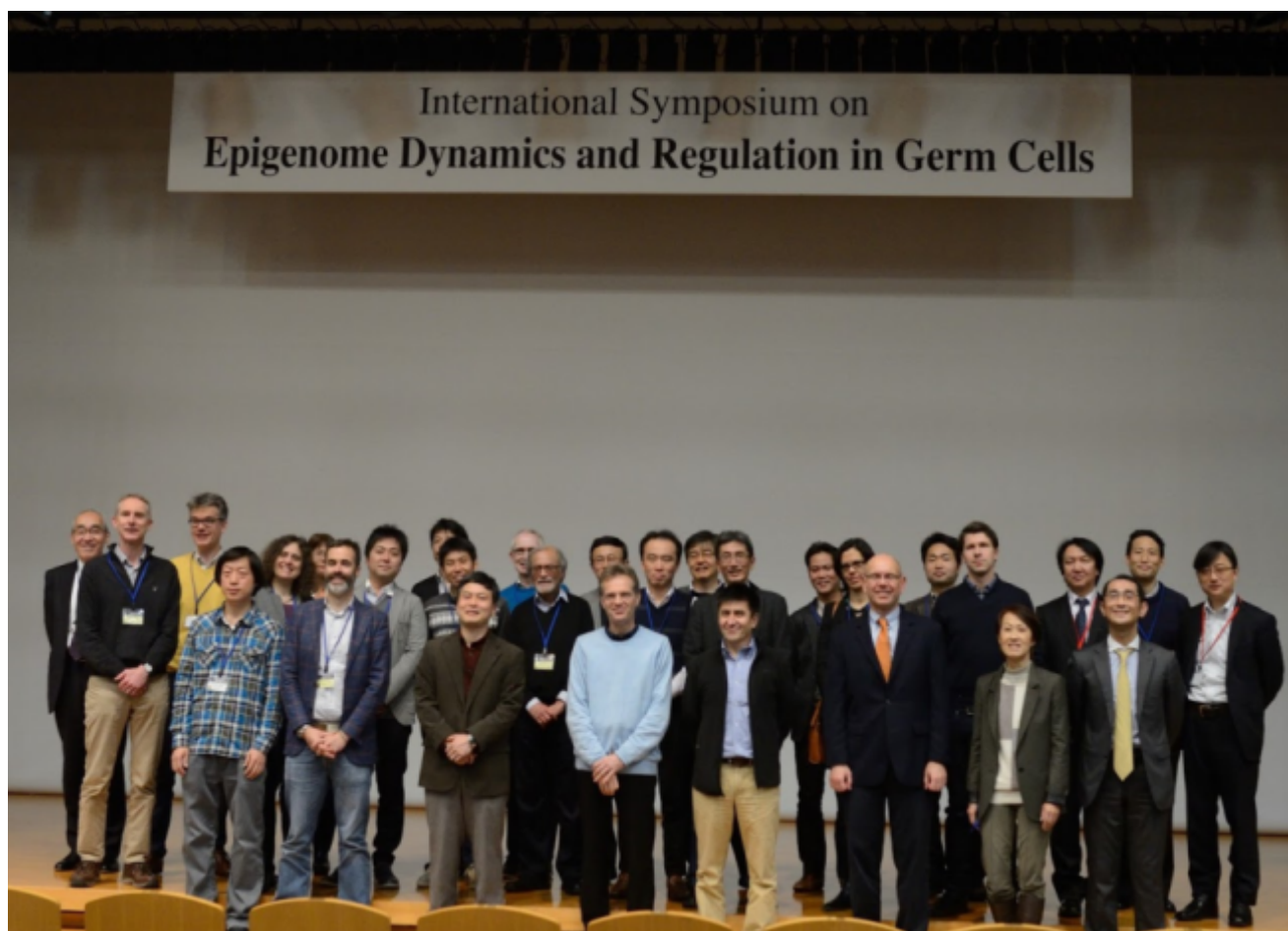
第4回公開シンポジウム＠三島市民文化会館
2016年11月16日−17日
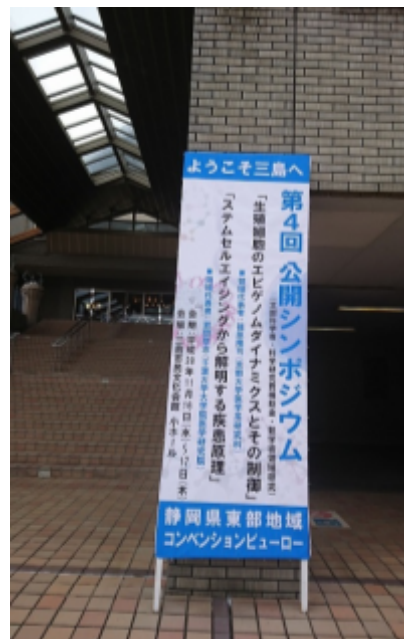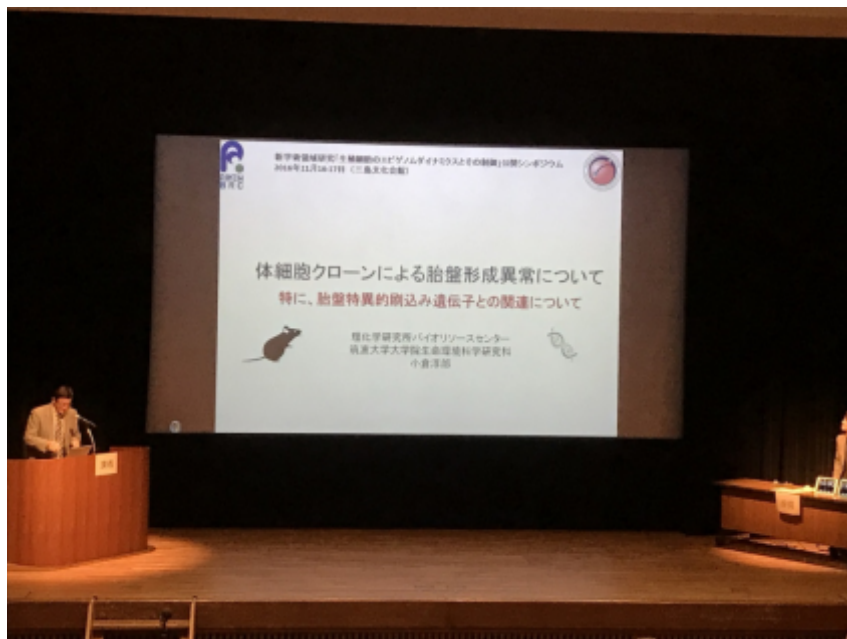
第5回公開シンポジウム＠つくばノバホール
2017年11月16日−17日
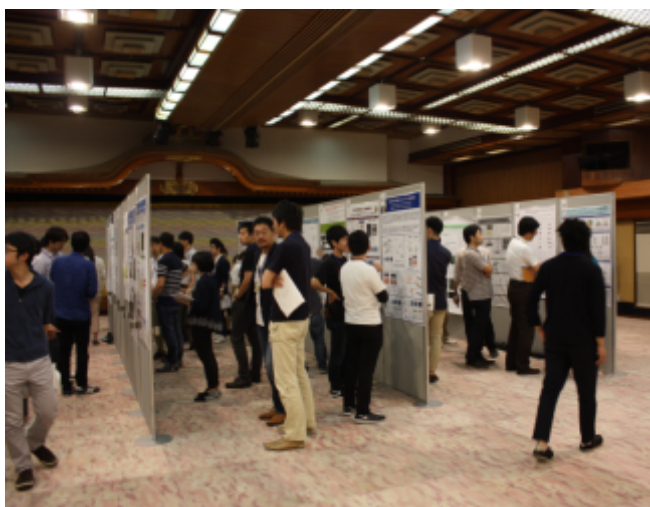
2014年若手勉強会　　2014年7月16日−18日
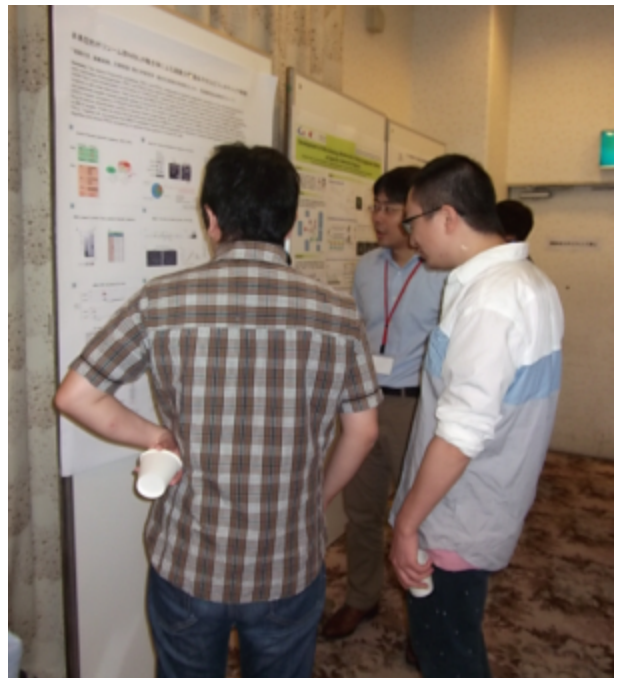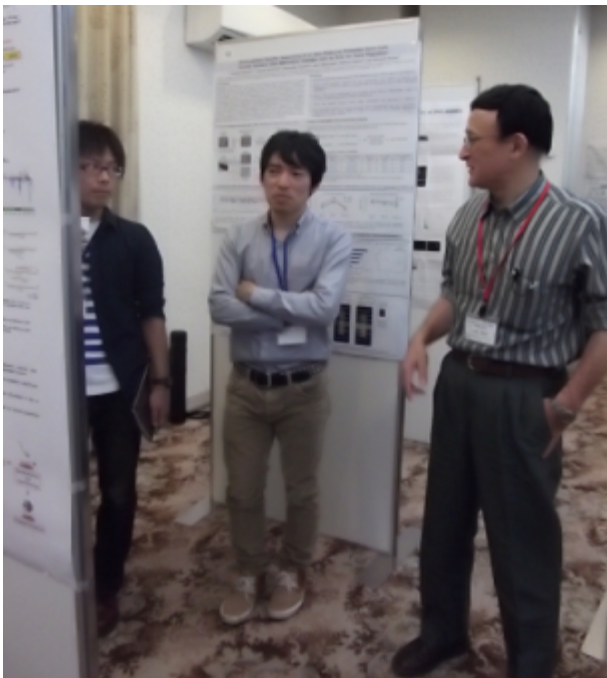
2015年若手勉強会　　2015年7月22日−24日
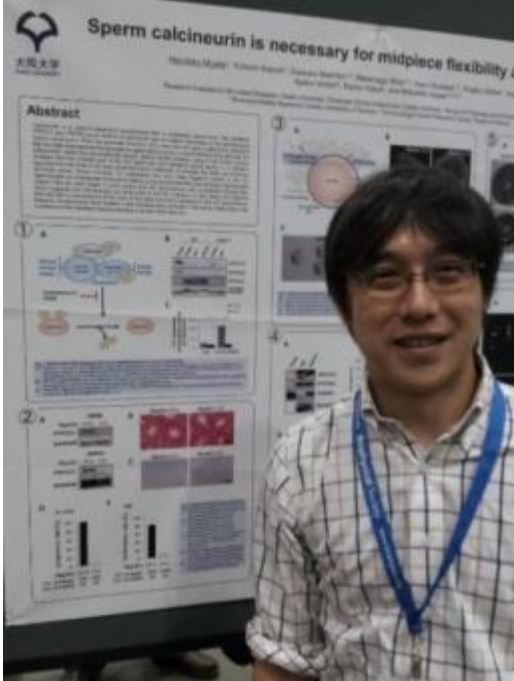
2016年若手勉強会　　2016年7月27日-29日
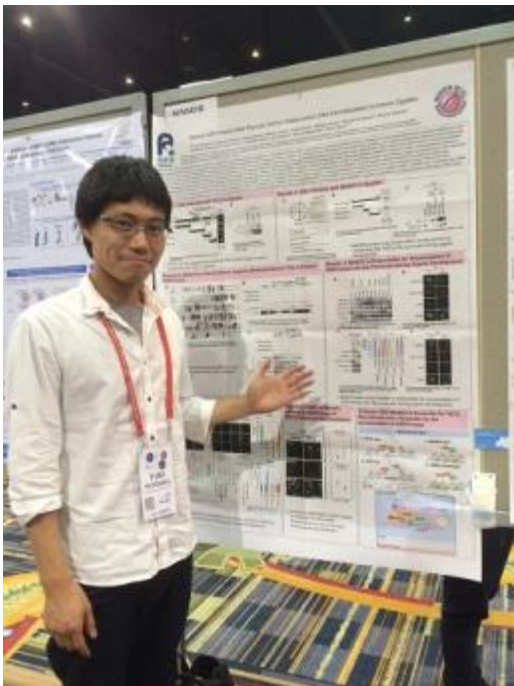

2017年若手勉強会　　2017年6月7日-9日

若手海外派遣

宮田治彦（伊川班）が優秀論文受賞として
海外発表 （2016.02.27-03.02@Biophysical Society
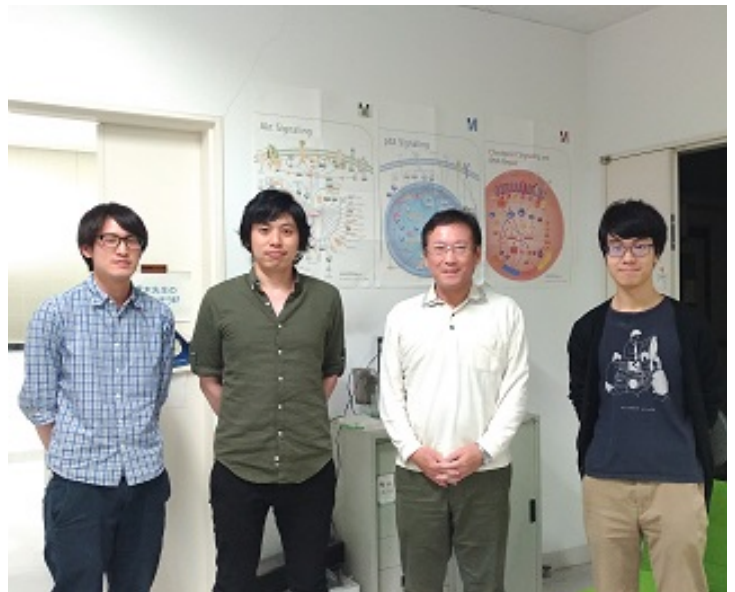60th Annual Meeting）

前之原章司（佐々木班）が国際コンファレンスにてベスト
ポスター賞を受賞 （2016.05.09-13@The 4th Cold Spring
Harbor Asia conference on Chromatin, Epigenetics and
Transcription）

畑中勇輝特別研究員（小倉班）がMouse
Genetics 2016で海外発表
（2016.07.13-16@Mouse Genetics 2016）

阿部健一郎（青木班）が国際支援班の援助（優秀論
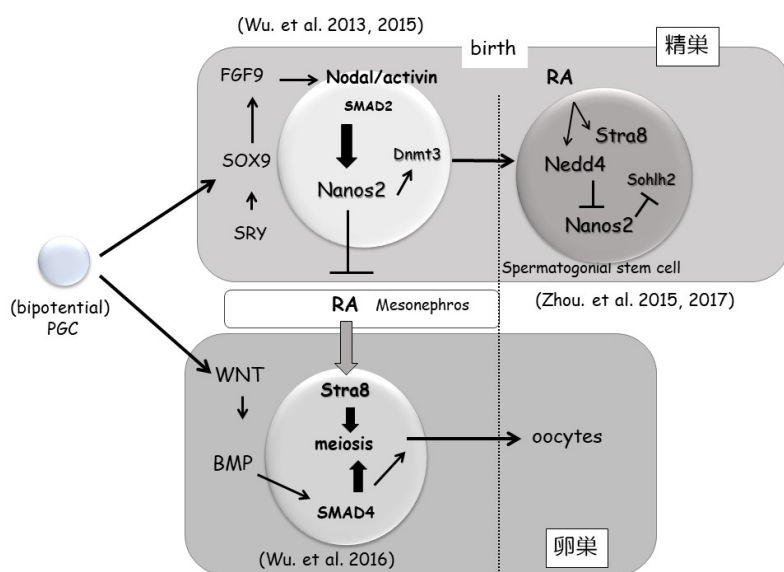文賞）でドイツの研究室に在籍中（2017.02）

研究成果

RNA 制御を介した生殖細胞の性特異的エピゲノムの確立		平成 25–29 年
研究代表者	相賀裕美子	情報・システム研究機構、国立遺伝学
	計画	研究所・系統生物研究センター

＜研究の目的＞

生殖細胞の性分化は胎生期におこる。性的に未分化な PGC が体細胞環境（精巣あるいは卵巣）の影響下で性分化を開始し胎生期に性特異的エピゲノムを確立する。体細胞の性分化シグナルはすでに同定、解析されていたが、生殖細胞の性分化に関わる因子は不明であった。生殖細胞の雄性化には我々が以前に同定した RNA 結合タンパク質 Nanos2 が重要な役割を果たす。Nanos2 は胎児精巣に入った生殖細胞特異的に発現し、主に標的遺伝子の抑制を介して、雌化の抑制及び、雄化遺伝子の発現誘導を促す。この研究計画では、胎仔精巣で Nanos2 を誘導するシグナル系を探索するとともに、胎仔卵巣で生殖細胞を雌化する因子を探索する。一方、精子幹細胞における Nanos2 の機能をモデルとして Nanos2 の下流カスケード制御の分子機構の解明を目指す。

＜研究成果＞

Nanos2 の上流機構の解析過程で、生殖細胞の性分化に TGF-b シグナル系が寄与することを明らかにした。特に雄性分化には Nodal/activin-SMAD2 経路、雌性分化には BMP-SMAD4 経路が重要であることを明らかにした。特に雌生殖細胞で SMAD4 に加えて RA シグナルを欠損させると、卵巣内であっても、生殖細胞が雄化し性転換が誘導できることを発見した(Wu et al. 2015, 2016)。この発見は、生殖細胞の雌化因子の発見と共に、雄化には、精巣特異的な誘導因子は必須でないという予想外のモデルを提唱できた。また Nanos2 の機能に関して、その機能発現に P-body の構造が必須であることが、P-body 構成因子 DDX6 の生殖細胞特異的遺伝子 KO により証明できた（未発表）。またこの解析は、マウス作成を介さず、キメラ解析により非常に短期間で条件付き遺伝子 KO が有効な手段であることを証明するとともに、効率的な解析を可能にする ES 細胞の確立と有効性を証明できた。また、精子幹細胞における Nanos2 のタンパク質の安定性が RA によって誘導される NEDD4 ユビキチン系に制御されており精子形成の最初のトリ

ガーが RA による Nanos2 の分解である可能性が示唆された。また精子幹細胞における Nanso2 の標的は分化因子 Sohlh2 であることが、遺伝学的及び分子生物学的解析により明らかになった(Zhou et al. 2015, 2017)。

＜研究の意義・展望＞
生殖細胞の性分化は体細胞環境によって決定するという事実はよく知られていたが、実際にどのような因子が実際に生殖細胞の性を決定するかは不明であった。我々の生殖細胞特異的遺伝子(SMAD4, STRA8)KO により、卵巣内で体細胞環境に関係なく生殖細胞が雄化するという事実は、生殖細胞の性決定においては精巣における環境は必要ないという、これまで構築されてきた体細胞性分化における雄優位の概念を変えるインパクトをもつ。我々の解析結果によると生殖細胞は、雌性化因子がない状態では雄性化する性質を持つ。最近、培養系で生殖細胞の雌性化に成功したという報告がある。しかし、その際に雌性化因子不在下でも、雄性化するわけではない。今後培養系の解析から雄性化因子も同定されるであろうが、in vivo における検証は必須である。我々が構築したキメラ解析系の利用により、機能解析がさらに推進できると考えている。

＜主な研究発表論文＞

1. Zhou, Z., Shirakawa, T., Ohbo, K., Sada, A., Wu, Q., Hasegawa, K., Saba, R., and *Saga, Y. (2015). RNA Binding Protein Nanos2 Organizes Post-transcriptional Buffering System to Retain Primitive State of Mouse Spermatogonial Stem Cells. Dev Cell *34*, 96-107.

2. Wu, Q., Fukuda, K., Weinstein, M., Graff, J.M., and *Saga, Y. (2015). SMAD2 and p38 signaling pathways act in concert to determine XY primordial germ cell fate in mice. Development 142, 575-586.

3. Kato, Y., Katsuki, T., Kokubo, H., Masuda, A., and *Saga, Y. (2016). Dazl is a target RNA suppressed by mammalian NANOS2 in sexually differentiating male germ cells. Nat Commun *7*, 11272.

4. Wu, Q., Fukuda, K., Kato, Y., Zhou, Z., Deng, C.X., and *Saga, Y. (2016). Sexual Fate Change of XX Germ Cells Caused by the Deletion of SMAD4 and STRA8 Independent of Somatic Sex Reprogramming. PLoS Biol *14*, e1002553.

5. Zhou, Z., Kawabe, H., Suzuki, A., Shinmyozu, K., and *Saga, Y. (2017). NEDD4 controls spermatogonial stem cell homeostasis and stress response by regulating messenger ribonucleoprotein complexes. Nat Commun *8*, 15662.

精子幹細胞のエピゲノム安定性と発がんとの関係の解析		平成 25-29 年
研究代表者	篠原隆司	京都大学大学院医学研究科
	計画	遺伝医学講座分子遺伝学
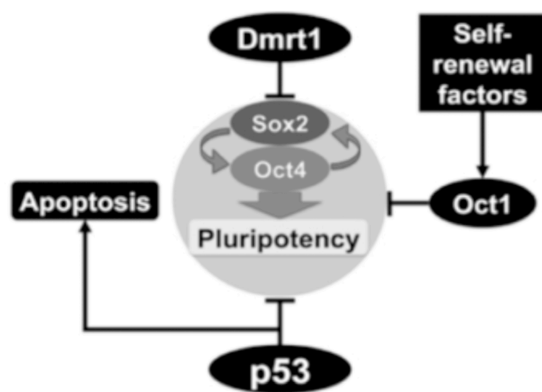
＜研究の目的＞

　生殖細胞は次世代に遺伝子を伝達するのみならず、奇形腫へ変化することにより様々な種類の体細胞へと分化するユニークな能力を持っている。しかしながら、その体細胞への発生能力を抑制している分子機構は未解明である。生殖細胞の腫瘍化に関わる因子の多くが ES 細胞の未分化性制御因子であることから生殖細胞がんの発生と細胞分化能のリプログラミングには密接な関係があると考えられている。例えば、生殖細胞腫瘍で高頻度に重複が見られる 12 番染色体短腕には Nanog, Gdf3, Edr1 など ES 細胞で高発現している複数個の遺伝子が局在しており、ES 細胞関連遺伝子群の高発現が生殖細胞腫瘍の発生を促進するのではないかと指摘されている。また、これらの因子は生殖細胞の発生にも重要であることから、体細胞への発生能力の抑制とリプログラミング・がん化は密接な関係があると予想される。

　我々のグループは 2003 年に精子幹細胞の長期培養に成功し、この細胞（Germline stem, GS 細胞）を利用して精子幹細胞の研究を行って来た。我々は GS 細胞の自己複製過程の研究で、この細胞がさまざまな種類の生殖細胞がんへと変化することを明らかにしてきた。例えば 2004 年に我々は GS 細胞が奇形腫を作る ES 細胞様の幹細胞である multipotent GS (mGS) 細胞に高頻度で変換することを見いだした。この GS 細胞から mGS 細胞への変換はがん抑制遺伝子である p53 の欠損により促進され、mGS 細胞はその表現型のみならず、キメラ形成能も持つ点で ES 細胞と酷似している。興味深いことに、mGS 細胞においてはインプリンティング遺伝子である H19 は全例で脱メチル化が起こっており、ヒトの生殖細胞腫瘍でもほぼ全例で DNA の脱メチル化が起こっていることを鑑みると、インプリンティング遺伝子のメチル化制御は発がんの過程に深く関わる可能性が高いのではないかと考えられる。

　そこで本研究では私たちはこれらのインプリンティング遺伝子の制御異常が精子幹細胞の体細胞への分化能力の脱抑制を引き起こし、リプログラミング・生殖細胞の腫瘍化を引き起こすのではないかと仮説を立て、この仮説の検証を試みた。

＜研究成果＞

　我々はがん抑制遺伝子である p53 と DNA のメチル化維持酵素である Dnmt1 を同時の抑制すると GS 細胞から mGS 細胞を誘導することができることを見出した。p53 と Dnmt1 の抑制はグローバルな DNA 脱メチル化を引き起こし、遺伝子導入された GS 細胞はほぼ前例で mGS 細胞へと変化した。p53 の抑制は GS 細胞の細胞死を抑制するために必要であったが、細胞死を抑制するために Bax の抑制を行った場合には多能性を誘導することが出来なかったため、p53 の抑制は単なる細胞死のためではなく、多能性の誘導に積極的に関わっている可能性がある。我々は p53 と Dnmt1 遺伝子の抑制は体細胞でも発がんを誘導することから、この遺伝子操作が生殖細胞の発がん遺伝子の発現上昇を誘導しているのではないかと考えた。

　そこで、ヒト生殖細胞関連遺伝子（例えば、Kitl, Atf7ip, Tert など）とエピジ

ェネティック因子群（ヒストン修飾酵素、DNA メチル化酵素、ポリコーム関連因子、Piwi-interacting 因子, microRNA 経路を含む）を候補として p53 KO GS 細胞を用いて、候補遺伝子の発現異常を誘導し、多能性細胞への変化を引き起こす遺伝子のスクリーニングを行った。その結果、Dmrt1 遺伝子を抑制した場合に GS 細胞の脱分化を誘導できることがわかった。Dmrt1 遺伝子は発がんに関わる遺伝子として知られているが、発がん以外にも性決定と同時に減数分裂制御にも関与する遺伝子として知られている。Dmrt1 遺伝子を抑制すると Sox2 ならびに Oct4 遺伝子の発現が上昇することから、GS 細胞においては多能性幹細胞で発現する Sox2 遺伝子の mRNA の発現を抑制していることが明らかとなった (Takashima et al., 2013)。

　Sox2 は ES 細胞の多能性維持に極めて重要な遺伝子であることが知られていたが、GS 細胞では Sox2 mRNA の発現があるものの、タンパク質の発現はないことが報告されており、その制御については未だ判っていない。Oct4 についても ES 細胞に比較すると mRNA の発現はかなり低いものの、タンパク質の発現は GS 細胞で確認されており、これらのいずれかの遺伝子を GS 細胞で強制発現すると、この場合にも mGS 細胞を誘導することが可能であった。

　これらの結果は GS 細胞におけるエピゲノムの不安的性が Dmrt1 の発現異常を引き起こし、その結果 Sox2 の発現が上昇することが mGS 細胞の発生の原因となっていることを示唆する。

＜研究の意義・展望＞

　体細胞と生殖細胞の違いは大きいのを実感した。我々の結果からは Dmrt1 が多能性に関与することが明らかになったが、未だになぜ p53 が関与するのかは不明のままである。いくら山中因子を導入しても GS 細胞は多能性を獲得しないのは、これと関係しているのではなかろうか？精子幹細胞のもつ多能性が性決定遺伝子に影響されるとは意外な結果であった。

＜主な研究発表論文＞

1. Takashima, S.,, Hirose, M., Ogonuki, N., Ebisuya, M., Inoue, K., Kanatsu-Shinohara, M., Tanaka, T., Nishida, E., Ogura, A., and Shinohara, T. (2013). Regulation of pluripotentcy in male germine stem cells by Dmrt1. Genes Dev. *27*, 1949-1958.

2. Morimoto, H., Iwata, K., Ogonuki, N., Inoue, K., Ogura, A., Kanatsu-Shinohara, M., Morimoto, T., Yabe-Nishimura, C., and Shinohara, T. (2013). ROS are required for mouse spermatogonial stem cell self-renewal. Cell Stem Cell *12*, 774-786.

3. Kanatsu-Shinohara, M., Onoyama, I., Nakayama, K. I., and Shinohara, T. (2014). Skp1-Cullin-F-box (SCF)-type ubiquitin ligase FBXW7 negatively regulates spermatogonial stem cell self-renewal. Proc. Natl. Acad. Sci. USA *111*, 8826-8831.

4. Kanatsu-Shinohara, M., Tanaka, T., Ogonuki, N., Ogura, A., Morimoto, H., Cheng, P. F., Eisenman, R. N., Trumpp, A., and Shinohara, T. (2016). Myc/Mycn-mediated glycolysiss enhances mouse spermatogonial stem cell self-renewal. Genes Dev. *30*, 2637-2648.

5. Kanatsu-Shinohara, M., Naoki, H., and Shinohara, T. (2016). Nonrandom germline transmission of mouse spermatogonial stem cells. Dev. Cell *38*, 248-261.

生殖幹細胞の減数分裂移行を制御する ゲノム–エピゲノムプログラム		平成 25-29 年
研究代表者	中馬新一郎	京都大学ウイルス・再生医科学研究所 発生エピゲノム研究分野
	計画	

＜研究の目的＞

　生殖細胞は、遺伝情報を体細胞よりも厳密に継承するものと考えられるが、減数分裂期には逆にゲノム DNA を積極的に組換えると共に、クロマチン構造の大規模な変換が起こる。哺乳類では古典的にはレチノイン酸が減数分裂をスタートするトリガーであるものと考えられてきたが、レチノイン酸は pleiotropic な因子であり、生殖細胞への分化能を持つ胚性多能性幹（ES）細胞に添加しても神経分化誘導等が起こり、減数分裂は起こらない。これは、生殖細胞には減数分裂を誘導する特異的なメカニズム(meiosis priming)がある事を示唆していたが、その実体は理解されていなかった。申請者はマウス生殖幹（GS）細胞株が体細胞型増殖から第1減数分裂に移行する培養条件を作出し、マルチオミクス解析による多能性幹細胞株や体細胞等との比較、また遺伝子機能スクリーニングにより、生殖細胞が減数分裂に移行する分子プログラムの理解を目標として研究を行った。

＜研究成果＞

　マウス生殖系列サイクルを通じた減数分裂プログラムの成立について、以下の主要な結果が得られた。(1) 生殖幹細胞は未分化状態で体細胞型増殖を行う一方、減数分裂を開始するための遺伝子発現パターンやエピゲノムプログラムをレチノイン酸非依存的に発生過程を通じて予め獲得している事（meiosis priming）、(2) レチノイン酸は、(1) の準備が既に整っている生殖幹細胞の減数分裂開始を誘導する「最後の一押し」の分子として働く事、(3) 生殖幹細胞の減数分裂制御は germline signature であるトランスポゾン抑制経路（*tudor*、*piwi* 遺伝子群等）と共発現制御を示す事、(4) 熊本大学の石黒博士との共同研究により(1)の meiosis priming を獲得した生殖幹細胞の減数分裂を誘導する十分因子（レチノイン酸をバイパスする因子）を同定した事、(5) RAR、non canonical PRC、STRA8、(4)の因子等の減数分裂制御の主要なプレーヤーと、(1) の meiosis priming を併せて、生殖幹細胞の体細胞分裂から減数分裂移行の分子プログラムの概要を説明可能となった事、等の成果を得た（論文準備中）。また、生殖細胞

のゲノム・エピゲノム情報をレトロトランスポゾン活性から保護する piRNA 経路について研究を進めると共に (Pandey et al., 2013;Chuma, 2014, Yoshimura et al.,2018 等)、多能性幹細胞と生殖幹細胞で高い発現を示す DNA 組換抑制遺伝子 *Pari* ノックアウトマウス作成により、内因性 DNA 複製ストレスの適切な抑制が細胞および個体の遺伝情報の安定性維持に働くメカニズムを明らかにした（Mochizuki et al., 2017)。

＜研究の意義・展望＞

「生殖細胞のエピゲノムダイナミクス解明」についてエピゲノム制御、転写制御、翻訳調節等のゲノムワイドなプロファイリングと個別因子の機能解析を行い、「遺伝情報の維持と再編」の機能調節が生殖系列サイクルのエピゲノムダイナミクスの中核の一つである事を示す事が出来た。これら研究成果は、生殖系列サイクルの遺伝情報の継承と再編の分子基盤の理解を前進させると共に、将来的には幹細胞リソースや個体の遺伝的安定性や相同組換え効率を制御する方法論の探索にも寄与する可能性がある。
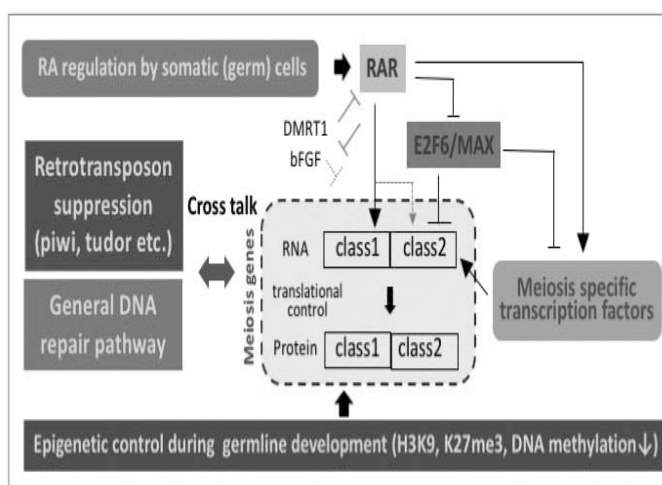
Meiosis priming in the germline stem cell cycle in mice

＜主な研究発表論文＞

Yoshimura, T., Watanabe, T., Kuramochi-Miyagawa, S., Takemoto, N., Shiromoto, Y., Kudo, A., Kanai-Azuma, M., Tashiro, F., Miyazaki, S., Katanaya, A., Chuma, S., and Miyazaki, J.I. (2018). Mouse GTSF1 is an essential factor for secondary piRNA biogenesis. EMBO Rep *19,* e42054.

Mochizuki, A.L., Katanaya, A., Hayashi, E., Hosokawa, M., Moribe, E., Motegi, A., Ishiai, M., Takata, M., Kondoh, G., Watanabe, H., Nakatsuji N, and Chuma S. (2017). PARI Regulates Stalled Replication Fork Processing To Maintain Genome Stability upon Replication Stress in Mice. Mol Cell Biol. *37,* e00117-17.

Chuma, S. (2014). LINE-1 of evidence for fetal oocyte attrition by retrotransposon. Dev Cell. *29,* 501-502.

Pandey, R.R., Tokuzawa, Y., Yang, Z., Hayashi, E., Ichisaka, T., Kajita, S., Asano, Y., Kunieda, T., Sachidanandam, R., Chuma, S., et al. (2013). Tudor domain containing 12 (TDRD12) is essential for secondary PIWI interacting RNA biogenesis in mice. Proc Natl Acad Sci USA. *110,* 16492-16497.

| 小分子 RNA が誘導するエピゲノム形成の分子機構		平成 25-29 年
研究代表者	齋藤都暁	慶應義塾大学医学部
	計画	国立遺伝学研究所

＜研究の目的＞

　ショウジョウバエをモデル動物として用い、Piwi-piRNA 複合体によるレトロトランスポゾン抑制機構を解明することを目指す。ショウジョウバエ卵巣由来培養細胞 (OSC)では piRNA が発現し、トランスフェクション法、ノックダウン法など様々な生化学的実験手法が開発済みであることから、単純化された実験系を駆使することで piRNA によるヘテロクロマチン形成誘導機構に迫りたい。具体的には、(a)Piwi-piRNA 複合体によるレトロトランスポゾン認識機構の解明、(b)レトロトランスポゾン領域のエピゲノム変化の同定と誘導機構解明、(c)エピゲノム変化を誘導する蛋白質因子群の同定と、その役割の解明、(d)エピゲノム変化の誘導に至るカスケードの解明、(e)小分子 RNA によるエピゲノム変化が周囲のクロマチン領域に与える影響、を解明する。最終的に piRNA によって誘導されるエピジェネティックマークとその誘導機構を関連蛋白質群の機能解明を通じて理解する。

＜研究成果＞

　研究開始当初はpiRNA と結合する Piwi タンパク質が核内で働くことがレトロトランスポゾンの抑制に重要であることが分かっていたが、抑制段階に働く因子は報告されていなかった。OSC においてレトロトランスポゾン mdg1 の発現を指標にレトロトランスポゾン抑制因子の探索を行った。100 以上の候補遺伝子群に対して siRNA によるノックダウンを行った結果、CG3893 遺伝子を含む複数のレトロトランスポゾン抑制候補遺伝子を見いだした。CG3893 遺伝子をDmGTSF1 と命名し、更にその機能解明を行った。はじめにノザンブロット法によって piRNA 生合成への関与を検討した。DmGTSF1 のノックダウン細胞ではpiRNA 量に変動が認められなかった。したがって、DmGTSF1 遺伝子は piRNA 生合成に関与しないことが明確となった。更に、細胞内局在を検討した結果、核に局在することが明らかとなった。DmGTSF1 遺伝子のハエ個体での機能を検討するため、DmGTSF1 変異ハエ系統を確立した。DmGTSF1 変異ハエを用いて解析下結果、著しく卵巣形成が阻害され、Piwi 変異ハエ同様、不稔となることを見いだした。次にトランスポゾンの発現について RT-qPCR 法で検討したところ、DmGTSF1 変異ハエでは、レトロトランスポゾンの発現が上昇していることが分かった。次に、DmGTSF1 の分子機能に迫るため、Piwi との相互作用の有無を IP-western blot 法で検討した。その結果、Piwi は DmGTSF1 と蛋白質間相互作用することを見いだした。次に、DmGTSF1 は CHHC type の Zn-finger ドメインを有することから、そのレトロトランスポゾンサイレンシングへの重要性を検討することとした。OSC を用いたレスキュー実験において、Zn-finger の点突然変異型は、Piwi と相互作用するものの、レトロトランスポゾンの抑制能を消失することが明らかとなった。以上のことから、DmGTSF1 は Piwi と核内で相互

作用し、その Zn-finger ドメインを介して機能することで piRNA の標的となるレトロトランスポゾンの発現を抑制していることが明らかとなった(Ohtani et al., 2013)。

　更に Piwi-piRNA 複合体によるエピゲノム制御の分子機構に迫るため、Piwi と相互作用する新たな核内因子を探索した。OSC の核抽出液を用いて、抗 Piwi 抗体による免疫沈降解析を行った結果、Piwi がリンカーヒストン H1 と蛋白質間相互作用することを見いだした。H1 が実際に Piwi と相互作用するかを IP-western blot 法や GST-pull down 法によって確認したところ、Piwi と H1 は蛋白質間相互作用することが明らかとなった。次に H1 が Piwi 同様レトロトランスポゾンの抑制に関与するか否かを OSC で検討した。mRNA-seq 解析の結果、Piwi 同様、H1 のノックダウンでレトロトランスポゾンの発現が上昇した。次に H1 と Piwi のエピゲノムへの寄与を検討するため、抗 H1 マウスモノクローナル抗体を作製し、クロマチン免疫沈降(ChIP)解析を行った。その結果、Piwi のノックダウンによって、H1 のレトロトランスポゾン上での密度が優位に減少することを見いだした。すなわち、Piwi は H1 の密度を正に制御すると考えられた。次に、ChIP-seq、ATAC-seq 法を駆使し、H1 の制御が Piwi によるクロマチン凝集制御に必須であることを見いだし、以上の結果を報告した(Iwasaki et al., 2016)。
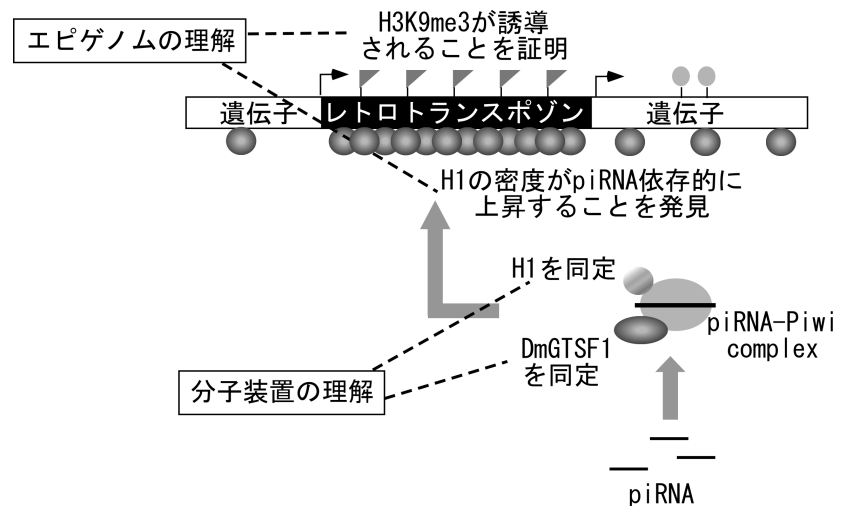
＜研究の意義・展望＞

　クロマチン制御マシナリーの新規分子を同定した結果、10 以上の因子が関わる複雑な機構が働くことが分かった。今後はこれを最少化、もしくはエピゲノム制御に至る過程をスキップするような系を開発することで、小分子 RNA による任意領域のエピゲノム改変を実現していきたい。

＜主な研究発表論文＞

1. Ohtani, H., Iwasaki, Y.W., Shibuya, A., Siomi, H., Siomi, M.C., and Saito, K. (2013). DmGTSF1 is necessary for Piwi-piRISC-mediated transcriptional transposon silencing in the Drosophila ovary. Genes Dev. *27*, 1656-1661.
2. Iwasaki, Y.W., Murano, K., Ishizu, H., Shibuya, A., Iyoda, Y., Siomi, M.C., Siomi, H., and Saito, K. (2016). Piwi modulates chromatin accessibility by regulating multiple factors including histone H1 to represss transposons. Mol. Cell *63*, 408-419.

着床前胚のエピゲノムダイナミクスと制御		平成 25-29 年
研究代表者	中村肇伸	長浜バイオ大学バイオサイエンス学部
	計画	エピジェネティック制御学研究室

＜研究の目的＞

初期の着床前胚は、胎仔と胎盤の両方に分化できる「全能性」細胞であり、胎仔のみに分化できる ES/iPS 細胞の「多能性」を凌ぐ能力を有している。しかし、初期の着床前胚は、幹細胞ではないためにその利用は限定されている。受精卵の全能性は、精子と卵子に刷り込まれたエピゲノム情報がリプログラミングされることにより再獲得される。

この過程には、DNA の脱メチル化、胚性遺伝子の活性化、母性 RNA の分解、および母性タンパク質の分解等が重要であることが明らかとなっている。しかしながら、リプログラミングの分子メカニズムについては、不明な点が多く残されている。本研究では、全能性を有する初期の着床前胚に特異的、あるいは高い発現を示す機能未知遺伝子の機能解析を通して、リプログラミングの分子機構を明らかにすることを目的とした。また、研究成果に立脚した新たなリプログラミング法の開発にも挑戦した。
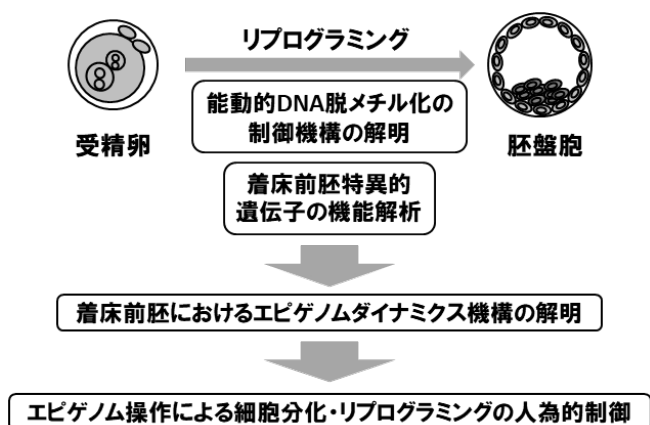
＜研究成果＞

本研究では、初期の着床前胚に特異的、あるいは高い発現を示す遺伝子を 8 個（Klf17、Btg4、Pramef12、Trim61、Rfpl4、Zc3h6、Zbed3、および Zfp92）同定した。全ての遺伝子のノックアウトマウスを作製し、生体内での機能を解析したところ、解析中の Zfp92 を除く 7 遺伝子中 5 個の遺伝子が正常発生に必須の母性効果遺伝子であることを明らかにした。また、Klf17 と Btg4 については、それぞれ胚性遺伝子の活性化と母性 RNA の分解に必要であることも示した。さらに、Pramef12 は精子形成に必須であること、母性 Trim61 と胚性 Trim61 が正常発生に必要であることを明らかにした（右表）。

Gene	Phenotype
Klf17	Female infertility / Required for major zygotic gene activation
Btg4	Female infertility / Required for maternal RNA degradation
Pramef12	Male infertility / Required for spermatogenesis
Trim61	Maternal and zygotic Trim61 is required for preimplantation development
Rfpl4	Maternal effect gene required for preimplantation development
Zc3h6	Maternal effect gene required for preimplantation development
Zbed3	Maternal effect gene required for preimplantation development
Zfp92	Under investigation

受精後の DNA 脱メチル化に関与する Tet3 制御タンパクの機能解析として、ES 細胞において Tet1/2 によりクロマチンにリクルートされることが明らかにされている O-linked N-acetylglucosamine transferase（OGT）に着目して研究を行った。その結果、受精卵において雄性クロマチン特異的にヒストン H2B の 112 番目のセリンがアセチルグルコサミン化 (H2B S112GlcNAc)されていることを見出した。また、このヒストン修飾を触媒する OGT の雌性クロマチンへの結合は PGC7 により阻害されていることを明らかにした。さらに、H2B S112A 変異体を用いて受精卵に存在する H2B S112GlcNAc を消去しても、雄性クロマチンにおける 5 メチル化シトシン（5mC）から 5 ヒドロキシルメチル化シトシン（5hmC）への変換に影響を及ぼさないことが明らかとなった。また、受精卵において Tet3 をノックダウンしても、H2B S112GlcNAc を消去しても転写に影響はなかったが、Tet3 をノックダウンした受精卵から H2B S112GlcNAc を消去した場合には、雄性クロマチンからの転写が抑制されることを見出した。これらのことから、受精卵の胚性遺伝子の活性化には、5hmC に加えて特異的なヒストン修飾が重要な役割を果たすことを明らかにした（右図）。
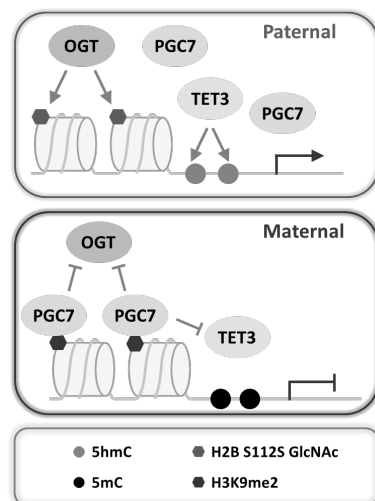
　本研究では、iPS 細胞を樹立する際に Oct3/4、Klf4、Sox2、および c-Myc に加えて、全能性細胞で高発現する PGC7 を用いることにより、iPS 細胞で頻繁に異常が認められる *Dlk1-Dio3* imprinting locus における遺伝子発現の異常を改善できることを明らかにした。また、PGC7 は IG-DMR と結合することにより、Dnmt3a による異所的なメチル化を阻害することを見出した。さらに、PGC7 ノックアウトの MEF に Oct3/4、Klf4、Sox2、および c-Myc を発現させても、野生型の MEF の場合とは異なり、内在性の多能性関連因子の発現がほとんど見られず、リプログラミングが不完全であることが示された。これらのことから、PGC7 は体細胞から iPS 細胞への完全なリプログラミングと *Dlk1-Dio3* imprinting locus のメチル化の維持に重要な役割を果たすことが明らかとなった（右図）（Xu X et al., 2015）。
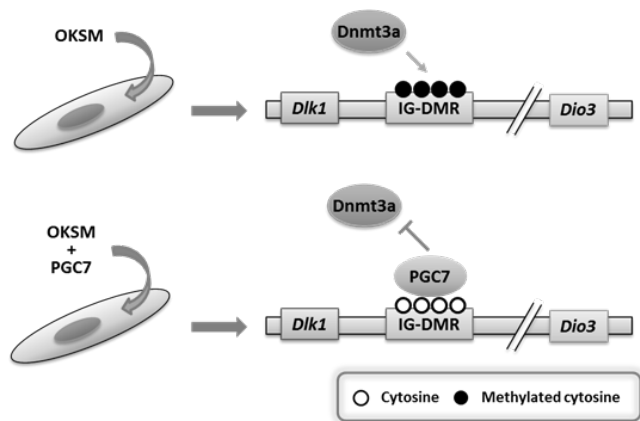
＜研究の意義・展望＞

　受精後のリプログラミングに必須の遺伝子を 6 個同定することができた。また、着床前胚で高発現する PGC7 を用いることにより、高い分化能を持つ iPS 細胞を作製することに成功した。今後、これらの遺伝子の詳細な機能を解析することにより、リプログラミングの分子機構の解明に寄与できると考えられる。

| 受精を介した経世代エピゲノム変化の解明と制御		平成 25-29 年
研究代表者	伊川　正人	大阪大学微生物病研究所
	計画	遺伝子機能解析分野

＜研究の目的＞

　精子と卵子の使命は父方と母方由来のゲノム情報を受精により子に伝えることにあるが、正常な個体発生には、DNA メチル化やクロマチン修飾などを含めたエピゲノム情報の伝達と、受精後にエピゲノム情報がリプログラミングされる必要がある。ところで体外受精という技術は安全な生殖補助医療として広く社会に受け入れられており、今や日本を含む先進諸国では約 20 人に 1 人が体外受精児である。しかしその一方で、乏精子症患者サンプルでのヒストン:プロタミン比の異常や、体外受精児の一部に H19 座などのエピゲノム異常とそれに伴う疾病の可能性が指摘されている。本研究では、ゲノム・エピゲノム編集技術の開発と、その技術を用いた遺伝子改変マウスの作製を通じて、配偶子の成熟と受精・発生に及ぼす影響について解析することを目的とした。

＜研究成果＞

　研究開始当初、我々は TALEN を用いたゲノム編集システムを導入していたが、2013 年に Science 誌に CRISPR/Csa9 を用いた哺乳類ゲノム編集技術が報告されたのを機に方針転換した。その結果、Cas9 と gRNA を同時発現するプラスミドを受精卵前核に注入することで、迅速・簡便に遺伝子破壊 (KO) マウスを作製する系を構築した (Mashiko et al., Sci Rep 2013)。本システムにより順次、精巣特異的発現遺伝子について KO マウスを作製し、個体レベルで妊孕性の確認を行った。解析した約 80 遺伝子の内、約 70%に相当する 54 もの遺伝子が、精巣特異的もしくは精巣で多く発現するにも関わらず、精子受精能力・発生能力に必須ではなかった。この結果は、組織特異的な発現パターンからでは遺伝子の重要性は計り知れないことを示すものであると同時に、KO マウスを作製して遺伝子機能の重要性を調べることは、コストパフォーマンスも高く、重要遺伝子の絞込みに有効であることを示す結果となった (Miyata et al., PNAS 2016)。

　なお Protamine1 や Centrin1 など、精子核タンパク質をコードする遺伝子を破壊した場合には、精子頭部の奇形が多くみられ雄性不妊を示したものの、顕微授精により正常な産仔が得られることを確認した。また予期せぬ結果として、精子特異的に発現するカルシニューリンの KO マウスでは、精子鞭毛の屈曲が障害され、雄性不妊となることを見出した (Miyata et al., Science 2015)。さらに我々は、受精メカニズムの解明に取り組み、精子膜タンパク質 IZUMO1 と卵子 GPI アンカー型膜タンパク質 JUNO の相互作用部位の同定を行った。東京大学の濡木理教授との共同研究により解明された JUNO タンパク質について、アミノ酸置換したタンパク質を Juno KO マウス卵子に mRNA 注入して発現させて精子との融合能力を測定した結果、JUNO の N 型糖鎖は受精に不要である一方、62 番目のトリプトファンが IZUMO との結合および精子・卵子の融合に必須であることを見出した (Kato et al., Nat Commun 2016)。

また我々は、精子由来で卵子を活性化する因子の同定に取り組んだ。候補因子の KO マウスを作製するアプローチから同定を試みた結果、PLCZ1 の KO マウスから得られた精子を顕微授精しても卵子活性化が起きないことを見出し、20 年以上に渡り不明とされてきた卵活性化因子が PLCZ1 であることを明らかにした。さらに詳細な解析から、PLCZ1 欠損精子であっても、膜融合を介した受精であれば弱いながらも卵子を活性化できること、さらにその弱い活性であっても一定頻度 (2 割程度) で発生を開始して産仔に発生することを報告した (Nozawa et al., Sci Rep 2018)。
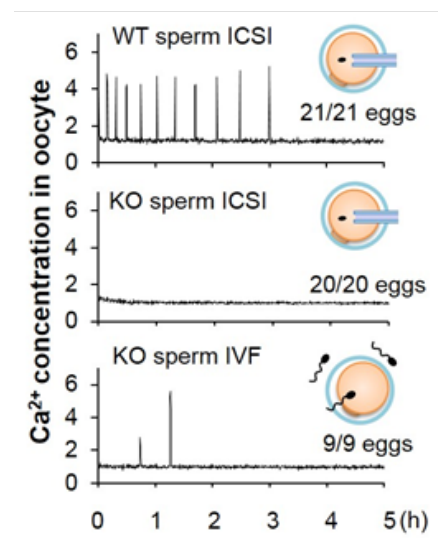
＜研究の意義・展望＞

CRISPR/Cas9 システムの出現により、ゲノム編集を用いた精子・卵子での遺伝子機能解析が簡便で効率よく実施できることを示すことができた。体細胞型カルシニューリンの阻害剤であるシクロスポリン A や、FK506 を投与したマウスでは同様に不妊となるものの、投薬を中止すると妊孕性が回復することを見出したことは、予期せぬ成果であるが、精子カルシニューリンが男性用避妊薬の標的となりえる成果として、国際的にも高い評価を得ることができ、生殖不全の診断・治療だけでなく、避妊薬開発にも貢献できると考えている。また卵子活性化不全は、不妊患者でも散見されることから、PLCZ1 異常との関連を調べると同時に、PLCZ1 補充による治療法開発などに発展が期待される。

＜主な研究発表論文＞

1. Mashiko, D., Fujihara, Y., Satouh, Y., Miyata, H., Isotani, A., and Ikawa, M. (2013). Generation of mutant mice by pronuclear injection of circular plasmid expressing Cas9 and single guided RNA. Sci Rep *3*, 3355.
2. Miyata, H., Satouh, Y., Mashiko, D., Muto, M., Nozawa, K., Shiba, K., Fujihara, Y., Isotani, A., Inaba, K., and Ikawa M. (2015). Sperm calcineurin inhibition prevents mouse fertility with implications for male contraceptive. Science *350*, 442-445.
3. Miyata, H., Castaneda, J.M., Fujihara, Y., Yu, Z., Archambeault, D.R., Isotani, A., Kiyozumi, D., Kriseman, M.L., Mashiko, D., Matsumura, T. Matzuk MM., Mori M., Noda T., Oji A., Okabe M., Prunskaite-Hyyrylainen R., Ramirez-Solis R., Satouh Y., Zhang Q., Ikawa M., and Matzuk MM. (2016). Genome engineering uncovers 54 evolutionarily conserved and testis-enriched genes that are not required for male fertility in mice. Proc Natl Acad Sci U S A *113*, 7704-7710.
4. Kato, K., Satouh, Y., Nishimasu, H., Kurabayashi, A., Morita, J., Fujihara, Y., Oji, A., Ishitani, R., Ikawa, M., and Nureki, O. (2016). Structural and functional insights into IZUMO1 recognition by JUNO in mammalian fertilization. Nat Commun *7*, 12198.
5. Nozawa, K., Satouh, Y., Fujimoto, T., Oji, A., and Ikawa, M. (2018). Sperm-borne phospholipase C zeta-1 ensures monospermic fertilization in mice. Sci Rep *8*, 1315.

| 卵および初期胚のエピゲノム制御機構	平成 25-29 年
研究代表者　束田裕一	九州大学
計画	稲盛フロンティア研究センター 先端生命情報研究部門

<研究の目的>

　我々ヒトを含めた哺乳類では、個体を構成する種々の細胞は分化の過程で異なる遺伝子発現プログラムを受け、細胞運命が決定される。分化した細胞では遺伝子発現プログラムが固定されるが、一部の細胞ではリプログラミングされる。生体内で起こる究極のゲノムリプログラミングは、高度に最終分化した配偶子が、受精を介して一個体を形成できる全能性を獲得する過程である。ゲノムリプログラミングでは、エピゲノム制御が果たす役割が非常に大きく、人為的ゲノムリプログラミング産物であるクローン動物、iPS 細胞では不十分なゲノムリプログラミングによるエピゲノム異常が明らかにされている。特に注目すべきは、エピゲノム異常の中心が DNA とヒストンのメチル化修飾という点である。エピゲノム変化では、クロマチン上の古い化学修飾の消去と新しい修飾の付加が起こるが、メチル化修飾はその可逆性が近年まで不明であり大きな議論の的となっていた修飾である。我々は、そのメチル化修飾消去機構の解明に取り組み、世界で初めて新規のヒストン脱メチル化酵素ファミリーとして JmjC ドメイン含有タンパク質ファミリーを同定し、ヒストンの脱メチル化が真核生物に共通したメチル化の制御機構であることを証明することで、エピジェネティクス研究にパラダイムシフトを起こした。一方で、この研究から学んだのは、メチル化修飾消去機構をはじめ、エピゲノム制御は生物種、生理過程及び細胞種により異なるメカニズムを用いているということでもあった。特に、哺乳類のエピゲノム制御機構については、体細胞を中心に研究が進められ、生殖細胞・着床前初期胚における制御機構はその生化学的解析の困難さと相俟って不明な点が多く残されている。生殖細胞・着床前初期胚では体細胞には存在しないような制御因子が存在するため、生殖細胞・着床前初期胚のエピゲノム制御機構を解明するには、生殖細胞・着床前初期胚特異的な制御因子の同定・機能解析が必要不可欠である。そこで本研究では、卵・初期胚におけるクロマチンメチル化を中心としたエピゲノム制御マシナリーの同定と機能解析により、全能性獲得のためのゲノムリプログラミングにおけるエピゲノム制御機構の解明を目的とする。

<研究成果>

　本研究で我々は、マウスの卵・着床前初期胚におけるエピゲノム制御因子の *in silico* スクリーニングにより得られた JmjC ファミリーに属するヒストン脱メチル化酵素 KDM7 とメチル化 DNA 酸化酵素 TET3 が、ゲノムリプログラミングにおいて果たす役割を明らかにした。まず、ヒストンのメチル化について、卵母細胞に特異的に高発現し、発生に伴い発現が速やかに減少するヒストン脱メ

チル化酵素 KDM7 の卵母細胞特異的コンディショナルノックアウトマウスを作製し、KDM7 が卵形成・受精・初期発生において果たす役割を解析した。その結果、母性 KDM7 欠損は卵形成、受精、初期発生、および産仔数への顕著な影響が見られず、KDM7 は卵・着床前初期胚に特異的高発現しているにも関わらず、胚発生に必要なゲノムリプログラミングに必須ではないことが示唆された。次に、DNA のメチル化について、KDM7 と同様に卵母細胞に特異的に高発現し、発生に伴い発現が速やかに減少するメチル化 DNA 酸化酵素 TET3 の解析を行った。哺乳類では、受精後の 1 細胞期胚において、雄性 DNA のゲノムワイドな脱メチル化が起こる。この DNA 脱メチル化には、メチル化 DNA の酸化が関与していることが報告され、メチル化 DNA 酸化酵素 TET3 がその責任分子である可能性が示唆された。我々もそれらの報告と独立して同様の結果を見出していたため、ゲノムリプログラミングの中心的エピゲノム制御機構と考えられていた雄性 DNA 脱メチル化（酸化）の発生およびエピゲノム制御機構における役割について、TET3 の卵母細胞特異的コンディショナルノックアウトマウスを作製して解析した。その結果、TET3 が受精卵における DNA 酸化の責任分子であることを確認したが、母性 TET3 の欠損は卵形成、受精、初期発生、および産仔数への顕著な影響を与えず、胚発生に必須ではないことを明らかにした (Tsukada et al., 2015)。本成果は、これまでの概念と異なり、初期胚で起こるメチル化 DNA の酸化が胚発生に必要なゲノムリプログラミングに必須ではないことを示唆するものである。さらに、母性 TET3 欠損は受精胚の発生には必須ではないが、体細胞核移植胚の発生には必須であるというユニークなエピゲノム制御因子であ

ることも明らかにした。本成果は、受精胚と体細胞核移植胚が異なるメカニズムでゲノムリプログラミングを行っていることを示唆するものであり、これまで明らかにされていない体細胞核移植胚特異的ゲノムリプログラミング因子の発見となった（図）。
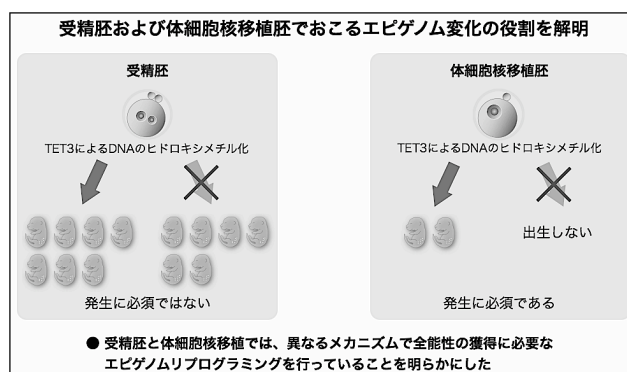
<研究の意義・展望>
　卵・着床前初期胚におけるエピゲノムダイナミクスについては、その観察までに留まる研究が多く、生理的役割・意義までを明らかにしている研究は少ない。本研究は、大方の予想に反し、初期胚で観察される雄性メチル化 DNA のゲノムワイドな酸化が、胚発生に必要なゲノムリプログラミングに必須ではないという意外な結果と世界初の体細胞特異的ゲノムリプログラミング因子の発見に繋がった。現在解析中のエピゲノム制御マシナリーの研究を継続し、ゲノムリプログラミングに必要なエピゲノム制御機構の全貌を明らかにしたい。

<主な研究発表論文>
Tsukada, Y., Akiyama, T., and Nakayama, K. I. (2015). Maternal TET3 is dispensable for embryonic development but is required for neonatal growth. Sci. Rep. *5*, 15876.

核移植技術を用いた生殖サイクルのエピジェネティクス変化の解析		平成 25-29 年
研究代表者	小倉淳郎	理化学研究所
	計画	バイオリソース研究センター
研究分担者	幸田　尚	山梨大学大学院総合研究部
		生命環境学域

＜研究の目的＞

　哺乳類の生殖サイクルにはいくつかの重要なエピジェネティクス転換期が存在する。ゲノムワイドな転換期として、受精、着床、そして生殖細胞分化が挙げられ、小規模でも発生に大きく影響を与えるものとして、ゲノム刷込みと X 染色体不活化が挙げられる。これらのエピジェネティクス変化の特徴を維持するために、ゲノム上には DNA メチル化、ヒストン修飾、クロマチン構造、核内コンポーネント構成などあらゆるエピジェネティクス制御が動員されると予想される。しかしこれらの直接的な解析のみで発生生物学的な意義に結びつけることは難しい。本研究の代表者小倉らは、着床、胎盤形成、生殖細胞分化など大きな転換期に依存するエピゲノム記憶は、卵子を用いた核移植では再プログラム化されにくいことを明らかにした。そこで、本研究では、クローン胚に受け継がれたドナー細胞ゲノム情報を時空間的に解析し、生殖サイクルにおけるエピジェネティクス変換期、特に着床と胎盤形成におけるエピジェネティクス変化を明らかにした。

＜研究成果＞

　これまでの解析により、体細胞クローン胚における *Xist* 遺伝子の異所性発現および H3K9me3 の残存が明らかになっている。そこで *Xist* ノックアウトおよび Kdm4d mRNA の注入を組み合わせることにより、これら 2 つの障害の除去を試みた。産子率（胚移植あたり）は卵丘細胞クローンで 18.7%、セルトリ細胞クローンで 23.5%まで改善し、これまでの最高値を得た(Matoba et al., 2018)。しかし、ICSI の産子率（60%以上）に比べると低いため、他の異常を検索したところ、H3K27me3 依存性のゲノム刷込みが消失(LOI)していることが明らかになった。
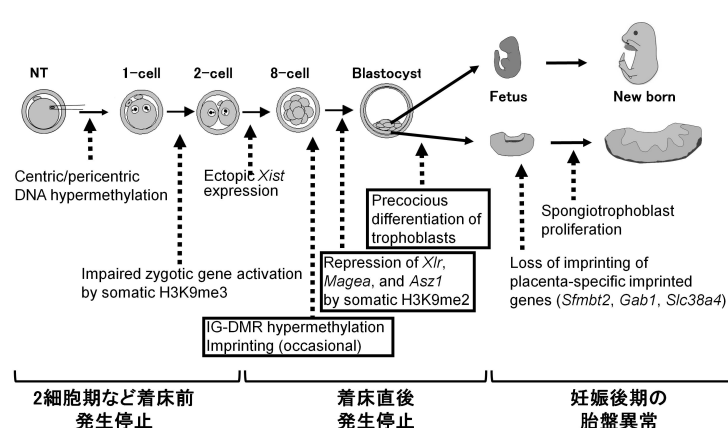
これらのうち少なくとも 5 つは胎盤特異的な刷込み遺伝子として働くため、体細胞クローン胎盤で両アリル性の発現になっていることが予想された。そこで体細胞核移植由来 trophoblast stem cell （TSC）を解析した結果、調査した *Sfmbt2*、*Slc38a4*、*Gab1* の

３遺伝子すべてが LOI により両アリル性発現になっていることを確認した。これらの異常がクローン胎盤の過形成の原因になっている可能性を探るため、母方ノックアウトドナー細胞を使って発現を正常化した。その結果、*Sfmbt2*、*Slc38a4*、*Gab1* いずれの発現を正常化させても胎盤の形態は異常なままであった。一方、*Sfmbt2* のイントロン 10 でクラスターを形成するマイクロ(mi)RNA 群 (Inoue et al. Cell Rep 2017)も、クローン胎盤において過剰発現（おそらく両アレル発現）をしていることが明らかになった。そこでこれらの miRNA 群を母方ノックアウトにより発現を正常化させたところ、クローン胎盤の重量が減少し、組織学的にも正常に近づくことが明らかになった。これらの miRNA 群のターゲット遺伝子は多数あるため、具体的な胎盤異常の原因となる coding 遺伝子は特定できていないが、本研究により初めてクローン胎盤の異常の原因が判明した。しかしながらいずれの遺伝子の母方ノックアウト体細胞クローンにおいても出生率は有意に上昇しなかった。今後、残っているクローン胚の主なエピジェネティクス異常である IG-DMR の高メチル化と一部の遺伝子の H3K9me2 残存などの影響を明らかにする予定である（上図の囲み）。

＜研究の意義・展望＞

　クローン胎盤異常の改善が出生率の向上につながらなかったことは意外であったが、本研究を通じて H3K9me3、H3K27me3、*Xist* 刷込みなどの生殖サイクルにおける意義を明らかにすることができた。今後、マウスクローンのさらなる改善により、哺乳類クローンの実用性向上に貢献するものと期待される。

＜主な研究発表論文＞

1. Hatanaka, Y., Inoue, K., Oikawa, M., Kamimura, S., Ogonuki, N., Kodama, E.N., Ohkawa, Y., Tsukada, Y., and Ogura, A. (2015) Histone chaperone CAF-1 mediates repressive histone modifications to protect preimplantation mouse embryos from endogenous retrotransposons. Proc. Natl. Acad. Sci. U. S. A. *112*, 14641-14646.
2. Hatanaka, Y., Tsusaka, T., Shimizu, N., Morita, K., Suzuki, T., Machida, S., Satoh, M., Honda, A., Hirose, M., Kamimura, S., Ogonuki, N., Nakamura, T., Inoue, K., Hosoi, Y., Dohmae, N., Nakano, T., Kurumizaka, H., Matsumoto, K., Shinkai, Y., and Ogura, A. (2017) Histone H3 methylated at arginine 17 is essential for reprogramming the paternal genome in zygotes. Cell Rep. *20*, 2756-2765.
3. Kaminuma, O., Katayama, K., Inoue, K., Saeki, M., Nishimura, T., Kitamura, N., Shimo, Y., Tofukuji, S., Ishida, S., Ogonuki, N., Kamimura, S., Oikawa, M., Katoh, S., Mori, A., Shichijo, M., Hiroi, T., and Ogura, A. (2017) Hyper-reactive cloned mice generated by direct nuclear transfer of antigen-specific CD4(+) T cells. EMBO Rep. *18*, 885-893
4. Inoue, K., Hirose, M., Inoue, H., Hatanaka, Y., Honda, A., Hasegawa, A., Mochida, K., and Ogura, A. (2017) The rodent-specific microRNA cluster within the *Sfmbt2* gene is imprinted and essential for placental development. Cell Rep. *19*, 949-956.
5. Matoba, S., Wang, H., Jiang, L., Lu, F., Iwabuchi, K.A., Wu, X., Inoue, K., Yang, L., Press, W., Lee, J.T., Ogura, A., Shen, L., and Zhang, Y. (2018) Loss of H3K27me3 imprinting in somatic cell nuclear transfer embryos disrupts post-implantation development. Cell Stem Cell (2018) *23*, 343-354.

| ゲノムインプリンティングと DNA メチル化の ダイナミクスと制御		平成 25-29 年
研究代表者	佐々木裕之	九州大学生体防御医学研究所 エピゲノム制御学分野
	計画	

＜研究の目的＞

　DNA メチル化などのエピゲノム修飾は、哺乳類の生殖細胞形成から受精後の初期発生にかけて大規模なリプログラミングを受ける。一方、ゲノム刷り込みにより確立された配偶子特異的な修飾（インプリント）や転移性遺伝因子（以下トランスポゾン）を抑制する修飾は、リプログラミングに抵抗して受精後の胚へ安定に継承される。この変化と継承の機構を明らかにすることを本研究の目的とした。そのため、微量サンプルへ適用可能な網羅的エピゲノム解析技術と微細な遺伝子変異を導入可能なゲノム編集技術を駆使した研究を行った。

＜研究成果＞

　まず、マウスの生殖細胞形成及び初期発生におけるエピゲノム変化を詳細に記述した。オスの生涯にわたる精子形成を支える精子幹細胞は、出生後の精巣で初めて出現する。我々は前駆細胞から精子幹細胞が分化する過程で、DNA メチル化と遺伝子発現がダイナミックに変化することを詳細に報告した（Kubo et al., 2015）。また、これらの細胞における非 CG メチル化と 5 ヒドロキシメチルシトシンのユニークな蓄積を発見した。一方、領域内の栗林ら（京大・斎藤通紀研）との共同研究により、培養下でマウスの多能性幹細胞から始原生殖細胞様細胞（PGCLC）を誘導する過程で、DNA メチル化と遺伝子発現が大規模に変化することを報告した（Shirane et al., 2016）。少数の細胞では把握が困難であった事実が初めて明らかになり、メスの多能性幹細胞及びそれから誘導された PGCLC では生体内で見られない極度の脱メチル化が生じることも判明した。

DNA methylation reprogramming during germ cell development in vitro

ESC / ICM → (Epiblast formation / Reorganization and elevation) → EpiLC / Epiblast → (Germ cell specification / Uniform erasure) → PGCLC / PGC

　さらに、マウスの卵巣体細胞との共培養により、ヒトの PGCLC から卵原細胞を誘導できることが分かり、この過程で生じるエピゲノムリプログラミングについても検討した。その結果、正常なリプログラミングであるインプリント消去が生じることを確認したほか、多能性幹細胞における DNA メチル化異常も正常に復することを明らかにできた（Yamashiro et al., 2018）。

　DNA メチル化を制御する因子の探索とメカニズム解明に関しては、始原生殖細胞で発現するヒストン H3K9 メチル化酵素 Setdb1 がゲノムの保護（トランスポゾンの抑制）と配偶子形成の両方に重要であること、DNA メチル化の促進因子である Dnmt3l が精子幹細胞の生存と維持に重要であること、精子形成過程におけるトランスポゾンの抑制機構は分化段階により転写後抑制（小分子 RNA）
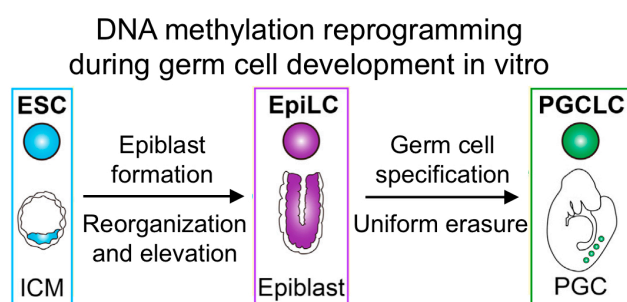
から転写抑制（DNA メチル化）へと切り替わることなどを発見した。また、領域内の仲野、中馬らとの共同研究により、卵子形成過程における小分子 RNA 生合成因子（MILI、PLD6 など）を同定し、その作用が精子形成過程のそれと異なることを明らかにした（Kabayama et al., 2017）。さらに、維持 DNA メチル化因子 Uhrf1 の卵子特異的な欠損マウスを作成し、この因子が初期胚における維持メチル化に必須の母性因子として働くことを示したほか、卵子由来の DNA メチル化酵素 Dnmt3a により胚ゲノムに導入された 5 メチルシトシンが、受精後のこの塩基の水酸化を誘導し、ゲノム全体のリプログラミングに一役買っているという想定外の発見もあった（Amouroux et al., 2016）。

　以上、主にマウスにおいて配偶子形成から初期胚に至るエピゲノムの変化を詳細に記述し、DNA メチル化の変化と維持に関わる因子を同定し、そのメカニズムの解明に貢献した。


＜研究の意義・展望＞
　哺乳類の卵子のような微量サンプルからも十分な質と量のオミックスデータを取得することができることを示し、この研究分野が新たな時代に入ったことを示した。目標のひとつであった新たな継承因子としての KRAB フィンガータンパク質の同定には至らず、必ずしも似た構造のタンパク質が似た機能を担うとは限らないという生物の本質を改めて実感した。

＜主な研究発表論文＞
1. Kubo, N., Toh, H., Shirane, K., Shirakawa, T., Kobayashi, H., Sato, T., Sone, H., Sato, Y., Tomizawa, S., Tsurusaki, Y., Shibata, H., Saitsu, H., Suzuki, Y., Matsumoto, N., Suyama, M., Kono, T., Ohbo, K., and Sasaki, H. (2015). DNA methylation and gene expression dynamics during spermatogonial stem cell differentiation in the early postnatal mouse testis. BMC Genomics *16*, 624.
2. Amouroux, R., Nashun, B., Shirane, K., Nakagawa, S., Hill, P.W., D'Souza, Z., Nakayama, M., Matsuda, M., Turp, A., Ndjetehe, E., Encheva, V., Kudo, N.R., Koseki, H., Sasaki, H., and Hajkova, P. (2016). De novo DNA methylation drives 5hmC accumulation in mouse zygotes. Nat. Cell Biol. *18*, 225-233.
3. Shirane, K., Kurimoto, K., Yabuta, Y., Yamaji, M., Satoh, J., Ito, S., Watanabe, A., Hayashi, K., Saitou, M., and Sasaki, H. (2016). Global landscape and regulatory principles of DNA methylation reprogramming for germ cell specification by mouse pluripotent stem cells. Dev. Cell *39*, 87-103.
4. Kabayama, Y., Toh, H., Katanaya, A., Sakurai, T., Chuma, S., Kuramochi-Miyagawa, S., Saga, Y., Nakano, T., and Sasaki, H. (2017). Roles of MIWI, MILI, and PLD6 in small RNA regulation in mouse growing oocytes. Nucl. Acids Res. *45*, 5387-5398.
5. Yamashiro, C., Sasaki, K., Yabuta, Y., Kojima, Y., Nakamura, T., Okamoto, I., Yokobayashi, S., Murase, Y., Ishikura, I., Shirane, K., Sasaki, H., Yamamoto, T., and Saitou, M. (2018). Generation of human oogonia from induced pluripotent stem cells in vitro. Science *362*, 356-360.

女性の生殖可能期間を支える原始卵胞活性化とエピゲノム修飾	平成 26〜27 年
研究代表者　　　　鈴木　仁美　　　　　東京医科歯科大学	
酵母	統合研究機構
研究分担者	

＜研究の目的＞
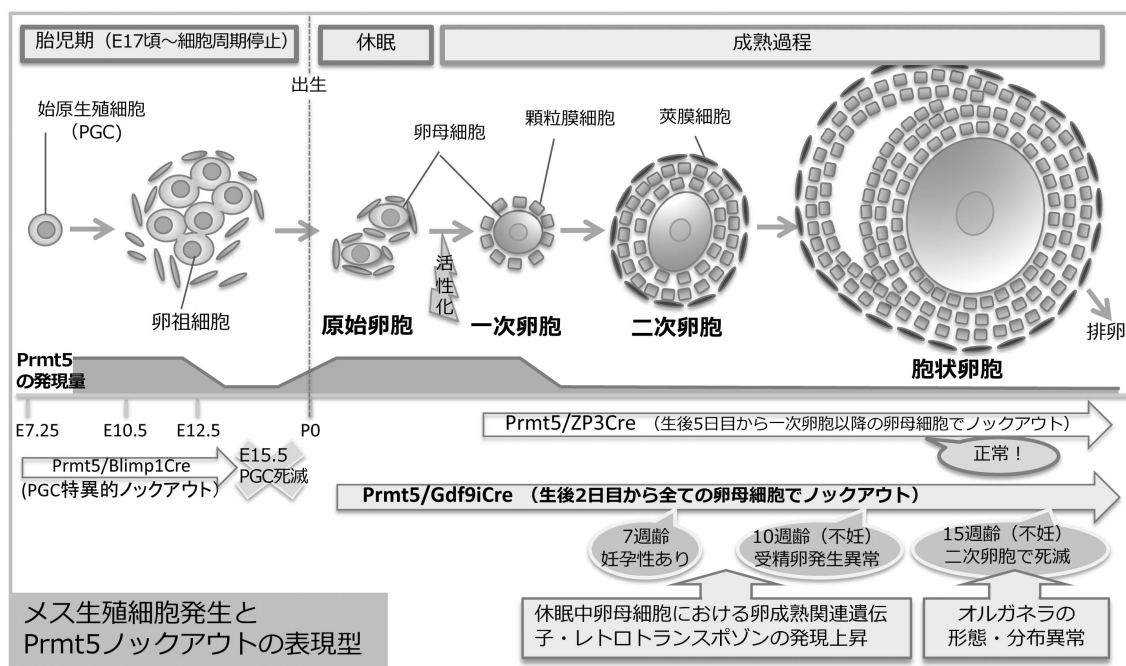
健康なヒト女性は約 40 年という長い生殖可能期間を維持する。これは未成熟な卵母細胞を含む「原始卵胞」を休眠状態で長期間維持し、その質を担保する機構が働いているからだ。哺乳類卵巣には様々な成熟段階の卵胞が存在するが、転写因子 Sohlh1 は最も未成熟な「原始卵胞」と、活性化して成熟段階初期に入った「一次卵胞」の卵母細胞にのみ発現し、原始卵胞活性化の抑制と活性化後の卵胞生存に必須であることが明らかになっている。申請者はこれまでに、マウス Sohlh1 の結合因子としてアルギニンメチル基転移酵素 Prmt5 を同定した。

タンパク質アルギニンメチル化酵素 Prmt5 は、始原生殖細胞（PGC）において発生初期から強く発現し、ヒストン修飾 H2A/H4R3Me2s を介した転写制御を行なっていることがしられている。Prmt5 を Blimp1-Cre でノックアウトした PGC はレトロトランスポゾンの上昇等によってゲノムインテグリティを失い死滅する。また、他の細胞においては、p53 や Foxo ファミリーといった転写因子をメチル化することによって転写活性の制御を行う機能があることが知られている。本研究の目的は、原始卵胞維持 Prmt5 の卵母細胞における生理的役割を明らかにすることである。

＜研究成果＞
　本研究では、Prmt5 が生後の卵母細胞においてもヒストン修飾 H2A/H4R3Me2s を介した転写制御に関与し、卵母細胞の生存とゲノムインテグリティに寄与していることを明らかにした。
　生殖細胞における Prmt5 の発現は、胎児期に一過的に減少するが、出生直前に再び上昇し、卵母細胞に強く発現することを発見した。卵母細胞における Prmt5 の発現は Sohlh1 と酷似しており、未成熟な休眠中原始卵胞と初期の一次卵胞にもっとも強く、二次卵胞までにほとんど消失することが明らかになった。そこで、一次卵胞からノックアウトする Prmt5/ZP3-Cre と原始卵胞からノックアウトする Prmt5/Gdf9-iCre を比較すると、Prmt5/ZP3-Cre がまったく正常で妊孕性に問題がなかったのに対し、Prmt5/Gdf9-iCre は 10 週齢頃から不妊を呈する早発性卵巣不全症様の表現型を示した。このとき、排卵された卵の 50%が減数分裂異常で受精不可能、残り 50%は胚盤胞までに死滅していた。Prmt5/Gdf9-iCre は 2 週齢までに Prmt5 がノックアウトされているが、ヒストンのメチル化修飾（H4/H2AR3Me2s）は 7 週齢まで保持され、9 週齢頃に消えていたことから、Prmt5 が卵母細胞におけるヒストン修飾の維持に寄与していることが強く示唆された。休眠中卵母細胞を FACS にてソートし、次世代シーケンサーによる解析をおこなったところ、本来なら休眠中卵母細胞では発現せず、活性化後の成熟過程にある卵母細胞で発現する遺伝子群が上昇していることが明らかになった。したがって、Prmt5 はヒストン修飾を介してこれらの遺伝子群の抑制を行うことで、休眠中卵母細胞のゲノムインテグリティを保障し、長期の休眠と生存に寄与しているのだと考えられる。
　本研究結果は現在論文投稿中である。

＜研究の意義・展望＞
　これまで Prmt 5 の卵母細胞における機能は無いと、Prmt5/ZP3-Cre ノックアウトマウスの解析によって主張されていた。しかし本研究では Prmt5/Gdf9-iCre ノックアウトマウスを使用することによって、Prmt 5 が休眠中卵母細胞のゲノムインテグリティの保持にあり、その生存に寄与していることを明らかにした。今後は ChIP-seq 等によって直接の転写調節標的を探索するとともに、結合因子である Sohlh1 との関係性について明らかにしていく必要があると考えている。

＜主な研究発表論文＞

1. <u>Suzuki H,</u> Dann CT, and Rajkovic A. (2013). Generation of a germ cell-specific mouse transgenic CHERRY reporter, Sohlh1-mCherry-Flag. Genesis *51*(1), 50-8.
2. Ren Y, <u>Suzuki H,</u> Jagarlamudi K, Golnoski K, McGuire M, Lopes R, Pachnis V, Rajkovic A. (2015). Lhx8 regulates primordial follicle activation and postnatal folliculogenesis. BMC Biol *13*(1), 39.
3. Hirate Y, Suzuki H, Kawasumi M, Takase HM, Igarashi H, Naquet P, Kanai Y, Kanai-Azuma M. (2016). Mouse Sox17 haploinsufficiency leads to female subfertility due to impaired implantation. Sci Rep. *6*, 24171

H3K9 脱メチル化エピゲノムによる生殖細胞の機能制御		平成 26-27 年
H3K9 脱メチル化エピゲノムによる生殖細胞の機能制御		平成 28-29 年
研究代表者	立花誠	大阪大学生命機能研究科
	公募	エピゲノムダイナミクス研究室

＜研究の目的＞

　1 つの受精卵から多細胞生物の体ができていく過程は、様々な細胞種における遺伝子発現プロファイルの経時的な変化の総和として捉えることができる。発生・分化特異的な遺伝子の発現には、エピジェネティック制御系が重要な役割を果たしている。ヒストン H3 の 9 番目のリジン残基（H3K9）のメチル化は分裂酵母からヒトまで高度に保存された転写抑制
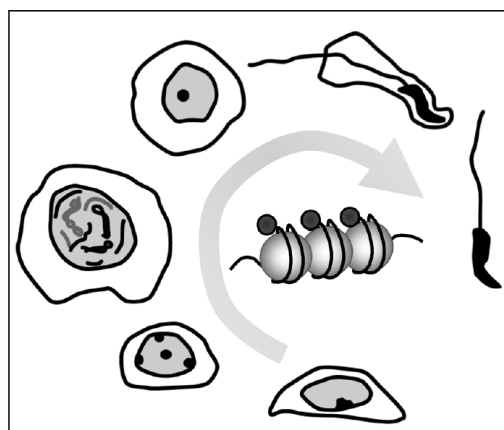
のピジェネティックマークである。申請者はこれまで、H3K9 メチル化エピゲノム構築系によるほ乳類の発生・分化制御の研究を進めてきた。

　本申請課題では、H3K9 の脱メチル化酵素が雄性生殖細胞の分化と機能をどのように調節しているのかについて細胞・分子レベルで明らかにする。生殖細胞の出現から配偶子形成に至る過程では、多彩なクロマチン修飾酵素によって時期・細胞特異的エピゲノムの確立・維持・消去がおこなわれる。なかでも、胎生期の雄性生殖細胞では H3K9 のメチル化レベルが体細胞に比べて顕著に低いことが、これまでの申請者らの研究によって明らかになっている。さらに、この H3K9 の低低メチル化は H3K9 メチル化酵素の発現では説明できず、積極的な脱メチル化の関与が推察された（Deguchi et al., *Biol. Reprod.* 2013）。よって本申請課題では、雄性生殖細胞の分化における H3K9 脱メチル化の役割を明らかにしていく。

＜研究成果＞

　H3K9 脱メチル化酵素である Jmjd1a とそのホモログである Jmjd1b に着目した。Jmjd1a と Jmjd1b のコンディショナルアリルを有するマウスを作製し、Vasa-Cre

マウスと交配した。得られたマウスの表現型を解析したところ、Jmjd1a と Jmjd1b の遺伝子量に依存した表現型を示すことが明らかになった。更に詳細な解析を進めたところ、Jmjd1a/Jmjdb 欠損マウスの雄性生殖細胞は生生後 15 日にはほぼ完全に欠落することが分った。この知見は雄性生殖細胞の維持に Jmjd1a と Jmjd1b が必須であることを意味した。生後 7 日目の Jmjd1a/Jmjd1b 欠損有性生殖細胞の性質を調べところ、cKit や PLZF といった典型的な spermatogonia（精原細胞）のマーカー遺伝子が発現しておらず、Jmjd1a と Jmjd1b を欠損させると機能的な spermatogonia ができないことを示唆した（図2）。さらに、prospermatogonia（前精原細胞）における Jmjd1a/Jmjd1b の機能を調べる目的で、生後 3 日目の雄性生殖細胞のトランスクリプトーム解析を行なった。Jmjd1a と Jmjd1b を欠損させると、Gfra1、Oct3/4、Plzf といった未分化性の維持に関わる遺伝子群の発現が軒並み低下していることが分った。以上まとめると、本研究は、Jmjd1 ファミリー分子の以下の機能を明らかにした。

1．prospermatogonia から spermatogonia への移行に必要である。
2．生殖細胞の未分化性を担保する遺伝子群の発現を正に制御する。

＜研究の意義・展望＞

　始原生殖細胞や精原細胞に比べ、prospermatogonia の生理機能は謎が多かったが、本研究は prospermatogonia の極めて重要な機能を解明した。このことは、生殖細胞の発生過程の理解を大きく前進させると考える。

　投稿に必要なデータは全て揃ったので、現在論文を執筆中です。「生殖エピゲノム」の領域の成果として、できるだけ早期に公表できればと思っています。

＜主な研究発表論文＞

1．Kuroki S, Okashita N, Baba S, Maeda R, Miyawaki S, Yano M, Yamaguchi M, Kitano S, Miyachi H, Itoh A, Yoshida M, **Tachibana M**. (2017). Rescuing the aberrant sex development of H3K9 demethylase Jmjd1a-deficient mice by modulating H3K9 methylation balance. PLoS Genet 13, e1007034.
2．Kuroki S, Nakai Y, Maeda R, Okashita N, Akiyoshi M, Yamaguchi Y, Kitano S, Miyachi S, Nakato R, Ichiyanagi K, Shirahige K, Kimura H, Shinkai Y, **Tachibana M**. (2018). Combined Loss of JMJD1A and JMJD1B Reveals Critical Roles for H3K9 Demethylation in the Maintenance of Embryonic Stem Cells and Early Embryogenesis. Stem Cell Reports 10, 1340-1354.

piRNA を介したエピゲノム操作法の開発とその利用		平成 26-27 年
研究代表者	宮川さとみ	大阪大学大学院生命機能研究科
	公募	時空生物学講座病因解析学

<研究の目的>

　遺伝子発現制御に、非コード RNA が重要な機能を有することが報告されている。我々は、胎仔期のマウス雄性生殖細胞において、生殖細胞特異的な非コード小分子 RNA である piRNA（PIWI interacting RNA）が、レトロトランスポゾン遺伝子の DNA メチル化に、そして、メチル化を介した遺伝子発現のサイレンシングに関与することを明らかにしてきた。その時期の piRNA の多くが、レトロトランスポゾン配列を持つこと、piRNA クラスターと呼ばれる遺伝子領域に由来すること、から、piRNA の産生には、レトロトランスポゾン配列に何らかの意義があるのではないか、また、piRNA クラスターに由来する長い RNA 転写産物が必要なのではないか、と考えられてきた。しかし、我々は、これに対して、単に、センス鎖とアンチセンス鎖の RNA が存在しさえすれば、piRNA の産生に必要十分ではないかという仮説を立て、EGFP 遺伝子のセンス鎖とアンチセンス鎖を発現するトランスジェニックマウスを用いたモデル系を構築した。予備的研究から、仮説通りに、このモデル系では、EGFP に対する piRNA が産生され、それを介した DNA のメチル化により EGFP 遺伝子のサイレンシングが生じる、という成果を得た。この研究を展開し、piRNA による遺伝子サイレンシングのメカニズムを詳細に解析していく。また、この方法論を用いて、内在性の遺伝子を piRNA 経路依存的にサイレンシングするシステムの開発をおこなう。

<研究成果>

　piRNA 依存的な遺伝子発現抑制機構をレトロトランスポゾン以外の遺伝子に応用できれば、雄性生殖細胞の発生・分化において特定の遺伝子に *de novo* DNA メチル化を生じさせ、遺伝子発現を抑制できるのではないかと考え、人為的

piRNA 誘導による遺伝子サイレンシングシステムの開発を試みた。胎仔期雄性生殖細胞において *EGFP* を発現するトランスジェニックマウスに、アンチセンス鎖の *EGFP* (*asEGFP*) を発現させると、*EGFP* の発現が piRNA 依存的に抑制された。そこで、次に、内在性の遺伝子にもこの方法論を利用できるかどうかを明らかにするため胎仔期雄性生殖細胞で発現する DNA メチル化酵素 *Dnmt3L* をターゲットにした実験をおこなった。胎仔期精巣においてアンチセンス鎖の *Dnmt3L* (*asDnmt3L*) を発現するトランスジェニックマウス（Tg-asDnmt3L）を作製したところ、*Dnmt3L* に対する piRNA が産生されること、その結果、*Dnmt3L* がサイレンシングされること、そして、DNMT3L 欠損マウスと同様に、精子形成の減数分裂期で形成不全が生じ、不稔になることが明らかとなった (Itou et al., 2015)。
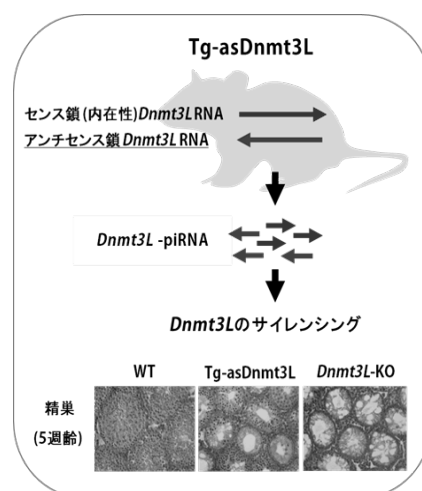
センス鎖とアンチセンス鎖の発現が重要という我々の主張に対して、piRNAクラスターとよばれるpiRNAが数多く産生されるゲノム領域にトランスジーンが挿入されており、そのクラスターからの転写がpiRNA産生に重要なのではないか、と指摘を受けたため、さらに解析を続けた。Tg-asDnmt3Lマウスにおけるトランスジーンのゲノム挿入部位を全ゲノムシークエンスにより解析したところ、18番染色体のqB3領域とqE1領域であることがわかった。挿入部位とサイレンシングの関係を明らかにするため戻し交配をおこない、片方のトランスジーンのみを持つマウス二系統を分離し、解析をおこなった。その結果、18qB3領域のみに挿入されたマウスはTg-asDnmt3Lマウスと同様に、精子形成が減数分裂期に停止する表現型を示したが、18qB3領域はpiRNAクラスターではないと考えられた。一方、18qE1領域はpiRNAクラスター領域と考えられるが、Dnmt3L遺伝子のサイレンシングは弱く精子形成は正常であった。このことは、これまで、「piRNAを介するサイレンシングにはpiRNAクラスター領域へのトランスジーンの挿入が重要である」と考えられてきたが、必ずしもそうではないと考えられた。
　さらに、トランスジーンが18qE1領域のみに挿入されたマウスでは、精子形成不全は生じていないにもかかわらず、DNMT3Lの標的遺伝子のメチル化の低下がみとめられた。

## ＜研究の意義・展望＞
　これまでの研究から、piRNAの前駆体となるためには、piRNAクラスターから転写されることが重要であると考えられている。ところが、この二系統のマウスはこれまでのpiRNA産生とpiRNAクラスターの関係から考えられる予想に反しており、その解析は、小分子RNA依存的な遺伝子サイレンシングのあらたなメカニズムの発見につながる可能性を秘めている。
　さらに、DNMT3Lのサイレンシングが弱い系統では、レトロトランスポゾンのDNAメチル化が低下しているにもかかわらず、精子形成が進んでいた。この系統のTg-asDnmt3Lマウスを用いれば、精子におけるDNAメチル化異常が、受精後に次世代のエピジェネティック状態や発生過程に与える影響を解析することが可能となると考えられる。

＜主な研究発表論文＞
1. Itou D, Shiromoto Y, Yukiho SY, Ishii C, Nishimura T, Ogonuki N, Ogura A, Hasuwa H, Fujihara Y, Kuramochi-Miyagawa S, Nakano T. (2015) Induction of DNA methylation by artificial piRNA production in male germ cells. Curr Biol. 25, 901-906.
2. Nagamori I, Kobayashi H, Shiromoto Y, Nishimura T, Kuramochi-Miyagawa S, Kono T, Nakano T. (2015) Comprehensive DNA Methylation Analysis of Retrotransposons in Male Germ Cells. Cell Rep. 12, 1541-1547.
3. Kojima-Kita K, Kuramochi-Miyagawa S, Nagamori I, Ogonuki N, Ogura A, Hasuwa H, Akazawa T, Inoue N, Nakano T. (2016) MIWI2 as an Effector of DNA Methylation and Gene Silencing in Embryonic Male Germ Cells. Cell Rep. 16, 2819-2828.

Max 遺伝子発現コントロールによる生殖細胞発生プログラム誘導の分子メカニズム	平成 26-27 年
MAX タンパク質の減数分裂抑制因子としての役割とその分子作用機序	平成 28-29 年

研究代表者	奥田晶彦	埼玉医科大学　ゲノム医学研究センター　発生・分化・再生部門
	公募	
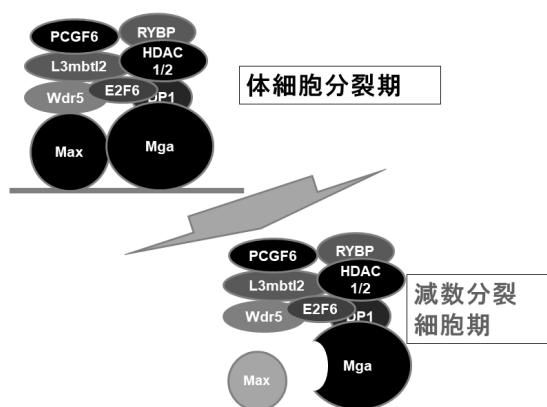
生殖細胞の体細胞分裂からの減数分裂への切り替え期でのPRC1.6複合体におけるMAX及びMGAの変化

＜研究の目的＞

減数分裂は生殖細胞固有の細胞分裂の様式である。但し、生殖細胞といえども、通常の細胞と同様に体細胞分裂を行う能力は有しており、特に未分化な状態では活発に体細胞分裂を繰り返している。従って、生殖細胞には、体細胞分裂を止めて減数分裂を開始する為の明確な分子基盤が存在する筈だが、そこにはレチノイン酸-*Stra8* の経路が関わっているということを除きほとんどわかっていない。私は、ES 細胞における Myc 全般の機能を明らかにすることを目的に MYC が転写因子として機能する上で必須なパートナー因子である MAX をコードする遺伝子についてホモ欠失 ES 細胞を樹立した。その結果、期待通りに ES 細胞の増殖速度低下であるとか細胞分化など Myc 全般の機能の低下に伴ったフェノタイプが観察された。しかし、それらの結果に加えて、生殖関連遺伝子群、中でも減数分裂に関わっている遺伝子群の高度な発現上昇という結果も得られた。後者の結果については予想していなかったものではあったが、その結果は、ES 細胞が生殖細胞でないにも関わらず減数分裂を開始する潜在能力を有するという新知見の確立につながることと、この *Max* ホモ欠失 ES 細胞を用いた実験系が生殖細胞における本来の減数分裂開始の機構の解明にも繋がる可能性が考えられたので、それら 2 点のことを研究目的として本公募研究を遂行することにした。なお、私は、公募研究員として 2 期に渡って活動させていただいたが、I 期目と II 期目についてはそれぞれ培養細胞とマウスを用いた研究を中心に研究を進めた。

＜研究成果＞

Max ホモ欠失 ES 細胞での減数分裂関連遺伝子の高度な発現上昇は、シナプトネマ複合体の主要コンポーネントの一つである SYCP3 に対する抗体を用いた免疫染色という細胞生物的な解析からも認められた。*Max* ホモ欠失 ES 細胞の中で免疫組織学的にも減数分裂様の変化を呈したのは全体の 5%程度で、そのほとんどは減数分裂開始後の極めて初期の段階に相当する Preleptotene を思わせる像を示したものであったが、中には、Leptotene、Zygotene 期と類似した像を示す

細胞も見られた。但し、明らかに Pachytene 期と断定できる像を呈する細胞は見当たらず、従って、Pachytene 期に入るか入らない段階で細胞は全て死滅していることが示唆された。このように、*Max* ホモ欠失 ES 細胞が呈する減数分裂様の変化は、減数分裂の極めて早い時期に破綻してしまっていることがわかったが、レチノイン酸-*Stra8* 遺伝子経路の存在に依存しているなど、この現象が、生殖細胞における生理的な減数分裂を忠実に反映していることを強く示唆するデータを数多く得ることができた。さらには、生殖細胞は、減数分裂を開始する際に、まさにこの MAX 依存的な減数分裂に対する抑制から解放されるべき生理的に *Max* 遺伝子の発現を下げていることも明らかにした。なお、生化学的・分子生物学的な解析から、私たちが見出した Max 依存的な減数分裂抑制機構には Myc は無関係で、6 種類の存在が知られている PRC1 複合体の中で最も非典型的と称される PRC1.6 複合体の中のサブユニットの一つとしての機能を反映していることが明らかになった(Suzuki et al., 2016)。

　マウス個体を用いた解析としては、*Max* 遺伝子コンディショナルノックアウトと生殖細胞特異的に CreERT2 を発現する Oct-3/4 promoter/CreERT2 トランスジェニックとの掛け合わせとタモキシフェン投与によって、本来減数分裂を起こさない胎生期にある雄の生殖細胞においても減数分裂関連遺伝子群の発現が高度に誘導されることを見出した。

　その他、PRC1.6 複合体の中での MAX に対するパートナーである MGA タンパク質をコードする遺伝子から、MAX とは相互作用できない MGA タンパク質をコードする *Mga* バリアントが、減数分裂時期にある生殖細胞で産生されていることを見つけた。従って、生殖細胞は、減数分裂を開始する際に、*Max* 遺伝子の発現を低下させるだけではない、MAX とは相互作用できない MGA タンパク質を作り出すことによっても PRC1.6 複合体の機能の不活化を達成していることが想定された。

＜研究の意義・展望＞

　減数分裂は成熟した精子・卵子を形成する上で最も重要なステップであるいっても過言ではないが、生殖細胞が体細胞分裂を止めて減数分裂を開始する為の機構については、そこにレチノイン酸-*Stra8* 遺伝子の経路が関わるということを除きほとんどわかっておらず、私たちは、MAX を含む PRC1.6 複合体がそれに深く関わっていることを見出した。この発見は、減数分裂開始の為の分子機構の解明の為の手掛かりになることは間違いなく、今後も、この発見を土台として、本機構の完全解明に努めたい。

＜主な研究発表論文＞

Suzuki, A., Hirasaki, M., Hishida, T., Wu, J., Okumura, D., Ueda, A., Nishimoto, M., Nakachi, Y., Mizuno, Y., Okazaki, Y., et al. (2016). Loss of MAX results in meiotic entry in mouse embryonic and germline stem cells. Nat Commun 7, 11056.

GS 細胞を用いた雄性エピゲノム形成の分子機構の解明と新規解析技術の開発	平成 26-27 年
研究代表者 　山中総一郎	慶應義塾大学
公募	医学部　分子生物学教室

＜研究の目的＞

　トランスポゾンとその残滓は、ヒトゲノムでは 45%もの領域を占める。トランスポゾンの持つ転移能は宿主個体に有害であり、特に生殖細胞におけるトランスポゾンの発現抑制は次世代への正確な遺伝情報の伝達を考えた場合に、生物にとって喫緊の課題である。一方、トランスポゾンが初期発生の時期に必要な遺伝子群のプロモーター活性を制御することがこれまでに明らかになっており、「トランスポゾンによる能動的なクロマチン構造制御」に関しても研究が盛んに行われている。特に受精直後の受精卵において、特定のトランスポゾンの働きを抑えると、それが発生異常を引き起こすことが知られている。以上の現象は、個体進化の過程でゲノムに侵入したトランスポゾンを、ホストが自己のシステムの一部として取り込んできたことを端的に示している。では、この「非自己から自己への変換」は"いつどこで"起きているのだろうか。以上の謎を解明するために、私は、胎児生殖細胞のエピゲノム形成とトランスポゾンとの関係を明らかにすることに加えて、ゲノム上のトランスポゾン認識因子を生化学的に同定する手法の開発に取り組んできた。

＜研究成果＞

　本研究で私は、以下の二種類の方向性で生殖細胞のエピゲノムの解析を試みた。

(1)ゴノサイトエピゲノムの解析
哺乳類の生活環の中でゲノムワイドなリプログラミングは二度起こる。一度目は受精卵、そして二度目は生殖細胞で起こる。その結果、胚盤胞と胎生 13.5 日目 (E13.5)の生殖細胞でゲノムのメチル化レベルは基底状態となる。その後生殖細胞では、ゴノサイトの時期にゲノムワイドなメチロ

(1) ゴノサイトエピゲノムの解析

E13.5　　E17.5　　P0　　P2

ChIP-seq, ATAC-seq, RNA-seq, Hi-C

(2) トランスポゾン認識因子の解析手法の開発

トランスポゾン認識因子

トランスポゾン　TALE　Flag

免疫沈降

ームが確立する。メチロームの形成は発生に必須であり、この過程に重要な働きを持つ Dnmt3a や Dnmt3l を欠失させた個体はそれぞれ胚性致死や不稔の表現型を示す。そこで、ゴノサイトでのクロマチン状態遷移を次世代シーケンサをベースにした手法で解析した結果、E17.5 というタイミングで一過的に開いたクロマチン構造を取るゲノム領域を発見し、それを Differentially Accessible Domain(DAD)と名付けた。また、DAD は体細胞期ではヘテロクロマチン構造を取
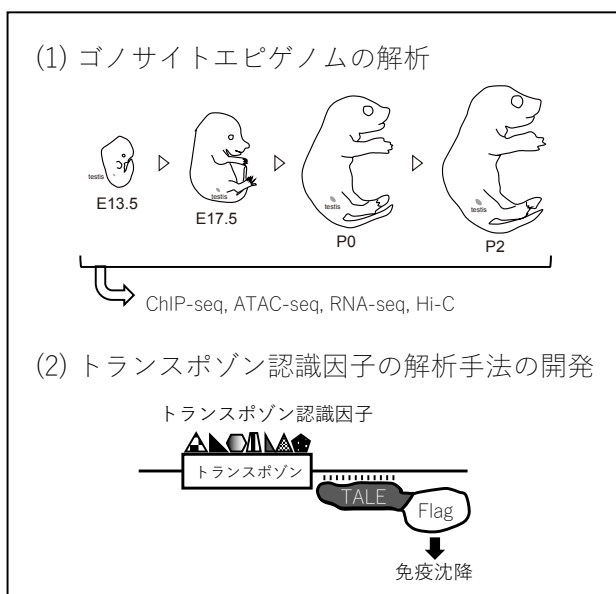
っているが、ゴノサイトの時期にユークロマチン構造となる。これらに加えて、以下の4つの実験結果を得ている。1)DADはゲノム上の「遺伝子砂漠」や「遺伝子クラスター」上に形成される。2)DADにおいてトランスポゾンのプロモーター領域が特に「開いたクロマチン構造」を取る。3)DAD領域が緩んだ後、当該領域のDNAメチル化が誘導される。4)ゴノサイトクロマチンの3D構造が一過的に緩む。

　体細胞で親細胞のエピゲノム状態は、DNA複製の際に働く機構によって娘細胞でも維持される。ゲノム上のコンパクトなクロマチン領域であるヘテロクロマチンでも、複製フォーク上でそのゲノムが一時的にほどかれる。この局所的なクロマチンの緩みにより、ヘテロクロマチン状態を維持する酵素群が娘鎖に一時的に接近できる。しかし、細胞周期アレストを起こしているゴノサイトにはS期に依存する緩みが存在せず、いかにしてメチロームが確立しているか謎であった。今回の私の実験結果は、ゴノサイトのクロマチンがダイナミックに緩むことでDNAメチル化酵素を呼び込んでいるというモデルを支持する。

(2)トランスポゾン認識因子の解析手法の開発
培養細胞を用いて、ゲノム上の特定領域に存在するタンパク質群を生化学的に同定する手法の開発に取り組んできた。CRISPR/Cas9を用いて配列特異性を持たせ、それを細胞に導入、および細胞固定をした後に、Cas9を免疫沈降し、共沈するタンパク質群を同定した。現在までに、クロマチンに結合するタンパク質群を純度良く精製することに成功している。しかし、依然として配列特異的なタンパク質群を発見するまでに至っていない。

＜研究の意義・展望＞
　ゴノサイトのクロマチン状態を詳細に解析した結果、予想に反してこの時期のクロマチン状態が極めてダイナミックに変動していることがわかった。今後、ゴノサイトのクロマチン状態を制御する因子群の同定を行うことで、この時期のクロマチン状態が果たす生殖能への役割の全貌を解明していきたい。
　上記研究結果の(2)に相当する部分では、近年CRISPR/Cas9とAPEXを組み合わせた研究手法が発表された。これにより、配列特異的にクロマチンタンパク質を同定することに成功している。しかし当該手法においては、テロメアタンパク質などゲノム上でリピートを形成しているゲノム領域を標的としている。そこで、今後私はCRISPR/Cas9-APEXによる手法を取り入れるとともに、単一のゲノム領域に対してもこれを応用していきたい。

＜主な研究発表論文＞
Yashiro, R., Murota, Y., Nishida, K.M., Yamashiro, H., Fujii, K., Ogai, A., Yamanaka, S., Negishi, L., Siomi, H., and Siomi, M.C. (2018). Piwi Nuclear Localization and Its Regulatory Mechanism in Drosophila Ovarian Somatic Cells. Cell Rep 23, 3647–3657.

始原生殖細胞によるエピゲノムリプログラミング 始原生殖細胞によるエピゲノムリプログラミング とその人為的制御		平成 26-27 年 平成 28-29 年
研究代表者	関　由行	関西学院大学理工学部 生命医化学科
	公募	

＜研究の目的＞

　生殖細胞は次世代へ遺伝情報を伝達するのみならず、ゲノムに後天的に付加された化学修飾、いわゆるエピゲノム情報を初期化することで全能性を獲得し、次世代の個体形成を保証している（エピゲノムリプログラミング）。生殖細胞の発生、分化、成熟、受精過程には様々なエピゲノムリプログラミング機構の存在が報告されているが、特に、始原生殖細胞の形成、分化過程及び受精直後にはDNAの脱メチル化などエピゲノム情報の大規模な再編成が起こる。これらの段階におけるエピゲノムリプログラミングの実体については明らかになりつつあるが、その分子基盤並びに生物学的意義については不明な点が多い。そこで、本研究では始原生殖細胞におけるエピゲノムリプログラミングを制御する分子基盤を同定し、さらにその分子基盤の一部を人為的に改変することで、エピゲノムリプログラミングの持つ生命機能の解明を目指した。

＜研究成果＞

　我々は以前、転写因子 Prdm14 が始原生殖細胞特異的に発現し、機能的にも始原生殖細胞の初期発生に重要であることを示していたが、詳細な分子機構は未知であった。Prdm14 は in vivo においてエピブラストに発現し、始原生殖細胞形成を誘導する。そこで、ES 細胞をエピブラストと性質が類似しているエピブラスト様細胞（EpiLC）に分化させた後に、人為的に Prdm14 を発現させることで、*in vivo* と同じ環境を *in vitro* で再現し、その後の変化を解析した。Prdm14 を EpiLC に発現させた 2 日後に細胞の形態が ES 細胞に類似した形態へと変化し、この細胞をヌードマウスの皮下に移植したところ、3 胚葉への分化が確認された。さらに、遺伝子発現パターン変化をマイクロアレイで解析したところ、ES 細胞と同様の遺伝子発現パターンを示したことから、EpiLC に Prdm14 を発現させ接着培養を行うことで、ES 細胞への脱分化を誘導できることを明らかにした（Okashita et al., 2016）。

　Prdm14 は、メチルシトシンの酸化反応を介して能動的に DNA を脱メチル化する活性があったため、PRDM14 による能動的脱メチル化反応と ES 細胞への脱分化誘導活性の関係を検証した。その結果、PRDM14 は多能性関連遺伝子の転写制御領域に存在する DNA メチル化を脱メチル化すること
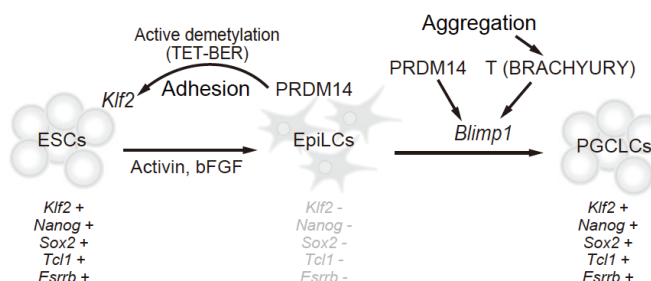
で、OCT3/4 による転写活性を促進することを見出した。この結果から、始原生殖細胞によるエピゲノムリプログラミング機構は多能性獲得に重要なステップであることが明らかとなった。

PRDM14 は、標的遺伝子に対応して転写活性と転写抑制活性を使い分けている。そこで、標的領域依存的な機能切替機構を解明するために、PRDM14 の複合体解析を行った。その結果、ポリコーム複合体（PRC2）と結合する転写制御因子 CTBP2 を同定することに成功した。PRDM14 による転写制御における CTBP2 の機能解析を行うために、CTBP1/2 欠損 ES 細胞を用いて解析したところ、PRDM14 は、CTBP2 との結合を介して PRC2 をリクルートすることで、転写抑制を行なっていることが明らかとなった。

＜研究の意義・展望＞

転写因子 PRDM14 は、マウスでの発現パターンや機能解析の結果をみると始原生殖細胞のためだけに重要な因子であると推測していた。しかしながら、今回の研究成果から、PRDM14 は始原生殖細胞形成よりもむしろ多能性細胞の誘導・維持に重要な因子であることが考えられる。興味深いことに、近年の他の哺乳動物であるヒトやブタなどの解析から、PRDM14 は始原生殖細胞よりもエピブラストで高発現していることが示されており、むしろマウスでの発現や機能がげっ歯類特異的な側面を見ている可能性が高いのではないかと考えている。また、我々の解析から原始的な後口動物のナメクジウオの初期胚において Prdm14 は多能性細胞や生殖細胞では全く発現しておらず、運動ニューロンで発現していることも見出しており、この運動ニューロンでの発現はゼブラフィッシュでも保存されている。この様な Prdm14 の進化的発現比較から、四肢動物の出現前後で Prdm14 の発現が多能性細胞で「転用」され、また、哺乳類の出現後にげっ歯類特異的にエピブラストでの発現を消失した可能性が考えられる。げっ歯類の初期胚は他の哺乳動物とは異なり、円筒形の特殊なエピブラスト構造を持ち、初期胚の遺伝子発現パターンがヒトやサルなどと大きく異なることが示されつつある。したがって、今後、運動ニューロンから多能性細胞への変化、またげっ歯類特異的なエピブラストでの発現消失機構を解明することで、げっ歯類特異的な初期胚形態及び遺伝子カスケード獲得の進化的経緯の解明に繋がることが期待できる。

＜主な研究発表論文＞

1.Okashita, N., Suwa, Y., Nishimura, O., Sakashita, N., Kadota, M., Nagamatsu, G., Kawaguchi, M., Kashida, H., Nakajima, A., Tachibana, M., Seki Y. (2016). PRDM14 Drives OCT3/4 Recruitment via Active Demethylation in the Transition from Primed to Naive Pluripotency. Stem Cell Reports *7*, 1072-1086.

2. Seki, Y. (2018). PRDM14 Is a Unique Epigenetic Regulator Stabilizing Transcriptional Networks for Pluripotency. Front Cell Dev Biol *6*, 12.

発生転換点におけるエピゲノム機能制御とヒト-マウス比較エピゲノミクス		平成 26-29 年
研究代表者	阿部訓也	理化学研究所バイオリソース研究センター
	公募	

<研究の目的>

　本研究では、初期胚に存在する多能性細胞から、始原生殖細胞、配偶子へと至る一連の細胞系譜で働く遺伝子の機能解析、網羅的遺伝子発現解析、さらに DNA メチル化等のエピゲノム解析を実施し、この細胞系譜の発生過程において劇的にエピゲノムが変動する「変曲点」を同定する。本研究では、これまで培った微量遺伝子発現解析、微量エピゲノム解析、イメージング技術等の新手法を駆使し、これらの変曲点における時空間的エピゲノムダイナミクスとその意義を追求することを目的とする。具体的には、1) 着床前後のマウス胚を構成する各組織、およびその in vitro モデルである多能性幹細胞の naive-primed 転換過程の遺伝子発現を詳細に解析するとともに、その制御に関わるエピゲノム状態を検索し、胚発生の「青写真」作成のためのエピゲノム制御に対する理解を深める、2) gonocyte から未分化精原細胞へ至る雄性生殖細胞の発生プロセスと GS 細胞における遺伝子発現プロファイルを詳細に比較検討することにより、生殖幹細胞の維持・分化に必要な遺伝子群の同定とそのエピゲノム発現制御に関する知見を得ることを目指す。

<研究成果>

　1) 着床前後における遺伝子発現変動と naïve-primed 転換過程の一細胞オミックス解析

　着床前後のマウス胚を構成する各組織を単離し、その発現プロファイルを解析した結果、内部細胞塊からエピブラストが形成される過程で、大規模な遺伝子発現変動が起きており、特に着床直後の 4.5 日胚のエピブラストにおける発現プロファイルは、3.5 日胚や 5.5 日胚の多能性細胞の発現プロファイルと大きく異なっていることが見出され、子宮への着床を契機に多能性細胞系譜ではその細胞特性が一過性に大きく変化していることが示唆された。この細胞特性の変換プロセスを詳細に解析するためのモデル実験系として、Wnt シグナルの阻害剤を用いることにより、naïve 型幹細胞であるマウス ES 細胞から primed 型幹細胞である EpiSC 様細胞を高効率で誘導する実験系を確立することに成功した。この in vitro 実験系を用いて、雌 ES 細胞から EpiSC 様細胞への分化誘導を行い、その過程のシングルセル RNA-Seq 解析およびエピゲノム解析を実施し、クラスター解析や差次的発現遺伝子の検出等の情報学的解析を行った。その結果、naïve-primed 変換過程において、細胞集団中の個々の細胞の発現プロファイルの多様性が一過的に増大し、その後、primed 型へと収束していくことが認められた。偽時間推定および t-SNE 解析により、この変換プロセスにおいては、ES、EpiSC と異なる細胞集団が少なくとも 2 つ存在することが明らかとなった。一つは、エピゲノム再編の代表的な事例であるランダム X 染色体不活性化が開始す

る直前の細胞群に相当し、もう一つはX染色体不活性化が完了し、primed 型への移行が進んでいる細胞集団であった。しかし、この後者の細胞集団は、EpiSC に類似しているが、その発現プロファイルは完全に一致しておらず、特に上皮間充織転換に関わる遺伝子の発現が異なっており、いわゆる ES と EpiSC の中間の性質を維持し、継代可能な新規多能性幹細胞であることが示唆された。最近、naïve と primed の中間段階にある細胞状態として、formative 型細胞が提唱されているが(Smith A., Development, 2017)、今回我々が得た EpiSC 様細胞は、これまで仮想的な存在であった formative 型多能性細胞の実態を追究するための非常に有効な材料となる可能性が示唆された。

　以上述べた 2 つの細胞集団は、これまで用いられていた細胞集団のマス解析では発見不可能であり、1 細胞解析の技術的有効性が改めて確認された。

2）naïve-primed 転換過程における DNA メチル化の意義の解明
naïve-primed 転換過程に特徴的なエピゲノム変動として、ゲノムワイドな DNA メチル化の増大が知られている。このゲノム修飾変化の意義を調べるため、3 種の DNA メチル化転移酵素を欠損した ES 細胞（TKO ES)から、EpiSC 様細胞を誘導可能かを検討した。DNA メチル化は、naïve 型細胞の自己複製には必須ではないが、細胞分化には必要であると予想されていたが、驚くべきことに形態的に EpiSC に酷似した EpiSC 様細胞株(TKO EpiSC)を樹立することが可能であった。この細胞は EpiSC と類似した発現プロファイルを有しているが、DNA メチル化は完全に喪失していた。しかし、この細胞の分化能を検討したところ、通常の EpiSC は Gata6 遺伝子を導入しても胚体外内胚葉細胞へ分化することは出来ないが、TKO EpiSC では Gata6 導入による胚体外内胚葉への分化誘導が可能であった。これらの結果から、DNA メチル化の増大は EpiSC 様細胞の分化誘導自体には不要と考えられるが、primed 型幹細胞の分化能を制限するための epigenetic barrier の形成に必要であることが示唆された。

3)精原細胞分化、GS 細胞におけるシングルセル遺伝子発現解析
gonocyte から精原細胞への分化プロセスの詳細な記述を目指し、受精後 17.5 日の胎児、生後 1 日、3 日、7 日の精巣から生殖細胞、および精原細胞から樹立される生殖幹細胞（GS 細胞）について、1 細胞レベルの RNA-Seq 解析を実施した。総計 977 個の細胞の解析の結果、これらの細胞は 9 つの集団に分類され、3880 の差次的発現遺伝子が検出された。生後 1 日の生殖細胞は gonocyte と未分化精原細胞の中間段階にあり、GS 細胞は未分化精原細胞に類似した発現プロファイルを持つことが明らかとなった。また、生後 3 日、7 日の生殖細胞は、いわゆる spermatogonial stem cells と progenitor 細胞に大別されるが、GS 細胞もこの 2 種類の細胞が混在する不均一な集団であり、培養条件等により、その比率が変動することが示唆された。

　この度得られた結果は、今後の生殖幹細胞の維持・分化に必要な遺伝子群の同定と機能解析のための重要な基礎的情報として利用されることが期待される。

ヒト生殖細胞のエピゲノムダイナミクスとその制御機構		平成 26-27 年
研究代表者	岡江寛明	東北大学大学院医学系研究科
	公募	情報遺伝学分野

＜研究の目的＞

DNA メチル化は核のリプログラミング、ゲノムインプリンティング、X 染色体不活性化、レトロトランスポゾンの抑制などに必須であり、その異常は様々なヒト疾患の原因となる。DNA メチル化状態は体細胞では比較的安定に維持されるが、生殖細胞および初期胚ではダイナミックに制御される。本研究開始時において、マウス生殖細胞および初期胚の DNA メチル化の全体像は既に明らかとなっていたが、ヒトでの解析はほとんど進んでいなかった。そこで、ヒト初期発生過程における DNA メチル化ダイナミクスを明らかにすることを目的に、次世代シーケンサーを用いた一塩基解像度でのゲノムワイドな DNA メチル化解析を行った。

＜研究成果＞

ヒト生殖細胞および初期胚の全ゲノムバイサルファイトシークエンシング解析を行い、ゲノム中の全 CpG サイトのうち 87-96%について DNA メ

ヒトとマウスの初期発生過程におけるDNAメチル化ダイナミクス
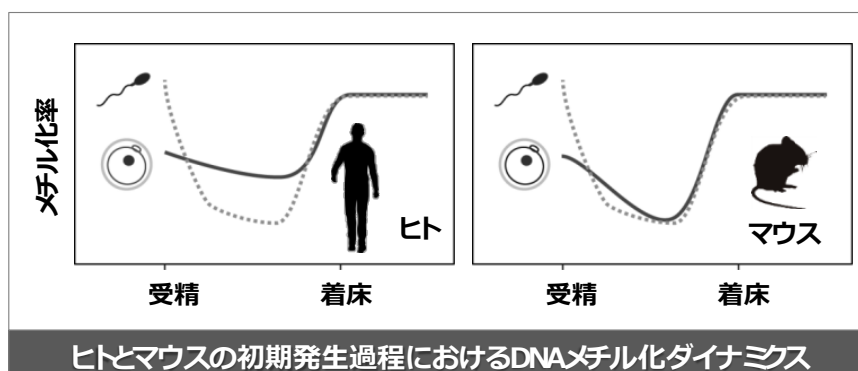
チル化率を決定した。卵子、精子、胚盤胞における平均メチル化率はそれぞれ 54、76、 26％であり、受精前後で DNA メチル化状態が大きく変化することを見出した。次に、インプリント領域・CpG island・リピート配列・プロモーター・Gene body などに着目し、受精後の DNA メチル化状態の経時的変化を詳細に解析した。その結果、①雄性ゲノムに比べて雌性ゲノムの脱メチル化の程度は非常に弱いこと、②ヒトには生殖細胞で獲得されるインプリント領域が少なくとも 46 領域存在し、このうち 15 領域は胎盤のみで維持されること、③SVA などのタンデムリピートを含むトランスポゾンが雄性ゲノムの脱メチル化から特異的に保護されること、④卵子では転写領域が高メチル化状態であり、他の領域は低メチル化状態であることなどを明らかにした。また、マウスとの比較を行い、ヒトではマウスに比べて雌性ゲノムの脱メチル化の程度が非常に弱いこと、ヒトではマウスの 2 倍程度のインプリント領域が存在すること、ZFP57 や DNMT3L などの DNA メチル化制御因子の発現パターンがヒトとマウスで大きく異なることを明らかにした（Okae et al., 2014, Hamada et al., 2016）。

＜研究の意義・展望＞

これまでにもヒト卵子や着床前胚の部分的な DNA メチル化解析は行われて

いたが、全ゲノムレベルでの解析に成功したのは本研究が初めてである。本研究の成果は、ゲノムインプリンティングの確立・維持機構、初期胚におけるユニークな遺伝子発現制御、世代を超えたエピジェネティック変化の遺伝などを理解するための重要な基盤となる。さらに、ヒト生殖補助医療の安全性評価や改良にも貢献すると期待される。今後はヒト・マウス以外の哺乳類における DNAメチル化ダイナミクスを解析することにより、哺乳類の受精後 DNA メチル化リプログラミングの共通原理を明らかにしていきたい。

＜主な研究発表論文＞

1. Okae, H., Chiba, H., Hiura, H., Hamada, H., Sato, A., Utsunomiya, T., Kikuchi, H., Yoshida, H., Tanaka, A., Suyama, M., and Arima, T. (2014). Genome-wide analysis of DNA methylation dynamics during early human development. PLoS Genet. *10*, e1004868.

2. Hamada, H., Okae, H., Toh, H., Chiba, H., Hiura, H., Shirane, K., Sato, T., Suyama, M., Yaegashi, N., Sasaki, H., and Arima, T. (2016). Allele-specific methylome and transcriptome analysis reveals widespread imprinting in the human placenta. Am. J. Hum. Genet. *99*, 1045-1058.

3. Kobayashi, N., Okae, H., Hiura, H., Chiba, H., Shirakata, Y., Hara, K., Tanemura, K., and Arima, T. (2016). Genome-scale assessment of age-related DNA methylation changes in mouse spermatozoa. PLoS One *11*, e0167127.

4. Kobayashi, N., Miyauchi, N., Tatsuta, N., Kitamura, A., Okae, H., Hiura, H., Sato, A., Utsunomiya, T., Yaegashi, N., Nakai, K., and Arima, T. (2017). Factors associated with aberrant imprint methylation and oligozoospermia. Sci. Rep. *7*, 42336.

5. Okae, H., Toh, H., Sato, T., Hiura, H., Takahashi, S., Shirane, K., Kabayama, Y., Suyama, M., Sasaki, H., and Arima, T. (2018). Derivation of human trophoblast stem cells. Cell Stem Cell *22*, 50-63 e56.

マウス・ゲノム刷り込み制御配列のエピゲノムダイナミクス		平成 26-27 年
研究代表者	谷本啓司	筑波大学生命環境系
	公募	ゲノム情報生物学

＜研究の目的＞
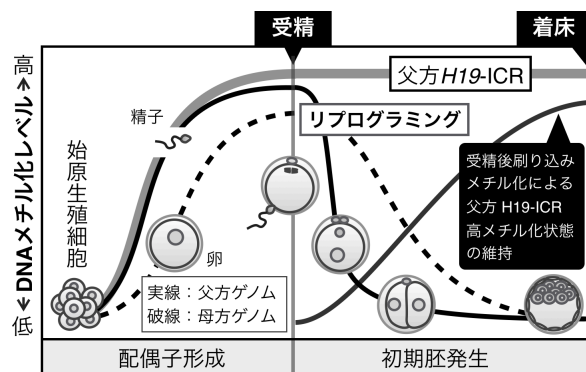
哺乳動物の一部遺伝子は、由来する親の性別に依存した片親性発現を示し、ゲノム刷り込みと呼ばれる。これら刷り込み遺伝子座の近傍には、アリル間で DNA メチル化状態の異なる領域が存在し、Differentially Methylated Region (DMR)と呼ばれる。DMR の非対称性メチル化は生殖細胞形成時に確立し、受精後も維持されることで、刷り込み遺伝子発現の分子基盤となる。一方、精子や卵は、それぞれが高度に分化した細胞であるため、独自のエピゲノム修飾を受けており、DNA のメチル化状態も大きく異なる。しかしながら、受精後、リプログラミングの過程で両アリルの DNA メチル化状態は低下し、エピゲノムの非対称性は解消される。初期胚発生過程のこのような環境下で、刷り込み遺伝子座の DMR のみが、いかにして DNA メチル化の非対称性を維持できるのかについてはよく分かっていなかった。

Igf2/H19 遺伝子座における刷り込み遺伝子発現の基盤は、遺伝子座中央に位置する DMR、すなわち Imprinting Control Region (*H19*-ICR)のアリル特異的な DNA メチル化である。同配列は精子特異的にメチル化され、同修飾は受精後も維持されることから、この刷り込みメチル化こそが、由来する親の性を見分けるためのマークであると考えられている。申請者は、トランスジェニック・マウス(TgM)を用いることで、「2.9-kb の *H19*-ICR 配列内に、刷り込みメチル化に必要・十分な情報が存在するが、アリル特異的メチル化は受精後に起きる」ことを発見し、同現象を受精後刷り込みメチル化と命名した(Tanimoto *et al.*, 2015)。

そこで、本研究の目的を「精子における *H19*-ICR エピゲノム刷り込みの分子メカニズム理解のために、受精後刷り込みメチル化に必要十分な DNA 配列を特定し、また、受精後刷り込みメチル化の生物学的意義を明らかにすること」とした。

＜研究成果＞

本研究で我々は、精子での DNA メチル化が起こらない TgM の系を用いることで、受精後刷り込みメチル化に必要な配列を 765-bp の範囲に限定した(Matsuzaki *et al.*, 2015)。さらにその後、多数の欠失変異体 TgM や内在遺伝子座のノックアウト・マウスを作製・解析することで、その範囲をさらに限局することに成功した。一方、受精後刷り込みメチル化活性をもつ人工 DMR の作製もおこなった。刷り込みメチル化は受けないものの、*H19*-ICR と CpG 配列の含量

が似ている λ-DNA に対して、*H19*-ICR 由来の特定 *cis* DNA 配列を移植した結果、母方アリルの低メチル化状態の確立と維持には、CTCF と Oct/Sox 因子の結合配列で十分なこと、父方アリルの高メチル化状態の受精後確立と維持には、上記 765-bp 中の、478-bp 配列で十分なことが分かった（Matsuzaki *et al.*, 2018）。

　次に、受精後刷り込みメチル化現象の生物学的意義の検証を行った。同目的のために、先述の 765-bp 必要配列をマウス内在遺伝子座より欠失するアリルを作製した。同変異型アリルを母親から受け継いだ場合、*H19*-ICR は野性型のそれと同様に、低メチル化状態であった。一方で、精子における変異型 *H19*-ICR のメチル化レベルは正常に高かったが、受精後、維持されるはずの *H19*-ICR の高メチル化レベルが、変異型では部分的に低下し、ゲノム刷り込み発現も破綻（*Igf2* 遺伝子の発現低下と *H19* 遺伝子の発現上昇）した。さらにこの結果、同マウスは成長遅延をおこした（Matsuzaki *et al.*, 2015）。以上の結果から、*H19*-ICR 配列の受精後刷り込みメチル化活性は、受精後の積極的な脱メチル化（リプログラミング）に抗して同配列を *de novo* メチル化することで、同配列のアリル間で非対称的な DNA メチル化の維持に関わるという生物学的意義を見いだせた。

<研究の意義・展望>
　我々による受精後刷り込みメチル化現象の発見の後、刷り込みメチル化の本質は「生殖細胞でのランダムなメチル化と、受精後のアリル特異的な維持」という理解へと変わっていった。しかし、アリル特異的に DNA メチル化が生き残るためには、受精後にアリルの区別が必須であり、DMR には DNA メチル化以外のエピジェネティック・マークが付加される可能性が考えられる。今後、精子で *H19*-ICR 配列に付加される、未知のマークの探索を行う。

　また我々は、TgM において、人工 DMR が *H19*-ICR と同様に、受精後、アリル特異的にメチル化されることを見いだした。そこで、人工配列を内在 *H19*-ICR と置換することで、精子においてメチル化されるようになるのか、その機能同等性を検証する。

　さらに、受精後刷り込みメチル化に必須の 478-bp 配列を介して機能する *trans* 因子を同定することで、同メカニズムの全貌を明らかにしたい。

　最後になりましたが、本領域に参加させていただいたおかげで、生殖細胞や初期発生、エピゲノムを専門とされる先生方から、たくさんの有り難いご助言をいただけましたこと、大変感謝いたします。

<主な研究発表論文>
1. Matsuzaki, H., Okamura, E., Takahashi, T., Ushiki, A., Nakamura, T., Nakano, T., Hata, K., Fukamizu, A., and <u>Tanimoto, K.</u> (2015). *De novo* DNA methylation through the 5′-segment of the *H19* ICR maintains its imprint during early embryogenesis Development. *142*, 3833-3844.
2. Matsuzaki, H., Okamura, E., Kuramochi, D., Ushiki, A., Hirakawa, K., Fukamizu, A., and <u>Tanimoto, K.</u> (2018). Synthetic DNA fragments bearing ICR *cis* elements become differentially methylated and recapitulate genomic imprinting in transgenic mice. Epigenetics & Chromatin. *11*, 36.

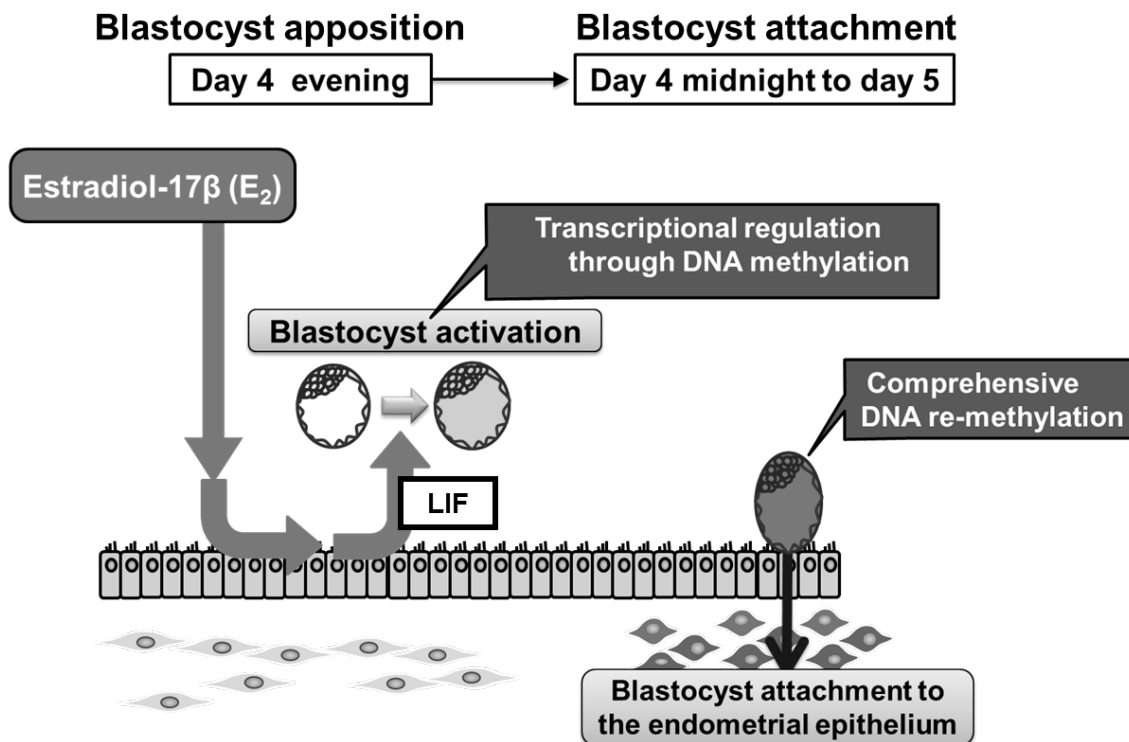| 子宮－胚間の協調的なエピゲノム調節と胚の活性化		平成 26-27 年
研究代表者	廣田泰	東京大学医学部附属病院
	公募	女性診療科・産科

＜研究の目的＞

　着床直前の胚盤胞は子宮との相互作用によりダイナミックな転写産物発現変化を起こす。この変化は胚盤胞活性化と呼ばれるが、この遺伝子発現変化に対するDNAメチル化調節の存在については明らかでない。本研究では胚盤胞活性化に伴っておこる着床直前の胚のDNAメチル化及びこの時期のDNAメチル化制御を受ける遺伝子を網羅的に解析した。

＜研究成果＞

　約15%の遺伝子で休眠胚盤胞と活性化胚盤胞の間で2倍以上のtranscript発現変化が認められ、胚盤胞活性化の存在が示された。休眠胚盤胞と活性化胚盤胞のゲノム全体のDNAメチル化の状態に差を認めず、着床直前の胚盤胞活性化によってゲノム全体のDNAメチル化の状態は変化しないことが判明した。胚が子宮に接着したのちにゲノムのDNAメチル化が急激に促進されることが推測された。Pathway解析によりDNAメチル化の制御を受け遺伝子発現変化をきたす遺伝子群の関連するPathwayの存在が認められ、子宮内で起こるエピジェネティックな遺伝子調節の存在が示された。一方で胚接着が起こらない子宮のLIF欠損マウスでは胚盤胞活性化が認められなかった。本研究により、着床の場で起こる受精卵のエピゲノム調節の詳細が明らかとなった。

＜研究の意義・展望＞

　本研究により着床に関する独自のin vivo評価系を用いて子宮内の胚のエピゲノム変化をとらえ、子宮内環境によるエピゲノム修飾と胚発生に関する新たな知見が得られた。子宮内環境による胚発生への直接的な影響を明らかにすることができ、子宮と胚の相互作用を介した着床制御の一端を解明できた。本研究を進展させ、未だブラックボックスである着床という生理的現象の解明につなげていきたい。

Blastocyst apposition
Day 4 evening →

Blastocyst attachment
Day 4 midnight to day 5

Estradiol-17β (E$_2$)

Transcriptional regulation through DNA methylation

Blastocyst activation

Comprehensive DNA re-methylation

LIF

Blastocyst attachment to the endometrial epithelium

＜主な研究発表論文＞

1．Haraguchi H, Saito-Fujita T, Hirota Y, Egashira M, Matsumoto L, Matsuo M, Hiraoka T, Koga K, Yamauchi N, Fukayama M, Bartos A, Cha J, Dey SK, Fujii T, Osuga Y. (2014). MicroRNA-200a locally attenuates progesterone signaling in the cervix, preventing embryo implantation. Mol. Endocrinol. 28, 1108-1117.
2．Hiraoka T, Hirota Y, Saito-Fujita T, Matsuo M, Egashira M, Matsumoto L, Haraguchi H, Dey SK, Furukawa KS, Fujii T, Osuga Y. (2016). STAT3 accelerates uterine epithelial regeneration in a mouse model of decellularized uterine matrix transplantation. JCI insight. 1, e87591.
3．Deng W, Cha J, Yuan J, Haraguchi H, Bartos A, Leishman E, Viollet B, Bradshaw HB, Hirota Y, Dey SK. (2016). p53 coordinates decidual sestrin 2/AMPK/mTORC1 signaling to govern parturition timing. J. Clin. Invest. 126, 2941-2954.
4．Egashira M, Hirota Y, Shimizu-Hirota R, Saito-Fujita T, Haraguchi H, Matsumoto L, Matsuo M, Hiraoka T, Tanaka T, Akaeda S, Takehisa C, Saito-Kanatani M, Maeda KI, Fujii T, Osuga Y. (2017). F4/80+ macrophages contribute to clearance of senescent cells in the mouse postpartum uterus. Endocrinology. 158, 2344-2353.
5．Matsumoto L, Hirota Y, Saito-Fujita T, Takeda N, Tanaka T, Hiraoka T, Akaeda S, Fujita H, Shimizu-Hirota R, Igaue S, Matsuo M, Haraguchi H, Saito-Kanatani M, Fujii T, Osuga Y. (2018). HIF2α in the uterine stroma permits embryo invasion and luminal epithelium detachment. J. Clin. Invest. 128, 3186-3197.

母性mRNAの分解に着目したゲノムリプログラミングの調節機構の解明		平成 26-27 年
受精前の卵子は最終分化した細胞なのか：全能性獲得の準備段階としての卵子		平成 28-29 年
研究代表者	青木　不学	東京大学大学院新領域創成科学研究科先端生命科学
	公募	

<研究の目的>
　受精前の卵は分化した細胞であるが、受精後の１細胞期胚は全能性を獲得し、受精前とは異なる新しい遺伝子発現プログラムをスタートさせる。このような遺伝子発現の変化は遺伝子発現のリプログラミングと呼ばれており、本研究の目的はこのリプログラミングのメカニズムを明らかにすることである。

<研究成果>
　遺伝子発現のリプログラミングのメカニズムを解明するためには、まずその前提として実際に受精前後でどのように遺伝子発現パターンが変化しているかについての情報が必須である。しかし、本研究プロジェクトをスタートさせた時点では、受精直後に発現する遺伝子についての情報がほとんどなかった。そこでまず、RNAseq を行い、受精後の１細胞期胚で遺伝子間領域を含む無秩序な転写が起こっていることを明らかにした（Abe et al., 2015）。このような無秩序な転写は、転写に抑制的に働くクロマチン構造が原因となっているのではないかと考え、fluorescent recovery after photobleaching (FRAP)法による解析を行ったところ、1 細胞期胚ではクロマチン構造が極度に緩んでいることが分かった（Ooga et al., 2016）。また、クロマチン構造の緩みは卵成長の段階から見られ、受精後にさらに大きく緩むことが明らかとなった（Ooga et al., 2018）。そして、このクロマチン構造の緩みには、H1 および H3 変異体が関与していることを明らかにした（Funaya et al., 2018; 未発表データ）。
　また、1 細胞期の転写産物はスプライシングがなされていないため、その大部分からは正常なタンパク質が作られないが、その転写を一過的に抑制すると 2 細胞期での遺伝子発現に異常をきたし発生が停止した（Abe et al., 2018）。したがって、1 細胞期において転写が起こることによりクロマチン構造に何らかの変化が生じ、2 細胞期の遺伝子発現が引き起こされることが明らかとなった。

1.　Abe, K., Yamamoto, R., Franke, V., Cao, M., Suzuki, Y., Suzuki, M.G., Vlahovicek, K., Svoboda, P., Schultz, R.M., and Aoki, F. (2015). The first murine zygotic transcription is promiscuous and uncoupled from splicing and 3' processing. EMBO J. *34*, 1523-1537.

2.　Ooga, M., Fulka, H., Hashimoto, S., Suzuki, M.G., and Aoki, F. (2016). Analysis of chromatin structure in mouse preimplantation embryos by fluorescent recovery after

photobleaching. Epigenetics *11*, 85-94.

3. Funaya, S., Ooga, M., Suzuki, M.G., and Aoki, F. (2018). Linker histone H1FOO regulates the chromatin structure in mouse zygotes. FEBS Lett. *592*, 2414-2424.

4. Ooga, M., Funaya, S., Hashioka, Y., Fujii, W., Naito, K., Suzuki, M.G., and Aoki, F. (2018). Chd9 mediates highly loosened chromatin structure in growing mouse oocytes. Biochem. Biophys. Res. Comm. *500*, 583-588.

5. Abe, K.-I., Funaya, S., Tsukioka, D., Kawamura, M., Suzuki, Y., Suzuki, M.G., Schultz, R.M., and Aoki, F. (2018). Minor zygotic gene activation is essential for mouse preimplantation development, Proc. Natl. Acad. Sci. USA, *115*, E6780-E6788.
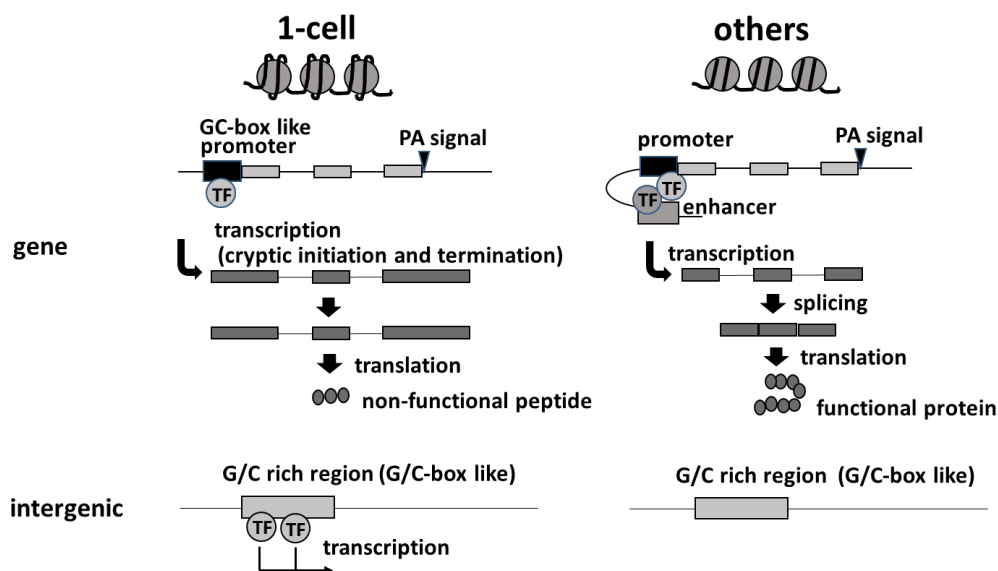
Regulation of gene expression in 1-cell stage embryos

＜研究の意義・展望＞

　これまで、受精後の遺伝子発現プログラム、さらには受精前後の遺伝子発現リプログラミングの調節機構についてはわずかの知見しか得られていなかった。その原因として、受精後に最初に転写される遺伝子が明らかにされていなかったことがある。本研究により、受精後の１細胞期胚の転写パターンが明らかとなり、さらにその調節にヒストン変異体が関わっていることが示されたことで、今後、当該研究分野が大きく発展することが期待される。

　また、本研究により、受精前後におけるエピゲノムの変化と遺伝子発現リプログラミングの関連が明らかになった。この成果は、本研究プロジェクトのテーマの１つであるエピゲノムダイナミクスの生殖サイクルへの関与について、その一部を明らかにしたものであると考えられる。

非典型的ポリコーム群 MBLR 複合体による減数分裂遺伝子のエピジェネティック制御	平成 26-27 年
研究代表者	遠藤充浩	シンガポール国立大学がん科学研究所、熊本大学国際先端医学研究機構
	公募	

＜研究の目的＞

マウスの始原生殖細胞において、減数分裂の前にゲノム全体のエピジェネティックな変化が大規模に起こることが知られるが、減数分裂に関連する遺伝子のエピジェネティックな発現制御機構についてはあまり良く分かっていない。本研究では、MBLR (PCGF6)が形成する非典型的ポリコーム群複合体 PRC1.6 による減数分裂・生殖関連遺伝子群のエピジェネティック制御の分子メカニズムとその生物学的意義を解明するため、遺伝子改変マウスや多能性幹細胞を用いた研究を行った。

＜研究成果＞

ナイーブ型の多能性幹細胞において、PCGF6 複合体の精製を行ったところ、RING1A/B, RYBP/YAF2, L3MBTL2 などのクロマチン因子に加え、転写因子 MGA が含まれることが分かった。PCGF6 をゲノムの特定領域に人工的に de
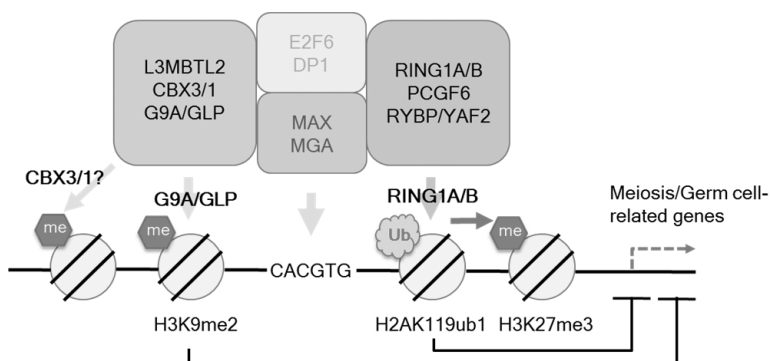
novo に結合させると、これら構成因子を含むいわゆる PRC1.6 複合体がリクルートされ、ヒストン H2A のモノユビキチン化修飾 (H2AK119ub1) とヒストン H3-K27 のトリメチル化修飾 (H3K27me3) が起こることが分かった。ナイーブ型の多能性幹細胞において PCGF6 が結合するゲノム領域について ChIP-seq 解析を行った結果、PCGF6 は減数分裂・生殖細胞関連遺伝子群の転写開始点周辺に結合することが分かった。またこれらの PCGF6 標的遺伝子の配列には E ボックス配列が含まれており、PRC1.6 複合体の構成因子である転写因子 MGA/MAX ヘテロダイマーがこれを認識して結合することにより、PRC1.6 複合体がリクルートされることが分かった（モデル図参照）。ナイーブ型の多能性幹細胞で PCGF6 を欠損させると、細胞の増殖及び生存の低下が起こり、減数分裂・生殖細胞関連遺伝子群への RING1B/RYBP の結合及び H2AK119ub1 / H3K27me3 修飾が消失して、これらの遺伝子の脱抑制が起こる。さらに、ナイーブ型の多能性幹細胞における PCGF6 による減数分裂・生殖細胞関連遺伝子群の抑制には、RING1B が媒介する H2AK119ub1 修飾が必要であることも分かった。一方プライム型の多能性幹細胞であるエピブラスト幹細胞においては、PRC1.6 複合体の減数分裂・生殖細胞関連遺伝子群への結合が見られず、PCGF6 あるいは RING1A/B を欠損させてもこれらの遺伝子の脱抑制は起こらなかった。PCGF6 欠損マウスは胚発生の過程で死亡する確率が野生型に比べて有意に高く、着床前胚から死亡

し始めること、着床後胚の胎盤形成に異常があることも分かり、以上の研究成果を国際科学雑誌 eLife で発表した。

＜研究の意義・展望＞

DNA メチル化がグローバルに低メチル化状態であるナイーブ型の多能性幹細胞において、減数分裂・生殖関連遺伝子は不完全な DNA メチル化を受ける遺伝子群である。本研究成果は、PRC1.6 複合体が不完全な DNA メチル化を受ける遺伝子領域の E ボックスに結合して、補完的に転写抑制を担う仕組みである可能性を示唆しており、これは DNA メチル化と排他的であることが知られる従来の PRC1 複合体とは対照的な性質である。今後、脱メチル化過程の DNA、例えば 5-ハイドロキシメチルシトシン(5-hmc)や 5-ホルミルシトシン(5-fC)などの修飾を持つ E ボックスと PRC1.6 複合体の関係を調べることにより、エピジェネティックリプログラミングが起こっている細胞に特有の転写抑制システムの一つとして PRC1.6 複合体を位置づけることができるかもしれない。
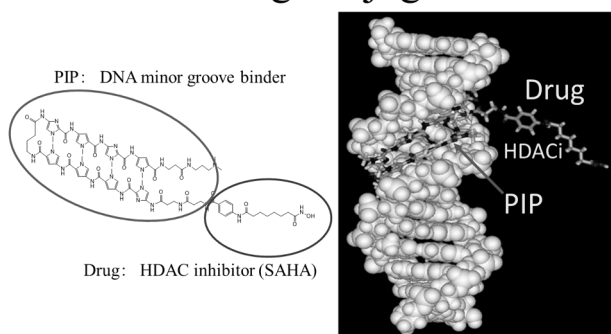
＜主な研究発表論文＞

1. Arner, E., Daub, C.O., Vitting-Seerup, K., Andersson, R., Lilje, B., Drablos, F., Lennartsson, A., Ronnerblad, M., Hrydziuszko, O., Vitezic, M.,…, Endoh, M., et al. (2015). Transcribed enhancers lead waves of coordinated transcription in transitioning mammalian cells. Science *347*, 1010-1014. (23th author)
2. Ikawa, T., Masuda, K., Endo, T.A., Endo, M., Isono, K., Koseki, Y., Nakagawa, R., Kometani, K., Takano, J., Agata, Y., et al. (2016). Conversion of T cells to B cells by inactivation of polycomb-mediated epigenetic suppression of the B-lineage program. Genes Dev *30*, 2475-2485.
3. Endoh, M., Endo, T.A., Shinga, J., Hayashi, K., Farcas, A., Ma, K.W., Ito, S., Sharif, J., Endoh, T., Onaga, N., et al. (2017). PCGF6-PRC1 suppresses premature differentiation of mouse embryonic stem cells by regulating germ cell-related genes. eLife *6*. e21064.
4. Noguchi, S., Arakawa, T., Fukuda, S., Furuno, M., Hasegawa, A., Hori, F., Ishikawa-Kato, S., Kaida, K., Kaiho, A., Kanamori-Katayama, M.,…, Endoh, M., et al. (2017). FANTOM5 CAGE profiles of human and mouse samples. Sci Data *4*, 170112. (49th author)
5. Baba, M., Endoh, M., Ma, W., Toyama, H., Hirayama, A., Nishikawa, K., Takubo, K., Hano, H., Hasumi, H., Umemoto, T., et al. (2018). Folliculin Regulates Osteoclastogenesis Through Metabolic Regulation. J Bone Miner Res. *10*, 1785-1798.

ゲノム認識エピジェネティック変更化合物の開発		平成 26-27 年
研究代表者	永瀬浩喜	千葉県がんセンター
	公募	研究所　がん遺伝創薬研究室

<研究の目的>

PIP-Drug conjugate

PIP: DNA minor groove binder

Drug

HDACi

PIP

Drug: HDAC inhibitor (SAHA)

エピジェネティック（後天的）な遺伝子制御の情報をリセットする生殖細胞のユニークな性質とその後のそれぞれの体細胞への分化プロセスを理解するうえでヒストン修飾酵素をゲノム領域特異的に制御し機能解析する方法が求められ、この実現は時空間軸をふまえ4次元的な生殖細胞エピゲノムのダイナミクスを解析する重要な手段となると考えられた。

我々は、ゲノム配列特異的に薬剤を送達する技術により HDACi をゲノムの一定領域に送達させる技術を開発し、特定のゲノム領域のヒストンアセチル化を変更することに成功した。さらに、この方法論は、他のヒストン修飾酵素阻害剤を特定のゲノムに送達させる新たなエピゲノム解析・制御技術として開発できると考えた。本研究課題では、本技術による SAHA-PIP および他のヒストン修飾阻害剤と PIP とのコンジュゲートを合成し、新たな標的領域特異的なエピゲノム変更技術を確立すること、および生体内生殖細胞に本化合物を送達させ、生殖エピゲノムを変更することを目的に研究を開始した。

<研究成果>

　　本研究では、SAHA-PIP 化合物によるエピゲノム介入を試みるため、まず皮膚繊維芽細胞より多能性幹細胞の創出が可能かを試み、マウスおよびヒトにおいてもスフェアを形成し、アルカリフォスファターゼ陽性、ES 類似発現パターン（幹細胞マーカー陽性）を示す細胞を PIP-SAHA 化合物で誘導できることを確認した（Pandian et al., 2014）。さらにヒストン脱アセチル化酵素阻害剤である SAHA に加えヒストンアセチル化酵素活性化剤 CTB によって、同じ配列認識する PIP とのコンジュゲートにおいて同様の遺伝子発現が誘導されることも確認した。化合物投与による幹細胞様の表現型が得られたことを数理的解析等により、複数の多能性関連遺伝子が関与することで幹細胞誘導が行われる可能性が発見され、さらに、異なる少なくとも4つのパスウェイの下流遺伝子が誘導されることにより、幹細胞誘導が誘導される可能性を確認した（Pandian et al., 2014）。化合物はマウスの精巣内細胞の核内にも送達できたため生体精巣細胞でのエピゲノム変更による、精子分化誘導への影響を確認できる可能性が示唆された。

<研究の意義・展望>

　体細胞と生殖細胞の違いは大きく、通常の低分子化合物は、生殖細胞では排

除され、体細胞で見られる効果を生殖細胞では期待できない。これは生殖細胞においては外部からの刺激や薬剤により影響を受けないように薬物トランスポーターが活性化され薬剤が速やかに細胞外に排泄されることがその一つの理由として考えられている。我々はPIP化合物では核内DNAと配列特異的に結合することで、生体内で薬物トランスポーターの影響を受けにくく、核内に薬剤が迅速に移行し貯留すること（Inoue et al., 2018）、生殖細胞内に薬剤が排泄されることなく存在すること、核内の特定の遺伝子領域に送達させ、インプリンティングも操作できること（Yoshizawa et al., 2015）を確認した。さらに、インフォーマティクス解析によりゲノム上の薬剤送達部位を確認する技術を創出したこと（Lin et al., 2016）で、この技術が、今後生体内において様々な細胞のエピゲノムを変更する技術に発展すると期待される。但し、生殖細胞及びその発生においては、*ex vivo*(試験管内)等での操作等が可能である。つまり細胞内送達技術を利用すれば既存のゲノム編集技術を応用することで特定領域のエピゲノムを変更することが可能であるため、本技術はDDSが必要ない技術ではあるが、その有意性は限定されるものと考えられた。このため、本技術は、現状では個体の体細胞における生体内機構へのエピゲノム介入への有効性に比べ生殖細胞研究では重要性、有用性が低いと考えられた。但し多くのゲノム領域を一度にエピジェネティックに改変すること等の用途や植物などの細胞壁を有する種等の生殖研究が今後必要となれば本技術は、生殖細胞などの解析においても有用となるものと考える。

＜主な研究発表論文＞

1. Pandian, G.N., Sato, S., Anandhakumar, C., Taniguchi, J., Takashima, K., Syed, J., Han, L., Saha, A., Bando, T., Nagase, H., and Sugiyama, H. (2014) Identification of a Small Molecule That Turns ON the Pluripotency Gene Circuitry in Human Fibroblasts. ACS Chem. Biol. *9*, 2729–2736.
2. Fujiwara, K., Ghosh, S., Liang, P., Morien, E., Soma, M., and Nagase, H. (2015) Genome-wide screening of aberrant DNA methylation which associated with gene expression in mouse skin cancers. Molecular Carcinogenesis *54*,178-188.
3. Yoshizawa, S., Fujiwara, K., Sugito, K., Uekusa, S., Kawashima, H., Hoshi, R., Watanabe, Y., Hirano, T., Furuya, T., Masuko, T., Ueno, T., Fukuda, N., Soma, M., Ozaki, T., Koshinaga, T., and Nagase, H. (2015) Pyrrole-Imidazole (PI) polyamide-mediated silencing of KCNQ1OT1 expression induces cell death in Wilms tumor cells. International Journal of Oncology *47*, 115-21.
4. Lin, J., Hiraoka, K., Watanabe, T., Kuo, T., Shinozaki, Y., Takatori, A., Koshikawa, N., Chandran, A., Otsuki, J., Sugiyama, H., Horton, P., and Nagase, H. (2016) Identification of Binding Targets of a Pyrrole-Imidazole Polyamide KR12 in the LS180 Colorectal Cancer Genome. PLOS ONE *11*, e0165581.
5. Inoue, T., Shimozato, O., Matsuo, N., Mori, Y., Shinozaki, Y., Lin, J., Watanabe, T., Takatori, A., Koshikawa, N., Ozaki, T., and Nagase, H. Hydrophobic structure of hairpin ten-ring pyrrole-imidazole polyamides enhanced tumor tissue accumulation/retention in vivo. Bioorganic & Medicinal Chemistry *26*, 2337-2344.

piRNA 生合成経路による翻訳制御機構		平成 28-29 年
研究代表者	石津大嗣	慶應義塾大学医学部
	公募	分子生物学教室

＜研究の目的＞

　小分子 RNA による遺伝子発現抑制機構は RNA サイレンシングと総称され，発生における分化制御や外来遺伝子からの防御機構などあらゆる生命現象に関与している．生殖細胞特異的に発現する小分子 RNA である PIWI-interacting RNA (piRNA)は，PIWI タンパク質と RNA 誘導型サイレンシング複合体を形成し，相補配列を持つ標的遺伝子の発現を抑制する．piRNA の主な標的はレトロトランスポゾンであり，piRNA は次世代に遺伝情報を継承する生殖細胞において，転移因子からゲノムの安定性を護る役割を担っている．また，piRNA には，レトロトランスポゾン を標的とするものの他に，特定のタンパク質コード遺伝子の 3′UTR から産生される genic piRNA が存在することが知られている．しかし，ほとんどの genic piRNA の標的は未知であり，それらの機能には不明な点が多い．genic piRNA をコードする遺伝子にとって，piRNA 生合成経路は mRNA 分解を促進する経路として作用する．つまり，piRNA 生合成経路が mRNA を不安定化させることでタンパク質翻訳効率の調整機構として働いている可能性がある．しかし，これまでの研究では，piRNA が標的とする遺伝子のサイレンシング機構に焦点が置かれており，piRNA 生合成経路の基質となる mRNA の視点からの研究は行われていない．そこで，本研究では，piRNA 生合成経路が genic piRNA コード遺伝子の翻訳効率に影響を与えるかどうかを調べることで，piRNA が生殖細胞においてレトロトランスポゾンの発現抑制だけでなく，転写後制御による適切なタンパク質量調整に関与するエピゲノム制御機構として機能するかどうかを明らかにすることを目的とした．また，genic piRNA が生成される特定の mRNA がどのように選別されるのか，その識別機構の解明を目指した．

genic piRNA coding mRNA
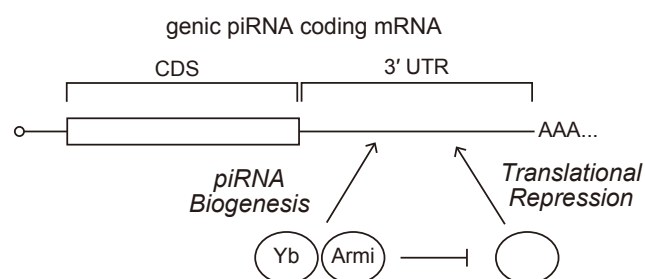
＜研究成果＞

　これまでに，piRNA 生合成経路が保存されたショウジョウバエ卵巣由来培養細胞株 OSC を用いた解析から，piRNA 生合成に必須の因子として RNA 結合タンパク質である fs(1)Yb（Yb）と Armitage（Armi）が同定されていた．これらの因子が，mRNA の翻訳に関与するかどうかを RNAi 法による阻害実験により調べた．*traffic jam*（*tj*）は 3′UTR から多くの piRNA を産生する遺伝子として知られている．Yb，または Armi をノックダウンし，ノーザンブロット法により *tj* mRNA の半減期を定量したところ，mRNA 半減期には影響がなかった．一方で，Tj タンパク質の量をウェスタンブロット法により定量した結果，タンパク質量

が減少することがわかった．これらの結果は，mRNA 分解を伴う piRNA 生合成経路は，翻訳効率を低下させるという当初の予想に反し，翻訳を安定化する効果を有することを示唆した．piRNA 生合成因子である Yb と Armi は，3′UTR の分解を引き起こす一方で，同じ 3′UTR に結合して翻訳抑制に作用するそのほかの RNA 結合タンパク質に干渉することで，翻訳効率の安定化に寄与することが考えられる．Armi は RNA ヘリケースドメインを持ち，*in vitro* の実験系から RNA 上を 5′から 3′方向に移動する活性を持つことを明らかにした．この RNA ヘリケース活性が RNPase として機能することで，翻訳抑制に作用するその他のタンパク質の 3′UTR への結合を阻害すると考えられる．

　Armi や Yb の piRNA 生合成経路における機能を解析するために Individual-nucleotide resolution crosslinking-immunoprecipitation（iCLIP）法を行った．iCLIP 法により，Armi と Yb は piRNA の前駆体となる RNA に結合することが明らかとなった．また，Armi をノックダウンした場合，Yb の結合 RNA への影響はなかったのに対して，Yb をノックダウンした場合，Armi の piRNA 前駆体への結合が阻害された．このことから，Armi の前駆体 RNA への結合は Yb 依存的であることが明らかとなり，Armi が結合する RNA は piRNA 生合成過程の中間体であると予想された．そこで，Armi が piRNA 中間体に結合していることを証明するために，Armi 結合 RNA の 5′末端を同定する CLIP followed by parallel analysis of RNA end(CLIPPARE)法を開発し，解析を行った結果，Armi が piRNA 中間体に結合することを明らかにした．以上の結果から，piRNA 前駆体は Yb によって選別された後，Armi によって成熟型 piRNA へのプロセシングが進められることが示唆された．

＜研究の意義・展望＞
　本研究により，piRNA は標的遺伝子の抑制に寄与するだけでなく，生合成の基質となる mRNA の翻訳制御にも関与することが示唆された．3′UTR に結合し，翻訳制御に関与する因子として Yb と Armi を同定し，これらの機能解析を行った結果，これらが同じ 3′UTR に結合する翻訳抑制因子のアンタゴニストとして機能するという仮説を提唱するに至った．今後は，この仮説を検証していく予定である．

＜主な研究発表論文＞
1.　Guida V, Cernilogar FM, Filograna A, De Gregorio R, Ishizu H, Siomi MC, Schotta G, Bellenchi GC, Andrenacci D. (2016). Production of small noncoding RNAs from the flamenco locus is regulated by the gypsy retrotransposon of *Drosophila melanogaster*. Genetics. 204, 631-644.
2. Iwasaki YW, Murano K, Ishizu H, Shibuya A, Iyoda Y, Siomi MC, Siomi H, Saito K. (2016). Piwi modulates chromatin accessibility by regulating multiple factors including histone H1 to repress transposons. Mol Cell. 63, 408-419.
3. Ishizu H, Sumiyoshi T, Siomi MC. (2017) Use of the CRISPR-Cas9 system for genome editing in cultured *Drosophila* ovarian somatic cells. Methods. 126, 186-192.

生殖細胞のエピゲノムリプログラミング過程における 多能性転写因子群の制御基盤の解明		平成 28-29 年
研究代表者	栗本一基	奈良県立医科大学 発生・再生医学講座
	公募	
研究分担者		

＜研究の目的＞

　始原生殖細胞は、DNA メチル化を始めとするエピゲノム情報を一旦初期化（リプログラミング）し、次世代個体の発生能獲得に備えると考えられる。その過程で、始原生殖細胞は多能性に関わる基盤転写因子群を発現し、潜在的に、多能性を再獲得もしくは保持する。一方で、始原生殖細胞は、原腸形成期において体細胞への分化を抑制する転写因子 BLIMP1 を発現し続けるなど、多能性幹細胞とは顕著に異なる特性を示す。これらの特性の組み合わせが、生殖細胞に全発生能を付与するエピゲノム的基盤であると考えられるが、その詳細は明らかではない。本研究では、エピゲノムリプログラミング過程にある始原生殖細胞における、多能性制御の核内基盤の解明を目指す。

＜研究成果＞

　本研究では、始原生殖細胞形成過程におけるゲノム DNA のメチル化リプログラミング過程を、始原生殖細胞の試験管内再構成系を用いて詳細に解析した。その結果、多能性幹細胞からのエピブラスト再構成過程、すなわち胚盤胞の着床に対応する過程においては、ゲノム DNA メチル化の急激な増加と、そのメチル化パターンの大規模な変動が見出された。一方で、再構成エピブラストからの始原生殖細胞の再構成、すなわちエピブラストから始原生殖細胞への分化に対応する過程においては、ゲノム DNA のメチル化パターンを維持したまま、メチル化率のみが漸進的に減少することが見出された。さらに低メチル化を示すゲノム部位を、多能性幹細胞と再構成始原生殖細胞の間で比較すると、前者では転写活性化される部位（H3K27ac）が、後者ではポリコームによる転写不活化部位（H3K27me3）が対応した。これらの結果から、着床前胚（多能性幹細胞）と始原生殖細胞は、ゲノム全体の低メチル化という共通した性質を持ちつつも、その制御の実態は全く異なることが明らかになった (Shirane et al., 2016)。

　さらに、再構成始原生殖細胞を平面培養して、DNA メチル化リプログラミングが完了する過程を再現することが出来た。この過程は、胚体内の発生過程においては始原生殖細胞に影響を与え得る体細胞が、存在しない状態で進行する。胚体内の生殖細胞は、DNA メチル化リプログラミングの完了時点で、すでに、遺伝子発現プロファイルの顕著な性的二型を示す。一方、体外で DNA メチル化

リプログラミングを進行させた再構成始原生殖細胞は、著明な性分化を示すことなく、初期の始原生殖細胞に酷似した遺伝子発現と活性化エンハンサーのプロファイルを示した。このことは、DNA の脱メチル化自体は遺伝子発現に大きく影響しないことを示唆する。一方、プロモーターでの DNA メチル化消去には、H3K27me3 の増加が付随した。すなわち、発現抑制機構の DNA メチル化からポリコームへのシフトが、潜在的多能性を持つ始原生殖細胞におけるエピゲノムリプログラミングの特徴であり、多能性幹細胞との重要な差異であると考えられる (Ohta et al., 2017)。

　また転写因子 BLIMP1 の結合部位を、初期の再構成始原生殖細胞と、後期の始原生殖細胞の間で比較した。この解析によって、BLIMP1 により制御される遺伝子のレパートリーが、始原生殖細胞発生の初期と後期で大きく異なる一方で、BLIMP1 の結合パターン自体は、初期に確立されたまま変化しないことが判明した。すなわち、始原生殖細胞の発生後期における BLIMP1 の転写制御機能が、発生初期にすでに準備されていることが示唆される (Mitani et al., 2017)。また、OCT4, SOX2, NANOG の各アレルにタグ挿入した組換え ES 細胞を作成し、SOX2 と NANOG について設計通りのタグ付きタンパク質の発現が認められた。

＜研究の意義・展望＞
　多能性幹細胞の「顕在化した多能性」と、始原生殖細胞の「潜在的な多能性」を分かつゲノム制御基盤は興味深い。また、定量的な比較解析の重要性を再認識した。
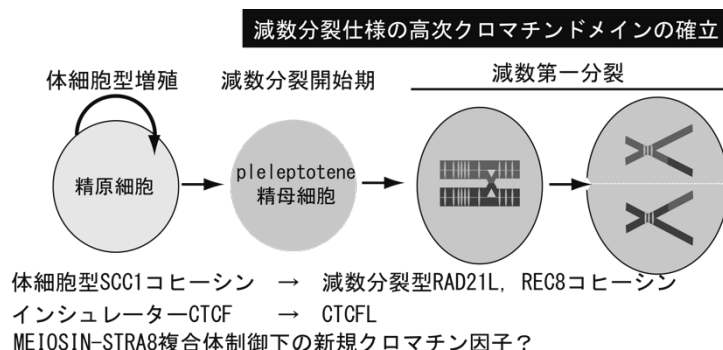

＜主な研究発表論文＞
1. Shirane, K., Kurimoto, K., Yabuta, Y., Yamaji, M., Satoh, J., Ito, S., Watanabe, A., Hayashi, K., Saitou, M., and Sasaki, H. (2016). Global Landscape and Regulatory Principles of DNA Methylation Reprogramming for Germ Cell Specification by Mouse Pluripotent Stem Cells. Dev Cell *39*, 87-103.
2. Ohta, H[§]., Kurimoto, K[§]., Okamoto, I., Nakamura, T., Yabuta, Y., Miyauchi, H., Yamamoto, T., Okuno, Y., Hagiwara, M., Shirane, K*., et al.* (2017). In vitro expansion of mouse primordial germ cell-like cells recapitulates an epigenetic blank slate. EMBO J.　[§]Co-first authors
3. Mitani, T., Yabuta, Y., Ohta, H., Nakamura, T., Yamashiro, C., Yamamoto, T., Saitou, M*., and Kurimoto, K*. (2017). Principles for the regulation of multiple developmental pathways by a versatile transcriptional factor, BLIMP1. Nucleic Acids Res *45*, 12152-12169. *Co-corresponding authors.

減数分裂型 cell cycle による生殖細胞エピゲノム制御機構		平成 28-29 年
研究代表者	石黒啓一郎	熊本大学　発生医学研究所
	公募	

＜研究の目的＞

　本研究は生殖細胞系列と体細胞系列の核内高次クロマチンドメインの違いを規定するメカニズムの解明を目的とする。とりわけ、減数第一分裂期ではおいては減数分裂型コヒーシンが体細胞型と置き換わるなど染色体構造が減数分裂仕様に劇的に変化を遂げることが明らかにされているが、基盤となるクロマチンドメインの成り立ちについては不明な点が多い。また体細胞ではインスレータータンパク質CTCFが発現してコヒーシンと協調して高次クロマチンドメインを形成するのに対して、減数分裂において同様の機構が見られるのかについても不明な点が多い。本研究では減数分裂期における、(1)減数分裂型コヒーシンおよび(2)CTCF-Like(CTCFL)の相互作用因子の同定とその解析を行った。また(3)我々が最近同定した減数分裂開始因子MEIOSINの転写制御下にある新規クロマチン結合タンパク質の同定を行った。さらに、(4) 2-cell stageマーカーとして知られるZSCAN4のGV oocyte核内の局在について検討を行った。

減数分裂仕様の高次クロマチンドメインの確立

体細胞型SCC1コヒーシン　→　減数分裂型RAD21L, REC8コヒーシン
インシュレーターCTCF　→　CTCFL
MEIOSIN-STRA8複合体制御下の新規クロマチン因子？

＜研究成果＞

減数分裂型コヒーシンの染色体へのloading機構とその土台となる高次クロマチンドメインを明らかにするため、減数分裂型コヒーシンRAD21LとREC8それぞれの内在性遺伝子にゲノム編集を行ってtag付きタンパクを発現するノックインマウスを作製した。精巣クロマチンより精製したタンパク質複合体のMS解析により、REC8はpre-meiotic S期のMCM複合体との相互作用によりDNA複製とcoupleしてクロマチンにloadされること、さらにRAD21Lはpre-meiotic S期より遅れてDNA複製装置に依存せずにloadされることが示唆された。興味深いことに、pre-meiotic S期の進行に伴いそのパラログCTCF-Like(CTCFL)がCTCFと置き換わることによってクロマチンドメインの変換が起きている可能性が示唆された。両者はターゲットとなるDNA結合配列を共通としながらも、N末側の違いが結合

因子を変えることにより異なる機能を示すと推測される。これらの知見に基づいてpre-meiotic S期におけるCTCFL会合タンパク質の同定と高次クロマチン構造形成への寄与について検討している。

　さらに、我々はStra8と複合体を形成する新規タンパク質MEIOSINを同定した。MEIOSIN-Stra8質複合体は、減数分裂に関連する遺伝子のプロモーターに結合するマスター転写因子であることが判明した(未発表)。ChIP-seq解析により、MEIOSIN-Stra8タンパク質複合体によって制御される未解析のhypothetical geneが複数同定された。これらの未解析因子には新規クロマチン結合タンパク質が含まれる可能性があるため、受精卵でのゲノム編集による表現型解析と免疫染色によるクロマチン局在について検討している。

　内在性 *Zscan4* 遺伝子クラスター領域内の Zscan4c 遺伝子座に GFP をノックインしたマウスを作製して解析を行った(Ishiguro et al., 2017a)。2-cell stage のみならず、GV oocyte で Zscan4 の発現が見られることが判明した。興味深いことに、GV oocyte のうち NSN と呼ばれる集団では Zscan4 は核内に均一に観察されるのに対して、RNA pol II による転写が不活性化されている SN と呼ばれる集団では dot 状の核内配置を示すことが明らかとなった(Ishiguro et al., 2017a)。これらの結果は Zscan4 が着床前初期胚のみならず生殖細胞においても何らかの機能を持つことを示唆している。

　　＜研究の意義・展望＞
CTCFL や減数分裂型コヒーシン RAD21L と REC8 の相互作用因子、さらに MEIOSIN-STRA8 制御下の新規クロマチン因子の手掛かりが得られたことは大きな成果であった。これらの解析に向けた準備が完了し、生殖細胞系列と体細胞系列の核内高次クロマチンドメインの違いを規定するメカニズムの解明に大いに資することが期待される。

＜主な研究発表論文＞

1. Ishiguro, K., Nakatake, Y., Chikazawa, N., Kimura, H., Akiyama, T., Oda, M., Ko, SBH., Ko, MS. (2017a). Expression analysis of the endogenous Zscan4 locus and its coding proteins in mouse ES cells and preimplantation embryos. In Vitro Cell Dev Biol Anim. *53*, 179-190.

2. Ishiguro, K., Monti, M., Akiyama, T., Kimura, H., Chikazawa, N., Sakota, M., Sato, S., Redi, CA., Ko, SBH., Ko, MS. (2017b). Zscan4 is expressed specifically during late meiotic prophase in both spermatogenesis and oogenesis. In Vitro Cell Dev Biol Anim. *53*, 167

生殖細胞のヒストン置換に関わる因子の同定および機能解析		平成 28-29 年
研究代表者	品川敏恵	理化学研究所 石井分子遺伝学研究室
	公募	（現・野崎徳州会病院附属研究所 再生医学研究部）

＜研究の目的＞

　精子形成の過程で、DNA を巻き付けていたヒストンは最終的にプロタミンに置換される。このエピゲノム変化は、ほぼゲノム全体にわたって起きる大規模なもので、機能的精子の形成に重要である。ヒストンの置換は Transition protein (TNP) への置換を経てプロタミンへと段階的に起きるが、、そのメカニズムについては不明な点が多い。我々は、カノニカルなヒストン H2A/H2B は、まず生殖細胞に特異的なヒストンバリアント TH2A/TH2B に置換される必要があり、Th2a/Th2b 欠損マウスではヒストンから TNP やプロタミンへの置換が進行せず、成熟精子が形成されないことを見いだした (Shinagawa et al., 2015)。H2A/H2B は自律的にヌクレオソームを形成できないので、ヌクレオソームを形成する際には、H3/H4 や DNA の他に NAP1 のようなヒストンシャペロンが必要であることが知られている。近年、H3.3 には HIRA、H2A.Z には ANP32E というようにヒストンバリアントにはそれぞれに特異的なヒストンシャペロンが存在することが明らかとなり、各ヒストンバリアントのゲノム上の特徴的な分布とその機能を考える上で、ヒストンシャペロンの役割が再評価されてきている。TH2A/TH2B の場合も同様と考えられるが、どのようなヒストンシャペロンが TH2A/TH2B と相互作用するのか分かっていない。本研究では、TH2A/TH2B のヒストンシャペロンを同定し、ヒストンの置換がどのような仕組みで起きるのか明らかにすることを目的とした。

＜研究成果＞

　細胞核の可溶画分にはヌクレオソーム構築前複合体が存在していると考えられたので、精子細胞核の可溶画分から TH2A/TH2B 含有蛋白質複合体の精製をおこなった。大腸菌で発現させた His タグ付きリコンビナント TH2A または H2A を磁気ビーズに固定し、野生型マウスの精巣の核可溶画分と反応させてアフィニティ精製をおこない、SDS-PAGE のあと質量分析によって蛋白質を同定した。His タグ付きリコンビナント TH2B と H2B についても同様の実験をおこなった。TH2A と H2A の間で結合に差のある蛋白質は観察されなかったが、TH2B と H2B に結合する精巣の核内蛋白質を比較することにより、TH2B に特異性の高い一群の蛋白質を同定することができ

Protein X

H2A/TH2B

H2A/TH2B-DNA aggregate
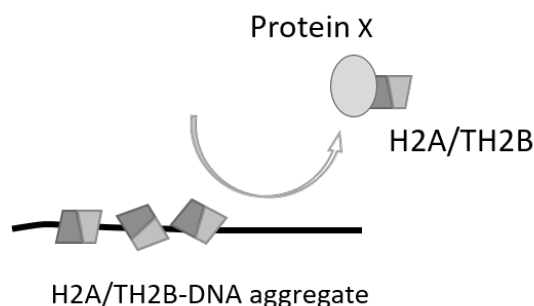
た。

　ヒストンシャペロンかどうかの基準の一つは、DNA とヒストンの非特異的凝集の形成を阻害し、すでに形成された凝集を解消する活性を持っていることである。そこで DNA 断片とリコンビナント TH2A, TH2B, H3, H4 の混合物に TH2B に特異性の高かった蛋白質のリコンビナントを加えて反応させ、電気泳動して凝集の形成が阻害・解消されるか調べた。その中の一つは DNA と H2A/TH2B の凝集体から H2A/TH2B を除去する活性を有しており、TH2B のクロマチンからの排除に寄与していると考えられた。
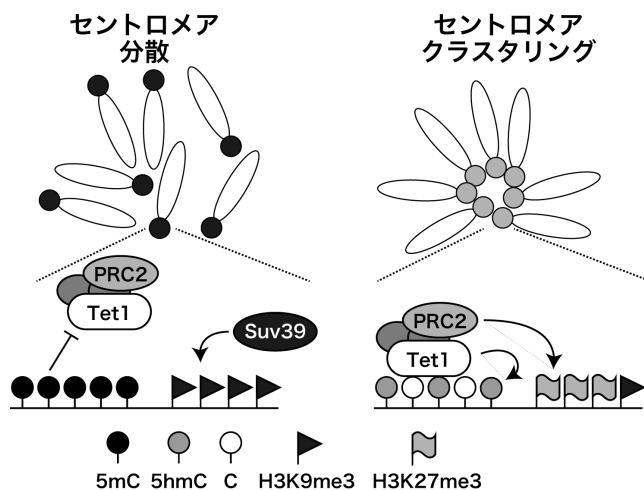
＜研究の意義・展望＞

　この研究で見つかったヒストンシャペロンは、DNA と H2A/TH2B の凝集体から H2A/TH2B を除去する活性を持っていた。同じヒストンシャペロンが TH2B がヌクレオソームを形成にも関わっているのか明らかにしていきたい。

＜主な研究発表論文＞

1. Padavattan S., Thiruselvam V., Shinagawa T., Hasegawa K., Kumasaka T., Ishii S., Kumarevel T. (2017) Structural analyses of the nucleosome complexes with human testis-specific histone variants, hTh2a and hTh2b. Biophys Chem. 221:41-48.

始原生殖細胞特異的なヘテロクロマチン動態の解析		平成 28-29 年
研究代表者	山口新平	大阪大学大学院医学系研究科
	公募	幹細胞病理学

セントロメア分散　セントロメアクラスタリング

5mC　5hmC　C　H3K9me3　H3K27me3

＜研究の目的＞

　生殖細胞は次世代へと遺伝情報を受け継ぐ唯一の細胞であり、その発生過程でダイナミックなエピジェネティック状態の変化が生じる。5-メチル化シトシン（5mC）を 5-ヒドロキシメチル化シトシン（5hmC）に酸化する酵素である Tet1 は、その過程において、減数分裂関連遺伝子の発現などに重要な役割を果たしている。Tet1 は主に開かれたクロマチンに酸化反応を生じさせると考えられており、実際に、体細胞では閉じられたクロマチンであるペリセントロメア領域に Tet1 は局在せず、5mC から 5hmC への変換も生じない。しかし、始原生殖細胞（PGC）のペリセントロメア領域は構成的ヘテロクロマチンの特徴を備えているにも関わらず 5hmC が存在していた。これらのことから、始原生殖細のペリセントロメア領域は、体細胞と異なるエピジェネティック状態を有していること、そして、それが生殖細胞発生にも影響を与える可能性があることが考えられたが、その機構も意義も未解明であった。

＜研究成果＞

　本研究で着目したリプログラミング期の PGC は、着床直後の胚で発生する微少な細胞集団であり、遺伝子改変実験が技術的に困難であった。そこで、PGC 同様に低メチル化状態を示す Dnmt1 欠損 ES 細胞を用いて解析を行った。その結果、野生型の ES 細胞ではペリセントロメア領域に 5hmC は局在しないが、Dnmt1 欠損 ES 細胞においては 5hmC が認められた。さらに、Dnmt1 欠損 ES 細胞では、構成的ヘテロクロマチンでは認められないヒストン H3 の 27 番目のリジンのトリメチル化（H3K27me3）が局在しており、構成的ヘテロクロマチンから条件的ヘテロクロマチンへのリモデリングが生じていた。Dnmt1 /Tet1 二重欠損 ES 細胞では 5hmC だけでなく、H3K27me3 も消失していたことから、このリモデリングは Tet1 に依存的であることがわかった。また 5mC および 5hmC が完全に消失する Dnmt1/3a/3b 三重欠損 ES 細胞においてもペリセントロメア領域に H3K27me3 が認められたが、Dnmt1/3a/3b/Tet1 四重欠損 ES 細胞では消失していたことから、リモデリングは 5hmC ではなく、Tet1 タンパク自体がエピゲノム因子をリクルートして生じていることが示唆された。ペリセントロメア領域の H3K27me3 は、PGC においても、特に雌において顕著に認められ、共通の機構で生じていることが示唆された。

Tet1 によるヘテロクロマチン・リモデリング現象をさらに検証するために、dCas9-SunTag システムを用いて Tet1 の酵素活性ドメインを人為的にペリセントロメア領域に誘導する、エピゲノム編集を行った。その結果、エピゲノム編集を行った ES 細胞では、上述の結果と矛盾せず、ペリセントロメア領域での 5hmC と H3K27me3 の集積が認められた。一方で、高メチル化状態となる、分化した ES 細胞では、エピゲノム編集を行っても 5hmC と H3K27me3 の集積は認められず、リモデリングは低メチル化状態にある細胞に特異的に生じることが示唆された。エピゲノム編集した ES 細胞では、クロモセンターが核内で集合して巨大化する、クラスタリングが生じていた。クロモセンターに局在するセントロメアは、減数分裂前期にクラスタリングすること、および、これが正常な減数分裂の進行に重要であることが報告されている。この結果と矛盾せず、ヘテロクロマチンのリモデリングが異常となる、Tet1 欠損マウスの雌の生殖細胞では、セントロメアのクラスタリングに異常が認められた。このことから、Tet1 は低メチル化状態の PGC において、ペリセントロメア領域のヘテロクロマチン・リモデリングを誘導し、そのクラスタリングに機能していることが示唆された。

　近年、MEK 阻害剤を含む 2i 条件で培養した ES 細胞では、低メチル化状態が顕著になり、ヘテロクロマチン・リモデリングが低頻度で生じていることが報告された。Tet1 によるメチル化状態依存的なクロマチンリモデリング現象の解析を進めるためには、より胚盤胞に近いエピゲノム状態を維持した ES 細胞の樹立が必要だと考えた。そこで、ES 細胞の樹立と維持の過程で要求される条件の解析を行い、MEK 阻害剤をほとんど用いない条件で ES 細胞を樹立、維持できる手法を開発した（Konishi et al., 2018）。

＜研究の意義・展望＞
　Tet1 は生殖細胞において、特定の遺伝子の DNA のメチル化を制御していることがわかっていたが、本研究の結果、ヒストン修飾の制御にも機能している予想外の結果が得られた。Tet1 を欠損した雌マウスでは、卵子の数および、妊孕性が顕著に低下している。代表者らは、以前、Tet1 欠損マウスの PGC では減数分裂関連遺伝子の発現が低下していること、および、減数分裂前期に生じている対合が不全となった結果、アポトーシスを起こしていること、を報告していた。しかし、減数分裂関連遺伝子の発現異常と対合異常との因果関係が未解明であり、他に直接的な原因が存在する可能性が考えられた。Tet1 によるヘテロクロマチン・リモデリングがセントロメアのクラスタリングに機能しているという本研究での発見は、この未解決の問題に回答を与えうるものだと考えている。今後は、ヘテロクロマチンのリモデリングがどのようにセントロメアのクラスタリングを誘導するのか、という点を解決する必要がある。

＜主な研究発表論文＞
1. Konishi, R., Nakano, T., and Yamaguchi, S. (2018). Distinct requirements for the maintenance and establishment of mouse embryonic stem cells. Stem Cell Res. *31*, 55-61.

体細胞核の全能性獲得に関わる分子機構		平成 28-29 年
研究代表者	宮本　圭	近畿大学生物理工学部
	公募	分子発生工学研究室

＜研究の目的＞

　卵子は精子との受精後に全ての細胞へと分化する能力である全能性を獲得する。一方、分化した体細胞核を卵細胞質内に移植すると、体細胞核に初期化が誘導され、クローン個体を得ることが可能である。しかし、体細胞核が初期化され、全能性を獲得する分子的背景は多くが謎に包まれており、クローン個体の作出効率も低い(Teperek and Miyamoto, 2013)。近年、クローン胚のエピジェネティック状態を変化させることにより、胚の発生率向上とクローン個体の作出効率改善が報告されている。また、発生率改善が見られたクローン胚では、遺伝子発現パターンが正常受精胚へと近づくことも報告されている。これは、全能性獲得へと繋がる体細胞核の初期化には、移植した体細胞核より胚性遺伝子が正常に活性化される必要があることを示唆している。そこで本研究では、クローン胚の発生率改善に伴って発現上昇する胚性遺伝子に着目し、それらの遺伝子がクローン胚の全能性獲得に関わる分子機序の解明を目指す。また、クローン胚の培養培地中へ小分子を添加することによって、胚のエピジェネティック状態や遺伝子発現を変化させ、クローン個体の作出効率改善も試みる。

＜研究成果＞

　我々は、クローン胚のエピジェネティック状態を変化させる方法として、ヒストン脱アセチル化酵素阻害剤 Tricostatin A（TSA）と Vitamin C（VC）を脱イオン化処理をしたウシ血清アルブミンを含む胚培養培地へ加え、TSA と VC の添加濃度と処理時間を詳細に検討した。その結果、核移植後 8 時間の TSA 処理とそれに続く 7 時間の VC 処理により、マウスクローン個体の作出効率が大幅に向上することを発見した（Miyamoto et al., 2017; Azuma et al., 2018）。本条件下では、安定して約 15％ものマウス体細胞クローン個体の作出が可能となる。さらに、当該条件下で発現上昇する遺伝子の内、正常受精胚と比較した際に通常の体細胞クローン胚（発見した条件で処理していないクローン胚）で発現が有意に低下する遺伝子 16 個を同定した。この 16 個の遺伝子の中から胚の全能性獲

得に必要な遺伝子のスクリーニングを行った。その結果、16 個の内、2 個の遺伝子が正常受精胚の発生に必要であることを発見した。この 2 遺伝子の発現様式を体細胞クローン胚で調べたところ、正常受精胚と比較して異常を示すことを見出した。核移植胚
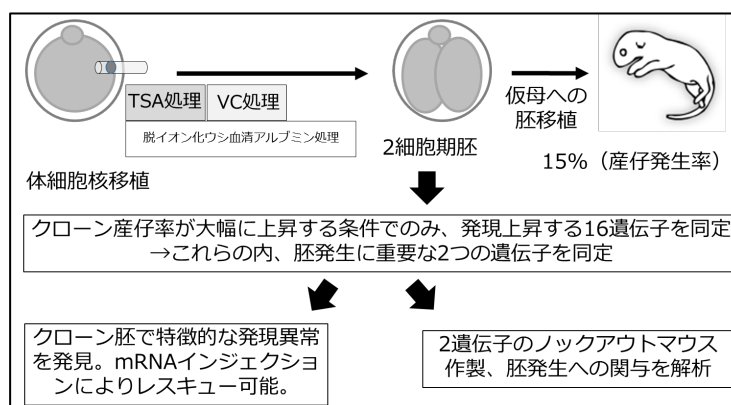
における異常な発現パターンは過剰発現によりレスキュー可能であることも発見した。これら2遺伝子については、伊川班との領域内共同研究によりノックアウトマウスを作製した。以上の結果より、体細胞クローン胚で発現異常を示す2遺伝子の同定に成功し、これらの遺伝子が胚発生に重要な役割を果たすことを示した。

＜研究の意義・展望＞
　培地中への小分子添加という簡易な方法で、安定してクローンマウスを作出する実験系を示した。また、クローン胚において、胚発生に必要であるにもかかわらず、活性化に失敗する特定の遺伝子の同定に至った。これらの遺伝子が体細胞核の全能性獲得にどのように関わるかを今後の研究で明らかにすることによって、クローン胚が発生に失敗する理由を特定の遺伝子レベルで説明できる可能性がある。また、これらの遺伝子がクローン胚で活性化に失敗する分子機構については現在検討中であるが、遺伝子の発現異常の主たる原因として考えられているヒストンH3K9me3が原因ではない可能性を示唆するデータを得ている。即ち、新規の遺伝子発現抑制機構の存在を示唆している。最近研究代表者は、遺伝子発現の初期化を誘導する分子機構を研究する過程で、体細胞核におけるクロマチン構造が遺伝子発現に大幅な影響を及ぼすことを発見した（Miyamoto et al., 2018）。今後は体細胞核のクロマチン構造がマウスクローン胚の遺伝子発現異常と発生不全に及ぼす影響を調べることによって、新たな遺伝子発現制御機構の発見につながる可能性がある。また、クロマチン構造に影響を与える因子として最近証明された核内のアクチンも（Baarlink et al., 2017）、遺伝子発現の初期化と全能性獲得との関係性を知る上で興味深い研究対象である。

＜主な研究発表論文＞

Azuma, R., Miyamoto, K., Oikawa, M., Yamada, M., and Anzai, M. (2018). Combinational treatment of Trichostatin A and vitamin C improves the efficiency of cloning mice by somatic cell nuclear transfer. J. Vis. Exp. *134*, e57036.

Baarlink, C., Plessner, M., Sherrard, A., Morita, K., Misu, S., Virant, D., Kleinschnitz, E.M., Harniman, R., Alibhai, D., Baumeister, S., Miyamoto, K., Endesfelder, U., Kaidi, A., and Grosse R. (2017). A transient pool of nuclear F-actin at mitotic exit controls chromatin organization. Nat. Cell. Biol. *19*, 1389-1399.

Miyamoto, K., Tajima, Y., Yoshida, K., Oikawa, M., Azuma, R., Allen, G.E., Tsujikawa, T., Tsukaguchi, T., Bradshaw, C.R., Jullien, J., Yamagata, K., Matsumoto, K., Anzai, M., Imai, H., Gurdon, J., and Yamada, M. (2017). Reprogramming towards totipotency is greatly facilitated by synergistic effects of small molecules. Biol. Open. *6*, 415-424.

Miyamoto, K., Nguyen, K.T., Allen, G.E., Jullien, J., Kumar, D., Otani, T., Bradshaw C.R., Livesey, F.J., Kellis, M., and Gurdon J.B. (2018). Chromatin accessibility impacts transcriptional reprogramming in oocytes. Cell. Rep. *24*, 304-311.

Teperek, M., and Miyamoto, K. (2013). Nuclear reprogramming of sperm and somatic nuclei in eggs and oocytes. Reprod. Med. Biol. *12*, 133-149.

| 卵母細胞の巨大な細胞サイズの意義		平成 28-29 年
研究代表者	北島智也	理化学研究所
	公募	生命機能科学研究センター

＜研究の目的＞

　卵母細胞は減数分裂を経て卵子となり、受精により胚となる。成長した卵母細胞は巨大な細胞質を持つ。この細胞質サイズは受精後の胚発生を支持するためと考えられているが、どのような細胞内プロセスを介して支持するのかは明らかではない。また、巨大な細胞質サイズが受精前の減数分裂において果たす役割は分かっていない。そこで本研究では、顕微操作とライブイメージングを合わせた生殖工学的かつ細胞生物学的アプローチから、マウス卵母細胞の細胞質サイズが減数分裂と胚発生に与える影響と役割を明らかにする。

＜研究成果＞

　まず、卵母細胞の細胞質サイズが減数分裂に与える影響について調べた。成長したマウス卵母細胞（卵核胞期）の細胞質を顕微操作により半分あるいは二倍にする系を確立した。半分の細胞質を持つ卵母細胞は、マイクロピペットにより細胞質を吸引除去することで作出した。二倍の細胞質を持つ卵母細胞は、除核した細胞質を追加融合することで作出した。これらの細胞に微小管と染色体のマーカーを発現させ、ライブイメージングにより減数分裂の分裂期をモニターした。微小管と染色体の動態について定量的な解析を行った結果、細胞質サイズは紡錘体サイズと分裂後期への進行時間に顕著な影響を与えることが分かった。細胞質サイズが大きいほど紡錘体サイズは大きくなり、それは紡錘体極の機能性を低下させていた。また、細胞質サイズが大きいほど分裂後期への進行時間が早くなり、それは紡錘体チェックポイントの厳密性が低下したためであった。これらの結果から、卵母細胞の巨大な細胞質サイズは紡錘体の機能性を制限し、染色体分配エラーを起こしやすくしていることが明らかになった

(Kyogoku & Kitajima 2017 Dev Cell)。

　続いて、卵母細胞の細胞質サイズが受精後の胚発生に与える影響について調べた。細胞質サイズを変化させた卵母細胞にICSI を行い、その胚発生をモニターする系を確立した。ライブイメージングによる解析の結果、細胞質サ

イズは前核のサイズに顕著な影響を与えることが分かった。そこで、核内のヒ
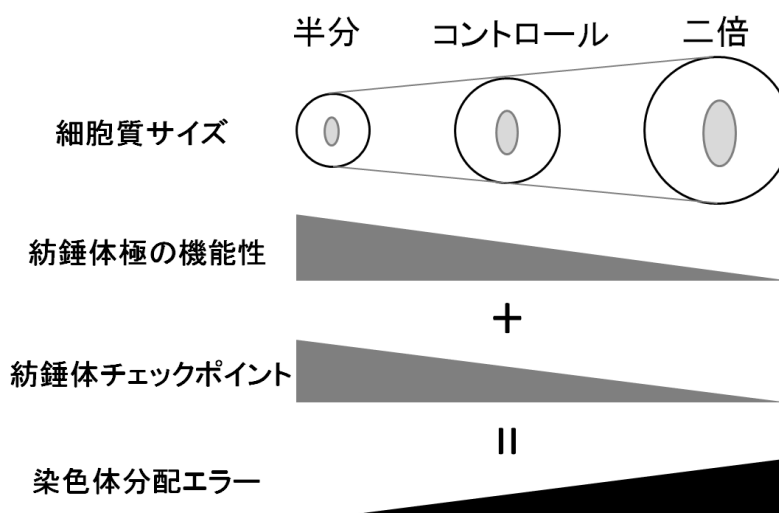
ストン修飾に着目して解析を行ったところ、特に雌性前核のヒストン修飾の量が細胞質サイズに顕著に影響することが分かった。これらの結果から、巨大な細胞質サイズは受精後の核形成を促進し、ヒストン修飾などエピゲノム制御に関わるという可能性が考えられる。

＜研究の意義・展望＞

　エピゲノム研究分野では主流のアプローチではないライブイメージングを用いることで、卵母細胞および胚のエピゲノム制御を細胞学的視点から理解する手がかりを与えることができた。卵母細胞の細胞質サイズがエラーを起こしやすい性質と結びついていることを示した研究成果は、流産や先天性疾患の原因である染色体数異常を理解するための基盤となるだろう。細胞質サイズが受精後の胚発生をどのように支持するのかについては、研究を継続して行う必要がある。今回用いた実験系は人工的に細胞質サイズを変化させるアプローチであったが、胚発生においては、細胞質サイズ減少は卵割にともなって行われる通常のイベントであり、その物理的変化が胚発生の何らかの過程を駆動するのであれば大変興味深い。

＜主な研究発表論文＞

1. Niwayama R, Nagao H, Kitajima TS, Hufnagel L, Shinohara K, Higuchi T, Ishikawa T, and Kimura A. (2016). Bayesian inference of forces causing cytoplasmic streaming in Caenorhabditis elegans embryos and mouse oocytes. PLOS One. *11*, e0159917.
2. Kyogoku, H., and Kitajima, T.S. (2017). Large cytoplasm is linked to the error-prone nature of oocytes. Dev. Cell *41*, 287-298.
3. Kyogoku H., Wakayama T., Kitajima, T.S., and Miyano T. (2018). Single nucleolus precursor body formation in the pronucleus of mouse zygotes and SCNT embryos. PLOS One 13(8): e0202663.
4. Ding, Y., Kaido, M., Llano, E., Pendas, A.M., and Kitajima, T.S. (2018). The post-anaphase SUMO pathway ensures the maintenance of centromeric cohesion through meiosis I-II transition in mammalian oocytes. Curr. Biol. 28(10), 1661-1669.

（総説）
1. 北島智也 (2017) 卵子の染色体数異常の細胞生物学的な原因　日本卵子学会誌 2(2), 39-44.
2. Kitajima, T.S. (2018). Mechanisms of kinetochore-microtubule attachment errors in mammalian oocytes. Dev. Growth Differ. 60(1), 33-43.
3. 北島智也 (2018) 哺乳類卵母細胞における染色体分配—細胞の特異性に対する染色体分配の恒常性と破綻を理解する　実験医学 36(17), 157-162.

生殖細胞におけるヒストンバリアントによるゲノムマーキング機構の解明	平成 28-29 年

研究代表者	原田哲仁	九州大学生体防御医学研究所
	公募	トランスクリプトミクス分野
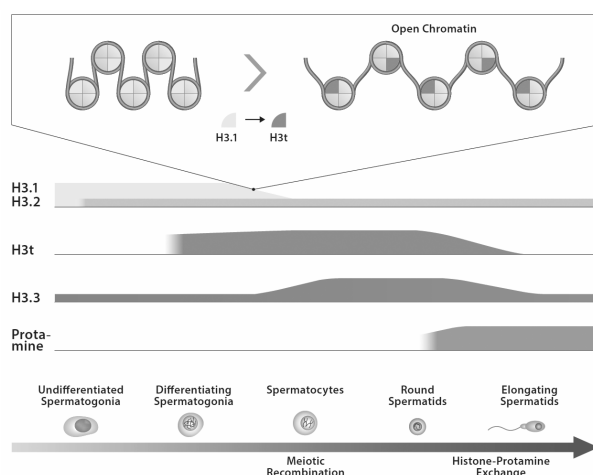
<研究の目的>

　個体が遺伝形質を次世代に伝える際に基盤となるのは、生殖細胞におけるゲノム DNA である。その一方で、近年の解析により、TH2A、TH2B 等の生殖細胞特異的なヒストンバリアントの同定が進み、精子形成にヒストンバリアントが必要であることが明らかとなっている。申請者らは 2015 年にヒト及びマウスゲノムにおいて、未知のヒストンバリアント遺伝子を網羅的に同定した。さらに、その中に生殖組織に特異的に発現する H3 バリアント群の存在を明らかとした。先行研究の結果、新たに同定した精巣特異的に発現するマウス H3 バリアント H3t は精子形成に不可欠であった。これらの事実は精子形成に新規ヒストンバリアント群が必須であることを示している。しかしながら、精巣組織には他にも特異的に発現するヒストンバリアントが存在しており、精子形成や精子の機能、そして受精後のエピジェネティックな遺伝に至る生殖系列サイクルで、どのような役割を担っているか未だ解明されていない。そこで、本研究では、未知ヒストンバリアントを含めた精巣に発現するヒストンバリアントの解析を行う。その方法として、精子あるいは精巣に含まれるヒストンのゲノムワイドな局在とヒストン修飾を明らかにし、精子形成過程において各バリアントが関わるヒストン修飾酵素、クロマチン構造変換酵素群を同定する。

そこで本研究では、生殖細胞におけるヒストンによって構成されるクロマチン基盤を明らかにすることで、生殖系列サイクルにおけるヒストンバリアントの機能解明を目的とする。

<研究成果>

　2015 年にマウスゲノムに存在する未知のヒストン H3 様のバリアント遺伝子を 14 種同定した。そのうち精巣特異的に発現する H3t が構成するクロマチン構造およびその機能解明を本研究で進めている。本年度ではマウスにおける精巣特異的ヒストンバリアント H3t の解析を重点的に行った。ヒストン H3t を破壊したノックアウトマウスは見かけ上、正常に発育する一方で、雄が無精子症となり完全に不妊となる。H3t 欠損により萎縮した精巣および生後 10 日目マウス精巣を用いた微量 RNA-seq 解析により、H3t 欠損マウスの精巣で発現が優位に低下していた遺伝子は主に第一減数分裂に関わる遺伝子であることが明らかと

なった(Ueda et al, Cell Reports., 2017)。さらに、H3t が取り込まれる領域を特定するために H3t 抗体を用いた ChIP-seq 解析を行った。その結果、H3t は遺伝子領域ではなく非遺伝子領域に分布していることが明らかとなった。これらのことから、H3t は減数分裂初期に非遺伝子領域に取り込まれゲノムの自由度を変化させている可能性が示唆された。

　また、ヒトヒストン H3 バリアントついては、我々が同定したヒト H3 バリアント H3.6, H3.7, H3.8 の発現部位を mRNA-seq データ及び作製した特異的モノクローナル抗体を用いた免疫組織化学染色により同定した(Taguchi et al., Biochemistry., 2017)。また、H3.5 が、非閉塞性無精子症の患者では発現が低いこと、ホルモン療法により H3.5 の発現が回復することを明らかにした(Shiraishi et al., Andrology., 2018)。

＜研究の意義・展望＞
　本研究により、ヒストンバリアントがエピゲノム因子の一つとして精子形成を制御していることが示唆された。特に H3t は精子形成の初期に発現していることから、H3t の発現を起点として様々なヒストンバリアントの発現が制御されている可能性がある。今後は、H3t を起点とした生殖細胞特異的なヒストンバリアントで構成されるクロマチン構造解析により、精子形成においてヒストンソースを変化させながらプロタミン置換に至る重要性を明らかにしていきたい。また、H3.5 は霊長類の精巣特異的ヒストン H3 バリアントであるのに対し、H3T はヒト、マウスを含め哺乳動物で広く保存されていることから、両者の機能を比較解析することで精子形成過程における霊長類で獲得された精子形成機構の同定につながることが期待される。

＜主な研究発表論文＞
1. Shiraishi, K., Shindo, A., Harada, A., Kurumizaka, H., Kimura, H., Ohkawa, Y., and Matsuyama, H. (2018). Roles of histone H3.5 in human spermatogenesis and spermatogenic disorders. Andrology 6, 158-165.

2. Taguchi, H., Xie, Y., Horikoshi, N., Maehara, K., Harada, A., Nogami, J., Sato, K., Arimura, Y., Osakabe, A., Kujirai, T., et al. (2017). Crystal Structure and Characterization of Novel Human Histone H3 Variants, H3.6, H3.7, and H3.8. Biochemistry 56, 2184-2196.

3. Ueda, J., Harada, A., Urahama, T., Machida, S., Maehara, K., Hada, M., Makino, Y., Nogami, J., Horikoshi, N., Osakabe, A., et al. (2017). Testis-Specific Histone Variant H3t Gene Is Essential for Entry into Spermatogenesis. Cell Rep 18, 593-600.

代表論文

Sexual Fate Change of XX Germ Cells Caused by the Deletion of SMAD4 and STRA8 Independent of Somatic Sex Reprogramming

Quan Wu[1,2], Kurumi Fukuda[1,2], Yuzuru Kato[2], Zhi Zhou[2], Chu-Xia Deng[3], Yumiko Saga[1,2,4]*

1 Department of Genetics, Sokendai, Mishima, Japan, 2 Division of Mammalian Development, National Institute of Genetics, Mishima, Japan, 3 Faculty of Health Sciences, University of Macau, Macau SAR, China, 4 Department of Biological Sciences, Graduate School of Science, The University of Tokyo, Tokyo, Japan

* ysaga@nig.ac.jp

Abstract

The differential programming of sperm and eggs in gonads is a fundamental topic in reproductive biology. Although the sexual fate of germ cells is believed to be determined by signaling factors from sexually differentiated somatic cells in fetal gonads, the molecular mechanism that determines germ cell fate is poorly understood. Herein, we show that mothers against decapentaplegic homolog 4 (SMAD4) in germ cells is required for female-type differentiation. Germ cells in *Smad4*-deficient ovaries respond to retinoic acid signaling but fail to undergo meiotic prophase I, which coincides with the weaker expression of genes required for follicular formation, indicating that SMAD4 signaling is essential for oocyte differentiation and meiotic progression. Intriguingly, germline-specific deletion of *Smad4* in *Stra8*-null female germ cells resulted in the up-regulation of genes required for male gonocyte differentiation, including *Nanos2* and *PLZF*, suggesting the initiation of male-type differentiation in ovaries. Moreover, our transcriptome analyses of mutant ovaries revealed that the sex change phenotype is achieved without global gene expression changes in somatic cells. Our results demonstrate that SMAD4 and STRA8 are essential factors that regulate the female fate of germ cells.

Author Summary

Mammalian sex depends on a male-specific gene, sex-determining region Y (SRY), which is located on the Y chromosome. Individuals lacking this gene will develop as female. Accordingly, germ cell fate also changes from male to female in the absence of SRY. Therefore, it is thought that somatic cells regulate germ cells to become sperm or oocytes. However, it is largely unknown what factor is responsible for sexual fate determination in germ cells. In fetal ovaries, retinoic acid (RA) initiates STRA8 expression in germ cells and induces meiosis. Female germ cells without STRA8 fail to enter meiosis but still progress to oogenesis and form oocyte-like cells, indicating that RA is not the

regulator of oogenesis. Here, we found that female germ cells lacking both SMAD4 and STRA8 (but not a single knockout) develop as male gonocyte-like cells in ovaries, indicating that these two factors work as female germ cell determinants. To our surprise, the sexual fate switch observed in the double knockout ovary is not accompanied by gene expression changes in somatic cells, revealing the unexpected finding that somatic factors controlled by SRY are dispensable for the upregulation of male-specific genes in germ cells.

Introduction

Primordial germ cells (PGCs) that emerge in the early mouse embryo have the capability to become either spermatocytes or oocytes and are enclosed by somatic cells in embryonic testes or ovaries. The sexual fate of germ cells in gonads is thought to be determined by factors derived from somatic cells because somatic sex determination precedes germ cell sex determination, and sex reversal in somatic cells leads to sex reversal in germ cells [1]. However, when and how germ cells receive such signals, and the determinants of germ cell sex, remain unknown. Understanding the mechanism of sex determination in germ cells requires elucidation of the pathways associated with male and female differentiation events.

The earliest sign of sexual differentiation in male germ cells is the entry into cell cycle arrest that is likely due to the suppression of retinoic acid (RA) signaling caused by upregulation of the RA-metabolizing enzyme CYP26B1 in somatic cells [2–4]. Simultaneously, the male-specific factor NANOS2 is induced by mothers against decapentaplegic homolog (Smad) 2 signaling in germ cells, and the expression is maintained during the embryonic stage [5–8]. The sex of germ cells in testes is determined by NANOS2 function, as the absence of NANOS2 impedes male differentiation and results in the induction of female characteristics, such as meiotic initiation and upregulation of genes associated with oocyte differentiation [9,10]. Inversely, if *Nanos2* is ectopically induced in female germ cells, the cells fail to enter meiosis and begin male-specific gene expression, such as DNA methyltransferase 3-like protein (*Dnmt3L*) and *MIWI2*, which are required for male-specific de novo DNA methylation in embryonic testes [10–13]. The somatic factor sex-determining region Y (SRY) and its downstream effectors SRY-box (SOX) 9 and fibroblast growth factor 9 (FGF9) are essential for the male fate decision because their deletions lead to male-to-female sex reversal, germ cells included [14–19]. Among these factors, FGF9 is considered to work directly in germ cells to induce *Nanos2* [16,20]. However, a recent report showed that the deletion of a female-specific gene, wingless-related MMTV integration site 4 (*WNT4*), in *Fgf9*-null testes rescues the switch from male to female, which suggests that FGF9 acts by suppressing WNT4 expression rather than by actively directing male fate [21]. Thus, the signal that induces the male fate decision remains unknown.

The sexual fate of germ cells in ovaries appears to be induced by two distinct processes—meiosis and oocyte differentiation—that proceed simultaneously [22]. Upon receiving an RA signal, XX germ cells express genes such as stimulated by retinoic acid 8 (*Stra8*) and *Rec8* [2,23,24]. After pre-meiotic DNA replication controlled by STRA8, germ cells enter meiotic prophase I, during which homologous chromosome pairing and recombination occurs in a series of stages: leptotene, zygotene, pachytene, and diplotene. Therefore, sexual differentiation in the ovary is associated with meiotic initiation, a process that is never observed in wild-type testes during the embryonic stage. In *Stra8*-deficient ovaries, XX germ cells enter neither meiosis nor mitosis and retain DNA content as 2N [23]. However, a recent study showed that

oocyte-like cells are generated without premeiotic replication in *Stra8*-deficient ovaries, which indicates that the feminization of germ cells occurs independent of meiosis and that factors other than RA must be involved in the induction of oocyte differentiation [22]. FOXL2 and WNT4 are possible somatic factors required for female fate determination, as evidenced by the sex reversal of XX PGCs caused by the deletion of *Foxl2* and *Wnt4* [25]. However, it is controversial whether the effector of Wnt signaling, β-catenin, functions in somatic cells or germ cells [26–28]. Therefore, the somatic factors downstream of FOXL2 and WNT4 signals that directly induce oocyte differentiation are unclear.

To clarify the signals that lead to the sexual determination of germ cells, we have focused on the transforming growth factor β (TGFβ) signaling pathway. We have shown that nodal/activin signaling is activated in germ cells in embryonic testis but not in ovaries, and is required for the induction of the male determinant NANOS2 [5,8]. In this study, we investigated the possible role of bone morphogenetic protein (BMP) signaling in the sexual differentiation of germ cells in ovaries because a previous study suggested that *Bmp2* expression was under the control of Wnt signaling, although the function of BMP2 remains unknown [29]. BMP signaling is mediated by SMAD 1, 5, or 8 and their common mediator Co-SMAD4 [30]. To determine the function of BMP signaling, we deleted *Smad4* in a germ-line-specific manner. We here provide evidence that Smad4 signaling plays essential roles in the induction of oocyte-specific regulators as well as in meiotic progression. Notably, the suppression of Smad4 and RA signaling in germ cells is sufficient to direct the cells to take a male pathway even in the absence of male somatic cells.

Results

Smad4 Signaling Is Required for Germ Cell Survival in the Fetal Ovary

To investigate any involvement of BMP signaling in the fetal ovary, we used immunostaining to examine the expression pattern of phosphorylated SMAD (pSMAD) 1/5/8. pSMAD1/5/8 was detected in both germ and somatic cells in ovaries from E11.5 to E13.5, suggesting that BMP signaling is activated in both cell types (S1A Fig). pSMAD1/5/8 requires SMAD4 to activate downstream genes even though these factors can enter the nucleus upon ligand binding [31]. Thus, we used a floxed allele of *Smad4* encoding the Co-SMAD protein to analyze the function of BMP signaling in ovaries. Although SMAD4 may mediate other TGFβ-signaling pathways mediated by SMAD2 and 3, previous studies have shown that phosphorylated SMAD2 was not detectable in ovaries at this stage [5,32]. Therefore, we reasoned that the deletion of *Smad4* may disrupt pSMAD1/5/8-dependent BMP signaling rather than pSMAD2/3-dependent signaling in the ovary, but we do not exclude the possibility that SMAD4 is also involved in other signaling pathways.

Smad4 was deleted in a germ cell-specific manner by using a transgenic *Stella-MerCreMer* line [33], in which Cre recombinase activity was induced by tamoxifen (TM) administration under the regulation of the element that controls *Stella* (a gene specifically expressed in germ cells) expression. We injected TM at E9.5 and E10.5 to delete *Smad4* in germ cells (Fig 1A). We refer to this mouse model as the *Smad4 (Stella)* mutant unless otherwise specified. The efficiency of Cre activity was variable, but was as high as 80% based on the reporter gene expression (S1B Fig). We found that the germ cell number decreased in the mutant ovaries at E16.5 and E17.5 (Fig 1B and 1C). As the reduction of female germ cells was correlated with the increase of cleaved-caspase3 positive germ cells at E16.5 (Fig 1D), it is likely that the observed germ cell loss was due to apoptotic cell death. These results indicate that *Smad4* is required for female germ cell survival.
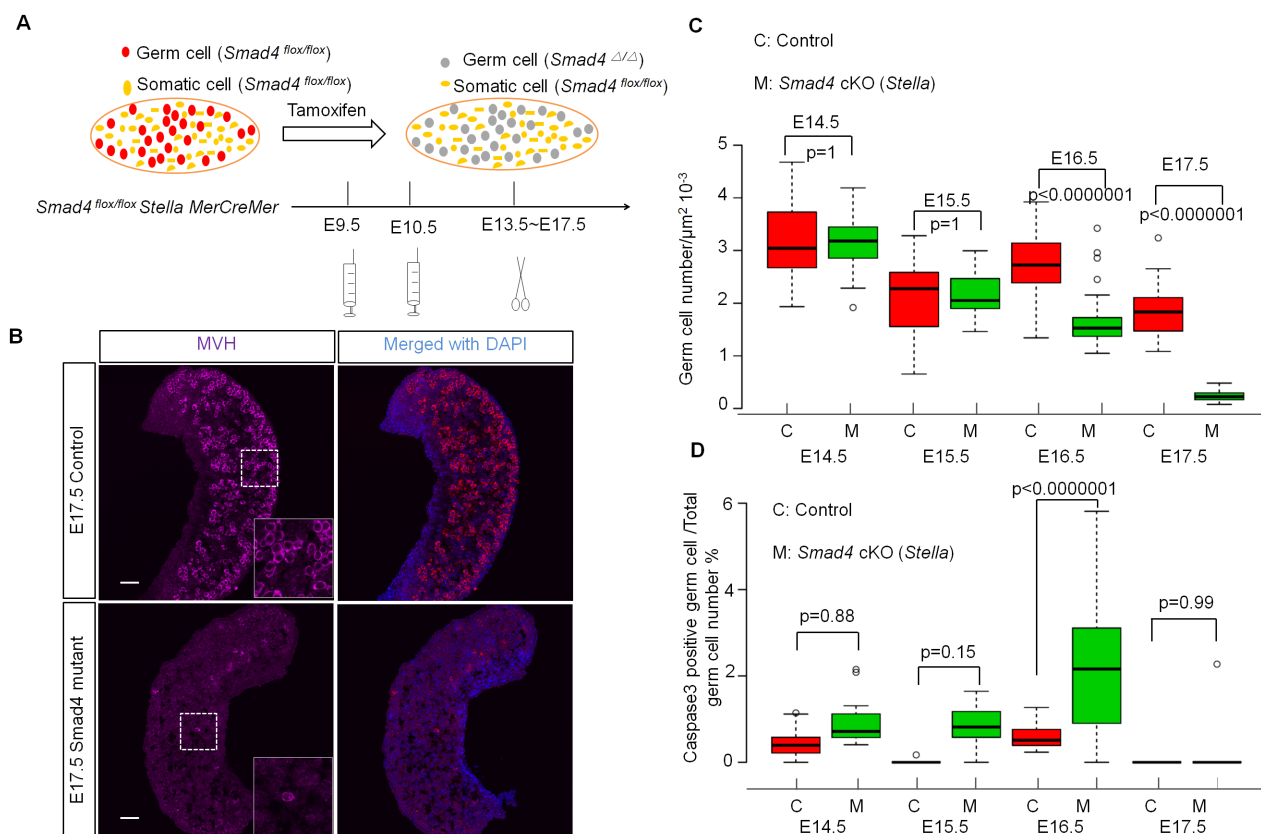
Fig 1. Smad4 signaling is required for germ cell survival. (A) Scheme of germ-cell-specific knockout strategy. Tamoxifen was injected at E9.5 and E10.5, and ovaries were recovered at indicated stages. (B) Representative image of E17.5 *Smad4 (Stella)* mutant and control ovarian tissue sections stained for MVH and DAPI. (C,D) Temporal changes of germ cell number (C) and cleaved-caspase3 positive germ cells (D) in control and *Smad4 (Stella)* mutant ovaries. Sample numbers used for counting were indicated in S1 Data. Significance was assessed using one-way ANOVA followed by Tukey's post-hoc tests for selected pairs of genotypes. Scale bars: 50 μm. We used *Smad^{flox/flox}*, *Smad4^{flox/+}*, and *Smad4^{flox/+} StellaMerCreMer* ovaries as the control.

doi:10.1371/journal.pbio.1002553.g001

Crucial Role of Smad4 Signaling in Female Germ Cell Differentiation Independent of RA Signaling

To investigate the cause of germ cell death and understand the function of SMAD4, we examined the gene expression changes that occurred before apoptosis. As female differentiation consists of meiosis and oocyte differentiation pathways, we first examined the expression of *Stra8*, a gene involved in pre-meiotic DNA replication [3,23]. In normal ovaries, STRA8 is expressed in germ cells from E13.5, and most of the germ cells lost this expression at E15.5 due to the progression of meiotic prophase I (Fig 2A). Even in *Smad4 (Stella)* mutant ovaries, STRA8 expression was observed from E13.5 as well, indicating that the deletion of *Smad4* does not interfere with RA signaling. However, its expression was retained up to E15.5 (Fig 2A), suggesting that *Smad4*-deficiency influences the progression of meiosis.

To evaluate *Smad4*-deficiency defects after the initiation of *Stra8* expression, we performed a cytological examination with *Smad4 (Stella)* mice at E15.5. In control ovaries, immunodetection of synaptonemal complex proteins (SYCPs) 1 and 3 in meiocyte spreads revealed normal meiotic progression: germ cells were found at leptotene (20/104 = 19.2%), zygotene (41/104 = 39.4%), or pachytene (43/104 = 41.3%) stages (Fig 2B). However, in *Smad4 (Stella)* ovaries, we found that 22.4% (26/116) of TRA98 (a germ cell marker)-positive cells showed weak
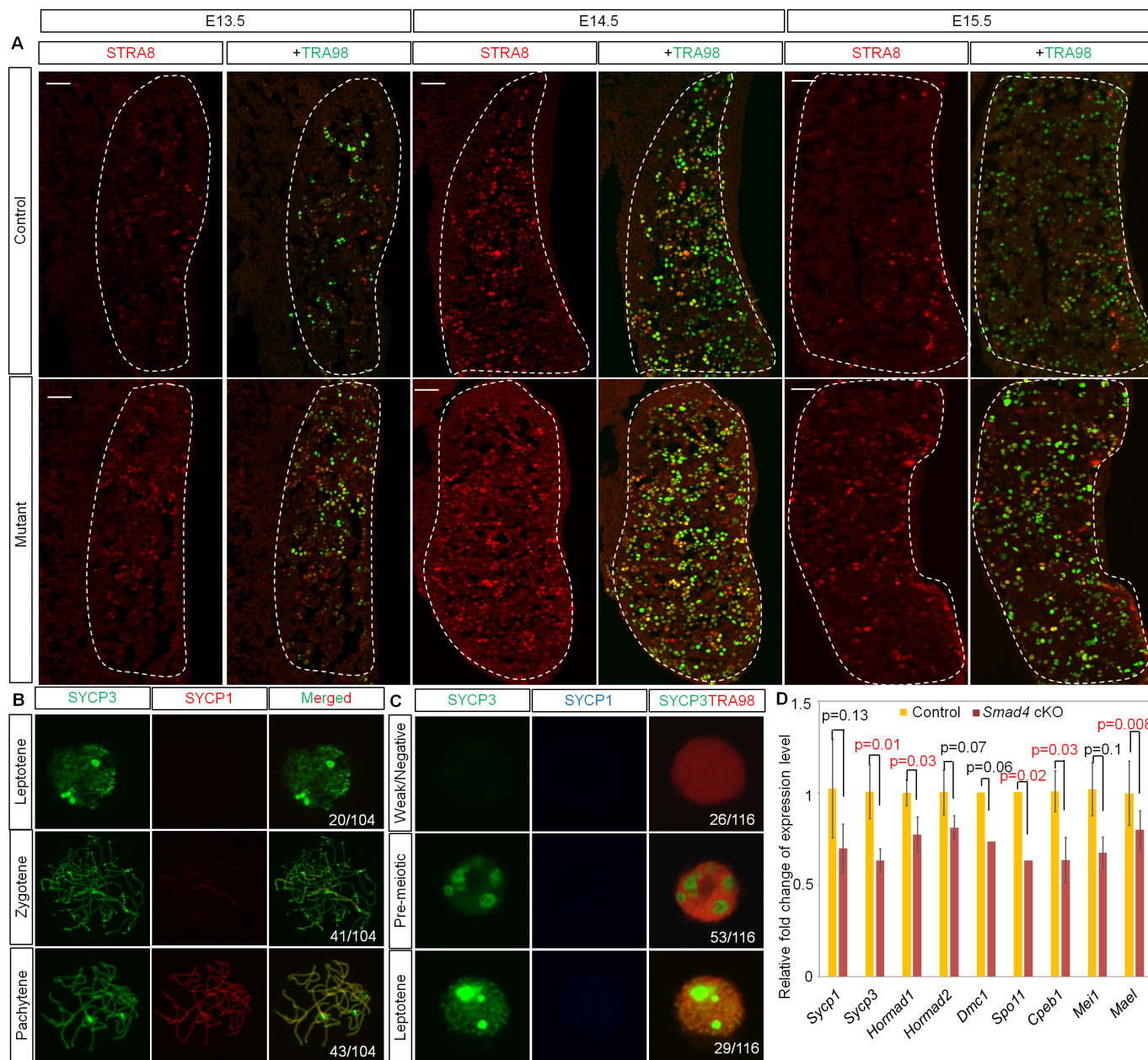
Fig 2. Initiation of meiosis but failure of meiotic progression in *Smad4 (Stella)* germ cells. (A) Representative image of the indicated ovary sections stained for STRA8 and TRA98 at E13.5, E14.5, and E15.5 in control and *Smad4 (Stella)* mutant ovaries. Ovaries were marked by dotted lines. Scale bars: 50 μm. (B) Representative images of leptotene, zygotene, and pachytene stage oocytes stained with SYCP3 and SYCP1 in control ovaries at E15.5. Number of oocytes in each stage is shown. (C) Representative images of different patterns of germ cells stained with SYCP3 and SYCP1 in *Smad4 (Stella)* ovaries at E15.5. Number of germ cells in each pattern is shown. (D) Expression level of meiosis-related genes in control and *Smad4 (Stella)* ovaries at E14.5 (*n* = 3 each). Data was extracted from microarray analysis (see S1 Data). Data is shown by a bar graph with *p*-value calculated by Student's *t* test. Error bars indicate standard deviation.

doi:10.1371/journal.pbio.1002553.g002

or negative SYCP3 signals (Fig 2C, upper panel). Furthermore, SYCP3 localized in nucleoli in 45.7% (53/116) of *Smad4(Stella)* germ cells (Fig 2C, middle panel), similar to that observed in pre-meiotic female germ cells and *Stra8*-null germ cells at E15.5 [23]. The remaining 25.0% (29/116) and 6.9% (8/116) of *Smad4 (Stella)* germ cells were at the leptotene stage lacking the

central synaptonemal complex (SC) marker SYCP1 (Fig 2C, lower panel) or at the zygotene stage, respectively. No pachytene-stage germ cells were observed in *Smad4*-deficient ovaries. The failure of meiosis progression was also examined by expression analyses of meiosis-related genes at E14.5. These genes included *Sycp1*, *Sycp3*, *Cpeb1*, *Mei1*, *Hormad1*, and *Hormad2* [34–37], which are related to the formation of SC protein and *Spo11*, *Dmc1*, and *Mael*, which are required for the induction, formation, and repair of double strand breaks and repression of transposable elements [38–40]. The expression levels of five out of nine genes were lower in the mutant than in the controls (Fig 2D). These results suggest that Smad4 signaling is required for meiotic progression independent of RA signaling.
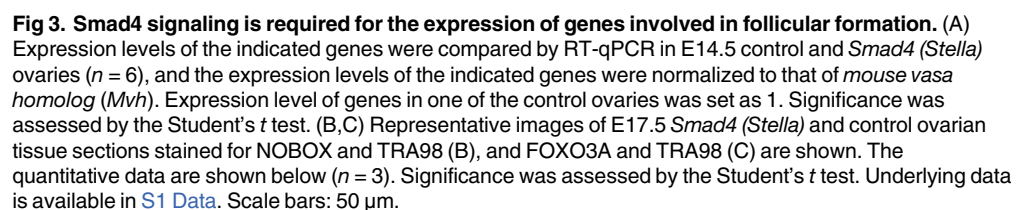
Next, we investigated the expression of genes involved in oocyte differentiation. We found that the expression of *Figla*, a key transcription factor required for primordial follicle formation, was decreased in *Smad4 (Stella)*-mutant ovaries; however, two other regulators, *Lhx8* and *Sohlh1* [41], were either not decreased (*Lhx8*) or significantly increased (*Sohlh1*) at E14.5 (Fig 3A). Although apoptosis occurred in *Smad4*-null germ cells at E16.5, some germ cells still survived. However, the number of newborn ovary homeobox protein (NOBOX)- and Forkhead box O3a (FOXO3A)-positive germ cells was fewer in *Smad4*-deficient ovaries than in the control at E17.5 (Fig 3B and 3C). These data suggest that SMAD4 plays a role in oogenic gene expression, although it is unclear whether SMAD4 directly controls these gene expressions or not.

SMAD4 in Somatic Cells Does Not Contribute to Female-Type Differentiation of Germ Cells

Next, we examined whether SMAD4 in somatic cells contributes to the female differentiation of germ cells. To delete *Smad4* from somatic cells, we used *WT1-CreERT2* mice. In this mouse line, *CreERT2* was inserted into the *Wt1* locus, and WT1 is expressed in genital ridges beginning at around E9.5 [42,43]. We injected TM into *Smad4$^{flox/flox}$*/*WT1-CreERT2* mice at E10.5 and E11.5 to delete *Smad4* in somatic cells. *Smad4* expression was repressed, but this had no effect on *Figla* and *Lhx8* expression; however, *Sohlh1* expression was slightly upregulated at E14.5 (S2A and S2B Fig). As most embryos died at E15.5 under our experimental conditions, we therefore cultured embryonic gonads for 3 days from E14.5 and examined the germ cell characteristics. We found that the differentiation of female germ cells was unaffected based on a comparison of NOBOX-positive germ cells in control and mutant ovaries (S2C Fig). In contrast, ubiquitous deletion of *Smad4* in *Smad4$^{flox/flox}$*/*Rosa-CreERT2* ovaries showed results similar to those observed in *Smad4 (Stella)* ovaries (S3 Fig). Expression of many meiotic marker genes as well as genes involved in follicle formation (*Lhx8* and *Figla*) was downregulated, while *Stra8* and *Rec8* expressions were not decreased (S3B Fig). Therefore, we concluded that Smad4 signaling acts in germ cells rather than somatic cells to control differentiation of germ cells in ovaries.

Suppression of Smad4 and RA Signaling Induces Ectopic NANOS2 Expression in the Ovary

To further examine the function of SMAD4 in the early germ cell differentiation pathway, we examined pluripotency-related genes. In germ cells of normal ovaries, the expression of the pluripotency-related genes *Sox2*, octamer-binding transcription factor 4 (*Oct4*), *Nanog*, and undifferentiated embryonic cell transcription factor 1 (UTF1) is downregulated at E14.5 accompanied by the upregulation of genes involved in female differentiation, which indicates that the downregulation is associated with female differentiation (Fig 4) [44,45]. In *Smad4*-deficient germ cells, however, these gene expressions were retained at high levels (Fig 4 and

112

Fig 3. Smad4 signaling is required for the expression of genes involved in follicular formation. (A) Expression levels of the indicated genes were compared by RT-qPCR in E14.5 control and *Smad4 (Stella)* ovaries (*n* = 6), and the expression levels of the indicated genes were normalized to that of *mouse vasa homolog* (*Mvh*). Expression level of genes in one of the control ovaries was set as 1. Significance was assessed by the Student's *t* test. (B,C) Representative images of E17.5 *Smad4 (Stella)* and control ovarian tissue sections stained for NOBOX and TRA98 (B), and FOXO3A and TRA98 (C) are shown. The quantitative data are shown below (*n* = 3). Significance was assessed by the Student's *t* test. Underlying data is available in S1 Data. Scale bars: 50 µm.

doi:10.1371/journal.pbio.1002553.g003

S3D Fig), indicating that SMAD4 is involved in the suppression of pluripotency-related genes upon entering a female differentiation pathway.

Since *Smad4-null* germ cells showed severe defects in female differentiation, we speculated that the sexual fate of these PGCs may have been switched from female to male. To test this possibility, we investigated whether NANOS2, a male- specific marker, is expressed in *Smad4-null* germ cells. However, we did not observe upregulation of NANOS2 in the *Smad4*-null germ cells (S4A Fig). We reasoned that the absence of *Nanos2* gene expression may be due to RA signaling, which blocks *Nanos2* activation in the testes [4,16], and predicted that simultaneous suppression of Smad4 and RA signaling may lead to *Nanos2* induction in XX germ cells.
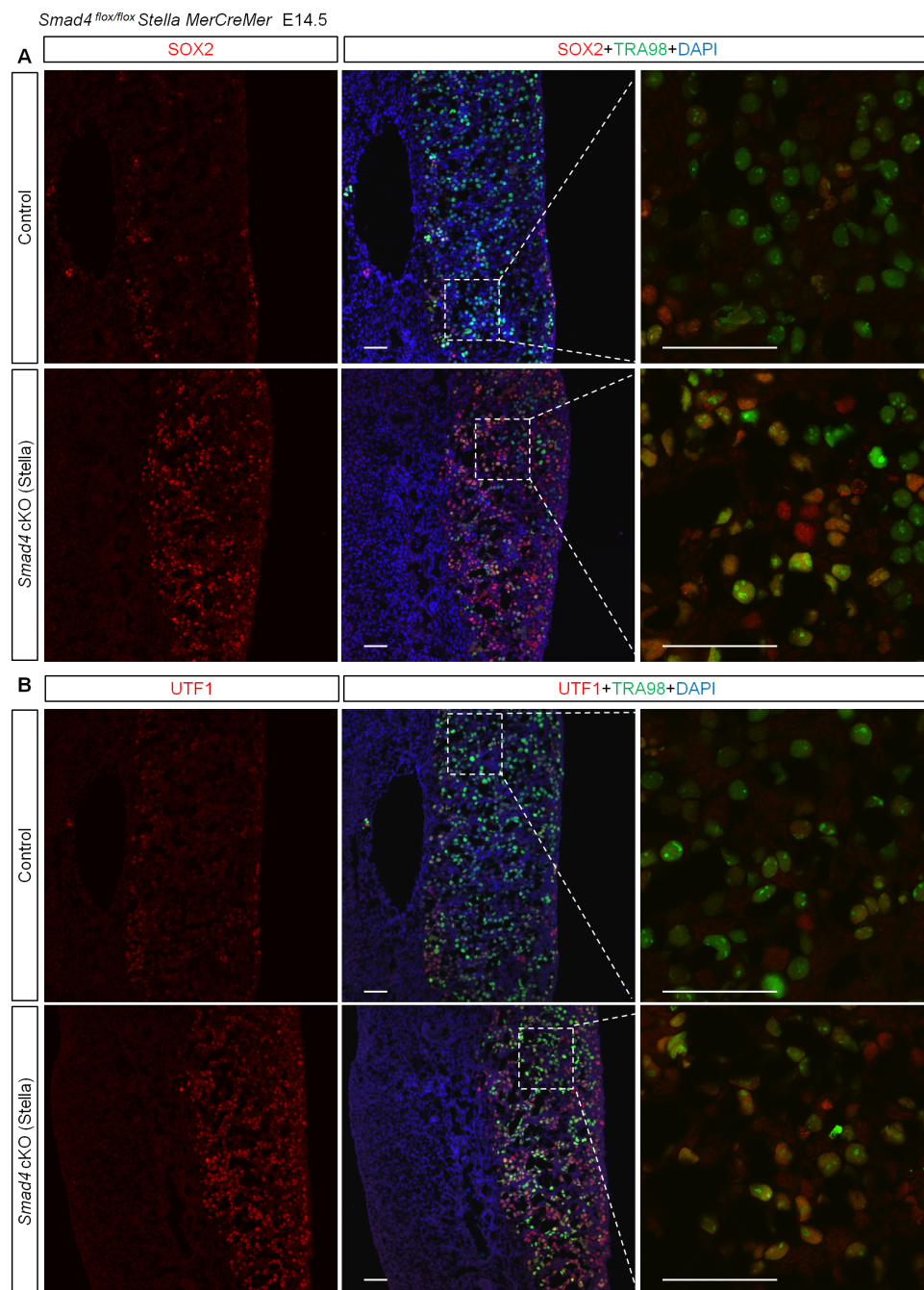
Smad4 _flox/flox_ Stella MerCreMer E14.5

Fig 4. Maintenance of pluripotency gene expression in XX germ cells in the absence of SMAD4. (A,B) Immunohistochemical detection of SOX2/TRA98 (A) and UTF1/TRA98 (B) in the E14.5 control and _Smad4 (Stella)_ ovaries. Scale bars: 50 μm.

doi:10.1371/journal.pbio.1002553.g004

To test this hypothesis, we collected ovaries of _Smad4 (Stella)_ carrying a Cre reporter _CAG-floxed-CAT-EGFP_ at E12.5 and cultured them with the RA receptor antagonist AGN193109. In this genetic background, _Smad4_-deficient cells could be detected through GFP reporter expression (Fig 5A). We found that 70% (302/431; _n_ = 5) of GFP-positive (_Smad4_-null) XX germ cells expressed NANOS2 only in the presence of RAR inhibitor (Fig 5B). Importantly, neither
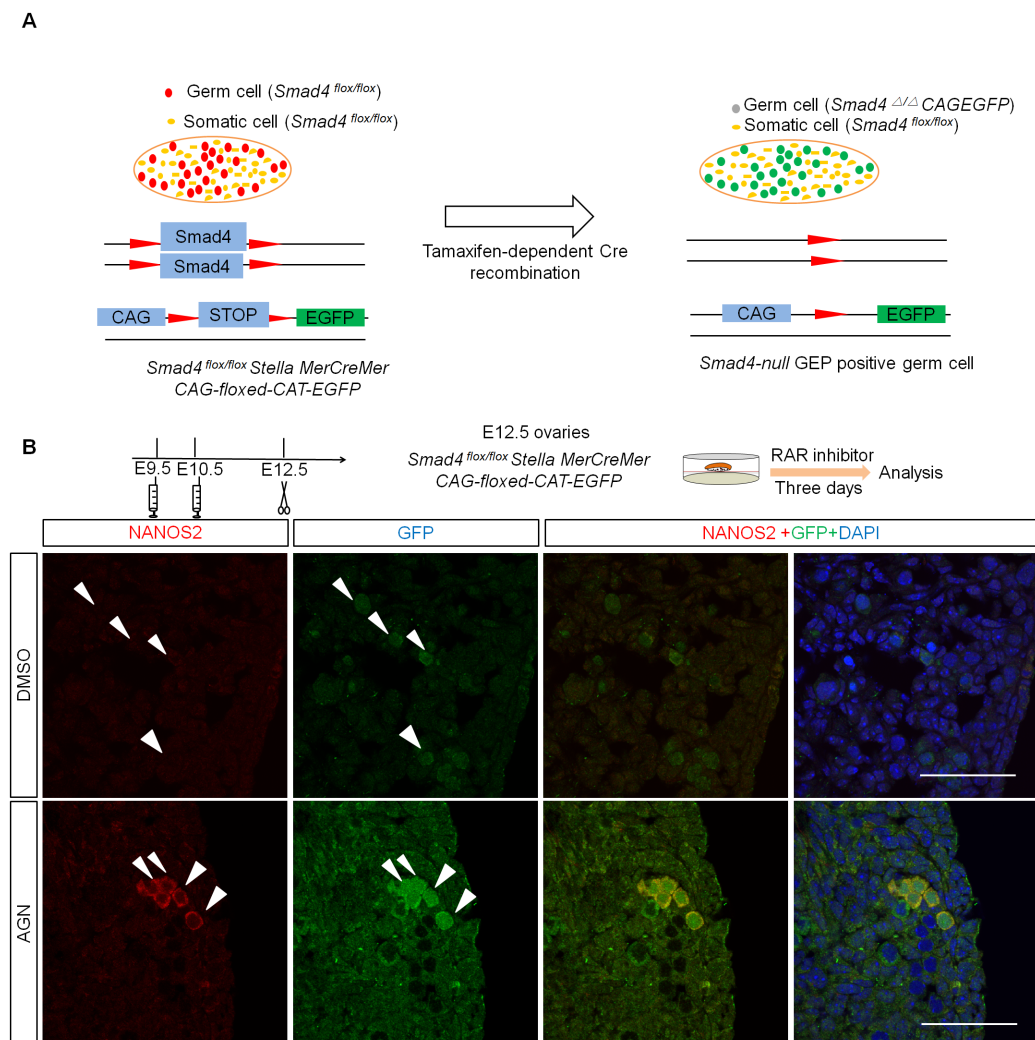
Fig 5. NANOS2 upregulation occurred in _Smad4_-null germ cells in the absence of RA signaling. (A) Scheme of strategy to trace the fate of _Smad4-null_ germ cells. Deletion of _Smad4_ by Cre recombination induces the expression of GFP, indicating _Smad4_-null germ cells. (B) Representative image of sections from _Smad4 (Stella)_ ovaries after DMSO or AGN193109 treatment stained for NANOS2 and GFP. White arrows indicate GFP-positive cells. Ovaries were cultured from E12.5 for 3 d with indicated drugs after injection of tamoxifen at E9.5 and E10.5. Scale bars: 50 μm.

doi:10.1371/journal.pbio.1002553.g005

ubiquitous deletion of _Smad4_ nor RAR inhibitor treatment in control ovaries alone induced _Nanos2_ expression (S4B–S4D Fig). These data suggest that Smad4 and RA signaling regulate female germ cell fate in a cooperative manner.

Germ Cell-Specific Deletion of _Smad4_ and _Stra8_ Resulted in Production of Male Gonocyte-Like Cells in Ovaries

To test the role of Smad4 and RA signaling in female fate determination in vivo, we deleted _Stra8_, a major target of RA signaling involved in the initiation of meiosis, together with _Smad4_, and compared phenotypes among _Smad4_-null (_Smad4(Stella)/Stra8$^{+/-}$_), _Stra8_-null (_Smad4$^{flox/flox}$/Stra8$^{-/-}$_), and _Smad4/Stra8_-DKO (_Smad4(Stella)/Stra8$^{-/-}$_) (referred to as DKO) germ cells. NANOS2-expressing germ cells were detected in the DKO mutants but not in _Smad4_ or _Stra8_

single-mutant ovaries (30.6 ± 16.5%, *n* = 4; Fig 6A). Conversely, SYCP3 expression disappeared in the NANOS2-expressing XX germ cells (Fig 6A). Intriguingly, the DKO XX germ cells also showed other male-like features: they began DNMT3L expression, a downstream factor of NANOS2 involved in de novo DNA methylation in fetal testes (13.2 ± 6.9%, n = 4; Fig 6B) [11,13], and retained E-cadherin expression (Fig 6C), a germ cell marker whose expression decreases in XX germ cells from E15.5 [46], as seen in XY germ cells (S5D and S5E Fig). These factors were never observed in *Stra8*-null ovaries (S5A and S5B Fig). These data indicate that SMAD4 and STRA8 are essential factors responsible for female fate determination.

To further trace the fate of germ cells in DKO mice, we cultured E14.5 DKO ovaries for 4 d, because all of the pregnant mice carrying DKO embryos aborted at E16.5 after TM injection. We examined two critical male gonocyte markers—5-methylcytosine (mC), a marker of DNA methylation, and promyelocytic leukemia zinc finger (PLZF) [47]—and found that most DNMT3L-positive germ cells exhibited strong 5-mC signals and some E-cadherin-positive cells had PLZF expression (Fig 6D and 6E), while no PLZF and 5-mC positive signals were detected in control ovaries (S5C Fig). These results suggest that DKO germ cells acquired an ability to enter the male gonocyte differentiation pathway.

Female-to-Male Gene Expression Changes in DKO Germ Cells without Somatic Sex Reversal

To examine to what extent expression pattern changes in the DKO ovary, we performed micro-array analyses. Total RNAs were extracted from control (*Smad4^{flox/+}*, *Smad4^{flox/flox}/Stra8^{+/-}*) testes and ovaries and from *Smad4 (Stella)* and DKO ovaries at E14.5. To examine genes expressed in germ or somatic cells separately, we first extracted 386 and 360 genes, specifically expressed in control E13.5 male and female germ cells, as well as 680 and 636 genes, specifically expressed in control E13.5 male and female somatic cells, respectively, from our previous data (see Materials and Methods section; also see S1 and S2 Tables) [48]. The upregulation of male-specific genes in DKO ovaries showed a 1-day delay compared with normal male differentiation of germ cells in testes (for example, DNMT3L positive germ cells appeared from E14.5 in control testes but from E15.5 in DKO ovaries judging by comparing S6A Fig and Fig 6B); thus, we considered the developmental time point at E14.5 in the DKO ovary equivalent to that at E13.5 in control samples.

First, principal component analysis (PCA) was performed based on all genes, somatic-specific genes, and germ-specific genes, respectively (Fig 7A–7C). In all cases, PCA divided these samples into two major populations according to a putative sex-dependent axis (PC1 value = 38.6%, 72.3%, and 72.8%, respectively). Male and female control samples were located at opposite ends, as expected. When PCA was performed with all genes or somatic-specific genes, the DKO did not show a strong bias (Fig 7A and 7B). In contrast, when PCA was performed with genes specific for germ cells, the DKO samples were shifted toward the male side compared with *Smad4*-single KO samples on the putative sex-dependent axis (Fig 7C). We also observed the differences between DKO and male samples on the *y*-axis, which might be ascribed to the presence of somatic cells and the incomplete knockout efficiency. Nevertheless, it should be noted that PC1 value is as high as 72.8% in this case, suggesting that most of the gene expression profile in DKO germ cells shifts from female to male.

Next, we examined how many germ-cell-specific gene expressions were changed in DKO ovaries. Among 386 male-specific genes that showed a 1.5-fold stronger expression in E13.5 testes than in ovaries (Fig 7D, green dots with *y*-value greater than $\log_2[1.5]$), more than half of the cognate genes (52.1%, 201/386) were 1.5-fold upregulated in the DKO ovaries than in the control ovaries (Fig 7D, green points with *x*-value greater than $\log_2[1.5]$). Similarly, the
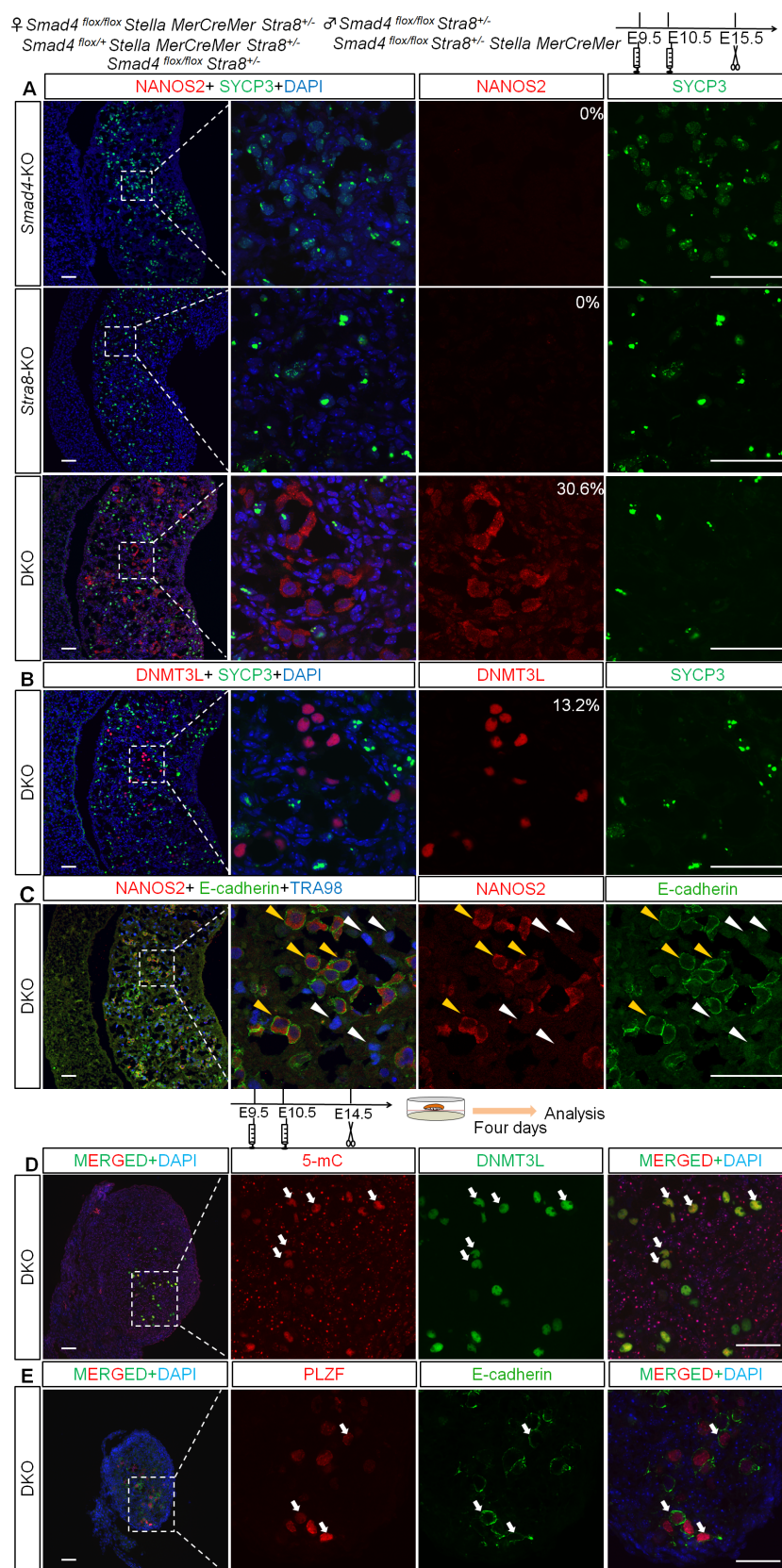
Fig 6. Deletion of *Smad4* and *Stra8* induces XX germ cells to adopt a male fate. (A–C) Representative image of E15.5 *Smad4*-KO (*Smad4 (Stella)*, *Stra8*^{+/-}), *Stra8*-KO (*Smad4*[f/f], *Stra8*^{-/-}), and DKO ovary sections stained for SYCP3/NANOS2 (A), SYCP3/DNMT3L (B), and E-CADHERIN/NANOS2/TRA98 (C). High

magnification images are shown in different channels. Numbers represent the percentage (%) of NANOS2-positive cells among SYCP3 -positive cells. Yellow arrowheads indicate NANOS2/E-CADHERIN/TRA98 triple-positive cells, and white arrowheads indicate TRA98-single positive cells. (D,E) Representative images of DKO ovary sections stained for 5-mC/DNMT3L and PLZF/E-CADHERIN. Tamoxifen was injected at E9.5 and E10.5. Gonads were cultured for 4 d from E14.5. White arrows in D and E indicate 5-mC-positive and PLZF-positive germ cells, respectively. Scale bars: 50 μm.
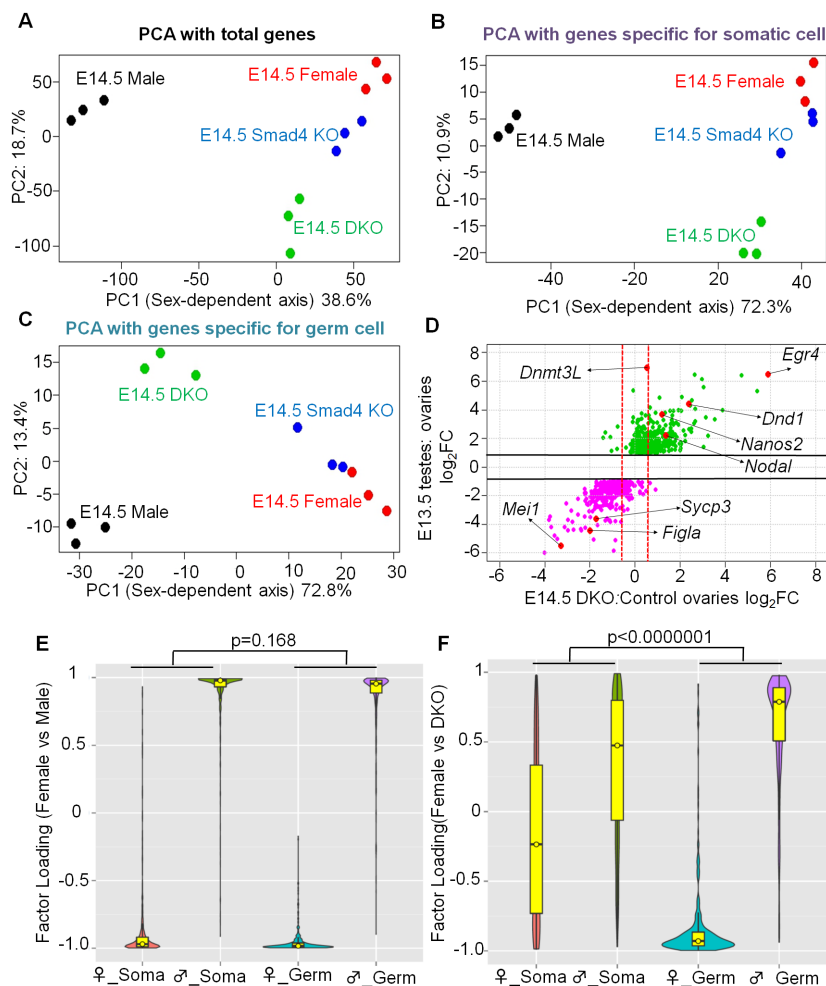
doi:10.1371/journal.pbio.1002553.g006

Fig 7. Sexual fate change of mutant XX germ cells was not accompanied by somatic sex reprogramming. (A–C) Principal component analyses of indicated samples for total genes (A), somatic-specific genes (B), and germ cell specific genes (C). (D) Scatter-plot analysis comparing germ-cell-specific gene expression changes between E13.5 Nanos3$^{+/−}$ male and female gonads (data from [48]) and between E14.5 DKO ovaries and control ovaries. For each point (gene), the *y*-value represents the expression change comparing E13.5 testes with E13.5 ovaries and the *x*-value represents the expression change comparing E14.5 DKO ovaries and control ovaries. Thus, green and pink spots indicate 1.5-fold upregulated or downregulated expression in E13.5 testes versus ovaries (*y*-value greater than $\log_2[1.5]$ for green spots and *y*-value less than $-\log_2[1.5]$ for pink spots: the cut-off lines are indicated by horizontal lines). These spots are considered as genes that are specifically expressed in either male (green) or female (pink) germ cells, and their expression changes between DKO and control ovaries can be judged by the *x*-value. Red spots indicate specific gene examples. Genes located right of the rightmost dotted red line show more than a 1.5-fold increase in DKO, and genes located left of the leftmost dotted red line show less than a 1.5-fold decrease in DKO compared with control ovaries. Because genes that are specifically expressed in germ cells and somatic cells were extracted using microarray data of Nanos3$^{+/−}$ ovaries and testes, we used Nanos3$^{+/−}$ ovaries and testes as control. (E,F) Factor loading of indicated gene groups to principle component. PCA analysis was performed using E13.5 Nanos3$^{+/−}$ male and female gonads (E) and E14.5 double-mutant and control ovaries (F). See text for details.

doi:10.1371/journal.pbio.1002553.g007

expression levels of 71.1% (256/360) female-specific genes (Fig 7D, pink points whose *x*-value is less than -log$_2$[1.5]) were 1.5-fold downregulated in the DKO ovaries. The results of microarray analysis were supported by RT-qPCR, in which eight out of eleven male-specific genes were upregulated in DKO ovaries (S6A Fig). Although *Dnmt3l* mRNA expression was not yet increased at E14.5, immunostaining data showed it was upregulated at E15.5 (Fig 6B). These data indicate that not only the representative genes but also a substantial number of germ-cell-specific genes were shifted to male in DKO ovaries.

The results of PCA analysis were further supported by factor loading analysis (Fig 7E and 7F). Theoretically, the genes that give a more positive contribution to the classification will have a factor loading value (*y*-axis in Fig 7E and 7F) closer to 1 or -1. In the control, the factor loading value of most of the female-specific genes (both somatic and germ cell specific) was close to -1, and that of the male-specific genes was close to 1, indicating that somatic and germ cells contribute equally to the female versus male diversification of developing gonads (see Fig 7E [*p* = 0.168]). Notably, the comparison of the DKO and control ovaries showed that the factor loading value of most of the germ-cell-specific genes, but not the somatic-cell-specific genes, was closer to 1 or -1, indicating that germ-cell-specific genes contribute much more than somatic-cell-specific genes in distinguishing DKO and control ovaries (*p* < 0.0000001; Fig 7F). Indeed, somatic cells differentiated to pregranulosa cells marked by FOXL2, but did not differentiate to Sertoli cells, as revealed by the negative signal for SOX9, in DKO ovaries (S6A and S6B Fig, also see S4D Fig). These results suggest that the observed sexual fate change of XX PGCs in DKO ovaries occurs independently from global gene expression change in the somatic cells.

Discussion

In this study, we investigated the function of Smad4 signaling in the sexual differentiation of germ cells in ovaries and clarified the roles of Smad4 and RA signaling in germ cell fate determination (Fig 8). Three important outcomes in this study deserve particular attention.

First, we provided an insight into the critical question in reproductive biology: what factors determine female germ cell fate? RA-Stra8 signaling was once considered to determine female germ cell fate by inducing meiosis. However, a recent study showed a case where female germ cells can complete oogenesis even in the absence of *Stra8*, indicating that these two pathways are independent [22]. Therefore, uncovering the factors that determine female germ cell fate has been long awaited. Given that the genes involved in follicular formation were compromised in *Smad4*-deficient germ cells without affecting initiation of *Stra8* expression and knocking out of both *Smad4* and *Stra8* resulted in up-regulation of male-specific germ cell genes, we propose that SMAD4 is a strong candidate for a sexual fate determinant in female germ cells. *Lhx8* and *Figla* may be the potential targets of SMAD4, but we do not exclude that other factors may also be regulated by SMAD4. Future studies to identify the target gene(s) of SMAD4 along with functional studies would facilitate our understanding for the regulators of oogenesis. In addition, what signal SMAD4 mediates in female germ cells remains an open question. In this regard, a deduced candidate is BMP2. As BMP2 is expressed in ovarian somatic cells under the control of Wnt4 [29], we speculate that BMP2 initiates Smad4 signaling. However, we cannot exclude the possibility that other TGFβ ligands activate the pathway as well. Further analysis is required to elucidate the signaling pathway.

We conclude that Smad4 signaling in germ cells functions independent of somatic cells during the sexual fate determination of XX germ cells based on the fact that expression levels of oocyte-specific regulators in *Smad4*$^{flox/flox}$/*WT1CreERT2* mutant ovaries were not significantly different from those of control ovaries at approximately E17.5. However, in the maturation
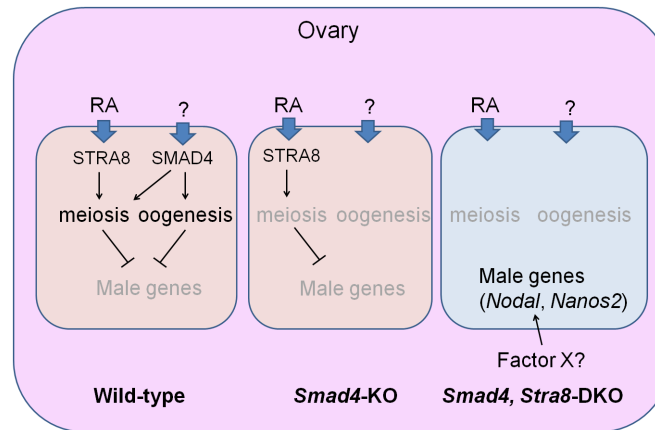
Fig 8. Sexual fate change in DKO germ cells in ovary. In the ovary, two signaling pathways are involved in germ cell fate determination; one is an RA-Stra8 pathway that initiates meiosis and the other is a SMAD4 pathway that is activated via a currently unknown factor. In the absence of SMAD4, germ cells fail to proceed through normal meiosis and fail to make any oocytes. SMAD4 acts in germ cells cell-autonomously and regulates the fate of female germ cells because loss of SMAD4 and STRA8 leads to the upregulation of *Nodal* and NANOS2 expression as well as other male-specific genes. In this situation, somatic cell fate was unchanged and germ cells in the DKO may determine their fate in a cell-autonomous manner or another common factor (X) from female somatic cells is also required.

doi:10.1371/journal.pbio.1002553.g008

stages of oocytes after birth, the deletion of *Smad4* from somatic cells (granulosa cells) is accompanied by precocious luteinization and cumulus cell defects [49]. Therefore, the function of SMAD4 is highly stage-dependent in ovaries.

Second, we found that SMAD4 or its downstream signaling regulates meiotic progression during oogenesis. Although controversial [50,51], it is widely accepted that RA induces meiosis in germ cells. However, whether RA alone supports meiotic progression or requires other signals remains unknown. RA alone could not induce meiosis in vitro, which implies that factors other than RA are involved in meiotic progression [52]. The results of our study showed that *Smad4*-null germ cells expressed *Stra8* and *Rec8*, but most showed meiotic defects before the pachytene stage accompanied by a failure to upregulate genes involved in meiosis (Fig 2 and S3B Fig). Notably, most of these genes were also inactivated in *Stra8* mutant ovaries (for example, *Sycp1*, *Sycp3*, *Dmc1*, *Spo11*, *Mei1*, and *Hormad1*) [53], which implies that SMAD4 and STRA8 regulate the same downstream factors to promote meiosis. Moreover, a Stra8-dependent pathway is reportedly responsible for the downregulation of *Stra8* and *Rec8* expression levels [53]. We speculated that this pathway is inactivated by the deletion of *Smad4* because the expression level of *Stra8* in mutant germ cells was higher than that in normal ovaries (Fig 2A and S3B Fig). Overall, the results of the present study indicated that in addition to RA-dependent meiotic initiation, Smad4 signaling is required for meiotic progression, consistent with the study that successful induction of meiosis requires Activin A, BMP, and RA [52]. This finding is a critical clue for understanding the mechanisms involved in meiosis.

Third, we found profound properties of DKO germ cells. These germ cells became positive for male factors NANOS2 and DNML3L, and some of those cells showed 5-mC, indicating DNA methylation, all of which are normally observed only in male gonocytes. The transcriptome analyses of DKO embryos showed that more than 50% of male-type genes were up-regulated and more than 70% of female type genes were downregulated, indicating that male pathway is promoted when female germ cell development is suppressed by the lack of *Stra8* and *Smad4*. However, as seen in PCA analyses, DKO germ cells were not equal to male germ cells and not all DKO germ cells expressed NANOS2. This may be due to the effects from

ovarian somatic cells; some factor(s) may act to suppress or promote the male pathway. Importantly, however, we showed that the female-to-male sexual fate change of XX germ cells occurred independent of the sexual switch of somatic cells as revealed by sustained FOXL2 expression in DKO ovaries. A similar phenotype was also observed in the ubiquitous *Smad4*-cKO (via Rosa-CreERT) with an RA inhibitor (S4C and S4D Fig). Owing to the lack of a Y chromosome in XX ovaries, the induction of male-like characteristics in DKO germ cells is not linked to any somatic factors, such as FGF9 and SOX9, which are controlled by SRY. Therefore, our results raise the unexpected possibility that male-specific factors in somatic cells are unnecessary for the male fate determination of germ cells even in the testes, although we do not exclude the possibility that other somatic factors (X) existing in both testes and ovaries are involved in the induction of maleness in germ cells (Fig 8). Consistent with this hypothesis, a recent study has shown that disruption of the germ-cell-specific factor FOXL3 in XX medaka (*Oryzias latipes*) leads to male differentiation even in ovaries [54]. In the case of our mouse model, however, we cannot expect to induce functional sperm in DKO ovaries, because the deletion of *Stra8* leads to meiotic defects, and spermatogenesis requires an appropriate microenvironment supported by Sertoli cells that cannot be provided in mouse ovaries.

In summary, we analyzed the functions of SMAD4 in fetal female germ cells and found that SMAD4 is required for sexual differentiation of female germ cells. We further proved that SMAD4 and STRA8 were crucial for female sex determination, because germ cells lacking these two factors became male gonocyte-like cells, even if these germ cells were surrounded with female somatic cells. Our results provide foundational information for understanding the sex determination system in mammals, which may contribute to the goal of direct gamete induction in vitro.

Materials and Methods

Ethics

All mouse experiments were approved by the Animal Experimentation Committee at the National Institute of Genetics. Permission number for animal experiment is 27–13.

Mice

Generation of floxed *Smad4* alleles and *Stra8* knockout mice has been described previously [48,55]. *Stella-MerCreMer* was established previously [33]. *Rosa-CreERT2* mice were purchased from Artemis Pharmaceuticals GmbH. *WT1-CreERT2* mice were purchased from Jackson Laboratory. *Gt(ROSA)26Sor^{tm1Sor}*/J and *CAG-floxed-CAT-EGFP* mouse lines were established previously [56,57]. All of these mice lines were kept in a mixed background. TM was diluted in sesame oil (Nacalai Tesque) at a concentration of 10 mg/ml, and 0.5 ml of the diluted TM was injected each time. To induce recombination in *Stella-MerCreMer* mice, TM was injected at E9.5 and E10.5. To induce recombination in *Rosa-CreERT2* or *WT1-CreERT2* mice, TM was injected at E10.5 and E11.5. ICR strain mice (Clea Japan) were used as control in some cases (S1A, S5D and S5E and S6B Figs).

Microarray and Data Analysis

RNA samples were prepared from E14.5 testes, ovaries, *Smad4* mutant ovaries, and double mutant embryos ($n = 3$ for each case). For each hybridization assay, 200 ng of total RNA was labeled with Cy3 and hybridized to a Whole Mouse Genome Oligo Microarray (G4122F; Agilent) in accordance with the manufacturer's protocol using a Quick Amp Labeling Kit (Cat

121

#51900424), One Color (Agilent), and Gene Expression Hybridization Kit (Agilent). Data have been deposited in Gene Expression Omnibus under accession number: GSE68773.

Extraction of genes specifically expressed in female somatic cells, male somatic cells, and male germ cells was performed using microarray data from [48] by R. To extract genes specifically expressed in male or female germ cells at E13.5, genes showing 1.5-fold changes in expression levels between $Nanos3^{+/-}$ testes and $Nanos3^{+/-}$ ovaries were defined as sex-specific genes. Then, genes showing 1.5-fold changes in expression levels between $Nanos3^{+/-}$ testes and $Nanos3^{-/-}$ testes and between $Nanos3^{+/-}$ ovaries and $Nanos3^{-/-}$ ovaries were defined as germ cell-specific genes, because $Nanos3^{-/-}$ gonads (both ovaries and testes) lack germ cells at E13.5. Genes specifically expressed in male or female germ cells were obtained by the intersection of genes in the two lists. Similarly, genes specifically expressed in male or female somatic cells (if genes are not germ-cell-specific) at E13.5 were also isolated. PCA was analyzed by R using genes in the above lists.

Organ Culture

Gonads were cultured in 24-well culture plates with DMEM containing 10% horse serum at 37°C on 5-μm nucleopore filters [58,59]. Some gonads were cultured in medium containing 4-hydroxytamoxifen (2 μM; Sigma-Aldrich), DMSO (Sigma-Aldrich), and AGN 193109 (5 μM; Toronto Research Chemical Inc.). For the experiments shown in S4B Fig, tamoxifen was injected at E10.5 and E11.5, and ovaries obtained at E12.5 were further cultured with DMSO (control) or AGN 193109 (5 μM) for 2 d or 3 d with 4-hydroxytamoxifen (2 μM) to further induce Cre-mediated Smad4 deletion during cultivation. For the experiments shown in Fig 5, tamoxifen was injected at E9.5 and E10.5, and ovaries obtained at E12.5 were further cultured with DMSO (control) or AGN 193109 (5 μM) for 3 d with 4-hydroxytamoxifen (2 μM). For the experiments shown in Fig 6D and 6E, tamoxifen was injected at E9.5 and E10.5, and ovaries obtained at E14.5 were further cultured for 4 d.

Reverse Transcription Real-Time Quantitative Polymerase Chain Reaction (RT-qPCR)

Total RNA was prepared from the fetal gonads of mutant embryos and the gonads of ICR strain embryos at each embryonic stage using RNeasy Mini Kits (Qiagen). Total RNA was then used for cDNA synthesis using PrimeScript RT Reagent Kits with gDNA Erase (Takara). PCR was performed with KAPA SYBR FAST qPCR Kits using a thermal cycler dice real time system (Takara). The primer pairs used for PCR amplification are listed in S3 Table.

Histological Analysis

Histological analysis was performed as previous reported [5,8]. Briefly, gonads were fixed in 4% paraformaldehyde, embedded in OCT compound (Tissue-Tek; Sakura), and sectioned (6 μm) using a cryostat. After preincubation with 3% skim milk powder in PBST for 30 min, the sections were stained with primary antibodies: anti-TRA98 (1:10000; a gift from Y. Nishimune), anti-undifferentiated embryonic cell transcription factor 1 (1:200; Abcam), anti-SOX2 (1:200; Santa Cruz), anti-SOX9 (1:250; a gift from Y. Kanai, The University of Tokyo, Tokyo, Japan), anti-NANOS2 (1:200) [60], anti-FOXL2 (1:200; Abcam), anti-STRA8 (1:200; Abcam), anti-SCP1 (1:1000; Abcam), anti-SCP3 (1:1000; Abcam), anti-GFP (1:400; Aves labs), anti-DNMT3L (1:200; a gift from S. Yamanaka, Kyoto University, Kyoto, Japan), anti-Cleaved-Caspase-3 (1:200; Cell Signaling Technology), anti-MVH (1:400; Abcam), anti-E-Cadherin (1:100; R&D systems) anti-NOBOX (1:200; Abcam), anti-PLZF (1:200; SantaCruz), anti-5mC (1:200; Activemotife), anit-FOXO3A (1:200; Cell signaling Technology), and anti-pSMAD1/5/8

(1:200; Cell Signaling Technology). The sections were then incubated with donkey anti-rabbit/rat/goat/mouse or anti-chick IgG secondary antibodies conjugated with either Alexa 488, Alexa 594, or cy5 (1:400; Invitrogen). Primary antibodies were diluted in 3% skim milk powder in PBST. Secondary antibodies were diluted in PBST. Slides were mounted for observation under a scanning confocal microscope (Olympus FV1200 IX83). The method for LacZ staining (S1B Fig) was reported previously [61].

Cell Counting

To trace the cell fate of *Smad4*-null germ cells in *Smad4^{flox/flox}/Stella-MerCreMer* ovaries, tamoxifen was injected at E9.5 and E10.5, and samples were harvested from E14.5 to E17.5. Ovaries were sectioned and immunostained with different markers: NOBOX (Fig 3B), FOXO3A (Fig 3C), and Cleaved-Caspase3 (Fig 1D), together with germ cell markers TRA98 or MVH. Germ cells on all these sections were counted as TRA98- or MVH-positive cells (Fig 1C). Underlying data used for counting were presented in S1 Data.

Statistical Analysis

Statistical analysis was performed as previous reported [5,8]. For quantitative analyses between two different samples, significance was assessed by Student's *t* test. For quantitative analyses among multiple samples, significance was assessed using one-way ANOVA followed by Tukey's post-hoc tests for selected pairs of genotypes.

Supporting Information

S1 Data. Underlying data used for quantitative analysis.
(XLSX)

S1 Fig. Examination of pSMAD1/5/8 expression and Stella-MerCreMer activity in embryonic ovaries. (A) Immunohistochemical detection of pSMAD1/5/8 and TRA98 (a germ cell marker) in indicated ovaries. White arrows indicated germ cells. (B) X-gal staining followed by TRA98 immunostaining of ovary section of ROSA26-Cre reporter strain, *Gt(ROSA)26Sor^{tm1Sor}/*J) crossed with a *Stella-MerCreMer* male mouse. Tamoxifen was injected at E9.5 and E10.5, and ovaries harvested at E14.5 were subjected to X-gal staining.
(TIF)

S2 Fig. Smad4 signaling in somatic cells is not involved in sex determination of germ cells. (A) Scheme of somatic-cell-specific knockout strategy. Tamoxifen was injected at E10.5 and E11.5, and ovaries were harvested at E14.5 (B) or cultured for 3 d (C). (B) Expression levels of the indicated genes were compared by RT-qPCR in control (*n* = 6) and *Smad4* mutant (via WT1-CreERT2; briefly WT1) ovaries (*n* = 4). The expression levels of the indicated genes were normalized to that of *Mvh* or *G3phd* (for *Smad4*). (C) Quantitative analysis of NOBOX-positive germ cells in *Smad4* mutant (WT1) (*n* = 3) and control ovaries (*n* = 4). Significance was assessed by Student's *t* test. Error bars indicate SD. Underlying data is available in S1 Data.
(TIF)

S3 Fig. Ubiquitous deletion of *Smad4* reproduced the phenotype of germ-line-specific *Smad4* deletion in ovaries. (A) Schematic drawing of ubiquitous knockout strategy. Tamoxifen was injected at E10.5 and E11.5, and ovaries were harvested at E14.5. (B) Expression level of meiosis-related genes in control and *Smad4* mutant (Rosa) ovaries. Data are represented as a heat map and the *p*-value was calculated by Student's *t* test. (C,D) Expression levels of the indicated genes were compared by RT-qPCR in control (set as 1) and *Smad4* mutant (Rosa) ovaries

(*n* = 4). The expression levels of the indicated genes were normalized to that of mouse vasa homolog (*Mvh*). Significance was assessed using Student's *t* test for one pair of genotypes and one-way ANOVA followed by Tukey's post-hoc tests for selected pairs of genotypes. Error bars indicate SD. Underlying data is available in S1 Data.
(TIF)

S4 Fig. Suppression of Smad4 or RA signaling alone does not result in sex reversal of XX PGCs. (A) Expression level of indicated genes in control and *Smad4 (Stella)* ovaries at E14.5. Data was extracted from microarray analysis. (B) Experimental scheme for (C,D). (C) RT-qPCR analysis of *Stra8* and *Nanos2* expression in control and *Smad4*-cKO (Rosa) mutant ovaries that were or were not treated with the RA receptor antagonist AGN 193109 for 2 d. Error bars indicate SD. Underlying data is available in S1 Data. (D) Representative image of sections from *Smad4*-cKO (Rosa) ovaries stained for NANOS2 and FOXL2 after treatment with AGN or DMSO for 3 d. Scale bar: 50 μm.
(TIF)

S5 Fig. Induction of male-specific genes was not observed in either *Stra8*-KO or wild-type ovaries. (A,B) Representative images of *Stra8*-KO ovary sections (littermate control of Fig 6B and 6C). (C) Representative images of wild-type ovaries incubated for 4 d with normal medium and stained for 5-mC and PLZF (negative control). (D,E) Wild-type testes stained for E-CADHERIN, PLZF, DNMT3L, and 5-mC, related to Fig 6D and 6E. Scale bars: 50 μm.
(TIF)

S6 Fig. Induction of male-specific genes occurred independently of sex reversal of somatic cells in DKO ovaries. (A) Expression levels of the indicated genes were compared by RT-qPCR in control male (set as 1) and female gonads, and in double mutant ovaries (*n* = 3). Tamoxifen was injected at E9.5 and E10.5, and gonads were recovered at E14.5. The expression levels of the indicated genes were normalized to that of mouse vasa homolog (*Mvh*). Significance was assessed using Student's *t* test. Error bars indicate SD. Underlying data is available in S1 Data. (B) Representative image of E15.5 DKO ovarian tissue section stained for FOXL2 and SOX9, and wild-type testis section stained for SOX9 and TRA98. Scale bars: 50 μm.
(TIF)

S1 Table. Fold change of male germ-cell-specific genes in DKO ovaries compared with control ovaries.
(DOCX)

S2 Table. Fold change of female germ-cell-specific genes in DKO ovaries compared with control ovaries.
(DOCX)

S3 Table. Primer set used for RT-qPCR.
(DOCX)

Acknowledgments

Author Contributions

Conceptualization: QW YS.

Formal Analysis: QW KF YK ZZ.

Methodology: QW CXD YS.

Investigation: QW KF.

Writing – original draft: QW YS.

Writing – review & editing: QW YK YS.

References

1. Bowles J, Koopman P. Sex determination in mammalian germ cells: extrinsic versus intrinsic factors. Reproduction. 2010; 139(6):943–58. Epub 2010/04/17. REP-10-0075 [pii] doi: 10.1530/REP-10-0075 PMID: 20395427.

2. Bowles J, Knight D, Smith C, Wilhelm D, Richman J, Mamiya S, et al. Retinoid signaling determines germ cell fate in mice. Science. 2006; 312(5773):596–600. Epub 2006/04/01. 1125691 [pii] doi: 10.1126/science.1125691 PMID: 16574820.

3. Koubova J, Menke DB, Zhou Q, Capel B, Griswold MD, Page DC. Retinoic acid regulates sex-specific timing of meiotic initiation in mice. Proc Natl Acad Sci U S A. 2006; 103(8):2474–9. Epub 2006/02/08. 0510813103 [pii] doi: 10.1073/pnas.0510813103 PMID: 16461896; PubMed Central PMCID: PMC1413806.

4. Saba R, Wu Q, Saga Y. CYP26B1 promotes male germ cell differentiation by suppressing STRA8-dependent meiotic and STRA8-independent mitotic pathways. Dev Biol. 2014. Epub 2014/03/01. S0012-1606(14)00093-1 [pii] doi: 10.1016/j.ydbio.2014.02.013 PMID: 24576537.

5. Wu Q, Kanata K, Saba R, Deng CX, Hamada H, Saga Y. Nodal/activin signaling promotes male germ cell fate and suppresses female programming in somatic cells. Development. 2013; 140(2):291–300. Epub 2012/12/12. doi: 10.1242/dev.087882 dev.087882 [pii]. PMID: 23221368; PubMed Central PMCID: PMC3597207.

6. Souquet B, Tourpin S, Messiaen S, Moison D, Habert R, Livera G. Nodal signaling regulates the entry into meiosis in fetal germ cells. Endocrinology. 2012; 153(5):2466–73. Epub 2012/03/08. en.2011-2056 [pii] doi: 10.1210/en.2011-2056 PMID: 22396454.

7. Miles DC, Wakeling SI, Stringer JM, van den Bergen JA, Wilhelm D, Sinclair AH, et al. Signaling through the TGF beta-activin receptors ALK4/5/7 regulates testis formation and male germ cell development. PLoS ONE. 2013; 8(1):e54606. Epub 2013/01/24. doi: 10.1371/journal.pone.0054606 PONE-D-12-29514 [pii]. PMID: 23342175; PubMed Central PMCID: PMC3546992.

8. Wu Q, Fukuda K, Weinstein M, Graff JM, Saga Y. SMAD2 and p38 signaling pathways act in concert to determine XY primordial germ cell fate in mice. Development. 2015; 142(3):575–86. Epub 2015/01/22. doi: 10.1242/dev.119446 142/3/575 [pii]. PMID: 25605784.

9. Suzuki A, Saba R, Miyoshi K, Morita Y, Saga Y. Interaction between NANOS2 and the CCR4-NOT deadenylation complex is essential for male germ cell development in mouse. PLoS ONE. 2012; 7(3):e33558. Epub 2012/03/27. doi: 10.1371/journal.pone.0033558 PONE-D-11-20898 [pii]. PMID: 22448252; PubMed Central PMCID: PMC3308992.

10. Suzuki A, Igarashi K, Aisaki K, Kanno J, Saga Y. NANOS2 interacts with the CCR4-NOT deadenylation complex and leads to suppression of specific RNAs. Proc Natl Acad Sci U S A. 2010; 107(8):3594–9. Epub 2010/02/06. 0908664107 [pii] doi: 10.1073/pnas.0908664107 PMID: 20133598; PubMed Central PMCID: PMC2840499.

11. Suzuki A, Saga Y. Nanos2 suppresses meiosis and promotes male germ cell differentiation. Genes Dev. 2008; 22(4):430–5. Epub 2008/02/19. 22/4/430 [pii] doi: 10.1101/gad.1612708 PMID: 18281459; PubMed Central PMCID: PMC2238665.

12. Carmell MA, Girard A, van de Kant HJ, Bourc'his D, Bestor TH, de Rooij DG, et al. MIWI2 is essential for spermatogenesis and repression of transposons in the mouse male germline. Dev Cell. 2007; 12 (4):503–14. Epub 2007/03/31. S1534-5807(07)00100-1 [pii] doi: 10.1016/j.devcel.2007.03.001 PMID: 17395546.

13. Bourc'his D, Bestor TH. Meiotic catastrophe and retrotransposon reactivation in male germ cells lacking Dnmt3L. Nature. 2004; 431(7004):96–9. Epub 2004/08/20. doi: 10.1038/nature02886 nature02886 [pii]. PMID: 15318244.

125

14. Koopman P, Munsterberg A, Capel B, Vivian N, Lovell-Badge R. Expression of a candidate sex-determining gene during mouse testis differentiation. Nature. 1990; 348(6300):450–2. Epub 1990/11/29. doi: 10.1038/348450a0 PMID: 2247150.

15. Colvin JS, Green RP, Schmahl J, Capel B, Ornitz DM. Male-to-female sex reversal in mice lacking fibroblast growth factor 9. Cell. 2001; 104(6):875–89. Epub 2001/04/06. S0092-8674(01)00284-7 [pii]. PMID: 11290325.

16. Bowles J, Feng CW, Spiller C, Davidson TL, Jackson A, Koopman P. FGF9 suppresses meiosis and promotes male germ cell fate in mice. Dev Cell. 2010; 19(3):440–9. Epub 2010/09/14. S1534-5807(10)00385-0 [pii] doi: 10.1016/j.devcel.2010.08.010 PMID: 20833365.

17. Kent J, Wheatley SC, Andrews JE, Sinclair AH, Koopman P. A male-specific role for SOX9 in vertebrate sex determination. Development. 1996; 122(9):2813–22. Epub 1996/09/01. PMID: 8787755.

18. Schmahl J, Kim Y, Colvin JS, Ornitz DM, Capel B. Fgf9 induces proliferation and nuclear localization of FGFR2 in Sertoli precursors during male sex determination. Development. 2004; 131(15):3627–36. Epub 2004/07/02. doi: 10.1242/dev.01239 dev.01239 [pii]. PMID: 15229180.

19. Sekido R, Lovell-Badge R. Sex determination involves synergistic action of SRY and SF1 on a specific Sox9 enhancer. Nature. 2008; 453(7197):930–4. Epub 2008/05/06. nature06944 [pii] doi: 10.1038/nature06944 PMID: 18454134.

20. Barrios F, Filipponi D, Pellegrini M, Paronetto MP, Di Siena S, Geremia R, et al. Opposing effects of retinoic acid and FGF9 on Nanos2 expression and meiotic entry of mouse germ cells. J Cell Sci. 2010; 123 (Pt 6):871–80. Epub 2010/02/18. PMID: 20159962.

21. Jameson SA, Lin YT, Capel B. Testis development requires the repression of Wnt4 by Fgf signaling. Dev Biol. 2012; 370(1):24–32. Epub 2012/06/19. doi: 10.1016/j.ydbio.2012.06.009 S0012-1606(12)00318-1 [pii]. PMID: 22705479.

22. Dokshin GA, Baltus AE, Eppig JJ, Page DC. Oocyte differentiation is genetically dissociable from meiosis in mice. Nat Genet. 2013; 45(8):877–83. Epub 2013/06/19. doi: 10.1038/ng.2672 ng.2672 [pii]. PMID: 23770609; PubMed Central PMCID: PMC3747777.

23. Baltus AE, Menke DB, Hu YC, Goodheart ML, Carpenter AE, de Rooij DG, et al. In germ cells of mouse embryonic ovaries, the decision to enter meiosis precedes premeiotic DNA replication. Nat Genet. 2006; 38(12):1430–4. Epub 2006/11/23. ng1919 [pii] doi: 10.1038/ng1919 PMID: 17115059.

24. Koubova J, Hu YC, Bhattacharyya T, Soh YQ, Gill ME, Goodheart ML, et al. Retinoic acid activates two pathways required for meiosis in mice. PLoS Genet. 2014; 10(8):e1004541. Epub 2014/08/08. doi: 10.1371/journal.pgen.1004541 PGENETICS-D-14-00436 [pii]. PMID: 25102060; PubMed Central PMCID: PMC4125102.

25. Ottolenghi C, Pelosi E, Tran J, Colombino M, Douglass E, Nedorezov T, et al. Loss of Wnt4 and Foxl2 leads to female-to-male sex reversal extending to germ cells. Hum Mol Genet. 2007; 16(23):2795–804. Epub 2007/08/31. ddm235 [pii] doi: 10.1093/hmg/ddm235 PMID: 17728319.

26. Liu CF, Bingham N, Parker K, Yao HH. Sex-specific roles of beta-catenin in mouse gonadal development. Hum Mol Genet. 2009; 18(3):405–17. Epub 2008/11/05. doi: 10.1093/hmg/ddn362 ddn362 [pii]. PMID: 18981061; PubMed Central PMCID: PMC2638797.

27. Maatouk DM, DiNapoli L, Alvers A, Parker KL, Taketo MM, Capel B. Stabilization of beta-catenin in XY gonads causes male-to-female sex-reversal. Hum Mol Genet. 2008; 17(19):2949–55. Epub 2008/07/12. doi: 10.1093/hmg/ddn193 ddn193 [pii]. PMID: 18617533; PubMed Central PMCID: PMC2536503.

28. Chassot AA, Gregoire EP, Lavery R, Taketo MM, de Rooij DG, Adams IR, et al. RSPO1/beta-catenin signaling pathway regulates oogonia differentiation and entry into meiosis in the mouse fetal ovary. PLoS ONE. 2011; 6(10):e25641. Epub 2011/10/13. doi: 10.1371/journal.pone.0025641 PONE-D-11-12306 [pii]. PMID: 21991325; PubMed Central PMCID: PMC3185015.

29. Yao HH, Matzuk MM, Jorgez CJ, Menke DB, Page DC, Swain A, et al. Follistatin operates downstream of Wnt4 in mammalian ovary organogenesis. Dev Dyn. 2004; 230(2):210–5. Epub 2004/05/27. doi: 10.1002/dvdy.20042 PMID: 15162500.

30. Dutko JA, Mullins MC. SnapShot: BMP signaling in development. Cell. 2011; 145(4):636.e1–2. Epub 2011/05/14. doi: 10.1016/j.cell.2011.05.001 S0092-8674(11)00487-9 [pii]. PMID: 21565618.

31. Massague J, Chen YG. Controlling TGF-beta signaling. Genes Dev. 2000; 14(6):627–44. Epub 2000/03/25. PMID: 10733523.

32. Spiller CM, Feng CW, Jackson A, Gillis AJ, Rolland AD, Looijenga LH, et al. Endogenous Nodal signaling regulates germ cell potency during mammalian testis development. Development. 2012; 139 (22):4123–32. Epub 2012/10/05. doi: 10.1242/dev.083006 dev.083006 [pii]. PMID: 23034635.

33. Hirota T, Ohta H, Shigeta M, Niwa H, Saitou M. Drug-inducible gene recombination by the Dppa3-MER Cre MER transgene in the developmental cycle of the germ cell lineage in mice. Biol Reprod. 2011; 85

(2):367–77. Epub 2011/04/29. biolreprod.110.090662 [pii] doi: 10.1095/biolreprod.110.090662 PMID: 21525417.

34. Yuan L, Liu JG, Zhao J, Brundell E, Daneholt B, Hoog C. The murine SCP3 gene is required for synaptonemal complex assembly, chromosome synapsis, and male fertility. Mol Cell. 2000; 5(1):73–83. Epub 2000/03/11. S1097-2765(00)80404-9 [pii]. PMID: 10678170.

35. Wojtasz L, Cloutier JM, Baumann M, Daniel K, Varga J, Fu J, et al. Meiotic DNA double-strand breaks and chromosome asynapsis in mice are monitored by distinct HORMAD2-independent and -dependent mechanisms. Genes Dev. 2012; 26(9):958–73. Epub 2012/05/03. doi: 10.1101/gad.187559.112 26/9/958 [pii]. PMID: 22549958; PubMed Central PMCID: PMC3347793.

36. Tay J, Richter JD. Germ cell differentiation and synaptonemal complex formation are disrupted in CPEB knockout mice. Dev Cell. 2001; 1(2):201–13. Epub 2001/11/13. S1534-5807(01)00025-9 [pii]. PMID: 11702780.

37. Libby BJ, De La Fuente R, O'Brien MJ, Wigglesworth K, Cobb J, Inselman A, et al. The mouse meiotic mutation mei1 disrupts chromosome synapsis with sexually dimorphic consequences for meiotic progression. Dev Biol. 2002; 242(2):174–87. Epub 2002/02/01. doi: 10.1006/dbio.2001.0535 S0012160601905354 [pii]. PMID: 11820814.

38. Mahadevaiah SK, Turner JM, Baudat F, Rogakou EP, de Boer P, Blanco-Rodriguez J, et al. Recombinational DNA double-strand breaks in mice precede synapsis. Nat Genet. 2001; 27(3):271–6. Epub 2001/03/10. doi: 10.1038/85830 PMID: 11242108.

39. Yoshida K, Kondoh G, Matsuda Y, Habu T, Nishimune Y, Morita T. The mouse RecA-like gene Dmc1 is required for homologous chromosome synapsis during meiosis. Mol Cell. 1998; 1(5):707–18. Epub 1998/07/14. S1097-2765(00)80070-2 [pii]. PMID: 9660954.

40. Soper SF, van der Heijden GW, Hardiman TC, Goodheart M, Martin SL, de Boer P, et al. Mouse maelstrom, a component of nuage, is essential for spermatogenesis and transposon repression in meiosis. Dev Cell. 2008; 15(2):285–97. Epub 2008/08/13. S1534-5807(08)00240-2 [pii] doi: 10.1016/j.devcel.2008.05.015 PMID: 18694567; PubMed Central PMCID: PMC2546488.

41. Pangas SA, Choi Y, Ballow DJ, Zhao Y, Westphal H, Matzuk MM, et al. Oogenesis requires germ cell-specific transcriptional regulators Sohlh1 and Lhx8. Proc Natl Acad Sci U S A. 2006; 103(21):8090–5. Epub 2006/05/13. 0601083103 [pii] doi: 10.1073/pnas.0601083103 PMID: 16690745; PubMed Central PMCID: PMC1472434.

42. Hu YC, Okumura LM, Page DC. Gata4 is required for formation of the genital ridge in mice. PLoS Genet. 2013; 9(7):e1003629. Epub 2013/07/23. doi: 10.1371/journal.pgen.1003629 PGENETICS-D-13-00597 [pii]. PMID: 23874227; PubMed Central PMCID: PMC3708810.

43. Zhou B, Ma Q, Rajagopal S, Wu SM, Domian I, Rivera-Feliciano J, et al. Epicardial progenitors contribute to the cardiomyocyte lineage in the developing heart. Nature. 2008; 454(7200):109–13. Epub 2008/06/24. PMID: 18568026; PubMed Central PMCID: PMC2574791. doi: 10.1038/nature07060

44. Yamaguchi S, Kimura H, Tada M, Nakatsuji N, Tada T. Nanog expression in mouse germ cell development. Gene Expr Patterns. 2005; 5(5):639–46. Epub 2005/06/09. S1567-133X(05)00021-9 [pii] doi: 10.1016/j.modgep.2005.03.001 PMID: 15939376.

45. Pesce M, Wang X, Wolgemuth DJ, Scholer H. Differential expression of the Oct-4 transcription factor during mouse germ cell differentiation. Mech Dev. 1998; 71(1–2):89–98. Epub 1998/06/20. PMID: 9507072.

46. Di Carlo A, De Felici M. A role for E-cadherin in mouse primordial germ cell development. Dev Biol. 2000; 226(2):209–19. Epub 2000/10/12. doi: 10.1006/dbio.2000.9861 S0012-1606(00)99861-0 [pii]. PMID: 11023681.

47. Costoya JA, Hobbs RM, Barna M, Cattoretti G, Manova K, Sukhwani M, et al. Essential role of Plzf in maintenance of spermatogonial stem cells. Nat Genet. 2004; 36(6):653–9. Epub 2004/05/25. doi: 10.1038/ng1367 ng1367 [pii]. PMID: 15156143.

48. Saba R, Kato Y, Saga Y. NANOS2 promotes male germ cell development independent of meiosis suppression. Dev Biol. 2014; 385(1):32–40. Epub 2013/11/05. doi: 10.1016/j.ydbio.2013.10.018 S0012-1606(13)00562-9 [pii]. PMID: 24183939.

49. Pangas SA, Li X, Robertson EJ, Matzuk MM. Premature luteinization and cumulus cell defects in ovarian-specific Smad4 knockout mice. Mol Endocrinol. 2006; 20(6):1406–22. Epub 2006/03/04. me.2005-0462 [pii] doi: 10.1210/me.2005-0462. PMID: 16513794

50. Kumar S, Chatzi C, Brade T, Cunningham TJ, Zhao X, Duester G. Sex-specific timing of meiotic initiation is regulated by Cyp26b1 independent of retinoic acid signalling. Nat Commun. 2011; 2:151. Epub 2011/01/13. ncomms1136 [pii] doi: 10.1038/ncomms1136 PMID: 21224842; PubMed Central PMCID: PMC3034736.

51. Kumar S, Cunningham TJ, Duester G. Resolving molecular events in the regulation of meiosis in male and female germ cells. Sci Signal. 2013; 6(288):pe25. Epub 2013/08/15. doi: 10.1126/scisignal. 2004530 scisignal.2004530 [pii]. PMID: 23943607; PubMed Central PMCID: PMC3784405.

52. Zhou Q, Wang M, Yuan Y, Wang X, Fu R, Wan H, et al. Complete Meiosis from Embryonic Stem Cell-Derived Germ Cells In Vitro. Cell Stem Cell. 2016; 18(3):330–40. Epub 2016/03/01. doi: 10.1016/j. stem.2016.01.017 S1934-5909(16)00018-7 [pii]. PMID: 26923202.

53. Soh YQ, Junker JP, Gill ME, Mueller JL, van Oudenaarden A, Page DC. A Gene Regulatory Program for Meiotic Prophase in the Fetal Ovary. PLoS Genet. 2015; 11(9):e1005531. Epub 2015/09/18. doi: 10.1371/journal.pgen.1005531 PGENETICS-D-15-01590 [pii]. PMID: 26378784; PubMed Central PMCID: PMC4574967.

54. Nishimura T, Sato T, Yamamoto Y, Watakabe I, Ohkawa Y, Suyama M, et al. Sex determination. foxl3 is a germ cell-intrinsic factor involved in sperm-egg fate decision in medaka. Science. 2015; 349 (6245):328–31. Epub 2015/06/13. science.aaa2657 [pii]. PMID: 26067255.

55. Yang X, Li CL, Herrera PL, Deng CX. Generation of Smad4/Dpc4 conditional knockout mice. Genesis. 2002; 32(2):80–1. doi: 10.1002/gene.10029. WOS:000174169900007. PMID: 11857783

56. Kawamoto S, Niwa H, Tashiro F, Sano S, Kondoh G, Takeda J, et al. A novel reporter mouse strain that expresses enhanced green fluorescent protein upon Cre-mediated recombination. FEBS Lett. 2000; 470(3):263–8. Epub 2000/04/04. S0014579300013387 [pii]. PMID: 10745079.

57. Soriano P. Generalized lacZ expression with the ROSA26 Cre reporter strain. Nat Genet. 1999; 21 (1):70–1. Epub 1999/01/23. doi: 10.1038/5007 PMID: 9916792.

58. Hiramatsu R, Harikae K, Tsunekawa N, Kurohmaru M, Matsuo I, Kanai Y. FGF signaling directs a center-to-pole expansion of tubulogenesis in mouse testis differentiation. Development. 2010; 137(2):303–12. Epub 2009/12/31. 137/2/303 [pii] doi: 10.1242/dev.040519 PMID: 20040496.

59. Harikae K, Miura K, Shinomura M, Matoba S, Hiramatsu R, Tsunekawa N, et al. Heterogeneity in sexual bipotentiality and plasticity of granulosa cells in developing mouse ovaries. J Cell Sci. 2013; 126(Pt 13):2834–44. Epub 2013/04/25. doi: 10.1242/jcs.122663 jcs.122663 [pii]. PMID: 23613466.

60. Suzuki A, Tsuda M, Saga Y. Functional redundancy among Nanos proteins and a distinct role of Nanos2 during male germ cell development. Development. 2007; 134(1):77–83. Epub 2006/12/02. dev.02697 [pii] doi: 10.1242/dev.02697 PMID: 17138666.

61. Saga Y, Yagi T, Ikawa Y, Sakakura T, Aizawa S. Mice develop normally without tenascin. Genes Dev. 1992; 6(10):1821–31. Epub 1992/10/01. PMID: 1383086.

Regulation of pluripotency in male germline stem cells by Dmrt1

Seiji Takashima,[1] Michiko Hirose,[2] Narumi Ogonuki,[2] Miki Ebisuya,[3] Kimiko Inoue,[2]
Mito Kanatsu-Shinohara,[1] Takashi Tanaka,[1] Eisuke Nishida,[4] Atsuo Ogura,[2] and Takashi Shinohara[1,5,6]

[1]Department of Molecular Genetics, Graduate School of Medicine, Kyoto University, Kyoto 606-8501, Japan; [2]RIKEN
Bioresource Center, Tsukuba 305-0074, Japan; [3]Career-Path Promotion Unit for Young Life Scientists, Kyoto University,
Kyoto 606-8501, Japan; [4]Department of Cell and Developmental Biology, Graduate School of Biostudies, Kyoto University, Kyoto
606-8501, Japan; [5]Japan Science and Technology Agency, CREST, Kyoto 606-8501, Japan

Spermatogonial stem cells (SSCs) present the potential to acquire pluripotency under specific culture conditions. However, the frequency of pluripotent cell derivation is low, and the mechanism of SSC reprogramming remains unknown. In this study, we report that induction of global DNA hypomethylation in germline stem (GS) cells (cultured SSCs) induces pluripotent cell derivation. When DNA demethylation was triggered by Dnmt1 depletion, GS cells underwent apoptosis. However, GS cells were converted into embryonic stem (ES)-like cells by double knockdown of Dnmt1 and p53. This treatment down-regulated Dmrt1, a gene involved in sexual differentiation, meiosis, and pluripotency. Dmrt1 depletion caused apoptosis of GS cells, but a combination of Dmrt1 and p53 depletion also induced pluripotency. Functional screening of putative Dmrt1 target genes revealed that Dmrt1 depletion up-regulates *Sox2*. Sox2 transfection up-regulated *Oct4* and produced pluripotent cells. This conversion was enhanced by Oct1 depletion, suggesting that the balance of Oct proteins maintains SSC identity. These results suggest that spontaneous SSC reprogramming is caused by unstable DNA methylation and that a Dmrt1–Sox2 cascade is critical for regulating pluripotency in SSCs.

Germ cells are thought to have pluripotency potential because they form teratomas. Teratomas are spontaneously formed in mice on a 129 background, and this strain was used to derive embryonic stem (ES) cells (Evans and Kaufman 1981; Stevens 1984). Although the frequency of spontaneous teratoma development was found to be limited to ~2%, studies have shown that primordial germ cells (PGCs) in the fetus can be induced to form teratomas by transplanting the genital ridges of midgestational embryos into ectopic locations in other animals (Stevens 1984). In the most successful cases, teratomas were found in ~80% of the PGC transplants. PGCs have pluripotency potential up until 12.5 d post-coitum (dpc). Although these classic experiments provided the foundation for teratoma studies, the mechanism of teratoma development has remained unknown. However, in 1992, two groups (Matsui et al. 1992; Resnick et al. 1992) demonstrated that PGCs can become ES-like pluripotent embryonic germ (EG) cells in vitro when they are cultured

with Kit ligand (KitL), fibroblast growth factor2 (FGF2), and leukemia inhibitory factor (LIF). EG cells are similar to ES cells, except in their DNA methylation patterns, and formed chimeras when the cells were transferred into blastocysts (Matsui et al. 1992; Labosky et al. 1994). The frequency of EG cell formation decreases gradually during development, and such potential pluripotency is no longer found in the germline later than 12.5 dpc (Labosky et al. 1994).

In 2003, a long-term culture system for spermatogonial stem cells (SSCs), in which SSCs proliferated in vitro in the presence of FGF2 and glial cell line-derived neurotrophic factor (GDNF), was developed (Kanatsu-Shinohara et al. 2003). Cultured SSCs, designated as germline stem (GS) cells, form grape-like clusters of spermatogonia in vitro but reinitiate spermatogenesis when transplanted into seminiferous tubules of infertile testes. Although GS cells are unipotent and produce sperm, they were subsequently found to transform into ES-like cells (Kanatsu-Shinohara et al. 2004). These ES-like cells, called multipotent GS (mGS) cells, often appear as sheets of epiblast-like cells, which transformed into ES-like compact colonies upon passaging. Despite their spermatogonial origin, they proliferate without GDNF and produce teratomas

in seminiferous tubules but are able to contribute to the blastocyst, thereby producing germline chimeras. Additional studies revealed that GS cells directly transform into mGS cells (Kanatsu-Shinohara et al. 2008), and similar cells were also derived from other species, including humans, although some of these results are being questioned (Ko et al. 2010b; Tapia et al. 2011).

While these results showed the pluripotency potential of SSCs, several critical issues remain to be answered. One is their low derivation frequency: mGS cells develop in only one out of every ~30 testes during GS cell derivation (Kanatsu-Shinohara et al. 2004). Although several groups also reported the derivation of pluripotent cells from postnatal male germ cells, discrepancies exist among these studies in terms of the nature and efficiency of reprogramming (Geijsen and Hochedlinger 2009). For example, one study showed the usefulness of LIF and obtained four lines from 21 mice (Guan et al. 2006). However, multipotent adult GS (maGS) cells produced in this study were unique in that they contribute to not only spermatogenesis but also embryogenesis, but the result of this study is being questioned (Geijsen and Hochedlinger 2009). Although beneficial effects of coculturing on testicular CD34+ stromal cells in pluripotency induction were reported in another study (Seandel et al. 2007), even better results were obtained by low-cell-density culture on mouse embryonic fibroblasts (MEFs), and six ES-like germline-derived pluripotent stem (gPS) cells were derived from eight testes within 4 wk in the most successful case (Ko et al. 2012). However, the quality of MEFs is still a critical factor, and an additional 3–4 wk are required when ES-like cells do not appear by low-cell-density cultures (Ko et al. 2010a). In addition to the variation in induction procedure, the difference in DNA methylation patterns in the differentially methylated region (DMR) of *H19* is also pointed out. While gPS cells show androgenetic DNA methylation patterns, maGS cells exhibit somatic cell DNA methylation patterns (Guan et al. 2006; Ko et al. 2009). It also should be noted here that many of these studies claimed derivation of ES-like cells from 129 or C57BL/6 (B6) mice, whose SSCs never proliferate without augmenting GDNF signal by GFRα1 supplementation (Kubota and Brinster 2008).

Such low or inconsistent derivation efficiency has made it difficult to study the molecular mechanism underlying pluripotency induction. We initially noticed that mGS cells often develop during initiation of GS cell cultures and that p53 deficiency improves their derivation (Kanatsu-Shinohara et al. 2004). We also found that mGS cells occasionally appear after freezing–thawing or electroporation (Kanatsu-Shinohara et al. 2005, 2008). Unexpectedly, GS cells were resistant to transfection of Yamanaka factors and did not become pluripotent (Morimoto et al. 2012). However, the mechanism of pluripotency regulation in SSCs has remained unknown. Thus, there is clearly a need to develop a fast and efficient system to induce SSC reprogramming, which will enable us to dissect the molecular mechanism involved in this process.

Here, we report a critical role of *Dmrt1* (a gene involved in sex determination) (Raymond et al. 2000) in GS cell reprogramming. We found previously that mGS cells often exhibit abnormal DNA methylation in DMRs of imprinted genes (Kanatsu-Shinohara et al. 2004). Because Dnmt1 is responsible for maintaining genomic methylation, we depleted Dnmt1 and found that Dnmt1 knockdown induces *H19* demethylation and mGS cell formation. Furthermore, Dnmt1 knockdown in GS cells was accompanied by the down-regulation of *Dmrt1*, a gene involved in sex differentiation (Raymond et al. 2000). Although this gene is thought to be responsible for meiotic induction in spermatogonia (Matson et al. 2010), Dmrt1 knockdown in GS cells up-regulates *Sox2* and efficiently induces mGS cells, suggesting that Dmrt1 plays a crucial role in repression of pluripotency in SSCs. We also propose a model in which spermatogonial identity is regulated by the balance of Oct proteins.

Results

Reprogramming of GS cells by induction of DNA demethylation

Global methylation of genomic DNA in GS cells is significantly higher than those in mGS and ES cells (Fig. 1A). Because DNA demethylation is often found in DMRs of *H19*-imprinted genes after reprogramming into mGS cells, we directly examined the role of Dnmt1, which maintains DNA methylation. To induce DNA demethylation, we used a Dnmt1 knockdown vector. When we induced demethylation by Dnmt1 knockdown, the majority of cells underwent p53-dependent apoptosis (Fig. 1B), but no mGS cells were found. However, because Dnmt1 is a maintenance methylase and passive demethylation due to Dnmt1 depletion requires multiple cell divisions (Jackson-Grusby et al. 2001), poor proliferation of GS cells in these cultures probably prevented efficient global DNA demethylation at 7 d. Therefore, GS cells from p53 knockout mice were transduced with a Dnmt1 knockdown vector and kept for ~1 mo. Although extensive apoptosis occurred after knockdown, some cells divided slowly and formed GS cell colonies. Using this protocol, mGS cells were obtained within 4 wk after Dnmt1 knockdown (Fig. 1C; Table 1; Supplemental Table S1). The morphology and the proliferation pattern of the Dnmt1 knockdown-induced mGS (Dnmt1-mGS) cells were indistinguishable from those of cells that developed spontaneously. Real-time PCR confirmed down-regulation of *Dnmt1* expression after knockdown (Supplemental Fig. S1A). Examination of global DNA methylation showed 3.7% ± 0.6% reduction in total methylcytosine levels by Dnmt1 knockdown 2 wk after transfection ($n = 3$; $P < 0.05$ by t-test). Combined bisulfite restriction analysis (COBRA) showed progressive demethylation of *H19* (Fig. 1D).

To examine whether the wild-type GS cells also transform into mGS cells, we established GS cells from transgenic pups carrying an enhanced green fluorescent protein (*EGFP*) gene (green mouse). Logarithmically growing GS cells were transduced with Dnmt1 and p53 knockdown vectors. Real-time PCR confirmed down-regulation of both p53 and Dnmt1 (Supplemental Fig. S1B,C). Wild-
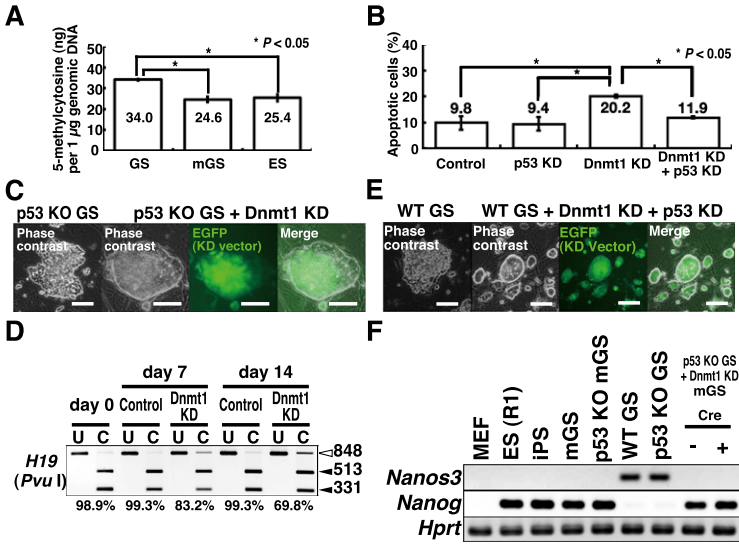
Figure 1. Development of mGS cells after Dnmt1 knockdown (KD). (*A*) Global DNA methylation levels in GS, mGS, and ES cells ($n = 3$). (*B*) Suppression of Dnmt1 knockdown-induced apoptosis by p53 knockdown. For each cell type, at least 99 cells were counted 7 d after transfection ($n = 5$). pSicoR was used as a control. (*C*) Development of mGS cells from p53 knockout (KO) GS cells after Dnmt1 knockdown. (*D*) COBRA of cultured cells. Open arrowheads indicate the sizes of the unmethylated DNA fragments, and closed arrowheads denote the sizes of the methylated DNA fragments. PCR products were digested with the indicated enzymes. Percent methylation is shown below the gel. pSicoR was used as a control. (*E*) Development of mGS cells from wild-type (WT) ROSA26 GS cells after double knockdown of Dnmt1 and p53. (*F*) RT–PCR analysis. Bars: *C,E*, 100 μm.

type GS cells produced mGS cells within 4 wk (Fig. 1E; Supplemental Table S1). RT–PCR confirmed *Nanog* expression in Dnmt1-mGS cells, which was accompanied by loss of *Nanos3* expression, suggesting that GS cells lost their spermatogonial identity and became ES-like cells (Fig. 1F). We did not find mGS cells using 5-azacytidine treatment using both wild-type and p53 knockout GS cells.

Dmrt1 knockdown induces mGS cells

Because Dnmt1 knockdown causes tumors in somatic cells without p53 (Gaudet et al. 2003), we hypothesized that DNA demethylation might have changed the expression of genes responsible for germ cell tumor (GCT) development. We therefore examined the impact of 14 GCT candidate genes by deregulating their expression in

a p53 knockout GS cell line. Dnmt1 knockdown down-regulated the expression of several genes, including Dnd1 and Dmrt1, both of which are implicated in the formation of teratomas from PGCs (Fig. 2A; Supplemental Fig. S2A,B; Gilbert et al. 2011). When we carried out knockdown experiments, knockdown of Dnd1 or Dmrt1 yielded mGS cell colonies within 4 wk (Supplemental Table S1). However, none of the other genes showed evidence of conversion.

To confirm the effects of Dnd1 and Dmrt1 knockdown on wild-type GS cells, we cotransfected each knockdown vector with a p53 knockdown vector. Although we obtained no mGS cells with Dnd1 knockdown, Dmrt1 knockdown successfully yielded mGS cells (Table 1). Compared with Dnmt1 knockdown, Dmrt1 knockdown induced mGS cells at a higher frequency with a shorter incubation time, and colony development was observed as early as 12 d.

Table 1. *Summary of mGS induction efficiency*

Gene transduction	Multiplicity of infection	Number of wells cultured	Number of wells with mGS cells	mGS colonies per 10^6 cells	Day colonies examined
p53 knockdown	10	22	0	0	28
Dnmt1 knockdown, p53 knockdown	10	12	9	13.7 ± 4.1	28
Dmrt1 knockdown, p53 knockdown	2,10	21	12	47.1 ± 17.1	28
Sox2 overexpression, p53 knockdown	10	6	4	2.3 ± 1.0	21
Oct4 overexpression, p53 knockdown	10	31	12	2.0 ± 0.7	21
Oct1 knockdown, p53 knockdown	10	12	3	1.0 ± 0.6	21
Oct4 overexpression, Oct1 knockdown, p53 knockdown	10	15	8	6.3 ± 1.9	21
Oct4 overexpression, Oct1 overexpression, p53 knockdown	10	8	3	2.5 ± 1.3	21
Oct6 knockdown, p53 knockdown	10	12	0	0	21

Values are mean ± SEM. Cells (5×10^5) were cultured in six-well plates. All experiments were carried out with wild-type GS cells.
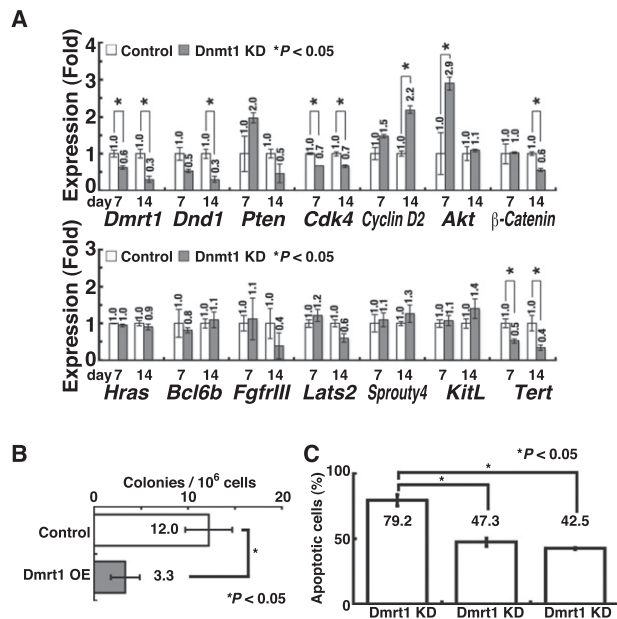
Takashima et al.

Figure 2. Development of mGS cells after Dmrt1 knockdown (KD). (A) Real-time PCR analysis of GCT candidate gene expression in p53 knockout (KO) GS cells after Dmrt1 knockdown (n = 3). pSicoR was used as a control. (B) Suppression of mGS cell development by Dmrt1 overexpression (OE) 28 d after Dmrt1 knockdown (n = 9). CSII-EF1α-IRES2-Venus was used as a control. (C) Suppression of Dmrt1-induced apoptosis by p53 or Bax knockdown. For each cell type, at least 68 cells were counted 7 d after transfection (n = 5).

Concurrent overexpression of Dmrt1 cDNA with a Dnmt1 knockdown vector significantly reduced mGS cell development (Fig. 2B), which suggests that *Dmrt1* downregulation is responsible for Dnmt1 knockdown-induced pluripotency. As in Dnmt1-mGS cells, simultaneous p53 knockdown was necessary because cells underwent apoptosis due to Dmrt1 knockdown (Fig. 2C). Although Bax knockdown was able to rescue cells from Dmrt1 knockdown-induced apoptosis, we were unable to observe mGS cells (Fig. 2C), suggesting that p53 knockdown has an additional function to promote pluripotency.

Because of the relatively high efficiency of mGS cell formation, we used this system to characterize the reprogramming process. As previously noted for spontaneously developed mGS cells, Dmrt1-mGS cell development is often accompanied by sudden generation of an epiblast-like sheet, which has Nanog expression in the center (Supplemental Fig. S3A). All Dmrt1-mGS cell colonies expressed Nanog on the day when colonies were discovered. This protocol was useful in deriving mGS cells from all seven tested wild-type GS cell lines, and mGS cells were obtained from not only pups but also adults (Supplemental Fig. S3B). These results suggest that Dmrt1 regulates pluripotency in GS cells.

Characterization of Dnmt1- and Dmrt1-mGS cells

RT–PCR and flow cytometry indicated that both Dnmt1- and Dmrt1-mGS cells have typical features of ES cells

(Supplemental Fig. S4A,B). They expressed high levels of *Oct4* and *Sox2* and were positive for Nanog in immunohistochemical analyses (Supplemental Fig. S4C). However, several lines of Dnmt1- or Dmrt1-mGS cells expressed *Neurog3* or *Sohlh1*, which suggested that the cells retain a spermatogonial phenotype (Supplemental Fig. S4A). We carried out bisulfite sequencing analysis to check the DNA methylation patterns in imprinted genes. Consistent with previous studies (Kanatsu-Shinohara et al. 2004), GS cells showed typical androgenetic DNA methylation patterns: hypermethylation in *H19* and hypomethylation in *Igf2r* (Supplemental Fig. S4D). In contrast, Dnmt1- and Dmrt1-mGS cells showed demethylation in *H19*. Although we occasionally observed *Igf2r* methylation in mGS cells, no apparent difference in *Igf2r* was found, regardless of the induction method.

Functional characterization of Dnmt1- and Dmrt1-mGS cells

To determine whether Dnmt1- and Dmrt1-mGS cells are functionally similar to ES cells, we examined their differentiation potential. In these experiments, Dnmt1-mGS cells were produced by shRNA transfection, and the shRNA was removed by cre treatment (Supplemental Fig. S4E,F). We first induced neuroectodermal differentiation in adherent monocultures (Ying and Smith 2003). The cultured cells successfully differentiated into cells expressing βIII-tubulin, a neuronal marker. We then generated embryoid bodies (EBs) in vitro and examined whether the cells could differentiate into other lineages (Fig. 3A). After 5 d of culture on gelatin-coated dishes, the EBs were
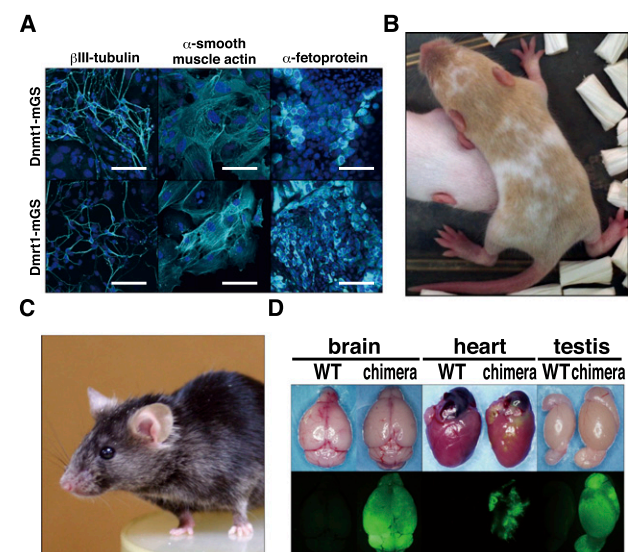
Figure 3. Differentiation potential of Dnmt1- and Dmrt1-mGS cells. (A) Neuronal or EB-mediated differentiation of mGS cells. (B,C) A live chimera formed by microinjection of Dnmt1-mGS cells (B) or Dmrt1-mGS cells (C) into ICR or B6 blastocyst, respectively. The cinnamon coat color represents the contribution of the Dnmt1- or Dmrt1-mGS cells on a DBA/2 background. (D) Contribution of Dmrt1-mGS cells to various organs, as indicated by EGFP fluorescence. Bar: A, 100 μm.

132

stained with several antibodies. Some cells stained positively for α-smooth muscle actin, a mesodermal marker, while others expressed cells with α-fetoprotein expression, suggesting that they belong to the endodermal lineage. We found no obvious difference between Dnmt1- and Dmrt1-mGS cells in terms of differentiation patterns and efficiencies. We also transplanted both cell types under the subcutaneous tissues of nude mice to examine their teratoma-forming potential. All clones produced tumors within 4 wk after transplantation. Histological analyses showed that the transplanted cells produced teratomas with the ectoderm (neural tube), mesoderm (chondrocytes), and endoderm (gut epithelium) (Supplemental Fig. S4G).

To test whether these mGS cells contribute to embryonic development, we microinjected them into blastocysts (Supplemental Table S2). In this experiment, GS cells from ROSA26 mice were used to derive Dnmt1-mGS cells, which were treated with cre to remove shRNA for Dnmt1 and p53 before the chimera experiment. On the other hand, we used green GS cells and transfected siRNAs for *Dmrt1* and *p53* to avoid vector integration for Dmrt1-mGS cell production. Both Dnmt1- and Dmrt1-mGS cells could produce chimeric offspring, albeit at low efficiency (Fig. 3B–D; Supplemental Table S2). Low efficiency of chimera production could be due to residual expression of *Neurog3* in these cells (Supplemental Fig. S4H). Nevertheless, both offspring were apparently normal, and Dmrt1-mGS-derived F1 offspring were born by natural mating. No abnormalities in *H19* were found by COBRA in these offspring (Supplemental Fig. S4I).

Identification of Dmrt1 target genes

In the next set of experiments, we sought to identify target genes regulated by Dmrt1. A previous study showed that Dmrt1 regulates >1400 genes in spermatogonia (Murphy et al. 2010). Among the diverse types of genes, we focused on those associated with cell cycle regulation (*p18* and *p19*) and pluripotency (*Nr5a1*, *Utf1*, *Sox2*, and *Zic3*) because we reasoned that deregulation of these genes can potentially stimulate GCT formation. We analyzed the expression levels of these candidate genes in p53 knockout GS cells by real-time PCR after Dmrt1 knockdown (Fig. 4A). The analyses revealed that while *Sox2* and *Utf1* were upregulated by Dmrt1 knockdown, *Nr5a1* and *Zic3* were down-regulated, which suggests that *Nr5a1* and *Zic3* are dispensable for reprogramming. Both *p18* and *p19* cyclin-dependent kinase inhibitors (CDKIs) were down-regulated, which may facilitate teratoma formation. Although similar results were obtained using wild-type GS cells with p53 knockdown, we failed to find statistically significant down-regulation of *p19* (Supplemental Fig. S5).

Based on this observation, we screened for genes that trigger pluripotency in GS cells. We overexpressed pluripotency-related genes or depleted the expression of CDKIs in wild-type GS cells. All transfection experiments were carried out by cotransfection with a p53 knockdown vector. Although Utf1 transfection did not result in mGS cell development, transfection of Sox2 yielded mGS cells using three different wild-type GS cell lines (Table 1;
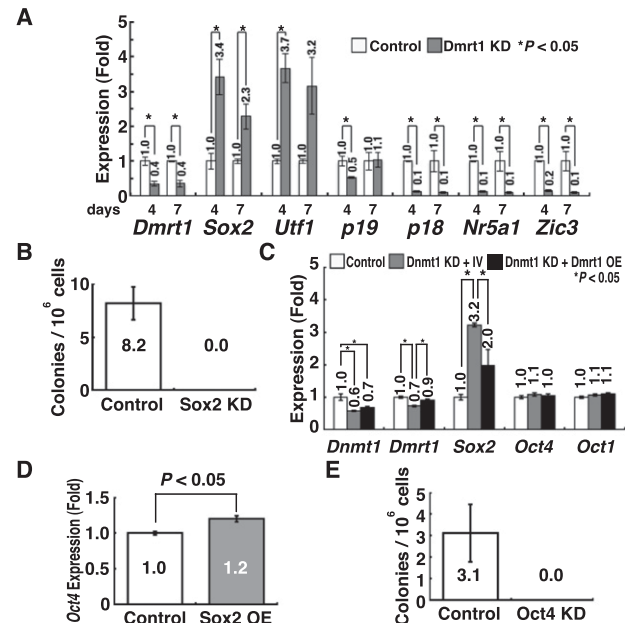
Figure 4. Development of mGS cells after Sox2 or Oct4 overexpression (OE). (*A*) Real-time PCR analysis of Dmrt1 target genes in p53 knockout (KO) GS cells after Dmrt1 knockdown (KD) ($n = 3$). pLKO.1 EGFP was used as a control. (*B*) Suppression of mGS cell development by Sox2 knockdown 28 d after Dmrt1 knockdown ($n = 13$). pLKO.1 EGFP was used as a control. (*C*) Real-time PCR analysis of *Dnmt1*, *Dmrt1*, *Sox2*, and *Oct1/4* expression in p53 knockout GS cells 14 d after Dmrt1 knockdown ($n = 4$). pSicoR was used as a control. For concurrent Dmrt1 overexpression, CSII-EF1α-IRES2-Venus was a control. (*D*) Real-time PCR analysis of *Oct4* expression in p53 knockout GS cells 14 d after Sox2 overexpression ($n = 3$). CSII-EF1α-IRES2-hKO1 was used as a control. (*E*) Reduced Sox2-mGS cell development 28 d after Oct4 knockdown ($n = 9$).

Supplemental Table S1; Supplemental Fig. S2C). Many cells underwent p53-dependent apoptosis after Sox2 overexpression (Supplemental Fig. S6A), but the remaining cells transformed into mGS cells, a pattern similar to that for Dmrt1 knockdown. Sox2 knockdown inhibited Dmrt1-mGS cell development (Fig. 4B; Supplemental Fig. S2A). Neither p18 nor p19 knockdown resulted in mGS cell production. Because concurrent Dmrt1 overexpression suppressed Sox2 expression induced by Dnmt1 depletion, the Dmrt1–Sox2 axis also appears to operate in Dnmt1-mGS cell development (Fig. 4C; Supplemental Fig. S2C).

Sox2 is necessary to regulate transcription factors that affect *Oct4* expression in ES cells (Masui et al. 2007). Although GS cells express *Oct4*, its level is significantly lower than that found in ES cells (Imamura et al. 2006). However, we noted that *Oct4* mRNA and protein expression were up-regulated in Sox2 transfected GS cells (Fig. 4D; Supplemental Fig. S7). Moreover, Oct4 knockdown prevented mGS cell development after Sox2 overexpression (Fig. 4E). Although apparent changes in Oct4 expression were not observed after Dmrt1 knockdown (Fig. 4C), we reasoned that this could be due to the relatively variable timing and small number of pluripotent colonies

133

Takashima et al.

by Dnmt1 knockdown. Because Sox2 maintains the requisite level of *Oct4* in ES cells and Oct4 overexpression can sustain Sox2-null ES cells (Masui et al. 2007), we tested the possibility that Oct4 overexpression may abolish the need for Sox2 transfection. Transfection of Oct4 induced mGS cell formation using three different wild-type GS cell lines (Table 1; Supplemental Table S1). Unlike Sox2 overexpression, Oct4 overexpression did not induce GS cell apoptosis (Supplemental Fig. S6B) but did require p53 knockdown for mGS cell formation. These results suggest that Sox2 is responsible for Dmrt1-mGS cell generation and that increased *Sox2* expression up-regulates *Oct4*, thereby inducing the formation of pluripotent cells.

Increased mGS cell development following Oct1 knockdown

Although these results show the importance of Oct4 regulation, the role of this protein in SSCs has been controversial. One study reported that *Oct4* down-regulation induces GS cell apoptosis (Dann et al. 2008), while another study showed that Oct6, but not Oct4, is indispensable for SSCs (Wu et al. 2010). However, we noted that GS cells express *Oct1* (Fig. 5A). Oct1 mRNA was down-regulated upon FGF2 or GDNF treatment, and Western blot analysis

also confirmed this result (Fig. 5B,C). Although we did not observe apparent changes in Oct4 and Oct6 expression at mRNA levels, Western blotting showed that both Oct4 and Oct6 protein levels were slightly up-regulated by cytokine treatment. These results suggested that regulation of Oct1 and Oct4/6 expression is different. Because Oct1 often has the same targets as Oct4 (Kang et al. 2009), we reasoned that the relative balance of Oct proteins is important for regulating pluripotency in SSCs.

To test this hypothesis, we examined the impact of Oct knockdown in GS cells. Knockdown of Oct1 or Oct4 induced GS cell apoptosis in a p53-dependent manner (Supplemental Fig. S6C). Oct6 knockdown also caused apoptosis, which was not rescued by p53 deficiency. We transfected wild-type GS cells with Oct1 or Oct6 knockdown vectors together with a p53 knockdown vector. Knockdown of Oct1, but not Oct6, yielded mGS cells using two different wild-type GS cell lines (Table 1). The efficiencies of Oct4 overexpression and Oct1 knockdown were comparable, but combining Oct4 overexpression and Oct1 knockdown synergistically improved mGS cell derivation efficiency ($P < 0.05$ by ANOVA), and mGS cells were obtained (Table 1). While Oct4 overexpression increased *Sox2* expression (Fig. 5D), Oct1 knockdown increased not only *Sox2* expression but also *Oct4* expression (Fig. 5E). On the other hand, Oct4 knockdown decreased *Sox2* expression, suggesting that Oct4 is positively regulating Sox2 (Fig. 5F). Although Oct1 overexpression decreased *Oct4* and *Sox2* expression (Fig. 5G), it was not possible to suppress Oct4-mGS cell development, suggesting that Oct1 is necessary but not sufficient for suppressing pluripotency. Because neither Oct4 nor Sox2 overexpression influenced *Oct1* expression (Fig. 5D,H), it is likely that Oct1 is regulated independently of Oct4 and Sox2. When we examined whether changes in Oct1/4 expression in GS cells can influence genes that are regulated by Oct4 in ES cells (van den Berg et al. 2010), several genes changed expression by Oct1 overexpression or knockdown (Supplemental Fig. S8). In particular, Utf1, one of the Dmrt1 target genes, was down-regulated by Oct1 overexpression, while it was up-regulated by Oct1 knockdown. There results suggest that Oct1 suppresses pluripotency in GS cells by competing with Oct4 for several pluripotency-related target genes.

Characterization of Sox2- and Oct4-mGS cells

Both Sox2- and Oct4-mGS cells were phenotypically similar to Dnmt1- and Dmrt1-mGS cells and were able to differentiate into cells of the three germ layers in vitro (Supplemental Fig. S9A–E). However, their global gene expression profiles were slightly different from those of ES cells (Fig. 6A; Supplemental Fig. S10). To confirm their pluripotency, we introduced Sox2 or Oct4 cDNA into a floxed vector that was transfected with a p53 knockdown vector. After transformation into mGS cells, the transgenes were removed by cre-mediated deletion (Supplemental Fig. S9F,G). The ability of the resulting cells to form chimeras by blastocyst injection was then tested (Supplemental Table S2). Chimeric offspring were obtained

Figure 5. Development of mGS cells after Oct1 knockdown (KD). (*A*) RT–PCR analysis of *Oct* gene expression in GS cells during logarithmic growth phase. (*B*) Real-time PCR analysis of Oct expression after cytokine stimulation. GS cells were starved for 3 d and restimulated with the indicated cytokines for 24 h before sample collection (*n* = 6). (*C*) Western blot analysis of Oct expression after cytokine stimulation. GS cells were starved for 3 d and restimulated with the indicated cytokines for 24 h before sample collection. (*D–G*) Real-time PCR analysis of *Oct1/4* and *Sox2* expression 14 d after Oct4 overexpression (OE) (*D*), Oct1 knockdown (*E*), Oct4 knockdown (*F*), or Oct1 overexpression (*G*) (*n* = 3). CSII-EF1α-IRES2-Venus was used as a control for Oct1 and Oct4 overexpression. pLKO.1 was a control for Oct1 and Oct4 knockdown. (*H*) Real-time PCR analysis of *Oct1* and *Sox2* expression 14 d after Sox2 overexpression (*n* = 3). CSII-EF1α-IRES2-hKO1 was used as a control.

134

Figure 6. Development of normal offspring from Sox2- or Oct4-mGS cells. (*A*) Hierarchical clustering of gene expression by microarray. (*B,C*) A live chimera formed by microinjection of Sox2-mGS cells (*B*) and Oct4-mGS cells (*C*) into B6 and ICR blastocysts, respectively. (*Inset*) Offspring produced after germline transmission. While Sox2-mGS cell origin was identified by the EGFP expression (*B*), Oct4-mGS cell origin was confirmed by the cinnamon coat color (*C*). (*D*) A model to explain the mechanism of pluripotency regulation in SSCs.

from both Sox2- and Oct4-mGS cells (Fig. 6B,C). Both types of mGS cells showed germline transmission by natural mating. These results suggest that Sox2- and Oct-4 mGS cells are pluripotent.

Discussion

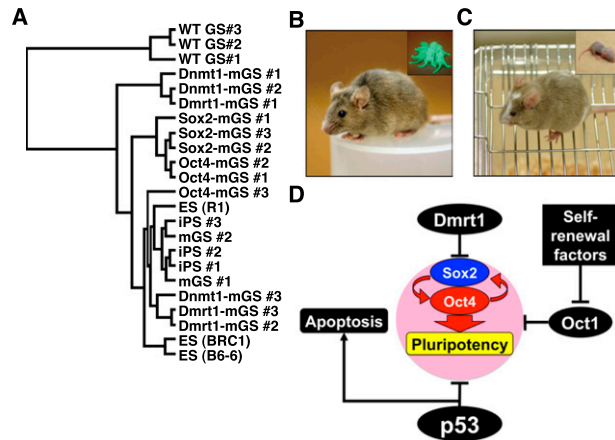The molecular mechanism of culture-induced pluripotency is not well understood. While DNA methylation patterns in ES cells often change within several months, GS cells maintain a stable karyotype and DNA methylation patterns in imprinted genes for >2 yr (Kanatsu-Shinohara et al. 2005). Because demethylation of *H19* DMRs is almost always found in spontaneously developed mGS cells, we reasoned that DNA demethylation might have contributed to the reprogramming of GS cells. To test our hypothesis directly, we used Dnmt1 knockdown to induce hypomethylation in GS cells. Unlike ES cells, which can proliferate without *Dnmt* genes (Tsumura et al. 2006), GS cell survival depends critically on *Dnmt1* expression (Takashima et al. 2009). Although Dnmt1 knockdown resulted in apoptosis of GS cells, simultaneous p53 knockdown successfully induced mGS cell formation, suggesting that DNA demethylation and suppression of p53 function are necessary for dedifferentiation of GS cells into pluripotent cells.

In our previous study, we did not observe mGS cells by Dnmt1 knockdown, probably because of the higher virus titer and shorter incubation time (Takashima et al. 2009), and *H19* DMR demethylation was not confirmed. The higher virus titer induced extensive apoptosis of GS cells, and the shorter incubation time (~3 wk) was probably insufficient to induce passive demethylation by cell replication because the current study shows that most of

the mGS cell colonies developed after 3 wk. Because deficiency of *Dnmt1* causes somatic cell tumors (Gaudet et al. 2003), acquisition of pluripotency in GS cells is suggested to share similarities with tumorigenesis. Consistent with this notion, *H19* is often demethylated in human GCTs (Looijenga et al. 1998). In particular, seminomas and nonseminomas generally show biallelic expression of the *H19* gene. Moreover, we also recently showed *H19* demethylation in ES-like colonies produced by in vitro transformation of mouse SSCs with activated Ras, c-myc, and p53 dominant-negative constructs (Morimoto et al. 2012). Although the roles of imprinted genes in GCTs are unknown, similarities between GCT formation and GS cell reprogramming led us to examine whether GCT candidate genes are deregulated as a result of global DNA hypomethylation.

Dmrt1 was one of the several candidate genes that were influenced by Dnmt1 knockdown, and Dmrt1 knockdown successfully induced mGS cell formation. *Dmrt1* is one of a group of conserved transcriptional regulators of sexual differentiation that share a Doublesex/Mab-3 (DM) domain DNA-binding motif and is required for testicular development in vertebrates (Raymond et al. 2000). In mice, this gene is expressed only in the gonad and is essential for differentiation of germ cells and Sertoli cells. Strikingly, testes without Dmrt1 show ovarian differentiation even at the adult stage (Matson et al. 2011). Humans lacking one copy of *Dmrt1* exhibit testicular dysgenesis and in some cases are feminized (Krentz et al. 2009). In germ cells, this gene is responsible for the formation of teratomas from PGCs, but it is limited to the 129 background (Krentz et al. 2009). In the postnatal testis, Dmrt1 has been considered as a transcriptional gatekeeper that controls mitosis versus meiosis in germ cells (Matson et al. 2010). Undifferentiated spermatogonia without Dmrt1 showed precocious entry into meiosis and reached meiotic prophase by skipping amplifying divisions of the differentiating spermatogonia population, but no tumor formation was reported in postnatal animals without Dmrt1. In contrast, Dmrt1 overexpression is thought to cause spermatocytic seminomas in human adults by increasing Ret expression (Krentz et al. 2009).

Although regulation of pluripotency by Dmrt1 in spermatogonia has not been reported, we speculate that the discrepancy between our results and previous studies is due to two factors. One is the suppression of apoptosis by p53 knockdown. Dmrt1 is involved in germ cell survival, and while Dmrt1 deficiency in PGCs caused teratomas on a 129 background, germ cell loss was observed in non-129 strains (Krentz et al. 2009). Apoptosis of germ cells is probably caused by reduced GDNF signaling because analyses of mutant testes showed that both GFRα1 and Ret are down-regulated, which suggests that Dmrt1 influences the responsiveness to GDNF. In the present study, we also observed that simple Dmrt1 knockdown induced apoptosis of GS cells, but simultaneous p53 knockdown rescued them from apoptosis, resulting in mGS cell formation. The other factor is the differentiation status of the target cells. In the previous study, analysis of Dmrt1 function in spermatogonia was carried out using cre

Takashima et al.

driven by a *Neurog3* promoter (Matson et al. 2010). However, *Neurog3* is thought to be expressed in a subpopulation of SSCs in a reversible manner (Yoshida 2010). Therefore, some SSCs may not have undergone *Neurog3*-cre-mediated *Dmrt1* deletion, and the function of Dmrt1 in the remaining SSC population is not known. The differentiation level of the target cell population is important for germ cell transformation because cells enriched for SSCs showed a higher frequency of development into transformed cells than committed spermatogonia after transfection of oncogenes or Yamanaka factors (Morimoto et al. 2012).

Knockdown of two GCT candidate genes, *Dnd1* and *Dmrt1*, induced pluripotency in p53 knockout GS cells. Dnd1 is an RNA-binding protein that regulates PGC viability and suppresses teratoma formation (Zhu et al. 2007). It is similar to Dmrt1 in that it only causes teratomas on a 129 background. However, the mechanism of pluripotency regulation seems to differ between these two genes. Although we were able to obtain mGS cells by Dnd1 or Dmr1 knockdown using p53 knockout GS cells, only Dmrt1 was useful for deriving mGS cells from wild-type cells. In fact, studies on PGCs also suggest that they have independent functions (Krentz et al. 2009). For example, Dnd1 mutants undergo a severe loss of germ cells before 11.5 dpc, whereas those in Dmrt1 mutants survive until birth. Although Pten deficiency induces teratomas in PGCs on non-129 backgrounds, Dmrt1 deficiency did not change levels of Pten or Akt phosphorylation (Kimura et al. 2003; Krentz et al. 2009). These results suggested that Dmrt1 acts either independently of Pten or downstream from the Pten pathway in PGCs. Although p53 deficiency also causes teratomas on non-129 backgrounds, it is distinct from Pten in that Pten-deficient gonocytes and spermatogonia do not show pluripotency (Goertz et al. 2011). Therefore, p53 and Dmrt1 seem to be guardians of pluripotency at both embryonic and postnatal stages.

Of the Dmrt1 target genes, our functional screening suggested that Sox2 acts downstream from Dmrt1 to induce reprogramming. *Sox2* mRNA is expressed from the early stages of PGC development, but Sox2 protein decreases from 13.5 dpc to 17.5 dpc in fetal gonocytes and is absent in spermatogonia (Imamura et al. 2006; Campolo et al. 2013). Dmrt1 protein expression is absent by 15.5 dpc but is re-expressed in spermatogonia (Lei et al. 2007). This suggests that Dmrt1 protein expression is discrepant with Sox2 protein expression, which apparently involves additional molecules. On the other hand, although the Oct4 protein is expressed in GS cells, its level is only 10% of that found in ES cells; Oct4/Sox2 sites in GS cells are not occupied by Oct4 and Sox2 despite their hypomethylated status, possibly due to the smaller amount of Oct4 and the absence of Sox2 (Imamura et al. 2006). Nevertheless, our results showed that Sox2 and Oct4 expression levels are closely correlated in GS cells. Although the role of Oct4 in SSCs is still under debate (Wu et al. 2010), high expression of Sox2 appears to overcome *Sox2* repression at the translational level and tip the balance toward pluripotency by up-regulating *Oct4*. Although changes in Oct4 levels were modest, this may have a large impact on pluripotency regulation, considering that the threshold for inducing differentiation in ES cells is set at 50% above or below the normal Oct4 expression (Niwa et al. 2000). Because Oct1 knockdown also induced up-regulation of Oct4, Sox2, and Utf1, relative reduction in Oct1 may perhaps induce pluripotency genes by increasing the access of Oct4 to target genes to regulate several pluripotency-related genes (Fig. 6C). However, given our production of mGS cells by Dnd1 knockdown in p53 knockout GS cells and the fact that Oct1 overexpression could not suppress Oct4-mGS cell development, suppression of pluripotency probably involves additional molecules. Identifying other genes that modulate the response of GS cells to Sox2 overexpression is warranted.

Because mGS cells can be derived without genetic manipulation, SSCs represent a unique resource for deriving pluripotent cells. However, conflicting reports on the induction method and nature of SSC-derived PS cells need to be reconciled. In particular, it still remains unknown why mGS cell development is often accompanied by epiblast-like colony formation, while similar colonies were not reported in other studies (Seandel et al. 2007; Geijsen and Hochedlinger 2009). Such discrepancies could be due to the differences in the cell of origin and/or mode of reprogramming. This may also explain why mGS cell formation occurred at relatively lower frequency compared with gPS cells (0.0047% vs. 0.01%), which gradually form ES-like colonies over several weeks. We also do not know how p53 is involved in pluripotency regulation. Because mGS cell development often occurred after freezing–thawing or electroporation, we think that such changes in culture conditions induce cellular stress, which may influence p53 levels. However, because Bax knockdown could not induce mGS cells, the role of p53 knockdown is not simply rescuing apoptosis but has an additional role in pluripotency regulation. Because we can reproducibly obtain mGS cells with our new protocol, analysis of reprogramming mechanisms is now possible, which will improve our understanding of how pluripotency is suppressed in germ cells despite their similarity to ES cells.

Materials and methods

Cell culture

GS cells were derived from the transgenic mouse lines C57BL6/Tg14(act-EGFP-OsbY01) and B6-TgR(ROSA26)26Sor, as previously described (Kanatsu-Shinohara et al. 2003, 2004, 2011). GS cells were also established from the transgenic mouse line Tg(Nanog-GFP, Puro)1Yam (Okita et al. 2007). GS cells from p53 knockout mice were previously described (Kanatsu-Shinohara et al. 2004). Culture medium was based on StemPro-34 SFM (Invitrogen) as previously described (Kanatsu-Shinohara et al. 2003). We also used mGS cells on a DBA/2 background that spontaneously developed during green GS cell derivation (Kanatsu-Shinohara et al. 2004). Growth factors used were 10 ng/mL human FGF2 and 15 ng/mL recombinant rat GDNF (both from Peprotech). ES cells (R1) were a generous gift from Dr. M. Ikawa (Osaka University, Suita, Japan). ES cells (BRC1 and B6-6) were provided by RIKEN BRC.

136

All pluripotent cell lines were maintained on MEFs in Dulbecco's modified Eagle's medium (DMEM) supplemented with 15% fetal bovine serum (FBS), 1000 U/mL LIF (ESGRO; Merck Millipore), nonessential amino acid mixture (Invitrogen), and 0.1 mM 2-mercaptoethanol (2-ME). We also used 2 μM PD0325901 (Selleck Chemicals), 3 μM CHIR99021 (Biovision, Inc.), and 1000 U/mL LIF in N2B27 medium to maintain these cells for chimera production (Ying and Smith 2003).

For differentiation into neuronal lineages, cells were cultured on gelatin-coated plates for 8 d in N2B27 medium. Neural cell differentiation was induced by replating on a LAB-TEK chamber slide (Thermo Fisher Scientific) coated with 0.2 mg/mL fibronectin (Invitrogen) and maintenance in N2B27 medium supplemented with 20 ng/mL FGF2 for 10 d (Ying and Smith 2003). For EB formation, cells were suspended in DMEM supplemented with 20% FBS, 10 μM 2-ME, and nonessential amino acid mixture and plated on a low-cell-binding plate at a density of 7.5×10^4 cells per 9.6 cm^2. Two days after culture, the serum concentration was reduced to 15% FBS, and the cells were cultured for 8 d. EBs were then transferred to a LAB-TEK chamber slide coated with 0.1% gelatin and cultured for 5 d.

Statistical analyses

The results are presented as the mean ± SEM. Significant differences between means for single comparisons were identified using Student's t-test. Multiple comparison analyses were performed using ANOVA followed by Tukey's HSD test.

Accession number

Raw data sets have been submitted to the Gene Expression Omnibus database (http://www.ncbi.nlm.nih.gov/geo) and are available under the accession number GSE43850.

Acknowledgments

References

Campolo F, Gori M, Favaro R, Nicolis S, Pellegrini M, Botti F, Rossi P, Jannini EA, Dolci S. 2013. Essential role of Sox2 for the establishment and maintenance of the germ cell line. *Stem Cells* **31:** 1408–1421.

Dann CT, Alvarado AL, Molyneux LA, Denard BS, Garbers DL, Porteus MH. 2008. Spermatogonial stem cell self-renewal requires OCT4, a factor downregulated during retinoic acid-induced differentiation. *Stem Cells* **26:** 2928–2937.

Evans MJ, Kaufman MH. 1981. Establishment in culture of pluripotential cells from mouse embryos. *Nature* **292:** 154–156.

Gaudet F, Hodgson JG, Eden A, Jackson-Grusby L, Dausman J, Gray JW, Leonhardt H, Jaenisch R. 2003. Induction of tumors in mice by genomic hypomethylation. *Science* **300:** 489–492.

Geijsen N, Hochedlinger K. 2009. gPS navigates germ cells to pluripotency. *Cell Stem Cell* **5:** 3–4.

Gilbert D, Rapley E, Shipley J. 2011. Testicular germ cell tumours: Predisposition genes and the male germ cell niche. *Nat Rev Cancer* **11:** 278–288.

Goertz MJ, Wu Z, Gallardo TD, Hamra FK, Castrillon DH. 2011. Foxo1 is required in mouse spermatogonial stem cells for their maintenance and the initiation of spermatogenesis. *J Clin Invest* **121:** 3456–3466.

Guan K, Nayernia K, Maier LS, Wagner S, Dressel R, Lee JH, Nolte J, Wolf F, Li M, Engel W, et al. 2006. Pluripotency of spermatogonial stem cells from adult mouse testis. *Nature* **440:** 1199–1203.

Imamura M, Miura K, Iwabuchi K, Ichisaka T, Nakagawa M, Lee J, Kanatsu-Shinohara M, Shinohara T, Yamanaka S. 2006. Transcriptional repression and DNA hypermethylation of a small set of ES cell marker genes in male germline stem cells. *BMC Dev Biol* **6:** 34.

Jackson-Grusby L, Beard C, Possemato R, Tudor M, Fambrough D, Csankovszki G, Dausman J, Lee P, Wilson C, Lander E, et al. 2001. Loss of genomic methylation causes p53-dependent apoptosis and epigenetic deregulation. *Nat Genet* **27:** 31–39.

Kanatsu-Shinohara M, Ogonuki N, Inoue K, Miki H, Ogura A, Toyokuni S, Shinohara T. 2003. Long-term proliferation in culture and germline transmission of mouse male germline stem cells. *Biol Reprod* **69:** 612–616.

Kanatsu-Shinohara M, Inoue K, Lee J, Yoshimoto M, Ogonuki N, Miki H, Baba S, Kato T, Kazuki Y, Toyokuni S, et al. 2004. Generation of pluripotent stem cells from neonatal mouse testis. *Cell* **119:** 1001–1012.

Kanatsu-Shinohara M, Ogonuki N, Iwano T, Lee J, Kazuki Y, Inoue K, Miki H, Takehashi M, Toyokuni S, Shinkai Y, et al. 2005. Genetic and epigenetic properties of mouse male germline stem cells during long-term culture. *Development* **132:** 4155–4163.

Kanatsu-Shinohara M, Lee J, Inoue K, Ogonuki N, Miki H, Toyokuni S, Ikawa M, Nakamura T, Ogura A, Shinohara T. 2008. Pluripotency of a single spermatogonial stem cell in mice. *Biol Reprod* **78:** 681–687.

Kanatsu-Shinohara M, Inoue K, Ogonuki N, Morimoto H, Ogura A, Shinohara T. 2011. Serum- and feeder-free culture of mouse germline stem cells. *Biol Reprod* **84:** 97–105.

Kang J, Shakya A, Tantin D. 2009. Stem cells, stress, metabolism and cancer: A drama in two Octs. *Trends Biochem Sci* **34:** 491–499.

Kimura T, Suzuki A, Fujita Y, Yomogida K, Lomeli H, Asada N, Ikeuchi M, Nagy A, Mak TW, Nakano T. 2003. Conditional loss of PTEN leads to testicular teratoma and enhances embryonic germ cell production. *Development* **130:** 1691–1700.

Ko K, Tapia N, Wu G, Kim JB, Bravo MJA, Sasse P, Glaser T, Ruau D, Han DW, Greber B, et al. 2009. Induction of pluripotency in adult unipotent germline stem cells. *Cell Stem Cell* **5:** 87–96.

Ko K, Araúzo-Bravo MJ, Kim J, Stehling M, Schöler HR. 2010a. Conversion of adult mouse unipotent germline stem cells into pluripotent stem cells. *Nat Protoc* **5:** 921–928.

Ko K, Araúzo-Bravo MJ, Tapia N, Kim J, Lin Q, Bernemann C, Han DW, Gentile L, Reinhardt P, Greber B, et al. 2010b. Human adult germline stem cells in question. *Nature* **465:** E1.

Ko K, Wu G, Araúzo-Bravo MJ, Kim J, Francine J, Greber B, Mühlisch J, Joo JY, Sabour D, Fruhwald MC, et al. 2012. Autologous pluripotent stem cells generated from adult mouse testicular biopsy. *Stem Cell Rev* **8:** 435–444.

Krentz AD, Murphy MW, Kim S, Cook MS, Capel B, Zhu R, Matin A, Sarver AL, Parker KL, Griswold MD, et al. 2009. The DM domain protein DMRT1 is a dose-sensitive regulator of fetal germ cell proliferation and pluripotency. *Proc Natl Acad Sci* **106:** 22323–22328.

Kubota H, Brinster RL. 2008. Culture of rodent spermatogonial stem cells, male germline stem cells of the postnatal animal. *Methods Cell Biol* **86:** 59–84.

Labosky PA, Barlow DP, Hogan BLM. 1994. Mouse embryonic germ (EG) cell lines: Transmission through the germline and

Takashima et al.

differences in the methylation imprint of insulin-like growth factor 2 receptor (Igf2r) gene compared with embryonic stem (ES) cell lines. *Development* **120:** 3197–3204.

Lei N, Hornbaker KI, Rice DA, Karpova T, Agbor VA, Heckert LL. 2007. Sex-specific differences in mouse DMRT1 expression are both cell type- and stage-dependent during gonad development. *Biol Reprod* **77:** 466–475.

Looijenga LHJ, Verkerk AJMH, Dekker MC, van Gurp RJHLM, Gillis AJM, Oosterhuis JW. 1998. Genomic imprinting in testicular germ cell tumours. *APMIS* **106:** 187–197.

Masui S, Nakatake Y, Toyooka Y, Shimosato D, Yagi R, Takahashi K, Okochi H, Okuda A, Matoba R, Sharov AA, et al. 2007. Pluripotency governed by Sox2 via regulation of Oct3/4 expression in mouse embryonic stem cells. *Nat Cell Biol* **9:** 625–635.

Matson CK, Murphy MW, Griswold MD, Yoshida S, Bardwell VJ, Zarkower D. 2010. The mammalian Doublesex homologue DMRT1 is a transcriptional gatekeeper that controls the mitosis versus meiosis decision in male germ cells. *Dev Cell* **19:** 612–624.

Matson CK, Murphy MW, Sarver AL, Griswold MD, Bardwell VJ, Zarkower D. 2011. DMRT1 prevents female reprogramming in the postnatal mammalian testis. *Nature* **476:** 101–104.

Matsui Y, Zsebo K, Hogan BLM. 1992. Derivation of pluripotential embryonic stem cells from murine primordial germ cells in culture. *Cell* **70:** 841–847.

Morimoto H, Lee J, Tanaka T, Ishii K, Toyokuni S, Kanatsu-Shinohara M, Shinohara T. 2012. In vitro transformation of mouse testis cells by oncogene transfection. *Biol Reprod* **86:** 1–11.

Murphy MW, Sarver AL, Rice D, Hatzi K, Ye K, Melnick A, Heckert LL, Zarkower D, Bardwell VJ. 2010. Genome-wide analysis of DNA binding and transcriptional regulation by the mammalian Doublesex homolog DMRT1 in the juvenile testis. *Proc Natl Acad Sci* **107:** 13360–13365.

Niwa H, Miyazaki J-I, Smith AG. 2000. Quantitative expression of Oct-3/4 defines differentiation, dedifferentiation or self-renewal of ES cells. *Nat Genet* **24:** 372–376.

Okita K, Ichisaka T, Yamanaka S. 2007. Generation of germline-competent induced pluripotent stem cells. *Nature* **448:** 313–317.

Raymond CS, Murphy MW, O'Sullivan MG, Bardwell VJ, Zarkower D. 2000. Dmrt1, a gene related to worm and fly sexual regulators, is required for mammalian testis differentiation. *Genes Dev* **14:** 2587–2595.

Resnick JL, Bixler LS, Cheng L, Donovan PJ. 1992. Long-term proliferation of mouse primordial germ cells in culture. *Nature* **359:** 550–551.

Seandel M, James D, Shmelkov SV, Falciatori I, Kim J, Chavala S, Scherr DS, Zhang F, Torres R, Gale NW, et al. 2007. Generation of functional mutipotent adult stem cells from GPR125^{+} germline progenitors. *Nature* **449:** 346–350.

Stevens LC. 1984. Spontaneous and experimentally induced testicular teratomas in mice. *Cell Differ* **15:** 69–74.

Takashima S, Takehashi M, Lee J, Chuma S, Okano M, Hata K, Suetake I, Nakatsuji N, Miyoshi H, Tajima S, et al. 2009. Abnormal DNA methyltransferase expression in mouse germline stem cells results in spermatogenic defects. *Biol Reprod* **81:** 155–164.

Tapia N, Araúzo-Bravo MJ, Ko K, Schöler HR. 2011. Concise review: Challenging the pluripotency of human testis-derived ESC-like cells. *Stem Cells* **29:** 1165–1169.

Tsumura A, Hayakawa T, Kumaki Y, Takebayashi S, Sakaue M, Matsuoka C, Shimotohno K, Ishikawa F, Li E, Ueda HR, et al. 2006. Maintenance of self-renewal ability of mouse embryonic stem cells in the absence of DNA methyltransferases Dnmt1, Dnmt3a and Dnmt3b. *Genes Cells* **11:** 805–814.

van den Berg DL, Snoek T, Mullin NP, Yates A, Bezstarosti K, Demmers J, Chambers I, Poot RA. 2010. An Oct4-centered protein interaction network in embryonic stem cells. *Cell Stem Cell* **6:** 369–381.

Wu X, Oatley JM, Oatley MJ, Kaucher AV, Avarbock MR, Brinster RL. 2010. The POU domain transcription factor POU3F1 is an important intrinsic regulator of GDNF-induced survival and self-renewal of mouse spermatogonial stem cells. *Biol Reprod* **82:** 1103–1111.

Ying QL, Smith AG. 2003. Defined conditions for neural commitment and differentiation. *Methods Enzymol* **365:** 327–341.

Yoshida S. 2010. Stem cells in mammalian spermatogenesis. *Dev Growth Differ* **52:** 311–317.

Zhu R, Bhattacharya C, Matin A. 2007. The role of dead-end in germ-cell tumor development. *Ann N Y Acad Sci* **1120:** 181–186.
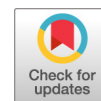
138

American Society for Microbiology

Molecular and Cellular Biology®

PARI Regulates Stalled Replication Fork Processing To Maintain Genome Stability upon Replication Stress in Mice

Ayako L. Mochizuki,[a] Ami Katanaya,[a] Eri Hayashi,[a] Mihoko Hosokawa,[a]
Emiko Moribe,[a] Akira Motegi,[b] Masamichi Ishiai,[c] Minoru Takata,[c] Gen Kondoh,[a]
Hitomi Watanabe,[a] Norio Nakatsuji,[a,d] Shinichiro Chuma[a]

Institute for Frontier Life and Medical Sciences, Kyoto University, Kyoto, Japan[a]; Department of Radiation Genetics, Kyoto University Graduate School of Medicine, Kyoto, Japan[b]; Laboratory of DNA Damage Signaling, Radiation Biology Center, Kyoto University, Kyoto, Japan[c]; iCeMS, Kyoto University, Kyoto, Japan[d]

ABSTRACT DNA replication is frequently perturbed by intrinsic, as well as extrinsic, genotoxic stress. At damaged forks, DNA replication and repair activities require proper coordination to maintain genome integrity. We show here that PARI antirecombinase plays an essential role in modulating the initial response to replication stress in mice. PARI is functionally dormant at replisomes during normal replication, but upon replication stress, it enhances nascent-strand shortening that is regulated by RAD51 and MRE11. PARI then promotes double-strand break induction, followed by new origin firing instead of replication restart. Such PARI function is apparently obstructive to replication but is nonetheless physiologically required for chromosome stability *in vivo* and *ex vivo*. Of note, *Pari*-deficient embryonic stem cells exhibit spontaneous chromosome instability, which is attenuated by differentiation induction, suggesting that pluripotent stem cells have a preferential requirement for PARI that acts against endogenous replication stress. PARI is a latent modulator of stalled fork processing, which is required for stable genome inheritance under both endogenous and exogenous replication stress in mice.

KEYWORDS genome stability, homologous recombination, replication stress, embryonic stem cells

DNA replication is vulnerable to hampering by various environmental agents, as well as intrinsic cellular conditions. Impaired replication forks, if not properly processed, result in genetic instability, including DNA mutations and structural and numerical chromosome aberrations, which are detrimental to normal cellular proliferation and differentiation (1, 2). Particularly sensitive to replication perturbation are highly proliferative cells, e.g., early embryonic cells, which exhibit rapid DNA replication and cell division with a short gap (G_1) phase and ineffective DNA damage checkpoints (3). Such a truncated cell cycle in early embryos is evolutionarily conserved and supposedly developmentally programmed to promptly achieve sufficient cell numbers for early embryonic morphogenesis (4, 5) but is at the same time intrinsically associated with genome instability due to high replication stress. After embryonic cell proliferation, postnatal stem cell lineages continue to self-renew and produce differentiated progeny and thus are also inherently vulnerable to replication perturbation during their lifelong proliferation (6). Such replication-associated genome instability poses potential risks of cellular transformation or cell death, which in multicellular organisms is linked to cancer predisposition, premature aging, developmental disorders, etc. (7).

To protect cells and organisms from these detrimental consequences, DNA repair mechanisms, together with cell cycle checkpoints, act to sense and restore impaired replication fork structures (8). Upon replication stalling, cell cycle checkpoint mecha-

nisms stabilize replisomes to later resume DNA synthesis (9) and several different pathways, including replication restart by fork regression, translesion synthesis, and repriming, act to restore DNA replication at and around stalled forks (10). After prolonged replication stalling, however, replisomes collapse, followed by new origin firing (NOF) and DNA double-strand break (DSB) induction, which subsequently are repaired by homology-dependent repair or nonhomologous end-joining pathways (11). How these distinct replication recovery pathways are properly integrated at damaged forks is under active investigation.

Central to the replication fork recovery mechanisms is homology-dependent repair. At stalled replication forks, RAD51 recombinase is recruited to extended single-stranded DNA (ssDNA) stretches, where RAD51 either promotes DNA strand annealing and homologous recombination (recombinogenic function) (12) or protects newly synthesized DNA strands from exonucleolytic resection by MRE11 (non- or prerecombinogenic function) (13). RAD51 activity is intricately controlled by pro- and antirecombination factors, such as *RAD52* epistasis group genes and *RecQ* family genes, respectively, whose functions have been well studied with regard to general DSB repair (14, 15). In contrast, much less is understood about how recombination activity is regulated at damaged replication forks in proper coordination with replication machineries (16). For instance, it is still largely unclear what specific factors and mechanisms act at damaged forks to modulate recombinogenic or nonrecombinogenic activities and how such specific regulation, if any, influences the replication fidelity and genome stability of cells. Also, the question of whether developmental-stage-specific and/or cellular-context-dependent control of replication stress response operates in multicellular organisms for proper coordination of cell proliferation, differentiation, and homeostasis remains mostly unaddressed.

Pari (also known as *Parpbp*) is one of the most recently identified antirecombinase genes, which is related to the *Saccharomyces cerevisiae* Srs2 and bacterial UvrD genes (17). Almost all other antirecombinases, such as RecQ family members (BLM, WRN, and RECQL in mammals) (15) and Srs2/UvrD-related family members (RTEL1 and FBH1 in mammals) (18, 19), are functional helicases, but PARI lacks a full repertoire of helicase motifs, discriminating it from other antirecombinase helicases. Previous studies have shown that PARI associates with PCNA, a sliding clamp for DNA polymerases (20), and it dissociates RAD51-ssDNA and PCNA-DNA polymerase δ interactions *in vitro* (17, 21). However, it remained to be determined how PARI actually controls DNA replication during normal, as well as damaged, fork processing. It is also unknown whether PARI has any physiological function in multicellular organisms.

In this study, we generated a *Pari* gene-targeted mouse line and show that *Pari* deficiency does not lead to immediate lethality, but upon replication stress, genome instability became evident *in vivo* and *ex vivo*. Specifically, PARI functions to reduce nascent DNA strand lengths at stalled forks and promotes DSB induction followed by NOF instead of replication restart. Such PARI function to enhance replication fork breakdown appears to be deleterious to stable replication recovery, but it is necessary for chromosome stability of proliferative cells, including somatic and germ line cells, upon replication stress in mice. Further, PARI acts to maintain the genetic stability of embryonic stem (ES) cells, but not their differentiated progeny, in the absence of exogenous replication stress, suggesting that pluripotent stem cells derived from early embryos have a developmental requirement for PARI-mediated control against endogenous replication stress to maintain their genome integrity.

RESULTS

PARI domain architecture and tissue expression in mice. We carried out *in silico* screening of the mouse genome to identify putative homologues of DNA repair pathway genes in yeast and bacteria, focusing on preferential tissue expression in pluripotent stem cells and germ cells. With this criterion, *4930547N16Rik* (Riken FANTOM database [22]) was shown to exhibit sequence similarity to *uvrD* in *Escherichia coli* and *SRS2* in yeast.
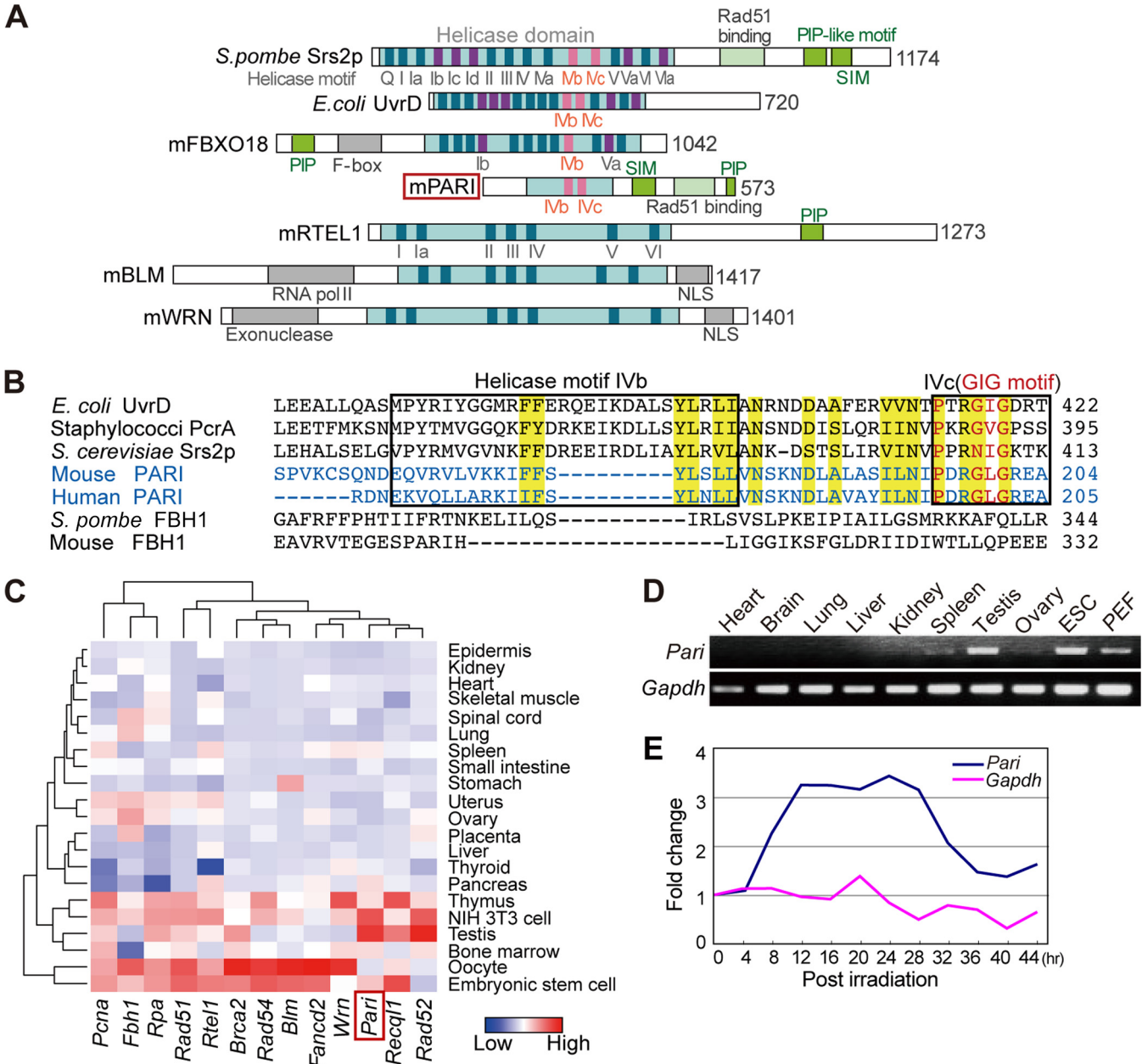
FIG 1 PARI domain architecture and tissue expression in mice. (A) Protein domain architectures of PARI, Srs2, UvrD, and other selected antirecombinase helicases. Light-blue boxes, helicase domains; dark-blue boxes, highly conserved motifs common to helicase superfamilies 1 and 2; purple and pink boxes, helicase motifs uniquely found in Srs2/UvrD family members. (B) Amino acid sequence alignment of helicase motifs IVb and IVc (boxed) of mouse and human PARI and other selected Srs2/UvrD family members. The conserved GIG motif (red) is in motif IVc. Highly conserved amino acids in the Srs2-related family are highlighted in yellow. (C) Heat map representation of the mRNA expression levels of *Pari* and other selected recombination and replication genes in representative tissues and cells in mice. The data were extracted from a published microarray data set (GEO accession no. GSE1133). (D) RT-PCR analysis of *Pari* expression in selected tissues of adult mice, embryonic stem cells (ESC), and PEF. *Gapdh* was used as a control. (E) Quantitative RT-PCR analysis for *Pari* and *Gapdh* expression in X-ray-irradiated (20 Gy) ES cells. The data were normalized to gene expression values of control ES cells without irradiation, and fold changes of *Pari* and *Gapdh* expression are shown as means from triplicate PCRs.

4930547N16Rik was then found to be the orthologue of human *PARI* (*PARPBP*) during our analysis of the mouse gene in this study (17, 21, 23, 24).

Mouse PARI exhibited partial homology to helicase superfamily 1 and 2 proteins but lacked most of the conserved functional helicase motifs (Fig. 1A), suggesting that it does not possess an actual helicase activity, as was reported for human PARI. The sequence similarity of mouse PARI with other UvrD/Srs2 family members was observed in the IVb and IVc helicase motifs (25), including a PXXGXG sequence (the "GIG" motif,

FIG 2 Generation of *Pari* gene-targeted mice. (A) *Pari* gene-targeting construct. Exons are shown as boxes, and *loxP* sites are shown as arrowheads. S, ScaI; B, BstXI; P, PflFI. (B) Southern blot of genomic DNA from *Pari*$^{+/+}$, *Pari*$^{+/-}$, and *Pari*$^{-/-}$ mice digested with BstXI. The probe position is indicated in panel A. (C) RT-PCR analysis of *Pari* expression in *Pari*$^{+/+}$ and *Pari*$^{-/-}$ adult testes. *Gapdh* was used as a control. (D) The number of live births of each genotype obtained by crossing *Par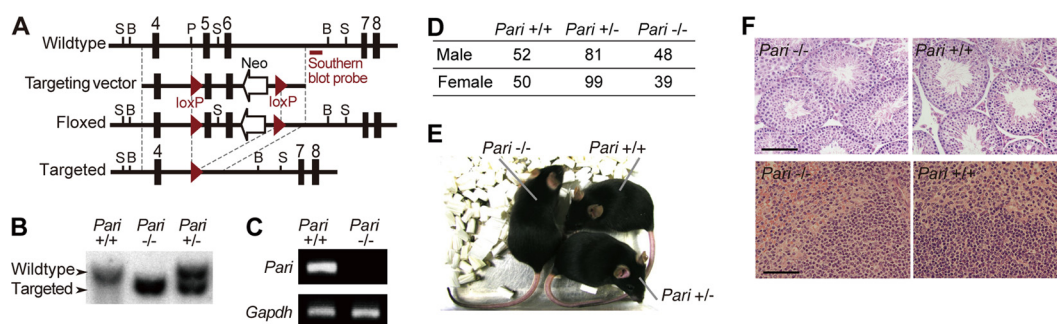i*$^{+/-}$ mice (44 females × 19 males; 72 litters). (E) Gross appearance of *Pari*$^{+/+}$, *Pari*$^{+/-}$, and *Pari*$^{-/-}$ sibling mice. (F) HE-stained sections of testes (top) and spleens (bottom) of *Pari*$^{+/+}$ and *Pari*$^{-/-}$ mice. Scale bars, 100 μm.

which binds DNA) (Fig. 1B). Mouse PARI also possesses a PCNA interaction peptide (PIP) box, a SUMO interaction motif (SIM), and a putative RAD51 binding domain, all of which are conserved in yeast Srs2 and human PARI (Fig. 1A) (17).

The expression of *Pari* mRNA was detected in various tissues at basal levels in expressed sequence tag (EST) (NCBI Unigene Mm.179378) and microarray (NCBI GEO GSE1133 [26]) (Fig. 1C) data sets but was preferentially abundant in the testis, which contains highly proliferative cells. By reverse transcription (RT)-PCR, *Pari* mRNA was abundant in ES cells and to a lesser extent in embryonic fibroblasts, in addition to testis and spleen, among the tissues we examined (Fig. 1D). *Pari* expression was also regulated by DNA damage, as exemplified by its increased expression following ionizing radiation of ES cells (Fig. 1E). Radiation-induced *Pari* upregulation was also seen in a public transcriptome sequencing (RNA-seq) data set (PRJNA268981 [27]) of irradiated microglial cells in C56BL/6 mice (transcript per million values [$n = 2$]: control, 0.067 and 0.076; irradiated, 0.14 and 0.22; mean fold change, 2.5). These tissue and cell expression profiles and DNA damage-induced upregulation suggested a role of *Pari* in proliferative cells and DNA damage response in mice.

Pari deficiency causes preferential sensitivity to replication stress. We generated a *Pari* gene-targeted mouse line with deletion of exons 5 and 6, which encode the conserved IVb and IVc motifs (Fig. 2A to C). *Pari*$^{-/-}$ mice were obtained in the expected Mendelian ratio and were viable and fertile (Fig. 2D and E). Under standard housing conditions, no gross pathological changes were discernible in *Pari*$^{-/-}$ mouse tissues, including testis and spleen, which expressed high levels of *Pari* mRNA in wild-type mice. (Fig. 2F).

We then examined the DNA damage response in *Pari*-deficient cells. *Pari*$^{-/-}$ ES cells and primary embryonic fibroblasts (PEF), expanded under standard culture conditions, exhibited normal cell proliferation and cell cycle profiles compared to wild-type cells (Fig. 3A to C). However, when exogenous genotoxic agents were applied, *Pari*$^{-/-}$ ES cells and PEF both exhibited increased cellular sensitivity to hydroxyurea (HU), a replication inhibitor that depletes deoxynucleoside triphosphate (dNTP) pools, and to mitomycin C (MMC), a cross-linking agent that disturbs replication and transcription (Fig. 3D, F, I, and K). In contrast, weak or no significant responses were observed with etoposide, a topoisomerase II inhibitor, and gamma ray irradiation (Fig. 3G, H, L, and M). These results indicated that *Pari* deficiency provokes a preferential sensitivity to replication stress rather than general DNA damage. Of note, *Pari* deficiency conferred transient cellular resistance to short-term treatment with the replication inhibitor HU (Fig. 3E and J), whereas prolonged exposure resulted in increased sensitivity compared with wild-type cells (Fig. 3F and K). These results suggested that *Pari* deficiency temporarily suppresses cell cycle arrest or apoptosis, which are usually provoked by cell cycle checkpoints triggered by DSBs or ssDNA gaps in the short term, whereas
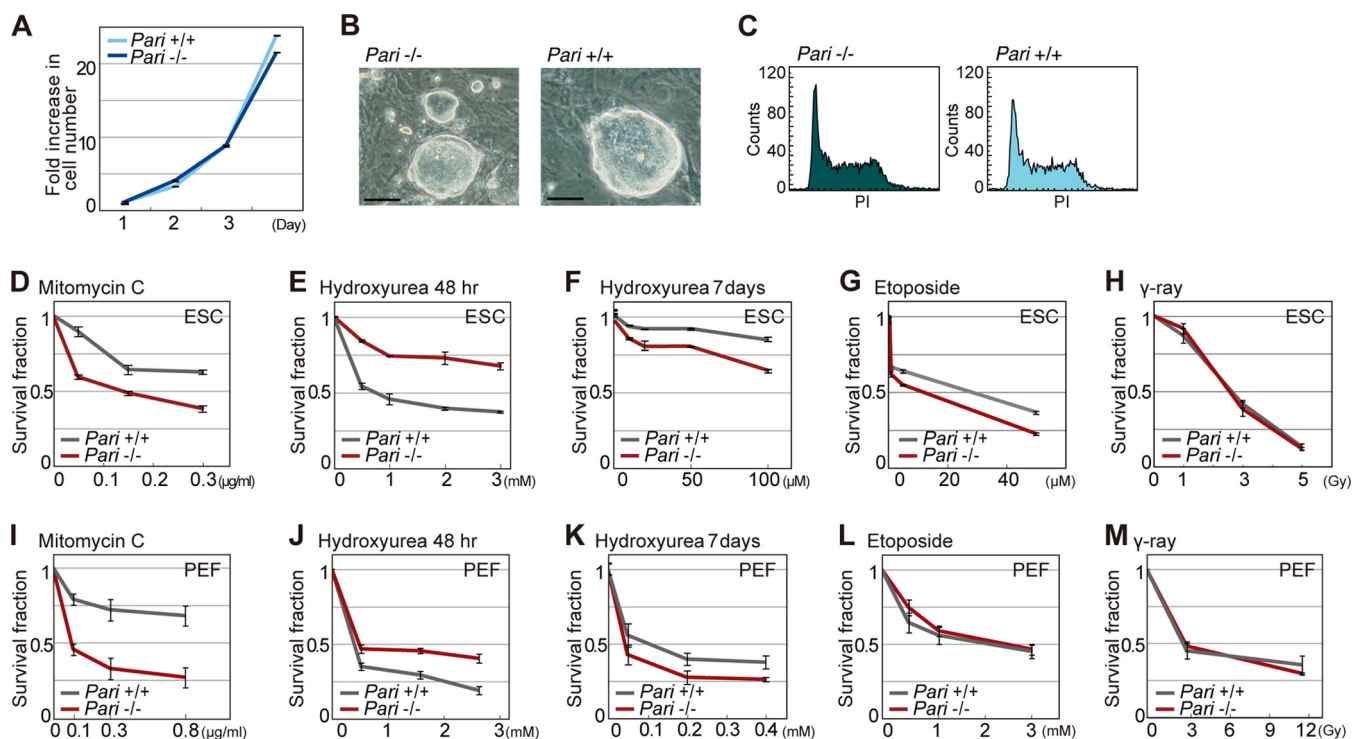
FIG 3 Genotoxic sensitivity of *Pari*-deficient cells. (A) Growth curve of *Pari*$^{+/+}$ and *Pari*$^{-/-}$ ES cells under standard culture conditions. (B) ES cell colonies established from *Pari*$^{+/+}$ and *Pari*$^{-/-}$ sibling blastocysts. Scale bars, 50 μm. (C) fluorescence-activated cell sorter (FACS) analysis of cell cycle profiles (DNA content stained with propidium iodide [PI]) of *Pari*$^{+/+}$ and *Pari*$^{-/-}$ ES cells under standard culture conditions. (D to H) Cellular sensitivity of *Pari*$^{+/+}$ and *Pari*$^{-/-}$ ES cells to mitomycin C (D), hydroxyurea (E and F), etoposide (G), and gamma rays (H). Treatment times were 24 h (D, G, and H), 48 h (E), and 7 days (F). Means $\pm$ standard errors (SE) from three independent cultures are shown. (I to M) Cellular sensitivity of *Pari*$^{+/+}$ and *Pari*$^{-/-}$ PEF to mitomycin C (I), hydroxyurea (J and K), etoposide (L), and gamma rays (M). Treatment times were 24 h (I, L, and M), 48 h (J), and 7 days (K). Means $\pm$ SE from three independent cultures are shown.

prolonged replication stress impairs cell proliferation or survival, possibly due to accumulated genome damage in the long term.

PARI localization at replisomes and recruitment to DNA damage sites. PARI interacts with PCNA, a component of replisomes, via its PIP box (17). In order to examine the subcellular localization of PARI under normal and replication stress conditions, we transiently expressed FLAG- and 6$\times$His-tagged PARI in human 293T and mouse 3T3 cells (Fig. 4A). Both PARI constructs expressed in the two cell lines exhibited similar discrete nuclear foci, which were reminiscent of replication complexes in the S phase. These PARI foci overlapped almost completely with those of PCNA throughout the S phase (Fig. 4B) and colocalized with pulse-labeled bromodeoxyuridine (BrdU) signals (Fig. 4C), demonstrating that PARI resides at ongoing replication forks. The association of PARI with nascent replication forks was further corroborated by an iPOND (isolation of proteins on nascent DNA) analysis (28, 29) of 293T cells expressing FLAG-tagged PARI (Fig. 4D). Of note, PARI localization at replisomes (i.e., colocalization with PCNA nuclear foci) did not change in the presence of MMC (Fig. 4E), indicating that PARI stably associates with replisomes irrespective of replication stress. As expected, PARI localization at replisomes depends on the PIP box (Fig. 4F).

We then conducted a laser microirradiation experiment using green fluorescent protein (GFP)-tagged human PARI in U2OS cells. In the S phase, when GFP-tagged PARI exhibited nuclear foci corresponding to replisomes, laser microirradiation did not apparently alter the localization pattern of PARI (Fig. 4G, left). In contrast, in the G_1/G_2 phases, when PARI was mostly diffusely distributed under unstressed conditions, rapid accumulation of PARI at laser-induced DNA damage sites was observed within a few seconds (Fig. 4G, right). This laser-induced relocalization of PARI is likely attributable to the PIP-mediated PARI-PCNA association, considering that PCNA is recruited to DNA
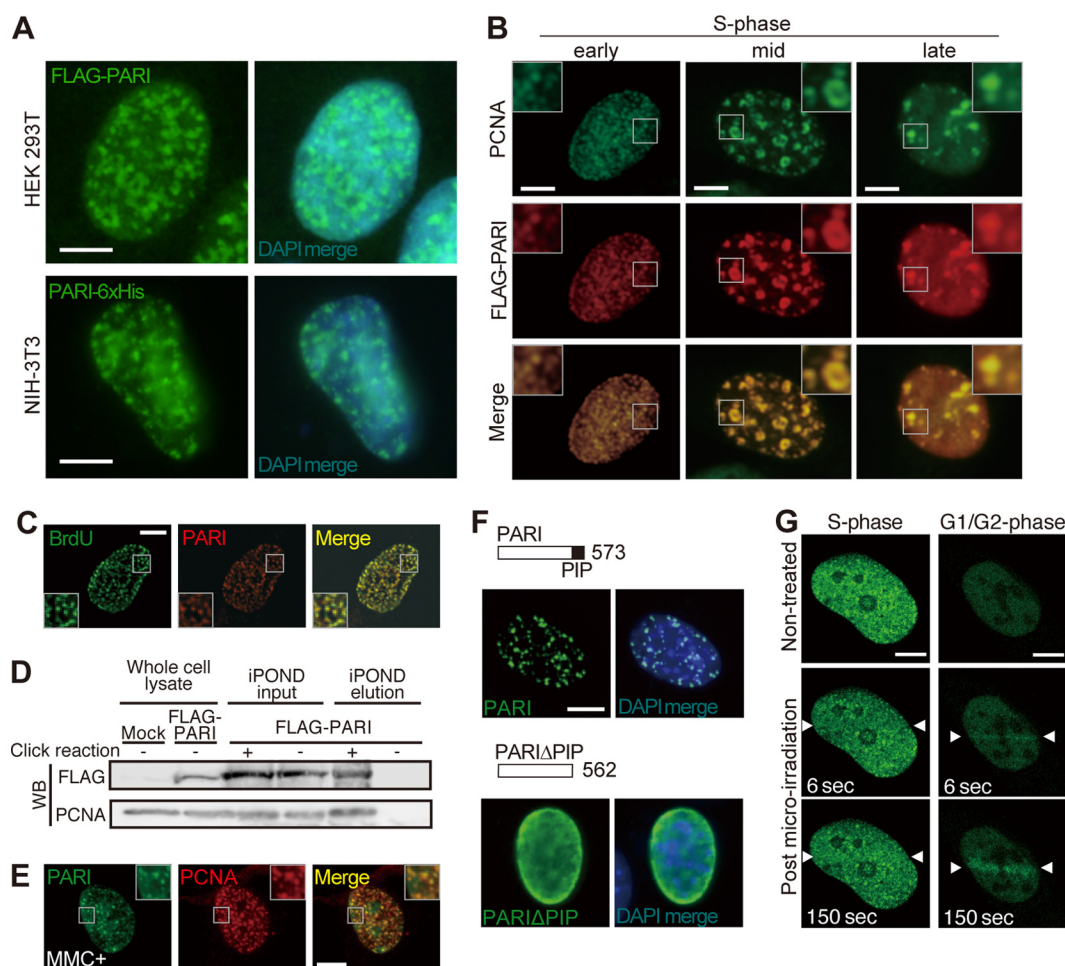
FIG 4 PARI localization at replication forks and DNA damage sites. (A) HEK 293T (top) and NIH 3T3 (bottom) cells transiently transfected with pCAG-FLAG-PARI and pCAG-PARI-6×His plasmids were immunostained with anti-FLAG and anti-6×His antibodies, respectively. DAPI was used to visualize the nuclei. Scale bars, 5 μm. (B) NIH 3T3 cells transiently transfected with pCAG-FLAG-PARI immunostained for FLAG (red) and PCNA (green). Representative images of early, mid-, and late S phase cells are presented. The insets show higher-magnification views of the boxed regions. Scale bars, 5 μm. (C) NIH 3T3 cells transiently transfected with pCAG-FLAG-PARI and pulse-labeled with BrdU were stained with anti-FLAG (red) and anti-BrdU (green) antibodies. (D) iPOND analysis of 293T cells transfected with pCAG-FLAG-PARI and pulse-labeled with EdU. Nascent replication forks were captured by the click reaction, and FLAG-PARI and PCNA were detected by Western blotting (WB). The input lanes represent 2.4% of the cell lysates used for the iPOND elution. (E) NIH 3T3 cells transiently transfected with pCAG-FLAG-PARI were treated with MMC for 24 h and immunostained for FLAG (green) and PCNA (red). (F) NIH 3T3 cells transiently transfected with plasmids that express FLAG-tagged full-length PARI (top) or PIP box deletion mutant PARIΔPIP (bottom) constructs were stained with anti-FLAG antibody (green). Nuclei were counterstained with DAPI (blue). (G) U2OS cells transfected with a plasmid that expresses GFP-human PARI were laser irradiated (between arrowheads) during S phase (left) or G1/G2 phase (right), and live-cell imaging was carried out. Representative images at the indicated time points are shown. Scale bars, 5 μm.

damage sites outside the S phase (30). The reasons why PARI localization to laser-irradiated sites was not discernible in S phase cells may include the following: (i) PARI forms bright, discrete foci at replisomes, which might have masked the detection of PARI at laser-irradiated sites (31) or (ii) PCNA is not stably localized at DNA damage sites in S phase cells (30) and, accordingly, does not efficiently recruit PARI. Together, these results suggested that PARI, which primarily acts at replisomes, may also play a role outside the S phase at DNA damage sites.

PARI promotes stalled fork processing and modulates replication repair pathway choice. We next employed the DNA fiber assay to focus on a possible molecular function of PARI at replication forks. $Pari^{-/-}$ and wild-type ES cells were pulse-labeled with nucleoside analogues, iododeoxyuridine (IdU) and/or chlorodeoxyuridine (CldU), and then DNA fiber spreads were immunostained for these nucleoside analogues to measure replication tracts. In our preliminary experiments, ES cells exhibited similar

rates of replication in the presence of both low and high (20 μM and 200 μM) concentrations of the nucleoside analogues (Fig. 5A). Therefore, these two concentrations were used for DNA fiber analyses (20 μM for the first label and 200 μM for the second label) in this study.

Under standard culture conditions, $Pari^{-/-}$ and wild-type ES cells exhibited similar rates of replication fork progression (Fig. 5B, IdU), indicating that normal replication kinetics is not disturbed by $Pari$ deficiency. In contrast, in the presence of replication stress (HU), $Pari^{-/-}$ ES cells showed substantially longer replication tracts than wild-type controls (Fig. 5C, CldU). Similarly, replication tract lengths that were pulse-labeled before HU treatment were longer in $Pari^{-/-}$ ES cells than in wild-type cells (Fig. 5D). These observations indicated that PARI reduces nascent-strand lengths following replication stress, possibly through (i) the enhancement of nascent-strand degradation or (ii) the suppression of replication fork progression in response to replication stress. In addition to ES cells, we examined replication fork kinetics of $Pari^{-/-}$ and wild-type PEF and observed that nascent-strand lengths were again more stable in $Pari^{-/-}$ PEF than in wild-type controls in the presence of HU (Fig. 5E). Of note, wild-type ES cells and PEF were different in that it took longer for PEF to exhibit a significant difference in nascent-strand shortening (12 to 24 h) than ES cells (1 to 5 h) under replication stress (Fig. 5D and E and 6C). One explanation for this is that the kinetics of replication stress response is different between ES cells and PEF, which have distinct proliferative capacities and cell cycle structures.

We then carried out add back experiments in $Pari^{-/-}$ ES cells with full-length PARI (wtPARI), PARI lacking the PIP box (PARIΔPIP), and PARI lacking the UvrD homology domain (PARIΔUvrD) (Fig. 5F). Under standard culture conditions, the expression of these three constructs in $Pari^{-/-}$ ES cells did not affect replication tract lengths (Fig. 5F, top). In the presence of HU, on the other hand, wtPARI expression in $Pari^{-/-}$ ES cells restored nascent-strand shortening, indicating that the knockout phenotype was rescued (Fig. 5F, bottom). In contrast, PARIΔUvrD failed to restore the mutant phenotype of $Pari^{-/-}$ ES cells, whereas PARIΔPIP exhibited intermediate phenotype recovery (Fig. 5F, bottom), suggesting that the UvrD homology domain is necessary and the PIP box is partially required for PARI function to regulate nascent-strand shortening in response to replication stress. A plausible explanation for the intermediate phenotype of PARIΔPIP could be that PARI lacking the PIP box still binds and inhibits RAD51 (and possibly other targets) that acts to protect nascent strands (see below).

The activity of PARI, which is functionally latent at replisomes during normal replication but acts to reduce nascent-strand lengths at stalled forks, is distinct from previously reported functions of most other antirecombinases that also localize at replisomes, such as RTEL1. By RNA interference (RNAi) knockdown of $Rtel1$ in ES cells, replication fork speed was slowed down under unperturbed culture conditions, as previously reported (Fig. 5G) (32), but nascent-strand lengths were not further diminished in the presence of HU (Fig. 5H). Thus, PARI and RTEL1, both belonging to the Srs2-related family (17, 18), play distinct roles in normal replication fork progression and stalled fork processing.

Previous studies have shown that nascent DNA strands are resected by MRE11 nuclease following replication fork stalling (33). The degradation of newly synthesized DNA by MRE11 is alleviated by the recombination-independent function of RAD51, which covers ssDNA gaps at stalled forks (34). To see whether PARI operates in the RAD51-MRE11 pathway, we carried out DNA fiber experiments in combination with chemical inhibitors of MRE11 and RAD51, mirin (35) and B02 (36), respectively (Fig. 5I). Mirin inhibits MRE11 by binding close to the exonuclease active site, and B02 associates with RAD51 to suppress RAD51-ssDNA nucleofilament formation. Both mirin and B02 did not interfere with normal replication tracts without HU in both $Pari^{-/-}$ and $Pari^{+/+}$ ES cells (Fig. 5I, panels a and b).

In wild-type ES cells, nascent-strand resection by HU was attenuated by MRE11 inhibition by mirin and enhanced by RAD51 inhibition by B02, in accord with previous reports (Fig. 5I, panels c to e) (34, 37). When both MRE11 and RAD51 were inhibited in
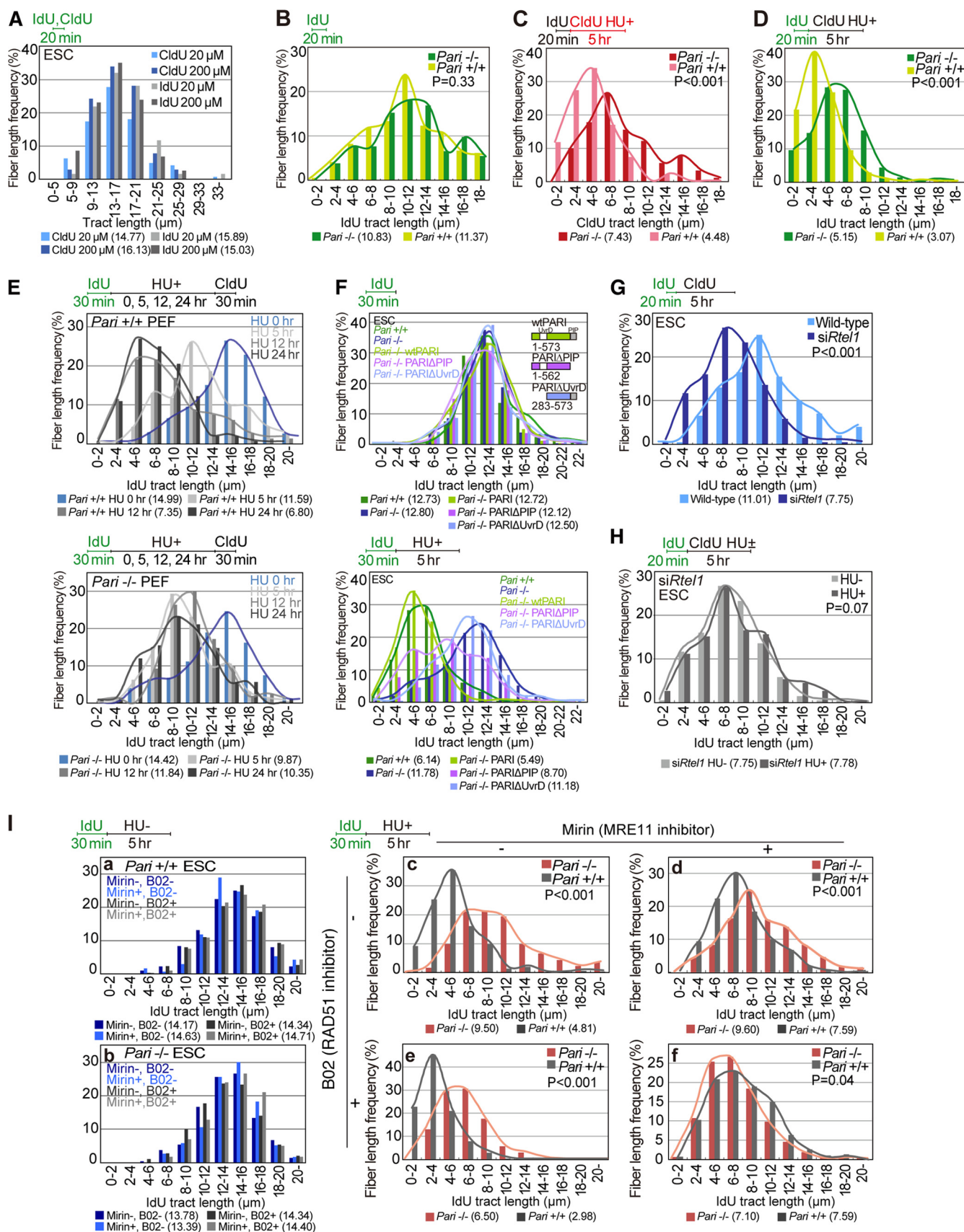
FIG 5 PARI promotes nascent-strand processing in response to replication stress. (A) DNA fiber analyses of wild-type ES cells pulse-labeled with a low (20 μM) or high (200 μM) concentration of nucleoside analogues (IdU or CldU) for 20 min under normal culture conditions. Median tract lengths are given in

(Continued on next page)

wild-type ES cells by simultaneous treatment with mirin and B02, nascent-strand shortening by HU was suppressed and was similar to that of MRE11 inhibition (mirin) alone, suggesting that MRE11 acts downstream of RAD51 (Fig. 5I, panel f) (13, 34).

In contrast to wild-type ES cells, nascent-strand shortening in $Pari^{-/-}$ ES cells in the presence of HU was not significantly altered by MRE11 inhibition (mirin), and $Pari^{-/-}$ and $Pari^{+/+}$ ES cells treated with mirin exhibited similar degrees of nascent-strand shortening upon HU treatment (Fig. 5I, panels c and d), indicating that MRE11 and PARI function in the same or overlapping pathways. RAD51 suppression by B02, on the other hand, enhanced nascent-strand shortening by HU in both $Pari^{-/-}$ and $Pari^{+/+}$ ES cells (Fig. 5I, panel e). This was in accord with previous observations that RAD51 protects nascent DNA strands (13, 34) and that PARI counteracts RAD51 (17). Together, these results indicated that PARI regulates nascent-strand processing in the same pathway as MRE11 and RAD51 and were in accord with the presumed functional relationship wherein PARI suppresses RAD51, which inhibits MRE11 that executes nascent-strand degradation upon replication stress.

We then examined whether PARI affects the pathway choice of replication repair after release from replication stress. To this end, we followed the fate of stalled replication forks after HU treatment by using another DNA fiber assay that distinguishes between (i) NOF (CldU only), (ii) stalled forks without replication restart (IdU only), and (iii) replication restart from stalled forks (IdU plus CldU) (Fig. 6A). Following a short-term treatment of ES cells with HU (1 h), stalled replication forks resumed DNA synthesis with similar efficiencies (>85%) in $Pari^{-/-}$ and wild-type ES cells. In contrast, after prolonged HU exposure (3 and 5 h), $Pari^{-/-}$ and wild-type ES cells exhibited distinct responses. In wild-type cells, the efficiency of fork restart was substantially decreased (<20%), and instead, the frequency of NOF increased (>50%). In contrast, $Pari^{-/-}$ cells retained higher efficiencies of replication restart from stalled/collapsed forks (>70% and >45% after 3 and 5 h of HU treatment, respectively) than wild-type cells, while NOF frequencies remained low (Fig. 6A).

If PARI regulates the replication repair pathway choice between fork restart and NOF following replication stress, then the interorigin distances (IOD) should be different between $Pari^{-/-}$ and wild-type cells. Indeed, although IOD of $Pari^{-/-}$ and wild-type ES cells were similar under normal culture conditions (average, around 30 μm), replication stress (HU) induced a greater decrease in IOD of wild-type ES cells (41% reduction compared to the HU^- condition) than in those of $Pari^{-/-}$ ES cells (12% reduction compared to the HU^- condition) (Fig. 6B). Therefore, PARI regulates the pathway choice of replication recovery, i.e., it increases NOF rather than replication restart following replication perturbation. This function of PARI again is distinct from the previously reported roles of most other antirecombinases, such as BLM, which promotes replication restart from stalled forks (38). We then examined whether PARI modulates nascent-strand lengths after release from replication stress. However, replication tract lengths were similar in $Pari^{-/-}$ and wild-type ES cells after the removal of HU (Fig. 6D), suggesting that PARI does not play a significant role in nascent-strand processing following replication restart, unlike BLM (34), etc.

***Pari* deficiency leads to chromosome instability in response to replication stress *in vivo* and *ex vivo*.** In wild-type cells, prolonged replication stalling provokes

FIG 5 Legend (Continued)
parentheses below each DNA fiber graph. (B) DNA fiber analyses of replication fork progression in $Pari^{+/+}$ and $Pari^{-/-}$ ES cells pulse-labeled with IdU (20 min) under normal culture conditions. IdU tract lengths ($n > 250$) are shown with P values obtained from the Mann-Whitney U test. (C and D) DNA fiber analyses of $Pari^{+/+}$ and $Pari^{-/-}$ ES cells pulse-labeled with IdU (20 min), followed by CldU labeling in the presence of HU (5 h). CldU (C) and IdU (D) tract lengths ($n > 250$) are shown. (E) DNA fiber analyses of $Pari^{+/+}$ and $Pari^{-/-}$ PEF pulse-labeled with IdU (30 min) and treated with HU for 5, 12, and 24 h or without HU treatment (0 h), followed by CldU postlabeling (30 min). IdU tract lengths ($n > 300$) are shown. (F) DNA fiber analyses of ES cells transiently transfected with plasmids that express FLAG-tagged full-length PARI (wtPARI), a PIP box deletion mutant (PARIΔPIP), or a UvrD homology domain deletion mutant (PARIΔUvrD). The cells were pulse-labeled with IdU (30 min) under normal culture conditions and treated with HU for 5 h (bottom) or without HU (top). IdU tract lengths ($n > 300$) are shown. (G) DNA fiber analyses of wild-type and $Rtel1$ knockdown ES cells pulse-labeled with IdU (20 min), followed by CldU labeling (5 h) under normal culture conditions. IdU tract lengths ($n > 300$) are shown. (H) DNA fiber analysis of $Rtel1$ knockdown ES cells pulse-labeled with IdU (20 min) under normal culture conditions, followed by CldU labeling in the presence or absence of HU (5 h). IdU tract lengths ($n > 300$) are shown. (I) Nascent-strand lengths of $Pari^{+/+}$ and $Pari^{-/-}$ ES cells in the presence or absence of MRE11 inhibitor (30 μM mirin) and/or RAD51 inhibitor (50 μM B02) with (c to f) or without (a and b) HU for 5 h. IdU tract lengths ($n > 300$) are shown.
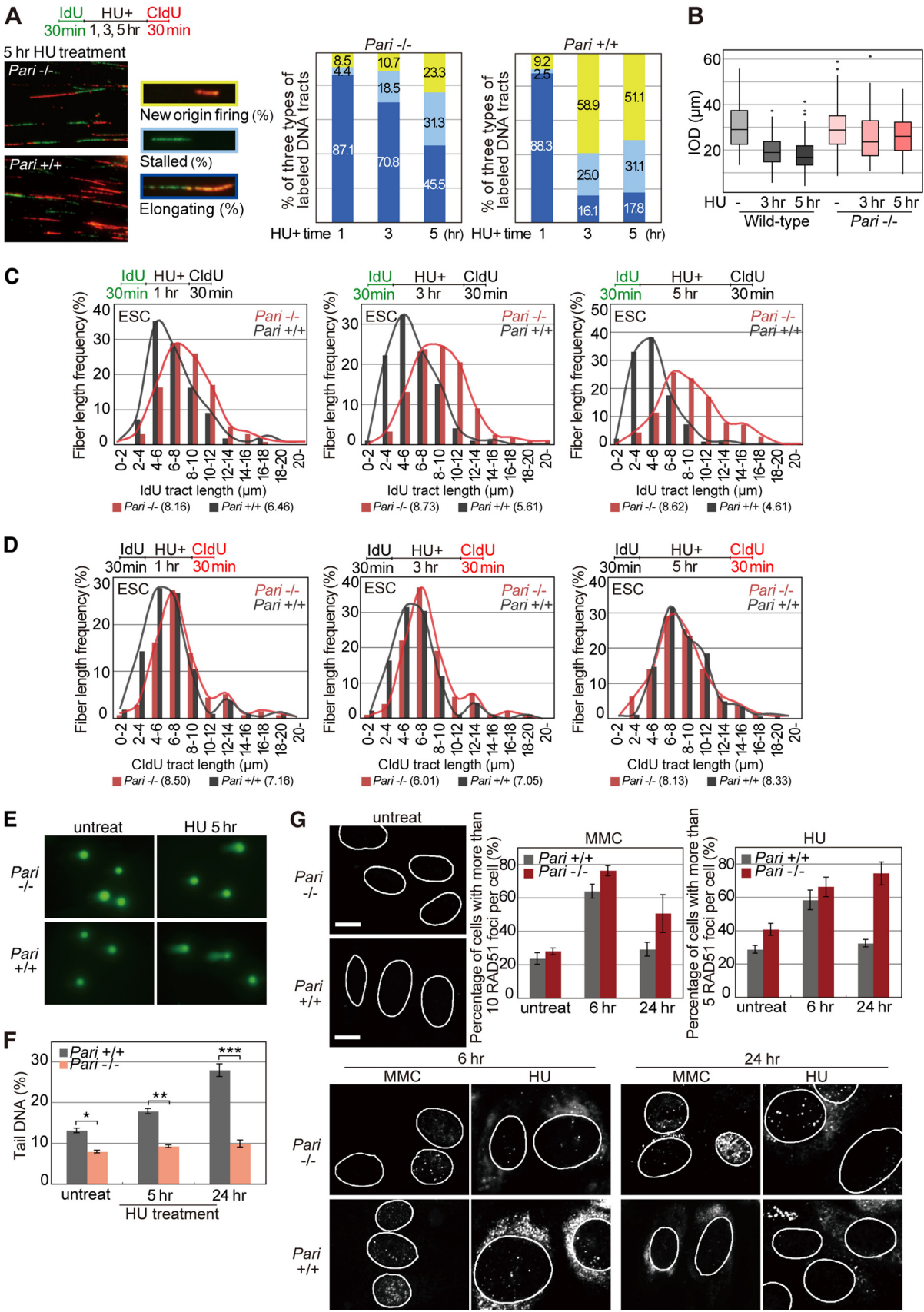
FIG 6 PARI controls the pathway choice of replication recovery. (A) Pari$^{+/+}$ and Pari$^{-/-}$ ES cells pulse-labeled with IdU and treated with HU for 1, 3, and 5 h, followed by CldU postlabeling. Representative images of DNA fibers of Pari$^{+/+}$ and Pari$^{-/-}$ ES cells treated with HU for 5 h

(Continued on next page)

replisome collapse and induces DSBs (11). These DSBs are processed by one-ended DSB repair or by two-ended DSB repair subsequent to NOF and replication fork merging (39). In $Pari^{-/-}$ ES cells, however, DSBs were not increased even after prolonged replication inhibition, as evidenced by the comet assay (Fig. 6E and F). DSB suppression (Fig. 6F), together with nascent-strand stabilization (Fig. 5C and D), in $Pari^{-/-}$ cells seemed to be a protective mechanism of damaged forks. However, it has been proposed that replication restart from stalled forks, involving template switching and homologous recombination, is a more complicated process than NOF-mediated replication recovery in mammalian cells, and illegitimate increase in such replication restart likely leads to the accumulation of unresolved recombination intermediates (40). In agreement with this notion, $Pari^{-/-}$ ES cells exhibited higher levels of RAD51 nuclear foci than wild-type cells after prolonged replication stress (HU and MMC for 24 h) (Fig. 6G). This, together with the suppression of DSBs (Fig. 6F), suggested that $Pari^{-/-}$ ES cells accumulate unresolved recombination intermediates after prolonged replication stress, which should then interfere with chromosome segregation in subsequent mitotic division.

Chromosome aberrations were indeed more increased in $Pari^{-/-}$ ES cells than in wild-type cells in the presence of replication inhibitors (HU and MMC) (Fig. 7A to C for HU and D to F for MMC). Sister chromatid exchange (SCE), a measure of recombination repair, was also elevated in $Pari^{-/-}$ ES cells in response to replication stress (MMC) (Fig. 7G and H). In addition to ES cells that were expanded *in vitro*, we observed that chromosome aberrations were also increased in $Pari^{-/-}$ bone marrow cells (BMC) and spermatogonial cell populations, both of which have high proliferative capacities, after *in vivo* induction of replication stress by MMC in mice (Fig. 8A to D).

We then examined a possible role of *Pari in vivo* under physiological conditions that induce extensive cell proliferation and replication stress. As a model system to address this, we studied phenylhydrazine (PHZ)-induced acute anemia in $Pari^{-/-}$ and $Pari^{+/+}$ mice. PHZ denatures hemoglobin and causes severe hemolytic anemia (41–43) without causing systemic defects, unlike general replication inhibitors, and thus enabled us to observe cell-type-specific (i.e., erythroid lineage) proliferation during the process of recovery from acute anemia. $Pari^{-/-}$ and $Pari^{+/+}$ mice raised under standard conditions both showed normal hematologic indices (Fig. 8E), including red blood cell (RBC) counts and hemoglobin levels. PHZ administration (40 mg/kg of body weight on days 0, 1, and 3) induced a severe decrease in the number of RBCs and in hematocrit indices in both $Pari^{-/-}$ and $Pari^{+/+}$ mice (Fig. 8F and G, day 4), but the subsequent recovery (Fig. 8F and G, day 7) was delayed in $Pari^{-/-}$ mice compared to $Pari^{+/+}$ mice, suggesting that acute cell proliferation of the erythroid lineage in response to PHZ-induced anemia was impaired by *Pari* deficiency. In addition, we also found that the Howell-Jolly body was more frequent in $Pari^{-/-}$ erythrocytes than in wild-type controls following PHZ administration (Fig. 8H). The Howell-Jolly body corresponds to the micronucleus, which is derived from a chromosome(s) or its fragment(s) missegregated during cell division, and increase in the Howell-Jolly body/micronucleus frequency indicates genome damage, including replication stress. Together, these results suggested that *Pari* deficiency impairs the process of recovery from PHZ-induced acute anemia with an indication of chromosome segregation deficiency.

FIG 6 Legend (Continued)

and relative frequencies of three types of labeled tracks, i.e., stalled forks (IdU only), fork elongation (IdU plus CldU), and new origin firing (CldU only), are shown. The data were obtained from >300 labeled tracts/sample. P values between $Pari^{+/+}$ and $Pari^{-/-}$ ES cells calculated by Pearson's chi-square test were 0.65 for HU treatment for 1 h and <0.001 for HU treatment for 3 and 5 h. (B) IOD of $Pari^{+/+}$ and $Pari^{-/-}$ ES cells pulse-labeled with IdU and treated with HU for 3 and 5 h, followed by CldU postlabeling. The data were obtained from >100 labeled tracts/sample. (C and D) IdU (C) and CldU (D) tract lengths of the same experiment shown in panel A. These data represent DNA tract lengths ($n > 250$) of $Pari^{+/+}$ and $Pari^{-/-}$ ES cells before (C) and after (D) HU treatment for 1, 3, and 5 h. Median tract lengths are given in parentheses. (E and F) Neutral comet assay of $Pari^{+/+}$ and $Pari^{-/-}$ ES cells with or without HU treatment for 5 and 24 h. Representative images (E) and tail DNA percentages measured from >100 cells/sample (F) are shown. *, $P < 1E-4$; **, $P < 1E-8$; ***, $P < 1E-9$ (Mann-Whitney U test). (G) Immunofluorescence staining for RAD51 of untreated $Pari^{+/+}$ and $Pari^{-/-}$ PEF (top left) or $Pari^{+/+}$ and $Pari^{-/-}$ PEF treated with MMC or HU for 6 and 24 h (bottom). Nuclei are outlined in white. (Top right) Percentages (±SE) of $Pari^{+/+}$ and $Pari^{-/-}$ PEF with >10 (MMC) and >5 (HU) RAD51 foci in the nuclei. Scale bars, 10 μm.
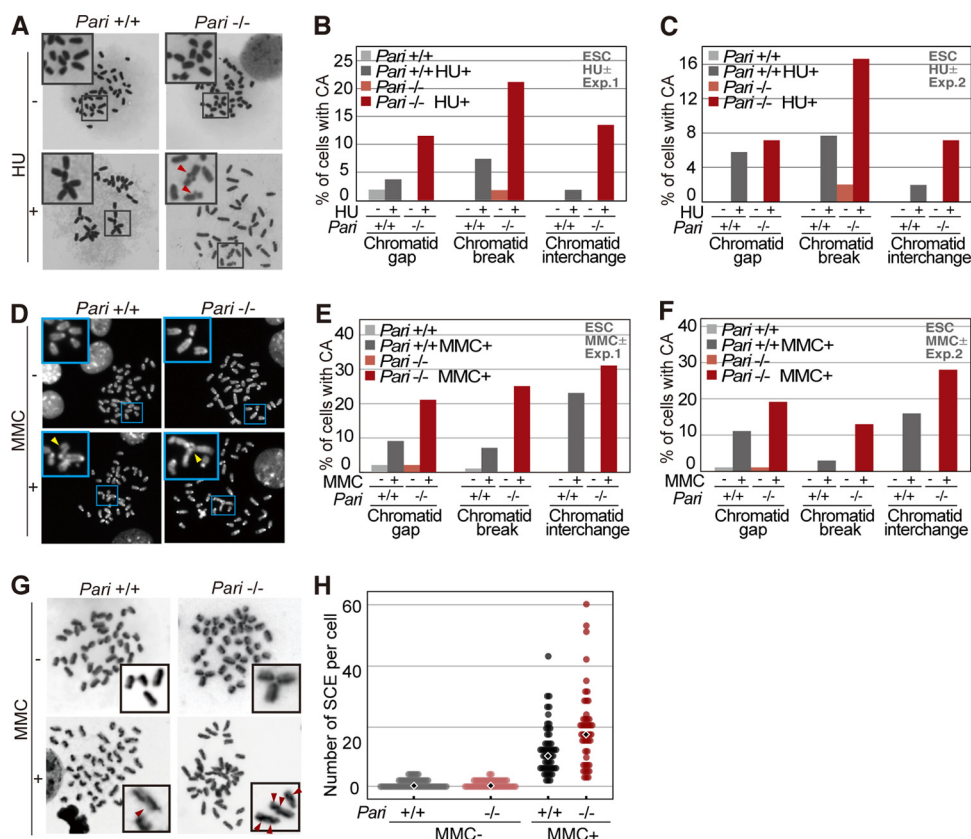
FIG 7 Chromosome instability of *Pari*-deficient ES cells in response to replication stress. (A) Metaphase spreads (Giemsa) of *Pari*⁺/⁺ and *Pari*⁻/⁻ ES cells cultured in the presence or absence of HU (2 mM). Representative images are shown, with chromosome aberrations indicated by the arrowheads. The insets are higher magnifications of the boxed regions. (B and C) Quantification (percentages) of *Pari*⁺/⁺ and *Pari*⁻/⁻ ES cells at the metaphase stage with each type of chromosome aberration (chromatid gap, break, and interchange) in the presence or absence of HU. The data represent the results of two independent experiments. (D) Metaphase spreads (DAPI) of *Pari*⁺/⁺ and *Pari*⁻/⁻ ES cells cultured in the presence or absence of 0.4 μg/ml MMC. Representative images are shown, with chromosome aberrations indicated by the arrowheads. The insets are higher magnifications of the boxed regions. (E and F) Quantification (percentages) of *Pari*⁺/⁺ and *Pari*⁻/⁻ ES cells at the metaphase stage, with chromatid gap, break, and interchange, in the presence or absence of MMC. The data shown represent the results of two independent experiments. (G) SCE analysis of *Pari*⁺/⁺ and *Pari*⁻/⁻ ES cells cultured in the presence or absence of MMC (0.4 μg/ml). (Insets) SCE sites are indicated by the arrowheads. (H) Quantification of frequencies of SCE of *Pari*⁺/⁺ and *Pari*⁻/⁻ ES cells in the presence or absence of MMC from the experiment shown in panel G. The diamonds indicate median frequencies of SCE.

We then asked whether PARI might participate in meiosis, in which homologous recombination plays an essential role. We examined recombination nodules in meiotic spermatocytes from *Pari*⁻/⁻ and wild-type male mice (Fig. 8I and J). Although the number of recombination nodules was slightly increased in *Pari*⁻/⁻ spermatocytes, such a difference is occasionally seen between different strains of wild-type mice. This suggested that *Pari* does not play a major role, if any, in meiotic recombination control in mice. In accord with this, *Pari*⁻/⁻ male mice exhibited normal fertility comparable to that of wild-type male mice (pregnancy rates for *Pari*⁻/⁻ and *Pari*⁺/⁺ males mated with wild-type females were 0.64 and 0.67; mean litter sizes for *Pari*⁻/⁻ and *Pari*⁺/⁺ mice were 6.7 and 7.3; $n = 4$ [*Pari*⁻/⁻] and 3 [*Pari*⁺/⁺]).

Spontaneous genome instability in *Pari*⁻/⁻ ES cells and its attenuation by differentiation induction. During the expansion of *Pari*⁻/⁻ ES cells, we noticed that *Pari*⁻/⁻ ES cells exhibited higher frequencies of spontaneous aneuploidy than wild-type controls under standard culture conditions (Fig. 9A and B). This propensity for spontaneous aneuploidy without exogenous replication stress was observed in two independently established *Pari*⁻/⁻ ES cell lines. In contrast, other cell types we examined, including PEF expanded *ex vivo* and bone marrow cells and spermatogonial cells *in vivo*,
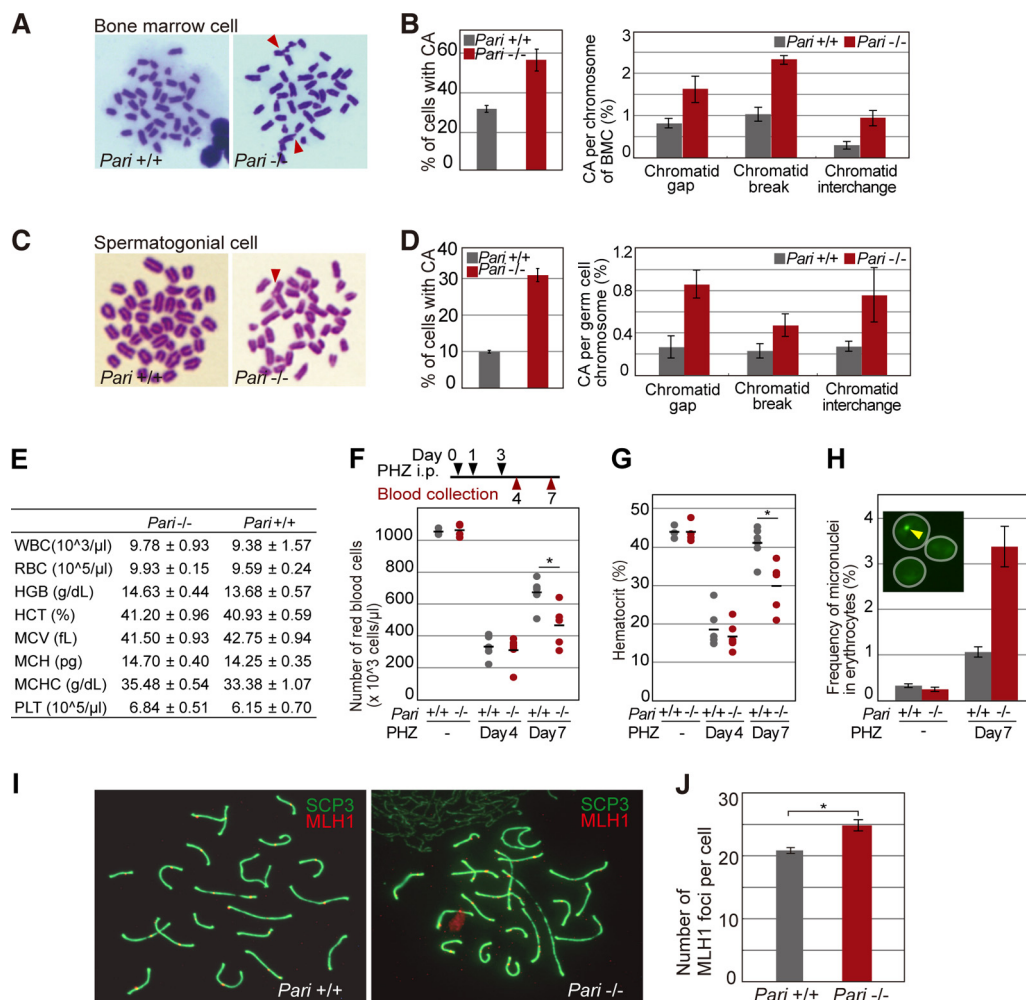
FIG 8 Chromosome instability of *Pari*-deficient cells in response to replication stress *in vivo*. (A) Metaphase spreads (Giemsa) of bone marrow cells from *Pari*$^{+/+}$ and *Pari*$^{-/-}$ mice injected with MMC (15 mg/kg). Chromosome aberrations are indicated with arrowheads. (B) Quantification (percentages) of chromosome aberrations in bone marrow cells from the experiment shown in panel A. Percentages of metaphase cells with chromosome aberrations (left) and each type of chromosome aberration (right) are shown. Means ± SE were obtained from >70 metaphases/sample from four pairs of *Pari*$^{+/+}$ and *Pari*$^{-/-}$ mice. (C) Metaphase spreads (Giemsa) of spermatogonial cells from *Pari*$^{+/+}$ and *Pari*$^{-/-}$ males injected with MMC (8 mg/kg). (D) Quantification (percentages) of chromosome aberrations in spermatogonial cells from the experiment shown in panel C. Percentages of metaphase cells with chromosome aberrations (left) and each type of chromosome aberration (right) are shown. Means ± SE were obtained from >70 metaphases/sample from three pairs of *Pari*$^{+/+}$ and *Pari*$^{-/-}$ mice. (E) Hematological values in *Pari*$^{+/+}$ and *Pari*$^{-/-}$ mice under standard housing conditions (means ± SE; *n* = 4). WBC, white blood cells; HGB, hemoglobin; HCT, hematocrits; MCV, mean corpuscular volume; MCH, mean corpuscular hemoglobin; MCHC, mean corpuscular hemoglobin concentration; PLT, platelets. (F and G) Numbers of red blood cells (F) and hematocrit values (G) of peripheral blood collected from *Pari*$^{-/-}$ and *Pari*$^{+/+}$ mice treated (days 4 and 7) or not with intraperitoneal injections of PHZ (40 mg/kg) (*n* = 6). Each dot represents a single mouse, and the bars indicate the means. *P* = 0.81 (day 4) and *P* < 0.05 (day 7) (F) and *P* = 0.70 (day 4) and *P* < 0.01 (day 7) (G) (Mann-Whitney U test). (H) Frequencies of micronuclei in >2,000 erythrocytes in peripheral blood from *Pari*$^{-/-}$ and *Pari*$^{+/+}$ mice treated (day 7) or not with PHZ. The data represent means ± SE (*n* = 3). (Inset) Representative image of erythrocytes (white circles) stained with acridine orange. The arrowhead indicates a micronucleus. (I) Surface spreads of meiotic spermatocytes from *Pari*$^{+/+}$ and *Pari*$^{-/-}$ male mice immunostained for MLH1 (red) and SYCP3 (green). (J) Numbers of MLH1 foci (recombination nodules) on synaptonemal complexes (SYCP3) per spermatocyte from the experiment shown in panel I. Means ± SE from the results of three independent experiments are presented. Fifty spermatocytes were analyzed for each experiment. *, *P* < 0.001 (Mann-Whitney U test).

did not exhibit such intrinsic predisposition to aneuploidy due to *Pari* deficiency (Fig. 9C).

Since aneuploidy primarily arises from chromosome missegregation (44), we examined whether chromosome segregation was impaired in *Pari*$^{-/-}$ ES cells in the absence of exogenous replication stress using micronucleus formation and lagging-
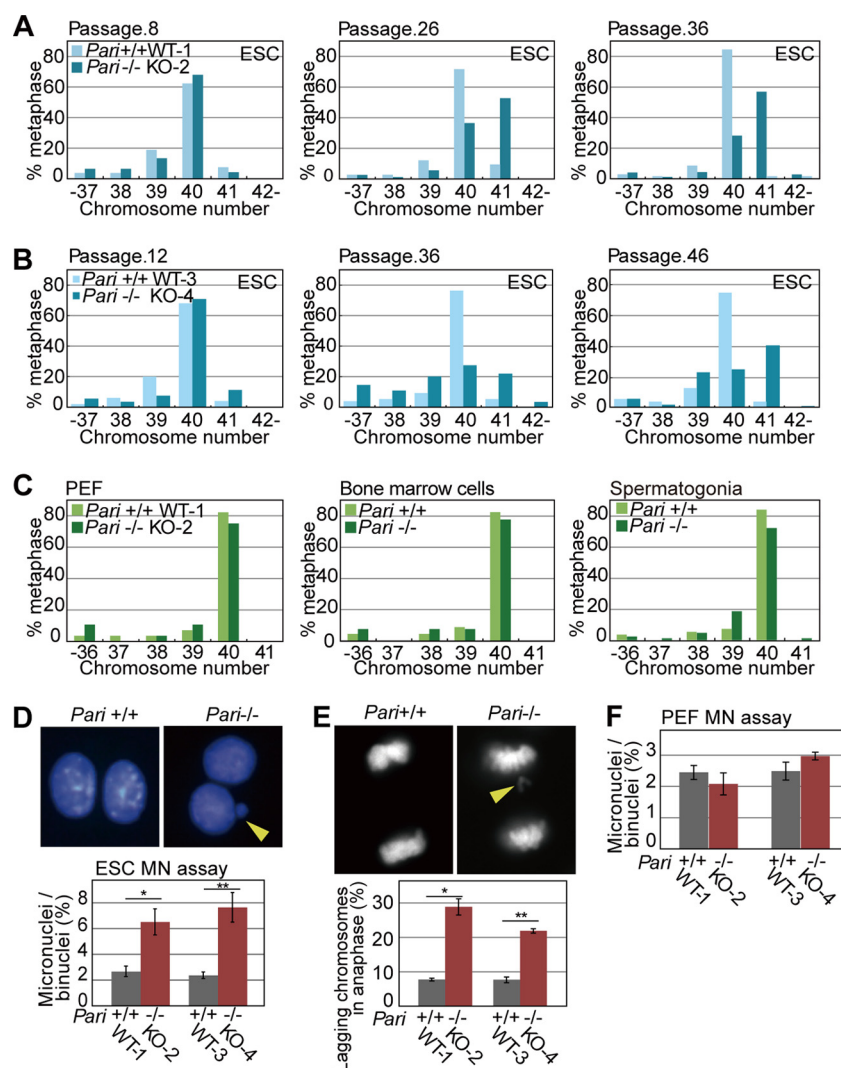
FIG 9 Spontaneous chromosome instability in *Pari*-deficient ES cells. (A and B) Numbers of chromosomes in *Pari*$^{+/+}$ and *Pari*$^{-/-}$ ES cell lines at early (left), middle (middle), and late (right) passages. *Pari*$^{+/+}$ (WT-1) and *Pari*$^{-/-}$ (KO-2) (A) and *Pari*$^{+/+}$ (WT-3) and *Pari*$^{-/-}$ (KO-4) (B) ES cell lines were established from two independent pairs of sibling blastocysts. (C) Numbers of chromosomes in PEF (left) obtained from *Pari*$^{+/+}$ and *Pari*$^{-/-}$ embryos and in bone marrow cells (middle) and spermatogonial cells (right) obtained from *Pari*$^{+/+}$ and *Pari*$^{-/-}$ mice. (D) Cytokinesis block micronucleus (MN) assay of *Pari*$^{+/+}$ and *Pari*$^{-/-}$ ES cells. Representative images (top) and frequencies of micronuclei in >500 binuclei per sample (bottom) are shown. ES cell lines established from two independent pairs of sibling blastocysts (*Pari*$^{+/+}$ [WT-1] versus *Pari*$^{-/-}$ [KO-2] and *Pari*$^{+/+}$ [WT-3] versus *Pari*$^{-/-}$ [KO-4], as shown in panels A and B) were used for the experiment. The data are means ± SE (*n* = 4). *, *P* < 0.05; **, *P* < 0.05 (Mann-Whitney U test). The arrowhead indicates a micronucleus. (E) Lagging-chromosome assay of *Pari*$^{+/+}$ and *Pari*$^{-/-}$ ES cells. Representative images (top) and frequencies of anaphase cells with a lagging chromosome(s) (bottom) are shown. Fifty anaphase cells were examined per sample. The data are means ± SE (*n* = 4). *, *P* < 0.05; **, *P* < 0.05 (Mann-Whitney U test). The arrowhead indicates a lagging chromosome. (F) Cytokinesis block micronucleus assay of *Pari*$^{+/+}$ and *Pari*$^{-/-}$ PEF. Frequencies of micronuclei in >500 binuclei per sample are shown. PEF expanded from two independent pairs of *Pari*$^{+/+}$ and *Pari*$^{-/-}$ embryos (WT-1 versus KO-2 and WT-3 versus KO-4) were used for the experiment. The data are means ± SE (*n* = 4). *P* = 0.49 and *P* = 0.34 (Mann-Whitney U test).

chromosome frequency assays (45, 46). These assays are generally more sensitive for detecting aneugenic and clastogenic effects than the chromosome aberration test, which detects only clastogenic events. In *Pari*$^{-/-}$ ES cells, spontaneous micronucleus and lagging-chromosome frequencies were both higher than in wild-type cells in the absence of exogenous replication stress (Fig. 9D and E). In contrast, no such difference was observed between *Pari*$^{-/-}$ and wild-type PEF (Fig. 9F), suggesting that ES cells are
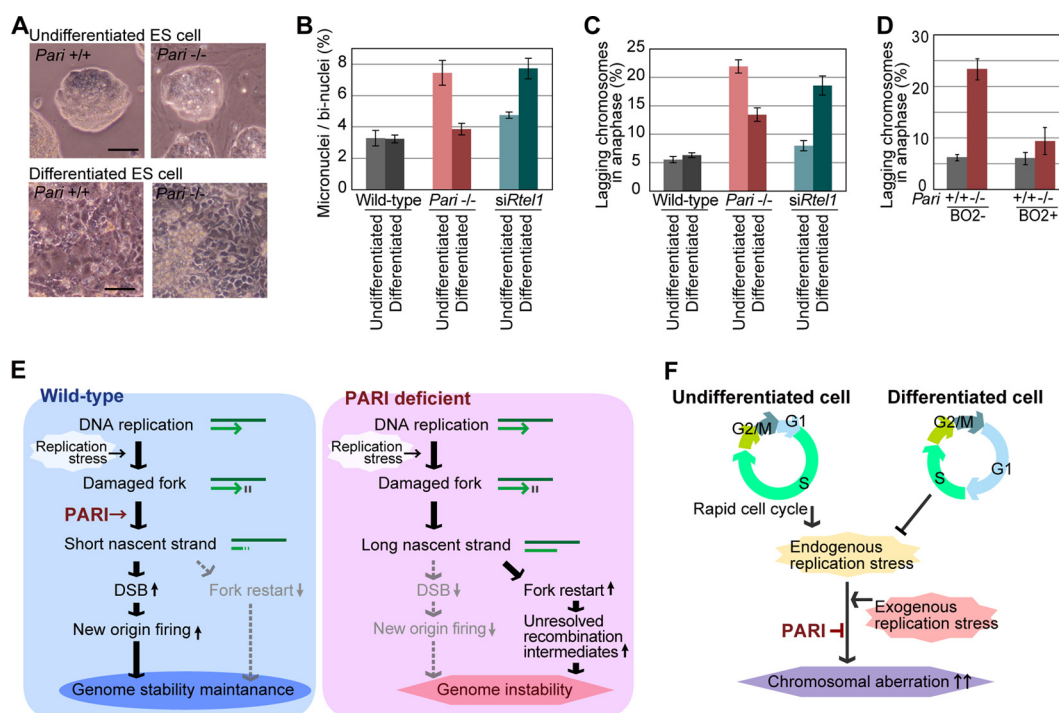
FIG 10 Preferential requirement for PARI function in undifferentiated ES cells to maintain chromosome stability. (A) Phase-contrast microscope images of undifferentiated $Pari^{+/+}$ and $Pari^{-/-}$ ES cell colonies (top) and their differentiated progeny (bottom). Scale bars, 50 μm. (B) Micronucleus frequencies (percentages) of wild-type, $Pari^{-/-}$, and $Rtel1$ knockdown (si$Rtel1$) ES cells and their differentiated progeny; >500 binucleated cells were examined for each sample. The data are means ± SE ($n = 4$). (C) Frequencies of anaphase cells with a lagging chromosome(s) in wild-type, $Pari^{-/-}$, and $Rtel1$ knockdown (si$Rtel1$) ES cells and their differentiated progeny; 50 anaphase cells were examined for each sample. The data are means ± SE ($n = 4$). (D) Frequencies of lagging chromosomes in $Pari^{+/+}$ and $Pari^{-/-}$ ES cells cultured or not with the RAD51 inhibitor B02 (50 μM) for 24 h. Fifty anaphase cells were examined per sample. The data are means ± SE ($n = 4$). (E) Schematic model of PARI function during DNA replication. PARI constitutively resides at replisomes but is functionally dormant during normal replication. Upon replication stress, PARI acts to reduce nascent-strand lengths through the RAD51-MRE11 pathway. PARI-DNA polymerase competition may also be involved in the nascent-strand shortening (see Discussion). Short nascent strands then promote DSB, together with NOF, and suppress the formation of unresolved recombination intermediates that interfere with proper chromosome segregation. (F) Developmental requirement for PARI function in ES cells. Undifferentiated ES cells undergo rapid self-renewal with an atypical cell cycle structure with short gap phases and inefficient checkpoints (see the introduction and Discussion). These cellular characteristics of ES cells inherently induce high endogenous replication stress and invoke an increased requirement for PARI-mediated control of stalled fork processing to ensure genome integrity.

more sensitive to $Pari$ deficiency than differentiated cells in terms of spontaneous chromosome segregation defects. Consistent with this notion, in $vitro$ differentiation induction of $Pari^{-/-}$ ES cells (Fig. 10A) attenuated intrinsic chromosome segregation errors (Fig. 10B and C), indicating that PARI has a developmentally regulated function to maintain chromosome stability in undifferentiated ES cells. Of note, this preferential requirement for $Pari$ in ES cells is not a general feature of other antirecombinases that act at replisomes. RNAi knockdown of $Rtel1$ resulted in an increase in chromosome segregation errors after, but not before, in $vitro$ differentiation induction from undifferentiated ES cells (47) (Fig. 10B and C). Hence, $Pari$ and $Rtel1$ play nonoverlapping and developmentally opposing functions to maintain chromosome stability in undifferentiated ES cells and their differentiated progeny, respectively.

Recent studies have shown that ES cells are under high intrinsic replication stress owing to their rapid proliferation and the lack of a G_1 checkpoint (48, 49). We reasoned that spontaneous chromosome instability in $Pari^{-/-}$ ES cells might be a secondary consequence of intrinsic replication stress that causes illegitimate accumulation of unresolved recombination intermediates, which then interfere with normal chromosome segregation. Consistent with this, RAD51 inhibition by B02, which attenuates the $Pari$-deficient phenotype in the S phase (Fig. 5I), suppressed chromosome missegregation in $Pari^{-/-}$ ES cells (Fig. 10D). The observation indicated that chromosome insta-

bility resulting from *Pari* deficiency originates from the primary function of PARI to antagonize RAD51 during DNA replication, and this activity of PARI is responsible for the chromosome stability of undifferentiated ES cells.

DISCUSSION

Maintaining genetic integrity is essential for all living cells and organisms. However, genome DNA is not ensured to be stable by default but, rather, is always under attack by numerous environmental sources, as well as metabolic processes. Naturally occurring frequencies of DNA damage that arise in a mammalian cell, for example, are estimated to be tens of thousands in a day (50), necessitating highly efficient pathways of DNA repair, which, however, are not complete or accurate. Unrepaired DNA damage interferes with DNA replication, which is also frequently perturbed by intrinsic replication barriers, including DNA binding proteins, transcription machinery, and unusual DNA structures. Such impediments to DNA replication need to be resolved by proper cooperation and choice between DNA repair and replication activities, such as fork stabilization versus fork processing, depending on the types of replication damage and possibly cellular and organismal states.

In this study, we demonstrated that PARI plays a pivotal role in modulating the initial processing of stalled replication forks in mice. PARI is constitutively associated with replisomes independently of the presence or absence of replication stress, and this persistent localization of PARI at replisomes should enable PARI to perform its molecular function immediately upon replication fork perturbation (Fig. 10E). Previous biochemical studies have shown that (i) PARI displaces RAD51 from ssDNA through its antirecombinase activity (17) and (ii) PARI competes for PCNA with DNA polymerase δ at D loop recombination intermediates (21). However, the exact physiological significance of PARI during DNA replication and repair under normal, as well as stressed, conditions remained unknown. By DNA fiber analyses, we showed that PARI does not affect replication kinetics during normal cell proliferation (Fig. 5B) but reduces nascent-strand lengths (Fig. 5D) and enhances DSB (Fig. 6F) in response to replication perturbation. The nascent-strand shortening can be explained by PARI function (i) to counteract the nonrecombinogenic role of RAD51, which protects nascent strands from nucleolytic degradation (17), or (ii) to compete for PCNA with DNA polymerase δ, which extends nascent strands (21). Nascent-strand shortening enhanced by PARI should then repress replication restart from stalled forks and instead provoke NOF to complete genome duplication. PARI thereby plays a pivotal role in determining how stalled forks are processed and DNA replication is recovered upon replication stress. As mentioned above, such PARI functioning contrasts with that of other antirecombinases, which generally act to protect stalled forks. Our results show that antirecombinases exert opposing control over impaired replication forks, i.e., to enhance (PARI) or to suppress (BLM, WRN, etc. [51]) nascent-strand processing, and both activities are necessary for faithful completion of genome duplication and maintaining genetic stability.

In order to investigate the physiological function of *Pari* in multicellular organisms, we generated a gene-targeted mouse line. In *Pari*-deficient mice, chromosome instability became evident in proliferative cells, including bone marrow and spermatogenic cells, upon exposure to replication inhibitors. We also showed that *Pari* plays an *in vivo* role to ensure cell proliferation and chromosome stability during accelerated recovery from acute anemia. Such a phenotype of *Pari*-deficient mice is in accord with the role of PARI during DNA replication, which is latent at normal replisomes but exerts its function in response to replication stress, which arises in the presence of replication perturbation and/or during extensive cell proliferation (Fig. 10E).

We observed spontaneous chromosome instability in *Pari*$^{-/-}$ ES cells. ES cells, which are established from early preimplantation embryos, are characterized by pluripotency to differentiate into all three germ layers and have unique cell cycle properties, including a rapid cell cycle (approximately 8 to 12 h for mouse ES cells), short gap phases, and lack of the G_1 checkpoint (52). These cell cycle characteristics are supposed to be developmentally programmed in early embryos, whose morphogenesis should

rely on rapid and synchronized cell proliferation. Such extensive cell proliferation is inherently associated with endogenous replication stress, and indeed, ES cells exhibit elevated levels of spontaneous γH2AX signals, together with increased ssDNA breaks, in the absence of exogenous genotoxic agents (53, 54), both of which are thought to arise from intrinsic replication damage. The lack of a G_1 checkpoint is possibly another cause of replication stress, since DNA damage imposed before the S phase potentially remains unrepaired and hampers DNA replication. Our results indicate that ES cells with early embryonic cell cycle profiles depend more on specific factors and mechanisms, including PARI, that act against endogenous replication stress than later differentiated progeny, which generally slow down cell proliferation rates (Fig. 10F). We propose that the functional status of PARI, and possibly other factors involved in DNA replication repair, has a significant impact on the genome stability of pluripotent stem cells, which often are expanded under highly proliferative conditions for use in both basic biological research and clinical applications.

Besides ES cells derived from early embryos, other cell types that also experience high physiological replication stress, such as cancer cells and aging stem cells, may also be prone to spontaneous chromosome instability due to *Pari* deficiency. In relation to this, recent studies reported that *Pari* expression is aberrantly upregulated in pancreatic cancer cell lines, and its RNAi knockdown reduces their cell viability (23, 24). A possible cancer-associated, as well as aging-related, phenotype(s) in *Pari* gene-targeted mice warrants future investigation. The mechanisms and factors underlying the genome instability associated with endogenous replication stress are still poorly understood, and their elucidation should be of fundamental importance in understanding the development, homeostasis, and diseases of long-lived organisms, including humans.

MATERIALS AND METHODS

Generation of *Pari* gene-targeted mice. The *Pari* gene-targeting plasmid was electroporated into KY1.1 mouse ES cells (kindly provided by Junji Takeda). After G418 drug selection, three subclones identified as correctly targeted were injected into C57BL/6 × DBA/2 blastocysts. Chimeric males were mated with C57BL/6 females. To excise *loxP*-flanked exons 5 and 6, floxed males were mated with *CMV-Cre* transgenic females (55). To induce acute anemia, the mice were injected intraperitoneally with 40 mg/kg of PHZ (TCI, Japan) three times on days 0, 1, and 3. All animal experiments were performed according to the institution's ethical guidelines.

Establishment of *Pari*$^{+/+}$ and *Pari*$^{-/-}$ ES cells. *Pari*$^{+/+}$ and *Pari*$^{-/-}$ sibling blastocysts were collected at 4.5 days postcoitum (dpc) from *Pari*$^{+/-}$ pregnant females mated with *Pari*$^{+/-}$ males. The zona pellucida was removed with acidic Tyrode's solution. Zona-free blastocysts were cultured in embryonic stem cell culture medium supplemented with 2i (PD032591 and CHIR99021; Axon Medchem) and LIF (Millipore) (56) on MMC-treated primary mouse embryonic fibroblasts. The inner cell masses of outgrowing blastocysts were picked up by using a glass capillary and then trypsinized and expanded to establish ES cell lines.

***Pari*$^{+/+}$ and *Pari*$^{-/-}$ primary embryonic fibroblasts.** *Pari*$^{+/+}$ and *Pari*$^{-/-}$ primary embryonic fibroblasts were prepared from *Pari*$^{+/+}$ and *Pari*$^{-/-}$ sibling embryos at 13.5 dpc. Briefly, after removal of the head, limbs, and internal organs, each embryo was mechanically minced, and a culture dish was plated with the minced embryos in standard Dulbecco's modified Eagle's medium (DMEM)-based culture medium. Primary embryonic fibroblasts were passaged by trypsinization and used for experiments between passage numbers 3 and 6.

Cell culture medium. Mouse ES cells were maintained in DMEM–F-12 medium supplemented with 15 to 20% fetal calf serum, L-glutamine, penicillin-streptomycin, sodium pyruvate, sodium bicarbonate, nonessential amino acids, LIF (Millipore), and 2i (PD032591 and CHIR99021) (56). Mouse primary embryonic fibroblasts and mouse NIH 3T3 and human HEK 293T cells were cultured in high-glucose DMEM supplemented with 10% fetal calf serum and penicillin-streptomycin at 37°C under 5% CO_2.

Assay of cell sensitivity to genotoxic agents. *Pari*$^{+/+}$ and *Pari*$^{-/-}$ ES cells were plated in 96-well plates (5 × 10^3 cells/well) and cultured in the presence or absence of genotoxic agents for the times indicated in the figures. Relative cell numbers were determined by using the Cell Titer Blue assay kit (Promega) and a microplate reader (iMark; Bio-Rad). For embryonic fibroblasts, 4 × 10^4 cells were seeded in each well of 12-well plates. The numbers of cells were determined by using a Countess cell counter (Life Technologies). HU and etoposide were purchased from Sigma-Aldrich and MMC from Kyowa Hakko Kirin, Japan. The cells were irradiated with gamma rays from a cesium 137 source in a Gammacell 40 Exactor (Best Theratronics).

Histological examination. Tissues were fixed in Bouin's solution, embedded in paraffin, and cut into 7-μm-thick sections. Paraffin sections were stained with hematoxylin and eosin (HE) and examined by light microscopy.

Southern blot analysis. For Southern blot analysis, 5 μg genomic DNA was digested with restriction enzymes PflFI and BstXI. The digested DNA was separated by agarose gel electrophoresis, transferred to

a Hybond N$^+$ membrane (GE Healthcare), hybridized with [α-32P]dCTP-labeled *Pari* probe (Fig. 2A), and exposed to X-ray film.

RT-PCR. Cells and tissues were lysed in TRIzol reagent (Life Technologies). Total RNA was extracted according to the manufacturer's instructions, and then, cDNA was synthesized by using a high-capacity RNA-to-cDNA kit (Life Technologies) and used as the template for RT-PCR. The PCR primers for *Pari* were 5'-GGGAGAGAGGCCTTCACCAACTTG-3' and 5'-CTGTGGCCTTTGATCAGCTGCATC-3', and those for *Gapdh* were 5'-ACGGCCGCATCTTCTTGTGC-3' and 5'-CCCTTTTGGCTCCACCCTTCAAGT-3'.

Cell cycle analysis. ES cells were trypsinized to a single-cell suspension and stained with propidium iodide in the presence of RNase (Guava cell cycle reagent kit; Millipore), and the DNA contents were analyzed by flow cytometry (Guava easyCyte flow cytometer; Millipore).

Plasmid construction and transfection. pCAG-FLAG-PARI and pCAG-3$\times$ FLAG-PARI encode the full-length of PARI tagged with a single or triple FLAG tag, respectively. pCAG-FLAG-PARIΔPIP encodes FLAG-tagged truncated PARI lacking the C-terminal PIP box. pCAG-FLAG-PARIΔUvrD encodes FLAG-tagged truncated PARI lacking the N-terminal UvrD domain. All the plasmids were constructed by inserting cDNA fragments between ClaI and ScaI sites downstream of the CAG promoter of pCAGGS. Transient transfection was carried out using Lipofectamine 2000 reagent (Life Technologies) according to the manufacturer's instructions. Human *PARI* cDNA was cloned from normal human peripheral blood cells by RT-PCR. The primer pair used was 5'-TGGCTGTGTTTAATCAGAAG-3' and 5'-TTATAGTCTAAAAA ACTGAG-3'. The human *PARI* cDNA was subcloned into the pENTR plasmid and then fused in frame to *EGFP* of the destination vector by the Gateway LR reaction (Life Technologies).

Immunocytochemistry. Cells were cultured in 8-well glass chamber slides (Nunc Lab-Tek chamber slide), fixed with 2% paraformaldehyde (PFA) in phosphate-buffered saline (PBS), permeabilized with 0.1% Triton X-100 in PBS, blocked with Blocking One (Nacalai Tesque, Japan), and then immunostained with primary antibodies diluted in Blocking One solution, followed by secondary antibodies conjugated with Alexa Fluor 488 or 555 (Life Technologies). The primary antibodies used were anti-FLAG polyclonal antibody (1:1,000; Sigma-Aldrich), anti-FLAG M2 monoclonal antibody (1:1,000; Sigma-Aldrich), anti-PCNA monoclonal antibody (1:500; PC10; Biolegend), anti-RAD51 (1:100; H-92; Santa Cruz), anti-BrdU antibody (1:400; BD); and anti-γH2AX (1:500; JBW301; Millipore). Nuclei were counterstained with DAPI (4',6-diamidino-2-phenylindole).

DNA fiber assay. DNA fiber assays were carried out as previously described (57). Briefly, ES cells and PEF were cultured in the presence of 20 μM IdU (1st label) for the indicated periods of time, washed twice with PBS, and then cultured in the presence of 200 μM CldU (2nd label). Replication stress was induced with 2 mM HU as indicated in the figures. The cells were trypsinized and resuspended in ice-cold PBS or 70% ethanol at a concentration of 7.5 $\times$ 10^5 cells/ml, and then 2 μl of the cell suspension was spotted onto amino silane-coated slide glass. The cell suspension was briefly dried, and then 7 to 15 μl of lysis solution (50 mM EDTA and 0.5% SDS in 200 mM Tris-HCl, pH 7.5) was applied to the cells and gently mixed. To spread DNA fibers, the slides were tilted at 15° and air dried. DNA fibers on the slides were fixed in Carnoy's solution for 10 min and then denatured in 2.5 M HCl for 80 min. The slides were blocked with Blocking One (Nacalai Tesque) and immunostained with mouse anti-BrdU antibody (1:500; BD Biosciences; 347580) for IdU and rat anti-BrdU antibody (1:800; Abcam; ab6326) for CldU detection. The secondary antibodies used were Alexa Fluor 488- and 555-conjugated anti-mouse and -rat IgG antibodies (Life Technologies). Mirin MRE11 inhibitor and B02 RAD51 inhibitor were purchased from Sigma-Aldrich. For *Rtel1* knockdown, small interfering RNAs (siRNAs) were transfected 36 h before DNA fiber experiments. Replication tract lengths were measured for 250 to 400 IdU- and/or CldU-labeled DNA fibers (1 to 3 independent experiments) using ImageJ. *P* values were calculated by the Mann-Whitney test.

RNA interference. For RNA interference of *Rtel1*, siRNA was purchased from GE Healthcare. Nontarget siRNA was used as a control. *Pari*$^{+/+}$ and *Pari*$^{-/-}$ ES cells were plated at a density of 1 $\times$ 10^6 cells per well of a 12-well plate. After 16 h, 100 fmol siRNAs was transfected with 2 μl of DharmaFect 1 reagent (Thermo Scientific) per well.

Neutral comet assay. A neutral comet assay was carried out using a comet assay kit (Trevigen) following the manufacturer's instructions. Briefly, 500 ES cells were mixed with molten low-melting-point agarose and spread onto a comet slide. The slide was placed flat in a humid chamber at 4°C for gelation and then incubated in the lysis solution for 2 h at 4°C. Electrophoresis was carried out in neutral electrophoresis buffer (100 mM Tris-HCl and 300 mM sodium acetate at pH 9.0) for 45 min at 4°C. DNA in the gel was precipitated with 7.5 M ammonium acetate in 95% ethanol, and then the gel was dried at 37°C. The slides were stained with SYBR Gold dye (Life Technologies). Images were taken with a fluorescence microscope (BX61; Olympus) and analyzed using ImageJ software with an Open Comet plug-in (58).

Metaphase spread preparation of embryonic stem cells. *Pari*$^{+/+}$ and *Pari*$^{-/-}$ ES cells were cultured in the presence of 60 ng/ml colcemid for 1 h before harvest. A single-cell suspension obtained by trypsinization was treated in hypotonic solution (75 mM KCl) for 5 to 10 min, fixed with Carnoy's solution (methanol-acetic acid, 3:1), and then stored at −30°C overnight. The fixed cell suspensions were dropped onto clean glass slides and allowed to spread on a hot plate at 60°C under humidified conditions. The slides were stained with Giemsa solution and analyzed by light microscopy.

Chromosome aberration test of bone marrow cells and spermatogonial cells. For the bone marrow chromosome aberration assay, *Pari*$^{+/+}$ and *Pari*$^{-/-}$ mice were injected intraperitoneally with 15 mg/kg MMC 24 h and 4 mg/kg colchicine 1 h before sacrifice. Bone marrow cells were flushed out from dissected femurs with a 27-gauge needle and a 1-ml syringe and incubated in prewarmed hypotonic solution (0.9% trisodium citrate dihydrate) at 37°C for 10 to 15 min. The cells were then fixed with

Carnoy's solution without resuspension for 10 min and rinsed with the fixative solution twice. Using a 26-gauge needle, the cell pellet was dispersed to a single-cell suspension. Metaphase spreads were prepared as described above. For the spermatogonial chromosome aberration test, male mice were administered 8 mg/kg MMC 24 h and 4 mg/kg colchicine 4 h before sacrifice. The tunica albuginea was removed from each testis, and the seminiferous tubules were teased apart and minced in PBS using fine forceps. The seminiferous tubule fragments were incubated in 0.5 mg/ml collagenase in PBS for 15 min at 37°C, and then spermatogonia were released into suspension by careful pipetting. The cells were rinsed with 2.2% sodium citrate (trisodium citrate) solution, followed by hypotonic treatment with 0.9% sodium citrate solution. Carnoy's fixative was added to the cells and incubated for 10 min on ice. Metaphase spreads were prepared as described above. The slides were stained with Giemsa solution and analyzed by light microscopy.

Sister chromatid exchange assay. ES cells were cultured in the presence of 10 μM BrdU for 24 h in the dark with 0.4 μg/ml MMC added during the last 12 h and 50 ng/ml colcemid added for the last 1 h before harvest. Metaphase spreads were prepared as described above. Differential staining of sister chromatids was carried out as described previously (59). Briefly, slides were stained with Hoechst 33258, rinsed with 2× SSC (1× SSC is 0.15 M NaCl plus 0.015 M sodium citrate), exposed to UV light, washed in 2× SSC, and then stained with Giemsa solution. The slides were mounted with DPX (Merck) and examined under light microscopy.

Surface spreading of meiotic chromosomes. Seminiferous tubules of $Pari^{+/+}$ and $Pari^{-/-}$ testes were mechanically dissected, and germ cells, including meiotic spermatocytes (as well as spermatids, etc.), were squeezed out using fine forceps. Hypotonic extraction buffer (30 mM Tris-HCl, pH 8.3, 5 mM EDTA, 1.7% sucrose, and 0.5% trisodium citrate dihydrate) was added to an equal volume of the cell suspension. The cells were then centrifuged and resuspended in 100 mM sucrose solution. A few drops of the cell suspension were spotted onto glass slides prewetted with 1% PFA and 0.15% Triton X-100 solution. The slides were then incubated in a humid chamber for 12 h at 4°C, washed with PBS, and air dried. Immunostaining was carried out with anti-SYCP3 (60), anti-MLH1 (1:100; BD Pharmingen), Alexa Fluor 488-conjugated anti-rabbit IgG, and Alexa Fluor 555-conjugated anti-mouse IgG antibodies.

Micronucleus formation assay and lagging-chromosome assay. The cytokinesis block micronucleus formation assay was carried out as described previously (46). Briefly, cells were cultured in the presence of 4.5 μg/ml cytochalasin for 8 h (ES cells) or 20 h (PEF) in standard culture medium. After trypsinization, a single-cell suspension was treated with hypotonic solution (75 mM KCl) for 3 min and fixed with Carnoy's solution. Cells were spread on glass slides and stained with DAPI (nuclei) and fluorescein isothiocyanate (FITC) (cytoplasm). Five hundred to 1,000 binucleated cells/sample were analyzed for the presence of micronuclei under fluorescence microscopy. For the lagging-chromosome assay, cells were trypsinized and resuspended in PBS, and an equal volume of 2% PFA was added. The cell suspension was then spread on glass slides and air dried. Nuclei were stained with DAPI, and then the frequencies of lagging chromosomes in anaphase cells were scored.

***In vitro* differentiation of mouse ES cells.** To induce *in vitro* differentiation, $Pari^{+/+}$ and $Pari^{-/-}$ ES cells were cultured in the absence of LIF, PD032591, and CHIR99021 on gelatin-coated dishes in the absence of feeder cells for 5 passages in 10 days.

Laser microirradiation experiments. Human U2OS cells in 35-mm glass bottom culture dishes (Iwaki) were transiently transfected with the GFP-human PARI-expressing plasmid using Lipofectamine 3000 reagent (Life Technologies) according to the manufacturer's instructions. Prior to laser irradiation, the cells were treated with 10 μg/ml Hoechst 33258 for 10 min. DNA damage was introduced into the nuclei of the cells by microirradiation with a pulsed 405-nm laser (TCS-SP5; Leica), and time-lapse imaging was performed using the FRAP Wizard system (Leica). During microirradiation and imaging, the cell culture plate was maintained at 37°C and 5% CO_2 using the INUH-SFB incubation system for microscopes (Tokai Hit, Japan). Cell cycle phases were determined by the subcellular localization of GFP-PARI, i.e., distinct and bright nuclear foci (S phase) or more diffuse distribution in the nucleus (G_1/G_2 phase).

iPOND experiments. iPOND experiments were carried out as previously described (28, 29). Briefly, 1×10^8 293T cells were transiently transfected with the pCAG-FLAG-PARI plasmid and pulse-labeled with 20 μM EdU (Thermo Scientific) for 30 min. The cells were cross-linked with 1% PFA and 2 mM DSP (Thermo Scientific) for 10 min, and then, the fixatives were quenched with 125 mM glycine and fetal calf serum. The cross-linked cells were permeabilized with 0.25% Triton-X for 30 min, and then a click reaction was carried out using 100 μM biotin-polyethylene glycol 4-azide (Thermo Scientific) in 10 mM sodium-L-ascorbate and 5 mM $CuSO_4$ solution. The cells were lysed in 1% SDS, 50 mM Tris-HCl, pH 8.0, and sonicated with an ultrasonicator (S220; Covaris). After centrifugation, protease inhibitor cocktail (Roche) was added to the supernatant, incubated with streptavidin-agarose resin beads (Novagen), and washed with PBS, followed by a high-stringency wash with 1 M NaCl and 0.5% SDS in 25 mM Tris-HCl, pH 8.0, solution. Then, the beads were eluted with standard SDS-PAGE loading buffer for 25 min at 95°C. SDS-PAGE and Western blotting were carried out according to standard procedures using anti-FLAG polyclonal antibody (1:2,000; Sigma-Aldrich) and anti-PCNA monoclonal antibody (1:1,000; PC10; Biolegend).

Hematological analysis. Peripheral blood from 14- to 16-week-old mice was collected from the tail in EDTA-coated vials (Terumo, Japan), and blood cell parameters were measured with a Celltac analyzer (Nihon Kohden, Japan). To quantify micronuclei in erythrocytes, blood smears were stained with 0.007% acridine orange, and more than 2,000 erythrocytes were analyzed.

REFERENCES

1. Aguilera A, Gómez-González B. 2008. Genome instability: a mechanistic view of its causes and consequences. Nat Rev Genet 9:204–217. https://doi.org/10.1038/nrg2268.
2. Branzei D, Foiani M. 2010. Maintaining genome stability at the replication fork. Nat Rev Mol Cell Biol 11:208–219. https://doi.org/10.1038/nrm2852.
3. Tichy ED, Stambrook PJ. 2008. DNA repair in murine embryonic stem cells and differentiated cells. Exp Cell Res 314:1929–1936. https://doi.org/10.1016/j.yexcr.2008.02.007.
4. Mac Auley A, Werb Z, Mirkes PE. 1993. Characterization of the unusually rapid cell cycles during rat gastrulation. Development 117:873–883.
5. Solter D, Škreb N, Damjanov I. 1971. Cell cycle analysis in the mouse EGG-cylinder. Exp Cell Res 64:331–334. https://doi.org/10.1016/0014-4827(71)90084-X.
6. Adams PD, Jasper H, Rudolph KL. 2015. Aging-induced stem cell mutations as drivers for disease and cancer. Cell Stem Cell 16:601–612. https://doi.org/10.1016/j.stem.2015.05.002.
7. Zeman MK, Cimprich KA. 2014. Causes and consequences of replication stress. Nat Cell Biol 16:2–9. https://doi.org/10.1038/ncb2897.
8. Sancar A, Lindsey-Boltz LA, Ünsal-Kaçmaz K, Linn S. 2004. Molecular mechanisms of mammalian DNA repair and the DNA damage checkpoints. Annu Rev Biochem 73:39–85. https://doi.org/10.1146/annurev.biochem.73.011303.073723.
9. Lopes M, Cotta-Ramusino C, Pellicioli A, Liberi G, Plevani P, Muzi-Falconi M, Newlon CS, Foiani M. 2001. The DNA replication checkpoint response stabilizes stalled replication forks. Nature 412:557–561. https://doi.org/10.1038/35087613.
10. Mourón S, Rodriguez-Acebes S, Martínez-Jiménez MI, García-Gómez S, Chocrón S, Blanco L, Méndez J. 2013. Repriming of DNA synthesis at stalled replication forks by human PrimPol. Nat Struct Mol Biol 20:1383–1389. https://doi.org/10.1038/nsmb.2719.
11. Petermann E, Helleday T. 2010. Pathways of mammalian replication fork restart. Nat Rev Mol Cell Biol 11:683–687. https://doi.org/10.1038/nrm2974.
12. Saleh-Gohari N, Bryant HE, Schultz N, Parker KM, Cassel TN, Helleday T. 2005. Spontaneous homologous recombination is induced by collapsed replication forks that are caused by endogenous DNA single-strand breaks. Mol Cell Biol 25:7158–7169. https://doi.org/10.1128/MCB.25.16.7158-7169.2005.
13. Hashimoto Y, Ray Chaudhuri A, Lopes M, Costanzo V. 2010. Rad51 protects nascent DNA from Mre11-dependent degradation and promotes continuous DNA synthesis. Nat Struct Mol Biol 17:1305–1311. https://doi.org/10.1038/nsmb.1927.
14. Helleday T. 2003. Pathways for mitotic homologous recombination in mammalian cells. Mutat Res 532:103–115. https://doi.org/10.1016/j.mrfmmm.2003.08.013.
15. Croteau DL, Popuri V, Opresko PL, Bohr VA. 2014. Human RecQ helicases in DNA repair, recombination, and replication. Annu Rev Biochem 83:519–552. https://doi.org/10.1146/annurev-biochem-060713-035428.
16. Lundin C, Schultz N, Arnaudeau C, Mohindra A, Hansen LT, Helleday T. 2003. RAD51 is involved in repair of damage associated with DNA replication in mammalian cells. J Mol Biol 328:521–535. https://doi.org/10.1016/S0022-2836(03)00313-9.
17. Moldovan GL, Dejsuphong D, Petalcorin MI, Hofmann K, Takeda S, Boulton SJ, D'Andrea AD. 2012. Inhibition of homologous recombination by the PCNA-interacting protein PARI. Mol Cell 45:75–86. https://doi.org/10.1016/j.molcel.2011.11.010.
18. Barber LJ, Youds JL, Ward JD, McIlwraith MJ, O'Neil NJ, Petalcorin MI, Martin JS, Collis SJ, Cantor SB, Auclair M, Tissenbaum H, West SC, Rose AM, Boulton SJ. 2008. RTEL1 maintains genomic stability by suppressing homologous recombination. Cell 135:261–271. https://doi.org/10.1016/j.cell.2008.08.016.
19. Fugger K, Mistrik M, Danielsen JR, Dinant C, Falck J, Bartek J, Lukas J, Mailand N. 2009. Human Fbh1 helicase contributes to genome maintenance via pro- and anti-recombinase activities. J Cell Biol 186:655–663. https://doi.org/10.1083/jcb.200812138.
20. Moldovan G-L, Pfander B, Jentsch S. 2007. PCNA, the maestro of the replication fork. Cell 129:665–679. https://doi.org/10.1016/j.cell.2007.05.003.
21. Burkovics P, Dome L, Juhasz S, Altmannova V, Sebesta M, Pacesa M, Fugger K, Sorensen CS, Lee MY, Haracska L. 2016. The PCNA-associated protein PARI negatively regulates homologous recombination via the inhibition of DNA repair synthesis. Nucleic Acids Res 44:3176–3189. https://doi.org/10.1093/nar/gkw024.
22. Okazaki Y, Furuno M, Kasukawa T, Adachi J, Bono H, Kondo S, Nikaido I, Osato N, Saito R, Suzuki H, Yamanaka I, Kiyosawa H, Yagi K, Tomaru Y, Hasegawa Y, Nogami A, Schonbach C, Gojobori T, Baldarelli R, Hill DP, Bult C, Hume DA, Quackenbush J, Schriml LM, Kanapin A, Matsuda H, Batalov S, Beisel KW, Blake JA, Bradt D, Brusic V, Chothia C, Corbani LE, Cousins S, Dalla E, Dragani TA, Fletcher CF, Forrest A, Frazer KS, Gaasterland T, Gariboldi M, Gissi C, Godzik A, Gough J, Grimmond S, Gustincich S, Hirokawa N, Jackson IJ, Jarvis ED, Kanai A, Kawaji H, Kawasawa Y, Kedzierski RM, King BL, Konagaya A, Kurochkin IV, Lee Y, Lenhard B, Lyons PA, Maglott DR, Maltais L, Marchionni L, McKenzie L, Miki H, Nagashima T, Numata K, Okido T, Pavan WJ, Pertea G, Pesole G, Petrovsky N, Pillai R, Pontius JU, Qi D, Ramachandran S, Ravasi T, Reed JC, Reed DJ, Reid J, Ring BZ, Ringwald M, Sandelin A, Schneider C, Semple CA, Setou M, Shimada K, Sultana R, Takenaka Y, Taylor MS, Teasdale RD, Tomita M, Verardo R, Wagner L, Wahlestedt C, Wang Y, Watanabe Y, Wells C, Wilming LG, Wynshaw-Boris A, Yanagisawa M, Yang I, Yang L, Yuan Z, Zavolan M, Zhu Y, Zimmer A, Carninci P, Hayatsu N, Hirozane-Kishikawa T, Konno H, Nakamura M, Sakazume N, Sato K, Shiraki T, Waki K, Kawai J, Aizawa K, Arakawa T, Fukuda S, Hara A, Hashizume W, Imotani K, Ishii Y, Itoh M, Kagawa I, Miyazaki A, Sakai K, Sasaki D, Shibata K, Shinagawa A, Yasunishi A, Yoshino M, Waterston R, Lander ES, Rogers J, Birney E, Hayashizaki Y, FANTOM Consortium, RIKEN Genome Exploration Research Group Phase I and II Team. 2002. Analysis of the mouse transcriptome based on functional annotation of 60,770 full-length cDNAs. Nature 420:563–573. https://doi.org/10.1038/nature01266.
23. Piao L, Nakagawa H, Ueda K, Chung S, Kashiwaya K, Eguchi H, Ohigashi H, Ishikawa O, Daigo Y, Matsuda K, Nakamura Y. 2011. C12orf48, termed PARP-1 binding protein, enhances poly(ADP-ribose) polymerase-1 (PARP-1) activity and protects pancreatic cancer cells from DNA damage. Genes Chromosomes Cancer 50:13–24. https://doi.org/10.1002/gcc.20828.
24. O'Connor KW, Dejsuphong D, Park E, Nicolae CM, Kimmelman AC, D'Andrea AD, Moldovan GL. 2013. PARI overexpression promotes

genomic instability and pancreatic tumorigenesis. Cancer Res 73:2529–2539. https://doi.org/10.1158/1538-7445.AM2013-2529.

25. Lee JY, Yang W. 2006. UvrD helicase unwinds DNA one base pair at a time by a two-part power stroke. Cell 127:1349–1360. https://doi.org/10.1016/j.cell.2006.10.049.

26. Su AI, Wiltshire T, Batalov S, Lapp H, Ching KA, Block D, Zhang J, Soden R, Hayakawa M, Kreiman G. 2004. A gene atlas of the mouse and human protein-encoding transcriptomes. Proc Natl Acad Sci U S A 101:6062–6067. https://doi.org/10.1073/pnas.0400782101.

27. Li MD, Burns TC, Kumar S, Morgan AA, Sloan SA, Palmer TD. 2015. Aging-like changes in the transcriptome of irradiated microglia. Glia 63:754–767. https://doi.org/10.1002/glia.22782.

28. Sirbu BM, Couch FB, Feigerle JT, Bhaskara S, Hiebert SW, Cortez D. 2011. Analysis of protein dynamics at active, stalled, and collapsed replication forks. Genes Dev 25:1320–1327. https://doi.org/10.1101/gad.2053211.

29. Sirbu BM, Couch FB, Cortez D. 2012. Monitoring the spatiotemporal dynamics of proteins at replication forks and in assembled chromatin using isolation of proteins on nascent DNA. Nat Protoc 7:594–605. https://doi.org/10.1038/nprot.2012.010.

30. Essers J, Theil AF, Baldeyron C, van Cappellen WA, Houtsmuller AB, Kanaar R, Vermeulen W. 2005. Nuclear dynamics of PCNA in DNA replication and repair. Mol Cell Biol 25:9350–9359. https://doi.org/10.1128/MCB.25.21.9350-9359.2005.

31. Davis AJ, Chi L, So S, Lee K-J, Mori E, Fattah K, Yang J, Chen DJ. 2014. BRCA1 modulates the autophosphorylation status of DNA-PKcs in S phase of the cell cycle. Nucleic Acids Res 42:11487–11501. https://doi.org/10.1093/nar/gku824.

32. Vannier JB, Sandhu S, Petalcorin MI, Wu X, Nabi Z, Ding H, Boulton SJ. 2013. RTEL1 is a replisome-associated helicase that promotes telomere and genome-wide replication. Science 342:239–242. https://doi.org/10.1126/science.1241779.

33. Ying S, Hamdy FC, Helleday T. 2012. Mre11-dependent degradation of stalled DNA replication forks is prevented by BRCA2 and PARP1. Cancer Res 72:2814–2821. https://doi.org/10.1158/1538-7445.AM2012-2814.

34. Schlacher K, Wu H, Jasin M. 2012. A distinct replication fork protection pathway connects Fanconi anemia tumor suppressors to RAD51-BRCA1/2. Cancer Cell 22:106–116. https://doi.org/10.1016/j.ccr.2012.05.015.

35. Dupre A, Boyer-Chatenet L, Sattler RM, Modi AP, Lee J-H, Nicolette ML, Kopelovich L, Jasin M, Baer R, Paull TT, Gautier J. 2008. A forward chemical genetic screen reveals an inhibitor of the Mre11-Rad50-Nbs1 complex. Nat Chem Biol 5:119–125. https://doi.org/10.1038/nchembio.63.

36. Huang F, Motlekar NA, Burgwin CM, Napper AD, Diamond SL, Mazin AV. 2011. Identification of specific inhibitors of human RAD51 recombinase using high-throughput screening. ACS Chem Biol 6:628–635. https://doi.org/10.1021/cb100428c.

37. Schlacher K, Christ N, Siaud N, Egashira A, Wu H, Jasin M. 2011. Double-strand break repair-independent role for BRCA2 in blocking stalled replication fork degradation by MRE11. Cell 145:529–542. https://doi.org/10.1016/j.cell.2011.03.041.

38. Davies SL, North PS, Hickson ID. 2007. Role for BLM in replication-fork restart and suppression of origin firing after replicative stress. Nat Struct Mol Biol 14:677–679. https://doi.org/10.1038/nsmb1267.

39. Petermann E, Luis Orta M, Issaeva N, Schultz N, Helleday T. 2010. Hydroxyurea-stalled replication forks become progressively inactivated and require two different RAD51-mediated pathways for restart and repair. Mol Cell 37:492–502. https://doi.org/10.1016/j.molcel.2010.01.021.

40. Gelot C, Lopez BS. 2015. Replication stress in mammalian cells and its consequences for mitosis. Genes 6:267–298. https://doi.org/10.3390/genes6020267.

41. Itano HA, Hirota K, Hosokawa K. 1975. Mechanism of induction of haemolytic anaemia by phenylhydrazine. Nature 256:665–667. https://doi.org/10.1038/256665a0.

42. Paulson RF, Shi L, Wu D-C. 2011. Stress erythropoiesis: new signals and new stress progenitor cells. Curr Opin Hematol 18:139. https://doi.org/10.1097/MOH.0b013e32834521c8.

43. Farres J, Llacuna L, Martin-Caballero J, Martínez C, Lozano J, Ampurdanés C, López-Contreras A, Florensa L, Navarro J, Ottina E. 2015. PARP-2 sustains erythropoiesis in mice by limiting replicative stress in erythroid progenitors. Cell Death Differ 22:1144. https://doi.org/10.1038/cdd.2014.202.

44. Ganem NJ, Godinho SA, Pellman D. 2009. A mechanism linking extra centrosomes to chromosomal instability. Nature 460:278–282. https://doi.org/10.1038/nature08136.

45. Fenech M. 2000. The in vitro micronucleus technique. Mutat Res 455:81–95. https://doi.org/10.1016/S0027-5107(00)00065-8.

46. Fenech M. 1993. The cytokinesis-block micronucleus technique: a detailed description of the method and its application to genotoxicity studies in human populations. Mutat Res 285:35–44. https://doi.org/10.1016/0027-5107(93)90049-L.

47. Ding H, Schertzer M, Wu XL, Gertsenstein M, Selig S, Kammori M, Pourvali R, Poon S, Vulto I, Chavez E, Tam PPL, Nagy A, Lansdorp PM. 2004. Regulation of murine telomere length by Rtel: an essential gene encoding a helicase-like protein. Cell 117:873–886. https://doi.org/10.1016/j.cell.2004.05.026.

48. Burdon T, Smith A, Savatier P. 2002. Signalling, cell cycle and pluripotency in embryonic stem cells. Trends Cell Biol 12:432–438. https://doi.org/10.1016/S0962-8924(02)02352-8.

49. Ahuja AK, Jodkowska K, Teloni F, Bizard AH, Zellweger R, Herrador R, Ortega S, Hickson ID, Altmeyer M, Mendez J. 2016. A short G_1 phase imposes constitutive replication stress and fork remodelling in mouse embryonic stem cells. Nat Commun 7:10660. https://doi.org/10.1038/ncomms10660.

50. Lindahl T, Barnes DE. 2000. Repair of endogenous DNA damage. Cold Spring Harbor Symp Quant Biol 65:127–133. https://doi.org/10.1101/sqb.2000.65.127.

51. Sidorova JM, Kehrli K, Mao F, Monnat R, Jr. 2013. Distinct functions of human RECQ helicases WRN and BLM in replication fork recovery and progression after hydroxyurea-induced stalling. DNA Repair 12:128–139. https://doi.org/10.1016/j.dnarep.2012.11.005.

52. White J, Dalton S. 2005. Cell cycle control of embryonic stem cells. Stem Cell Rev 1:131–138. https://doi.org/10.1385/SCR:1:2:131.

53. Chuykin IA, Lianguzova MS, Pospelova TV, Pospelov VA. 2008. Activation of DNA damage response signaling in mouse embryonic stem cells. Cell Cycle 7:2922–2928. https://doi.org/10.4161/cc.7.18.6699.

54. Banath J, Banuelos C, Klokov D, MacPhail S, Lansdorp P, Olive P. 2009. Explanation for excessive DNA single-strand breaks and endogenous repair foci in pluripotent mouse embryonic stem cells. Exp Cell Res 315:1505–1520. https://doi.org/10.1016/j.yexcr.2008.12.007.

55. Schwenk F, Baron U, Rajewsky K. 1995. A cre-transgenic mouse strain for the ubiquitous deletion of loxP-flanked gene segments including deletion in germ cells. Nucleic Acids Res 23:5080. https://doi.org/10.1093/nar/23.24.5080.

56. Ying Q-L, Wray J, Nichols J, Batlle-Morera L, Doble B, Woodgett J, Cohen P, Smith A. 2008. The ground state of embryonic stem cell self-renewal. Nature 453:519-U5. https://doi.org/10.1038/nature06968.

57. Schwab RA, Niedzwiedz W. 2011. Visualization of DNA replication in the vertebrate model system DT40 using the DNA fiber technique. J Vis Exp 56:e3255. https://doi.org/10.3791/3255.

58. Gyori BM, Venkatachalam G, Thiagarajan P, Hsu D, Clement M-V. 2014. OpenComet: an automated tool for comet assay image analysis. Redox Biol 2:457–465. https://doi.org/10.1016/j.redox.2013.12.020.

59. Wolff S, Perry P. 1974. Differential Giemsa staining of sister chromatids and the study of sister chromatid exchanges without autoradiography. Chromosoma 48:341–353. https://doi.org/10.1007/BF00290991.

60. Chuma S, Nakatsuji N. 2001. Autonomous transition into meiosis of mouse fetal germ cells in vitro and its inhibition by gp130-mediated signaling. Dev Biol 229:468–479. https://doi.org/10.1006/dbio.2000.9989.

Molecular Cell

Piwi Modulates Chromatin Accessibility by Regulating Multiple Factors Including Histone H1 to Repress Transposons

Graphical Abstract
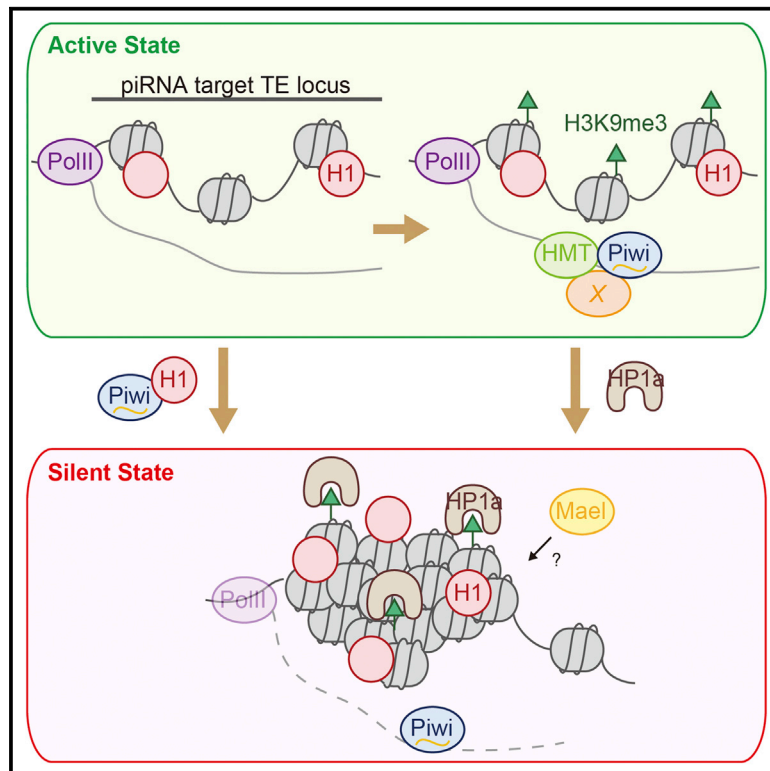
Authors

Yuka W. Iwasaki, Kensaku Murano, Hirotsugu Ishizu, ..., Mikiko C. Siomi, Haruhiko Siomi, Kuniaki Saito

Correspondence

awa403@keio.jp (H.S.),
saito@z6.keio.jp (K.S.)

In Brief

Piwi-piRNA complexes silence transposons in animal gonads. Iwasaki et al. identify linker histone H1 as a component of nuclear Piwi-piRNA complexes and show that Piwi-piRNA complexes require both H1 and HP1a to repress targets and that the transcriptional silencing is correlated with the chromatin state rather than H3K9me3 marks.

Highlights

- Piwi forms a complex with H1 to regulate H1 association to target transposon loci

- H1 regulates Piwi target transposons independently of H3K9me3 modification

- Piwi transcriptionally silences its targets by modulating chromatin accessibility

- H1 and HP1a interdependently regulate chromatin accessibility at Piwi target loci

Accession Numbers

GSE81434

CellPress

Piwi Modulates Chromatin Accessibility by Regulating Multiple Factors Including Histone H1 to Repress Transposons

Yuka W. Iwasaki,[1] Kensaku Murano,[1] Hirotsugu Ishizu,[2] Aoi Shibuya,[1] Yumiko Iyoda,[1] Mikiko C. Siomi,[2] Haruhiko Siomi,[1,*] and Kuniaki Saito[1,*]

[1]Department of Molecular Biology, Keio University School of Medicine, Tokyo 160-8582, Japan
[2]Department of Biological Sciences, Graduate School of Science, The University of Tokyo, Tokyo 113-0032, Japan
*Correspondence: awa403@keio.jp (H.S.), saito@z6.keio.jp (K.S.)
http://dx.doi.org/10.1016/j.molcel.2016.06.008

SUMMARY

PIWI-interacting RNAs (piRNAs) mediate transcriptional and post-transcriptional silencing of transposable element (TE) in animal gonads. In *Drosophila* ovaries, Piwi-piRNA complexes (Piwi-piRISCs) repress TE transcription by modifying the chromatin state, such as by H3K9 trimethylation. Here, we demonstrate that Piwi physically interacts with linker histone H1. Depletion of Piwi decreases H1 density at a subset of TEs, leading to their derepression. Silencing at these loci separately requires H1 and H3K9me3 and heterochromatin protein 1a (HP1a). Loss of H1 increases target loci chromatin accessibility without affecting H3K9me3 density at these loci, while loss of HP1a does not impact H1 density. Thus, Piwi-piRISCs require both H1 and HP1a to repress TEs, and the silencing is correlated with the chromatin state rather than H3K9me3 marks. These findings suggest that Piwi-piRISCs regulate the interaction of chromatin components with target loci to maintain silencing of TEs through the modulation of chromatin accessibility.

INTRODUCTION

Movement of mobile DNA elements such as transposable elements (TEs) can result in deleterious mutations on the host genome (Goodier and Kazazian, 2008). piRNAs are a class of small non-coding RNAs that associate with PIWI proteins and guide piRNA-induced silencing complexes (piRISCs) to target and repress TEs (Ge and Zamore, 2013; Iwasaki et al., 2015). PIWI proteins and piRNAs are expressed almost exclusively in the animal germline, and defects of Piwi-piRNA silencing result in activation of TEs and a sterile phenotype, underlining the importance of TE regulation and maintenance of genome integrity.

Among three PIWI proteins expressed in the *Drosophila* ovary, Aubergine (Aub) and AGO3 cleave complementary TE transcripts by small RNA-guided endoribonuclease (Slicer) activity in the cytoplasm of germline cells (Brennecke et al., 2007; Gunawardane et al., 2007). In contrast, Piwi is located in the nucleus of both germline cells and surrounding somatic cells (Cox et al., 2000). TE silencing by Piwi operates at the transcriptional level in a slicer-independent manner (Klenov et al., 2011; Le Thomas et al., 2013; Rozhkov et al., 2013; Saito et al., 2010; Sienski et al., 2012; Wang and Elgin, 2011). piRNAs form a complex with Piwi at the cytoplasmic Yb-body, and only Piwi proteins loaded with a piRNA are imported into the nucleus to silence their targets. Within the nucleus, Piwi-piRISCs repress TEs transcriptionally, and H3K9 trimethylation (H3K9me3) coincides with silenced TEs. Piwi is expressed in the cell line Ovarian Somatic Cell (OSC) (Saito et al., 2009). Earlier studies showed that OSC reproduces the Piwi-piRNA pathway observed in somatic cells of *Drosophila* ovaries (Dönertas et al., 2013; Ishizu et al., 2015; Muerdter et al., 2013; Ohtani et al., 2013; Post et al., 2014; Saito et al., 2009, 2010; Sienski et al., 2012), and therefore the cell line represents a very powerful system to elucidate how Piwi-piRISCs repress TEs.

Heterochromatin is characterized by H3K9me3 repressive epigenetic marks (Nakayama et al., 2001; Rea et al., 2000; Schotta et al., 2002), associated with Heterochromatin protein 1 (HP1a in *Drosophila*) (Bannister et al., 2001; Eissenberg et al., 1990; Lachner et al., 2001). Spread of H3K9me3 marks leads to heterochromatin formation on target TE loci (Le Thomas et al., 2013; Rozhkov et al., 2013; Sienski et al., 2012; Wang and Elgin, 2011). Maelstrom (Mael), DmGTSF1/Asterix (Arx), and HP1a are putative Piwi cofactors (Brower-Toland et al., 2007; Czech et al., 2013; Dönertas et al., 2013; Le Thomas et al., 2013; Muerdter et al., 2013; Ohtani et al., 2013; Sienski et al., 2012; Wang and Elgin, 2011), and recent genetic screening studies suggested several other factors are involved in Piwi-mediated transcriptional silencing (Czech et al., 2013; Handler et al., 2013; Muerdter et al., 2013). Mael and DmGTSF1/Arx regulate RNA polymerase II recruitment and RNA levels of Piwi target TEs (Dönertas et al., 2013; Muerdter et al., 2013; Ohtani et al., 2013; Sienski et al., 2012). HP1a regulates many TEs including those targeted by Piwi, and loss of Piwi reduces HP1a association to Piwi target TE loci (Brower-Toland et al., 2007; Le Thomas et al., 2013; Wang and Elgin, 2011). However, depletion of piRNA pathway genes leads to different outcomes at the level of H3K9me3 (Dönertas et al., 2013; Klenov et al., 2014; Muerdter et al., 2013; Ohtani et al., 2013; Sienski et al., 2012). Piwi
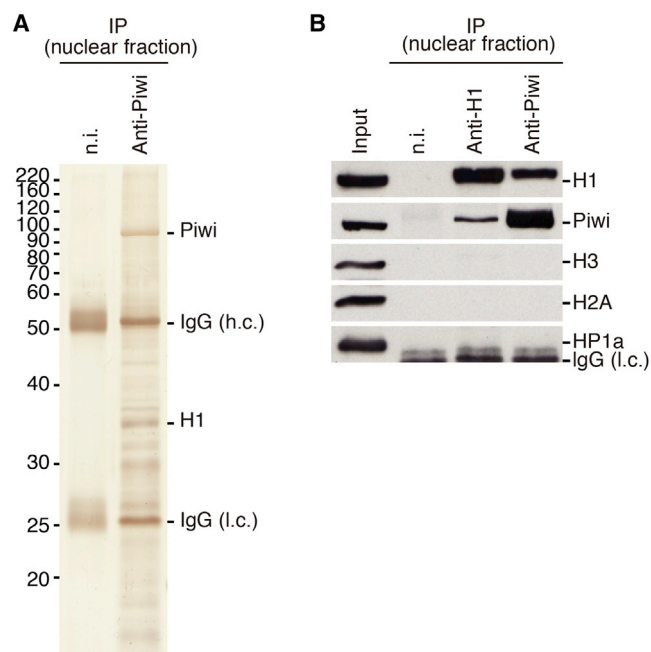
Figure 1. H1 Physically Associates with Nuclear Piwi

(A) Silver staining of nuclear protein components in the anti-Piwi immunoprecipitated complex. Immunoprecipitation was performed using OSC nuclear extracts under stringent conditions. h.c., heavy chain; l.c., light chain of the antibody.

(B) Western blot showing H1, Piwi, H3, H2A, and HP1a protein levels in the nuclear complex immunoprecipitated from OSCs using indicated antibodies. Mouse immunoglublin G (IgG) (n.i.) was used for control immunoprecipitations.

See also Figures S1 and S2.

knockdown (KD) or DmGTSF1/Arx-KD decreases H3K9me3 levels at Piwi target TE loci, whereas Mael-KD does not, suggesting that H3K9me3 per se is not the final silencing mark for transcriptional gene silencing mediated by Piwi-piRNA complexes. Thus, it is unclear how H3K9me3 mark contributes to Piwi-piRISC-mediated TE silencing, and the final effector of this transcriptional silencing pathway is unknown.

Chromatin compaction by heterochromatin results in repression of genes encoded at corresponding regions (Li and Reinberg, 2011). Linker histone H1 confers higher-order organization to chromatin by direct binding with nucleosomes, making genes inaccessible to specific transcription factors to prevent their expression (Buttinelli et al., 1999; Laybourn and Kadonaga, 1991; Pennings et al., 1994). However, interaction of H1 with nucleosomes is only transient; its nucleosome residing time is modulated by posttranslational modifications in H1 or by nuclear proteins that interact with H1 or compete with H1 for nucleosome binding sites (Bustin et al., 2005; Misteli et al., 2000). Recently, H1 was reported to be required for TE repression in *Drosophila* (Lu et al., 2013; Vujatovic et al., 2012). H1 may recruit Su(var)3-9 methyltransferase to TE loci, resulting in the addition of H3K9me3 marks (Lu et al., 2013). However, a systematic understanding of how H1 is recruited to specific TE loci and how H3K9me3 modification induces TE silencing is unclear.

In this study, we identified H1 as a component of a nuclear Piwi complex. Using OSCs, we found that loss of Piwi results in a specific decrease of H1 density at Piwi target TE loci and their surrounding genomic regions, suggesting that Piwi enforces association of H1 to its target TE loci. Depletion of H1 derepresses a variety of TEs and their surrounding genes, including those normally silenced by Piwi-piRISCs, without affecting the density of H3K9me3 mark and HP1a at target TE loci. We demonstrated that chromatin accessibility at Piwi target TE loci is modulated by H1. Notably, depletion of HP1a also resulted in increased chromatin accessibility at Piwi target TE loci. These findings suggest that Piwi-piRISCs adopt interdependent actions of H1 and HP1a to maintain silencing of the TE state by modulating the chromatin state.

RESULTS

Piwi Forms a Complex with Linker Histone H1

To gain insights into the molecular pathway leading to Piwi-piRISC-mediated TE silencing, we immunopurified Piwi-associated complexes from OSC nuclear lysates. These complexes were subjected to SDS-PAGE gel electrophoresis followed by silver staining. Several specific protein bands were observed, and mass spectrometric analyses identified a 34-kDa band as linker histone H1, suggesting that H1 associates with Piwi in the nucleus (Figures 1A and S1A). To confirm the H1-Piwi association, we produced a specific monoclonal antibody against H1. Western blotting showed a discrete band at 34 kDa in OSC and ovary lysates but not in OSCs where H1 was depleted by RNAi, indicating that the antibody specifically recognizes H1 (Figure S1B). Using the antibody, we immunopurified H1-associated complexes from OSC nuclear lysates or *Drosophila* ovary lysates. Western blots of immunoprecipitates confirmed that Piwi, but not the core nucleosome proteins, histone H3 and H2A or HP1a, was present in the H1-associated complex (Figures 1B, S1C, and S1D). Thus, although H1 is a highly charged abundant nuclear protein, it specifically interacts with Piwi (Figure S1E).

We also performed an in vitro pull-down assay using recombinant H1 fused to glutathione S-transferase (GST-H1) and crude OSC lysates (Figure S1F). Piwi was detected in GST-H1 pull-down products, confirming the association in vitro. Because it is unlikely that GST-H1 is modified at specific H1 amino acid residues, which may occur in vivo (Bonet-Costa et al., 2012), specific protein modifications do not appear to require this interaction. Moreover, the addition of DNase or RNase did not affect interactions between H1 and Piwi (Figure S1G).

H1 Is Required for TE Silencing

To explore whether H1 is involved in Piwi-piRISC-mediated transcriptional silencing of TEs in OSCs, we depleted H1 by RNAi (Figure S2A). We isolated total RNA from 4-day KD samples, performed RNA-sequencing (RNA-seq) analysis, and compared RNA expression profiles with control EGFP RNAi. Overall, 82 (63.6%) TE transcripts of 129 annotated TEs were increased >2-fold, whereas 999 (7.1%) protein-coding genes were upregulated >2-fold in H1-depleted cells, revealing a major repressive effect of H1 on OSC TE expression (Figure 2A). Furthermore, qRT-PCR of *mdg1*, a TE regulated by the somatic Piwi-piRNA
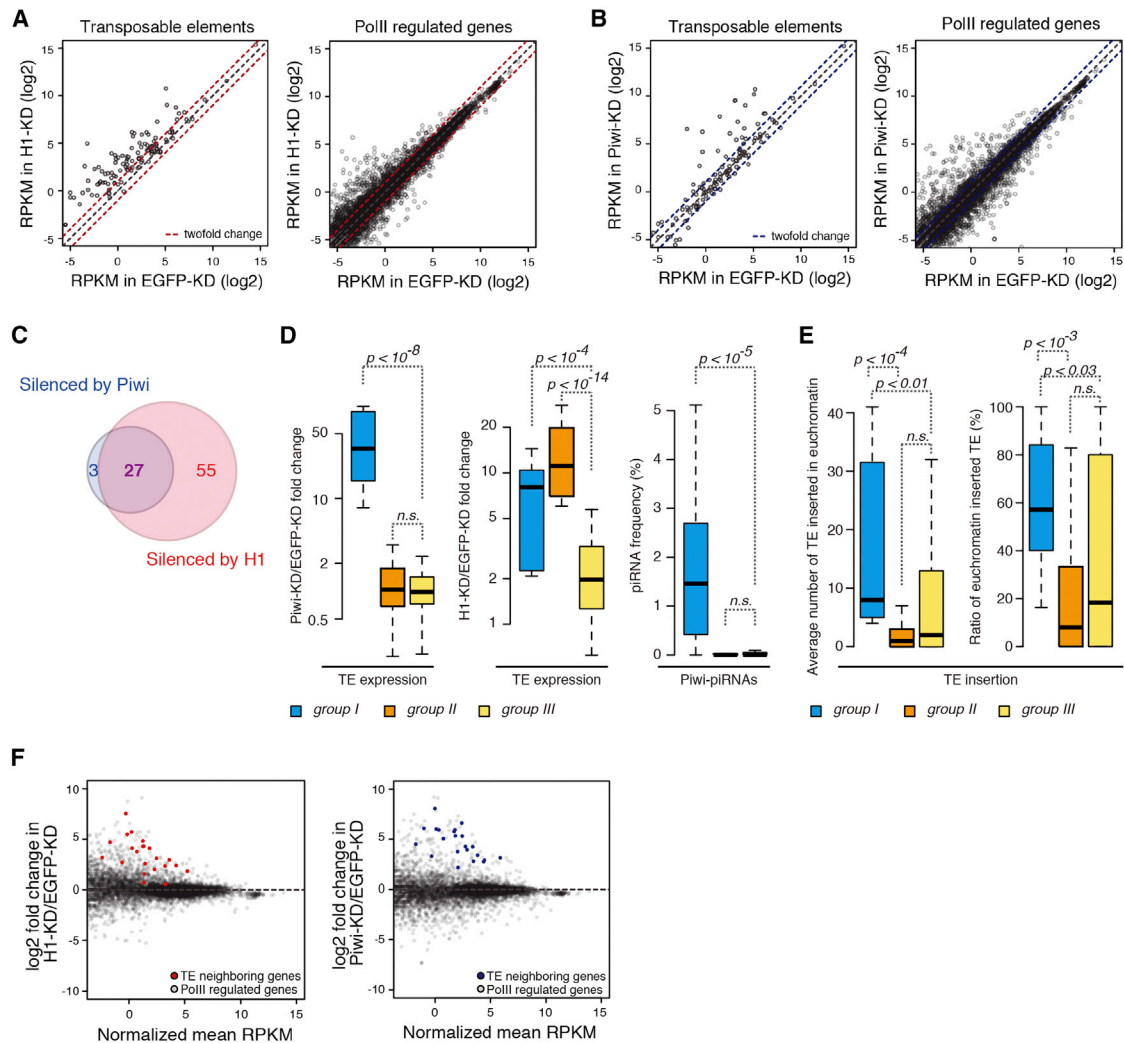
Figure 2. H1 Is Essential for Silencing of TEs Targeted by the Piwi-piRNA Pathway

(A) Scatterplot of RPKM values (log$_2$) for 129 TEs (left) or 14,145 Pol II-regulated genes (right) in EGFP-KD (control, x axis) or H1-KD (y axis) samples examined by RNA-seq. Red diagonal lines indicate 2-fold change.

(B) Scatterplot as in (A) for EGFP-KD (x axis) or Piwi-KD (y axis) samples. Blue diagonal lines indicate 2-fold change.

(C) Venn diagram displaying the number of >2-fold upregulated TEs upon depletion of Piwi (blue) or H1 (red).

(D) Boxplots showing fold changes in the expression of group I, II, and III TEs based on RNA-seq upon Piwi (left)- or H1 (center)-KD. Boxplot on the right shows frequency of piRNAs targeting group I, II, and III TEs. Boxplot whiskers show maxima and minima. p values were calculated by Wilcoxon rank-sum test, and y axis is log$_2$ scale. n.s.; not significant (p > 0.05).

(E) Boxplots, as in (D), show average number of TEs inserted in euchromatin (left) or ratio of euchromatin-inserted TEs (right) in group I, II, and III TEs.

(F) MA plot showing changes in RNA abundance for set of Pol II-regulated genes upon H1 (left)- or Piwi (right)-KD based on RNA-seq. Twenty-two genes with TE insertions either in the gene body or close proximity (<5 kb away) and upregulated <4-fold in Piwi-KD cells are plotted in red (left) or blue (right), while other genes are plotted in gray.

See also Figures S2 and S3.

pathway (Sienski et al., 2012), confirmed that its expression was activated as much as 80-fold in H1-KD cells (Figure S2B). Under conditions where endogenous H1 was depleted, expression of myc-H1r, which was designed to be RNAi insensitive, rescued *mdg1* repression (Figure S2C). Thus, activation of TE expression results from H1 protein decrease in OSCs. H1 loss did not affect the nuclear localization of Piwi (Figure S2D). Moreover, expression levels of piRNAs, which were severely decreased by the loss of Piwi were unaffected by H1 loss (Figure S2E).

We confirmed this by deep sequencing of Piwi-associated piR-NAs upon control (EGFP) and H1-KD (Figures S2F and S2G). Levels of piRNAs mapped to the somatic piRNA cluster *flamenco* and the genic piRNA locus *traffic jam*, and those mapped to TEs remained unchanged upon H1-KD (Figures S2H–S2J), indicating that general piRNA biogenesis does not require H1. An exception was an increase of piRNAs mapped to *roo*, which was consistent with a previous study (Lu et al., 2013). Expression of *roo* TE, how-ever, was unchanged by either H1- or Piwi-KD (Figure S3). These

163

results suggest that H1 is involved in the silencing step, rather than piRNA biogenesis, of the Piwi-piRNA pathway.

We delineated the region of H1 responsible for TE silencing. H1 is a tripartite protein consisting of a central globular DNA-binding domain flanked by lysine-rich regions at both N- and C-terminal domains (Figure S2K). Absence of C-terminal or N-terminal regions had no effect on nuclear localization (Figure S2L), and deletion of the C-terminal but not N-terminal region failed to rescue *mdg1* repression, indicating the requirement of the C-terminal region for TE silencing (Figure S2M). This C-terminal region of the H1 protein is sufficient for Piwi binding (Figure S2N). However, the same region of H1 is also known to be important for condensing chromatin in general (Zhou et al., 2013, 2015). We also found that the N-terminal region (amino acids 1–130) of the Piwi protein is essential for H1 interaction (Figure S2O). The N-terminal region (amino acids 1–72) of Piwi is known to be responsible for its nuclear localization (Saito et al., 2009), and, as we expected, Piwi lacking the N-terminal region (amino acids 1–130) was unable to localize to the nucleus (data not shown). These results show that the C-terminal region of H1 and the N-terminal region of Piwi interact with each other. However, it is difficult to definitively rule out the possibility that the regions responsible for this interaction are also essential for other functions.

H1 Regulates TEs, Including Those Targeted by the Piwi-piRNA Pathway

Over 60% of TE transcripts were increased >2-fold in H1-depleted cells (Figure 2A). To compare transcript levels in H1- or Piwi-depleted OSCs, we analyzed our RNA-seq data. Consistent with previous studies (Ohtani et al., 2013; Sienski et al., 2012), only a limited number of TE families (30/129, 23.3%) were increased >2-fold upon Piwi-KD (Figure 2B), almost all of which (27/30, 90%) were increased in H1-KD cells (Figures 2A–2C). Based on RNA-seq data, we classified TEs into three groups. TEs without mapped reads were excluded, because they are likely to be "dead" TEs. Thirteen TEs in group I exhibited >6-fold increase of mRNA expression in Piwi-KD cells. The 6-fold increase was used as a threshold based on the average fraction of piRNA frequency per TEs (Figure S3A, top). Of the remaining TEs, 29 upregulated expression >6-fold in H1-KD and were classified as group II. Other TEs (n = 76) were categorized as group III and underwent moderate changes of expression upon Piwi- or H1-KD (Figure S3B). Importantly, the Piwi-KD fold-change threshold was compatible with the fraction of TEs regulated by H1 (Figure S3A, bottom), supporting that H1 correlates with Piwi-regulated TE silencing and has a role in the piRNA pathway. Group II TEs were significantly repressed by H1 but not Piwi, implying that H1 may discriminate TEs in a piRNA-dependent (group I) or -independent manner (group II), while some TEs were independent of regulation by Piwi or H1 (group III) (Figures 2D and S3C). Selected examples of each group were analyzed by qRT-PCR to confirm the RNA-seq data (Figure S3D).

Both group I and group II TEs were regulated by H1, but only group I TEs were targeted by piRNAs (Figure 2D). Thus, we investigated features to separate these two groups. Most TEs in group I were long terminal repeat (LTR) elements (92.3%), except for the DNA element *transib2* (Figure S3C). In contrast,

only 58.6% of group II TEs were LTR elements. Genomic insertion sites and numbers of each TE indicated that group I TEs had significantly larger numbers of insertions in euchromatin regions compared to group II TEs ($p < 10^{-4}$) (Figure 2E, left). Additionally, the ratio of euchromatic insertions against the total number of the genomic insertions was higher for group I TEs ($p < 10^{-3}$) (Figure 2E, right). Thus, group I TEs are mostly LTR elements, which accumulate in euchromatic regions, whereas group II TEs tend to consist of various elements inserted in both euchromatic and heterochromatic regions.

Depletion of piRISC components influences the expression of a subset of protein-coding genes near TE insertions (Ohtani et al., 2013; Sienski et al., 2012). To assess the role of H1, we analyzed RNA-seq data of 22 genes, for which TE insertions were either in the gene body or in close proximity (<5 kb away) and which were upregulated in Piwi-KD OSCs (Sienski et al., 2012). As expected, >90% (20 of 22) of genes with a 4-fold change upon Piwi-KD were also highly upregulated upon H1-KD (Figure 2F). Moreover, variation in expression of TE neighboring genes was highly comparable between H1- and Piwi-KD cells (r = 0.95; Figure S3E). Collectively, these data strongly support the notion that H1 is a component of the Piwi-piRNA-mediated silencing pathway.

Piwi Regulates Association of H1 to Piwi-piRNA Target TE Loci

To elucidate how H1 functions in Piwi-mediated TE silencing, we verified H1 binding to chromatin in OSCs. Because H1 association with DNA inhibits nucleosome mobility and transcription in vitro (Laybourn and Kadonaga, 1991; Pennings et al., 1994), and that H1 is required for Piwi-dependent transcriptional silencing (Figure 2), we hypothesized that Piwi may act upstream of H1 by regulating its association with the target TE locus. To test this, we studied the association of H1 with TE loci using chromatin immunoprecipitation sequencing (ChIP-seq) analysis under Piwi-KD. Piwi-KD reduced H1 density throughout the entire TE consensus sequences on group I but not group II or III TEs (Figure 3A). We further confirmed the group I TE (*mdg1*)-specific decrease in the H1 ChIP signal upon Piwi-KD by ChIP-qPCR analyses (Figure S4A). These data indicated that Piwi is specifically required for H1 to associate with group I TEs.

Previously, Piwi-KD was shown to increase the occupancy of Pol II within an ∼15-kb region flanking euchromatic TE insertions (Sienski et al., 2012). We analyzed the H1 density in regions flanking euchromatic TE insertions and found that the ∼15-kb extension feature was also observed in H1 density (Figure 3B) on group I, but not group II or group III TE insertions, indicating that the H1 association with group I TEs is controlled by the Piwi-piRNA pathway. Because we focused on several representative TEs in each group (Figures 3A and 3B), we analyzed ChIP-seq data of the complete set of group I, II, and III TEs to determine whether Piwi-regulated H1 association with TE loci was reflected within the entire set of group I TEs. Comparison of ChIP-seq signal fold changes demonstrated a significant decrease in H1 occupancy upon Piwi loss for group I TEs compared with group III TEs ($p < 0.02$) (Figure 3C). Moreover, H1 occupancy was further decreased ($p < 10^{-3}$) when we collected TEs derepressed >20-fold upon Piwi loss (group I-20; Figure S3C). By contrast, no
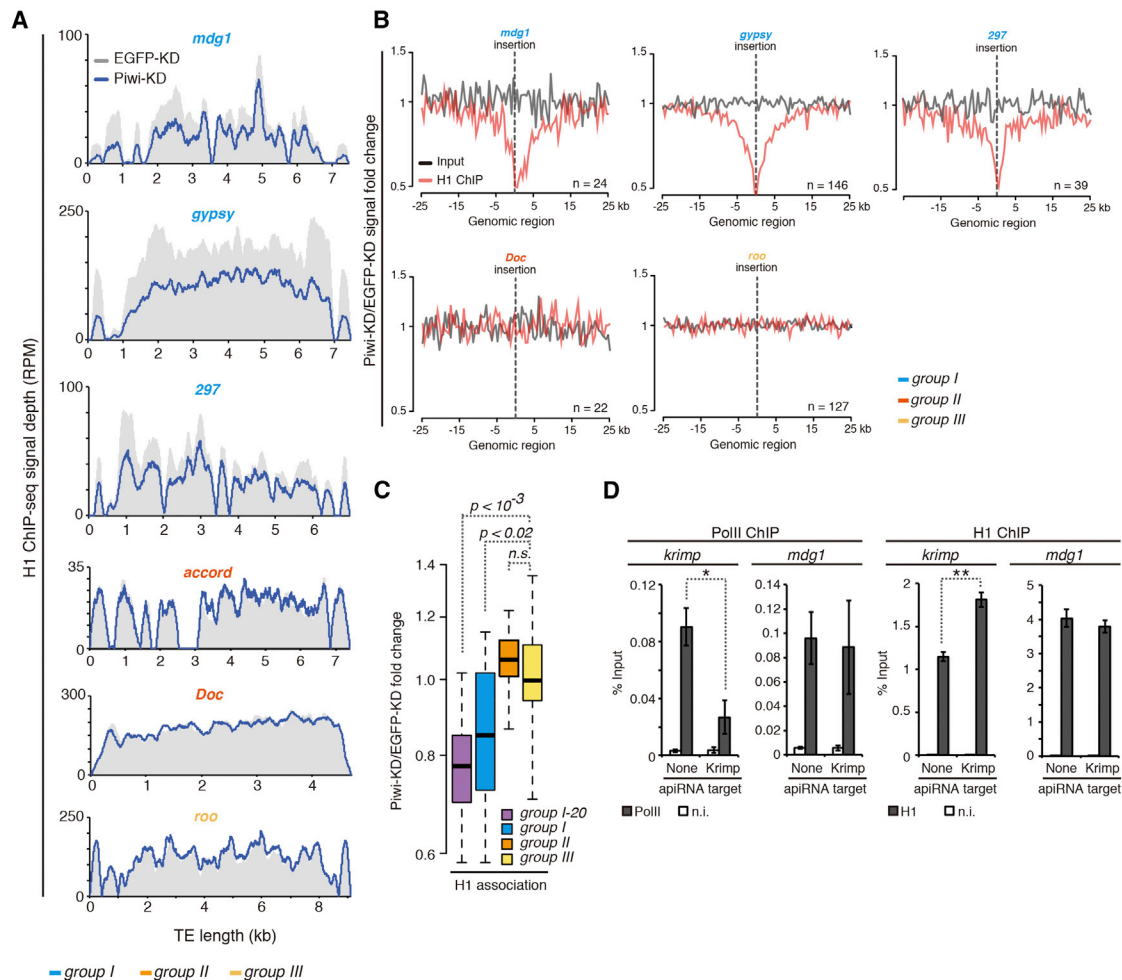
164

Figure 3. Association of H1 with piRNA Target TE Loci Is Regulated by Piwi

(A) Density plots for normalized H1 ChIP-seq signals over consensus sequences from group I, II, and III TEs in EGFP (control)- or Piwi-KD cells. ChIP signal depths on EGFP (gray)- and Piwi (blue)-KD samples are shown. Note that *accord* had only one euchromatic insertion, and therefore metaplot could not be calculated.

(B) Metaplots showing signal of H1 ChIP-seq for genomic regions around euchromatin insertions of group I, II, and III TEs. Fold-change in Piwi-KD compared with EGFP-KD is shown for H1 ChIP (red) and Input (gray) signals. y axis is $\log_2$ scale.

(C) Boxplot, as in Figure 2, showing fold changes in the association of H1 with group I, II, and III TEs upon depletion of Piwi, based on ChIP-seq. Group I-20 TEs are a population of group I TEs whose expression fold change was >20 in Piwi-KD samples compared with EGFP-KD samples.

(D) ChIP-qPCR analysis of RNA PolII (left) and H1 (right) occupancy on the *krimp* and *mdg1* promoter region, following expression of *krimp* targeting artificial piRNA (apiRNA). apiRNAs expressed without target genes (None) were used as a negative control. Error bars represent means ± SEM values of three independent experiments. *p < 0.05; **p < 0.005.

See also Figure S4.

significant difference was observed between group II and III TEs (Figure 3C), whose expression levels were unaffected by Piwi-KD (Figure 2D). Thus, the Piwi-regulated H1 occupancy on TE loci correlated with the degree of TE expression regulated by Piwi and supported our notion that H1 density on group I TEs is regulated by the Piwi-piRNA pathway.

To corroborate our data, we applied an artificial piRNA (apiRNA) production system that targets and transcriptionally silences a gene of interest in OSCs (Figure S4B, left) (Ishizu et al., 2015). We confirmed that the expression of apiRNAs against *krimper (krimp)*, a protein coding gene expressed in naive OSCs, decreased Krimper protein levels and occupancy of Pol

II (Figures 3D, left, and S4B, right). Analysis of the level of H1 association with the *krimp* promoter region indicated that H1 density increased 1.6-fold by expression of apiRNA (Figure 3D, right) without affecting levels of *mdg1* TE. These results showed that apiRNAs induce the association of H1 with a target gene in a sequence-specific manner.

Piwi and H1 Regulate Targets by Modulating Chromatin Accessibility

Stable association of H1 functions in the compaction of chromatin into higher order structures, resulting in regulation of the encoded genes (Buttinelli et al., 1999; Laybourn and Kadonaga,
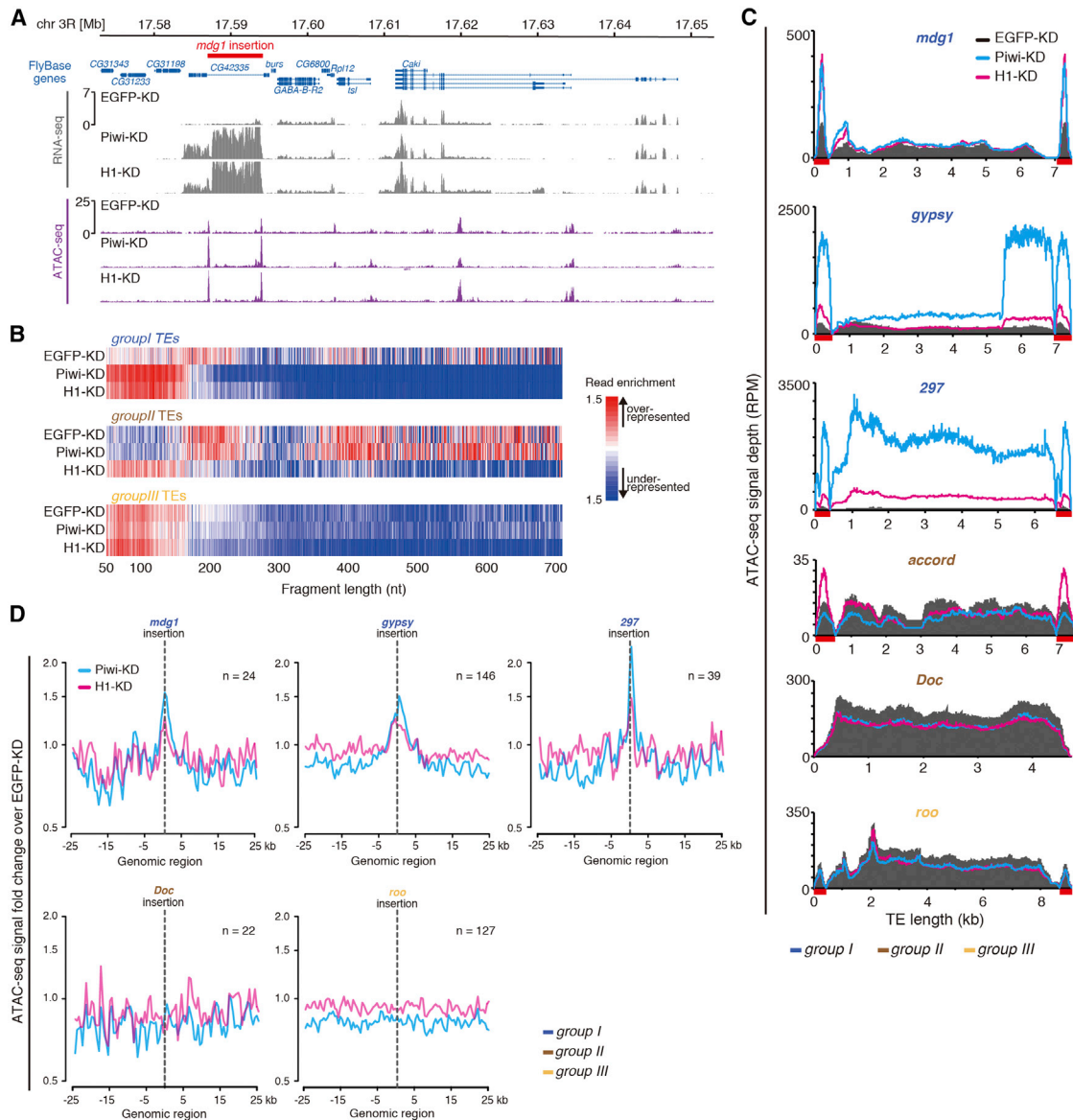
Figure 4. Piwi and H1 Modify Chromatin Accessibility to Silence Their Target TEs

(A) RNA-seq and ATAC-seq signal densities at genomic regions neighboring *mdg1* insertion are shown for OSCs with EGFP (control)- Piwi- or H1-KD. FlyBase protein-coding genes are indicated at the top, together with chromosome position.

(B) Read enrichments for three groups of TEs upon Piwi or H1-KD. Distributions of paired-end sequencing fragment sizes were calculated, and reads were normalized by percent maximal within each group of TEs. Enrichment was calculated relative to the genome-wide set of fragment sizes.

(C) Density plots for normalized ATAC-seq signals over consensus sequences from group I, II, and III TEs in EGFP-, Piwi- or H1-KD cells. ATAC-seq signal depths on EGFP (black)-, Piwi (blue)-, and H1 (pink)-KD samples are shown. LTR regions are shown by red line under x axis.

(D) Metaplots showing signal of ATAC-seq signal for genomic regions around euchromatin insertions of group I, II, and III TEs. Fold change in Piwi (blue)- or H1 (pink)-KD compared to EGFP-KD is shown. y axis is log2 scale.

See also Figure S4.

1991; Pennings et al., 1994). We hypothesized that Piwi-mediated recruitment of H1 resulted in chromatin compaction, leading to downregulation of Piwi-piRNA target TE expression. We performed transposase-accessible chromatin (ATAC)-seq analysis (Buenrostro et al., 2013) to profile open chromatin structures. ATAC-seq probe chromatin accessibility with Tn5 transposase, which integrates into accessible chromatin re-

gions. Therefore, genomic regions with open chromatin regions, such as transcription start sites (TSSs), result in accumulated ATAC-seq reads, whereas chromatin-dense regions result in decreased ATAC-seq signals (Figure 4A). Notably, only TSSs and not the gene body of transcribed genes had increased ATAC-seq signals, suggesting that ATAC-seq may be used to detect TSSs of coding genes. Indeed, we determined

ATAC-seq peaks from EGFP-, Piwi-, and H1-KD samples, and peaks commonly detected in EGFP- and Piwi/H1-KD samples were enriched in genomic regions neighboring TSSs (Figure S4C). In contrast, most peaks detected specifically in Piwi/H1-KD samples corresponded to intron or intergenic regions where TEs are enriched, rather than TSSs neighboring regions of genes (Figures S4C and S4D). Therefore, we further analyzed ATAC-seq signals at TE regions. First, we checked ATAC-seq fragment size, because accessible chromatin regions are enriched for short fragments, whereas regions with low chromatin accessibility are depleted of short fragments and enriched for phased multinucleosomal inserts (Buenrostro et al., 2013). The increase of short fragments for group I TEs after depletion of Piwi or H1 was detected, suggesting that Piwi and H1 are responsible for the regulation of chromatin accessibility at group I TEs. In contrast, increased shorter fragments were observed only in H1-KD samples for group II TEs, and Piwi or H1-KD did not affect the fraction size for group III TEs (Figure 4B). At steady state (EGFP-KD sample), shorter fragments were relatively under-represented in group II TEs compared to group I TEs. In agreement with the result showing that group I consists of larger fractions of TEs with euchromatic insertions (Figure 2E), these data suggest that group I TEs are located at regions with higher chromatin accessibility compared to group II TEs. Group III TEs tend to consist of TEs with shorter ATAC-seq fragment sizes, suggesting that these TEs are inserted in open chromatin regions. Group III TEs may be more ancient, degenerated TEs with lower transcriptional activity caused by mutations in their promoter region, or regulation by other mechanisms, and no longer pose a threat to *Drosophila*.

Distributions of ATAC-seq fragments within TE consensus sequences were analyzed upon Piwi and H1-KD. Depletion of Piwi and H1 increased ATAC-seq signal density for group I TEs (p < 10^{-5}, p < 10^{-3}) (Figures 4C and S4E). Increased ATAC-seq signals in Piwi- and H1-KD suggest that both modify chromatin accessibility at group I TE loci. Although the distribution of ATAC-seq fragments on each TE consensus sequence suggests a greater effect of Piwi than H1 on chromatin accessibility (Figure 4C), this may be explained by differences in efficiency of RNAi-KD (Figure S2A) or the other factor acting in parallel with H1 for modulation of chromatin accessibility. The distributions of ATAC-seq reads upon Piwi/H1-KD were commonly increased at LTR regions for each member of group I TEs. However, the distribution on the internal portion differed among TEs. We also profiled chromatin accessibility in regions flanking euchromatic TE insertions and found that the ∼5-kb extension feature was observed in ATAC-seq tag density (Figure 4D) on group I, but not group II or group III TE insertions, consistent with the result of H1-ChIP-seq analysis. This indicated that the effect on the state of chromatin also spreads to the flanking region of group I, but not group II or group III TE insertions. Together, these results show that the Piwi-piRNA pathway regulates its targets by recruiting H1 to modify chromatin accessibility.

H1 Is Required for TE Silencing but Not H3K9me3 Modification

To address how H1 affects chromatin states, we analyzed H3K9me3 signals by ChIP-seq. Consistent with previous studies

(Ohtani et al., 2013; Sienski et al., 2012), Piwi-KD significantly decreased H3K9me3 signals on group I TE loci (Figure 5A). By contrast, we observed only a slight difference in H3K9me3 density between H1-KD and EGFP-KD on group I TEs (p < 0.04) (Figures 5A and S5A, right). Moreover, no significant differences were observed for group I-20 TEs compared with group III TEs (Figure S5A, right), showing that, unlike Piwi-KD (Figure S5A, left), H1-KD does not significantly affect H3K9me3 levels. Meta-analysis of TE insertion sites and closer inspection of loci that harbor TE insertions showed that H1-KD does not affect H3K9me3 signals (Figures 5B and 5C), in contrast with earlier models suggesting that H1 recruits H3K9 methyltransferase Su(var)3-9 to chromatin (Lu et al., 2013). Increased Pol II occupancy on group I TEs in H1-KD cells (Figure S5B), and upregulation of TEs and their neighboring genes coupled with open chromatin structure and unaffected H3K9me3 marks upon depletion of H1, suggests that modulation of chromatin accessibility by H1 is responsible for transcriptional silencing, and that H3K9me3 itself is not the final silencing mark.

Several factors have been identified in the Piwi-piRNA pathway, including Mael and HP1a, which regulate expression of Piwi-piRNA target TEs but not H3K9me3 marks (Le Thomas et al., 2013; Sienski et al., 2012; Wang and Elgin, 2011). Because H1 acts downstream of or in parallel to H3K9me3, we analyzed the relationship between H1 and these factors within the Piwi-piRNA pathway. We performed H1 ChIP-seq analysis upon depletion of Mael or HP1a. Mael-KD did not result in a significant decrease of H1 ChIP-seq signals distributed at group I, II, and III TEs, and effects on neighboring regions of group I TE insertion sites were limited (Figures S5C–S5F). HP1a-KD resulted in a relatively mild decrease of H1 distribution at group I TEs and their neighboring regions (Figures S5G–S5J). For example, reads mapped to *mdg1*, *gypsy,* or *297* consensus TE decreased to 83.0%, 78.3%, or 76.0% upon HP1a-KD, where it decreased to 64.3%, 58.4%, or 69.7% upon Piwi-KD (Figures 3A and S5G). Additionally, Mael and HP1a were not detected in the complex containing Piwi and H1 (Figures 1B and S1E), suggesting that recruitment of H1 to group I TE loci is independent of Mael or HP1a.

H1 and HP1a Interdependently Modulate Chromatin Accessibility in the Piwi-piRNA Pathway

Previously, it was shown that H1 interacts with HP1a in mammals and *Drosophila* (Hale et al., 2006; Lu et al., 2013; Nielsen et al., 2001) and that H3K9me stabilizes the binding of HP1a to chromatin using mammals and yeast models (Bannister et al., 2001; Jacobs and Khorasanizadeh, 2002; Lachner et al., 2001; Nakayama et al., 2001). To analyze whether HP1a in the Piwi-piRNA pathway is regulated by H1 or H3K9me3 marks, we performed HP1a ChIP-seq analysis upon Piwi- or H1-KD. Consistent with previous studies showing that association of HP1a on several Piwi target TEs are regulated by Piwi (Wang and Elgin, 2011), and recruitment of HP1a to artificial piRNA target loci (Le Thomas et al., 2013), we observed the downregulation of HP1a signals upon Piwi-KD specifically at group I TEs (p < 10^{-3}) (Figures 6A and S6A), suggesting that HP1a also acts downstream of Piwi. However, H1-KD did not affect HP1a signal levels at the same loci (Figures 6A and S6A), and the effect of
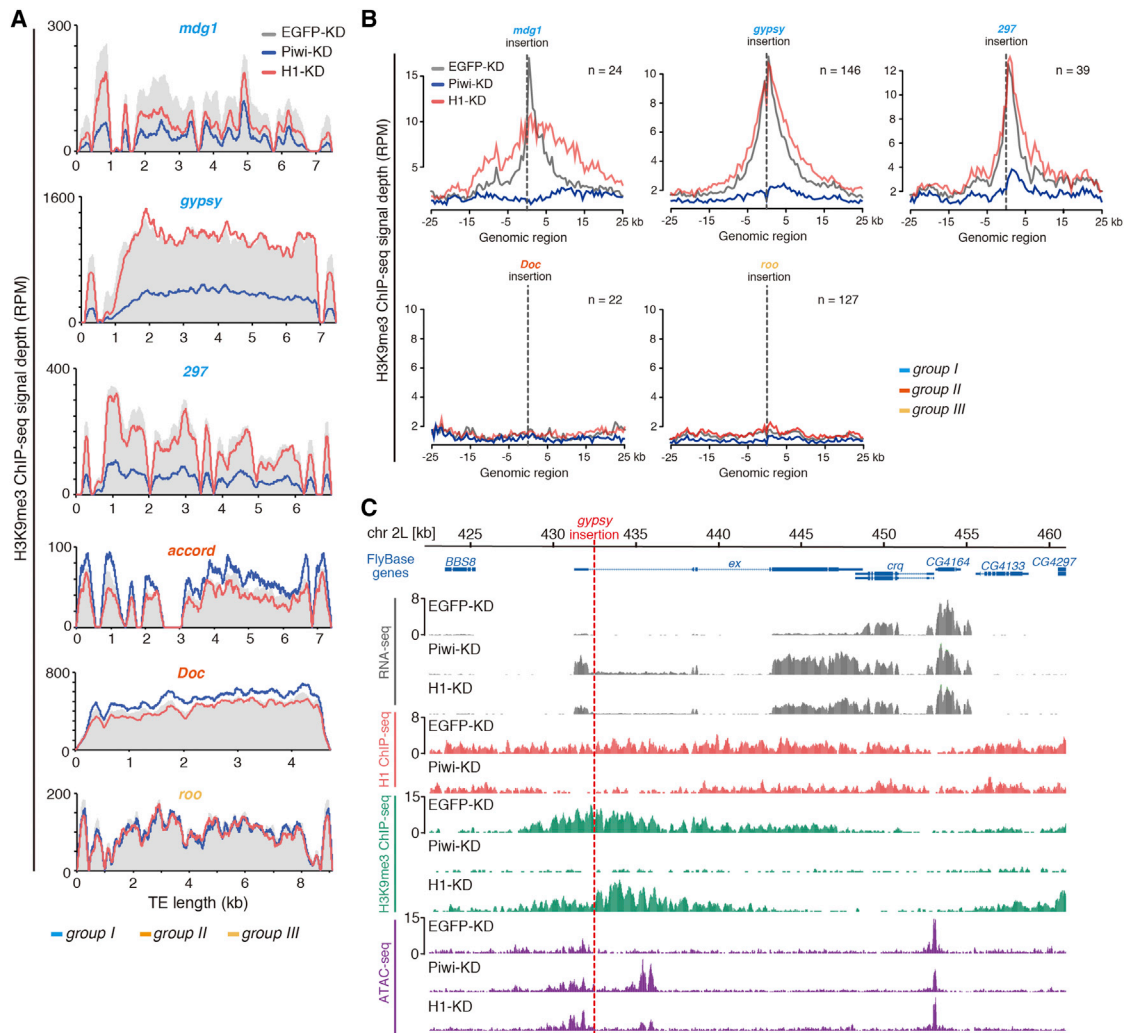
Figure 5. H1 Is Responsible for Transcriptional Silencing and Chromatin Accessibility but Not for H3K9me3 Marks

(A) Density plots for normalized H3K9me3 ChIP-seq signals over consensus sequences from group I, II, and III TEs in EGFP (control)-, Piwi-, or H1-KD cells. ChIP signal depths on EGFP (gray)-, Piwi (blue)-, and H1 (red)-KD samples are shown. x axis of LTR regions are highlighted in red.

(B) Metaplots showing H3K9me3 ChIP-seq signal for genomic regions around euchromatin insertions of group I, II, and III TEs. Normalized ChIP-seq reads in EGFP (gray)-, Piwi (blue)-, and H1 (red)-KD are shown.

(C) RNA levels (RNA-seq signal density), H1 association (H1 ChIP-seq signal density), H3K9me3 association (H3K9me3 ChIP-seq signal density), and chromatin structure (ATAC-seq signal density) at the genomic region flanking the *gypsy* insertion (red dashed line) are shown for OSCs with EGFP-, Piwi-, and H1-KD. FlyBase protein-coding genes are indicated at the top, together with chromosome position.

See also Figure S5.

HP1a-KD on H1 distribution was limited compared to that of Piwi (Figures 3 and S5G–S5J). A similar effect was observed by meta-analysis of genomic regions surrounding euchromatic TE insertions (Figures 6B and S5H). Importantly, we observed a synergistic effect on the derepression of *mdg1* upon H1- and HP1a-KD (Figures 6C and S6B). These data suggest that H1 and HP1a play an interdependent role in the effector step of the Piwi-piRNA pathway.

Distribution of HP1a ChIP-seq signals upon Piwi- and H1-KD (Figures 6A and 6B) was similar to H3K9me3 ChIP-seq signals upon Piwi- or H1-KD (Figures 5A and 5B). Therefore, we studied the relationship between HP1a and H3K9me3 marks. We deter-

mined H3K9me3 peaks using H3K9me3 ChIP-seq data and analyzed the overlap of HP1a and H1 ChIP-seq signals, by displaying HP1a and H1 signals in a metaplot centered on H3K9me3 peak summit. Significant enrichment of HP1a signals was observed at H3K9me3 peaks, suggesting, as expected, that HP1a is probably recruited by H3K9me3 marks (Figure 6D). In contrast, H1 was not accumulated at H3K9me3-enriched sites (Figure 6D). Additionally, as previously reported (Sienski et al., 2012), obvious enrichment of H3K9me3 signals on TE loci and flanking regions of TE insertions was observed. HP1a signal was similarly enriched, whereas the enrichment was not detected for H1 signals (Figure S6C). Combined with data showing
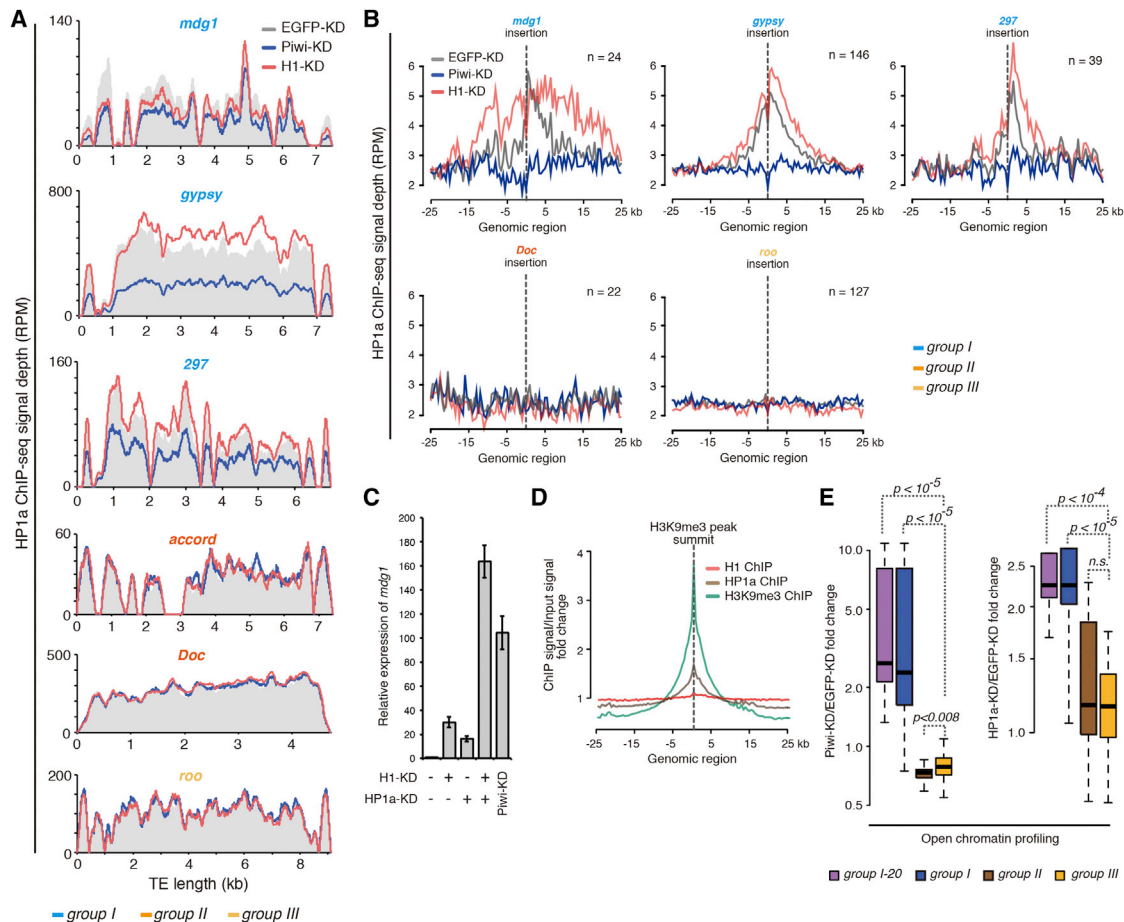
Figure 6. HP1a Functions in Parallel to H1 to Silence Piwi-piRNA Target TEs

(A) Density plots for normalized HP1a ChIP-seq signals over consensus sequences from group I, II, and III TEs in EGFP (control)-, Piwi-, or H1-KD cells. ChIP signal depths on EGFP (gray)-, Piwi (blue)-, and H1 (red)-KD samples are shown.

(B) Metaplots showing HP1a ChIP-seq signal for genomic regions around euchromatin insertions of group I, II, and III TEs. Normalized ChIP-seq reads in EGFP (gray)-, Piwi (blue)-, and H1 (red)-KD are shown.

(C) *mdg1* mRNA levels were quantified by qRT-PCR upon depletion of EGFP, H1, HP1a, and Piwi. Amount of siRNA efficient for limited KD conditions of H1 and HP1a were determined pre-experimentally. Error bars represent mean ± SEM values of three independent experiments.

(D) Metaplots of H3K9me3, HP1a, and H1 signals normalized to the Input signal for the 50-kb window flanking the H3K9me3 peak summit.

(E) Boxplot, as in Figure 3, showing fold changes in normalized ATAC-seq reads for group I, II, and III TEs upon depletion of Piwi or HP1a. Number of reads shorter than 100 bp were counted.

See also Figures S5 and S6.

---

independency of HP1a and H1 distributions (Figures 6A–6C and S5G–S5J), our data indicate that the H3K9me3 mark itself may contribute to HP1a association, but not to H1 association with chromatin.

To check the dependency on chromatin accessibility for TE silencing by the Piwi-piRNA pathway, we performed ATAC-seq experiments upon HP1a- and Mael-KD. As for H1, loss of HP1a and Mael resulted in an increase of chromatin accessibility, supporting our hypothesis that compaction of chromatin structure is the final effector of Piwi-piRNA silencing (Figures 6E and S6D–S6J). Depletion of Mael did not alter H1 accumulation (Figures S5C–S5F) or H3K9me3 levels (Sienski et al., 2012), suggesting that Mael functions downstream or in parallel to H1 and H3K9me3 modifications to modify chromatin accessibility.

Depletion of HP1a resulted in shorter ATAC-seq fragments that mapped to group I TEs (Figure S6D), and reads mapped to group I TEs significantly increased upon HP1a-KD ($p < 10^{-5}$) (Figures 6E and S6E). A similar effect was observed for flanking euchromatic regions of group I TE insertion sites (Figure S6F). Thus, HP1a is also indispensable for modification of chromatin accessibility, leading to silencing of TEs in the Piwi-piRNA pathway. As for H1, the impact of HP1a-KD on chromatin accessibility was not as potent as for Piwi-KD (Figures 6E and S6E). Because HP1a couples with H3K9me3 modification and functions in parallel to H1, we propose that Piwi regulates interdependent pathways, mediated by H1 and HP1a, to achieve highly dense chromatin compaction to maintain TE silencing (Figure S6K).

DISCUSSION

Modulation of Chromatin Accessibility by H1 and Piwi-piRNA Pathways

Based on our data, we propose a model where the association of Piwi-piRISCs with H1 enforces the sustained binding of H1 to target TE chromatin, which is probably mediated by the base-pairing of piRNAs with target nascent transcripts (Le Thomas et al., 2013; Post et al., 2014; Rozhkov et al., 2013; Sienski et al., 2012). This then exerts selective transcriptional silencing of TEs mediated by the regulation of chromatin accessibility (Figure S6K). H1 is distributed evenly throughout chromatin with a propensity for paucity at TSSs (Braunschweig et al., 2009), and the distribution of ATAC-seq reads shows clear enrichment at TSSs (Buenrostro et al., 2013). Consistently, our H1 ChIP-seq reads were depleted and ATAC-seq reads were accumulated at TSSs in OSCs (Figure S4C; data not shown). It is conceivable that H1 distributes evenly throughout chromatin and only genes depleted with H1 become transcriptionally active. We thus postulate that Piwi-target TEs may actively remove H1 from their chromatin loci by currently unknown mechanisms to activate their transcription. Indeed, H1 is depleted at target TE loci in Piwi-KD cells (Figure 3). Piwi-piRNA complexes actively recruit H1 to target TE chromatin loci and stabilize its association to modify the chromatin state at the loci to repress TEs.

Although H3K9me3 accumulation on target TE loci coincides with the continual activities of the Piwi-piRNA complexes, our results show that H1 is involved, in parallel with H3K9me3, in Piwi-piRISC-mediated TE silencing. The common feature of H1- and H3K9me3-mediated transcriptional silencing is the compaction of chromatin into higher-order structures. H3K9me3 modification is required for binding of HP1, which initiates heterochromatin formation (Grewal and Jia, 2007). Our data show that HP1a also regulates chromatin accessibility (Figures 6E and S6D–S6F). HP1a slightly affects H1 binding on TE loci (Figures S5G–S5J), suggesting that HP1a may stabilize chromatin formation, thereby maintaining H1 association with piRNA target loci. Furthermore, Mael is also responsible for modifying chromatin accessibility at Piwi target loci (Figures S6G–S6J). Thus, Piwi regulates mutually interdependent pathways that alter chromatin formation, suggesting that each pathway may induce repressive chromatin states to cooperatively reinforce TE silencing. This supports an obligatory functional relationship between H1, HP1a, and Mael as effectors of Piwi-mediated TE silencing.

Although most of the ATAC-seq peaks detected specifically in Piwi/H1-KD samples corresponded to TEs (Figures 4 and S4C), we also detected 84 genes with enriched ATAC-seq peaks in both Piwi- and H1-KD samples. Of these 84 genes, 18 were located near group I TEs. Gene Ontology analysis of the remaining genes (66 genes) suggested enrichment of terms such as "development of primary sexual characteristics" and "sex differentiation" (Figure S4D), which might be useful to study the role of Piwi in germline development.

Molecular Mechanism of TE Silencing in the Piwi-piRNA Pathway

Several important points remain to explain this pathway fully. Piwi was shown to regulate the association of HP1a and H3K9 methyl-ation at piRNA target locus (Brower-Toland et al., 2007; Le Thomas et al., 2013; Wang and Elgin, 2011). Recently, Panoramix/Silencio was demonstrated to be responsible for the recruitment of H3K9me3 marks in this process (Yu et al., 2015; Sienski et al., 2015). Because our data suggest H1 and HP1a/H3K9me3 function interdependently in the Piwi-piRNA pathway (Figure 6), we speculate that Piwi regulates H1 in parallel to Panoramix/Silencio and H3K9me3, to modulate chromatin accessibility and induces silencing of their target TEs. Further analysis is necessary to reveal the precise relationship between H1 and Panoramix/Silencio.

The concept that H3K9me and HP1 serve as a recruiting platform for various effectors, including HDACs, which, in turn, mediate heterochromatic silencing, is well developed in the *S. pombe* system (Grewal and Jia, 2007). Moreover, loss of HDACs associated with the H3K9me-HP1 platform or defects in RNAi components involved in targeting H3K9me result in increased turnover of nucleosomes and loss of heterochromatic repression (Aygün et al., 2013). Piwi-bound H1 and effectors associated with H3K9me-HP1 might similarly prevent histone turnover to repress TEs. The changes detected in ATAC-seq may reflect changes in histone dynamics. Therefore, analysis of the effects of H1 and Piwi on histone turnover may provide a unifying theme underlying the assembly of repressive chromatin.

Piwi-piRNA complexes in OSCs repress only a subset of TEs (Figure 2A), consistent with previous studies (Le Thomas et al., 2013; Ohtani et al., 2013; Sienski et al., 2012). In line with a previous study (Lu et al., 2013), our data also suggest that H1 regulates TEs other than those targeted by the Piwi-piRNA pathway (Figure 2B), indicating that the overlap between TEs regulated by Piwi and H1 is rather limited. Previously, H1 was shown to regulate TEs ubiquitously, by recruiting H3K9 methyltransferase Su(var)3-9 (Lu et al., 2013). Our results indicated that loss of H1 did not affect H3K9me3 marks on Piwi-piRNA target TEs (Figure 5). Additionally, loss of Su(var)3-9 did not affect *mdg1* expression levels (data not shown), suggesting that piRNA-mediated TE regulation differs from ubiquitous TE regulation by H1, as far as Su(var)3-9 dependency is concerned. We therefore hypothesize that the Piwi-piRNA pathway utilizes the ability of H1 to silence TEs in order to silence their targets.

Overall, we proposed chromatin accessibility functions as the final effector of Piwi-piRNA-mediated TE silencing. Interdependent pathways are responsible for this: (1) recruitment of H1 by Piwi, and (2) H3K9me3-mediated recruitment of HP1a. These pathways coordinately regulate chromatin formation to regulate genome-wide piRNA target TEs.

EXPERIMENTAL PROCEDURES

Cell Culture and Transfection

OSCs were cultured in Shields and Sang M3 Insect Medium (Sigma) supplemented with 10% fly extract, 10% fetal bovine serum, 0.6 mg/ml glutathione, and 10 mU/ml insulin as described (Niki et al., 2006; Saito et al., 2009). Transfection of siRNAs was performed using Cell Line 96-well Nucleofector Kit SF and 96-well Shuttle Device (Lonza). Details are given in the Supplemental Information.

Production of Anti-H1 Monoclonal Antibody

A 148-amino-acid C-terminal fragment of H1, fused with glutathione S-transferase (GST), was used as the antigen to immunize mice. Details are given in the Supplemental Information.

RNA-seq Analysis

Poly(A)$^+$ RNA libraries were prepared as described (Ohtani et al., 2013) and analyzed by Illumina HiSeq (Hokkaido Systems Science). This yielded ~20–25 million genome-mapped reads in each sample transfected with siRNA. Computational analyses are described in Supplemental Information.

ChIP and ChIP-seq Analysis

ChIP was performed as described (Ohtani et al., 2013) with modifications. To prepare ChIP-seq libraries, DNA fragments from the ChIP experiment were sheared to ~200 bases using Covaris S220. These were used for library preparation with the NEBNext Ultra DNA Library Prep Kit for Illumina (NEB) following the manufacturer's protocol. Details are given in the Supplemental Information.

ATAC Sequencing Analysis

ATAC sequencing (ATAC-seq) analysis was performed as described (Buenrostro et al., 2013, 2015) with some modifications. Details are given in the Supplemental Information.

ACCESSION NUMBERS

The accession number for the deep sequencing datasets reported in this paper is NCBI GEO: GSE81434.

SUPPLEMENTAL INFORMATION

Supplemental Information includes Supplemental Experimental Procedures, six figures, and one table and can be found with this article online at http://dx.doi.org/10.1016/j.molcel.2016.06.008.

REFERENCES

Aygün, O., Mehta, S., and Grewal, S.I. (2013). HDAC-mediated suppression of histone turnover promotes epigenetic stability of heterochromatin. Nat. Struct. Mol. Biol. 20, 547–554.

Bannister, A.J., Zegerman, P., Partridge, J.F., Miska, E.A., Thomas, J.O., Allshire, R.C., and Kouzarides, T. (2001). Selective recognition of methylated lysine 9 on histone H3 by the HP1 chromo domain. Nature 410, 120–124.

Bonet-Costa, C., Vilaseca, M., Diema, C., Vujatovic, O., Vaquero, A., Omeñaca, N., Castejón, L., Bernués, J., Giralt, E., and Azorín, F. (2012). Combined bottom-up and top-down mass spectrometry analyses of the pattern of post-translational modifications of Drosophila melanogaster linker histone H1. J. Proteomics 75, 4124–4138.

Braunschweig, U., Hogan, G.J., Pagie, L., and van Steensel, B. (2009). Histone H1 binding is inhibited by histone variant H3.3. EMBO J. 28, 3635–3645.

Brennecke, J., Aravin, A.A., Stark, A., Dus, M., Kellis, M., Sachidanandam, R., and Hannon, G.J. (2007). Discrete small RNA-generating loci as master regulators of transposon activity in Drosophila. Cell 128, 1089–1103.

Brower-Toland, B., Findley, S.D., Jiang, L., Liu, L., Yin, H., Dus, M., Zhou, P., Elgin, S.C.R., and Lin, H. (2007). Drosophila PIWI associates with chromatin and interacts directly with HP1a. Genes Dev. 21, 2300–2311.

Buenrostro, J.D., Giresi, P.G., Zaba, L.C., Chang, H.Y., and Greenleaf, W.J. (2013). Transposition of native chromatin for fast and sensitive epigenomic profiling of open chromatin, DNA-binding proteins and nucleosome position. Nat. Methods 10, 1213–1218.

Buenrostro, J.D., Wu, B., Chang, H.Y., and Greenleaf, W.J. (2015). ATAC-seq: a method for assaying chromatin accessibility genome-wide. Curr. Protoc. Mol. Biol. 109, 21–29.

Bustin, M., Catez, F., and Lim, J.H. (2005). The dynamics of histone H1 function in chromatin. Mol. Cell 17, 617–620.

Buttinelli, M., Panetta, G., Rhodes, D., and Travers, A. (1999). The role of histone H1 in chromatin condensation and transcriptional repression. Genetica 106, 117–124.

Cox, D.N., Chao, A., and Lin, H. (2000). piwi encodes a nucleoplasmic factor whose activity modulates the number and division rate of germline stem cells. Development 127, 503–514.

Czech, B., Preall, J.B., McGinn, J., and Hannon, G.J. (2013). A transcriptome-wide RNAi screen in the Drosophila ovary reveals factors of the germline piRNA pathway. Mol. Cell 50, 749–761.

Dönertas, D., Sienski, G., and Brennecke, J. (2013). Drosophila Gtsf1 is an essential component of the Piwi-mediated transcriptional silencing complex. Genes Dev. 27, 1693–1705.

Eissenberg, J.C., James, T.C., Foster-Hartnett, D.M., Hartnett, T., Ngan, V., and Elgin, S.C.R. (1990). Mutation in a heterochromatin-specific chromosomal protein is associated with suppression of position-effect variegation in Drosophila melanogaster. Proc. Natl. Acad. Sci. USA 87, 9923–9927.

Ge, D.T., and Zamore, P.D. (2013). Small RNA-directed silencing: the fly finds its inner fission yeast? Curr. Biol. 23, R318–R320.

Goodier, J.L., and Kazazian, H.H., Jr. (2008). Retrotransposons revisited: the restraint and rehabilitation of parasites. Cell 135, 23–35.

Grewal, S.I., and Jia, S. (2007). Heterochromatin revisited. Nat. Rev. Genet. 8, 35–46.

Gunawardane, L.S., Saito, K., Nishida, K.M., Miyoshi, K., Kawamura, Y., Nagami, T., Siomi, H., and Siomi, M.C. (2007). A slicer-mediated mechanism for repeat-associated siRNA 5′ end formation in Drosophila. Science 315, 1587–1590.

Hale, T.K., Contreras, A., Morrison, A.J., and Herrera, R.E. (2006). Phosphorylation of the linker histone H1 by CDK regulates its binding to HP1alpha. Mol. Cell 22, 693–699.

Handler, D., Meixner, K., Pizka, M., Lauss, K., Schmied, C., Gruber, F.S., and Brennecke, J. (2013). The genetic makeup of the Drosophila piRNA pathway. Mol. Cell 50, 762–777.

Ishizu, H., Iwasaki, Y.W., Hirakata, S., Ozaki, H., Iwasaki, W., Siomi, H., and Siomi, M.C. (2015). Somatic Primary piRNA Biogenesis Driven by cis-Acting RNA Elements and trans-Acting Yb. Cell Rep. 12, 429–440.

Iwasaki, Y.W., Siomi, M.C., and Siomi, H. (2015). PIWI-Interacting RNA: Its Biogenesis and Functions. Annu. Rev. Biochem. 84, 405–433.

Jacobs, S.A., and Khorasanizadeh, S. (2002). Structure of HP1 chromodomain bound to a lysine 9-methylated histone H3 tail. Science 295, 2080–2083.

Klenov, M.S., Sokolova, O.A., Yakushev, E.Y., Stolyarenko, A.D., Mikhaleva, E.A., Lavrov, S.A., and Gvozdev, V.A. (2011). Separation of stem cell maintenance and transposon silencing functions of Piwi protein. Proc. Natl. Acad. Sci. USA 108, 18760–18765.

Klenov, M.S., Lavrov, S.A., Korbut, A.P., Stolyarenko, A.D., Yakushev, E.Y., Reuter, M., Pillai, R.S., and Gvozdev, V.A. (2014). Impact of nuclear Piwi elimination on chromatin state in *Drosophila* melanogaster ovaries. Nucleic Acids Res. 42, 6208–6218.

Lachner, M., O'Carroll, D., Rea, S., Mechtler, K., and Jenuwein, T. (2001). Methylation of histone H3 lysine 9 creates a binding site for HP1 proteins. Nature 410, 116–120.

Laybourn, P.J., and Kadonaga, J.T. (1991). Role of nucleosomal cores and histone H1 in regulation of transcription by RNA polymerase II. Science 254, 238–245.

Le Thomas, A., Rogers, A.K., Webster, A., Marinov, G.K., Liao, S.E., Perkins, E.M., Hur, J.K., Aravin, A.A., and Tóth, K.F. (2013). Piwi induces piRNA-guided transcriptional silencing and establishment of a repressive chromatin state. Genes Dev. 27, 390–399.

Li, G., and Reinberg, D. (2011). Chromatin higher-order structures and gene regulation. Curr. Opin. Genet. Dev. 21, 175–186.

Lu, X., Wontakal, S.N., Kavi, H., Kim, B.J., Guzzardo, P.M., Emelyanov, A.V., Xu, N., Hannon, G.J., Zavadil, J., Fyodorov, D.V., and Skoultchi, A.I. (2013). Drosophila H1 regulates the genetic activity of heterochromatin by recruitment of Su(var)3-9. Science 340, 78–81.

Misteli, T., Gunjan, A., Hock, R., Bustin, M., and Brown, D.T. (2000). Dynamic binding of histone H1 to chromatin in living cells. Nature 408, 877–881.

Muerdter, F., Guzzardo, P.M., Gillis, J., Luo, Y., Yu, Y., Chen, C., Fekete, R., and Hannon, G.J. (2013). A genome-wide RNAi screen draws a genetic framework for transposon control and primary piRNA biogenesis in Drosophila. Mol. Cell 50, 736–748.

Nakayama, J., Rice, J.C., Strahl, B.D., Allis, C.D., and Grewal, S.I. (2001). Role of histone H3 lysine 9 methylation in epigenetic control of heterochromatin assembly. Science 292, 110–113.

Nielsen, A.L., Oulad-Abdelghani, M., Ortiz, J.A., Remboutsika, E., Chambon, P., and Losson, R. (2001). Heterochromatin formation in mammalian cells: interaction between histones and HP1 proteins. Mol. Cell 7, 729–739.

Niki, Y., Yamaguchi, T., and Mahowald, A.P. (2006). Establishment of stable cell lines of Drosophila germ-line stem cells. Proc. Natl. Acad. Sci. USA 103, 16325–16330.

Ohtani, H., Iwasaki, Y.W., Shibuya, A., Siomi, H., Siomi, M.C., and Saito, K. (2013). DmGTSF1 is necessary for Piwi-piRISC-mediated transcriptional transposon silencing in the Drosophila ovary. Genes Dev. 27, 1656–1661.

Pennings, S., Meersseman, G., and Bradbury, E.M. (1994). Linker histones H1 and H5 prevent the mobility of positioned nucleosomes. Proc. Natl. Acad. Sci. USA 91, 10275–10279.

Post, C., Clark, J.P., Sytnikova, Y.A., Chirn, G.W., and Lau, N.C. (2014). The capacity of target silencing by Drosophila PIWI and piRNAs. RNA 20, 1977–1986.

Rea, S., Eisenhaber, F., O'Carroll, D., Strahl, B.D., Sun, Z.W., Schmid, M., Opravil, S., Mechtler, K., Ponting, C.P., Allis, C.D., and Jenuwein, T. (2000). Regulation of chromatin structure by site-specific histone H3 methyltransferases. Nature 406, 593–599.

Rozhkov, N.V., Hammell, M., and Hannon, G.J. (2013). Multiple roles for Piwi in silencing Drosophila transposons. Genes Dev. 27, 400–412.

Saito, K., Inagaki, S., Mituyama, T., Kawamura, Y., Ono, Y., Sakota, E., Kotani, H., Asai, K., Siomi, H., and Siomi, M.C. (2009). A regulatory circuit for piwi by the large Maf gene traffic jam in Drosophila. Nature 461, 1296–1299.

Saito, K., Ishizu, H., Komai, M., Kotani, H., Kawamura, Y., Nishida, K.M., Siomi, H., and Siomi, M.C. (2010). Roles for the Yb body components Armitage and Yb in primary piRNA biogenesis in Drosophila. Genes Dev. 24, 2493–2498.

Schotta, G., Ebert, A., Krauss, V., Fischer, A., Hoffmann, J., Rea, S., Jenuwein, T., Dorn, R., and Reuter, G. (2002). Central role of Drosophila SU(VAR)3-9 in histone H3-K9 methylation and heterochromatic gene silencing. EMBO J. 21, 1121–1131.

Sienski, G., Dönertas, D., and Brennecke, J. (2012). Transcriptional silencing of transposons by Piwi and maelstrom and its impact on chromatin state and gene expression. Cell 151, 964–980.

Sienski, G., Batki, J., Senti, K.A., Dönertas, D., Tirian, L., Meixner, K., and Brennecke, J. (2015). Silencio/CG9754 connects the Piwi-piRNA complex to the cellular heterochromatin machinery. Genes Dev. 29, 2258–2271.

Vujatovic, O., Zaragoza, K., Vaquero, A., Reina, O., Bernués, J., and Azorín, F. (2012). Drosophila melanogaster linker histone dH1 is required for transposon silencing and to preserve genome integrity. Nucleic Acids Res. 40, 5402–5414.

Wang, S.H., and Elgin, S.C. (2011). Drosophila Piwi functions downstream of piRNA production mediating a chromatin-based transposon silencing mechanism in female germ line. Proc. Natl. Acad. Sci. USA 108, 21164–21169.

Yu, Y., Gu, J., Jin, Y., Luo, Y., Preall, J.B., Ma, J., Czech, B., and Hannon, G.J. (2015). Panoramix enforces piRNA-dependent cotranscriptional silencing. Science 350, 339–342.

Zhou, B.R., Feng, H., Kato, H., Dai, L., Yang, Y., Zhou, Y., and Bai, Y. (2013). Structural insights into the histone H1-nucleosome complex. Proc. Natl. Acad. Sci. USA 110, 19390–19395.

Zhou, B.R., Jiang, J., Feng, H., Ghirlando, R., Xiao, T.S., and Bai, Y. (2015). Structural mechanisms of nucleosome recognition by linker histones. Mol. Cell 59, 628–638.

ARTICLE

Dppa3 expression is critical for generation of fully reprogrammed iPS cells and maintenance of *Dlk1-Dio3* imprinting

Xingbo Xu[1,*], Lukasz Smorag[1,*], Toshinobu Nakamura[2,*], Tohru Kimura[3], Ralf Dressel[4], Antje Fitzner[5], Xiaoying Tan[1], Matthias Linke[5], Ulrich Zechner[5], Wolfgang Engel[1] & D.V. Krishna Pantakani[1]

Reprogramming of mouse somatic cells into induced pluripotent stem cells (iPSCs) often generates partially reprogrammed iPSCs (pre-iPSCs), low-grade chimera forming iPSCs (lg-iPSCs) and fully reprogrammed, high-grade chimera production competent iPSCs (hg-iPSCs). Lg-iPSC transcriptome analysis revealed misregulated *Dlk1-Dio3* cluster gene expression and subsequently the imprinting defect at the *Dlk1-Dio3* locus. Here, we show that germ-cell marker *Dppa3* is present only in lg-iPSCs and hg-iPSCs, and that induction with exogenous *Dppa3* enhances reprogramming kinetics, generating all hg-iPSCs, similar to vitamin C (Vc). Conversely, *Dppa3*-null fibroblasts show reprogramming block at pre-iPSCs state and *Dlk1-Dio3* imprinting defect. At the molecular level, we show that Dppa3 is associated with *Dlk1-Dio3* locus and identify that Dppa3 maintains imprinting by antagonizing Dnmt3a binding. Our results further show molecular parallels between Dppa3 and Vc in *Dlk1-Dio3* imprinting maintenance and suggest that early activation of *Dppa3* is one of the cascades through which Vc facilitates the generation of fully reprogrammed iPSCs.

[1] Institute of Human Genetics, University of Goettingen, Heinrich-Dueker-Weg 12, 37073 Goettingen, Germany. [2] Department of Bio-Science, Nagahama Institute of Bio-Science and Technology, Shiga 526-0829, Japan. [3] Department of Biosciences, Kitasato University School of Science, Kanagawa 252-0373, Japan. [4] Department of Cellular and Molecular Immunology, University of Goettingen, Humboldtallee 34, 37073 Goettingen, Germany. [5] Institute of Human Genetics, Johannes Gutenberg-University Mainz, Langenbeckstraße 1, 55131 Mainz, Germany. * These authors contributed equally to this work. Correspondence and requests for materials should be addressed to D.V.K.P. (email: krishna.if1@gmail.com).

Pluripotent stem cells boast the differentiation potential virtually into any cell type of the body, and hence hold a great promise for regenerative medicine applications[1]. Recent advances in reprogramming strategies unveiled the induction of pluripotency in somatic cells by using few transcription factors resulting in the generation of induced pluripotent stem cells (iPSCs)[2,3]. Reprogramming of mouse somatic cells into iPSCs often generates partially reprogrammed iPSCs (pre-iPSCs), low-grade iPSCs (lg-iPSCs) that produce only low-grade chimeras and completely reprogrammed, high-grade iPSCs (hg-iPSCs) that support high-grade chimerism[4–8]. Pre-iPSCs are characterized by the lack of endogenous pluripotency markers expression and show residual expression of reprogramming factors, absence of chimera formation and defects at the genetic and epigenetic level[4–7]. Lg-iPSCs are morphologically indistinguishable from hg-iPSCs; however, they show abnormal hypermethylation of the imprinted *Dlk1-Dio3* locus and contribute to low-grade chimeras with or without germline transmission[8,9]. The transcriptome analysis of lg-iPSCs in comparison to embryonic stem cells (ESCs) revealed that the expression of coding and non-coding genes encoded by the *Dlk1-Dio3* imprinting cluster is misregulated due to the aberrant acquisition of DNA methylation at the maternal allele along with the normally methylated paternal allele[8]. Recently, addition of vitamin C (Vc) during reprogramming was shown to result in iPSCs with normal *Dlk1-Dio3* imprinting, yet the factor expressed in a Vc-dependent manner was not identified[10].

Genomic imprinting is an epigenetic phenomenon established during gametogenesis and involves differential DNA methylation and post-translational histone modifications. Short DNA sequences called imprinting control regions (ICRs) are methylated on either the maternal or paternal allele to regulate expression of the imprinted gene in *cis*[11]. These marks lead to exclusive or preferential parent-specific monoallelic expression of imprinted genes[12,13]. During embryonic development, a pool of primordial germ cells (PGCs) gives rise to progenitors of adult gametes. After their specification and up on their arrival at the genital ridge, these PGCs undergo demethylation of the whole genome including an erasure of parent-specific methylation marks of imprinted genes, the so-called imprints[14]. The reestablishment of genomic imprinting in germ cells (GCs) according to the sex of the embryo is initiated after the entry of PGCs into gonads and continues through germ-cell differentiation[15,16].

The imprint acquisition according to the sex of the embryo is regulated by several components, such as primary sequence specificity, chromatin configuration, non-histone proteins and transcriptional events (reviewed by Arnaud[17]). Specifically, the *de novo* DNA methyltransferase Dnmt3a and its related protein Dnmt3l that has no methyltransferase activity, were shown to be essential for imprint establishment at several imprinted loci[18–20]. In addition to the DNA methylation machinery, several other DNA-binding proteins, such as Zfp57, Nlrp2, Nlrp7, Ctcfl and Prmt7, are implicated in the establishment of imprints in a sex-specific manner[21–25]. Once established in GCs, several factors are known to faithfully maintain and transmit the imprints during the early stages of embryogenesis to all somatic lineages (reviewed by Arnaud[17]). Dppa3/PGC7 is one such factor expressed mainly in GCs and known to protect some of the maternal as well as paternal imprints during the wave of DNA demethylation occurring in early embryogenesis[26].

Previously, we have shown that GC marker genes, such as *Blimp1*, *Fragilis* and *Dppa3*, are expressed in all pluripotent cell types and emerge early during somatic cell reprogramming into iPSCs[27]. In the present study, we evaluate whether these GC marker genes, in particular *Dppa3*, play any role in the maintenance of *Dlk1-Dio3* imprinting during the generation of

iPSCs. Interestingly, *Dppa3* is expressed only in lg-iPSCs and hg-iPSCs, but not in pre-iPSCs. Reprogramming studies in the presence of *Dppa3*, in addition to classical reprogramming factors (OSKM), show that supplementation of *Dppa3* enhances reprogramming kinetics and generates all hg-iPSCs. In line with these observations, reprogramming studies with *Dppa3*-knock out (*Dppa3*-KO) fibroblasts reveal a reprogramming arrest in pre-iPSC state along with *Dlk1-Dio3* imprinting defect. At the molecular level, we observe that Dppa3 is required for the suppression of virus-mediated reprogramming factors and endogenous retroviral elements (ERVs). Furthermore, Dppa3 is found to be associated with the intergenic differentially methylated region (IG-DMR) of the *Dlk1-Dio3* and to counteract the binding of Dnmt3a to this region during reprogramming.

Results

Dppa3 is present in lg-iPSCs and hg-iPSCs, not in pre-iPSCs. Advances in understanding the process of somatic cell reprogramming towards iPS cells have proposed three phases in reprogramming: *initiation*, marking mesenchymal-to-epithelial transition; *maturation and stabilization*, with pre-iPSCs and characterized by silencing of exogenous reprogramming factors and activation of endogenous pluripotency-related genes, such as *Dppa3*, *Sox2* and *Dnmt3l*[7] (Fig. 1a). Progression through these phases generates fully reprogrammed hg-iPSCs, while failure to undergo the faithful reprogramming process yields pre-iPSCs or lg-iPSCs with imprinting defect at the *Dlk1-Dio3* locus[4,6–9]. However, the molecular mechanisms and the determining factor(s) of these cell states are yet to be identified.

To decipher the cause of aberrant *Dlk1-Dio3* imprinting, we established several iPSC lines from mouse embryonic fibroblasts (MEFs) using the classical Yamanaka's method[3]. We found clones (iPSC-1 and -2) that displayed mRNA expression of *Gtl2* (also known as *Meg3*), a maternally expressed non-coding transcript from the imprinted *Dlk1-Dio3* locus, above the threshold level typically found in ESCs (*Gtl2*^{on})[8], and other clones (iPSC-3, -4, -5 and -6) that showed *Gtl2* mRNA expression below that level (*Gtl2*^{off}) (Fig. 1b). Consistent with the expression pattern of *Gtl2*, iPSC-1 and -2 showed normal, 40–60% DNA methylation at the *Dlk1-Dio3* IG-DMR, whereas the other clones showed DNA hypermethylation (Fig. 1c). Then we analysed the mRNA expression of pluripotency-related genes in all six iPSC lines and detected no expression in iPSC-3 and -4, but similar expression levels to control were found in iPSC-1, -2, -5 and -6 (Fig. 1d). These results led us to conclude that iPSC-1 and -2 are fully reprogrammed iPSCs, while iPSC-3 and -4 are in pre-iPSC state and iPSC-5 and -6 are in lg-iPSC state.

Recently, we showed that the expression of *Dppa3/PGC7*, a GC marker gene, precedes the expression of endogenous pluripotency marker genes, such as *Oct3/4*, *Sox2*, *Nanog* and *Klf4*, during somatic cell reprogramming[27]. *Dppa3* is known to protect some maternal as well as paternal imprints during the first wave of DNA demethylation occurring in early embryogenesis and was also implicated in the regulation of DNA methylation at ERVs, such as intracisternal A-particles (IAPs)[26]. To determine whether *Dppa3* functions in establishment/maintenance of *Dlk1-Dio3* imprinting during somatic cell reprogramming, we analysed iPSC colonies for the Dppa3 RNA and protein expression. The expression of Dppa3 was observed both in lg-iPSCs and hg-iPSCs, but not in pre-iPSCs (Fig. 1d,e). In line with these results, protein expression analysis of two *Gtl2*^{off} (R21-5-OFF and 159-3-OFF) clones and one *Gtl2*^{on} clone (R-21-4-ON) from the study of Stadtfeld et al.[8], detected the expression of Dppa3 in all the three clones, indicating that the *Gtl2*^{off} clones from their study might
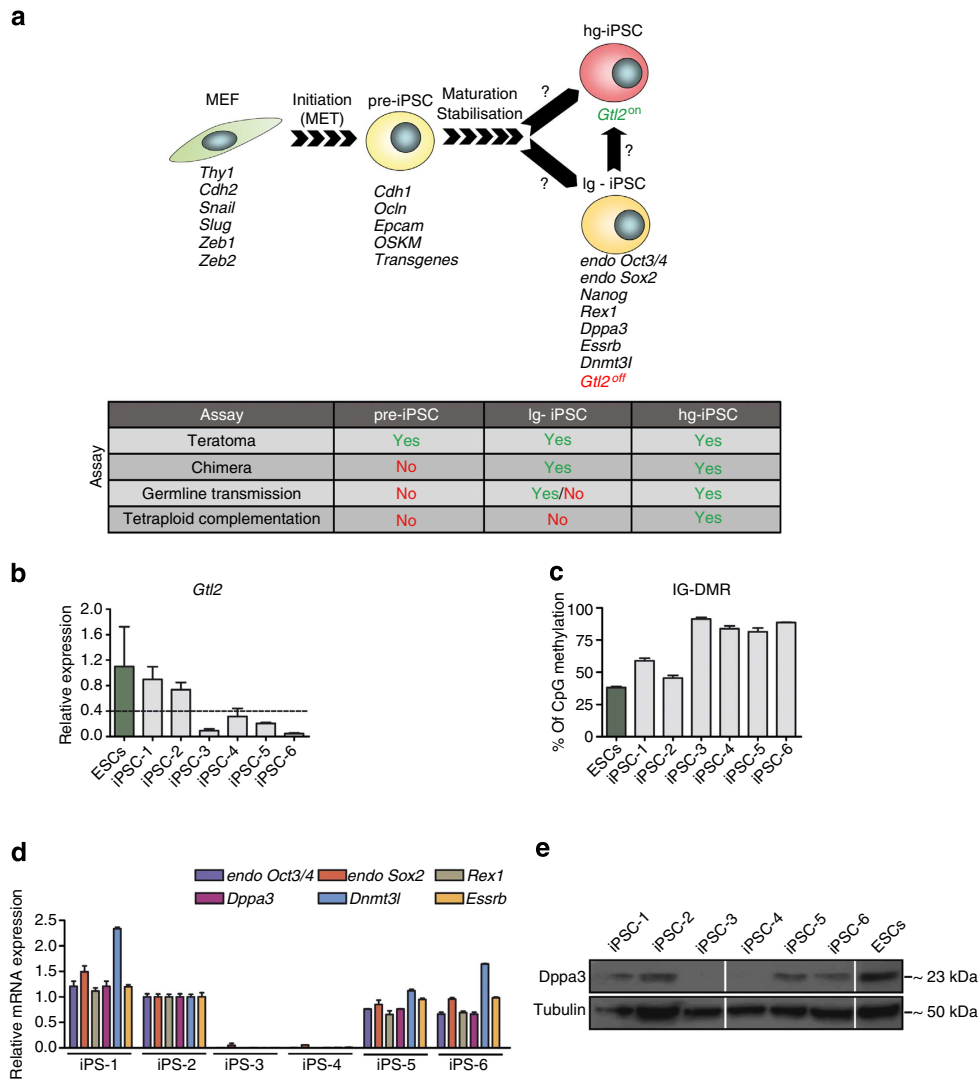
Figure 1 | Stages of somatic cell reprogramming and Dppa3 expression status. (**a**) Schematic representation of somatic cell reprogramming, in which somatic cell (mouse embryonic fibroblast, MEF) transduced with OSKM reprogramming factors passes through initiation, maturation and stabilization phases to establish fully reprogrammed iPSC. Failure in proceeding to maturation and stabilization phases results in pre-iPSC. Similarly, defects occurring during maturation and stabilization phases result in lg-iPSC. Finally, faithful progression through all these phases results in establishment of hg-iPSC. The factor(s) responsible for conversion from pre-iPSC to either lg-iPSC or hg-iPSC, as well as from lg-iPSC to hg-iPSC are not known (?). Expression of several marker genes are indicated below each stage and pluripotency capabilities of various stages are indicated in a table. MET, mesenchymal–epithelial transition. (**b**) qRT–PCR data showing expression of *Gtl2* RNA above the threshold (dotted line) of expression typically found in ESCs, in only two iPSC clones generated with classical Yamanaka factors (OSKM). *Gtl2* RNA expression and associated error bars, representing mean ± s.d. ($n = 3$), were normalized to expression level in ESCs (green). (**c**) DNA methylation analysis of the *Dlk1-Dio3* IG-DMR in OSKM-derived iPSC clones showed normal methylation levels of 40–60% only in iPSC-1 and -2, whereas iPSC-3, -4, -5 and -6 displayed hypermethylation. Genomic DNA from ESCs (green) served as a control. Error bars represent mean ± s.d. ($n = 2$). (**d**) qRT–PCR data showing expression of various pluripotency marker genes only in iPSC-1, -2, -5 and -6, but not in iPSC-3 and -4. Gene expression and associated error bars, representing mean ± s.d. ($n = 3$), were normalized to expression level in iPS-2. (**e**) Western blot analysis showing expression of Dppa3 in all iPSCs, with the exception of iPSC-3 and -4. ESC protein extract was used as a control.

be lg-iPSCs (Supplementary Fig. 1a). To check if *Dppa3*-deficient ESCs[26] show any imprinting defect at the *Dlk-Dio3* locus, we performed RNA expression analysis for *Gtl2* and *Dlk1* and found no obvious differences in their expression levels between *Dppa3*-deficient and control ESCs (Supplementary Fig. 1b). Further, DNA methylation analysis of the *Dlk1-Dio3* IG-DMR revealed no significant differences with ∼50% methylation levels in *Dppa3*-deficient and control ESCs (Supplementary Fig. 1c). One imprinted paternally methylated locus, *H19*, was hypermethylated in both ESC types, whereas another, *Rasgrf1*, showed 40–57% methylation in control and hypomethylation in *Dppa3*-deficient, ESCs (Supplementary Fig. 1c).

Dppa3 enhances reprogramming and generates all hg-iPSCs. To analyse the effect of exogenous *Dppa3* expression on maintenance of *Dlk1-Dio3* imprinting, we reprogrammed *Nanog*-EGFP MEFs with *Dppa3* (D) and Yamanaka factors (OSKM). OSKM + D-transduced MEFs formed colonies already by day 8 and activated *Nanog*-EGFP by day 14 of reprogramming, whereas OSKM-only-transduced cells formed colonies only by day 12 and were EGFP-positive by day 18 (Fig. 2a,b). OSKM + D transduction greatly enhanced the number of alkaline phosphatase (AP)- and EGFP-positive colonies (Fig. 2c). The *Gtl2* mRNA expression analysis in OSKM + D iPSC colonies revealed that the addition of Dppa3 results in 100% *Gtl2*[on] colonies, while
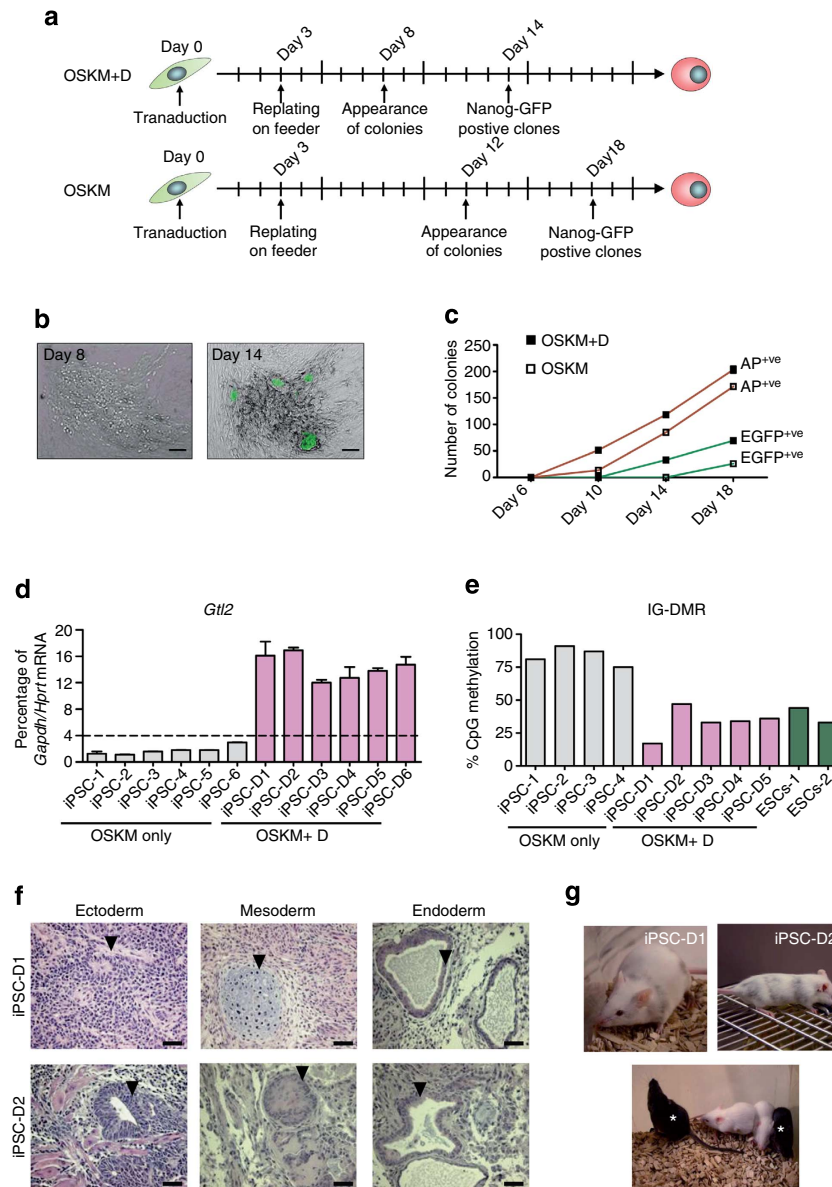
Figure 2 | Dppa3 enhances reprogramming and generates fully pluripotent iPSCs. (**a**) Time scale showing the start of viral transduction followed by the appearance of ESC-like and *Nanog*-EGFP-positive colonies during iPSC generation using either OSKM or OSKM in combination with Dppa3 (OSKM + D). (**b**) Bright-field image showing the appearance of ESC-like colonies by day 8 of reprogramming using OSKM + D (left panel). The same colony was positive for *Nanog*-driven EGFP on day 14 (right panel). Scale bars correspond to 100 μm. (**c**) Line graph showing the number of AP-positive (AP^{+ve}) and EGFP-positive (EGFP^{+ve}) colonies during the reprogramming time course in the presence of OSKM or OSKM + D. (**d**) *Gtl2* RNA expression analysis in iPSCs generated using either OSKM (grey) or OSKM + D (purple). *Gtl2* RNA expression and associated error bars, representing mean ± s.d. ($n = 3$), were normalized to housekeeping genes, *Gapdh* and *Hprt*, and presented as percentage of expression. (**e**) DNA methylation analysis of *Dlk1-Dio3* IG-DMR in OSKM-only (grey) and OSKM + D (purple) iPSCs. ESC genomic DNA (green) was used as a control. (**f**) Light micrographs of hematoxylin and eosin-stained sections of teratomas obtained from OSKM + D iPSCs showing the presence of cell type derivatives of all three germ layers. Arrowheads indicate presence of representative tissue/cell type in respective germ layer. Scale bars correspond to 200 μm. (**g**) Images of chimeras obtained from OSKM + D iPSCs (upper panel) and their F1 progeny resulting from germline transmission (lower panel). *, pup derived from the germline-competent OSKM + D iPSCs.

OSKM-only generated *Gtl2*^{off} colonies exclusively (Fig. 2d). The *Dlk1-Dio3* IG-DMR showed moderate hypomethylation in OSKM + D *Gtl2*^{on} and hypermethylation in OSKM-only-derived *Gtl2*^{off}, iPSCs (Fig. 2e). To confirm *Dppa3*-mediated maintenance of *Dlk1-Dio3* imprinting, we generated additional OSKM + D clones. All were *Gtl2*^{on} (Supplementary Fig. 2a) and expressed paternally expressed *Dlk1* (Supplementary Fig. 2b) and several *Dlk1-Dio3* cluster-encoded miRNAs (Supplementary Fig. 2c–e) at ESC-comparable levels. We further confirmed AP, *Nanog*-EGFP and pluripotency marker genes expression in several OSKM + D

clones (Supplementary Fig. 2f,g). These clones generated teratomas consisting of all three germ-layer derivatives and chimeras with germline transmission (Fig. 2f,g). Genotyping of F1 progeny confirmed the presence of OSKM + D constructs (Supplementary Fig. 3). Next, we investigated whether *Dppa3* can replace any of the reprogramming factors during iPSCs generation. MEFs supplemented with *Dppa3*, replacing any Yamanaka factor, failed to generate iPSCs (Supplementary Fig. 4), suggesting that *Dppa3* cooperates with other reprogramming factors, but cannot drive reprogramming if any are lacking.

Modified StemPro medium generates exclusively $Gtl2^{on}$ iPSCs. During the course of this study, we investigated whether Stem-Pro-based low-serum medium (SPVc), which we regularly use for the culture of spermatogonial stem cells [28], can generate all $Gtl2^{on}$ iPSCs with greater efficiency. To this end, we reprogrammed *Nanog*-EGFP MEFs with OSKM in SPVc medium and found ESC-like colonies already by day 6 of reprogramming that finally resulted in a two-fold increase in AP- and *Nanog*-EGFP-positive colonies (Fig. 3a,b). All SPVc-derived lines analysed were $Gtl2^{on}$ (Fig. 3c) and expressed maternally expressed miRNAs, validating activation of *Dlk1-Dio3* locus genes (Fig. 3d). These results led us

to hypothesize that the components of SPVc help in proper maintenance of imprinting at the *Dlk1-Dio3* locus during reprogramming. The SPVc medium inherently contains Vc that was reported to protect against the loss of *Dlk1-Dio3* imprinting during reprogramming[10]. It was shown that Vc functions primarily by preserving active chromatin structure at the *Dlk1-Dio3* locus and by preventing recruitment of Dnmt3a, a *de novo* DNA methyltransferase, to this locus. Hence, we asked whether StemPro-based low-serum medium depleted of Vc (SP) can also generate exclusively $Gtl2^{on}$ iPSCs with reprogramming kinetics similar to SPVc. However, the use of SP medium resulted in
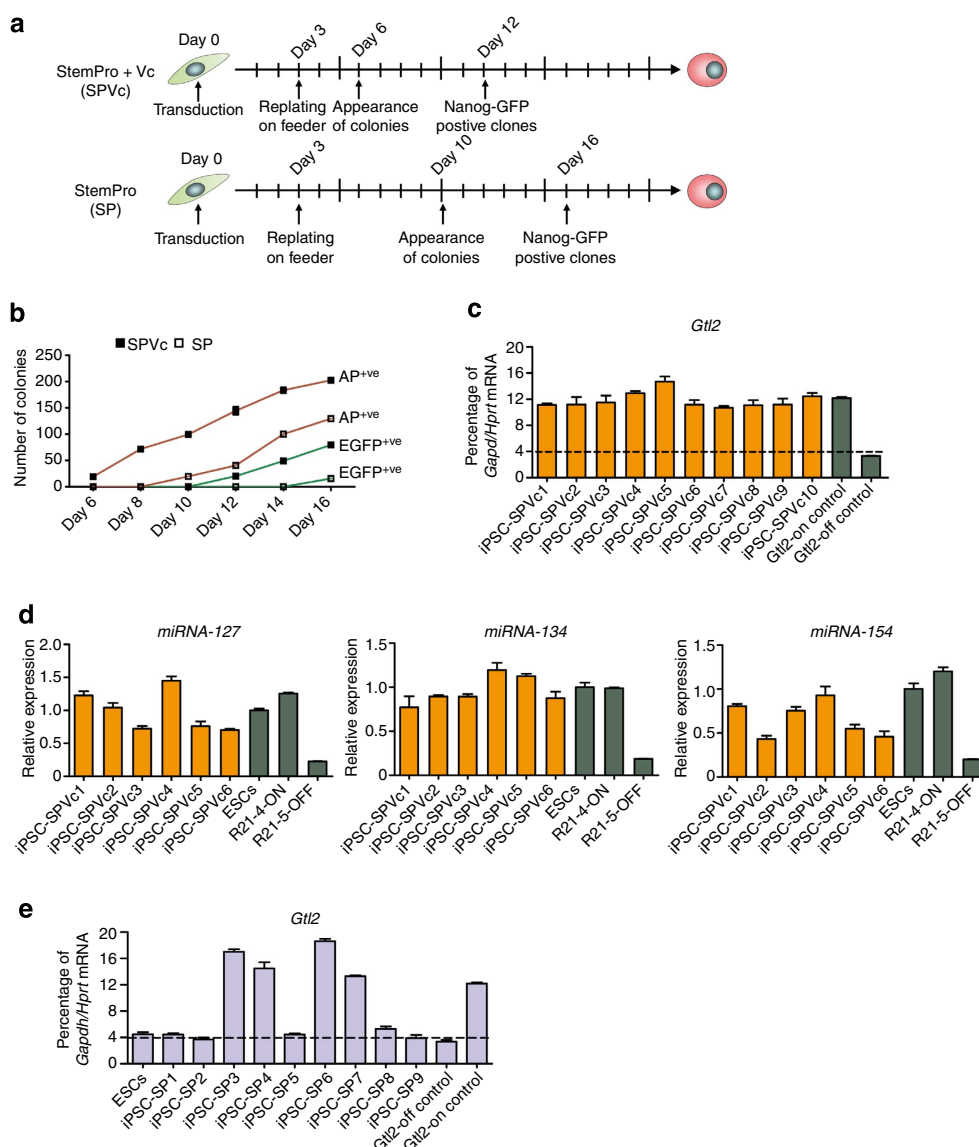

Figure 3 | Vitamin C (Vc) enhances reprogramming and generates fully pluripotent iPSCs in low-serum medium. (**a**) Time scale showing the start of viral transduction followed by appearance of ESC-like and *Nanog*-EGFP-positive colonies during iPSC generation using OSKM in the low-serum medium StemPro (SP) in the presence (SPVc) or absence (SP) of supplementation with Vc. (**b**) Line graph showing the number of AP-positive (AP^{+ve}) and EGFP-positive (EGFP^{+ve}) colonies during the reprogramming time course in the presence of SP or SPVc. (**c**) qRT–PCR data showing the expression of *Gtl2* RNA in iPSC clones generated using SPVc (iPSC-SPVc). Previously generated $Gtl2^{off}$ and $Gtl2^{on}$ iPSC clones were used as controls. *Gtl2* RNA expression and associated error bars, representing mean ± s.d. ($n = 3$), were normalized to housekeeping genes, *Gapdh* and *Hprt* and presented as percentage of expression. (**d**) qRT–PCR data showing the expression of miRNA-127, miRNA-134, and miRNA-154 in iPSC-SPVc clones. ESCs, R21-4-ON ($Gtl2^{on}$) and R21-5-OFF ($Gtl2^{off}$) were used as controls. *miRNA* expression and associated error bars, representing mean ± s.d. ($n = 3$), were normalized to expression level in ESCs. (**e**) qRT–PCR data showing the expression of *Gtl2* RNA in iPSC clones generated using SP only (iPSC-SP). Previously generated $Gtl2^{off}$ and $Gtl2^{on}$ iPSC clones were again used as controls. *Gtl2* RNA expression and associated error bars, representing mean ± s.d. ($n = 3$), were normalized to housekeeping genes, *Gapdh* and *Hprt* and presented as percentage of expression.

slower reprogramming kinetics and only four of nine iPSC clones (SP-iPSC) were $Gtl2^{on}$ (Fig. 3b,e).

Dppa3-deficient fibroblasts arrest in pre-iPSC state. On the basis of parallels between Dppa3 and Vc in preventing *Dlk1-Dio3* imprinting loss, we investigated whether Vc treatment compensates for the Dppa3 absence during reprogramming. Towards this end, we reprogrammed MEFs derived from the *Dppa3*-knockout (KO)/*Oct4*-EGFP animals (KO_MEFs) (Supplementary Fig. 5) in the presence and absence of Vc and in the presence of exogenous *Dppa3*. Reprogramming of KO_MEFs with OSKM-only resulted in iPSC-like colonies that, however, failed to activate the *Oct3/4*-driven EGFP, whereas cells reprogrammed with OSKM+Vc or OSKM+D showed efficient activation of the *Oct3/4*-EGFP (Fig. 4a). The mRNA expression analysis for pluripotency marker genes revealed that KO_MEFs reprogrammed with OSKM-only (iPSC_K4) are arrested in the pre-iPSC state, as they could not activate the endogenous pluripotency network, whereas the cells reprogrammed with OSKM+Vc (iPSC_KV) or OSKM+D (iPSC_K5) showed expression levels comparable to control cells (Fig. 4b). Silencing of exogenous reprogramming factors is crucial for proper transition from maturation-to-stabilization phase during the reprogramming and transition failure results in loss of endogenous pluripotency network activation[6]. Interestingly, OSKM-only-reprogrammed cells failed to inactivate viral transgenes, as indicated by higher levels of total *Oct3/4* mRNA levels derived from the transgene (Fig. 4b). iPSC_K4 clones showed very low *Gtl2* mRNA levels and IG-DMR hypermethylation, whereas clones derived from OSKM+Vc (iPSC_KV) or OSKM+D (iPSC_K5) conditions showed normal *Gtl2* expression and methylation (Fig. 4c,d). The DNA methylation analysis of two additional imprinted loci, *H19* and *Snrpn*, showed normal DNA methylation levels in iPSC clones form all three conditions (Supplementary Fig. 6a,b), indicating that Dppa3 depletion specifically affects the *Dlk1-Dio3* imprinting. It is known that Dppa3 suppresses ERVs such as IAPs and LINEs during early embryogenesis[26]. To determine whether ERVs are suppressed in iPSCs derived from *Dppa3*-KO fibroblasts, we performed quantitative reverse transcription PCR (qRT–PCR) analysis for their expression and found that IAPs are significantly activated in OSKM-only, but not in OSKM+Vc or OSKM+D, iPSCs (Fig. 4e).

To verify whether Vc functions in conversion of pre-iPSCs derived from KO_MEFs towards lg-iPSCs or hg-iPSCs, we cultured these cells with Vc and could observe the activation of *Oct3/4*-EGFP (Fig. 4f). These colonies resembled lg-iPSCs and showed no *Gtl2* expression at a global level (data not shown), suggesting that Vc can overcome the reprogramming block, but cannot restore the imprinting defect in the resulting lg-iPSCs. To determine whether exogenous Dppa3 can rescue the reprogramming block seen in KO_MEFs-derived pre-iPSCs, we supplemented these clones with retroviral Dppa3 and observed neither *Gtl2* activation nor morphological changes (Supplementary Fig. 7a–c).

Vitamin C (Vc) mediates early activation of Dppa3. We hypothesized that Vc might activate *Dppa3*, which is ultimately responsible for maintenance of proper imprinting during early stages of reprogramming. To verify this hypothesis, we reprogrammed *Nanog*-MEFs using OSKM in standard ESC medium in the presence or absence of Vc and investigated changes in chromatin modifications and pluripotency marker expression. After day 5 of reprogramming, MEFs treated with Vc (+Vc) showed enrichment for H3K4me3, a histone modification mark associated with active gene transcription, whereas MEFs treated without Vc (−Vc) showed basal H3K4me3 levels (Fig. 5a,b).

In contrast to H3K4me3, the levels of H3K27me3, a histone mark associated with transcription repression, were reduced in +Vc, but not in −Vc cells (Fig. 5a,b). These changes were also evident at day 7 of reprogramming (Fig. 5a,b). Endogenous *Oct3/4* and *Sox2* mRNA expression was activated at least two days earlier in +Vc than in −Vc cells (Fig. 5c). Further, by day 12 of reprogramming, we observed much higher levels of endogenous *Oct3/4* and *Sox2* mRNA levels in +Vc cells compared with −Vc cells (Fig. 5c). Surprisingly, *Dppa3* mRNA expression was already detected by day 2 of reprogramming in +Vc treated MEFs, but only by day 6 of reprogramming in control −Vc cells (Fig. 5c). Correlating early *Dppa3* activation with potential Vc-induced chromatin changes, we hypothesized that exogenous reprogramming factor(s) might gain access to the *Dppa3* promoter and activate its expression early in Vc-treated cells. To ascertain this assumption, we searched publicly available chromatin immunoprecipitation (ChIP)-Seq data for *Oct3/4*- and *Sox2*-binding sites/targets across the ESC genome (http://promotion.molgen.mpg.de/gb2/gbrowse/Mm.enhancer/) and found *Oct3/4* and *Sox2* binding sites at the *Dppa3* promoter region[29] (Fig. 5d). To validate these global ChIP-Seq data, we performed ChIP assays with anti-Oct3/4 and anti-Sox2 antibodies and quantitative PCR (qPCR) analysis of two PCR amplicons in the *Dppa3* promoter region. The qPCR data clearly showed that Oct3/4 and Sox2 bind *Dppa3* promoter region (Fig. 5e).

Dppa3 binds to the IG-DMR of the Dlk1-Dio3 cluster. Dppa3 is considered as a DNA-binding protein and indeed *in vitro* studies have shown that it binds DNA non-specifically[26]. To test the hypothesis that Dppa3 is physically associated with the IG-DMR of the *Dlk1-Dio3* region, we performed ChIP assay with Dppa3 antibody and ESC chromatin. As the IG-DMR spans around 4.2 kb in the *Dlk1-Dio3* cluster, we designed eight PCR amplicons (P1–P8) covering the entire region (Fig. 6a). ChIP assays revealed that Dppa3 specifically binds the IG-DMR region represented by amplicons P2 and P3 (Fig. 6b). Recent data showed that Dnmt3a is highly enriched at the IG-DMR during somatic cell reprogramming; probably leading to the silencing of maternal allele and that this effect can be counteracted by the addition of Vc[10]. This led us to analyse whether exogenous Dppa3 can also counteract Dnmt3a binding at the IG-DMR. Interestingly, Dnmt3a association with P2 and P3 was significantly reduced in OSKM+D-transduced cells on day 9 of reprogramming, whereas OSKM-only-transduced cells showed Dnmt3a enrichment (Fig. 6c). Similar results were obtained at day 12 of reprogramming (Fig. 6d), confirming that Dppa3 prevents IG-DMR hypermethylation by preventing Dnmt3a binding. These results indicate that Vc facilitates *Dppa3* transcription during early stages of reprogramming leading to the initiation of maturation process, binding of Dppa3 to the *Dlk1-Dio3* cluster and restriction of Dnmt3a access to this locus.

Discussion
By identifying Dppa3 expression in lg-iPSCs ($Gtl2^{off}$) and hg-iPSCs ($Gtl2^{on}$), but not in pre-iPSCs, we hypothesized that the temporal expression of Dppa3 is crucial for the maintenance of *Dlk1-Dio3* imprinting in lg-iPSCs. This assumption was supported by our observation that *Dppa3*-KO fibroblasts undergoing reprogramming were arrested in pre-iPSCs state and that the addition of Vc to these pre-iPSCs can only convert them to lg-iPSCs, which show abnormal *Dlk1-Dio3* imprinting. Further, we identified that in the absence of Dppa3, the ERVs as well as exogenous retrovirus-mediated reprogramming factors remain unsilenced leading to maturation-to-stabilization transition failure. Collectively, our results reveal that the temporal
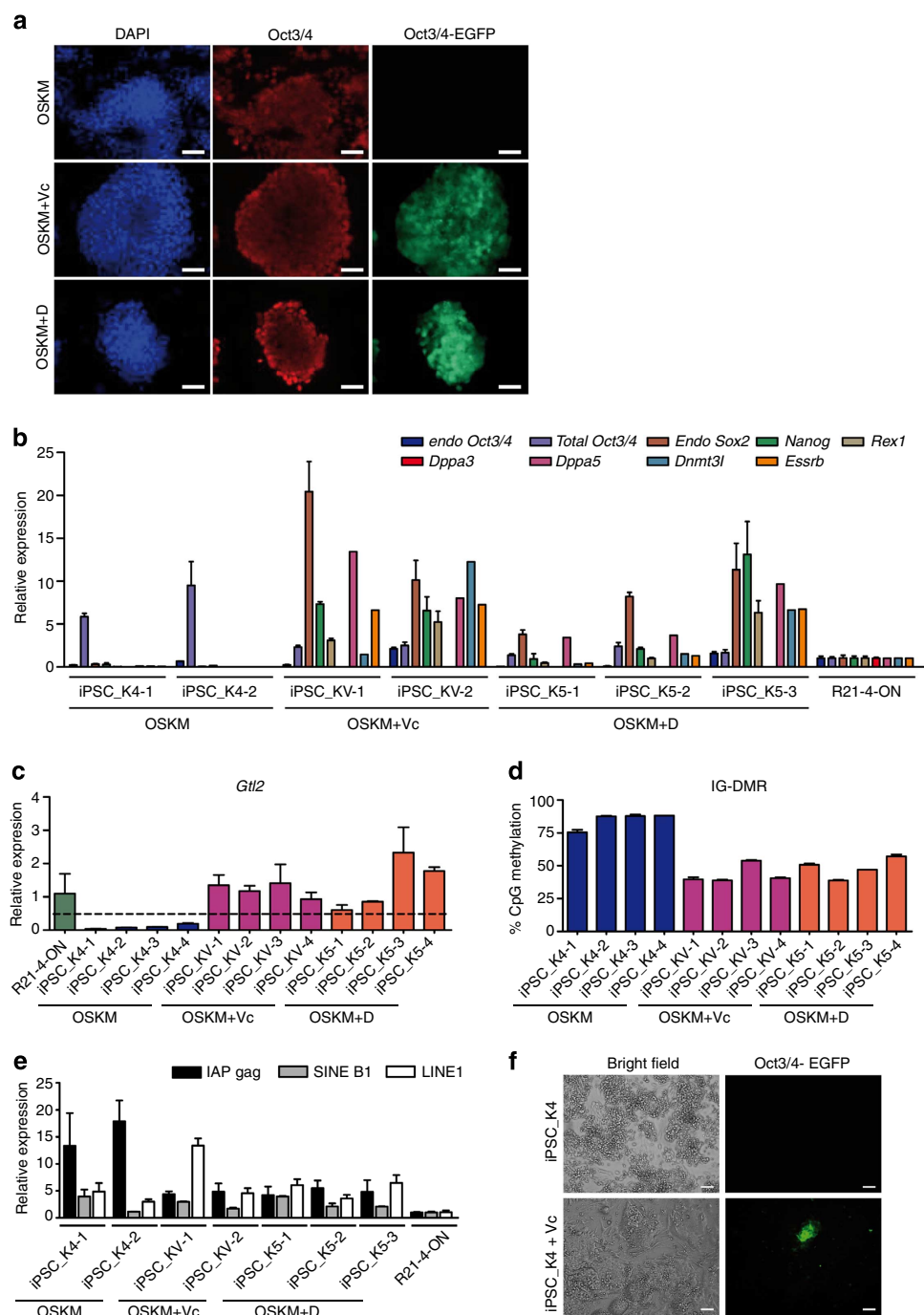
Figure 4 | *Dppa3*-knockout (KO) fibroblasts are arrested in pre-iPSC state during reprogramming. (**a**) Immunofluorescence images showing Oct3/4-positivity and activation of *Oct3/4*-driven EGFP in *Dppa3*-KO fibroblasts reprogrammed either with OSKM (upper panel), OSKM + Vc (middle panel) or OSKM + Dppa3 (lower panel). Nuclei were counterstained with DAPI. Scale bars correspond to 50 μm. (**b**) qRT–PCR data showing the expression of various pluripotency marker genes in the indicated *Dppa3*-KO-derived iPSCs generated with OSKM + Vc and OSKM + D, but not in OSKM-only-generated iPSCs. Gene expression and associated error bars, representing mean ± s.d. (*n* = 3), were normalized to expression level in *Gtl2*[on] iPSC clone[6] (R21-4-ON). (**c**) qRT–PCR data showing expression of *Gtl2* RNA in *Dppa3*-KO-derived iPSCs in presence of OSKM (blue), OSKM + Vc (purple) or OSKM + Dppa3 (red). *Gtl2* RNA expression and associated error bars, representing mean ± s.d. (*n* = 3), were normalized to expression level in *Gtl2*[on] iPSC clone[6] (R21-4-ON). (**d**) DNA methylation analysis of the *Gtl2* IG-DMR in iPSCs generated from *Dppa3*-KO fibroblasts with OSKM-only (blue), OSKM + Vc (purple) and OSKM + Dppa3 (red). Error bars represent mean ± s.d. (*n* = 2). (**e**) qRT–PCR data showing expression of retrotransposons, intracisternal A-particles (IAP gag, black), short interspersed nuclear elements (SINE B1, grey), and long interspersed nuclear elements (LINE 1, white), in *Dppa3*-KO-derived iPSCs in presence of OSKM, OSKM + Vc or OSKM + Dppa3. Retrotransposons expression and associated error bars, representing mean ± s.d. (*n* = 3), were normalized to expression level in *Gtl2*[on] iPSC clone[6] (R21-4-ON). (**f**) Bright-field image (left panel) showing colony morphology and fluorescence image (right panel) showing the activation of *Oct3/4*-driven EGFP in iPSCs derived from *Dppa3*-KO fibroblasts with OSKM (upper panel) and the same clones treated with Vc (iPSC_K4 + Vc) (lower panel). Scale bars correspond to 200 μm.
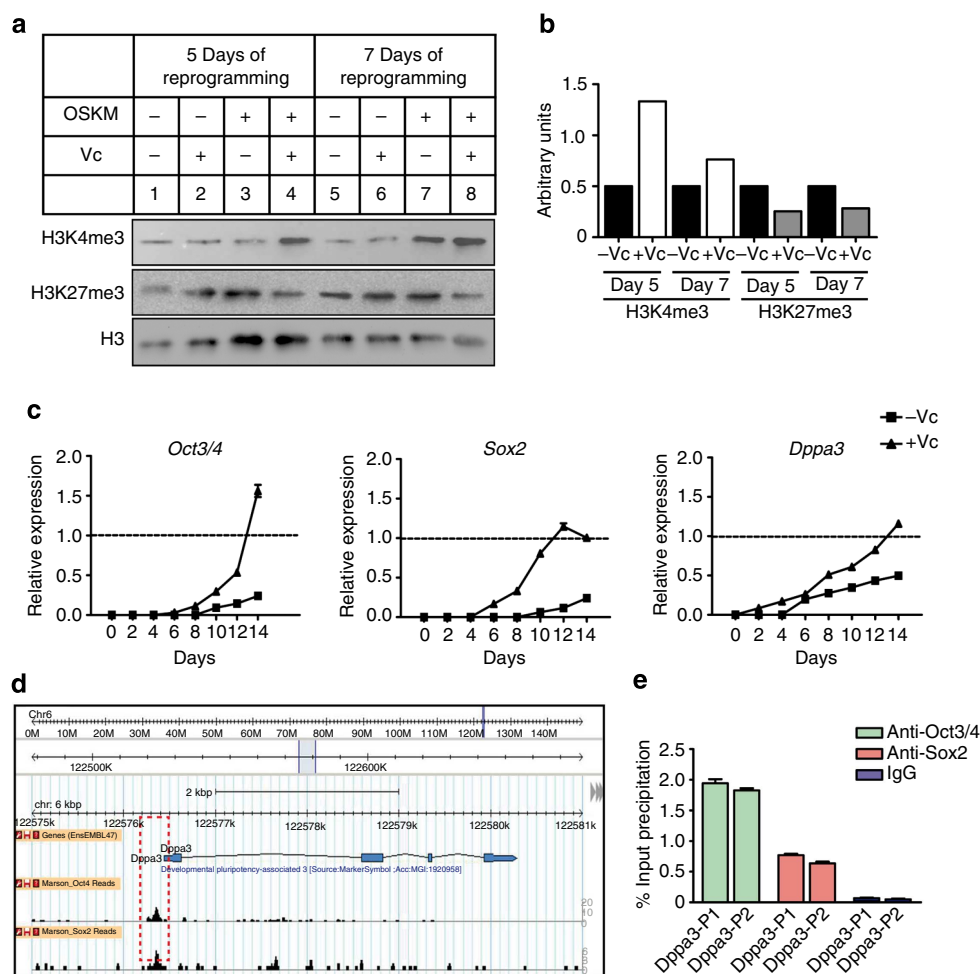
Figure 5 | Vitamin C mediates global chromatin relaxation and early activation of pluripotency-related genes. (**a**) Western blots showing expression of histone modifications during OSKM reprogramming on days 5 and 7 in standard ESC culture medium in the presence and absence of Vc. MEFs supplemented with no OSKM or Vc (lanes 1 and 5), either Vc only (lanes 2 and 6), or OSKM only (lanes 3 and 7) served as controls. All blots were reprobed with an anti-total Histone 3 (H3) antibody, and one representative blot shows loading control. (**b**) Quantification of densitometric intensity of H3K4me3 and H3K27me3 bands shown in (**a**). (**c**) qRT–PCR data showing the expression of *Oct3/4* (left panel), *Sox2* (middle panel), and *Dppa3* (right panel) mRNAs during the OSKM reprogramming time course in standard ESC culture medium in the presence (+ Vc) or absence (− Vc) of Vc. Gene expression and associated error bars, representing mean ± s.d. ($n = 3$), were normalized to expression level in ESCs (dotted line). (**d**) Publicly available ChIP-Seq data showing the binding of Oct3/4 and Sox2 (black peaks) in the *Dppa3* promoter region (red box). (**e**) ChIP–qPCR analysis showing the binding of Oct3/4 (green) and Sox2 (maroon) at the *Dppa3* promoter region (amplicons Dppa3-P1 and Dppa3-P2) in ESCs. ChIP with IgG (blue) served as a negative control. The ChIP data, representing mean ± s.d. ($n = 2$), is presented as percent of input DNA. a.u., arbitrary units.

expression of Dppa3 is crucial not only for maintaining the *Dlk1-Dio3* imprinting, but also for transition from pre-iPSC-to-lg-iPSC and to establish the authentic induced pluripotency.

Dppa3 is highly expressed during embryonic development, as well as in germ cells and pluripotent stem cells[30,31]. Gene ablation studies of *Dppa3* in mice revealed that it functions during early embryonic development to protect the maternal genome against the first wave of active DNA demethylation[26]. Moreover, *Dppa3* was also shown to be essential for protecting several but not all imprinted loci and ERVs against DNA demethylation during post-fertilization events[26]. Interestingly, the paternally methylated *Dlk1-Dio3* region was not affected in *Dppa3*-null fertilized oocytes, whereas *H19* and *Rasgrf1*, the two other paternally methylated imprinted loci, showed partial loss of imprints[26]. Similarly, our current analysis of *Dppa3*-deficient ESCs also revealed no obvious defects in *Dlk1-Dio3* imprinting. In contrast to these observations, *Dppa3*-deficient fibroblasts failed to reprogram, arrested in pre-iPSCs state and showed imprinting defect at the *Dlk1-Dio3* cluster. This discrepancy could be mainly

due to artificial reprogramming of somatic cells versus normal early embryonic development. Another explanation would be that the oocyte-delivered Dppa3 might maintain stable *Dlk1-Dio3* imprinting in $Dppa3^{−/−}$ embryos and ESCs derived thereof. Supporting this view, imprinting of paternally methylated *H19* and *Rasgrf1* is markedly disturbed in ESCs derived from $Dppa3^{−/−}$ embryos, whereas the *Dlk1-Dio3* imprinting is stable and normal.

A recent report described that Dppa3 binds to nucleosomes containing an H3K9me2[32]. Our ChIP analysis showed that Dppa3 binds to a specific region in the *Dlk1-Dio3* IG-DMR, which also suggests that the interaction might involve modified histones. Unlike many imprinted loci, the IG-DMR of the *Dlk1-Dio3* cluster was reported to contain negligible H3K9me2 (ref. 32). Thus, it is possible that the association of Dppa3 with the IG-DMR is mediated by histone modifications other than H3K9me2 or another interaction protein.

Recently, Stadtfeld et al.[10] showed that Vc can prevent the *Dlk1-Dio3* imprinting defect during reprogramming mainly by
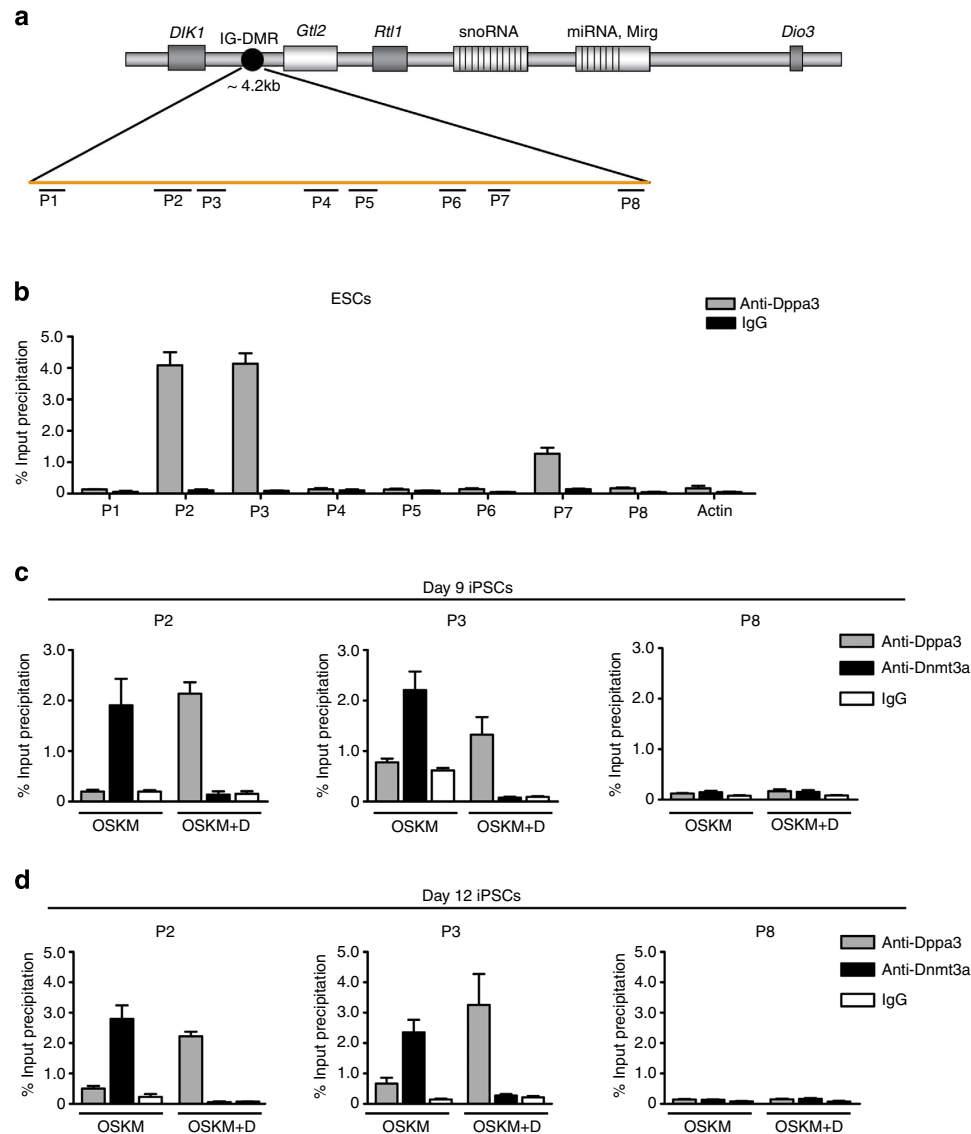
Figure 6 | Dppa3 binds to a specific region within the IG-DMR of the *Dlk1-Dio3* imprinted cluster and prevents the recruitment of Dnmt3a.
(**a**) Simplified schematic diagram showing the *Dlk1-Dio3* imprinted cluster together with paternally expressed genes (dark grey boxes) and maternally expressed genes (light grey boxes). The ~4.2 kb long IG-DMR (black circle), representing the imprinted control region, and the eight ChIP–qPCR amplicons (P1–P8) spanning the entire IG-DMR are indicated. (**b**) ChIP–qPCR analysis of Dppa3-binding sites (grey) across the eight PCR amplicons of the IG-DMR in ESCs. ChIP with IgG (black) was used as a negative control. The ChIP data, representing mean ± s.d. ($n = 2$), is presented as percent of input DNA. (**c,d**) ChIP–qPCR of Dppa3 (grey) and Dnmt3a (black) binding at the P2, P3 and P8 amplicons of the IG-DMR in OSKM and OSKM + D on day 9 (**c**) and day 12 (**d**) of reprogramming. ChIP with IgG (white) was used as a negative control. The ChIP data, representing mean ± s.d. ($n = 3$), is presented as percent of input DNA.

preserving the active chromatin structure at this locus. The resulting active chromatin was suggested to counteract the recruitment of Dnmt3a, a *de novo* DNA methyltransferase, to this locus thus maintaining the normal imprinting in Vc-treated cells[10]. Our results are in consistent with observations of Stadtfeld *et al.*[10], indicating that Vc enhances reprogramming kinetics and prevents *Dlk1-Dio3* imprinting loss. Moreover, the comparison of reprogramming kinetics between Vc and OSKM + D showed that Vc treatment resulted in appearance of iPSC colonies at least 2 days earlier than with OSKM + D, indicating that Vc broadly impacts reprogramming. Recently, it was reported also that culturing of pre-iPSCs in the presence of Vc establishes chimera forming iPSCs; however, germline transmission and *Dlk1-Dio3* imprinting status have not been tested[4]. We observed that although Vc can overcome the pre-iPSCs arrest of Dppa3-KO

cells and result in lg-iPSCs establishment, it could not establish the normal imprinting at *Dlk1-Dio3* locus. These results highlight that Vc-mediated chromatin changes or gene expression during early stages of reprogramming are crucial for maintenance of *Dlk1-Dio3* imprinting.

Dppa3's role in preventing the *Dlk1-Dio3* imprinting defect suggests that Vc functions through *Dppa3* activation, or Vc and *Dppa3* function independently in a similar mechanistic pathway. The former cooperative model is supported by the observation that *Dppa3* transcripts are upregulated in Vc-treated cells. The acceleration and efficiency of reprogramming seen with Vc[4,10,33] is also observed with exogenous Dppa3, indicating that Dppa3 either alone or in cooperation with other yet unknown factor(s) might implement Vc-mediated maintenance of *Dlk1-Dio3* imprinting. Moreover, the early Dppa3 expression is crucial for

timely suppression of virus-mediated reprogramming factors and transition of pre-iPSC into lg-iPSC state. On the basis of our observations, we propose that early Dppa3 expression, by exogenous induction or Vc exposure, is followed by Dppa3 binding to the IG-DMR and probably to other genomic regions. Bound Dppa3 prevents Dnmt3a recruitment to the IG-DMR, maintaining the imprinting and expression of imprinted *Dlk1-Dio3* genes. In line with this hypothesis, it was recently shown that the forced expression of Dppa3 in NIH3T3 cells causes the global DNA demethylation by counteracting the recruitment of Dnmt1, a maintenance DNA methyltransferase[34]. The observed counteracting mechanism was partially mediated by Dppa3 competing for the interaction with Uhrf1/Np95, a protein known to recruit Dnmt1 to hemimethylated DNA and to maintain the DNA methylation during replication[34–36]. Considering these above observations along with the fact that *de novo* DNA methylation process requires cooperation between Dnmt3a and Dnmt1 enzymes[37], we suggest that Dppa3 is functioning in a similar way to block the accession of Dnmt3a to *Dlk1-Dio3* locus during somatic reprogramming. In the second scenario, the function of Dppa3 is compensated by other Dppa family members or unknown factors, which also implement Vc-mediated imprinting maintenance.

Methods

Cell culture. Mouse ESCs and induced pluripotent stem cells (iPSCs) were cultured in Dulbecco's Modified Eagle Medium (DMEM) (PAN, Germany) supplemented with 15% foetal calf serum (FCS; PAN), 2 mM L-glutamine (PAN), 50 μM β-mercaptoethanol (Gibco/Life Technologies), 1% non-essential amino acids (NEAA) (Gibco/Life Technologies), 1% sodium pyruvate (Gibco/Life Technologies), 1% penicillin/streptomycin (PAN), and 1,000 U ml^{-1} leukemia inhibitory factor (LIF) (Millipore, Germany). For reprogramming studies with low-serum medium, cells were cultured in StemPro medium (Invitrogen/Life Technologies) supplemented with StemPro supplement (Invitrogen/Life Technologies), 1% FCS, 2 mM L-Glutamine, 1 mM sodium pyruvate, 1% NEAA, 100 μM β-mercaptoethanol and 1000 U ml^{-1} LIF in the presence or absence of 50 μg ml^{-1} vitamin C (Sigma-Aldrich).

Preparation of *Dppa3*-KO/*Oct4*-EGFP fibroblasts (MEFs). *Dppa3*-KO mice were generated using the conventional knockout strategy, and were maintained in a 129/Sv and C57BL/6 mixed background[26]. *Oct4*-EGFP transgenic mice were maintained in a DBA2 and C57BL/6 mixed background[38]. The animals were cared for in accordance with the guidelines of Osaka University Animal Care and Use Committee. To prepare *Dppa3*-KO/*Oct4*-EGFP MEFs, *Dppa3*$^{-/-}$ male mice carrying the *Oct4*-EGFP transgene were crossed with *Dppa3*$^{+/-}$ female mice carrying the *Oct4*-EGFP transgene. The morning on which a copulation plug was noted was defined as embryonic day 0.5 (E0.5). MEFs were isolated from E13.5 embryos. After the removal of the head, visceral tissues and gonads, the remaining bodies were washed with phosphate-buffered saline, minced and dissociated with 0.1% Trypsin/1mM EDTA solution. MEFs from each embryo were plated on individual 0.1% gelatin-coated 100 mm dishes and incubated at 37 °C with 5% CO$_2$. We used the MEFs within two passages from initial plating to avoid replicative senescence. The embryo heads were used for genotyping *Dppa3* as described previously[26]. The sex of the embryos and the presence of the *Oct4*-EGFP transgene were determined by morphology and EGFP fluorescence of gonads, respectively. *Dppa3*-KO MEFs preparations were approved by Osaka University Animal Care and Use Committee.

Generation of iPSCs. We used retroviral expression vectors for *Oct3/4*, *Sox2*, *Klf4* and *c-Myc* either in presence or absence of *Dppa3* (ref. 3) to reprogram MEFs into iPSCs. Briefly, MEFs isolated from transgenic *Nanog*-EGFP mice[39] or *Dppa3*-KO/*Oct4*-EGFP mice were transduced with retroviral particles as described[27]. To establish iPSC lines, colonies appearing 8–12 days after transduction were selected and cultured in 24-well plates under standard ESC culture conditions and monitored for ESC-like morphology using an Olympus IX71 inverted microscope (Olympus). Further, several independent iPSC lines were established from each combination to examine the expression of *Gtl2*, as well as for further characterization. Alternatively, iPSCs were generated in low-serum medium, as described above.

Immunostaining and alkaline phosphatase (AP) staining. Immunostaining was performed as described previously[40] using mouse monoclonal antibodies to SSEA1. Cytochemical staining for AP was performed using the Leukocyte Alkaline Phosphatase Kit (Sigma-Aldrich).

Total protein extraction and western blotting. Total protein extracts were prepared using lysis buffer (10 mM Tris-HCl, pH 8.0, 1 mM EDTA, 2.5% SDS, 100 mM phenylmethylsulfonyl fluoride (PMSF)) containing protease inhibitor cocktail (Roche). Protein samples were resolved on 4–12% SDS–PAGE gels (Life Technologies) and transferred onto nitrocellulose membranes (Amersham Biosciences/GE Healthcare). Membranes were processed using standard western blot protocols, and signals were detected using a chemiluminescence kit (Santa Cruz Biotechnology). Antibody sources are listed in Supplementary Table 1.

RNA extraction and real-time PCR (qRT–PCR) analysis. Total RNA was extracted from cells using NucleoSpin miRNA kit (Machery-Nagel) following the manufacturer's protocols. For the mRNA quantification experiment, 5 μg total RNA was converted into complementary DNA (cDNA) using the SuperScript II System (Invitrogen/Life Technologies). For the miRNA quantification experiment, 1 μg total RNA was used for cDNA synthesis using the miScript II RT Kit (Qiagen). For qRT–PCR analysis, diluted cDNA (1/10) was used as a template in QuantiFast SYBR Green (Qiagen) assays on an ABI7900HT Real-Time PCR System (Applied Biosystems). The qRT–PCR data were normalized to the expression of house-keeping genes (*Hprt* and *Gapdh*) and presented as percent expression of the mean of the two housekeeping genes. Primers used in qRT–PCR are listed in Supplementary Table 2.

Bisulfite sequence analysis. WT or *Dppa3*-KO ES cells were bisulfite-treated using the EpiTect Bisulfite Kit (Qiagen). To amplify the DMRs of *H19*, *Dlk1/Gtl2* and *Rasgrf1*, fully or seminested PCR was performed. The first and second rounds of PCR were performed using AccuPrime Taq DNA polymerase (Invitrogen) and ExTaq HS (Takara Bio), respectively. The first round of PCR consisted of the following cycling conditions: 2 min at 94 °C for 1 cycle and 30 s at 94 °C, 30 s at 50 °C and 1 min at 68 °C for 30 cycles. The second round of PCR consisted of the following cycling conditions: 2 min at 94 °C for 1 cycle and 30 s at 94 °C, 30 s at 55 °C and 1 min at 72 °C for 30 cycles. The sequences of the PCR primers have been described previously[26]. The PCR products were purified using the QIAEX II Gel Extraction Kit (QIAGEN), cloned into the pGEM-T Vector (Promega) and sequenced using an ABI PRISM 3100 Genetic Analyzer (Applied Biosystems).

Methylation analysis of the *Gtl2* IG-DMR. Genomic DNA isolation from cells and bisulfite pyrosequencing were performed as previously described[41]. Briefly, Genomic DNA of MEFs, iPSCs and ESCs was extracted with the GentraPuregeneKit (Qiagen) according to the manufacturer's instructions and quantified using a NanoDrop 2000 spectrophotometer. Bisulfite conversion of 500 ng genomic DNA per sample was performed with the EpiTect Bisulfite Kit (Qiagen) according to the manufacturer's specifications. Quantification of DNA methylation was carried out by PCR of Bisulfite-converted DNA and pyrosequencing. PCR and sequencing primers for bisulfite pyrosequencing were designed using the Pyrosequencing Assay Design Software 2.0 (Qiagen) and are listed in Supplementary Table 2. For pyrosequencing, a PyroMark Q96 ID instrument (Qiagen) and PyroMark Gold Q96 reagents (Qiagen) were used. Data were analysed using the PyroMark CpG Software 1.0.11 (Qiagen).

Chromatin immunoprecipitation (ChIP) assay. ChIP assays were performed on ESCs and MEFs undergoing reprogramming using the Diagenode OneDay ChIP kit (Diagenode). Briefly, the cells (3×10^6 cells per pull-down) were crosslinked using formaldehyde and lysed using the shearing kit (Diagenode), followed by sonication using a bioruptor (Diagenode, UCD-200 TM) to obtain an average chromatin size of 400 bp. Then, the sheared chromatin was immunoprecipitated with 5 μg of indicated antibodies, and the Diagenode OneDay ChIP protocol was followed to extract the chromatin bound to each specific antibody. Rabbit IgG was used as a control in mock ChIP experiments. Quantitative analysis was performed using qRT–PCR and the primers listed in Supplementary Table 2. The ChIP-qPCR data were analysed using ΔCt method in which the immunoprecipitated (IPed) sample Ct value was normalized to the input DNA Ct value and the percentage of precipitation was calculated using the following formula- %input = 2^-(Ct Input— Ct IPed) × dilution factor of Input DNA × 100%. All fold enrichment values are means of three independent experiments.

Teratoma formation assay. The teratoma formation assay was performed as previously described[42,43]. Briefly, iPSCs (1×10^6 cells) were injected subcutaneously into RAG2$^{-/-}$γc$^{-/-}$ mice lacking T, B and natural killer (NK) cells. Tumour growth was monitored weekly by palpation and size was measured using linear calipers. Animals were sacrificed when a tumour diameter of 1 cm was reached. Autopsies were performed and tumour tissue was placed in phosphate-buffered 4% formalin for 16 h and then embedded in paraffin. For histological analysis, the specimens were stained with hematoxylin and eosin (HE).

Replicates. Unless otherwise stated, all results presented are representative of two or more independent experiments. All qRT–PCR data for RNA expression analysis were calculated using either the standard curve method or comparative Ct method.

References

1. Grabel, L. Prospects for pluripotent stem cell therapies: into the clinic and back to the bench. *J. Cell. Biochem.* **113,** 381–387 (2012).
2. Takahashi, K. *et al.* Induction of pluripotent stem cells from adult human fibroblasts by defined factors. *Cell* **131,** 861–872 (2007).
3. Takahashi, K. & Yamanaka, S. Induction of pluripotent stem cells from mouse embryonic and adult fibroblast cultures by defined factors. *Cell* **126,** 663–676 (2006).
4. Chen, J. *et al.* H3K9 methylation is a barrier during somatic cell reprogramming into iPSCs. *Nat. Genet.* **45,** 34–42 (2013).
5. Mattout, A., Biran, A. & Meshorer, E. Global epigenetic changes during somatic cell reprogramming to iPS cells. *J. Mol. Cell. Biol.* **3,** 341–350 (2011).
6. Silva, J. *et al.* Promotion of reprogramming to ground state pluripotency by signal inhibition. *PLoS Biol.* **6,** e253 (2008).
7. Sridharan, R. *et al.* Role of the murine reprogramming factors in the induction of pluripotency. *Cell* **136,** 364–377 (2009).
8. Stadtfeld, M. *et al.* Aberrant silencing of imprinted genes on chromosome 12qF1 in mouse induced pluripotent stem cells. *Nature* **465,** 175–181 (2010).
9. Liu, L. *et al.* Activation of the imprinted Dlk1-Dio3 region correlates with pluripotency levels of mouse stem cells. *J. Biol. Chem.* **285,** 19483–19490 (2010).
10. Stadtfeld, M. *et al.* Ascorbic acid prevents loss of Dlk1-Dio3 imprinting and facilitates generation of all-iPS cell mice from terminally differentiated B cells. *Nat. Genet.* **44,** 398–405 S391-392 (2012).
11. Spahn, L. & Barlow, D. P. An ICE pattern crystallizes. *Nat. Genet.* **35,** 11–12 (2003).
12. Ferguson-Smith, A. C. & Surani, M. A. Imprinting and the epigenetic asymmetry between parental genomes. *Science* **293,** 1086–1089 (2001).
13. Tycko, B. & Efstratiadis, A. Genomic imprinting: piece of cake. *Nature* **417,** 913–914 (2002).
14. Brandeis, M. *et al.* The ontogeny of allele-specific methylation associated with imprinted genes in the mouse. *EMBO J.* **12,** 3669–3677 (1993).
15. Allegrucci, C., Thurston, A., Lucas, E. & Young, L. Epigenetics and the germline. *Reproduction* **129,** 137–149 (2005).
16. Lucifero, D., Mertineit, C., Clarke, H. J., Bestor, T. H. & Trasler, J. M. Methylation dynamics of imprinted genes in mouse germ cells. *Genomics* **79,** 530–538 (2002).
17. Arnaud, P. Genomic imprinting in germ cells: imprints are under control. *Reproduction* **140,** 411–423 (2010).
18. Bourc'his, D., Xu, G. L., Lin, C. S., Bollman, B. & Bestor, T. H. Dnmt3L and the establishment of maternal genomic imprints. *Science* **294,** 2536–2539 (2001).
19. Hata, K., Okano, M., Lei, H. & Li, E. Dnmt3L cooperates with the Dnmt3 family of de novo DNA methyltransferases to establish maternal imprints in mice. *Development* **129,** 1983–1993 (2002).
20. Kaneda, M. *et al.* Essential role for de novo DNA methyltransferase Dnmt3a in paternal and maternal imprinting. *Nature* **429,** 900–903 (2004).
21. Jelinic, P., Stehle, J. C. & Shaw, P. The testis-specific factor CTCFL cooperates with the protein methyltransferase PRMT7 in H19 imprinting control region methylation. *PLoS Biol.* **4,** e355 (2006).
22. Kou, Y. C. *et al.* A recurrent intragenic genomic duplication, other novel mutations in NLRP7 and imprinting defects in recurrent biparental hydatidiform moles. *Mol. Hum. Reprod.* **14,** 33–40 (2008).
23. Li, X. *et al.* A maternal-zygotic effect gene, Zfp57, maintains both maternal and paternal imprints. *Dev. Cell.* **15,** 547–557 (2008).
24. Meyer, E. *et al.* Germline mutation in NLRP2 (NALP2) in a familial imprinting disorder (Beckwith-Wiedemann Syndrome). *PLoS Genet.* **5,** e1000423 (2009).
25. Murdoch, S. *et al.* Mutations in NALP7 cause recurrent hydatidiform moles and reproductive wastage in humans. *Nat. Genet.* **38,** 300–302 (2006).
26. Nakamura, T. *et al.* PGC7/Stella protects against DNA demethylation in early embryogenesis. *Nat. Cell. Biol.* **9,** 64–71 (2007).
27. Xu, X. *et al.* Stage-specific germ-cell marker genes are expressed in all mouse pluripotent cell types and emerge early during induced pluripotency. *PLoS ONE* **6,** e22413 (2011).
28. Smorag, L. *et al.* MicroRNA signature in various cell types of mouse spermatogenesis: evidence for stage-specifically expressed miRNA-221, -203, and -34b-5p mediated spermatogenesis regulation. *Biol. Cell.* **104,** 677–692 (2012).
29. Marson, A. *et al.* Connecting microRNA genes to the core transcriptional regulatory circuitry of embryonic stem cells. *Cell* **134,** 521–533 (2008).
30. Payer, B. *et al.* Stella is a maternal effect gene required for normal early development in mice. *Curr. Biol.* **13,** 2110–2117 (2003).
31. Sato, M. *et al.* Identification of PGC7, a new gene expressed specifically in preimplantation embryos and germ cells. *Mech. Dev.* **113,** 91–94 (2002).
32. Nakamura, T. *et al.* PGC7 binds histone H3K9me2 to protect against conversion of 5mC to 5hmC in early embryos. *Nature* **486,** 415–419 (2012).
33. Esteban, M. A. *et al.* Vitamin C enhances the generation of mouse and human induced pluripotent stem cells. *Cell Stem Cell* **6,** 71–79 (2010).
34. Funaki, S. *et al.* Inhibition of maintenance DNA methylation by Stella. *Biochem. Biophys. Res. Commun.* doi:10.1016/j.bbrc.2014.09.101 (2014).
35. Bostick, M. *et al.* UHRF1 plays a role in maintaining DNA methylation in mammalian cells. *Science* **317,** 1760–1764 (2007).
36. Sharif, J. *et al.* The SRA protein Np95 mediates epigenetic inheritance by recruiting Dnmt1 to methylated DNA. *Nature* **450,** 908–912 (2007).
37. Fatemi, M., Hermann, A., Gowher, H. & Jeltsch, A. Dnmt3a and Dnmt1 functionally cooperate during de novo methylation of DNA. *Eur. J. Biochem.* **269,** 4981–4984 (2002).
38. Yoshimizu, T. *et al.* Germline-specific expression of the Oct-4/green fluorescent protein (GFP) transgene in mice. *Dev. Growth Differ.* **41,** 675–684 (1999).
39. Okita, K., Ichisaka, T. & Yamanaka, S. Generation of germline-competent induced pluripotent stem cells. *Nature* **448,** 313–317 (2007).
40. Khromov, T. *et al.* Global and gene-specific histone modification profiles of mouse multipotent adult germline stem cells. *Mol. Hum. Reprod.* **17,** 166–174 (2011).
41. Zechner, U. *et al.* Comparative methylation profiles and telomerase biology of mouse multipotent adult germline stem cells and embryonic stem cells. *Mol. Hum. Reprod.* **15,** 345–353 (2009).
42. Dressel, R. *et al.* Multipotent adult germ-line stem cells, like other pluripotent stem cells, can be killed by cytotoxic T lymphocytes despite low expression of major histocompatibility complex class I molecules. *Biol. Direct.* **4,** 31 (2009).
43. Dressel, R. *et al.* Pluripotent stem cells are highly susceptible targets for syngeneic, allogeneic, and xenogeneic natural killer cells. *FASEB J.* **24,** 2164–2177 (2010).

Author contributions

X.X., L.S., W.E. and D.V.K.P. conceived the experiments and analysed the data. X.X., L.S. and X.T. performed reprogramming studies and analysed the data. T.N. performed DNA methylation and qRT–PCR analyses of Dppa3$^{-/-}$ ESCs. T.N. and T.K. provided Dppa3-KO fibroblasts. A.F., M.L. and U.Z. performed DNA methylation analysis of iPSC clones and analysed the data. R.D. performed teratoma experiments. X.X. and D.V.K.P. wrote the manuscript. U.Z. and W.E. edited the manuscript.

Additional information

REPRODUCTIVE BIOLOGY

Sperm calcineurin inhibition prevents mouse fertility with implications for male contraceptive

Haruhiko Miyata,[1] Yuhkoh Satouh,[1] Daisuke Mashiko,[1,2] Masanaga Muto,[1,3] Kaori Nozawa,[1,2] Kogiku Shiba,[4] Yoshitaka Fujihara,[1] Ayako Isotani,[5] Kazuo Inaba,[4] Masahito Ikawa[1,2,3,5]*

Calcineurin inhibitors, such as cyclosporine A and FK506, are used as immunosuppressant drugs, but their adverse effects on male reproductive function remain unclear. The testis expresses somatic calcineurin and a sperm-specific isoform that contains a catalytic subunit (PPP3CC) and a regulatory subunit (PPP3R2). We demonstrate herein that male mice lacking *Ppp3cc* or *Ppp3r2* genes (knockout mice) are infertile, with reduced sperm motility owing to an inflexible midpiece. Treatment of mice with cyclosporine A or FK506 creates phenocopies of the sperm motility and morphological defects. These defects appear within 4 to 5 days of treatment, which indicates that sperm-specific calcineurin confers midpiece flexibility during epididymal transit. Male mouse fertility recovered a week after we discontinued treatment. Because human spermatozoa contain PPP3CC and PPP3R2 as a form of calcineurin, inhibition of this sperm-specific calcineurin may lead to the development of a reversible male contraceptive that would target spermatozoa in the epididymis.

Calcineurin is a Ca^{2+}- and calmodulin-dependent serine-threonine phosphatase that plays a major role in calcium signaling (*1, 2*). In the immune system, calcineurin activates T cells by dephosphorylating the transcription factor NFAT (nuclear factor of activated T cells), and the dephosphorylated NFAT up-regulates the expression of interleukin-2 (*1, 2*). This process is suppressed by calcineurin inhibitors, such as cyclosporine A (CsA) and FK506, that are mainstays of immunosuppressive therapy after organ transplantation (*1, 2*). In the male re-productive system, animal experiments have revealed that CsA and FK506 have deleterious effects on spermatogenesis and epididymal sperm maturation (*3, 4*). Further, in vitro treatment of spermatozoa with these drugs impairs sperm motility and the acrosome reaction (*5, 6*). These data suggest important roles of calcineurin in male fertility; however, the existence of several isoforms expressed in the testis hampered the clarification of their functions and pharmacological processes.

Calcineurin exists as a heterodimer composed of a catalytic and a regulatory subunit. In mammals, three isoforms of the catalytic subunit (PPP3CA, PPP3CB, and PPP3CC) and two isoforms of the regulatory subunit (PPP3R1 and PPP3R2) have been identified. *Ppp3ca*, *Ppp3cb*, and *Ppp3r1* are expressed ubiquitously, whereas *Ppp3cc* and *Ppp3r2* are expressed strongly in the mouse testis (fig. S1A) (*7*). PPP3CC and PPP3R2 were not detected in the testis and epididymis of c-Kit[w/wv]

mice, which lack differentiating germ cells (Fig. 1A). This indicates that *Ppp3cc* and *Ppp3r2* are the only subunits expressed in spermatogenic cells. In mature spermatozoa, both PPP3CC and PPP3R2 are localized in the tail (Fig. 1B). Consistent with the existence of the calcineurin iso-forms, Ca^{2+}-dependent phosphatase activity is inhibited by CsA in mouse spermatozoa (fig. S1B). When mouse *Ppp3cc* and *Ppp3r2* were expressed in human embryonic kidney 293T (HEK293T) cells, heterodimerizaion of PPP3CC and PPP3R2 stabilized the calcineurin complex (Fig. 1C). This is consistent with genetic deletion of *Ppp3r1*, which leads to loss of PPP3CA and/or PPP3CB (*8*). Protein extracts from transfected cells contain Ca^{2+}-dependent phosphatase activity that was blocked by CsA (Fig. 1D). Thus, we conclude that the PPP3CC-PPP3R2 complex is the sperm-specific calcineurin (sperm calcineurin).

To elucidate the physiological functions of sperm calcineurin, we deleted (i.e., knocked out) the *Ppp3cc* gene in mice (fig. S2, A and B). We confirmed that PPP3CC was depleted in both testis and spermatozoa in *Ppp3cc*^{−/−} males (fig. S2C). The PPP3R2 signal was less in *Ppp3cc*-null testis and spermatozoa, which further indicated that PPP3CC stabilizes PPP3R2 (fig. S2D). As expected, Ca^{2+}-dependent phosphatase activity was reduced in *Ppp3cc*-null spermatozoa (fig. S2E). In *Ppp3cc*^{−/−} mice, there were no overt abnormalities in spermatogenesis, epididymal sperm morphology, or sperm counts (fig. S3, A to F).

Although *Ppp3cc*^{−/−} males copulated, they were infertile (Fig. 2A). When we investigated sperm migration in the female reproductive tract using transgenic spermatozoa that have DsRed2 in the mitochondria (*9*), fewer spermatozoa reached the ampulla compared with those of controls (fig. S4A). Although this could explain, in part, the male infertility, the presence of spermatozoa in the ampulla suggests that there are other factors that render the *Ppp3cc*^{−/−} males infertile. To examine other possible factors, we performed in vitro fertilization (IVF) and found that *Ppp3cc*-null spermatozoa cannot fertilize cumulus-intact oocytes (Fig. 2B). Further analysis revealed that *Ppp3cc*-null spermatozoa could pass through the cumulus cell layers (fig. S4B) and could bind to the zona pellucida (ZP) (Fig. 2C) but failed to fertilize cumulus-free ZP intact oocytes (fig. S4C);

[1]Research Institute for Microbial Diseases, Osaka University, Suita, Osaka 565-0871, Japan. [2]Graduate School of Medicine, Osaka University, Suita, Osaka 565-0871, Japan. [3]School of Pharmaceutical Sciences, Osaka University, Suita, Osaka 565-0871, Japan. [4]Shimoda Marine Research Center, University of Tsukuba, 5-10-1 Shimoda, Shizuoka 415-0025, Japan. [5]Immunology Frontier Research Center, Osaka University, Suita, Osaka 565-0871, Japan.
*Corresponding author. E-mail: ikawa@biken.osaka-u.ac.jp

Fig. 1. Sperm calcineurin is a complex of PPP3CC and PPP3R2. (**A**) Both PPP3CC and PPP3R2 were detected in differentiating germ cells. (**B**) Both PPP3CC and PPP3R2 are localized in the sperm tail. IZUMO1 localized in the head and BASIGIN localized in the tail were used as controls. (**C**) Mouse PPP3CC-FLAG (cc-FLAG) and/or mouse PPP3R2 (r2) were overexpressed in HEK293T cells. (**D**) HEK293T cells that overexpressed both PPP3CC-FLAG and PPP3R2 have Ca^{2+}-dependent phosphatase activity that is blocked by 100 nM CsA. *n* = 3.

184

therefore, the ZP was the site of the problem. Once the ZP was removed, *Ppp3cc*-null spermatozoa could fuse with oocytes (fig. S4D), which confirmed that *Ppp3cc*-null spermatozoa are defective in zona penetration. When IVF was performed in a medium containing glutathione as a reducing agent to destabilize the ZP (fig. S5A) (*10*, *11*), oocytes were fertilized by *Ppp3cc*-null spermatozoa (Fig. 2D and fig. S5A). These fertilized eggs developed to term (Fig. 2E and fig. S5B), which indicates that sperm calcineurin is not required for sperm genomic integrity. Fertility of *Ppp3cc*⁻/⁻ males was also rescued by expressing mCherry-tagged *Ppp3cc* transgene under a testis-specific *Clgn* promoter (fig. S6, A to C) (*12*).

To understand why null spermatozoa could not penetrate the ZP, we investigated the acrosome reaction, as this is a prerequisite for spermatozoa to penetrate through the ZP (*13*). However, the acrosome reaction occurred normally in *Ppp3cc*-null spermatozoa (fig. S7, A and B). Next, we investigated sperm motility using computer-assisted sperm analysis. Although there were no differences in the percentage of motile spermatozoa (fig. S7C), velocity parameters of *Ppp3cc*-null spermatozoa (C57BL6/DBA2 background) were lower than those of control C57BL6/DBA2 spermatozoa (Fig. 3A). However, knockout (KO) sperm motility was still comparable to that of C57BL6 wild-type (WT) mice (table S1). Therefore, differences in velocities alone cannot explain the penetration defect.

We then investigated the percentage of hyperactivated spermatozoa and discovered that it was significantly lower in *Ppp3cc*⁻/⁻ mice than in control spermatozoa (Fig. 3B and fig. S7D), which suggests that *Ppp3cc*-null spermatozoa are defective in ZP penetration due to impaired hyperactivation. To elucidate why *Ppp3cc*-null

spermatozoa fail to exhibit hyperactivation, we further analyzed sperm motility. Although beat frequencies of *Ppp3cc*-null spermatozoa were normal (fig. S7E), the midpiece of null spermatozoa bent slightly in a direction opposite from the hook of the acrosome (anti-hook) (99%, 110 out of 111 spermatozoa) (*14*) and was inflexible (Fig. 3, C and D, and movies S1 to S4). In contrast, defects were not observed in the principal piece of null spermatozoa (Fig. 3C). When WT spermatozoa are hyperactivated, the curvature of the midpiece bend increases (*14*); however, *Ppp3cc*-null spermatozoa do not exhibit this increase. Thus, PPP3CC is required to develop the flexible midpiece for hyperactivation and to penetrate the ZP. Identical phenotypes were observed in *Ppp3r2* KO mice (fig. S8, A to F), which reconfirmed the importance of sperm calcineurin in midpiece flexibility and male fertility.

PPP3CC is localized close to CATSPER1, a Ca²⁺ channel required for hyperactivation (*15*, *16*). To investigate whether PPP3CC is downstream of CATSPER1, we analyzed sperm motility of *Catsper1*⁻/⁻ mice. However, the midpiece of *Catsper1*-null spermatozoa was not rigid (fig. S8G), which indicates that sperm calcineurin is activated by calcium influx from different calcium channels and/or internal calcium stores.

To understand why the *Ppp3cc*-null midpiece remains rigid, we investigated microtubule (MT) sliding using spermatozoa from which membranes had been removed. MTs extend from the neck region in both control and null spermatozoa with comparable frequencies, which suggests that axonemal dyneins can slide the MTs even in the KO midpiece (fig. S9, A to C, and movie S5). The midpiece that was bent in the direction of the hook of the acrosome (pro-hook) appeared in null spermatozoa (fig. S9A) (32% ± 8.0, no. of

males = 3, no. of spermatozoa = 55). Because the mitochondrial sheath was removed in this assay (*17*), the mitochondrial sheath may contribute to the rigid midpiece bending in an anti-hook direction. Interaction between the mitochondrial sheath and the outer dense fibers may keep the midpiece rigid (*18*).

To further analyze the function of sperm calcineurin, we treated WT spermatozoa in vitro with CsA or FK506. Sperm motility and midpiece flexibility of these mature spermatozoa were not affected by calcineurin inhibitors (fig. S10, A and B). Furthermore, WT spermatozoa were able to fertilize normally in vitro, even in the presence of CsA or FK506 in the media (fig. S10C). Thus, sperm calcineurin activity is no longer necessary to confer midpiece flexibility in mature spermatozoa collected from the cauda epididymis.

To determine the effects of immunosuppressant drugs on immature spermatozoa, WT male mice were treated with CsA or FK506 for 2 weeks; these males became infertile (Fig. 4A), and spermatozoa from treated mice did not fertilize in vitro (Fig. 4B). When sperm motility was investigated, their midpiece was as inflexible as *Ppp3cc*- or *Ppp3r2*-null spermatozoa (Fig. 4C, movie S6 to S9). These results indicate that sperm calcineurin activity is important during the later stages of spermatogenesis or during sperm maturation in the epididymis. To elucidate where sperm calcineurin works, we administered CsA or FK506 for short periods. Spermatozoa with rigid midpieces appeared as early as 5 days after CsA administration and 4 days after FK506 administration (Fig. 4D). Because it takes ~10 days for spermatozoa to transit the epididymis (*19*), these results indicate that sperm calcineurin is essential to confer midpiece flexibility during epididymal transit. This is consistent with the fact that the sperm midpiece becomes flexible during epididymal transit (fig. S11A) (*20*). Fast transit of spermatozoa through the epididymis suggests that male fertility may recover quickly after stopping drug administration. As expected, fertility of male mice treated with CsA or FK506 recovered 1 week after halting drug administration (Fig. 4E). Sperm motility and midpiece flexibility also recovered after treatment (fig. S11, B to D). Considering these results in mice, we suggest that sperm calcineurin may be a target for reversible and rapidly acting human male contraceptives.

In human spermatozoa, the catalytic subunit of calcineurin was detected using a pan-calcineurin antibody (*21*). With specific antibodies, we confirmed the existence of PPP3CC and PPP3R2 but not PPP3CA and PPP3CB in human spermatozoa (fig. S12A). The recombinant human PPP3CC-PPP3R2 exhibited Ca²⁺-dependent phosphatase activity that was blocked by CsA (fig. S12, B and C). Thus, human spermatozoa contain PPP3CC-PPP3R2 as a functional calcineurin. In support of this idea, it has been reported that human spermatozoa exhibit Ca²⁺-dependent phosphatase activity (*21*). In humans, sperm motility develops during epididymal transit (*22*). Although male patients treated with a therapeutic dosage of CsA did not show signs of infertility (*23*), there are

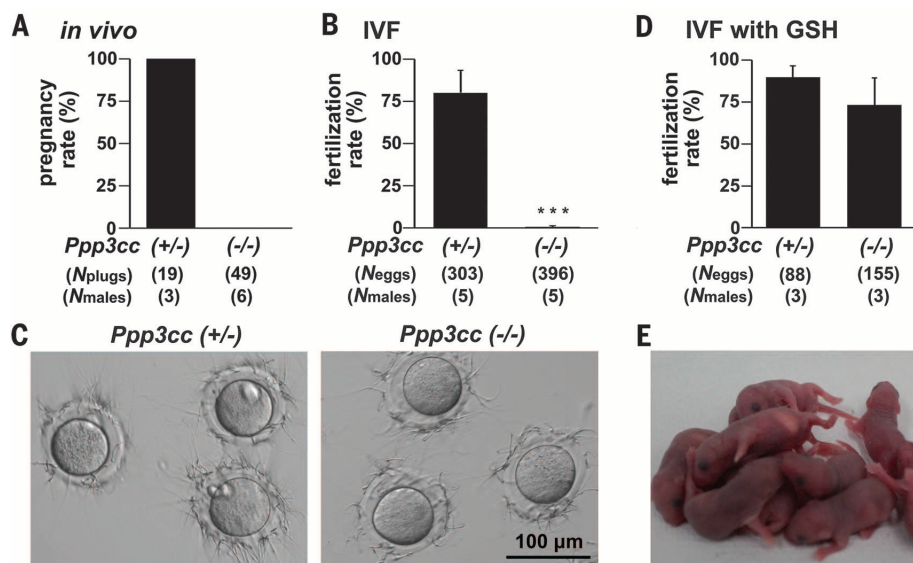**Fig. 2. *Ppp3cc*⁻/⁻ male is infertile because of impaired ZP penetration.** (**A**) Pregnancy rate (pregnancy over vaginal plug) is presented as a percentage. (**B**) IVF with cumulus-intact oocytes. (**C**) Sperm-ZP binding assay in vitro. (**D**) IVF with cumulus-intact oocytes in medium containing glutathione (GSH). (**E**) Pups were obtained from eggs fertilized with *Ppp3cc*-null spermatozoa in (D).
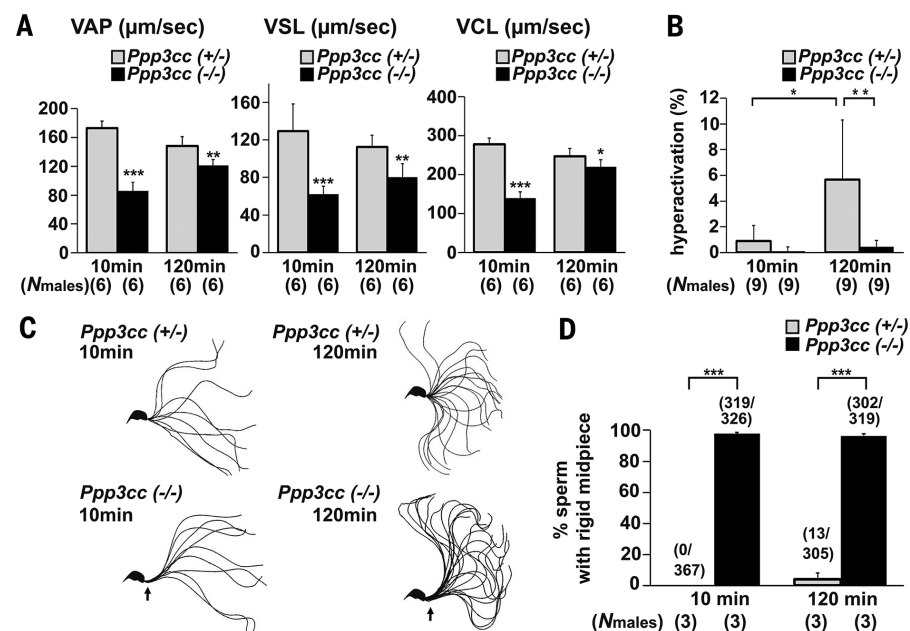
185

Fig. 3. Sperm calcineurin is necessary for a flexible midpiece. (**A**) Sperm motility at 10 min and 120 min after sperm suspension. VAP, average path velocity; VSL, straight-line velocity; and VCL, curvilinear velocity. (**B**) The percentage of hyperactivated spermatozoa. (**C**) Flagellar bending patterns. Single frames throughout one beating cycle are superimposed. The midpiece (black arrow) was inflexible in the *Ppp3cc*-null spermatozoa. (**D**) The percentage of the spermatozoa with a rigid midpiece. The number of spermatozoa with a rigid midpiece over the number of spermatozoa examined is presented in the parentheses above the column.

Fig. 4. Sperm calcineurin confers midpiece flexibility during epididymal transit. (**A** and **B**) Male mice were treated with CsA or FK506 for 2 weeks, and we analyzed their in vivo fertility using superovulated females (A), and fertilization rate in vitro (with cumulus cells) (B). (**C**) The percentage of spermatozoa with a rigid midpiece. The number of spermatozoa with a rigid midpiece over the number of spermatozoa examined was 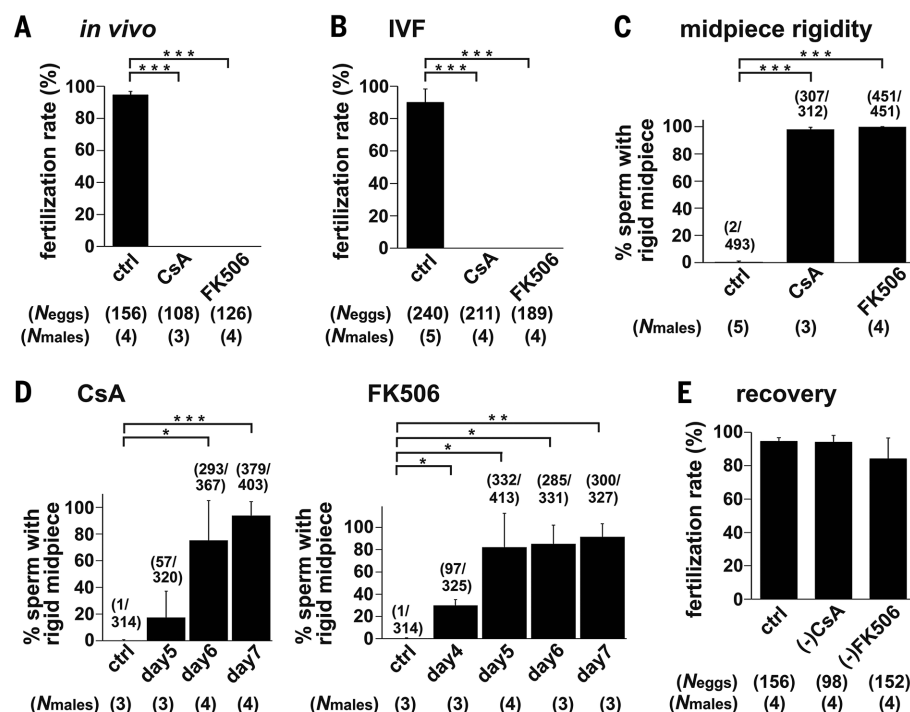presented in the parentheses above the column. (**D**) Male mice were treated with CsA or FK506 for a short period, and their midpiece was analyzed. (**E**) Male mice were treated with CsA or FK506 for 2 weeks, and their in vivo fertility was analyzed 1 week after stopping drug administration. Drug concentration for CsA, 80 mg/kg per day, and for FK506, 8 mg/kg per day.

studies showing that CsA treatment impairs the motility of spermatozoa (*24*). Further, the concentration of CsA in the blood correlates inversely with sperm motility (*25*), which suggests that the PPP3CC-PPP3R2 complex is also involved in sperm motility development in humans.

In the present study, we demonstrated that PPP3CC associates with PPP3R2 to form sperm calcineurin during spermatogenesis. Our KO mice reveal that sperm calcineurin is not essential for spermatogenesis. The impaired spermatogenesis reported with CsA and FK506 treatment could be attributed to the inhibition of somatic calcineurin and/or nonspecific inhibition of other molecules. We conclude that sperm calcineurin confers midpiece flexibility during epididymal transit, and this process is required to generate fertilization-competent spermatozoa. In the immune system, calcineurin dephosphorylates the transcription factor NFAT (*1*, *2*); however, in spermatozoa, calcineurin plays roles in the epididymis after transcription has ceased. Therefore, sperm calcineurin does not confer midpiece flexibility by dephosphorylating transcription factors such as NFAT. Specific inhibition of sperm calcineurin or its interaction with substrates may lead to the development of reversible and rapidly acting male contraceptives that target spermatozoa in the epididymis but leave testicular function intact.

REFERENCES AND NOTES

1. C. B. Klee, H. Ren, X. Wang, *J. Biol. Chem.* **273**, 13367–13370 (1998).
2. F. Rusnak, P. Mertz, *Physiol. Rev.* **80**, 1483–1521 (2000).
3. L. Seethalakshmi, M. Menon, R. K. Malhotra, D. A. Diamond, *J. Urol.* **138**, 991–995 (1987).
4. A. Hisatomi et al., *Toxicology* **109**, 75–83 (1996).
5. M. M. Misro, S. P. Chaki, M. Srinivas, S. K. Chaube, *Arch. Androl.* **43**, 215–220 (1999).
6. J. Castillo Bennett, C. M. Roggero, F. E. Mancifesta, L. S. Mayorga, *J. Biol. Chem.* **285**, 26269–26278 (2010).
7. T. Muramatsu, P. R. Giri, S. Higuchi, R. L. Kincaid, *Proc. Natl. Acad. Sci. U.S.A.* **89**, 529–533 (1992).
8. H. Zeng et al., *Cell* **107**, 617–629 (2001).
9. H. Hasuwa et al., *Exp. Anim.* **59**, 105–107 (2010).
10. M. L. Bath, *PLOS ONE* **5**, e9387 (2010).
11. T. Takeo, N. Nakagata, *Biol. Reprod.* **85**, 1066–1072 (2011).
12. M. Ikawa et al., *Dev. Biol.* **240**, 254–261 (2001).
13. R. Yanagimachi, in *The Physiology of Reproduction*, E. Knobil, J. D. Neil, Eds. (Raven Press, New York, 1988), vol. 1, chap. 5.
14. S. Ishijima, S. A. Baba, H. Mohri, S. S. Suarez, *Mol. Reprod. Dev.* **61**, 376–384 (2002).
15. J. J. Chung et al., *Cell* **157**, 808–822 (2014).
16. D. Ren et al., *Nature* **413**, 603–609 (2001).
17. M. Kinukawa, M. Nagata, F. Aoki, *Reproduction* **128**, 813–818 (2004).
18. D. M. Woolley, J. Neesen, G. G. Vernon, *Cell Motil. Cytoskeleton* **61**, 74–82 (2005).
19. M. L. Meistrich, T. H. Hughes, W. R. Bruce, *Nature* **258**, 145–147 (1975).
20. C. Jeulin, L. M. Lewin, C. Chevrier, D. Schoevaert-Brossault, *Cell Motil. Cytoskeleton* **35**, 147–161 (1996).
21. K. Ahmad, G. E. Bracho, D. P. Wolf, J. S. Tash, *Arch. Androl.* **35**, 187–208 (1995).
22. C. H. Yeung, T. G. Cooper, F. Oberpenning, H. Schulze, E. Nieschlag, *Biol. Reprod.* **49**, 274–280 (1993).
23. J. Haberman et al., *J. Urol.* **145**, 294–296 (1991).
24. Z. G. Cao et al., *Zhonghua Nan Ke Xue* **12**, 405–407 (2006).
25. M. M. Eid, I. A. Abdel-Hamid, M. A. Sobh, M. A. el-Saied, *Int. J. Androl.* **19**, 338–344 (1996).

SCIENTIFIC REP⚙RTS

OPEN

Maternal TET3 is dispensable for embryonic development but is required for neonatal growth

Yu-ichi Tsukada[1,2], Tomohiko Akiyama[3] & Keiichi I. Nakayama[4]

The development of multicellular organisms is accompanied by reprogramming of the epigenome in specific cells, with the epigenome of most cell types becoming fixed after differentiation. Genome-wide reprogramming of DNA methylation occurs in primordial germ cells and in fertilized eggs during mammalian embryogenesis. The 5-methylcytosine (5mC) content of DNA thus undergoes a marked decrease in the paternal pronucleus of mammalian zygotes. This loss of DNA methylation has been thought to be mediated by an active demethylation mechanism independent of replication and to be required for development. TET3-mediated sequential oxidation of 5mC has recently been shown to contribute to the genome-wide loss of 5mC in the paternal pronucleus of mouse zygotes. We now show that TET3 localizes not only to the paternal pronucleus but also to the maternal pronucleus and oxidizes both paternal and maternal DNA in mouse zygotes, although these phenomena are less pronounced in the female pronucleus. Genetic ablation of TET3 in oocytes had no significant effect on oocyte development, maturation, or fertilization or on pregnancy, but it resulted in neonatal sublethality. Our results thus indicate that zygotic 5mC oxidation mediated by maternal TET3 is required for neonatal growth but is not essential for development.

DNA methylation, the covalent addition of a methyl group to the C-5 position of cytosine (C), is a common epigenetic modification in most eukaryotes and is implicated in numerous biological processes including genomic imprinting, transcriptional silencing of retrotransposons, and X chromosome inactivation[1]. DNA methylation underlies heritable and long-term silencing of gene transcription that is critical for the development and survival of an organism, and it is therefore considered to be a relatively stable modification compared with other epigenetic marks. However, replication-independent demethylation of DNA has been observed under various circumstances including at specific stages of development[2–6], in association with the transcriptional response to specific signals[7–11], and during artificial reprogramming of differentiated cells[12]. In particular, genome-wide DNA demethylation occurs at two different stages of mammalian development: the migration of primordial germ cells toward the genital ridge[4–6], and the pronuclear stage of fertilized eggs[2,3]. In the latter instance, immunostaining with antibodies to 5-methylcytosine (5mC) revealed a genome-wide loss of 5mC in the paternal pronucleus of mammalian zygotes that begins at sperm decondensation and is marked in extent before replication of DNA, whereas 5mC in the maternal pronucleus was found to be resistant to such depletion[2,13–15]. Although the mechanism of replication-independent demethylation of DNA in mammals has been a recurrent subject of uncertainty and controversy[16,17], substantial progress in understanding that of the genome-wide loss of 5mC in the paternal pronucleus of zygotes has been recently achieved. 5-Methylcytosine has thus been

[1]Division of Molecular Immunology, Medical Institute of Bioregulation, Kyushu University, 3-1-1 Maidashi, Higashi-ku, Fukuoka 812-8582, Japan. [2]Advanced Biological Information Research Division, INAMORI Frontier Research Center, Kyushu University, 744 Motooka, Nishi-ku, Fukuoka 819-0395, Japan. [3]Department of Systems Medicine, Sakaguchi Laboratory, Keio University School of Medicine, 35 Shinanomachi, Shinjuku, Tokyo 160-8562, Japan. [4]Division of Cell Regulation Systems, Medical Institute of Bioregulation, Kyushu University, 3-1-1 Maidashi, Higashi-ku, Fukuoka 812-8582, Japan. Correspondence and requests for materials should be addressed to Y.T. (email: ytsukada@ifrc.kyushu-u.ac.jp)

187

found to be oxidized to 5-hydroxymethylcytosine (5hmC), 5-formylcytosine, and 5-carboxylcytosine by the DNA oxidase TET3 in the paternal pronucleus of mouse zygotes, suggesting that the genome-wide loss of 5mC in the paternal pronucleus is attributable mostly to the conversion of 5mC to its derivatives mediated by this enzyme[18–20]. Furthermore, the generated 5mC derivatives are diluted during preimplantation development by DNA replication, similar to the passive DNA demethylation that occurs in the maternal pronucleus[20,21].

The genome-wide loss of 5mC in the paternal pronucleus of mammalian zygotes has been thought to play an important role in mammalian development. This notion is supported by the fact that the phenomenon is conserved among mammalian species including mouse, rabbit, cow, and human[18,22–24]. It is also supported indirectly by the observed inefficiency of DNA demethylation in cloned animals[25–28]. However, other evidence suggests that the genome-wide loss of 5mC in the paternal pronucleus of zygotes is dispensable for mammalian development. Mouse zygotes that were generated by round spermatid injection and in which this process was impaired were thus found to develop normally[29]. In addition, the genome-wide loss of 5mC in the paternal pronucleus is not conserved among all mammalian species, having not been observed in sheep, goat, and pig[30–32]. Thus, in contrast to the advances in understanding the mechanism of this process, its biological relevance remains unclear. Given that the genome-wide loss of paternal 5mC in zygotes has been attributed to the oxidation of 5mC[18,19,33], elucidation of the biological relevance of 5mC oxidation may shed light on that of the loss of paternal 5mC. Few studies have examined the role of zygotic 5mC oxidation in mammalian development, however[19,34], although zygotes depleted of maternal TET3 have been generated and studied with regard to elucidation of the molecular mechanism of paternal DNA demethylation[18,33–36].

We have now evaluated the biological relevance of zygotic 5mC oxidation in mice by depleting oocytes of TET3. We found that attenuation of 5mC oxidation in zygotes resulting from genetic ablation of maternal TET3 is compatible with embryonic development but leads to neonatal sublethality. Our findings thus refine current knowledge of the biological role of 5mC oxidation in zygotes.

Results

TET3 mediates 5mC oxidation in both paternal and maternal DNA in zygotes.

To elucidate the biological relevance of TET3-mediated 5mC oxidation in mammalian zygotes, we generated mouse oocytes deficient in TET3. To this end, we first produced mice harboring a "floxed" allele of *Tet3*, in which exon 3 is flanked by *loxP* sites (Fig. 1a). We then crossed these mice with mice harboring a *cre* transgene under the control of the promoter for the zona pellucida glycoprotein 3 gene (*Zp3*). Female mice in which exon 3 of *Tet3* was conditionally ablated as a result of *Zp3* promoter–driven expression of Cre recombinase would be expected to produce oocytes deficient in TET3 (Fig. 1b). To confirm the ablation of TET3 in zygotes derived from oocytes of [*Zp3-cre*, *Tet3*F/−] female mice fertilized with wild-type (WT) mouse sperm, we performed immunostaining with antibodies to (anti-) the NH_2-terminal (N) or COOH-terminal (C) regions of mouse (m) TET3. Signals for both mTET3(N) and mTET3(C) were prominent in the paternal pronucleus of control zygotes derived from oocytes of [*Zp3-cre*, *Tet3*F/+] female mice (Fig. 1c), consistent with the previous observation that TET3 predominantly localizes to paternal pronuclei[19,33,37]. A small amount of mTET3 immunoreactivity was also detected in the maternal pronucleus of such control zygotes (Fig. 1c), however, suggesting that TET3 may also oxidize 5mC in maternal DNA. In contrast, signals for both mTET3(N) and mTET3(C) were virtually absent from both paternal and maternal pronuclei of zygotes derived from oocytes of [*Zp3-cre*, *Tet3*F/−] female mice (Fig. 1c). The presence of pronuclei in these zygotes was confirmed by staining of DNA with Sytox (Fig. 1c). These results thus indicated that TET3 in oocytes of [*Zp3-cre*, *Tet3*F/−] female mice is depleted efficiently.

Given that TET3 is thought to be responsible for the oxidation of 5mC in zygotes[18,19,33], we next investigated the effect of maternal TET3 depletion on this process. Consistent with previous findings[19–21,33,37], simultaneous staining of zygotes with anti-5hmC and anti-5mC revealed that the signal for 5mC was prominent in the maternal pronucleus but was virtually absent from the paternal pronucleus of control zygotes derived from oocytes of [*Zp3-cre*, *Tet3*F/+] female mice, whereas the opposite pattern was observed for the 5hmC signal (Fig. 1d). Furthermore, loss of the 5hmC signal and an increase in the 5mC signal were apparent in the paternal pronucleus of TET3-deficient zygotes derived from oocytes of [*Zp3-cre*, *Tet3*F/−] female mice (Fig. 1d). A small but detectable amount of 5hmC immunoreactivity was observed in the maternal pronucleus of the control zygotes (Fig. 1d), consistent with the low level of TET3 immunoreactivity detected in the maternal pronucleus (Fig. 1c). On the other hand, the signal for 5hmC was virtually undetectable in the maternal pronucleus of TET3-deficient zygotes derived from oocytes of [*Zp3-cre*, *Tet3*F/−] female mice, with the exception of staining in a small portion of the periphery of the nucleolus-like body[38] (Fig. 1d). Together, these results not only verified that maternal TET3 is responsible for the oxidation of paternal 5mC in mouse zygotes, but also suggested that TET3 oxidizes maternal 5mC, albeit to a lesser extent than paternal 5mC.

To verify that the signal for 5hmC detected in a small portion of the periphery of the nucleolus-like body of the maternal pronucleus in TET3-deficient zygotes derived from oocytes of [*Zp3-cre*, *Tet3*F/−] female mice was not attributable to TET3-mediated oxidation of 5mC, we examined the expression pattern of TET3 and the effect of maternal TET3 depletion on 5mC and 5hmC status in fully grown (FG) oocytes at the germinal vesicle (GV) stage. FG oocytes manifest two distinct types of chromatin configuration: the surrounded nucleolus (SN) type, in which chromatin is highly condensed and surrounds
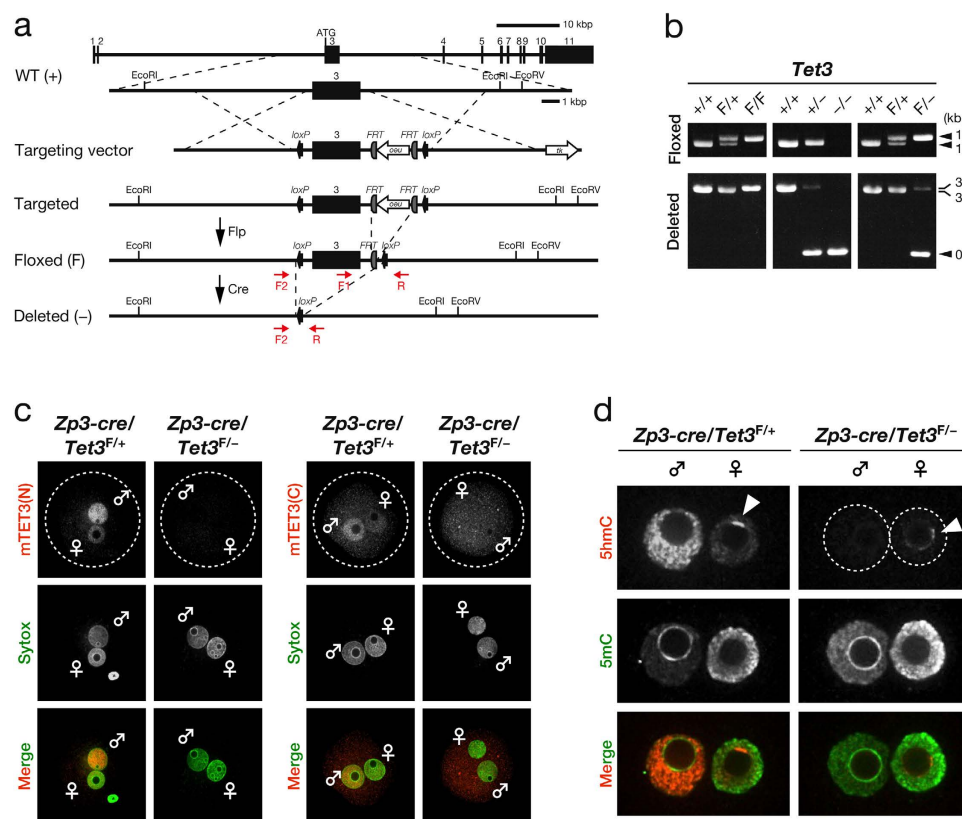
Figure 1. Generation of TET3-depleted oocytes and loss of 5mC oxidation in zygotes derived therefrom.
(**a**) Strategy for targeted disruption of mouse *Tet3*. Exons and primers for genotyping are shown as numbered black boxes and red arrows, respectively. See Methods for details. (**b**) Representative genotyping of mice by PCR analysis. The primers F1 and R were used for detection of WT (1.2 kbp) and floxed (1.4 kbp) alleles, whereas primers F2 and R were used for that of WT (3.0 kbp), floxed (3.2 kbp), and deleted (0.5 kbp) alleles. (**c**) Representative images showing depletion of maternal TET3 in zygotes derived from oocytes of [*Zp3-cre*, *Tet3*^F/−] female mice compared with those derived from oocytes of [*Zp3-cre*, *Tet3*^F/+] female mice. Zygotes were stained with anti-mTET3(N) or anti-mTET3(C) (red in merged images). Pronuclei were revealed by staining of DNA with Sytox (green in merged images). Dashed circles, ♂, and ♀ indicate the rim of the zygote, the paternal pronucleus, and the maternal pronucleus, respectively. (**d**) Representative images showing the loss of 5hmC in both pronuclei of zygotes derived from oocytes of [*Zp3-cre*, *Tet3*^F/−] female mice compared with those derived from oocytes of [*Zp3-cre*, *Tet3*^F/+] female mice. Pronuclei were stained with anti-5hmC (red in merged images) and anti-5mC (green in merged images). ♂, ♀, dashed circles, and arrowheads indicate the paternal pronucleus, the maternal pronucleus, the rim of each pronucleus, and the periphery of the nucleolus-like body, respectively.

the nucleolus, and the non–surrounded nucleolus (NSN) type, in which chromatin is less condensed and does not surround the nucleolus[39]. DNA methyltransferase 3a (DNMT3a) localizes predominantly to the nucleus of FG oocytes[40]. Immunostaining with anti-DNMT3a confirmed that the DNMT3a signal was prominent in both SN and NSN types of nuclei in control FG oocytes from [*Zp3-cre*, *Tet3*^F/+] female mice (Fig. 2a). In contrast, signals for both mTET3(N) and mTET3(C) were virtually absent from both SN and NSN types of nuclei in FG oocytes from both [*Zp3-cre*, *Tet3*^F/+] and [*Zp3-cre*, *Tet3*^F/−] female mice (Fig. 2b, Supplementary Fig. S1). Simultaneous staining of FG oocytes with anti-5hmC and anti-5mC revealed a small but detectable amount of 5hmC immunoreactivity in both types of nuclei of FG oocytes obtained from both [*Zp3-cre*, *Tet3*^F/+] and [*Zp3-cre*, *Tet3*^F/−] female mice (Fig. 2c). In particular, the signal for 5hmC was prominent in a small portion of the periphery of the nucleolus of the SN-type nucleus in FG oocytes, similar to the pattern observed in the maternal pronucleus of zygotes. Furthermore, a reduction in the 5hmC signal or increase in the 5mC signal was not apparent in FG oocytes obtained from [*Zp3-cre*, *Tet3*^F/−] female mice compared with those from [*Zp3-cre*, *Tet3*^F/+] females (Fig. 2c), consistent with the expression pattern of TET3 in FG oocytes (Fig. 2b, Supplementary Fig. S1). Together, these results suggested that the 5hmC observed in a small portion of the periphery of the nucleolus-like body of the maternal pronucleus in zygotes is produced during oocyte development before the GV stage and is not generated by TET3-mediated oxidation of 5mC.
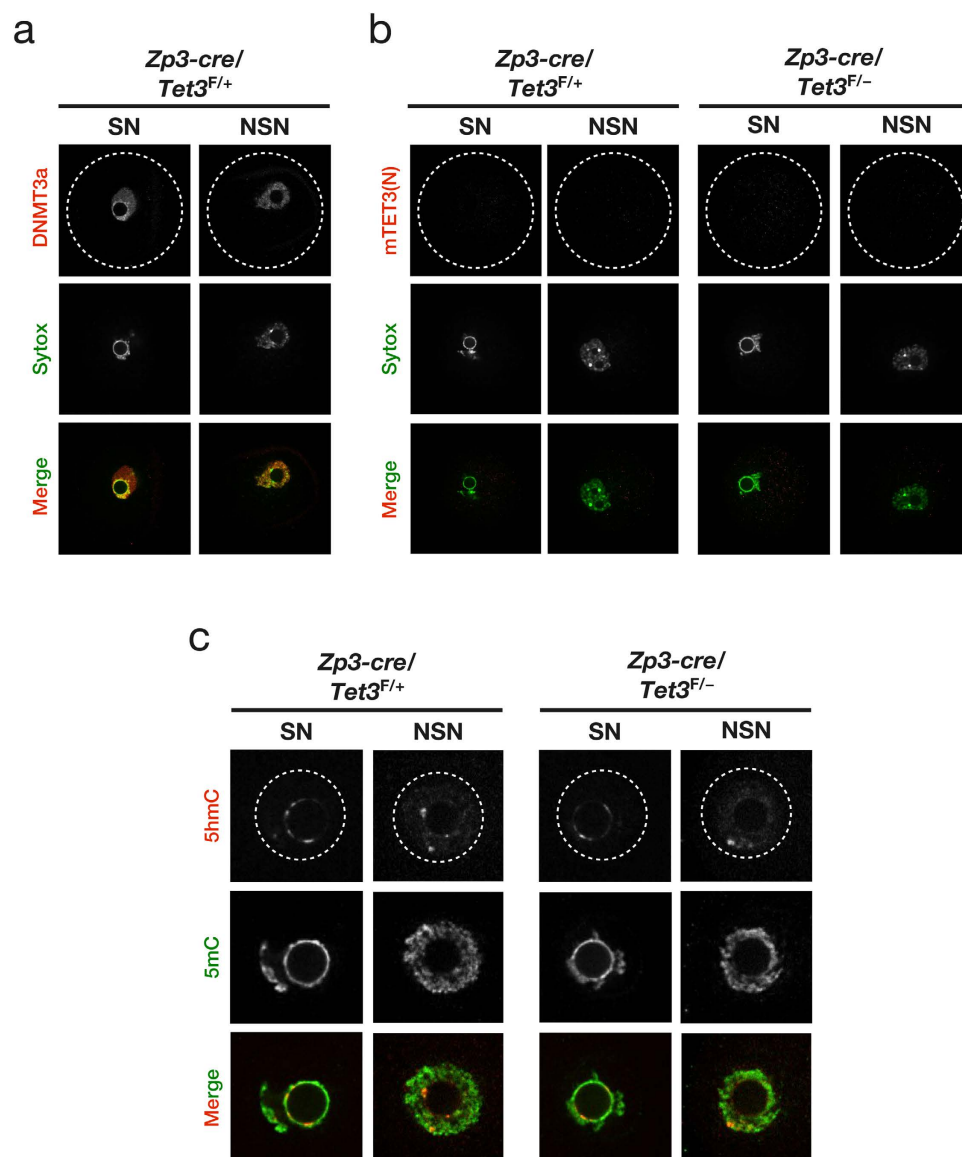
Figure 2. Effect of maternal TET3 depletion on 5mC and 5hmC levels in FG oocytes at the GV stage.
(**a**) Representative images showing the accumulation of DNMT3a in both SN and NSN types of nuclei in FG oocytes of [*Zp3-cre*, *Tet3*F/+] female mice. Oocytes were stained with anti-DNMT3a (red in merged images), and nuclei were revealed by staining of DNA with Sytox (green in merged images). Dashed circles indicate the rim of the oocyte. (**b**) Representative images showing the absence of maternal TET3 in both SN and NSN types of nuclei in FG oocytes of [*Zp3-cre*, *Tet3*F/+] or [*Zp3-cre*, *Tet3*F/−] female mice. Oocytes were stained with anti-mTET3(N) (red in merged images), and nuclei were revealed by staining of DNA with Sytox (green in merged images). Dashed circles indicate the rim of the oocyte. (**c**) Representative images showing the presence of 5hmC in both types of nuclei in FG oocytes of both [*Zp3-cre*, *Tet3*F/−] and [*Zp3-cre*, *Tet3*F/+] female mice. Nuclei were stained with anti-5hmC (red in merged images) and anti-5mC (green in merged images). Dashed circles indicate the rim of the nucleus.

TET3 is dispensable for oocyte development, maturation, and fertilization. Given that we confirmed that TET3 is responsible for 5mC oxidation in zygotes, we evaluated the effect of maternal TET3 depletion on oocyte development, maturation, and fertilization. We collected oocytes at the metaphase II (MII) stage from 8- to 9-week-old [*Zp3-cre*, *Tet3*F/+] and [*Zp3-cre*, *Tet3*F/−] female mice in which "superovulation" had been induced by injection of pregnant mare serum gonadotropin (PMSG) and human chorionic gonadotropin (hCG). The oocytes were then fertilized with WT sperm *in vitro*. Consistent with previous observations[19], the number of ovulated oocytes obtained from [*Zp3-cre*, *Tet3*F/−] female mice and their fertilization rate did not differ significantly from those for [*Zp3-cre*, *Tet3*F/+] female mice (Fig. 3a,b; Supplementary Table S1), suggesting that TET3-mediated 5mC oxidation is dispensable
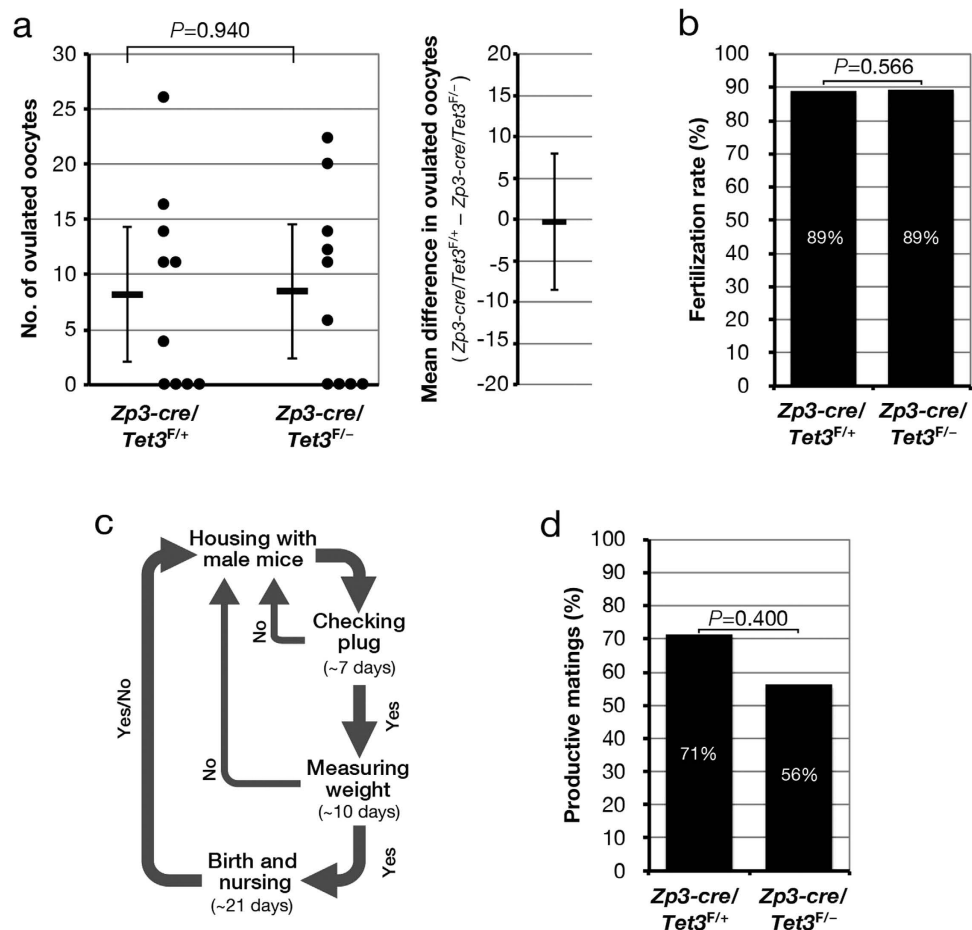
Figure 3. TET3 is dispensable for oocyte development, maturation, and fertilization as well as for pregnancy. (**a**) Number of MII stage oocytes obtained per ovulation for [*Zp3-cre*, *Tet3*[F/+]] ($n = 10$) and [*Zp3-cre*, *Tet3*[F/−]] ($n = 10$) female mice that were treated with PMSG and hCG. The number of ovulated MII stage oocytes for each mouse (circles) as well as the overall mean value (horizontal bar) and 95% confidence interval (CI) are shown in the left panel. The average difference in the number of ovulated MII stage oocytes between [*Zp3-cre*, *Tet3*[F/+]] and [*Zp3-cre*, *Tet3*[F/−]] female mice and its 95% CI are indicated in the right panel. Normality and homoscedasticity of the data were verified by the Shapiro-Wilk test ($\alpha = 0.05$) and F test ($\alpha = 0.05$), respectively. The *P* value was determined by the two-sided Student's *t* test. (**b**) Oocytes obtained from [*Zp3-cre*, *Tet3*[F/+]] ($n = 82$) and [*Zp3-cre*, *Tet3*[F/−]] ($n = 85$) mice as in (**a**) were exposed to WT (ICR) spermatozoa *in vitro* for determination of the rate of fertilization, which was judged by the presence of two pronuclei in zygotes. The *P* value was determined by the one-sided Fisher's exact probability test. (**c**) Strategy for evaluation of productive mating performed over a 2-month observation period. (**d**) [*Zp3-cre*, *Tet3*[F/+]] ($n = 10$) and [*Zp3-cre*, *Tet3*[F/−]] ($n = 10$) female mice were housed with WT (C57BL/6J) male mice as in (**c**) for determination of the number of matings (judged on the basis of plug formation) and the percentage of productive matings (based on the total number of litters produced relative to the total number of matings). The *P* value was determined by the one-sided Fisher's exact probability test.

for oocyte development after the primary follicle stage (at which expression of the *cre* transgene is initiated as a result of activation of the *Zp3* promoter) as well as for oocyte maturation and fertilization.

We next determined whether maternal TET3 deficiency affects pregnancy rate. [*Zp3-cre*, *Tet3*[F/+]] or [*Zp3-cre*, *Tet3*[F/−]] female mice were housed with WT males, and the pregnancy rate was evaluated over a 2-month observation period (Fig. 3c). The pregnancy rate was determined as successful pregnancy per mating and did not differ significantly between [*Zp3-cre*, *Tet3*[F/+]] female mice (71%) and [*Zp3-cre*, *Tet3*[F/−]] female mice (56%) (Fig. 3d, Supplementary Table S2). Although this finding is not consistent with previous results obtained with [*Tnap-cre*, *Tet3*[F/+]] and [*Tnap-cre*, *Tet3*[F/−]] female mice, which had pregnancy rates of 96.3% and 43.8%, respectively ($P < 0.0001$)[19], the discrepancy might be explained by differences in the experimental conditions including the genetic background of the mice, the deleted region of *Tet3*, and the promoter regulating the expression of *cre*. Our results thus suggested that TET3-mediated 5mC oxidation in zygotes is not essential for pregnancy.

TET3-mediated 5mC oxidation in zygotes is not essential for mouse development but is required for neonatal growth. Given that we found that TET3 is dispensable for oocyte development, maturation, and fertilization, we evaluated the effect of maternal TET3 deficiency on fecundity. [*Zp3-cre*, *Tet3*^F/+] or [*Zp3-cre*, *Tet3*^F/−] female mice were housed with WT males and were assessed for fecundity (litter size) over a 2-month period as indicated in Fig. 3c. The mean litter sizes of [*Zp3-cre*, *Tet3*^F/+] and [*Zp3-cre*, *Tet3*^F/−] females were 7.4 and 5.7 (23% reduction, $P = 0.074$), respectively (Fig. 4a, Supplementary Table S3), suggesting that TET3 deficiency tends to reduce litter size, possibly as a result of increased developmental failure. Although the effect of maternal TET3 deficiency on litter size was not as marked as that described previously for [*Tnap-cre*, *Tet3*^F/−] female mice (litter size of 2.8, compared with a value of 8.4 for [*Tnap-cre*, *Tet3*^F/+] females; 67% reduction, $P < 0.0001$)[19], this discrepancy again might be attributable to differences in experimental conditions between the two studies. Our results thus suggested that attenuation of zygotic 5mC oxidation is compatible with mouse development.

We next assessed the effect of maternal TET3 deficiency on neonatal and postnatal growth by examining the progeny of [*Zp3-cre*, *Tet3*^F/+] and [*Zp3-cre*, *Tet3*^F/−] female mice mated with WT males. Offspring were nursed for 21 days after birth and then weaned (Fig. 3c). The mean number of weaned pups for [*Zp3-cre*, *Tet3*^F/−] dams was significantly reduced compared with that for [*Zp3-cre*, *Tet3*^F/+] dams (4.6 versus 7.0) (Fig. 4b, Supplementary Table S3), whereas the percentage of dead pups was significantly greater for [*Zp3-cre*, *Tet3*^F/−] female mice (19.3%) than for [*Zp3-cre*, *Tet3*^F/+] female mice (5.4%) (Fig. 4c). All pups that were alive at 7 days after birth survived and were weaned at 21 days after birth. We confirmed that all of the weaned pups of [*Zp3-cre*, *Tet3*^F/−] female mice and about half of those of [*Zp3-cre*, *Tet3*^F/+] female mice were heterozygous for *Tet3* (Fig. 4d, Supplementary Table S4), indicating that the floxed *Tet3* allele is efficiently ablated by Cre recombinase produced from *Zp3-cre*. These results thus suggested that deficiency of maternal TET3 leads to neonatal sublethality.

Maternal TET3 contributes to the fine-tuning of zygotic transcription after DNA synthesis. Given that the onset of zygotic transcription as well as that of oxidation of 5mC occurs shortly after pronucleus formation in zygotes, we investigated the effect of maternal TET3 depletion on zygotic transcription. To this end, we analyzed RNA synthesis by measuring the incorporation of 5-ethynyl uridine (5EU) into newly synthesized RNA. The signal for 5EU was detected in zygotes derived from oocytes of both [*Zp3-cre*, *Tet3*^F/+] and [*Zp3-cre*, *Tet3*^F/−] female mice as early as 6 to 8 h postinsemination (hpi), but it was not detected before 6 hpi (Fig. 5a,b). Although transcribed RNA accumulated to similar extents in zygotes derived from oocytes of both [*Zp3-cre*, *Tet3*^F/+] and [*Zp3-cre*, *Tet3*^F/−] female mice until 10 hpi, the amount of transcribed RNA was significantly increased in both maternal and paternal pronuclei of zygotes derived from oocytes of [*Zp3-cre*, *Tet3*^F/−] females after 10 hpi (Fig. 5). Zygotes treated with α-amanitin, an inhibitor of RNA polumerase II, did not yield a signal for 5EU (Supplementary Fig. S2), indicating that the detected 5EU signals were indeed attributable to zygotic transcribed RNA. These results thus suggested that maternal TET3 or its oxidation of 5mC restrains zygotic transcription.

To exclude the possibility that the observed effect of maternal TET3 depletion on zygotic transcription might be attributable to a difference in cell cycle progression between zygotes derived from oocytes of [*Zp3-cre*, *Tet3*^F/+] or [*Zp3-cre*, *Tet3*^F/−] female mice, we examined the effect of maternal TET3 depletion on the cell cycle of zygotes. We analyzed DNA synthesis by measurement of the incorporation of 5-ethynyl-2′-deoxyuridine (5EdU) into newly synthesized DNA. A homogeneous signal for 5EdU in both pronuclei, a feature of the early replication stage[41], was detected in ~90% of zygotes derived from oocytes of both [*Zp3-cre*, *Tet3*^F/+] and [*Zp3-cre*, *Tet3*^F/−] female mice as early as 4 to 6 hpi, indicating that most zygotes entered S phase of the cell cycle (Supplementary Fig. S3a,b). A signal for 5EdU at the periphery of the nucleolus-like body in the maternal pronucleus and at the periphery of the paternal pronucleus, a feature of late replication[41], was detected in 27% of zygotes derived from oocytes of both [*Zp3-cre*, *Tet3*^F/+] and [*Zp3-cre*, *Tet3*^F/−] female mice, whereas a signal was not detected in the remaining zygotes, at 9 to 10 hpi (Supplementary Fig. S3a,b), indicating that >70% of zygotes had exited S phase of the cell cycle. Zygotes treated with aphidicolin, an inhibitor of B-family DNA polymerases, did not yield a signal for 5EdU (Supplementary Fig. S3c), indicating that the signals attributed to newly synthesized DNA were specific. These results suggested that maternal TET3 depletion has no obvious effect on cell cycle progression but enhances zygotic transcription after completion of DNA replication.

Discussion

We have here shown that the loss of maternal TET3 results in attenuation of 5mC oxidation in mouse zygotes and neonatal sublethality. Our genetic evidence suggests that TET3 oxidizes not only paternal 5mC but also, albeit to a lesser extent, maternal 5mC, consistent with the relative extent of its localization to the two pronuclei of zygotes. Our data further indicate that TET3-mediated oxidation of paternal and maternal 5mC in zygotes is not essential for mouse development but is required for neonatal growth.

It has been thought that paternal DNA is subject to a genome-wide loss of 5mC, whereas 5mC of maternal DNA is resistant to this process. This notion was based on the initial observation that genome-wide loss of 5mC occurs asymmetrically in mouse zygotes[2,3]. Consistent with this notion, only paternal 5mC was found to be oxidized concomitantly with the loss of 5mC[19–21,33,37], and TET3, which is responsible for the oxidation of 5mC in zygotes, was found to localize specifically to the paternal pronuclus[19,33,37]. Recent studies indicate that TET3 activity is regulated by a cullin–RING finger ligase–4 complex[42,43].
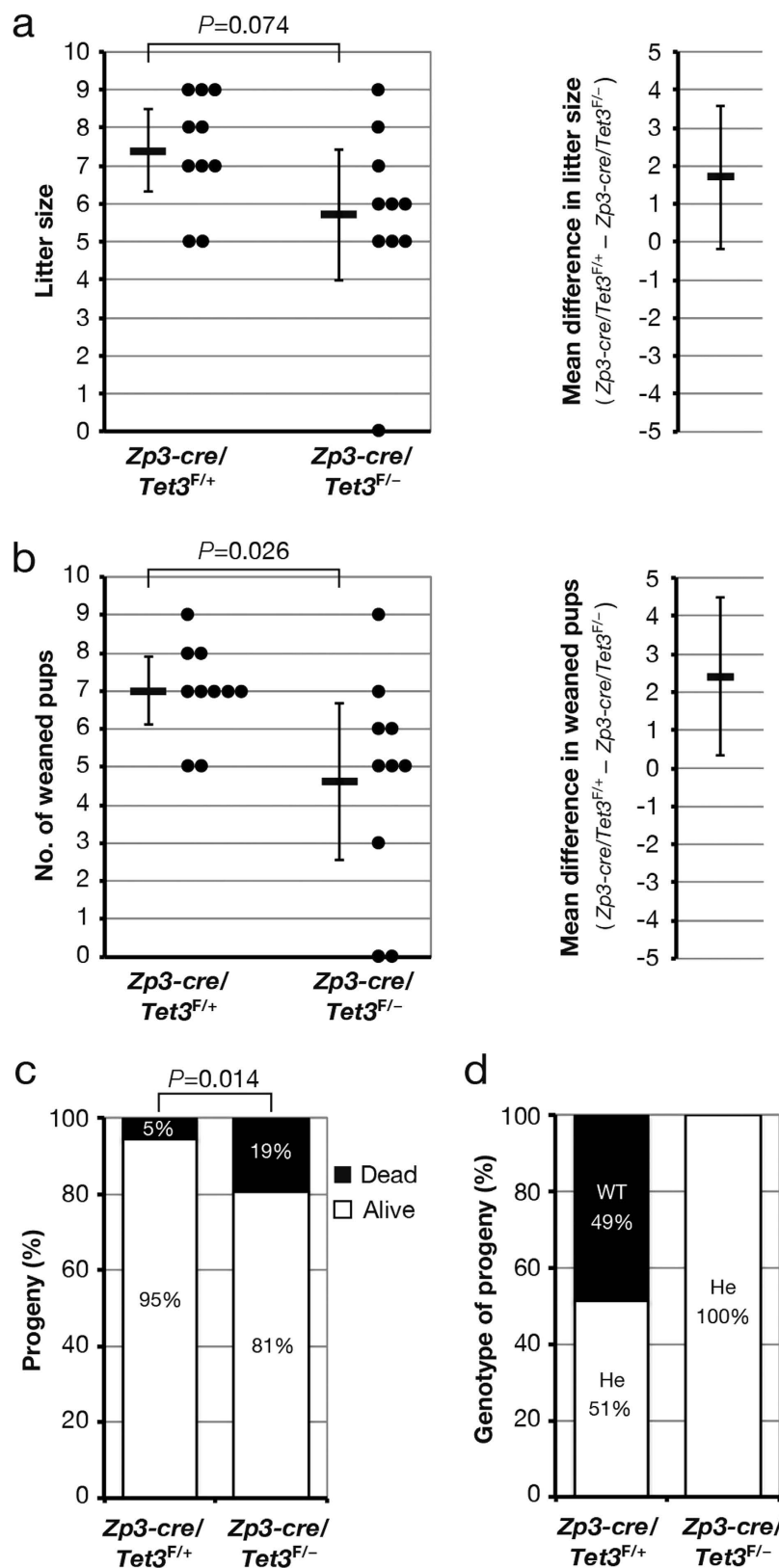
Figure 4. TET3-mediated 5mC oxidation in the zygote is not required for mouse development. (a,b) [*Zp3-cre, Tet3*F/+] ($n = 10$) or [*Zp3-cre, Tet3*F/−] ($n = 10$) female mice were housed with WT (C57BL/6J) males as in Fig. 3c, and both litter size (**a**) and the number of weaned pups (**b**) were determined. Litter size and the number of weaned pups for each female (circles) as well as the overall mean values (horizontal bars) and 95% CIs are shown in the left panels, and the average difference in litter size or the number of weaned pups between [*Zp3-cre, Tet3*F/+] and [*Zp3-cre, Tet3*F/−] dams and its 95% CI are indicated in the right panels. Normality and homoscedasticity of the data were verified by the Shapiro-Wilk test ($\alpha = 0.05$) and F test

($\alpha = 0.05$), respectively. The P values were determined by the two-sided Student's t test. (**c**) The offspring produced in (**a**) ([*Zp3-cre*, *Tet3*$^{F/+}$] dams, $n = 74$; [*Zp3-cre*, *Tet3*$^{F/-}$] dams, $n = 57$) were counted at 7 days after birth, and the percentages of live and dead pups were determined. The P value was determined by the one-sided Fisher's exact probability test. (**d**) *Tet3* genotype of weaned mice in (**b**) ([*Zp3-cre*, *Tet3*$^{F/+}$] dams, $n = 70$; [*Zp3-cre*, *Tet3*$^{F/-}$] dams, $n = 46$). He, heterozygous.

....

However, other studies have found no dynamic reciprocal changes in the levels of 5mC and its oxidation product[41,44]. We have now shown that TET3 is present not only in the paternal pronucleus but also in the maternal pronucleus of mouse zygotes. Consistent with the presence of TET3 in both pronuclei, oxidation of 5mC to 5hmC was detected in both paternal and maternal pronuclei. However, the oxidation of maternal 5mC was less pronounced compared with that of paternal 5mC, corresponding to the lesser extent of TET3 localization to the maternal pronucleus than to the paternal pronucleus. Furthermore, other groups have recently described similar observations[34,36]. Our data coupled with these previous observations support the notion that not only paternal DNA but also maternal DNA in zygotes is subject to TET3-mediated oxidation of 5mC, although such oxidation occurs to a lesser extent in maternal DNA.

Pericentric heterochromatin is arranged in the region surrounding the nucleolus in FG oocytes[45]. This organization of pericentric heterochromatin is reiterated later in the zygote[46] and correlates with the developmental competence of the embryo[47,48]. Similar to previous observations[18,41], we found that 5hmC accumulates in a region of the periphery around the nucleolus-like body in the maternal pronucleus of zygotes. However, this accumulation of 5hmC was not completely abrogated in zygotes deficient in TET3, in contrast to the complete loss of 5hmC from the nucleoplasm apparent in TET3-depleted zygotes. We also detected TET3-independent generation of 5hmC in both SN and NSN types of FG oocytes at the GV stage. Given that 5hmC is enriched in a subset of pericentric heterochromatin of primordial germ cells (PGCs) and that this pattern of 5hmC subcellular localization is maintained even in mature oocytes[49], it is likely that the accumulation of 5hmC in a region of the periphery around the nucleolus-like body in the maternal pronucleus of zygotes is established in PGCs and corresponds to pericentric heterochromatin of a subset of chromosomes. Pericentric 5hmC in PGCs was recently suggested to be generated by TET1[50]. Although the meiotic phenotype of *Tet1* knockout female PGCs suggests that TET1 may have an important role in germ cell development[50], its roles in the zygote as well as in embryonic development are unclear. Whether pericentric 5hmC in the maternal pronucleus of zygotes is important for embryonic development warrants further investigation.

A genome-wide loss of 5mC in the paternal pronucleus of zygotes has been thought to play an important role in mammalian development. Consistent with this notion, TET3-mediated oxidation of paternal 5mC has also been thought to be required for mouse development[51–53]. However, our genetic evidence now suggests that TET3-mediated oxidation of paternal 5mC in zygotes is not essential for mouse development. We have shown that TET3 is dispensable for oocyte development, maturation, and fertilization, consistent with the results of a previous study[19]. Deficiency of TET3 and the accompanying attenuation of 5mC oxidation in zygotes appeared to result in a small but nonsignificant increase in developmental failure of embryos (23% reduction in litter size, $P = 0.074$). However, this result contrasts with the pronounced developmental failure of embryos with maternal TET3 deficiency observed in a previous study (67% reduction in litter size, $P < 0.0001$)[19]. This phenotypic difference may be attributable to differences in experimental conditions between the two studies. First, we used the *Zp3* promoter to control expression of *cre* and thereby to achieve oocyte-specific deletion of *Tet3* from the primary follicle stage, whereas the *Tnap* promoter was used in the previous study to achieve germline-specific deletion of *Tet3* in PGCs. Ablation of *Tet3* in different cell types as well as at different developmental stages might lead to distinct phenotypes. Second, we deleted exon 3 of *Tet3*, whereas exons 8 and 9 were eliminated in the previous study[19]. The deleted genomic regions might contain functional elements such as enhancers or produce noncoding RNAs, and their loss might therefore have phenotypic consequences. Third, we studied mice with a C57BL/6 genetic background, whereas the mice in the previous study had a mixed C57BL/6–129Sv genetic background[19]. Genetic background might have a substantial effect on the phenotype associated with loss of chromatin modifiers. For example, deficiency of the histone demethylase Jumonji domain–containing protein 1A (JMJD1A, also known as KDM3A), which controls *Sry* expression by regulating H3K9me2 (dimethylation at Lys[9] of histone H3) marks, results in a male-to-female sex-reversal phenotype[54]. However, this phenotype is dependent not only on the loss of *Jmjd1a* but also on the genetic origin of the Y chromosome. The proportion of JMJD1A-deficient mice that manifested abnormal sex differentiation was thus 88% with a Y chromosome of CBA origin but only 14% with one of C57BL/6J origin, even though the H3K9me2 levels at the *Sry* locus in the JMJD1A-deficient gonads at embryonic day 11.5 were indistinguishable between these genetic backgrounds. During the revision of our manuscript, another group using complementary methods independently found that TET3-mediated oxidation of paternal 5mC is dispensable for mouse development[55]. Our data coupled with this new study thus strongly support the notion that oxidation of 5mC mediated by maternal TET3 in zygotes is not essential for mouse development.

Recent genome-scale sequence analysis revealed that a much smaller proportion of 5mC is oxidized in the paternal genome of zygotes than previously thought[34,36]. In addition, oxidized 5mC was found to
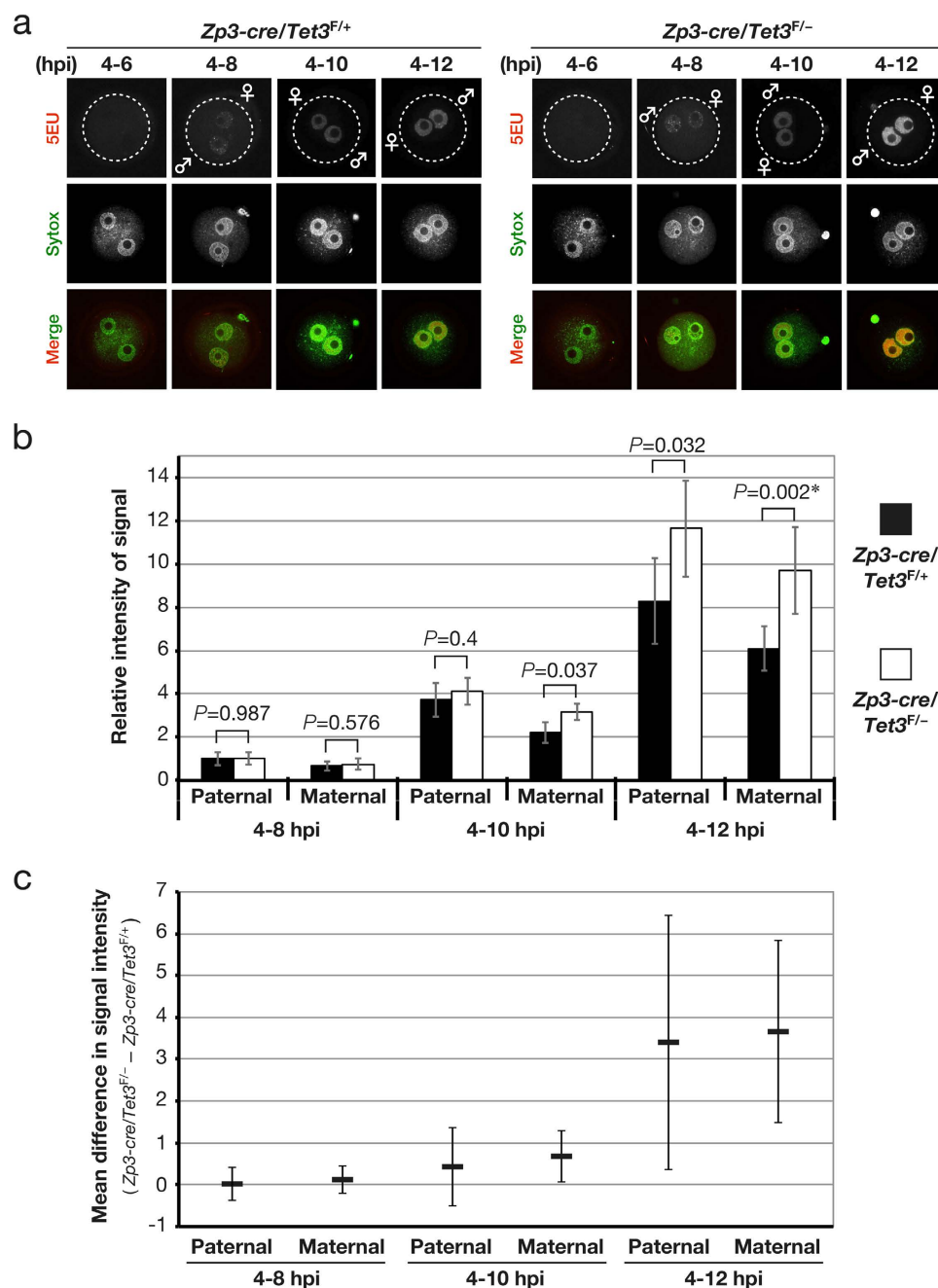
Figure 5. Depletion of maternal TET3 in zygotes enhances zygotic transcription. (**a**) Representative images showing accumulation of incorporated 5EU in zygotes derived from oocytes of [*Zp3-cre*, *Tet3*F/+] or [*Zp3-cre*, *Tet3*F/−] female mice. Zygotes were pulse-labeled with 5EU from 4 to 6, 8, 10, or 12 hpi, incorporated 5EU was then observed (red in merged images). Pronuclei were revealed by staining of DNA with Sytox (green in merged images). Dashed circles, ♂, and ♀ indicate the rim of the zygote, the paternal pronucleus, and the maternal pronucleus, respectively. (**b,c**) The signal intensity for incorporated 5EU in the paternal and maternal pronuclei of zygotes derived from oocytes of [*Zp3-cre*, *Tet3*F/−] (4–8 hpi, $n = 11$; 4–10 hpi, $n = 15$; 4–12 hpi, $n = 15$) or [*Zp3-cre*, *Tet3*F/+] (4–8 hpi, $n = 9$; 4–10 hpi, $n = 11$; 4–12 hpi, $n = 10$) female mice was quantified, normalized by that of Sytox, and expressed relative to the normalized value for the paternal pronucleus of zygotes (4–8 hpi) derived from oocytes of [*Zp3-cre*, *Tet3*F/+] females. The overall mean values and 95% CIs are shown in (**b**), and the average difference (and its 95% CI) in the normalized values between zygotes derived from oocytes of [*Zp3-cre*, *Tet3*F/−] female mice and those derived from oocytes of [*Zp3-cre*, *Tet3*F/+] females is indicated in (**c**). Normality and homoscedasticity of the data were verified by the Shapiro-Wilk test ($\alpha = 0.05$) and F test ($\alpha = 0.05$), respectively. The *P* values were determined by the two-sided Student's *t* test, with the exception of that indicated by the asterisk, which was determined by the two-sided Welch's *t* test because of unequal sample variance.

be diluted in a manner dependent on DNA replication[20,21]. These findings indicate that the oxidation of 5mC contributes to DNA demethylation in zygotes to a lesser extent than previously thought and are therefore consistent with our results showing that deficiency of TET3 and consequent attenuation of 5mC oxidation in zygotes are compatible with mouse development. This compatibility might be attributable to compensation for TET3 deficiency by replication-dependent successive dilution of 5mC as well as by oxidation of 5mC mediated by TET1 or TET2 during preimplantation development. Although TET3-mediated 5mC oxidation is not essential for embryonic development, we found that maternal TET3 is required for neonatal growth. Given that *Tet3* homozygous mutant mice manifest neonatal lethality, the observed neonatal sublethality of *Tet3* heterozygous progeny of [*Zp3-cre*, *Tet3*$^{F/-}$] female mice might be expected to be attributable to the haploinsufficiency of *Tet3*. [*Zp3-cre*, *Tet3*$^{F/+}$] female mice mated with WT males also generate *Tet3* heterozygous progeny at a theoretical proportion of 50%. If these latter pups exhibit neonatal sublethality due to haploinsufficiency of *Tet3*, then this predicted ratio would be affected. However, the ratio of *Tet3* genotypes for the weaned progeny matched the theoretical one, eliminating the possibility that haploinsufficiency of *Tet3* has a sublethal effect. During the revision of our manuscript, another group using complementary methods independently found that deficiency of maternal TET3 leads to neonatal sublethality[55]. Our data coupled with this new study thus strongly support the notion that TET3 is required for neonatal growth.

The oocyte-to-embryo transition is accompanied by a marked reprogramming of gene expression. Mammalian FG oocytes are transcriptionally quiescent, with oocytes after this stage as well as zygotes utilizing only transcripts synthesized and stored during early oocyte development until zygotic genome activation. The timing of zygotic genome activation is species dependent, and the onset of zygotic transcription as well as that of oxidation of 5mC occurs shortly after pronucleus formation in mouse zygotes. Our genetic evidence now suggests that TET3 or its oxidation of 5mC in zygotes represses zygotic transcription. We found that depletion of maternal TET3 did not influence cell cycle progression, however. Deficiency of TET3 and the associated attenuation of 5mC oxidation in zygotes thus appear to result in an increase in zygotic transcription after DNA replication. Although RNA interference–mediated depletion of maternal TET3 was previously shown to have no apparent effect on zygotic transcription (as determined by measurement of 5-bromouridine-5′-triphosphate incorporation into permeabilized zygotes over 15 min)[33], our measurement of 5EU incorporation into intact living zygotes over 2 to 8 h revealed that maternal TET3 may function as a transcriptional repressor in zygotes. TET proteins have been expected to regulate transcription by adjusting the level of DNA methylation at promoters[55]. However, the extent of transcriptional activation by TET1 was found to be less pronounced than its observed repressive function mediated through the recruitment of polycomb repressive complex 2 and the Sin3A corepressor complex[56]. The repressive effect of TET3 on zygotic transcription observed in the present study might thus be explained by a mechanism similar to that described for TET1. Given that epigenetic mutations tend to have a milder phenotype compared with genetic mutations, the accumulation of moderate effects of maternal TET3 depletion each occurring during a narrow time window, such as the effect on zygotic transcription described here, may give rise to the neonatal sublethality apparent in *Tet3* heterozygous progeny of [*Zp3-cre*, *Tet3*$^{F/-}$] female mice. Further studies are thus required to determine why TET3 is required for neonatal growth.

Methods

Generation of *Tet3* conditional knockout mice.　To generate *Tet3* conditional knockout mice, we inserted two *loxP* sequences into the *Tet3* locus by homologous recombination. For construction of the targeting vector, a 6.3-kbp mouse genomic fragment of the 5′ proximal region of *Tet3*, a 2.4-kbp fragment containing exon 3, and a 5.5-kbp fragment containing intron 3 (Gene ID, 194388; RefSeq, NM_183138) were amplified by the polymerase chain reaction (PCR) from genomic DNA of RENKA embryonic stem (ES) cells (C57BL/6N)[57]. The 2.4-kbp amplified fragment containing exon 3 was cloned between the two *loxP* sites of a vector containing both a PGK_neo cassette (neomycin resistance gene driven by the phosphoglycerate kinase 1 gene promoter) as a positive selection marker flanked by *FRT* sequences as well as a PGK_TK cassette (thymidine kinase gene driven by the phosphoglycerate kinase 1 gene promoter) as a negative selection marker. The 6.3- and 5.5-kbp fragments were then also subcloned into the resulting plasmid. The resulting targeting vector contains a 5′ homologous region of 6.3 kbp, the first *loxP* site, the 2.4-kbp floxed genomic region containing exon 3, the PGK_neo cassette flanked by *FRT* sites, the second *loxP* site, a 3′ homologous region of 5.5 kbp, and the PGK_TK cassette (Fig. 1a). The targeting vector was linearized and introduced into RENKA ES cells by electroporation. The cells were subjected to selection with geneticin and ganciclovir, resistant clones were isolated, and their DNA was screened for homologous recombination by nested-PCR analysis with the primers *3AR4* (5′-TCACCTGGTCTATACATCTG AATGC-3′) and *neo_108r* (5′-CCTCAGAAGAACTCGTCAAGAAG-3′) for the first PCR and *3AR3* (5′-CAGTCACTCAATATTTCAACACTCC-3′) and *neo_100* (5′-AGGTGAGATGACAGGAGATC-3′) for the nested PCR. PCR-positive ES clones were expanded, and their isolated DNA was further analyzed by PCR with the primers *5AF3* (5′-AAGTCTCAAACTCTTCTCTGTGTCC-3′) and *neo_marker_sense* (5′-ATTCGCAGCGCATCGCCTTCTATCGCCTTC-3′) for amplification of the 5′ region, *3AR3* and *neo_100* for amplification of the 3′ region, and *DAF2* (5′-AAAGTCGACCCAGCTAGAAGGTGTAGA CTGAGGC-3′) and *R65462* (5′-CGTAAGATGACACAGCTTCG-3′) for amplification of the first *loxP*

region. Homologous recombination in these clones was also confirmed by genomic Southern hybridization with a probe for the neomycin resistance gene.

Homologous recombinant ES cell clones were aggregated with ICR eight-cell embryos to generate chimeric mice. Chimeric mice with a high contribution of the RENKA background were crossed with C57BL/6N mice to obtain offspring heterozygous for the modified *Tet3* allele. The targeted allele was identified by PCR analysis with the primer sets *3AR3* and *neo_100* as well as *DAF2* and *R65462*. The positive selection marker (PGK_neo cassette) was removed from the genome by crossing the heterozygous mice with C57BL/6J mice harboring a *Flp* transgene. The resulting offspring were then crossed with mice harboring a *cre* transgene under the control of the *Zp3* promoter[58]. For genotyping of mice, DNA was extracted from embryos or the tail tip and was subjected to PCR analysis with the primers F1 (5′-TGTTAGGCAGATTGTTCTGG-3′) and R (5′-GAAGGCCTCTGTGATGTCAG-3′) for detection of the floxed allele as well as F2 (5′-GGAGAACCTGCAAGGAAAGCG-3′) and R for detection of the deleted allele.

Generation of antibodies to TET3. Plasmids encoding glutathione S-transferase (GST) fusion proteins of mTET3 were constructed by PCR amplification with cDNA prepared from NIH 3T3 cells. Plasmids encoding GST-mTET3(N) (RefSeq NP_898961, amino acids 1–200) or GST-mTET3(C) (RefSeq NP_898961, amino acids 1300–1506) were generated by insertion of the coding sequence into the SmaI and HindIII sites of a modified pGEX-2T vector (GE Healthcare Bio-Sciences). All constructs were verified by sequencing. The GST-mTET3 fusion proteins were purified as previously described[59]. Polyclonal antibodies to mTET3(N) and to mTET3(C) were generated by injection of rabbits with the corresponding recombinant proteins and were then purified as previously described[60].

Isolation of spermatozoa and oocytes as well as *in vitro* fertilization. All mice were maintained under the specific pathogen–free condition, and all animal experiments were approved by the animal care and use committee of Kyushu University and were performed in accordance with the regulations for animal experiments at Kyushu University. FG oocytes at the GV stage were obtained from 8- to 9-week-old [*Zp3-cre*, *Tet3*^F/−] or [*Zp3-cre*, *Tet3*^F/+] female mice that had been treated with PMSG (ASKA Pharmaceutical Co.). The ovaries were removed from the mice and transferred to modified human tubal fluid (HTF) medium (Irvine Scientific). The ovarian follicles were punctured with a 27-gauge needle, and the cumulus cells were gently removed from the cumulus-oocyte complexes with the use of a narrow-bore glass pipette. MII stage oocytes were collected from the oviducts of 8- to 9-week-old [*Zp3-cre*, *Tet3*^F/−] or [*Zp3-cre*, *Tet3*^F/+] female mice that had been treated with PMSG and hCG (ASKA Pharmaceutical Co.), and spermatozoa were collected from the cauda epididymis of 10- to 15-week-old ICR or C57BL/6J male mice (CLEA Japan). For *in vitro* fertilization, MII stage oocytes were placed in HTF medium supplemented with bovine serum albumin (BSA) at 10 mg/ml (Sigma-Aldrich) and were exposed to spermatozoa in which capacitation had been induced by prior incubation for 1.5 h in HTF medium supplemented with BSA at 4 mg/ml. At 5 h after insemination, fertilized oocytes with two pronuclei were washed and cultured under a humidified atmosphere of 5% CO_2/5% O_2/90% N_2 at 37 °C in HTF medium supplemented with BSA (4 mg/ml). The fertilization rate of oocytes was judged on the basis of the presence of two pronuclei in zygotes at 8 h after insemination.

Immunostaining of oocytes and zygotes. FG oocytes at the GV stage and zygotes produced by *in vitro* fertilization were fixed for 20 min at room temperature with 4% paraformaldehyde in phosphate-buffered saline (PBS) containing 0.2% Triton X-100. They were then washed with PBS containing 0.05% Tween 20 (PBST) before incubation first for 1 h at room temperature with 1% BSA in PBST and then overnight at 4 °C with rabbit anti-mTET3(N), anti-mTET3(C), or anti-DNMT3a (Imgenex) (each at a 1:1000 dilution). They were then washed with PBST, incubated for 1 h at room temperature with Alexa Fluor 568–conjugated goat antibodies to rabbit immunoglobulin G (Molecular Probes–Invitrogen), washed with PBST, and mounted in SlowFade Gold antifade reagent (Molecular Probes–Invitrogen) containing Sytox (Molecular Probes–Invitrogen). For immunostaining of 5hmC and 5mC, FG oocytes at the GV stage and zygotes were fixed with 4% paraformaldehyde in PBS for 30 min at room temperature and then permeabilized with 0.4% Triton X-100 for 30 min at room temperature. They were then washed with PBST, treated with 4 M HCl for 10 min at room temperature, neutralized with 0.1 M Tris-HCl (pH 8.5) for 10 min, and washed with PBST containing 0.5 M NaCl. For the following steps, all solutions contained 0.5 M NaCl. The oocytes and zygotes were incubated first for 1 h at room temperature with 1% BSA in PBST and then overnight at 4 °C with rabbit anti-5hmC (1:1000 dilution, Active Motif) and mouse anti-5mC (1:100, Eurogentec). They were then washed with PBST, incubated for 1 h at room temperature with Alexa Fluor 488–conjugated goat antibodies to mouse immunoglobulin G and Alexa Fluor 568–conjugated goat antibodies to rabbit immunoglobulin G (Molecular Probes–Invitrogen), washed with PBST, and mounted in SlowFade Gold antifade reagent. Fluorescence images were acquired at multiple 2-μm intervals in the *z*-axis with the use of a confocal microscope (CV1000, Yokogawa).

5EU and 5EdU incorporation assays. Incorporation of 5EU and 5EdU in zygotes was monitored on the basis of their fluorescence labels with the use of a Click-iT RNA Imaging Kit and a Click-iT EdU Imaging Kit (Life Technologies), respectively. The zygotes were mounted in SlowFade Gold antifade

reagent containing Sytox. Fluorescence images were acquired at multiple 2-μm intervals in the *z*-axis with the use of a confocal microscope (CV1000, Yokogawa), and the intensity of fluorescence signals for incorporated 5EU and for Sytox was quantified with the use of MetaMorph software (Universal Imaging Co.).

Fecundity test.   Eight-week-old [*Zp3-cre*, *Tet3*$^{F/-}$] or [*Zp3-cre*, *Tet3*$^{F/+}$] female mice were housed with 8-week-old WT (C57BL/6J) male mice, and a check for plug formation was performed daily each morning for 7 days. If no plug was detected, the male mouse was replaced with another one. The weight of female mice was measured at 10 days after plug formation. If no increase in weight was observed, the female mouse was housed with another WT male. Dams were allowed to nurse their pups for 21 days after delivery and were then again housed with a WT male. Weaned pups were counted at 21 days after birth. This fecundity test was conducted over a 2-month observation period.

Statistical analysis.   Data are presented and were analyzed as described in legends. A *P* value of <0.05 was considered statistically significant.

References

1. Jaenisch, R. & Bird, A. Epigenetic regulation of gene expression: how the genome integrates intrinsic and environmental signals. *Nat. Genet.* **33** (suppl.)**,** 245–254 (2003).
2. Mayer, W., Niveleau, A., Walter, J., Fundele, R. & Haaf, T. Demethylation of the zygotic paternal genome. *Nature* **403,** 501–502 (2000).
3. Oswald, J. *et al.* Active demethylation of the paternal genome in the mouse zygote. *Curr. Biol.* **10,** 475–478 (2000).
4. Hajkova, P. *et al.* Epigenetic reprogramming in mouse primordial germ cells. *Mech. Dev.* **117,** 15–23 (2002).
5. Lee, J. *et al.* Erasing genomic imprinting memory in mouse clone embryos produced from day 11.5 primordial germ cells. *Development* **129,** 1807–1817 (2002).
6. Yamazaki, Y. *et al.* Reprogramming of primordial germ cells begins before migration into the genital ridge, making these cells inadequate donors for reproductive cloning. *Proc. Natl. Acad. Sci. USA* **100,** 12207–12212 (2003).
7. Bruniquel, D. & Schwartz, R. H. Selective, stable demethylation of the interleukin-2 gene enhances transcription by an active process. *Nat. Immunol.* **4,** 235–240 (2003).
8. Kangaspeska, S. *et al.* Transient cyclical methylation of promoter DNA. *Nature* **452,** 112–115 (2008).
9. Kim, M. S. *et al.* DNA demethylation in hormone-induced transcriptional derepression. *Nature* **461,** 1007–1012 (2009).
10. Martinowich, K. *et al.* DNA methylation-related chromatin remodeling in activity-dependent BDNF gene regulation. *Science* **302,** 890–893 (2003).
11. Metivier, R. *et al.* Cyclical DNA methylation of a transcriptionally active promoter. *Nature* **452,** 45–50 (2008).
12. Bhutani, N. *et al.* Reprogramming towards pluripotency requires AID-dependent DNA demethylation. *Nature* **463,** 1042–1047 (2010).
13. Santos, F., Hendrich, B., Reik, W. & Dean, W. Dynamic reprogramming of DNA methylation in the early mouse embryo. *Dev. Biol.* **241,** 172–182 (2002).
14. Santos, F. & Dean, W. Epigenetic reprogramming during early development in mammals. *Reproduction* **127,** 643–651 (2004).
15. Wossidlo, M. *et al.* Dynamic link of DNA demethylation, DNA strand breaks and repair in mouse zygotes. *EMBO J.* **29,** 1877–1888 (2010).
16. Ooi, S. K. & Bestor, T. H. The colorful history of active DNA demethylation. *Cell* **133,** 1145–1148 (2008).
17. Tsukada, Y. Hydroxylation mediates chromatin demethylation. *J. Biochem.* (*Tokyo*) **151,** 229–246 (2012).
18. Wossidlo, M. *et al.* 5-Hydroxymethylcytosine in the mammalian zygote is linked with epigenetic reprogramming. *Nat. Commun.* **2,** 241 (2011).
19. Gu, T. P. *et al.* The role of Tet3 DNA dioxygenase in epigenetic reprogramming by oocytes. *Nature* **477,** 606–610 (2011).
20. Inoue, A., Shen, L., Dai, Q., He, C. & Zhang, Y. Generation and replication-dependent dilution of 5fC and 5caC during mouse preimplantation development. *Cell Res.* **21,** 1670–1676 (2011).
21. Inoue, A. & Zhang, Y. Replication-dependent loss of 5-hydroxymethylcytosine in mouse preimplantation embryos. *Science* **334,** 194 (2011).
22. Lepikhov, K. *et al.* Evidence for conserved DNA and histone H3 methylation reprogramming in mouse, bovine and rabbit zygotes. *Epigenet Chromatin* **1,** 8 (2008).
23. Reis Silva, A. R. *et al.* Dynamics of DNA methylation levels in maternal and paternal rabbit genomes after fertilization. *Epigenetics* **6,** 987–993 (2011).
24. Guo, H. *et al.* The DNA methylation landscape of human early embryos. *Nature* **511,** 606–610 (2014).
25. Dean, W. *et al.* Conservation of methylation reprogramming in mammalian development: aberrant reprogramming in cloned embryos. *Proc. Natl. Acad. Sci. USA* **98,** 13734–13738 (2001).
26. Kang, Y. K. *et al.* Aberrant methylation of donor genome in cloned bovine embryos. *Nat. Genet.* **28,** 173–177 (2001).
27. Humpherys, D. *et al.* Epigenetic instability in ES cells and cloned mice. *Science* **293,** 95–97 (2001).
28. Inoue, K. *et al.* Faithful expression of imprinted genes in cloned mice. *Science* **295,** 297 (2002).
29. Polanski, Z., Motosugi, N., Tsurumi, C., Hiiragi, T. & Hoffmann, S. Hypomethylation of paternal DNA in the late mouse zygote is not essential for development. *Int. J. Dev. Biol.* **52,** 295–298 (2008).
30. Beaujean, N. *et al.* Non-conservation of mammalian preimplantation methylation dynamics. *Curr. Biol.* **14,** R266–R267 (2004).
31. Jeong, Y. S. *et al.* DNA methylation state is preserved in the sperm-derived pronucleus of the pig zygote. *Int. J. Dev. Biol.* **51,** 707–714 (2007).
32. Park, J. S., Lee, D., Cho, S., Shin, S. T. & Kang, Y. K. Active loss of DNA methylation in two-cell stage goat embryos. *Int. J. Dev. Biol.* **54,** 1323–1328 (2010).
33. Inoue, A., Matoba, S. & Zhang, Y. Transcriptional activation of transposable elements in mouse zygotes is independent of Tet3-mediated 5-methylcytosine oxidation. *Cell Res.* **22,** 1640–1649 (2012).
34. Shen, L. *et al.* Tet3 and DNA replication mediate demethylation of both the maternal and paternal genomes in mouse zygotes. *Cell Stem Cell* **15,** 459–470 (2014).
35. Santos, F. *et al.* Active demethylation in mouse zygotes involves cytosine deamination and base excision repair. *Epigenet. Chromatin* **6,** 39 (2013).
36. Guo, F. *et al.* Active and passive demethylation of male and female pronuclear DNA in the mammalian zygote. *Cell Stem Cell* **15,** 447–458 (2014).

198

37. Nakamura, T. *et al.* PGC7 binds histone H3K9me2 to protect against conversion of 5mC to 5hmC in early embryos. *Nature* **486,** 415–419 (2012).
38. Probst, A. V. & Almouzni, G. Heterochromatin establishment in the context of genome-wide epigenetic reprogramming. *Trends Genet.* **27,** 177–185 (2011).
39. Debey, P. *et al.* Competent mouse oocytes isolated from antral follicles exhibit different chromatin organization and follow different maturation dynamics. *Mol. Reprod. Dev.* **36,** 59–74 (1993).
40. Hirasawa, R. *et al.* Maternal and zygotic Dnmt1 are necessary and sufficient for the maintenance of DNA methylation imprints during preimplantation development. *Genes Dev.* **22,** 1607–1616 (2008).
41. Salvaing, J. *et al.* 5-Methylcytosine and 5-hydroxymethylcytosine spatiotemporal profiles in the mouse zygote. *PloS One* **7,** e38156 (2012).
42. Yu, C. *et al.* CRL4 complex regulates mammalian oocyte survival and reprogramming by activation of TET proteins. *Science* **342,** 1518–1521 (2013).
43. Yu, C., Xu, Y. W., Sha, Q. Q. & Fan, H. Y. CRL4DCAF1 is required in activated oocytes for follicle maintenance and ovulation. *Mol. Hum. Reprod.* **21,** 195–205 (2015).
44. Li, Y. & O'Neill, C. 5′-Methylcytosine and 5′-hydroxymethylcytosine each provide epigenetic information to the mouse zygote. *PloS One* **8,** e63689 (2013).
45. Zuccotti, M., Piccinelli, A., Giorgi Rossi, P., Garagna, S. & Redi, C. A. Chromatin organization during mouse oocyte growth. *Mol. Reprod. Dev.* **41,** 479–485 (1995).
46. Probst, A. V., Santos, F., Reik, W., Almouzni, G. & Dean, W. Structural differences in centromeric heterochromatin are spatially reconciled on fertilisation in the mouse zygote. *Chromosoma* **116,** 403–415 (2007).
47. Zuccotti, M. *et al.* The analysis of chromatin organisation allows selection of mouse antral oocytes competent for development to blastocyst. *Zygote* **10,** 73–78 (2002).
48. De La Fuente, R. *et al.* Major chromatin remodeling in the germinal vesicle (GV) of mammalian oocytes is dispensable for global transcriptional silencing but required for centromeric heterochromatin function. *Dev. Biol.* **275,** 447–458 (2004).
49. Yamaguchi, S. *et al.* Dynamics of 5-methylcytosine and 5-hydroxymethylcytosine during germ cell reprogramming. *Cell Res.* **23,** 329–339 (2013).
50. Yamaguchi, S. *et al.* Tet1 controls meiosis by regulating meiotic gene expression. *Nature* **492,** 443–447 (2012).
51. Messerschmidt, D. M., Knowles, B. B. & Solter, D. DNA methylation dynamics during epigenetic reprogramming in the germline and preimplantation embryos. *Genes Dev.* **28,** 812–828 (2014).
52. Seisenberger, S., Peat, J. R. & Reik, W. Conceptual links between DNA methylation reprogramming in the early embryo and primordial germ cells. *Curr. Opin. Cell Biol.* **25,** 281–288 (2013).
53. Wu, H. & Zhang, Y. Reversing DNA methylation: mechanisms, genomics, and biological functions. *Cell* **156,** 45–68 (2014).
54. Kuroki, S. *et al.* Epigenetic regulation of mouse sex determination by the histone demethylase Jmjd1a. *Science* **341,** 1106–1109 (2013).
55. Inoue, A., Shen, L., Matoba, S. & Zhang, Y. Haploinsufficiency, but not defective paternal 5mC oxidation, accounts for the developmental defects of maternal Tet3 knockouts. *Cell Rep.* **10,** 463–470 (2015).
56. Williams, K., Christensen, J. & Helin, K. DNA methylation: TET proteins—guardians of CpG islands? *EMBO Rep.* **13,** 28–35 (2012).
57. Mishina, M. & Sakimura, K. Conditional gene targeting on the pure C57BL/6 genetic background. *Neurosci. Res.* **58,** 105–112 (2007).
58. De Vries, W. N. *et al.* Expression of Cre recombinase in mouse oocytes: a means to study maternal effect genes. *Genesis* **26,** 110–112 (2000).
59. Tsukada, Y. *et al.* Histone demethylation by a family of JmjC domain-containing proteins. *Nature* **439,** 811–816 (2006).
60. Tsukada, Y., Ishitani, T. & Nakayama, K. I. KDM7 is a dual demethylase for histone H3 Lys 9 and Lys 27 and functions in brain development. *Genes Dev.* **24,** 432–437 (2010).

Acknowledgements

Author Contributions

Y.T. conceived the project, designed and performed the experiments, and wrote the manuscript. T.A. and K.I.N. provided technical support for experiments and contributed to revision of the manuscript.

Additional Information

Supplementary information accompanies this paper at http://www.nature.com/srep

Competing financial interests: The authors declare no competing financial interests.

How to cite this article: Tsukada, Y. *et al.* Maternal TET3 is dispensable for embryonic development but is required for neonatal growth. *Sci. Rep.* **5**, 15876; doi: 10.1038/srep15876 (2015).
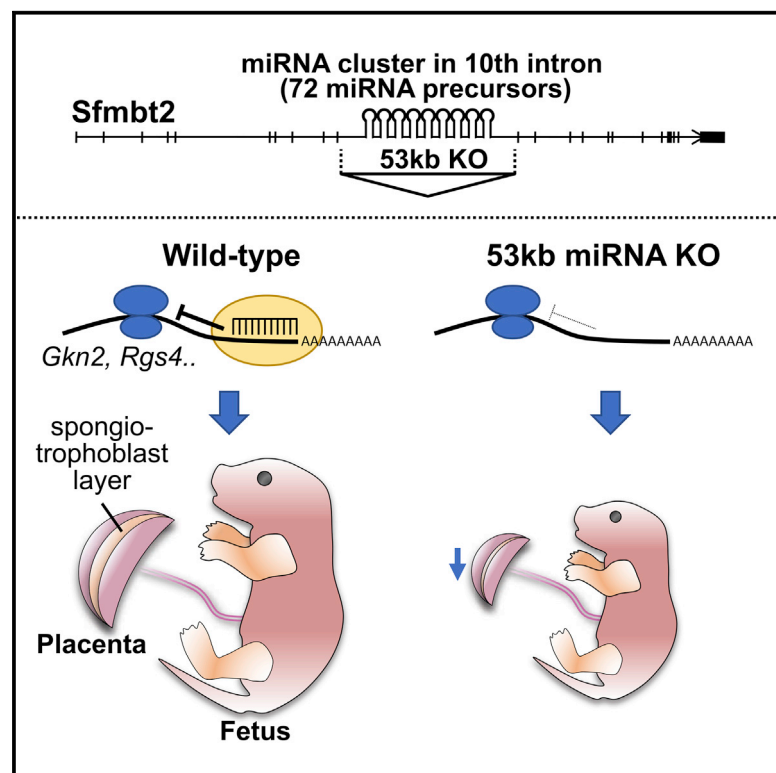
Cell Reports

The Rodent-Specific MicroRNA Cluster within the *Sfmbt2* Gene Is Imprinted and Essential for Placental Development

Graphical Abstract

Authors

Kimiko Inoue, Michiko Hirose, Hiroki Inoue, ..., Ayumi Hasegawa, Keiji Mochida, Atsuo Ogura

Correspondence

inoue@rtc.riken.jp (K.I.),
ogura@rtc.riken.go.jp (A.O.)

In Brief

Inoue et al. use 53-kb knockout mice to uncover the function of the miRNAs that comprise the largest cluster in mice. These miRNAs promote spongiotrophoblast cell proliferation by suppressing target genes with cell-proliferation-regulator or tumor-repressor functions, in cooperation with the host *Sfmbt2* gene under the same imprinted placental expression control.

Highlights

- One of the largest miRNA clusters in the *Sfmbt2* gene is paternally expressed in mice

- Loss of *Sfmbt2* miRNA results in severely impaired development of the placenta

- Impaired placental development is associated with developmental delay of fetuses

- *Sfmbt2* miRNAs may promote proliferation by silencing tumor suppressors

Accession Numbers

GSE82055

CrossMark

CellPress

200

The Rodent-Specific MicroRNA Cluster within the *Sfmbt2* Gene Is Imprinted and Essential for Placental Development

Kimiko Inoue,[1,2,5,*] Michiko Hirose,[1] Hiroki Inoue,[1,3] Yuki Hatanaka,[1] Arata Honda,[1,4] Ayumi Hasegawa,[1] Keiji Mochida,[1] and Atsuo Ogura[1,2,*]

[1]Bioresource Engineering Division, BioResource Center, RIKEN, Tsukuba, Ibaraki 305-0074, Japan
[2]Graduate School of Life and Environmental Sciences, University of Tsukuba, Tsukuba, Ibaraki 305-8572, Japan
[3]Graduate School of Agricultural Science, Faculty of Agriculture, Tohoku University, Sendai, Miyagi 981-8555, Japan
[4]Organization for Promotion of Tenure Track, University of Miyazaki, Miyazaki 889-1692, Japan
[5]Lead Contact
*Correspondence: inoue@rtc.riken.jp (K.I.), ogura@rtc.riken.go.jp (A.O.)
http://dx.doi.org/10.1016/j.celrep.2017.04.018

SUMMARY

MicroRNAs (miRNAs) represent small noncoding RNAs that are involved in physiological and developmental processes by posttranscriptionally inhibiting gene expression. One of the largest miRNA clusters in mice is located in intron 10 of the *Sfmbt2* gene, containing 72 miRNA precursor sequences. In this study, we generated mice lacking the entire *Sfmbt2* miRNA cluster to elucidate its functions during development. The *Sfmbt2* miRNAs were expressed predominantly from the paternal allele in the placenta, as is the host *Sfmbt2* gene. Loss of the paternal allele resulted in severely impaired development of the placenta, especially the spongiotrophoblast layer, and frequent lethality or defects of fetuses. The predicted target sequences of the miRNAs and gene expression analysis defined at least nine putative target genes, which function as tumor suppressors or apoptosis inducers. Our study has provided experimental evidence for the indispensable roles of placental miRNAs in trophoblast proliferation and thus fetal development.

INTRODUCTION

MicroRNAs (miRNAs) represent a family of short noncoding RNAs and function as negative regulators of posttranscriptional products. Systems for gene silencing by miRNAs are well conserved from invertebrate to higher vertebrate organisms, and more than 2,000 miRNAs exist in humans and mice, according to the miRBase public database. miRNA regulation systems are involved in wide-ranging biological processes, including tissue development, cell proliferation, and cancer progression. They act by induction of translational repression in distinct ways: the inhibition of translation at the initiation or post-initiation stage, and the repression of translation by inducing

deadenylation and/or subsequent degradation of target mRNA (Jonas and Izaurralde, 2015).

Many animal miRNA genes are distributed in clusters to gain a functional advantage, and clustered miRNAs are often processed from the same polycistronic precursor transcript (Bartel, 2004). If the clustered miRNAs have similar sequences, the cohort of gene products may contribute additively to the regulation of a set of mRNA targets. When they include miRNAs with distinct sequences, these miRNAs are deployed coordinately toward their various mRNA targets. Notably, large miRNA clusters in mammals are located near or within imprinted genes, which are expressed monoallelically in parent-of-origin fashion. Such large clusters include the chromosome 19 microRNA cluster (C19MC) and *Dlk1-Dio3* and *Sfmbt2* miRNA clusters. C19MC is primate specific, and in humans spans over 100 kb at chromosome 19q13.41 (Noguer-Dance et al., 2010). The C19MC miRNAs are exclusively expressed in the placenta from the paternal allele, and their association with eclampsia (Buckberry et al., 2014) and antiviral defenses during maternal-fetal infections (Delorme-Axford et al., 2013) has been demonstrated. The miR-379/miR-410 miRNA cluster located in the *Mirg* gene within the *Dlk1-Dio3* imprint region is a maternally expressed cluster of genes observed throughout eutherian mammals (Seitz et al., 2004). The function of the miR-379/miR-410 cluster was investigated using conventional knockout mice with a deletion of the corresponding 59-kb region of the *Mirg* gene (Labialle et al., 2014). The mutants showed partially penetrant postnatal death, which was caused by defects in the maintenance of energy homeostasis. Thus, C19MC and *Dlk1-Dio3* miRNA clusters are under imprinted control but appear to exert their differential effects on pre- and postnatal development, respectively.

The third large miRNA cluster is located within the *Sfmbt2* gene (Zheng et al., 2011). The coding region of *Sfmbt2* configures four malignant brain tumor (MBT) domains and is well conserved throughout eutherian mammals (Kuzmin et al., 2008; Wang et al., 2011). It is expressed robustly in the placentas of all mammalian species examined but shows imprinted expression only in Old World rodents, including rats and mice. Intriguingly, its encompassed miRNA cluster is found in these
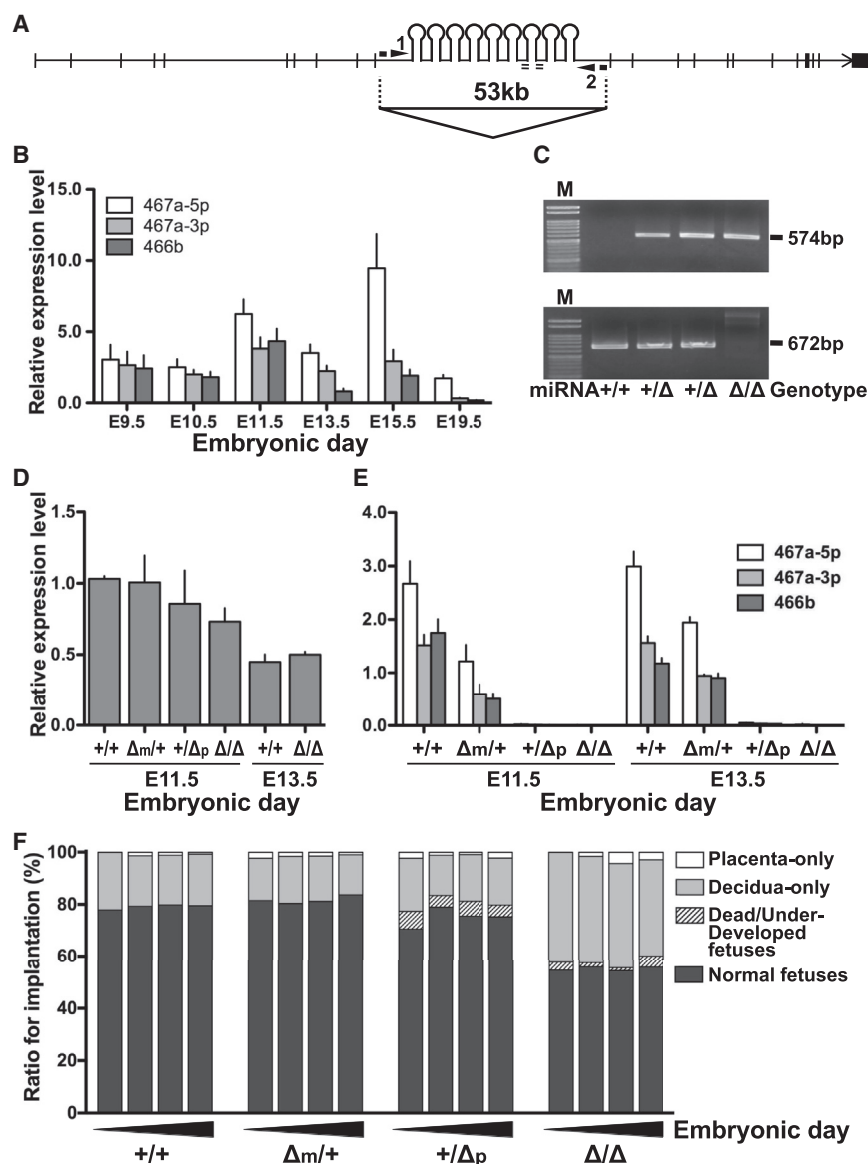
Figure 1. Generation of *Sfmbt2* miRNA Cluster-Deleted Mice and Expression Level of *Sfmbt2* mRNA and miRNAs

(A) Genomic structure of *Sfmbt2*. Vertical bars indicate exons, and the miRNA cluster is located in intron 10 of the mouse *Sfmbt2* gene. The CRISPR/Cas9 system can induce an approximately 53-kb deletion. Solid and double lines indicate the binding of the primer sets for detection of deleted and wild-type alleles as shown in (C).

(B) Expression level of miRNAs in placentas derived from E9.5 to 19.5 embryos. White and light and dark gray bars indicate mmu-miR467a-5p, -467a-3p, and -466b-3p, respectively. miRNA expression level was the highest at E15.5 (467a-5p) or E11.5 (467a-3p and 466b). Error bars indicate SEM.

(C) Confirmation by PCR of the large-scale deletion of the *Sfmbt2* miRNA cluster. Products of 574 bp indicate the presence of the 53-kb deletion induced by the CRISPR/Cas9 system (upper panel). Homo- and heterozygous deletions were confirmed by genomic PCR of the wild-type allele (bottom panel). M; size marker.

(D) *Sfmbt2* mRNA levels in placentas from the four genotypes. Expression levels on the same embryonic days were not significantly different (Kruskal–Wallis test for E11.5, and unpaired t test for E13.5). Error bars indicate SEM.

(E) *Sfmbt2* miRNA levels in placentas from the four genotypes. miRNAs were barely expressed in miRNA +/Δp and Δ/Δ placentas. Error bars indicate SEM.

(F) Developmental abilities of embryos derived from the four genotypes. Ratios of fetuses (dark gray) were significantly decreased in Δ/Δ compared with +/+ or Δm/+ (p < 0.01 or p < 0.05 by one-way ANOVA), and underdeveloped fetuses (hatched lines) were observed only in +/Δp and Δ/Δ. The ratio was calculated from the cumulative numbers showing embryonic growth. Bars indicate embryonic days 11.5, 13.5, 15.5, and 19.5 in the four genotypes.

two species but not in humans, bovines, or pigs. This may indicate that the miRNA cluster in *Sfmbt2* emerged recently in the rodent genome, probably coincidental with the acquisition of the imprinted control of *Sfmbt2* (Lehnert et al., 2011; Wang et al., 2011; Zheng et al., 2011). The miRBase database records that the *Sfmbt2* miRNA cluster is located in intron 10 of the *Sfmbt2* gene and contains 72 stem-loop structures. The *Sfmbt2* gene is paternally expressed in the mouse placenta and is essential for trophoblast maintenance, as confirmed by knockout mice with paternal deletion of the gene (Kuzmin et al., 2008; Miri et al., 2013). However, the function of any miRNAs in this cluster is still unknown because of the high similarity of their sequences, which span over 50 kb in intron 10 of *Sfmbt2*. In this study, we sought to define the expressed allele and the functions of the *Sfmbt2* miRNAs during mouse development. For this purpose, we generated knockout mice with a large-scale deletion of the

entire *Sfmbt2* miRNA region using the CRISPR/Cas9-dual-sgRNA (single-guide RNA) system.

RESULTS

The *Sfmbt2* miRNAs Are Paternally Expressed in the Placenta

The mouse *Sfmbt2* gene contains 72 miRNA precursor sequences located in intron 10 (Figure 1A). First, we analyzed the expression profiles of the miRNAs in embryonic day (E)11.5 placentas using an Agilent miRNA microarray (version 17), which covers 55 mature miRNAs within the *Sfmbt2* miRNA cluster. We identified that at least 28 miRNAs in this cluster were highly expressed in E11.5 placentas (Table S1). We then examined whether the expression levels of *Sfmbt2* miRNAs changed with the day of pregnancy. The expression levels of three mature

Table 1. Segregation Pattern of the *Sfmbt2* miRNA Cluster Deletion in the F1 to F3 Generations

Generations					
Offspring (Mother × Father)	F1 (F0 × WT)	F2 (F1 × WT)	F2 (WT × F1)	F3 (F2 × WT)	– (F2 × F1)
Mother	*Sfmbt2* miRNA +/Δ	*Sfmbt2* miRNA +/Δ	wild-type	*Sfmbt2* miRNA +/Δ	*Sfmbt2* miRNA +/Δ
×	×	×	×	×	×
Father	wild-type	wild-type	*Sfmbt2* miRNA +/Δ	wild-type	*Sfmbt2* miRNA +/Δ
No. of litters	7	6	6	7	2
Total no. of mice	44	54	55	48	16
No. of *Sfmbt2* miRNA +/Δ (%)	10 (22.7)	33 (61.1)*	17 (30.9)**	26 (54.2)*	9 (56.3)
Female:male	5:5	22:11	12:5	13:13	8:6
No. of *Sfmbt2* miRNA Δ/Δ (%)	–	–	–	–	2 (12.5)
Female:male	–	–	–	–	0:2

*versus **: p < 0.05 (chi-square test).

miRNAs, mmu-miR-467a-5p (467a-5p), mmu-miR-467a-3p (467a-3p), and mmu-miR-466b-3p (466b), which were highly expressed at E11.5, were measured by reverse transcription-quantitative real-time PCR (RT-qPCR) using placentas from E9.5 to E19.5. The three miRNAs were expressed at all the stages examined, but each miRNA showed stage-specific expression patterns (Figure 1B): 467a-3p and 466b were most highly expressed at E11.5, whereas 467a-5p was most highly expressed at E15.5. In E19.5 term placentas, the expression was decreased to the lowest detectable level.

To define the functional roles of *Sfmbt2* miRNAs, we used the CRISPR/Cas9 system to produce mice that lacked the *Sfmbt2* miRNA cluster. We used Cas9 plasmid vector pX330 with dual sgRNAs designed to target either end of the miRNA cluster (target IDs 1 and 2 in Figure 1A and Table S2). Using information from a public database (GEO: GSE40667, GSE51511, and GSE29218), we confirmed that in placenta or extraembryonic cultured cells, this region included no specific binding motifs for major regulatory factors such as SOX2 or CDX2 (data not shown). The plasmid was introduced into the male pronucleus of one-cell-stage fertilized embryos. The sequence containing the 53-kb deletion was amplified by primer sets designed to recognize outside the targeted sequences (Figures 1A and 1C), and the deletion was confirmed by DNA sequencing of PCR products.

We finally obtained one founder (F0) heterozygous mutant (*Sfmbt2* miRNA +/Δ) female (Table S2). Forty-four F1 mice, ten (22.7%) of which were heterozygous mutants (+/Δ), were obtained by mating the founder female with wild-type (+/+) males (Table 1). In the F2 and F3 generations produced by the same cross (heterozygous [+/Δ] females × wild-type [+/+] males), 61.1% (33/54) and 54.2% (26/48), respectively, were heterozygous mutants (+/Δ), proportions that did not differ significantly from the expected segregation ratio (50%). However, when the F2 generation was produced by crossing wild-type (+/+) females and heterozygous (+/Δ) males, 30.9% (17/55) were heterozygous mutants (+/Δ), a significantly lower proportion than for the reciprocal cross. By crossing heterozygous (+/Δ) parents, we confirmed that at least some homozygous mutant (Δ/Δ) embryos survived to term (2 of 16 pups born).

We examined wild-type (+/+), maternal mutant (Δm/+), paternal mutant (+/Δp), and homozygous mutant (Δ/Δ) embryos

for their gene expression patterns. There was no significant difference between these genotypes in the level of expression of *Sfmbt2* mRNA in E11.5 or E13.5 placentas (p = 0.70 and p = 0.45, respectively), indicating that the absence of the miRNA cluster had no effect on the transcription of the host gene (Figure 1D). Next, to examine the allelic expression pattern of the *Sfmbt2* miRNAs, we examined the expression levels of three miRNAs in E11.5 and E13.5 placentas of the four genotypes. All miRNAs were highly expressed in wild-type (+/+) and maternal knockout (Δm/+) placentas. In contrast, no or very low miRNA expression was found in paternal knockout (+/Δp) and homozygous knockout (Δ/Δ) placentas (Figure 1E). This indicated that, like the host *Sfmbt2* gene, the *Sfmbt2* miRNAs are paternally expressed.

Paternal Deletion of the *Sfmbt2* miRNA Cluster Causes Partial Embryonic Lethality

To clarify the reasons for the decreased numbers of paternal knockout (+/Δp) and homozygous knockout (Δ/Δ) fetuses, we examined the implantation sites at E11.5, E13.5, E15.5, and E19.5 following in vitro fertilization and embryo transfer. The parents used were homozygous, either wild-type (+/+) or mutant (Δ/Δ), so that we could obtain a set of embryos with the same expected genotypes. The implantation rates were not significantly different between the genotypes, ranging from 80% to 100%. The proportions of normal fetuses, dead or underdeveloped fetuses, placentas without fetuses (placenta only), and implantation scars (decidua only) did not differ significantly between the +/+, Δm/+, and +/Δp genotypes (Figure 1F). However, in the Δ/Δ genotype, the proportion of normal fetuses was significantly lower than in the +/+ and Δm/+ genotypes (Figure 1F). Furthermore, both +/Δp and Δ/Δ genotypes were characterized by the presence of dead or underdeveloped fetuses (in total, 4.5% in +/Δp and 4.2% in Δ/Δ, at term), whereas Δm/+ conceptuses were indistinguishable from the wild-type (+/+) (Figures 1F and 2A–2E). The +/Δp and Δ/Δ fetuses that reached term had significantly lower body weights (Figure 2F). After birth, more than 85% of live newborns survived to weaning (day 21) irrespective of the genotype (Figure S1). After weaning, one +/Δp male died for an unknown reason, but the other individuals grew into normal adults. Thus, a significant proportion of +/Δp and Δ/Δ fetuses died or
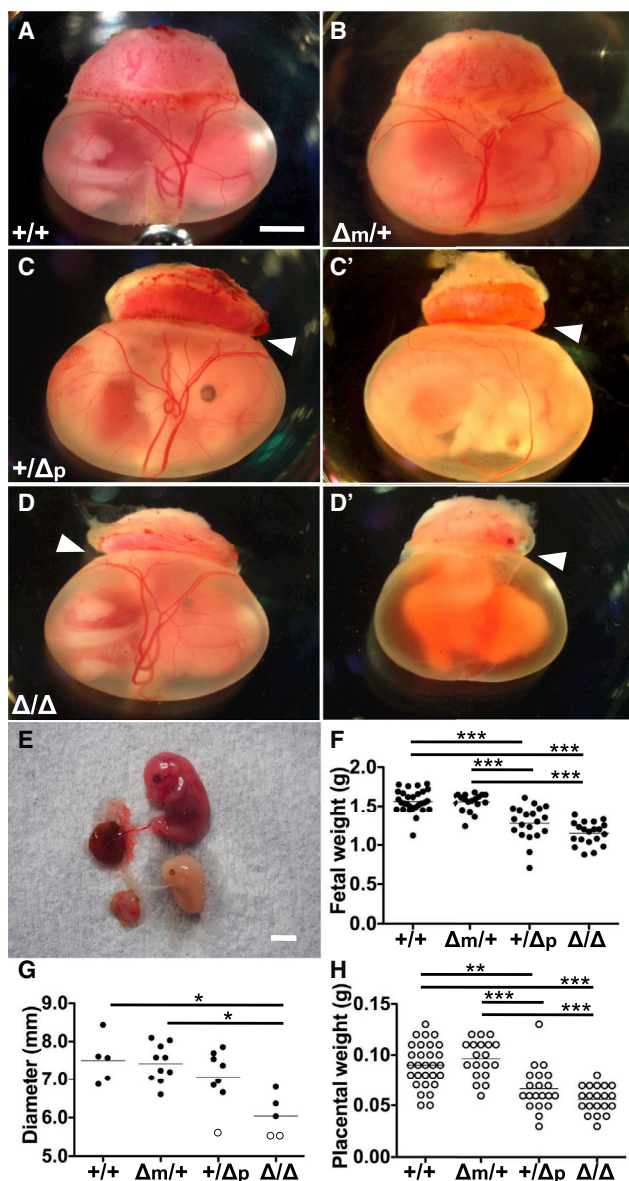
Figure 2. Representative Appearance of E13.5 Whole Embryos and Fetal and Placental Development for the Four Genotypes

(A–D) Disruption of the parietal yolk was not observed in miRNA +/+ (A) and Δm/+ (B) genotypes, but a gap (infolding) was created between the placenta and the visceral yolk sac in +/Δp (C) and Δ/Δ (D) genotypes (white arrowheads). Several underdeveloped or dead fetuses were observed in +/Δp (C′) and Δ/Δ (D′) genotypes. Scale bar, 2 mm.

(E) Live and dead fetuses observed in the E15.5 +/Δp genotype. Scale bar, 4 mm.

(F) E19.5 fetal weights of the four genotypes. Lines within graphs indicate mean values. ***p < 0.005 (Kruskal–Wallis test).

(G) Diameters of E13.5 placentas of the four genotypes. Open circles show placentas of underdeveloped or dead fetuses. Lines within the graph indicate mean values. Diameters of miRNA Δ/Δ placentas were significantly smaller than those of +/+ and Δm/+ placentas. *p < 0.05 (Kruskal–Wallis test).

(H) E19.5 placental weights of the four genotypes. Lines within graphs indicate mean values. **p < 0.01 and ***p < 0.005 (Kruskal–Wallis test).

were developmentally delayed before midgestation, but thereafter most surviving fetuses reached term and survived to adulthood.

The placentas in the Δ/Δ and +/Δp genotypes showed a characteristic impaired phenotype. The mean diameters of Δ/Δ and +/Δp placentas at E13.5 were smaller than those of Δm/+ and +/+ placentas, and those bearing a dead or underdeveloped fetus were the smallest in size (Figures 2A–2D′ and 2G). The mean placental weight at term was significantly lower in the Δ/Δ and +/Δp genotypes than in the Δm/+ and +/+ genotypes (Figure 2H).

To define the reason for the impaired development of Δ/Δ and +/Δp placentas, we examined their histological features. The mouse placental area can be roughly divided into three layers: the maternal decidua and the fetal labyrinthine and spongiotrophoblast layers (Figure 3A). At E11.5, the two fetal layers in Δ/Δ and +/Δp placentas were smaller than those of the wild-type, whereas the maternal decidua was of normal thickness (Figures 3A–3D). In particular, the spongiotrophoblast layer was extremely thin, containing only a few layers of trophoblastic cells. By contrast, Δm/+ placentas showed normal histology and were indistinguishable from +/+ placentas. These alterations were confirmed by measurement of the area of each layer (Figure S2). The spongiotrophoblast layer in Δ/Δ and +/Δp placentas was significantly smaller than that in Δm/+ and +/+ placentas. The defective structure of the spongiotrophoblast layers in the +/Δp and Δ/Δ placentas was also found at E13.5 (Figures S2 and S3) and persisted to term (Figures 3A′–3D′).

We also noted another minor phenotype in +/Δp and Δ/Δ placentas. When we retrieved the conceptuses from the uteri at E11.5 or E13.5, a gap (infolding) was created between the placenta and the yolk sac (white arrowheads in Figures 2C, 2C′, 2D, and 2D′). This was caused by the disruption of the parietal yolk sac at this region. At the histological level, the parietal yolk sac in these knockout conceptuses was characterized by a thin Reichert's membrane and a decreased number of endoderm cells (insets in Figures 3A and 3D).

These histological phenotypes in miRNA-knockout placentas were evident as early as E8.5; very few trophoblastic cells (future spongiotrophoblast cells) were present under the parietal yolk sac. The parietal yolk sac showed a sparse distribution of endoderm cells on the Reichert's membrane (Figures S3E–S3H).

Next, we attempted to establish trophoblast stem (TS) cells from hetero- and homozygous embryos to investigate in vitro the characteristics of these genotypes. We confirmed that TS cell lines were able to be established from Δ/Δ embryos (Table S3), although the proportion of established TS cell lines derived from cultured Δ/Δ blastocysts was slightly lower than that for wild-type (70.0% versus 46.4%, p > 0.05, chi-square test), and that Δm/+ and +/Δp TS cell lines were also able to be established with comparable efficiency to wild-type. There were also no genotype-dependent differences in the expression levels of CDX2, a TS cell marker protein, even after a 48-h differentiation culture (Figure S4A). When gene expression levels were compared in undifferentiated and 48-h differentiated cells, expression of *Gcm1* (labyrinthine marker), *Pr3d1* (PL-1; trophoblast giant cell marker), and *Ascl1* (spongiotrophoblast marker) showed trends toward decreasing in Δ/Δ cell lines, although the differences were not significant (Figure S4B). These results suggested that
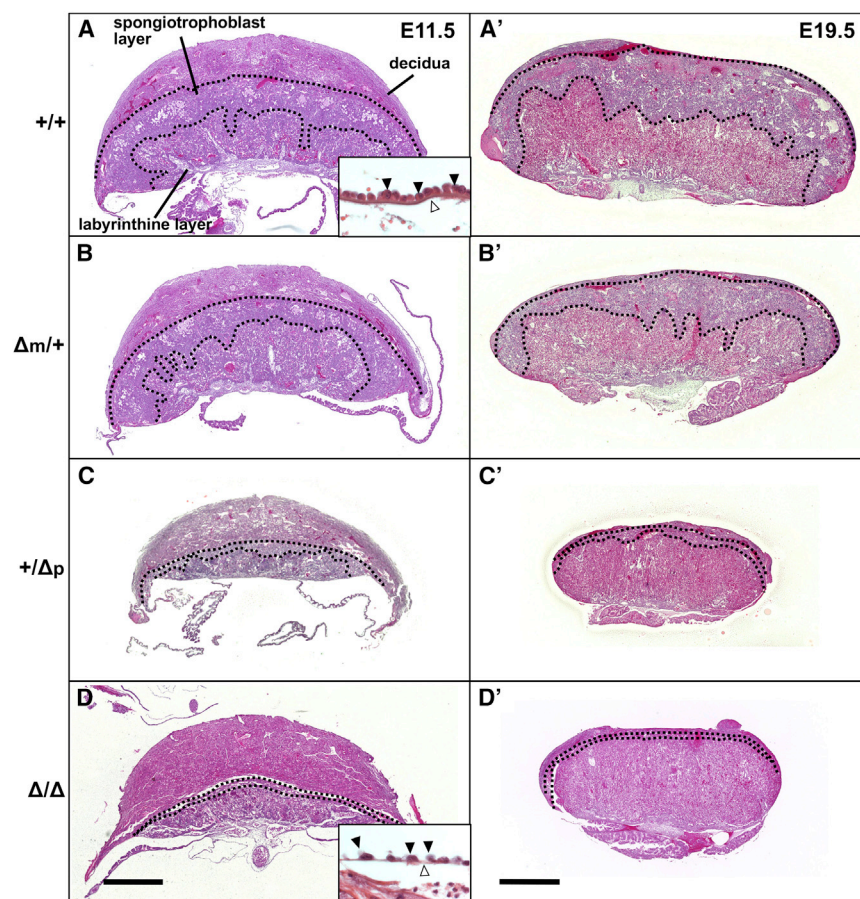
Figure 3. Tissue Sections of Placentas Derived from the Four Genotypes at E11.5 and E19.5

(A–D) Placentas at E11.5 (A–D) and E19.5 (A′–D′). Placentas derived from miRNA +/+ (A and A′), Δm/+ (B and B′), +/Δp (C and C′), and Δ/Δ (D and D′) genotypes. The three principal layers (maternal decidua, fetal spongiotrophoblast, and labyrinthine layers) are divided by dotted lines. Insets in (A) and (D) show endoderm cells (black arrowheads) and Reichert's membrane (white arrowheads) at E11.5. Scale bars, 1 mm. See also Figures S2 and S3.

regulating genes (*Fst*, *Dlx4*, *Fgfrl1*, *Bmper*, and *Car8*), and a gene with unknown function (*Sh3d21*). *Gkn2* expression is localized to the spongiotrophoblast layer and the endoderm cell layer of the mouse placenta (Antas et al., 2014; Fahlbusch et al., 2015). GKN2 was implicated in the migration of trophoblasts within the placentas and hematopoietic progenitors from the yolk sac to the embryo proper. Numerous studies have reported antiproliferative activity for GKN-family proteins in gastric epithelial cells and loss of GKN expression in cancer cells (Menheniott et al., 2013). *Rgs4* may also function as a tumor-suppressor gene by preventing G protein activation (Richardson et al., 2001). This gene is known to be expressed in human placenta, but is downregulated in a placenta-derived choriocarcinoma cell line (Kobayashi et al., 2013). *Fndc1* (also known as *Ags8* in humans) is a hypoxia-induced apoptosis gene (Sato et al., 2009), and may be activated in mouse placentas that are exposed to hypoxic stress during angiogenesis (Iwawaki et al., 2009). *Fst* is the gene for follistatin, which functions as an antagonist of activin A (Hemmati-Brivanlou et al., 1994). Follistatin is distributed in the extracellular matrix of the spongiotrophoblast layer (Candeloro and Zorn, 2007) and inhibits the proliferation of TS cells in vitro by suppressing activin A activity (Erlebacher et al., 2004). Thus, these known functions and distributions described for the four upregulated genes (*Gkn2*, *Rgs4*, *Fndc1*, and *Fst*) are in good accordance with the poor development of the spongiotrophoblast layer associated with *Sfmbt2* miRNA-knockout placentas. Although further experiments are necessary to identify the exact causal relationship between these genes and the placental phenotype in the *Sfmbt2* miRNA-knockout placentas, we can speculate that the *Sfmbt2* miRNAs are responsible for the maintenance of the normal size and structure of mouse placentas by negatively regulating target genes that have antiproliferative effects.

deletion of *Sfmbt2* miRNAs had some, but not significant, effects on the establishment efficiency and in vitro differentiation ability of TS cells.

Prediction of *Sfmbt2* miRNA Target Genes

We next sought to identify candidate target genes of the 28 *Sfmbt2* miRNAs that were expressed in E11.5 placentas (Table S1). By 60k microarray analysis of mRNAs, we found that the expression of 3,118 probes was significantly increased in miRNA Δ/Δ placentas compared with +/+ placentas. To predict the possible target sequences, we selected genes at the intersection of two computational target-prediction searches, TargetScan and microRNA.org. Of the 3,118 upregulated probes, 102 contained possible target sequences for these miRNAs in their 3′ untranslated regions. To strengthen the prediction of target genes, we next compared the gene expression pattern of both genotypes in E8.5 extraembryonic tissues. We identified 7,839 probes upregulated in miRNA Δ/Δ placentas compared with wild-type placenta; 251 probes were included in the target prediction by both algorithms. Finally, we narrowed the candidate target genes down to 15 genes that were upregulated in both developmental stages (Table S4). RT-qPCR validation confirmed that 9 of the 15 genes were significantly upregulated (Figure 4). These nine genes included tumor-suppressor genes (*Gkn2* and *Rgs4*), an apoptosis-inducing gene (*Fndc1*), differentiation/patterning-

DISCUSSION

In mammals, miRNA families are often located in large clusters near or within imprinted genes, probably because of the
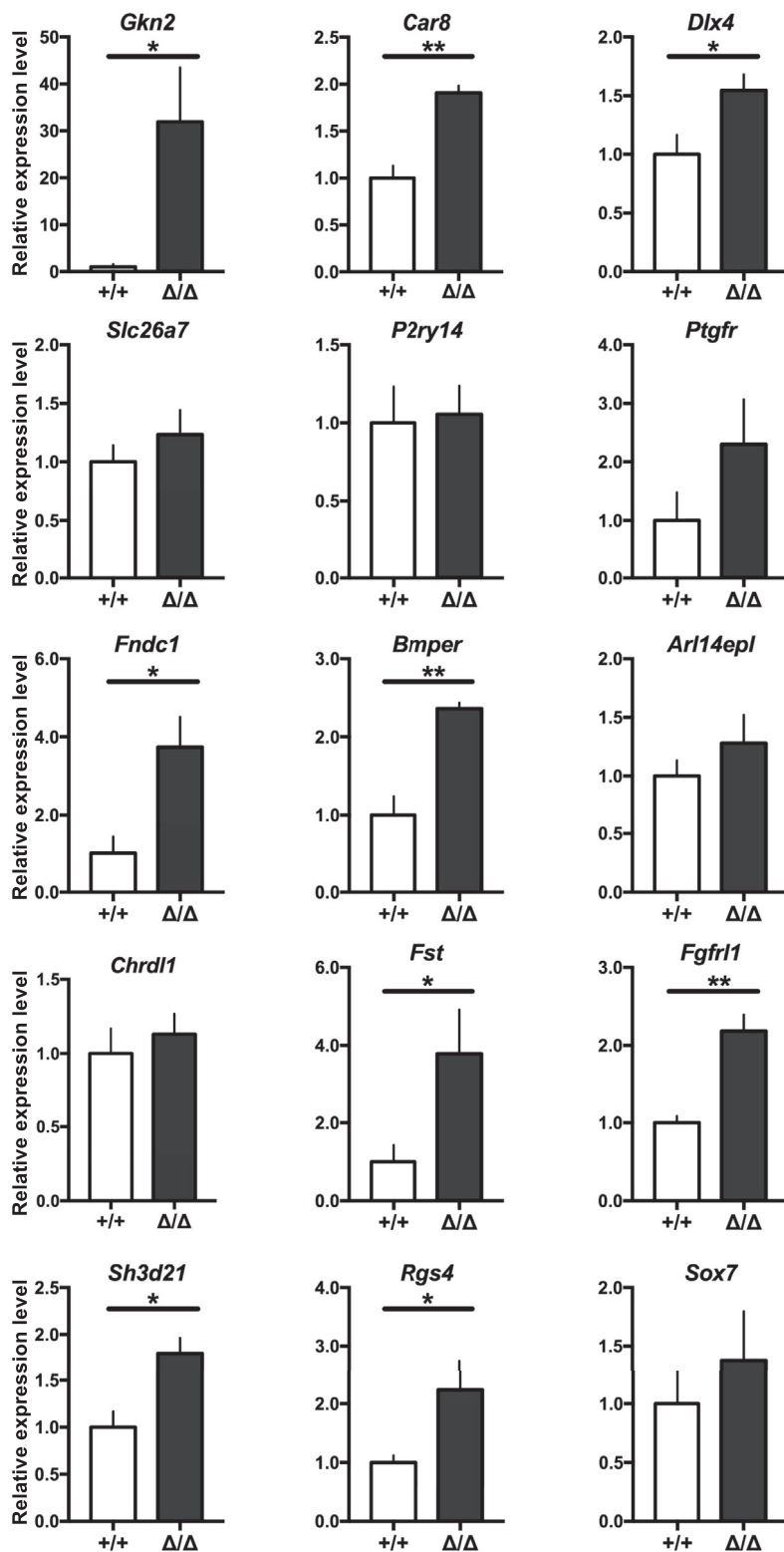
Figure 4. Gene Expression Validation of 15 Putative Target Genes by RT-qPCR
White and dark gray bars indicate miRNA +/+ and Δ/Δ, respectively. *p < 0.05 and **p < 0.01 (unpaired t test). Error bars indicate SEM.

to delete multiple miRNA-family genes in a single step, using the CRISPR/Cas9 system with dual sgRNAs. As a result, we could demonstrate that the *Sfmbt2* miRNA cluster is under imprinted control and is essential for normal placental development. Although miRNA-mediated regulation of trophoblast development has been suggested by the altered expression of miRNAs in human placental diseases such as preeclampsia (Buckberry et al., 2014; Chen and Wang, 2013), there has been no experimental evidence that supports this concept. The results of our study provide a demonstration that miRNAs are involved in the balance of trophoblast proliferation and apoptosis (or cell-cycle arrest) that is critically important for normal placental development. It has been reported that mouse *miR-127*, one of the miRNAs processed from an antisense transcript of *Rtl1* (*Rtl1as*), may repress its target *Rtl1* in the labyrinthine zone (Ito et al., 2015). However, *Rtl1* and *Rtl1as* have a one-to-one relationship and are expressed in fetal epithelial cells, not trophoblast cells, to form the fetal capillaries in the labyrinthine zone (Sekita et al., 2008). Therefore, this *Rtl1-Rtl1as* system may be distinct from other miRNA-mediated gene regulatory systems in placental development, perhaps because of its evolutionarily unusual retrotransposon origin.

We identified a characteristic phenotype in the developing placentas that lacked the *Sfmbt2* miRNAs. The spongiotrophoblast layer of +/Δp (and also Δ/Δ) embryos was very thin, although it normally occupies about half the volume of the fetal placenta. It is most likely that the *Sfmbt2* miRNAs are transcribed in the spongiotrophoblast layer, because the host *Sfmbt2* gene is highly expressed in this layer (Miri et al., 2013). *Sfmbt2* is also expressed in embryonic tissues but is not imprinted. Therefore, any expression of the *Sfmbt2* miRNAs in embryonic tissues may not be imprinted. From these data, we may presume that the retarded development or lethality in miRNA +/Δp embryos is not a direct effect of the loss of the miRNAs on the embryonic side but a consequence of the impaired development of the placenta, especially the spongiotropho-

evolutionary advantage of sharing common allele- and developmental stage-specific expression with the host gene. In this study, we took advantage of the clustering nature of miRNAs

blast layer. The fate of most +/Δp embryos is probably determined by midgestation, as suggested by the survival rates through the postimplantation and postnatal stages (Figure 1F).

This is consistent with the high expression of the miRNAs at E9.5 and the appearance of the earliest placental abnormalities at E8.5. The development of fetuses might be affected at midgestation (around E9.5 to E10.5), because from this point on, they depend more on the chorioallantoic placenta than the yolk sac placenta. In addition, our miRNA-knockout study has implications for the interpretation of the previous *Sfmbt2*-knockout study by Miri et al. (2013), who reported that all fetuses with the paternal knockout allele showed a more severe phenotype and died by E12.5. They produced *Sfmbt2*-null mice by inserting a gene-trap allele including a splicing acceptor and a strong poly(A) signal to induce the translation of truncated SFMBT2 protein. Because the *Sfmbt2* mRNA level was significantly decreased in the knockout placenta, it was probable that the expression of miRNAs was also repressed. Thus, the severe phenotype observed in *Sfmbt2*-null mice might be attributable in part to this miRNA repression.

In this study, miRNA Δ/Δ embryos showed more severe phenotypes than +/Δp embryos. The rate of surviving fetuses with the Δ/Δ genotype was significantly lower than that of those with the +/Δp genotype (54.3%–55.7% versus 70.4%–78.9% at E11.5 to 19.5). This may be explained by some leakage of expression of miRNAs from the maternal allele in +/Δp embryos. Indeed, RT-qPCR analysis detected low but significant miRNA expression in +/Δp placentas but not in Δ/Δ placentas (0.017 versus 0.004 on average at E11.5). Consistent with this, Miri et al. (2013) reported a considerable level of *Sfmbt2* transcripts from the maternal allele in *Sfmbt2* paternal knockout placentas. Because the *Sfmbt2* miRNAs consist of four major miRNA families with a high level of redundancy in their target sequences, even small amounts of some miRNAs from the maternal allele might have ameliorated the phenotypes.

The list of predicted targets of the *Sfmbt2* miRNAs included some genes that play roles in tumor repression or apoptosis (*Gkn2*, *Rgs4*, *Fndc1*, and *Fst*). *Gkn2*, for example, was originally discovered as a gene expressed in stomach epithelium (Dai et al., 2014), and has been recognized as a tumor-suppressor gene that suppresses proliferation, migration, and invasion of gastric cancer cells. *Gkn2* is known to be expressed in extraembryonic tissues including yolk sac and spongiotrophoblast cells (Antas et al., 2014; Fahlbusch et al., 2015), which exactly matches the sites we found to be affected by knockout of the *Sfmbt2* miRNAs. The knowledge and analytical technologies for investigating miRNA are developing rapidly. Therefore, future analysis of possible targets of *Sfmbt2* miRNAs might identify another set of genes under the control of these miRNAs. In such future analysis, our knockout mice would also be a valuable tool for confirming these new miRNA-target gene interactions and the mechanisms underlying mouse placentation, especially the development of the spongiotrophoblast layer.

EXPERIMENTAL PROCEDURES

Animals

The animals were provided with water and commercial laboratory mouse chow ad libitum and housed under controlled lighting conditions (daily light from 0700 to 2100 hours). They were maintained under specific-pathogen-free conditions. All animal experiments were carried out in accordance with the approved guidelines of the RIKEN BioResource Center. All experimental protocols were approved by the Animal Care and Use Committee of the RIKEN BioResource Center.

Generation of CRISPR/Cas9 Mice

PX330 vectors were injected into the pronucleus of (C57BL/6 × DBA/2) F1 (BDF1) × C57BL/6 in-vitro-fertilized embryos, and injected embryos that had reached the two-cell stage after 24 hr in culture were transferred into the oviducts of pseudopregnant ICR female mice on day 0.5 (the day following sterile mating with a vasectomized male mouse). On day 19.5, pups were delivered by caesarean section and the live ones were nursed by lactating ICR strain female mice. Vector information is indicated in Supplemental Experimental Procedures.

REFERENCES

Antas, V.I., Brigden, K.W.L., Prudence, A.J., and Fraser, S.T. (2014). Gastrokine-2 is transiently expressed in the endodermal and endothelial cells of the maturing mouse yolk sac. Gene Expr. Patterns *16*, 69–74.

Bartel, D.P. (2004). MicroRNAs: genomics, biogenesis, mechanism, and function. Cell *116*, 281–297.

Buckberry, S., Bianco-Miotto, T., and Roberts, C.T. (2014). Imprinted and X-linked non-coding RNAs as potential regulators of human placental function. Epigenetics *9*, 81–89.

Candeloro, L., and Zorn, T.M.T. (2007). Distribution and spatiotemporal relationship of activin A and follistatin in mouse decidual and placental tissue. Am. J. Reprod. Immunol. *58*, 415–424.

Chen, D.B., and Wang, W. (2013). Human placental microRNAs and pre-eclampsia. Biol. Reprod. *88*, 130.

Dai, J., Zhang, N., Wang, J., Chen, M., and Chen, J. (2014). Gastrokine-2 is downregulated in gastric cancer and its restoration suppresses gastric tumorigenesis and cancer metastasis. Tumour Biol. *35*, 4199–4207.

Delorme-Axford, E., Donker, R.B., Mouillet, J.F., Chu, T., Bayer, A., Ouyang, Y., Wang, T., Stolz, D.B., Sarkar, S.N., Morelli, A.E., et al. (2013). Human

placental trophoblasts confer viral resistance to recipient cells. Proc. Natl. Acad. Sci. USA 110, 12048–12053.

Erlebacher, A., Price, K.A., and Glimcher, L.H. (2004). Maintenance of mouse trophoblast stem cell proliferation by TGF-beta/activin. Dev. Biol. 275, 158–169.

Fahlbusch, F.B., Ruebner, M., Huebner, H., Volkert, G., Bartunik, H., Winterfeld, I., Hartner, A., Menendez-Castro, C., Noegel, S.C., Marek, I., et al. (2015). Trophoblast expression dynamics of the tumor suppressor gene gastrokine 2. Histochem. Cell Biol. 144, 281–291.

Hemmati-Brivanlou, A., Kelly, O.G., and Melton, D.A. (1994). Follistatin, an antagonist of activin, is expressed in the Spemann organizer and displays direct neuralizing activity. Cell 77, 283–295.

Ito, M., Sferruzzi-Perri, A.N., Edwards, C.A., Adalsteinsson, B.T., Allen, S.E., Loo, T.H., Kitazawa, M., Kaneko-Ishino, T., Ishino, F., Stewart, C.L., and Ferguson-Smith, A.C. (2015). A trans-homologue interaction between reciprocally imprinted miR-127 and Rtl1 regulates placenta development. Development 142, 2425–2430.

Iwawaki, T., Akai, R., Yamanaka, S., and Kohno, K. (2009). Function of IRE1 alpha in the placenta is essential for placental development and embryonic viability. Proc. Natl. Acad. Sci. USA 106, 16657–16662.

Jonas, S., and Izaurralde, E. (2015). Towards a molecular understanding of microRNA-mediated gene silencing. Nat. Rev. Genet. 16, 421–433.

Kobayashi, Y., Banno, K., Shimizu, T., Ueki, A., Tsuji, K., Masuda, K., Kisu, I., Nomura, H., Tominaga, E., Nagano, O., et al. (2013). Gene expression profile of a newly established choriocarcinoma cell line, iC3-1, compared to existing choriocarcinoma cell lines and normal placenta. Placenta 34, 110–118.

Kuzmin, A., Han, Z., Golding, M.C., Mann, M.R.W., Latham, K.E., and Varmuza, S. (2008). The PcG gene Sfmbt2 is paternally expressed in extraembryonic tissues. Gene Expr. Patterns 8, 107–116.

Labialle, S., Marty, V., Bortolin-Cavaillé, M.-L., Hoareau-Osman, M., Pradère, J.-P., Valet, P., Martin, P.G., and Cavaillé, J. (2014). The miR-379/miR-410 cluster at the imprinted Dlk1-Dio3 domain controls neonatal metabolic adaptation. EMBO J. 33, 2216–2230.

Lehnert, S., Kapitonov, V., Thilakarathne, P.J., and Schuit, F.C. (2011). Modeling the asymmetric evolution of a mouse and rat-specific microRNA gene cluster intron 10 of the Sfmbt2 gene. BMC Genomics 12, 257.

Menheniott, T.R., Kurklu, B., and Giraud, A.S. (2013). Gastrokines: stomach-specific proteins with putative homeostatic and tumor suppressor roles. Am. J. Physiol. Gastroint. Liver Physiol. 304, G109–G121.

Miri, K., Latham, K., Panning, B., Zhong, Z., Andersen, A., and Varmuza, S. (2013). The imprinted polycomb group gene Sfmbt2 is required for trophoblast maintenance and placenta development. Development 140, 4480–4489.

Noguer-Dance, M., Abu-Amero, S., Al-Khtib, M., Lefèvre, A., Coullin, P., Moore, G.E., and Cavaillé, J. (2010). The primate-specific microRNA gene cluster (C19MC) is imprinted in the placenta. Hum. Mol. Genet. 19, 3566–3582.

Richardson, R.M., Marjoram, R.J., Barr, A.J., and Snyderman, R. (2001). RGS4 inhibits platelet-activating factor receptor phosphorylation and cellular responses. Biochemistry 40, 3583–3588.

Sato, M., Jiao, Q., Honda, T., Kurotani, R., Toyota, E., Okumura, S., Takeya, T., Minamisawa, S., Lanier, S.M., and Ishikawa, Y. (2009). Activator of G protein signaling 8 (AGS8) is required for hypoxia-induced apoptosis of cardiomyocytes: role of G betagamma and connexin 43 (CX43). J. Biol. Chem. 284, 31431–31440.

Seitz, H., Royo, H., Bortolin, M.L., Lin, S.P., Ferguson-Smith, A.C., and Cavaillé, J. (2004). A large imprinted microRNA gene cluster at the mouse Dlk1-Gtl2 domain. Genome Res. 14, 1741–1748.

Sekita, Y., Wagatsuma, H., Nakamura, K., Ono, R., Kagami, M., Wakisaka, N., Hino, T., Suzuki-Migishima, R., Kohda, T., Ogura, A., et al. (2008). Role of retrotransposon-derived imprinted gene, Rtl1, in the feto-maternal interface of mouse placenta. Nat. Genet. 40, 243–248.

Wang, Q., Chow, J., Hong, J., Smith, A.F., Moreno, C., Seaby, P., Vrana, P., Miri, K., Tak, J., Chung, E.D., et al. (2011). Recent acquisition of imprinting at the rodent Sfmbt2 locus correlates with insertion of a large block of miRNAs. BMC Genomics 12, 204.

Zheng, G.X.Y., Ravi, A., Gould, G.M., Burge, C.B., and Sharp, P.A. (2011). Genome-wide impact of a recently expanded microRNA cluster in mouse. Proc. Natl. Acad. Sci. USA 108, 15804–15809.

208

Developmental Cell

Global Landscape and Regulatory Principles of DNA Methylation Reprogramming for Germ Cell Specification by Mouse Pluripotent Stem Cells

Graphical Abstract
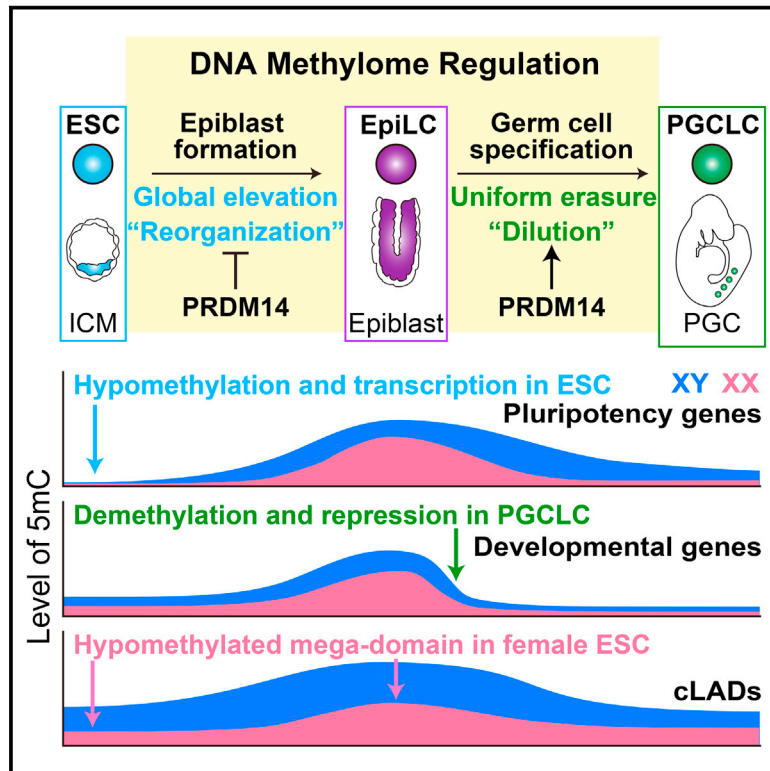
Authors

Kenjiro Shirane, Kazuki Kurimoto, Yukihiro Yabuta, ..., Katsuhiko Hayashi, Mitinori Saitou, Hiroyuki Sasaki

Correspondence

saitou@anat2.med.kyoto-u.ac.jp (M.S.), hsasaki@bioreg.kyushu-u.ac.jp (H.S.)

In Brief

DNA methylation reprogramming is important for germ cell development and embryogenesis. Shirane et al. constructed DNA methylation maps of mouse primordial germ cell (PGC)-like cells, produced from embryonic stem-cell-derived epiblast-like cells, as a model of PGC specification. These analyses suggest distinct methylation regulation in stem cells versus germ cells.

Highlights

- In vitro primordial germ cell specification from mouse ESCs models in vivo process

- PGCLC methylome is derived from progressive dilution of epiblast-like cell methylome

- PRDM14 differentially impacts the hypomethylation in ESCs and PGCLCs

- Female ESCs, but not PGCLCs, create hypomethylated lamina-associated domains

Accession Numbers

DRA003471

CrossMark

CellPress

Global Landscape and Regulatory Principles of DNA Methylation Reprogramming for Germ Cell Specification by Mouse Pluripotent Stem Cells

Kenjiro Shirane,[1,2] Kazuki Kurimoto,[3,4] Yukihiro Yabuta,[3,4] Masashi Yamaji,[3,4,10] Junko Satoh,[5] Shinji Ito,[5] Akira Watanabe,[6,7] Katsuhiko Hayashi,[3,8,9] Mitinori Saitou,[3,4,6,7,*] and Hiroyuki Sasaki[1,11,*]

[1]Division of Epigenomics and Development, Medical Institute of Bioregulation, and Epigenome Network Research Center, Kyushu University, Maidashi 3-1-1, Higashi-ku, Fukuoka 812-8582, Japan
[2]Graduate School of Medical Sciences, Kyushu University, Maidashi 3-1-1, Higashi-ku, Fukuoka 812-8582, Japan
[3]Department of Anatomy and Cell Biology, Graduate School of Medicine, Kyoto University, Yoshida-Konoe-cho, Sakyo-ku, Kyoto 606-8501, Japan
[4]JST, ERATO, Yoshida-Konoe-cho, Sakyo-ku, Kyoto 606-8501, Japan
[5]Medical Research Support Center, Graduate School of Medicine, Kyoto University, Yoshida-Konoe-cho, Sakyo-ku, Kyoto 606-8501, Japan
[6]Center for iPS Cell Research and Application, Kyoto University, 53 Kawahara-cho, Shogoin, Sakyo-ku, Kyoto 606-8507, Japan
[7]Institute for Integrated Cell-Material Sciences, Kyoto University, Yoshida-Ushinomiya-cho, Sakyo-ku, Kyoto 606-8501, Japan
[8]Department of Developmental Stem Cell Biology, Faculty of Medical Sciences, Kyushu University, Maidashi 3-1-1, Higashi-ku, Fukuoka 812-8582, Japan
[9]JST, PRESTO, Maidashi 3-1-1, Higashi-ku, Fukuoka 812-8582, Japan
[10]Present address: Howard Hughes Medical Institute, Laboratory of RNA Molecular Biology, The Rockefeller University, 1230 York Avenue, Box #186, New York, NY 10065-6399, USA
[11]Lead Contact
*Correspondence: saitou@anat2.med.kyoto-u.ac.jp (M.S.), hsasaki@bioreg.kyushu-u.ac.jp (H.S.)
http://dx.doi.org/10.1016/j.devcel.2016.08.008

SUMMARY

Specification of primordial germ cells (PGCs) activates epigenetic reprogramming for totipotency, the elucidation of which remains a fundamental challenge. Here, we uncover regulatory principles for DNA methylation reprogramming during in vitro PGC specification, in which mouse embryonic stem cells (ESCs) are induced into epiblast-like cells (EpiLCs) and then PGC-like cells (PGCLCs). While ESCs reorganize their methylome to form EpiLCs, PGCLCs essentially dilute the EpiLC methylome at constant, yet different, rates between unique sequence regions and repeats. ESCs form hypomethylated domains around pluripotency regulators for their activation, whereas PGCLCs create demethylation-sensitive domains around developmental regulators by accumulating abundant H3K27me3 for their repression. Loss of PRDM14 globally upregulates methylation and diminishes the hypomethylated domains, but it preserves demethylation-sensitive domains. Notably, female ESCs form hypomethylated lamina-associated domains, while female PGCLCs effectively reverse such states into a more normal configuration. Our findings illuminate the unique orchestration of DNA methylation and histone modification reprogramming during PGC specification.

INTRODUCTION

Epigenetic reprogramming of the developmental potency during the germline cycle is vital for ensuring a continuous generation of totipotent zygotes (Lee et al., 2014; Saitou et al., 2012; Sasaki and Matsui, 2008). Key reprogramming events that occur during specification and development of primordial germ cells (PGCs) include global DNA demethylation as well as histone modification reprogramming. Recent studies showed that, after the specification period, PGCs at embryonic day 9.5 (E9.5) or later undergo replication-coupled passive demethylation, compensated by an active mechanism acting on specific loci (Arand et al., 2015; Gkountela et al., 2015; Guo et al., 2015; Hackett et al., 2013; Kagiwada et al., 2013; Kobayashi et al., 2013; Seisenberger et al., 2012; Tang et al., 2015; Yamaguchi et al., 2013). However, questions arise as to the mechanism that directs epigenetic reprogramming during PGC specification, relationships between the changes in DNA methylation and histone modifications, differences in the epigenome regulation between PGCs, their precursors, and pluripotent stem cells, and the impact of epigenetic reprogramming on subsequent gametogenesis. Systematic exploration of such issues has been difficult, due to the limited amount of materials available from PGCs and the lack of an in vitro system that recapitulates germ cell development.

Recent studies showed that mouse epiblast-like cells (EpiLCs) induced from pluripotent stem cells (i.e., embryonic stem cells [ESCs] and induced pluripotent stem cells [iPSCs]) cultured in the presence of inhibitors of the mitogen-activated protein kinase pathway (MEKi) and the glycogen synthase kinase 3 pathway (GSK3i), known as 2i (Ying et al., 2008), can be further induced into primordial germ cell-like cells (PGCLCs), which

show robust capacity for spermatogenesis and oogenesis (Hayashi et al., 2011, 2012). This PGCLC induction system has also been demonstrated as a precise reconstitution of PGC specification by the proper reprogramming of the gene-expression profile (Hayashi et al., 2011, 2012). Accordingly, the PGCLC induction system has been exploited for identification of transcription factors involved in PGC induction (Murakami et al., 2016; Nakaki et al., 2013), clarification of signaling mechanisms for PGC specification (Aramaki et al., 2013), and, more recently, development of a PGCLC induction system in human ESCs and iPSCs, which provides a foundation for understanding and reconstituting human germ cell development in vitro (Irie et al., 2015; Sasaki et al., 2015).

Using the mouse PGCLC induction system, we recently reported large-scale histone modification reprogramming during PGC specification and a potential mechanism for this reprogramming (Kurimoto et al., 2015). Here, using the same system, we study the comprehensive picture of the dynamic DNA methylation reprogramming that occurs during PGC specification and its relationship with the histone modification reprogramming.

RESULTS

Design of the Study

At the outset, we determined the levels of unmodified cytosine (C), 5-methylcytosine (5mC), and 5-hydroxymethylcytosine (5hmC) (Kriaucionis and Heintz, 2009; Tahiliani et al., 2009) in key cell types of the mouse PGCLC induction system (male ESCs, EpiLCs, and day-6 [d6] PGCLCs [*Blimp1-mVenus*-positive cells; Hayashi et al., 2011]) by mass spectrometry (MS) and whole-genome bisulfite sequencing (WGBS) (Figure 1 and Table S1). The MS analysis revealed a rapid increase in 5mC level upon transition from ESC to EpiLC, followed by an acute decrease during PGCLC induction (Figure 1B). In contrast, the 5hmC level remained very low (1%–3% of 5mC level) in all cell types (Figure 1B). The results from the WGBS were essentially identical to those obtained by MS (Figure 1C and Table S1). Furthermore, biological replicates showed excellent reproducibility in WGBS (Figures 1C and 1D; Table S1) and, therefore, we performed more detailed WGBS data analysis in single replicates (Figure 1D and Table S1). Since the 5hmC level was negligible (Figure 1B), and since bisulfite sequencing does not distinguish 5mC from 5hmC (Hayatsu and Shiragami, 1979), we describe both modified bases as 5mC in this study. We focused on the 5mCs in CpG contexts, since CpH (where H = A, C, or T) methylation was limited in these cells (Figure 1C and Table S1) and had no known biological role in mammalian cells (Schubeler, 2015). We also analyzed the transcriptomes of all cell types by RNA sequencing (RNA-seq) (Table S2).

As a key parameter for the global DNA methylation state, we determined the average 5mC level of the total unique sequence regions (unique regions; in 2-kb windows with 1-kb overlaps). We separately determined the 5mC levels of the promoters (divided into high [HCPs], intermediate [ICPs], and low CpG density promoters [LCPs]) (Weber et al., 2007), consensus sequences of the repeat elements (long interspersed nuclear element 1 [LINE1]; intracisternal A particle [IAP]; endogenous retroviruses [ERVs] other than IAP; major and minor satellites)

(Table S3), and imprint control regions (ICRs) associated with the imprinted genes. We also determined the 5mC levels of non-promoter CpG islands (CGIs) (Illingworth et al., 2010), exons, introns, intergenic regions, cell-specific enhancers (Kurimoto et al., 2015), and evolutionarily young short interspersed nuclear elements B1 (SINE B1) (Table S3).

EpiLCs Reorganize the ESC Methylome

We first characterized the methylome of ESCs derived and cultured in 2i in comparison with that of the inner cell mass (ICM) of E3.5 blastocysts. We used an MEKi concentration of 0.4 μM instead of the original 1 μM (Ying et al., 2008), since ESCs cultured with this concentration of MEKi adhere to dishes more efficiently and serve as a more suitable source for EpiLC induction (Hayashi et al., 2011). When published data of the ICM (Wang et al., 2014) was reprocessed, low 5mC levels were evident in the unique regions (average 23%) and all three classes of promoters (Figure S1A). Published data from ESCs cultured with 1 μM MEKi (Habibi et al., 2013) revealed a global 5mC level similar to that of the ICM (21%) with smaller variations (Figures S1A and S1B). In contrast, ESCs cultured with 0.4 μM MEKi showed higher 5mC levels in the unique regions (58%) and promoters (particularly ICPs and LCPs), but not in the repeats, than those cultured with 1 μM MEKi and the ICM (Figures S1A and S1B). Notably, the 5mC distributions in the unique regions and promoters (and to a lesser extent, in the repeats) were divergent between ESCs and the ICM (Figures S1B and S1C). These findings highlight the differences between the ESC and ICM methylomes and the key role of MEKi in decreasing the global 5mC level in a dose-dependent fashion. It is notable that the repeats generally show relatively constant 5mC levels (Figure S1B).

The ESC-to-EpiLC transition resulted in an increase in 5mC level in the unique regions (from 58% to 73%) and promoters (particularly the ICPs and LCPs), but not the repeats, and consequently, EpiLCs acquired a methylome highly similar to that of the epiblast at E6.5 (70%) (Seisenberger et al., 2012) (Figures S1A–S1C and Table S1). The increase observed during this transition was not even, with the unique regions and promoters of the 10%–75% 5mC range showing a greater increase, indicating significant methylome reorganization (Figure S1B). We compared the methylome of EpiLCs with that of neural progenitor cells (NPCs) induced from ESCs (Stadler et al., 2011) and found that NPCs show higher 5mC levels in the unique regions (average 85%) and many promoters (Figures S1A and S1B; Table S1). Thus, EpiLCs had a 5mC level intermediate between ESCs and NPCs, recapitulating the state of the epiblast, which is intermediate between the ICM and somatic tissues (Wang et al., 2014). Collectively, EpiLCs recapitulate the methylome of the epiblast, which probably represents an epigenome appropriate for differentiation toward somatic lineages (higher 5mC level) as well as the germ cell lineage (lower 5mC level).

PGCLCs Progressively Dilute the EpiLC Methylome

The high similarity between the EpiLC and epiblast methylomes suggests that the EpiLC methylome would give an appropriate reference for DNA methylation changes that occur during PGCLC specification. The PGCLC induction from EpiLCs resulted in a decrease in 5mC level in essentially all genomic regions (Figures 2A, 2B, and S2A). The methylome of d2 PGCLCs
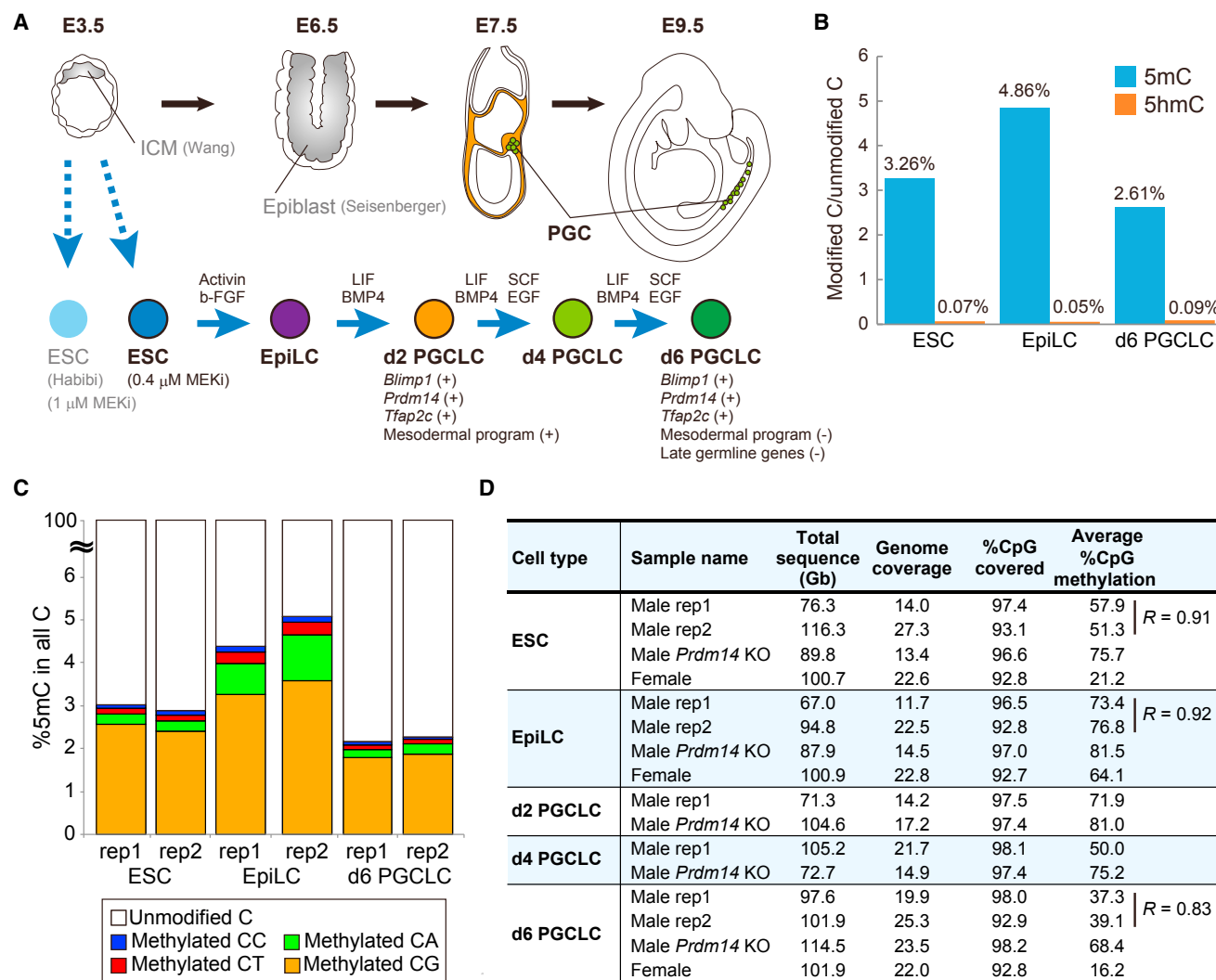
Figure 1. Design and Summary of WGBS

(A) Schematic representation of PGC specification and PGCLC induction.

(B) Levels of 5mC (blue) and 5hmC (orange) relative to unmodified C determined by MS. The average values from two independent experiments are shown.

(C) Fractions of 5mCs present in the respective dinucleotide context determined by WGBS. The results from biological replicates are shown separately. Color coding is as indicated.

(D) Summary of the WGBS.

was still similar to that of EpiLCs, but demethylation proceeded steadily during continued culture (37% in d6 PGCLCs), while still preserving the 5mC distribution pattern established in EpiLCs (Figure 2B). The rate of demethylation was greater in the unique regions and promoters than in the repeats. Consequently, d6 PGCLCs showed about half the 5mC levels of EpiLCs in the unique regions and promoters (0.46- and 0.49-fold, respectively), and a 0.78-fold level in the repeats (Figure 2B). The degree of demethylation was relatively constant in the respective categories (Figure S2B). Thus, the global demethylation that occurs upon PGCLC induction is essentially a dilution of the EpiLC methylome with different kinetics for the unique regions/promoters and repeats.

We next examined the demethylation kinetics of individual genomic elements during PGCLC induction. Similar 5mC levels

and demethylation kinetics were observed for the LCPs, exons, introns, and intergenic regions, which were essentially identical to those for the unique regions (Figures 2C and 2D). The HCPs, ICPs, non-promoter CGIs, and cell-specific enhancers had lower 5mC levels (Figures 2C and S2C) and, among them, the non-promoter CGIs and some cell-specific enhancers showed different 5mC dynamics (Figures 2D and S2C). Thus, the ESC- and EpiLC-specific enhancers, marked by histone H3 lysine-27 acetylation (H3K27ac) in the respective cell types (Kurimoto et al., 2015), showed an initial small increase and a subsequent decrease in 5mC level upon PGCLC induction. In contrast, the d2 and d6 PGCLC-specific enhancers showed demethylation kinetics similar to those of the unique regions (Figures 2C, 2D, and S2C). Among the repeats and ICRs, IAPs, LINE1s, the maternally methylated ICRs, and the major and minor satellites showed
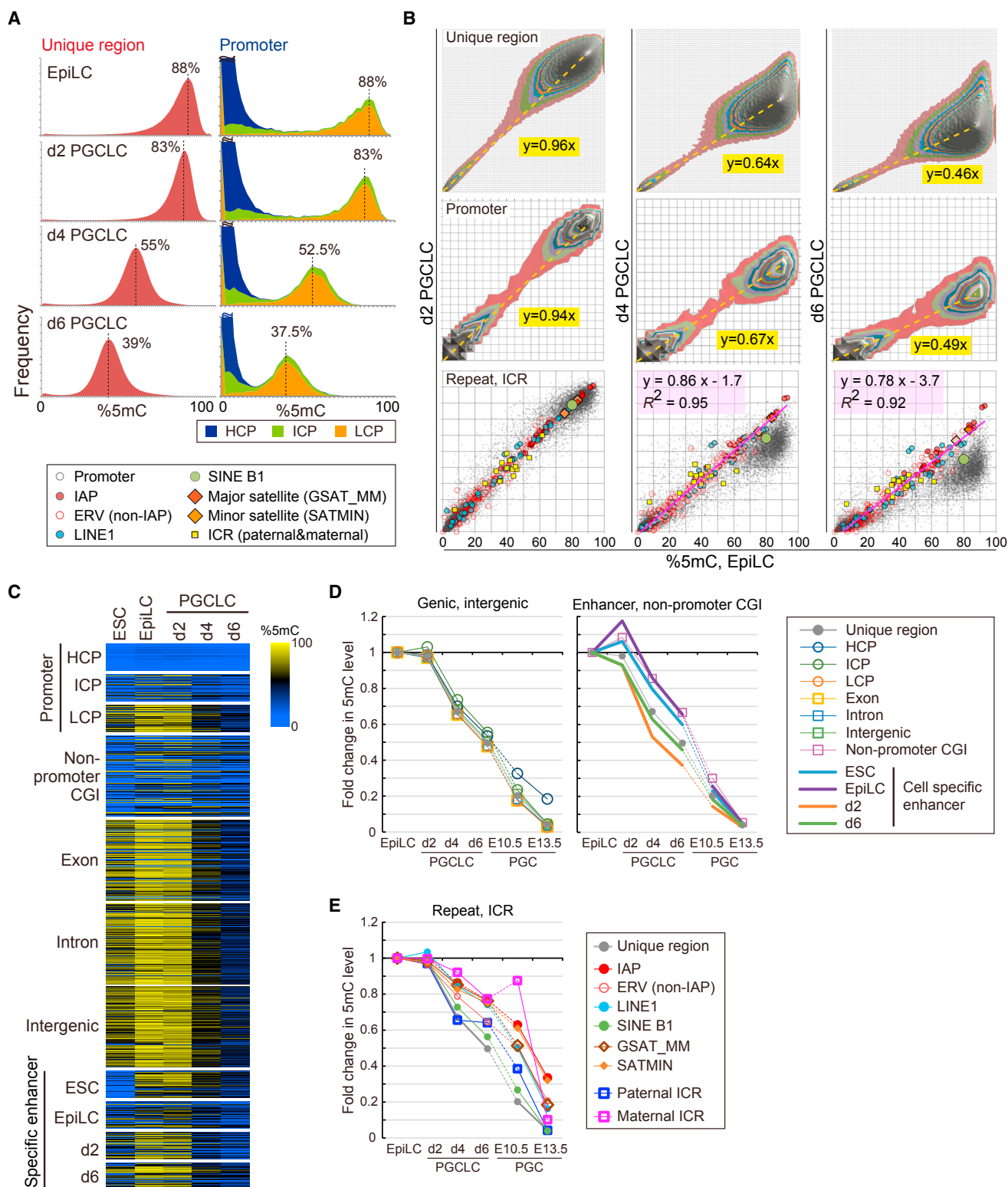
Figure 2. PGCLCs Dilute the EpiLC Methylome

(A) Histograms showing the distributions of the unique regions (2-kb windows) (left) and promoters (right) across 5mC levels in indicated cells. The mode 5mC level is indicated for the unique regions and LCPs. Color coding is as indicated.

(B) Comparisons of the 5mC levels of indicated genomic elements between indicated cells. Contour-plot (for the unique regions [2-kb windows] and promoters) (top and middle) or scatterplot representation (for the repeats and ICRs) (bottom) is used. Contour lines are drawn with an interval of 100 windows or 25 promoters.

(legend continued on next page)

slower and lesser demethylation (Figure 2E). ERVs other than IAPs and the paternally methylated ICRs showed a demethylation rate intermediate between the above repeats and unique regions (Figure 2E). Among the paternally methylated ICRs, the *H19* and *Rasgrf1* ICRs showed faster demethylation than the *Dlk1-Gtl2* ICR (Figure S2D).

Consistent with the notion that d6 PGCLCs correspond to E9.5 PGCs in vivo (Hayashi et al., 2011) and that developing PGCs have a progressively lower 5mC level, the level was lower in E10.5 and E13.5 PGCs (Kobayashi et al., 2013) than in d6 PGCLCs (Figures 2D, 2E, S2E, and S2F; Table S1). Importantly, the 5mC distribution patterns were highly similar between d6 PGCLCs and E10.5 PGCs (Figure S2F), indicating that E10.5 PGCs have a methylome corresponding to a diluted state of the d6 PGCLC methylome. These results further demonstrate the precise recapitulation of PGC specification and development by the PGCLC induction system.

ESCs and PGCLCs Show Distinct Correlations between DNA Hypomethylation, Histone Modification, and Gene Expression

Next, we wanted to correlate the changes in DNA methylation, histone modifications, and gene transcription in ESCs and PGCLCs. To this end, we identified regions (2-kb windows) showing significantly higher/lower 5mC levels in ESCs compared with EpiLCs and those showing relatively greater sensitivity/resistance to demethylation in d6 PGCLCs (Figure 3A). Such regions often formed clusters: we designated both singlet regions and clusters selected under certain criteria as domains (see Experimental Procedures). We thus identified hypo-/hypermethylated domains in ESCs and demethylation-sensitive/-resistant domains in PGCLCs (Figure 3B). There were 11 domains that were hypermethylated in ESCs but less so in EpiLCs, but these were not studied further because of the lack of associated genes.

Hypomethylated Domains in ESCs

The domains significantly hypomethylated in ESCs compared with EpiLCs (3,309 in total) occupied 2.1% of the genome and showed higher (G + C) content than the total unique regions (Figures 3C and 3D; Table S4). Upon ESC-to-EpiLC transition, the hypomethylated state of the domains became less recognizable with an increase in their 5mC level and, upon PGCLC induction, became even less so with a progressive dilution of the methylome (Figure 3E). Thus, these hypomethylated domains were specifically observed in ESCs.

The hypomethylated domains in ESCs were gene rich (Figure 3C), and 2,929 promoters (1,958 HCPs, 399 ICPs, and 572 LCPs) were located in and around these domains (Figure S3A). A gene ontology (GO) analysis revealed their association with negative/positive regulation of transcription and chromosome organization, and the gene list included key regulators of pluripotency and components of polycomb repressive complexes (PRCs) (Figure 3F). Based on our histone mark data (Kurimoto et al., 2015), these domains were depleted of H3K27 trimethylation (H3K27me3), enriched in H3K27ac, particularly in ESCs (Figure 3G), and associated with the majority of ESC-specific enhancers (972 of 1,193) (Kurimoto et al., 2015) (Figure S3B). Some of these domains coincided with superenhancer domains formed in CTCF-mediated chromatin loops (Dowen et al., 2014) (Figure S3C). Furthermore, the promoters located in and around the domains were frequently marked by H3K4me3, depleted of H3K27me3, and highly active in ESCs (Figures 3H and 3I). Thus, the hypomethylated domains represent active chromatin associated with robust transcription in ESCs.

Demethylation-Sensitive Domains in PGCLCs

The demethylation-sensitive domains in PGCLCs (91 in total) occupied 0.05% of the genome and were (G + C) rich (Figures 3C and 3D; Table S4). These domains showed faster demethylation than the rest of the genome, reaching the minimum 5mC level of 12.5% in d6 PGCLCs (Figure 3E).

The demethylation-sensitive domains in PGCLCs were gene rich (Figure 3C), and 153 promoters (103 HCPs, 40 ICPs, and 10 LCPs) were found in and around the domains (Figure S3A). These genes were often involved in pattern specification or embryonic morphogenesis (Figure 3F). Only 6.5% of these genes overlapped with those identified in and around the hypomethylated domains in ESCs (Figure S3D). To explore this point further, we examined ESCs cultured with 1.0 μM MEKi (Habibi et al., 2013) and found that, although the hypomethylated domains expanded greatly to encompass about half of all genes (Figures S3E and S3F), more than 70% of the genes found in and around the demethylation-sensitive domains in PGCLCs were still excluded (Figure S3F). Thus, the mechanism and targets of demethylation mediated by MEKi in ESCs are distinct from those observed in PGCLC development.

The demethylation-sensitive domains were marked by H3K27me3, devoid of H3K27ac in both d2 and d6 PGCLCs (Figure 3G), and identified previously as "d2 or d6 PGCLC PRC2 targets" (112 of 153) (Kurimoto et al., 2015) (Figure S3G). Consistently, the promoters of the genes identified in and around these domains were marked by H3K27me3, depleted of H3K4me3, and transcriptionally repressed in d6 PGCLCs (Figures 3H and 3I). Thus, the demethylation-sensitive domains in PGCLCs assume repressive chromatin and show no or only low transcriptional activity.

Demethylation-Resistant Domains in PGCLCs

The relatively demethylation-resistant domains in PGCLCs (340 in total) accounted for 0.1% of the genome and showed (G + C) content similar to that of the total unique regions (Figures

The background plots in the bottom panels are from the promoters (middle). A yellow dotted line connects the origin and mode. The regression line for the repeats is colored in magenta. Color coding is as indicated in the lower panel of (A).

(C) Heatmaps showing the 5mC levels of indicated genomic elements in indicated cells. One hundred promoters and enhancers of each class (Kurimoto et al., 2015) and 400 non-promoter CGIs (Illingworth et al., 2010), exons, introns, and intergenic regions (2-kb windows) are randomly selected and analyzed. Color coding is as indicated.

(D and E) Relative changes in 5mC level of indicated elements during PGCLC induction and PGC development (Kobayashi et al., 2013). The 5mC levels determined in EpiLCs are used as reference. Color coding is as indicated.

214
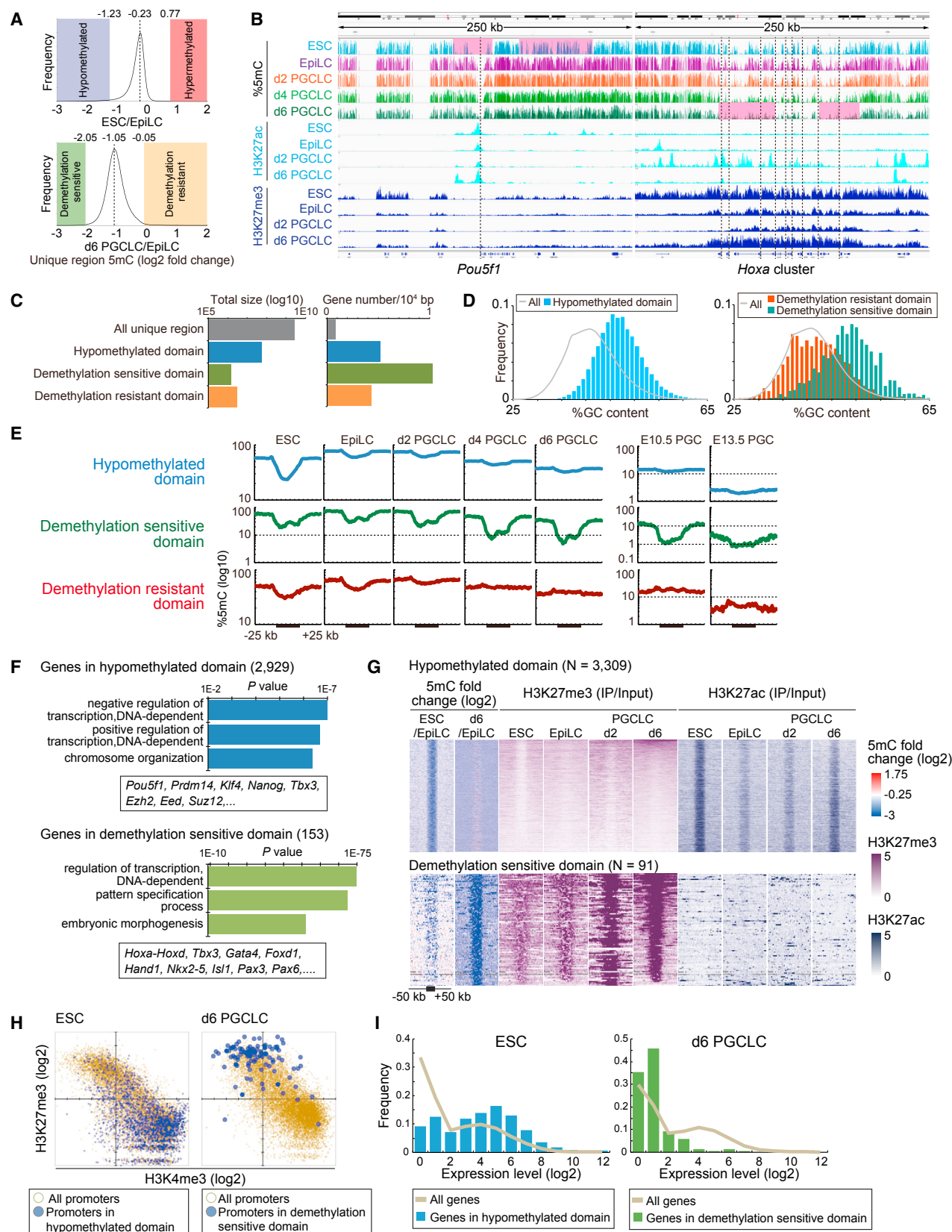
(legend on next page)

3C and 3D; Table S4). They were considerably methylated, but at slightly lower 5mC levels compared with the adjacent regions, in both ESCs and EpiLCs (Figure 3E). These domains had a highest 5mC level in d2 PGCLCs, and showed resistance to demethylation in d4 and d6 PGCLCs, maintaining the relatively high 5mC levels in d6 PGCLCs (Figure 3E). About 20% of the demethylation-resistant domains were located on the Y chromosome (Table S4).

The demethylation-resistant domains were gene rich (Figure 3C) and, based on our previous data (Kurimoto et al., 2015), marked by H3K27ac in d6 PGCLCs (Figure S3H). A total of 136 promoters (64 HCPs, 37 ICPs, and 35 LCPs) were identified in and around the domains (Figure S3A), which overlapped significantly with those identified in and around the hypomethylated domains in ESCs (95 of 136, 70%) (Figure S3D). These genes showed association with cell-cell adhesion or transcription (Figure S3I). The H3K27me3 and H3K4me3 levels and transcriptional activity of the promoters were similar to those of all promoters (Figures S3J and S3K). Thus, despite the demethylation resistance and retention of considerable levels of 5mC, these promoters showed activity in d6 PGCLCs.

Promoter and Enhancer Methylation and Transcription

We next explored the influence of promoter methylation on gene expression. More than 96% of the promoters that showed ≥20% methylation in at least one cell type were ICPs and LCPs, and the vast majority of HCPs stayed hypomethylated (<20%) (Figure 4A). Since all cell types predominantly express HCP genes (Kurimoto et al., 2015), the DNA methylation reprogramming appeared to regulate only a small set of genes during PGCLC induction.

We identified promoters showing significant hypomethylation in ESCs compared with EpiLCs (930) (there were none with significant hypermethylation in ESCs) and those showing sensitivity (179) or resistance (258) to demethylation in d6 PGCLCs (Figure 4B). We noted overlaps between the categories: 67 of the 930 hypomethylated-in-ESC promoters were demethylation sensitive and another set of 67 were demethylation resistant in d6 PGCLCs (Table S5). Figures 4C and S4A show the changes in 5mC and expression levels observed with the promoters representative of the three categories. While the hypomethylated-in-ESC promoters were enriched for genes involved in im-

mune response and showed an expected reverse correlation between the 5mC and expression levels, the demethylation-sensitive promoters were enriched for genes involved in embryonic morphogenesis and showed a less significant correlation between the 5mC and expression levels (Figures 4D and 4E). Notably, the demethylation-resistant promoters showed enrichment for genes involved in meiosis, gained methylation in d2 PGCLCs, and showed a reverse correlation between 5mC and expression (Figures 4B, 4D, and 4E). This is consistent with the notion that the germline genes are tightly regulated by DNA methylation (Seisenberger et al., 2012). While 32% of the hypomethylated-in-ESC promoters were located in the hypomethylated domains, only 12% and 10% of the demethylation-sensitive and -resistant promoters, respectively, were located within the corresponding domains in d6 PGCLCs (Figure 4F). Thus, the regulation of DNA methylation at the demethylation-resistant promoters of the meiosis-related genes appears local.
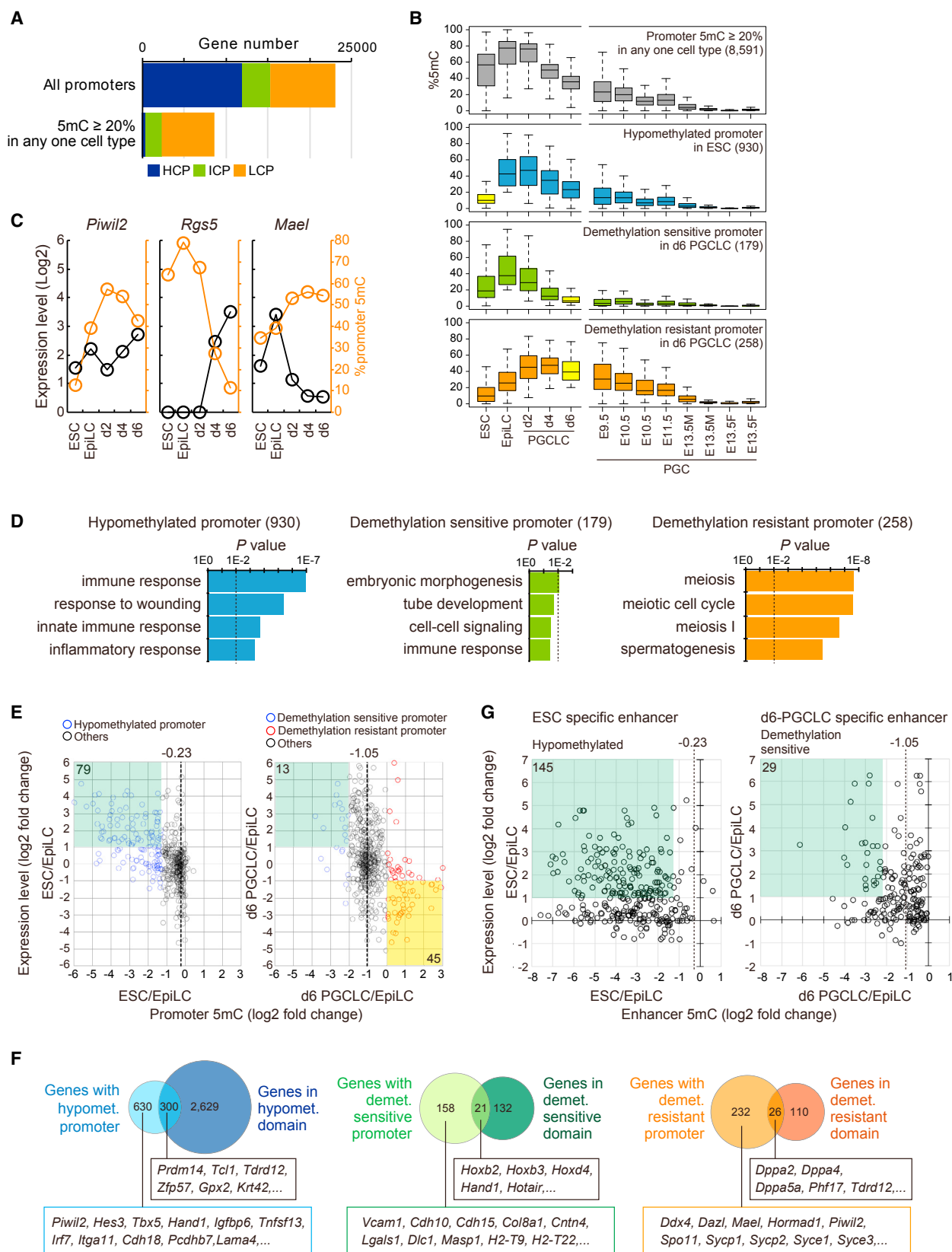
We tried to correlate the 5mC levels of the ESC- and d6-PGCLC-specific enhancers, marked by H3K27ac in the corresponding cell types (Kurimoto et al., 2015), with the expression levels of the nearby genes. While many ESC-specific enhancers showed hypomethylation in ESCs, only a few d6-PGCLC-specific enhancers were sensitive to demethylation in d6 PGCLCs (Figure 4G). Thus, promoter/enhancer hypomethylation, expression, and domain-wide hypomethylation showed a good correlation in ESCs but not in PGCLCs.

Role of PRDM14 in DNA Methylation Reprogramming

We next explored the impact of loss of PRDM14, a key regulator of naive pluripotency and PGC specification (Ma et al., 2011; Yamaji et al., 2008, 2013), on the transcriptome and methylome during PGCLC induction. It was previously shown that ablation of *Prdm14* in mice results in inefficient derivation and survival of ESCs, impaired PGC development, and infertility (Yamaji et al., 2008, 2013). Compared with wild-type cells, *Prdm14*$^{-/-}$ ESCs showed altered expression (≥2-fold) of 504 genes, but only 139 genes were affected in mutant EpiLCs (Figure 5A). The functional significance of PRDM14 became greater again upon PGCLC induction: 415 genes were affected in mutant d6 PGCLCs (Figure 5A). Only a small number of genes showed consistently higher or lower expression in both mutant ESCs

Figure 3. Distinct Correlations between DNA Hypomethylation, Histone Modifications, and Transcription in ESCs and d6 PGCLCs
(A) Histograms showing the distributions of the unique regions (2-kb windows) across 5mC fold changes in ESC and EpiLC (top) and in d6 PGCLC and EpiLC (bottom). The mode values and criteria for hypo-/hypermethylated domains in ESCs and demethylation-sensitive/-resistant domains in PGCLCs are indicated.
(B) Screenshots of the 5mC, H3K27ac, and H3K27me3 distributions in representative regions. Hypomethylated domains in ESCs (*Pou5f1*) and demethylation-sensitive domains in PGCLCs (*Hoxa*) are highlighted in pink. Positions of the transcription start sites are indicated by vertical dotted lines.
(C) Total sizes (left) and gene densities (right) of the unique regions, hypomethylated domains in ESCs, and demethylation-sensitive/-resistant domains in PGCLCs.
(D) Histograms showing the distributions of 2-kb windows from the hypomethylated domains in ESCs (left) and demethylation-sensitive/-resistant domains in PGCLCs (right) across (G + C) content. The distribution of all unique regions is shown for comparison.
(E) Aggregation plots showing the 5mC levels in and around indicated domains in indicated cells. Published data are used for PGCs (Kobayashi et al., 2013).
(F) GO term enrichment and representative genes in and around indicated domains.
(G) Heatmaps showing the 5mC fold changes and H3K27me3 and H3K27ac levels in and around the hypomethylated domains in ESCs and demethylation-sensitive domains in PGCLCs in indicated cells. Color coding is as indicated.
(H) Scatterplots showing the correlations between the H3K4me3 and H3K27me3 levels at the promoters located in and around the hypomethylated domains in ESCs (left) and demethylation-sensitive domains in d6 PGCLCs (right). The correlations at all promoters are shown for comparison.
(I) Histograms showing the distributions of the genes in and around the hypomethylated domains in ESCs (left) and demethylation-sensitive domains in d6 PGCLCs (right) across expression levels. The distribution of all genes is shown for comparison.

216

A

Gene number

B

C

Piwil2   *Rgs5*   *Mael*

Promoter 5mC ≥ 20%
in any one cell type (8,591)

Hypomethylated promoter
in ESC (930)

Demethylation sensitive promoter
in d6 PGCLC (179)

Demethylation resistant promoter
in d6 PGCLC (258)

D

Hypomethylated promoter (930)

P value

immune response
response to wounding
innate immune response
inflammatory response

Demethylation sensitive promoter (179)

P value

embryonic morphogenesis
tube development
cell-cell signaling
immune response

Demethylation resistant promoter (258)

P value

meiosis
meiotic cell cycle
meiosis I
spermatogenesis

E

○ Hypomethylated promoter
○ Others

○ Demethylation sensitive promoter
○ Demethylation resistant promoter
○ Others

G

ESC specific enhancer
Hypomethylated

d6-PGCLC specific enhancer
Demethylation sensitive

F

Genes with hypomet. promoter — Genes in hypomet. domain
630 | 300 | 2,629
Prdm14, Tcl1, Tdrd12, Zfp57, Gpx2, Krt42,...
Piwil2, Hes3, Tbx5, Hand1, Igfbp6, Tnfsf13, Irf7, Itga11, Cdh18, Pcdhb7, Lama4,...

Genes with demet. sensitive promoter — Genes in demet. sensitive domain
158 | 21 | 132
Hoxb2, Hoxb3, Hoxd4, Hand1, Hotair,...
Vcam1, Cdh10, Cdh15, Col8a1, Cntn4, Lgals1, Dlc1, Masp1, H2-T9, H2-T22,...

Genes with demet. resistant promoter — Genes in demet. resistant domain
232 | 26 | 110
Dppa2, Dppa4, Dppa5a, Phf17, Tdrd12,...
Ddx4, Dazl, Mael, Hormad1, Piwil2, Spo11, Sycp1, Sycp2, Syce1, Syce3,...

(legend on next page)

217

and d6 PGCLCs (Figure 5B), suggesting that PRDM14 regulates different sets of genes in ESCs and PGCLCs.

In *Prdm14*$^{-/-}$ PGCLCs, expression of *Tfap2c*, *Nanos3*, and *Sox2*, which are the key genes for PGC specification and potential pluripotency, was delayed (Figure 5C), suggesting that PRDM14 is important for timely induction of these genes. Consistent with the previous report (Yamaji et al., 2013), mutant ESCs derepressed *Dnmt3a*, *Dnmt3b*, and *Dnmt3l* (Figure 5C), supporting the notion that PRDM14 plays an important role in repressing de novo DNA methylation. Importantly, mutant PGCLCs failed to repress *Uhrf1*, a key regulator of maintenance methylation (Bostick et al., 2007; Sharif et al., 2007), and *Dnmt3* (Figure 5C), suggesting that PRDM14 represses these genes for global demethylation. Since the loss of *Prdm14* did not affect *Uhrf1* expression in ESCs (Figure 5C), ESCs and PGCLCs have differential requirements for PRDM14 in the regulation of maintenance methylation activity.

Consistent with the previous work on limited loci (Yamaji et al., 2013) and also with the expression profile described above, *Prdm14*$^{-/-}$ ESCs and EpiLCs showed higher global 5mC levels (76% and 82%, respectively) compared with wild-type cells (58% and 73%, respectively) (Figures 5D and S5A; Table S1). Mutant cells also showed higher 5mC levels in the promoters, particularly in the ICPs and LCPs (Figure 5D). Upon PGCLC induction, mutant cells underwent progressive, but slower and lesser demethylation. Thus, the global 5mC level was 68% in mutant d6 PGCLCs compared with 37% in wild-type cells (Figures 5D and S5A; Table S1). Since mutant PGCLCs showed a cell-cycle profile similar to that of wild-type cells (Figures S5B and S5C), the slower demethylation was not due to less frequent DNA replication. Scatterplot comparisons of the 5mC levels between mutant EpiLCs and d6 PGCLCs revealed uneven demethylation (Figure 5E), suggesting the existence of regions more/less sensitive to the mutation. Indeed, the HCPs, ICPs, non-promoter CGIs, and EpiLC- and PGCLC-specific enhancers were less sensitive to the mutation than the other elements (Figure 5F). In contrast, the repeats and ICRs were clearly sensitive and showed higher 5mC levels in mutant PGCLCs (Figures 5E and S5D), indicating that these elements require PRDM14 for demethylation in PGCLCs.

There were 3-fold fewer hypomethylated domains, with a smaller average size, in *Prdm14*$^{-/-}$ ESCs compared with wild-type cells (Figure S5E and Table S4). With an exception of genes associated with stem cell maintenance, many genes located in

and around the hypomethylated domains in wild-type ESCs were no more associated with such domains in mutant cells (Figure 5G). In contrast, the number and size of demethylation-sensitive domains were comparable between mutant and wild-type d6 PGCLCs (Figure S5E and Table S4). Thus, the same developmental genes marked by H3K27me3 (see above) were found in the demethylation-sensitive domains in both wild-type and mutant PGCLCs (Figure 5G).

## DNA Methylation Reprogramming during Female PGCLC Specification

Female ESCs have two active X chromosomes (Xa) and show extremely lower global 5mC levels than male ESCs (Habibi et al., 2013; Schulz et al., 2014; Zvetkova et al., 2005). Also, a majority of female EpiLCs maintain the XaXa pattern and, upon differentiation, undergo X chromosome inactivation. Female PGCLCs initially have one Xa and one inactive X chromosome (Xi) and gradually reactivate the Xi (Hayashi et al., 2012).

We first examined the methylomes of female ESCs, EpiLCs, and d6 PGCLCs, and found that not only ESCs but also other cell types have lower 5mC levels in the unique regions and promoters in females compared with males (Figures 6A and 6B). We then examined the transcriptomes of these cells. Female ESCs, EpiLCs, and d6 PGCLCs respectively express 341, 321, and 322 genes at higher levels (≥2-fold) and 464, 105, and 208 genes at lower levels (≤0.5-fold), compared with male counterparts (Figure 6C). Thus, the global hypomethylation affects gene expression in either direction. Only a small subset of genes consistently showed higher or lower expression in all female cells (Figure 6D). Consistent with the XaXa state, expression of X-linked genes was 1.9-fold higher in female ESCs and EpiLCs, and 1.5-fold higher in female d6 PGCLCs compared with male counterparts (Figure S6A). The key genes for PGC specification and DNA methylation/demethylation were expressed similarly in males and females during PGCLC development, except for *Tcl1* and *Dnmt3l*, which showed higher expression in female cells (Figure 6E).

Upon ESC-to-EpiLC transition, female cells drastically increased the global 5mC level (from 21% to 64%), acquiring a reorganized methylome similar to that of male cells (Figures 6A, 6F, and S6B; Table S1). Female PGCLCs then rapidly lost methylation (0.5-fold per 2 days) and reached the global 5mC level of 16% in d6 PGCLCs (Figures 6A, 6F, and S6B; Table S1), acquiring essentially a diluted version of the EpiLC

Figure 4. Promoter and Enhancer Methylation and Transcription

(A) Proportions of HCP, ICP, and LCP in all promoters and in those showing 5mC level ≥20% in at least one cell type.

(B) Box-and-whisker plots of the 5mC levels of indicated promoters during PGCLC induction and PGC development (Kobayashi et al., 2013; Seisenberger et al., 2012). M, male; F, female.

(C) Changes in promoter 5mC level (orange) and expression level (black) of *Piwil2* (a promoter hypomethylated in ESCs and demethylation-resistant in d6 PGCLCs), *Rgs5* (demethylation-sensitive), and *Mael* (demethylation-resistant) during PGCLC induction.

(D) GO term enrichment for indicated promoters.

(E) Scatterplots showing the correlations between the fold changes in 5mC and expression in ESCs and EpiLCs (left) and in d6 PGCLCs and EpiLCs (right) for indicated promoter categories. Dotted lines indicate the mode values of the 5mC fold changes in all unique regions (Figure 3A). The numbers of genes showing positive and negative correlations are indicated.

(F) Venn diagrams showing the overlaps between the genes identified by 5mC change in domains and those identified by 5mC change in promoters. Demet., demethylation; hypomet., hypomethylation.

(G) Scatterplots showing the correlations between the fold changes in 5mC and expression in ESCs and EpiLCs (left) and in d6 PGCLCs and EpiLCs (right) for indicated enhancer categories. Dotted lines indicate the mode values of the 5mC fold changes in all unique regions (Figure 3A). The numbers of genes showing expected positive correlations are indicated.

A

B

Up in *Prdm14*⁻/⁻   Down in *Prdm14*⁻/⁻

C

D

E

F

G
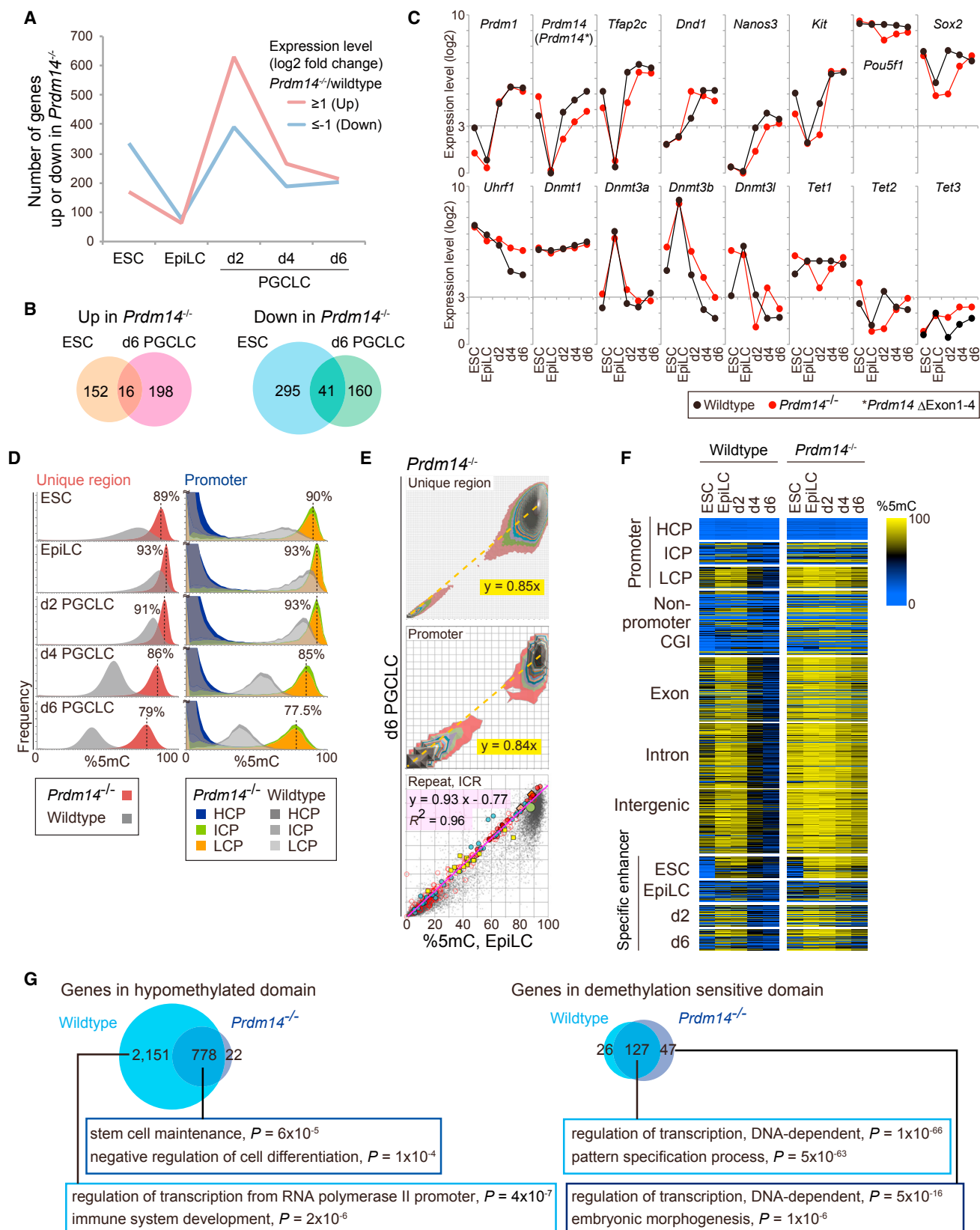
(legend on next page)

methylome (Figure 6F). Thus, female cells essentially follow the changes observed in male cells. However, severe loss of 5mC occurred in almost all ICRs in female cells: the DNA methylation imprints were lost in ESCs, not re-established in EpiLCs except for the *Rasgrf1* and *H19* ICRs, and erased further in d6 PGCLCs (Figures 6F, S6C, and S6D). In contrast, the 5mC levels of many repeats, including IAPs and satellites, were better preserved (Figure 6F). Thus, upon PGCLC induction, female cells undergo DNA methylation reprogramming under the principle similar to that of male cells, with more acute global changes and distinct impacts on specific elements.

We identified hypomethylated domains in female ESCs and demethylation-sensitive/-resistant domains in female PGCLCs (Figure S6E and Table S4). There were 4-fold more hypomethylated domains in female ESCs compared with male cells, with twice the average size of those in male cells (see next section). A large number of genes existed in and around the hypomethylated domains of female ESCs, including those found in such domains of male cells (Figure 6G). Although there were more, and larger, demethylation-resistant domains in female d6 PGCLCs compared with male cells, the demethylation-sensitive domains showed modest differences between male and female cells (Figures 6G and S6E; Table S4).

Hypomethylated Mega-Domains in Female ESCs

When we compared the 5mC levels of the unique regions between male and female ESCs in 500-kb windows, two distinct populations of genomic domains were noted. One population showed a relatively even and proportional decrease in 5mC level in female ESCs compared with male cells, while the other showed greater and uneven decreases in female cells (Figure 7A). The two populations were also distinguishable in ESCs cultured with serum or with 1 μM MEKi (Habibi et al., 2013) (Figure S7A). The domains of the latter population often existed next to each other and formed mega-domains as large as 12.5 Mb (average 1.9 Mb) (Figure S7B and Table S4). These mega-domains showed lower 5mC levels compared with the adjacent regions in female ESCs and EpiLCs, but not in their male counterparts, or in d6 PGCLCs and E13.5 PGCs of either sex (Figure 7B). Thus, female PGCLCs effectively reverse the hypomethylated states of such domains into a more normal configuration.

The hypomethylated mega-domains in female ESCs showed low (G + C) content and low gene density (Figures 7C and 7D) and overlapped significantly with constitutive lamina-associated domains (cLADs), which are marked by H3K9me2 (Guelen et al.,

2008; Peric-Hupkes et al., 2010) (Figures 7E and S7B). The promoters located in the hypomethylated mega-domains were predominantly LCPs (Figure S7C) and stayed silenced in both male and female ESCs, EpiLCs, and PGCLCs (Figure 7F). We recently reported large partially methylated domains in prospermatogonia (PSGs) and more differentiated spermatogenic cells (Kubo et al., 2015), which essentially overlap with the cLADs. As expected, the hypomethylated mega-domains overlapped well with the partially methylated domains identified in E16.5 PSGs and adult spermatozoa (Kobayashi et al., 2013; Kubo et al., 2015) (Figure S7B). Although less prominent, the hypomethylated mega-domains were also present in germinal-vesicle oocytes (Shirane et al., 2013) (Figure 7B). The methylome of female ESCs correlated relatively well with that of E16.5 PSGs, but less so with those of sperm and germinal-vesicle oocytes, which have the established methylomes (Figure S7D). These findings suggest unique methylome regulation in female ESCs, the mechanism of which might operate during the de novo methylation process in germ cell development.
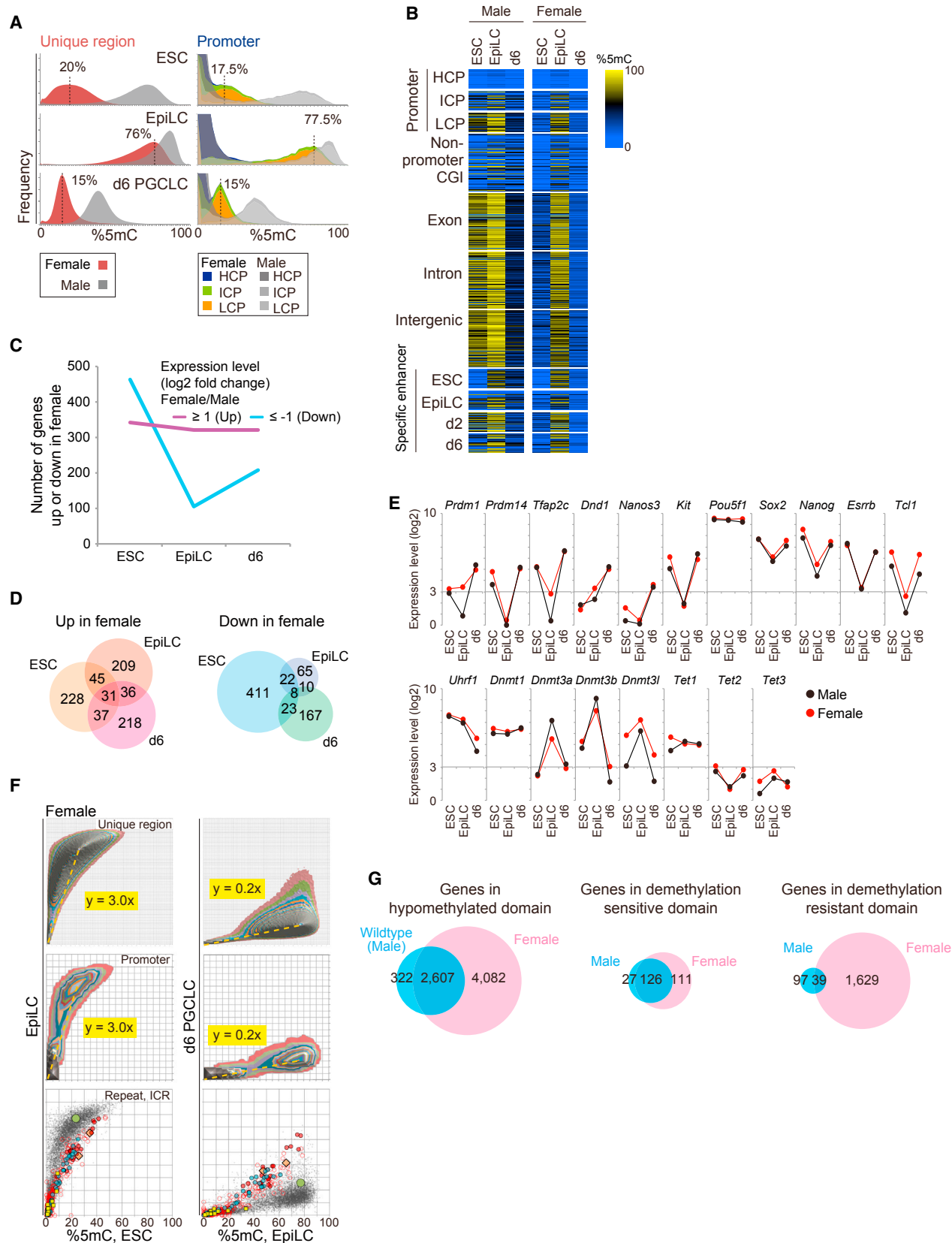
DISCUSSION

The present study uncovers the dynamic DNA methylation reprogramming at the outset of mouse germ cell development in the in vitro PGCLC induction system and, combined with our previous work (Kurimoto et al., 2015), illuminates the unique orchestration of DNA methylation and histone modification reprogramming. As summarized in Figure 7G, ESCs reorganize their methylome, especially around pluripotency regulators, by de novo DNA methylation and H3K27ac removal, to form EpiLCs. Then the PGCLCs essentially dilute the EpiLC methylome and deposit H3K27me3 around developmental regulators for their repression. PRDM14 plays an important role in these processes, especially in maintaining the hypomethylated state of pluripotency regulators in ESCs and establishing the global hypomethylation state in PGCLCs. Although female cells generally show lower methylation levels compared with male cells, the regulatory principle for DNA methylation reprogramming is essentially the same in both sexes. Interestingly, hypomethylated mega-domains exist in female ESCs and EpiLCs, overlapping with the cLADs marked by H3K9me2, but disappear upon PGCLC differentiation to form a more normal methylome (Figure 7G).

Our data suggest that the global DNA demethylation during PGCLC specification proceeds primarily via a replication-coupled passive mechanism through repression of DNA

Figure 5. Role of PRDM14 in DNA Methylation Reprogramming

(A) Numbers of genes showing higher (red) and lower expression (blue) in *Prdm14*^{−/−} cells compared with wild-type cells.

(B) Venn diagrams showing the overlaps between the genes showing higher expression in *Prdm14*^{−/−} ESCs and in d6 PGCLCs (left) and between the genes showing lower expression in the two cell types (right).

(C) Expression levels (log$_2$[FPKM + 1]) of key genes in *Prdm14*^{−/−} (red) and wild-type cells (black) during PGCLC induction. An asterisk indicates the transcripts from the mutated *Prdm14* allele (exons 1–4 deleted).

(D) Histograms showing the distributions of the unique regions (2-kb windows) (left) and promoters (right) across 5mC levels in indicated *Prdm14*^{−/−} cells. The mode 5mC levels are indicated for the unique regions and LCPs. Histograms from wild-type cells (Figure 2A) are shown for comparison. Color coding is as indicated.

(E) Comparisons of the 5mC levels of indicated genomic elements between indicated *Prdm14*^{−/−} cells. Details are as for Figure 2B.

(F) Heatmaps showing the 5mC levels of indicated genomic elements in indicated *Prdm14*^{−/−} cells. Heatmaps from wild-type cells (Figure 2C) are shown for comparison. Details are as for Figure 2C.

(G) Venn diagrams showing the overlaps between the genes identified in *Prdm14*^{−/−} and wild-type cells. The genes identified in and around the hypomethylated domains in ESCs (left) and demethylation-sensitive domains in PGCLCs (right) are separately shown. GO term enrichment is shown for indicated genes.

A

Unique region · Promoter

ESC — 20% / 17.5%

EpiLC — 76% / 77.5%

d6 PGCLC — 15% / 15%

Frequency vs %5mC

Female · Male

Female: HCP, ICP, LCP
Male: HCP, ICP, LCP

B

Male · Female

ESC EpiLC d6 · ESC EpiLC d6

%5mC 100 / 0

Promoter: HCP, ICP, LCP
Non-promoter CGI
Exon
Intron
Intergenic
Specific enhancer: ESC, EpiLC, d2, d6

C

Expression level (log2 fold change) Female/Male

≥ 1 (Up) · ≤ -1 (Down)

Number of genes up or down in female

ESC · EpiLC · d6

D

Up in female

ESC EpiLC
228 · 45 · 209
31 · 36
37 · 218
d6

Down in female

ESC EpiLC
411 · 22 · 65
8 · 10
23 · 167
d6

E

Prdm1 Prdm14 Tfap2c Dnd1 Nanos3 Kit Pou5f1 Sox2 Nanog Esrrb Tcl1

Expression level (log2)

ESC EpiLC d6

Uhrf1 Dnmt1 Dnmt3a Dnmt3b Dnmt3l Tet1 Tet2 Tet3

Expression level (log2)

Male · Female

F

Female

Unique region — y = 3.0x
Promoter — y = 3.0x
Repeat, ICR

EpiLC

d6 PGCLC — y = 0.2x
y = 0.2x

%5mC, ESC · %5mC, EpiLC

G

Genes in hypomethylated domain

Wildtype (Male) · Female
322 · 2,607 · 4,082

Genes in demethylation sensitive domain

Male · Female
27 · 126 · 111

Genes in demethylation resistant domain

Male · Female
97 · 39 · 1,629

(legend on next page)

methyltransferase (DNMT) activity (Figures 1, 2, and 5), as reported for more developed PGCs (E9.5 and later) (Arand et al., 2015; Kagiwada et al., 2013; Seisenberger et al., 2012). Consistent with this notion, mutant PGCLCs, deficient in proper repression of *Uhrf1* and *Dnmt3b*, fail to erase the EpiLC methylome (Figure 5). Together with the data showing the lack of both TET activation and 5hmC accumulation (Figures 1 and 5), our study discounts the other possible mechanism involving global 5hmC accumulation followed by dilution or active demethylation. In this regard, it is interesting that the global demethylation in ESCs cultured in 2i also occurs by a passive mechanism, involving a reduction in UHRF1 protein, but not mRNA, and global loss of H3K9me2, which is required for chromatin binding of UHRF1 (von Meyenn et al., 2016).

Interestingly, while the rate of this demethylation is 0.7-fold per 2 days in wild-type male PGCLCs (Figure 2), the cells proliferate 2-fold per 2 days (Hayashi et al., 2011). Thus, there should be a mechanism that withstands the replication-coupled halving of the 5mC level. Notably, the repeat elements generally show greater resistance against the 5mC dilution than the rest of the genome (0.86-fold per 2 days) (Figure 2). We assume that residual DNMT activity in PGCLCs would preferentially target the repeats. Interestingly, female PGCLCs show a faster demethylation rate, consistent with the replication-coupled halving (0.5-fold per 2 days) (Figure 6). Since female and male PGCLCs repress *Uhrf1* and *Dnmts* to similar extents (Figure 6), female cells may lack a mechanism for stabilizing the residual DNMT activity or for recruiting such activity to replication foci, possibly due to the upregulation of X-linked genes (Figure S6).

A previous study suggested similarities between ESCs cultured in 2i and in vivo PGCs regarding the methylome and demethylation mechanism (Ficz et al., 2013). Although both ESCs cultured in 2i and PGCLCs appear to employ a passive mechanism for global demethylation (see above), we note differential regulation of *Uhrf1* by PRDM14 between ESCs and PGCLCs (Figure 5). Moreover, we find that ESCs, but not PGCLCs, maintain pluripotency regulators in a discretely hypomethylated state (Figure 3), while PGCLCs rapidly accumulate high levels of H3K27me3 in developmental regulators for their repression (Kurimoto et al., 2015). The H3K27me3 deposition is well correlated with the rapid loss of 5mC from the demethylation-sensitive domains, which could be brought about by tight exclusion of residual DNMT activity by PRCs (Deaton and Bird, 2011). In this regard, it is notable that loss of PRDM14 leads to drastic shrinkage and even disappearance of the hypomethylated domains in ESCs but not the demethylation-sensitive domains in PGCLCs (Figure 5). Similarly, while

female ESCs have larger hypomethylated domains compared with male cells, female PGCLCs do not show changes in the demethylation-sensitive domains (Figure 6). Altogether, we find some fundamental differences between ESCs and PGCLCs regarding the methylome regulation.

We also uncover the existence of hypomethylated mega-domains in female ESCs, which broadly overlap the cLADs (Figure 7). Although the average 5mC level is higher, the hypomethylated mega-domains consistently exist as 5mC valleys in EpiLCs, E16.5 PSGs, sperm, and germinal-vesicle oocytes (Figure 7). It would be interesting to explore whether the hypomethylated mega-domains also exist in the ICM and early epiblast of female embryos (Okamoto et al., 2004). The hypomethylated mega-domains observed in female ESCs overlap very well with the partially methylated domains that we recently reported in male germ cells (Kubo et al., 2015). Notably, partially methylated domains, which primarily overlap the cLADs, also exist in cultured cells and cancers, but not in their normal in vivo counterparts (Berman et al., 2012; Hansen et al., 2011; Hon et al., 2012; Lister et al., 2009, 2011; Raddatz et al., 2012). Cells that have hypomethylated mega-domains or partially methylated domains might have similar nuclear architecture, DNMT regulation, or both, but the underlying mechanism and functional significance warrant further investigation.

In summary, our study highlights the unique regulation of the DNA methylation reprogramming during PGCLC specification and, together with our previous report on histone modification reprogramming (Kurimoto et al., 2015), provides an important resource for further mechanistic studies. Reconstitution of germ cell development beyond d6 PGCLCs will be critical for the study of many fundamental questions regarding, for example, the mechanisms of upregulation of germline genes, further maturation of the PGC epigenome, and initiation of spermatogenic and oogenic differentiation.

EXPERIMENTAL PROCEDURES

All animal experiments were performed under the ethical guidelines of Kyoto University and Kyushu University. The experimental procedures for MS, cell-cycle analyses of PGCLCs, analysis of ICRs and repeat elements, and definition of hypo-/hypermethylated domains/promoters in ESCs and demethylation-sensitive/-resistant domains/promoters in d6 PGCLCs are available in Supplemental Experimental Procedures.

Induction and Isolation of PGCLCs
ESCs were cultured in a medium containing 2iLIF (3 μM GSKi [CHIR99021], 0.4 μM MEKi [PD0325901], and 1 U/μL LIF) and induced into EpiLCs, from

Figure 6. DNA Methylation Reprogramming during Female PGCLC Induction
(A) Histograms showing the distributions of the unique regions (2-kb windows) (left) and promoters (right) across 5mC levels in indicated female cells. The mode 5mC level is indicated for the unique regions and LCPs. Histograms from male cells (Figure 2A) are shown for comparison. Color coding is as indicated.
(B) Heatmaps showing the 5mC levels of indicated genomic elements in indicated female cells. Heatmaps from male cells (Figure 2C) are shown for comparison. Details are as for Figure 2C.
(C) Numbers of genes showing higher (red) and lower (blue) expression in female cells compared with male cells.
(D) Venn diagrams showing the overlaps between the genes showing higher (left) or lower (right) expression in female ESCs, EpiLCs, and d6 PGCLCs compared with corresponding male cells.
(E) Expression levels (log2[FPKM + 1]) of key genes in female (red) and male (black) cells during PGCLC induction.
(F) Comparisons of the 5mC levels of indicated genomic elements between indicated female cells. Details are as for Figure 2B.
(G) Venn diagrams showing the overlaps between the genes identified in male and female cells. The genes identified in and around the respective domains are separately shown.
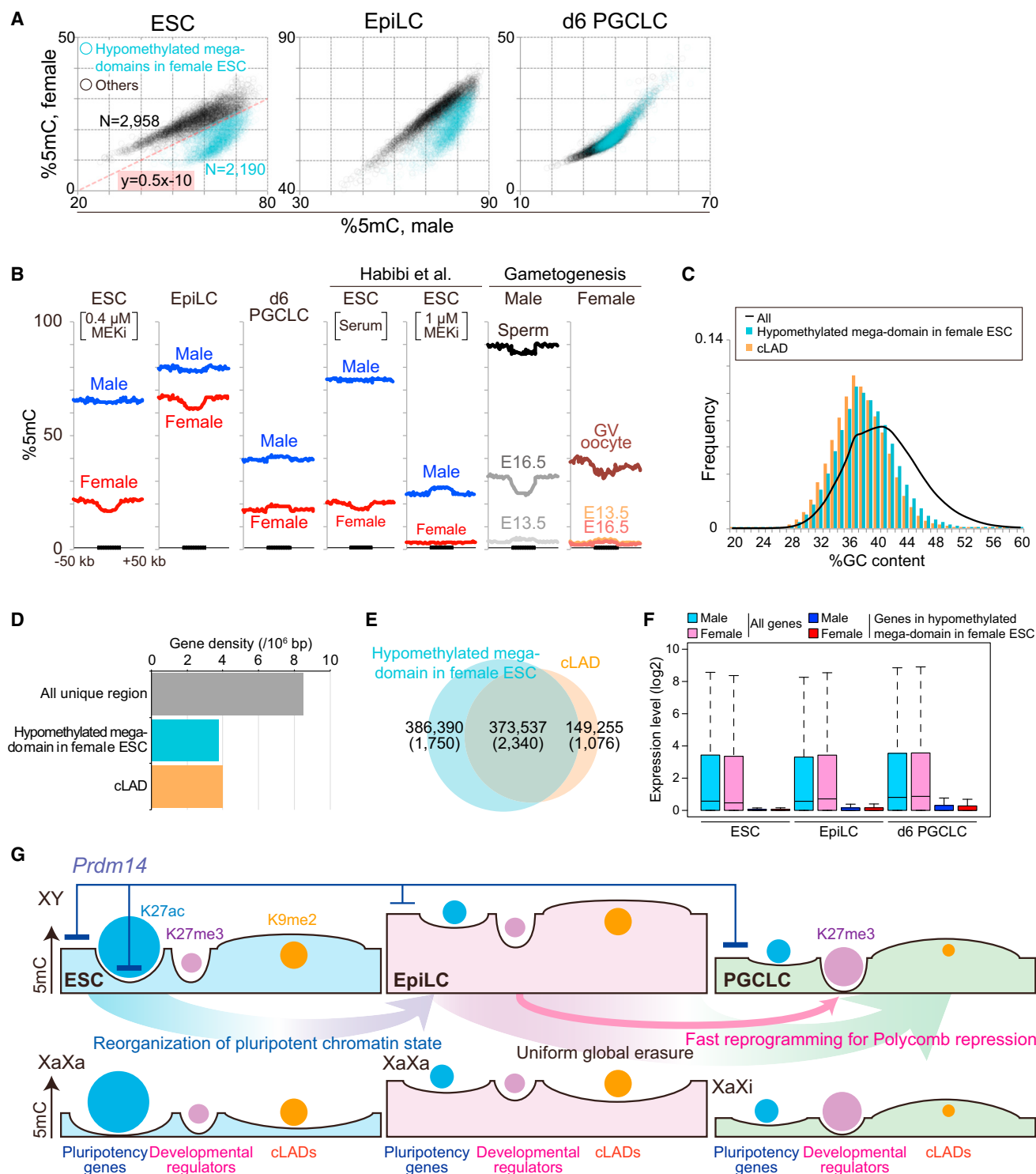
Figure 7. Hypomethylated Mega-Domains in Female ESCs

(A) Scatterplots showing the 5mC levels of the unique regions (500-kb windows) between indicated male and female cells. The hypomethylated mega-domains in female ESCs (blue dots) are defined as domains in $y < 0.5x - 10$, where x and y denote the 5mC levels in male and female ESCs, respectively.

(B) Aggregation plots showing the 5mC levels in and around the hypomethylated mega-domains in indicated male and female cells. Published data are used for ESCs cultured with serum and with 1 μM MEKi (Habibi et al., 2013), PGCs (Kobayashi et al., 2013), sperm (Kubo et al., 2015), and germinal-vesicle oocytes (Shirane et al., 2013).

(C) Histograms showing the (G + C) content of the hypomethylated mega-domains (2-kb windows), cLADs (Guelen et al., 2008; Peric-Hupkes et al., 2010), and all unique regions.

which PGCLCs were induced as described previously (Hayashi et al., 2011). PGCLCs were purified with a fluorescence-activated cell sorter using the *Blimp1-mVenus* reporter as described previously (Hayashi et al., 2011).

WGBS

Genomic DNA of 50–200 ng spiked with 0.5%–1.0% (w/w) unmethylated lambda phage DNA (Promega) was subjected to bisulfite conversion and library construction for amplification-free WGBS, using the post-bisulfite adaptor tagging method as described previously (Kobayashi et al., 2013; Miura et al., 2012; Shirane et al., 2013). Massively parallel sequencing was performed on an Illumina HiSeq 1500/2500 to generate 101-nt single-end or paired-end sequence reads. Cluster generation and sequencing were performed in single-read/paired-end mode using the TruSeq SR/PE Cluster Kit v3-cBot-HS and the TruSeq SBS Kit v3-HS (Illumina) according to the manufacturer's protocols.

Processing, Mapping, and Conversion of the Data for WGBS

For quality control of the data, we trimmed away 4 and 15 bases from the 5′ ends for single- and paired-end reads, respectively, one base at the 3′ ends, low-quality bases from the 3′ ends (quality score <20), and the adaptor sequences of the libraries, by using the TrimGalore program (http://www.bioinformatics.babraham.ac.uk/projects/trim_galore/). We mapped the processed reads to the mouse reference genome (mm10/GRCM38) using the Bismark program with the options of "-X 1000 –pbat -un" for paired-end reads and "–pbat" for single-end reads (Krueger and Andrews, 2011), and only uniquely mapped reads were used for subsequent analyses. For the paired-end data, we remapped unmapped reads as single-end for read1 with "–pbat" and read2 with default options, and the mapped reads from the single- and paired-end data were combined. The numbers of converted/unconverted CpGs in both strands were combined to determine 5mC levels. To estimate the bisulfite conversion rate, we mapped the processed reads to the lambda phage genome. The sequencing and mapping statistics are shown in Table S1. CpG sites covered by less than five reads and more than 200 reads were excluded; thus the minimum sequence depth to call 5mC level was 5.

Analysis of DNA Methylation in Unique Regions and Promoters

For the unique regions, 5mC levels were determined in 2-kb sliding windows with 1-kb overlaps. Promoters were defined as regions from 0.9 kb upstream to 0.4 kb downstream of the transcription start sites and classified into HCPs, ICPs, and LCPs depending on their (G + C) content and CpG density as described previously (Weber et al., 2007). Promoters with at least five CpG sites were used for methylation analysis. To determine fold changes in 5mC levels between different cell types, we used only unique regions (2-kb windows) and promoters fulfilling the following criteria: (1) 5mC level >20% for either cell type and (2) >0% for both cell types. This effectively excluded contributions by unique regions and promoters showing large fold changes in a low-5mC level range ($\leq$20%).

RNA-Seq

Total RNA of 75–100 ng was used for library construction for RNA-seq analysis. Libraries were prepared using a TruSeq Stranded mRNA Sample Prep Kit (Illumina) according to the manufacturer's instructions, and sequenced on HiSeq1500/2500 to generate 101-nt paired-end sequence reads as described above. After trimming of Illumina adaptor sequences and low-quality bases from the 3′ end (quality score <20) by TrimGalore, the read tags were aligned to mouse RefSeq transcripts by TopHat with the following options: "-g 1 –no-mixed –no-discordant –library-type fr-firststrand." Reads uniquely mapped to gene exons were normalized by total mapped reads and exon lengths (fragments per kilobase of exon per million mapped sequence reads [FPKM])

by the Cufflinks program (Trapnell et al., 2009). The biological replicates of RNA-seq showed good reproducibility (the correlation coefficients were 0.99 for ESCs, EpiLCs, and d6 PGCLCs). We defined genes differentially expressed between two cell types as follows: (1) $\log_2$(FPKM + 1) > 3 in at least one cell type, and (2) difference in $\log_2$(FPKM + 1) $\geq$ 1 (2-fold). The read depth corresponding to $\log_2$ (FPKM + 1) = 3 was in the range of 408–19,551 reads. The sequencing and mapping statistics are shown in Table S2.

See also Supplemental Experimental Procedures.

REFERENCES

Aramaki, S., Hayashi, K., Kurimoto, K., Ohta, H., Yabuta, Y., Iwanari, H., Mochizuki, Y., Hamakubo, T., Kato, Y., Shirahige, K., et al. (2013). A mesodermal factor, T, specifies mouse germ cell fate by directly activating germline determinants. Dev. Cell *27*, 516–529.

Arand, J., Wossidlo, M., Lepikhov, K., Peat, J.R., Reik, W., and Walter, J. (2015). Selective impairment of methylation maintenance is the major cause of DNA methylation reprogramming in the early embryo. Epigenetics Chromatin *8*, 1.

Berman, B.P., Weisenberger, D.J., Aman, J.F., Hinoue, T., Ramjan, Z., Liu, Y., Noushmehr, H., Lange, C.P., van Dijk, C.M., Tollenaar, R.A., et al. (2012). Regions of focal DNA hypermethylation and long-range hypomethylation in colorectal cancer coincide with nuclear lamina-associated domains. Nat. Genet. *44*, 40–46.

(D) Gene densities in the unique regions, hypomethylated mega-domains, and cLADs.

(E) Venn diagram showing the overlap between the hypomethylated mega-domains and cLADs. The numbers indicate the overlap in kilobases with gene number in parentheses.

(F) Box-and-whisker plots showing the expression levels of the genes in the hypomethylated mega-domains and all genes in indicated male and female cells. Color coding is as indicated.

(G) Model of the regulatory logic for the DNA methylation and histone modification reprogramming during in vitro PGC specification.

Bostick, M., Kim, J.K., Esteve, P.O., Clark, A., Pradhan, S., and Jacobsen, S.E. (2007). UHRF1 plays a role in maintaining DNA methylation in mammalian cells. Science *317*, 1760–1764.

Deaton, A.M., and Bird, A. (2011). CpG islands and the regulation of transcription. Genes Dev. *25*, 1010–1022.

Dowen, J.M., Fan, Z.P., Hnisz, D., Ren, G., Abraham, B.J., Zhang, L.N., Weintraub, A.S., Schuijers, J., Lee, T.I., Zhao, K., et al. (2014). Control of cell identity genes occurs in insulated neighborhoods in mammalian chromosomes. Cell *159*, 374–387.

Ficz, G., Hore, T.A., Santos, F., Lee, H.J., Dean, W., Arand, J., Krueger, F., Oxley, D., Paul, Y.L., Walter, J., et al. (2013). FGF signaling inhibition in ESCs drives rapid genome-wide demethylation to the epigenetic ground state of pluripotency. Cell Stem Cell *13*, 351–359.

Gkountela, S., Zhang, K.X., Shafiq, T.A., Liao, W.W., Hargan-Calvopina, J., Chen, P.Y., and Clark, A.T. (2015). DNA demethylation dynamics in the human prenatal germline. Cell *161*, 1425–1436.

Guelen, L., Pagie, L., Brasset, E., Meuleman, W., Faza, M.B., Talhout, W., Eussen, B.H., de Klein, A., Wessels, L., de Laat, W., et al. (2008). Domain organization of human chromosomes revealed by mapping of nuclear lamina interactions. Nature *453*, 948–951.

Guo, F., Yan, L., Guo, H., Li, L., Hu, B., Zhao, Y., Yong, J., Hu, Y., Wang, X., Wei, Y., et al. (2015). The transcriptome and DNA methylome landscapes of human primordial germ cells. Cell *161*, 1437–1452.

Habibi, E., Brinkman, A.B., Arand, J., Kroeze, L.I., Kerstens, H.H., Matarese, F., Lepikhov, K., Gut, M., Brun-Heath, I., Hubner, N.C., et al. (2013). Whole-genome bisulfite sequencing of two distinct interconvertible DNA methylomes of mouse embryonic stem cells. Cell Stem Cell *13*, 360–369.

Hackett, J.A., Sengupta, R., Zylicz, J.J., Murakami, K., Lee, C., Down, T.A., and Surani, M.A. (2013). Germline DNA demethylation dynamics and imprint erasure through 5-hydroxymethylcytosine. Science *339*, 448–452.

Hansen, K.D., Timp, W., Bravo, H.C., Sabunciyan, S., Langmead, B., McDonald, O.G., Wen, B., Wu, H., Liu, Y., Diep, D., et al. (2011). Increased methylation variation in epigenetic domains across cancer types. Nat. Genet. *43*, 768–775.

Hayashi, K., Ohta, H., Kurimoto, K., Aramaki, S., and Saitou, M. (2011). Reconstitution of the mouse germ cell specification pathway in culture by pluripotent stem cells. Cell *146*, 519–532.

Hayashi, K., Ogushi, S., Kurimoto, K., Shimamoto, S., Ohta, H., and Saitou, M. (2012). Offspring from oocytes derived from in vitro primordial germ cell-like cells in mice. Science *338*, 971–975.

Hayatsu, H., and Shiragami, M. (1979). Reaction of bisulfite with the 5-hydroxymethyl group in pyrimidines and in phage DNAs. Biochemistry *18*, 632–637.

Hon, G.C., Hawkins, R.D., Caballero, O.L., Lo, C., Lister, R., Pelizzola, M., Valsesia, A., Ye, Z., Kuan, S., Edsall, L.E., et al. (2012). Global DNA hypomethylation coupled to repressive chromatin domain formation and gene silencing in breast cancer. Genome Res. *22*, 246–258.

Illingworth, R.S., Gruenewald-Schneider, U., Webb, S., Kerr, A.R., James, K.D., Turner, D.J., Smith, C., Harrison, D.J., Andrews, R., and Bird, A.P. (2010). Orphan CpG islands identify numerous conserved promoters in the mammalian genome. PLoS Genet. *6*, e1001134.

Irie, N., Weinberger, L., Tang, W.W., Kobayashi, T., Viukov, S., Manor, Y.S., Dietmann, S., Hanna, J.H., and Surani, M.A. (2015). SOX17 is a critical specifier of human primordial germ cell fate. Cell *160*, 253–268.

Kagiwada, S., Kurimoto, K., Hirota, T., Yamaji, M., and Saitou, M. (2013). Replication-coupled passive DNA demethylation for the erasure of genome imprints in mice. EMBO J. *32*, 340–353.

Kobayashi, H., Sakurai, T., Miura, F., Imai, M., Mochiduki, K., Yanagisawa, E., Sakashita, A., Wakai, T., Suzuki, Y., Ito, T., et al. (2013). High-resolution DNA methylome analysis of primordial germ cells identifies gender-specific reprogramming in mice. Genome Res. *23*, 616–627.

Kriaucionis, S., and Heintz, N. (2009). The nuclear DNA base 5-hydroxymethylcytosine is present in Purkinje neurons and the brain. Science *324*, 929–930.

Krueger, F., and Andrews, S.R. (2011). Bismark: a flexible aligner and methylation caller for Bisulfite-Seq applications. Bioinformatics *27*, 1571–1572.

Kubo, N., Toh, H., Shirane, K., Shirakawa, T., Kobayashi, H., Sato, T., Sone, H., Sato, Y., Tomizawa, S., Tsurusaki, Y., et al. (2015). DNA methylation and gene expression dynamics during spermatogonial stem cell differentiation in the early postnatal mouse testis. BMC Genomics *16*, 624.

Kurimoto, K., Yabuta, Y., Hayashi, K., Ohta, H., Kiyonari, H., Mitani, T., Moritoki, Y., Kohri, K., Kimura, H., Yamamoto, T., et al. (2015). Quantitative dynamics of chromatin remodeling during germ cell specification from mouse embryonic stem cells. Cell Stem Cell *16*, 517–532.

Lee, H.J., Hore, T.A., and Reik, W. (2014). Reprogramming the methylome: erasing memory and creating diversity. Cell Stem Cell *14*, 710–719.

Lister, R., Pelizzola, M., Dowen, R.H., Hawkins, R.D., Hon, G., Tonti-Filippini, J., Nery, J.R., Lee, L., Ye, Z., Ngo, Q.M., et al. (2009). Human DNA methylomes at base resolution show widespread epigenomic differences. Nature *462*, 315–322.

Lister, R., Pelizzola, M., Kida, Y.S., Hawkins, R.D., Nery, J.R., Hon, G., Antosiewicz-Bourget, J., O'Malley, R., Castanon, R., Klugman, S., et al. (2011). Hotspots of aberrant epigenomic reprogramming in human induced pluripotent stem cells. Nature *471*, 68–73.

Ma, Z., Swigut, T., Valouev, A., Rada-Iglesias, A., and Wysocka, J. (2011). Sequence-specific regulator Prdm14 safeguards mouse ESCs from entering extraembryonic endoderm fates. Nat. Struct. Mol. Biol. *18*, 120–127.

Miura, F., Enomoto, Y., Dairiki, R., and Ito, T. (2012). Amplification-free whole-genome bisulfite sequencing by post-bisulfite adaptor tagging. Nucleic Acids Res. *40*, e136.

Murakami, K., Gunesdogan, U., Zylicz, J.J., Tang, W.W., Sengupta, R., Kobayashi, T., Kim, S., Butler, R., Dietmann, S., and Surani, M.A. (2016). NANOG alone induces germ cells in primed epiblast in vitro by activation of enhancers. Nature *529*, 403–407.

Nakaki, F., Hayashi, K., Ohta, H., Kurimoto, K., Yabuta, Y., and Saitou, M. (2013). Induction of mouse germ-cell fate by transcription factors in vitro. Nature *501*, 222–226.

Okamoto, I., Otte, A.P., Allis, C.D., Reinberg, D., and Heard, E. (2004). Epigenetic dynamics of imprinted X inactivation during early mouse development. Science *303*, 644–649.

Peric-Hupkes, D., Meuleman, W., Pagie, L., Bruggeman, S.W., Solovei, I., Brugman, W., Graf, S., Flicek, P., Kerkhoven, R.M., van Lohuizen, M., et al. (2010). Molecular maps of the reorganization of genome-nuclear lamina interactions during differentiation. Mol. Cell *38*, 603–613.

Raddatz, G., Gao, Q., Bender, S., Jaenisch, R., and Lyko, F. (2012). Dnmt3a protects active chromosome domains against cancer-associated hypomethylation. PLoS Genet. *8*, e1003146.

Saitou, M., Kagiwada, S., and Kurimoto, K. (2012). Epigenetic reprogramming in mouse pre-implantation development and primordial germ cells. Development *139*, 15–31.

Sasaki, H., and Matsui, Y. (2008). Epigenetic events in mammalian germ-cell development: reprogramming and beyond. Nat. Rev. Genet. *9*, 129–140.

Sasaki, K., Yokobayashi, S., Nakamura, T., Okamoto, I., Yabuta, Y., Kurimoto, K., Ohta, H., Moritoki, Y., Iwatani, C., Tsuchiya, H., et al. (2015). Robust in vitro induction of human germ cell fate from pluripotent stem cells. Cell Stem Cell *17*, 178–194.

Schubeler, D. (2015). Function and information content of DNA methylation. Nature *517*, 321–326.

Schulz, E.G., Meisig, J., Nakamura, T., Okamoto, I., Sieber, A., Picard, C., Borensztein, M., Saitou, M., Bluthgen, N., and Heard, E. (2014). The two active X chromosomes in female ESCs block exit from the pluripotent state by modulating the ESC signaling network. Cell Stem Cell *14*, 203–216.

Seisenberger, S., Andrews, S., Krueger, F., Arand, J., Walter, J., Santos, F., Popp, C., Thienpont, B., Dean, W., and Reik, W. (2012). The dynamics of genome-wide DNA methylation reprogramming in mouse primordial germ cells. Mol. Cell *48*, 849–862.

Sharif, J., Muto, M., Takebayashi, S., Suetake, I., Iwamatsu, A., Endo, T.A., Shinga, J., Mizutani-Koseki, Y., Toyoda, T., Okamura, K., et al. (2007). The SRA protein Np95 mediates epigenetic inheritance by recruiting Dnmt1 to methylated DNA. Nature *450*, 908–912.

225

Shirane, K., Toh, H., Kobayashi, H., Miura, F., Chiba, H., Ito, T., Kono, T., and Sasaki, H. (2013). Mouse oocyte methylomes at base resolution reveal genome-wide accumulation of non-CpG methylation and role of DNA methyl-transferases. PLoS Genet. *9*, e1003439.

Stadler, M.B., Murr, R., Burger, L., Ivanek, R., Lienert, F., Scholer, A., Wirbelauer, C., Oakeley, E.J., Gaidatzis, D., Tiwari, V.K., et al. (2011). DNA-binding factors shape the mouse methylome at distal regulatory regions. Nature *480*, 490–495.

Tahiliani, M., Koh, K.P., Shen, Y., Pastor, W.A., Bandukwala, H., Brudno, Y., Agarwal, S., Iyer, L.M., Liu, D.R., Aravind, L., et al. (2009). Conversion of 5-methylcytosine to 5-hydroxymethylcytosine in mammalian DNA by MLL partner TET1. Science *324*, 930–935.

Tang, W.W., Dietmann, S., Irie, N., Leitch, H.G., Floros, V.I., Bradshaw, C.R., Hackett, J.A., Chinnery, P.F., and Surani, M.A. (2015). A unique gene regulatory network resets the human germline epigenome for development. Cell *161*, 1453–1467.

Trapnell, C., Pachter, L., and Salzberg, S.L. (2009). TopHat: discovering splice junctions with RNA-Seq. Bioinformatics *25*, 1105–1111.

von Meyenn, F., Iurlaro, M., Habibi, E., Liu, N.Q., Salehzadeh-Yazdi, A., Santos, F., Petrini, E., Milagre, I., Yu, M., Xie, Z., et al. (2016). Impairment of DNA methylation maintenance is the main cause of global demethylation in naive embryonic stem cells. Mol. Cell *62*, 848–861.

Wang, L., Zhang, J., Duan, J., Gao, X., Zhu, W., Lu, X., Yang, L., Zhang, J., Li, G., Ci, W., et al. (2014). Programming and inheritance of parental DNA methylomes in mammals. Cell *157*, 979–991.

Weber, M., Hellmann, I., Stadler, M.B., Ramos, L., Paabo, S., Rebhan, M., and Schubeler, D. (2007). Distribution, silencing potential and evolutionary impact of promoter DNA methylation in the human genome. Nat. Genet. *39*, 457–466.

Yamaguchi, S., Shen, L., Liu, Y., Sendler, D., and Zhang, Y. (2013). Role of Tet1 in erasure of genomic imprinting. Nature *504*, 460–464.

Yamaji, M., Seki, Y., Kurimoto, K., Yabuta, Y., Yuasa, M., Shigeta, M., Yamanaka, K., Ohinata, Y., and Saitou, M. (2008). Critical function of Prdm14 for the establishment of the germ cell lineage in mice. Nat. Genet. *40*, 1016–1022.

Yamaji, M., Ueda, J., Hayashi, K., Ohta, H., Yabuta, Y., Kurimoto, K., Nakato, R., Yamada, Y., Shirahige, K., and Saitou, M. (2013). PRDM14 ensures naive pluripotency through dual regulation of signaling and epigenetic pathways in mouse embryonic stem cells. Cell Stem Cell *12*, 368–382.

Ying, Q.L., Wray, J., Nichols, J., Batlle-Morera, L., Doble, B., Woodgett, J., Cohen, P., and Smith, A. (2008). The ground state of embryonic stem cell self-renewal. Nature *453*, 519–523.

Zvetkova, I., Apedaile, A., Ramsahoye, B., Mermoud, J.E., Crompton, L.A., John, R., Feil, R., and Brockdorff, N. (2005). Global hypomethylation of the genome in XX embryonic stem cells. Nat. Genet. *37*, 1274–1279.

TECHNOLOGY REPORT

Generation of a Germ Cell-Specific Mouse Transgenic CHERRY Reporter, *Sohlh1-mCherryFlag*

Hitomi Suzuki,[1] **Christina Tenenhaus Dann,**[2] **and Aleksandar Rajkovic**[1]*

[1]Magee-Womens Research Institute, Department of Obstetrics, Gynecology, and Reproductive Sciences, University of Pittsburgh, Pittsburgh, Pennsylvania

[2]Department of Biology, Indiana University, Bloomington, Indiana

Summary: Visualization of differentiating germ cells is critical to understanding the formation of primordial follicles in the ovary, and the commitment of spermatogonial stem cells to differentiation. We engineered and generated a BAC transgenic mouse line, *Sohlh1-mCherryFlag* (*S1CF*), under the direction of the native *Sohlh1* promoter. *Sohlh1* is a germ cell-specific gene that encodes the basic helix-loop-helix (bHLH) transcriptional regulator that is essential in oogenesis and spermatogenesis. *Sohlh1* expression is unique, and is limited to perinatal and early follicle oocytes and differentiating spermatogonia. The *Sohlh1-mCherryFlag* transgene was engineered to fuse SOHLH1 to the red fluorescent protein CHERRY with 3-tandem-FLAG tags. *S1CF* animals fluoresce specifically in the oocytes of perinatal ovaries and small follicles in adult ovaries, as well as in spermatogonia, a pattern that is similar to endogenous SOHLH1. Moreover, *S1CF* rescued germ cell loss and infertility in both male and female *Sohlh1*$^{-/-}$ animals. The FLAG-tag on *S1CF* was effective for immunostaining and immunoprecipitation. The *Sohlh1-mCherryFlag* transgenic mouse provides a unique model to study early germ cell differentiation, as well as *in vivo* imaging and purification of differentiating germ cells. genesis 51:50–58, 2013. © 2012 Wiley Periodicals, Inc.

Key words: oocyte; oogenesis; spermatogonia; spermatogenesis; imaging

Live imaging is important in understanding the localization and movements of specific cell types and their responses to genetic and environmental manipulations. Fluorescent proteins engineered under the control of specific promoters are useful in the study of germ cell development. For example, *Ngn3/*EGFP transgenic mice express EGFP in spermatogonia, and time-lapse analyses have contributed significantly to our understanding of spermatogonial proliferation and renewal (Yoshida *et al.*, 2007). *Oct4-EGFP* transgenic mice have been useful in the study of PGC migration mechanisms (Molyneaux *et al.*, 2001, 2003; Runyan *et al.*, 2006; Takeuchi *et al.*, 2005). However, *Oct4* expression ceases around embryonic day (E) 16.5 in the ovary and re-establishes itself postnatally. Hence, *Oct4* is not useful in the study of perinatal events, such as the transition from germ cell cysts to primordial follicles. Promoters that drive *Gdf9* and *Zp3* expression act postnatally, and have been used to engineer *ZP3*-EGFP and *GDF9*-EGFP for various postnatal analyses such as cellular localization and functional analysis of promoter elements (Baibakov *et al.*, 2007; Hoodbhoy *et al.*, 2006; Philpott *et al.*, 1987; Yan *et al.*, 2006). *Sohlh1* expression is confined to the germ cell lineage in the mouse. Embryonic female gonads commence *Sohlh1* mRNA expression circa E15.5, at a time when most female germ cells entered meiosis, and continue to express *Sohlh1* mRNA until birth. Postnatally SOHLH1 protein is strongly expressed in oocytes where its expression is confined to the germ cell cysts and primordial follicles. In the adult ovary, SOHLH1 expression is uniquely
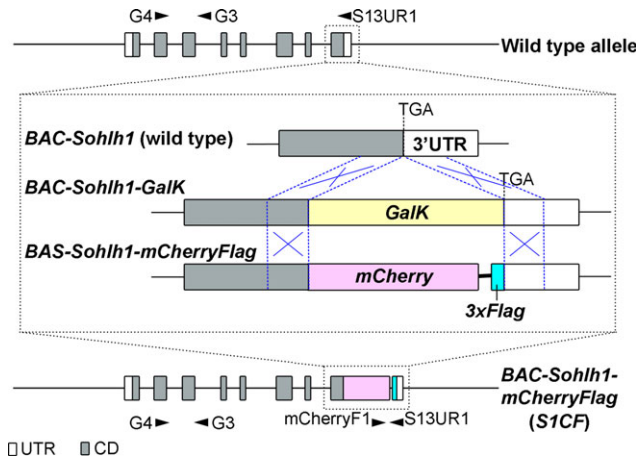
FIG. 1. *BAC-Sohlh1-mCherryFlag* engineering. The *GalK* sequence (yellow box) was first inserted just before the stop codon on the *Sohlh1* Exon 8, using a homologous recombination system in bacteria, followed by the replacement of *mCherry-3xFlag* (Magenta and turquoise boxes). Homologous regions used for recombination are indicated in blue break lines. PCR primer locations are shown with black arrowheads. Gray boxes represent the *Sohlh1* coding region (CD) and white boxes represent the untranslated region (UTR). The following primer sets were used for PCR: G4 and G3 for wild type (633 bp), mCherryF1 and S13UR1 for *S1CF* (313 bp). In matings with the *Sohlh1*$^{+/-}$, we also used HPRT2 and G3 primers previously described to detect the mutant allele (220 bp) (Pangas *et al.*, 2006).

observed in primordial and primary follicles but not in secondary or later stage ovarian follicles (Pangas *et al.*, 2006). We therefore generated a *Sohlh1* reporter mouse line that will be useful in studying perinatal female germ cells and small ovarian follicles.

We selected *Sohlh1*-containing BAC clone bMQ416B15 (129AB22 mouse strain), with 59 kb and 91 kb of 5′ and 3′-flanking sequences, respectively. This BAC clone was recombineered to produce a *BAC-Sohlh1-mCherryFlag (S1CF)* construct as previously described (Fig. 1) (Warming *et al.*, 2005). A *GalK* cassette was transiently inserted by recombineering right in front of the *Sohlh1* stop codon and then replaced by *mCherryFlag* cassette via recombineering (Fig. 1). The *S1CF* construct was designed to produce a protein fusion of SOHLH1 to CHERRY and three tandem FLAG tag repeats (S1CF protein). To study rescue of *Sohlh1*$^{-/-}$ mice by *S1CF*, we devised a PCR strategy using primers G4 and S13UR1 to distinguish *Sohlh1*$^{+/-}$/*S1CF* from *Sohlh1*$^{-/-}$/*S1CF* mice (Fig. 1). We identified five transgenic founder lines, and two of the five founder lines (*S1CF*#1 and #2) showed strong FLAG expression in the testis by Western blotting (Fig. 4e for #1 and data not shown for #2). *S1CF*#1 founder was selected for the current analysis. We observed bright CHERRY signals in *S1CF*#1 using either a dissection microscope with fluorescence filter or with confocal microscopy (Figs. 2 and 3 and data not shown).

We examined the expression pattern of CHERRY fluorescence in *S1CF* mice during female and male gonadal development. To avoid confusion with background staining of antibodies, we directly observed CHERRY signals in fixed tissues without immunostaining. In female gonads, the endogenous SOHLH1 expression was first observed circa embryonic day (E) 15.5 in a small subset of germ cells, and then expanded to all germ cells in the newborn ovary (Fig. 2a–c) (Pangas *et al.*, 2006). The expression of CHERRY in *S1CF* mice emerged by E17.5 in many germ cells (Fig. 2e,f). In postnatal ovaries, CHERRY expression was observed in primordial and primary follicles but not in secondary or later stage follicles, a pattern that was identical to endogenous SOHLH1 (Fig. 2g–i) (Pangas *et al.*, 2006). The subcellular localization of CHERRY was also similar to endogenous SOHLH1, being predominantly cytoplasmic in many oogonia and oocytes (Fig. 2c, inset of g, and f–i).

In male gonads, endogenous SOHLH1 expression commenced circa E14-15 in all germ cells, and was dramatically reduced in perinatal gonads (Fig. 3a–c,g). SOHLH1 expression resumed by postnatal day 4 in a subset of spermatogonia (Ballow *et al.*, 2006). *S1CF* CHERRY signal was observed in many male germ cells at E15.5 and mimicked endogenous SOHLH1 (Fig. 3a,b,d,e). Moreover, the CHERRY signal was cytoplasmic in location, as was the endogenous SOHLH1 protein. CHERRY signal was observed in postnatal day (PD) 1 gonocytes in which endogenous SOHLH1 was not detected (Fig. 3g,j), indicating that either CHERRY expression resumed earlier than endogenous SOHLH1; alternatively, the anti-SOHLH1 antibody may not be as sensitive at that stage. In adult testis, endogenous SOHLH1 was expressed in both undifferentiated and differentiating spermatogonia but not in GFRA1-positive spermatogonia (Suzuki *et al.*, 2012). GFRA1 marks the most primitive undifferentiated spermatogonia, including spermatogonial stem cells. CHERRY was also exclusively observed in GFRA1-negative undifferentiated spermatogonia and differentiating spermatogonia (Fig. 3h,i,k,l). Although endogenous SOHLH1 was clearly localized in the nuclei of spermatogonia, CHERRY was observed in both the cytoplasm and nuclei (inset of Fig. 3i,l) (Suzuki *et al.*, 2012).

Unexpectedly, CHERRY was not detected in all GFRA1-negative spermatogonia and early follicular stages of oocytes in *Sohlh1*$^{+/-}$/*S1CF*, cell types where endogenous SOHLH1 is usually expressed. However, when S1CF was expressed in *Sohlh1* deficient mice (*Sohlh*$^{-/-}$/*S1CF*), CHERRY expression was present in all GFRA1-negative spermatogonia and early follicular stages of oocytes (data not shown). These results suggest that the *S1CF* transgene expression maybe negatively regulated by endogenous SOHLH1.

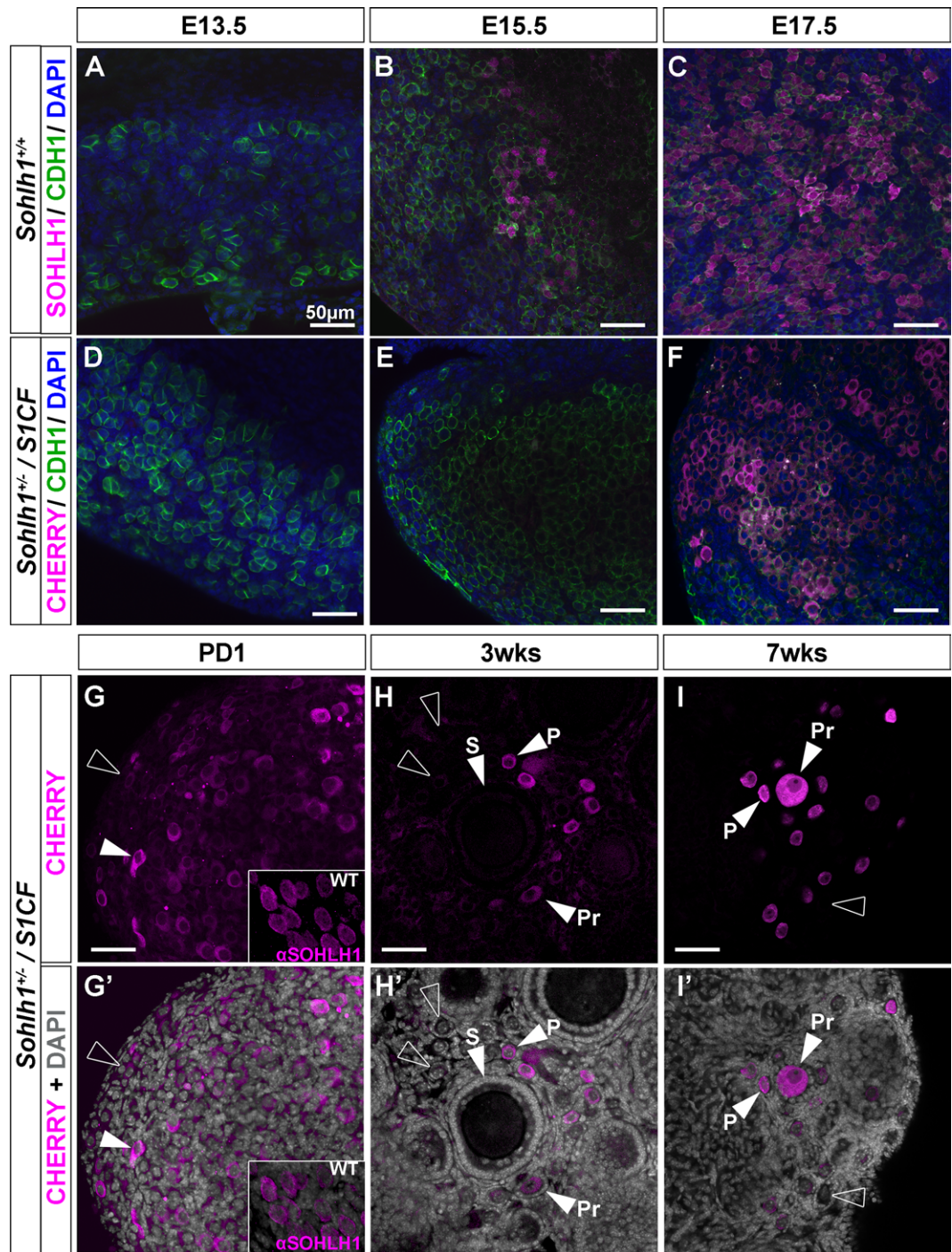We derived spermatogonial cell lines from the testes of PD21 *Sohlh1*$^{+/-}$/*S1CF* pups and nontransgenic sib-

FIG. 2. CHERRY expression mimics endogenous SOHLH1 expression in female gonads. Endogenous SOHLH1 (**a–c**) and CHERRY (**d–i**) expression in female gonads at E13.5 (a and d), E15.5 (b and e), E17.5 (c and f), postnatal 1 day (PD1; g and g′), 3-weeks old (h and h′) and 7-weeks old (i and i′). (a–f) Gonads were immunostained with anti-CDH1 (green) (a–f) and anti-SOHLH1 (magenta) (a–c), and counter stained with DAPI (blue). Native CHERRY fluorescence is shown in magenta. Genotypes are indicated. (g–i) Ovaries were counter stained with DAPI (gray in g′–i′). Native CHERRY fluorescence is shown in magenta (not immunostained). The endogenous SOHLH1 localization in wild type PD1 ovary is shown in insets of g and g′. P, primordial follicle; Pr, primary follicle; S, secondary follicle. White arrowheads indicate oocytes expressing CHERRY and open arrowheads indicate oocytes that do not express CHERRY. Scale bars represent 50 μm. Endogenous SOHLH1 expression commences between E14.5 and 15.5 in a subset of germ cells and expands to all germ cells by the time of birth. Endogenous SOHLH1 protein can be detected in germ cell cysts, primordial follicles and primary follicles but not in secondary follicles. Endogenous SOHLH1 was dominantly localized to the cytoplasm in most oocytes. CHERRY mimics endogenous SOHLH1 expression and developmental localization, however, the onset of CHERRY expression was slightly later than that of endogenous SOHLH1. We did not observe this delay when CHERRY was expressed on the background of *Sohlh1* deficient gonads, arguing that some negative regulation by endogenous SOHLH1 may exist.
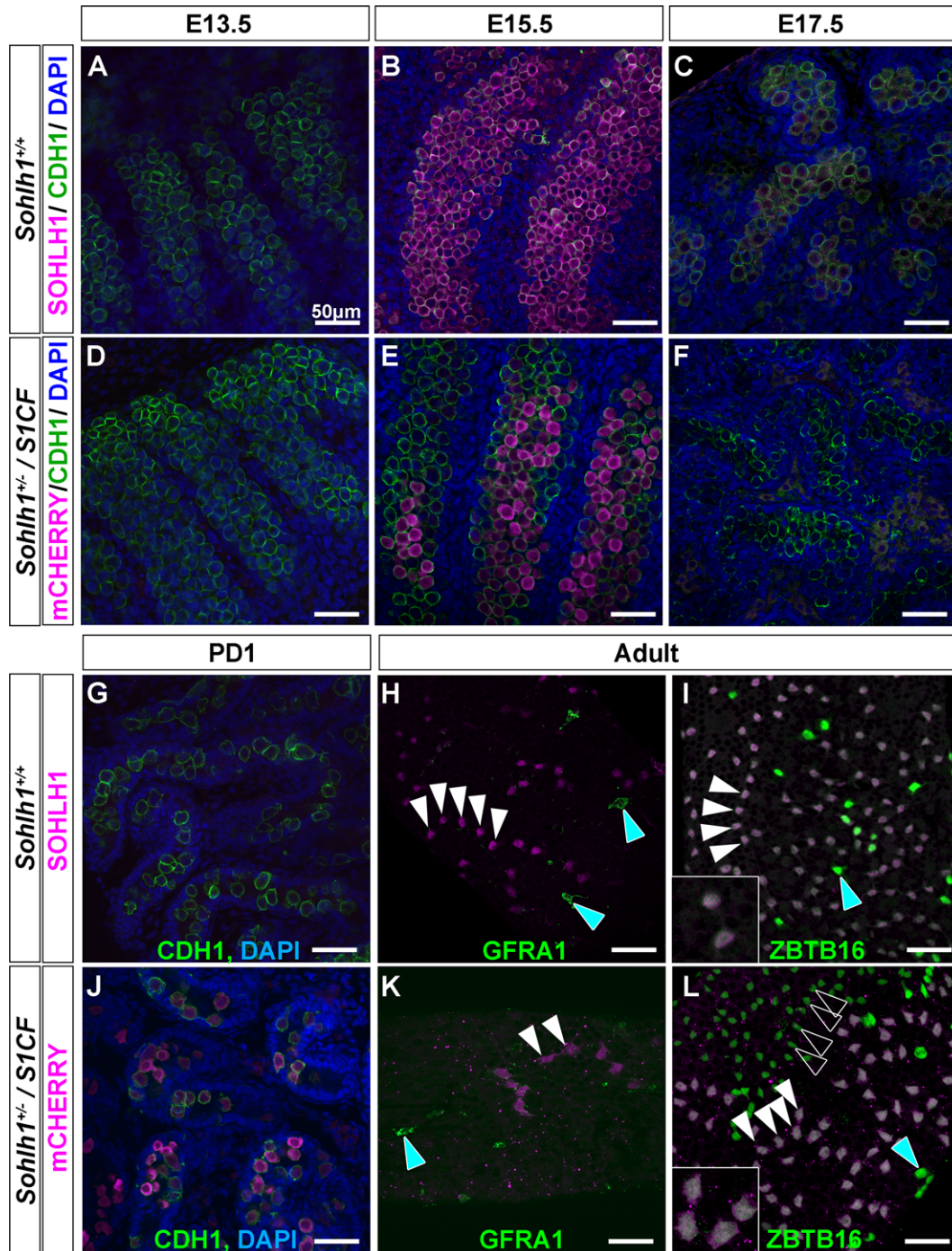
FIG. 3. CHERRY expression mimics endogenous SOHLH1 expression in male gonads. SOHLH1 (**a–c** and **g–i**) and CHERRY (**d–f** and **j–l**) expression in male gonads at E13.5 (a and d), E15.5 (b and e), E17.5 (c and f), PD1 (PD1; g and j) and 8-weeks-old adult (h, i, k, and l). Gonads were immunostained with anti-CDH1 (green) (a–g and j), anti-SOHLH1 (magenta) (d–f and g–i), anti-GFRA1 (green) (h and k) and ZBTB16 (green) (i and l), and counter stained with DAPI (blue) (a–g and j). Genotypes are indicated. CHERRY signals are shown in magenta (d–f and j–l). Cyan arrowheads indicate GFRA1-positive or ZBTB16 positive A_s undifferentiating spermatogonia that do not express SOHLH1 or CHERRY. White arrowheads indicate SOHLH1 or CHERRY positive spermatogonia. Open arrowheads indicate CHERRY negative differentiating spermatogonia that would be expected to express SOHLH1. Scale bars represent 50 μm. Endogenous SOHLH1 expression commences at around E15.5 and decreases in the perinatal testis until PD3, when SOHLH1 can be detected again in spermatogonia. Endogenous SOHLH1 protein was detected in both undifferentiated (h) and differentiating (i) sprematogonia, but was not observed in most of the GFRA1-positive undifferentiated sprematogonial population. CHERRY closely mimics this endogenous SOHLH1 expression throughout the development of male germ cells.
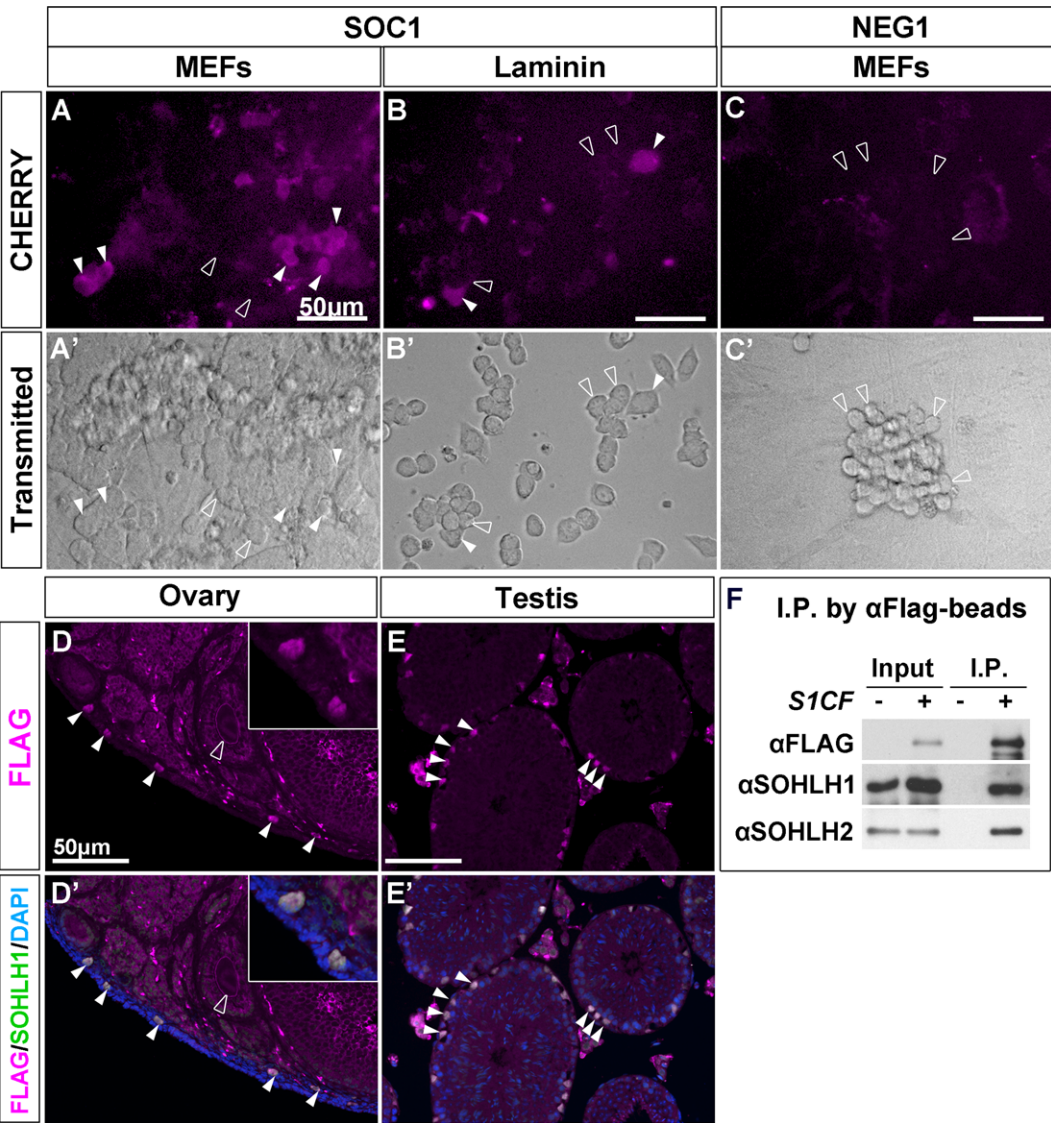
FIG. 4. *S1CF* is useful for multiple analysis. (**a–c**) Spermatogonial stem/progenitor cells derived from *Sohlh1*$^{+/-}$/*S1CF* (SOC1; a, b) or *Sohlh1*$^{+/-}$ (NEG1; c) were cultured on MEFs (a, c) or laminin (b). On MEFs the cultured cells proliferated to form large three-dimensional clusters of interconnected cells while on laminin the cultured cells exhibited a flatter morphology. CHERRY fluorescence was observed in a subset of the SOC1 spermatogonial population (a, b) but not in NEG1 (c). White arrowheads indicate spermatogonia expressing CHERRY and open arrowheads indicate spermatogonia that do not express CHERRY. Scale bars represent 50 μm. (**d** and **e**) Section immunofluorescence of adult ovary (d) and testis (e) harboring the *S1CF* transgene. Specimens were immunostained with anti-SOHLH1 (green) and anti-FLAG (magenta), and counter stained with DAPI (blue). White arrowheads indicate oocytes or spermatogonia stained with SOHLH1 and FLAG. The open arrowhead in a, a', and a" indicates an oocyte in the secondary follicle stage that expresses neither SOHLH1 nor FLAG. Scale bars represent 50 μm. (**f**) Immunoprecipitation–Western blot analyses of proteins from PD7 testes extracts of wild type and *S1CF* transgenic mice using anti-FLAG antibody conjugated beads. Each antibody used for western blot analysis is indicated at the left side of panel. Input: preimmunoprecipitation testes lysate (1%). S1CF was immunoprecipitated only from S1CF-positive lysate (I.P.). Endogenous SOHLH1 and SOHLH2 were coimmunoprecipitated with S1CF, indicating that SOHLH1 homodimerizes and heterodimerizes *in vivo* in the testis.

lings as a control ("SOC1" and "NEG1" cell lines, respectively) to examine whether the *S1CF* transgene could be utilized to visualize spermatogonial differentiation by *in vitro* live imaging. We used a method developed originally by Shinohara *et al.* (Kanatsu-Shinohara *et al.*, 2003) with which cultures can be established containing a mixture of spermatogonial stem cells and differentiating progenitor cells. Accordingly, we have previously observed that a subset of cells in such cultures expresses SOHLH1 protein (Dann *et al.*, 2008). Indeed, we observed CHERRY fluorescence in a small subset of the cultured spermatogonia in the transgenic SOC1 cells, but not in the NEG1 cells (Fig. 4a–c), consistent with the idea that the cultured cells comprise a
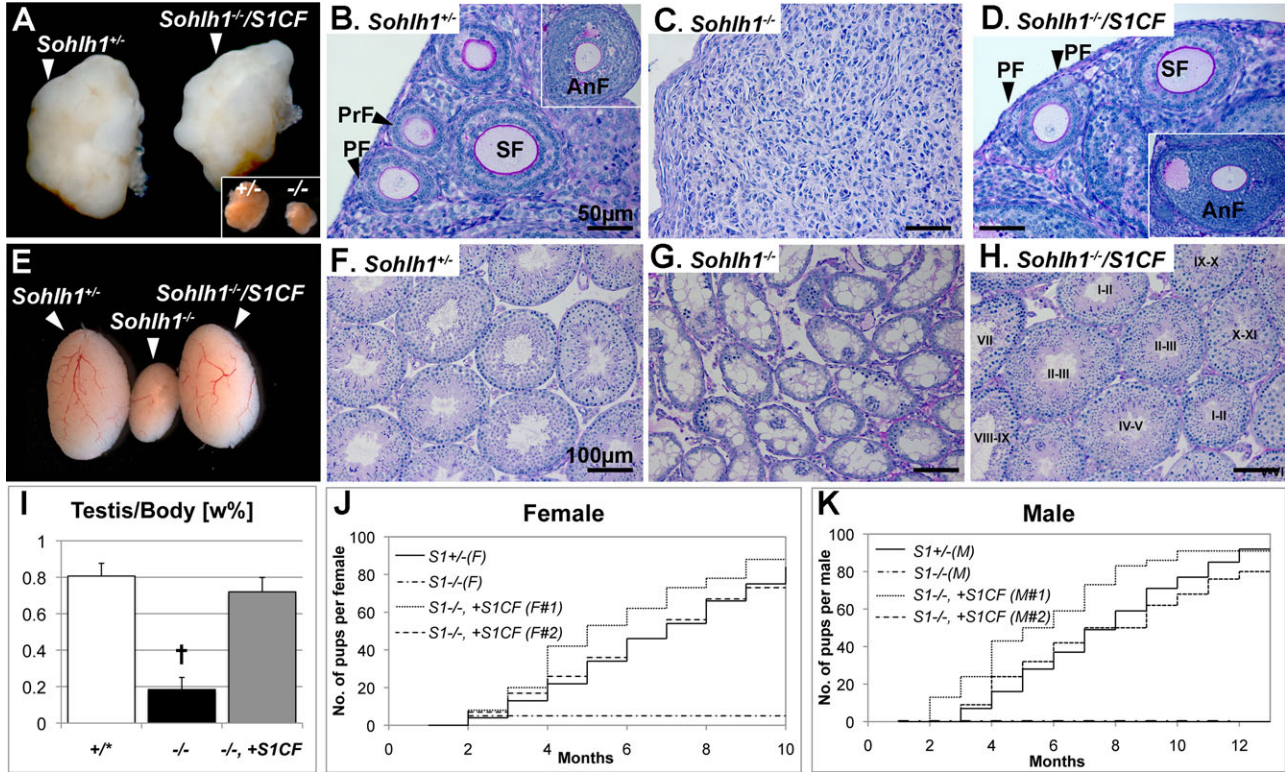
FIG. 5. *S1CF* transgene rescues the *Sohlh1*$^{-/-}$ phenotype in both males and females. *Sohlh1*$^{-/-}$/*S1CF* adult anatomy, histology, and cumulative number of pups from females (**a–d** and **j**) and males (**e–i** and **k**). (a) Ovaries shown under the same magnification for *Sohlh1*$^{+/-}$ (left), and knockout rescued by *S1CF*, *Sohlh1*$^{-/-}$/*S1CF* (right). Inset in the right lower corner shows that *Sohlh1*$^{-/-}$ ($^{-}/^{-}$) ovaries are one third the size of wild type or *Sohlh1*$^{+/-}$ ($+/^{-}$) ovaries as previously reported (Pangas *et al.*, 2006). (b–d) PAS-Hematoxylin staining of adult ovaries. Various stages of follicular development are shown, primordial (PF), primary (PrF), secondary (SF), and antral (AnF) follicles, in *Sohlh1*$^{+/-}$ (b) and *Sohlh1*$^{-/-}$/*S1CF* (d) ovaries but no follicles are visible in *Sohlh1*$^{-/-}$ at the same age (c). Scale bars represent 50 μm. (**e**) Gross testes dissected from *Sohlh1*$^{+/-}$ (left), *Sohlh1*$^{-/-}$ (middle) and *Sohlh1*$^{-/-}$/*S1CF* (right) mice. *Sohlh1*$^{-/-}$ testis size was recovered in the presence of *S1CF* and was equivalent to *Sohlh1*$^{+/-}$ testes. (**f–h**) PAS staining of adult testes. Various epithelial stages of seminiferous tubules were observed in *Sohlh1*$^{+/-}$ (f) and *Sohlh1*$^{-/-}$/*S1CF* (h) testis but not in *Sohlh1*$^{-/-}$ testes at the same age (g). Scale bars represent 100 μm. (**i**) Comparison of testes weights. *Sohlh1*$^{-/-}$ ($-/-$) testes weights recovered with *S1CF* ($-/-$, +S1CF), similarly as in *Sohlh1*$^{+/*}$ ($+/*$) (*Sohlh1*$^{+/+}$ or *Sohlh1*$^{+/-}$) ($P < 0.1$). More than three mice were examined for each genotype. Error bars show SE. Student *t* test was used to calculate *P* values. †, $P < 0.01$ against wild type. (j and **k**) Comparison of the cumulative number of pups per female (j) or male (k). Genotypes for each line are indicated in the figure. (j) *Sohlh1*$^{-/-}$ females are infertile, except for occasional, one-time litter observed among a subset of females prior to 8 weeks of age, but *Sohlh1*$^{-/-}$/*S1CF* ($n = 3$) fertility was comparable to *Sohlh1*$^{+/-}$ females. (k) *Sohlh1*$^{-/-}$ males were infertile and did not yield any pups, but *Sohlh1*$^{-/-}$/*S1CF* ($n = 8$) males fertility was comparable to *Sohlh1*$^{+/-}$ males.

heterogeneous population of undifferentiated spermatogonia with a subset of cells beginning to differentiate (Dann *et al.*, 2008). The number of cells expressing CHERRY was lower than anticipated and the low expression may have resulted from negative regulation by the endogenous SOHLH1. Nonetheless, the CHERRY expression from the S1CF transgene is expected to be a useful tool for live imaging analysis of spermatogonial differentiation for a variety of experiments.

We also examined whether the FLAG-tag is effective for immunostaining and immunoprecipitation. In paraffin sections, the anti-FLAG (M2) antibody clearly detected S1CF protein in adult oocytes and spermatogonia (Fig. 4d,e). Furthermore, the antibody immunoprecipitated S1CF from the PD7 testes lysates. The endogenous SOHLH2 protein was coimmunoprecipitated with S1CF by anti-FLAG as well as by the anti-SOHLH1 anti-

body (Suzuki *et al.*, 2012). The endogenous SOHLH1 was also co-immunoprecipitated with S1CF, indicating that SOHLH1 homodimerizes with the transgenic SOHLH1 protein *in vivo* (Fig. 4f).

Finally, we examined whether the S1CF fusion protein rescued *Sohlh1*$^{-/-}$ pathology. We crossed *Sohlh1*$^{+/-}$/*S1CF* males with *Sohlh1*$^{+/-}$ females and obtained *Sohlh1*$^{-/-}$/*S1CF* pups. Ovaries of *Sohlh1*$^{-/-}$ 7-weeks-old females were significantly smaller than wild type *Sohlh1*$^{+/-}$ ovaries due to the lack of oocytes (Fig. 5a–c) (Pangas *et al.*, 2006). *Sohlh1*$^{-/-}$/*S1CF* ovaries were comparable to *Sohlh1*$^{+/-}$ ovaries and were histologically indistinguishable from the wild type (Fig. 5a,b,d). We also tested *Sohlh1*$^{-/-}$/*S1CF* fertility by crossing adult *Sohlh1*$^{-/-}$/*S1CF* females with wild type males. The fertility of *Sohlh1*$^{-/-}$/*S1CF* females was comparable to that in *Sohlh1*$^{+/-}$ females (Fig. 5j). We

also tested the ability of the S1CF fusion protein to rescue male infertility due to *Sohlh1* deficiency. Testes of *Sohlh1*$^{-/-}$ 7-weeks-old males were significantly smaller than those of wild type or *Sohlh1*$^{+/-}$ males due to the defect in spermatogonial differentiation (Fig. 5e–g) (Ballow *et al.*, 2006). *Sohlh1*$^{-/-}$ testes were rescued in *Sohlh1*$^{-/-}$/*S1CF* males and were indistinguishable from *Sohlh1*$^{+/-}$ testes (Fig. 5e,f,h,i). *Sohlh1*$^{-/-}$/*S1CF* male fertility was comparable to *Sohlh1*$^{+/-}$ males, whereas *Sohlh1*$^{-/-}$ males without the S1CF fusion protein did not impregnate wild type females (Fig. 5k). It is also noteworthy that both *Sohlh1*$^{+/-}$/*S1CF* females and males retained normal fertility after 1 year or more (data not shown). *S1CF* homozygous animals did not display gross phenotypic abnormalities.

Our results indicate that the S1CF fusion protein, derived from the *S1CF* transgene, can support normal oogenesis and spermatogenesis. The *S1CF* transgenic line will be a useful model to study both female and male germ cell development.

MATERIAL AND METHODS

BAC-Sohlh1-mCherryFlag Construct

The BAC clone bMQ416B15 (129AB22 strain), containing a 59 kb 5′-flanking region and a 91 kb 3′-flanking region of the *Sohlh1* gene, was modified to ultimately generate a *BAC-Sohlh1-mCherryFlag* construct via recombineering as previously described (Warming *et al.*, 2005). Using pGalK as a template and Sohlh1-galK-F1 and Sohlh1-galK-R1 primers, a DNA fragment for homologous recombination was amplified by PCR using PrimeSTAR DNA HS polymerase (Takara Bio). The Sohlh1-galK-F1 primer contains a 50-bp 5′-flanking sequence of the *Sohlh1* stop codon and 20 bp of the galK homologous region including ATG. The Sohlh1-galK-R1 primer contains a 50 bp complement sequence of the 3′-flanking region of the *Sohlh1* stop codon and 20 bp of the galK complement sequence including the stop codon. Homologous recombination with this PCR fragment in the SW102 harboring BAC clone bMQ416B15 resulted in insertion of the *GalK* cassette into the *Sohlh1* COOH-terminal (*BAC-Sohlh1-GalK*). We also constructed pmCherry-3xFlag-C1 by inserting the 170-bp three-tandem-repeats of Flag (derived from pcDNA3.1-3xFlag kindly provided from A. Suzuki) into pmCherry-C1. Using pmCherry-3Flag-C1 as a template, and Sohlh1-mCherry-F1 and Sohlh1-Flag-R1 primers, a DNA fragment for a second homologous recombination was amplified by PCR using PrimeSTAR DNA HS polymerase. In the same manner as *GalK* insertion, Sohlh1-mCherry-F1 contains a 50-bp 5′-flanking sequence of the *Sohlh1* stop codon and 20 bp of the mCherry homologous region including ATG. The Sohlh1-Flag-R1 primer contains a 50 bp complement sequence of the

3′-flanking region of the *Sohlh1* stop codon and 20 bp of the galK complement sequence including stop codon. The homologous recombination with this PCR fragment in SW102 harboring *BAC-Sohlh1-GalK* resulted in insertion of *mCherry-3xFlag* into the *Sohlh1* c-terminal (*BAC-Sohlh1-mCherryFlag*). The following primer sequences were used: Sohlh1-galK-F1 (3′-GCCTGGCCCT GAAGGATGAA GCGGACAGCA TCTTCCCTGA CTTTTTCCCC CCTGTTGACA ATTAATCATC GGCA −5′), Sohlh1-galK-R1 (3′- CCAGGCACAG GACAGCTCCC CAGCAAACTA AACTCTGGGG GACTCAGCTA TCAG-CACTGT CCTGCTCCTT −5′), Sohlh1-mCherry-F1 (3′-GCCTGGCCCT GAAGGATGAA GCGGACAGCA TCTT-CCCTGA CTTTTTCCCC ATGGTGAGCA AGGGCGAGGA −5′) and Sohlh1-Flag-R1 (3′- AGCCCAAAAT ACAA-CACCCA GGCACAGGAC AGCTCCCCAG CAAACTAAAC TCTGGGGGAC TCAGCTATCA GTCATCGTCA TCCTT GTAAT −5′). Both PCR products were ∼1 kb.

Generation *of BAC-Sohlh1-mCherryFlag* Transgenic Mice and Animal Care

Following linearization by restriction enzyme pIsce-I (New England Biolabs), the DNA without vector sequences was gel purified using CHEF-DR II pulsed field electrophoresis systems (Bio-Rad). Purified DNA was microinjected into B6SJLF1/J oocytes at the transgenic and molecular core in Magee-Women's Research Institute. The *Sohlh1* mutant mouse was generated as previously described (Pangas *et al.*, 2006). All experimental and surgical procedures were in compliance with the Guide for the Care and Use of Laboratory Animals and were approved by the University of Pittsburgh IACUC. The *BAC-Sohlh1-mCherryFlag* transgenics will be available upon request to the research community.

Genotyping

Tail DNA was prepared in two ways, depending upon primer sets. For detection of *Sohlh1* wild type (primer G4 and G3, 633bp), targeted allele (primer HPRT2 and G3, 220bp) and *BAC-Sohlh1-mCherryFlag* (primer mCherryF1 and S13UR1, 313bp), tails were digested for 1 h at 100°C in 50 mM NaOH followed by neutralization with Tris-HCl (pH 8.0, 1M). PCR reactions were performed in 10 µl volumes containing 1-µl tail DNA, 5-µl amfiSure PCR Master Mix (GenDEPOT), 0.25-µl each of forward and reverse primers (10 µM), and 3.5 µl dH$_2$O. The PCR conditions were 95°C 4 min; (95°C 30 s, 60°C 30 s, 72°C 30 s) × 33 cycles; 72°C 5 min. For distinguishing *Sohlh1*$^{+/-}$/*S1CF* and *Sohlh*$^-$*1*$^{-/-}$/*S1CF* (primer G4 and S13UR1, 3.7 kb for wild type allele and 4.5 kb for *S1CF*), tail DNA was purified using a Gentra Puregene Kit (Qiagen). PCR reactions were performed in 20 µl volumes containing 25 ng of tail DNA, 4 µl 5× PrimeSTAR buffer (Takara Bio), 1.6 µl 25 mM dNTP, 0.5 µl each of forward and reverse primers (10 µM), 0.2 µl Pri-

meSTAR HS DNA Polymerase (Takara Bio) and 12.2 μl dH$_2$O. The PCR conditions were 98°C 3 min; (98°C 10 s, 60°C 5 s, 72°C 5 min) × 33 cycles; 72°C 5 min. The following primer sequences were used: G3 (3′-CTGGAGCC-CAAGAAGACAAG-5′), G4 (3′-GTCTTCGGAGAAACG TGGTC-5′), HPRT2, (3′-GCAGTGTTGGCTGTATTTTCC-5′), mCherry-F1 (3′-CACCATCGTGGAACAGTACG-5′) and S13UR1 (3′-GCCCTGCCAGGCTCCCTCAA-5′).

Immunofluorescence and Histology

For all fluorescence analyses, CHERRY was not immunostained with antibody and the original CHERRY signal was observed using confocal laser microscopy; Nikon A1 (Nikon). Male and female gonads were fixed in 4%PFA at 4°C overnight, protected from light. Postnatal ovaries were washed three times in PBS containing 0.1% TritonX-100 (0.1%PBS-Tr) for 5 min each and incubated with DAPI (PBS containing 0.2 μg ml^{-1} DAPI and 50 μg ml^{-1} RNase) at RT for 2 h. Ovaries were then washed three times in 0.1%PBS-Tr and mounted with ProLong Gold Antifade Reagent (Invitrogen) on a glass slide. Both 3-week-old and adult ovaries were sliced by scalpel before being mounted. Embryonic gonads and postnatal testis were also washed three times in 0.1%PBS-Tr. After 1.5 h of blocking with 3%BSA/0.1%PBS-Tr at RT, the tissues were incubated overnight at 4°C with primary antibodies in PBS containing 0.01% TritonX-100 (0.01% PBS-Tr). The following day, the tissues were washed six times in 0.01% PBS-Tr for 15 min each and then incubated with secondary antibodies and DAPI for 2 h at RT. Next, the tissues were again washed six times and mounted with ProLong Gold Antifade Reagent (Invitrogen) on a glass slide.

Ovaries and testes were fixed in 4%PFA at 4°C overnight and embedded in paraffin for sectioning. About 5-μm paraffin sections were deparafinized and hydrated, and incubated with primary antibodies in 0.1% PBS-Tr at 4°C overnight. Specimens were then washed three times in 0.1% PBS-Tr for 5 min each followed by incubation with secondary antibodies and DAPI at RT for 2 h. After washing three times, specimens were mounted with ProLong Gold Antifade Reagent. For histology, sections were stained by Periodic Acid Schiff-Hematoxylin (PAS-H) after hydration and mounted with Cytoseal 60 (Thermo scientific).

Primary antibodies were used at the following dilutions: goat anti-E-Cadherin/CDH1 (R&D systems, AF748) 1:500, goat anti-GFRα1 (R&D systems, AF560) 1:50, rabbit anti-Plzf/ZBTB16 (Santa Cruz, H-300, sc-22839) 1:500, armenian hamster anti-KIT (Yamatani et al., 2004) 1:500, rabbit anti-SOHLH1 (Pangas et al., 2006) 1:500 and mouse anti-FLAG (M2) (Sigma) 1:200. The following secondary antibodies were purchased from Jackson ImmunoResearch Laboratories and were used at a 1:500 dilution: Dylight 594 or 649 donkey anti-goat, 488, 594, or 649 donkey anti-rabbit, 594 goat anti-armenian hamster and 488 donkey anti-mouse.

Culture Spermatogonial Stem/Progenitor Cell

Spermatogonial stem/progenitor cell cultures were established and maintained using two media: F12GFB and SPGF. SPGF consisted of Stem Pro base with 1× Stem Pro supplement (Life Technologies), supplements according to Kanatsu-Shinohara et al. (2003), recombinant rat glial cell line derived neurotrophic factor (GDNF) at 10 ng ml^{-1} (Peprotech) , and recombinant human basic fibroblast growth factor (FGF2) at 10 ng ml^{-1} (Life Technologies). F12GFB media had a simpler composition than SPGF and consisted of DMEM/F-12 base, GDNF at 10 ng ml^{-1}, FGF2 at 10 ng ml^{-1} and supplements according to Dann et al. (2008). Spermatogonia grew as clusters of interconnected cells in both media; however F12GFB medium led to reduced adherence of the clusters to the substratum, compared to SPGF. A feeder layer of irradiated DR4 mouse embryonic fibroblasts (MEFs) was used, as described (Dann et al., 2008; Falciatori et al., 2008). Spermatogonial stem/progenitor cell cultures were derived from two PD 21 Sohlh$^{+/-}$/S1CF mice or two nontransgenic siblings (Sohlh1$^{+/-}$). The resulting cell lines were named SOC1 and NEG1, respectively. The procedure for cell line derivation was performed essentially as described, with modifications as follows (Falciatori et al., 2008; Kanatsu-Shinohara et al., 2003). Testes were shipped overnight in 1XPBS on ice. The tunica albuginea was removed, seminiferous tubules mechanically dispersed and then enzymatically dissociated in dispase (Becton Biosciences) at 37°C for 30 min. Dissociated cells were strained and plated on a gelatin coated well overnight in SPGF. Nonadherent and loosely bound cells were washed off the well and transferred to MEFs and cultured in F12GFB medium for 9 days. During this phase of culture the cells were transferred to new wells of MEFs every 3 days by gentle trituration to separate spermatogonia from adhering somatic cells. In F12GFB medium the spermatogonial clusters grew in suspension or loosely bound to the substratum, while somatic cells adhered to the plate. For subsequent culturing the cells were maintained in SPGF medium on MEFs and passaged by dissociating with 0.05% trypsin (Hyclone) (Falciatori et al., 2008). Images of spermatogonial stem/progenitor clusters were acquired using a BD Biosciences Pathway 435 High-Content Bioimager with a Lumenera-Infinity 3-1 cooled CCD camera and a 20× (U Apo/340 0.75 NA, Olympus) objective. Where indicated, spermatogonial stem/progenitor cells were plated without MEFs on laminin coated wells (0.016 mg ml^{-1}; Sigma) for 1 day prior to imaging.

Co-immunoprecipitation analysis

Four testes from PD7 Sohlh1$^{+/-}$ and Sohlh1$^{+/-}$/S1CF pups were used for immunoprecipitation by anti-

FLAG M2 Magnetic Beads (Sigma), as described previously (Suzuki *et al.*, 2012).

LITERATURE CITED

Baibakov B, Gauthier L, Talbot P, Rankin TL, Dean J. 2007. Sperm binding to the zona pellucida is not sufficient to induce acrosome exocytosis. Development 134:933–943.

Ballow D, Meistrich ML, Matzuk M, Rajkovic A. 2006. Sohlh1 is essential for spermatogonial differentiation. Dev Biol 294:161–167.

Dann CT, Alvarado AL, Molyneux LA, Denard BS, Garbers DL, Porteus MH. 2008. Spermatogonial stem cell self-renewal requires OCT4, a factor downregulated during retinoic acid-induced differentiation. Stem Cells 26:2928–2937.

Falciatori I, Lillard-Wetherell K, Wu Z, Hamra FK, Garbers DL. 2008. Deriving mouse spermatogonial stem cell lines. Methods Mol Biol 450:181–192.

Hoodbhoy T, Aviles M, Baibakov B, Epifano O, Jimenez-Movilla M, Gauthier L, Dean J. 2006. ZP2 and ZP3 traffic independently within oocytes prior to assembly into the extracellular zona pellucida. Mol Cell Biol 26:7991–7998.

Kanatsu-Shinohara M, Ogonuki N, Inoue K, Miki H, Ogura A, Toyokuni S, Shinohara T. 2003. Long-term proliferation in culture and germline transmission of mouse male germline stem cells. Biol Reprod 69:612–616.

Molyneaux KA, Stallock J, Schaible K, Wylie C. 2001. Time-lapse analysis of living mouse germ cell migration. Dev Biol 240:488–498.

Molyneaux KA, Zinszner H, Kunwar PS, Schaible K, Stebler J, Sunshine MJ, O'Brien W, Raz E, Littman D, Wylie C, Lehmann R. 2003. The chemokine SDF1/ CXCL12 and its receptor CXCR4 regulate mouse germ cell migration and survival. Development 130:4279–4286.

Pangas SA, Choi Y, Ballow DJ, Zhao Y, Westphal H, Matzuk MM, Rajkovic A. 2006. Oogenesis requires germ cell-specific transcriptional regulators Sohlh1 and Lhx8. Proc Natl Acad Sci USA 103:8090–8095.

Philpott CC, Ringuette MJ, Dean J. 1987. Oocyte-specific expression and developmental regulation of ZP3, the sperm receptor of the mouse zona pellucida. Dev Biol 121:568–575.

Runyan C, Schaible K, Molyneaux K, Wang Z, Levin L, Wylie C. 2006. Steel factor controls midline cell death of primordial germ cells and is essential for their normal proliferation and migration. Development 133:4861–4869.

Suzuki H, Ahn HW, Chu T, Bowden W, Gassei K, Orwig K, Rajkovic A. 2012. SOHLH1 and SOHLH2 coordinate spermatogonial differentiation. Dev Biol 361:301–312.

Takeuchi Y, Molyneaux K, Runyan C, Schaible K, Wylie C. 2005. The roles of FGF signaling in germ cell migration in the mouse. Development 132:5399–5409.

Warming S, Costantino N, Court DL, Jenkins NA, Copeland NG. 2005. Simple and highly efficient BAC recombineering using galK selection. Nucleic Acids Res 33:e36.

Yamatani H, Sato Y, Fujisawa H, Hirata T. 2004. Chronotopic organization of olfactory bulb axons in the lateral olfactory tract. J Comp Neurol 475:247–260.

Yan C, Elvin JA, Lin YN, Hadsell LA, Wang J, DeMayo FJ, Matzuk MM. 2006. Regulation of growth differentiation factor 9 expression in oocytes in vivo: a key role of the E-box. Biol Reprod 74:999–1006.

Yoshida S, Sukeno M, Nabeshima Y. 2007. A vasculature-associated niche for undifferentiated spermatogonia in the mouse testis. Science 317:1722–1726.

Stem Cell Reports

Article

Combined Loss of JMJD1A and JMJD1B Reveals Critical Roles for H3K9 Demethylation in the Maintenance of Embryonic Stem Cells and Early Embryogenesis

Shunsuke Kuroki,[1] Yuji Nakai,[2] Ryo Maeda,[1] Naoki Okashita,[1] Mika Akiyoshi,[3] Yutaro Yamaguchi,[3] Satsuki Kitano,[3] Hitoshi Miyachi,[3] Ryuichiro Nakato,[4] Kenji Ichiyanagi,[5] Katsuhiko Shirahige,[4] Hiroshi Kimura,[6] Yoichi Shinkai,[7] and Makoto Tachibana[1,3,*]

[1]Institute of Advanced Medical Sciences, Tokushima University, 3-18-15 Kuramoto-cho, Tokushima 770-8503, Japan
[2]Institute for Food Sciences, Hirosaki University, 2-1-1 Yanagawa, Aomori 038-0012, Japan
[3]Experimental Research Center for Infectious Diseases, Institute for Virus Research, Kyoto University, 53 Shogoin, Kawara-cho, Sakyo-ku, Kyoto 606-8597, Japan
[4]Research Center for Epigenetic Disease, The University of Tokyo, 1-1-1 Yayoi, Bonkyo-ku, Tokyo 113-0032, Japan
[5]Department of Applied Molecular Biosciences, Graduate School of Bioagricultural Sciences, Nagoya University, Furo-cho, Chikusa-ku, Nagoya 464-8601, Japan
[6]Graduate School of Bioscience and Biotechnology, Tokyo Institute of Technology, 4259 Nagatsuta, Midori-ku, Yokohama 226-8501, Japan
[7]Cellular Memory Laboratory, RIKEN Advanced Science Institute, 2-1 Hirosawa, Wako, Saitama 351-0198, Japan
*Correspondence: mtachiba@tokushima-u.ac.jp
https://doi.org/10.1016/j.stemcr.2018.02.002

SUMMARY

Histone H3 lysine 9 (H3K9) methylation is unevenly distributed in mammalian chromosomes. However, the molecular mechanism controlling the uneven distribution and its biological significance remain to be elucidated. Here, we show that JMJD1A and JMJD1B preferentially target H3K9 demethylation of gene-dense regions of chromosomes, thereby establishing an H3K9 hypomethylation state in euchromatin. JMJD1A/JMJD1B-deficient embryos died soon after implantation accompanying epiblast cell death. Furthermore, combined loss of JMJD1A and JMJD1B caused perturbed expression of metabolic genes and rapid cell death in embryonic stem cells (ESCs). These results indicate that JMJD1A/JMJD1B-mediated H3K9 demethylation has critical roles for early embryogenesis and ESC maintenance. Finally, genetic rescue experiments clarified that H3K9 overmethylation by G9A was the cause of the cell death and perturbed gene expression of JMJD1A/JMJD1B-depleted ESCs. We summarized that JMJD1A and JMJD1B, in combination, ensure early embryogenesis and ESC viability by establishing the correct H3K9 methylated epigenome.

INTRODUCTION

Posttranslational modifications in the tail region of core histones are important epigenetic marks linked to various nuclear functions, including transcriptional activity control. The discovery of enzymes that add/remove methyl groups to/from histones suggests that histone methylation levels are not statically but dynamically controlled (Kooistra and Helin, 2012). So far, individual functions of histone methyltransferases or demethylases have been studied extensively, but the role sharing between methyltransferases and demethylases for the correct establishment of histone methylated epigenome is not yet fully understood.

Histone H3 lysine 9 (H3K9) methylation is considered as an epigenetic mark of transcriptionally silenced heterochromatin. The JMJD1 family of proteins, which includes JMJD1A and its isozyme JMJD1B, reportedly possesses intrinsic H3K9 demethylating activity (Kim et al., 2012; Kuroki et al., 2013a; Yamane et al., 2006). JMJD1A plays important roles in several biological processes such as spermiogenesis (Liu et al., 2010; Okada et al., 2007), metabolism (Inagaki et al., 2009; Tateishi et al., 2009), and sex determination (Kuroki et al., 2013b). Recently, JMJD1B was shown to be required for female fertility (Liu et al., 2015). In contrast to the individual function of JMJD1A and JMJD1B in postnatal mice, the role of JMJD1 proteins in early embryogenesis and their functional redundancy are still unknown.

In this study, we demonstrated that JMJD1A and JMJD1B are redundantly but essentially required for mouse development immediately after implantation. We also demonstrated that JMJD1A and JMJD1B exhibit pivotal roles in mouse embryonic stem cell (ESC) function through the correct establishment of H3K9 methylated epigenome. Not a single depletion but depletion of both JMJD1A and JMJD1B induced a massive increase in H3K9 methylation accompanied by rapid cell death and perturbed gene expression. In control ESCs, dimethylated H3K9 (H3K9me2) was abundant in the gene-poor regions and scarce in the gene-dense regions of the chromosomes. Intriguingly, JMJD1A/JMJD1B deficiency induced a remarkable increase of H3K9me2 in the
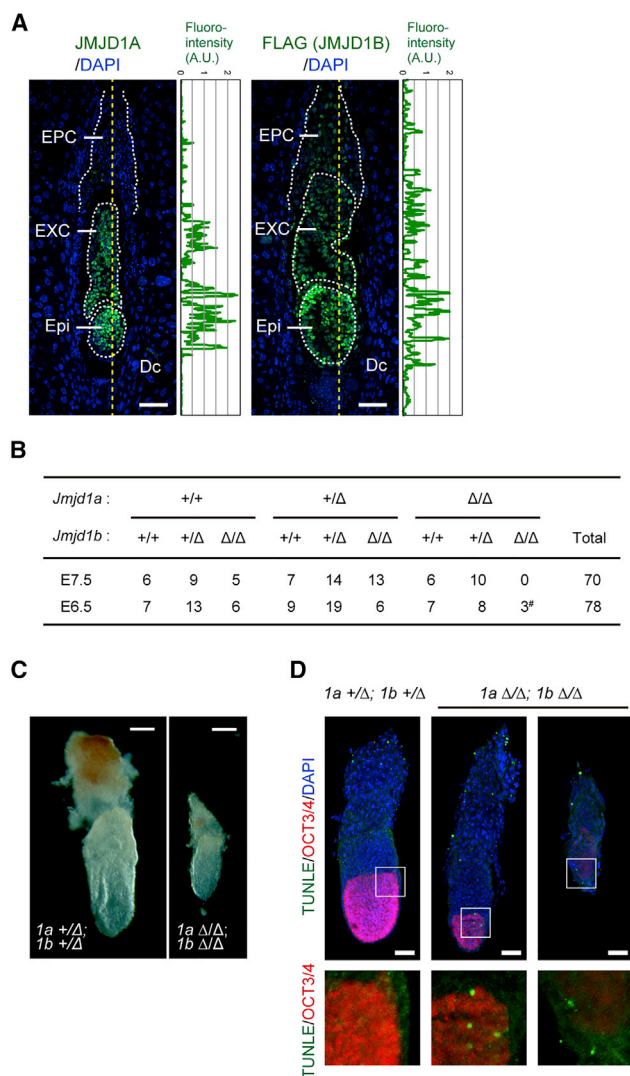
Figure 1. JMJD1A and JMJD1B Are Essential for Mouse Embryogenesis

(A) Immunofluorescence analysis of longitudinal sections of the E6.5 embryos with JMJD1A (left) and JMJD1B (right). E6.5 wild-type embryos were stained with anti-JMJD1A antibodies and DAPI (left). E6.5 $Jmjd1b^{+/Flag-KI}$ embryos were stained with anti-FLAG antibodies and DAPI (right). Fluorescence intensities along the dashed lines were quantified and plotted on the right side of the images. Scale bars, 100 μm. Epi, epiblast; EXC, extraembryonic ectoderm; EPC, ectoplacental cone; Dc, decidual cells. A.U., arbitrary unit.

(B) $Jmjd1a^{+/\Delta}$; $Jmjd1a^{+/\Delta}$ males and females were crossed, and the resultant embryos were genotyped at the indicated embryonic periods. $Jmjd1a^{\Delta/\Delta}$; $Jmjd1a^{\Delta/\Delta}$ embryos were found at E6.5, but not at E7.5. #, growth-retarded embryos.

(C) Gross appearances of $Jmjd1a/Jmjd1b$ double-deficient embryos at E6.5 (left) when compared with a littermate control (right). $1a$ and $1b$ represent $Jmjd1a$ and $Jmjd1b$, respectively. Scale bar, 100 μm.

(D) Whole-mount immunostaining analysis for the epiblast marker OCT3/4. Embryos were counterstained with DAPI and TUNEL to detect apoptotic cells. Scale bars, 100 μm.

(E) TUNEL-positive cells in the epiblast lineage were counted and summarized. $Jmjd1a^{+/\Delta}$; $Jmjd1a^{+/\Delta}$, n = 7; $Jmjd1a^{\Delta/\Delta}$; $Jmjd1a^{\Delta/\Delta}$, n = 3 different embryos (biological replicates). Data are presented as means ± SD. **p < 0.01 (Student's t test).

gene-dense regions, causing aberrant H3K9me2 distribution; high levels of H3K9me2 decorate chromosomes throughout. This result implies that JMJD1A/JMJD1B preferentially target H3K9 demethylation at the gene-dense euchromatin. Finally, we found that the additional mutation for an H3K9 methyltransferase G9A in a JMJD1A/JMJD1B-deficient background restored not only H3K9 overmethylation but also rapid cell death and perturbed gene expression phenotypes, indicating collaborative roles of JMJD1A/JMJD1B and G9A not only for the tuning of the H3K9 methylation levels but also for the regulation of ESC function. Taking these results together, we propose that JMJD1A/JMJD1B ensures cellular viability and transcription accuracy through the establishment of the correct H3K9 methylated epigenome in early mouse development.

RESULTS

JMJD1A and JMJD1B Are Essentially Required for Peri-implantation Development in Mice

Previous studies had demonstrated that JMJD1A and JMJD1B possess intrinsic H3K9 demethylating activity (Kim et al., 2012; Kuroki et al., 2013a; Yamane et al., 2006), suggesting that JMJD1A and JMJD1B may function in a redundant manner. To evaluate the roles of JMJD1A and JMJD1B in peri-implantation development, we examined the expression profiles of JMJD1A and JMJD1B in developing embryos (Figure 1A). Immunofluorescence analysis with anti-JMJD1A antibodies revealed that JMJD1A is expressed in the epiblast and extraembryonic ectoderm at embryonic day (E) 6.5 (Figure 1A, left). To detect the endogenous JMJD1B protein with an anti-FLAG tag antibody, we
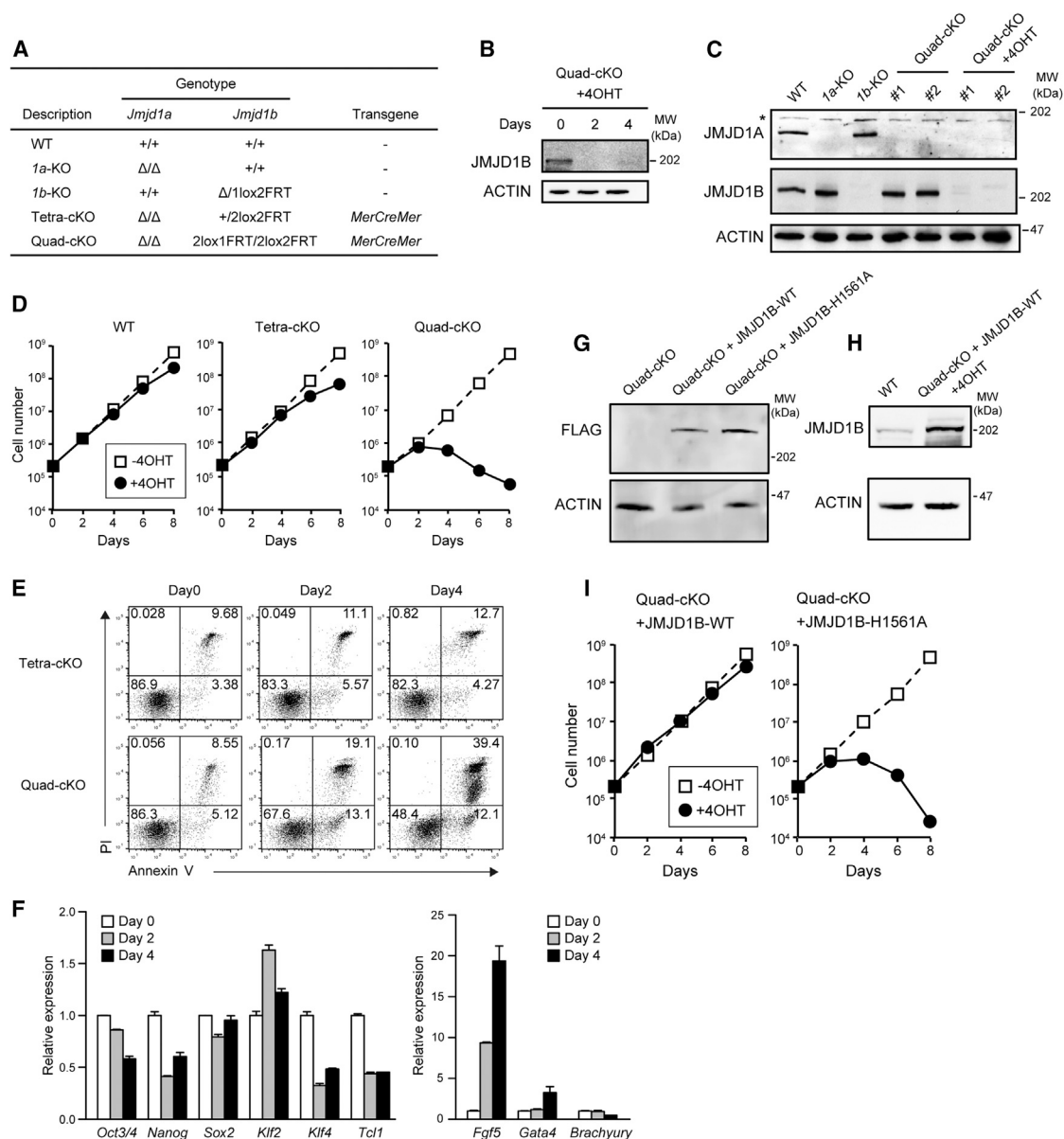
Figure 2. Depletion of JMJD1A and JMJD1B Induces Growth Arrest in ESCs

(A) List of the established ESC lines and their genotypes. MerCreMer, Cre flanked by mutated estrogen receptor ligand-binding domains.

(B) Time-course analysis of 4OHT-dependent depletion of JMJD1B in Quad-cKO cells.

(C) Immunoblot analyses of JMJD1A/JMJD1B-depleted ESC lines. Whole extracts of the indicated ESC lines were fractionated using SDS-PAGE and then applied to immunoblot analysis with antibodies against JMJD1A and JMJD1B. JMJD1A and JMJD1B were depleted in the Quad-cKO cell lines cultured with 800 nM 4OHT for 4 days. Asterisk (*) represents non-specific signals.

(D) The indicated ESC lines were cultured in the presence or absence of 4OHT. Cell numbers were determined every 2 days. Growth arrest became apparent when the Quad-cKO cell line was cultured in the presence of 4OHT for 4 days (right). In contrast, wild-type (left) and Tetra-cKO (middle) cells grew in the presence of OHT.

(E) Time-course analysis of JMJD1 depletion-induced cell death. The indicated ESC lines were cultured in the presence of 4OHT, following which the cells were stained with PI and annexin V and analyzed using flow cytometry.

(F) Expression levels of pluripotency-associated (left) and lineage-associated (right) genes in Quad-cKO cells treated with 4OHT were examined using RT-qPCR. We used *Fgf5*, *Gata4*, and *Brachyury* as the markers for primitive ectoderm, endoderm, and mesoderm, respectively. Representative data are presented from independent triplicate experiments. Error bars indicate means ± SD derived from technical replicates.

(legend continued on next page)

established knockin mouse and ESC lines carrying modified *Jmjd1b* allele (referred as *1b* hereafter). In the resultant lines, $1b^{+/Flag-KI}$ allele produces the JMJD1B protein with a carboxy-terminal FLAG tag (Figure S1). Immunofluorescence analysis of $1b^{+/Flag-KI}$ embryos with anti-FLAG tag antibody revealed that JMJD1B is expressed in the epiblast, extraembryonic ectoderm, and ectoplacental cone of E6.5 embryos (Figure 1A, right). We measured and plotted the signal intensities for JMJD1 proteins in the embryonic lineages (Figure 1A, plot analyses). Consequently, JMJD1A and JMJD1B were both found to be abundantly expressed in the epiblast of the developing embryos, indicating the potential roles of JMJD1A and JMJD1B in epiblast development.

We established mutant mice bearing the $1b^{\Delta}$ allele, which lacks exons 20–21, corresponding with a portion of the catalytic JmjC domain (Figure S1). The $1b^{\Delta/\Delta}$ mice were born at nearly the expected Mendelian ratio, but most of them died within a week after birth (Figure S2). Some of the $1b^{\Delta/\Delta}$ mice survived and developed into adults; however, their body weights were almost half those of the controls (Figure S2). These phenotypes are in accordance with those reported in a recent study (Liu et al., 2015). To evaluate the effects of compound depletion of JMJD1A and JMJD1B on mouse development, we examined postnatal animals and embryos derived from the mating of *1a*/*1b* double-heterozygous mutant mice. Among the 109 neonatal offspring, no JMJD1A/JMJD1B-deficient mice were found, strongly suggesting that JMJD1A/JMJD1B-deficient mice were embryonically lethal (Figure S2). Intriguingly, all of the mice carrying three mutant alleles of *1a* or *1b* were stillborn, indicating that the gene dosage of *1a*/*1b* is critical for prenatal development (Figure S2). Embryos bearing the *1a*/*1b* double-homozygous mutation were not found in 70 embryos at E7.5, whereas three embryos with this mutation were found in 78 embryos at E6.5 (Figure 1B). Notably, all JMJD1A/JMJD1B-deficient embryos were smaller than the controls at this stage (Figure 1C). These data suggest that JMJD1A/JMJD1B-deficient embryos display growth retardation and die around E6.5.

To examine the development of JMJD1A/JMJD1B-deficient embryos in more detail, we performed a whole-mount immunostaining analysis using antibodies against OCT3/4, which mark epiblast cells (Figure 1D). Apoptotic cells were detected by TUNEL labeling (Figure 1D). Strikingly, the mass size of OCT3/4-positive epiblasts in JMJD1A/JMJD1B-deficient embryos was smaller than those in the control embryos (Figure 1D, middle panels). We also found some JMJD1A/JMJD1B-deficient embryos without detectable epiblast cells (Figure 1D, right panels). TUNEL counterstaining analysis demonstrated a significant increase in the number of apoptotic cells in the epiblasts of JMJD1A/JMJD1B-deficient embryos (summarized in Figure 1E). These data indicate that growth retardation of JMJD1A/JMJD1B-deficient embryos can be attributed, in part, to the compromised development of the epiblast cells. We therefore conclude that JMJD1A and JMJD1B play redundant but essential roles for post-implantation development in mouse.

JMJD1A and JMJD1B Are Essentially Required for ESC Viability

To further address the roles of JMJD1-mediated H3K9 demethylation in early embryogenesis, we used mouse ESCs, which provide a good tool for studying the developmental process of pre- and post-implantation embryos. Immunoblot analysis indicated that JMJD1A and JMJD1B were both expressed in ESCs (Figure 2). We previously generated ESCs lacking JMJD1A by a simple targeting method (Inagaki et al., 2009). Also, we have established ESCs lacking JMJD1B in this study (Figure S1), indicating that neither JMJD1A nor JMJD1B is essential for ESC survival. To address the impact of JMJD1A and JMJD1B double-deficiencies in ESC function, we tried to establish an ESC line with conditionally depleted JMJD1 proteins. The conditional targeting vector of *Jmjd1b* was constructed and then introduced into the JMJD1A-deficient ESC line (Figure S1). To convert functional $1b^{2lox}$ alleles into defective $1b^{1lox}$ alleles in a 4-hydroxy tamoxifen (4OHT)-dependent manner, the MerCreMer (Cre flanked by mutated estrogen receptor ligand-binding domains) expression plasmid was also introduced into the homologous recombinant lines. We consequently obtained *1a*/*1b*-conditional knockout (KO) lines named Quad-cKO ($Jmjd1a^{\Delta/\Delta}$; $Jmjd1b^{2lox1FRT/2lox2FRT}$; *Mer-Cre-Mer*) (Figure 2A). Quad-cKO cell lines were cultured with 4OHT and then applied to immunoblot analysis (Figures 2B and 2C). Time-course

(G and H) Rescue of the growth arrest phenotype by exogenous introduction of JMJD1B into Quad-cKO cell line. (G) Expression vectors for FLAG-tagged wild-type JMJD1B or enzymatically inactive H1561A mutants of JMJD1B were individually and stably introduced into the Quad-cKO cell line. The expression levels of exogenously expressed proteins were compared by immunoblot analysis. (H) Comparison of protein expression levels of endogenously expressed JMJD1B and exogenously expressed JMJD1B using anti-JMJD1B antibody. JMJD1B expression levels were compared between wild-type ESCs and 4OHT-treated Quad-cKO cells expressing FLAG-JMJD1B-WT.
(I) Quad-cKO cell lines expressing wild-type JMJD1B (left) or the enzymatically inactive H1561A mutant of JMJD1B (right) were cultured in the presence of 4OHT. Exogenous expression of wild-type JMJD1B rescued the growth arrest phenotype of Quad-cKO cells in the presence of 4OHT, whereas the enzymatically inactive H1561A mutant did not.

experiments showed that JMJD1B signal disappeared after the 4OHT treatment for 2 days (Figure 2B). We confirmed the absence of JMJD1A signals, as well as JMJD1B signals, in the 4OHT-treated Quad-cKO cells (Figure 2C). We, thus, successfully generated ESC lines with conditionally depleted JMJD1 proteins.

Next, we examined the growth potential of Quad-cKO cell lines. Tetra-cKO ($Jmjd1a^{\Delta/\Delta}$; $Jmjd1b^{+/2lox2FRT}$; Mer-Cre-Mer) cells that carried two disrupted $Jmjd1a$ alleles and single conditional allele of $Jmjd1b$ were generated as controls (Figure 2A). The parental wild-type cells (TT2 line) and Tetra-cKO cells could grow exponentially in the presence of 4OHT (Figure 2D, left and middle panels, respectively). In contrast, when Quad-cKO cell lines were cultured in the presence of 4OHT, an increase in cell numbers was noted during the first 2 days, which was followed by a decrease in number (Figure 2D, right panel). Note that we could not establish cell lines lacking both JMJD1A and JMJD1B due to severe growth defect in the Quad-cKO cell lines when the two proteins were depleted. Taking these results together, we concluded that JMJD1A and JMJD1B are redundantly but essentially required for ESC survival.

To examine the cause of growth arrest in ESCs lacking JMJD1A and JMJD1B, we assessed the cell viability by staining with propidium iodide (PI) and annexin V (Figure 2E). The number of early apoptotic cells that stained positively with annexin V and negatively with PI increased when the Quad-cKO cell line was cultured in the presence of 4OHT for 2 days; remarkably, the number further increased with 4OHT treatment for another 2 days (Figure 2E, bottom panel). In addition, the number of dead cells that stained positively with both annexin V and PI simultaneously increased (Figure 2E, bottom panel). The progressive increase in the number of apoptotic cells might account for the growth defect of ESCs lacking JMJD1A and JMJD1B, at least in part. In contrast, 4OHT treatment had a moderate effect on the number of apoptotic and dead cells in the Tetra-cKO cell line (Figure 2E, top panel). We also conducted cell cycle analysis of Quad-cKO cells by measuring bromodeoxyuridine (BrdU) incorporation and the DNA contents (Figure S3). 4OHT treatment did not have a profound effect on cell cycle progression in both Quad-cKO and Tetra-cKO cell lines. Therefore, the growth defect phenotype in JMJD1A/JMJD1B-depleted ESCs partly results from an increase in the apoptotic cell death.

To investigate how JMJD1A/JMJD1B depletion influenced the pluripotency of ESCs, we examined mRNA expression levels of six pluripotency-associated genes (*Oct3/4*, *Nanog*, *Sox2*, *Klf2*, *Klf4*, and *Tcl1*) and three lineage-associated genes (*Fgf5*, *Gata4*, and *Brachyury*) in 4OHT-treated Quad-cKO cells (Figure 2F). The expression of four pluripotency-associated genes, *Oct3/4*, *Nanog*, *Klf4*, and *Tcl1*, was downregulated (Figure 2F, left), whereas that of the lineage-associated primitive endoderm marker gene *Fgf5* was upregulated in 4OHT-treated Quad-cKO cells (Figure 2F, right). These results indicate that JMJD1A/JMJD1B depletion in ESCs might compromise the self-renewal property of pluripotent ESCs and/or prompt their differentiation.

It is important to elucidate whether the growth arrest of JMJD1A/JMJD1B-depleted cells was dependent on JMJD1-mediated enzymatic activity. To address this issue, we performed rescue experiments using *Jmjd1b* expression vectors. Expression vectors for FLAG-tagged wild-type JMJD1B and catalytically defective JMJD1B^{H1561A} (Figure S3) were stably introduced into the Quad-cKO cells (Figure 2G). We confirmed that the protein expression levels of exogenously introduced JMJD1B were higher than that of endogenous JMJD1B (Figures 2G and 2H). As shown in Figure 2I, Quad-cKO cells carrying wild-type *Jmjd1b* transgene had a clearly restored growth potential in the presence of 4OHT. In contrast, the growth potential of Quad-cKO cells carrying *Jmjd1b*^{H1561A} transgene was not restored, even though the expression level of exogenously introduced JMJD1B^{H1561A} was higher than that of wild-type (Figure 2G). These findings indicate that the H3K9 demethylating activity of JMJD1 enzymes is absolutely required for ESC survival.

JMJD1A and JMJD1B Substantially Contribute to H3K9 Demethylation in ESCs

To address how JMJD1A and JMJD1B contribute to H3K9 methylation status of ESCs, we examined H3K9 methylation levels of mutant ESCs by immunoblot analysis (Figures 3A–3C). Dimethylated H3K9 (H3K9me2) was markedly increased in the Quad-cKO cell line when cultured in the presence of 4OHT for 2 days onward (Figure 3A). We next compared the H3K9 methylation levels among wild-type, JMJD1A-deficient, JMJD1B-deficient, and JMJD1A/JMJD1B-depleted ESCs using a panel of specific antibodies by immunoblot analysis (Figure 3B) (Kimura et al., 2008). H3K9me1 levels remained unchanged even after *1a*/*1b* compound mutation (summarized in Figure 3C, left panel). In contrast, the compound mutation led to robust increases in the levels of H3K9me2 and me3 (summarized in Figure 3C, middle and right panels, respectively). Single mutations of *1a* or *1b* led to only moderate increases in the levels of H3K9me2 and me3, indicating that JMJD1A and JMJD1B redundantly catalyze H3K9 demethylation in ESCs.

We compared nuclear distribution profiles of H3K9 methylation between wild-type and JMJD1A/JMJD1B-depleted ESCs by immunocytochemistry. Neither distribution nor intensity of H3K9me1 signals was affected by JMJD1A/JMJD1B depletion (Figure 3D). H3K9me2 signals
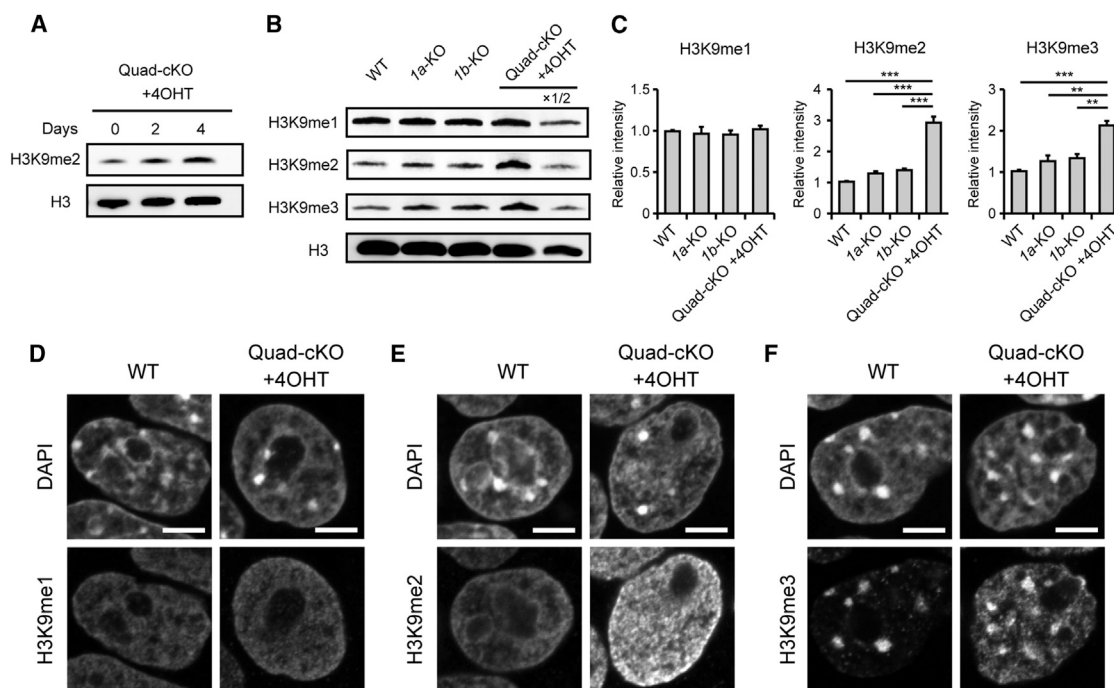
240

Figure 3. JMJD1A and JMJD1B Substantially Contribute to H3K9 Demethylation in ESCs

(A) Time-course analysis of JMJD1B-depletion-induced increase in H3K9me2 in 4OHT-treated Quad-cKO cells.

(B) Immunoblot analyses of H3K9 methylation levels in the indicated ESC lines.

(C) The methylation levels of H3K9me1 (left), H3K9me2 (middle), and H3K9me3 (right) in the indicated ESC lines were determined by immunoblot analysis. The intensities of H3K9me signals of wild-type cells were defined as 1. Data are presented as means ± SD (n = 3 independent experiments). **$p < 0.01$; ***$p < 0.001$ (Student's t test).

(D–F) Nuclear distribution profiles of H3K9me1 (D), H3K9me2 (E), and H3K9me3 (F) in JMJD1A/JMJD1B-depleted ESCs compared with those in the wild-type ESCs. Scale bars, 5 μm.

were detected mostly at the euchromatic regions in wild-type nuclei (Figure 3E, left panels). Distribution profiles of H3K9me2 signals seemed to be unaffected by JMJD1A/JMJD1B depletion; nevertheless, the signal intensities were dramatically increased (Figure 3E, right panels). H3K9me3 were detected mainly at the pericentric heterochromatin as dense signals in both wild-type and JMJD1A/JMJD1B-depleted cells (Figure 3F). Interestingly, we observed that JMJD1A/JMJD1B depletion led to a significant increase in H3K9me3 signals in the euchromatin (Figure 3F, right panels). These results strongly suggest that the increase in H3K9me2/3 in JMJD1A/JMJD1B-depleted ESCs is attributed to the increase in H3K9me2/3 in the euchromatin.

JMJD1A/JMJD1B-Mediated H3K9 Demethylation Targets Gene-Dense Regions of Chromosomes

The next important question is which loci are targeted by JMJD1A/JMJD1B-mediated H3K9 demethylation in ESCs. To address this issue, we performed chromatin immunoprecipitation (ChIP) analysis using antibodies against H3K9me2. Mononucleosome was prepared by enzymatic digestion of ESC chromatin and then applied to ChIP sequencing (ChIP-seq) analysis (Figure 4). Importantly, approximately 1.7 times more DNA was immunoprecipitated with anti-H3K9me2 antibody from JMJD1A/JMJD1B-depleted nuclei than from wild-type nuclei, indicating that JMJD1A/JMJD1B depletion resulted in a genome-wide increase in H3K9me2 (Figure S4). The distribution profile of H3K9me2 on chromosome 11 is representatively shown in Figure 4A; the relatively gene-poor region spans 10–50 M and relatively gene-dense region spans 50–120 M (Figure 4A, upper panel). H3K9me2 was detected throughout chromosome 11 in wild-type cells, indicating high abundance of the H3K9me2 marks (Figure 4A, middle panel). It is intriguing that H3K9me2 distributes evenly with high levels of methylation in the gene-poor region, whereas H3K9me2 distributes unevenly with high and low levels of methylation in the gene-dense region of chromosome 11 in wild-type cells. In the gene-dense region, we observed a typical feature between the gene densities and enrichment of H3K9me2 in wild-type ESCs; loci with low gene densities were heavily methylated, while those with high gene densities were hypomethylated
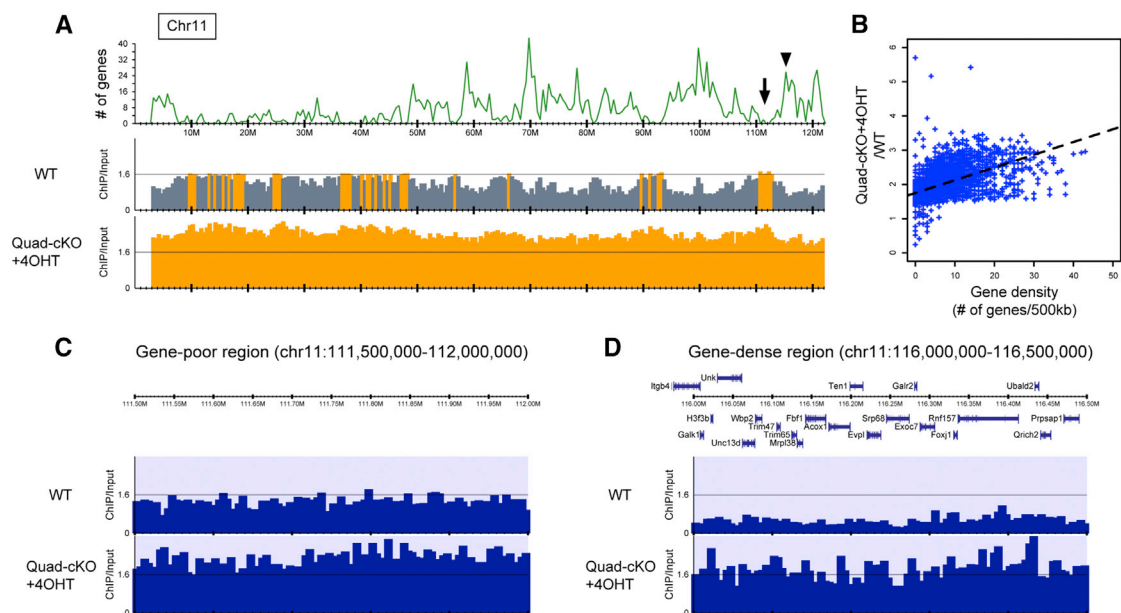
Figure 4. JMJD1A/JMJD1B-Mediated H3K9 Demethylation Targets Gene-Dense Euchromatin

(A) Distribution profiles of H3K9me2 along chromosome 11. The upper panel shows the number (#) of mm10 RefSeq genes smoothed with a width of 500 kb. The middle and lower panels represent the ratios of normalized read density between ChIP and whole-cell lysate (input) samples (ChIP/input) in wild-type and JMJD1A/JMJD1B-depleted cells (Quad-cKO+4OHT), respectively. The ratio of ChIP/input >1.6 is shown in orange.

(B) Correlation between gene density and increased H3K9me2 levels due to JMJD1A/JMJD1B depletion. The x and y axes indicate the number of mm10 RefSeq genes and the quotient of ChIP/input of Quad-cKO+4OHT divided by ChIP/input of wild-type (WT), respectively, smoothed with a 500 kb width. The dashed lines represent regression lines.

(C and D) Distribution profile of H3K9me2 in a gene-poor region (C), arrow showing the position in (A), or a gene-dense region (D), arrowhead showing the position in (A) within chromosome 11. The upper panels show the positions of the protein-coding genes, whereas lower tracks depict ChIP/input in the indicated samples.

(Figure 4A, middle panel). JMJD1A/JMJD1B depletion resulted in increased levels of H3K9me2 throughout chromosome 11 (Figure 4A, bottom panel). These characteristics were common in the other chromosomes (Figure S4). Notably, the increase in H3K9me2 levels due to JMJD1A/JMJD1B depletion in the gene-dense region seemed to be higher than that in the gene-poor region. To address this quantitatively, the relationship between the increased H3K9me2 levels due to JMJD1A/JMJD1B depletion and gene densities of all chromosomes was statistically evaluated by calculating the average levels of H3K9me2 in comparison with the gene densities (number of genes per 500 kb genome). As shown in Figure 4B, there was a positive correlation between the increased H3K9me2 levels due to JMJD1A/JMJD1B depletion and gene densities, implying that JMJD1A/JMJD1B preferentially targets H3K9 demethylation in these regions (Figure 4B). The distribution profiles of H3K9me2 with narrower windows in the gene-poor and gene-dense regions of chromosome 11 are shown in Figures 4C and 4D, respectively. In the gene-poor region, H3K9me2 levels of JMJD1A/JMJD1B-

depleted cells were approximately one and a half times higher than that of wild-type cells. In contrast, H3K9me2 levels of JMJD1A/JMJD1B-depleted cells were more than three times higher than that of wild-type cells, confirming that JMJD1A/JMJD1B preferentially targets H3K9 demethylation in gene-dense regions (Figures 4C and 4D).

Profound Effect of JMJD1A/JMJD1B Depletion on Gene Expression

As the enrichment of H3K9 methylation marks is relevant to transcriptionally silenced heterochromatin, the distorted distribution of H3K9me2 might induce the alteration of gene expression in JMJD1-depleted cells. To address this, we performed a microarray analysis using RNAs from wild-type, JMJD1B-deficient, JMJD1A-deficient (Quad-cKO cell lines), and JMJD1A/JMJD1B-depleted cells (Quad-cKO cell lines cultured in the presence of 4OHT). Hierarchical clustering analysis revealed that each of the genotype-identical sets forms the smallest clusters, indicating that it is not the clonal but the genetic difference that influences gene expression (Figure 5A). The cluster of
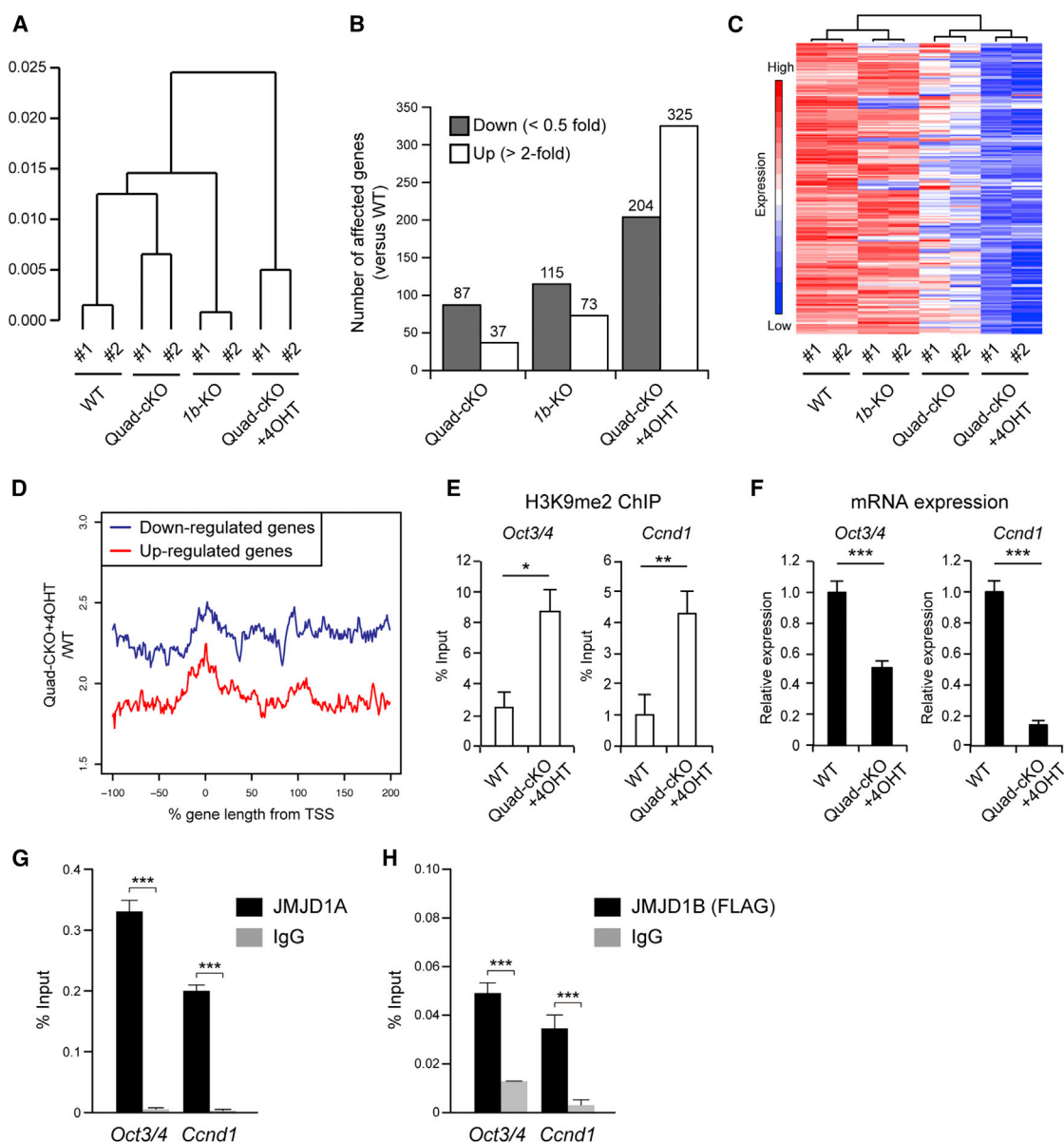
Figure 5. Depletion of JMJD1A and JMJD1B Alters Gene Expression Profile in ESCs

RNAs were prepared from ESCs and subjected to a microarray analysis using an Affymetrix mouse genome 430 2.0 array.

(A) Hierarchical clustering analysis of gene expression profiles in wild-type cells (TT2 lines), JMJD1A-deficient cells (Quad-cKO cell lines), JMJD1B-deficient cells, and JMJD1A/JMJD1B-double-depleted cells (Quad-cKO cell lines cultured with 4OHT). The farthest distance was observed between the cluster of JMJD1A/JMJD1B-double-depleted cells and the other cell clusters, indicating that the compound depletion of JMJD1A and JMJD1B has the most prominent effect on transcription.

(B) Numbers of genes affected by the JMJD1A and/or JMJD1B depletion in ESCs. Downregulated genes (<0.5-fold) and upregulated genes (>2.0-fold) due to each mutation are represented as dark and white bars, respectively.

(C) Comparison of mRNA levels in the 204 genes between the indicated samples, which were downregulated by JMJD1A/JMJD1B double depletion. Heatmap analysis demonstrated that single depletion had a moderate effect on the transcription of these genes compared with double depletion.

(D) Quantitative analysis of H3K9me2 levels of the genes regulated by JMJD1A and JMJD1B. Averaged increase in H3K9me2 around the gene bodies down- (blue) and upregulated (red) due to JMJD1A/JMJD1B depletion was plotted. The x axes indicate % gene length; 0% and 100% represent transcription start site and transcription end site, respectively. The y axes indicate the average of the quotient of ChIP/input of Quad-cKO+4OHT divided by ChIP/input of wild-type.

(legend continued on next page)

JMJD1A/JMJD1B-depleted cells was the farthest from those of the other cells, indicating that compound depletion of JMJD1A and JMJD1B has the most prominent effect on transcription. Based on this notion, the numbers of genes up- or downregulated by JMJD1A/JMJD1B double depletion were found to be larger than the numbers affected by single mutation (Figure 5B, genes are listed in Table S2).

Next, we examined the individual roles of JMJD1A and JMJD1B on the transcriptional regulation of the 204 genes that were downregulated by JMJD1A/JMJD1B double depletion. A heatmap analysis revealed that JMJD1A or JMJD1B deficiency alone had only moderate effects on the downregulation of those genes, indicating that JMJD1A and JMJD1B upregulate these genes in a redundant manner (Figure 5C). Among the 204 genes, 134 were downregulated only when both JMJD1A and JMJD1B were depleted (Figure S5). Gene ontology (GO) analyses demonstrated that metabolic processes such as one-carbon metabolism and amino acid biosynthesis were significantly enriched among the 134 genes (Figure S5). On the other hand, the genes of many pathways, such as reproductive process, inflammatory pathway, and cellular differentiation, were significantly enriched among the genes upregulated only when both JMJD1A and JMJD1B were depleted (Figure S5). To elucidate the cause of distorted gene expression in JMJD1A/JMJD1B-depleted cells, we examined H3K9 methylation levels in the genomic portion surrounding the down- and upregulated genes (Figure 5D). We found that JMJD1A/JMJD1B depletion increased H3K9 methylation levels of the downregulated genes more profoundly than those of the upregulated genes (Figure 5D). Therefore, it is conceivable that these genes are the direct targets of JMJD1A and JMJD1B.

Because previous studies have demonstrated that H3K9 methylation negatively controls the transcription of genes including *Oct3/4* (Feldman et al., 2006) and a D-type cyclin *Ccnd1* (Shirato et al., 2009), we hypothesized that JMJD1A/JMJD1B-mediated H3K9 demethylation will upregulate the transcription of *Oct3/4* and *Ccnd1*. To evaluate this hypothesis, we examined the H3K9 methylation levels of *Oct3/4* and *Ccnd1* promoters and the mRNA expression levels of *Oct3/4* and *Ccnd1* in JMJD1A/JMJD1B-depleted ESCs. As shown in Figures 5E and 5F, JMJD1A/JMJD1B depletion increased the levels of H3K9me2 at *Oct3/4* and *Ccnd1* and decreased their transcription. To further confirm the effect of JMJD1-mediated H3K9 demethylation on *Oct3/4* and *Ccnd1* regulation, we examined the enrichment of JMJD1A and JMJD1B at *Oct3/4* and *Ccnd1* loci. ChIP analysis revealed that JMJD1A was significantly enriched at the promoter regions of *Oct3/4* and *Ccnd1* in ESCs (Figure 5G). ChIP analysis of $1b^{+/Flag-KI}$ ESCs demonstrated that endogenous JMJD1B was significantly enriched at the promoter regions of *Oct3/4* and *Ccnd1* (Figure 5H). Taking these results together, we conclude that JMJD1A and JMJD1B catalyze H3K9 demethylation of *Oct3/4* and *Ccnd1* gene promoters, thereby activating their transcription.

Collaborative Roles of JMJD1A/JMJD1B Demethylases and G9A Methyltransferase for Tuning the H3K9 Methylation Levels and Regulation of ESC Function

The data presented here suggest that the excess accumulation of H3K9 methylation might cause rapid cell death and perturbed gene expression in JMJD1A/JMJD1B-depleted cells. To verify this possibility, we tried to identify the enzymes responsible for H3K9 overmethylation in JMJD1A/JMJD1B-depleted cells. We have previously demonstrated that GLP/G9A methyltransferase complex catalyzes H3K9 methylation in the euchromatin (Tachibana et al., 2002, 2005). Assuming the strong candidate of this complex for euchromatic H3K9 overmethylation in the JMJD1A/JMJD1B-depleted cells, we introduced G9A-conditional alleles into the Quad-cKO cell line. Consequently, Hexa-cKO cells, in which JMJD1A, JMJD1B, and G9A could be inducibly depleted, were obtained (Figure 6A). Surprisingly, the Hexa-cKO cells demonstrated normal growth when they were cultured in the presence of 4OHT (Figure 6B), suggesting that G9A depletion restored the growth potential of JMJD1A/JMJD1B-depleted ESCs. As expected by this finding, ESC lines lacking JMJD1A, JMJD1B, and G9A (named as JGTKO) were easily established from a pool of Hexa-cKO cells cultured with 4OHT, confirming that the triple-KO ESCs have normal growth potential (Figures 6A and 6C). Next, H3K9 methylation levels of the JGTKO lines were assessed by immunoblot analysis (Figures 6D–6F). The additional *G9a* mutation induced drastic reductions in H3K9me2 and H3K9me3 levels in ESCs with JMJD1A/JMJD1B-deficient background (Figures 6E and 6F). Taken together, we conclude that G9A is a bona fide enzyme responsible for the H3K9 overmethylation in

(E) H3K9 methylation levels of the promoter regions of *Oct3/4* (left) and *Ccnd1* (right) of the indicated ESCs.

(F) mRNA expression levels of *Oct3/4* (left) and *Ccnd1* (right) of the indicated ESCs.

(G) ChIP analysis for JMJD1A at the promoter regions of *Oct3/4* (left) and *Ccnd1* (right) with anti-JMJD1A antibodies.

(H) ChIP analysis of JMJD1B at the promoter regions of *Oct3/4* (left) and *Ccnd1* (right) using anti-FLAG antibody. To detect endogenous JMJD1B with anti-FLAG antibody, we established knockin ESC line carrying $1b^{+/Flag-KI}$ allele, in which the modified *1b* allele produces JMJD1B protein with a FLAG tag at its carboxy terminus (Figure S1).

For (E–H), data are presented as means ± SD from n = 3 independent experiments. *p < 0.05; **p < 0.01; ***p < 0.001 (Student's t test).
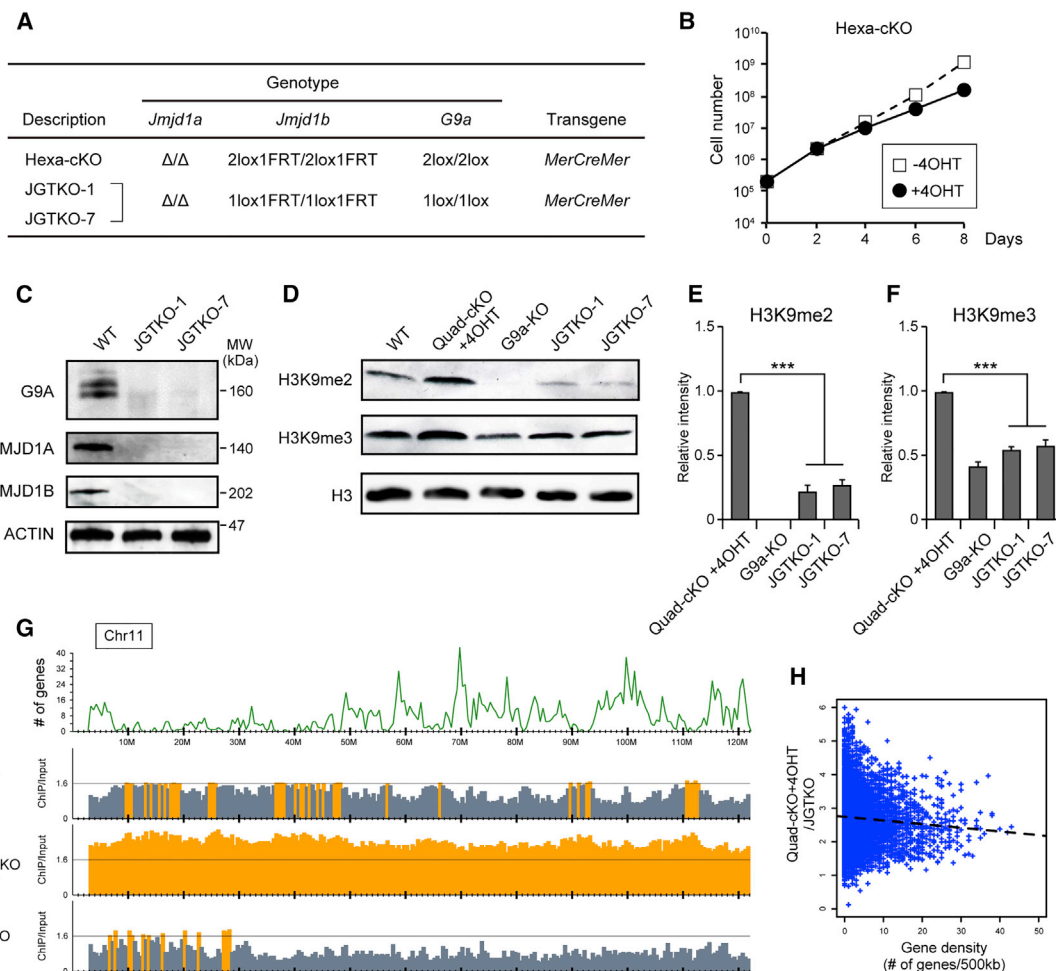
244

Figure 6. Collaborative Roles of JMJD1A/JMJD1B Demethylases and G9A Methyltransferase for Tuning the H3K9 Methylation Levels and Regulating ESC Function

(A) Genotypes of the established ESC line. Hexa-cKO cell line carries alleles for the null mutation of *Jmjd1a*, the conditional mutation of *Jmjd1b*, and the conditional mutation of *G9a*. ESC lines lacking JMJD1A, JMJD1B, and G9A (named JGTKO-1 and JGTKO-7) were established by cloning from a pool of Hexa-cKO cells cultured in the presence of 4OHT.

(B) Growth curve of Hexa-cKO cell line in the presence or absence of 4OHT.

(C) JMJD1A, JMJD1B, and G9A proteins were absent in JGTKO-1 and JGTKO-7 ESC lines. Whole-cell extracts were fractionated by SDS-PAGE, and then subjected to immunoblot analysis with the indicated antibodies.

(D–F) *G9a* mutation rescues the H3K9 overmethylation phenotype of JMJD1A/JMJD1B-double-depleted cells. H3K9me2 and H3K9me3 levels in the indicated cell lines were examined by immunoblot analysis (D) and summarized (E and F, respectively). The intensities of H3K9me signals of Quad-cKO + 4OHT were defined as 1. Data are presented as means ± SD from n = 3 independent experiments. ***p < 0.001 (Student's t test).

(G) Distribution profiles of H3K9me2 of JGTKO cells along chromosome 11. The top panel shows the number of mm10 RefSeq genes smoothed over 500 kb. The middle panels represent the ratios of normalized ChIP/input of ESCs of the indicated genotypes, including wild-type and JMJD1A/JMJD1B-depleted cells. The ratio of ChIP/input >1.6 is shown in orange.

(H) Correlation between gene density and decreased H3K9me2 levels due to *G9a* mutation in JMJD1A/JMJD1B-depleted cells. The x and y axes indicate the number of mm10 RefSeq genes and the quotient of ChIP/input of Quad-cKO+4OHT divided by ChIP/input of JGTKO cells, respectively, smoothed over 500 kb. Dashed lines represent regression curves.

JMJD1A/JMJD1B-depleted ESCs and that G9A-mediated H3K9 overmethylation is the cause of cell death in JMJD1A/JMJD1B-depleted ESCs.

To investigate how *G9a* mutation altered the genome-wide distribution of H3K9 methylation, we examined the H3K9me2 distribution profile of JGTKO cells by
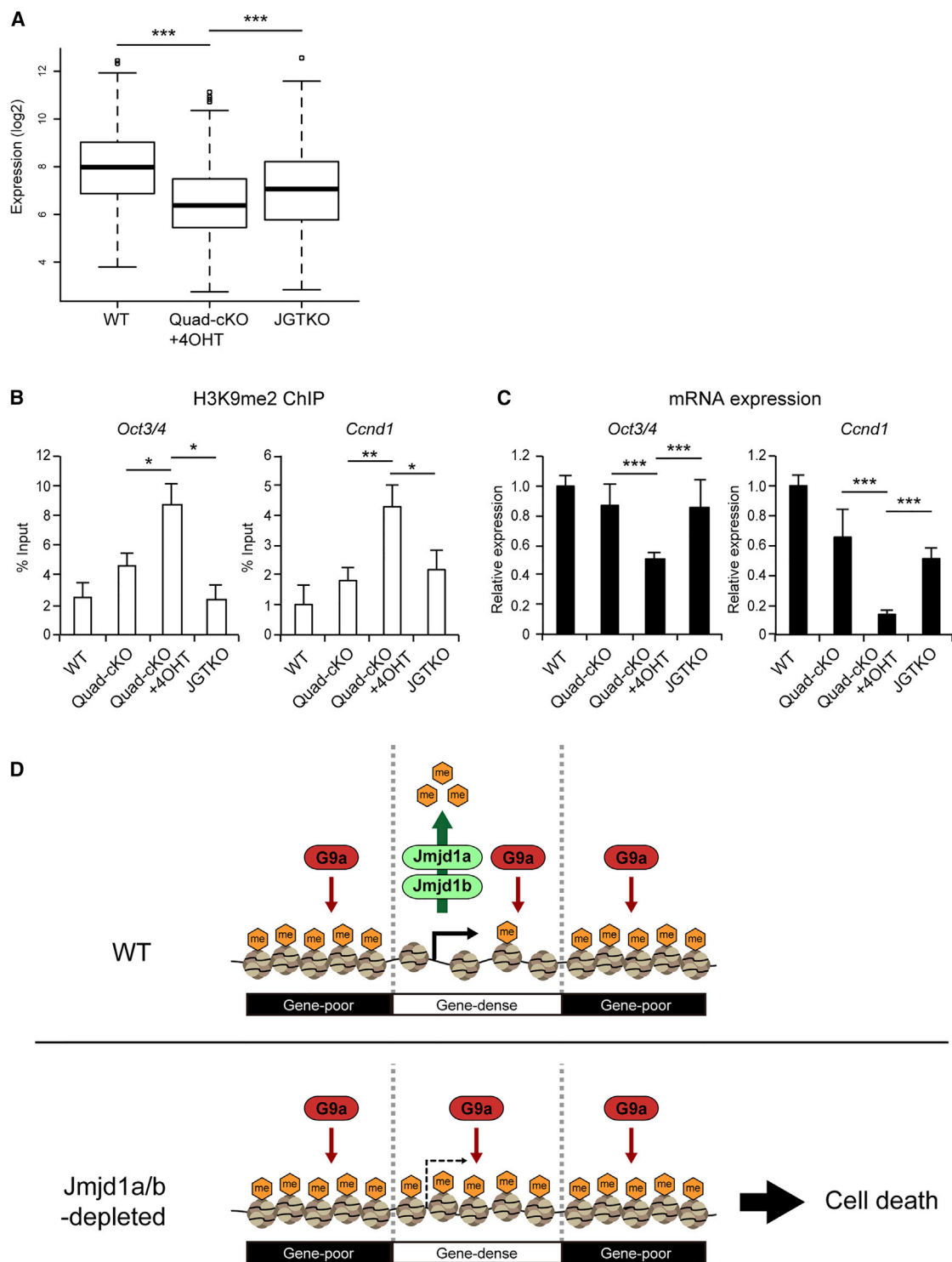
Figure 7. *G9a* Mutation Rescues JMJD1A/JMJD1B-Depletion-Induced Transcriptional Downregulation

(A) Comparison of average expression levels of 204 genes that were downregulated by JMJD1A/JMJD1B depletion between the mutant ESCs. Introduction of *G9a* mutation in JMJD1A/JMJD1B-deficient background significantly restored the expression levels of those genes. ***$p < 0.001$ (Student's t test).

(B and C) JMJD1A/JMJD1B and G9A antagonistically tune the H3K9 methylation levels of *Oct3/4* and *Ccnd1* to ensure accurate transcription. (B) The H3K9me2 levels in the promoter regions of *Oct3/4* (left) and *Ccnd1* (right) were examined by performing

(legend continued on next page)

ChIP-seq analysis (Figure 6G). Notably, less than half the amount of input DNA was immunoprecipitated with anti-H3K9me2 antibody from JGTKO cell nuclei than from JMJD1A/JMJD1B-depleted cell nuclei, indicating that G9A might actually contribute to H3K9 di-methylation in JMJD1A/JMJD1B-depleted cells (Figure S4). The distribution profile of H3K9me2 on chromosome 11 of JGTKO cells is shown in Figure 6G. We found that *G9a* mutation resulted in decreased H3K9me2 levels throughout chromosome 11, confirming that G9A substantially contributes to H3K9 di-methylation in JMJD1A/JMJD1B-depleted cells. To address the target preference of G9A-mediated H3K9 methylation, the relationship between the decreased H3K9me2 levels due to *G9a* mutation in JMJD1A/JMJD1-depleted cells and gene densities of all chromosomes was statistically evaluated as in Figure 4B. No significant differences were detected in G9A-mediated H3K9 methylation levels between the gene-poor and gene-dense regions (Figure 6H). These data suggest that the target preference of G9A-mediated H3K9 methylation is less strict than that of JMJD1A and JMJD1B-mediated H3K9 demethylation, which preferentially targets gene-dense regions (Figure 4B).

G9a Mutation Rescues JMJD1A/JMJD1B-Depletion-Induced Transcriptional Downregulation

To address the question of whether *G9a* mutation also restores gene expression profiles in JMJD1A/JMJD1B-depleted cells, we examined the expression levels of 204 genes in JGTKO cells that were downregulated due to JMJD1A/JMJD1B depletion. As shown in Figure 7A, *G9a* mutation remarkably restored the expression levels of those genes. To investigate the roles of JMJD1A/JMJD1B-mediated H3K9 demethylation and G9A-mediated H3K9 methylation in transcription regulation at single-gene level, we examined H3K9 methylation and mRNA expression of *Oct3/4* and *Ccnd1* in the serial mutant ESC lines (Figures 7B and 7C, respectively). ChIP analyses demonstrated that the elevated H3K9me2 levels were rescued by the introduction of *G9a* mutation (Figure 7B), strongly suggesting that H3K9me2 levels of *Oct3/4* and *Ccnd1* were regulated by both JMJD1A/JMJD1B-mediated H3K9 demethylation and G9A-mediated H3K9 methylation. mRNA

analyses indicated typical inverse correlations between the H3K9me2 levels and the expression levels of *Oct3/4* and *Ccnd1*; the decreased mRNA expression levels of *Oct3/4* and *Ccnd1* were rescued by *G9a* mutation (Figures 7B and 7C). Thus, we conclude that the antagonistic activities between JMJD1A/JMJD1B and G9A collaboratively contribute to the tuning of H3K9 methylation levels in *Oct3/4* and *Ccnd1*. We summarize the function of JMJD1A/JMJD1B in the maintenance of ESCs as follows: H3K9 demethylases JMJD1A and JMJD1B ensure cell viability and transcriptional accuracy by removing the H3K9 methylation marks deposited by G9A in the gene-dense euchromatin (Figure 7D).

As shown in Figure 6B, JMJD1A/JMJD1B- and G9A-triple-KO cells clearly re-acquired growth potential, indicating that ESCs can survive in the absence of JMJD1A/JMJD1B- and G9A-mediated H3K9 methylation tuning. To address the possible importance of JMJD1A/JMJD1B- and G9A-mediated H3K9 methylation tuning for differentiation of ESCs, we cultured the JMJD1A/JMJD1B/G9A-triple-deficient JGTKO-1 line under differentiating condition without leukemia inhibitory factor. As shown in Figure S6, the JGTKO cell line immediately lost growth potential in the differentiating condition. We further examined the kinetics of mRNA expression of several pluripotency-associated genes (Figure S6). In wild-type cells, pluripotency-associated genes were downregulated concomitantly with differentiation. In contrast, some pluripotency-associated genes were not downregulated in the JGTKO line in the differentiating condition (Figure S6). These results indicate that collaborative H3K9 methylation tuning by JMJD1A/JMJD1B and G9A plays an indispensable role in the suppression of pluripotency-associated genes when ESCs undergo differentiation.

DISCUSSION

We previously demonstrated that JMJD1A and JMJD1B have intrinsic enzymatic activities for H3K9 demethylation (Kuroki et al., 2013a). Here, we report the functional overlap of JMJD1A and JMJD1B in early embryogenesis and ESC maintenance in mice. As expected, JMJD1A and JMJD1B

ChIP-qPCR analyses. Increased H3K9me2 levels in these genes in JMJD1A/JMJD1B-double-depleted cells were rescued by G9A depletion. (C) The expression levels of *Oct3/4* (left) and *Ccnd1* (right) were examined by RT-qPCR analyses. Reduced expression levels of these genes in JMJD1A/JMJD1B-double-depleted cells were rescued by G9A depletion. mRNA expression levels of wild-type cells were defined as 1. For (B) and (C), data are presented as means ± SD. n = 3 independent experiments. *p < 0.05; **p < 0.01; ***p < 0.001 (Student's t test).

(D) Schematic representation of the roles of JMJD1A/JMJD1B in ESCs. JMJD1A/JMJD1B ensure cell viability and transcriptional accuracy by antagonizing G9a-mediated H3K9 overmethylation in gene-rich euchromatin in ESCs. In wild-type ESCs, JMJD1A/JMJD1B preferentially remove H3K9 methylation marks from gene-rich euchromatin. The compound loss of JMJD1A/JMJD1B results in G9a-mediated H3K9 overmethylation in euchromatin, thereby inducing cell death and impaired gene expression.

are both expressed in developing embryos and ESCs (Figures 1 and 2, respectively). On the other hand, *Jmjd1a* single-mutant mice display unique phenotypes, such as defects of spermiogenesis (Liu et al., 2010; Okada et al., 2007), metabolism (Inagaki et al., 2009; Tateishi et al., 2009), and sex determination (Kuroki et al., 2013b). We speculate that *Jmjd1a* is highly expressed in these tissues and therefore plays a dominant role in H3K9 demethylation. According to this notion, protein expression profiles of JMJD1A and JMJD1B are distinctive in the human tissues (http://www.humanproteomemap.org/).

We demonstrated that the combined depletion of JMJD1A and JMJD1B has a synergistic effect on gene expression (Figure 5). It is plausible that the growth defect phenotype of JMJD1A/JMJD1B-depleted ESCs is attributed to distorted gene expression, at least partly. Note that the GO terms for the multiple metabolic pathways downregulated by JMJD1A/JMJD1B deficiency include the one-carbon and amino acid biosynthetic pathways (Figure S5). It is feasible that disorders in multiple metabolic pathways might induce the loss of ESC viability.

Mammalian cells have multiple H3K9 methyltransferases and demethylases with different product/substrate specificities and target specificities (Greer and Shi, 2012; Kooistra and Helin, 2012). The antagonistic activities of H3K9 methyltransferase and demethylase are considered to contribute to the tuning of the H3K9 methylation levels, but how and which combination of methyltransferase/demethylase contributes to this regulation were still unresolved. Here, we demonstrated that JMJD1A/JMJD1B demethylases and G9A methyltransferase are involved in the tuning of the H3K9 methylation levels (summarized in Figure 7D). To the best of our knowledge, this is the first study revealing the role sharing between demethylase and methyltransferase for the correct establishment of histone methylated epigenome. In this context, G9A-mediated H3K9 methylation seems to exhibit less specificity for the target region of chromosomes (Figure 6H). According to this notion, a previous ChIP-seq analysis demonstrated that G9A is located in almost all chromosomal regions (Mozzetta et al., 2014). On the other hand, ChIP-seq analysis in our present study revealed that JMJD1A/JMJD1B-mediated H3K9 demethylation may preferentially target gene-dense euchromatin (Figure 4B). How JMJD1A/JMJD1B exerts target specificity toward euchromatin needs to be ascertained. Like most of the histone modification enzymes, JMJD1A and JMJD1B do not contain typical DNA recognition motifs, strongly suggesting that the target specificity of these proteins is dependent on the interaction of other proteins. JMJD1A and JMJD1B bear the signature LXXLL motif indicative of a protein-protein interaction with the nuclear receptors. It was reported that JMJD1A is recruited to androgen-receptor target genes in

a hormone-dependent manner (Yamane et al., 2006). A recent study revealed that phosphorylation of JMJD1A strengthens the binding capacity to binding partner proteins, such as PPARγ (Abe et al., 2015). However, as shown in Figure 4D, it seems likely that JMJD1A/JMJD1B-mediated H3K9 demethylation can target megabase ranges of the chromosomal region. Thus, it is also conceivable that JMJD1A/JMJD1B forms a complex with a nuclear protein, which can recognize the global chromatin structure rather than specific DNA sequences.

Unexpectedly, our results indicate that JMJD1A/JMJD1B- and G9A-mediated H3K9 methylation tuning is dispensable for the maintenance of ESCs (Figure 6B). On the other hand, this tuning machinery seems to play an indispensable role when ESCs undergo differentiation because the downregulation of pluripotency-associated genes was compromised in the JGTKO line when cultured in the differentiating condition (Figure S6). A previous study demonstrated that the forced expression of protein kinase A in ESCs induces cellular differentiation concomitantly with G9A-mediated H3K9 methylation of the *Oct3/4* locus (Yamamizu et al., 2012). We demonstrated that the *Oct3/4* locus undergoes not only G9A-mediated H3K9 methylation but also JMJD1A/JMJD1B-mediated H3K9 demethylation to ensure correct expression levels (Figures 7B and 7C). It is plausible that the collaboration of JMJD1A/JMJD1B-mediated H3K9 demethylation and G9A-mediated H3K9 methylation may be essentially required for the rearrangement of H3K9 methylated epigenome upon differentiation. Based on the result that *G9a* mutation rescued compromised gene expression due to JMJD1A/JMJD1B depletion (Figure 7A), we speculate that the fine-tuning of H3K9 methylation by JMJD1 and G9A may contribute to transcriptional regulation of not only *Oct3/4* but also other genes important for ESC function.

It has been demonstrated that lysine methyltransferases and demethylases regulate methylation dynamics not only for histones but also for non-histone proteins (Hamamoto et al., 2015). Most recently, it was demonstrated that the GLP/G9A complex methylates lysine residues within the TARK motif of DNA Ligase 1, which is similar to the H3K9 methylation within the TARK motif of histone H3 (Ferry et al., 2017). To the best of our knowledge, the contribution of JMJD1A and JMJD1B toward the demethylation of non-histone protein substrates has not been reported. The possibility that JMJD1A/JMJD1B and G9A regulate methylation of non-histone proteins warrants further investigation.

Note that the levels of H3K9me2 and H3K9me3 in the triple-KO cells were slightly but significantly higher than those in the *G9a*-deficient cells (Figures 6D–6F). These data indicate that JMJD1A and JMJD1B demethylate the H3K9me2 and H3K9me3 marks deposited by H3K9 methyltransferase(s) other than G9A. We propose that the

balance in H3K9 methylation levels is maintained in a highly orchestrated manner, governed by multiple enzymes for methylation and demethylation.

EXPERIMENTAL PROCEDURES

Generation of Mutant Mice and ESCs

Serial knockin targeting vectors were constructed by the bacterial artificial chromosome recombineering technique (Copeland et al., 2001) and then introduced into the ESC line TT2. Detailed information for the generation of mutant mice and ESCs is described in Supplemental Information. All animal experiments were performed under the animal ethical guidelines of Tokushima University (experiment number 14,108, approved by The Ethics Committee of Tokushima University for Animal Research) and Kyoto University (experiment number A12-6-2, approved by Animal Experimentation Committee of Kyoto University).

ACCESSION NUMBERS

The accession numbers for the microarray data and the ChIP-seq data reported in this paper are GEO: GSE98761 and DDBJ: DRA006496, respectively.

SUPPLEMENTAL INFORMATION

Supplemental Information includes Supplemental Experimental Procedures, six figures, and two tables and can be found with this article online at https://doi.org/10.1016/j.stemcr.2018.02.002.

REFERENCES

Abe, Y., Rozqie, R., Matsumura, Y., Kawamura, T., Nakaki, R., Tsurutani, Y., Tanimura-Inagaki, K., Shiono, A., Magoori, K., Nakamura, K., et al. (2015). JMJD1A is a signal-sensing scaffold that regulates acute chromatin dynamics via SWI/SNF association for thermogenesis. Nat. Commun. *6*, 7052.

Copeland, N.G., Jenkins, N.A., and Court, D.L. (2001). Recombineering: a powerful new tool for mouse functional genomics. Nat. Rev. Genet. *2*, 769–779.

Feldman, N., Gerson, A., Fang, J., Li, E., Zhang, Y., Shinkai, Y., Cedar, H., and Bergman, Y. (2006). G9a-mediated irreversible epigenetic inactivation of Oct-3/4 during early embryogenesis. Nat. Cell Biol. *8*, 188–194.

Ferry, L., Fournier, A., Tsusaka, T., Adelmant, G., Shimazu, T., Matano, S., Kirsh, O., Amouroux, R., Dohmae, N., Suzuki, T., et al. (2017). Methylation of DNA ligase 1 by G9a/GLP recruits UHRF1 to replicating DNA and regulates DNA methylation. Mol. Cell *67*, 550–565.e5.

Greer, E.L., and Shi, Y. (2012). Histone methylation: a dynamic mark in health, disease and inheritance. Nat. Rev. Genet. *13*, 343–357.

Hamamoto, R., Saloura, V., and Nakamura, Y. (2015). Critical roles of non-histone protein lysine methylation in human tumorigenesis. Nat. Rev. Cancer *15*, 110–124.

Inagaki, T., Tachibana, M., Magoori, K., Kudo, H., Tanaka, T., Okamura, M., Naito, M., Kodama, T., Shinkai, Y., and Sakai, J. (2009). Obesity and metabolic syndrome in histone demethylase JHDM2a-deficient mice. Genes Cells *14*, 991–1001.

Kim, J.Y., Kim, K.B., Eom, G.H., Choe, N., Kee, H.J., Son, H.J., Oh, S.T., Kim, D.W., Pak, J.H., Baek, H.J., et al. (2012). KDM3B is the H3K9 demethylase involved in transcriptional activation of lmo2 in leukemia. Mol. Cell Biol. *32*, 2917–2933.

Kimura, H., Hayashi-Takanaka, Y., Goto, Y., Takizawa, N., and Nozaki, N. (2008). The organization of histone H3 modifications as revealed by a panel of specific monoclonal antibodies. Cell Struct. Funct. *33*, 61–73.

Kooistra, S.M., and Helin, K. (2012). Molecular mechanisms and potential functions of histone demethylases. Nat. Rev. Mol. Cell Biol. *13*, 297–311.

Kuroki, S., Akiyoshi, M., Tokura, M., Miyachi, H., Nakai, Y., Kimura, H., Shinkai, Y., and Tachibana, M. (2013a). JMJD1C, a JmjC domain-containing protein, is required for long-term maintenance of male germ cells in mice. Biol. Reprod. *89*, 93.

Kuroki, S., Matoba, S., Akiyoshi, M., Matsumura, Y., Miyachi, H., Mise, N., Abe, K., Ogura, A., Wilhelm, D., Koopman, P., et al. (2013b). Epigenetic regulation of mouse sex determination by the histone demethylase Jmjd1a. Science *341*, 1106–1109.

Liu, Z., Chen, X., Zhou, S., Liao, L., Jiang, R., and Xu, J. (2015). The histone H3K9 demethylase Kdm3b is required for somatic growth and female reproductive function. Int. J. Biol. Sci. *11*, 494–507.

Liu, Z., Zhou, S., Liao, L., Chen, X., Meistrich, M., and Xu, J. (2010). Jmjd1a demethylase-regulated histone modification is essential for cAMP-response element modulator-regulated gene expression and spermatogenesis. J. Biol. Chem. *285*, 2758–2770.

Mozzetta, C., Pontis, J., Fritsch, L., Robin, P., Portoso, M., Proux, C., Margueron, R., and Ait-Si-Ali, S. (2014). The histone H3 lysine 9 methyltransferases G9a and GLP regulate polycomb repressive complex 2-mediated gene silencing. Mol. Cell *53*, 277–289.

Okada, Y., Scott, G., Ray, M.K., Mishina, Y., and Zhang, Y. (2007). Histone demethylase JHDM2A is critical for Tnp1 and Prm1 transcription and spermatogenesis. Nature *450*, 119–123.

Shirato, H., Ogawa, S., Nakajima, K., Inagawa, M., Kojima, M., Tachibana, M., Shinkai, Y., and Takeuchi, T. (2009). A jumonji (Jarid2) protein complex represses cyclin D1 expression by methylation of histone H3-K9. J. Biol. Chem. *284*, 733–739.

Tachibana, M., Sugimoto, K., Nozaki, M., Ueda, J., Ohta, T., Ohki, M., Fukuda, M., Takeda, N., Niida, H., Kato, H., et al. (2002). G9a histone methyltransferase plays a dominant role in euchromatic histone H3 lysine 9 methylation and is essential for early embryogenesis. Genes Dev. *16*, 1779–1791.

Tachibana, M., Ueda, J., Fukuda, M., Takeda, N., Ohta, T., Iwanari, H., Sakihama, T., Kodama, T., Hamakubo, T., and Shinkai, Y. (2005). Histone methyltransferases G9a and GLP form heteromeric complexes and are both crucial for methylation of euchromatin at H3-K9. Genes Dev. *19*, 815–826.

Tateishi, K., Okada, Y., Kallin, E.M., and Zhang, Y. (2009). Role of Jhdm2a in regulating metabolic gene expression and obesity resistance. Nature *458*, 757–761.

Yamamizu, K., Fujihara, M., Tachibana, M., Katayama, S., Takahashi, A., Hara, E., Imai, H., Shinkai, Y., and Yamashita, J.K. (2012). Protein kinase A determines timing of early differentiation through epigenetic regulation with G9a. Cell Stem Cell *10*, 759–770.

Yamane, K., Toumazou, C., Tsukada, Y., Erdjument-Bromage, H., Tempst, P., Wong, J., and Zhang, Y. (2006). JHDM2A, a JmjC-containing H3K9 demethylase, facilitates transcription activation by androgen receptor. Cell *125*, 483–495.

Current Biology

Induction of DNA Methylation by Artificial piRNA Production in Male Germ Cells

Graphical Abstract
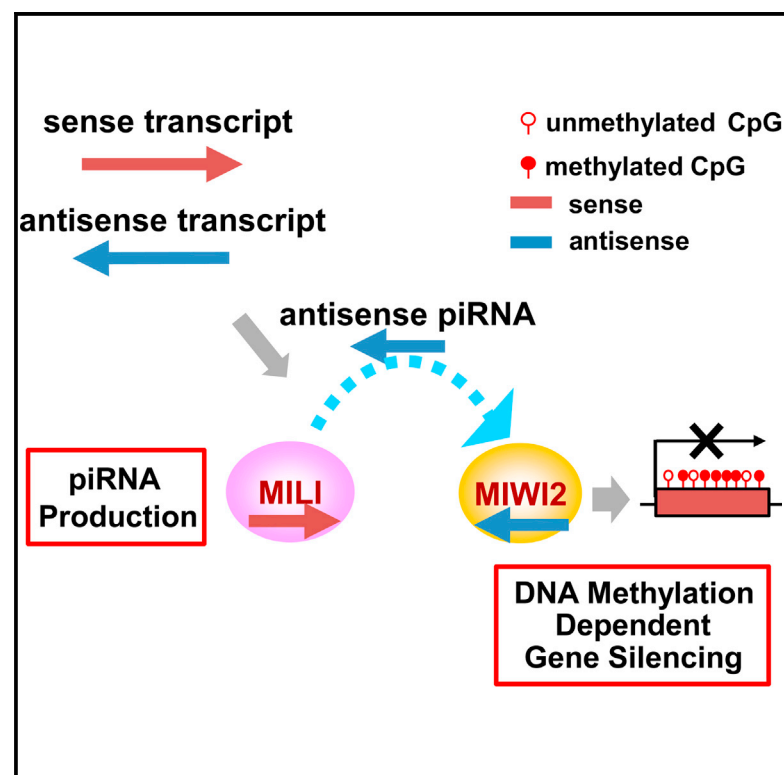
Authors

Daisuke Itou, Yusuke Shiromoto, ...,
Satomi Kuramochi-Miyagawa,
Toru Nakano

Correspondence

smiya@patho.med.osaka-u.ac.jp (S.K.-
M.),
tnakano@patho.med.osaka-u.ac.jp (T.N.)

In Brief

Itou et al. established an artificial piRNA production system by the concomitant expression of sense and antisense mRNAs in murine embryonic testes. This system made it possible to induce gene-specific DNA methylation by piRNAs in male germ cells and would be useful for the study of transgenerational epigenetic inheritance.

Highlights

- Concomitant expression of sense and antisense EGFP transgenes induced EGFP piRNAs

- EGFP transgenes were silenced by piRNA pathway-dependent DNA methylation

- piRNA-dependent gene silencing was introduced into the endogenous Dnmt3L gene

- Our piRNA induction system should be useful for the study of epigenetic inheritance

CrossMark

CellPress

CellPress

Induction of DNA Methylation by Artificial piRNA Production in Male Germ Cells

Daisuke Itou,[1,3] Yusuke Shiromoto,[2,3] Yukiho Shin-ya,[1,3] Chika Ishii,[1,3] Toru Nishimura,[1,3] Narumi Ogonuki,[4] Atsuo Ogura,[4] Hidetoshi Hasuwa,[5] Yoshitaka Fujihara,[5] Satomi Kuramochi-Miyagawa,[2,3,*] and Toru Nakano[1,2,3,*]

[1]Department of Pathology, Graduate School of Frontier Biosciences, Osaka University, Yamada-oka 2-2 Suita, Osaka 565-0871, Japan
[2]Medical School, Osaka University, Yamada-oka 2-2 Suita, Osaka 565-0871, Japan
[3]CREST, Japan Science and Technology Agency (JST), Saitama 332-0012, Japan
[4]RIKEN BioResources Center, Tsukuba 305-0074, Ibaraki, Japan
[5]Research Institute for Microbial Diseases, Osaka University, Yamada-oka 2-2 Suita, Osaka 565-0871, Japan
*Correspondence: smiya@patho.med.osaka-u.ac.jp (S.K.-M.), tnakano@patho.med.osaka-u.ac.jp (T.N.)
http://dx.doi.org/10.1016/j.cub.2015.01.060

SUMMARY

Global DNA demethylation and subsequent de novo DNA methylation take place in mammalian male embryonic germ cells [1–3]. P-element-induced wimpy testis (PIWI)-interacting RNAs (piRNAs), which are germline-specific small RNAs, have been postulated to be critically important for de novo DNA methylation of retrotransposon genes, and many proteins, including PIWI family proteins, play pivotal roles in this process [4–6]. In the embryonic mouse testis, two mouse PIWI proteins, mouse PIWI-like (MILI) and mouse PIWI2 (MIWI2), are involved in the biogenesis of piRNAs through the so-called ping-pong amplification cycle [7–10], and long single-stranded RNAs transcribed from the gene regions of piRNA clusters have been proposed to be the initial material [11–16]. However, it remains unclear whether transcription from the piRNA clusters is required for the biogenesis of piRNAs. To answer this question, we developed a novel artificial piRNA production system by simple expression of sense and antisense EGFP mRNAs in embryonic male germ cells in the piRNA biogenesis phase. EGFP expression was silenced by piRNA-dependent DNA methylation, indicating that concomitant expression of sense and antisense RNA transcripts is necessary and sufficient for piRNA production and subsequent piRNA-dependent gene silencing. In addition, we demonstrated that this artificial piRNA induction paradigm could be applied to an endogenous gene essential for spermatogenesis, DNMT3L [3, 17, 18]. This study not only provides novel insights into the molecular mechanisms of piRNA production, but also presents an innovative strategy for inducing epigenetic modification in germ cells.

RESULTS AND DISCUSSION

DNA Methylation of EGFP Transgene by Concomitant Expression of Antisense Transcripts

Comprehensive sequencing of piRNAs and genomic mapping of piRNAs suggest that long transcripts from piRNA clusters are required as the precursors for piRNAs [11–16]. There are two classes of murine piRNA clusters. One is embryonic piRNA clusters, which are important for MILI- and MIWI2-dependent retrotransposon-related ping-pong amplification of piRNAs. The other is pachytene piRNA clusters, which are MILI and MIWI dependent and related to intergenic sequences in general. Previous papers suggested that RNA transcripts containing retrotransposon sequences derived from the embryonic piRNA clusters were important for piRNA biogenesis [4]. However, how they are utilized as the substrate of piRNA and even whether they are a prerequisite for piRNA production have not yet been elucidated. It is also unknown why piRNAs corresponding to retrotransposons are preferentially produced. Our hypothesis, that neither long transcripts nor sequence preference is important for piRNA production, challenges the aforementioned two unproven general beliefs. In this study, we adopted a simple experimental system wherein sense and antisense EGFP transgenes were expressed in embryonic male germ cells during de novo DNA methylation. We used this paradigm to assess the induction of piRNA-dependent DNA methylation.

In the Oct4-EGFP mouse testis, EGFP expression was detectable from embryonic day 7 [19] to at least 2 weeks after birth (Figures 1A and S1B). Three lines of Miwi2-asEGFP transgenic mice (#1, #6, and #8), in which antisense EGFP mRNA expression was controlled by the 2.5-kb Miwi2 promoter, expressed antisense EGFP RNA transcripts in embryonic day 16.5 testes (Figures S1A and S1B). The antisense EGFP transcript was only expressed in the embryonic testis of the Miwi2-asEGFP mouse, consistent with the expression of MIWI2 [5, 6] (Figures S1B and S1C). We primarily used transgenic line #1 in subsequent experiments because of its high expression of antisense EGFP RNAs.

In double transgenic mice bearing both Oct4-EGFP and Miwi2-asEGFP transgenes, expression of EGFP was silenced

252

CrossMark

A

Wild Type

B

C

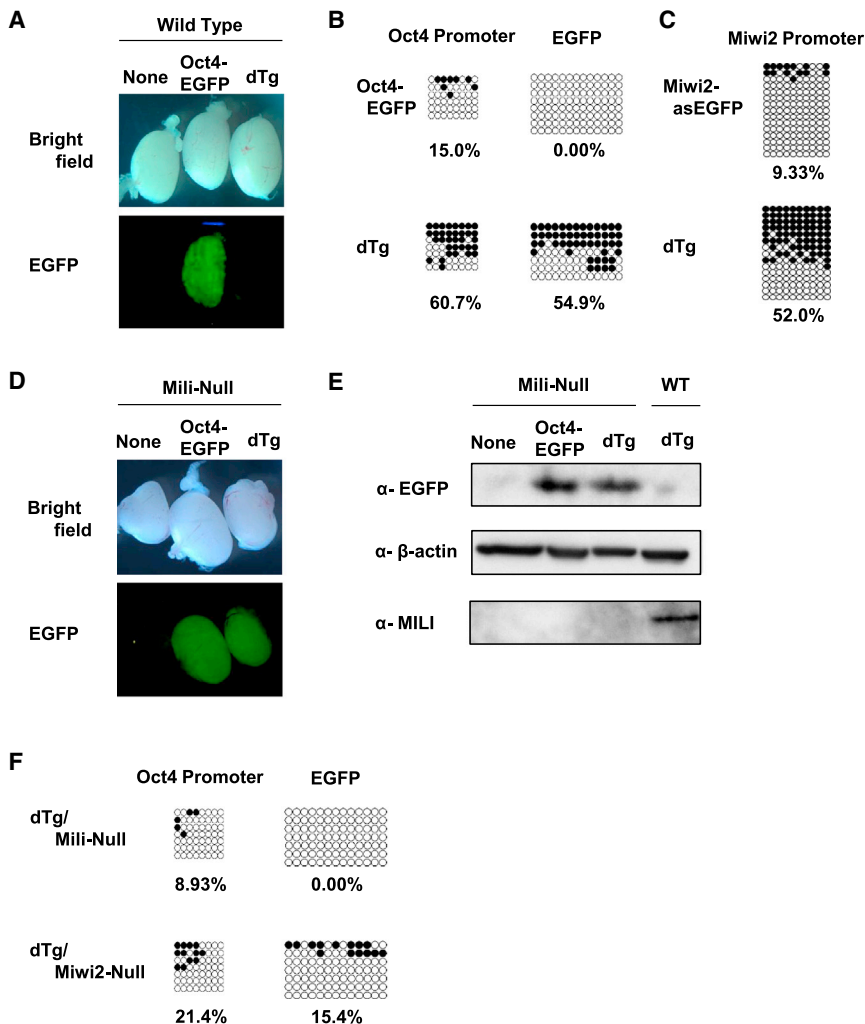Miwi2 Promoter

D

Mili-Null

E

F

Figure 1. Gene Silencing of EGFP by DNA Methylation in a piRNA-Dependent Manner

(A) Bright-field and fluorescent photographs of day 14 testes of wild-type, *Oct4-EGFP*, and double transgenic (dTg) mice, which were produced by crossing *Oct4-EGFP* mice with *Miwi2-asEGFP* mice.

(B) Bisulfite sequencing analysis of the *Oct4* promoter and *EGFP* gene of the *Oct4-EGFP* transgenic mice. Genomic DNA from day 14 EpCAM-positive germ cells from *Oct4-EGFP* transgenic mice and double transgenic mice was used to analyze *Oct4-EGFP*. White and black circles represent unmethylated and methylated cytosine, respectively.

(C) Bisulfite sequencing analysis of the *Miwi2-asEGFP* transgenes. Genomic DNA from E-CAD-HERIN-positive germ cells was used to analyze the *Miwi2*-promoter.

(D) Bright-field and fluorescent photographs of *Oct4-EGFP* and double transgenic mice testes under the MILI null condition. Data of the mice bearing no transgene (None), *Oct4-EGFP* transgene, and both *Oct4-EGFP* and *Miwi2-asEGFP* transgenes (dTg) are shown.

(E) Western blot analysis of day 14 *Oct4-EGFP* and double transgenic testes under the MILI null condition, using anti-EGFP and anti-MILI antibodies. β-ACTIN was used as an internal control.

(F) Bisulfite sequencing analysis of day 14 EpCAM-positive germ cells of double transgenic mice under MILI and MIWI2 null conditions.

at embryonic day 16.5 (Figure S1D) and at day 14 after birth (Figure 1A). Not only the representative *EGFP* antisense transgenic line (#1) but also the other lines (#6 and #8) showed essentially same silencing (Figure S1E). This suppression is unlikely to be a result of a direct effect of the antisense *EGFP* transcript because antisense *EGFP* was minimally or not at all expressed in male germ cells at day 14 (Figure S1C).

Next, we examined the DNA methylation status of the *Oct4-EGFP* transgene by bisulfite sequencing (Figure 1B). In male germ cells of double transgenic mice, methylation of the *Oct4-EGFP* promoter and the *EGFP*-coding region was significantly higher than that of the *Oct4-EGFP* mice. Although the expression of EGFP was utilized as a marker to visualize *EGFP* gene silencing, sense and antisense *EGFP* transgenes can be considered equivalent from the point of view of gene silencing through piRNA-dependent DNA methylation. Next, we examined the expression and DNA methylation of the *Miwi2-asEGFP* transgene (Figures S1F and 1C). Similar to the results for the *Oct4-EGFP* transgene, silenced expression of antisense *EGFP* and high DNA methylation of its promoter were detected in the double transgenic male germ cells. These data clearly demonstrate that expression of both sense and antisense transgenes was silenced by DNA methylation of their promoters. To exclude the possibility that the activity of the endogenous *Oct4* and *Miwi2* promoters in the double transgenic mice were affected by some unknown reasons, we carried out western blotting of the OCT4 and MIWI2 proteins (Figure S1G). The amounts of OCT4 and MIWI2 proteins in dTg embryonic testes were essentially the same as those in the control testes.

Involvement of Artificially Induced *EGFP*-Related piRNAs in the Gene Silencing of *EGFP* Transgenes

A critical question to answer was whether or not DNA methylation and subsequent gene silencing were dependent upon the piRNA pathway. To resolve this, we examined the expression of EGFP in double transgenic mice under *Mili*- and *Miwi2*-deficient conditions (described as dTg/*Mili* Null and dTg/*Miwi2* Null mice, respectively). Gross examination and western blotting analysis clearly demonstrated that the expression of EGFP, which was abrogated in the double transgenic mice, was recovered under *Mili* and *Miwi2* null conditions (Figures 1D and 1E and data not shown). Levels of methylation of the *Oct4-EGFP* promoter in the dTg/*Mili* Null and dTg/*Miwi2* Null mice were quite low, compared to the simple double transgenic mice (Figures 1B and 1F). These data demonstrate that gene silencing of *Oct4-EGFP* was dependent on MILI and MIWI2, i.e., the piRNA pathway.
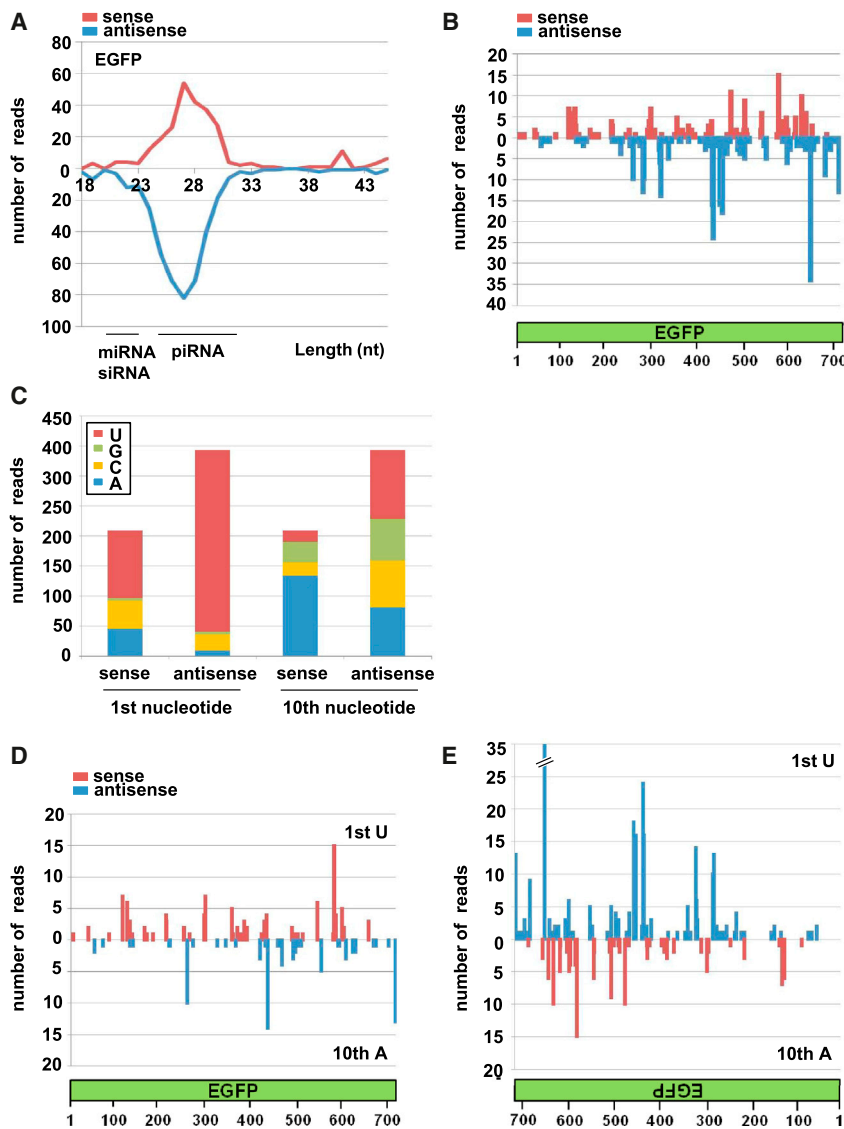
Figure 2. Deep Sequencing Analysis of Small RNAs in the Whole Embryonic Gonads of *EGFP* Double Transgenic

(A) Length distribution of the small RNAs corresponding to *EGFP*.

(B) Mapping of *EGFP* piRNAs. Red and blue bars indicate sense and antisense *EGFP* piRNAs, respectively.

(C) Numbers of the first and tenth nucleotides in *EGFP* piRNAs.

(D and E) Mapping of 1st U and 10th A *EGFP* piRNAs. Sense 1st U and antisense 10th A piRNAs corresponding to the sense *EGFP* are shown in (D). Antisense 1st U and sense 10th A piRNAs corresponding to the antisense *EGFP* are shown in (E).

orientations, and the results are shown in Figure S2. Approximately 50%–60% of the piRNAs matched the ping-pong signature (Figures S2A and S2C). Representative ping-pong signature data for sense and antisense *EGFP* sequences are shown in Figures S2B and S2D, respectively. These data clearly show that piRNAs for *EGFP* were produced via the ping-pong amplification cycle.

Silencing of *Dnmt3L* Gene through DNA Methylation Introduced by the Expression of Antisense *Dnmt3L*

Next, we aimed to establish whether this piRNA-dependent germ cell-specific gene silencing was applicable to endogenous genes. We selected *Dnmt3L* (DNA methyltransferase 3-like) as a model gene because it is expressed in embryonic male germ cells, and null mutant mice show defective DNA methylation of retrotransposon genes and impairment of spermatogenesis [3, 17, 18], similar to the *Mili* or *Miwi2* null mice [5, 6, 20]. We produced *Miwi2-asDnmt3L* transgenic mice expressing the antisense mRNA of *Dnmt3L* under the control of the *Miwi2* promoter. These transgenic mouse lines (#3 and #6, described as *asDnmt3L#3* and *asDnmt3L#6*, respectively) had significantly smaller testes than control mice (Figures 3A and S3A).

We used the *asDnmt3L#3* line in further experiments because it showed the more severe impairment of spermatogenesis (Figure S3B). Although *asDnmt3L#6* did not produce offsprings by natural mating, microscopic analysis showed some spermatogenesis in the mice. These germ cells possessed the fertilization ability when tested by intracytoplasmic sperm injection (ICSI) and elongating spermatid injection (ELSI) (Figure S3C). We assumed that this insufficient spermatogenesis was due to the lower DNA methylation level of the mice, presumably caused by the lower expression of the antisense transgene (Figure S3D).

DNMT3L proteins were drastically reduced in *asDnmt3L* embryonic testes, and spermatogenesis was severely impaired
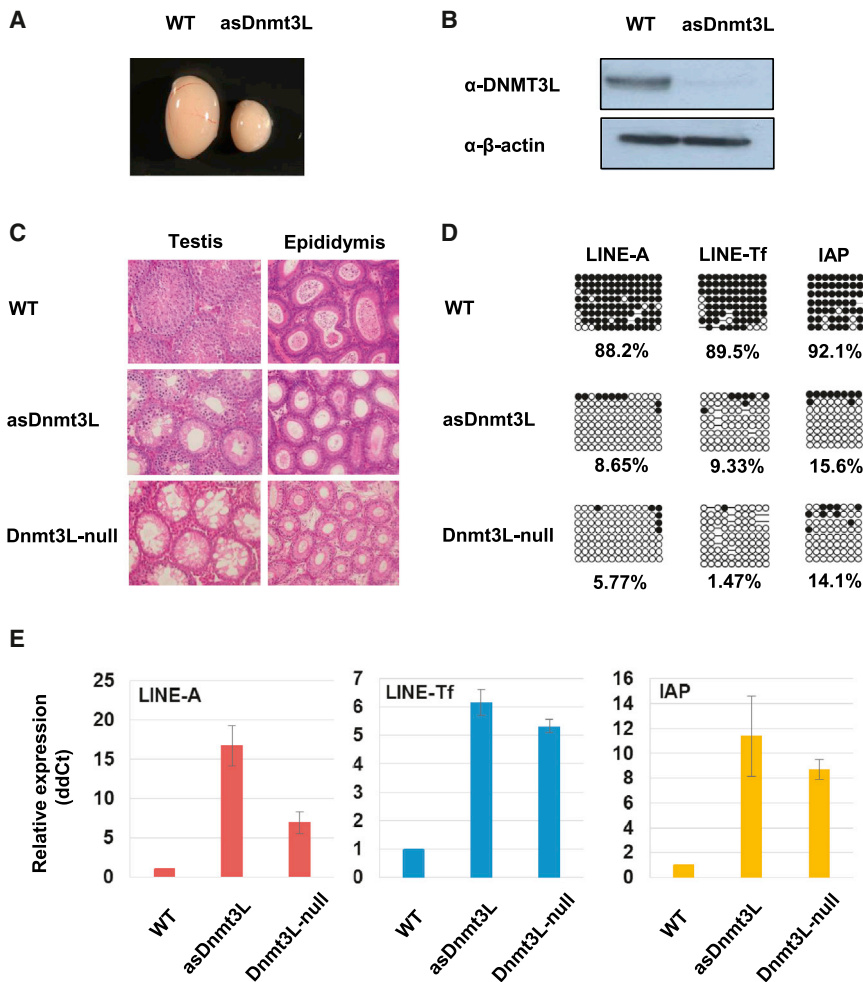
To examine the production of *EGFP*-related piRNAs, we carried out deep sequencing analysis of small RNAs in the whole embryonic gonads of double transgenic mice. A total of 552 reads of *EGFP*-related RNAs were obtained from the RNA sequence data (11,747,822) of 18–45 nt in length. The length of *EGFP*-related small RNAs showed a single peak of 25–31 nt (Figure 2A), which was consistent with the length of piRNAs. Both sense and antisense piRNAs related to *EGFP* were mapped to the entire *EGFP* sequence (Figure 2B). A strong sequence bias, namely, uracil in the first position (1st U) and adenine in the tenth position (10th A), has been reported as a signature of piRNA production [8–10]. As shown in Figure 2C, the majority of both sense and antisense *EGFP* piRNAs demonstrated a high 1st U bias (54% [113/209] and 88% [302/343], respectively). A strong 10th A bias was only evident in sense *EGFP*-piRNAs (64% [134/209]).

The distributions of 1st U and 10th A piRNAs against sense and antisense *EGFP* transgenes are shown in Figures 2D and 2E. These piRNAs were screened for the ping-pong signature (ten bases matching between 1st U and 10th A piRNAs with reverse

Figure 3. Impaired Spermatogenesis, Silencing of *Dnmt3L* Gene, and Increased Retrotransposon Expression in the Antisense *Dnmt3L* Transgenic Mouse

(A) Testes of 5-week-old wild-type and *asDnmt3L* mice.

(B) Western blotting analysis of embryonic day 16.5 wild-type and *asDnmt3L* testes, using anti-DNMT3L and anti-β-ACTIN antibodies.

(C) Hematoxylin-eosin staining of 5-week-old wild-type, *asDnmt3L*, and *Dnmt3L*-null mice.

(D) Bisulfite sequencing analysis of *LINE-A*, *LINE-Tf*, and *IAP* retrotransposon promoter regions. Genomic DNA was extracted from the EpCAM-positive germ cells of 2-week-old wild-type, *asDnmt3L*, and *Dnmt3L*-null mice.

(E) Quantitative RT-PCR analysis of *LINE-A*, *LINE-Tf*, and *IAP* retrotransposon expression. RNAs were extracted from whole testes of 2-week-old wild-type, *asDnmt3L*, and *Dnmt3L*-null mice. Error bars indicate SD of n = 3 biological replicates. *β-actin* was used as an internal control.

[14,069/22,266] antisense) and 10th A bias (70.7% [8,625/12,205] sense; 43.4% [9,670/22,266] antisense) (Figure 4E), and approximately 90% of *Dnmt3L* piRNAs harbored the ping-pong signature (Figure S4D). These data clearly demonstrate that expression of antisense *Dnmt3L* mRNA induces the production of corresponding *Dnmt3L* piRNAs and subsequent DNA methylation. We cannot exclude the possibility of post-transcriptional degradation of *Dnmt3L* because there exist antisense RNAs, which can potentially introduce the post-transcriptional modification. Transcriptional repression and post-transcriptional degradation are mutually unexclusive, and our results clearly showed that significant DNA methylation and subsequent transcriptional repression took place.

The absolute reads number of *Dnmt3L* piRNAs was much larger than that of *EGFP* piRNAs (34,471 and 552, respectively). Even taking the reads of miRNAs as an internal control (the reads of the dTg and *asDnmt3L* cells were 1,204,399 and 8,092,774, respectively), the relative amount of *Dnmt3L* piRNAs was still nine times higher compared to that of *EGFP* piRNAs (Figure S4E). Meanwhile, the characteristics of *Dnmt3L* piRNAs and *EGFP* piRNAs were a little different. Although sense and antisense *Dnmt3L* piRNAs showed the tendency of 10th A bias (Figure 4E), only antisense, but not sense, *EGFP* piRNAs possessed this preponderance (Figure 2C). These differences would be due to the amount of RNA transcripts, the balance between sense and antisense transcripts, and/or the sequence differences of the two kinds of genes.

(Figures 3B and 3C). DNA hypomethylation of the promoter regions of *LINE-1* and *IAP* retrotransposons and subsequent abrogation of gene silencing were observed in *asDnmt3L* male germ cells (Figures 3D and 3E). This phenotype was essentially identical to that of the *Dnmt3L*-null mice, strongly suggesting that piRNA-mediated gene silencing of *Dnmt3L* takes place in *asDnmt3L* embryonic testes. The DNA methylation status of control regions of the *Dnmt3L* gene, spanning from the promoter to the second exon [21–23], was significantly increased in the *asDnmt3L* male germ cells (Figure 4A). It is quite likely that the observed phenotype is manifested by DNA methylation of *Dnmt3L* in a piRNA-dependent manner. Otherwise, the phenotype of these transgenic mice cannot be explained.

Comprehensive Analysis of *Dnmt3L*-Related piRNAs

Next, we carried out deep sequencing analysis of small RNAs in the *asDnmt3L* whole embryonic gonads. Although there were very few *Dnmt3L*-related piRNAs in the control male embryonic germ cells, a significant number of piRNAs were observed in the transgenic mice (Figures 4B, 4C, and S4A–S4C). Mapping of *Dnmt3L*-associated piRNAs demonstrated that these piRNAs were produced from various regions of the *Dnmt3L* mRNAs (Figure 4D). In addition, both sense and antisense *Dnmt3L* piRNAs harbor high 1st U (43.6% [5,323/12,205] sense; 63.2%

Usefulness and Utility of Artificial piRNA Induction System

Our data support two important concepts. One is that retrotransposon sequences and transcription from piRNA clusters
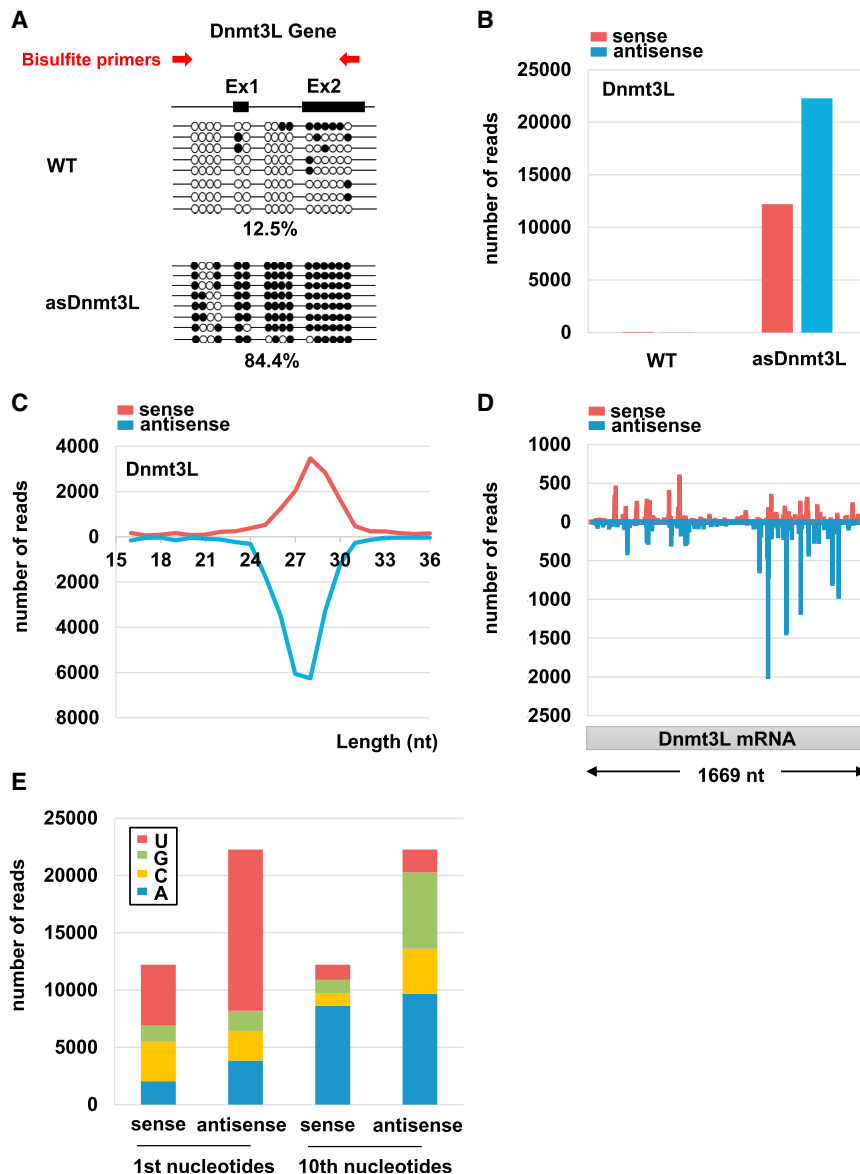
A Dnmt3L Gene

Bisulfite primers

Ex1 Ex2

WT

12.5%

asDnmt3L

84.4%

B Dnmt3L

- sense
- antisense

number of reads

WT asDnmt3L

C Dnmt3L

- sense
- antisense

number of reads

15 18 21 24 27 30 33 36

Length (nt)

D

- sense
- antisense

number of reads

Dnmt3L mRNA

1669 nt

E

- U
- G
- C
- A

number of reads

sense antisense sense antisense

1st nucleotides 10th nucleotides

Figure 4. Induction of *Dnmt3L* Gene piRNA Production and DNA Methylation by Expression of Antisense *Dnmt3L* mRNA

(A) Bisulfite sequencing of the control region of the *Dnmt3L* gene. Genomic DNA was extracted from EpCAM-positive germ cells of 2-day-old wild-type and *asDnmt3L* mice. Black bars indicate exons in the *Dnmt3L* promoter. Red arrows represent the primers used for the bisulfite sequence.

(B–E) Deep sequencing analysis of small RNAs in *asDnmt3L* whole embryonic gonads. Numbers of small RNAs with 25–31 nt length corresponding to the *Dnmt3L* sequence are shown in (B). Length distribution of small RNAs corresponding to the *Dnmt3L* sequence is shown in (C). Mapping of *Dnmt3L* piRNAs is shown in (D). Red and blue bars indicate the sense and antisense strands, respectively. Numbers of the first and tenth nucleotides in *Dnmt3L* piRNAs are shown in (E).

notion that the transgene integration site was not in the active piRNA clusters. Thus, our data suggest that the transcription from the piRNA cluster is not necessarily a critical factor for piRNA biogenesis if sense and antisense RNAs are co-expressed.

There were *EGFP*-related piRNAs in the *Oct4-EGFP* and *Miwi2-asEGFP* transgenic mice embryonic testes (8 in 22,098,877 and 273 in 18,792,650 of the RNAs with 18 to 45 nt length, respectively). Similarly, although the numbers were quite low, there were endogenous sense piRNAs including the piRNAs corresponding to *Dnmt3L* in the control embryonic male germ cells (Figures S4A–S4C). Such "seed" *EGFP* and *Dnmt3L* piRNAs may have some roles in the initial step of ping-pong cycle in the dTg and *Dnmt3L* antisense

are irrelevant to the piRNA biosynthesis of embryonic mouse male germ cells. Recently, it was demonstrated that *EGFP*-related piRNAs were produced in flies, mice, and cultured silkworm ovary cells, as shown by inserting an *EGFP* sequence into their piRNA clusters, suggesting that the locus of the gene is important for piRNA production [24–26]. These papers highlighted the importance of the piRNA cluster region in piRNA production. To identify the insertion sites of *Miwi2-asEGFP* transgenes, capture sequence analysis was performed as described in Figure S2E and Table S1. In silico piRNA cluster analysis by proTRAC [27] showed that there were 821 typical piRNA clusters in the dTg mice and that the genomic insertion sites of the transgenes were not in the piRNA clusters (Table S2). RT-PCR analysis using the primers between the exogenous *Miwi2* promoter and the antisense *EGFP* revealed that there were no RNA transcripts from the upstream regions of antisense *EGFP* (data not shown). These data supported the

transgenic mice. However, considering that there were many more abundant sense piRNAs in these transgenic mice embryonic testes, both sense and antisense transcripts should have been necessary for the efficient piRNA production even in this case.

The second important finding is the utility of piRNA-dependent silencing of endogenous gene(s). Our simple experimental system for inducing artificial piRNAs and subsequent DNA methylation-dependent gene silencing provides a novel procedure for induction of DNA methylation to inhibit gene expression during spermatogenesis. Now we are producing transgenic mouse lines that express antisense RNAs of various genes in the embryonic germ cells under the control of *Miwi2* promoter. Moreover, we believe that sperm containing abnormal DNA methylation patterns introduced by piRNA represent a useful tool for the study of transgenerational epigenetic inheritance.

EXPERIMENTAL PROCEDURES

Details are shown in the Supplemental Experimental Procedures. All animal experiments were performed in accordance with the general guidelines of The Institute of Experimental Animal Sciences, Osaka University Medical School.

SUPPLEMENTAL INFORMATION

Supplemental Information includes Supplemental Experimental Procedures, four figures, and two tables and can be found with this article online at http://dx.doi.org/10.1016/j.cub.2015.01.060.

REFERENCES

1. Aravin, A.A., and Bourc'his, D. (2008). Small RNA guides for de novo DNA methylation in mammalian germ cells. Genes Dev. *22*, 970–975.

2. Saitou, M., Kagiwada, S., and Kurimoto, K. (2012). Epigenetic reprogramming in mouse pre-implantation development and primordial germ cells. Development *139*, 15–31.

3. Bourc'his, D., and Bestor, T.H. (2004). Meiotic catastrophe and retrotransposon reactivation in male germ cells lacking Dnmt3L. Nature *431*, 96–99.

4. Aravin, A.A., Sachidanandam, R., Bourc'his, D., Schaefer, C., Pezic, D., Toth, K.F., Bestor, T., and Hannon, G.J. (2008). A piRNA pathway primed by individual transposons is linked to de novo DNA methylation in mice. Mol. Cell *31*, 785–799.

5. Carmell, M.A., Girard, A., van de Kant, H.J., Bourc'his, D., Bestor, T.H., de Rooij, D.G., and Hannon, G.J. (2007). MIWI2 is essential for spermatogenesis and repression of transposons in the mouse male germline. Dev. Cell *12*, 503–514.

6. Kuramochi-Miyagawa, S., Watanabe, T., Gotoh, K., Totoki, Y., Toyoda, A., Ikawa, M., Asada, N., Kojima, K., Yamaguchi, Y., Ijiri, T.W., et al. (2008). DNA methylation of retrotransposon genes is regulated by Piwi family members MILI and MIWI2 in murine fetal testes. Genes Dev. *22*, 908–917.

7. Castel, S.E., and Martienssen, R.A. (2013). RNA interference in the nucleus: roles for small RNAs in transcription, epigenetics and beyond. Nat. Rev. Genet. *14*, 100–112.

8. Siomi, M.C., Sato, K., Pezic, D., and Aravin, A.A. (2011). PIWI-interacting small RNAs: the vanguard of genome defence. Nat. Rev. Mol. Cell Biol. *12*, 246–258.

9. Ishizu, H., Siomi, H., and Siomi, M.C. (2012). Biology of PIWI-interacting RNAs: new insights into biogenesis and function inside and outside of germlines. Genes Dev. *26*, 2361–2373.

10. Aravin, A.A., Hannon, G.J., and Brennecke, J. (2007). The Piwi-piRNA pathway provides an adaptive defense in the transposon arms race. Science *318*, 761–764.

11. Aravin, A.A., Sachidanandam, R., Girard, A., Fejes-Toth, K., and Hannon, G.J. (2007). Developmentally regulated piRNA clusters implicate MILI in transposon control. Science *316*, 744–747.

12. Rangan, P., Malone, C.D., Navarro, C., Newbold, S.P., Hayes, P.S., Sachidanandam, R., Hannon, G.J., and Lehmann, R. (2011). piRNA production requires heterochromatin formation in Drosophila. Curr. Biol. *21*, 1373–1379.

13. Zhang, F., Wang, J., Xu, J., Zhang, Z., Koppetsch, B.S., Schultz, N., Vreven, T., Meignin, C., Davis, I., Zamore, P.D., et al. (2012). UAP56 couples piRNA clusters to the perinuclear transposon silencing machinery. Cell *151*, 871–884.

14. Pane, A., Jiang, P., Zhao, D.Y., Singh, M., and Schüpbach, T. (2011). The Cutoff protein regulates piRNA cluster expression and piRNA production in the Drosophila germline. EMBO J. *30*, 4601–4615.

15. Watanabe, T., Tomizawa, S., Mitsuya, K., Totoki, Y., Yamamoto, Y., Kuramochi-Miyagawa, S., Iida, N., Hoki, Y., Murphy, P.J., Toyoda, A., et al. (2011). Role for piRNAs and noncoding RNA in de novo DNA methylation of the imprinted mouse Rasgrf1 locus. Science *332*, 848–852.

16. Gu, W., Lee, H.C., Chaves, D., Youngman, E.M., Pazour, G.J., Conte, D., Jr., and Mello, C.C. (2012). CapSeq and CIP-TAP identify Pol II start sites and reveal capped small RNAs as C. elegans piRNA precursors. Cell *151*, 1488–1500.

17. Hata, K., Kusumi, M., Yokomine, T., Li, E., and Sasaki, H. (2006). Meiotic and epigenetic aberrations in Dnmt3L-deficient male germ cells. Mol. Reprod. Dev. *73*, 116–122.

18. Webster, K.E., O'Bryan, M.K., Fletcher, S., Crewther, P.E., Aapola, U., Craig, J., Harrison, D.K., Aung, H., Phutikanit, N., Lyle, R., et al. (2005). Meiotic and epigenetic defects in Dnmt3L-knockout mouse spermatogenesis. Proc. Natl. Acad. Sci. USA *102*, 4068–4073.

19. Yoshimizu, T., Sugiyama, N., De Felice, M., Yeom, Y.I., Ohbo, K., Masuko, K., Obinata, M., Abe, K., Schöler, H.R., and Matsui, Y. (1999). Germline-specific expression of the Oct-4/green fluorescent protein (GFP) transgene in mice. Dev. Growth Differ. *41*, 675–684.

20. Kuramochi-Miyagawa, S., Kimura, T., Ijiri, T.W., Isobe, T., Asada, N., Fujita, Y., Ikawa, M., Iwai, N., Okabe, M., Deng, W., et al. (2004). Mili, a mammalian member of piwi family gene, is essential for spermatogenesis. Development *131*, 839–849.

21. Hu, Y.G., Hirasawa, R., Hu, J.L., Hata, K., Li, C.L., Jin, Y., Chen, T., Li, E., Rigolet, M., Viegas-Péquignot, E., et al. (2008). Regulation of DNA methylation activity through Dnmt3L promoter methylation by Dnmt3 enzymes in embryonic development. Hum. Mol. Genet. *17*, 2654–2664.

22. Shovlin, T.C., Bourc'his, D., La Salle, S., O'Doherty, A., Trasler, J.M., Bestor, T.H., and Walsh, C.P. (2007). Sex-specific promoters regulate Dnmt3L expression in mouse germ cells. Hum. Reprod. *22*, 457–467.

23. O'Doherty, A.M., Rutledge, C.E., Sato, S., Thakur, A., Lees-Murdock, D.J., Hata, K., and Walsh, C.P. (2011). DNA methylation plays an important role in promoter choice and protein production at the mouse Dnmt3L locus. Dev. Biol. *356*, 411–420.

24. Kawaoka, S., Mitsutake, H., Kiuchi, T., Kobayashi, M., Yoshikawa, M., Suzuki, Y., Sugano, S., Shimada, T., Kobayashi, J., Tomari, Y., and Katsuma, S. (2012). A role for transcription from a piRNA cluster in de novo piRNA production. RNA *18*, 265–273.

25. Muerdter, F., Olovnikov, I., Molaro, A., Rozhkov, N.V., Czech, B., Gordon, A., Hannon, G.J., and Aravin, A.A. (2012). Production of artificial piRNAs in flies and mice. RNA *18*, 42–52.

26. Yamamoto, Y., Watanabe, T., Hoki, Y., Shirane, K., Li, Y., Ichiiyanagi, K., Kuramochi-Miyagawa, S., Toyoda, A., Fujiyama, A., Oginuma, M., et al. (2013). Targeted gene silencing in mouse germ cells by insertion of a homologous DNA into a piRNA generating locus. Genome Res. *23*, 292–299.

27. Rosenkranz, D., and Zischler, H. (2012). proTRAC—a software for probabilistic piRNA cluster detection, visualization and analysis. BMC Bioinformatics *13*, 5.

Loss of MAX results in meiotic entry in mouse embryonic and germline stem cells

Ayumu Suzuki[1], Masataka Hirasaki[1], Tomoaki Hishida[1,2], Jun Wu[2], Daiji Okamura[2,3], Atsushi Ueda[1], Masazumi Nishimoto[1], Yutaka Nakachi[4,5], Yosuke Mizuno[5], Yasushi Okazaki[4,5], Yasuhisa Matsui[6,7], Juan Carlos Izpisua Belmonte[2] & Akihiko Okuda[1]

Meiosis is a unique process that allows the generation of reproductive cells. It remains largely unknown how meiosis is initiated in germ cells and why non-germline cells do not undergo meiosis. We previously demonstrated that knockdown of *Max* expression, a gene encoding a partner of MYC family proteins, strongly activates expression of germ cell-related genes in ESCs. Here we find that complete ablation of *Max* expression in ESCs results in profound cytological changes reminiscent of cells undergoing meiotic cell division. Furthermore, our analyses uncovers that *Max* expression is transiently attenuated in germ cells undergoing meiosis *in vivo* and its forced reduction induces meiosis-like cytological changes in cultured germline stem cells. Mechanistically, *Max* depletion alterations are, in part, due to impairment of the function of an atypical PRC1 complex (PRC1.6), in which MAX is one of the components. Our data highlight MAX as a new regulator of meiotic onset.

[1] Division of Developmental Biology, Research Center for Genomic Medicine, Saitama Medical University, Yamane Hidaka, Saitama 350-1241, Japan. [2] Gene Expression Laboratory, Salk Institute for Biological Studies, 10010 North Torrey Pines Road, La Jolla, California 92037, USA. [3] Universidad Católica San Antonio de Murcia (UCAM) Campus de los Jerónimos, No. 135, Guadalupe, 30107 Murcia, Spain. [4] Division of Translational Research, Research Center for Genomic Medicine, Saitama Medical University, Yamane Hidaka, Saitama 350-1241, Japan. [5] Division of Functional Genomics and Systems Medicine, Research Center for Genomic Medicine, Saitama Medical University, Yamane Hidaka, Saitama 350-1241, Japan. [6] Cell Resource Center for Biomedical Research, Institute of Development, Aging and Cancer, Tohoku University, Sendai 980-8575, Japan. [7] Japan Agency for Medical Research and Development and Development-Core Research for Evolutionary Science and Technology (AMED-CREST), Tokyo 100-0004, Japan. Correspondence and requests for materials should be addressed to J.C.I.B. (email: belmonte@salk.edu) or to A.O. (email: akiokuda@saitama-med.ac.jp).

Meiosis is a specialized cell division process that produces gametes with a haploid genome[1]. Up to date, several reports have demonstrated significant conservation among species in the molecular basis underlying meiosis[2]. However, the molecular mechanisms that allow switching from mitotic to meiotic cell division in germ cells do not appear to be conserved across species or even between sexes within the same species. *Stra8*, whose expression is upregulated by retinoic acid (RA), has been shown to play crucial roles in premeiotic DNA replication[3–6] and constitutes a physiological and crucial regulator of the initiation of meiosis in both sexes[7–10]. In addition to the RA–Stra8 signalling pathway, it is plausible that unknown negative regulator of meiosis may prevent its premature entry in germ cells or ectopic induction in non-germ cells.

Recently, we demonstrated that knockdown of expression of the *Max* gene, encoding an indispensable partner for transcription factor c-MYC in embryonic stem cells (ESCs), leads to strong induction of germ cell-related gene expressions[11]. Notably, loss of *Max* expression in ESCs does not significantly alter the expression levels of primordial germ cell (PGC) specification genes such as *Blimp1* and *Stella* (also known as *Prdm1* and *Dppa3*, respectively), but rather selectively upregulates expression of genes related to meiotic cell division[11]. This preferential expression of meiosis-related genes in *Max* knockdown ESCs prompted us to explore the possibility that MAX might be part of the mechanism that safeguards meiosis by controlling the physiological timing of meiosis onset and preventing ectopic meiosis.

In this study, we found that *Max* depletion in ESCs not only upregulated the expression of meiosis-related genes but also induced the cytological changes reminiscent of germ cells at leptotene and zygotene stages of meiosis. Furthermore, our data revealed that these cytological changes even occurred in ESCs cultured in stringent 2i condition that renders ESCs refractory to cellular differentiation. This implies a direct conversion of *Max*-null ESCs to a meiosis-like state bypassing PGC differentiation. Moreover, we demonstrated that *Stra8*, but not *Blimp1*, was required for these cytological changes. Our analyses revealed that the *Max* gene undergoes a strong decline in expression during physiological meiosis in both male and female germs cells. Forced reduction of *Max* expression levels in germline stem cells (GSCs)[12,13] by lentivirus-mediated knockdown induced meiosis-like cytological changes. Our findings in *Max*-null ESCs may reflect a physiological role for MAX during *in vivo* meiosis. *Max*-null ESCs may serve as a useful *in vitro* tool for studying the molecular mechanisms governing mitotic versus meiotic cell divisions. Mechanistically, our data indicate that these cytological changes are the result of loss of function of a variant PRC1 complex (PRC1.6) in which MAX is a component[14,15].

Results

Induction of meiosis-related genes in *Max*-null ESCs. Our previous RNA interference screen uncovered *Max* as a strong suppressor of the expression of germ cell-related genes such as *Ddx4* (also known as *Mvh*, mouse Vasa homologue) and *Dazl*, in ESCs[11]. Owing to residual *Max* expression in knockdown experiments, we hypothesized that *Max* knockout may elicit more profound effects. We first analysed our *Max*-null ESC transcriptome data set (GSE27881) reported previously. In these cells, the endogenous *Max* gene was homozygously disrupted, and doxycycline (Dox)-regulatable expression of MAX was introduced using the tetracycline-off system[16]. Consistent with our hypothesis, expression levels of many germ cell-related genes were elevated in *Max*-null ESCs, of which most are

meiosis-related (Fig. 1a,b and Supplementary Fig. 1). Some of the meiotic genes, such as *Stra8* and *Dazl*, showed progressive increase in the expression levels following Dox treatment, while expression of others, such as *Hormad1* and *Stk31*, peaked at around day 4 and abruptly dropped thereafter. However, it is unknown whether the latter expression dynamics are caused by a negative feedback loop of regulation of these meiotic genes or simply a consequence of extensive cell death phenotype associated with meiotic-like *Max*-null ESCs. Unlike meiosis-related genes, PGC specification genes such as *Blimp1* and *Dppa3* did not show appreciable alterations in their expression levels on Dox treatment. We also noted that the expression levels of genes encoding meiosis-specific cohesion components, such as *Rec8* and *Smc1b*, were elevated, to a lesser extent, in Dox-treated cells compared with untreated controls. We also examined the expression of genes encoding key regulators of DNA recombination and found most of them remained unchanged, although a modest increase was evident in *Spo11* expression. These results implied that *Max*-null ESCs exhibited a partial, but not complete, gene expression pattern characteristic of meiotic cells (Supplementary Fig. 1). In addition, we also observed increased expression of two-cell embryo signature genes such as *Zscan4* and *Dub1* (refs 17,18; Fig. 1a,b and Supplementary Fig. 1). However, flow cytometric analyses of Dox-inducible *Max*-null ESCs bearing a DsRed reporter gene, which faithfully recapitulates the endogenous *Zscan4* expression profile with an aid of 5'-flanking region of the gene, indicated that DsRed- and STRA8-positive cells, both of which became prominent after *Max* depletion in ESCs, did not significantly overlap, but were rather mutually exclusive (Supplementary Fig. 2). These data implied that meiosis-like induction and activation of two-cell embryo gene signatures are independent phenomena. As expected, gene ontology (GO) analysis revealed over-representation of genes related to meiosis and sexual reproduction (Fig. 1c).

Max-null ESCs show meiosis-like cytological changes. Expression of meiosis-related genes led us to examine cytological changes in *Max*-null ESCs. To this end we performed immunocytochemical analyses with an antibody against SYCP3, one of the major components of the synaptonemal complex[19,20]. After 8 days of Dox treatment, about 4–5% of *Max*-null ESCs showed a SYCP3-immunostaining pattern that is reminiscent of germ cells undergoing meiosis (Fig. 2a,b). We observed about 20% STRA8-positive cells among all *Max*-null ESCs treated with Dox for 6 days (Supplementary Fig. 2). Most STRA8-positive cells, however, failed to proceed to the stage acquiring a meiosis-like SYCP3-staining pattern. To assess the stages of meiosis in meiosis-like cells from *Max*-null ESCs, we established a criterion to distinguish the stages based on the average length of SYCP3-stained regions observed in the chromosomes of germ cells in seminiferous tubules of the testis (Supplementary Fig. 3). Our analyses indicated that meiosis-like cells derived from *Max*-null ESCs following 6 days' Dox treatment were mostly preleptotene-like, with some cells progressed to the leptotene-like state. And longer Dox treatment (8 or 10 days) increased the percentages of these cells and also yielded cells bearing SYCP3-staining patterns similar to germ cells at zygotene stages of meiotic cell division (Fig. 2b). However, no cell was scored as pachytene-like even with extended Dox treatment (Fig. 2a,b). To confirm these observations, we conducted co-staining with antibodies against SYCP3 together with other meiotic markers. First, similar to the normal progression of meiosis, we found that STRA8 expression was more enriched in cells representing the early stages of meiosis and much less in cells at a more advanced
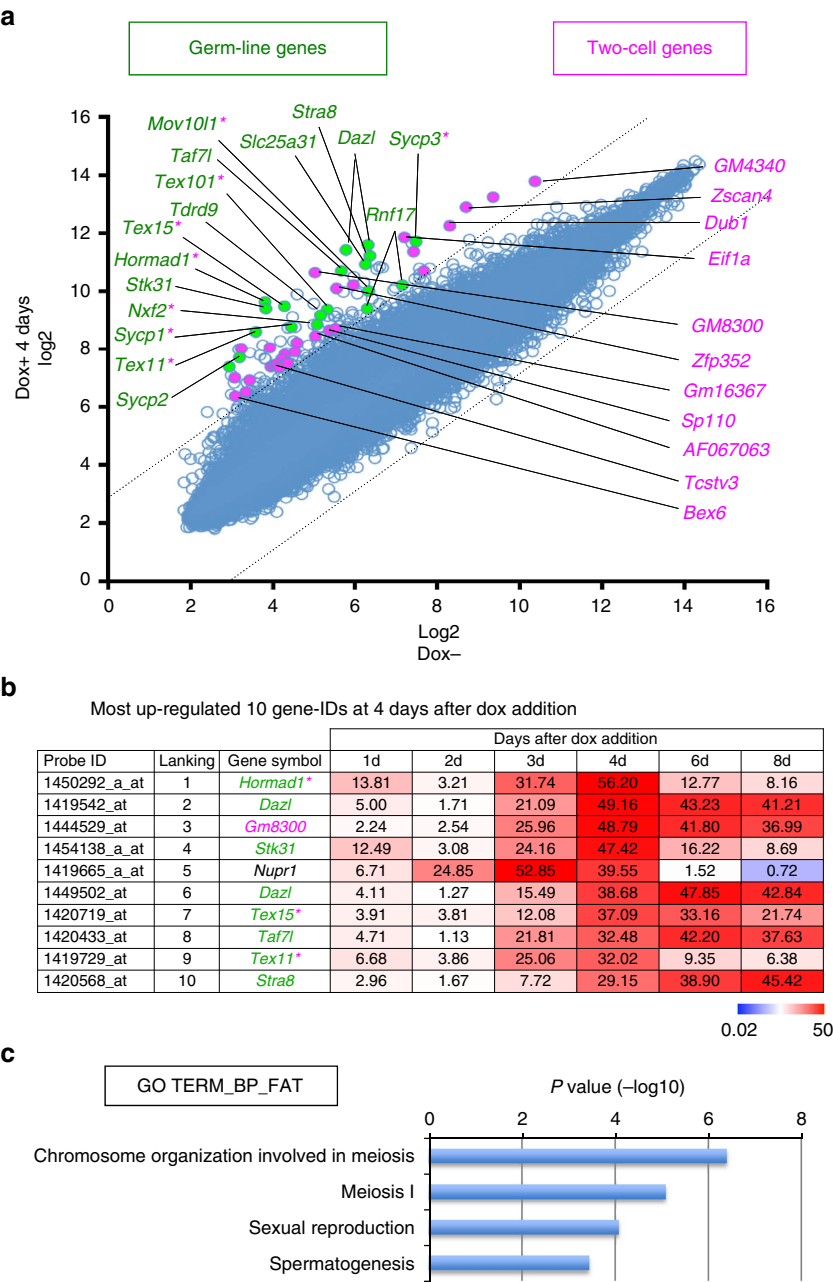
Figure 1 | Elevation of germ cell- and two-cell embryo-related genes in ESCs subjected to *Max* expression ablation. (**a**) Scatter plots of DNA microarray data from untreated and Dox-treated *Max*-null ESCs for 4 days using our previously deposited DNA microarray data under accession number GSE27881. Among genes with highly elevated expression in Dox-treated *Max*-null ESCs compared with that in untreated control cells (eightfold or higher), genes related to germ cells (green) and/or two-cell embryos denoted by Macfarlan *et al.*[18] (pink) are highlighted. Genes belonging to both categories are green with pink asterisks added to the gene names. (**b**) List of probe identifications (IDs) that showed the most conspicuous upregulation (top 10) in *Max*-null ESCs treated with Dox for 4 days (4d) and their expression changes during *Max* expression ablation in ESCs. *Dazl* is duplicated with different probe IDs. (**c**) GO analyses of genes showing more than eightfold higher expression in Dox-treated *Max*-null ESCs using DAVID software. The *P* value cutoff was set to $<1 \times 10^{-3}$.

stage with a zygotene-like SYCP3-staining pattern (Fig. 2c). We also found that cells with a leptotene-like SYCP3-staining pattern showed a strong γH2AX signal, similar to meiotic cells at this stage (Fig. 2d). Furthermore, REC8 and SYCP3 were co-localized in some, but not all, of the cells with a zygotene-like SYCP3-staining pattern (Supplementary Fig. 4a), likely due to less conspicuous induction of *Rec8* compared with that of other meiotic marker genes such as *Stra8* and *Sycp3* (Supplementary Fig. 1). We also conducted immunostaining with an antibody against SYCP1 that is known to play a crucial role in the formation of the synaptonemal complex at the pachytene stage

of meiosis, in which two paired homologous chromosomes (four chromosomes in total) are brought into a juxtaposition as a prerequisite step for the subsequent crossover[21–23]. Although SYCP1 expression was detected in some cells, we did not observe extensive overlap of SYCP1 signals with that of the SYCP3 on chromosomes (Supplementary Fig. 4b). These results were consistent with the data shown in Fig. 2b and imply that *Max* deficiency arrests ESCs at the crux of the pachytene stage of meiosis-like processes. Because aurora kinase is a known critical regulator of meiosis[24], we examined changes in the expression of aurora kinase A, B and C in *Max*-null ESCs by western blot
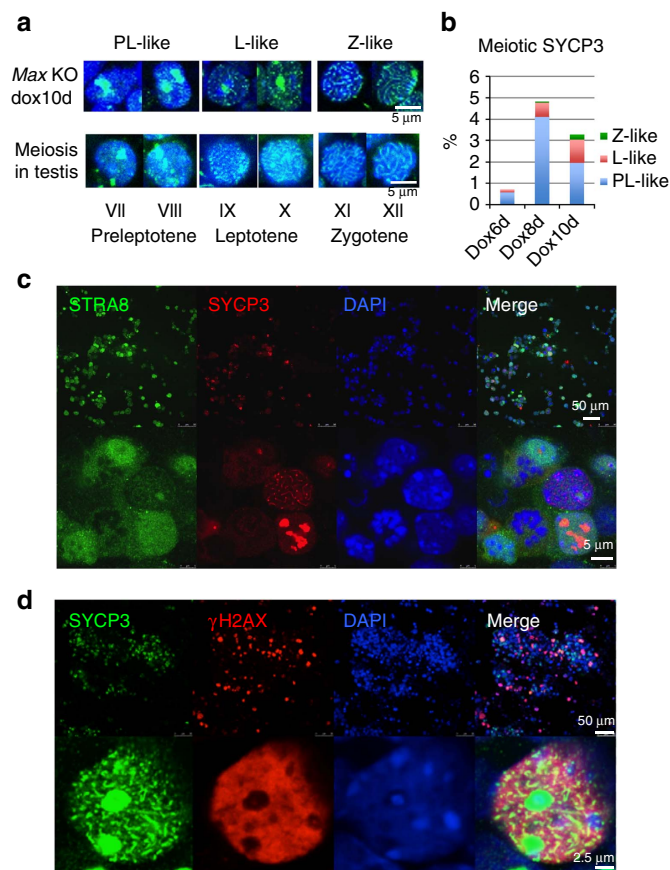
Figure 2 | Cytological changes reminiscent of cells undergoing meiotic cell division processes. (**a**) Meiosis-like SYCP3-staining patterns in *Max*-null ESCs treated with Dox for 10 days. The meiosis-like SYCP3-staining patterns in *Max*-null ESCs were classified as preleptotene (PL)-, leptotene (L)- and zygotene (Z)-like patterns according to the criteria shown in Supplementary Fig. 3. (**b**) Frequency of preleptotene-, leptotene- and zygotene-like SYCP3-staining patterns in *Max*-null ESCs at the indicated days after Dox administration. (**c**) Co-immunostaining analyses of *Max*-null ESCs treated with Dox for 9 days with antibodies against SYCP3 and STRA8. (**d**) *Max*-null ESCs treated with Dox for 10 days were co-immunostained for SYCP3 and γH2A.X.

analyses. All three aurora kinases exhibited reductions in their protein expression levels, although the reduction of aurora kinase C was marginal (Supplementary Fig. 5a). Next, we examined the effect of a pan-aurora kinase inhibitor, VX680, and found that it did not noticeably alter the magnitude of meiosis-like changes in *Max*-null ESCs (Supplementary Fig. 5b,c). Because aurora kinase C is the only aurora kinase with an unequivocal contribution to meiosis among the three aurora kinases and localization of aurora kinase C at chromocentres becomes apparent at the diplotene stage[24], no apparent effect of the aurora kinase inhibitor may be reasonable in our system in which the meiotic process was arrested at or before the pachytene stage (Fig. 2). Next, we examined whether loss of *Max* expression in ESCs was accompanied by alterations in genomic DNA methylation levels. To this end we compared the levels of 5-methyl cytosine (5mC) and 5-hydroxymetyl cytosine (5hmC) between Dox-untreated and -treated ESCs for 8 days. Although 5mC levels remained rather constant on *Max* depletion, our analyses demonstrated an elevation in the levels of 5hmC by about twofold in Dox-treated *Max*-null ESCs (Supplementary Fig. 6a). We also examined the methylation status of imprinting genes because erasure of

imprinting is one of the hallmarks of germ cell development. We found that differentially methylated regions (DMRs) of maternally methylated *Snrpn* and *Igf2r* genes were almost completely demethylated in *Max* expression-ablated ESCs, implying that activation of the meiotic programme in these cells was coupled with imprinting erasure (Supplementary Fig. 6b,c). We also found similar, but less significant, induction of demethylation in one of the DMRs in the paternally methylated *H19* gene (Supplementary Fig. 6d). The almost complete methylation of DMRs in the *H19* gene of Dox-untreated ESCs reflects the usual DNA methylation status of this locus in mouse ESCs cultured in conventional mouse ESC medium[25–27].

Vitamin C enhances meiosis-related changes in *Max*-null ESCs. Since apoptosis is a prominent phenotype of *Max*-null ESCs, we investigated whether apoptosis might be triggered by meiosis-like changes or elevated levels of reactive oxygen species in *Max*-null ESCs[16]. Towards this end we treated *Max*-null ESCs with vitamin C, a compound that has been described both as an antioxidant and as a potentiating factor in meiosis through activation of ten-eleven translocation 1 (Tet1)[28,29]. Vitamin C treatment of *Max*-null ESCs did not reduce but instead significantly accelerated cell apoptosis (Fig. 3a). This was accompanied by elevated *Stra8* expression (Fig. 3b). Vitamin C treatment also increased the frequency of meiosis-like SYCP3-staining patterns and yielded cells representing more advanced stages of meiosis compared with Dox treatment alone (Fig. 3c,d). These results implied that the meiosis-related changes rather than reactive oxygen species in *Max*-null ESCs are closely linked to apoptosis. To further explore the relationship between the meiosis-like changes and apoptotic cell death in *Max*-null ESCs, we suppressed the levels of apoptosis by treatment with the caspase inhibitor Z-VAD-FMK. We found that Z-VAD-FMK treatment increased the frequency of cells with meiosis-like changes, especially cells with preleptotene- and leptotene-like SYCP3-staining patterns (Supplementary Fig. 7). These observations implied that a substantial portion of meiotic-like *Max*-null ESCs were eliminated at rather early stages before proceeding to more advanced stages of meiosis. Apoptosis occurred likely as a result of the ESC culture condition, which is different from the niche environment found within the seminiferous tubules of the testis and the female genital ridge.

Meiosis-like changes in *Max*-null ESCs depend on *Stra8* gene. To explore the relationship between the induction of *Stra8* gene expression and the meiosis-like SYCP3-staining patterns in our system, we knocked out the *Stra8* gene in *Max*-null ESCs using the CRISPR-Cas9 system[30] (Fig. 4a). Immunocytochemical (Fig. 4b) and western blot (Fig. 4c) analyses confirmed that *Max* depletion-mediated induction of *Stra8* expression did not occur in *Stra8*-knockout ESCs. More importantly, loss of *Stra8* gene functions resulted in marked suppression of incidences of meiosis-like SYCP3-staining patterns in Dox-treated *Max*-null ESCs (Fig. 4d). We also found that disruption of the *Stra8* gene led to a significant reduction in γH2AX signals, a characteristic feature observed strongly at leptotene stages of meiosis (Fig. 4e). These data implied that, similar to normal meiotic cell division, expression of *Stra8* is indispensable for induction of meiotic-like patterns in *Max*-null ESCs[3–6]. It is also worth noting that *Stra8* knockout not only impaired the cytological changes reminiscent of meiosis but also significantly alleviated apoptotic cell death phenotype associated with *Max* knockout (Fig. 4f,g). Therefore, these results further suggest that the extensive cell death observed in *Max*-null ESCs is, at least in part, due to induction of meiosis.
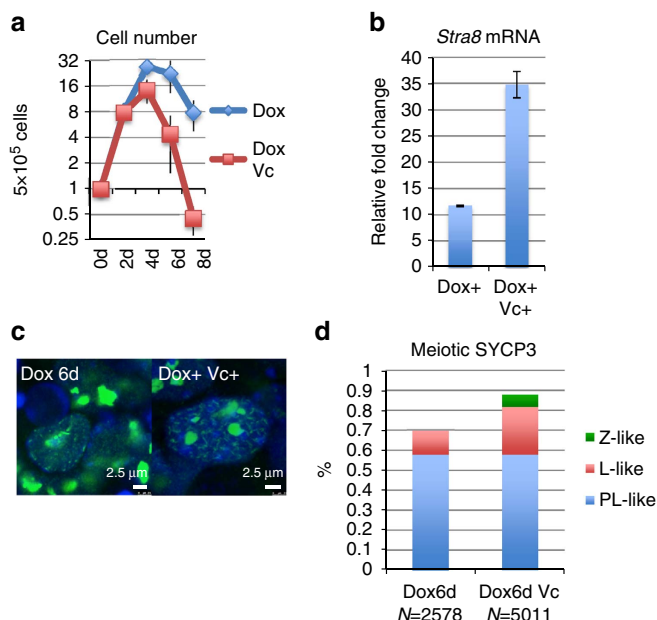
Figure 3 | Vitamin C enhances meiosis-related changes in *Max* expression-ablated ESCs. (**a**) Total number of viable Dox-treated *Max*-null ESCs cultured in the presence or absence of vitamin C at the indicated days after Dox addition. The number of cells at day 0 (0d) was arbitrarily set to one ($n = 3$, means ± s.d.). (**b**) Expression levels of the *Stra8* gene in Dox-treated *Max*-null ESCs cultured in the presence or absence of vitamin C for 4 days (4d). The expression level of the *Stra8* gene in untreated control *Max*-null ESCs was arbitrarily set to one ($n = 3$, means ± s.d.). (**c**) Representative meiosis-like SYCP3-staining patterns in Dox-treated *Max*-null ESCs cultured in the absence or presence of vitamin C for 6 days (6d). (**d**) Frequency of meiosis-like SYCP3-staining patterns in *Max*-null ESCs treated only with Dox for 6 days or together with vitamin C.

Meiosis-like changes in *Max*-null ESCs under 2i condition. We have previously demonstrated that *Max*-null ESCs in the 2i + leukaemia inhibitory factor (LIF) condition with two kinase inhibitors against MEK and GSK3β (ref. 31), but not in conventional ESC medium, maintain normal expression levels of pluripotency markers such as OCT3/4, SOX2 and NANOG, and are able to self-renew indefinitely[16]. In this context, we sought to determine whether *Max* depletion leads to the activation of germ cell-related genes in ESCs even if the vast majority of cells maintain their pluripotent properties. First, DNA microarray analyses showed that the expression levels of germ cell-related genes were elevated even in Dox-treated *Max*-null ESCs under the 2i + LIF condition, although the induction levels were not as conspicuous as those observed in *Max*-null ESCs under conventional LIF + serum conditions (Fig. 5a). Quantitative PCR confirmed the induction of *Stra8* gene expression in both conditions (Fig. 5b). These results prompted us to investigate whether the cytological changes reminiscent of meiotic cell division also occur in Dox-treated *Max*-null ESCs under the 2i + LIF condition. We found that accumulation of STRA8 protein as well as meiosis-like SYCP3 staining became evident on loss of *Max* expression in ESCs under the 2i + LIF condition (Fig. 5c,d), although the frequency of these cytological changes was about half of that observed in conventional ESC culture conditions (Fig. 5e).

Implications of direct onset of meiosis in *Max*-null ESCs. It has been shown that the 2i + LIF condition renders ESCs refractory

to cellular differentiation[32]. The changes in meiosis reported in *Max*-null ESCs, even in the 2i + LIF condition, indicate that this induction occurs without passing through a PGC state that first becomes evident at around 7.0 days post coitum (dpc; early gastrulation stage) in mouse embryos[33]. This is supported by the fact that *Max* ablation in ESCs led to elevated expression levels of late PGC and meiosis-related genes, but did not elicit prominent induction of PGC specification genes. To further address this issue, and taking into account the fact that *Blimp1* is known to play crucial roles in the induction and maintenance of PGCs[34,35], we knocked out the *Blimp1* gene in *Max*-null ESCs using the CRISPR-Cas9 system. After homozygous knockout of the *Blimp1* gene (Supplementary Fig. 8), the ESCs were treated with Dox to suppress *Max* expression for 9 days and then subjected to co-immunocytochemical analyses with antibodies against SYCP3 and STRA8. Strong induction of STRA8 as well as meiosis-like SYCP3-staining patterns became evident in the ESCs after loss of *Max* expression, even without a functional *Blimp1* gene (Fig. 5f–h), indicating that *Max*-null ESCs bypassed the PGC state and directly acquired features reminiscent of meiosis I phase.

Meiosis-related changes in ESCs depend on retinoid. Retinoid[7–10] and LIF[36] signalling are critical players in the onset of meiosis in germ cells. We thus decided to examine the effects of RA and LIF on *Max*-null ESCs. Similarly to vitamin C, RA treatment further enhanced the meiosis-related changes in *Max*-null ESCs (Fig. 6a–c). With respect to LIF, although its withdrawal from culture showed little to no effect on *Stra8* expression, it facilitated meiosis-related cytological changes in *Max*-null background (Fig. 6c). We also found that the number of viable cells was inversely correlated with the magnitude of meiosis-like changes (Fig. 6d), again implying that meiosis-like changes in ESCs are accompanied by apoptotic cell death. Our analyses with the RA receptor inhibitor AGN193109 (AGN; Fig. 6e and Supplementary Fig. 9a,b) and forced expression of *Cyp26b1* encoding an RA-degrading enzyme (Fig. 6f, Supplementary Fig. 9c,d) also confirmed the crucial involvement of RA, likely present in fetal bovine serum used, in meiotic changes in *Max* expression-ablated ESCs. To confirm this, we conducted experiments using serum- and RA-free N2B27 medium. Without exogenous supply of RA, induction of *Stra8* was barely detectable, irrespective of the presence or absence of *Max* expression in N2B27 medium. Interestingly, RA supplementation augmented *Stra8* expression levels dose-dependently even in the presence of *Max* expression, although much more profound induction was attained in the absence of *Max* expression. These results suggest that RA is essential for the induction of *Stra8* expression and that *Max* expression-ablated background sensitized ESCs to the RA-mediated change (Fig. 6g).

Blockade of meiosis by MAX/MGA-containing atypical PRC1. To explore the molecular mechanisms underlying the meiosis-related changes associated with *Max* depletion in ESCs, we first searched for factors in the MYC superfamily, whose deficiency caused meiosis-related changes in ESCs, similar to MAX ablation. We found that lentivirus-mediated knockdown of *Mga* and *Max*, but not those of other MYC superfamily members, were coupled with induction of the expression of meiotic genes *Stra8*, *Taf7l* and *Slc25a31* (Fig. 7a and Supplementary Fig. 10). *Mga* knockdown-mediated induction of STRA8 expression was also confirmed by immunostaining (Fig. 7b). Because both MAX and MGA were recently demonstrated to be a part of an atypical PRC1 complex (PRC1.6)[14,15], we next examined the consequence of forced reduction of the expression of the *L3mbtl2* gene that
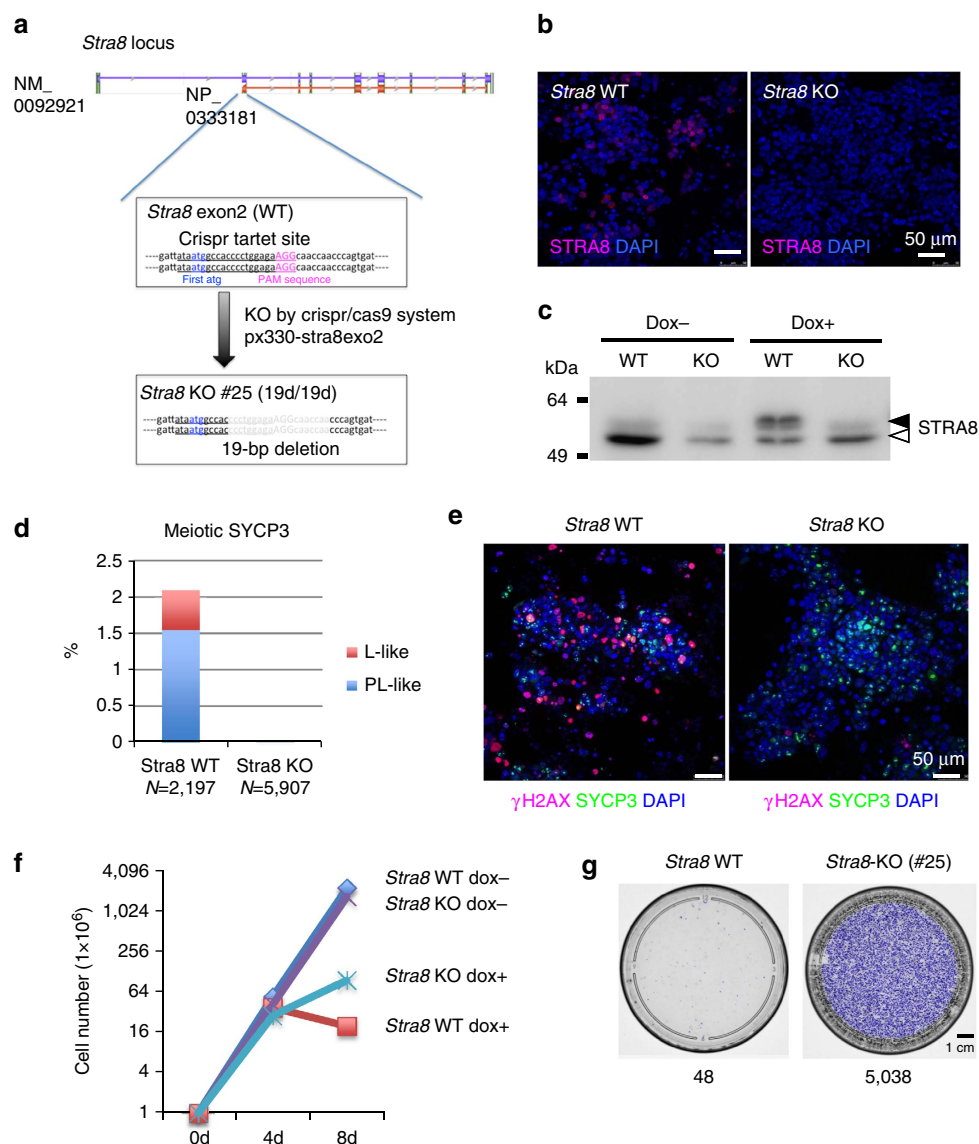
Figure 4 | Induction of the *Max* expression ablation-mediated meiosis-like SYCP3-staining pattern in ESCs depends on the presence of a functional *Stra8* gene. (**a**) Schematic representation of CRISPR-Cas9-mediated disruption of the *Stra8* gene. Genomic analyses revealed that *Stra8* KO #25 clone had an out-of-frame mutation in both loci of the *Stra8* gene due to homozygous deletion of 19 base pairs located immediately downstream of the ATG initiation codon in exon 2 of the gene. (**b**) Confirmation of the absence of functional *Stra8* genes in the *Stra8* KO #25 *Max*-null ESC clone. The *Stra8* KO #25 clone and parental *Max*-null ESCs were treated with Dox for 9 days and then subjected to immunocytochemical analyses with an antibody against STRA8. (**c**) Western blot analyses of STRA8 in *Stra8* KO #25 clone and parental *Max*-null ESCs cultured in the presence or absence of Dox. Solid and open arrowheads indicate specific and non-specific bands, respectively. (**d**) Frequency of preleptotene-, leptotene- and zygotene-like staining patterns in the *Stra8* KO #25 clone and parental *Max*-null ESCs treated with Dox for 9 days. (**e**) Immunostaining analyses of γH2AX and SYCP3 in the Dox-treated (9 days) *Stra8* KO #25 clone and parental *Max*-null ESCs. (**f**) Increase in the recovery of viable Dox-treated *Max*-null ESCs due to homozygous knockout of the *Stra8* gene. The number of cells at day 0 was arbitrarily set to one. (**g**) *Max*-null ESCs (1×10^5) with or without functional *Stra8* genes were individually transferred to 10-cm dishes and treated with Dox for 12 days. The cells were then subjected to Leishman's staining. Numbers under the dishes are the number of stained cell colonies. d, day; KO, knockout; WT, wild type.

also encodes one of the components of PRC1.6. Knockdown of *L3mbtl2* expression also led to significant elevation in the expression levels of meiotic genes, although the expression levels of the *Stra8* gene were not affected (Fig. 7c). Next, to assess whether elevation of meiotic gene expression is the direct consequence of *Max* expression ablation or secondary in nature, we examined whether MAX protein binds to the meiosis-related genes. To this end, we conducted chromatin immunoprecipitation (ChIP) analyses with an anti-MAX antibody. Our data clearly demonstrated that MAX bound to *Ddx4*, *Slc25a31* and *Sycp3* genes in Dox-untreated ESCs (Fig. 7d).

However, such signals were attenuated on *Max* expression ablation by Dox treatment. These results indicated that the MAX-containing complex directly bound to meiosis-related genes and repressed their expression in ESCs, and upregulation of these genes in *Max*-null ESCs reflects the liberation from such MAX-dependent repression. We also conducted ChIP analyses with an antibody against L3MBTL2. Although the immunoprecipitation efficiency was not as high with the antibody against L3MBTL2 compared with the anti-MAX antibody, our data indicated that L3MBTL2 directly bound to the examined meiotic genes. Furthermore, our data demonstrated that the
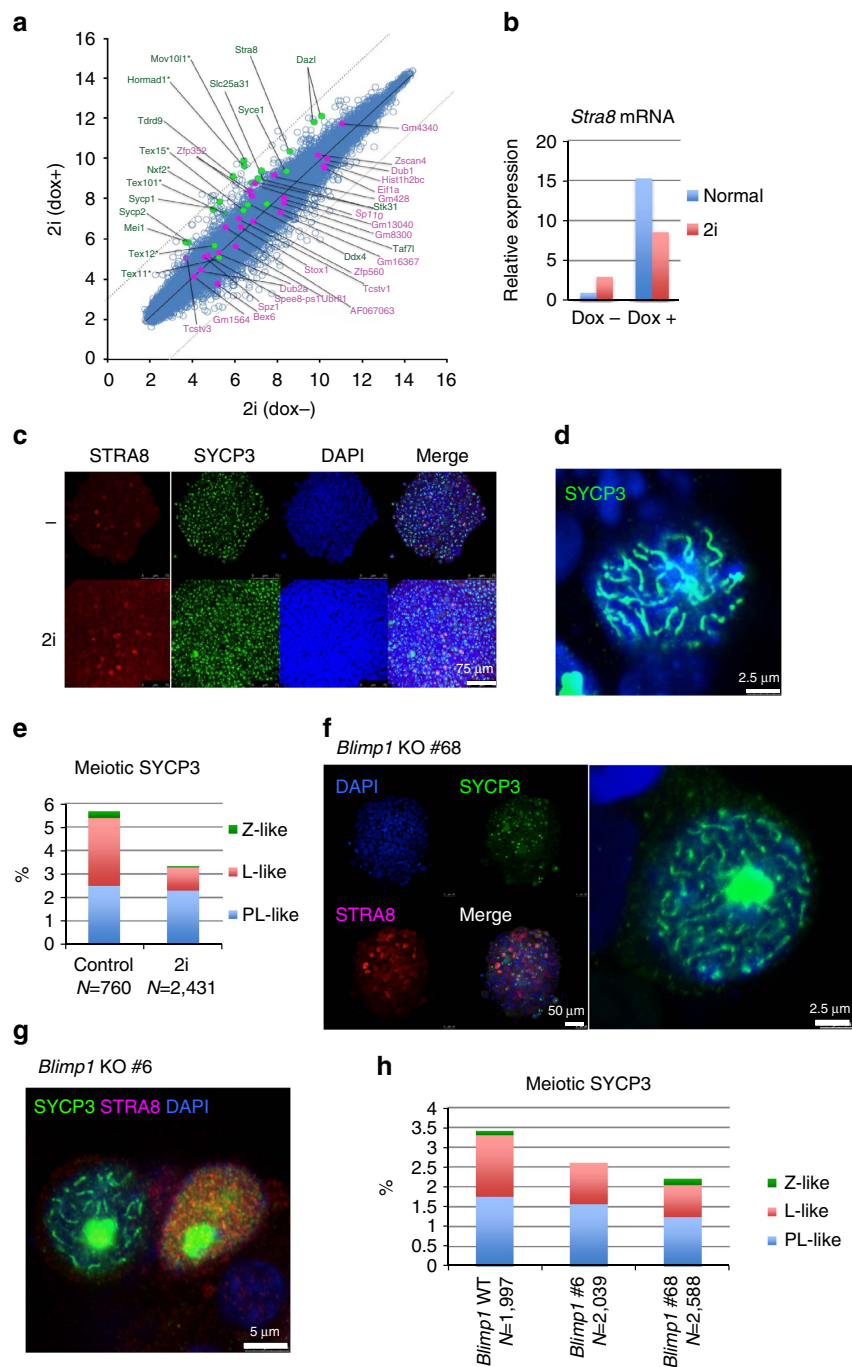
Figure 5 | Occurrence of meiosis-like changes in *Max* expression-ablated ESCs without passing through the PGC state. (**a**) Scatter plots of DNA microarray data from untreated and Dox-treated *Max*-null ESCs cultured under the 2i + LIF condition. Genes highlighted in Fig. 1a are indicated by the same colours (green: germ cell-specific genes; pink: two-cell embryo-specific genes; green with an asterisk: genes belonging to both categories). (**b**) Measurement of *Stra8* mRNA levels by quantitative PCR in Dox-untreated and -treated *Max*-null ESCs cultured under conventional mouse ESC or 2i + LIF culture conditions. (**c**) Immunocytochemical analyses of STRA8 and SYCP3 in Dox-treated *Max*-null ESCs cultured under conventional mouse ESC or 2i + LIF culture conditions. (**d**) Representative image of the zygotene-like SYCP3-staining pattern observed in Dox-treated *Max*-null ESCs cultured under the 2i + LIF condition. (**e**) Frequency of meiosis-like SYCP3-staining patterns in Dox-treated *Max*-null ESCs cultured under conventional mouse ESC or 2i + LIF culture conditions. (**f**) Immunocytochemical analyses of STRA8 and SYCP3 in the Dox-treated *Blimp1* KO #68 *Max*-null ESC clone. Right panel shows a representative zygotene-like SYCP3-staining pattern. In this mutant clone, a single adenine nucleotide was inserted into both loci of exon 3 in the *Blimp1* gene, causing an out-of-frame mutation (for details, see Supplementary Fig. 8). (**g**) Leptotene-like immunostaining pattern of SYCP3 with high STRA8 expression (right) and the zygotene-like SYCP3-staining pattern (left) with low STRA8 expression in the Dox-treated *Blimp1* KO #6 *Max*-null ESC clone in which a large deletion had occurred in the region encompassing exon 3 and intron 3 in both loci of the gene (for details, see Supplementary Fig. 8). (**h**) Frequency of meiosis-like SYCP3-staining patterns in Dox-treated *Max*-null ESCs of *Blimp1* KO #68 and #6 clones. KO, knockout.
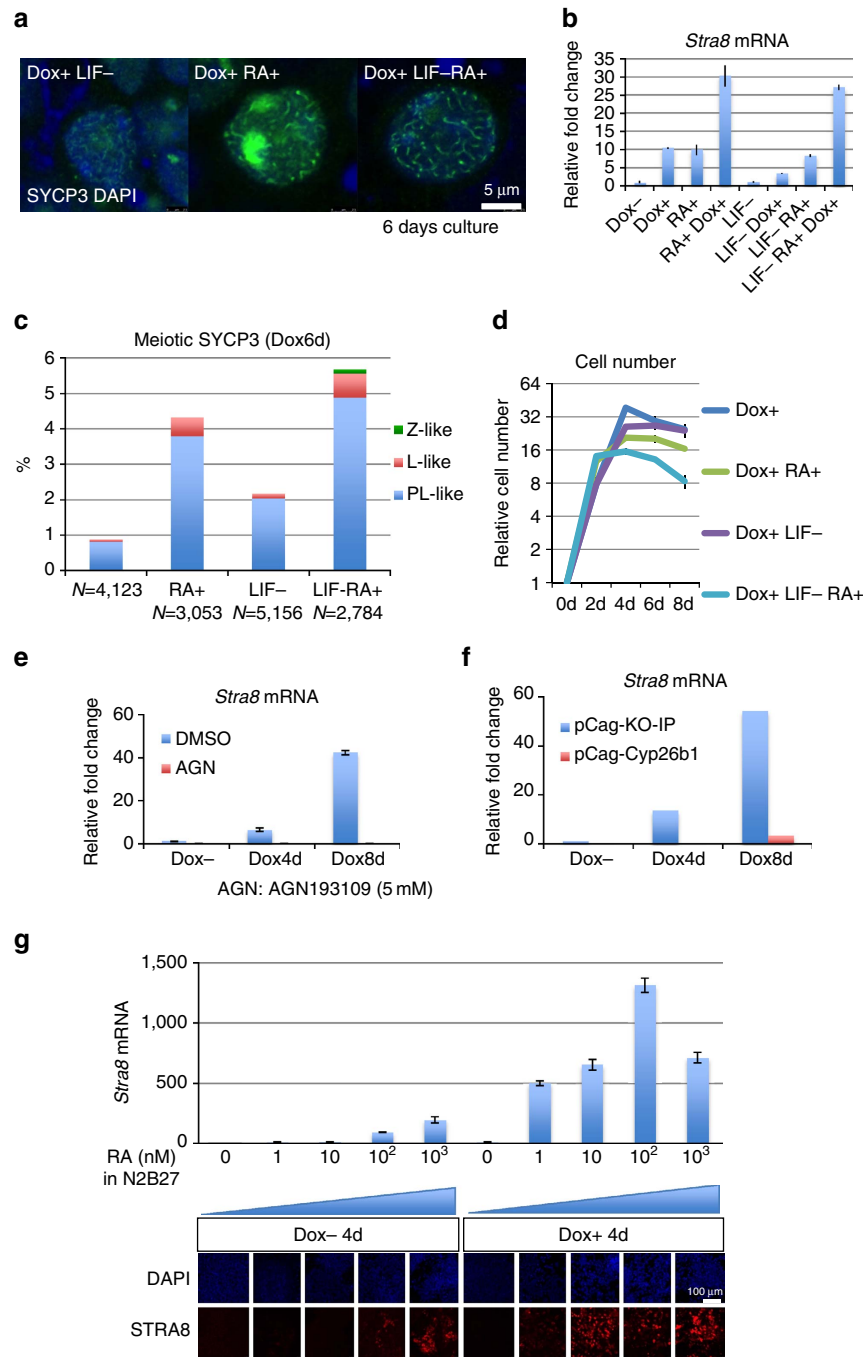
Figure 6 | RA treatment potentiates meiosis-related changes in *Max* expression-ablated ESCs. (**a**) Representative images of meiosis-like SYCP3-staining patterns in Dox-treated *Max*-null ESCs cultured with or without RA in the presence or absence of LIF for 6 days. (**b**) Expression levels of the *Stra8* gene in Dox-treated *Max*-null ESCs cultured under the indicated conditions for 6 days. The *Stra8* gene expression level in Dox-untreated control *Max*-null ESCs cultured in the presence of LIF was arbitrarily set to one ($n = 3$, means ± s.d.). (**c**) Frequency of meiosis-like SYCP3-staining patterns in *Max*-null ESCs treated with Dox for 6 days or together with RA in the presence or absence of LIF. (**d**) Effect of RA on the recovery of viable Dox-treated *Max*-null ESCs cultured with or without LIF. The number of cells at day 0 was arbitrarily set to one ($n = 3$, means ± s.d.). (**e**) Quantification of *Stra8* mRNA levels in Dox-treated or -untreated *Max*-null ESCs cultured in the presence or absence of the RA receptor inhibitor AGN for the indicated days ($n = 3$, means ± s.d.). (**f**) Effect of the expression of *Cyp26b1* on *Stra8* expression levels in *Max*-null ESCs. (**g**) Dose-dependent effect of RA on *Stra8* expression levels in *Max*-null ESCs cultured in N2B27 with no RA as basal medium ($n = 3$, means ± s.d.).

binding signal was greatly diminished on *Max* expression ablation, implying that binding of L3MBTL2 on the meiotic genes is dependent on the presence of MAX (Fig. 7d). This finding further supported the notion that PRC1.6 complex is involved in the repression of meiotic genes in ESCs. Next, we examined the expression levels of genes encoding the *Myc* superfamily and those encoding either one of the components of the PRC1.6 complex after *Max* expression ablation in ESCs. We found that many of the genes, including *L3mbtl2*, showed slight decline in their expression levels following *Max* depletion in ESCs, while expression level of *Mga* was initially elevated (up to 4 days) but declined thereafter (Supplementary Fig. 11).
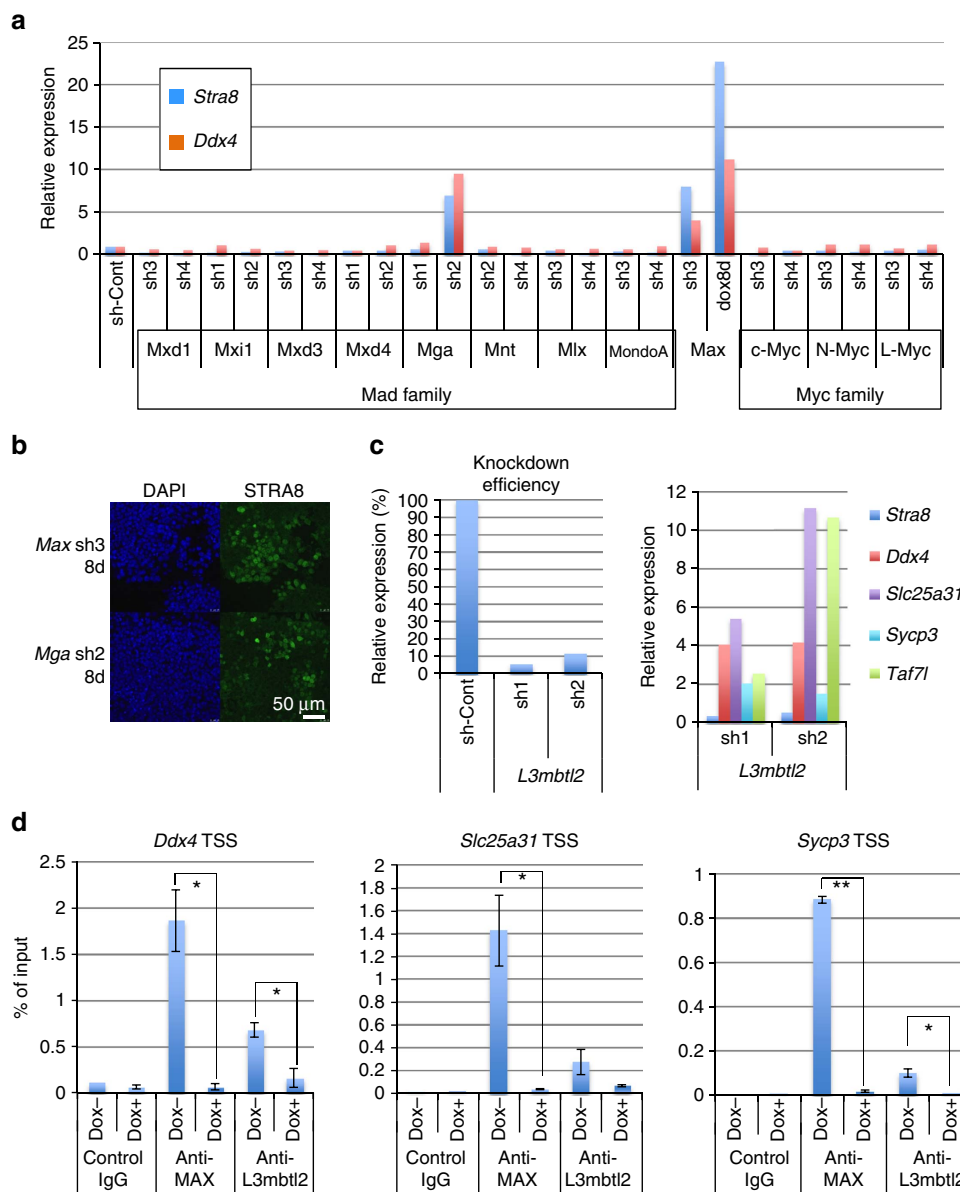
Figure 7 | Implication of the MAX-containing PRC1.6 complex in the blockade of meiosis-related gene expression in ESCs. (**a**) Effect of knockdown of *Myc* superfamily genes on the expression of *Stra8* and *Ddx4* genes in ESCs. Expression levels of *Stra8* and *Ddx4* genes were quantitated in Dox-untreated *Max*-null ESCs subjected to lentivirus-mediated stable knockdown of the indicated genes. Expression levels of *Stra8* and *Ddx4* genes in cells subjected to knockdown with a scrambled sequence was arbitrarily set to one. Knockdown efficiency of each gene is shown in Supplementary Fig. 10a. (**b**) Immunocytochemical analyses of STRA8 in Dox-untreated *Max*-null ESCs in which expression of *Max* (upper) and *Mga* (lower) was subjected to lentivirus-mediated stable knockdown. (**c**) Effect of *L3mbtl2* knockdown on meiotic gene expression in ESCs. Lentivirus-mediated knockdown was conducted as described in **a**. Expression of *Stra8*, *Ddx4*, *Slc25a31*, *Sycp3* and *Tafl7* was determined by TaqMan-based quantitative PCR. (**d**) ChIP analyses of meiotic gene promoters with antibodies against MAX and L3MBLT2. Dox-untreated and -treated *Max*-null ESCs for 4 days were subjected to ChIP with either anti-MAX or L3MBLT2 antibodies. A ChIP reaction was also performed with control IgG. The genomic DNAs recovered by these ChIP reactions were individually subjected to quantitative PCR to quantify the relative amounts of *Ddx4*, *Slc25a31* and *Sycp3* gene promoters compared with those used as input samples ($n = 3$, means ± s.d.). Unpaired *t*-test was done to compare immunoprecipitation efficiency statistically between Dox-untreated and -treated *Max*-null ESCs (*$P < 0.05$; **$P < 0.01$).

Meiosis-like changes in ESCs with a MYC/MAX complex. We have previously demonstrated that the detrimental phenotype of *Max*-null ESCs could be rescued by c-MYC and MAX mutants bearing modifications in their leucine zipper dimerization domains[16,36]. Because of these modifications, c-MYC and MAX mutants, designated as c-MYC-EG and MAX-EG, respectively, do not bind to other endogenous partners, but dimerize efficiently with each other to function as a c-MYC/MAX transcriptional complex. Therefore, *Max*-null ESCs bearing these mutants are able to maintain MYC activity but lack a functional PRC1.6 complex because the MAX-EG mutant does not interact with the endogenous MGA protein. We examined whether meiosis-like changes were evident in *Max*-null ESCs expressing c-MYC-EG and MAX-EG. Consistent with our previous report, *Max*-null ESCs bearing these mutants were able to maintain cell viability (Fig. 8a,b). However, our analyses revealed that the induction of expression of meiotic genes and production of STRA8 protein were also observed in these cells (Fig. 8c,d). Furthermore,

266
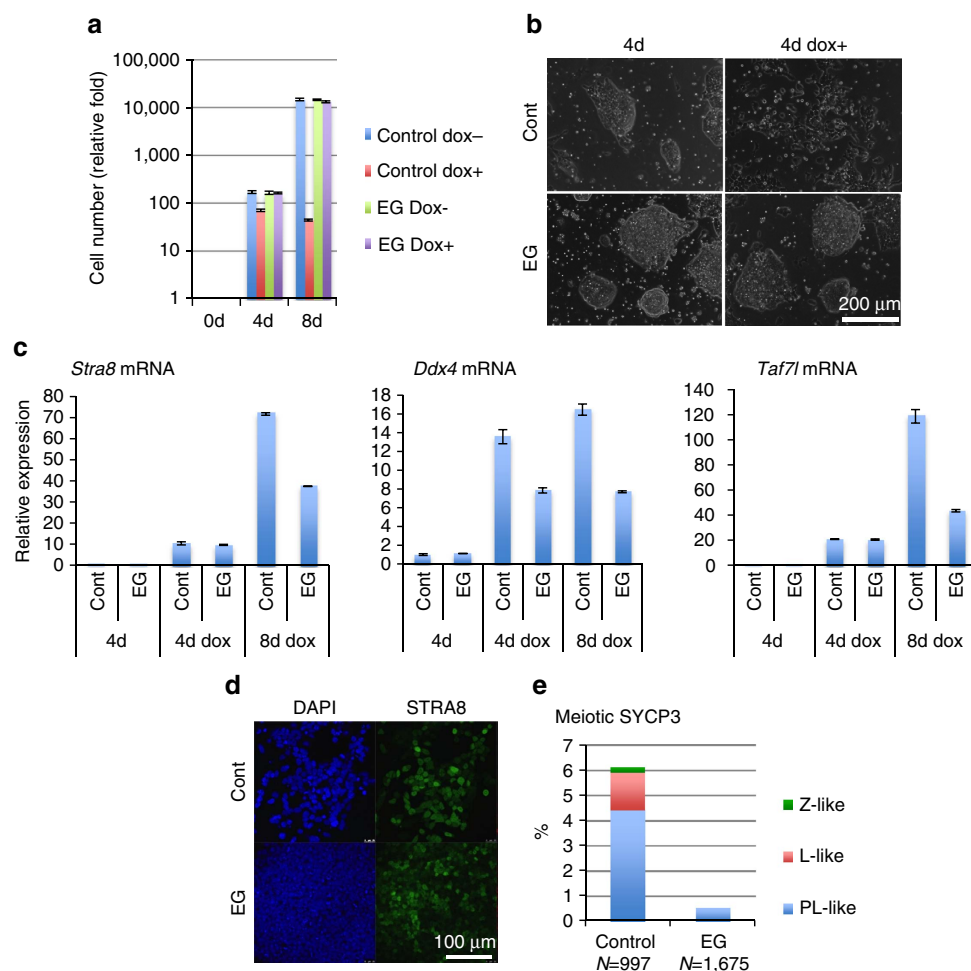
Figure 8 | Meiosis-like changes in Dox-treated *Max*-null ESCs with rescued viability by mutant c-MYC/MAX. (**a**) *Max*-null ESCs with or without mutant c-MYC/MAX, whose expression was under the control of the constitutive β-actin promoter, were treated with Dox for the indicated days, and then viable cell numbers were counted. The number of cells at day 0 (0d) was arbitrarily set to one (*n* = 3, means ± s.d.). (**b**) Microscopic inspection of Dox-treated and -untreated *Max*-null ESCs for 4 days (4d) with or without mutant c-MYC/MAX. (**c**) Examination of the expression levels of meiotic genes in Dox-treated and untreated *Max*-null ESCs with or without mutant c-MYC/MAX. Expression levels of *Stra8*, *Ddx4* and *Tafl7l* were examined by TaqMan-based quantitative PCR (*n* = 3, means ± s.d.). (**d**) *Max*-null ESCs with or without mutant c-MYC/MAX were treated with Dox for 8 days (8d) and then subjected to immunostaining with antibodies against STRA8. (**e**) Frequency of the meiosis-like SYCP3-staining pattern in Dox-treated *Max*-null ESCs with or without mutant c-MYC/MAX for 8 days. Cont, control.

meiosis-like cytological changes were detected as well (Fig. 8e). These meiotic-like changes were found, however, to a lesser degree when compared with control *Max*-null ESCs. These results suggest that a PRC1.6-independent MYC/MAX activity may also help guard meiosis entry in ESCs.

***In vivo* meiosis is coupled with a decline in *Max* expression.** Since meiosis-like cytological changes could be induced in *Max* expression-ablated ESCs, we decided to examine whether *Max* expression levels decline during normal meiotic cell division in testes. To this end we performed immunohistochemical analyses of testis sections. In addition to an antibody against MAX, antibodies against PLZF and cKIT, which mark spermatogonial stem/progenitor cells and differentiating spermatogonia, respectively, were used in the analyses to facilitate staging of cells undergoing meiosis[37]. We found that MAX expression, which is generally thought to be ubiquitous[38], was extremely low in cKIT-positive differentiating spermatogonia and premeiotic type B spermatogonia at stage VI compared with PLZF-positive spermatogonial stem/progenitor cells (Fig. 9a–c).

This low level of MAX expression in differentiating spermatogonia persisted up to the early pachytene stage but increased again during the pachytene stage (Supplementary Fig. 12). Whereas the meiotic cell division begins in testes after birth in males, meiosis commences in the genital ridges at the midgestation stage in females[39]. Therefore, we examined whether the meiotic processes in female mice are also accompanied by downregulation of MAX expression. Indeed, we found that MAX expression levels were extremely low in SYCP3-positive female PGCs at 13.5 dpc, which coincides with meiosis initiation, but were much higher in E13.5 male PGCs (Fig. 9d). These results reveal that, although occurs at different timing, meiosis in both sexes is coupled with downregulation of MAX expression. To assess whether there is also a difference in *Max* mRNA levels between male and female PGCs, we inspected DNA microarray data of PGCs deposited by Kagiwada *et al.*[40] We found that *Max* expression levels in female PGCs was lower compared with those of male PGCs, especially at the initiation of meiosis (13.5 dpc; Supplementary Fig. 13a), implicating that the lower level of MAX protein in female PGCs revealed by immunostaining was at least in part due to lower levels of *Max* mRNA in female PGCs
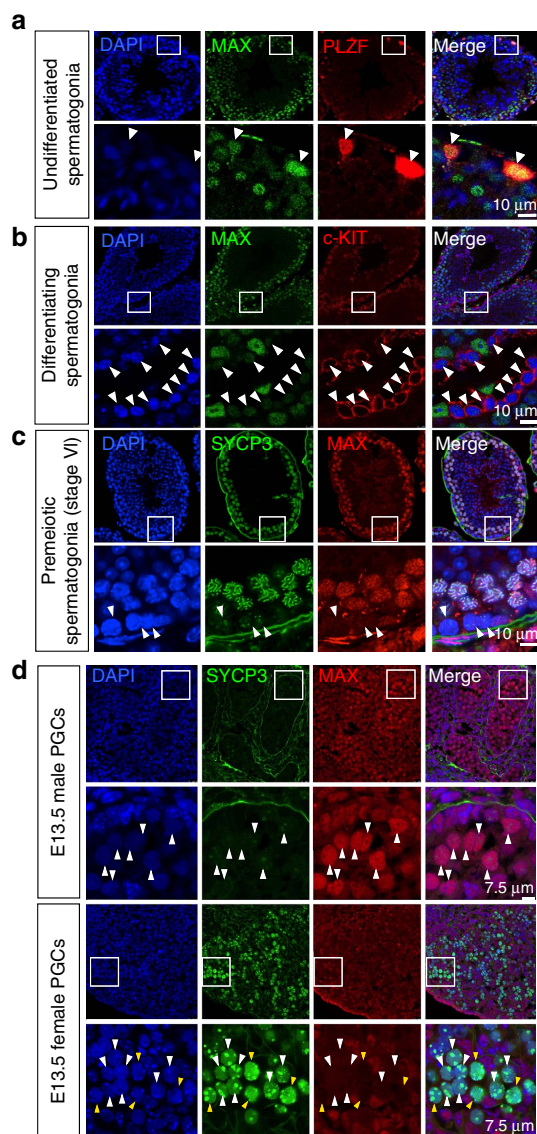
Figure 9 | *Max* expression dynamics in normal gametogenesis. Frozen sections of testes from adult male mice were prepared and immunostained for MAX. The sections were also co-immunostained for PLZF (**a**), cKIT (**b**) or SYCP3 (**c**). Arrowheads in **a,b** and **c** indicate PLZF-positive undifferentiated spermatogonia that are strongly positive for MAX, cKIT-positive differentiating spermatogonia that are weak for MAX and cells undergoing meiotic cell division (presumable premeiotic type B spermatogonia) that are weak for both SYCP3 and MAX, respectively. (**d**) Decline of MAX expression levels in female, but not in male, PGCs of 13.5 dpc embryos. Male and female embryos (13.5 dpc) were recovered from a single pregnant female mouse, and then the genital ridges were recovered individually. After processing, sections were prepared and subjected to co-immunostaining with antibodies against MAX and SYCP3. Arrowheads shown in male genital ridges represent PGCs with strong and weak signals for MAX and SYCP3, respectively. Corresponding female PGCs with strong expression of SYCP3 are also indicated by arrowheads in which white and yellow indicate weak and almost no MAX expression, respectively.

those categorized into both germline and two-cell signature genes shown in Supplementary Fig. 1 also had strong elevations in their expression levels during midgestation (E10.5–13.5; Supplementary Fig. 13b). Interestingly, most meiotic genes showed significant elevations in their expression levels not only in female PGCs but also in male PGCs during gestation, although the magnitude of the elevation was not as prominent as that observed in female PGCs. More remarkably, most of the genes that were significantly or modestly activated in *Max*-null ESCs were also, respectively, activated in similar manners during PGCs development, providing additional evidence that our *Max* expression ablation system in ESCs represents a *bona fide* model of meiosis. However, genes categorized exclusively as two-cell signature genes did not show any tendency of activation, but rather decreased their expression levels during PGCs development. These results further suggest that activation of these genes in *Max* expression-ablated ESCs is not related to meiosis-like changes (Supplementary Fig. 13b).

Meiotic induction in GSCs by *Max* knockdown. We next examined the consequence of forced reduction of *Max* expression in GSCs. We not only found that *Stra8* expression level was elevated (Fig. 10a) but also detected cytological changes reminiscent of meiosis in GSCs on *Max* knockdown (Fig. 10b,c). Of note is that these cytological changes were only observed in cells with reduced *Max* expression. Because knockdown of *Max* expression was insufficient, but *Max* expression should be completely ablated in ESCs to induce meiosis-related cytological changes, our data with GSCs suggested that GSCs are more competent for meiosis-like cytological changes than ESCs. Next, we conducted knockdown of *Max* expression in mouse embryonic fibroblasts, NIH3T3 cells and induced pluripotent stem cells (iPSCs). Although lentivirus-mediated knockdown of *Max* expression enhanced *Stra8* gene expression levels in iPSCs, no such induction was evident in mouse embryonic fibroblasts or NIH3T3 cells (Fig. 10d). Induction of STRA8 in iPSCs was confirmed by immunostaining (Fig. 10e). Therefore, we conclude that meiosis-related changes due to *Max* expression deficiency are specific to germ and pluripotent cells.

Discussion

In this study we have uncovered an intriguing meiosis-like programme in ESCs triggered by loss of function of *Max*. Our results show that the loss of *Max* expression in ESCs not only activates germ cell-related genes but also leads to cytological changes resembling leptotene and zygotene stages of meiosis.

Our functional screening of the *Myc* superfamily led to the identification of MGA, whose absence also triggered the meiosis-like changes. Our subsequent analyses revealed that a MAX-containing atypical PRC1 complex (PRC1.6) is responsible for the molecular blockade of meiotic onset. There are six distinct PRC1 complexes with variations in their components, but only in PRC1.6 (ref. 14) are both MAX and MGA present. A unique characteristic of PRC1.6 is that this variant PRC1 does not co-localize with PRC2 at their target sites[15]. Therefore, PRC1.6 must bind to DNA stably without PRC2, and possible molecules responsible for such stable DNA binding include MAX and its association factor MGA. In this context, it is of interest to mention that the MAX-containing PRC1 complex has been shown to be linked to the E box sequence that serves as a binding site for MAX and MGA[15].

We provide evidence of the existence of a transient decline in *Max* expression during physiological gametogenesis in both male and female germ cells. This lead us to assume that the same or at least a similar process of MAX-dependent blockade of meiosis is
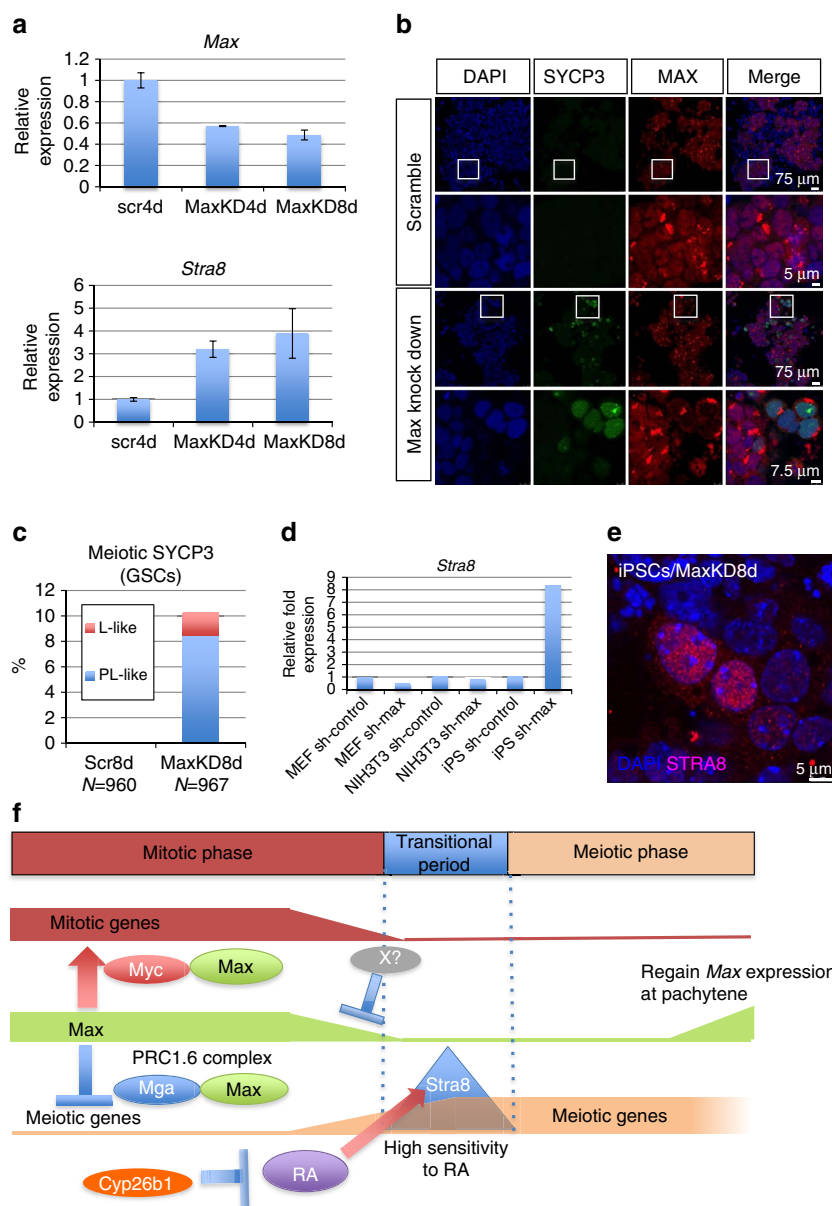
compared with that in male PGCs. However, our data do not exclude the possibility that MAX protein levels were also controlled post-translationally.

We also used these DNA microarray data to study the expression dynamics of genes whose expression levels were elevated in *Max*-null ESCs. Both germline-specific genes and

Figure 10 | Induction of meiosis-like changes in GSCs by knockdown of *Max* expression. (**a**) Effect of *Max* knockdown in GSCs on expression of the *Stra8* gene. Lentivirus-mediated knockdown was conducted as described in Fig. 7. Upper panel shows the knockdown efficiency of *Max* expression ($n = 3$, means ± s.d.). (**b**) Effect of *Max* knockdown in GSCs on induction of the meiosis-like SYCP3-staining pattern. GSCs were subjected to knockdown with scrambled or specific sequences for *Max* expression and then applied to co-immunostaining analyses with antibodies against MAX and SYCP3. (**c**) Frequency of the meiosis-like SYCP3-staining pattern in GSCs subjected to lentivirus-mediated knockdown of *Max* expression. (**d**) Effect of *Max* knockdown in MEFs, NIH3T3 cells and iPSCs on the induction of *Stra8* expression. The levels of *Stra8* expression were measured by quantitative PCR. (**e**) Immunocytochemical analyses of iPSCs subjected to lentivirus-mediated knockdown of *Max* expression with an antibody against STRA8. (**f**) Schematic representation of possible inverse regulation of the expression of meiotic and mitotic genes through the control of *Max* expression for efficient meiosis. MAX is known to play important roles in preserving the stem cell properties of ESCs and GSCs by functioning as an obligated partner for MYC transcription factors. Our present study demonstrates that MAX also contributes to the maintenance of stemness of these cells by blocking expression of meiotic genes. Artificial and physiological declines in *Max* expression levels in ESCs and GSCs, respectively, enhance and reduce expression of meiotic and mitotic genes, respectively, through liberation from the MAX/MGA-dependent repression mechanism and the loss of MYC/MAX complex-dependent transcriptional activation. The former potentiates meiotic progression, whereas the latter results in disruption of the stem/progenitor properties and, therefore, facilitates cellular differentiation. Our data suggest that the MAX-containing PRC1.6 complex is the molecule responsible for the MAX-mediated repression of meiotic genes. However, it is unknown at present what lowers *Max* expression levels at the onset of meiosis in GSCs.

present in GSCs. GSCs should be liberated from such blockades by a physiological decline in *Max* expression to proceed with meiosis during their differentiation. This assumption was further corroborated by data demonstrating that knockdown of *Max* expression in GSCs also led to meiosis-like cytological changes. It

is noteworthy that MYC family proteins, including c-MYC and N-MYC, play crucial roles in preservation of the self-renewal properties of both ESCs[41] and GSCs[42] in which MAX functions as an indispensable partner. Thus, as depicted in Fig. 10f, loss of MAX may promote meiosis not only by activating the expression

of meiotic genes but also by facilitating cellular differentiation through impairment of the self-renewal of ESCs and GSCs because of the loss of MYC functions. The differences in efficiencies in the induction of meiosis-like changes between *Max*-null ESCs bearing c-MYC, MAX mutants and control *Max*-null ESCs may be explained by the preservation of MYC functions in the former, but not in the latter cells. It is noteworthy that Yokobayashi et al.[43] have demonstrated that the PRC1 complex acts negatively against RA signalling through maintenance of the transcriptionally repressed state of the *Stra8* gene. Similarly, our data demonstrated that *Max* expression ablation in ESCs, which is coupled to disruption of the PRC1.6 complex, sensitized RA-mediated induction of *Stra8* gene expression. This finding further strengthens the notion that the meiotic onset in ESCs faithfully recapitulates the *in vivo* meiotic onset. Observations made by Yokobayashi et al.[43] on the loss of function of PRC1 in germ cells may not reflect impairment of the general functions of PRC1, but might be due to disruption of the MAX-containing atypical PRC1 complex.

Max expression ablation appears to induce meiotic onset in ESCs in a physiologically relevant manner. However, such meiosis-like cells are arrested at rather early stages and do not proceed beyond the crux of the pachytene-like stage. To overcome this problem, development of improved culture conditions suitable for meiosis and/or the forced expression of inefficiently induced meiotic genes such as *Rec8* and *Sycp1* will be needed. Although we are far from a complete understanding of the mechanisms involved in generating haploid cells, the results and methodologies here described may open up new avenues towards achieving this goal.

Methods

Animal ethics. This study was carried out under strict accordance with the international and institutional guidelines. The protocol was approved by the institutional review boards on the Ethics of Animal Experiments of the Saitama Medical University, with the permission number of 1518.

Mouse ESC and GSC culture. *Max*-null ESCs with Max cDNA under the control of the tetracycline-off system were cultured in conventional ESC culture medium with LIF and serum, or the 2i condition with inhibitors of MEK (PD0325901) and GSK3β (CHIR99021) with the concentrations of 1 and 3 μM, respectively. N2B27 not containing vitamin A was used as basal medium for the experiments shown in Fig. 6g. The following reagents were used at the indicated concentration unless stated otherwise: $1 \mu g\,ml^{-1}$ Dox (631311, Clontech); 100 nM VX680 (A10981-25, ADG); 20 μM Z-VAD-FMK (627610, Calbiochem); 5 μM AGN193109 (sc210768, Santa Cruz Biotechnology); 1 μM all-trans retinoic acid (R2625, Sigma); and $50 \mu g\,ml^{-1}$ vitamin C (A4544, SIGMA). Mouse GSCs were cultured with Stem Pro-34 SFM medium (10639-011, Invitrogen) with the ingredients of $25 \mu g\,ml^{-1}$ insulin (1882, Sigma), $100 \mu g\,ml^{-1}$ transferrin (Sigma, T1147), 60 μM putrescine (P7505, Sigma), 30 nM sodium selenite (214485, Sigma), $6\,mg\,ml^{-1}$ D-(+)-glucose (G7021, Sigma), $30 \mu g\,ml^{-1}$ pyruvic acid (107360, Sigma), $1 \mu g\,ml^{-1}$ DL-lactic acid (4263, Sigma), $5\,mg\,ml^{-1}$ bovine serum albumin (15561-020, Invitrogen), 2 mM L-glutamine, 50 nM 2-mercaptoethanol, MEM vitamin solution (11120-052, Invitrogen), 0.1 mM nonessential amino acid solution (11140-050, Invitrogen), $30\,ng\,ml^{-1}$ β-estradiol (E2758, Sigma), $60\,ng\,ml^{-1}$ progesterone (P8783, Sigma), $10 \mu g\,ml^{-1}$ D-biotin (B4501, Sigma), 100 mM ascorbic acid (A4544, Sigma), $20\,ng\,ml^{-1}$ mouse epidermal growth factor (2028-EG, R&D systems), $10\,ng\,ml^{-1}$ human basic fibroblast growth factor (13256-029, Becton Dickinson), $1,000\,U\,ml^{-1}$ mouse leukaemia inhibitory factor (02740, Stem Cell Technologies), $10\,ng\,ml^{-1}$ rat glial cell line-derived neurotrophic factor (512-GF, R&D systems) and 1% fetal bovine serum.

Plasmid constructions. Construction of expression vectors for c-MYC and MAX mutants, designated as c-MYC-MG and MAX-EG, respectively, which do not bind to their endogenous partners, but bind efficiently with each other, was described previously[16,36]. CYP26B1 expression vector was constructed by PCR amplification using cDNA from mouse ESCs and subcloned into pCAG-IP vector bearing puromycin resistant gene.

Quantitative reverse transcription (RT)-PCR analysis. Quantitative RT–PCR (qRT–PCR) was performed using the StepOnePlusTM Real-Time PCR System (Applied Biosystems), with cDNAs generated by reverse transcription.

TaqMan-based reactions (Invitrogen) quantified the expression levels of *Stra8* (Mm00486473_m1), *Slc25a31* (Mm00617754_m1), *Sycp3* (Mm00488519_m1), *Taf7l* (Mm00459354_m1), *Ddx4* (Mm00802445_m1), *c-Myc* (Mm00487803_m1), *N-Myc* (Mm00476449_m1), *L-Myc* (Mm03053598_s1) and *Max* (Mm00484802_g1), while qRT–PCR for other genes, including quantification of other *Myc* superfamily genes such as *Mxd1* (Supplementary Fig. 10), was done by SYBR Green-based method with the following oligonucleotides.

L3mbtl2: 5′-TACCTCATGAAGCGGTTGGT-3′ and 5′-CAACCCACTGGGTGGATC-3′

Mxd1: 5′-AGATGCCTTCAAACGGAGGAA-3′ and 5′-CAAGCTCAGAGTGGTGTGTCG-3′

Mxi1: 5′-AACATGGCTACGCCTCATCG-3′ and 5′-CGGTTCTTTTCCAACTCATTGTG-3′

Mxd3: 5′-GAGGCAGAGCACGGTTATG-3′ and 5′-TGTAGTGTATCGGGTACAGTCAA-3′

Mxd4: 5′-ATGGAGCTGAACTCTCTGCTG-3′ and 5′-GTGAAGACCTGTTGTTCGGGG-3′

Mga: 5′-GAGGAGCACCTACCTACCTTCTTTGT-3′ and 5′-ACGGGCATCTCGATTAGTAACT-3′

Mnt: 5′-TCCTGTAGTGACCAATTCCCC-3′ and 5′-TGGCTCCTTAATGCTGAGTCC-3′

Mlx: 5′-GAGGACAGTGATTATCAGCAGGA-3′ and 5′-CATCCCTTCTCTTCTGTTCAGC-3′

MondoA: 5′-GACTCGGACACAGACGAGC-3′ and 5′-GGAGAGGACACCATGAAGTGG-3′

Immunostaining. For immunocytochemistry, cells were plated on 0.1% gelatin-coated Cell Disks (MS-92132, SUMITOMO BAKELITE Co., Tokyo, Japan) and cultured for an appropriate period. Then the cells were fixed with 4% paraformaldehyde for 20 min at room temperature. After extensive washes with phosphate-buffered saline (PBS), the cells were permeabilized and blocked in blocking buffer (PBS containing 0.3% Triton X-100, and 5% fetal bovine serum) for 60 min at room temperature. Subsequently, the cells were washed with PBS and then incubated with primary antibodies in blocking buffer at 4 °C overnight. After three washes with PBS, the cells were incubated with the appropriate Alexa Fluor dye-conjugated secondary antibodies (Invitrogen) and $3 \mu g\,ml^{-1}$ 4′,6-diamidino-2-phenylindole (DAPI) in blocking buffer at 37 °C for 1 h. The cells were washed and observed under a confocal laser scanning microscope (TCS SP8, Leica Microsystems) and analysed with ImageJ computer software. For immuno-histochemistry, male testes and the genital ridges of male and female siblings were isolated from 8-week-old male mice and 13.5 dpc embryos, respectively. After fixing with 4% paraformaldehyde, the tissues were embedded in optimal cutting temperature (OCT) compound and frozen. Sections prepared from the frozen tissues were mounted on glass slides and subjected to immunostaining procedures as described above. The primary antibodies used were as follows: anti-SYCP1 (1:400, ab15090), anti-SYCP3 (1:400, ab97672), anti-STRA8 (1:400, ab49602), anti-REC8 (1:100, ab192241) and anti-Aurora B (1:1,000, ab2254) from Abcam; anti-MAX (1:100, sc-197), anti-L3mbtl2 (1:100, sc-134879) and anti-PLZF (1:100, sc28319) from Santa Cruz Biotechnology; 5-methylcytosine (1:100, 61255) and 5-hydroxymethylcytosine (1:100, 39791) from Active Motif; anti-γH2AX (1:1,000, #2577, Cell Signaling Technology); anti-cKIT (1:100, 553352) from BD Pharmingen; and Anti-Aurora A/B/C (1:300, BS-2445R) from Bioss Antibodies.

Estimation of meiotic stages from SYCP3-stainig length. Germ cells in preleptotene, leptotene, zygotene, pachytene and diplotene stages were identified the ordinary way, with testis sections immunostained and counterstained with anti-SYCP3 antibody and DAPI, respectively. Subsequently, actual lengths of SYCP3-stainig regions were measured with respect to five representative chromosomes of each cell. Some cells with large dots, the width of which was more than 1.5 μm, often found in cells at preleptotene and leptotene stages, were eliminated from the analyses. Exploration of the relationship between averages of these measurements and meiotic stages led to the following criteria: preleptotene-like, <1.2 μm; leptotene-like, 1.2∼3.0 μm; zygotene-like, 3.0∼7.5 μm; and pachytene or diplotene-like, >7.5 μm. This method did not allow us to distinguish between pachytene and diplotene stages. These criteria were used to assign the stages of meiosis-like cells from *Max*-null ESCs. For details, see Supplementary Fig. 3.

Gene disruption. The CRISPR/Cas9 system was used to conduct homozygous knockout of *Stra8* and *Blimp1* genes. The following oligonucleotides were used to edit exon 2 and exon 3 of *Stra8* and *Blimp1* genes, respectively.

Stra8: 5′-CACCGATAATGGCCACCCCTGGAGA-3′ and 5′-AAACTCTCCAGGGGTGGCCATTATC-3′.

Blimp1: 5′-CACCGATCATGAAAATGGACATGG-3′ and 5′-AAACCCATGTCCATTTTCATGATC-3′.

Sequences from the original genomic DNA are underlined. The oligonucleotides were annealed and subcloned into the Bbs1 site of the pX330-U6-Chimeric_BB_CBh-hSpCas9 vector[44]. The vector was then co-transfected with pCAG-IP into *Max*-null ESCs using lipofectamine 2000 (Invitrogen, Life Technology) and then subjected to puromycin selection. The resulting ESC

colonies were individually cloned and used to prepare cell stocks and genomic DNA. Subsequently, PCRs were conducted to identify clones with homozygous knockout by direct DNA sequencing of the PCR products. Details of mutations in *Stra8* and *Blimp1* genes are shown in Fig. 4a and Supplementary Fig. 8, respectively.

Lentivirus-mediated knockdown. Lentivirus-mediated knockdown of the expression of *Myc* superfamily genes and the *L3mbtl2* gene was conducted as described previously[45]. Sequences used for knockdown are shown in Supplementary Table 1.

ChIP-PCR analyses. ChIP analyses were done with Dox-untreated and -treated *Max*-null ESCs for 4 days using antibodies against MAX or L3MBTL2. Primers used for amplifying promoter regions of *Ddx4*, *Slc25a31* and *Sycp3* genes, which were described by Maeda et al.[11], Okashita et al.[46] and Yamaguchi et al.[28], respectively, are as follows:

Ddx4: 5′-ACTCACCTCTCCGCTCCAG-3′ and 5′-GTCGCCTGATGCTAT TTGTTGT-3′.

Slc25a31: 5′-AAAGCTGCTGTGCACTGATTG-3′ and 5′-CTGAGGATGCTG GGAGAACAG-3′.

Sycp3: 5′-GGGGCCGGACTGTATTTACT-3′ and 5′-CTCCCCCATCTCCTT ACCTC-3′.

DNA microarray and GO analyses. Biotin-labelled cRNA was synthesized and then hybridized to Affymetrix GeneChip Mouse Genome 430 2.0 arrays (Affymetrix) according to the manufacturer's instructions. Microarray expression data were background subtracted and normalized by the robust multi-array analysis method using statistical software R. GO analyses were conducted using DAVID web tools (http://david.abcc.ncifcrf.gov). To eliminate redundancy, the selected GO terms were subjected to further analyses using AmiGO1 (http://amigo1.geneontology.org/cgi-bin/amigo/go.cgi) and REVIGO (http://revigo.irb.hr) web sites.

DNA blot and bisulfite sequencing analyses. DNA blot analyses of global changes in 5mC and 5hmC due to *Max* expression ablation in ESCs were performed using genomic DNAs from Dox-untreated and -treated *Max*-null ESCs for 8 days as described by Blaschke et al.[29]. Bisulfite sequencing analyses of *Snrpn*, *Igf2r* and *H19* genes were performed with the same set of genomic DNAs using the following oligonucleotides, which are described by Lucifero et al.[47]

Snrpn first PCR: 5′-TATGTAATATGATATAGTTTAGAAATTAG-3′ and 5′-A ATAAACCCAAATCTAAAATATTTTAATC-3′

Snrpn second PCR: 5′-AATTTGTGTGATGTTTGTAATTATTTGG-3′ and 5′-ATAAAATACACTTTCACTACTAAAATCC-3′

Igf2r first PCR: 5′-TTAGTGGGGTATAAAAGGTTAATGAG-3′ and 5′-AAAT ATCCTAAAAATACAAACTACAC-3′

Igf2r second PCR: 5′-GTGTGGTATTTTTATGTATAGTTAGG-3′ and 5′-AA ATATCCTAAAAATACAAACTACAC-3′

H19 first PCR: 5′-GAGTATTTAGGAGGTATAAGAATT-3′ and 5′-ATCAAA AACTAACATAAACCCCT-3′

H19 second PCR: 5′-GTAAGGAGATTATGTTTATTTTTGG-3′ and 5′-CCTC ATTAATCCCATAACTAT-3′

Uncropped versions of western blots shown in Fig. 4c and Supplementary Fig. 5a are shown in Supplementary Fig. 14a,b, respectively.

References

1. Ginsburg, M., Snow, M. H. & McLaren, A. Primordial germ cells in the mouse embryo during gastrulation. *Development* **110**, 521–528 (1990).
2. Brar, G. A. & Amon, A. Emerging roles for centromeres in meiosis I chromosome segregation. *Nat. Rev. Genet.* **9**, 899–910 (2008).
3. Menke, D. B., Koubova, J. & Page, D. C. Sexual differentiation of germ cells in XX mouse gonads occurs in an anterior-to-posterior wave. *Dev. Biol.* **262**, 303–312 (2003).
4. Baltus, A. E. et al. In germ cells of mouse embryonic ovaries, the decision to enter meiosis precedes premeiotic DNA replication. *Nat. Genet.* **38**, 1430–1434 (2006).
5. Anderson, E. L. et al. Stra8 and its inducer, retinoic acid, regulate meiotic initiation in both spermatogenesis and oogenesis in mice. *Proc. Natl Acad. Sci. USA* **105**, 14976–14980 (2008).
6. Koubova, J. et al. Retinoic acid activates two pathways required for meiosis in mice. *PLoS Genet.* **10**, e1004541 (2014).
7. Koubova, J. et al. Retinoic acid regulates sex-specific timing of meiotic initiation in mice. *Proc. Natl Acad. Sci. USA* **103**, 2474–2479 (2006).
8. Bowles, J. et al. Retinoid signaling determines germ cell fate in mice. *Science* **312**, 596–600 (2006).
9. Ohta, K., Lin, Y., Hogg, N., Yamamoto, M. & Yamazaki, Y. Direct effects of retinoic acid on entry of fetal male germ cells into meiosis in mice. *Biol. Reprod.* **83**, 1056–1063 (2010).
10. Raverdeau, M. et al. Retinoic acid induces Sertoli cell paracrine signals for spermatogonia differentiation but cell autonomously drives spermatocyte meiosis. *Proc. Natl Acad. Sci. USA* **109**, 16582–16587 (2012).
11. Maeda, I. et al. Max is a repressor of germ cell-related gene expression in mouse embryonic stem cells. *Nat. Commun.* **4**, 1754 (2013).
12. Kanatsu-Shinohara, M. et al. Long-term proliferation in culture and germline transmission of mouse male germline stem cells. *Biol. Reprod.* **69**, 612–616 (2003).
13. Kanatsu-Shinohara, M. et al. Genetic and epigenetic properties of mouse male germline stem cells during long-term culture. *Development* **132**, 4155–4163 (2005).
14. Gao, Z. et al. PCGF homologs, CBX proteins, and RYBP define functionally distinct PRC1 family complexes. *Mol. Cell* **45**, 344–356 (2012).
15. Qin, J. et al. The polycomb group protein L3mbtl2 assembles an atypical PRC1-family complex that is essential in pluripotent stem cells and early development. *Cell Stem Cell* **11**, 319–332 (2012).
16. Hishida, T. et al. Indefinite self-renewal of ESCs through Myc/Max transcriptional complex-independent mechanisms. *Cell Stem Cell* **9**, 37–49 (2011).
17. Zalzman, M. et al. Zscan4 regulates telomere elongation and genomic stability in ES cells. *Nature* **464**, 858–863 (2010).
18. Macfarlan, T. S. et al. Embryonic stem cell potency fluctuates with endogenous retrovirus activity. *Nature* **487**, 57–63 (2012).
19. Heyting, C. Synaptonemal complexes: structure and function. *Curr. Opin. Cell Biol.* **8**, 389–396 (1996).
20. Kee, K., Angeles, V. T., Flores, M., Nguyen, H. N. & Reijo Pera, R. A. Human DAZL, DAZ and BOULE genes modulate primordial germ-cell and haploid gamete formation. *Nature* **462**, 222–225 (2009).
21. Meuwissen, R. L. et al. A coiled-coil related protein specific for synapsed regions of meiotic prophase chromosomes. *EMBO J.* **11**, 5091–5100 (1992).
22. Ollinger, R., Alsheimer, M. & Benavente, R. Mammalian protein SCP1 forms synaptonemal complex-like structures in the absence of meiotic chromosomes. *Mol. Biol. Cell* **16**, 212–217 (2005).
23. de Vries, F. A. et al. Mouse Sycp1 functions in synaptonemal complex assembly, meiotic recombination, and XY body formation. *Genes Dev.* **19**, 1376–1389 (2005).
24. Tang, C. J., Lin, C. Y. & Tang, T. K. Dynamic localization and functional implications of Aurora-C kinase during male mouse meiosis. *Dev. Biol.* **290**, 398–410 (2006).
25. Seisenberger, S. et al. The dynamics of genome-wide DNA methylation reprogramming in mouse primordial germ cells. *Mol. Cell* **48**, 849–862 (2012).
26. Ficz, G. et al. FGF signaling inhibition in ESCs drives rapid genome-wide demethylation to the epigenetic ground state of pluripotency. *Cell Stem Cell* **13**, 351–359 (2013).
27. Leung, D. et al. Regulation of DNA methylation turnover at LTR retrotransposons and imprinted loci by the histone methyltransferase Setdb1. *Proc. Natl Acad. Sci. USA* **111**, 6690–6695 (2014).
28. Yamaguchi, S. et al. Tet1 controls meiosis by regulating meiotic gene expression. *Nature* **492**, 443–447 (2012).
29. Blaschke, K. et al. Vitamin C induces Tet-dependent DNA demethylation and a blastocyst-like state in ES cells. *Nature* **500**, 222–226 (2013).
30. Hsu, P. D., Lander, E. S. & Zhang, F. Development and applications of CRISPR-Cas9 for genome engineering. *Cell* **157**, 1262–1278 (2014).
31. Ying, Q. L. et al. The ground state of embryonic stem cell self-renewal. *Nature* **453**, 519–523 (2008).
32. Hackett, J. A. & Surani, M. A. Regulatory principles of pluripotency: from the ground state up. *Cell Stem Cell* **15**, 416–430 (2014).
33. Magnusdottir, E. & Surani, M. A. How to make a primordial germ cell. *Development* **141**, 245–252 (2014).
34. Ohinata, Y. et al. Blimp1 is a critical determinant of the germ cell lineage in mice. *Nature* **436**, 207–213 (2005).
35. Nakaki, F. et al. Induction of mouse germ-cell fate by transcription factors in vitro. *Nature* **501**, 222–226 (2013).
36. Amati, B. et al. Oncogenic activity of the c-Myc protein requires dimerization with Max. *Cell* **72**, 233–245 (1993).
37. Kanatsu-Shinohara, M. & Shinohara, T. Spermatogonial stem cell self-renewal and development. *Annu. Rev. Cell Dev. Biol.* **29**, 163–187 (2013).
38. Baudino, T. A. & Cleveland, J. L. The Max network gone mad. *Mol. Cell. Biol.* **21**, 691–702 (2001).
39. Feng, C. W., Bowles, J. & Koopman, P. Control of mammalian germ cell entry into meiosis. *Mol. Cell. Endocrinol.* **382**, 488–497 (2014).
40. Kagiwada, S., Kurimoto, K., Hirota, T., Yamaji, M. & Saitou, M. Replication-coupled passive DNA demethylation for the erasure of genome imprints in mice. *EMBO J.* **32**, 340–353 (2013).
41. Kim, J. et al. A Myc network accounts for similarities between embryonic stem and cancer cell transcription programs. *Cell* **143**, 313–324 (2010).

42. Kanatsu-Shinohara, M., Onoyama, I., Nakayama, K. I. & Shinohara, T. Skp1-Cullin-F-box (SCF)-type ubiquitin ligase FBXW7 negatively regulates spermatogonial stem cell self-renewal. *Proc. Natl Acad. Sci. USA* **111,** 8826–8831 (2014).

43. Yokobayashi, S. *et al.* PRC1 coordinates timing of sexual differentiation of female primordial germ cells. *Nature* **495,** 236–240 (2013).

44. Cong, L. *et al.* Multiplex genome engineering using CRISPR/Cas systems. *Science* **339,** 819–823 (2013).

45. Hishida, T. *et al.* Sirt1, p53, and p38(MAPK) are crucial regulators of detrimental phenotypes of embryonic stem cells with Max expression ablation. *Stem Cells* **30,** 1634–1644 (2012).

46. Okashita, N. *et al.* PRDM14 promotes active DNA demethylation through the ten-eleven translocation (TET)-mediated base excision repair pathway in embryonic stem cells. *Development* **141,** 269–280 (2014).

47. Lucifero, D., Mertineit, C., Clarke, H. J., Bestor, T. H. & Trasler, J. M. Methylation dynamics of imprinted genes in mouse germ cells. *Genomics* **79,** 530–538 (2002).

Acknowledgements

Author contributions

Additional information

Cell Reports

Piwi Nuclear Localization and Its Regulatory Mechanism in *Drosophila* Ovarian Somatic Cells

Graphical Abstract

Authors

Ryu Yashiro, Yukiko Murota,
Kazumichi M. Nishida, ..., Lumi Negishi,
Haruhiko Siomi, Mikiko C. Siomi

Correspondence

siomim@bs.s.u-tokyo.ac.jp

In Brief

Piwi represses transposons transcriptionally to maintain genome integrity. Yashiro et al. show that Importinα plays a pivotal role in Piwi nuclear localization and that Piwi has a bipartite nuclear localization signal at the N terminus. Piwi autoregulates its nuclear localization by exposing the nuclear localization signal to Impα upon piRNA loading.

Highlights

- Importinα plays a pivotal role in Piwi nuclear localization in OSCs

- Piwi has a classical bipartite nuclear localization signal at the N terminus

- piRNA loading triggers conformational change in Piwi

- Piwi autoregulates its nuclear localization by exposing NLS to environment

CellPress

Article

Piwi Nuclear Localization and Its Regulatory Mechanism in *Drosophila* Ovarian Somatic Cells

Ryu Yashiro,[1,5] Yukiko Murota,[1,5] Kazumichi M. Nishida,[1] Haruna Yamashiro,[1] Kaede Fujii,[2] Asuka Ogai,[2] Soichiro Yamanaka,[3] Lumi Negishi,[4] Haruhiko Siomi,[3] and Mikiko C. Siomi[1,6,*]

[1]Department of Biological Sciences, Graduate School of Science, The University of Tokyo, Tokyo 113-0032, Japan
[2]Yokohama City University School of Medicine, Yokohama, Kanagawa 236-0004, Japan
[3]Department of Molecular Biology, Keio University School of Medicine, Tokyo 160-8582, Japan
[4]Institute of Molecular and Cellular Biosciences, The University of Tokyo, Tokyo 113-0032, Japan
[5]These authors contributed equally
[6]Lead Contact
*Correspondence: siomim@bs.s.u-tokyo.ac.jp
https://doi.org/10.1016/j.celrep.2018.05.051

SUMMARY

In *Drosophila* ovarian somatic cells (OSCs), Piwi represses transposons transcriptionally to maintain genome integrity. Piwi nuclear localization requires the N terminus and PIWI-interacting RNA (piRNA) loading of Piwi. However, the underlying mechanism remains unknown. Here, we show that Importinα (Impα) plays a pivotal role in Piwi nuclear localization and that Piwi has a bipartite nuclear localization signal (NLS). Impα2 and Impα3 are highly expressed in OSCs, whereas Impα1 is the least expressed. Loss of Impα2 or Impα3 forces Piwi to be cytoplasmic, which is rectified by overexpression of any Impα members. Extension of Piwi-NLS with an additional Piwi-NLS leads Piwi to be imported to the nucleus in a piRNA-independent manner, whereas replacement of Piwi-NLS with SV40-NLS fails. Limited proteolysis analysis suggests that piRNA loading onto Piwi triggers conformational change, exposing the N terminus to the environment. These results suggest that Piwi autoregulates its nuclear localization by exposing the NLS to Impα upon piRNA loading.

INTRODUCTION

PIWI proteins are a subclade of the Argonaute family of proteins enriched in the gonads, where PIWI binds PIWI-interacting RNAs (piRNAs) to assemble piRNA-induced silencing complexes (piRISCs) to repress transposons to maintain genome integrity (Aravin et al., 2007; Ghildiyal and Zamore, 2009; Iwasaki et al., 2015; Juliano et al., 2011; Malone and Hannon, 2009; Yamashiro and Siomi, 2018). Loss-of-function mutations of PIWI proteins and piRNA factors essential in the pathway cause defects in the genome surveillance system, leading to transposon derepression, failures in gametogenesis, and infertility (Khurana and Theurkauf, 2010).

Drosophila expresses three genes encoding members of the PIWI protein family, Piwi, Aubergine (Aub), and Ago3 in both ovaries and testes (Cox et al., 1998; Li et al., 2009; Nagao et al., 2011; Schmidt et al., 1999). In the ovaries, Aub and Ago3 are expressed specifically in germ cells, where they silence transposons post-transcriptionally by cleaving their transcripts using their endonuclease activity known as Slicer (Brennecke et al., 2007; Gunawardane et al., 2007; Li et al., 2009; Nishida et al., 2007). Aub- and Ago3-bound piRNAs are mainly antisense and sense to transposon-coding sequences, respectively, and Aub and Ago3 reciprocally cleave transposon mRNAs and antisense transcripts, respectively. The resultant RNA fragments are further processed to mature piRNAs; thereby Aub/Ago3-Slicer-dependent transposon silencing in germ cells is considered to be coupled with piRNA biogenesis.

Piwi is expressed in both germ cells and ovarian somatic cells (OSCs), and in both cell types, Piwi is localized to the nucleus and silences transposons transcriptionally by inducing heterochromatinization at the target loci with co-factors such as Panoramix/Silencio, Asterix/GTSF1, Maelstrom (Mael), and linker histone H1 (Czech et al., 2013; Dönertas et al., 2013; Handler et al., 2013; Iwasaki et al., 2016; Kalmykova et al., 2005; Le Thomas et al., 2013; Muerdter et al., 2013; Ohtani et al., 2013; Saito et al., 2006, 2010; Sienski et al., 2012, 2015; Yu et al., 2015). Piwi nuclear localization requires both the N-terminal region of Piwi and piRNA loading onto Piwi, which may be particularly obvious in OSCs (Klenov et al., 2011; Saito et al., 2009, 2010). A proportion of Piwi in germ (nurse) cells may be translocated to the nucleus even under conditions where the piRNA binding activity was impeded by mutations (Le Thomas et al., 2013). This layered, "gatekeeping" mechanism ensures Piwi-piRISC-mediated nuclear transposon silencing, because piRNA-free Piwi in the nucleus would be useless with no ability to find its targets (Ishizu et al., 2011). However, how piRNA loading-dependent Piwi nuclear localization is regulated mechanistically is still unclear. The nuclear import machinery required for Piwi nuclear import also remains unclear.

The N-terminal region of Piwi, which has been shown to be necessary for its nuclear import, is rich in basic residues, a characteristic typical of classical nuclear localization signals (NLSs) whose nuclear import is mediated by an Importin α/β (Impα/β) heterodimer (Görlich, 1998; Stewart, 2007). The NLS of SV40 large T antigen (SV40-NLS) (PKKKRKV) (Kalderon et al., 1984) and that of *Xenopus laevis* nucleoplasmin (NP-NLS) (KRPAATKKAGQAKKKK) (Robbins et al., 1991) are the

prototypic monopartite and bipartite NLSs, respectively (Gold-farb et al., 2004; Stewart, 2007). Monopartite NLSs consist of a single stretch of basic residues, while bipartite NLSs contain two stretches of basic residues with a linker region between them. In the Impα/β pathway, the adaptor molecule Impα protein first binds cargos in the cytoplasm through their NLSs. Then, Impβ associates with the heterodimer through the Impβ binding (IBB) domain of Impα to assemble a NLS-cargo/Impα/Impβ trimeric complex, which facilitates the nucleocytoplasmic translocation of the complex across the nuclear pores located on the nuclear envelope. Upon transport, RanGTP in the nucleus binds and disassembles the complex, releasing the cargos to the nucleoplasm, where they exert their nuclear functions (Görlich, 1998; Stewart, 2007).

Members of the Impα family of proteins can be divided into three phylogenetic clades, α1, α2, and α3 (Mason et al., 2009; Pumroy and Cingolani, 2015). *Drosophila* contains a single representative of each clade, Impα1, Impα2, and Impα3 (Küssel and Frasch, 1995; Goldfarb et al., 2004; Török et al., 1995; Mason et al., 2002, 2003). All Impα proteins contain one IBB domain at the N-terminal end, and the rest of the sequence contains 10 Armadillo (ARM) repeats, which were originally identified in the protein encoded by the *Drosophila* segment polarity gene *armadillo* (Riggleman et al., 1989). While the IBB domain binds Impβ during nuclear import through the nuclear pore, the ARM repeats assemble a scaffold structure that can accommodate monopartite or bipartite NLSs (Conti et al., 1998; Fontes et al., 2003). When the ARM repeats are not bound with cargos, the IBB domain binds the ARM repeats intramolecularly, autoinhibiting nuclear import of cargo-free Impα (Kobe, 1999; Stewart, 2007). *Drosophila* possibly contains a fourth Impα member, Impα4, which, however, lacks the IBB domain and is testis specific (Phadnis et al., 2012). A single *Impβ* gene known as *ketel* was found in the *Drosophila* genome (Lippai et al., 2000). *Drosophila Impα1* null flies developed to adulthood but showed severe defects in gametogenesis and infertility (Ratan et al., 2008). Similarly, homozygous *Impα2* mutants developed normally to adulthood, but mutant females, and not males, were completely sterile (Mason et al., 2002). Impα3 mutants showed embryonic lethality (Mason et al., 2003).

On the basis of all these earlier findings, we speculated that Impα may be responsible for Piwi nuclear localization. To test this, we first examined the levels of Impα proteins in cultured OSCs. To this end, we produced monoclonal antibodies for each Impα member and performed western blotting, which revealed that Impα2 and Impα3 were fairly highly expressed in OSCs, whereas Impα1 was the least expressed. Loss of Impα2 or Impα3 by RNAi treatment disturbed nuclear localization of Piwi. However, nuclear localization of SV40-NLS-cargo was not affected, suggesting that Piwi-NLS may have lower nuclear localization efficiency than SV40-NLS. We defined the N-terminal 36 residues of Piwi as a bipartite NLS. Interestingly, bipartite NP-NLS-cargo behaved similarly to Piwi in OSCs lacking Impα2 or Impα3. Impα proteins may prioritize monopartite NLSs over bipartite NLSs, at least in OSCs. Replacement of Piwi-NLS with SV40-NLS failed to obviate the requirement of piRNA loading in Piwi nuclear localization. However, Piwi was imported to the nucleus piRNA independently upon duplication of the

Piwi-NLS. Substitution of the second NLS with a peptide that lacks the NLS activity little changed the outcome. Limited proteolysis assays showed that about 90 residues in the N-terminal end of Piwi were inaccessible when Piwi was free from piRNAs, but piRNA loading made the region accessible to the environment, most likely through a conformational change in Piwi. piRNA loading increased the ability of Piwi to interact with Impα2 and Impα3. Thus, Piwi autoregulates its nuclear localization by exposing the NLS to Impα upon piRNA loading. Addition of Piwi-NLS caused the otherwise cytoplasmic Aub to be imported to the nucleus in a piRNA-dependent manner, as was Piwi. Piwi-NLS may have a unique property to be "hidden" intramolecularly prior to piRNA loading, possibly by domains conserved in PIWI members.

RESULTS

Our previous RNA-sequencing data (Sumiyoshi et al., 2016) suggested that *Impα2* was relatively highly expressed in OSCs, accounting for 70.7% of the total *Impα* expression, while the expression level of *Impα1* was much lower (4.0%) (Figure S1A). The expression level of *Impα3* was between those of *Impα2* and *Impα1* (25.3%) (Figure S1A). To estimate the levels of the Impα proteins by western blotting, we first produced monoclonal antibodies against each of the proteins (Figures S1B and S1C). Comparison of the signals of the endogenous Impα proteins in OSCs with those of recombinant Impα proteins suggested that the ratio of abundance levels of Impα1, Impα2, and Impα3 proteins in OSCs was about 5:77.5:17.5 (Figures S1A and S1D). The corresponding monoclonal antibodies detected each Impα protein in OSCs in immunofluorescence analyses (Figure S1E).

To examine whether Impα was responsible for Piwi nuclear localization, we expressed myc-Piwi in OSCs in which each Impα had been individually depleted by RNAi. The efficiency and specificity of the RNAi treatment were determined by western blotting (Figure S2A). Immunofluorescence showed that myc-Piwi still accumulated in the nucleus in Impα1-depleted OSCs, as it did in normal OSCs (Figure 1A). We considered these results to be reasonable because Impα1 was the least abundant Impα in the OSCs (Figure S1A), and Impα2 and Impα3 remained highly abundant in OSCs even after RNAi treatment (Figure S2A). However, myc-Piwi was no longer restricted in the nucleus and was detected in the cytoplasm in Impα2- and Impα3-depleted OSCs (Figures 1B and 1C). piRNA loading of myc-Piwi was barely affected by lack of Impα2 and Impα3 (Figure S2B; data not shown). These results support our original idea that Impα plays a role in Piwi nuclear localization.

Impα2 accounted for about 78% of total Impα proteins in the OSCs (Figure S1A). Therefore, after depletion of Impα2, the amounts of Impα1 and Impα3 proteins in the OSCs may not be enough to import all cargos to the nucleus. Indeed, depletion of Impα2 strongly affected the cellular localization of Piwi (Figure 1B). However, after depletion of Impα3, the amount of Impα2 remained high in OSCs (Figure S2A). Therefore, the finding that Piwi nuclear localization was affected by loss of Impα3 (Figure 1C) was somewhat confusing. The simplest explanation for this result is that Piwi nuclear localization requires both Impα2 and Impα3 simultaneously. To test this hypothesis, we
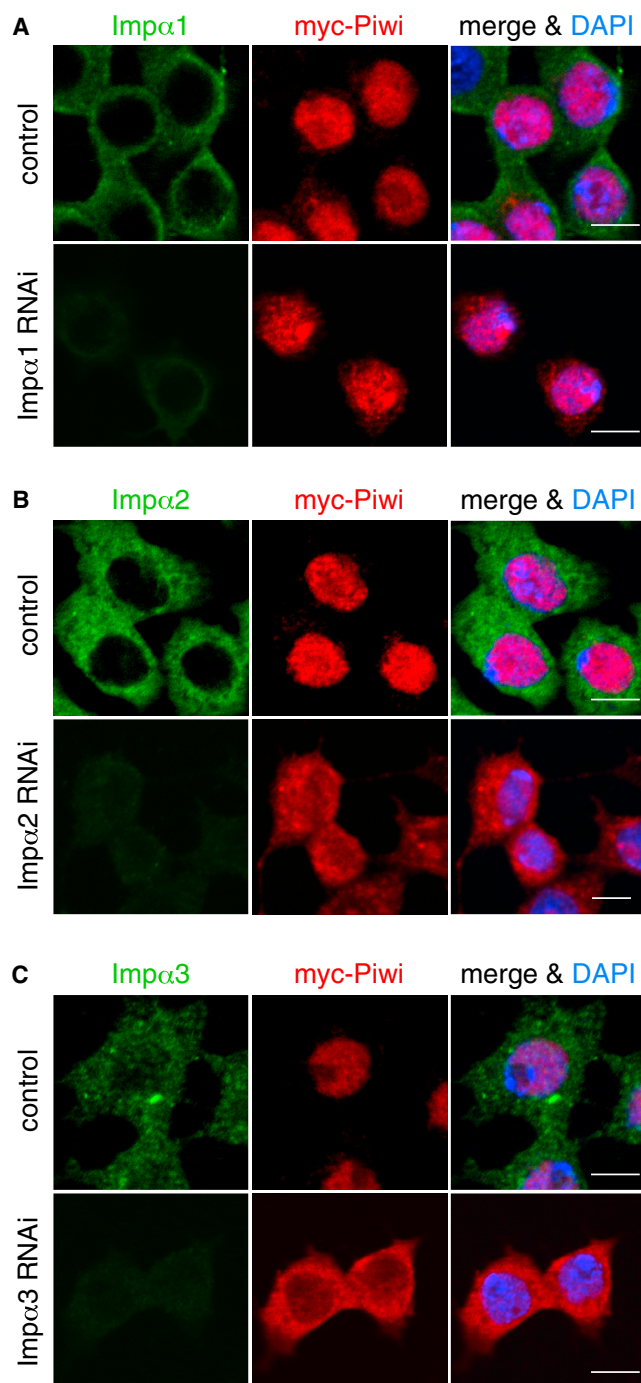
Figure 1. Requirement of Impα in Piwi Nuclear Localization in OSCs
(A) Nuclear localization of myc-Piwi (red) was not affected by loss of Impα1 (green) in OSCs. EGFP siRNA was used as a control. DAPI signals (blue) show the nuclei. Scale bars, 5 μm.
(B) Nuclear localization of myc-Piwi (red) was affected by loss of Impα2 (green) in OSCs. EGFP siRNA was used as a control. DAPI signals (blue) show the nuclei. Scale bars, 5 μm.
(C) Loss of Impα3 (green) also affected nuclear localization of myc-Piwi (red) in OSCs. EGFP siRNA was used as a control. DAPI signals (blue) show the nuclei. Scale bars, 5 μm.
See also Figures S1 and S2 and Table S1.

performed rescue experiments. First, Impα2- and Impα3-lacking OSCs were prepared; then each *Impα* gene was expressed by cotransfection with FLAG-Piwi in the cells. If both Impα2 and Impα3 were simultaneously required for Piwi nuclear localization, ectopic expression of *Impα3* in Impα2-lacking OSCs would not restore Piwi nuclear localization, while ectopic expression of *Impα2* should rescue the defective phenotype. Examination revealed that not only *Impα2* expression, but also *Impα1* and *Impα3* expression (all *Impα* genes were RNAi-resistant) rectified Piwi nuclear localization (Figure 2A). Similarly, ectopic expression of all individual *Impα* genes rescued the defective phenotype caused by depletion of Impα3 (Figure 2B). Therefore, the idea that Impα2 and Impα3 were simultaneously required for Piwi nuclear localization was excluded.

An alternative explanation may be that the binding activity of Piwi-NLS to Impα2 was relatively low, and therefore Impα2 prioritized cargos other than Piwi in nuclear import when the total amount of Impα proteins was reduced, albeit only by about 18%, as a consequence of, for instance, Impα3 depletion. To check this, we examined whether the subcellular localization of SV40-NLS-cargo was affected by lack of Impα3 as well as Impα2. To this end, Mael fused with a myc-tag, and a monopartite SV40-NLS at the N- and C-terminal ends of Mael, respectively, was employed. Mael is one of the piRNA factors required in germ cells, but is dispensable for the somatic piRNA pathway in OSCs (Matsumoto et al., 2015; Sienski et al., 2012). We found that depletion of neither Impα2 nor Impα3 affected cellular localization of myc-Mael-SV40-NLS (cargo-SV40-NLS in Figures 3A and 3B), suggesting that efficiency of nuclear import of Piwi-NLS was somewhat lower than that of monopartite SV40-NLS.

Previously, we showed that a Piwi mutant Piwi-ΔN that lacked 72 amino acid residues from the N-terminal end was mislocalized to the cytoplasm, although Piwi-ΔN formed piRISCs with piRNAs as well as wild-type (WT) Piwi (Saito et al., 2009). The 72 residues were very basic, and arginine and lysine residues together accounted for 23.6% (17 out of 72 residues), which is a typical feature of classical NLSs bound with Impα proteins (Figure 4A). We fused the peptide consisting of the 72 residues to EGFP and found that this fusion protein was localized exclusively to the nucleus (Figure 4B). However, the peptide was too long to be defined as a monopartite or bipartite NLS. Thus, we deleted 36 N-terminal residues from Piwi and examined the cellular localization. This mutant Piwi-ΔN36 failed to accumulate in the nucleus (Figure 4C). We then fused the 36 residues to EGFP and found that this fusion protein, Piwi-N36-EGFP, strongly accumulated in the nucleus similar to Piwi-N72-EGFP (Figure 4C). In contrast, Piwi-N20-EGFP, which contained only 20 residues from the N-terminal end of Piwi, was found to be throughout the cells, the same as EGFP alone (Figures 4B and 4C), although the 20 residues included a basic stretch 7-RGRRR-11. Based on these results, we defined the 1–36 residues at the N-terminal end of Piwi as the Piwi-NLS.

Next, we produced a series of Piwi-NLS mutants in the context of full-length Piwi. We first mutated four residues 9-RRRP-12 of Piwi to four alanine residues. This mutant Piwi-NLS-M1 appeared mostly in the cytoplasm, but was slightly detected also in the nucleus (Saito et al., 2009) (Figure 4D). Piwi-NLS-M2, where Arg22 was mutated to alanine, was nearly exclusively
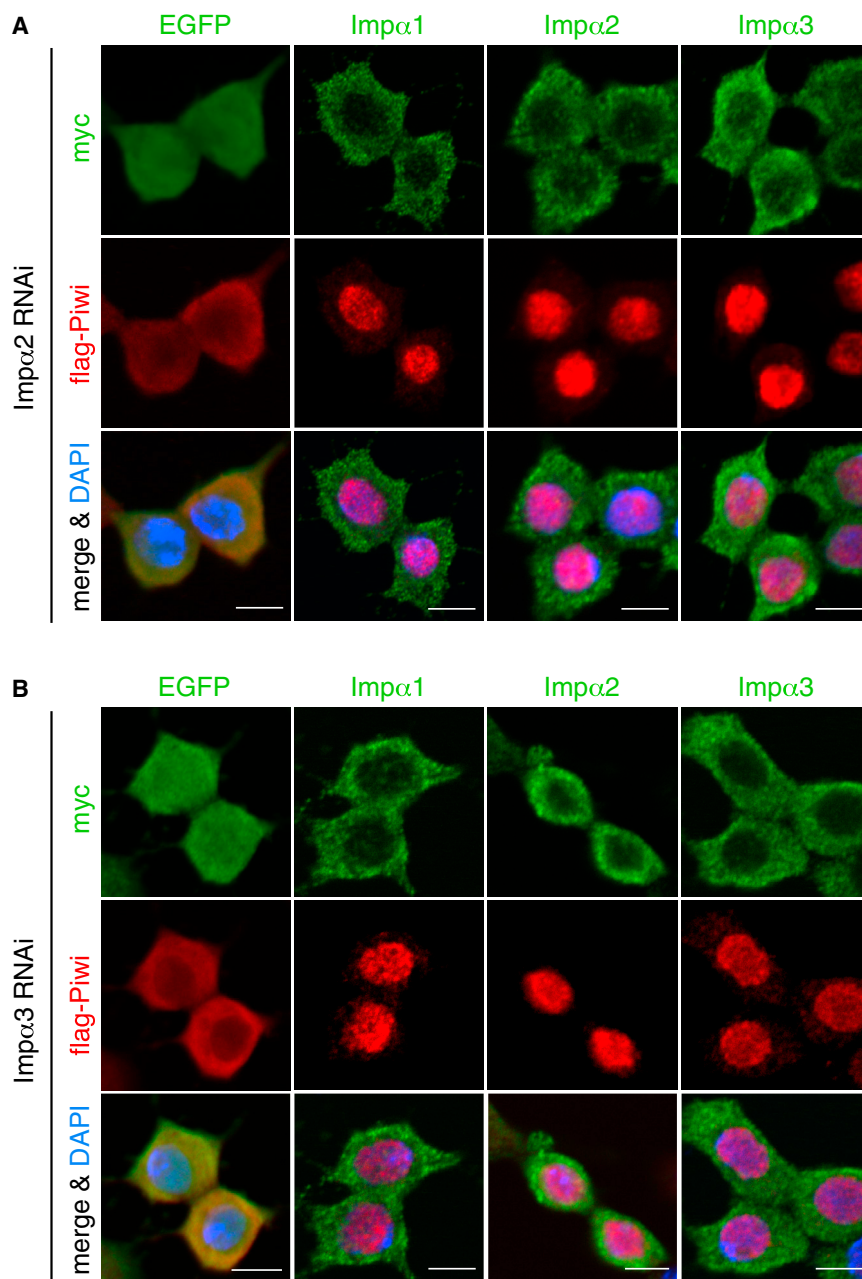
A

B

Figure 2. All Three Impα Members Restore Piwi Nuclear Localization Affected by Loss of Impα2 and Impα3 in OSCs

(A) Expression of individual Impα members (green), but not EGFP, in Impα2-depleted OSCs restored nuclear localization of Piwi (red). DAPI signals (blue) show the nuclei. Scale bars, 5 μm.

(B) Expression of individual Impα proteins (green) in Impα3-depleted OSCs restored nuclear localization of Piwi (red). DAPI signals (blue) show the nuclei. Scale bars, 5 μm.

See also Table S1.

(sDMA) (Figure S3A). sDMA is one of the post-translational modifications that are observed in the majority of PIWI proteins across species (Yamashiro and Siomi, 2018). Arginines within Piwi-NLS may also be sDMA-modified, but only weakly (Figure S3A). Piwi was undetected with Y12 and SYM11, the antibodies specifically reacting to sDMAs (Figure S3B and data not shown). These results suggest that sDMA modification of Piwi hardly impacts on Piwi nuclear localization in OSCs.

We then took NP-NLS, a representative of bipartite NLSs, and fused it to EGFP to produce NP-NLS-EGFP. In contrast to SV40-NLS-containing cargo (Figures 3A and 3B), NP-NLS-EGFP was localized exclusively to the nucleus of normal OSCs, as expected, but was detected in the cytoplasm under conditions where Impα2 or Impα3 had been depleted (NP-NLS-cargo in Figures 4E and 4F), similar to Piwi (Figures 1B and 1C). These results suggest that the sensitivity that Piwi showed to a subtle reduction in the total amount of Impα proteins in OSCs was not unique to Piwi, and that monopartite NLSs likely have higher efficiency in nuclear transport than bipartite NLSs, at least in OSCs.

Piwi nuclear localization requires not only its NLS but also piRNA loading, sug-

localized to the nucleus (Figure 4D), and Piwi-NLS-M3, where Arg34 was mutated to alanine, was found in both the nucleus and the cytoplasm nearly evenly. However, Piwi-NLS-M4 and Piwi-NLS-M5, where Lys31 and Lys31/Arg34 were mutated to alanine residues, respectively, were not localized to the nucleus (Figure 4D). Piwi-NLS-M1 and Piwi-NLS-M5 only weakly bound to Impα3 (Figure S2C). In summary, two small basic islands around 9-RRRP-12 and 31-KVFR-34 within the 36-residue Piwi-NLS sequence were necessary for Piwi nuclear localization. Thus, we defined Piwi-NLS as a bipartite NLS.

Mass spectrometric analysis of Piwi in OSCs showed that Arg82 might be deeply modified to be a symmetric dimethyl arginine
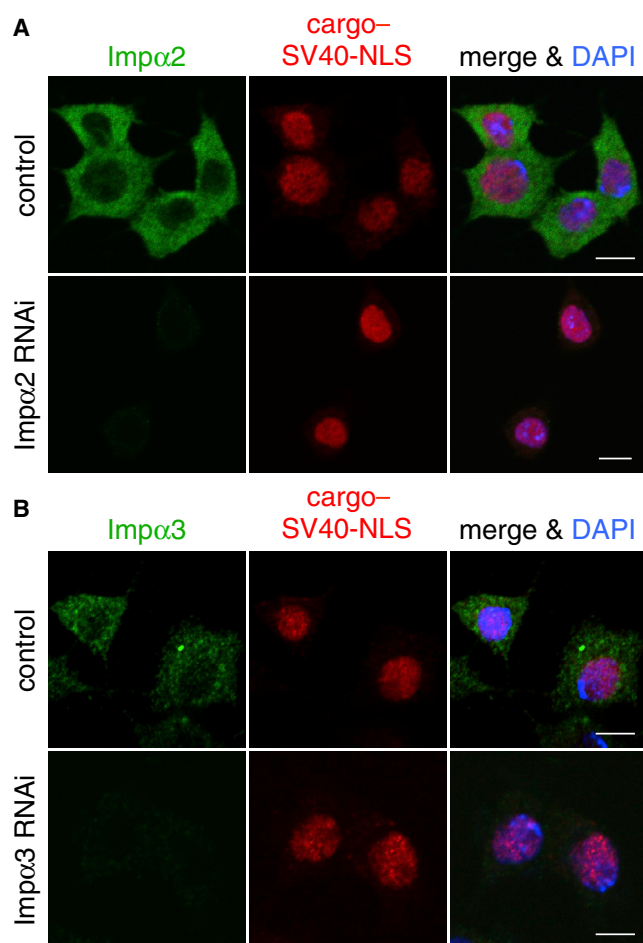
gesting that Piwi-NLS is not accessible for Impα in the cytosol until Piwi is loaded with piRNA. One hypothesis was that an unknown protein (temporally termed as protein X) specifically occupied the NLS of piRNA-free Piwi, blocking Impα binding to the NLS. Then, piRNA loading onto Piwi triggered displacement of the protein X from Piwi-NLS, allowing Piwi-piRISC to be successfully localized to the nucleus. To test this model, we exchanged Piwi-NLS with SV40-NLS to determine whether the Piwi mutant SV40-NLS-Piwi-ΔN required piRNA loading or not to be localized to the nucleus. Because SV40-NLS-containing cargo was localized to the nucleus with no specific treatments (Figures 3A and 3B), we assumed that SV40-NLS-Piwi-ΔN would

277

A

B

Figure 3. Effects of Impα Depletion on SV40-NLS Localization in OSCs

(A and B) Depletion of Impα2 (green in A) and Impα3 (green in B) only marginally affected cellular localization of cargo-SV40-NLS (myc-Mael-SV40-NLS) (red) in OSCs. DAPI signals (blue) show the nuclei. Scale bars, 5 μm.
See also Table S1.

also be translocated to the nucleus without piRNA loading. However, against our expectation, the mutant failed to be localized to the nucleus when piRNA biogenesis had been compromised by Yb depletion (Figure 5A). Thus, the "protein X" hypothesis was unlikely.

An alternative model is that Piwi can hide its own NLS intramolecularly from Impα until piRNA is loaded onto Piwi. To examine this possibility, we fused another Piwi-NLS composed of 36 residues to the N-terminal end of WT Piwi (Figure 5B). This process extended the NLS by duplication of the sequence in the context of full-length Piwi by fusing Piwi-NLS to the N terminus of WT Piwi. If this additional Piwi-NLS projected into the cellular environment beyond the surface of piRNA-free Piwi, we considered Impα would bind to it and translocate the mutant Piwi-NLS-Piwi to the nucleus, regardless of piRNA loading. Indeed, Piwi-NLS-Piwi was localized to the nucleus even after Yb depletion. Two independent Piwi-NLS-Piwi mutants in which the second NLS was mutated to impede the activity as NLS behaved similarly

to Piwi-NLS-Piwi (Figures S4A and S4B), suggesting the internal NLS in Piwi-NLS-Piwi is dispensable for rendering the piRNA-independent, nuclear localization activity to the protein.

Human Ago2 (hAgo2) that was not bound with guide RNA was fragmented to domains in limited proteolysis assays, but guide RNA loading made hAgo2 resistant to the proteolysis treatment (Elkayam et al., 2012). We tested whether Piwi behaved similarly in the assays. To this end, we expressed Piwi in cultured *Drosophila* Schneider 2 (S2) cells, which are non-gonadal somatic cells, so they do not operate the piRNA pathway. Indeed, Piwi expressed in S2 cells was devoid of piRNAs or any other RNAs, and was cytoplasmic (Figures S5A and S5B). We then immunopurified piRNA-free Piwi from S2 cells using anti-Piwi monoclonal antibody 3G11. In parallel, Piwi-piRISC was immunopurified from OSCs using 3G11. The epitope of 3G11 was within the 20 residues at the N-terminal end that corresponded to the first half of the Piwi-NLS (Figure S5C). In accordance with this fact, we found that immunopurification of piRNA-free Piwi from S2 cells was much more difficult than immunopurification of Piwi-piRISC from OSCs, so to obtain comparable amounts of Piwi, we prolonged the duration of immunoprecipitation from S2 cells. Also, the cell number of S2 cells used was about 10 times higher compared with that of OSCs. Both Piwi fractions were subjected to limited proteolysis assays. First, we used thermolysin because it was employed in the original hAgo2 study (Elkayam et al., 2012). However, even a low final thermolysin concentration of 0.08 ng/μL nearly completely degraded even Piwi-piRISC (data not shown). We then used chymotrypsin, which we found successfully released a large portion of Piwi-piRISC to the supernatant (Figure 5C), as was the case for Siwi-piRISC in our previous study (Siwi is one of two PIWI members in silkworm; Matsumoto et al., 2016). The large portion of Piwi in the supernatant was detected by another anti-Piwi monoclonal antibody 4D2 (Saito et al., 2009) by western blotting. The epitope of 4D2 was determined to be located between Trp72 and Lys89 (Figure S5D), suggesting that the proteolysis occurred upstream of the 4D2 epitope. In contrast, for piRNA-free Piwi, multiple 4D2-positive bands appeared exclusively in the bead fraction, implying that proteolysis occurred at multiple sites downstream of the 4D2 epitope. These results strongly suggest that the N-terminal region of approximately 90 residues of Piwi (including Piwi-NLS and 3G11/4D2 epitopes) was hardly accessible when Piwi was devoid of piRNAs, but piRNA loading induced a major conformational change in Piwi, as in hAgo2, exposing the N-terminal region to the environment.

Similar results were obtained when Piwi (with no tag) exogenously expressed in OSCs before and after depletion of Gasz, an essential piRNA biogenesis factor (Handler et al., 2013), was employed (Figure 5D). In this particular experiment, we knocked down Gasz, but not Yb, because piRNA-free Piwi was somewhat more stable than that in Yb-depleted cells (data not shown). Thus, our earlier observation that Piwi-piRISC (from OSCs) and piRNA-free Piwi (from S2 cells) showed distinct proteolytic patterns (Figure 5C) was not because of use of two different cell lines in the assays.

We then examined whether Piwi binding with Impα is affected by piRNA loading status of Piwi. To this end, we expressed FLAG-Piwi in Gasz-depleted OSCs, immunoprecipitated the
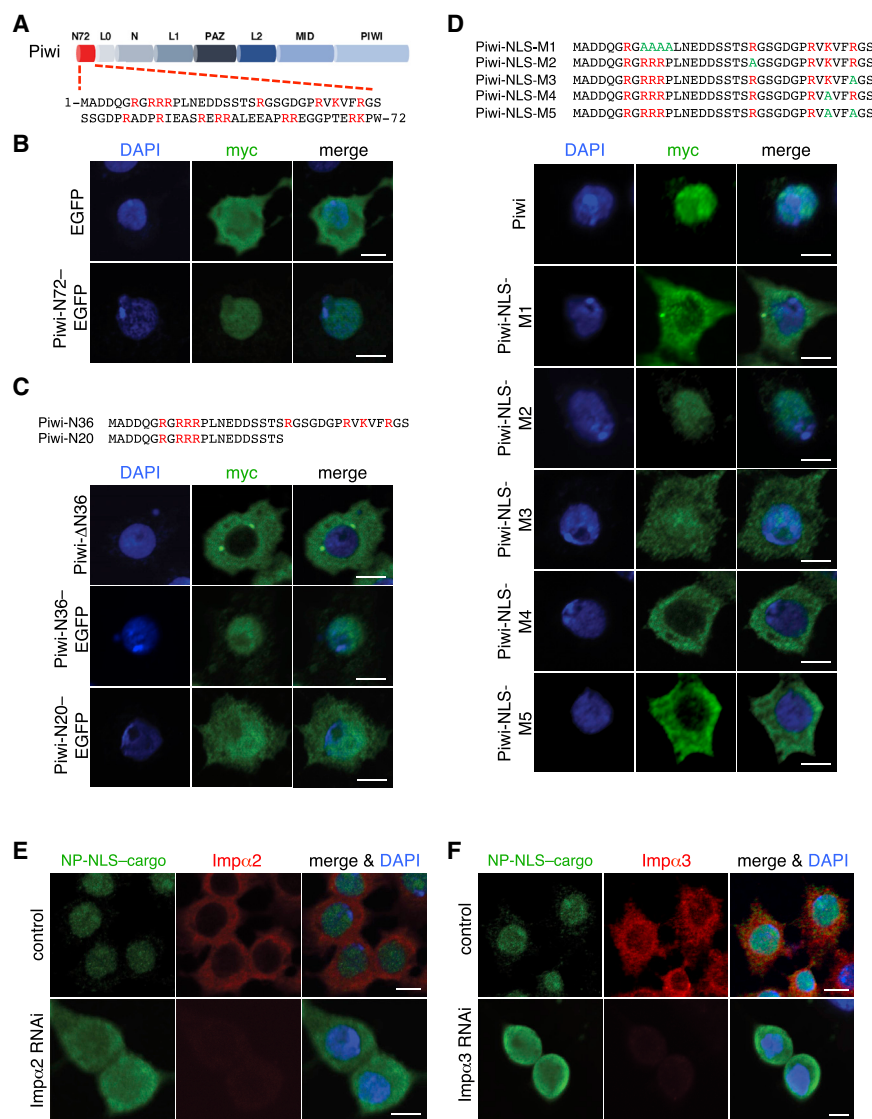
Figure 4. Piwi Contains a Bipartite NLS at the N-Terminal End

(A) Domain structure and amino acid sequence of the N-terminal 72 residues of Piwi (N72) are shown. L0 domain: 38 residues (Y76–R113); N domain: 73 residues (I114–I186); L1 domain: S187–T263 (77 residues); PAZ domain: I264–T371 (108 residues); L2 domain: G372–T470 (99 residues); MID domain: P471–I601 (131 residues); PIWI domain: E602–L843 (242 residues). Three residues, 73-GDQ-75, do not belong to any of the domains indicated. The domain structure was defined by sequence alignment with the peptide sequence of Siwi (Matsumoto et al., 2016). Lysine and arginine residues are shown in red.

(B) myc-Piwi-N72-EGFP (green), but not myc-EGFP, was exclusively localized to the nucleus. EGFP has a small molecular weight (about 25 kDa), which allows EGFP to diffuse passively in and out of the nucleus in a receptor-independent fashion. DAPI signals (blue) show the nuclei. Scale bars, 5 μm.

(C) Deletion of 36 residues from the N-terminal end of Piwi caused mislocalization of Piwi (green: myc-Piwi-ΔN36) in the cytoplasm. Piwi-N36-EGFP (green), but not Piwi-N20-EGFP, was nearly exclusively localized to the nucleus. DAPI signals (blue) show the nuclei. Scale bars, 5 μm.

(D) myc-Piwi and myc-Piwi-NLS-M2 were nearly exclusively localized to the nucleus. Piwi-NLS-M3 can be detected in both the nucleus and the cytoplasm evenly in OSCs. Piwi-NLS-M1, -M4, and -M5 strongly accumulated in the cytoplasm. DAPI signals (blue) show the nuclei. Scale bars, 5 μm.

(E and F) Depletion of Impα2 (in E) and Impα3 (in F) affects cellular localization of NP-NLS-cargo (green: myc-NP-NLS-EGFP) in OSCs. DAPI signals (blue) show the nuclei. Scale bars, 5 μm.

See also Figures S2 and S3 and Table S1.

Impα3 complex, and probed it with anti-FLAG antibody. As expected, depletion of Gasz severely reduced the levels of Piwi-Impα3 interaction (Figure 5E). The level of Piwi-Impα2 interaction was similarly reduced (Figure S5E). These results strongly support our original idea that Piwi-piRNA loading is necessary for Piwi being tightly associated with Impα *in vivo*. It was experimentally confirmed that Piwi exogenously expressed in Gasz-depleted OSCs was loaded with piRNAs to a much lesser extent than Piwi expressed in normal OSCs (Figures S5F and S5G).

Aub exogenously expressed in OSCs by transfection was loaded with piRNAs that are normally loaded onto endogenous Piwi in the cells (Sato et al., 2015). However, Aub-piRISC remained to be in the cytoplasm, as was the case in germ cells, because it did not possess an NLS. We then fused Piwi-NLS to Aub and found that the Piwi-NLS-Aub protein was imported to the nucleus in OSCs (Figure 6A). However, Aub was forced to be in the cytoplasm when Yb was depleted to block piRNA

biogenesis, as was found for Piwi (Figure 6A). Similar results were obtained when Aub was fused to SV40-NLS (Figure 6A). Both Piwi-NLS-EGFP and SV40-NLS-EGFP were insensitive to Yb depletion and localized to the nucleus in Yb-depleted OSCs (Figure 6B). Addition of another Piwi-NLS to Piwi-NLS-Aub caused the protein to be nuclear localized in a manner independent of piRNAs (Figure S5H). These results suggest that piRNA loading-driven conformational change, which controls the accessibility of the PIWI N terminus, is a common feature of PIWI proteins.

DISCUSSION

In this study, we revealed that Impα played a vital role in Piwi nuclear localization in OSCs, and that Piwi autoregulated its cellular localization by controlling the accessibility of its own N-terminal bipartite NLS to Impα, by changing the structure in a piRNA loading-dependent manner. With this "layered" regulation, Piwi was strictly localized to the cytoplasm before piRNA loading.
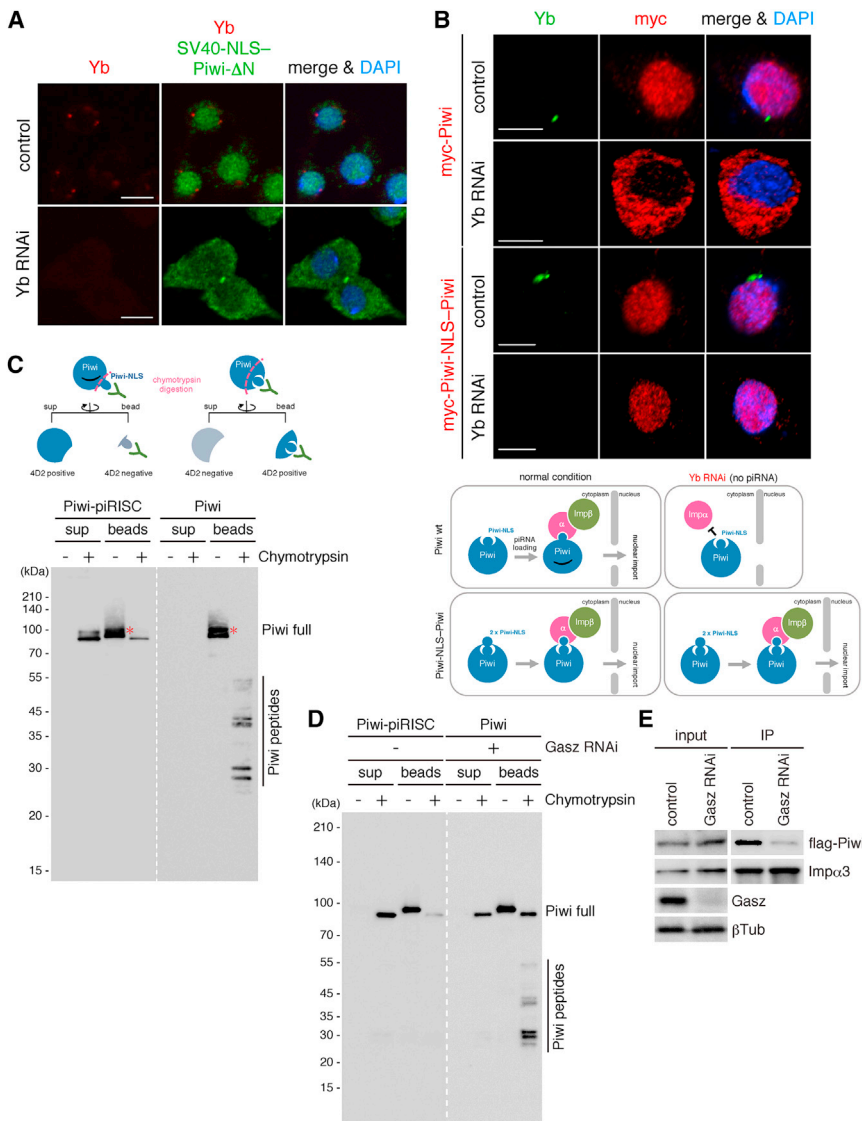
Figure 5. Addition of Piwi-NLS to Full-Length Piwi Achieves piRNA-Independent Piwi Nuclear Localization

(A) SV40-NLS-Piwi-ΔN (green) requires piRNA loading for Piwi to be localized to the nucleus in OSCs. Yb was detected in the control using anti-Yb antibody (red dots). DAPI signals (blue) show the nuclei. Scale bars, 5 μm.

(B) Piwi-NLS-Piwi (red) is imported to the nucleus piRNA independently in OSCs. Yb was detected in the control using anti-Yb antibody (green dots). Scale bars, 5 μm. The proposed models are shown (bottom).

(C) Limited proteolysis of Piwi immunoisolated from S2 cells (i.e., piRNA-free Piwi) and OSCs (i.e., piRNA-bound Piwi). The anti-Piwi antibody 3G11 that reacts with the N-terminal end (1–20 residues) of Piwi (Figure S5C) was used for immunoprecipitation. Western blotting using 4D2 whose epitope was between Try72–Lys89 of Piwi (Figure S5D) shows that piRNA-bound Piwi was digested between the 3G11 and 4D2 epitopes, so the majority of the core region of Piwi positive for 4D2 was detected in the supernatant after chymotrypsin treatment. piRNA-free Piwi was digested downstream of the 4D2 epitope, so the N-terminal regions containing both 3G11 and 4D2 epitopes mostly remained in the bead fraction (Piwi peptides), suggesting that the N-terminal region containing approximately 90 residues of Piwi was difficult to access when Piwi was free from piRNA. The bands indicated with asterisks correspond to full-length Piwi.

(D) Limited proteolysis of Piwi exogenously expressed (with no tag) in and immunoisolated from OSCs using anti-Piwi antibody before (Piwi-piRISC) and after (piRNA-free Piwi) Gasz depletion. It should be noted that the latter material also contains endogenous Piwi-piRISC (~50%) that was formed before Gasz depletion.

(E) Depletion of Gasz severely reduced the activity of Piwi to interact with Impα3 in OSCs.

See also Figures S4 and S5 and Table S1.

However, once piRNA was loaded onto Piwi, Piwi-NLS was exposed to the cellular environment, where the adaptor protein Impα bound to it and triggered the nuclear import of Piwi-piRISC together with Impβ. Unfortunately, depletion of Impβ in OSCs by RNAi caused severe damage to the cells; thus, the necessity of Impβ in the processing remains unclear.

The limited proteolysis analysis provided compelling evidence that Piwi drastically changed the conformation in a piRNA-dependent manner, similar to what was reported for hAgo2. However, direct evidence is still missing. For this, crystal structural analysis of Piwi in the presence and absence of piRNAs is desirable. However, this is currently difficult because it is extremely challenging to purify a large amount of recombinant PIWI proteins without piRNAs owing to their high instability in cellular environments. Nonetheless, we recently solved the crystal structure of Siwi-piRISC (Matsumoto et al., 2016). To make the crystals, we collected endogenous Siwi-piRISC by immunoi-

solating the complex from cultured BmN4 cells using anti-Siwi antibody. Because the vast majority of Siwi in BmN4 cells are loaded with piRNAs and the interaction between them is so tight, removing piRNAs from the piRISCs was the issue to be solved. Using a powerful electron-cryo-microscopy may be another way to go; however, the molecular mass of PIWI proteins is around 90–100 kDa, which may be too small for this type of analysis. We are currently exploring gentle but efficient ways of removing piRNAs from PIWI-piRISCs.

Our rescue experiments revealed that all three Impα proteins could individually rescue mislocalization of Piwi to the cytoplasm caused by loss of Impα2 and Impα3 in OSCs. This clearly excludes a paralog-specific role of Impα in Piwi nuclear localization. However, previous genetic studies showed that sterility caused by *Impα2* mutations was not rescued by ectopic expression of *Impα1* or *Impα3*, although the levels of *Impα* mRNAs (and Impα proteins) ectopically expressed in the mutant ovaries were
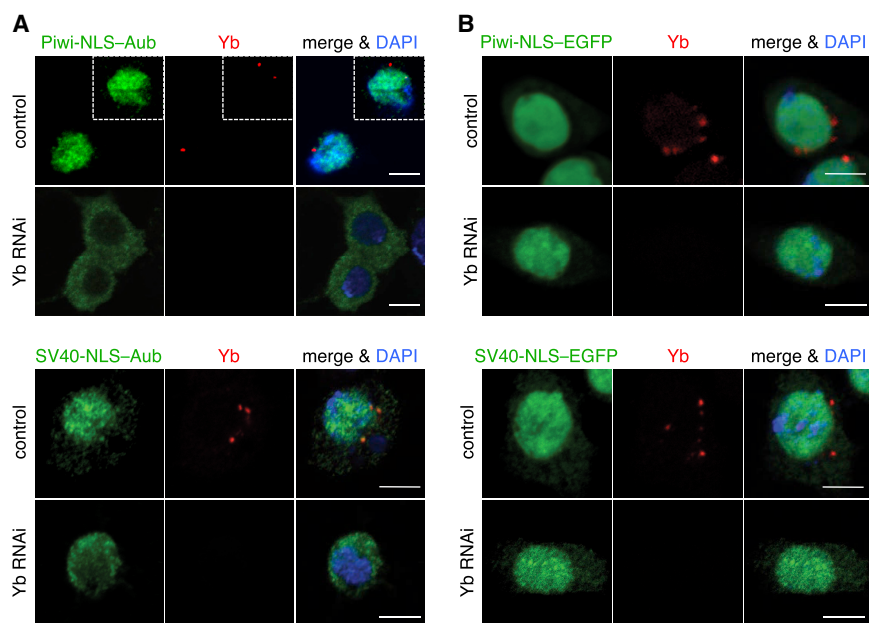
A

B

Figure 6. SV40-NLS-Aub and Piwi-NLS-Aub Were Imported to the Nucleus in a piRNA-Dependent Manner, Similar to Piwi, in OSCs
(A) Both Piwi-NLS-Aub and SV40-NLS-Aub (green) were imported to the nucleus in OSCs. Their import was blocked when piRNA biogenesis was impaired by Yb RNAi, so Piwi-NLS-Aub and SV40-NLS-Aub were localized in the cytoplasm. Yb was detected in the control using anti-Yb antibody (red dots). DAPI signals (blue) show the nuclei. Scale bars, 5 μm.
(B) Nuclear localization of Piwi-NLS-EGFP and SV40-NLS-EGFP (green) was unaffected by Yb depletion in OSCs. Scale bars, 5 μm.
See also Figure S5 and Table S1.

heterochromatinization of the loci. Aub exhibits a strong Slicer activity, so nuclear Aub-piRISC may immediately cleave the target RNAs upon association. If this were the case, Aub-piRISC, even after being successfully localized to the nucleus in a similar way as Piwi-piRISC, would not induce transcriptional silencing, as opposed to Piwi-piRISC, which can. However, Aub-piRISC would efficiently cleave transposon mRNAs Slicer dependently even in the nucleus, which should lead to post-transcriptional silencing of transposons. We are currently examining the effect of nuclear Aub-piRISC in transposon silencing.

A recent *Arabidopsis* study showed that heterochromatic small interfering RNAs (siRNAs) (hc-siRNAs) drive AGO4, a ubiquitously expressed Argonaute member, into the nucleus to facilitate target gene silencing via DNA methylation (Ye et al., 2012). In the study, however, not only AGO4 WT but also AGO4 mutant incapable of unwinding hc-siRNA duplexes to single-strand remained to be cytoplasmic, suggesting that the siRNA duplex loading onto AGO4 was insufficient for driving nuclear localization of AGO4. Rather, it further required AGO4 endonuclease-dependent, passenger strand cleavage and displacement, i.e., activation of AGO4-RISC. The Ye et al. (2012) report also revealed that AGO4 contains a monopartite NLS at Asp176-Pro183 residues (DRKRLRRP), and the relocation of NLS to the very N-terminal end of AGO4 drove AGO4 nuclear localization in an hc-siRNA-independent manner. Furthermore, dissociation of a protein chaperone Hsc70/HSP90 from AGO4 was also necessary for AGO4-RISC nuclear localization. Therefore, *Drosophila* Piwi and *Arabidopsis* AGO4 show rather distinct features regarding their nuclear localization, although both Argonaute proteins are key components of nuclear transcriptional silencing in the respective species.

comparable with endogenous ones (Mason et al., 2002). Embryonic lethality of Impα3 mutants was also not rescued by overexpression of *Impα1* or *Impα2* (Mason et al., 2003). These results suggest that some cargo proteins, crucial for gonadal development and fertility in *Drosophila*, were forced to remain cytoplasmic under the circumstance where other Impα isoforms were expressed in the mutant ovaries. Identification of cargos for which nuclear import is tightly controlled by a particular Impα protein is awaited.

Piwi bears a bona fide bipartite NLS. Why a bipartite, not monopartite, NLS evolved in Piwi is still unknown. Our results revealed that bipartite NLSs, from both Piwi and NP, showed less efficiency in nuclear import than monopartite NLSs, at least in OSCs. Therefore, it might be expected that having a monopartite NLS would simply be more effective and secure for exerting Piwi function in the nucleus. However, interestingly, our results also showed that Piwi containing its own NLS was clearly more sensitive to loss of piRNA than Piwi bearing SV40-NLS instead of its own NLS. This result suggests that Piwi autoregulation may be more controllable with bipartite NLSs than with monopartite NLSs, and this is most likely the reason why Piwi evolutionally acquired a bipartite NLS rather than a monopartite NLS. Notably, the N-terminal sequence of MIWI2, one of three PIWI proteins expressed in mouse testis whose nuclear localization and subsequent piRNA-mediated transposon silencing in the nucleus also requires piRNA loading (Carmell et al., 2007; Siomi et al., 2011), is similar to the N-terminal sequence of Piwi, including the NLS. It is likely that MIWI2 also evolutionally acquired a bipartite NLS rather than a monopartite NLS (Figure S5I).

Piwi-NLS-Aub was able to be localized in the OSCs in a piRNA-dependent manner, similar to endogenous Piwi protein. To accomplish transposon transcriptional silencing, Piwi-piRISC has to target and remain bound with nascent transcripts that are attached to the target loci upon transcription to efficiently induce

EXPERIMENTAL PROCEDURES

Cell Culture, RNAi, and Transfection with Plasmids
OSCs and S2 cells were cultured as described previously (Miyoshi et al., 2005; Saito et al., 2009). To perform RNAi, we transfected OSCs with 200 pmol siRNAs using Nucleofector 2b (Lonza). The siRNA sequences used in this study are listed in Table S1. OSC transfection with plasmids was carried out

using Xfect Transfection Reagent (Clontech) as described previously (Murota et al., 2014). S2 cells were transfected using Lipofectamine Transfection Reagents (Invitrogen).

Production of Anti-Impα Monoclonal Antibodies

Recombinant proteins of full-length Impα1, Impα2, and Impα3 fused to glutathione S-transferase (GST) (GST-Impα1, GST-Impα2, and GST-Impα3) were expressed in and purified from *E. coli* and then injected into mice for immunization. Production and selection of hybridomas that produced anti-Impα monoclonal antibodies were performed as described previously (Nishida et al., 2015). To examine the specificity of anti-Impα monoclonal antibodies raised in this study, we performed western blotting as described previously (Miyoshi et al., 2005) using OSC lysates before and after RNAi treatment for each Impα member. β-Tubulin (βTub) was detected as a loading control using anti-βTub mouse monoclonal antibody (1:2,500 dilution; obtained from the Developmental Studies Hybridoma Bank).

Plasmid Construction

We used plasmids pAcM-Piwi and pAcM-EGFP that were constructed and used previously (Saito et al., 2009) to express myc-Piwi and myc-EGFP in OSCs. To yield pAcF-Piwi for expressing FLAG-Piwi in OSCs and S2 cells, we exchanged the region encoding a myc peptide in pAcM-Piwi with a DNA fragment encoding a FLAG peptide using NEBuilder HiFi DNA Assembly Master Mix (NEB). The PCR primers used were F-Piwi-I-F/F-Piwi-I-R and F-Piwi-V-F/F-Piwi-V-R (Table S1). Construction of all other plasmids is described in the Supplemental Information.

Estimation of Impα Protein Levels in OSCs

Recombinant GST-Impα proteins isolated from *E. coli* and BSA (NEB) were run on protein gels. Protein concentrations of full-length GST-Impα in each solution were estimated by staining them with Coomassie Brilliant Blue (CBB) and comparing them with BSA stained with CBB. Western blotting was then performed using anti-Impα monoclonal antibodies (this study) on GST-Impα and OSC whole lysates. Signal intensity was calculated using ImageJ (NIH).

Immunofluorescence

Immunofluorescence was performed as described previously (Saito et al., 2010). The primary antibodies used in this study were anti-Impα monoclonal antibodies (this study), anti-myc rabbit polyclonal antibodies (1:500 dilution; Sigma), anti-FLAG mouse monoclonal antibody (1:1,000 dilution; Sigma), anti-myc mouse monoclonal antibody (1:1,000 dilution; Sigma), and anti-Yb monoclonal antibody (1:500 dilution) (Murota et al., 2014). The secondary antibodies used were Alexa 488-conjugated anti-mouse immunoglobulin M (IgM; Abcam), Alexa 488-conjugated anti-mouse IgG (Molecular Probes), Alexa 488-conjugated anti-rabbit IgG (Molecular Probes), Alexa 546-conjugated anti-mouse IgG (Molecular Probes), and Alexa 546-conjugated anti-rabbit IgG (Molecular Probes). Transfection of OSCs prior to immunofluorescence with plasmids was performed as described previously (Saito et al., 2009). Impα and Yb were depleted by RNAi by introducing Impα-siRNAs and Yb-siRNA into OSCs prior to overexpression of myc-Piwi (Figure 1), myc-Mael-SV40-NLS (Figure 3), myc-NP-NLS-EGFP (Figures 4E and 4F), myc-SV40-NLS-Piwi-ΔN (Figure 5A), myc-Piwi, (Figure 5B), myc-Piwi-NLS-Piwi (Figure 5B), myc-Piwi-NLS-Aub (Figure 6A), myc-SV40-NLS-Aub (Figure 6A), myc-Piwi-NLS-EGFP (Figure 6B), and myc-SV40-NLS-EGFP (Figure 6B). EGFP-siRNA or luciferase (luc)-siRNA was used as a negative control. Between 12 and 15 cells were analyzed per Impα member, where individual Impα proteins were efficiently depleted, and representative images were shown in corresponding figures (Figures 1A–1C, 3A, 3B, 4E, and 4F). Between 10 and 16 cells were analyzed before and after Yb depletion, and representative images were shown in corresponding figures (Figures 5A, 5B, 6A, 6B, S4A, S4B, and S5H). Approximately 10 cells were analyzed, and representative images were shown in corresponding figures (Figures 4B–4D).

Rescue Assays

To knock down *Impα1*, *Impα2*, and *Impα3* in OSCs, we introduced Impα1-siRNAs, Impα2-siRNAs, and Impα3-siRNAs separately into OSCs. Two days later, the cells were transfected again with the Impα-siRNAs to raise the RNAi effect. Plasmids to overexpress FLAG-Piwi, together with myc-Impα1, myc-Impα2, or myc-Impα3, were simultaneously introduced into the cells. Myc-EGFP was expressed as a negative control. One day later, immunofluorescence was performed as described above (see Immunofluorescence). Between 15 and 18 cells were analyzed per Impα member, and representative images were shown in corresponding figures (Figures 2A and 2B).

Limited Proteolysis Assays

Piwi with no tags was expressed in S2 cells by transfection and then immunoprecipitated using anti-Piwi antibody 3G11, to obtain piRNA-free Piwi. Piwi-piRISC was immunoprecipitated from OSCs using 3G11. After extensive washing, chymotrypsin was added to both immunoprecipitated samples to give a final concentration of 2.0 ng/μL. After incubation at 37°C for 30 min, the bead fractions were separated from the supernatants, and both fractions were subjected to western blotting using 4D2. Western blotting was performed as described previously (Miyoshi et al., 2005). To perform RNAi, we transfected OSCs with 200 pmol EGFP-siRNA or Gasz-siRNA using Nucleofector 96-well shuttle (Lonza). To obtain piRNA-free Piwi and Piwi-piRISC, Piwi with no tag was expressed in OSCs treated with EGFP-siRNA or Gasz-siRNA using Nucleofector 2b in Nucleofection Solution (5 mM KCl, 15 mM MgCl$_2$, 50 mM D-mannitol) added to 180 mM Church phosphoric acid buffer (pH 7.2) instead of 60 mM Na$_2$PO$_4$ and 60 mM NaH$_2$PO$_4$ (Nye et al., 2014) and then immunoprecipitated using anti-Piwi antibody 3G11. After extensive washing, chymotrypsin was added to both immunoprecipitated samples to give a final concentration of 2.0 ng/μL. After incubation at 37°C for 30 min, the beads fractions were separated from the supernatants, and both fractions were subjected to western blotting using 4D2.

AUTHOR CONTRIBUTIONS

R.Y., H.S., and M.C.S. conceived the project and designed the experiments. R.Y., Y.M., K.M.N., H.Y., and S.Y. performed the experiments with K.F.'s and A.O.'s help. L.N. performed mass spectrometric analysis. R.Y., Y.M., K.M.N., H.S., and M.C.S. analyzed the data and wrote the paper.

DECLARATION OF INTERESTS

The authors declare no competing interests.

REFERENCES

Aravin, A.A., Hannon, G.J., and Brennecke, J. (2007). The Piwi-piRNA pathway provides an adaptive defense in the transposon arms race. Science *318*, 761–764.

Brennecke, J., Aravin, A.A., Stark, A., Dus, M., Kellis, M., Sachidanandam, R., and Hannon, G.J. (2007). Discrete small RNA-generating loci as master regulators of transposon activity in *Drosophila*. Cell *128*, 1089–1103.

Carmell, M.A., Girard, A., van de Kant, H.J., Bourc'his, D., Bestor, T.H., de Rooij, D.G., and Hannon, G.J. (2007). MIWI2 is essential for spermatogenesis and repression of transposons in the mouse male germline. Dev. Cell *12*, 503–514.

Conti, E., Uy, M., Leighton, L., Blobel, G., and Kuriyan, J. (1998). Crystallographic analysis of the recognition of a nuclear localization signal by the nuclear import factor karyopherin α. Cell *94*, 193–204.

Cox, D.N., Chao, A., Baker, J., Chang, L., Qiao, D., and Lin, H. (1998). A novel class of evolutionarily conserved genes defined by *piwi* are essential for stem cell self-renewal. Genes Dev. *12*, 3715–3727.

Czech, B., Preall, J.B., McGinn, J., and Hannon, G.J. (2013). A transcriptome-wide RNAi screen in the *Drosophila* ovary reveals factors of the germline piRNA pathway. Mol. Cell *50*, 749–761.

Dönertas, D., Sienski, G., and Brennecke, J. (2013). *Drosophila* Gtsf1 is an essential component of the Piwi-mediated transcriptional silencing complex. Genes Dev. *27*, 1693–1705.

Elkayam, E., Kuhn, C.-D., Tocilj, A., Haase, A.D., Greene, E.M., Hannon, G.J., and Joshua-Tor, L. (2012). The structure of human argonaute-2 in complex with miR-20a. Cell *150*, 100–110.

Fontes, M.R., Teh, T., Toth, G., John, A., Pavo, I., Jans, D.A., and Kobe, B. (2003). Role of flanking sequences and phosphorylation in the recognition of the simian-virus-40 large T-antigen nuclear localization sequences by importin-alpha. Biochem. J. *375*, 339–349.

Ghildiyal, M., and Zamore, P.D. (2009). Small silencing RNAs: an expanding universe. Nat. Rev. Genet. *10*, 94–108.

Goldfarb, D.S., Corbett, A.H., Mason, D.A., Harreman, M.T., and Adam, S.A. (2004). Importin α: a multipurpose nuclear-transport receptor. Trends Cell Biol. *14*, 505–514.

Görlich, D. (1998). Transport into and out of the cell nucleus. EMBO J. *17*, 2721–2727.

Gunawardane, L.S., Saito, K., Nishida, K.M., Miyoshi, K., Kawamura, Y., Nagami, T., Siomi, H., and Siomi, M.C. (2007). A slicer-mediated mechanism for repeat-associated siRNA 5′ end formation in *Drosophila*. Science *315*, 1587–1590.

Handler, D., Meixner, K., Pizka, M., Lauss, K., Schmied, C., Gruber, F.S., and Brennecke, J. (2013). The genetic makeup of the *Drosophila* piRNA pathway. Mol. Cell *50*, 762–777.

Ishizu, H., Nagao, A., and Siomi, H. (2011). Gatekeepers for Piwi-piRNA complexes to enter the nucleus. Curr. Opin. Genet. Dev. *21*, 484–490.

Iwasaki, Y.W., Siomi, M.C., and Siomi, H. (2015). PIWI-interacting RNA: its biogenesis and functions. Annu. Rev. Biochem. *84*, 405–433.

Iwasaki, Y.W., Murano, K., Ishizu, H., Shibuya, A., Iyoda, Y., Siomi, M.C., Siomi, H., and Saito, K. (2016). Piwi modulates chromatin accessibility by regulating multiple factors including histone H1 to repress transposons. Mol. Cell *63*, 408–419.

Juliano, C., Wang, J., and Lin, H. (2011). Uniting germline and stem cells: the function of Piwi proteins and the piRNA pathway in diverse organisms. Annu. Rev. Genet. *45*, 447–469.

Kalderon, D., Richardson, W.D., Markham, A.F., and Smith, A.E. (1984). Sequence requirements for nuclear location of simian virus 40 large-T antigen. Nature *311*, 33–38.

Kalmykova, A.I., Nurminsky, D.I., Ryzhov, D.V., and Shevelyov, Y.Y. (2005). Regulated chromatin domain comprising cluster of co-expressed genes in *Drosophila melanogaster*. Nucleic Acids Res. *33*, 1435–1444.

Khurana, J.S., and Theurkauf, W. (2010). piRNAs, transposon silencing, and *Drosophila* germline development. J. Cell Biol. *191*, 905–913.

Klenov, M.S., Sokolova, O.A., Yakushev, E.Y., Stolyarenko, A.D., Mikhaleva, E.A., Lavrov, S.A., and Gvozdev, V.A. (2011). Separation of stem cell mainte-

nance and transposon silencing functions of Piwi protein. Proc. Natl. Acad. Sci. USA *108*, 18760–18765.

Kobe, B. (1999). Autoinhibition by an internal nuclear localization signal revealed by the crystal structure of mammalian importin α. Nat. Struct. Biol. *6*, 388–397.

Küssel, P., and Frasch, M. (1995). Pendulin, a *Drosophila* protein with cell cycle-dependent nuclear localization, is required for normal cell proliferation. J. Cell Biol. *129*, 1491–1507.

Le Thomas, A., Rogers, A.K., Webster, A., Marinov, G.K., Liao, S.E., Perkins, E.M., Hur, J.K., Aravin, A.A., and Tóth, K.F. (2013). Piwi induces piRNA-guided transcriptional silencing and establishment of a repressive chromatin state. Genes Dev. *27*, 390–399.

Li, C., Vagin, V.V., Lee, S., Xu, J., Ma, S., Xi, H., Seitz, H., Horwich, M.D., Syrzycka, M., Honda, B.M., et al. (2009). Collapse of germline piRNAs in the absence of Argonaute3 reveals somatic piRNAs in flies. Cell *137*, 509–521.

Lippai, M., Tirián, L., Boros, I., Mihály, J., Erdélyi, M., Belecz, I., Máthé, E., Pósfai, J., Nagy, A., Udvardy, A., et al. (2000). The *Ketel* gene encodes a *Drosophila* homologue of importin-β. Genetics *156*, 1889–1900.

Malone, C.D., and Hannon, G.J. (2009). Small RNAs as guardians of the genome. Cell *136*, 656–668.

Mason, D.A., Fleming, R.J., and Goldfarb, D.S. (2002). *Drosophila melanogaster* importin α1 and α3 can replace importin α2 during spermatogenesis but not oogenesis. Genetics *161*, 157–170.

Mason, D.A., Máthé, E., Fleming, R.J., and Goldfarb, D.S. (2003). The *Drosophila melanogaster* importin α3 locus encodes an essential gene required for the development of both larval and adult tissues. Genetics *165*, 1943–1958.

Mason, D.A., Stage, D.E., and Goldfarb, D.S. (2009). Evolution of the metazoan-specific importin α gene family. J. Mol. Evol. *68*, 351–365.

Matsumoto, N., Sato, K., Nishimasu, H., Namba, Y., Miyakubi, K., Dohmae, N., Ishitani, R., Siomi, H., Siomi, M.C., and Nureki, O. (2015). Crystal structure and activity of the endoribonuclease domain of the piRNA pathway factor Maelstrom. Cell Rep. *11*, 366–375.

Matsumoto, N., Nishimasu, H., Sakakibara, K., Nishida, K.M., Hirano, T., Ishitani, R., Siomi, H., Siomi, M.C., and Nureki, O. (2016). Crystal structure of silkworm PIWI-clade Argonaute Siwi bound to piRNA. Cell *167*, 484–497.e9.

Miyoshi, K., Tsukumo, H., Nagami, T., Siomi, H., and Siomi, M.C. (2005). Slicer function of *Drosophila* Argonautes and its involvement in RISC formation. Genes Dev. *19*, 2837–2848.

Muerdter, F., Guzzardo, P.M., Gillis, J., Luo, Y., Yu, Y., Chen, C., Fekete, R., and Hannon, G.J. (2013). A genome-wide RNAi screen draws a genetic framework for transposon control and primary piRNA biogenesis in *Drosophila*. Mol. Cell *50*, 736–748.

Murota, Y., Ishizu, H., Nakagawa, S., Iwasaki, Y.W., Shibata, S., Kamatani, M.K., Saito, K., Okano, H., Siomi, H., and Siomi, M.C. (2014). Yb integrates piRNA intermediates and processing factors into perinuclear bodies to enhance piRISC assembly. Cell Rep. *8*, 103–113.

Nagao, A., Sato, K., Nishida, K.M., Siomi, H., and Siomi, M.C. (2011). Gender-specific hierarchy in nuage localization of PIWI-interacting RNA factors in *Drosophila*. Front. Genet. *2*, 55.

Nishida, K.M., Saito, K., Mori, T., Kawamura, Y., Nagami-Okada, T., Inagaki, S., Siomi, H., and Siomi, M.C. (2007). Gene silencing mechanisms mediated by Aubergine piRNA complexes in *Drosophila* male gonad. RNA *13*, 1911–1922.

Nishida, K.M., Iwasaki, Y.W., Murota, Y., Nagao, A., Mannen, T., Kato, Y., Siomi, H., and Siomi, M.C. (2015). Respective functions of two distinct Siwi complexes assembled during PIWI-interacting RNA biogenesis in *Bombyx* germ cells. Cell Rep. *10*, 193–203.

Nye, J., Buster, D.W., and Rogers, G.C. (2014). The use of cultured *Drosophila* cells for studying the microtubule cytoskeleton. Methods Mol. Biol. *1136*, 81–101.

283

Ohtani, H., Iwasaki, Y.W., Shibuya, A., Siomi, H., Siomi, M.C., and Saito, K. (2013). DmGTSF1 is necessary for Piwi-piRISC-mediated transcriptional transposon silencing in the *Drosophila* ovary. Genes Dev. *27*, 1656–1661.

Phadnis, N., Hsieh, E., and Malik, H.S. (2012). Birth, death, and replacement of karyopherins in *Drosophila*. Mol. Biol. Evol. *29*, 1429–1440.

Pumroy, R.A., and Cingolani, G. (2015). Diversification of importin-α isoforms in cellular trafficking and disease states. Biochem. J. *466*, 13–28.

Ratan, R., Mason, D.A., Sinnot, B., Goldfarb, D.S., and Fleming, R.J. (2008). *Drosophila* importin α1 performs paralog-specific functions essential for gametogenesis. Genetics *178*, 839–850.

Riggleman, B., Wieschaus, E., and Schedl, P. (1989). Molecular analysis of the armadillo locus: uniformly distributed transcripts and a protein with novel internal repeats are associated with a *Drosophila* segment polarity gene. Genes Dev. *3*, 96–113.

Robbins, J., Dilworth, S.M., Laskey, R.A., and Dingwall, C. (1991). Two interdependent basic domains in nucleoplasmin nuclear targeting sequence: identification of a class of bipartite nuclear targeting sequence. Cell *64*, 615–623.

Saito, K., Nishida, K.M., Mori, T., Kawamura, Y., Miyoshi, K., Nagami, T., Siomi, H., and Siomi, M.C. (2006). Specific association of Piwi with rasiRNAs derived from retrotransposon and heterochromatic regions in the *Drosophila* genome. Genes Dev. *20*, 2214–2222.

Saito, K., Inagaki, S., Mituyama, T., Kawamura, Y., Ono, Y., Sakota, E., Kotani, H., Asai, K., Siomi, H., and Siomi, M.C. (2009). A regulatory circuit for *piwi* by the large Maf gene *traffic jam* in *Drosophila*. Nature *461*, 1296–1299.

Saito, K., Ishizu, H., Komai, M., Kotani, H., Kawamura, Y., Nishida, K.M., Siomi, H., and Siomi, M.C. (2010). Roles for the Yb body components Armitage and Yb in primary piRNA biogenesis in *Drosophila*. Genes Dev. *24*, 2493–2498.

Sato, K., Iwasaki, Y.W., Shibuya, A., Carninci, P., Tsuchizawa, Y., Ishizu, H., Siomi, M.C., and Siomi, H. (2015). Krimper enforces an antisense bias on piRNA pools by binding AGO3 in the *Drosophila* germline. Mol. Cell *59*, 553–563.

Schmidt, A., Palumbo, G., Bozzetti, M.P., Tritto, P., Pimpinelli, S., and Schäfer, U. (1999). Genetic and molecular characterization of sting, a gene involved in crystal formation and meiotic drive in the male germ line of *Drosophila melanogaster*. Genetics *151*, 749–760.

Sienski, G., Dönertas, D., and Brennecke, J. (2012). Transcriptional silencing of transposons by Piwi and maelstrom and its impact on chromatin state and gene expression. Cell *151*, 964–980.

Sienski, G., Batki, J., Senti, K.A., Dönertas, D., Tirian, L., Meixner, K., and Brennecke, J. (2015). Silencio/CG9754 connects the Piwi-piRNA complex to the cellular heterochromatin machinery. Genes Dev. *29*, 2258–2271.

Siomi, M.C., Sato, K., Pezic, D., and Aravin, A.A. (2011). PIWI-interacting small RNAs: the vanguard of genome defence. Nat. Rev. Mol. Cell Biol. *12*, 246–258.

Stewart, M. (2007). Molecular mechanism of the nuclear protein import cycle. Nat. Rev. Mol. Cell Biol. *8*, 195–208.

Sumiyoshi, T., Sato, K., Yamamoto, H., Iwasaki, Y.W., Siomi, H., and Siomi, M.C. (2016). Loss of *l(3)mbt* leads to acquisition of the ping-pong cycle in *Drosophila* ovarian somatic cells. Genes Dev. *30*, 1617–1622.

Török, I., Strand, D., Schmitt, R., Tick, G., Török, T., Kiss, I., and Mechler, B.M. (1995). The overgrown hematopoietic organs-31 tumor suppressor gene of *Drosophila* encodes an Importin-like protein accumulating in the nucleus at the onset of mitosis. J. Cell Biol. *129*, 1473–1489.

Yamashiro, H., and Siomi, M.C. (2018). PIWI-Interacting RNA in *Drosophila*: Biogenesis, Transposon Regulation, and Beyond. Chem. Rev. *118*, 4404–4421.

Ye, R., Wang, W., Iki, T., Liu, C., Wu, Y., Ishikawa, M., Zhou, X., and Qi, Y. (2012). Cytoplasmic assembly and selective nuclear import of Arabidopsis Argonaute4/siRNA complexes. Mol. Cell *46*, 859–870.

Yu, Y., Gu, J., Jin, Y., Luo, Y., Preall, J.B., Ma, J., Czech, B., and Hannon, G.J. (2015). Panoramix enforces piRNA-dependent cotranscriptional silencing. Science *350*, 339–342.

284

Stem Cell Reports

Article

ISSCR

OPEN ACCESS

PRDM14 Drives OCT3/4 Recruitment via Active Demethylation in the Transition from Primed to Naive Pluripotency

Naoki Okashita,[1,4] Yoshiaki Suwa,[1] Osamu Nishimura,[2] Nao Sakashita,[1] Mitsutaka Kadota,[2] Go Nagamatsu,[3] Masanori Kawaguchi,[1] Hiroki Kashida,[1] Ayaka Nakajima,[1] Makoto Tachibana,[4] and Yoshiyuki Seki[1,*]

[1]Department of Biomedical Chemistry, School of Science and Technology, Kwansei Gakuin University, 2-1, Gakuen, Sanda, Hyogo 669-1337, Japan
[2]Phyloinformatics Unit, RIKEN Center for Life Science Technologies, 2-2-3 Minatojima-minami, Kobe 650-0047, Japan
[3]Department of Stem Cell Biology and Medicine, Graduate School of Medical Science, Kyushu University, Fukuoka 812-8582, Japan
[4]Department of Enzyme Chemistry, Institute for Enzyme Research, Tokushima University, Tokushima 770-8503, Japan
*Correspondence: yseki@kwansei.ac.jp
http://dx.doi.org/10.1016/j.stemcr.2016.10.007

SUMMARY

Primordial germ cells (PGCs) are specified from epiblast cells in mice. Genes associated with naive pluripotency are repressed in the transition from inner cell mass to epiblast cells, followed by upregulation after PGC specification. However, the molecular mechanisms underlying the reactivation of pluripotency genes are poorly characterized. Here, we exploited the in vitro differentiation of epiblast-like cells (EpiLCs) from embryonic stem cells (ESCs) to elucidate the molecular and epigenetic functions of PR domain-containing 14 (PRDM14). We found that *Prdm14* overexpression in EpiLCs induced their conversion to ESC-like cells even in the absence of leukemia inhibitory factor in adherent culture. This was impaired by the loss of Kruppel-like factor 2 and ten-eleven translocation (TET) proteins. Furthermore, PRDM14 recruited OCT3/4 to the enhancer regions of naive pluripotency genes via TET-base excision repair-mediated demethylation. Our results provide evidence that PRDM14 establishes a transcriptional network for naive pluripotency via active DNA demethylation.

INTRODUCTION

Cells in the human body can be broadly classified as two major types, germline and somatic cells. The fusion of fully differentiated germ cells (i.e., sperm and oocyte) produces a totipotent zygote. Since all cells harbor the same genetic code, differentiation depends on the epigenetic state of each cell; germ cells reprogram epigenetic information during their specification, development, and maturation to acquire toti- or pluripotency. Germ cells in mice are specified from proximal epiblast cells that lack expression of some subsets of pluripotency genes such as *Nanog*, Kruppel-like factor 2 (*Klf2*), and T cell leukemia/lymphoma 1 (*Tcl1*), which are regulated by the transcription factors B lymphocyte-induced maturation protein 1 (BLIMP1), PR domain-containing 14 (PRDM14), and transcription factor AP-2 gamma (TFAP2C) (Nakaki et al., 2013; Ohinata et al., 2005, 2009; Weber et al., 2010; Yabuta et al., 2006; Yamaji et al., 2008). Specified PGCs reactivate pluripotency-associated genes and can be used to derive embryonic germ cells (EGCs) via stimulation with three cytokines, basic fibroblast growth factor (bFGF), stem cell factor (SCF), and leukemia inhibitory factor (LIF) (Matsui et al., 1992). Migrating PGCs in the hindgut replace repressive DNA methylation and H3K9 methylation marks with a repressive H3K27 trimethylation mark in their genome during migration (Seki et al., 2005, 2007). DNA demethylation occurs as a two-step process: the first demethylation wave occurs in a genome-wide manner during migration and a second wave occurs in a locus-specific manner, for example

at germline-specific genes and imprinted loci at the time when PGCs arrive at the gonads (Seisenberger et al., 2012). CpG methylation marks can be removed via replication-dependent and independent mechanisms (Wu and Zhang, 2010). The former is regulated by inhibition of DNA methyltransferase activity during de novo DNA synthesis, whereas the latter (also known as active demethylation) is triggered by oxidation of 5-methylcytosine catalyzed by ten-eleven translocation (TET) proteins, which is followed by base excision repair (BER) (Hackett et al., 2012). PGCs use both active and passive demethylation to erase genome-wide methylation marks (Hajkova et al., 2008; Kagiwada et al., 2013; Kawasaki et al., 2014; Ohno et al., 2013; Popp et al., 2010). Global hypomethylation is induced in the transition from metastable embryonic stem cells (ESCs) cultured with serum plus LIF to ground-state ESCs cultured with 2i plus LIF, which is similar to the first wave of DNA demethylation in migratory PGCs (Ficz et al., 2013).

We have previously shown that PRDM14 is transiently expressed in the inner cell mass (ICM) of blastocysts at embryonic day 3.5 (E3.5) and reactivated in specifying PGCs at approximately E6.25 (Yamaji et al., 2008). Knockout (KO) studies have demonstrated that expression of *Prdm14* in the ICM is required for priming of the epiblast cells for proper somatic differentiation (Payer et al., 2013), and that expression of PGCs is critical for establishment of the germline in mice (Yamaji et al., 2008). Furthermore, induction of PRDM14 in epiblast-like cells (EpiLCs) induced from ESCs is sufficient for PGC-like cell (PGCLC) induction

in aggregate culture (Hayashi et al., 2011). KO and overexpression studies of *Prdm14* suggest that PRDM14 is a critical determinant for PGC specification in mice. However, recent studies regarding human PGC induction from pluripotent cells have clarified a difference in expression of *Prdm14* between mice and humans during the transition from pluripotent cells to PGCs (Irie et al., 2015; Sasaki et al., 2015). Interestingly, *PRDM14* is consistently expressed at moderate levels in pluripotent cells, i.e., primitive streak cells, which are precursors of PGCs in human, and PGCs, suggesting that PRDM14 is not a critical determinant for PGC specification in humans.

Here, we exploited adherent culture of EpiLCs in which *Prdm14* expression is controlled by doxycycline (Dox) to reveal the molecular and epigenetic function of PRDM14 during the transition from epiblast cells to PGCs in mice. We showed that inducing *Prdm14* expression in EpiLCs in adherent culture promotes pluripotency and self-renewal, resulting in conversion from EpiLCs to ESC-like cells (ESCLCs).

RESULTS

PRDM14 Overexpression Converts EpiLCs to ESC-like Cells

Prdm14 is expressed in proximal epiblast cells at around E6.5 that constitute PGC precursors in mice. In three-dimensional aggregate culture of EpiLCs, PRDM14 has been shown to be sufficient to induce PGCLCs (Nakaki et al., 2013). To exclude the effect of cell-cell contact in three dimensions and investigate the direct function of PRDM14 in PGC development, we exploited adherent culture of EpiLCs, in which *Prdm14* expression was controlled by Dox treatment (ROSA-Tet-off [Figures 1 and 5] and piggyBac Tet-on [Figures 2, 3, 4, and 6]) (Figures 1A and 1B) (Hayashi et al., 2011). ESCs were transferred onto fibronectin and stimulated with bFGF and activin A in N2B27 medium containing 1% KO serum replacement (KSR), and 2 days after EpiLC induction, *Prdm14* expression was induced by removal of Dox in Glasgow minimum essential medium containing 15% KSR (GK15), which is the basic medium used for PGCLC induction (Figures 1C and 1D) (Ohinata et al., 2009). The morphology of EpiLCs expressing *Prdm14* changed from flattened to small, compact colonies, and the cells regained alkaline phosphatase (AP) activity to a degree similar to that of ESCs, which was associated with the reactivation of pluripotency genes (Figures 1E and 1F). Interestingly, the expression of early PGC markers in EpiLCs expressing PRDM14 was comparable with that in ESCs, and we were able to expand EpiLCs expressing PRDM14 at multiple passages, which clearly indicates that PRDM14 induction in EpiLCs does not induce PGCLCs (Figure S1A). To evaluate

the self-renewal capacity and pluripotency of *Prdm14*-expressing EpiLCs, we assessed colony formation along with AP activity in ESCs grown at low density under standard culture conditions (serum plus LIF). The number of AP-positive colonies was higher for EpiLCs overexpressing PRDM14 than for control EpiLCs (Figure 1G). Interestingly, despite the absence of LIF, we were able to expand PRDM14-expressing EpiLCs several times, and these cells retained expression of pluripotency genes except for *Klf4*, which is a direct target of LIF signaling (Figure S1B). Moreover, the cells formed three germ layers in the subcutaneous region of nude mice, indicating that PRDM14 expression confers self-renewal capacity and pluripotency in EpiLCs independent of LIF signaling (Figure 1H).

To determine the transcriptional dynamics in PRDM14-expressing EpiLCs, we performed a microarray analysis using total RNA from ESCs, EpiLCs at day 2 (d2), EpiLCs + PRDM14, and EpiLCs (d4). Unsupervised hierarchical clustering revealed that the global gene expression profile of EpiLCs + PRDM14 was more similar to that of ESCs than that of EpiLCs (Figure 2A). Scatterplots of EpiLCs (d2) and EpiLCs + PRDM14 showed that 669 genes, including those associated with pluripotency, were upregulated, and 480 genes, including those encoding DNA methyltransferases or associated with differentiation, were downregulated by *Prdm14* expression in EpiLCs (Figure 2B). Unsupervised hierarchical clustering of genes up- or downregulated by PRDM14 in EpiLCs formed four clusters (Figure 2C). Genes in cluster 1 did not show a significant change in the transition from ESCs to EpiLCs, but were upregulated thereafter, whereas cluster-2 genes showed downregulation from ESCs to EpiLCs, followed by upregulation. Genes in cluster 3 showed relatively high expression from ESCs to EpiLCs followed by downregulation, whereas those in cluster 4 showed upregulation from ESCs to EpiLCs before subsequent downregulation. According to gene ontology (GO) functional annotations, stem cell maintenance (e.g., *Tcl1*, *Nanog*, *nuclear receptor subfamily* [*Nr*]5a2, and estrogen-related receptor β [*Esrrb*]), and DNA methylation (e.g., *Dnmt3a/b*) genes were enriched in clusters 2 and 4, respectively (Figures 2C and 2D). PRDM14 overexpression in epiblast stem cells (EpiSCs) partially activated pluripotency genes without inducing their conversion to ESCs, even in the presence of LIF (Gillich et al., 2012). To identify candidate genes regulated by PRDM14 that can account for the difference between EpiLC and EpiSC conversion to ESCs, we compared the top 1,000 probes that were differentially upregulated by PRDM14 overexpression in EpiLCs and EpiSCs according to published data (Gillich et al., 2012). Critical pluripotency factors such as *Tcl1*, *Nanog*, *Nr5a2*, transcription factor CP2-like 1 (*Tfcp2l1*), and *T-box 3* (*Tbx3*) were upregulated by PRDM14 in EpiLCs but not in EpiSCs (Figure 2E), suggesting that differences in the
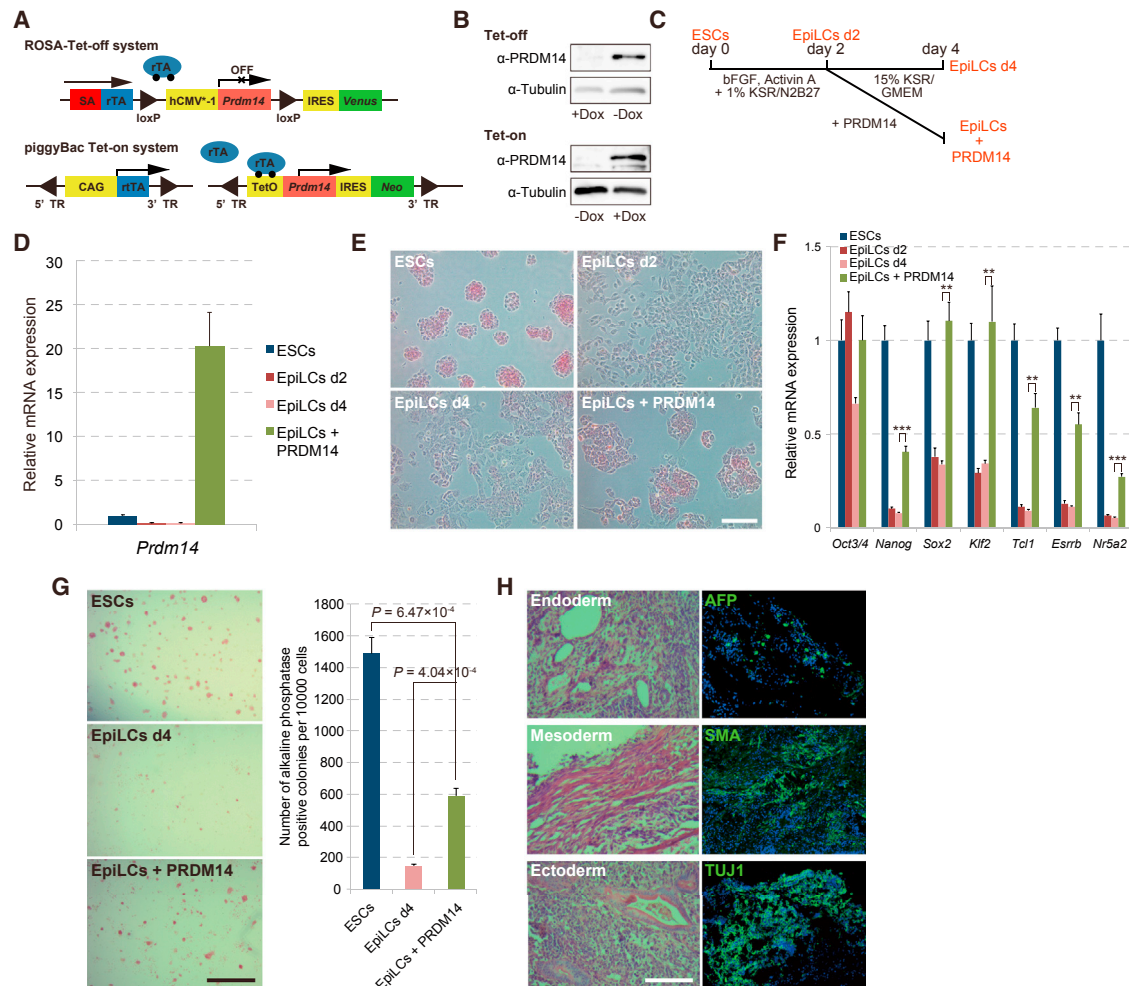
Figure 1. PRDM14 Induces the Transition of EpiLCs to ESCLCs

(A) Constructs of the ROSA-Tet-off system and piggyBac Tet-on system.

(B) Western blotting of PRDM14 and tubulin.

(C) Scheme of the transition of ESCs to EpiLCs and of EpiLCs to ESCLCs.

(D) qRT-PCR analysis of *Prdm14* expression in ESCs, EpiLCs (d2), EpiLCs (d4), and EpiLCs + PRDM14. Error bars indicate ±SD of a biological triplicate.

(E) AP staining of ESCs, EpiLCs (d2), EpiLCs (d4), and EpiLCs + PRDM14. Scale bar, 50 μm.

(F) qRT-PCR analysis of pluripotency genes in ESCs, EpiLCs (d2), EpiLCs (d4), and EpiLCs + PRDM14. Error bars indicate ±SD of a biological triplicate.

(G) Colony formation by ESCs, EpiLCs (d4), and EpiLCs + PRDM14 was assessed by AP staining over 3 days in the presence of serum + LIF. Error bars indicate ±SD of biological triplicates. p Values were calculated with the Student's t test. Scale bar, 200 μm.

(H) (Left) Teratoma formation by EpiLCs expressing *Prdm14* cultured in the absence of LIF. (Right) Immunofluorescent staining of α-fetoprotein (AFP), smooth muscle actin (SMA), and class III β-tubulin (TUJ1) in teratoma sections. Scale bar, 200 μm.

$**p < 0.01$, $***p < 0.001$, Student's t test.

epigenetic landscape of pluripotency-associated genes between EpiLCs and EpiSCs may be critical for their activation by PRDM14. In the case of genes downregulated by PRDM14, epigenetic modifiers controlling DNA and H3K9 methylation—including *Dnmt3a*, *Dnmt3l*, *ubiquitin-like PHD* and *RING finger domain-containing protein 1* (*Uhrf1*), *helicase lymphoid-specific* (*Hells*), and *suppressor of variegation 3–9 homolog 1* (*Suv39h1*)—were downregulated by PRDM14 only in EpiLCs (Figure S2A), which may be necessary for the establishment of an epigenetic background that ensures the conversion from EpiLCs to ESCLCs.

We used adherent EpiLC cultures to investigate the function of PRDM14 while excluding the effects of
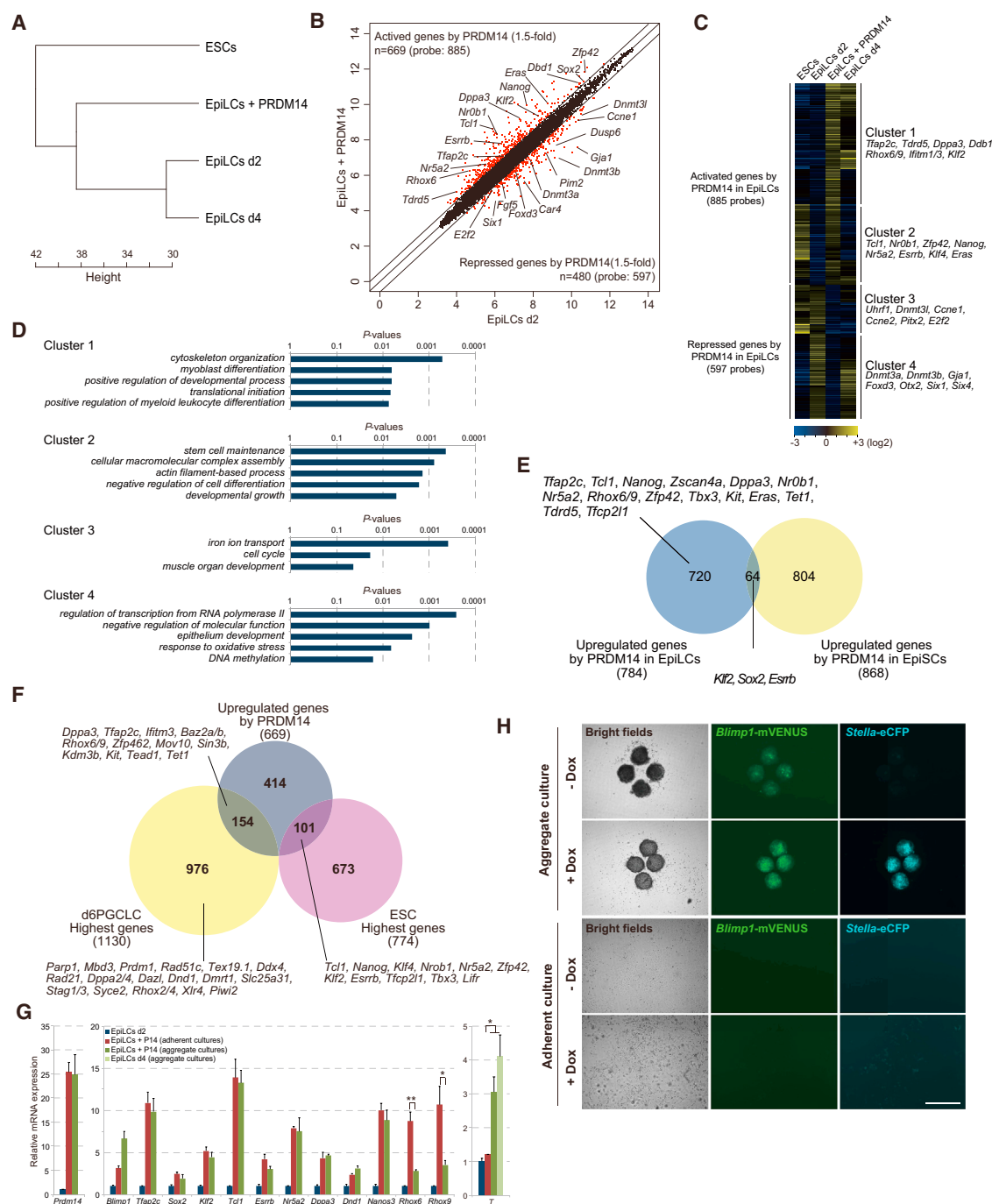
Figure 2. Global Gene Expression Profiles in the Transition from EpiLCs to ESCLCs

(A) Unsupervised hierarchical cluster analysis of ESCs, EpiLCs (d2), EpiLCs (d4), and EpiLCs + PRDM14.

(B) Scatter plots comparing the transcriptomes of EpiLCs + PRDM14 and EpiLCs (d2).

(C) Heatmap visualization of data obtained by unsupervised hierarchical cluster analysis of genes up- and downregulated by PRDM14 in EpiLCs.

(D) GO term overrepresentation analysis using DAVID.

(E) Comparison of genes upregulated by PRDM14 in EpiLCs versus EpiSCs.

(F) Comparison of genes upregulated by PRDM14 and those most highly expressed in ESCs and d6 PGCLCs (Kurimoto et al., 2015).

(legend continued on next page)
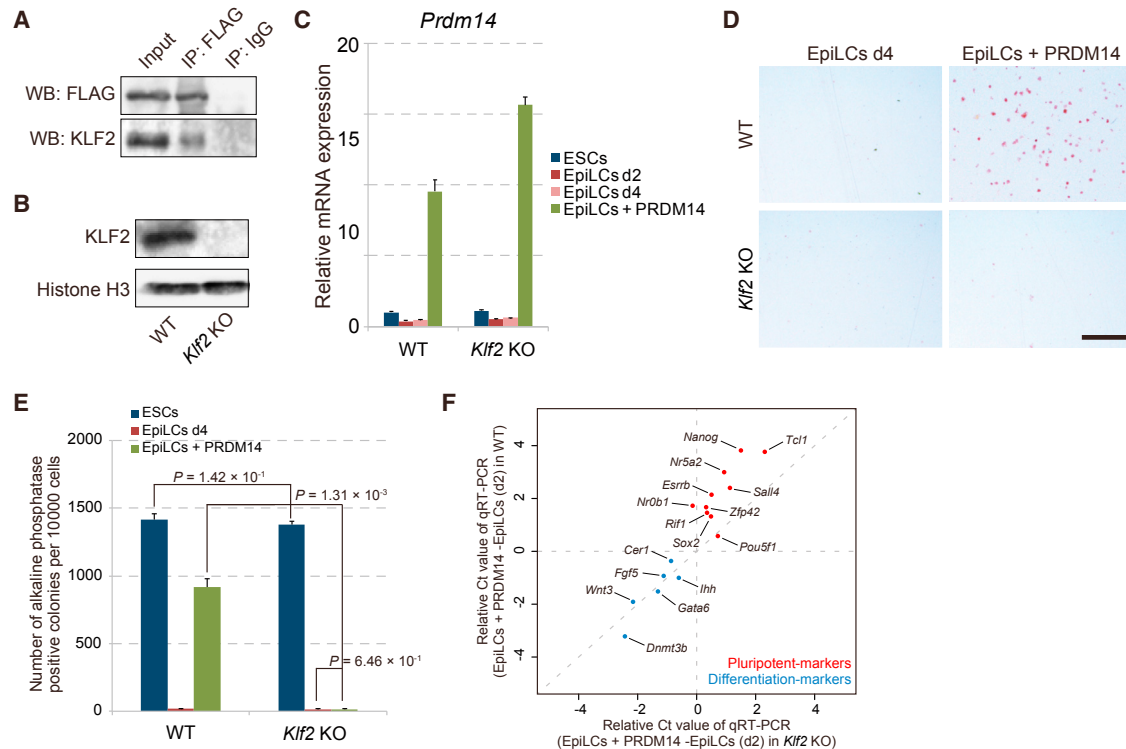
Figure 3. *Klf2* Is Required for the PRDM14-Induced Reversion of EpiLCs to ESCLCs

(A) Immunoprecipitation of PRDM14 with KLF2 in ESCs.

(B) Western blot analysis of KLF2 expression in WT and *Klf2* KO ESCs.

(C) qRT-PCR analysis of *Prdm14* expression in WT and *Klf2* KO ESCs. Error bars indicate ±SD of a biological triplicate.

(D) Colony formation by EpiLCs with or without *Prdm14* induction induced from WT or *Klf2* KO ESCs, as assessed by AP staining. Scale bar, 200 μm.

(E) Quantification of colony formation shown in (D). Error bars indicate ±SD of biological triplicates. p Values were calculated with Student's t test.

(F) Scatter plot shows relative Ct values of pluripotency-associated genes (red dots) and differentiation markers (blue dots) determined by qRT-PCR. The x axis indicates relative Ct values of each gene (EpiLCs + PRDM14 − EpiLCs [d2]) in WT, and the y axis indicates relative Ct values of each gene (EpiLCs + PRDM14 − EpiLCs [d2]) in *Klf2* KO.

three-dimensional cell-cell contact. EpiLCs expressing PRDM14 could be expanded for long time periods, implying that EpiLCs were not induced to become PGCLCs under our culture conditions. In contrast, forced expression of PRDM14 in aggregate EpiLC cultures induced PGCLCs but not ESCLCs (Nakaki et al., 2013). Germ cell specification consists of two major events: the acquisition of potential pluripotency (by reactivation of genes such as *Nanog*, *Klf2*, and *Tcl1*) and of germ cell character (by activation of *Blimp1*, *Nanos3*, and *dead-end protein homology 1*) (Kurimoto et al., 2008; Yamaji et al., 2008). The difference

in cell fate between PRDM14-expressing EpiLCs grown as adherent or aggregate cultures suggests that acquisition of pluripotency is directly controlled by PRDM14, while three-dimensional cell-cell interactions between EpiLCs are required for the induction of germ cell characteristics, including the activation of germline-specific genes. A recent analysis of global gene expression in the differentiation of ESCs to EpiLCs and of EpiLCs to PGCLCs identified genes that were enriched in ESCs, EpiLCs, and d2 and d6 PGCLCs (Kurimoto et al., 2015). We compared the characteristics of EpiLCs expressing PRDM14 grown under our

(G) qRT-PCR analysis of pluripotency and germ cell-related genes in EpiLCs, and EpiLCs expressing PRDM14 and grown as adherent or aggregate cultures. Error bars indicate ±SD of a biological triplicate. *p < 0.05, **p < 0.01, Student's t test.

(H) Comparison of the expression of PGC markers, Blimp1 (mVENUS) and stella (eCFP), between adherent culture and aggregate culture of EpiLCs with PRDM14. Scale bar, 200 μm.
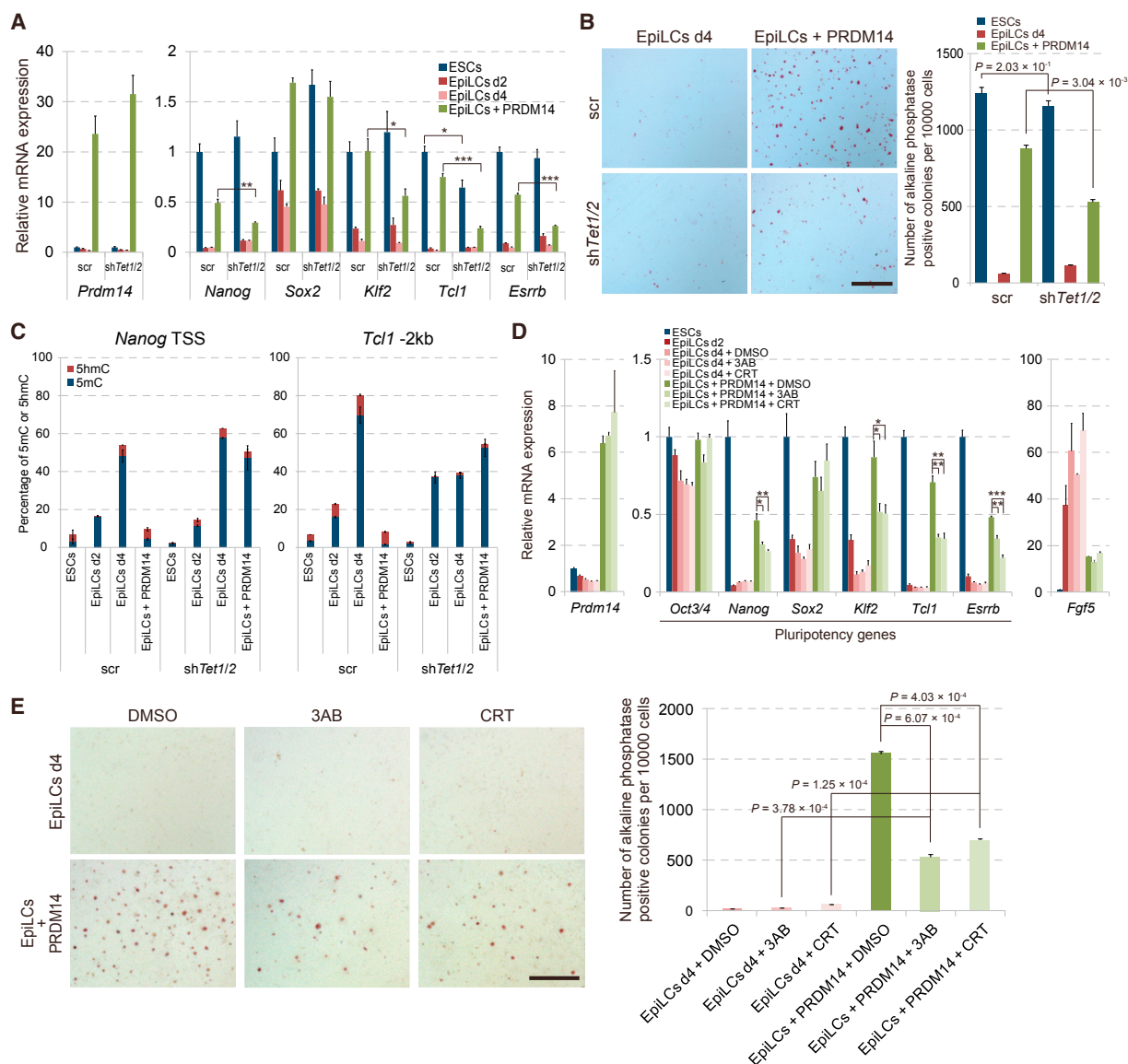
Figure 4. Reversion from Primed to Naive Pluripotency Induced by PRDM14 via the TET-BER Pathway

(A) qRT-PCR analysis of *Prdm14* and pluripotency genes in ESCs, EpiLCs (d2), EpiLCs (d4), and EpiLCs + PRDM14 in WT and *Tet1/2* KD backgrounds. Error bars indicate ±SD of a biological triplicate. *p < 0.05, **p < 0.01, ***p < 0.001, Student's t test.

(B) Colony formation by EpiLCs with or without *Prdm14* induction induced from WT and *Tet1/2* KD ESCs, as determined by AP staining. Scale bar, 200 μm. Error bars indicate ±SD of biological triplicates. p Values were calculated with Student's t test.

(C) Glucosylation of genomic DNA followed by methylation-sensitive (GlucMS)-qPCR analysis showing the percentage of 5mC and 5hmC marks in or near PRDM14 binding regions of the *Nanog* and *Tcl1* enhancers in ESCs, EpiLCs (d2), EpiLCs (d4), and EpiLCs + PRDM14 in WT and *Tet1/2* KD backgrounds. Error bars indicate ±SD of a biological triplicate.

(D) qRT-PCR analysis of *Prdm14*, pluripotency genes, and *Fgf5* in ESCs, EpiLCs (d2), EpiLCs (d4), and EpiLCs + PRDM14 treated with DMSO (control), 3-aminobenzamide (3AB), and CRT 004876 (CRT). Error bars indicate ±SD of a biological triplicate. *p < 0.05, **p < 0.01, ***p < 0.001, Student's t test.

(E) Colony formation by EpiLCs + PRDM14 treated with DMSO, 3AB, and CRT as assessed by AP staining. Error bars indicate ±SD of a biological triplicate. p Values were calculated with Student's t test. Scale bar, 200 μm.

culture conditions with ESC highest genes, d6 PGCLCs, and EpiLC highest genes in a Venn diagram. The majority of transcription factors critical for ESC pluripotency among ESC highest genes were upregulated by PRDM14 in adherent EpiLC cultures, while genes most highly expressed in d6 PGCLCs were generally not upregulated by

PRDM14 in these cultures including *Blimp1* (*Prdm1*), a critical determinant of germ cell specification (Ohinata et al., 2005) (Figures 2F and 2G). These findings led us to speculate that a combination of *Prdm14* induction and three-dimensional cell-cell contact is necessary for the induction of *Blimp1* expression in EpiLCs. To clarify the response of EpiLCs to PRDM14 induction in aggregate culture and adherent culture, we established PRDM14-inducible ESCs carrying two reporters, *Blimp1-mVENUS* (BV) and *stella-eCFP* (SC) (BVSC), and monitored the fluorescence of mVENUS and eCFP in different culture conditions (Hayashi et al., 2011). At 2 days after PRDM14 induction in EpiLCs at aggregate culture, the aggregates showed both BV and SC expression (Figure 2H), which provides evidence of PGCLC induction, as shown in a previous study (Nakaki et al., 2013). By contrast, adherent-cultured EpiLCs expressing PRDM14 showed no BV expression and weak SC expression, which is consistent with the expression profile in ESCs (Hayashi et al., 2011). *Blimp1* is upregulated by the mesoderm marker gene *T* (*Brachyury*) (Aramaki et al., 2013). We therefore compared *T* expression levels in adherent and aggregate EpiLC cultures. Interestingly, *T* was only upregulated in EpiLC aggregate cultures both with and without *Prdm14* induction (Figure 2G), suggesting that three-dimensional cell-cell interactions are required for *T* expression, which induces PGCs along with PRDM14. A comparison of genes downregulated by PRDM14 in adherent EpiLC cultures with EpiLC highest genes showed that many EpiLC highest genes including *Otx2* and *Foxd3* (Buecker et al., 2014; Respuela et al., 2016), which are known to important for the transition from naive to primed pluripotency, were repressed by PRDM14, indicating that PRDM14 suppresses epiblast characteristics (Figure S2B).

Klf2 Is Required for the Acquisition of Pluripotency by PRDM14

Adherent culture of EpiLCs with PRDM14 is a powerful tool to uncover the molecular and epigenetic mechanisms for potential re-establishment of pluripotency by PRDM14, because this system induces the conversion from EpiLCs to ESCLCs at high efficiency and uniformly. We first focused on the function of KLF2, which is activated soon after induction of PRDM14 in EpiLCs in adherent culture. KLF2 has been shown to act synergistically with PRDM14 in the reversion of EpiSCs to ESCs (Gillich et al., 2012); the interaction between the two proteins in ESCs was confirmed by immunoprecipitation (IP) (Figure 3A). To clarify the role of *Klf2* in the PRDM14-associated acquisition of pluripotency, we generated *Klf2* KO ESCs harboring a Dox-inducible *Prdm14* expression cassette using the clustered regularly interspaced short palindromic repeats (CRISPR)/Cas9 system (Figures 3B and 3C). Interestingly,

we did not observe AP-positive colonies in *Klf2*-null EpiLCs expressing PRDM14, which demonstrated that *Klf2* is essential for the PRDM14-induced conversion of EpiLCs to ESCLCs (Figure 3D and 3E). To clarify the cause of the loss of AP activity in EpiLCs + PRDM14 in *Klf2* KO, we compared the repression of differentiation markers and activation of pluripotency-associated markers by PRDM14 in wild-type (WT) and *Klf2* KO using qRT-PCR analysis. We plotted the relative Ct values of qRT-PCR data (EpiLCs + PRDM14 − EpiLCs [d2]) for WT (y axis) and *Klf2* KO (x axis). Consistent impairment of activation of pluripotent-associated genes by PRDM14 was observed, whereas the repression of differentiation markers by PRDM14 was relatively maintained in *Klf2* KO EpiLCs (Figure 3F). These results indicate that PRDM14 cooperates with KLF2 to convert EpiLCs to ESCLCs through the activation of pluripotency-associated genes.

PRDM14-Induced Acquisition of Pluripotency Occurs via TET-Dependent Active Demethylation

We previously showed that PRDM14 promotes active demethylation of pluripotency genes in ESCs via the TET-BER pathway (Okashita et al., 2014). To assess the role of the TET-BER pathway in PRDM14-induced acquisition of pluripotency, we established a *Tet1/Tet2* knockdown (KD) ESC line with a Dox-inducible *Prdm14* cassette (Figure S3A). *Tet1/Tet2* KD prevented the reactivation of *Nanog*, *Klf2*, *Tcl1*, and *Esrrb* but not of *Sox2* and also prevented AP-positive colony formation by PRDM14 under ESC culture conditions (Figures 4A and 4B), while the repression of *Dnmt3b* and differentiation markers by PRDM14 occurred normally in *Tet1/Tet2* KD EpiLCs (Figure S3B). CpG methylation level at PRDM14 binding regions of *Nanog* and *Tcl1* in ESCs substantially increased in the transition from ESCs to EpiLCs; these marks were rapidly removed by *Prdm14* induction (Figure 4C). In contrast, the removal of 5-methylcytosine (5mC) by PRDM14 at *Nanog* and *Tcl1* loci was impaired by *Tet1/Tet2* KD. Furthermore, treatment of EpiLCs expressing PRDM14 with pharmacological inhibitors of the BER components DNA endonuclease apurinic/apyrimidinic endonuclease (3-aminobenzamide) and poly(ADP-ribose) polymerase (CRT 004876) abrogated the reversion of EpiLCs to ESCLCs, similar to the *Tet1/Tet2* KD phenotype (Figures 4D and 4E). To investigate the role of TET proteins in global gene expression profiles regulated by PRDM14 in EpiLCs, we compared genes that were up- or downregulated by PRDM14 in WT and *Tet1/Tet2* KD EpiLCs by microarray analysis. Genes that were up- or downregulated by PRDM14 in WT EpiLCs showed corresponding up- and downregulation in *Tet1/Tet2* KD EpiLCs (Figure S4A). These genes were of four types: ESC-, PGC-, or EpiLC-enriched, or epigenetic modifiers. We examined the effect of *Tet1/Tet2* KD on the transcriptional regulation
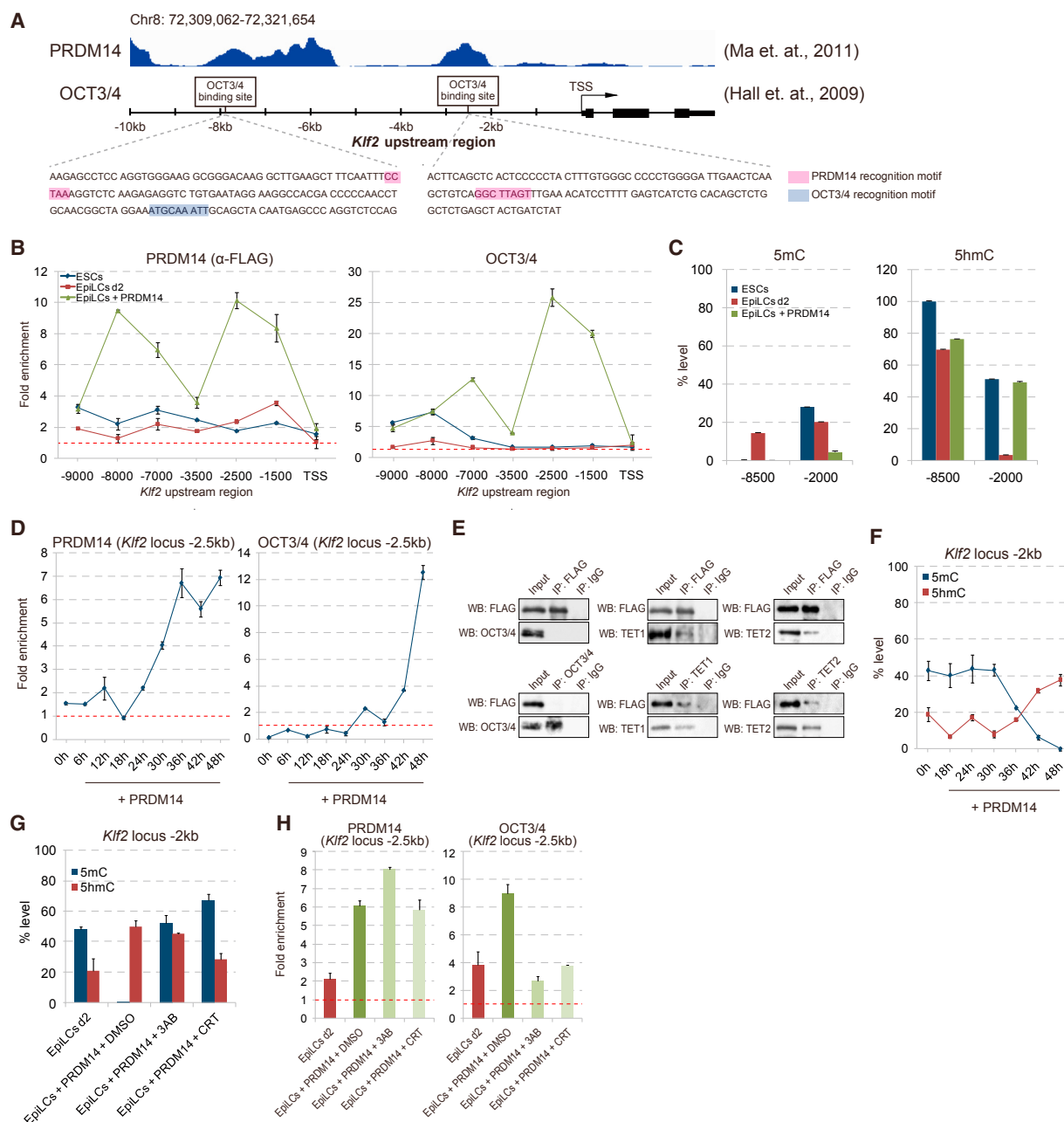
Figure 5. PRDM14 Increases OCT3/4 Recruitment to *Klf2* via the TET-BER Pathway

(A) Schematic representation of ChIP data for PRDM14 and OCT3/4 at the *Klf2* locus in ESCs (Hall et al., 2009; Ma et al., 2011) and PRDM14 and OCT3/4 recognition motifs at two enhancers.

(B) ChIP-qPCR analysis of PRDM14 (α-FLAG) and OCT3/4 at the *Klf2* locus in ESCs, EpiLCs (d2), and EpiLCs + PRDM14. Fold enrichment was calculated by comparing pre-immune immunoglobulin G (IgG) control (red dotted line) with each antibody. Error bars indicate ±SD of a technical duplicate.

(C) GlucMS-qPCR analysis showing the percentage of 5mC and 5hmC marks at two *Klf2* enhancers in ESCs, EpiLCs (d2), and EpiLCs + PRDM14. Error bars indicate ±SD of a technical duplicate.

(D) ChIP-qPCR analysis of PRDM14 (α-FLAG) and OCT3/4 at the *Klf2* locus every 6 hr after *Prdm14* induction. Error bars indicate ±SD of a technical duplicate.

(E) Western blot (WB) analysis of FLAG, OCT3/4, TET1, and TET2 levels following immunoprecipitation (IP) of EpiLCs + PRDM14 precipitated with an anti-FLAG antibody.

(legend continued on next page)

of these genes by PRDM14 in EpiLCs (Figure S4B). The expression of PGC- and EpiLC-enriched genes and epigenetic modifiers was unaltered by PRDM14 in *Tet1/Tet2* KD EpiLCs. In contrast, activation of ESC-enriched genes by PRDM14 was impaired in *Tet1/Tet2* KD EpiLCs. We observed, however, that ESC-enriched genes tended to be upregulated by PRDM14 even in *Tet1/Tet2* KD EpiLCs, suggesting that TET proteins cooperate with an unknown pathway regulated by PRDM14 to activate ESC-enriched genes in EpiLCs (Figure S4B).

PRDM14 Enhances OCT3/4 Binding to *Klf2* Enhancers via the TET-BER Pathway

Because *Klf2* activation is critical for acquisition of pluripotency by PRDM14, we investigated the molecular and epigenetic mechanisms of *Klf2* activation by PRDM14. Both PRDM14 and OCT3/4 bind to proximal and distal enhancers of the *Klf2* locus in ESCs (Figure 5A) (Hall et al., 2009; Ma et al., 2011). We therefore evaluated the binding of PRDM14 and OCT3/4 to the *Klf2* locus in the transition from ESCs to EpiLCs and dedifferentiation of EpiLCs to ESCLCs by chromatin IP (ChIP)-qPCR. Since ChIP-grade anti-PRDM14 antibody was unavailable, we detected the binding of exogenous FLAG-PRDM14 in EpiLCs using an anti-FLAG antibody (Figure 5B). After *Prdm14* expression was induced in EpiLCs, two distinct peaks appeared at the proximal and distal enhancers of *Klf2* (Figure 5B). Under our culture conditions, OCT3/4 was present only at distal enhancers of *Klf2*, and this peak disappeared in the transition from ESCs to EpiLCs (Figure 5B). Interestingly, induction of *Prdm14* expression enhanced the binding of OCT3/4 at both proximal and distal enhancers of *Klf2* in EpiLCs.

We next measured 5mC and 5hmC levels at two enhancers of *Klf2* in ESCs, EpiLCs, and EpiLCs + PRDM14. In ESCs, 5mC was detected only at proximal enhancers of *Klf2*, which was correlated with absence of OCT3/4 at the proximal enhancer (Figures 5B and 5C). At the distal enhancer of *Klf2*, 5mC level was transiently upregulated during the differentiation of ESCs to EpiLCs; this was followed by a downregulation induced by PRDM14. In contrast, the 5hmC level remained constant. To determine the temporal hierarchy of events (PRDM14 and OCT3/4 binding, 5mC removal, and activation of *Klf2* expression), we analyzed *Prdm14* and *Klf2* expression as well as PRDM14

and OCT3/4 binding, and 5mC and 5hmC distribution at the two *Klf2* enhancers every 6 hr after *Prdm14* induction in EpiLCs. *Prdm14* expression was detected starting 18 hr after induction; this was followed by increased PRDM14 binding at the two enhancers at 24 hr (Figures 5D, S5A, and S5B). In contrast, OCT3/4 binding at these sites first appeared 42 hr after *Prdm14* induction (Figures 5D and S5B). PRDM14 was found to interact with TET1 and TET2 but not with OCT3/4 in EpiLCs (Figure 5E), suggesting that PRDM14 indirectly enhances OCT3/4 recruitment to these enhancers. Interestingly, the level of 5mC rapidly reduced while that of 5hmC increased after PRDM14 recruitment to these enhancers (Figures 5F and S5C). To determine whether active demethylation by PRDM14 is required for OCT3/4 binding, we examined the effects of BER inhibitor (BERi) on 5mC removal from and OCT3/4 recruitment to these enhancers. BERi treatment completely disrupted the rapid removal of 5mC by PRDM14 at both *Klf2* enhancers in EpiLCs (Figures 5G and S5D). Under these conditions, OCT3/4 recruitment was abrogated although PRDM14 enrichment was unaltered (Figures 5H and S5E). Taken together, these data indicate that PRDM14 activates *Klf2* expression via active demethylation-mediated recruitment of OCT3/4 to the enhancers (Figure S5F).

To identify the genomic regions at which PRDM14 enhances OCT3/4 recruitment, we performed ChIP for OCT3/4 and PRDM14 (α-FLAG) followed by deep sequencing (ChIP-seq) in ESCs, EpiLCs, and EpiLCs expressing PRDM14, and identified 18,093, 8,136, and 13,882 OCT3/4 peaks, respectively, using the MACS2 callpeak (Feng et al., 2012). Next, to investigate the effects of PRDM14 on OCT3/4 binding, we compared the enrichment of OCT3/4 peaks among ESCs, EpiLCs, and EpiLCs expressing PRDM14 by using the MACS2 bdgdiff module (Feng et al., 2012). Over half of the OCT3/4 binding in ESCs was reduced and only 312 peaks increased in the transition of ESCs to EpiLCs (Figure 6A); 2 days after PRDM14 induction, 2,542 OCT3/4 binding peaks increased or had appeared, and those corresponding to 1,559 genes colocalized with PRDM14 binding peaks (Figure 6B). Approximately 6.3% (98 of 1,559) of genes in which OCT3/4 binding was enhanced by PRDM14 were upregulated by PRDM14, whereas approximately 2.8% (43 of 1,559) of genes in which OCT3/4 binding was upregulated by

(F) GlucMS-qPCR analysis of the percentage of 5mC and 5hmC marks at the *Klf2* locus every 6 hr after *Prdm14* induction. Error bars indicate ±SD of a technical duplicate.

(G) GlucMS-qPCR showing the percentage of 5mC and 5hmC marks at the *Klf2* locus in EpiLCs + PRDM14 treated with DMSO(DMSO; control), 3-aminobenzamide (3AB), or CRT 004876 (CRT). Error bars indicate ±SD of a technical duplicate.

(H) ChIP-qPCR analysis of PRDM14 (α- FLAG) and OCT3/4 at the *Klf2* locus in EpiLCs + PRDM14 treated with DMSO, 3AB, or CRT. Fold enrichment was calculated by comparing pre-immune IgG control (red dotted line) with each antibody. Error bars indicate +SD of a technical duplicate.
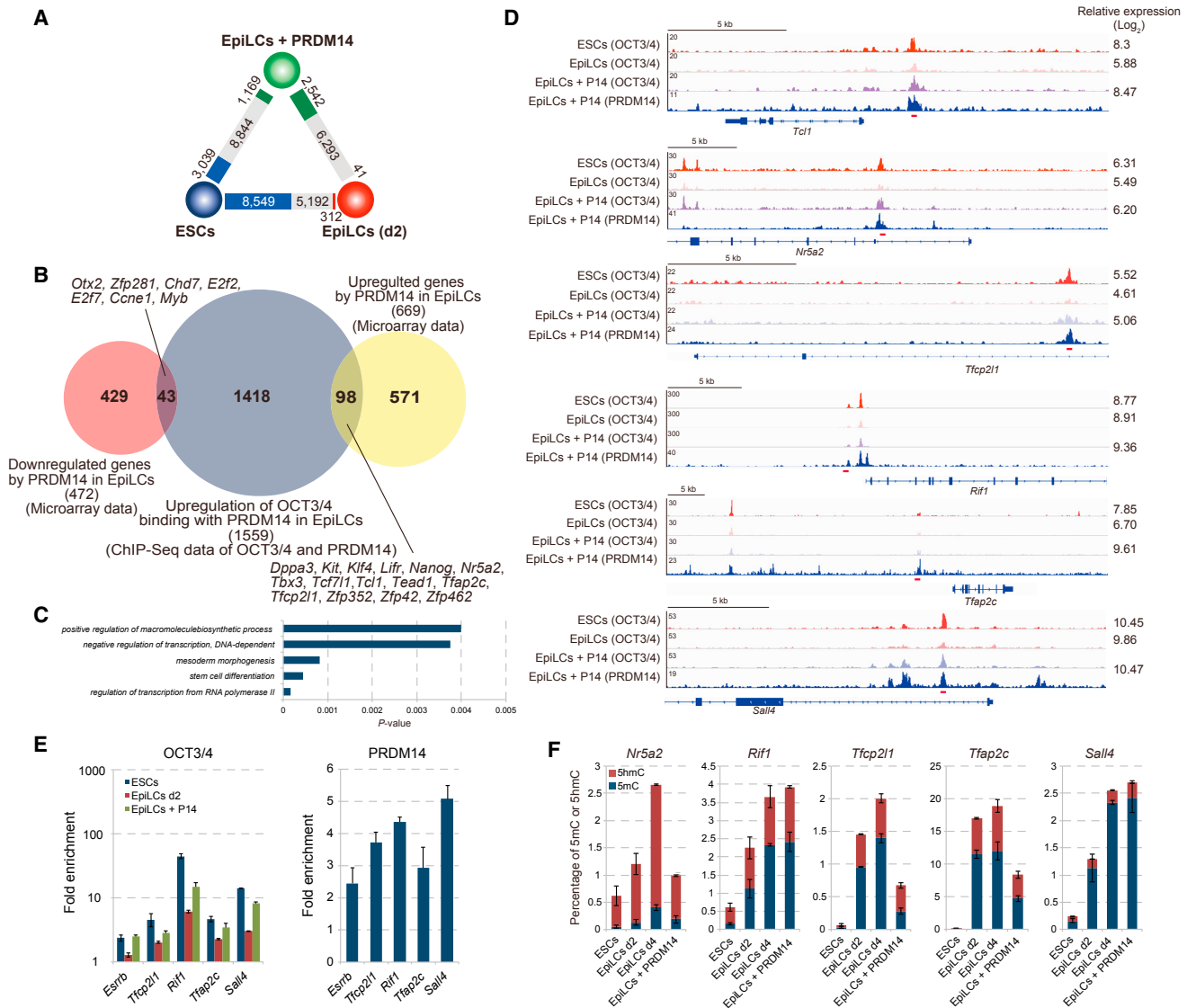
Figure 6. Enhancement of OCT3/4 Binding by PRDM14 during Reversion from Primed to Naive Pluripotency

(A) Comparison of OCT3/4 binding peaks between ESCs and EpiLCs (d2), EpiLCs (d2) and EpiLCs + PRDM14, and EpiLCs + PRDM14 and ESCs. Numbers in gray rectangles indicate peaks common to both cell types in each pair. Numbers in blue, red, and green rectangles indicate peaks specific to ESCs, EpiLCs (d2), and EpiLCs + PRDM14, respectively.

(B) Genes downregulated by PRDM14 during the transition from EpiLCs to ESCLCs (red circles). Genes associated with PRDM14 and OCT3/4 binding that were enhanced during the transition of EpiLCs to ESCs are indicated by navy circles; genes upregulated by PRDM14 in EpiLCs are shown by yellow circles.

(C) GO annotation of genes upregulated by PRDM14 in which OCT3/4 binding increased with PRDM14 binding (from EpiLCs to EpiLCs + PRDM14).

(D) ChIP-seq tracks of OCT3/4 and PRDM14 in ESCs, EpiLCs (d2), and EpiLCs + PRDM14. Intensity values of microarray data are shown on the right side. Red bar indicates the position of the primers for ChIP-qPCR and GlucMS-qPCR.

(E) ChIP-qPCR analysis of OCT3/4 and PRDM14 expression in ESCs, EpiLCs (d2), and EpiLCs + PRDM14. Fold enrichment indicates values of each IgG relative to input values using the same amount of DNA as template. Error bars indicate ±SD of a technical duplicate.

(F) GlucMS-qPCR analysis of the percentage of 5mC and 5hmC marks at pluripotency genes. Error bars indicate ±SD of a technical duplicate.

PRDM14 were downregulated by *Prdm14* induction in EpiLCs (Figure 6B). An overrepresentation analysis using DAVID (Huang et al., 2007) revealed that GO terms related to stem cell maintenance, including *Tcl1*, *Nr5a2*, and *Tfcp2l1*, were enriched among the upregulated genes (Figures 6C and 6D). Consistent with ChIP-seq data, the
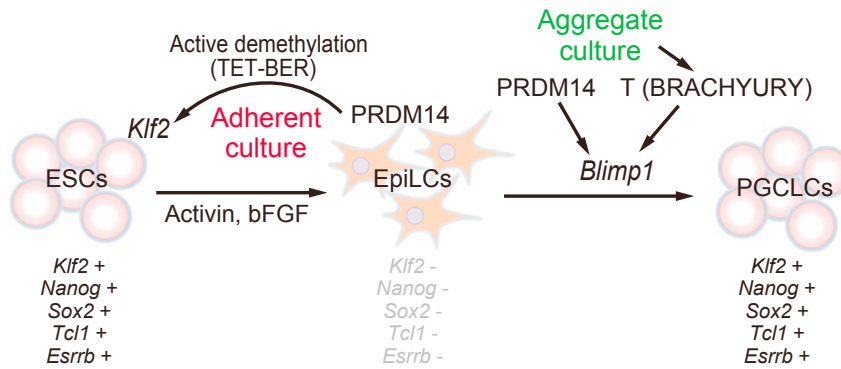
Figure 7. Working Model of the Role of PRDM14 in the Conversion of EpiLCs to ESCLCs and PGC Specification

enrichment of OCT3/4 binding at five of the genes decreased during differentiation of ESC to EpiLC, with a consequent increase in OCT3/4 binding peaks by PRDM14 binding-associated induction (Figure 6E). To determine whether PRDM14-mediated DNA demethylation modulates the recruitment of OCT3/4 to the five genes, we measured 5mC and 5hmC levels at the binding regions of OCT3/4 and PRDM14 by glucosylation of genomic DNA followed by methylation-sensitive (GlucMS)-qPCR (Figure 6F). 5mC levels were elevated at all genes analyzed during ESC-to-EpiLC differentiation, whereas at three of the five genes the levels decreased after PRDM14 induction in EpiLCs. These findings indicate that PRDM14 acts via DNA demethylation-dependent and -independent mechanisms to recruit OCT3/4.

DISCUSSION

This study provides evidence that PRDM14 confers pluripotency and self-renewal capacity to EpiLCs by reactivating pluripotency genes via TET-BER-mediated active demethylation (Figure 7). Nascent PGCs reactivate pluripotent-associated genes during specification from epiblast cells. Our data suggest that the activation of PRDM14 in epiblast is a key event for reactivation of pluripotent-associated genes and the acquisition of potential pluripotency. Our data demonstrate that EpiLC culture conditions (i.e., adherent versus aggregate) determine the expression of two key genes for PGC specification, *T* and *Blimp1* (Ohinata et al., 2005) (Figures 2G and 2H). Moreover, adherent EpiLC cultures with *Prdm14* induction resulted in the conversion of EpiLCs to ESCLCs, whereas three-dimensional aggregate cultures induced PGCLCs (Nakaki et al., 2013). It has been shown that the WNT3-β-catenin axis induces *T* expression in epiblast culture in aggregate culture of EpiLCs (Aramaki et al., 2013). Therefore, we consider that aggregate culture of EpiLCs enhance WNT3-β-catenin signaling to activate *T* expression. Further experiments are needed to clarify

whether the combination of PRDM14 with BLIMP1 or T can induce PGCLCs from EpiLCs in adherent culture.

Tet1/*Tet2* KD and BERi treatment impaired the reactivation of pluripotency genes by PRDM14, reducing the conversion efficiency of EpiLCs to ESCLCs. However, the reactivation of pluripotency genes by PRDM14 was partially inhibited by *Tet1*/*Tet2* KD and BERi treatment, implying that PRDM14 acts via a TET-BER-independent mechanism in this process. Furthermore, PRDM14-induced activation of PGC-enriched genes including *Tfap2c*, developmental pluripotency-associated 3 (*Dppa3*), and reproductive homeobox 6/9 (*Rhox6/9*) was normal in *Tet1*/*Tet2* KD EpiLCs. These data are consistent with the phenotype of *Tet1*/*Tet2* double KO (DKO) PGCs, and demonstrate normal PGC specification and development (Yamaguchi et al., 2012). Further studies examining the developmental potential of EGCs derived from *Tet1*/*Tet2* DKO PGCs are needed to clarify the function of TET1/TET2 in the acquisition of pluripotency by PGCs in vivo.

The concordance between ChIP-seq and microarray data provided evidence that PRDM14 recruits OCT3/4 to enhancer regions of pluripotency genes, leading to their transcription during the conversion from EpiLCs to ESCLCs. The 5mC marks at *Nr5a2*, *Tfcp2l1*, and *Tfap2c* enhancers were removed by PRDM14 in EpiLCs, while 5mC at replication timing regulatory factor 1 (*Rif1*) and spalt-like transcription factor 4 (*Sall4*) enhancers were unchanged. Interestingly, the reactivation of *Rif1* and *Sall4* by PRDM14 was impaired in *Tet1*/*Tet2* double KD EpiLCs (Figure S4B). These results suggest that TET proteins are involved in the reactivation of *Rif1* and *Sall4* by PRDM14 via DNA demethylation-independent mechanisms. In support of this possibility, TET proteins were required for the recruitment of O-linked N-acetylglucosamine (O-GlcNAc) transferase to target chromatin, which leads to its activation via O-GlucNAcylation of histone H2B (Chen et al., 2013; Vella et al., 2013).

Recently, various groups have independently succeeded in inducing human PGCLCs from human pluripotent

stem cells (PSCs) (Irie et al., 2015; Sasaki et al., 2015; Sugawa et al., 2015). For instance, human PGCLCs were more robustly induced from mesoderm-like cells (iMeLCs) and human ESCs cultured in medium containing four inhibitors, called "4i" medium; they expressed some mesoderm markers. Although most naive pluripotency genes are repressed in the transition from ESCs to EpiLCs in mice, most genes including *KLF2*, *TCL1A*, *ESRRB*, *TFCP2L1*, and nuclear receptor subfamily 0 B1 (*NR0B1*) showed low expression in human ESCs/induced PSCs (iPSCs). Although expression of *Prdm14* is closely associated with naive pluripotency in mice, primed human ESCs/iPSCs, primitive streak-like cells, iMeLCs, and 4i ESCs consistently express PRDM14 at moderate levels. Therefore, the specific upregulation of *Prdm14* observed during the transition from pluripotent cells to PGCs in mice does not occur in human PGC specification. The present study has clearly demonstrated that PRDM14 governs the transcriptional network for pluripotency in the absence of BLIMP1 in mice. In contrast to early mouse embryos, epiblast cells in human early embryos need to maintain pluripotency for longer than 10 days until the emergence of PGCs. Furthermore, primitive streak-like cells, which have a high capacity for PGC specification, retain pluripotency markers including NANOG and PRDM14 (Irie et al., 2015; Sasaki et al., 2015). On this basis, we hypothesize that continuous expression of PRDM14 is essential for the long-term maintenance of pluripotent cells to give rise to PGCs in humans. In contrast to our hypothesis, it has also been shown that PRDM14 KD ESCs are competent for PGCLC induction, which led to the conclusion that PRDM14 is not necessary for PGC induction in humans (Sugawa et al., 2015). However, another group has clearly shown that *PRDM14* KD induces human ESC differentiation (Chia et al., 2010), implying that the KD efficiency in the study of Sugawa et al. (2015) was quite low and that conclusions cannot be drawn regarding the role of PRDM14 in human PGC development. Therefore, additional KO studies are needed to clarify the molecular and epigenetic functions of PRDM14 in the human germline.

The conversion of EpiLCs to ESCLCs is similar to the late stage of somatic cell reprogramming, since activation of pluripotency genes by PRDM14 is associated with DNA demethylation of their promoters. Given these findings, we consider that PRDM14-dependent active demethylation of pluripotency genes is required for progression of the late stage of somatic cell reprogramming. This is supported by the fact that *Prdm14* KO fibroblasts failed to be converted to iPSCs in the absence of *Nanog* and *Sox2* reactivation under standard ESC culture conditions (Payer et al., 2013). Furthermore, epigenetic errors result in partially reprogrammed iPSCs and low-grade iPSCs (Stadtfeld et al., 2010; Tran et al., 2015). Our findings provide a framework for

understanding not only physiological but also artificial (e.g., iPSC derivation) and pathological (e.g., the appearance of cancer stem cells) reprogramming.

EXPERIMENTAL PROCEDURES

Cell Culture

E14tg2a ESCs were cultured in Glasgow minimum essential medium (Wako) containing 10% fetal calf serum (Invitrogen), 1 mM glutamine (Wako), nonessential amino acid (Wako), and 0.1 mM 2-mercaptoethanol (Wako). The culture was supplemented with LIF (Wako) in the absence of feeder cells.

Teratoma Formation and Histological Analysis

Approximately 5×10^6 EpiLCs expressing PRDM14, cultured without LIF, were injected subcutaneously into both the flanks of female nude mice. After 30 days, the tumors were excised, embedded in paraffin, and sectioned into 4-μm-thick slices. H&E staining was done according to the standard protocol. Markers for the three germ layers were monitored with immunofluorescence with antibodies: α-AFP (Proteintech; 14550-1-AP), α-SMA (Abcam; ab5694), and α-β-tubulin (Cell Signaling; catalog no. 2146). These experiments were conducted according to the Kwansei Gakuin University Regulation for Animal experimentation.

Generation of *Prdm14*-Inducible ESCs by ROSA-Tet-Off and piggyBac Tet-On

For the ROSA-Tet-off system, EBRTcH3 cells were transfected with pZhc-Prdm14 and pCAGGS-Cre (Masui et al., 2005). For the Tet-on system, E14tg2a ESCs and BVSC ESCs (Hayashi et al., 2011) were transfected with PB-TET-FLAG-*Prdm14*-IRES-Neo, PB-CA-rtTA Adv, pCAG-Pbase, and pGG131 (pCAG-DsRed-IRES-Hygro). The cells were grown in selective medium containing 1.5 μg/mL puromycin (Sigma-Aldrich) and 200 μg/mL hygromycin B (Wako) for 7 days (Okashita et al., 2014). Colonies were picked and analyzed by qRT-PCR and western blotting to determine PRDM14 expression levels, with and without doxycycline.

RNAi

Tet1 and *Tet2* small hairpin RNAs (shRNAs) were generated from pLKO.1-puro (Addgene; 8453) or pLKO.1-blast (Addgene; 26655). The *Tet1* and *Tet2* shRNAs were adapted for pLKO.1 plasmids. The RNAi target sequences are presented in Table S1. pLKO.1 lentiviruses were constructed according to the Addgene pLKO.1 protocol (http://www.addgene.org/). pLKO.1 plasmids were co-transfected with pCMV-VSV-G (Addgene; 8454) and pCMV-dR8.2 dvpr (Addgene; 8455) into HEK293T cells. Lentivirus-containing supernatants were centrifuge-filtered through a 0.45-μm filter. Clarified supernatants were combined using the Lenti-X Concentrator (Clontech) according to the manufacturer's protocol. The mixture was centrifuged, after which the supernatant was carefully removed and the pellet resuspended in DMEM.

For lentivirus transduction, subconfluent iP14 ESCs were incubated with lentivirus-containing DMEM supplemented with 8 μg/mL polybrene (Sigma-Aldrich) for 24 hr. After changing the spent medium with fresh medium, cells were selected with

2 μg/mL puromycin (Sigma-Aldrich) or 20 μg/mL blasticidin S hydrochloride (Calbiochem). Knockdown efficiency was analyzed by qRT-PCR and western blotting.

Generation of *Klf2*-Knockout ESCs Using a CRISPR/Cas9 System

Klf2 guide RNA was adapted for and generated from the pX330-U6-Chimeric_BB-CBh-hSpCas9 plasmid (Addgene; 42230). The *Klf2* guide RNA sequences are presented in Table S1. The established plasmid was co-transfected with pCAG-IRES-Puro into the induced PRDM14 ESCs, and the transfected cells were selected with 2 μg/mL puromycin. KLF2 expression was analyzed by western blot.

Induction of EpiLCs

ESCs were cultured in N2B27 basal medium containing 3 μM CHIR99021 (Wako), 0.4 μM PD0325901 (Wako), and LIF in a dish coated with 0.01% poly-L-ornithine (Millipore) and 10 ng/mL laminin (BD Biosciences). Induction of EpiLCs was performed as described previously (Hayashi et al., 2011). EpiLCs were induced from ESCs in N2B27 basal medium containing 20 ng/mL activin A (Peprotech), 12 ng/mL bFGF (Invitrogen), and 0.1–1% KSR for 2 days on a dish coated with 16.7 μg/mL human plasma fibronectin (Millipore). Two days after EpiLC induction, the cells were collected and replated (0.5–1.0 × 10^5) with or without doxycycline in GK15 medium on a dish coated with 16.7 μg/mL human plasma fibronectin. For the colony formation assay for AP-positive cells, ESCs, EpiLCs, and EpiLCs induced with or without PRDM14 were dissociated by TrypLE Select (Invitrogen). Cells (1.0 × 10^4) were cultured under standard ESC culture conditions. After culture for 3 days, the cells were stained for AP activity. The aggregate culture of EpiLCs was performed as previously reported (Nakaki et al., 2013). In brief, after 36 hr of EpiLC induction the cells were collected, and 2,000 cells per well were transferred to a low-cell binding 96-well plate (NUNC). The cells were grown for 2 days in GK15 medium with or without 1.5 μg/mL doxycycline.

qRT-PCR

Total RNA was extracted using TRIzol (Invitrogen). The ReverTra Ace qPCR RT kit (Toyobo) was used for cDNA synthesis according to the manufacturer's instructions. Subsequently, cDNA was used as a template for qPCR with the Thunderbird SYBR qPCR Mix (Toyobo) and gene-specific primers (Table S1) on a LightCycler 96 system (Roche).

Western Blot and Immunoprecipitation Analysis

Cells were lysed by boiling in SDS sample buffer (Wako). The total proteins from lysed cells were denatured by 2-mercaptoethanol and were then applied to polyacrylamide-SDS gels. The proteins were separated on polyacrylamide-SDS gels, blotted on polyvinylidene fluoride membrane, and probed using the following primary antibodies: α-PRDM14 (R & D Systems; MAB8097), α-tubulin (Sigma; T5168), α-histone H3 (Abcam; ab1791), α-FLAG (Sigma; F1804), α-KLF2 (Millipore; 09–820), α-TET1 (Millipore; 09–872), α-TET2 (Santa Cruz Biotechnology; sc-136926), and α-OCT3/4 (Santa Cruz; sc-8628). Following the primary antibody reaction, the membrane was incubated with secondary horseradish peroxi-

dase-coupled antibodies. Detection was achieved using the Luminata Forte Western HRP Substrate (Millipore). For immunoprecipitation analysis, extracts containing a protease inhibitor cocktail (Roche) were incubated with anti-PRDM14 antibody or anti-OCT3/4 antibody for 2 hr at 4°C, and captured with protein A beads. Protein complexes were washed with wash buffer (50 mM Tris-HCl [pH 8.0], 150 mM NaCl, 1% NP-40), and eluted by boiling with SDS sample buffer.

ACCESSION NUMBERS

Data from this study are available in GEO: GSE77622 (Microarray) and in DNA DataBank of Japan (DDBJ): DRA004294 (ChIP-seq).

SUPPLEMENTAL INFORMATION

Supplemental Information includes Supplemental Experimental Procedures, five figures, and one table and can be found with this article online at http://dx.doi.org/10.1016/j.stemcr.2016.10.007.

AUTHOR CONTRIBUTIONS

N.O. performed most experiments and analyzed data. Y. Suwa, N.S., M.K., H.K., and A.N. performed some experiments. O.N. and M.K. contributed ChIP-seq analysis. G.N. established ESC cell line. Y. Seki designed and performed experiments. M.T. contributed to the immunofluorescence study of teratoma tissue. N.O. and Y. Seki wrote the manuscript. Y. Suwa, O.N., and N.S. contributed equally to this work.

ACKNOWLEDGMENTS

REFERENCES

Aramaki, S., Hayashi, K., Kurimoto, K., Ohta, H., Yabuta, Y., Iwanari, H., Mochizuki, Y., Hamakubo, T., Kato, Y., Shirahige, K., et al. (2013). A mesodermal factor, T, specifies mouse germ cell fate by directly activating germline determinants. Dev. Cell 27, 516–529.

Buecker, C., Srinivasan, R., Wu, Z., Calo, E., Acampora, D., Faial, T., Simeone, A., Tan, M., Swigut, T., and Wysocka, J. (2014). Reorganization of enhancer patterns in transition from naive to primed pluripotency. Cell Stem Cell 14, 838–853.

Chen, Q., Chen, Y., Bian, C., Fujiki, R., and Yu, X. (2013). TET2 promotes histone O-GlcNAcylation during gene transcription. Nature 493, 561–564.

Chia, N.Y., Chan, Y.S., Feng, B., Lu, X., Orlov, Y.L., Moreau, D., Kumar, P., Yang, L., Jiang, J., Lau, M.S., et al. (2010). A genome-wide RNAi screen reveals determinants of human embryonic stem cell identity. Nature 468, 316–320.

Feng, J., Liu, T., Qin, B., Zhang, Y., and Liu, X.S. (2012). Identifying ChIP-seq enrichment using MACS. Nat. Protoc. 7, 1728–1740.

Ficz, G., Hore, T.A., Santos, F., Lee, H.J., Dean, W., Arand, J., Krueger, F., Oxley, D., Paul, Y.L., Walter, J., et al. (2013). FGF signaling inhibition in ESCs drives rapid genome-wide demethylation to the epigenetic ground state of pluripotency. Cell Stem Cell 13, 351–359.

Gillich, A., Bao, S., Grabole, N., Hayashi, K., Trotter, M.W., Pasque, V., Magnusdottir, E., and Surani, M.A. (2012). Epiblast stem cell-based system reveals reprogramming synergy of germline factors. Cell Stem Cell 10, 425–439.

Hackett, J.A., Zylicz, J.J., and Surani, M.A. (2012). Parallel mechanisms of epigenetic reprogramming in the germline. Trends Genetics 28, 164–174.

Hajkova, P., Ancelin, K., Waldmann, T., Lacoste, N., Lange, U.C., Cesari, F., Lee, C., Almouzni, G., Schneider, R., and Surani, M.A. (2008). Chromatin dynamics during epigenetic reprogramming in the mouse germ line. Nature 452, 877–881.

Hall, J., Guo, G., Wray, J., Eyres, I., Nichols, J., Grotewold, L., Morfopoulou, S., Humphreys, P., Mansfield, W., Walker, R., et al. (2009). Oct4 and LIF/Stat3 additively induce Kruppel factors to sustain embryonic stem cell self-renewal. Cell Stem Cell 5, 597–609.

Hayashi, K., Ohta, H., Kurimoto, K., Aramaki, S., and Saitou, M. (2011). Reconstitution of the mouse germ cell specification pathway in culture by pluripotent stem cells. Cell 146, 519–532.

Huang, D.W., Sherman, B.T., Tan, Q., Kir, J., Liu, D., Bryant, D., Guo, Y., Stephens, R., Baseler, M.W., Lane, H.C., et al. (2007). DAVID Bioinformatics Resources: expanded annotation database and novel algorithms to better extract biology from large gene lists. Nucleic Acids Res. 35, W169–W175.

Irie, N., Weinberger, L., Tang, W.W., Kobayashi, T., Viukov, S., Manor, Y.S., Dietmann, S., Hanna, J.H., and Surani, M.A. (2015). SOX17 is a critical specifier of human primordial germ cell fate. Cell 160, 253–268.

Kagiwada, S., Kurimoto, K., Hirota, T., Yamaji, M., and Saitou, M. (2013). Replication-coupled passive DNA demethylation for the erasure of genome imprints in mice. EMBO J. 32, 340–353.

Kawasaki, Y., Lee, J., Matsuzawa, A., Kohda, T., Kaneko-Ishino, T., and Ishino, F. (2014). Active DNA demethylation is required for complete imprint erasure in primordial germ cells. Sci. Rep. 4, 3658.

Kurimoto, K., Yabuta, Y., Ohinata, Y., Shigeta, M., Yamanaka, K., and Saitou, M. (2008). Complex genome-wide transcription dy-namics orchestrated by Blimp1 for the specification of the germ cell lineage in mice. Genes Dev. 22, 1617–1635.

Kurimoto, K., Yabuta, Y., Hayashi, K., Ohta, H., Kiyonari, H., Mitani, T., Moritoki, Y., Kohri, K., Kimura, H., Yamamoto, T., et al. (2015). Quantitative dynamics of chromatin remodeling during germ cell specification from mouse embryonic stem cells. Cell Stem Cell 16, 517–532.

Ma, Z., Swigut, T., Valouev, A., Rada-Iglesias, A., and Wysocka, J. (2011). Sequence-specific regulator Prdm14 safeguards mouse ESCs from entering extraembryonic endoderm fates. Nat. Struct. Mol. Biol. 18, 120–127.

Masui, S., Shimosato, D., Toyooka, Y., Yagi, R., Takahashi, K., and Niwa, H. (2005). An efficient system to establish multiple embryonic stem cell lines carrying an inducible expression unit. Nucleic Acids Res. 33, e43.

Matsui, Y., Zsebo, K., and Hogan, B.L. (1992). Derivation of pluripotential embryonic stem cells from murine primordial germ cells in culture. Cell 70, 841–847.

Nakaki, F., Hayashi, K., Ohta, H., Kurimoto, K., Yabuta, Y., and Saitou, M. (2013). Induction of mouse germ-cell fate by transcription factors in vitro. Nature 501, 222–226.

Ohinata, Y., Payer, B., O'Carroll, D., Ancelin, K., Ono, Y., Sano, M., Barton, S.C., Obukhanych, T., Nussenzweig, M., Tarakhovsky, A., et al. (2005). Blimp1 is a critical determinant of the germ cell lineage in mice. Nature 436, 207–213.

Ohinata, Y., Ohta, H., Shigeta, M., Yamanaka, K., Wakayama, T., and Saitou, M. (2009). A signaling principle for the specification of the germ cell lineage in mice. Cell 137, 571–584.

Ohno, R., Nakayama, M., Naruse, C., Okashita, N., Takano, O., Tachibana, M., Asano, M., Saitou, M., and Seki, Y. (2013). A replication-dependent passive mechanism modulates DNA demethylation in mouse primordial germ cells. Development 140, 2892–2903.

Okashita, N., Kumaki, Y., Ebi, K., Nishi, M., Okamoto, Y., Nakayama, M., Hashimoto, S., Nakamura, T., Sugasawa, K., Kojima, N., et al. (2014). PRDM14 promotes active DNA demethylation through the ten-eleven translocation (TET)-mediated base excision repair pathway in embryonic stem cells. Development 141, 269–280.

Payer, B., Rosenberg, M., Yamaji, M., Yabuta, Y., Koyanagi-Aoi, M., Hayashi, K., Yamanaka, S., Saitou, M., and Lee, J.T. (2013). Tsix RNA and the germline factor, PRDM14, link X reactivation and stem cell reprogramming. Mol. Cell 52, 805–818.

Popp, C., Dean, W., Feng, S., Cokus, S.J., Andrews, S., Pellegrini, M., Jacobsen, S.E., and Reik, W. (2010). Genome-wide erasure of DNA methylation in mouse primordial germ cells is affected by AID deficiency. Nature 463, 1101–1105.

Respuela, P., Nikolic, M., Tan, M., Frommolt, P., Zhao, Y., Wysocka, J., and Rada-Iglesias, A. (2016). Foxd3 promotes exit from naive pluripotency through enhancer decommissioning and inhibits germline specification. Cell Stem Cell 18, 118–133.

Sasaki, K., Yokobayashi, S., Nakamura, T., Okamoto, I., Yabuta, Y., Kurimoto, K., Ohta, H., Moritoki, Y., Iwatani, C., Tsuchiya, H., et al. (2015). Robust in vitro induction of human germ cell fate from pluripotent stem cells. Cell Stem Cell 17, 178–194.

Seisenberger, S., Andrews, S., Krueger, F., Arand, J., Walter, J., Santos, F., Popp, C., Thienpont, B., Dean, W., and Reik, W. (2012). The dynamics of genome-wide DNA methylation reprogramming in mouse primordial germ cells. Mol. Cell 48, 849–862.

Seki, Y., Hayashi, K., Itoh, K., Mizugaki, M., Saitou, M., and Matsui, Y. (2005). Extensive and orderly reprogramming of genome-wide chromatin modifications associated with specification and early development of germ cells in mice. Dev. Biol. 278, 440–458.

Seki, Y., Yamaji, M., Yabuta, Y., Sano, M., Shigeta, M., Matsui, Y., Saga, Y., Tachibana, M., Shinkai, Y., and Saitou, M. (2007). Cellular dynamics associated with the genome-wide epigenetic reprogramming in migrating primordial germ cells in mice. Development 134, 2627–2638.

Stadtfeld, M., Apostolou, E., Akutsu, H., Fukuda, A., Follett, P., Natesan, S., Kono, T., Shioda, T., and Hochedlinger, K. (2010). Aberrant silencing of imprinted genes on chromosome 12qF1 in mouse induced pluripotent stem cells. Nature 465, 175–181.

Sugawa, F., Arauzo-Bravo, M.J., Yoon, J., Kim, K.P., Aramaki, S., Wu, G., Stehling, M., Psathaki, O.E., Hubner, K., and Scholer, H.R. (2015). Human primordial germ cell commitment in vitro associates with a unique PRDM14 expression profile. EMBO J. 34, 1009–1024.

Tran, K.A., Jackson, S.A., Olufs, Z.P., Zaidan, N.Z., Leng, N., Kendziorski, C., Roy, S., and Sridharan, R. (2015). Collaborative rewiring of the pluripotency network by chromatin and signalling modulating pathways. Nat. Commun. 6, 6188.

Vella, P., Scelfo, A., Jammula, S., Chiacchiera, F., Williams, K., Cuomo, A., Roberto, A., Christensen, J., Bonaldi, T., Helin, K., et al. (2013). Tet proteins connect the O-linked N-acetylglucosamine transferase Ogt to chromatin in embryonic stem cells. Mol. Cell 49, 645–656.

Weber, S., Eckert, D., Nettersheim, D., Gillis, A.J., Schafer, S., Kuckenberg, P., Ehlermann, J., Werling, U., Biermann, K., Looijenga, L.H., et al. (2010). Critical function of AP-2 gamma/TCFAP2C in mouse embryonic germ cell maintenance. Biol. Reprod. 82, 214–223.

Wu, S.C., and Zhang, Y. (2010). Active DNA demethylation: many roads lead to Rome. Nat. Rev. Mol. Cell Biol. 11, 607–620.

Yabuta, Y., Kurimoto, K., Ohinata, Y., Seki, Y., and Saitou, M. (2006). Gene expression dynamics during germline specification in mice identified by quantitative single-cell gene expression profiling. Biol. Reprod. 75, 705–716.

Yamaguchi, S., Hong, K., Liu, R., Shen, L., Inoue, A., Diep, D., Zhang, K., and Zhang, Y. (2012). Tet1 controls meiosis by regulating meiotic gene expression. Nature 492, 443–447.

Yamaji, M., Seki, Y., Kurimoto, K., Yabuta, Y., Yuasa, M., Shigeta, M., Yamanaka, K., Ohinata, Y., and Saitou, M. (2008). Critical function of Prdm14 for the establishment of the germ cell lineage in mice. Nat. Genet. 40, 1016–1022.

ISSCR

OPEN ACCESS

A Simple and Robust Method for Establishing Homogeneous Mouse Epiblast Stem Cell Lines by Wnt Inhibition

Michihiko Sugimoto,[1,6] Masayo Kondo,[1] Yumiko Koga,[1] Hirosuke Shiura,[1] Rieko Ikeda,[1] Michiko Hirose,[2] Atsuo Ogura,[2] Ayumi Murakami,[3] Atsushi Yoshiki,[3] Susana M. Chuva de Sousa Lopes,[4] and Kuniya Abe[1,5,*]

[1]Technology and Development Team for Mammalian Genome Dynamics, RIKEN BioResource Center, 3-1-1 Koyadai, Tsukuba, Ibaraki 305-0074, Japan
[2]Bioresource Engineering Division, RIKEN BioResource Center, 3-1-1 Koyadai, Tsukuba, Ibaraki 305-0074, Japan
[3]Experimental Animal Division, RIKEN BioResource Center, 3-1-1 Koyadai, Tsukuba, Ibaraki 305-0074, Japan
[4]Department of Anatomy and Embryology, Leiden University Medical Center, 2333 ZC Leiden, the Netherlands
[5]Graduate School of Life and Environmental Sciences, University of Tsukuba, Ibaraki 305-8572, Japan
[6]Present address: Division of Developmental Genetics, Institute of Resource Development and Analysis, Kumamoto University, 2-2-1 Honjo, Kumamoto 860-0811, Japan
*Correspondence: abe@rtc.riken.jp
http://dx.doi.org/10.1016/j.stemcr.2015.02.014

SUMMARY

Epiblast stem cells (EpiSCs) are pluripotent stem cells derived from epiblasts of postimplantation mouse embryos, and thus provide a useful model for studying "primed" pluripotent states. Here, we devised a simple and robust technique to derive high-quality EpiSCs using an inhibitor of WNT secretion. Using this method, we readily established EpiSC lines with high efficiency and were able to use whole embryonic portions without having to separate the epiblast from the visceral endoderm (VE). Expression analyses revealed that these EpiSCs maintained a homogeneous, undifferentiated status, yet showed high potential for differentiation both in vitro and in teratomas. Unlike EpiSCs derived by the original protocol, new EpiSC lines required continuous treatment with the Wnt inhibitor, suggesting some intrinsic differences from the existing EpiSCs. The homogeneous properties of this new version of EpiSCs should facilitate studies on the establishment and maintenance of a "primed" pluripotent state, and directed differentiation from the primed state.

INTRODUCTION

Epiblast stem cells (EpiSCs) are pluripotent stem cells (PSCs) derived from the epiblasts of early postimplantation mouse embryos (Brons et al., 2007; Tesar et al., 2007). EpiSCs can proliferate indefinitely in culture and differentiate into derivatives of all three germ layers in vitro and in teratomas. However, EpiSCs possess several different characteristics compared with other PSCs such as mouse embryonic stem cells (mESCs). Whereas mESCs show dome-shaped colonies, EpiSCs show a flatter colony morphology. Other characteristics that differ between EpiSCs and mESCs are the status of X chromosome inactivation in female cells, the culture conditions needed, the expression of several genes/markers (e.g., mESC-specific *Pecam1* and EpiSC-specific *Fgf5*), and their clonogenicity and contribution to chimeras when injected into blastocysts (Brons et al., 2007; Nichols and Smith, 2009). Most of these cellular characteristics of EpiSCs are shared by human PSCs such as human ESCs (hESCs) and human induced PSCs (hiPSCs). EpiSCs and human PSCs are considered "primed" PSCs, in contrast to "naïve"-type stem cells such as mESCs (Nichols and Smith, 2009). Therefore, comparisons between EpiSCs and hESCs/hiPSCs should contribute to our understanding of the nature of the primed state and provide insights into the processes underlying the naive-to-primed state transition.

One difficulty in deriving EpiSCs is the need for microdissection of small postimplantation embryos. The original protocols used only the epiblast layer separated from the surrounding visceral endoderm (VE) tissue as a source of the cell lines. The overall efficiency of EpiSC derivation from epiblast explants varies from <10% to 40% (Brons et al., 2007; Tesar et al., 2007; Kojima et al., 2014; this study). Han et al. (2010) reported that EpiSCs carrying the *Oct4*-GFP transgene contained both GFP-positive and GFP-negative populations in culture, and that the *Oct4*-GFP-positive minor population could contribute to the tissues of chimeras constructed by blastocyst injection, whereas the GFP-negative population could not. It is also known that EpiSCs express marker genes for the mesoderm, endoderm, or primitive streak (albeit at low levels and in conjunction with pluripotency markers), and that some of these lineage markers show heterogeneous expression among cells within the same culture (Bernemann et al., 2011; Sumi et al., 2013). It has been suggested that this heterogeneous expression of lineage markers might predispose or prime EpiSCs toward particular cell lineages even while the cells remain pluripotent (Bernemann et al., 2011; Kojima et al., 2014). Alternatively, the heterogeneous expression could reflect some degree of spontaneous differentiation in cultures of EpiSCs.

Wnt signaling has been described as a positive regulator of self-renewal in mESCs (Hao et al., 2006; Ogawa et al.,

CrossMark

300

2006; Singla et al., 2006; ten Berge et al., 2011); however, the involvement of the canonical Wnt signaling pathway (i.e., β-catenin-dependent Wnt signaling, as opposed to non-canonical Wnt signaling, which is β-catenin independent) in pluripotency remains controversial (reviewed by Sokol, 2011). In fact, *β-catenin* null mESCs have been generated successfully in naive conditions (Lyashenko et al., 2011; Wray et al., 2011). Interestingly, Ying et al. (2008) showed that mESCs can be maintained in the ground state when cultured in medium containing leukemia inhibitory factor (LIF) plus two inhibitors (2i) for ERK signaling and GSK3 activity. However, although the GSK3 inhibitor they used was an effective agonist of the Wnt/β-catenin signaling pathway, the maintenance of ground-state mESCs requires dual inhibition. Blocking the secretion of all WNT proteins in ground-state mESCs by deleting the *Porcupine* gene also proved to be compatible with pluripotency, demonstrating that the WNT protein secretion may not be necessary for pluripotency (Biechele et al., 2013).

Given that the retention of β-catenin in the cytoplasm has been implicated in the self-renewal of both EpiSC and hESCs (Kim et al., 2013), we reasoned that inhibition of Wnt signaling might favor the growth of primed-state PSCs, i.e., EpiSCs. Here, we devised a simple and robust technique to derive high-quality EpiSCs using the small-molecule Wnt-inhibitor IWP-2, which acts on the protein Porcupine, blocking the secretion of WNT proteins and consequently pharmacologically inhibiting downstream Wnt signaling. Here, we show that the use of IWP-2 allows one to derive EpiSCs from epiblast cells without having to remove the VE, and to stably maintain EpiSCs by blocking the endogenous WNT-mediated spontaneous differentiation that otherwise would arise in culture. The homogeneous properties of the resulting EpiSCs at the cellular level, regarding morphology and expression of lineage markers, should facilitate studies on establishing and maintaining stable culture of cells in the primed pluripotent state, and directing differentiation from that state.

RESULTS

Critical Effect of Inhibiting WNT Secretion on EpiSC Derivation

To test our hypothesis that Wnt inhibition would enhance the efficiency of EpiSC derivation, we separated epiblasts of embryonic day 5.5 (E5.5) mouse embryos obtained from C57BL/6 (B6) × 129S2/Sv (129) strain crosses from the VE and cultured them in EpiSC medium with or without the Wnt inhibitor IWP-2, as described in the Experimental Procedures (Figure 1A). Epiblast explants attached to the substratum on day 2 of culture, and epiblast cells formed flat colonies on day 3 irrespective of the presence or absence of IWP-2 (Figure S1). By day 5, only the epiblast explants cultured with IWP-2 still showed flat colonies of compact cells characteristic of EpiSCs (Figure 1B). In contrast, explants cultured without IWP-2 gave rise to colonies with heterogeneous morphologies, and differentiated cells emerged in most cases (Figure 1C). At 1 or 2 days after passage 3 or 4, we examined the morphologies of ten colonies, and if more than eight of the colonies showed "good" undifferentiated morphologies (see Figure S1), we judged that EpiSC lines had been established. Expression of alkaline phosphatase was also examined (Figure S1). EpiSC lines were derived from E5.5 epiblasts in the presence of IWP-2 with high efficiency (5/5), whereas EpiSC lines were established at a much lower rate in the absence of IWP-2 under our culture conditions (3/16 hybrid embryo explants; 19%) (Table 1). Using E6.5 embryos, we obtained essentially similar results (two lines of 24 E6.5 epiblasts (8%) in the absence of IWP-2, versus 6/6 in the presence of IWP-2; Table S1). These results suggest that inhibition of WNT secretion greatly enhanced the derivation of EpiSC lines.

To simplify the procedure for EpiSC derivation even further, we next tested whether IWP-2 could facilitate EpiSC isolation from embryos when the VE was left intact. For this purpose, we used parts of E5.5 embryos without removing the VE (VE+ condition) and cultured them in EpiSC medium with or without IWP-2 (Figure 1D). On day 3 of culture, epiblast outgrowths were visible, whereas the VE tissues had shrunk in both conditions (Figure S1). Also, 86 EpiSC lines were eventually obtained from 97 VE+ embryo parts, but only when cultured with IWP-2. However, no EpiSC lines were isolated from VE+ conditions in the absence of IWP-2 (0/6 embryos; Figures 1E and 1F; Table 1). This result indicates that IWP-2 allowed EpiSC isolation even when the VE was present. To confirm the genome integrity of our EpiSCs, we selected two EpiSC lines obtained from a B6 × 129 strain cross and two lines from a 129 × B6 cross, and analyzed their karyotypes (Figures 1G–1I). In all cases, the cells possessed normal karyotypes: more than 85% of chromosome spreads had 40 chromosomes. No bias in the sex ratio was observed in these newly derived EpiSCs (Table 1).

We also tested another Wnt inhibitor, XAV939, which blocks the canonical pathway through inhibition of tankyrases (Huang et al., 2009). This inhibitor also promotes EpiSC derivation (Table 1; Sumi et al., 2013) and was found to be effective for stable maintenance of undifferentiated EpiSCs. Since both Wnt inhibitors with different modes of action showed similar promoting effects on EpiSC derivation, we conclude that Wnt inhibition is critical for establishing EpiSCs.
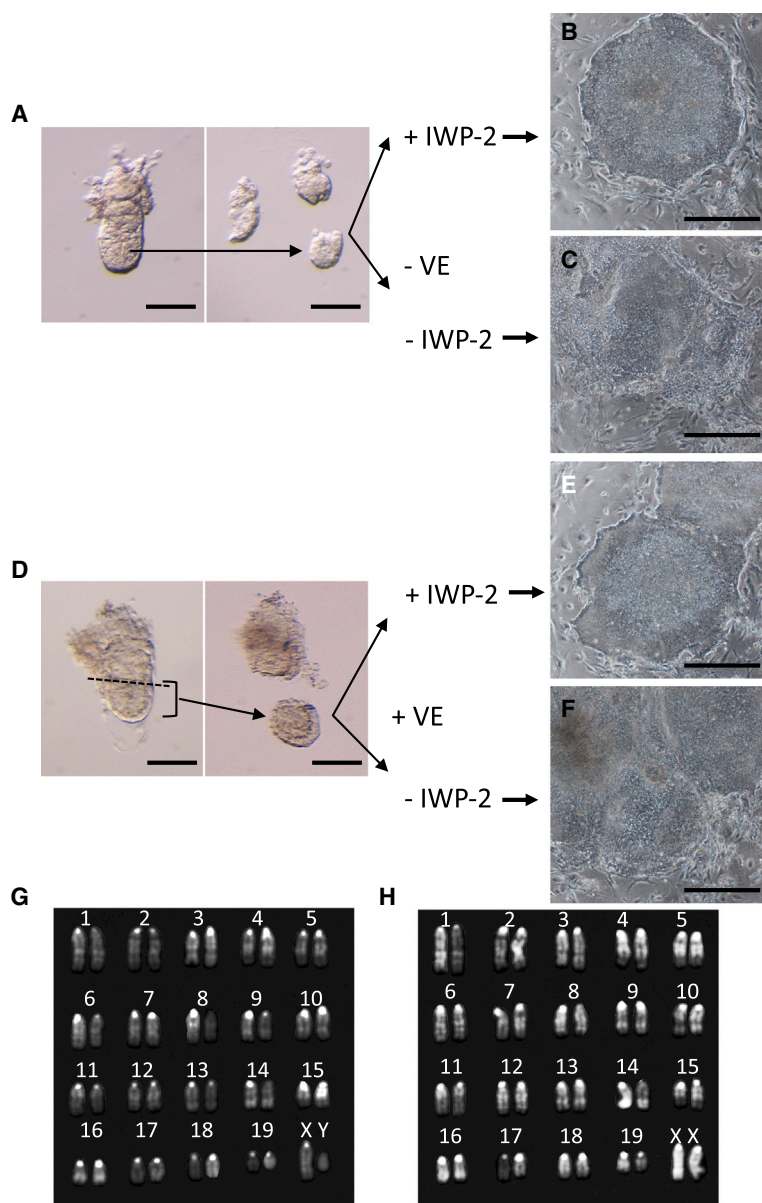
EpiSC lines	Genetic background	Method	Number (%) of metaphase No. Chr. < 40	= 40	40 <	Sex chr.
B129a7	C57BL/6N x 129/Sv	+ VE	8 (13.4)	52 (86.6)	0 (0.0)	XY
B129b1	C57BL/6N x 129/Sv	- VE	3 (5.0)	55 (91.7)	2 (3.3)	XX
129Ba1	129/Sv x C57BL/6N	+ VE	4 (6.7)	56 (93.3)	0 (0.0)	XY
129Ba2	129/Sv x C57BL/6N	+ VE	2 (3.2)	60 (96.8)	0 (0.0)	XX
BNa1	C57BL/6N	+ VE	2 (3.2)	59 (95.2)	1 (1.6)	XX
BNa17	C57BL/6N	+ VE	1 (1.7)	57 (95.0)	2 (3.3)	XY
BNa18	C57BL/6N	+ VE	2 (3.3)	59 (96.7)	0 (0.0)	XX

C57BL6 and its substrains are the most widely used mouse strains. They provide various biological resources and information, such as large numbers of genetically modified ESC lines and detailed available genomic data (e.g., Waterston et al., 2002). It is desirable to have EpiSC lines from a pure B6 strain, although to our knowledge, no EpiSC lines have been established from this strain to date. Therefore, we attempted to derive EpiSCs lines from C57BL/6N embryos. By culturing VE+ epiblasts from E5.5 B6 embryos, we successfully obtained 23 EpiSC lines in 30 trials with IWP-2, as opposed to one EpiSC line out of nine attempts in the absence of IWP-2 (Table 1). We

Table 1. EpiSC Lines Established from E5.5 Epiblasts with or without Wnt Inhibitor

Genetic Background	Visceral Endoderm	IWP2	XAV939	No. of Embryos	No. of Cell Lines (%)	Sex Ratio (Male/Female)	Total No. of Cell Lines/Embryos (%)
C57BL/6N × 129S2/Sv	−	−	−	16	3 (19)	2:1	IWP2(−) 4/31 (13)
C57BL/6N × C57BL/6N	−	−	−	9	1 (11)	1:0	
C57BL/6N × 129S2/Sv	+	−	−	6	0 (0)	ND	
C57BL/6N × 129S2/Sv	−	+	−	5	5 (100)	2:3	IWP2(+) 91/102 (89)
C57BL/6N × 129S2/Sv	+	+	−	36	34 (94)	18:16	
129S2/Sv × C57BL/6N	+	+	−	19	18 (95)	8:10	
129S2/Sv × 129S2/Sv	+	+	−	12	11 (92)	6:5	
C57BL/6N × C57BL/6N	+	+	−	30	23 (77)	10:13	
C57BL/6N × 129S2/Sv	+	−	+	6	6 (100)	2:4	XAV939(+) 12/13 (92)
129S2/Sv × C57BL/6N	+	−	+	7	6 (86)	4:2	
Total				146	107		

ND, not determined. See also Table S1.

obtained both male and female lines with no apparent sex bias, and we confirmed that three randomly selected EpiSC lines had normal karyotypes (Figure 1I).

Characterizations of EpiSCs Generated by Wnt Inhibition

To characterize our newly established EpiSCs, we examined the expression of pluripotency cell markers. Immunofluorescence analysis allowed us to detect the expression of SSEA1 and OCT4 in EpiSCs as well as in mESCs, whereas PECAM1 was detected only in mESCs, as reported previously (Figures 2A–2D; Rugg-Gunn et al., 2012). The NANOG protein was detected in the nuclei of mESCs and EpiSCs, albeit at much lower levels in the EpiSCs (Figures 2E and 2F). It is known that one of two X chromosomes in female EpiSCs is inactivated (Bao et al., 2009). As shown in Figures 2G and 2H, a single, strong immunofluorescence signal of histone H3K27 trimethylation (H3K27me3) was observed in the nuclei of female EpiSCs, whereas no such signals for H3K27me3 were observed in male EpiSCs, indicating that X inactivation occurred in our female EpiSC lines. Flow-cytometry analysis also confirmed that our EpiSCs were SSEA1-positive and PECAM1-negative (Figures 2I and 2J). Furthermore, we carried out qRT-PCR analyses to measure the expression levels of mRNAs for the mESC and EpiSC lines. As shown in Figure 2K, the EpiSC lines expressed *Oct4* and *Sox2* at levels similar to those observed in the mESCs. *Nanog* expression was much lower in our EpiSCs than in the mESCs, as expected from the immunofluorescence data described above. Three genes—*Rex1*, *Pecam1*, and *Dppa3* (which

are known to be highly expressed in naive mESCs)—were not detected in our EpiSC lines, consistent with previous reports (Brons et al., 2007; Tesar et al., 2007). Marker genes for epiblast (*Fgf5*, *Cldn6*, and *Otx2*) were expressed at much higher levels in the EpiSCs than in mESCs. We also examined marker gene expression in one of the EpiSC lines established by the original protocol, using the 129C1 line (Brons et al., 2007) (a gift from Dr. S. Pauklin) as a control. The expression profile of the marker genes in this cell line was essentially the same as those of our EpiSCs, except for *Dppa3*. These results indicate that the EpiSCs produced by our method using the Wnt inhibitor IWP-2 possess a transcription profile characteristic of "bona fide" EpiSCs.

The population doubling time of hESCs is ~36 hr, whereas mESCs have much shorter doubling times of 12–16 hr (Ware et al., 2006; Tamm et al., 2013). Although the growth rate of mouse EpiSCs was not defined in previous studies, EpiSCs are routinely passaged every 2–3 days (Tesar et al., 2007) or every 5 days (Brons et al., 2007), whereas mESCs are usually passaged every 2 days. Chang and Li (2013) reported that mESC-derived EpiSCs showed a population doubling time of ~36 hr. Thus, one would expect murine EpiSCs to grow more slowly than mESCs. However, we noted that our EpiSCs derived in the presence of IWP-2 proliferated rapidly, and to maintain these cell lines we had to passage them routinely every 2 days. We determined the growth rates of the EpiSC lines 129Ba1, 129Ba2, and BNa17 (listed in Figure 1I). The EpiSCs showed logarithmic growth for the first 3 days with doubling times of 11.7 hr for 129Ba1, 11.2 hr for
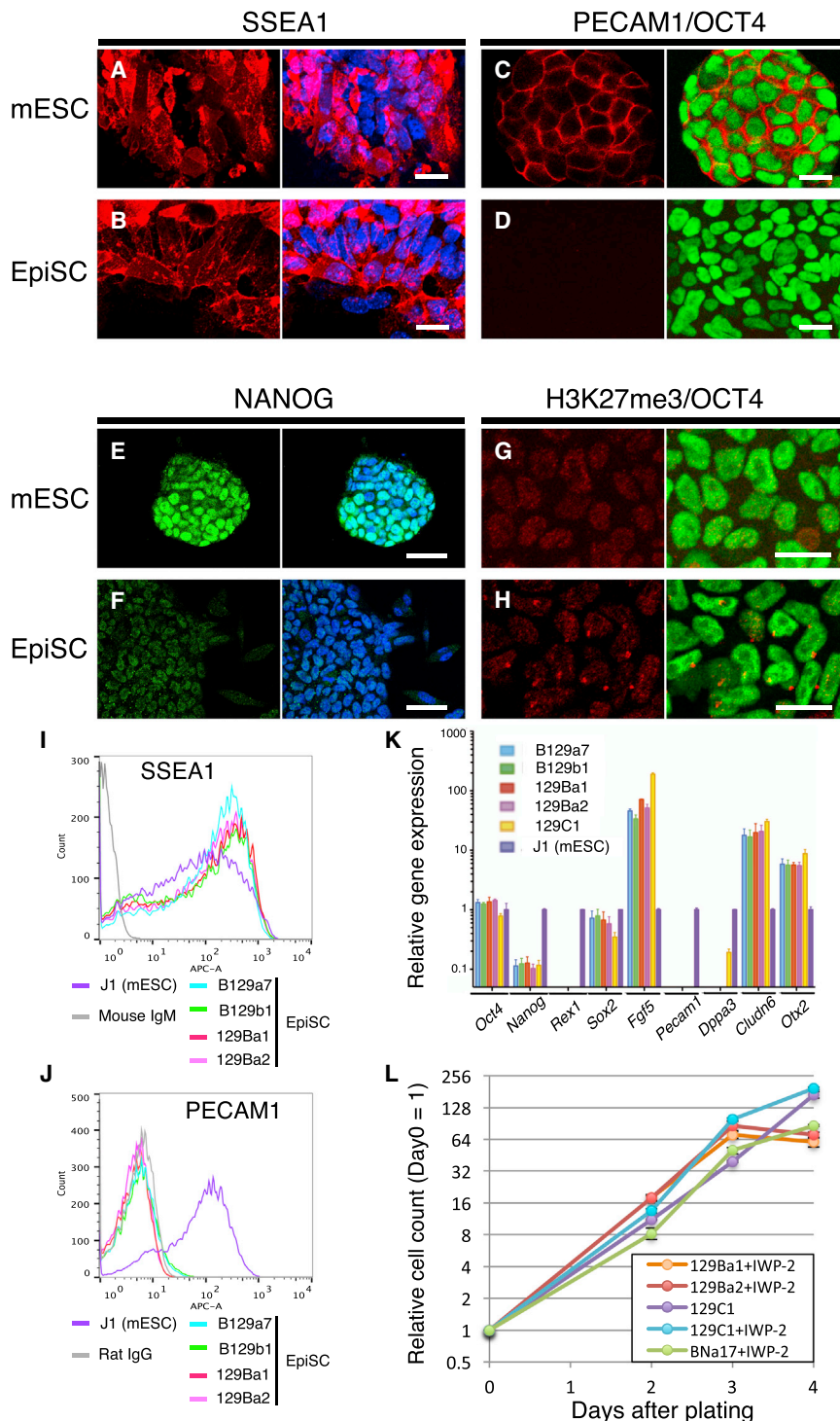
Figure 2. Cellular Pluripotency Marker Expression Levels in EpiSCs Derived by the IWP-2 Method

(A–J) Immunofluorescence images for SSEA1 (A and B), PECAM1 (red) and OCT4 (green, C and D), NANOG (E and F), and histone H3K27 trimethylation (G and H) in mESCs (A, C, E, and G) and EpiSCs (B, D, F, and H). Nuclear staining is shown using TO-PRO3 (blue). Cytograms of EpiSCs and mESCs are shown using anti-SSEA1 (I) and anti-PECAM1 (J) antibodies.

(K) Relative expression levels of marker genes in EpiSCs detected by qRT-PCR compared with J1 mESCs. For each gene, technical triplicate assays and two independent experiments were performed. Error bars represent the standard SEM.

(L) Growth curves of EpiSCs. At the indicated time points, 2.0×10^4 cells were plated and counted. Averaged data from three independent experiments were plotted.

Scale bars, 20 μm (A, B, C, D, G, and H) and 50 μm (E and F).

129Ba2, and 12.7 hr for BNa17 (Figure 2L). We also determined the growth rate of the 129C1 line cultured in the presence or absence of IWP-2. In regular culture conditions, 129C1 cells proliferated with a doubling time of 13.5 hr, whereas 129C1 cells in the IWP-2 medium proliferated with a 10.8 hr doubling time. We also determined the doubling time of the J1 mESC line for comparison and found it to be 16.4 hr.

We noted that the 129C1 EpiSCs cultured in the IWP-2 medium showed a more homogeneous morphology than the same line cultured without IWP-2. Thus, some cells within the colonies changed from exhibiting the typical

304

morphology of EpiSCs to displaying differentiated cells in the absence of IWP-2 (data not shown). Such spontaneous differentiation was rarely observed when the EpiSCs were cultured in the IWP-2 medium and passaged using a CTK cell dissociation solution (see Experimental Procedures).

EpiSCs Generated by the Wnt Inhibition Method Maintain Pluripotency

When IWP-2 was withdrawn from the EpiSC culture medium, our EpiSCs changed their morphologies and started to differentiate into cells expressing the mesoderm marker T or the endoderm marker GATA4 (Figures 3A, 3B, and S2). By contrast, 129C1, the EpiSC line established by the original protocol, could be maintained as an undifferentiated form in the absence of IWP-2. Flow-cytometry analysis of SSEA1-positive cells indicated that our EpiSC line downregulated SSEA1 expression, whereas a higher percentage of 129C1 cells continued to express SSEA1 4 days after IWP-2 removal (Figure S2).

We found that differentiating EpiSCs developed efficiently into cystic embryoid bodies (EBs) that often contained pulsating areas, most probably containing cardiomyocytes (Figure 3C). After 7 days of EB formation in medium containing 10% fetal bovine serum (FBS), EBs were transferred to adhesive culture plates. After 14 days of adhesive culture, neuroectodermal cells expressing NESTIN, and more mature neural cells expressing β-III tubulin (TUBB3) were detected by immunofluorescence analysis (Figure 3D). In addition, we readily observed cells expressing the neural cell markers in EpiSC-derived EBs cultured in serum-free conditions (Figure S2) that are known to promote neural differentiation efficiently in mESC-derived EBs.

To assess the EpiSCs' potency for developing into various tissues in vivo, we carried out teratoma-formation assays using two hybrid EpiSC lines and one B6 line. Clumps of EpiSCs were injected into the kidney capsule of immunodeficient SCID mice (Bosma et al., 1983). At 29 days and 72 days after transplantation of the hybrid EpiSC lines and the B6 line, respectively, teratomas were dissected out and subjected to histological analysis. The teratomas were found to contain extensively differentiated cell types from all three germ layers, including chondrocytes, skeletal myocytes, adipocytes, gastrointestinal epithelial cells, melanocytes, and neural cells (Figures 3E–3J). These results show unambiguously that the EpiSCs generated and maintained in the IWP-2 medium retained pluripotency and were able to differentiate efficiently into all three primary germ layers.

Differences in WNT Sensitivity between the EpiSCs Derived by the IWP-2 Method and Those Derived by the Original Protocol

As described above, EpiSC lines established in the presence of IWP-2 readily underwent differentiation after the withdrawal of IWP-2 (Figures 3A, 3B, S2A–S2D, and S2I–S2L), whereas the 129C1 line derived by the original method could be maintained even in the absence of IWP-2. Therefore, we investigated whether Wnt signals secreted from either feeder cells or the EpiSCs themselves caused EpiSC differentiation. We examined changes in the expression of OCT4 or SSEA1 in response to WNT stimulus by immunostaining and flow cytometry. As shown in Figures S3A and S3B, WNT3A administration induced loss of OCT4 expression in 129Ba1 cells, the EpiSC line established by the IWP-2 method. In the presence of IWP-2, 129Ba1 cells showed uniform OCT4 expression in their nuclei, whereas most of the cells lost OCT4 protein by WNT3A addition and only a small subset of cells retained OCT4 expression. Flow-cytometry analysis confirmed the immunostaining data (Figures S3E and S3F). Because IWP-2 is an inhibitor of WNT secretion, the direct supplementation of WNT protein to the culture medium overcomes the suppressive effect of IWP-2 on the Wnt pathway. We obtained essentially the same results from an SSEA1 expression analysis: WNT3A addition caused a reduction of SSEA1 expression in 129Ba1 culture (Figures S3I and S3J).

We performed similar experiments using 129C1 cells, the EpiSC line established by the original protocol (without using IWP-2). Unlike our 129Ba1 EpiSCs, the 129C1 cells could be maintained in an OCT4-positive pluripotent state without IWP-2, although we observed some spontaneous differentiation (Figure S3C). IWP-2 treatment reduced such spontaneous differentiation of 129C1, leading to a more homogeneous culture (not shown). In sharp contrast to 129Ba1, however, WNT3A addition to the 129C1 culture did not cause a reduction of OCT4-positive cells, as determined by both immunostaining and flow cytometry (Figures S3D, S3G, S3H, and S3M). Analysis of SSEA1 expression again confirmed that WNT3A addition caused only a small reduction in SSEA1 expression in the 129C1 line (Figures S3K, S3L, and S3N). These results suggest that the 129C1 cells cultured in the absence of IWP-2 may be less responsive to WNT ligands than EpiSC lines such as 129Ba1 (derived using IWP-2). This result might help explain the difference between 129Ba1 and 129C1 cells: Wnt pathway-dependent differentiation is promoted by WNT3A in the former cell line, but not efficiently in the latter one.

Molecular Characterization of EpiSC Lines Established in the Presence of IWP-2

To characterize the molecular features of our EpiSC lines, we determined global gene-expression profiles using microarrays and compared them with those of EpiSC lines established by other groups using conventional methods. The EpiSC lines 129Ba1 (XY) and 129Ba2 (XX) from E5.5 129 × B6 hybrid embryos, as well as BNa17 (XY) from E5.5 B6 embryos, were cultured in the IWP-2-containing medium and analyzed. The 129C1 EpiSC line (Brons et al., 2007) and Wt1 EpiSCs (derived from B6 × ICR embryos, a gift from Dr. M. Ema) were cultured in the absence of IWP-2 and analyzed. A 129C1 line cultured in IWP-2-containing medium was also analyzed. In addition to the EpiSC lines, two mESC lines and an mESC line cultured in 2i medium (Ying et al., 2008), and epiblast/embryonic ectoderm from E5.5, E6.5, and E7.5 mouse embryos were included in the analysis.

Principal-component analysis (PCA) of the expression profile data revealed that mESC lines, EpiSC lines, and epiblast/embryonic ectoderm were clustered at distinct positions on the PC1-PC2 plane (Figure 4A). Moreover, differences in the expression profiles of each group were revealed along the PC3 axis. For example, mESCs cultured in 2i medium were distantly located from mESCs cultured in KSR/FBS-containing medium, and EpiSC lines made by the IWP-2 method were located separately from the EpiSCs established by the original method. Hierarchical cluster analysis also revealed that three groups—mESCs, epiblast/ectoderm, and EpiSCs—displayed globally different expression profiles (Figure 4B; Table S2). Although the EpiSC lines generated by the IWP-2 method exhibited profiles similar to those of EpiSCs made by the original method, they were classified into different clusters. To examine differences among the EpiSC lines, we subjected 17,819 probes that showed differential expression among EpiSCs and epiblast/ectoderm to a k-means cluster analysis, which revealed nine clusters (Figure S4A). Clusters 2, 3, 6, and 8 represent probes that exhibited differences between EpiSCs and epiblast/ectoderm. Clusters 1 and 5 represent genes that were upregulated in 129C1 and Wt1 cells (the EpiSC lines established without IWP-2), and cluster 9 includes genes that were upregulated in the EpiSCs made by the IWP-2 method. Cluster 1 genes are particularly interesting because they were highly expressed in 129C1 cells but were repressed when 129C1 cells were cultured in the IWP-2 medium. These genes were also suppressed in 129Ba1, 129Ba2, and BNa17 cells cultured in the IWP-2 medium, suggesting that expression of the cluster 1 genes depends on WNT secretion, and therefore these genes function downstream of Wnt signaling.

We then studied genes that were differentially expressed between 129C1 cells and those cultured in the IWP-2 medium (p < 0.05, fold change ≥ 2.0), and performed k-means clustering again (Figure S4B). We found that 229 gene probes were clearly upregulated in 129C1 and Wt1 cells but were repressed in the 129C1+IWP-2, 129Ba1, 129Ba2,
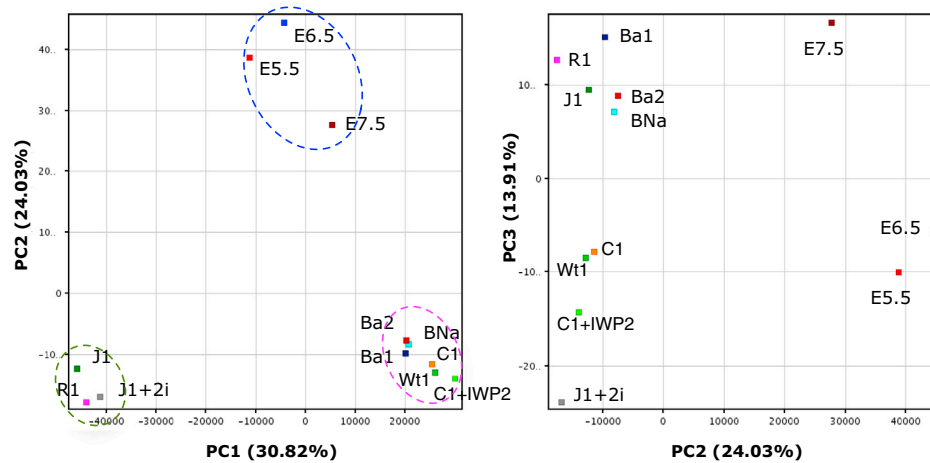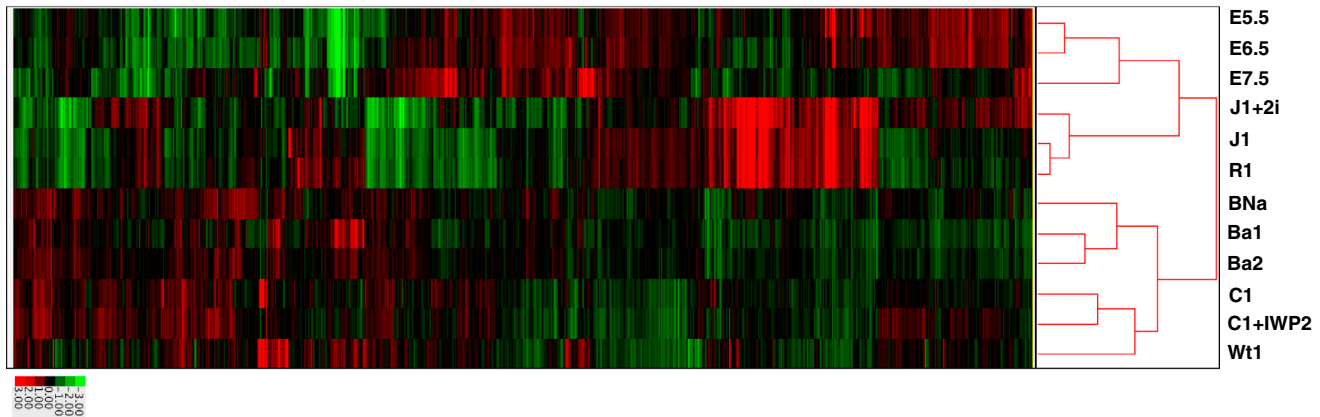
Figure 4. Global Gene-Expression Profiling of EpiSCs, mESCs, and Epiblasts

(A) PCA of global gene-expression profiles obtained from the indicated cell types. J1 and R1 are mESCs. J1+2i represents J1 cells cultured in 2i-containing medium. E5.5, E6.5, and E7.5 are epiblast cells isolated from embryos at the corresponding stages. Ba1, Ba2, BNa, Wt1, C1, and C1+IWP2 represent EpiSC lines 129Ba1, 129Ba2, 129BNa, Wt1, 129C1, and 129C1 cultured in the IWP-2-containing medium, respectively. Dotted circles indicate the mESC group (green), EpiSC group (pink), and epiblast group (blue).

(B) Hierarchical cluster analysis of expression profiles from EpiSCs, mESCs, and epiblast cells.

See also Figure S4 and Table S2.

and BNa17 EpiSCs (Figure S4B). Gene Ontology (GO) analysis suggested that GO terms such as "developmental process," "anatomical structure development," and "multicellular organismal development (biological process)" were enriched in these genes. Sixty-two of the 229 129C1-upregulated genes (34.4%) were associated with the GO term "developmental process" and included developmental regulatory genes such as *Cer1*, *Cfc1*, *Foxa2*, and *Sox17* (data not shown). In the GO category of molecular function, "sequence-specific DNA binding" was enriched, and transcription factors such as *Foxa2*, *Gata4*, *Gata6*, *Eomes*, *T*, and *Gsc* were included. In the cellular-component GO category, "extracellular region" was overrepresented in the 129C1-upregulated genes. Genes such as *Cer1*, *Dkk1*, and

Bmp2 are associated with this GO term. Collectively, many of the 129C1-upregulated genes that were suppressed by Wnt inhibition were developmental regulator genes acting in both extracellular and nuclear compartments.

Heterogeneous Expression of Developmental Regulators Was Suppressed in EpiSCs Cultured in the IWP-2 Medium

Next, we validated the suppression of several developmental regulators (GATA4, CER1, T, and SOX17) in 129C1 cells treated with IWP-2 by immunostaining (Figures 5 and S5). In 129C1 cells, GATA4- or SOX17-positive cells were clustered in OCT4-negative patches (Figures
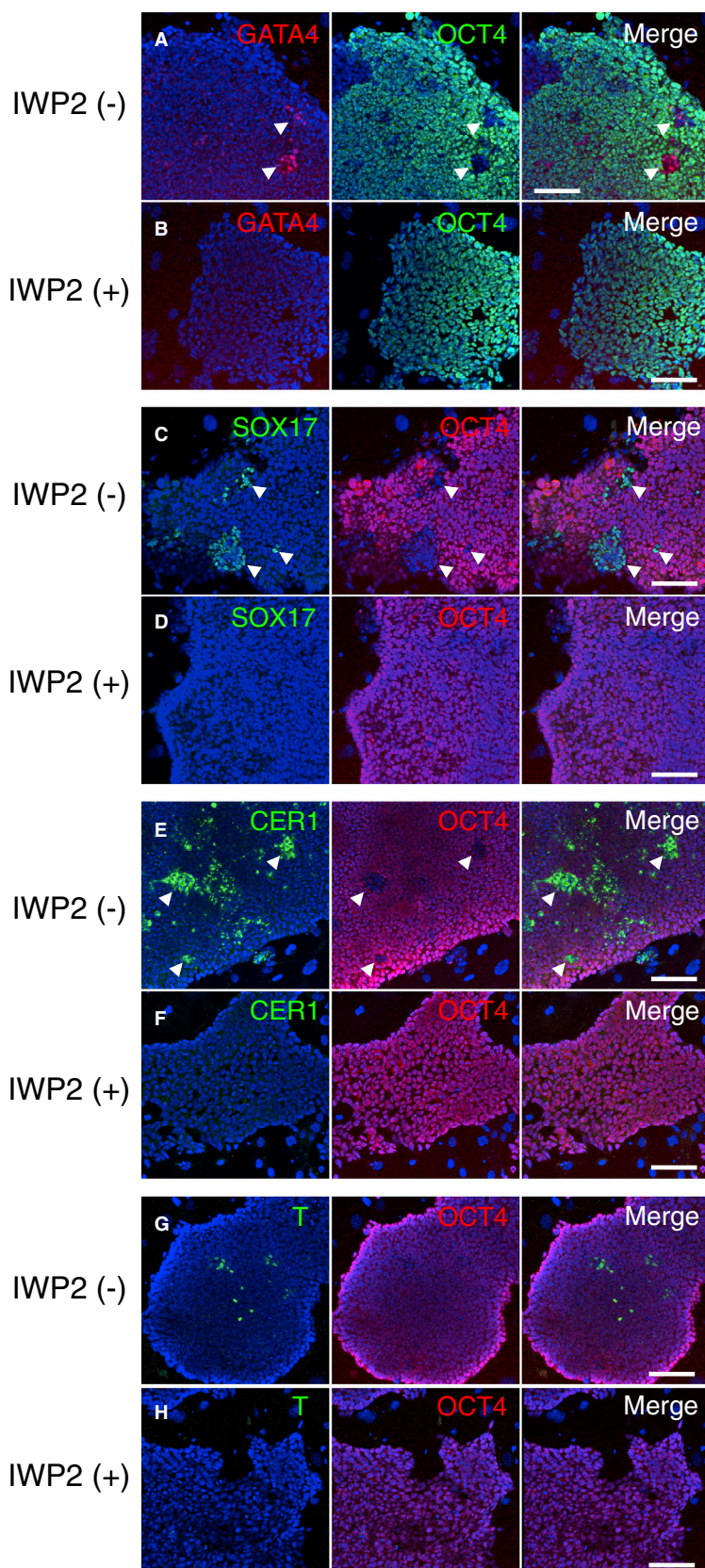
Figure 5. Effects of IWP-2 on Gene Expression in the 129C1 EpiSC Line

Immunofluorescence images for GATA4 (red) and OCT4 (green) (A and B), SOX17 (C and D), T (E and F), and CER1 (G and H) in EpiSCs cultured without IWP-2 (A, C, E, and G) or with IWP-2 (B, D, F, and H). Nuclei were stained with TO-PRO3 (blue). Scale bar, 100 μm. See also Figures S5 and S6.

5A–5D). However, such GATA4-positive cells or OCT4-negative regions were never observed in the EpiSCs cultured in the IWP-2 medium. Relatively large numbers of CER1-positive cells were found in the absence of IWP-2, whereas the IWP-2 treatment almost completely suppressed the expression of CER1. CER1-positive cells showed weaker OCT4 expression than the surrounding CER1-negative EpiSCs (Figure S5C). Small numbers of T-positive cells were found among the colonies in the absence of IWP-2 treatment, whereas T-positive cells were hardly seen in the IWP-2 cultures. T was expressed weakly in OCT4-positive cells, whereas cells weakly positive for OCT4 showed higher expression of this marker (Figure S5D). These results suggest that the EpiSC cultures were composed of subpopulations exhibiting different degrees of spontaneous differentiation: *Cer1* was expressed in cells weakly positive for OCT4, while *Gata4* and *Sox17* were expressed in OCT4-negative cells. The IWP-2 treatment suppressed such developmental regulators by inhibiting WNT secretion, reducing the degree of spontaneous differentiation and thus producing a more homogeneous population of pluripotent EpiSCs. Whether or not "undifferentiated" EpiSCs cultured with IWP-2 differ significantly from EpiSCs cultured without IWP-2 remains to be clarified.

To address this point, we sorted SSEA1-positive cells by fluorescence-activated cell sorting (FACS) from 129C1 cells cultured with or without IWP-2, and analyzed their global gene-expression profiles. The presence of SSEA1 likely represented "undifferentiated" EpiSCs, as SSEA1 was uniformly expressed in the IWP-2-treated (+) EpiSCs, but a small number of SSEA1-negative cells could be found in 129C1 cells cultured without IWP-2 (–). We collected both SSEA1 "high" and "low" fractions from cultures with or without IWP-2 (Figure S6) and performed microarray analysis. Although the overall profiles of the four kinds of samples were similar, significant differences could be detected. Out of 55,679 gene probes, 5,535 showed >2-fold differences between the SSEA1^{high};IWP-2(+) and SSEA1^{high};IWP-2(–) fractions. We found that 136 gene probes exhibited ≥10.0-fold differences between the two samples, and 101 of these were downregulated in the IWP-2(+) fraction. GO analysis of the up- or downregulated genes revealed that terms such as "pattern specification process," "regionalization," and "embryo development" were significantly enriched in the downregulated genes, whereas no GO terms were enriched in 35 upregulated genes. We noted that *Gata4* or *Sox17*, which showed differential expression between bulk 129C1 and 129C1(+)IWP-2 cells, were not included in the data set. We next selected representative genes that exhibited significant differences between bulk 129C1 and 129C1 IWP-2(+) cells, and examined their expression in the SSEA1^{high} cells treated with or without

IWP-2, and SSEA1^{low} cells treated with or without IWP-2 (Figure S6). We found that these genes could be classified into at least two classes. *Gata4*, *Sox17*, *Cfc1*, and *Cer1* were barely detectable in both SSEA1^{high};IWP-2(+) and SSEA1^{high};IWP-2(–) fractions, but were highly expressed in the SSEA1^{low}:IWP-2(–) cells, suggesting that these genes were more likely to be expressed in more differentiated cells than in the SSEA1^{high} cells, and that they could be suppressed by the Wnt inhibitor. This result is consistent with the immunostaining data showing that GATA4 and SOX17 were expressed in the OCT4-negative population of the EpiSC culture (Figures 5A–5D). By contrast, *Foxa2*, *Gsc*, *Evx1*, and *T* were highly expressed in the SSEA1^{high};IWP-2(–) samples, suggesting that these genes were expressed in the SSEA1^{high} cells in a Wnt signal-dependent manner.

DISCUSSION

We have shown here that inhibiting WNT secretion by IWP-2 treatment was highly effective for the derivation and maintenance of EpiSCs. Expression analyses of the EpiSCs obtained by the IWP-2 method revealed that this Wnt inhibitor suppressed the heterogeneous expression of marker genes specific to the mesoderm, endoderm, or primitive streak. Thus, this inhibitor appears to play at least two roles: it favors the rapid propagation of epiblast cells and it inhibits Wnt-dependent spontaneous differentiation into particular germ-layer derivatives. As a result, we were able to obtain a homogeneous population of high-quality pluripotent EpiSCs under the culture conditions we used. Cell detachment using the CTK solution was also effective for maintaining a homogeneous population. Reductions in heterogeneous gene expression have been observed in EpiSCs treated with a different Wnt inhibitor (Sumi et al., 2013), hESCs treated with IWP-2 (Blauwkamp et al., 2012), and hiPSCs cultured in medium containing IWP-2 (M.K., M.S., and K.A., unpublished observation). The effect of IWP-2 must be specific to the Wnt signaling pathway, as administration of the WNT ligand WNT3A could reverse the effect of IWP-2. We also demonstrated that inhibition of the Wnt canonical pathway by the tankyrase inhibitor XAV939 (Huang et al., 2009) resulted in the derivation of homogeneous EpiSC lines. The EpiSC lines established by our method exhibited the typical morphologies of primed PSCs, with less spontaneous differentiation compared with EpiSCs made by the original protocol, but still showed robust differentiation into various cell lineages in vitro and in teratomas.

Note that our EpiSC lines required continuous treatment with IWP-2 because removal of this Wnt inhibitor caused spontaneous differentiation. Since the original EpiSCs

can be propagated without IWP-2, our EpiSCs must be distinguished from them by some intrinsic difference. There may be heterogeneities in Wnt signaling activity among epiblast cell populations, as previously observed for hESCs (Blauwkamp et al., 2012). Given that the inhibition of WNT secretion (or inhibition of Wnt signaling) promotes rapid EpiSC expansion, cells with lower Wnt activity or responsiveness can be selected and established preferentially as EpiSCs under the original derivation conditions. On the other hand, IWP-2 blocks WNT secretion, leading to a reduced level of Wnt signaling. Since the WNT ligands available in culture would be greatly decreased, almost all of the epiblast cells, including cells with high Wnt responsiveness, would expand as EpiSCs. Therefore, EpiSCs derived by the IWP-2 method retain Wnt responsiveness and can differentiate in response to the Wnt stimulus. The fact that the 129C1 EpiSC line established by the original protocol (Brons et al., 2007) showed reduced responsiveness to WNT3A supports the notion described above.

Whether or not other existing EpiSC lines or primed PSC lines in general possess reduced Wnt responsiveness remains to be clarified. This is not a trivial question; because Wnt signaling is important for differentiation from pluripotent cells toward various cell lineages, reduced Wnt activity might hamper the subsequent differentiation processes. On the other hand, since stem cells established by the IWP-2 method retain robust Wnt responsiveness, they can be readily differentiated in various directions once IWP-2 is removed from the culture.

Global gene-expression analysis revealed that addition of IWP-2 to 129C1 EpiSC cultures suppressed the expression of a specific cluster of genes. This tight cluster of genes was highly expressed in EpiSC lines obtained by the original protocol (i.e., 129C1 and Wt1 cells), whereas it was barely detectable in the EpiSCs derived by the IWP-2 method, in 129C1 cells cultured with IWP-2, or in epiblast tissues from E5.5–E7.5 embryos. This cluster of genes is involved in the regulation of development into the mesoderm, endoderm, or primitive streak. Interestingly, some of these genes (e.g., *Cer1*, *Dkk1*, and *Sox17*) have been considered to be characteristic markers of EpiSCs (Brons et al., 2007; Tesar et al., 2007; Kojima et al., 2014). However, we show here that the expression of these marker genes is not essential for the derivation and self-renewal of EpiSC lines. Our EpiSCs made by the IWP-2 method appear to represent authentic pluripotent EpiSCs, but with low levels of Wnt-induced spontaneous differentiation. In a study using XAV939 together with the Rho kinase inhibitor Y27632, Sumi et al. (2013) suggested that Wnt signaling inhibition plays a role in promoting less spontaneous differentiation. In the present study, we further demonstrated that genes suppressed by Wnt inhibition could be classified into at least two groups: one expressed in a partially differ-

entiated subpopulation in EpiSC cultures (e.g., *Gata4* or *Sox17*), and one expressed in SSEA1^{high} undifferentiated EpiSCs, including *Foxa2*, *Gsc*, and *Evx1*. Expression of genes in both classes was dependent on Wnt signaling. Therefore, the Wnt inhibitor suppressed spontaneous, Wnt-induced differentiation to endoderm or mesoderm lineages, and also suppressed the expression of Wnt-dependent genes in SSEA1^{high} pluripotent cells.

As variations caused by Wnt signaling could be extinguished by the IWP-2 treatment of EpiSCs made by the original protocol, comparisons of IWP-2-treated EpiSCs should now reveal molecular differences caused by genetic differences or epigenetic features that arise during the establishment of these cell lines. Through further analyses of our new version of EpiSCs, the origins of inter- and intra-strain heterogeneities and their functional consequences, as well as common and distinct features of mouse EpiSCs and human PSCs, can now be addressed.

EXPERIMENTAL PROCEDURES

Mice and Embryo Dissection

The mouse strains C57BL/6NJcl (B6) (CLEA Japan) and 129S2/Sv (129) (RBRC00123, provided by RIKEN BRC through the National Bio-Resource Project of MEXT, Japan) were used to establish EpiSC lines. SCID mice (CLEA Japan) were used for teratoma-formation assays.

E5.5 embryos were obtained from crosses of the mouse strains B6 × 129, 129 × B6, 129 inter se, and B6 inter se. Embryos were dissected out from decidua in DMEM/F-12 containing 10% FBS, and Reichert's membrane was removed with finely sharpened tungsten needles. Epiblasts were separated from the other embryonic tissues as previously described (Sugimoto et al., 2012). In brief, embryos were incubated in pancreatin/trypsin enzyme solution (2.5% pancreatin, 0.5% trypsin, 0.5% polyvinylpyrrolidone in Ca^{2+}/Mg^{2+}-free Tyrode Ringer's saline) for 15 min on ice, and the enzyme reaction was stopped in culture medium with 10% FBS. The embryonic region containing both epiblast and VE was isolated by cutting embryos at the border of the embryonic-extraembryonic portions using a pair of fine tungsten needles. The epiblast was separated from the VE by pipetting through a fine glass capillary tube.

All animal experiments were approved by the Institutional Animal Experiment Committee of RIKEN Tsukuba Institute.

Derivation and Maintenance of EpiSCs

The EpiSC culture medium was composed of DMEM/F-12 GlutaMAX medium (Life Technologies) supplemented with 15% KSR (Life Technologies), 1× nonessential amino acids (Life Technologies), 0.1 mM 2-mercaptoethanol (Life Technologies), 0.5× penicillin/streptomycin mix (Life Technologies), 12 ng/ml of human basic fibroblast growth factor (FGF; Peprotech), and 20 ng/ml of activin A (Peprotech). The Wnt inhibitor IWP-2 (Stemgent) was added to the EpiSC medium at 2 μM when necessary. The tankyrase inhibitor XAV939 (X3004; Sigma-Aldrich) was added to the

medium at 10 μM when necessary. Single epiblast explants or embryonic parts of E5.5 embryos were placed in each well of four-well dishes (Thermo Scientific) and cultured in the EpiSC medium with or without IWP-2. The four-well dishes were precoated with FBS for 1 hr at 37°C, and mitomycin C (Sigma-Aldrich)-treated mouse embryonic fibroblast feeder cells were seeded at $1.25–2.50 \times 10^4$ cells/cm^2. After 4–7 days of explant culture in the EpiSC medium, emerging colonies were cut into several pieces using a sterile 25 G (0.5 mm) needle, and detached from the dishes by gentle pipetting or scraping. The cell clumps were then plated on new dishes. EpiSCs cultured in the EpiSC medium with IWP-2 were passaged every other day and ~1/8 of the cells were transferred regularly to new dishes in the same culture environment. EpiSCs were cryopreserved in FBS containing 10% DMSO (Sigma-Aldrich). Alternatively, EpiSCs were detached from the dishes by treating them with CTK solution containing 0.25% trypsin (215240; BD Diagnostic Systems), 1 mg/ml collagenase (17104-019; Life Technologies), 20% KSR, and 1 mM $CaCl_2$ in PBS (Suemori et al., 2006) for 1–3 min at room temperature. After excess CTK solution was removed, EpiSC colonies were resuspended in culture medium and dissociated into small cell clumps by gentle pipetting using a 1 ml micropipette. The cell clumps were plated onto new dishes for passaging.

To calculate doubling times, EpiSCs were precultured under feeder-cell-free conditions overnight. Cells were treated with 10 μM of the Rho-associated protein kinase inhibitor Y-27632 (Wako Pure Chemical Industries) for 1 hr before they were dissociated with 0.25% trypsin-EDTA (Life Technologies). EpiSCs that dissociated into single cells were suspended in EpiSC medium supplemented with 2 μM of IWP-2 and 10 μM of Y-27632, and plated into 24-well dishes precoated with FBS at concentrations of 2.0×10^4 cells/well. The medium was changed every 12 hr. Cell numbers were counted using an automated TC10 cell counter (Bio-Rad) every day or every other day after dissociation into single cells. The EpiSC lines described in this work will be made available to the research community through the Cell Bank of the RIKEN BioResource Center (http://cell.brc.riken.jp).

Culture of mESCs

The J1 mESC line (Sado et al., 2001) was a gift from Dr. Takashi Sado (Kinki University). The mESCs were maintained on a feeder layer in Glasgow-minimal essential medium (G-MEM; Sigma-Aldrich) supplemented with 14% KSR, 1% ESC culture-grade FBS (Life Technologies), 1 mM sodium pyruvate (Nacalai Tesque), 1× nonessential amino acids, 0.1 mM 2-mercaptoethanol, 0.25× penicillin/streptomycin mix, and 1,000 U/ml of LIF (ESGRO; Millipore).

Karyotyping

EpiSCs were cultured in EpiSC medium containing 20 ng/ml of colcemid (KaryoMAX; Life Technologies) for 30 min and dissociated into single cells using 0.25% trypsin-EDTA (Life Technologies). After hypotonic treatment with 0.075 M KCl, EpiSCs were fixed in Carnoy's solution (methanol/glacial acetic acid 3:1). Chromosome spreads were prepared by an air-drying method (Takagi et al., 1983) on clean glass slides and stained with Hoechst 33258 (Sigma-Aldrich).

EB Formation

EpiSCs were precultured in the EpiSC medium containing IWP-2 on FBS-coated dishes without feeder cells for 2 days. EpiSC colonies were cut into small fragments using a 25 G needle, and cell clumps were cultured on a 10 cm low-cell-binding dish (Lipidure Coat; NOF) in DMEM/F-12 GlutaMAX medium supplemented with 10% FBS, 1× nonessential amino acids, 0.1 mM 2-mercaptoethanol, and 0.5× penicillin/streptomycin mix.

For neural differentiation, EBs of day 7 cultures were plated on a gelatinized glass-bottomed dish and cultured for another 14 days in the FBS medium described above. Alternatively, 10% FBS was replaced with 15% KSR, and EBs were cultured to induce neural differentiation in this medium (Eiraku et al., 2008).

Immunofluorescence Analysis

EpiSCs and EBs were fixed with 4% paraformaldehyde in PBS at 4°C overnight. Samples were washed three times with a wash buffer (PBS containing 0.1% Tween-20), permeabilized with 0.5% Triton X-100, and incubated in 1% BSA (Sigma-Aldrich) or 5% goat serum (Jackson ImmunoResearch) to block any nonspecific binding of antibodies. Samples were incubated overnight at 4°C with a primary antibody diluted in blocking buffer (0.1% Triton X-100, 1% BSA in PBS). Primary antibodies were diluted as follows: anti-stage-specific mouse embryonic antigen (SSEA1; 1:100; Developmental Studies Hybridoma Bank); anti-OCT4 (1:300, sc-8628 [Santa Cruz Biotechnology] or ab19857 [Abcam]); anti-platelet/endothelial cell adhesion molecule 1 (PECAM1; 1:25, 550274; BD Biosciences); anti-NANOG (1:500, RCAB0001P; ReproCELL); anti-Brachyury (T, 1:300, sc-17743; Santa Cruz Biotechnology); anti-GATA4 (1:300, sc-9053; Santa Cruz Biotechnology); anti-neuron-specificβ-III tubulin (TUBB3; 1:100, MAB1195; R&D Systems); anti-NESTIN (1:1,000, ab81755; Abcam); anti-CER1 (1:200, AF1986; R&D Systems); and anti-histone H3K27 trimethylation (1:1,000, 07-449; Merck Millipore). The secondary antibodies were anti-mouse immunoglobulin M (IgM) tagged with Alexa Fluor 594 (1:500, A21044; Life Technologies); anti-rat IgG-Alexa Fluor 633 (1:500, A21094; Life Technologies); anti-goat IgG-Alexa Fluor 488 (1:500, A11055; Life Technologies); anti-rabbit IgG-Alexa Fluor 488 (1:500, A11008; Life Technologies); anti-rabbit IgG-Alexa Fluor 594 (1:500, A21207; Life Technologies); and anti-chicken IgY-DyLight 488 (1:500, 703-485-155; Jackson ImmunoResearch). Nuclei were stained with TO-PRO3 (Life Technologies). Immunofluorescence images were taken with an LSM510 meta confocal laser scanning microscope (Zeiss).

Flow Cytometry

EpiSCs or mESCs were dissociated with 0.25% trypsin-EDTA and plated for 30 min on a gelatinized dish to remove feeder cells. The cells were washed with ice-cold PBS containing 1% FBS (FBS/PBS) and then incubated at 4°C for 30 min with primary antibodies. Primary antibodies were diluted with FBS/PBS as follows: anti-SSEA1 (0.5 μg/ml, 560079; BD Biosciences) and anti-PECAM1 (1:25, 550274; BD Biosciences). As isotype controls, mouse IgMκ (0.5 μg/ml, 555581-81; BD Biosciences) and rat IgG2a (0.5 μg/ml, 14-4321-81; eBioscience) were used. The cells were then washed twice in ice-cold FBS/PBS and incubated at 4°C for 30 min with APC rat anti-mouse IgM (562032; BD Biosciences) or APC donkey

311

anti-rat IgG F(ab′)2 (17-4822-82; eBioscience). The cells were washed twice in ice-cold FBS/PBS and then stained with 7-amino-actinomycin D (7-AAD, 559925; BD Biosciences) for 10 min on ice to discriminate between dead and live cells. Usually, 2×10^4 live cells were analyzed using an LSRFortessa cell analyzer (BD Biosciences). For sorting of SSEA1-positive EpiSCs, Alexa Fluor 488 anti-mouse/human CD15 (SSEA1, 125609; BioLegend) was used.

RNA Extraction and qRT-PCR

Total RNAs were extracted from mESCs and EpiSCs using TRizol Reagent (Life Technologies) according to the manufacturer's procedure. Each sample was treated with RNase-free TURBO DNase (Life Technologies) to remove genomic DNA contamination. Then, 2 μg of total RNA was reverse-transcribed with SuperScript III Reverse Transcriptase (Life Technologies) and oligo dT_{18} primers. qRT-PCR was performed using a LightCycler 480 system (Roche Applied Science) with LightCycler 480 Probes Master mix (Roche Applied Science). Primer sequences were designed using the Roche Universal ProbeLibrary Assay Design Center web site.

Gene-Expression Profiling

A 60K mouse gene expression microarray (Agilent Technologies) was used for gene-expression profiling throughout this study. Hybridization was performed according to the protocol of the supplier. Hybridized slides were scanned using a microarray scanner (Agilent Technologies) and the signals were processed using Feature Extraction software (v. 10.5.1.1; Agilent Technologies). The processed signal data were normalized and analyzed using Gene Spring GX12.1 software (Agilent Technologies). The microarray experiments were conducted using duplicate samples.

Teratoma Formation

Teratoma formation assays were carried out as previously described (Honda et al., 2010). In brief, $1–2 \times 10^6$ EpiSCs were injected under the kidney capsule of SCID mice. At 29 days and 73 days after transplantation for two of the hybrid EpiSC lines and a B6 line, respectively, teratomas were dissected out and fixed with Bouin's solution. Teratomas embedded in polyester wax were sectioned and stained with H&E.

ACCESSION NUMBERS

The GEO accession number for the gene-expression microarray data reported in this paper is GSE58735.

SUPPLEMENTAL INFORMATION

Supplemental Information includes six figures and two tables and can be found with this article online at http://dx.doi.org/10.1016/j.stemcr.2015.02.014.

AUTHOR CONTRIBUTIONS

M.S., S.M.C.d.S.L., and K.A. conceived and designed the experiments. M.S., S.M.C.d.S.L., M.K., Y.K., H.S., M.H., R.I., and A.M. performed the experiments. M.S., S.M.C.d.S.L., A.O., A.Y., and K.A. analyzed the data. M.S., S.M.C.d.S.L., and K.A. wrote the paper.

REFERENCES

Bao, S., Tang, F., Li, X., Hayashi, K., Gillich, A., Lao, K., and Surani, M.A. (2009). Epigenetic reversion of post-implantation epiblast to pluripotent embryonic stem cells. Nature *461*, 1292–1295.

Bernemann, C., Greber, B., Ko, K., Sterneckert, J., Han, D.W., Araúzo-Bravo, M.J., and Schöler, H.R. (2011). Distinct developmental ground states of epiblast stem cell lines determine different pluripotency features. Stem Cells *29*, 1496–1503.

Biechele, S., Cockburn, K., Lanner, F., Cox, B.J., and Rossant, J. (2013). Porcn-dependent Wnt signaling is not required prior to mouse gastrulation. Development *140*, 2961–2971.

Blauwkamp, T.A., Nigam, S., Ardehali, R., Weissman, I.L., and Nusse, R. (2012). Endogenous Wnt signalling in human embryonic stem cells generates an equilibrium of distinct lineage-specified progenitors. Nat. Commun. *3*, 1070.

Bosma, G.C., Custer, R.P., and Bosma, M.J. (1983). A severe combined immunodeficiency mutation in the mouse. Nature *301*, 527–530.

Brons, I.G.M., Smithers, L.E., Trotter, M.W.B., Rugg-Gunn, P., Sun, B., Chuva de Sousa Lopes, S.M., Howlett, S.K., Clarkson, A., Ahrlund-Richter, L., Pedersen, R.A., and Vallier, L. (2007). Derivation of pluripotent epiblast stem cells from mammalian embryos. Nature *448*, 191–195.

Chang, K.-H., and Li, M. (2013). Clonal isolation of an intermediate pluripotent stem cell state. Stem Cells *31*, 918–927.

Eiraku, M., Watanabe, K., Matsuo-Takasaki, M., Kawada, M., Yonemura, S., Matsumura, M., Wataya, T., Nishiyama, A., Muguruma, K., and Sasai, Y. (2008). Self-organized formation of polarized cortical tissues from ESCs and its active manipulation by extrinsic signals. Cell Stem Cell *3*, 519–532.

Han, D.W., Tapia, N., Joo, J.Y., Greber, B., Araúzo-Bravo, M.J., Bernemann, C., Ko, K., Wu, G., Stehling, M., Do, J.T., and Schöler, H.R. (2010). Epiblast stem cell subpopulations represent mouse embryos of distinct pregastrulation stages. Cell *143*, 617–627.

Hao, J., Li, T.G., Qi, X., Zhao, D.F., and Zhao, G.Q. (2006). WNT/β-catenin pathway up-regulates Stat3 and converges on LIF to prevent differentiation of mouse embryonic stem cells. Dev. Biol. *290*, 81–91.

Honda, A., Hirose, M., Hatori, M., Matoba, S., Miyoshi, H., Inoue, K., and Ogura, A. (2010). Generation of induced pluripotent stem

cells in rabbits: potential experimental models for human regenerative medicine. J. Biol. Chem. *285*, 31362–31369.

Huang, S.-M.A., Mishina, Y.M., Liu, S., Cheung, A., Stegmeier, F., Michaud, G.A., Charlat, O., Wiellette, E., Zhang, Y., Wiessner, S., et al. (2009). Tankyrase inhibition stabilizes axin and antagonizes Wnt signalling. Nature *461*, 614–620.

Kim, H., Wu, J., Ye, S., Tai, C.-I., Zhou, X., Yan, H., Li, P., Pera, M., and Ying, Q.-L. (2013). Modulation of β-catenin function maintains mouse epiblast stem cell and human embryonic stem cell self-renewal. Nat. Commun. *4*, 2403.

Kojima, Y., Kaufman-Francis, K., Studdert, J.B., Steiner, K.A., Power, M.D., Loebel, D.A.F., Jones, V., Hor, A., de Alencastro, G., Logan, G.J., et al. (2014). The transcriptional and functional properties of mouse epiblast stem cells resemble the anterior primitive streak. Cell Stem Cell *14*, 107–120.

Lyashenko, N., Winter, M., Migliorini, D., Biechele, T., Moon, R.T., and Hartmann, C. (2011). Differential requirement for the dual functions of β-catenin in embryonic stem cell self-renewal and germ layer formation. Nat. Cell Biol. *13*, 753–761.

Nichols, J., and Smith, A. (2009). Naive and primed pluripotent states. Cell Stem Cell *4*, 487–492.

Ogawa, K., Nishinakamura, R., Iwamatsu, Y., Shimosato, D., and Niwa, H. (2006). Synergistic action of Wnt and LIF in maintaining pluripotency of mouse ES cells. Biochem. Biophys. Res. Commun. *343*, 159–166.

Rugg-Gunn, P.J., Cox, B.J., Lanner, F., Sharma, P., Ignatchenko, V., McDonald, A.C., Garner, J., Gramolini, A.O., Rossant, J., and Kislinger, T. (2012). Cell-surface proteomics identifies lineage-specific markers of embryo-derived stem cells. Dev. Cell *22*, 887–901.

Sado, T., Wang, Z., Sasaki, H., and Li, E. (2001). Regulation of imprinted X-chromosome inactivation in mice by *Tsix*. Development *128*, 1275–1286.

Singla, D.K., Schneider, D.J., LeWinter, M.M., and Sobel, B.E. (2006). wnt3a but not wnt11 supports self-renewal of embryonic stem cells. Biochem. Biophys. Res. Commun. *345*, 789–795.

Sokol, S.Y. (2011). Maintaining embryonic stem cell pluripotency with Wnt signaling. Development *138*, 4341–4350.

Suemori, H., Yasuchika, K., Hasegawa, K., Fujioka, T., Tsuneyoshi, N., and Nakatsuji, N. (2006). Efficient establishment of human embryonic stem cell lines and long-term maintenance with stable karyotype by enzymatic bulk passage. Biochem. Biophys. Res. Commun. *345*, 926–932.

Sugimoto, M., Kondo, M., Hirose, M., Suzuki, M., Mekada, K., Abe, T., Kiyonari, H., Ogura, A., Takagi, N., Artzt, K., and Abe, K. (2012). Molecular identification of t$^{(w5)}$: *Vps52* promotes pluripotential cell differentiation through cell-cell interactions. Cell Rep. *2*, 1363–1374.

Sumi, T., Oki, S., Kitajima, K., and Meno, C. (2013). Epiblast ground state is controlled by canonical Wnt/β-catenin signaling in the postimplantation mouse embryo and epiblast stem cells. PLoS ONE *8*, e63378.

Takagi, N., Yoshida, M.A., Sugawara, O., and Sasaki, M. (1983). Reversal of X-inactivation in female mouse somatic cells hybridized with murine teratocarcinoma stem cells in vitro. Cell *34*, 1053–1062.

Tamm, C., Pijuan Galitó, S., and Annerén, C. (2013). A comparative study of protocols for mouse embryonic stem cell culturing. PLoS ONE *8*, e81156.

ten Berge, D., Kurek, D., Blauwkamp, T., Koole, W., Maas, A., Eroglu, E., Siu, R.K., and Nusse, R. (2011). Embryonic stem cells require Wnt proteins to prevent differentiation to epiblast stem cells. Nat. Cell Biol. *13*, 1070–1075.

Tesar, P.J., Chenoweth, J.G., Brook, F.A., Davies, T.J., Evans, E.P., Mack, D.L., Gardner, R.L., and McKay, R.D.G. (2007). New cell lines from mouse epiblast share defining features with human embryonic stem cells. Nature *448*, 196–199.

Ware, C.B., Nelson, A.M., and Blau, C.A. (2006). A comparison of NIH-approved human ESC lines. Stem Cells *24*, 2677–2684.

Waterston, R.H., Lindblad-Toh, K., Birney, E., Rogers, J., Abril, J.F., Agarwal, P., Agarwala, R., Ainscough, R., Alexandersson, M., An, P., et al.; Mouse Genome Sequencing Consortium (2002). Initial sequencing and comparative analysis of the mouse genome. Nature *420*, 520–562.

Wray, J., Kalkan, T., Gomez-Lopez, S., Eckardt, D., Cook, A., Kemler, R., and Smith, A. (2011). Inhibition of glycogen synthase kinase-3 alleviates Tcf3 repression of the pluripotency network and increases embryonic stem cell resistance to differentiation. Nat. Cell Biol. *13*, 838–845.

Ying, Q.-L., Wray, J., Nichols, J., Batlle-Morera, L., Doble, B., Woodgett, J., Cohen, P., and Smith, A. (2008). The ground state of embryonic stem cell self-renewal. Nature *453*, 519–523.

313

PLOS | GENETICS

Genome-Wide Analysis of DNA Methylation Dynamics during Early Human Development

Hiroaki Okae[1,2], Hatsune Chiba[1,2], Hitoshi Hiura[1,2], Hirotaka Hamada[1,2], Akiko Sato[1,3], Takafumi Utsunomiya[3], Hiroyuki Kikuchi[4], Hiroaki Yoshida[4], Atsushi Tanaka[5], Mikita Suyama[2,6], Takahiro Arima[1,2]*

1 Department of Informative Genetics, Environment and Genome Research Center, Tohoku University Graduate School of Medicine, Sendai, Japan, 2 JST, CREST, Saitama, Japan, 3 St. Luke Clinic Laboratory, Oita, Japan, 4 Yoshida Ladies Clinic Center for Reproductive Medicine, Sendai, Japan, 5 St. Mother Clinic Laboratory, Kitakyushu, Fukuoka, Japan, 6 Division of Bioinformatics, Medical Institute of Bioregulation, Kyushu University, Maidashi 3-1-1, Fukuoka, Japan

Abstract

DNA methylation is globally reprogrammed during mammalian preimplantation development, which is critical for normal development. Recent reduced representation bisulfite sequencing (RRBS) studies suggest that the methylome dynamics are essentially conserved between human and mouse early embryos. RRBS is known to cover 5–10% of all genomic CpGs, favoring those contained within CpG-rich regions. To obtain an unbiased and more complete representation of the methylome during early human development, we performed whole genome bisulfite sequencing of human gametes and blastocysts that covered>70% of all genomic CpGs. We found that the maternal genome was demethylated to a much lesser extent in human blastocysts than in mouse blastocysts, which could contribute to an increased number of imprinted differentially methylated regions in the human genome. Global demethylation of the paternal genome was confirmed, but SINE-VNTR-Alu elements and some other tandem repeat-containing regions were found to be specifically protected from this global demethylation. Furthermore, centromeric satellite repeats were hypermethylated in human oocytes but not in mouse oocytes, which might be explained by differential expression of *de novo* DNA methyltransferases. These data highlight both conserved and species-specific regulation of DNA methylation during early mammalian development. Our work provides further information critical for understanding the epigenetic processes underlying differentiation and pluripotency during early human development.

Introduction

In mammals, DNA methylation is essential for normal development and plays critical roles in repression of transposable elements, maintaining genome stability, genomic imprinting and X-chromosome inactivation. DNA methylation patterns are relatively stable in somatic cells but genome-wide reprogramming of DNA methylation occurs in primordial germ cells and preimplantation embryos [1–3]. During mouse preimplantation development, the maternal genome is passively demethylated in a replication-dependent manner while some oocyte-specific methylated regions maintain maternal allele-specific methylation at the blastocyst stage [4,5]. In contrast, the paternal genome is actively and rapidly demethylated through the oxidation of 5-methylcytosine (5mC) to 5-hydroxymethylcytosine (5hmC) by ten-eleven translocation-3 [6]. In spite of the global demethylation, imprinted differentially methylated regions (DMRs) and some transposable elements (*e.g.* intracisternal A-particles (IAPs)) are specifically protected from demethylation [1].

During human preimplantation development, the paternal genome is reported to be actively demethylated as in the mouse [7,8], but the regulatory mechanism and the genome-wide DNA methylation patterns in early embryos are not well understood. Recently, two studies employed reduced representation bisulfite sequencing (RRBS) of human gametes and early embryos to characterize the human methylome very early in development [7,9]. According to these studies, the paternal genome is rapidly and globally demethylated after fertilization whereas demethylation of the maternal genome is more limited and some oocyte-specific methylated regions maintain monoallelic methylation during preimplantation development, similar to the mouse genome. RRBS is known to cover 5–10% of genomic CpGs, favoring those contained within CpG islands (CGIs) and promoter regions. To obtain an unbiased and more complete representation of the methylome during early human development, we performed whole genome bisulfite sequencing (WGBS) of human gametes and blastocysts that covered>70% of genomic CpGs. We found

314

Author Summary

DNA methylation reprogramming after fertilization is critical for normal mammalian development. Early embryos are sensitive to environmental stresses and a number of reports have pointed out the increased risk of DNA methylation errors associated with assisted reproduction technologies. Therefore, it is very important to understand normal DNA methylation patterns during early human development. Recent reduced representation bisulfite sequencing studies reported partial methylomes of human gametes and early embryos. To provide a more comprehensive view of DNA methylation dynamics during early human development, we report on whole genome bisulfite sequencing of human gametes and blastocysts. We show that the paternal genome is globally demethylated in blastocysts whereas the maternal genome is demethylated to a much lesser extent. We also reveal unique regulation of imprinted differentially methylated regions, gene bodies and repeat sequences during early human development. Our high-resolution methylome maps are essential to understand epigenetic reprogramming by human oocytes and will aid in the preimplantation epigenetic diagnosis of human embryos.

human-specific regulation of DNA methylation in various regions including oocyte-methylated CGIs, gene bodies and tandem repeat-containing regions.

Results

WGBS of human gametes and blastocysts

We performed WGBS of human oocytes, sperm, blastocysts and neonatal blood cells. For ethical reasons, we used only surplus germinal vesicle (GV) or metaphase I (MI) oocytes and blastocysts obtained from female patients undergoing *in vitro* fertilization (IVF) treatment. Sperm and blood cells were collected from healthy donors (see Materials and Methods for details). WGBS libraries were constructed using the amplification-free post-bisulfite adaptor tagging (PBAT) method [10] for all samples except the oocytes, which required PCR-amplification (PCR cycles $= 10$) to increase the read depth (Table 1). For each cell type, 87–96% of genomic CpGs were covered by at least one read, which was comparable to the reported methylome maps of mouse gametes [5,11,12] and human sperm [13]. We also compared two oocyte PBAT libraries prepared with and without PCR-amplification (Oocyte(+PCR) and Oocyte(−PCR)) (S1A Figure, S1B Figure, and Table 1). The methylation levels of individual CpGs were highly correlated ($r = 0.83$) between these two libraries. Furthermore, the average methylation levels were very similar: Oocyte(+PCR) at 53.1% versus Oocyte(−PCR) at 54.8%. These data demonstrate that our PCR-amplification protocol did not lead to significant bias in our data sets. Non-CpG methylation was observed in human oocytes, especially at CpA sites (mean $= 5.6\%$), with a positive correlation between CpG and non-CpG methylation (S1C Figure, S1D Figure). Non-CpG methylation was not a significant feature of sperm or blastocysts ($<1\%$). In the following analyses, only CpGs covered with ≥ 3 reads were considered for oocytes and those covered with ≥ 5 reads were considered for the other samples.

We confirmed that three imprinted DMRs and two pluripotency genes frequently observed to be abnormal in poor quality oocytes or embryos [14,15] were normally methylated in our WGBS data (S1E Figure). We also compared our WGBS data

with recently reported RRBS data of human oocytes, blastocysts and inner cell mass (ICM) and WGBS data of ICM [7,9]. Our data substantially increased the coverage of genomic CpGs compared with the reported data (S1F Figure, S1G Figure). The methylation levels of CGIs showed high correlations ($r = 0.96$) between our WGBS data and the reported RRBS data (oocyte: S1H Figure, blastocyst: S1I Figure), validating the WGBS data.

Global changes of DNA methylation during early human development

Similar to findings for the mouse, human oocytes showed an intermediate methylation level of CpGs and blastocysts were globally hypomethylated (Fig. 1A). To further characterize global DNA methylation changes, we used a system of sliding windows of 20 CpGs with a step size change of 10 CpGs. Windows were classified as increasing (or decreasing) if the methylation levels increased (or decreased) by $>20\%$ and the changes were statistically significant (Benjamini-Hochberg (BH) corrected $P<0.05$). We found that 57% and 83% of windows showed decreased methylation levels in blastocysts compared with oocytes and sperm, respectively (Fig. 1B). In contrast, $>90\%$ of windows showed increased methylation in ES or blood cells compared with blastocysts (Fig. 1B). To explore the differences in demethylation dynamics between parental genomes, we focused on windows hypermethylated in one gamete and hypomethylated in the other. In this study, we defined regions that were $\geq 80\%$ methylated as hypermethylated and those that were $\leq 20\%$ methylated as hypomethylated. Windows hypermethylated in sperm and hypomethylated in oocytes (sperm-specific methylated windows) were abundant in intergenic regions. In contrast, oocyte-specific ones showed a relatively uniform distribution (S2A Figure). In blastocysts, oocyte-specific methylated windows showed intermediate methylation levels (median $= 35.1\%$), in contrast to the nearly complete demethylation of sperm-specific ones (Fig. 1C). Almost all windows hypomethylated in both gametes remained hypomethylated and very few windows (0.04%) were hypermethylated in blastocysts, suggesting that genome-wide *de novo* methylation occurred after implantation (Fig. 1C and S2B Figure). Consistently, the methylation patterns of oocytes and blastocysts were very similar to each other (Figs. 1E, F), suggesting that the global methylation pattern of the maternal genome, but not the paternal genome, was inherited by blastocysts.

Next, we examined specific genomic features: CGIs, promoters and transposable elements. CGIs and promoters hypermethylated in sperm remained methylated in ES and blood cells. On the other hand, oocyte-specific methylated CGIs showed variable methylation levels and oocyte-specific methylated promoters were preferentially demethylated in ES and blood cells (S3A Figure and S3B Figure). In addition, the promoter methylation patterns of sperm, but not of oocytes, showed high correlations with those of ES and blood cells ($r>0.8$, Fig. 1D). These data highlighted the unique promoter methylation profile of oocytes. Short interspersed nuclear elements (SINEs), long interspersed nuclear elements (LINEs), long terminal repeats (LTRs) and DNA repeats were essentially highly methylated in ES and blood cells, whereas 20–30% and 3–8% of repeat copies were hypomethylated in oocytes and sperm, respectively (S2B Figure). These transposable elements were demethylated similarly to other genomic regions in blastocysts (S3 Figure).

Stability of imprinted DMRs and oocyte-specific methylated CGIs

Germline DMRs (gDMRs) frequently serve as imprinting control regions [16] and we were interested in how many gDMRs

315

Table 1. Summary of whole genome bisulfite sequencing.

Sample	Number	Mapped reads	Depth	≥1	≥3	≥5
Oocyte (+PCR)	79 oocytes	144,463,623	4.5	74.4%	56.9%	38.5%
Oocyte (−PCR)	123 oocytes	79,772,565	2.5	71.9%	26.9%	6.6%
Oocyte (Total)	202 oocytes	224,236,188	7.0	87.5%	71.0%	54.1%
Sperm (Donor-1)	-	243,284,702	7.6	90.7%	80.1%	68.5%
Sperm (Donor-2)	-	258,580,093	8.1	91.2%	80.8%	68.9%
Sperm (Donor-3)	-	280,502,462	8.8	91.3%	82.0%	71.8%
Sperm (Total)	3 individuals	782,367,257	24.5	94.9%	91.3%	88.2%
Blastocyst	80 embryos	750,044,631	23.5	95.7%	93.6%	91.3%
Blood (Donor-1)	-	102,369,166	3.2	81.4%	46.8%	21.8%
Blood (Donor-2)	-	107,690,372	3.4	84.0%	53.3%	26.7%
Blood (Donor-3)	-	98,147,071	3.1	83.4%	51.0%	24.1%
Blood (Donor-4)	-	100,978,105	3.2	83.5%	51.3%	24.9%
Blood (Donor-5)	-	113,611,080	3.6	76.8%	35.5%	11.4%
Blood (Total)	5 individuals	522,795,794	16.4	94.7%	90.4%	85.4%

Libraries were prepared without PCR-amplification except for Oocyte (+PCR). The proportion (%) of CpGs covered with over 1, 3 or 5 reads is indicated. Oocyte (Total), Sperm (Total) and Blood (Total) are used in most our analyses. Bisulfite conversion rates were >99% for all samples.
doi:10.1371/journal.pgen.1004868.t001

exist in the human genome. Among the 67 known imprinted DMRs [17], 46 DMRs were classified as gDMRs according to the following definition: DMRs hypermethylated in one gamete and hypomethylated in the other (Fig. 2A, B and S1 Table). Of these, 15 reportedly placenta-specific DMRs were lost in blood cells (Fig. 2A, C). The other 31 gDMRs showed intermediate methylation levels in blood cells, but about one-third of these gDMRs were not maintained in ES cells (H9 ES cells: Fig. 2A, H1 and HUES6 ES cells: S4A Figure), indicating the instability of gDMRs in human ES cells. Importantly, oocyte-specific methylated autosomal CGIs showed methylation levels very similar (median = 37.5%) to gDMRs (median = 39.2%) in human blastocysts (Fig. 2D). We confirmed monoallelic methylation of four autosomal CGIs in human blastocysts by using conventional bisulfite sequencing (Fig. 2E and S4B Figure). We also analyzed two X-linked CGIs hypermethylated in oocytes and found that these CGIs showed high methylation levels in male blastocysts (the X chromosome of male blastocysts is derived from oocytes) and monoallelic methylation in female blastocysts (Fig. 2F). Consistently, X-linked CGIs with oocyte-specific methylation showed higher methylation levels than autosomal ones in blastocysts (the WGBS data were derived from a pool of blastocysts) (Fig. 2D). A similar tendency was also observed in the sliding window-based analyses (S2C Figure). These data suggested that a substantial number of oocyte-specific methylated CGIs may maintain maternal allele-specific methylation in human blastocysts. In contrast, most oocyte-specific methylated CGIs were significantly demethylated compared with gDMRs in mouse blastocysts (Fig. 2D).

A bimodal gene body methylation pattern associated with transcription in human oocytes

In mouse oocytes, gene-body methylation levels are reported to positively correlate with the transcription levels [5]. In human oocytes, a positive correlation between gene-body methylation and transcription levels was also observed. Interestingly, there was an expression-level boundary at around $log_2(RPKM) = -5$ (RPKM: reads per kilobase per million) (Fig. 3A). Genes with

$log_2(RPKM) > -5$ and < -5 may be transcriptionally active and inactive genes, respectively (Fig. 3B). We analyzed previously reported mouse methylome and transcriptome data and found that a bimodal distribution of gene body methylation was also observed while there was a boundary at around $log_2(RPKM) = 0$ (Fig. 3A). It is unclear whether the difference between the human and mouse expression-level boundaries reflects experimental or functional differences. We found that 971 genes showed differential gene body methylation between human and mouse oocytes (Fig. 3C and S2 Table). Gene ontology (GO) analysis revealed an abundance of genes encoding cell adhesion molecules with human-specific gene body hypermethylation (Fig. 3D), which could have important roles during human oogenesis. In mouse oocytes, *Dnmt3l* and *Zfp57* are highly expressed and essential for DNA methylation regulation [18,19] whereas human *DNMT3L* is undetectable in oocytes [20]. Here we found that the gene body regions of *DNMT3L* and *ZFP57* were hypomethylated in human oocytes and neither gene was expressed (Figs. 3E, F), implying that *DNMT3L* and *ZFP57* might not be essential for regulation of DNA methylation in human oocytes.

Unique regulations of tandem repeat-containing regions

As described above, global methylation changes of SINEs, LINEs, LTRs and DNA repeats were very similar to other genomic regions in early human embryos (S3 Figure). We further analyzed mean methylation levels of CpGs in various classes of these transposable elements (Fig. 4A, see also S3 Table for details). These repeat classes showed similar methylation changes: ~60% methylated in oocytes, ~80% methylated in sperm, ES and blood cells and ~30% methylated in blastocysts. These data suggested that SINEs, LINEs, LTRs and DNA repeats were essentially not resistant to genome-wide demethylation after fertilization. Mouse IAPs are known to be protected from demethylation during preimplantation development [5,21]. To identify transposable elements specifically protected from demethylation during human preimplantation development, we screened repeat copies overlapping windows showing >70% methylation in blastocysts (0.3% of all windows) (S4 Table). We found that SINE-VNTR-Alu (SVA)
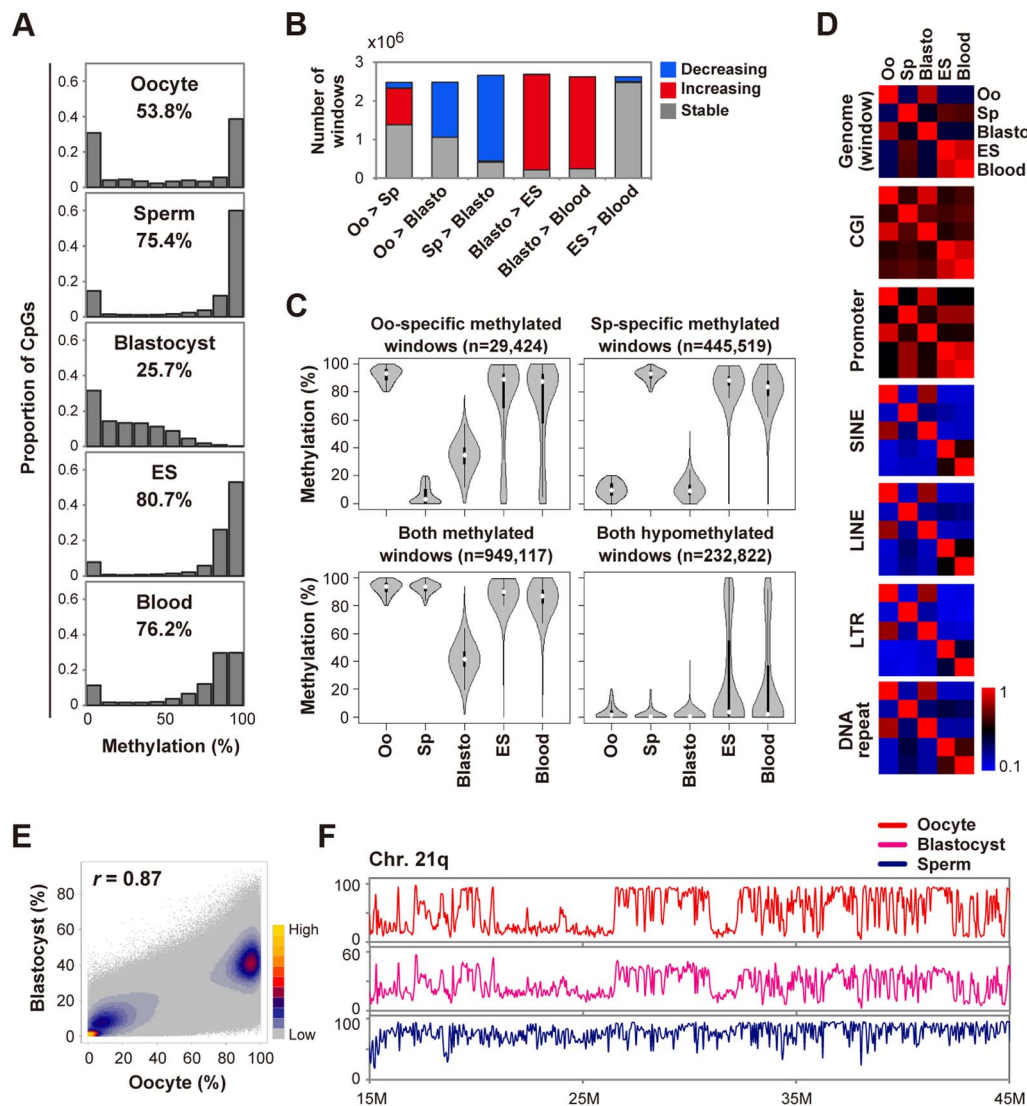
Fig. 1. Global changes of DNA methylation during early human development. A, Distribution of methylation levels of individual CpGs. The mean methylation levels of CpGs are also indicated. We included human H9 ES cells (GEO accession number: GSM706059) for comparison. **B,** Detection of dynamic methylation changes using a sliding window (window size = 20 CpGs, step size = 10 CpGs). Windows were classified as increasing (or decreasing) if the methylation levels increased (or decreased) by>20% and the changes were significant (BH-corrected $P<0.05$). The other windows were classified as stable. Oo: Oocyte; Sp: Sperm; Blasto: Blastocyst. **C,** Violin plots of mean methylation levels of windows hypermethylated (≥80%) or hypomethylated (≤20%) in one or both gametes. Oo-specific (Sp-specific) methylated windows are defined as windows hypermethylated in oocytes (sperm) and hypomethylated in sperm (oocytes). Thin and thick lines are box plots and white dots indicate the median. **D,** Heatmaps of Pearson correlation coefficients. Correlation coefficients were calculated based on the mean methylation levels of individual windows, CGIs, promoters and repeat copies. Correlation coefficients are color-coded as shown. **E,** A density scatterplot of mean methylation levels of the sliding windows. The Pearson correlation coefficient between oocytes and blastocysts was high ($r = 0.87$). The density is color-coded as indicated. **F,** Methylation levels across the long arm of chromosome 21 (smoothed using 50 kb non-overlapping windows). Similar methylation patterns were observed for oocytes and blastocysts whereas the methylation levels of blastocysts were low (note that the vertical maximum scale is 60% for blastocysts).
doi:10.1371/journal.pgen.1004868.g001

subfamilies, especially SVA_A, frequently overlapped the>70% methylated windows (Fig. 4B). SVA_A also showed the highest methylation level in blastocysts (59.2%) whereas the other repeat sequences were <50% methylated (Fig. 4A and S3 Table). SVA is a hominid-specific repeat family that remains active in the human genome [22]. Similar to mouse LTRs [5], methylation levels of CpGs within SVAs are positively correlated with CpG density in human oocytes and blastocysts (Fig. 4C and S5 Figure). LTR12 subfamilies, which are LTRs of HERV9, also tended to overlap the>70% methylated windows (Fig. 4B). Interestingly, both SVA

and LTR12 subfamilies contain CpG-rich variable number tandem repeats (VNTRs) [22,23]. We also noticed that whereas the MER34C2 consensus sequence does not contain VNTRs, MER34C2 copies overlapping the>70% methylated windows were all tandemly repeated in a single genomic locus (Fig. 4D). VNTRs were also found in the two paternal gDMRs (Fig. 4E). VNTRs were not a common feature of the maternal gDMRs, but a significantly higher proportion of the maternal gDMRs did contain VNTRs as compared with all CGIs (gDMRs: 11/44, CGIs: 1763/27718, chi-square $P=4.1\times10^{-7}$). Therefore, we
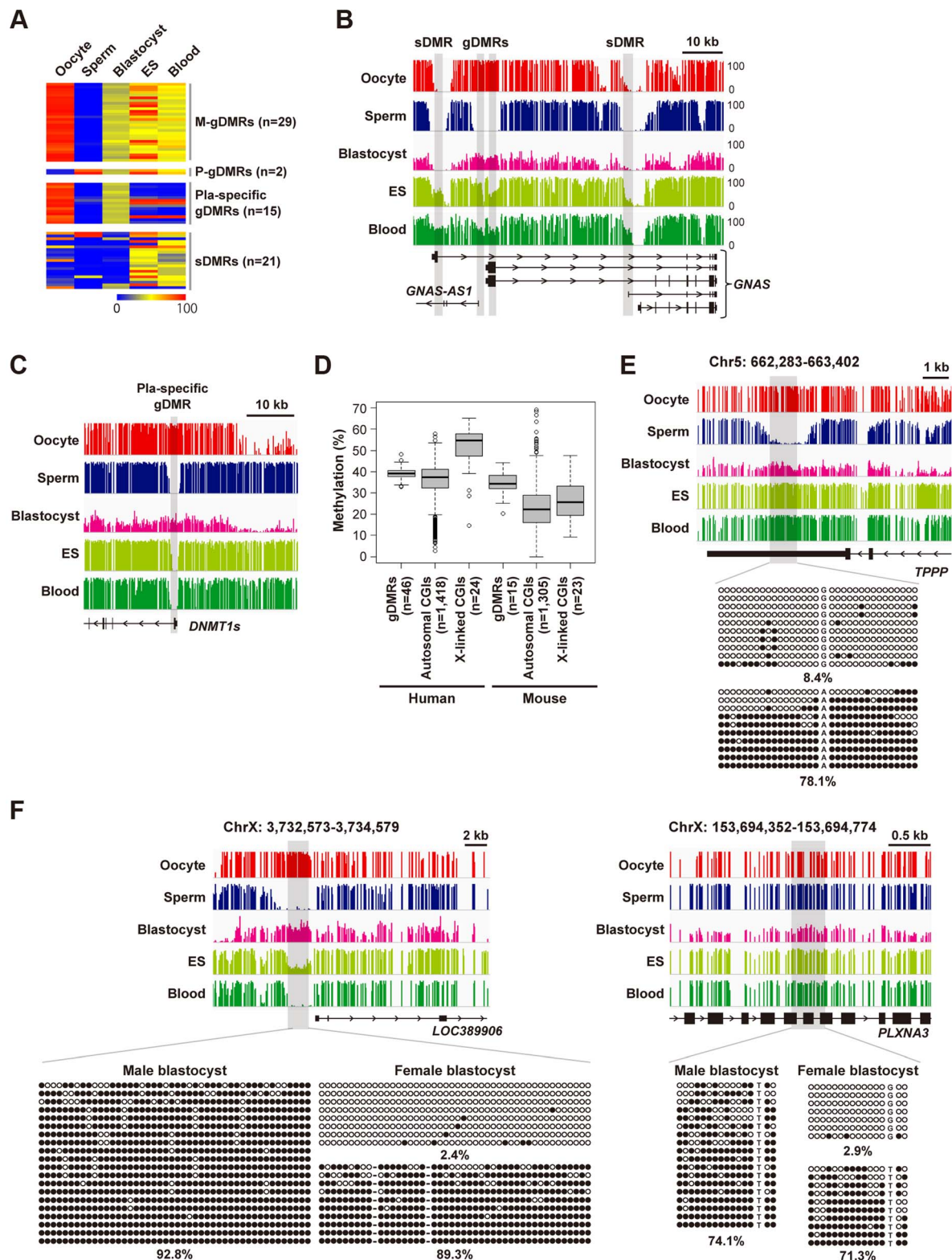
Fig. 2. Establishment and maintenance of imprinted DMRs. A, A heatmap of mean methylation levels of imprinted DMRs. We classified the 67 known human imprinted DMRs [17], and found that 44 were maternal germline DMRs (M-gDMRs), 2 were paternal germline DMRs (P-gDMRs) and 21 were secondary DMRs (sDMRs). 15 M-gDMRs are reported to be maintained only in the placenta and shown as ''Pla-specific gDMRs''. gDMRs other than placenta-specific ones showed 35–65% methylation levels in blood cells but the intermediate methylation levels were not well maintained in ES cells (11/31 showed>75% methylation). Methylation levels are color coded as indicated. The raw data are shown in S1 Table. **B,** Methylation patterns at the human *GNAS* locus. The vertical axis indicates the methylation level (%). In this locus, there were two gDMRs and two sDMRs. All DMRs overlap promoter regions. **C,** Methylation patterns at the human *DNMT1* locus. The promoter region of the somatic isoform of *DNMT1* (*DNMT1s*) is known to show maternal allele-specific methylation in the placenta [45]. The *DNMT1* DMR was hypomethylated in both ES and blood cells, suggesting placenta-

specific protection of the maternal allele from demethylation. **D,** Box plots of mean methylation levels of gDMRs and oocyte-specific methylated CGIs in blastocysts. Boxes represent lower and upper quartiles and horizontal lines indicate the median. Whiskers extend to the most extreme data points within 1.5 times the interquartile range from the boxes. The open circles indicate the data points outside the whiskers. Methylation levels of mouse gDMRs and oocyte-specific methylated CGIs [5] are shown for comparison. **E,** Methylation patterns of an oocyte-specific methylated CGI. A single blastocyst was used for the analysis. Black and white circles indicate methylated and unmethylated residues, respectively. The percentages of methylated CpG sites are indicated. **F,** Bisulfite sequencing analyses of X-linked CGIs hypermethylated in oocytes. A single blastocyst was used for each bisulfite sequencing analysis.

doi:10.1371/journal.pgen.1004868.g002
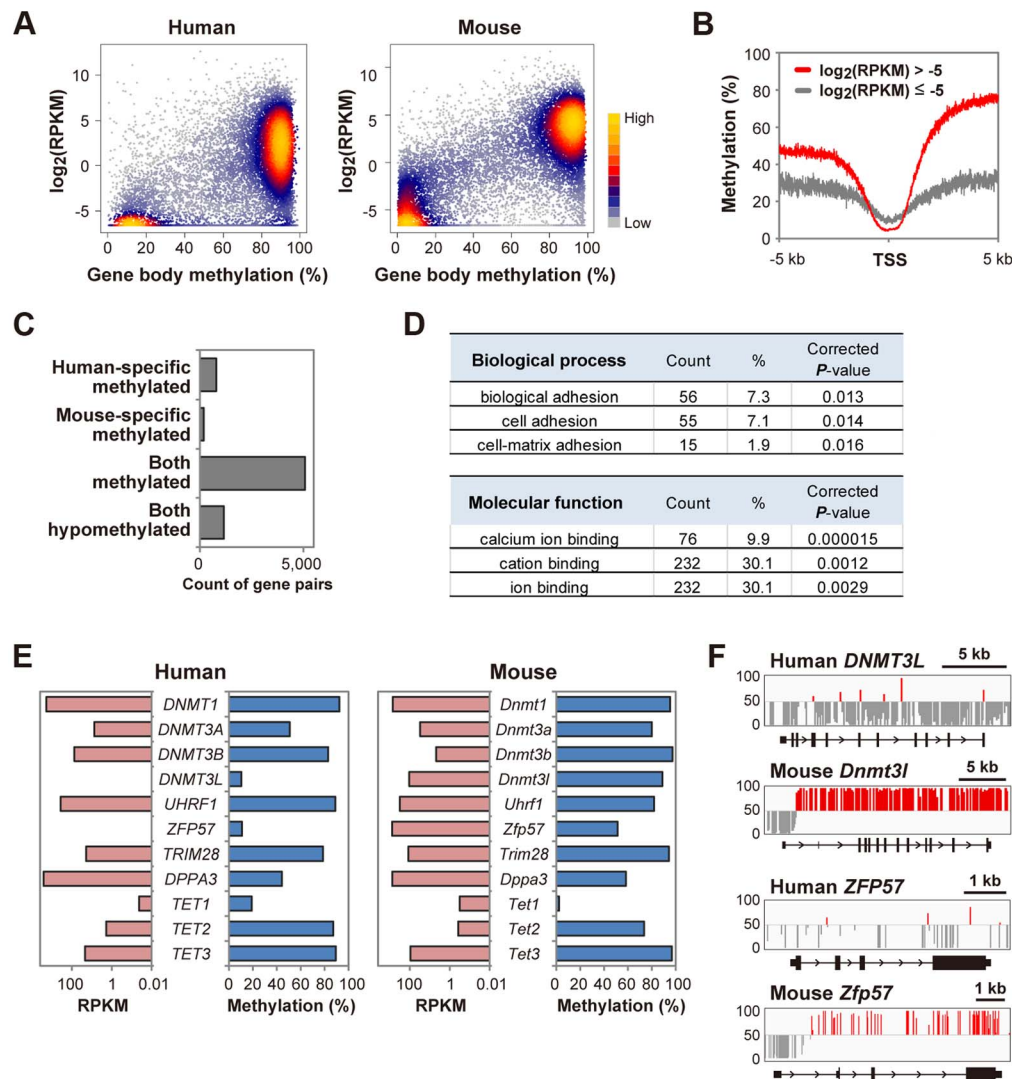
Fig. 3. A bimodal gene body methylation pattern associated with transcription in human oocytes. A, A density scatterplot of gene body methylation levels and transcription levels [43] in human oocytes. The data of mouse oocytes [5,11] are also shown for comparison. Only genes longer than 5 kb were analyzed. For genes with RPKM less than 0.01, RPKM was set as 0.01. The density is color-coded as indicated. **B,** Mean methylation levels within 5 kb of transcription start sites (TSS) in human oocytes. Genes (>5 kb) were classified into two groups ($\log_2(\text{RPKM}) > -5$ and ≤ -5). Methylation levels were smoothed using 5 bp non-overlapping sliding windows. **C,** Conservation of gene body methylation levels between human and mouse oocytes. 783 and 188 genes showed human-specific and mouse-specific gene body hypermethylation, respectively. 5076 and 1151 genes were hypermethylated and hypomethylated in both types of oocytes, respectively. The raw data are shown in S2 Table. **D,** GO analysis of 783 genes with human-specific gene body hypermethylation. The top three GO terms (biological process and molecular function) are indicated with gene counts, the proportion (%) and BH-corrected P-values. No GO term was enriched in genes with mouse-specific gene body hypermethylation. **E,** Gene body methylation levels and transcription levels of DNA methylation regulators in human and mouse oocytes. *DNMT3L* and *ZFP57* showed gene body hypomethylation and were not expressed (RPKM<0.01) in human oocytes. *DNMT3B* (RPKM = 76.0) showed 10-fold higher expression than *DNMT3A* (RPKM = 7.6) in human oocytes. In contrast, *Dnmt3b* (RPKM = 4.9) showed ~6-fold lower expression than *Dnmt3a* (RPKM = 30.6) in mouse oocytes. **F,** Methylation patterns at human *DNMT3L* and *ZFP57* loci and mouse *Dnmt3l* and *Zfp57* loci. The vertical line indicates the methylation level (%) and the baseline is set at 50% to highlight unmethylated CpGs. CpGs with>50% and <50% methylation are shown in red and grey, respectively.
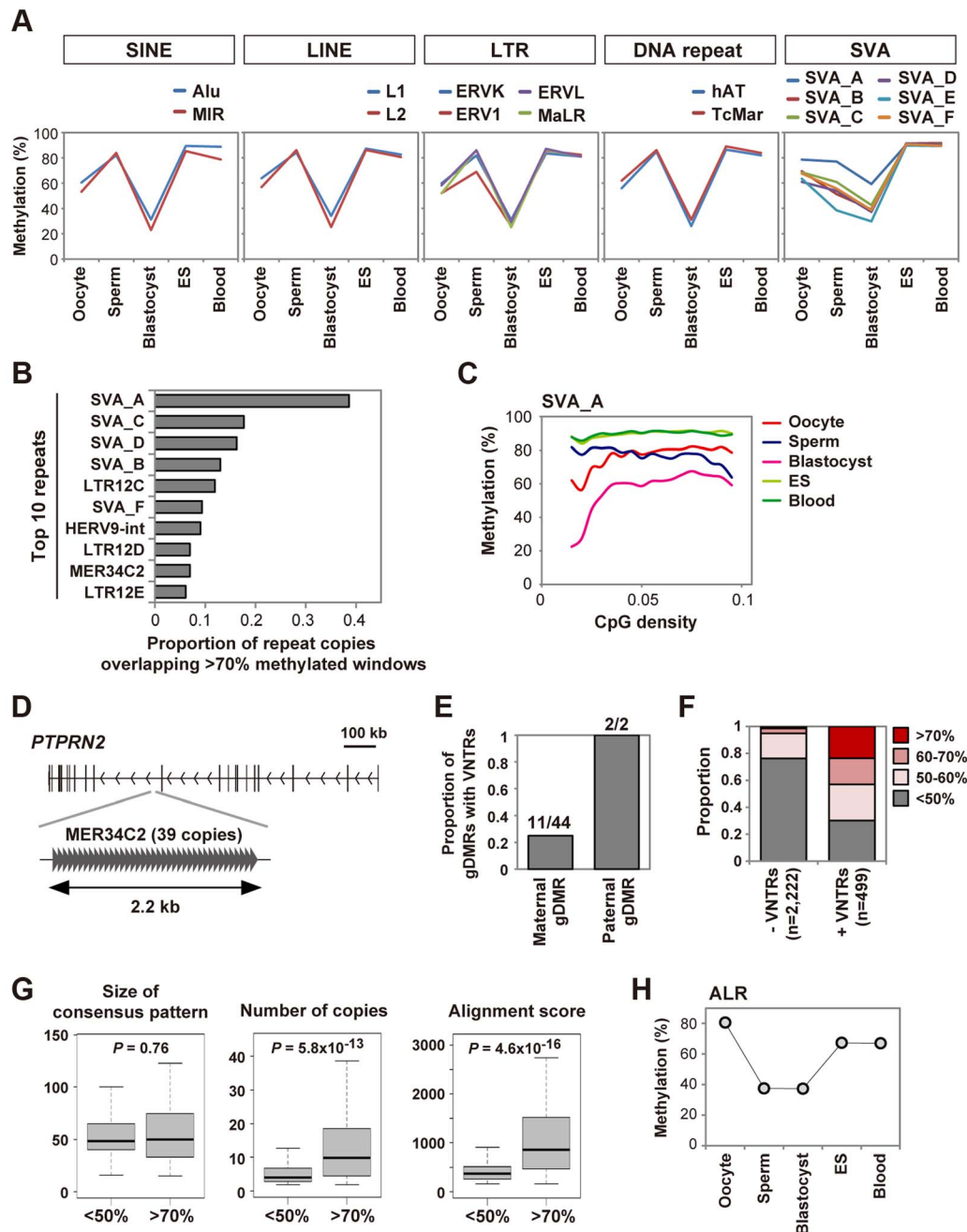
doi:10.1371/journal.pgen.1004868.g003

Fig. 4. Unique regulation of tandem repeat-containing regions. A, DNA methylation dynamics of transposable elements. Mean methylation levels of CpGs in various classes of SINEs, LINEs, LTRs and DNA repeats and SVA subfamilies are shown. SVA_A showed an especially high methylation level in blastocysts (59.2%). **B,** Proportions of repeat copies overlapping>70% methylated windows in human blastocysts. We analyzed only SINEs, LINEs, LTRs, DNA repeats, SVAs and satellites with>100 copies in the human genome. The top ten repeat names with the highest proportions are shown. The raw data are shown in S4 Table. **C,** Relationships between methylation levels and CpG densities. Mean methylation levels of CpGs in SVA_A are plotted against CpG densities. **D,** MER34C2 copies overlapping>70% methylated windows in human blastocysts. 39 MER34C2 copies are all tandemly repeated within the *PTPRN2* gene locus. **E,** Proportions of maternal and paternal gDMRs containing VNTRs. Counts of gDMRs with VNTRs and total gDMR are indicated. **F,** Proportions of mean methylation levels of CGIs with and without VNTRs in human blastocysts. Only autosomal CGIs hypermethylated in both gametes were analyzed. 118 of 499 CGIs with VNTRs and 31 of 2,222 CGIs without VNTRs showed>70% methylation ($P = 0$, chi-square test). **G,** Characteristics of VNTRs highly methylated in blastocysts. Using Tandem Repeats Finder [41], the size of the consensus pattern, the number of tandemly aligned copies and the alignment score were compared between VNTRs of <50% methylated CGIs and>70% methylated CGIs shown in (F). The alignment score calculated by Tandem Repeat Finder reflects the degree of similarity between repeat copies. When several VNTRs were found in a CGI, the VNTR with the highest alignment score was analyzed. Boxes represent lower and upper quartiles and horizontal lines indicate the median. Whiskers extend to the most extreme data points within 1.5 times the interquartile range from the boxes. The Mann-Whitney U test was used to calculate *P*-values. No sequence motif was found among the consensus patterns of the>70% methylated CGIs using DREME [42]. **H,** Mean methylation levels of CpGs in ALR. Oocytes showed the highest methylation level (80.6%).
doi:10.1371/journal.pgen.1004868.g004

focused on CGIs hypermethylated in both gametes and found that CGIs containing VNTRs were preferentially protected from demethylation in blastocysts (Fig. 4F). A comparison between VNTRs of >70% and <50% methylated CGIs in blastocysts revealed that VNTRs with more repeats tended to be protected from demethylation, whereas no sequence motif was found (Fig. 4G). These data suggested that VNTRs might underlie silencing of specific transposable elements and the protection of paternal gDMRs.

We also found that alpha satellite (ALR), which is a tandemly repeated DNA family found in centromeric and pericentromeric regions [24], was hypermethylated in human oocytes (80.6%) (Fig. 4H). Interestingly, DNMT3B was highly expressed in human oocytes (Fig. 3E), and DNMT3B is reported to interact with centromere protein CENP-C and contribute to DNA methylation of ALR [25]. Thus, it is possible that DNMT3B is involved in DNA methylation of ALR in human oocytes.

Discussion

This work reports the genome-wide DNA methylation patterns of human gametes and blastocysts at single-base resolution. Our WGBS data of oocytes and blastocysts substantially increase the coverage of genomic CpGs adding to the reported RRBS data of oocytes and blastocysts and WGBS data of ICM [7,9]. We confirmed that the paternal genome was globally demethylated as previously reported. However, the oocyte-specific methylated regions maintained intermediate methylation levels in human blastocysts (median = 35.1%). Consistently, the methylation patterns of oocytes and blastocysts were very similar to each other, suggesting that the global methylation pattern of the maternal genome was inherited by blastocysts. Furthermore, oocyte-specific methylated CGIs showed methylation levels very similar (median = 37.5%) to gDMRs (median = 39.2%). These data appear not to support replication-dependent global demethylation of the maternal genome during human early development, because oocyte-specific methylated regions should show ≤25% methylation after one replication-dependent global demethylation event. In mouse blastocysts, most oocyte-specific methylated CGIs were significantly demethylated compared with gDMRs, which may reflect the passive demethylation of the maternal genome [1,2]. These data strongly suggest that the maternal genome is demethylated to a much lesser extent in human blastocysts than in mouse blastocysts.

We classified known imprinted DMRs [17] and discovered that there were at least 46 gDMRs in the human genome including 15 specific to the placenta. Our data suggested that a substantial number of oocyte-specific methylated CGIs may also maintain mono-allelic methylation in human blastocysts whereas they were essentially lost through hypermethylation or hypomethyaltion in blood cells. It is suggested that a significant portion of gene transcripts show mono-allelic expression in human 8-cell embryos and morulae [26], and the oocyte-specific methylated CGIs could regulate mono-allelic expression of some genes in human preimplantation embryos. In the mouse genome, ~25 well defined gDMRs have been identified and only the Gpr1 DMR is reported to be placenta-specific [27,28]. The demethylation resistance of oocyte-specific methylated CGIs during early human development may, in part, explain the increased number of placenta-specific gDMRs in the human genome. Interestingly, we found that ZFP57 was not expressed in human oocytes. Because replication-dependent global demethylation of the maternal genome is not likely to occur during human preimplantation development, we speculate that the protection of gDMRs by ZFP57 may be dispensable in human oocytes. These data contribute to our understanding of the regulatory mechanism of human-specific genomic imprinting.

Both human and mouse oocytes showed bimodal gene body methylation patterns associated with transcription. While it is unclear whether transcription is the only determinant, transcription may be an important determinant of the oocyte methylomes. In mammals, DNMT3A and DNMT3B are de novo DNA methyltransferases whereas DNMT3L acts in a recruiting role. In mouse oocytes, Dnmt3a and Dnmt3l are essential for de novo DNA methylation, whereas Dnmt3b is poorly expressed and essentially dispensable [11,29]. In contrast, in human oocytes DNMT3B showed ~10-fold higher expression than DNMT3A, and DNMT3L was not expressed, suggesting that DNMT3B may be the critical de novo DNA methyltransferase during human oocyte growth. Interestingly, centromeric satellite repeats were highly methylated in human oocytes. These regions are known to be hypomethylated in mouse oocytes [30]. Human DNMT3B is reported to interact with centromere protein CENP-C and contribute to DNA methylation of centromeric satellite repeats [25]. Similarly, centromeric satellite repeats are demethylated in Dnmt3b mutant mice [31]. Therefore, the differential expression pattern of DNMT3B could explain this human-specific hyper-methylation of centromeric satellite repeats in oocytes.

It is suggested that evolutionarily young SINEs and LINEs are demethylated to a milder extent than older ones during human preimplantation development [7]. We found that SVAs and some LTRs containing CpG-rich VNTRs were much more preferentially protected from demethylation than SINEs and LINEs in human blastocysts. Paternal gDMRs also contained VNTRs and many VNTR-containing CGIs remained highly methylated in human blastocysts. Therefore, VNTRs might underlie the protection of paternal gDMRs and specific transposable elements from demethylation. The maintenance of DNA methylation of SVAs may be especially important because SVAs are currently active in the human genome and are involved in various human diseases [22,32]. While the underlying mechanism of the protection of VNTR-containing regions is currently unknown, it is noteworthy that VNTRs are related to RNA-directed DNA methylation in plants [33]. Many transposable elements including SVAs are expressed in human early embryos [7,9] and it is interesting to speculate that RNA might be involved in the demethylation resistance of VNTR-containing regions.

Overall, this work highlights both conserved and species-specific regulation of DNA methylation during early mammalian development. Our WGBS data of human gametes and blastocysts not only provide information to support our understanding of normal human developmental processes but also will be useful in interpreting studies on assisted reproductive technologies (ARTs). ARTs in humans are associated with an increased risk of imprinting disorders [34,35], and our data will aid in the safety evaluation of ARTs and the preimplantation epigenetic diagnosis of human embryos.

Materials and Methods

Sample collection

Human oocytes, sperm, blastocysts and umbilical cord blood cells were obtained with signed informed consent of the donors or the couples, and the approval of the Ethics Committee of Tohoku University School of Medicine (Research license 2013-1-57), associated hospitals, the Japan Society of Obstetrics and Gynecology and the Ministry of Education, Culture, Sports, Science and Technology (Japan). Altogether, 202 surplus oocytes and 80 surplus blastocysts were obtained from female patients (ages 26–

321

43) undergoing IVF treatment. The patients were healthy women with no habitual drug use and no particular past or familial disease history. We collected morphologically normal GV and MI oocytes from preovulatory follicles by intravaginal ultrasound-guided follicular aspiration after controlled ovarian hyperstimulation. To remove cumulus cells and the zona pellucida, oocytes were treated with hyaluronidase solution (JX Nippon Oil & Energy Corporation, Tokyo, Japan) and Tyrode's solution-Acidified (JX Nippon Oil & Energy Corporation) according to the manufacturer's instructions. Blastocysts were obtained by culturing early cleavage-stage embryos in Global Medium (LifeGlobal, Guilford, CT) overlaid with mineral oil. We used morphologically normal expanding or expanded blastocysts. The number of ICM cells is similar to, or a little lower than, that of trophectoderm (TE) cells in blastocysts at this stage [36]. Because ICM and TE cells show similar methylation levels [7,9] and the available embryos in this study were limited, we performed WGBS using whole blastocysts. Ejaculated sperm samples with normal volume, counting and rates of mortality were collected. Only motile sperm cells isolated by the swim-up method [37] were used.

Construction and sequencing of PBAT libraries

Oocytes and blastocysts were incubated in a lysis solution (0.1% SDS, 1 mg/ml proteinase K, 50 ng/μl carrier RNA (QIAGEN, Valencia, CA)) for 60 min at 37°C and then 15 min at 98°C. Genomic DNA was purified with phenol/chloroform extraction and ethanol precipitation. Sperm genomic DNA was prepared as described [38]. Genomic DNA of cord blood cells was purified with phenol/chloroform extraction and ethanol precipitation. Isolated genomic DNA was spiked with 5% (for oocytes and blastocysts) or 0.5% (for sperm and cord blood cells) unmethylated lambda DNA (Promega, Madison, WI). Bisulfite treatment was performed using the MethylCode Bisulfite Conversion Kit (Invitrogen, Carlsbad, CA).

PBAT libraries were prepared as previously described [10]. Briefly, the first-strand DNA was synthesized with the Klenow fragment (3′-5′ exo-) (NEB, Beverly, MA) using BioPEA2N4 (5′-biotin-ACA CTC TTT CCC TAC ACG ACG CTC TTC CGA TCT NNN N-3′). The biotinylated first-strand DNA was captured using Dynabeads M-280 Streptavidin (Invitrogen). The second-strand DNA was synthesized with the Klenow fragment (3′-5′ exo-) using PE-reverse-N4 (5′-CAA GCA GAA GAC GGC ATA CGA GAT NNN N-3′). After removing the first-strand DNA, the second strand was double stranded with Phusion Hot Start II High-Fidelity DNA Polymerase (Finnzymes, Woburn, MA) using Primer-3 (5′-AAT GAT ACG GCG ACC ACC GAG ATC TAC ACT CTT TCC CTA CAC GAC GCT CTT CCG ATC T-3′). For an oocyte PBAT library, PCR-amplification was performed with KAPA HiFi HotStart Uracil+ ReadyMix (2×) (Kapa Biosystems, Woburn, MA) using primers, (5′-CAA GCA GAA GAC GGC ATA CGA GAT-3′) and (5′- AAT GAT ACG GCG ACC ACC GAG ATC T-3′). The following program was used for the PCR-amplification: 10 cycles of 98°C for 15 sec, 65°C for 30 sec and 72°C for 30 sec. Concentrations of the PBAT libraries were measured by quantitative PCR (qPCR) using the Kapa Library Quantification Kit (Kapa Biosystems).

PBAT libraries were sequenced on the HiSeq 2000 or HiSeq 2500 platform (Illumina, CA, USA) with 100-bp single-end reads using the TruSeq SR Cluster Kit v3-cBot-HS and the TruSeq SBS Kit v3-HS (Illumina).

Mapping and methylation analysis

Sequenced reads were processed using the Illumina standard base-calling pipeline (v1.8.2) and the first 4 bases were trimmed to remove random primer sequences. The resulting reads were aligned to the reference genome (UCSC hg19) using Bismark [39] (v.0.9.0) with default parameters. For the oocyte library prepared with PCR-amplification, identical reads were treated as a single read to remove PCR duplicates. The methylation level of each cytosine was calculated using the Bismark methylation extractor. For CpG sites, reads from both strands were combined to calculate the methylation levels. Except for S1 Figure, methylation levels of CpGs covered with ≥3 reads were analyzed for oocytes and those of CpGs covered with ≥5 reads were analyzed for the other samples. Bisulfite conversion rates were estimated using reads that uniquely aligned to the lambda phage genome and were>99% for all samples. In this study, mC and hmC were indistinguishable because bisulfite sequencing cannot differentiate hmC from mC.

We also included available RRBS data of human oocytes, ICM and blastocysts [7,9] and WGBS data of human ICM [7], ES cells (H1, H9 and HUES6) and mouse oocytes [11]. Processed methylation data were downloaded from NCBI GEO (http://www.ncbi.nlm.nih.gov/geo) for ICM (Accession number: GSE49828 and GSE51239), blastocysts (Accession number: GSE51239), H1 (Accession number: GSM429321), H9 (Accession number: GSM706059) and HUES6 ES cells (Accession number: GSM1173778). The RRBS data from biological replicates were combined. For mouse oocytes [11], the raw reads were mapped to the reference genome (UCSC mm9) and analyzed as described above (only CpGs covered with ≥5 reads were used).

Annotations of genomic regions

Annotations of Refseq genes, CGIs and repeat sequences were downloaded from the UCSC Genome Browser. Refseq genes shorter than 300 bp (encoding microRNAs or small nucleolar RNAs in most cases) were excluded from our analyses. Promoters were defined as regions 1 kb upstream and downstream from transcription start sites of Refseq transcripts. For calculation of the mean methylation levels, we analyzed only CGIs and promoters containing ≥10 CpGs with sufficient coverage for calculation of the methylation levels. Similarly, we considered only repeat copies containing ≥5 CpGs for calculation of the mean methylation levels of repeat copies. The gene bodies were defined as transcribed regions of Refseq transcripts except for promoters. When several Refseq transcripts were assigned to a Refseq gene, the transcribed regions were merged into a single gene body. Regions and names of the 67 imprinted DMRs were defined as previously reported [17].

The CpG density was defined for each CpG site as the density of CpGs within 100 bp upstream and downstream regions (the number of CpGs was divided by 200). Gene ontology analyses were performed using the Database for Annotation, Visualization and Integrated Discovery (DAVID) [40]. The list of human and mouse homologs including HomoloGene IDs was downloaded from Mouse Genome Informatics (MGI, http://www.informatics.jax.org/). VNTRs were identified using Tandem Repeats Finder [41] (alignment parameters = 2, 5, 7; minimum alignment score = 150; maximum period size = 500). Sequence motifs among VNTRs were searched using DREME [42] (the consensus patterns of VNTRs of>70% and <50% methylated CGIs in Fig. 4G were used as positive and negative sequences, respectively).

Transcriptome analysis

Transcriptome data of human and mouse oocytes were previously reported [5,43]. The raw reads from biological replicates were combined and analyzed using Avadis NGS software with default parameters (version 1.5, Strand Scientific Intelligence).

Graphical presentation

Methylation levels of CpGs were visualized using Integrative Genomics Viewer (IGV) software (http://www.broadinstitute.org/igv/). Heatmaps and scatter plots were generated using the heatmap.2 function of the gplots package and the heatscatter function of the LSD package in R (http://www.R-project.org/), respectively. Violin plots were generated using the vioplot package (http://neoscientists.org/~plex/).

Sliding window-based analysis of methylation changes

We used a sliding window of 20 CpGs with a step size of 10 CpGs (the mean length was ~2 kb) for consideration of the successful identification of imprinted DMRs using sliding windows of 10 CpGs [44] and 25 CpGs [17]. We considered only windows containing ≥10 CpGs with sufficient coverage for calculation of the methylation levels (84% of windows were covered in all samples shown in Fig. 1). Windows were classified as increasing (or decreasing) if the methylation levels increased (or decreased) by > 20% and the changes were statistically significant according to Student's t-test with BH correction ($P<0.05$).

Bisulfite sequencing

DNA samples were treated with sodium bisulfite using an EZ DNA Methylation Kit (Zymo Research, Orange, CA) and PCR-amplified using TaKaRa EpiTaq^{TM} HS (Takara Bio, Shiga, Japan). The PCR products were cloned into the pGEM-T Easy vector (Promega) and individual clones were sequenced. The following primers were used: chr5: 662,283–663,402: (5′-GGG GTT AAG ATG GGA GTT ATG A-3′) and (5′-TAA ACA ACC CAA TCC CCA CA-3′), chr12: 20,704,525-20,706,004: (5′-GGG AGG AGG AGG AGT AGT AGG A-3′) and (5′-CCC ACT AAA AAC AAA ATC AAT ACC-3′), chr15: 89,952,271-89,953,061: (5′-GAT TTT TGT TAA TGA TTG GGT AGG A-3′) and (5′-CCC CAC AAT ATC TAC CCT CAT A-3′), chr21: 32,716,044-32,716,485: (5′-AGA AGT TAA GGG GGA AAG ATG A-3′) and (5′-TTC ACA AAT TAC ACC CAC TAC CTC-3′′), chrX: 3,732,573-3,734,579: (5′-TTA ATG GGG TAA AGG GGT TAG A-3′) and (5′-ACC AAA TAA ACC CCA CCC AAA C-3′), chrX: 153,694,352-153,694,774: (5′-GTG GGG TTT AAG GAA GGA GGT A-3′) and (5′-CAA TCA CCC ACA CAC AAC TCC-3′). The sex of blastocysts was determined by PCR amplification of the male-specific SRY locus using bisulfite-converted DNA with the following primers: Forward: (5′ -TGA AAT TAA ATA TAA GAA AGT GAG GGT TG- 3′) and Reverse: (5′ -CCA CAC ACT CAA AAA TAA AAC ACC A- 3′).

Accession number

All sequencing data are deposited in the Japanese Genotype-phenotype Archive under the accession number JGA S00000000006.

Supporting Information

S1 Figure Summary of whole genome bisulfite sequencing. A, Mean methylation levels of cytosines in oocytes. Methylation levels of individual cytosines covered with at least one read were analyzed. PCR amplification did not affect overall methylation levels of cytosines. H = A, T or C. **B,** Pearson correlation coefficients between replicates. Methylation levels of individual CpGs covered with at least 3 reads were used for the calculation. Correlation coefficients were high (>0.70) in all cases. **C,** Mean methylation levels of individual non-CpG sites. Non-CpG sites covered with at least one read were analyzed. **D,** A density scatterplot of CpG and non-CpG methylation levels of

oocytes. The methylation levels were calculated with a non-overlapping sliding window of 10 kb. Cytosines covered with at least one read were analyzed. The density is color-coded as indicated. **E,** Mean methylation levels of imprinted DMRs (*KvDMR1*, *MEST* and *H19*) and the promoters of pluripotency genes (*POU5F1* and *NANOG*). The *KvDMR1* and *MEST* DMR were hypermethylated and the *H19* DMR, *POU5F1* and *NANOG* were hypomethylated in oocytes. In blastocysts, imprinted DMRs showed intermediate methylation levels but the pluripotency genes were hypomethylated. These patterns are frequently disrupted in poor-quality oocytes or preimplantation embryos derived from patients undergoing ART [14,15]. **F,** Proportions of CpGs covered by the oocyte WGBS data from this study and RRBS data [7]. Only CpGs covered with ≥3 reads were considered. **G,** Proportions of CpGs covered by the blastocyst WGBS data of this study and previously reported blastocyst/ICM WGBS or RRBS data [7,9]. Only CpGs covered with ≥5 reads were considered. **H,** A density scatterplot of mean methylation levels of CGIs in oocytes. A high correlation was observed between our WGBS data and reported RRBS data [7]. The density is color-coded as indicated. **I,** A density scatterplot of mean methylation levels of CGIs in blastocysts. A high correlation was observed between our WGBS data and reported RRBS data [9].
(TIF)

S2 Figure DNA methylation levels of specific genomic regions. A, Genomic distribution of windows. The proportions of windows overlapping promoters, exons, introns and intergenic regions are indicated. If a window overlaps more than two categories, the priority is as follows: 1) promoter, 2) exon, 3) intron, 4) intergenic region (*e.g.* if a window overlaps a promoter and an exon, it is classified as "promoter"). Sperm-specific methylated windows were abundant in intergenic regions. More than half of the windows hypomethylated in both gametes overlapped promoters. **B,** Distribution of mean methylation levels of windows, CGIs, promoters and repeat copies. A high proportion of hypomethylated repeat copies is evident in oocytes and blastocysts. **C,** Box plots of mean methylation levels of the sliding windows in human blastocysts. Boxes represent lower and upper quartiles and horizontal lines indicate the median. Whiskers extend to the most extreme data points within 1.5 times the interquartile range from the boxes. X-linked windows hypermethylated in oocytes showed ~10% higher methylation levels than autosomal ones.
(TIF)

S3 Figure Region-specific methylation changes during early human development. A, Violin plots of mean methylation levels of CGIs. Thin and thick lines are box plots and white dots indicate the median. **B,** Violin plots of mean methylation levels of promoters. Oocyte-specific methylated promoters preferentially showed low methylation levels in ES and blood cells. **C–F,** Violin plots of mean methylation levels of repeat copies. SINEs, LINEs, LTRs and DNA repeats were demethylated similarly to other genomic regions in blastocysts.
(TIF)

S4 Figure Stability of gDMRs and oocyte-specific methylated CGIs. A, A heatmap of mean methylation levels of gDMRs in H1 (GEO accession number: GSM429321) and HUES6 (GEO accession number: GSM1173778) ES cells. Among gDMRs other than placenta-specific ones, 13 and 9 DMRs showed >75% methylation in H1 and HUES6 ES cells, respectively. Methylation levels are color-coded as indicated. **B,** Methylation patterns of three oocyte-specific methylated CGIs. Black and white circles indicate methylated and unmethylated

residues, respectively. The percentages of methylated CpG sites are indicated.
(TIF)

S5 Figure   Relationships between methylation levels and CpG densities. Mean methylation levels of CpGs in six repeat families are plotted against CpG densities. All genomic CpGs were also analyzed for comparison. Mean methylation levels were calculated only for CpG densities with>1000 CpG sites covered by all samples. Transposable elements were essentially highly methylated in ES and blood cells. Low methylation levels of CpGs were observed in oocytes and blastocysts regardless of the CpG density. In sperm, CpGs in SINEs, LTRs and satellites showed especially low methylation levels at high CpG densities.
(TIF)

S1 Table   DNA methylation levels of imprinted DMRs. DMRs are classified into four groups: Maternal gDMRs; oocyte-specific methylated gDMRs with 35–65% methylation levels in blood cells, Paternal gDMRs; sperm-specific methylated gDMRs with 35–65% methylation levels in blood cells, Placenta-specific maternal gDMRs; maternal gDMRs maintained only in the placenta, Secondary DMRs; DMRs other than gDMRs. For secondary DMRs, neighboring gDMRs are indicated. While the *ZC3H12C* and *LIN28B* DMRs are classified as secondary DMRs, these may be placenta-specific maternal gDMRs (the methylation levels in oocytes were 76.0% and 77.4%, respectively).
(XLSX)

S2 Table   Gene body methylation and transcription levels in human and mouse oocytes. Only genes longer than 5 kb were analyzed. Homologous genes between the human and mouse are shown with HomoloGene IDs.
(XLSX)

S3 Table   DNA methylation levels of repeat sequences. We analyzed SINEs, LINEs, LTRs, DNA repeats, SVAs and satellites with>100 copies in the human genome. Mean methylation levels of CpGs are shown.
(XLSX)

S4 Table   Proportion of repeat copies highly methylated in human blastocysts. We analyzed SINEs, LINEs, LTRs, DNA repeats, SVAs and satellites with>100 copies in the human genome. Proportions of repeat copies overlapping>70% methylated windows are indicated.
(XLSX)

Author Contributions

Conceived and designed the experiments: HO HC TA. Performed the experiments: HO HC HHi HHa. Analyzed the data: HO MS TA. Contributed reagents/materials/analysis tools: AS TU HK HY AT. Wrote the paper: HO HC TA.

References

1. Messerschmidt DM, Knowles BB, Solter D (2014) DNA methylation dynamics during epigenetic reprogramming in the germline and preimplantation embryos. Genes Dev 28: 812–828.
2. Smith ZD, Meissner A (2013) DNA methylation: roles in mammalian development. Nat Rev Genet 14: 204–220.
3. Saitou M, Kagiwada S, Kurimoto K (2012) Epigenetic reprogramming in mouse pre-implantation development and primordial germ cells. Development 139: 15–31.
4. Smallwood SA, Tomizawa S, Krueger F, Ruf N, Carli N, et al. (2011) Dynamic CpG island methylation landscape in oocytes and preimplantation embryos. Nat Genet 43: 811–814.
5. Kobayashi H, Sakurai T, Imai M, Takahashi N, Fukuda A, et al. (2012) Contribution of intragenic DNA methylation in mouse gametic DNA methylomes to establish oocyte-specific heritable marks. PLoS Genet 8: e1002440.
6. Kohli RM, Zhang Y (2013) TET enzymes, TDG and the dynamics of DNA demethylation. Nature 502: 472–479.
7. Guo H, Zhu P, Yan L, Li R, Hu B, et al. (2014) The DNA methylation landscape of human early embryos. Nature 511: 606–610.
8. Beaujean N, Hartshorne G, Cavilla J, Taylor J, Gardner J, et al. (2004) Non-conservation of mammalian preimplantation methylation dynamics. Curr Biol 14: R266–267.
9. Smith ZD, Chan MM, Humm KC, Karnik R, Mekhoubad S, et al. (2014) DNA methylation dynamics of the human preimplantation embryo. Nature 511: 611–615.
10. Miura F, Enomoto Y, Dairiki R, Ito T (2012) Amplification-free whole-genome bisulfite sequencing by post-bisulfite adaptor tagging. Nucleic Acids Res 40: e136.
11. Shirane K, Toh H, Kobayashi H, Miura F, Chiba H, et al. (2013) Mouse oocyte methylomes at base resolution reveal genome-wide accumulation of non-CpG methylation and role of DNA methyltransferases. PLoS Genet 9: e1003439.
12. Wang L, Zhang J, Duan J, Gao X, Zhu W, et al. (2014) Programming and inheritance of parental DNA methylomes in mammals. Cell 157: 979–991.
13. Molaro A, Hodges E, Fang F, Song Q, McCombie WR, et al. (2011) Sperm methylation profiles reveal features of epigenetic inheritance and evolution in primates. Cell 146: 1029–1041.
14. Al-Khtib M, Blachere T, Guerin JF, Lefevre A (2012) Methylation profile of the promoters of Nanog and Oct4 in ICSI human embryos. Hum Reprod 27: 2948–2954.
15. Denomme MM, Mann MR (2012) Genomic imprints as a model for the analysis of epigenetic stability during assisted reproductive technologies. Reproduction 144: 393–409.
16. Ferguson-Smith AC (2011) Genomic imprinting: the emergence of an epigenetic paradigm. Nat Rev Genet 12: 565–575.
17. Court F, Tayama C, Romanelli V, Martin-Trujillo A, Iglesias-Platas I, et al. (2014) Genome-wide parent-of-origin DNA methylation analysis reveals the intricacies of human imprinting and suggests a germline methylation-independent mechanism of establishment. Genome Res 24: 554–569.
18. Li X, Ito M, Zhou F, Youngson N, Zuo X, et al. (2008) A maternal-zygotic effect gene, Zfp57, maintains both maternal and paternal imprints. Dev Cell 15: 547–557.
19. Bourc'his D, Xu GL, Lin CS, Bollman B, Bestor TH (2001) Dnmt3L and the establishment of maternal genomic imprints. Science 294: 2536–2539.
20. Huntriss J, Hinkins M, Oliver B, Harris SE, Beazley JC, et al. (2004) Expression of mRNAs for DNA methyltransferases and methyl-CpG-binding proteins in the human female germ line, preimplantation embryos, and embryonic stem cells. Mol Reprod Dev 67: 323–336.
21. Smith ZD, Chan MM, Mikkelsen TS, Gu H, Gnirke A, et al. (2012) A unique regulatory phase of DNA methylation in the early mammalian embryo. Nature 484: 339–344.
22. Wang H, Xing J, Grover D, Hedges DJ, Han K, et al. (2005) SVA elements: a hominid-specific retroposon family. J Mol Biol 354: 994–1007.
23. Lania L, Di Cristofano A, Strazzullo M, Pengue G, Majello B, et al. (1992) Structural and functional organization of the human endogenous retroviral ERV9 sequences. Virology 191: 464–468.
24. Schueler MG, Sullivan BA (2006) Structural and functional dynamics of human centromeric chromatin. Annu Rev Genomics Hum Genet 7: 301–313.
25. Gopalakrishnan S, Sullivan BA, Trazzi S, Della Valle G, Robertson KD (2009) DNMT3B interacts with constitutive centromere protein CENP-C to modulate DNA methylation and the histone code at centromeric regions. Hum Mol Genet 18: 3178–3193.
26. Xue Z, Huang K, Cai C, Cai L, Jiang CY, et al. (2013) Genetic programs in human and mouse early embryos revealed by single-cell RNA sequencing. Nature 500: 593–597.
27. Kobayashi H, Yanagisawa E, Sakashita A, Sugawara N, Kumakura S, et al. (2013) Epigenetic and transcriptional features of the novel human imprinted lncRNA GPR1AS suggest it is a functional ortholog to mouse Zdbf2linc. Epigenetics 8: 635–645.
28. Proudhon C, Duffie R, Ajjan S, Cowley M, Iranzo J, et al. (2012) Protection against de novo methylation is instrumental in maintaining parent-of-origin methylation inherited from the gametes. Mol Cell 47: 909–920.
29. Hirasawa R, Chiba H, Kaneda M, Tajima S, Li E, et al. (2008) Maternal and zygotic Dnmt1 are necessary and sufficient for the maintenance of DNA

methylation imprints during preimplantation development. Genes Dev 22: 1607–1616.

30. Yamagata K, Yamazaki T, Miki H, Ogonuki N, Inoue K, et al. (2007) Centromeric DNA hypomethylation as an epigenetic signature discriminates between germ and somatic cell lineages. Dev Biol 312: 419–426.

31. Ueda Y, Okano M, Williams C, Chen T, Georgopoulos K, et al. (2006) Roles for Dnmt3b in mammalian development: a mouse model for the ICF syndrome. Development 133: 1183–1192.

32. Hancks DC, Kazazian HH, Jr. (2010) SVA retrotransposons: Evolution and genetic instability. Semin Cancer Biol 20: 234–245.

33. Chandler VL (2010) Paramutation's properties and puzzles. Science 330: 628–629.

34. van Montfoort AP, Hanssen LL, de Sutter P, Viville S, Geraedts JP, et al. (2012) Assisted reproduction treatment and epigenetic inheritance. Hum Reprod Update 18: 171–197.

35. Hiura H, Okae H, Miyauchi N, Sato F, Sato A, et al. (2012) Characterization of DNA methylation errors in patients with imprinting disorders conceived by assisted reproduction technologies. Hum Reprod 27: 2541–2548.

36. Hardy K, Handyside AH, Winston RM (1989) The human blastocyst: cell number, death and allocation during late preimplantation development in vitro. Development 107: 597–604.

37. Ushijima C, Kumasako Y, Kihaile PE, Hirotsuru K, Utsunomiya T (2000) Analysis of chromosomal abnormalities in human spermatozoa using multi-colour fluorescence in-situ hybridization. Hum Reprod 15: 1107–1111.

38. Bahnak BR, Wu QY, Coulombel L, Drouet L, Kerbiriou-Nabias D, et al. (1988) A simple and efficient method for isolating high molecular weight DNA from mammalian sperm. Nucleic Acids Res 16: 1208.

39. Krueger F, Andrews SR (2011) Bismark: a flexible aligner and methylation caller for Bisulfite-Seq applications. Bioinformatics 27: 1571–1572.

40. Huang da W, Sherman BT, Lempicki RA (2009) Systematic and integrative analysis of large gene lists using DAVID bioinformatics resources. Nat Protoc 4: 44–57.

41. Benson G (1999) Tandem repeats finder: a program to analyze DNA sequences. Nucleic Acids Res 27: 573–580.

42. Bailey TL (2011) DREME: motif discovery in transcription factor ChIP-seq data. Bioinformatics 27: 1653–1659.

43. Yan L, Yang M, Guo H, Yang L, Wu J, et al. (2013) Single-cell RNA-Seq profiling of human preimplantation embryos and embryonic stem cells. Nat Struct Mol Biol 20: 1131–1139.

44. Fang F, Hodges E, Molaro A, Dean M, Hannon GJ, et al. (2012) Genomic landscape of human allele-specific DNA methylation. Proc Natl Acad Sci U S A 109: 7332–7337.

45. Das R, Lee YK, Strogantsev R, Jin S, Lim YC, et al. (2013) DNMT1 and AIM1 Imprinting in human placenta revealed through a genome-wide screen for allele-specific DNA methylation. BMC Genomics 14: 685.

RESEARCH ARTICLE

De novo DNA methylation through the 5′-segment of the *H19* ICR maintains its imprint during early embryogenesis

Hitomi Matsuzaki[1,2], Eiichi Okamura[3], Takuya Takahashi[3], Aki Ushiki[3], Toshinobu Nakamura[4], Toru Nakano[5], Kenichiro Hata[6], Akiyoshi Fukamizu[1,2] and Keiji Tanimoto[1,2,*]

ABSTRACT

Genomic imprinting is a major monoallelic gene expression regulatory mechanism in mammals, and depends on gamete-specific DNA methylation of specialized *cis*-regulatory elements called imprinting control regions (ICRs). Allele-specific DNA methylation of the ICRs is faithfully maintained at the imprinted loci throughout development, even in early embryos where genomes undergo extensive epigenetic reprogramming, including DNA demethylation, to acquire totipotency. We previously found that an ectopically introduced *H19* ICR fragment in transgenic mice acquired paternal allele-specific methylation in the somatic cells of offspring, whereas it was not methylated in sperm, suggesting that its gametic and postfertilization modifications were separable events. We hypothesized that this latter activity might contribute to maintenance of the methylation imprint in early embryos. Here, we demonstrate that methylation of the paternally inherited transgenic *H19* ICR commences soon after fertilization in a maternal DNMT3A- and DNMT3L-dependent manner. When its germline methylation was partially obstructed by insertion of insulator sequences, the endogenous paternal *H19* ICR also exhibited postfertilization methylation. Finally, we refined the responsible sequences for this activity in transgenic mice and found that deletion of the 5′ segment of the endogenous paternal *H19* ICR decreased its methylation after fertilization and attenuated *Igf2* gene expression. These results demonstrate that this segment of the *H19* ICR is essential for its *de novo* postfertilization DNA methylation, and that this activity contributes to the maintenance of imprinted methylation at the endogenous *H19* ICR during early embryogenesis.

KEY WORDS: DNA methylation, Genomic imprinting, *Igf2/H19* locus, Early embryogenesis

INTRODUCTION

Genomic imprinting is an epigenetic phenomenon in mammals that causes parental-specific, monoallelic expression of a subset of autosomal genes. The unique expression patterns of imprinted genes are controlled by allele-specific DNA methylation of the *cis*-regulatory sequences, called the imprinting control regions (ICRs).

[1]Faculty of Life and Environmental Sciences, University of Tsukuba, Tsukuba, Ibaraki 305-8577, Japan. [2]Life Science Center of Tsukuba Advanced Research Alliance (TARA), University of Tsukuba, Tsukuba, Ibaraki 305-8577, Japan. [3]Graduate School of Life and Environmental Sciences, University of Tsukuba, Tsukuba, Ibaraki 305-8577, Japan. [4]Department of Animal Bio-Science, Nagahama Institute of Bio-Science and Technology, Nagahama, Shiga 526-0829, Japan. [5]Graduate School of Frontier Biosciences, Osaka University, Suita, Osaka 565-0871, Japan. [6]Department of Maternal-Fetal Biology, National Research Institute for Child Health and Development, Setagaya, Tokyo 157-8535, Japan.

*Author for correspondence (keiji@tara.tsukuba.ac.jp)

Because allelic DNA methylation of ICRs is acquired during gametogenesis, ICRs are also called germline differentially methylated regions (gDMRs) (Ferguson-Smith, 2011; Kelsey and Feil, 2013; Tomizawa and Sasaki, 2012). Recent genome-wide profiling has, however, revealed that the number of oocyte- or sperm-specific methylated genomic regions is far more than that of the known ICRs (Kobayashi et al., 2012; Smallwood et al., 2011). Therefore, germline methylation might not be restricted to ICRs, and both the ICRs and the other gDMRs could be methylated by a common mechanism without being strictly discriminated in the germ line (Kelsey and Feil, 2013).

During preimplantation development, although most gDMRs lose their gamete-derived methylation via epigenetic reprogramming activity, allelic methylation of ICRs is faithfully maintained (Kobayashi et al., 2012; Smallwood et al., 2011). Presumably, the methylation maintenance mechanism against genome-wide demethylation activity might operate at restricted genomic loci and selected alleles in preimplantation embryos. We and others have reported that Stella (also known as DPPA3) (Nakamura et al., 2007), KAP1 (also known as TRIM28) (Messerschmidt et al., 2012), and NuRD complex components (Ma et al., 2010; Reese et al., 2007), in addition to the maintenance methyltransferase DNMT1 (Hirasawa et al., 2008), help to maintain ICR methylation in preimplantation embryos. Because these factors have no sequence specificity for DNA binding or intrinsic DNA binding ability themselves, other sequence-specific DNA binding proteins must be required for their recruitment to specific target sites. The Krüppel-associated box (KRAB)-containing zinc-finger protein ZFP57, which was found to interact with KAP1, is a dominant candidate for such a protein (Li et al., 2008; Messerschmidt et al., 2012; Quenneville et al., 2011). However, because the depletion of ZFP57 did not always affect the methylation of ICRs (Li et al., 2008), other factors and their target *cis* elements are apparently engaged in the maintenance mechanism.

The *H19* ICR in the mouse *Igf2/H19* locus (Fig. 1A) is DNA-methylated by the DNMT3A-DNMT3L complex in prospermatogonia, the status of which is maintained on the paternal allele following fertilization (Kaneda et al., 2004; Tremblay et al., 1997), and it is thus classified as a gDMR. Whereas indispensable roles for CTCF (Matsuzaki et al., 2010; Schoenherr et al., 2003) and Sox-Oct binding motifs (Sakaguchi et al., 2013; Zimmerman et al., 2013) in maintaining maternal *H19* ICR hypomethylation during postimplantation periods are well established, little is known about the underlying mechanisms that maintain paternal *H19* ICR hypermethylation during preimplantation periods.

We previously tested the activity of the *H19* ICR in yeast artificial chromosome (YAC) transgenic mice (TgM), in which an *H19* ICR fragment (2.9 kb) was inserted into a YAC bearing the (nonimprinted) human β-globin locus (150 kb, Fig. 1B) to minimize position effects of transgene insertion sites (Tanimoto

3833

Fig. 1. DNA methylation status of the transgenic *H19* ICR in early embryos. (A) Structure of the mouse *Igf2/H19* locus. Mouse *Igf2* and *H19* (open boxes) are ~90 kb apart, and the expression of both genes depends on the shared 3′ enhancer (gray box). The *H19* ICR, located approximately at −4 to −2 kb relative to the transcription start site of *H19* is contained within a 2.9-kb *Sac*I (Sa)-*Bam*HI (B) fragment. Dots (1-4) indicate the position of CTCF binding sites. G; *Bgl*II site. (B) Structure of the ICR/β-globin YAC transgene. The 150-kb human β-globin locus YAC carries the LCR (gray box) and the β-like globin genes (open boxes). The 2.9-kb *H19* ICR fragment (inverted orientation) was introduced between the LCR and the ε-globin gene (Tanimoto et al., 2005). A gray bar below the map indicates sequences (region I′) analyzed by bisulfite sequencing. (C,D) Methylation status of the transgenic *H19* ICR in embryos. One- (C) or two-cell (D) embryos that inherited the ICR/β-globin YAC transgene (line 1048) either paternally (Pat.) or maternally (Mat.) were embedded in agarose beads (19-43 embryos per bead in C, 13-37 embryos per bead in D) and treated with sodium bisulfite. The beads were separately and directly used to amplify the region I′ of the transgenic *H19* ICR by nested PCR. PCR products were individually subcloned and sequenced. The results from single beads are presented together in a cluster. Each horizontal row represents a single DNA template molecule. The numbers on the right of each row indicate number of times the pattern was observed in the sequencing. Methylated and unmethylated CpG motifs are shown as filled and open circles, respectively. (E,F) A role of *de novo* DNA methyltransferases in the postfertilization methylation of the paternally inherited transgenic *H19* ICR. Two-cell (E) or blastocyst (F)-stage embryos were obtained from wild-type (WT), [*Dnmt3l*^{−/−}], [*Dnmt3a*^{2lox/2lox}, *Zp3-Cre*], or [*Dnmt3b*^{2lox/2lox}, *Zp3-Cre*] females crossed with the ICR/β-globin male TgM carrying WT Dnmts (5-24 embryos in E, 1-9 embryos in F). The methylation status of the paternally inherited transgenic *H19* ICR (region I′) was analyzed by bisulfite sequencing as described previously. (G) E8.5 embryos were obtained from WT or [*Dnmt3l*^{−/−}] females crossed with ICR/β-globin male TgM. Genomic DNA was extracted from each embryo and treated with sodium bisulfite, and region I′ of the transgenic *H19* ICR was amplified by nested PCR. PCR products were subcloned and sequenced. The results from single embryos are presented together in a cluster. Above each panel in E-G are genotypes of mothers.

et al., 2010; Park et al., 2004) suggested that two distinct methylation mechanisms operate at the endogenous *H19* ICR: one in the germ line, which is under the control of its surrounding sequences, and the other during the postfertilization period, which is governed by a hypothetical epigenetic mark preset within the *H19* ICR during gametogenesis. We speculated that the latter activity might be actively involved in the region-specific maintenance of allelic methylation at the endogenous *H19* ICR in preimplantation embryos.

In this study, we show that the paternal-allele-specific methylation of the transgenic *H19* ICR commences soon after fertilization in YAC-TgM, and that maternally supplied DNMT3A and DNMT3L are required for this process. By partially obstructing germline methylation of the endogenous *H19* ICR, we discovered that postfertilization methylation activity also exists at the endogenous *H19* ICR. Furthermore, in YAC-TgM, we substantially narrowed the responsible sequences for postfertilization methylation acquisition in the transgenic *H19* ICR. Finally, by deleting the responsible sequences from the endogenous locus, we noted a partial loss of methylation in the paternally inherited *H19* ICR after fertilization, diminished *Igf2* expression, and embryonic growth retardation in the offspring that paternally inherited the mutation. These results demonstrate that the postfertilization methylation imprinting activity of the *H19* ICR is essential for maintaining its imprinted methylation status once established during gametogenesis.

RESULTS
Methylation acquisition at the transgenic *H19* ICR in early embryos

The *H19* ICR fragment inserted into the β-globin YAC transgene (Fig. 1B) exhibited preferential DNA methylation in the somatic cells of offspring after paternal transmission, whereas it was not

et al., 2005). In somatic cells, the *H19* ICR fragment was preferentially methylated when paternally inherited, demonstrating that the 2.9-kb sequence contained sufficient information to recapitulate imprinted methylation. Surprisingly, however, the transgenic *H19* ICR was not methylated in the testes. In addition, randomly integrated *H19* ICR fragments in the mouse genome were hypermethylated in the paternal allele after fertilization, irrespective of their variable methylation levels in the testes of multiple TgM lines (Matsuzaki et al., 2009). It was therefore presumed that the *H19* ICR was marked by an epigenetic modification other than DNA methylation in the germ line, and that paternal allele-specific methylation was acquired after fertilization by referring to this hypothetical mark. Hence, our results and those of others (Gebert

DEVELOPMENT

methylated in sperm (Fig. S1A-C) (Tanimoto et al., 2005). As a first step in elucidating the mechanism of the allele-specific methylation of the transgenic *H19* ICR, we examined the timing of its acquisition in mouse early embryos. Bisulfite sequencing of the transgenic *H19* ICR (region I′ including the CTCF site 1, Fig. 1B) revealed that the paternally inherited ICR was moderately and heavily methylated in one- and two-cell stage embryos, respectively (Fig. 1C,D, Fig. S1D), the levels of which were substantially higher than in the maternally inherited alleles. While the DNA methylation level in region I′ in two-cell embryos was already high (Fig. 1D, Fig. S1D) and indistinguishable from that in blastocyst-stage embryos (Fig. S1E) (Matsuzaki et al., 2010), DNA methylation around CTCF binding site 4 of the paternally inherited *H19* ICR was low in blastocysts (region II, Fig. S1F), suggesting that DNA methylation acquisition directionally extends from a region near CTCF site 1. These results suggested that the paternally inherited transgenic *H19* ICR is recognized by the DNA methylation machinery soon after fertilization and becomes progressively methylated during embryonic development.

A role for DNMT3s in the postfertilization methylation of the transgenic *H19* ICR

Methylation acquisition in the endogenous *H19* ICR occurs in fetal prospermatogonia via the actions of DNMT3A and DNMT3L (Kaneda et al., 2004). However, the activity and targets, if any, of the DNMT3 family in early embryos remain obscure. We thus examined which DNMTs were involved in methylation acquisition in the transgenic *H19* ICR. Because the gene products present in early embryos soon after fertilization are mostly derived from oocytes, we assessed the roles of DNMTs on postfertilization methylation of the transgenic *H19* ICR after maternal disruption. To test the function of *Dnmt3l*, *Dnmt3l*-null (−/−) (Hata et al., 2002) females were mated with ICR/β-globin YAC transgenic (*Dnmt3l* wild-type) (Fig. 1B) (Tanimoto et al., 2005) males. Because *Dnmt3a*$^{-/-}$ or *Dnmt3b*$^{-/-}$ mice are not viable (Okano et al., 1999), we used Cre-loxP recombination to specifically eliminate these genes in growing oocytes via the *zona pellucida glycoprotein 3* (*Zp3*) promoter-*Cre* transgene (de Vries et al., 2000; Dodge et al., 2005; Kaneda et al., 2004). After confirming that *Dnmt3* gene products were depleted in both oocytes and early embryos by quantitative reverse transcription-polymerase chain reaction (RT-qPCR) (Fig. S2), we analyzed the methylation status of the transgenic *H19* ICR fragment. In *Dnmt3l*-deficient two-cell embryos, the paternally inherited transgenic *H19* ICR was hypomethylated (Fig. 1E). Depletion of maternally provided *Dnmt3a* gene product also caused hypomethylation of the transgenic *H19* ICR, whereas the loss of the *Dnmt3b* gene product did not affect its methylation (Fig. 1E). These results demonstrated that the postfertilization methylation acquisition of the paternally inherited transgenic *H19* ICR required both DNMT3A and DNMT3L, which were maternally provided to early embryos.

We next examined whether zygotic expression of Dnmts (Fig. S2) (Guenatri et al., 2013; Hu et al., 2008) would compensate for a loss of maternally provided DNMT3L in transgenic *H19* ICR methylation during embryogenesis. The paternally inherited transgenic *H19* ICR remained unmethylated in blastocyst-stage embryos derived from *Dnmt3l*$^{-/-}$ mothers (Fig. 1F). The unmethylated state of the transgenic *H19* ICR did not change even at embryonic day (E) 8.5, despite the fact that allele-nonspecific methylation, probably elicited by postimplantation *de novo* DNA methylation activity, was observed outside of the DMR (Fig. 1G).

(Matsuzaki et al., 2010). These results demonstrated that the paternally inherited transgenic *H19* ICR must be recognized by the DNA methylation machinery, including DNMT3A and DNMT3L, in early embryos to acquire imprinted methylation.

Evaluation of the postfertilization methylation activity at the endogenous *H19* ICR

Although the transgenic *H19* ICR possesses intrinsic activity to acquire paternal allele-specific methylation in early embryos, it is unclear whether this activity also exists at the endogenous locus. Because the endogenous *H19* ICR is fully methylated in sperm, the postfertilization methylation activity at the endogenous locus, if present, is normally difficult to reveal. Our previous results (Matsuzaki et al., 2009) and those of others (Gebert et al., 2010; Park et al., 2004; Puget et al., 2015) suggested that the gametic methylation of the *H19* ICR was governed by signals from surrounding sequences, i.e. those located outside the 2.9-kb *H19* ICR region. Therefore, by interfering with the transmission of these hypothetical signals and subsequent methylation during spermatogenesis, we sought to verify the postfertilization methylation imprinting activity at the endogenous locus. To this end, we inserted tandemly arrayed chicken HS4 core sequences, (cHS4c)$_2$,on both sides of the endogenous *H19* ICR (Fig. 2A), expecting that this would block a presumptive signal to direct DNA methylation of the *H19* ICR in the germ line, as the cHS4 itself was unmethylated in both germ and somatic cells when it was substituted for the endogenous *H19* ICR (Szabo et al., 2002). Importantly, during the postfertilization period, the same manipulation does not prevent methylation imprinting activity in the context of YAC-TgM (Okamura et al., 2013a). Embryonic stem cells (ESCs) were modified by homologous recombination, and accurate targeting events were confirmed by Southern blotting (Fig. S3A,B). Following the establishment of two knock-in mouse lines (Fig. S3B), the neo^r selectable marker was excised by mating them with Cre-expressing TgM (Fig. S3C).

Germline methylation of the endogenous *H19* ICR is inhibited by flanking insulator sequences

We examined the methylation status of the insulated *H19* ICR allele in sperm by bisulfite sequencing. The (cHS4c)$_2$ sequences on both sides of the *H19* ICR were hypomethylated (Fig. 2B). In addition, the *H19* ICR region containing CTCF sites 3 and 4 was also methylated at very low levels. Furthermore, the region around the CTCF sites 1 and 2 was significantly less methylated (Fig. 2B) in comparison to the fully methylated sequences in the wild-type allele (Fig. S3D) (*P*<0.0001, Mann–Whitney U-test; http://quma.cdb.riken.jp/). Southern blotting using methylation-sensitive restriction enzymes confirmed these results (Fig. S4A,B). These results indicated that the flanking (cHS4c)$_2$ fragments at the endogenous *H19* ICR inhibited its methylation acquisition during spermatogenesis. It was reported that USF1 binding to cHS4 sequences induces histone H3/H4 acetylation and H3K4 methylation, thereby interfering with the spread of repressive histone modifications (such as H3K9 methylation) and heterochromatin formation (West et al., 2004). We therefore infer that intrusion of the repressive chromatin state into the *H19* ICR from outside might be a prerequisite for its gametic methylation and that flanking cHS4c might block this process. Alternative hypotheses might be that VEZF1-bound cHS4c sequences or simply its CpG island-like nature somehow interfered with the *de novo* DNA methylation of the neighboring *H19* ICR only during spermatogenesis (Dickson et al., 2010; Kobayashi et al., 2012; Smallwood et al., 2011). It is also possible that cHS4c
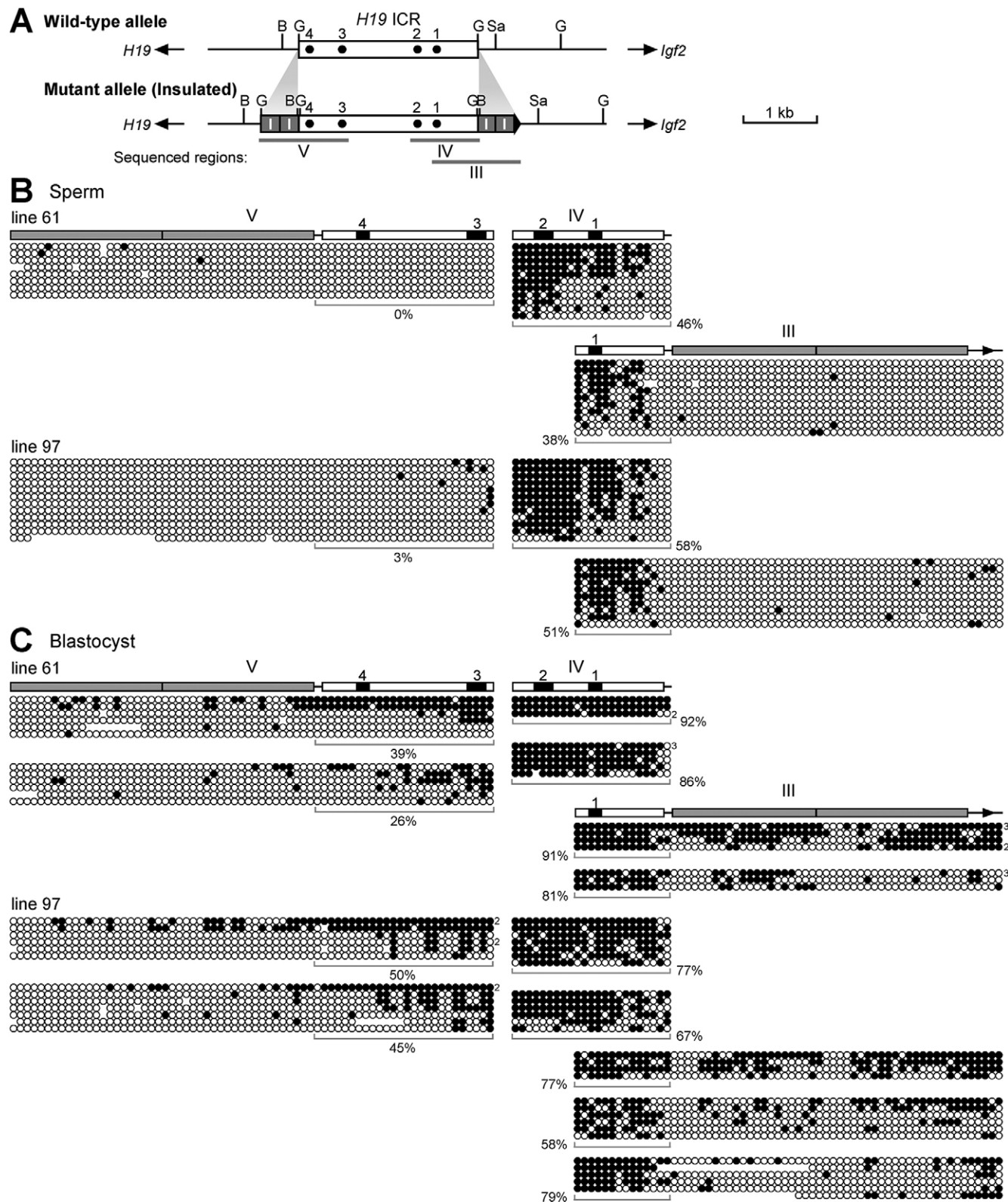
328

Fig. 2. DNA methylation status of the insulated *H19* ICR in sperm and blastocysts. (A) Map of the wild-type and mutant *H19* loci. Tandem cHS4 core fragments (gray rectangles, I for insulator) were inserted at both sides of the *H19* ICR [at *Bgl*II (G) sites: mutant allele] (see also Fig. S3). Three regions of the mutant allele (III, IV, and V; gray bars beneath the map) were analyzed by bisulfite sequencing in B and C. B, *Bam*HI; Sa, *Sac*I sites; dots 1-4, CTCF binding sites. (B) Genomic DNA extracted from sperm of mutant mice (lines 61 and 97) was digested with *Xba*I and treated with sodium bisulfite. Three regions of the mutant allele were amplified by PCR, subcloned, and sequenced. The overall percentage of methylated CpGs in region IV or those in the ICR portions of region III or V are indicated next to each panel. (C) Blastocyst-stage embryos that inherited the mutant allele paternally were embedded in agarose beads (6-12 embryos per bead) and treated with sodium bisulfite. The beads were used for amplifying three regions of the mutant allele by PCR, and the resulting fragments were individually subcloned and sequenced.

sequences interfered with transcription read-through at the *H19* ICR, which has been suggested to induce its methylation in male germ cells (Henckel et al., 2012).

Allele-specific postfertilization DNA methylation at the insulated *H19* ICR

We next examined the methylation status of the insulated *H19* ICR after fertilization. In blastocyst-stage embryos (Fig. 2C), as well as in the somatic cells of neonates (Fig. S4A,C-E), the paternally inherited insulated *H19* ICR exhibited higher methylation levels than those observed in sperm (Fig. 2B). The markedly elevated level of methylation in $(cHS4c)_2$ sequences on the paternal allele (Fig. S4E) was probably a secondary consequence of imprinted methylation of the adjacent *H19* ICR as the same sequences were unmethylated after maternal transmission. These results demonstrated that the endogenous *H19* ICR was methylated after fertilization in a paternal allele-specific manner, and that the methylation acquisition commenced during the preimplantation period.

In the YAC-TgM, transgenic *H19* ICR methylation in early embryos was dependent on maternally provided DNMT3L and DNMT3A (Fig. 1E,F). We therefore examined whether the same DNA methyltransferases were operating at the endogenous insulated *H19* ICR. When $Dnmt3l^{-/-}$ female mice were bred, the paternally inherited insulated *H19* ICR region (region IV in Fig. 3A) was less methylated in blastocyst (Fig. 3B) than in control embryos (WT), indicating that DNMT3L is involved in the methylation of the endogenous *H19* locus. In addition, the effect of maternal DNMT3L depletion on the postfertilization methylation at the endogenous insulated *H19* ICR was observed in as early as 2-cell embryos (Fig. 3C), the same timing when postfertilization methylation acquisition took place in the YAC TgM (Fig. 1D).

Taken together, these results suggest that postfertilization paternal allele-specific methylation activity also exists in the endogenous *H19* ICR, which is probably governed by a shared mechanism with the transgenic *H19* ICR.

Defining the *H19* ICR DNA sequences essential for allele-specific postfertilization DNA methylation in YAC-TgM

To further elucidate the mechanisms underlying the postfertilization methylation of the *H19* ICR, we sought to more precisely define its responsive sequences. To this end, we employed a YAC-TgM system, in which the methylation activity is clearly detectable after fertilization because of its unmethylated state in sperm. We previously demonstrated that the 1.7-kb 'ICR21' fragment covering CTCF sites 1 and 2 (Fig. 4A) was sufficient to recapitulate paternal allele-specific DNA methylation after fertilization in YAC-TgM (Okamura et al., 2013b). We thus generated a series of 5′-truncated *H19* ICR fragments: the ICR4321S fragment, in which the 5′-end of the 2.9-kb *H19* ICR fragment (766 bp) was deleted but all four CTCF sites remained; and the ICR432 fragment, which is 173 bp shorter than the ICR4321S fragment and lacks CTCF site 1 (Fig. 4A). To reduce the time required to obtain mouse lines carrying intact single-copy YAC transgenes, these two fragments were individually floxed using hetero-specific *loxP* sequences, combined to employ a co-placement strategy (Tanimoto et al., 2008), and introduced 3′ to the locus control region (LCR) in the human β-globin YAC (Fig. S5A). YAC-TgM were generated by pronuclear injection and intact, single-copy transgene carriers were identified (Fig. S5A,B). Parental YAC-TgM lines (Numbers 443 and 429) were crossed with Cre-TgM to initiate *in vivo* Cre-loxP recombination, which generated daughter lines carrying either the ICR4321S or ICR432
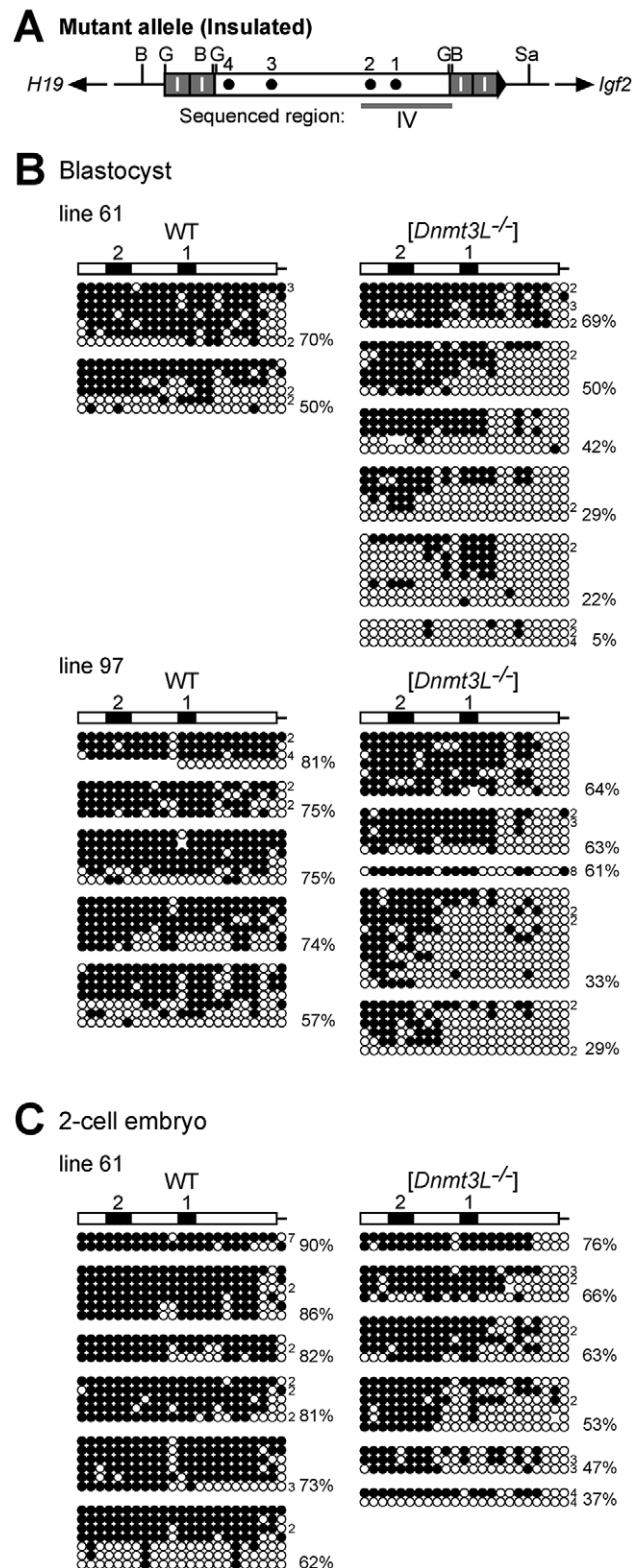
Fig. 3. Function of DNMT3L in postfertilization methylation of the paternally inherited insulated *H19* ICR. Blastocyst (lines 61 and 97) and 2-cell (line 61) stage embryos were obtained from wild-type (WT) or $[Dnmt3l^{-/-}]$ females crossed with male mice carrying mutant (insulated) *H19* ICR allele. DNA methylation status of region IV (shown in A, map legend as per Fig. 2A) of the paternally inherited mutant allele was analyzed by bisulfite sequencing, as described above, for blastocyst- (B) and 2-cell stage embryos (C). Three to 10 (blastocyst) or 13 to 30 (2-cell) embryos per agarose bead were used. Above each panel in B and C are genotypes of mothers.

transgene at the identical chromosomal integration site (Fig. 4B, Fig. S5C,D).

We examined the methylation status of the transgene fragments in somatic cells by Southern blotting (Fig. 4C). The ICR4321S fragment was hypomethylated regardless of its parental origin (Fig. 4D). The methylation status was also determined by bisulfite sequencing. Region VII, covering CTCF sites 3 and 4 (Fig. 5A), was hypomethylated regardless of parental origin (Fig. 5B). Although region VI, containing CTCF sites 1 and 2 (Fig. 5A), was partially methylated, its overall methylation level was low and equally observed on both alleles, implying that this methylation acquisition was allele-nonspecific (Fig. 5B). Because hypomethylation of the

paternally inherited ICR4321S fragment was also observed in two-cell embryos (Fig. 5C), it is suggested that the ICR4321S fragment lost its ability to acquire *de novo* DNA methylation in the early embryo. As was seen in the wild-type 2.9-kb *H19* ICR TgM (Fig. S1B,C) (Tanimoto et al., 2005), the ICR4321S fragment was not methylated in testis (Fig. S6E), indicating that the deleted sequence was not involved in methylation regulation of the *H19* ICR in male germ cells. Essentially the same phenotype, i.e. hypomethylation on both parental alleles in somatic cells (Fig. S6A-C) and in male germ cells (Fig. S6D), was observed in the shorter ICR432 fragment TgM. These results demonstrated that the 5′-region of the *H19* ICR is necessary for postfertilization allele-
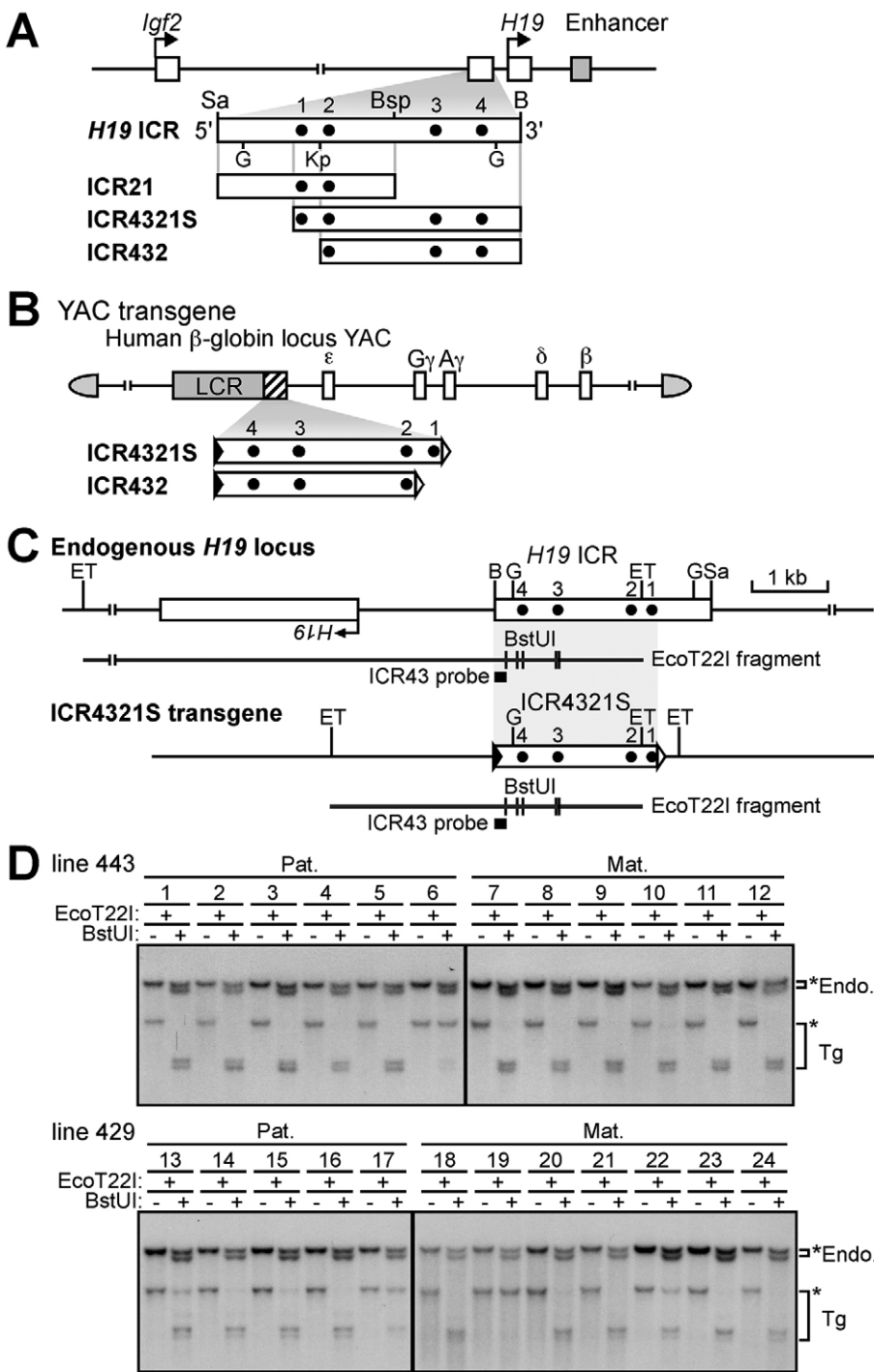
Fig. 4. Generation and DNA methylation analysis of the YAC-TgM carrying the 5′-truncated *H19* ICR fragments. (A) Schematic representation of the *H19* ICR, ICR21 (Okamura et al., 2013b), ICR4321S, and ICR432 DNA fragments. Sa, *Sac*I; B, *Bam*HI; Bsp, *Bsp*EI; G, *Bgl*II; Kp, *Kpn*I sites; dots 1-4, CTCF binding sites. (B) The ICR4321S and ICR432 fragments were inserted 3′ to the LCR in the human β-globin YAC, and YAC-TgM were generated (see also Fig. S5). (C) Partial restriction enzyme maps of the endogenous *H19* locus and the β-globin YAC transgene with the inserted ICR4321S fragment. Methylation-sensitive *Bst*UI sites in the *Eco*T22I (ET) fragments are displayed as vertical lines beneath each map. The ICR43 probe used for Southern blotting in D is shown as a filled rectangle. (D) DNA methylation status of the ICR4321S fragment in somatic cells of the YAC-TgM (lines 443 and 429) that inherited the transgenes either paternally (Pat.) or maternally (Mat.). Tail DNA was digested with *Eco*T22I and then *Bst*UI, and the blot was hybridized with the ICR43 probe. Endo., endogenous locus; Tg, transgene. Asterisks indicate the positions of parental or methylated undigested fragments.
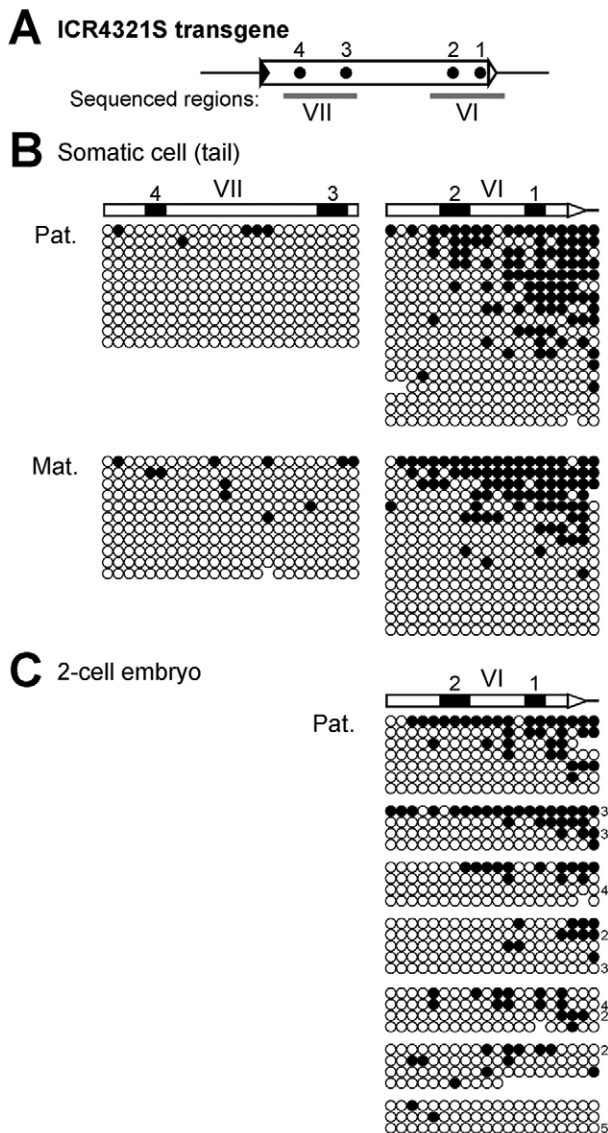
Fig. 5. DNA methylation status of the ICR4321S transgene in tail somatic cells and preimplantation embryos. (A) Map of the ICR4321S fragment. Two regions (VI and VII) analyzed by bisulfite sequencing in B and C are shown as gray bars beneath the map. (B) DNA methylation status of regions VI and VII in somatic cells of the ICR4321S YAC-TgM (line 443) that inherited the transgenes either paternally (Pat.) or maternally (Mat.). Tail DNA was digested with *Xba*I and treated with sodium bisulfite. Two regions were amplified by nested PCR, subcloned, and sequenced. (C) The DNA methylation status of region VI in 2-cell embryos that inherited the ICR4321S YAC transgene paternally (Pat.) (line 443) was analyzed by bisulfite sequencing as described previously. 16-38 embryos per bead were used.

specific methylation acquisition, which commences during early embryogenesis, in YAC-TgM.

The role of the 5′-region of the *H19* ICR in allele-specific methylation at the endogenous locus

To elucidate whether the 5′-end of the *H19* ICR was also essential for its allele-specific methylation at the endogenous locus, we removed a 765-bp sequence, which we deleted in the ICR4321S fragment, from the endogenous *H19* ICR (Fig. 6A, Fig. S7). ESCs were transformed with the targeting vector, in which the 765-bp sequence was flanked by *loxP* sequences (Fig. S7A). Properly targeted ESCs were identified by Southern blotting and used for

generating a knock-in mouse line (Fig. S7B). The 765-bp sequence and neo^r selectable marker were simultaneously excised from the parental allele by crossing with Cre-expressing TgM, and the precise recombination events were monitored by Southern blotting (5′ICR-KO allele; Fig. S7C).

We first examined the methylation status of the paternally inherited 5′ICR-KO allele in somatic cells (tail tips) of the mutant mice by Southern blotting. The methylation levels of the remaining *H19* ICR sequences were partially reduced in more than half of the offspring (Fig. 6A,B). To further clarify the methylation status, we conducted bisulfite sequencing analysis of the DNA region covering CTCF sites 1 and 2. Based on the Southern blotting results (Fig. 6B), DNA samples from mutant mice carrying highly (numbers 1 and 2) and partially (numbers 3-8 and 9-13) methylated paternally inherited knock out (KO) alleles were individually pooled and subjected to analysis. Consistent with the Southern blotting data, some sequenced clones exhibited partial loss of methylation, particularly around the internal region of the residual *H19* ICR. By contrast, the wild-type paternal allele was fully methylated (Fig. 6C). To explore the reason behind the diminished methylation on the paternal KO allele, we conducted methylation analysis of sperm and preimplantation embryos (1-cell, 2-cell and blastocyst stages). Although the KO allele was fully methylated in sperm (Fig. 6D), the paternally inherited KO allele exhibited a partial loss of methylation even in 1-cell stage embryos (Fig. 6E). These results suggested that the 5′-region of the *H19* ICR was essential for its *de novo* DNA methylation at the endogenous, as well as at the transgene loci, in early embryos, and contributed to ensuring the maintenance of differential methylation during this developmental period.

The partial loss of methylation on the paternal KO allele was also observed in E12.5 embryos (Fig. 7A). Because the *H19* ICR methylation status regulates *Igf2* and *H19* transcription (Bell and Felsenfeld, 2000; Hark et al., 2000; Srivastava et al., 2000), we analyzed the expression of these genes. The expression levels of *Igf2* and *H19* were decreased and increased, respectively, in the livers of E12.5 embryos inheriting the KO allele paternally, when compared with littermate controls (Fig. 7B). Importantly, the degree of methylation loss at the *H19* ICR in each embryo correlated highly with the change in gene expression levels. While the product of *Igf2* promotes fetal growth (DeChiara et al., 1991), that of *H19* [non-coding RNA, carrying a micro RNA (miR-675) sequence] has been proposed to act as a growth repressor (Gabory et al., 2010). In accordance with the expected functions of these genes, the embryos (E12.5) carrying a paternally inherited KO allele tended to be smaller than control embryos from the same litter (Fig. S8). These results suggested that the 5′-region of the *H19* ICR played an essential role in normal *Igf2/H19* expression and fetal growth through the maintenance of paternal allele-specific methylation status after fertilization.

DISCUSSION

Using a genetic strategy, we found that maternally supplied DNMT3A and DNMT3L enzymes are essential for the *de novo* DNA methylation of the paternally inherited transgenic *H19* ICR in preimplantation embryos (Fig. 1E). Even in the presence of these enzymes (Fig. S2) (Guenatri et al., 2013; Hirasawa et al., 2008), the maternally inherited transgenic (Fig. 1C,D) and endogenous *H19* ICRs do not acquire methylation. Therefore, it was strongly suggested that an epigenetic mark other than DNA methylation is set within the transgenic *H19* ICR during gametogenesis, and after fertilization, the mark is used for discriminating the parental alleles
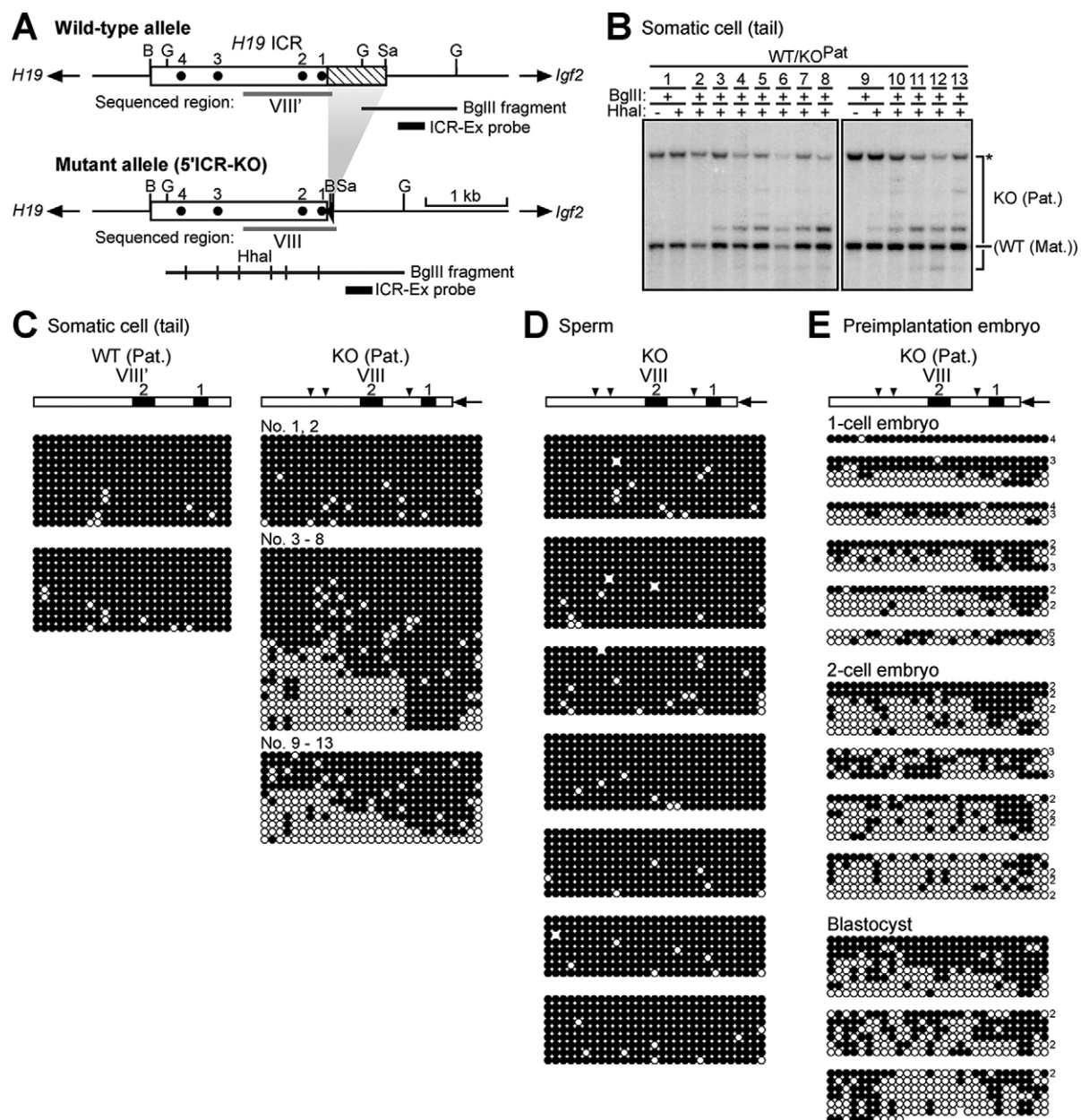
Fig. 6. DNA methylation status of the 5′-deleted endogenous *H19* ICR. (A) Map of the wild-type and mutant *H19* gene loci. The *H19* ICR 5′-region (765 bp, shaded area) was excised from the endogenous locus (mutant allele 5′ICR-KO; see also Fig. S7). Methylation-sensitive *Hha*I sites in the *Bgl*II (G) fragment are displayed as vertical lines beneath the mutant allele map. The ICR-Ex probe used for Southern blotting in B is shown as a filled rectangle. The *Bgl*II fragment detected in the wild-type allele does not have a *Hha*I site. Gray bars below each map (VIII and VIII′) indicate regions analyzed by bisulfite sequencing in C, D and E. B, *Bam*HI; Sa, *Sac*I sites; dots 1-4, CTCF binding sites. (B) DNA methylation status of the paternally inherited mutant (5′ICR-KO) allele in tail somatic cells. Tail DNA of mutant mice (WT/KO^pat) was digested with *Bgl*II and then *Hha*I, and the blot was hybridized with the ICR-Ex probe. Asterisks indicate the positions of parental or methylated, undigested fragments. (C) DNA methylation status of the paternally inherited wild-type (region VIII′) or 5′ICR-KO (region VIII) *H19* ICR in somatic cells. Tail DNA was pooled, digested with *Xba*I, and treated with sodium bisulfite. Each region was amplified by PCR, subcloned, and sequenced. The numbers above each panel in the 5′ICR-KO results are the ID numbers of pooled samples (in B). The position of the *Hha*I sites in region VIII are shown by arrowheads. (D) DNA methylation status of the 5′ICR-KO allele (region VIII) in sperm from 7 mutant males was analyzed by bisulfite sequencing. (E) DNA methylation status of the paternally inherited 5′ICR-KO allele (region VIII) in 1-cell, 2-cell, and blastocyst stage embryos was analyzed by bisulfite sequencing. 22-33 (1-cell stage), 23-47 (2-cell stage), and 4-12 (blastocyst stage) embryos per agarose bead were used.

by the DNMT complex. In support of this notion, it has been recently reported that several maternal ICRs (*PLAGL1*, *INPP5F_v2*, and *PEG3*) in the macaque appeared to acquire allele-specific methylation only after fertilization (Cheong et al., 2015).

The paternally inherited hypomethylated transgenic *H19* ICR in two-cell embryos lacking the maternally supplied DNMT3L (Fig. 1E, Fig. S2A) was not capable of acquiring allele-specific

methylation even after the implantation period (Fig. 1G), during which DNMT3L was zygotically expressed (Fig. S2A) (Guenatri et al., 2013; Hu et al., 2008). These results imply that the paternally inherited transgenic *H19* ICR must be recognized by the maternally supplied DNMT complex immediately after fertilization so that it is methylated during early embryogenesis. It is possible that *trans*-acting factors recruiting the DNMT complex to the epigenetically

DEVELOPMENT
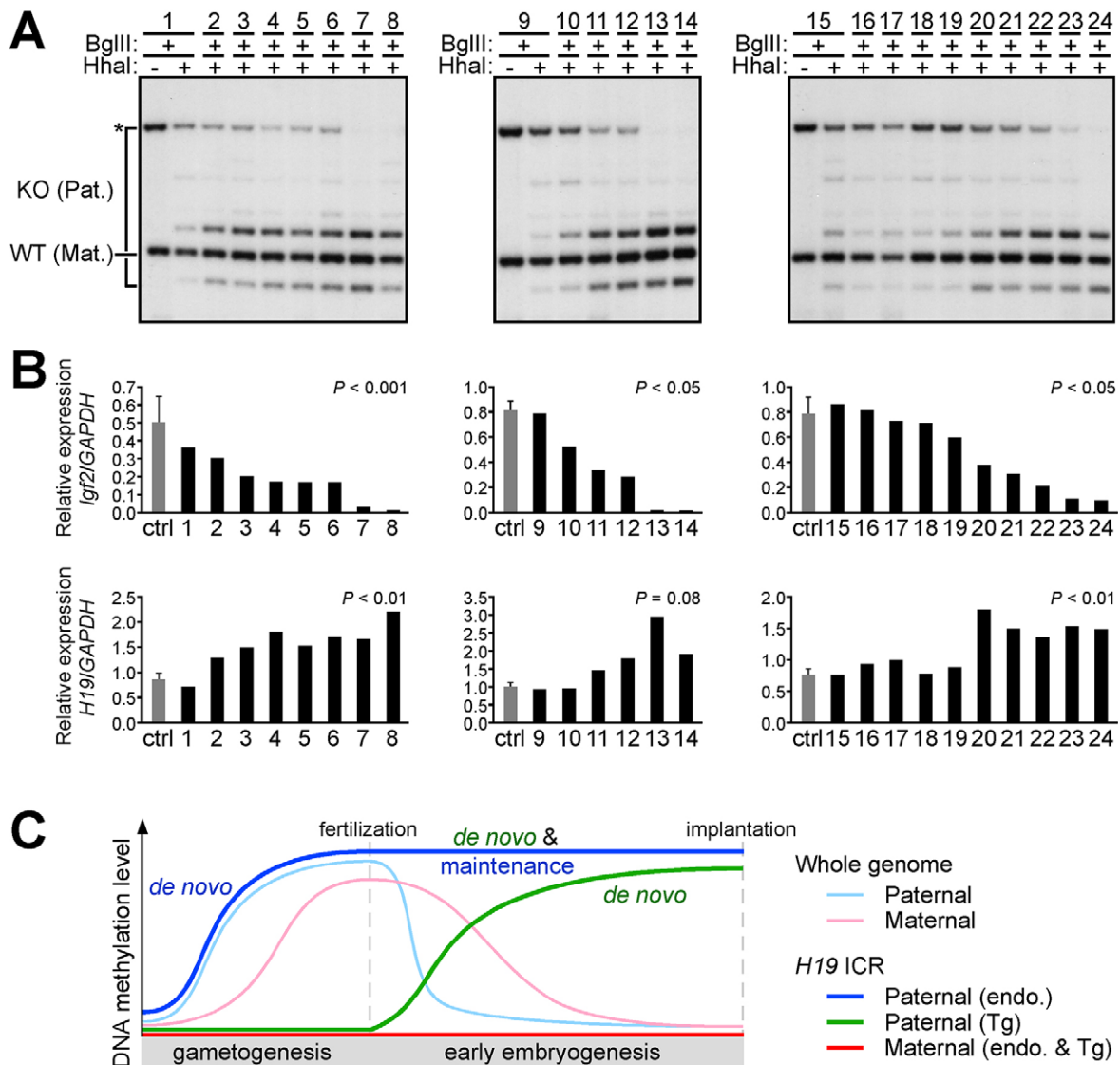
Fig. 7. *In vivo* role of the 5′-region of the endogenous *H19* ICR. (A) DNA methylation status of the paternally inherited mutant (5′ICR-KO) allele in the fetal liver. E12.5 embryos were obtained by mating wild-type females and hetero-KO males. The liver DNA of hetero-KO embryos (WT/KO[pat]) was extracted and analyzed by Southern blotting as described above. Each panel shows the results of embryos from a single litter. Samples are arranged in order of their *Igf2* gene expression levels determined in B. (B) Expression levels of *Igf2* and *H19* in fetal livers. Total RNA was extracted from the livers of hetero-KO embryos (WT/KO[pat]) and control (ctrl, WT/WT) littermates. The numbers correspond to those in A. The mRNA levels of *Igf2* (top) and *H19* (bottom) were measured by quantitative reverse transcription-PCR. Each value represents the ratio of *Igf2* or *H19* expression to that of *GAPDH*. For control embryos (sample numbers are 5, 8, and 5 in each litter: from left to right), the mean±s.d. is shown. The differences in the means between control and KO embryos were tested using an unpaired *t*-test. (C) A model of postfertlization maintenance of methylation imprint at the *H19* ICR. During early embryogenesis, mammalian genomes undergo extensive epigenetic reprogramming, such as genome-wide DNA demethylation. Even in this environment, the allelic DNA methylation of ICRs is faithfully maintained at the imprinted loci, suggesting their states are selectively protected. Based on our observations, we propose that the postfertilization, *de novo* DNA methylation activity of the *H19* ICR contributes to maintain its imprint in early embryos.

marked paternal *H19* ICR might be present only during this short period after fertilization. Alternatively, the hypothetical allele-specific epigenetic mark on the *H19* ICR itself might be lost as embryonic development proceeds.

Possible candidates for the epigenetic signatures marked during spermatogenesis are histone modifications and/or association with specific histone variants. In sperm, 1% and 15% of the genomes are associated with histones rather than protamines in mice and humans, respectively (Miller et al., 2010), and importantly, imprinted loci including the *Igf2/H19* locus are among those regions (Hammoud et al., 2009). We reported that, in sperm, H3K9me2 is preferentially enriched at the paternally methylated endogenous ICRs (e.g. *H19*

and *Rasgrf1* ICRs) (Nakamura et al., 2012). Therefore, histone modification or histone variants within the transgenic *H19* ICR might be transmitted to zygotes to attract the DNMT complex to introduce DNA methylation.

Methylation acquisition at the endogenous *H19* ICR that is flanked by cHS4c sequences was partially obstructed in sperm (Fig. 2B, Fig. S4B). After fertilization, its methylation level was moderately recovered (Fig. 2C, Fig. 3C, Fig. S4C,E), and maternally provided DNMT3L played a significant role in this process (Fig. 3). Therefore, similar to the transgenic *H19* ICR, the endogenous *H19* ICR likely acquired an unknown epigenetic mark during spermatogenesis, and after fertilization, the *de novo*

DNA methylation machinery recognized the mark for allele discrimination. If a common epigenomic state can be identified in the DNA-methylated endogenous *H19* ICR and unmethylated transgenic *H19* ICR sequences in sperm, that would constitute a strong candidate for the primary mark that instructs imprinted DNA methylation in early embryos, because the mark cannot be secondary to DNA methylation.

Although some maternally methylated ICRs (*Snrpn* and *Peg3*) have been suggested to acquire allele-specific methylation after fertilization in mouse, these cases were not maternal DNMT3L dependent (Arnaud et al., 2006; Henckel et al., 2009). Therefore, the mechanistic basis of postfertilization methylation in the *H19* and other ICRs might be distinct. Additionally, as far as we know our data also provide the first example demonstrating a role for DNMT3L during early embryogenesis.

We have previously proposed that, in early embryos, Stella was involved in the maintenance of the hypermethylation status of the endogenous *H19* ICR, by inhibiting Tet3-mediated conversion of 5-methylcytosine to 5-hydroxymethylcytosine (Nakamura et al., 2012). We therefore tested whether the methylation status of the transgenic *H19* ICR, established *de novo* by DNMT3A and DNMT3L was also protected by this molecule. Maternal deletion of the *Stella* gene in oocytes caused a partial loss of methylation at the paternally inherited transgenic *H19* ICR in two-cell embryos (Fig. S1G). It was therefore suggested that Stella plays a shared role in the endogenous and transgenic *H19* ICR.

To demonstrate a role for postfertilization paternal allele-specific methylation activity at the endogenous locus, we narrowed its essential sequences in YAC-TgM (Figs 4 and 5) (Okamura et al., 2013b) and deleted them from the endogenous paternal *H19* ICR. Although gametic methylation of the mutant, endogenous *H19* ICR was not affected, its methylation level was diminished soon after fertilization (Fig. 6), demonstrating that the deleted region contains *cis* elements required for maintaining allele-specific methylation levels during early embryogenesis. A DNA-binding protein complex recognizing this region might interact with the *de novo* DNMT complex or with factors involved in the regulation of the DNA methylation status of the *H19* ICR. Another possibility is that an epigenetic mark to designate its paternal origin might be set in this region of the *H19* ICR during spermatogenesis. Importantly, this is the first example of regulatory sequences that ensure a stable methylation level of the paternal *H19* ICR during preimplantation periods, because all the *cis* regulatory elements identified to date (such as CTCF or Sox-Oct binding motifs) function to maintain the unmethylated state of maternal *H19* ICR following implantation (Matsuzaki et al., 2010; Sakaguchi et al., 2013; Schoenherr et al., 2003; Zimmerman et al., 2013).

Paternal inheritance of the 5′ICR-KO allele resulted in its partial loss of DNA methylation (Fig. 7A), decreased and increased expression of *Igf2* and *H19*, respectively (Fig. 7B), and reduced body weight of the mutant embryos (Fig. S8). Because we observed partial penetrance of these phenotypes, we repeated these experiments after backcrossing the mutant mice onto C57BL/6 for five generations after which essentially the same results were obtained (data not shown). Therefore, any phenotypic variability among embryos is not attributable to genetic background. Some part of maintenance and/or *de novo* methylation machinery in early embryos might have a stochastic nature and contribute to generation of such variations.

In summary, we delineated the postfertilization allele-specific *de novo* DNA methylation activity in the transgenic *H19* ICR and identified its 5′-region as an essential element for this activity. Deletion of this element from the endogenous mouse *H19* ICR

resulted in a loss of methylation on the paternal allele, dysregulation of both *Igf2* and *H19* expression, and growth retardation. We propose that the activity we uncovered plays a role in maintaining allele-specific methylation at the endogenous *H19* ICR in preimplantation embryos, and that the *de novo* methylation imprinting activity at the *H19* ICR and genome-wide demethylation activity are in a state of dynamic equilibrium during this period (Fig. 7C).

MATERIALS AND METHODS
Mice
Transgenic mice carrying a human β-globin YAC, in which the 2.9-kb *H19* ICR fragment was inserted between the LCR and the ε-globin gene were described previously (Tanimoto et al., 2005). *Dnmt3l* KO mice were kindly provided by Dr En Li (Hata et al., 2002). *Dnmt3a-2lox* (RBRC03731) (Kaneda et al., 2004) and *Dnmt3b-2lox* (RBRC03733) (Dodge et al., 2005) mice were generous gifts from Dr Masaki Okano and provided by RIKEN BRC through the National Bio-Resource Project of the Ministry of Education, Culture, Sports, Science and Technology (MEXT), Japan. To conditionally disrupt the floxed alleles in oocytes, these mice were crossed with TgM carrying *Zp3-Cre* gene (Jackson Laboratory; de Vries et al., 2000). Insulated *H19* ICR knock-in mice, ICR4321S TgM, ICR432 TgM, and 5′ICR KO mice were generated as described in the supplementary materials and methods.

Animal experiments were performed in a humane manner and approved by the Institutional Animal Experiment Committee of the University of Tsukuba. Experiments were conducted in accordance with the Regulation of Animal Experiments of the University of Tsukuba and the Fundamental Guidelines for Proper Conduct of Animal Experiments and Related Activities in Academic Research Institutions under the jurisdiction of the MEXT.

Preparation of oocytes and embryos
Female mice were super-ovulated via injection of pregnant mare serum gonadotropin, followed by human chorionic gonadotropin (hCG) (47-48 h interval). Unfertilized oocytes were collected from oviducts 18 h after hCG injection, and cumulus cells were removed by hyaluronidase treatment. Fertilized one-cell zygotes were collected from mated females 24 h after hCG injection, and cumulus cells were removed. Two- and eight-cell embryos were flushed from oviducts at 44 and 68 h, respectively, after hCG injection. Embryos at E3.5 (blastocysts), E8.5, and E12.5 were obtained by natural mating.

DNA methylation analysis by bisulfite sequencing
Preimplantation embryos were embedded in agarose beads and treated with sodium bisulfite as described previously (Matsuzaki et al., 2009). Genomic DNA extracted from postimplantation embryos (E8.5), adult male sperm, or the tail tips of ~1-week-old animals was treated with sodium bisulfite using the EZ DNA Methylation Kit (Zymo Research). Sperm and tail tip DNA was digested with *Xba*I prior to the treatment. Subregions of the *H19* ICR in transgenic and knock-in/KO mice were amplified by nested and single-round PCR, respectively, and the fragments were subcloned into the pGEM-T Easy vector (Promega) for sequencing analyses. PCR primers are listed in Tables S1, S2. Nested PCR was employed to distinguish between the endogenous and transgenic *H19* ICR sequences.

DNA methylation analysis by Southern blotting
Genomic DNA from ICR4321S TgM and 5′ICR-KO mice were first digested by *Eco*T22I and *Bgl*II, respectively, to liberate the *H19* ICR region and subjected to the methylation-sensitive enzymes *Bst*UI and *Hha*I, respectively. Following size separation in agarose gels, Southern blots were hybridized with α-^{32}P-labeled probes and subjected to X-ray film autoradiography.

RT-qPCR
Total RNA of the liver at E12.5 was extracted by ISOGEN (Nippon Gene) and converted to cDNA using ReverTra Ace qPCR RT Master Mix with

gDNA Remover (TOYOBO). Quantitative amplification of cDNA was performed with the Thermal Cycler Dice (TaKaRa Bio) using SYBR Premix EX TaqII (TaKaRa Bio) and PCR primers listed in Table S3.

Supplementary information
Supplementary information available online at
http://dev.biologists.org/lookup/suppl/doi:10.1242/dev.126003/-/DC1

References
Arnaud, P., Hata, K., Kaneda, M., Li, E., Sasaki, H., Feil, R. and Kelsey, G. (2006). Stochastic imprinting in the progeny of Dnmt3L$^{-/-}$ females. *Hum. Mol. Genet.* **15**, 589-598.

Bell, A. C. and Felsenfeld, G. (2000). Methylation of a CTCF-dependent boundary controls imprinted expression of the Igf2 gene. *Nature* **405**, 482-485.

Cheong, C. Y., Chng, K., Ng, S., Chew, S. B., Chan, L. and Ferguson-Smith, A. C. (2015). Germline and somatic imprinting in the nonhuman primate highlights species differences in oocyte methylation. *Genome Res.* **25**, 611-623.

de Vries, W. N., Binns, L. T., Fancher, K. S., Dean, J., Moore, R., Kemler, R. and Knowles, B. B. (2000). Expression of Cre recombinase in mouse oocytes: a means to study maternal effect genes. *Genesis* **26**, 110-112.

DeChiara, T. M., Robertson, E. J. and Efstratiadis, A. (1991). Parental imprinting of the mouse insulin-like growth factor II gene. *Cell* **64**, 849-859.

Dickson, J., Gowher, H., Strogantsev, R., Gaszner, M., Hair, A., Felsenfeld, G. and West, A. G. (2010). VEZF1 elements mediate protection from DNA methylation. *PLoS Genet.* **6**, e1000804.

Dodge, J. E., Okano, M., Dick, F., Tsujimoto, N., Chen, T., Wang, S., Ueda, Y., Dyson, N. and Li, E. (2005). Inactivation of Dnmt3b in mouse embryonic fibroblasts results in DNA hypomethylation, chromosomal instability, and spontaneous immortalization. *J. Biol. Chem.* **280**, 17986-17991.

Ferguson-Smith, A. C. (2011). Genomic imprinting: the emergence of an epigenetic paradigm. *Nat. Rev. Genet.* **12**, 565-575.

Gabory, A., Jammes, H. and Dandolo, L. (2010). The H19 locus: role of an imprinted non-coding RNA in growth and development. *Bioessays* **32**, 473-480.

Gebert, C., Kunkel, D., Grinberg, A. and Pfeifer, K. (2010). H19 imprinting control region methylation requires an imprinted environment only in the male germ line. *Mol. Cell. Biol.* **30**, 1108-1115.

Guenatri, M., Duffie, R., Iranzo, J., Fauque, P. and Bourc'his, D. (2013). Plasticity in Dnmt3L-dependent and -independent modes of de novo methylation in the developing mouse embryo. *Development* **140**, 562-572.

Hammoud, S. S., Nix, D. A., Zhang, H., Purwar, J., Carrell, D. T. and Cairns, B. R. (2009). Distinctive chromatin in human sperm packages genes for embryo development. *Nature* **460**, 473-478.

Hark, A. T., Schoenherr, C. J., Katz, D. J., Ingram, R. S., Levorse, J. M. and Tilghman, S. M. (2000). CTCF mediates methylation-sensitive enhancer-blocking activity at the H19/Igf2 locus. *Nature* **405**, 486-489.

Hata, K., Okano, M., Lei, H. and Li, E. (2002). Dnmt3L cooperates with the Dnmt3 family of de novo DNA methyltransferases to establish maternal imprints in mice. *Development* **129**, 1983-1993.

Henckel, A., Nakabayashi, K., Sanz, L. A., Feil, R., Hata, K. and Arnaud, P. (2009). Histone methylation is mechanistically linked to DNA methylation at imprinting control regions in mammals. *Hum. Mol. Genet.* **18**, 3375-3383.

Henckel, A., Chebli, K., Kota, S. K., Arnaud, P. and Feil, R. (2012). Transcription and histone methylation changes correlate with imprint acquisition in male germ cells. *EMBO J.* **31**, 606-615.

Hirasawa, R., Chiba, H., Kaneda, M., Tajima, S., Li, E., Jaenisch, R. and Sasaki, H. (2008). Maternal and zygotic Dnmt1 are necessary and sufficient for the maintenance of DNA methylation imprints during preimplantation development. *Genes Dev.* **22**, 1607-1616.

Hu, Y.-G., Hirasawa, R., Hu, J.-L., Hata, K., Li, C.-L., Jin, Y., Chen, T., Li, E., Rigolet, M., Viegas-Pequignot, E. et al. (2008). Regulation of DNA methylation activity through Dnmt3L promoter methylation by Dnmt3 enzymes in embryonic development. *Hum. Mol. Genet.* **17**, 2654-2664.

Kaneda, M., Okano, M., Hata, K., Sado, T., Tsujimoto, N., Li, E. and Sasaki, H. (2004). Essential role for de novo DNA methyltransferase Dnmt3a in paternal and maternal imprinting. *Nature* **429**, 900-903.

Kelsey, G. and Feil, R. (2013). New insights into establishment and maintenance of DNA methylation imprints in mammals. *Philos. Trans. R. Soc. B Biol. Sci.* **368**, 20110336.

Kobayashi, H., Sakurai, T., Imai, M., Takahashi, N., Fukuda, A., Yayoi, O., Sato, S., Nakabayashi, K., Hata, K., Sotomaru, Y. et al. (2012). Contribution of intragenic DNA methylation in mouse gametic DNA methylomes to establish oocyte-specific heritable marks. *PLoS Genet.* **8**, e1002440.

Li, X., Ito, M., Zhou, F., Youngson, N., Zuo, X., Leder, P. and Ferguson-Smith, A. C. (2008). A maternal-zygotic effect gene, Zfp57, maintains both maternal and paternal imprints. *Dev. Cell* **15**, 547-557.

Ma, P., Lin, S., Bartolomei, M. S. and Schultz, R. M. (2010). Metastasis tumor antigen 2 (MTA2) is involved in proper imprinted expression of H19 and Peg3 during mouse preimplantation development. *Biol. Reprod.* **83**, 1027-1035.

Matsuzaki, H., Okamura, E., Shimotsuma, M., Fukamizu, A. and Tanimoto, K. (2009). A randomly integrated transgenic H19 imprinting control region acquires methylation imprinting independently of its establishment in germ cells. *Mol. Cell. Biol.* **29**, 4595-4603.

Matsuzaki, H., Okamura, E., Fukamizu, A. and Tanimoto, K. (2010). CTCF binding is not the epigenetic mark that establishes post-fertilization methylation imprinting in the transgenic H19 ICR. *Hum. Mol. Genet.* **19**, 1190-1198.

Messerschmidt, D. M., de Vries, W., Ito, M., Solter, D., Ferguson-Smith, A. and Knowles, B. B. (2012). Trim28 is required for epigenetic stability during mouse oocyte to embryo transition. *Science* **335**, 1499-1502.

Miller, D., Brinkworth, M. and Iles, D. (2010). Paternal DNA packaging in spermatozoa: more than the sum of its parts? DNA, histones, protamines and epigenetics. *Reproduction* **139**, 287-301.

Nakamura, T., Arai, Y., Umehara, H., Masuhara, M., Kimura, T., Taniguchi, H., Sekimoto, T., Ikawa, M., Yoneda, Y., Okabe, M. et al. (2007). PGC7/Stella protects against DNA demethylation in early embryogenesis. *Nat. Cell Biol.* **9**, 64-71.

Nakamura, T., Liu, Y.-J., Nakashima, H., Umehara, H., Inoue, K., Matoba, S., Tachibana, M., Ogura, A., Shinkai, Y. and Nakano, T. (2012). PGC7 binds histone H3K9me2 to protect against conversion of 5mC to 5hmC in early embryos. *Nature* **486**, 415-419.

Okamura, E., Matsuzaki, H., Fukamizu, A. and Tanimoto, K. (2013a). The chicken HS4 insulator element does not protect the H19 ICR from differential DNA methylation in yeast artificial chromosome transgenic mouse. *PLoS ONE* **8**, e73925.

Okamura, E., Matsuzaki, H., Sakaguchi, R., Takahashi, T., Fukamizu, A. and Tanimoto, K. (2013b). The H19 imprinting control region mediates preimplantation imprinted methylation of nearby sequences in yeast artificial chromosome transgenic mice. *Mol. Cell. Biol.* **33**, 858-871.

Okano, M., Bell, D. W., Haber, D. A. and Li, E. (1999). DNA methyltransferases Dnmt3a and Dnmt3b are essential for de novo methylation and mammalian development. *Cell* **99**, 247-257.

Park, K.-Y., Sellars, E. A., Grinberg, A., Huang, S.-P. and Pfeifer, K. (2004). The H19 differentially methylated region marks the parental origin of a heterologous locus without gametic DNA methylation. *Mol. Cell. Biol.* **24**, 3588-3595.

Puget, N., Hirasawa, R., Hu, N.-S. N., Laviolette-Malirat, N., Feil, R. and Khamlichi, A. A. (2015). Insertion of an imprinted insulator into the IgH locus reveals developmentally regulated, transcription-dependent control of V(D)J recombination. *Mol. Cell. Biol.* **35**, 529-543.

Quenneville, S., Verde, G., Corsinotti, A., Kapopoulou, A., Jakobsson, J., Offner, S., Baglivo, I., Pedone, P. V., Grimaldi, G., Riccio, A. et al. (2011). In embryonic stem cells, ZFP57/KAP1 recognize a methylated hexanucleotide to affect chromatin and DNA methylation of imprinting control regions. *Mol. Cell* **44**, 361-372.

Reese, K. J., Lin, S., Verona, R. I., Schultz, R. M. and Bartolomei, M. S. (2007). Maintenance of paternal methylation and repression of the imprinted H19 gene requires MBD3. *PLoS Genet.* **3**, e137.

Sakaguchi, R., Okamura, E., Matsuzaki, H., Fukamizu, A. and Tanimoto, K. (2013). Sox-Oct motifs contribute to maintenance of the unmethylated H19 ICR in YAC transgenic mice. *Hum. Mol. Genet.* **22**, 4627-4637.

Schoenherr, C. J., Levorse, J. M. and Tilghman, S. M. (2003). CTCF maintains differential methylation at the Igf2/H19 locus. *Nat. Genet.* **33**, 66-69.

DEVELOPMENT

336

Smallwood, S. A., Tomizawa, S.-i., Krueger, F., Ruf, N., Carli, N., Segonds-Pichon, A., Sato, S., Hata, K., Andrews, S. R. and Kelsey, G. (2011). Dynamic CpG island methylation landscape in oocytes and preimplantation embryos. *Nat. Genet.* **43**, 811-814.

Srivastava, M., Hsieh, S., Grinberg, A., Williams-Simons, L., Huang, S. P. and Pfeifer, K. (2000). H19 and Igf2 monoallelic expression is regulated in two distinct ways by a shared cis acting regulatory region upstream of H19. *Genes Dev.* **14**, 1186-1195.

Szabo, P. E., Tang, S. H., Reed, M. R., Silva, F. J., Tsark, W. M. and Mann, J. R. (2002). The chicken beta-globin insulator element conveys chromatin boundary activity but not imprinting at the mouse Igf2/H19 domain. *Development* **129**, 897-904.

Tanimoto, K., Shimotsuma, M., Matsuzaki, H., Omori, A., Bungert, J., Engel, J. D. and Fukamizu, A. (2005). Genomic imprinting recapitulated in the human beta-globin locus. *Proc. Natl. Acad. Sci. USA* **102**, 10250-10255.

Tanimoto, K., Sugiura, A., Kanafusa, S., Saito, T., Masui, N., Yanai, K. and Fukamizu, A. (2008). A single nucleotide mutation in the mouse renin promoter disrupts blood pressure regulation. *J. Clin. Invest.* **118**, 1006-1016.

Tomizawa, S.-i. and Sasaki, H. (2012). Genomic imprinting and its relevance to congenital disease, infertility, molar pregnancy and induced pluripotent stem cell. *J. Hum. Genet.* **57**, 84-91.

Tremblay, K. D., Duran, K. L. and Bartolomei, M. S. (1997). A 5′ 2-kilobase-pair region of the imprinted mouse H19 gene exhibits exclusive paternal methylation throughout development. *Mol. Cell. Biol.* **17**, 4322-4329.

West, A. G., Huang, S., Gaszner, M., Litt, M. D. and Felsenfeld, G. (2004). Recruitment of histone modifications by USF proteins at a vertebrate barrier element. *Mol. Cell* **16**, 453-463.

Zimmerman, D. L., Boddy, C. S. and Schoenherr, C. S. (2013). Oct4/Sox2 binding sites contribute to maintaining hypomethylation of the maternal igf2/h19 imprinting control region. *PLoS ONE* **8**, e81962.

DEVELOPMENT

HIF2α in the uterine stroma permits embryo invasion and luminal epithelium detachment

Leona Matsumoto, … , Tomoyuki Fujii, Yutaka Osuga

Research Article   Development   Reproductive biology

Graphical abstract
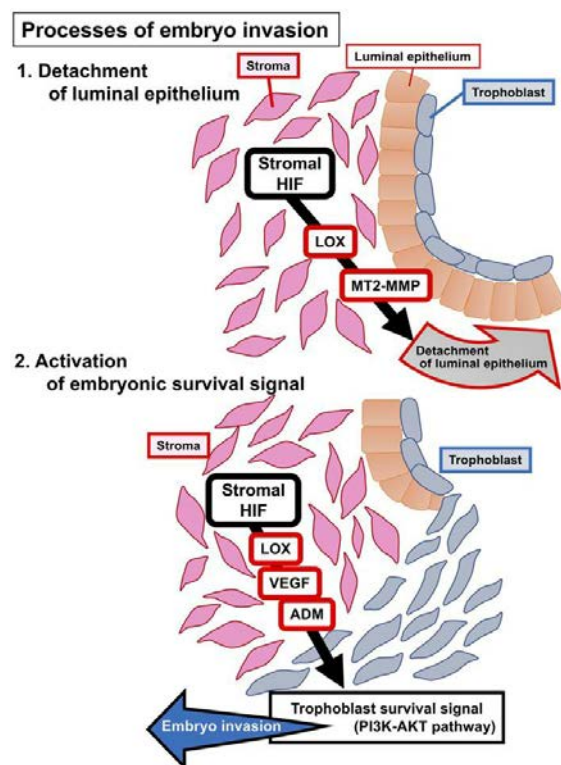
Find the latest version:

http://jci.me/98931/pdf

HIF2α in the uterine stroma permits embryo invasion and luminal epithelium detachment

Leona Matsumoto,[1] Yasushi Hirota,[1,2] Tomoko Saito-Fujita,[1] Norihiko Takeda,[3] Tomoki Tanaka,[1] Takehiro Hiraoka,[1] Shun Akaeda,[1] Hidetoshi Fujita,[4] Ryoko Shimizu-Hirota,[5] Shota Igaue,[1] Mitsunori Matsuo,[1] Hirofumi Haraguchi,[1] Mayuko Saito-Kanatani,[1] Tomoyuki Fujii,[1] and Yutaka Osuga[1]

[1]Department of Obstetrics and Gynecology, Graduate School of Medicine, The University of Tokyo, Bunkyo-ku, Tokyo, Japan. [2]Precursory Research for Innovative Medical Care (PRIME), Japan Agency for Medical Research and Development (AMED), Bunkyo-ku, Tokyo, Japan. [3]Department of Cardiovascular Medicine, Graduate School of Medicine, The University of Tokyo, Bunkyo-ku, Tokyo, Japan. [4]Department of Future Medical Science, Institute of Medical Science, Tokyo Medical University, Shinjuku-ku, Tokyo, Japan. [5]Department of Internal Medicine, Center of Preventive Medicine, School of Medicine, Keio University, Shinjuku-ku, Tokyo, Japan.

Although it has been reported that hypoxia inducible factor 2 α (*Hif2a*), a major transcriptional factor inducible by low oxygen tension, is expressed in the mouse uterus during embryo implantation, its role in pregnancy outcomes remains unclear. This study aimed to clarify functions of uterine HIF using transgenic mouse models. Mice with deletion of *Hif2a* in the whole uterus (*Hif2a*-uKO mice) showed infertility due to implantation failure. Supplementation with progesterone (P$_4$) and leukemia inhibitory factor (LIF) restored decidual growth arrest and aberrant position of implantation sites in *Hif2a*-uKO mice, respectively, but did not rescue pregnancy failure. Histological analyses in *Hif2a*-uKO mice revealed persistence of the intact luminal epithelium, which blocked direct contact between stroma and embryo, inactivation of PI3K-AKT pathway (embryonic survival signal), and failed embryo invasion. Mice with stromal deletion of *Hif2a* (*Hif2a*-sKO mice) showed infertility with impaired embryo invasion and those with epithelial deletion of *Hif2a* (*Hif2a*-eKO mice) showed normal fertility, suggesting the importance of stromal HIF2α in embryo invasion. This was reflected in reduced expression of membrane type 2 metalloproteinase (MT2-MMP), lysyl oxidase (LOX), VEGF, and adrenomedullin (ADM) in *Hif2a*-uKO stroma at the attachment site, suggesting that stromal HIF2α regulates these mediators to support blastocyst invasion. These findings provide new insight that stromal HIF2α allows trophoblast invasion through detachment of the luminal epithelium and activation of an embryonic survival signal.

Introduction

Infertility is a worldwide issue estimated to affect up to 30% of couples in both developed and developing countries (1). Infertile patients undergoing in vitro fertilization and embryo transfer (IVF-ET) are on the rise, and many of them experience recurrent implantation failure, which is a major problem in IVF-ET programs. The process of embryo implantation spanning blastocyst apposition and attachment with the uterine epithelium, along with invasion of blastocyst trophectoderm into the endometrium, is executed by molecular interactions between the embryo and uterus (2–5). Among others, progesterone (P$_4$) signaling, heparin-binding EGF-like growth factor (HB-EGF), and leukemia inhibitory factor–STAT3 (LIF-STAT3) signaling were reported as key molecular mediators of embryo apposition and attachment (6–11). However, other key molecules and pathways in these processes remain elusive.

Hypoxia inducible factor (HIF) is a major transcription factor that responds to low oxygen tension and induces the expression of hypoxia-related genes such as VEGF and erythropoietin (12). Through the induction of these genes, HIF is involved in vari-

ous physiological responses such as metabolism, cell death, and angiogenesis (13). HIF is composed of 2 subunits, α and β (14). The HIFα subunit has 3 isotypes, HIF1α, HIF2α, and HIF3α, whereas the HIFβ subunit has 2 types, ARNT1 and ARNT2 (14). A previous study showed that the expression of *Hif1a* is primarily in the uterine luminal epithelium during the peri-implantation period, and the expression of *Hif2a* is mainly in the stroma at the same time, whereas *Hif3a* is undetectable in the uterus (15). Notably, *Hif2a* is strongly expressed in the uterine stroma after embryo attachment (15). Based on expression patterns, we speculated that HIFα has functional roles in embryo implantation. *Hif1a* and *Hif2a* homozygous null embryos die during gestation (16, 17), impeding functional analysis of HIF in the reproductive system. To overcome this difficulty, we generated mice with uterine tissue–specific deletion of *Hif1a* and *Hif2a* using *Pgr*-Cre and *Ltf*-Cre drivers as previously described (18–21), and examined critical pregnancy events. Mice with *Hif2a* deletion in the entire uterus (*Hif2a*-uKO mice) were infertile, whereas mice with uterine deletion of *Hif1a* (*Hif1a*-uKO mice) showed subfertility, indicating the importance of uterine HIFα in fertility. The luminal epithelial barrier surrounding the embryo disappears just before embryo invasion in the littermate controls, whereas it persists and prevents embryo invasion in *Hif2a*-uKO mice, suggesting impairment of this invasion process as a cause of infertility in *Hif2a*-uKO mice. Importantly, detachment of luminal epithelium from stroma, which permits direct contact

between stroma and embryo, and activation of PI3K-AKT pathway as an embryonic survival signal are not observed in *Hif2a*-uKO mice (unlike the littermate controls), providing evidence for a role of HIF2α in embryo invasion. Our findings offer insights that uterine HIF2α is critical for embryo invasion through activation of an embryo survival signal and detachment of the luminal epithelium.

Results
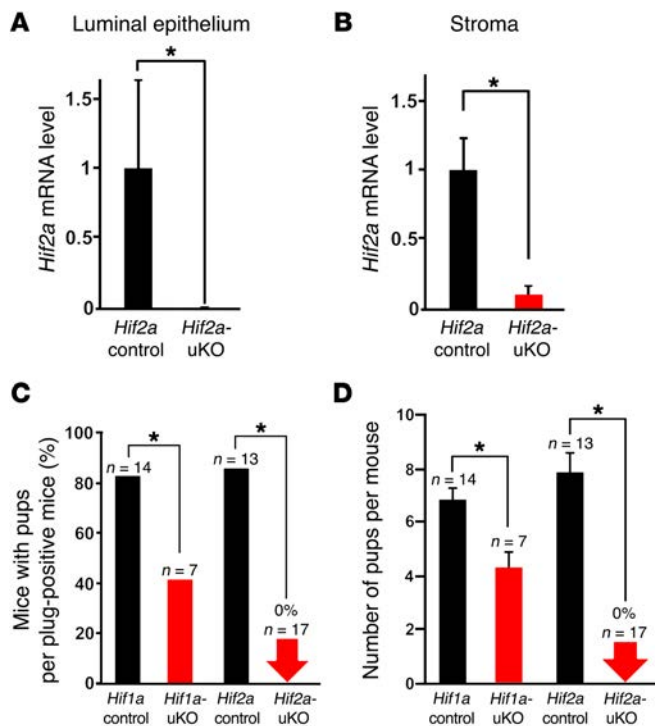
Mice with uterine deletion of Hif2a show infertility and those with uterine deletion of Hif1a show subfertility. To explore the role of uterine HIF in pregnancy, we generated females with deletion of *Hif1a* and *Hif2a* in the entire uterus (*Hif1a*-uKO and *Hif2a*-uKO, respectively) by crossing *Hif1a*- or *Hif2a*-loxP mice with *Pgr*-Cre mice. We first confirmed that HIF1α and HIF2α mRNA levels were significantly reduced in the uterus of *Hif1a*-uKO and *Hif2a*-uKO mice, respectively (Figure 1, A and B and Supplemental Figure 1; supplemental material available online with this article; https://doi.org/10.1172/JCI98931DS1). *Hif1a*-uKO mice, *Hif2a*-uKO mice, and their littermate controls (*Hif1a* control, *Hif2a* control) were mated with WT fertile male mice. We found that approximately 50% of the plug-positive *Hif1a*-uKO mice did not deliver any pups and the number of pups with *Hif1a*-uKO dams was significantly reduced (Figure 1, C and D). Surprisingly, we found that *Hif2a*-uKO mice were infertile (Figure 1, C and D), suggesting that uterine *Hifa*, especially *Hif2a*, is critical for successful pregnancy. Based on these results, we focused on the role of *Hif2a* in the uterus in the subsequent analyses by using *Hif2a*-uKO mice.

Hif2a-uKO mice showing normal ovulation and preimplantation embryo development undergo impaired embryo implantation. We examined ovulation and fertilization in *Hif2a*-uKO mice by flushing eggs and/or embryos on day 2 of pregnancy (day 1 = vaginal plug), and found both processes to be normal (Figure 2, A–C). We

also confirmed normal development of preimplantation embryos and their timely transport from the oviduct into uterine lumens of *Hif2a*-uKO mice by recording the number of blastocysts retrieved through flushing the uteri on day 4 of pregnancy (Figure 2, D and E). Successful implantation is the result of reciprocal interactions between the blastocyst and the receptive uterus. Stromal edema on day 4 morning leads to uterine luminal closure, placing the blastocyst in close apposition with the luminal epithelium. We previously reported that proliferation-to-differentiation switching, cessation of epithelial proliferation, and acceleration of stromal proliferation in the uterus on day 4 morning are hallmarks of uterine receptivity in embryo implantation (7). Immunostaining of Ki67, a cell proliferation marker, revealed that uteri of *Hif2a*-uKO mice had normal proliferation-to-differentiation switching, comparable to the controls (Supplemental Figure 2, A–C). Embryo apposition is followed by intimate adherence of the blastocyst trophectoderm to the luminal epithelium (attachment reaction), marking the first discernible sign of implantation from midnight of day 4 to day 5 morning. The attachment reaction coincides with increased stromal vascular permeability at the site of the blastocyst and can be demarcated by distinct blue bands along the uterus after intravenous injection of Chicago blue dye solution (8). We found that the number of distinct implantation sites in *Hif2a*-uKO mice was comparable to *Hif2a* controls on day 5 morning (Figure 2, F and G). With the implantation process in progress, stromal cells surrounding the implanting embryo undergo decidualization. The luminal epithelium surrounding the implantation sites disappears on day 5 evening, and embryo invasion into the stroma starts from day 5 night to day 6 morning. Decidual growth peaks on day 8 of pregnancy. To determine whether this process is normal in *Hif2a*-uKO mice, we counted the number of implantation sites in *Hif2a*-uKO mice and the controls on days 6 and 8 of pregnancy. The number of implantation sites remained comparable between the 2 groups on day 6 (Figure 2, H and I), but normal implantation sites with decidualization completely disappeared in *Hif2a*-uKO mice on day 8 (Figure 2, J and K). By H&E staining, we confirmed that embryos were completely degraded and decidualization was impaired in *Hif2a*-uKO mice on day 8 of pregnancy (Figure 2L), suggesting decidual growth arrest and implantation failure in *Hif2a*-uKO mice.

P$_4$ administration rescues decidualization in Hif2a-uKO mice but does not rescue pregnancy failure. It has been reported that murine decidua-derived factors serve as luteotrophins to prolong the life span of the corpus luteum and maintain luteal P$_4$ production (22–24). Prolactin-related factors *Prl3c1* and *Prlr* are hallmarks of decidual health and contribute to activation of the corpus luteum and ovarian secretion of P$_4$ in rodents (25–31). In *Hif2a*-uKO mice, the expression of *Prl3c1* and *Prlr* was significantly reduced (Figure 3, A–C), suggesting that unhealthy decidual condition compromises luteotrophy in *Hif2a*-uKO mice. As
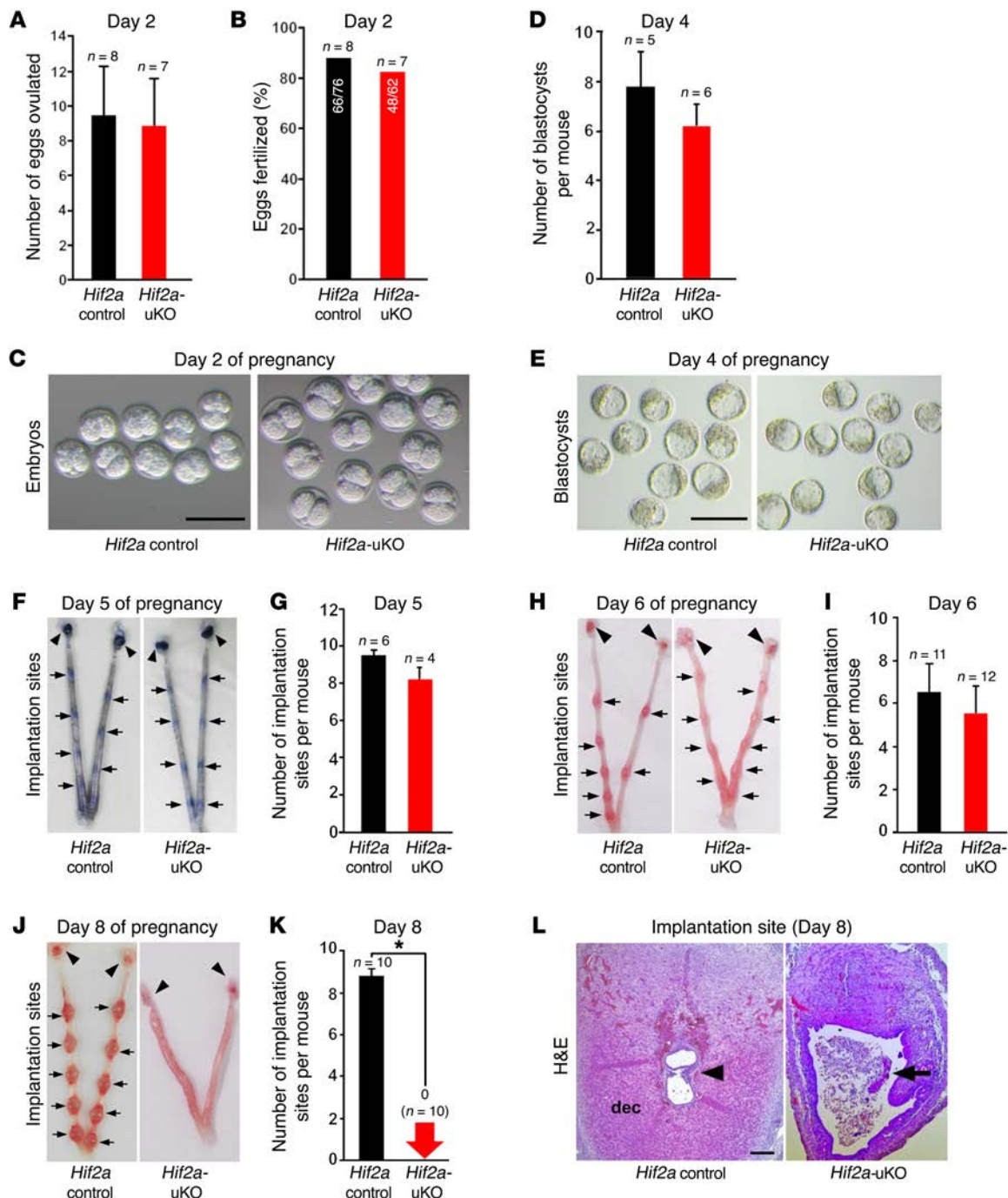
Figure 2. *Hif2a*-uKO mice show implantation failure. (**A–E**) Ovulation, fertilization, and development of preimplantation embryos were normal in *Hif2a*-uKO mice. **A** and **D**, $P > 0.05$, mean ± SEM, Student's *t* test; **B**, $P > 0.05$, Fisher's exact probability test; **C** and **E**, scale bar, 200 μm. (**F** and **G**) Attachment reaction occurred normally in *Hif2a*-uKO mice at 1000 hours on day 5. $P > 0.05$, mean ± SEM, Student's *t* test. Arrow and arrowhead indicate implantation site and ovary, respectively. (**H** and **I**) Decidualization was observed in *Hif2a*-uKO mice at 1000 hours on day 6. $P > 0.05$, mean ± SEM, Student's *t* test. (**J–L**) Embryo implantation and decidualization were completely disturbed in *Hif2a*-uKO mice at 1000 hours on day 8. In **K**, *$P < 0.05$, mean ± SEM, Student's *t* test. In **L**, arrowhead indicates an embryo; arrow, a destroyed embryo with blood cell infiltration; dec, decidua.

expected, serum P_4 levels are significantly reduced in *Hif2a*-uKO mice on days 6 and 8 of pregnancy when decidualization prominently occurs (Figure 3D). In contrast, serum estradiol-17β (E_2) levels on days 4, 5, 6, and 8 of pregnancy were comparable between controls and *Hif2a*-uKO mice (Figure 3E). To clarify whether the decreased levels of P_4 were involved in decidual growth arrest of *Hif2a*-uKO mice, we examined the effect of luteal support in *Hif2a*-uKO mice by daily subcutaneous injection of P_4 from day 2 of pregnancy (2 mg/mouse/day). P_4 administration successfully restored the number and weight of implantation sites in *Hif2a*-uKO mice on day 8 of pregnancy (Figure 3, F and G, and Supplemental Figure 3). The expression of decidualiza-
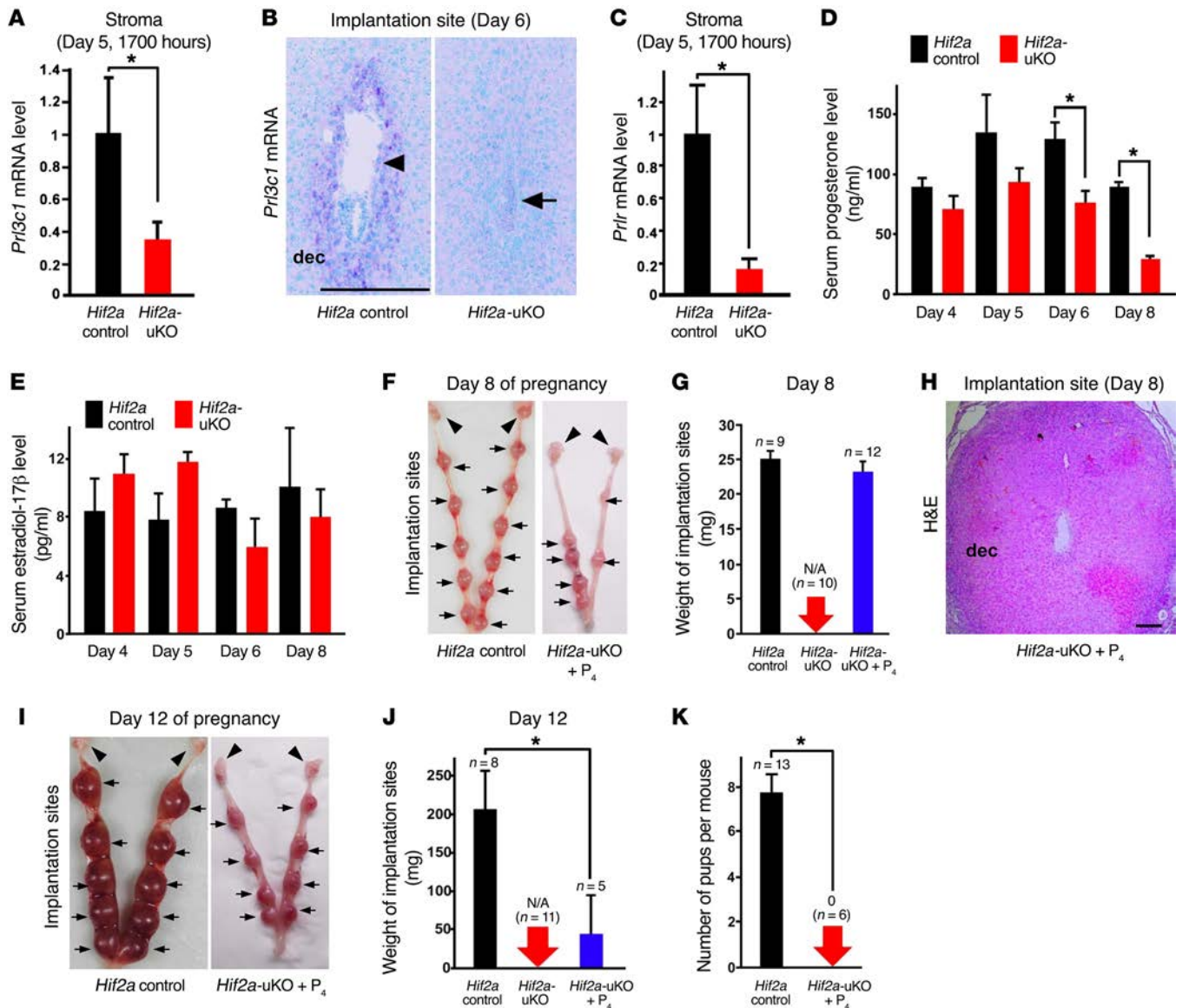
Figure 3. P$_4$ administration does not recover implantation failure but rescues decidualization in *Hif2a*-uKO mice. (**A–C**) Decidual prolactin-related factors *Prl3c1* and *Prlr*, hallmarks of decidual health and luteotrophin, were reduced in *Hif2a*-uKO mice during decidualization. In **A** and **C**, $n \geq 4$, *$P < 0.05$, mean ± SEM, Student's *t* test. In **B**, scale bar, 200 μm; arrowhead, an embryo; arrow, a destroyed embryo with blood cell infiltration; dec, decidua. (**D** and **E**) Serum P$_4$ levels were reduced in *Hif2a*-uKO mice compared with the controls on days 6 and 8 of pregnancy, whereas serum E$_2$ levels were comparable between them. *$P < 0.05$, mean ± SEM, Student's *t* test. (**F** and **G**) Daily injection of P$_4$ from day 2 of pregnancy (2 mg/mouse/day) restored decidualization in *Hif2a*-uKO mice on day 8 of pregnancy. $P > 0.05$, mean ± SEM, Student's *t* test. Arrow and arrowhead indicate implantation site and ovary, respectively. (**H**) P$_4$ supplementation did not recover embryo survival in *Hif2a*-uKO mice on day 8 of pregnancy. No embryo was observed at the implantation site of *Hif2a*-uKO mice with P$_4$ treatment. Scale bar, 200 μm; dec, decidua. (**I–K**) *Hif2a*-uKO mice with daily P$_4$ injection showed the reduced weight of implantation sites on day 12, and did not deliver any pups in parturition. *$P < 0.05$, mean ± SEM, Student's *t* test.

tion marker BMP2 (32, 33) was comparable between *Hif2a*-uKO mice with P$_4$ treatment and the control mice (Supplemental Figure 4), suggesting that P$_4$ supplementation rescues decidualization failure in *Hif2a*-uKO mice. However, H&E staining demonstrated that P$_4$ supplementation did not recover embryo survival in *Hif2a*-uKO mice on day 8 of pregnancy (Figure 3H). These findings indicate that P$_4$ reduction is not the cause of pregnancy failure in *Hif2a*-uKO mice. In fact, *Hif2a*-uKO mice with daily P$_4$ injection showed reduced weight of implantation sites on day 12 (Figure 3, I and J) and never delivered pups (Figure 3K).

Pregnancy failure in Hif2a-uKO mice is due to insufficiency of uterine factors. P$_4$ is a major ovarian factor essential for pregnancy, but the ovary produces other factors to support pregnancy. To evaluate the contribution of ovarian factors (including P$_4$) to the implantation phenotype in *Hif2a*-uKO mice, we performed transplantation of WT ovaries into *Hif2a*-uKO mice or littermate controls by ovariectomy to normalize ovarian functions (Figure 4A) and evaluated the implantation phenotype of these mice. Normal implantation sites were observed in control mice with transplantation of WT ovaries on day 8 of pregnancy, while normal

activation of STAT3, a downstream signaling effector of LIF (11), was eliminated in the implantation sites of *Hif2a*-uKO uteri, as evident from phosphorylated STAT3 immunostaining (Figure 5E). To evaluate whether the decrease of LIF in *Hif2a*-deficient uteri leads to implantation failure, we injected recombinant LIF (20 μg/mouse on day 4) intraperitoneally in *Hif2a*-uKO mice in addition to P_4 injection. Although LIF administration markedly normalized the positioning of embryo attachment to the crypt (Figure 5F and Supplemental Figure 5), it did not rescue pregnancy failure in *Hif2a*-uKO mice (Figure 5G). Since LIF is transcriptionally regulated by HIF (36, 37), uterine HIF2α may determine the positioning of the embryo through LIF induction.

Persistent preservation of the intact luminal epithelium surrounding the embryo is associated with failed embryo invasion in Hif2a-uKO mice. We next used histological analysis to evaluate the process of embryo invasion from day 5 to day 6 in *Hif2a*-uKO mice. We found that alignment of the luminal epithelium disappeared at the implantation site and that trophoblast invasion starts in control mice at 2100 hours on day 5 (Figure 6A). In contrast, alignment of luminal epithelium was intact at the implantation site and trophoblast invasion did not occur in *Hif2a*-uKO mice at the same time (Figure 6A). On day 6 morning, blood cell infiltration without the normal embryo structure was observed at the implantation site of *Hif2a*-uKO mice, whereas the stromal area with trophoblast invasion expanded in the controls (Figure 6A). At 1700 hours on day 5 just before initiation of embryo invasion, epithelial expression of E-cadherin, a tight junction regulator as well as a marker of epithelium, was eliminated. Epithelial alignment collapsed at the implantation sites of the controls, whereas both E-cadherin expression and epithelial alignment persisted in *Hif2a*-uKO mice (Figure 6B), suggesting that intact alignment of luminal epithelium is associated with failed embryo invasion.

Direct contact between embryo and uterine stroma is involved in embryonic cell survival and invasion. Although the disappearance of the luminal epithelium attached to the embryo occurred in control mice on day 5 evening, apoptosis of the luminal epithelium was not observed at that time (Figure 7A), suggesting that apoptosis is not a key mechanism for the elimination of the luminal epithelium around the embryo. In contrast, apoptosis was observed in the trophoblast attached to the intact luminal epithelium in *Hif2a*-uKO mice, indicating programmed death in embryos that fail to initiate direct contact with endometrial stroma. We next hypothesized that epithelial mesenchymal transition (EMT) could be involved in the disappearance of the luminal epithelium around the embryo;

implantation sites were never observed in *Hif2a*-uKO mice that received WT ovaries (Figure 4, B and C). P_4 supplementation did not recover implantation failure but did rescue decidualization in *Hif2a*-uKO mice with ovarian transplantation (Figure 4, B and C). These experiments using mice with ovarian transplantation did not rescue the similar phenotypes observed in those without ovarian transplantation, indicating that implantation failure in *Hif2a*-uKO mice is not derived from ovarian factors but from a uterine factor. Importantly, ovarian *Hif2a* mRNA levels were comparable between *Hif2a*-uKO mice and their controls (Figure 4D).

Uterine HIF2α confers appropriate homing of the implanting embryo in the crypt. To examine the detailed mechanism of implantation failure in *Hif2a*-uKO mice, we evaluated blastocyst attachment on day 5 morning. By histological analysis of *Hif2a*-deficient uteri, we found that the positioning of the embryo attachment at the bottom of the endometrial crypt was impaired in *Hif2a*-uKO mice (Figure 5A and Supplemental Figure 5). COX2, a marker of embryo attachment reaction (34), was similarly expressed in the implantation sites of both *Hif2a*-uKO and control mice (Figure 5, B and C). The expression of LIF, a key regulator of embryo attachment (9, 10, 35), was significantly decreased in *Hif2a*-deficient uteri on day 5 morning (Figure 5D). In accordance with LIF reduction,
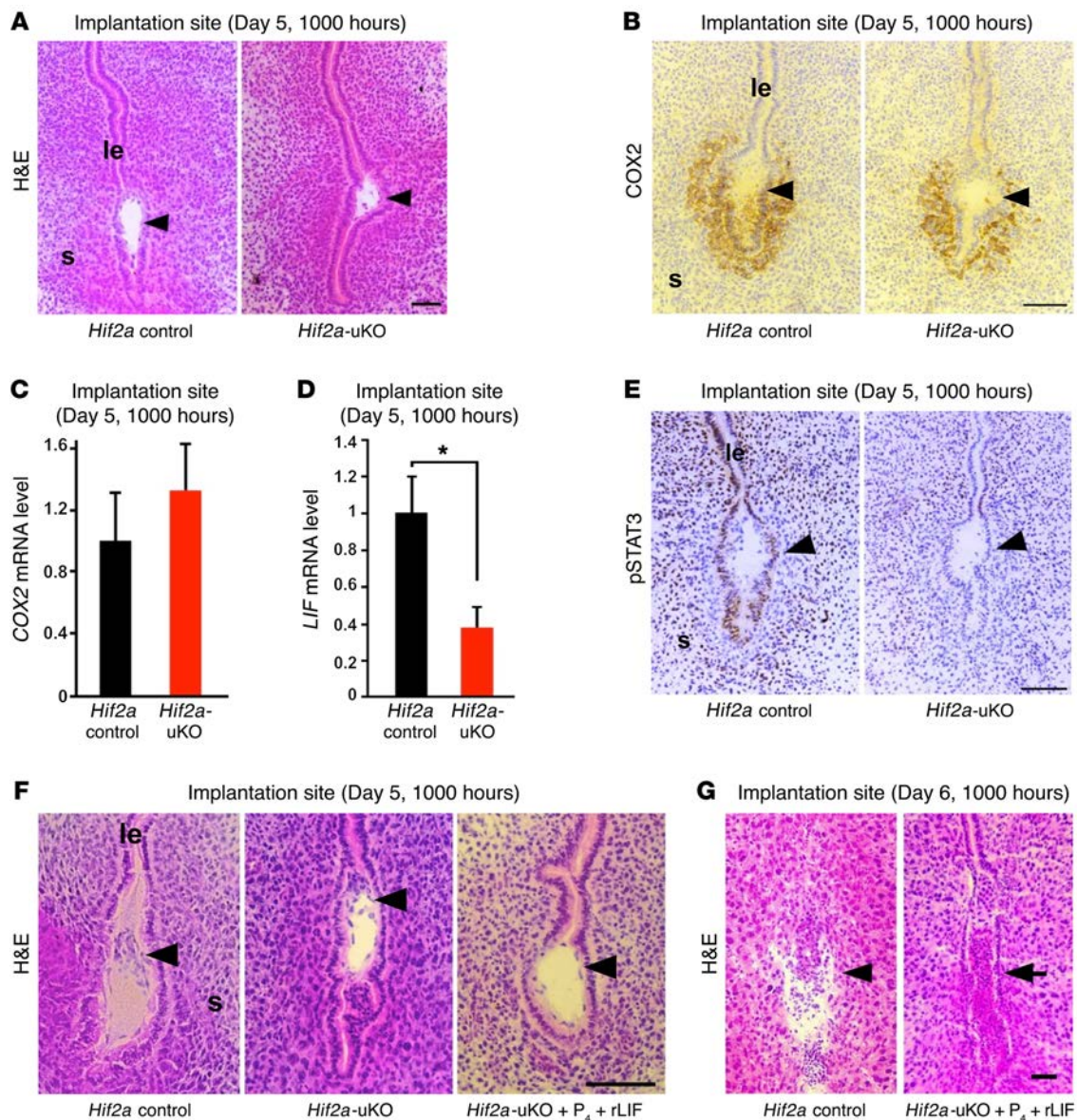
Figure 5. Uterine HIF2α places the implanting embryo in the bottom of the endometrial crypt through induction of LIF. (**A**) The positioning of embryo attachment at the bottom of the endometrial crypt was impaired in *Hif2a*-uKO mice at 1000 hours on day 5. Scale bar, 100 μm; arrowhead, an embryo; s, stroma; le, luminal epithelium. (**B** and **C**) COX2, a marker of embryo attachment reaction, was similarly expressed in the implantation sites of both *Hif2a*-uKO and control mice. *P* > 0.05, *n* ≥ 5, mean ± SEM, Student's *t* test. (**D**) The expression of LIF, a key regulator of embryo attachment, was decreased at the implantation site of *Hif2a*-uKO mice on day 5 morning. **P* < 0.05, *n* ≥ 5, mean ± SEM, Student's *t* test. (**E**) Activation of STAT3, a downstream signaling of LIF, was eliminated in the implantation site of *Hif2a*-uKO mice, as demonstrated by phosphorylated STAT3 immunostaining. (**F**) Intraperitoneal injection of recombinant LIF (20 μg/mouse on day 4) into *Hif2a*-uKO mice in addition to P$_4$ injection normalized the position of embryo attachment to the bottom of the endometrial crypt on day 5 morning. (**G**) LIF administration could not rescue implantation failure in *Hif2a*-uKO mice on day 6 morning (arrow, a destroyed embryo with blood cell infiltration).

we investigated this process using *R26GRR/Ltf-Cre* mice, which can be used for tracing cells with uterine epithelium origin. However, epithelium-derived cells were not observed in the uterine stroma surrounding the invading embryo (Supplemental Figure 6), suggesting that EMT does not play a key role in the elimination of the luminal epithelium around the embryo.

Transmission electron microscopic analyses of embryo-uterine interface at 1900 hours on day 5 showed newly formed gaps between the stroma and the luminal epithelium and the invading trophoblast within these gaps in the control mice, but not in

Hif2a-uKO mice (Figure 7B), suggesting a role for uterine HIF2α in the detachment of the luminal epithelium from uterine stroma along with trophoblast invasion by direct contact with the stroma. Of note, this epithelial detachment was similarly observed in ICR mice on a different genetic background (Supplemental Figure 7), indicating that loss of the epithelial barrier is a common critical phenomenon during implantation.

In terms of the detachment of luminal epithelium from stroma, mRNA expression of membrane type 2 metalloproteinase (MT2-MMP) and lysyl oxidase (LOX) at the stroma of implan-
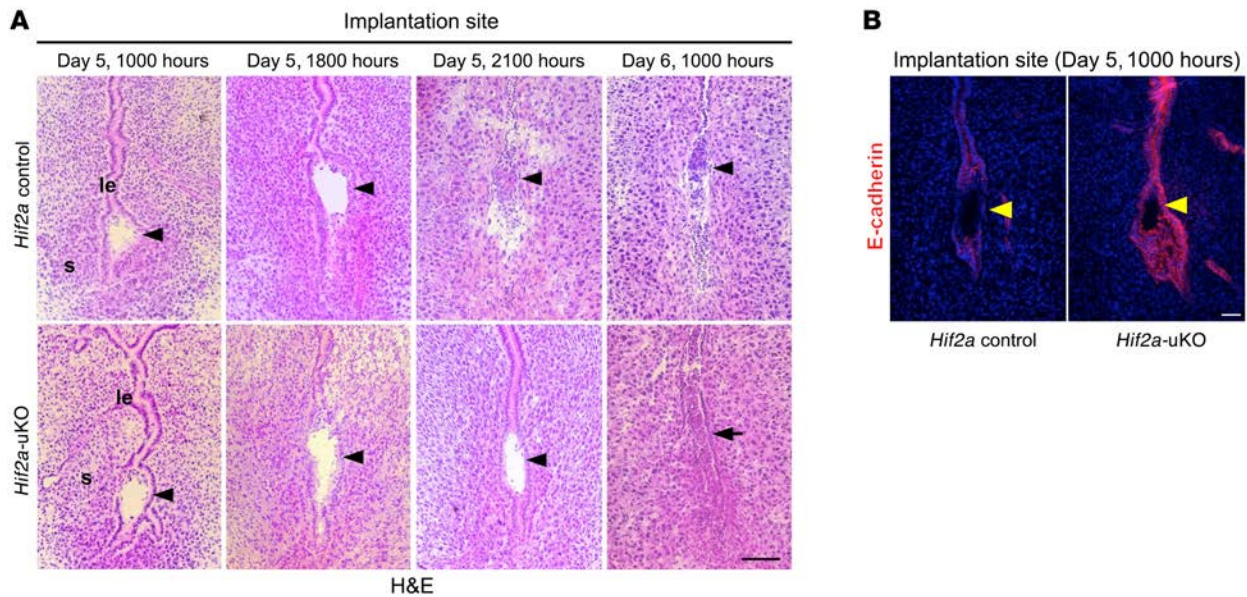
Figure 6. Intact alignment of luminal epithelium surrounding the embryo is associated with failed embryo invasion in *Hif2a*-uKO mice. (A) Alignment of luminal epithelium disappeared at the implantation site, and trophoblast invasion started in the control mice at 2100 hours on day 5. In contrast, alignment of luminal epithelium was intact at the implantation site, and trophoblast invasion did not occur in *Hif2a*-uKO mice at the same time. On day 6 morning, destroyed embryo with blood cell infiltration was observed at the implantation site of *Hif2a*-uKO mice, while the stromal area with trophoblast invasion expanded in the controls. Scale bar, 200 μm; arrowhead, an embryo; s, stroma; le, luminal epithelium; arrow, a destroyed embryo with blood cell infiltration. **(B)** Expression of E-cadherin, a tight junction regulator as well as a marker of epithelium, was eliminated and epithelial alignment was collapsed at implantation sites of the controls, while both E-cadherin expression and epithelial alignment were persistent in *Hif2a*-uKO mice on day 5 evening.

tation sites collected by laser capture microdissection (LCM) was downregulated in *Hif2a*-uKO mice compared with the controls (Figure 7, C and D). We also confirmed the downregulation of these genes by in situ hybridization (Supplemental Figures 8 and 9). MT2-MMP and LOX are known transcription targets of HIF (38, 39). MT2-MMP, located on the cellular membrane, activates MMP2 outside the cell wall (40, 41) and breaks extracellular matrices composed of basement membrane together with the secreted MMP2, thereby serving as a regulator of basement membrane remodeling (42, 43). MT2-MMP also cleaves E-cadherin at the epithelial junction and regulates epithelial cell remodeling (44). LOX, secreted by the stroma, remodels the extracellular matrix by facilitating covalent cross-linking (45) and promotes cancer metastasis and invasion (45, 46). LOX and MT2-MMP in the stroma may cooperatively promote basement membrane remodeling and weaken the stroma-to-epithelium contact by changing the distribution of E-cadherin and the conformation of extracellular matrices between luminal epithelium and stroma. Our findings indicate that stromal *Hif2a* induces MMPs and LOX, which release the luminal epithelium from the stroma and promote trophoblast invasion.

Stromal Hif2a is critical for embryo invasion and activation of the PI3K-AKT pathway in the implanting embryo. To clarify the importance of stromal HIF2α in embryo invasion, we generated mice with uterine stromal deletion of *Hif2a* (*Hif2a*-sKO mice, *Hif2a*-loxP/ *Amhr2*-Cre). We confirmed that *Hif2a* mRNA levels were significantly reduced in the stroma of *Hif2a*-sKO mice (Supplemental Figure 10, A and B). As expected, the similar infertility phenotype with both impaired embryo invasion and persistent presence of luminal epithelium was observed in *Hif2a*-sKO mice (Figure 8, A–C), sug-

gesting that stromal *Hif2a* controls embryo invasion. Moreover, we also generated mice with uterine epithelial deletion of *Hif2a* (*Hif2a*-eKO mice, *Hif2a*-loxP/*Ltf*-Cre) to evaluate the function of *Hif2a* in the luminal epithelium. *Hif2a* mRNA levels were significantly reduced in the luminal epithelium of *Hif2a*-eKO mice (Supplemental Figure 10, C and D). However, *Hif2a*-eKO mice demonstrated normal fertility (Figure 8D), emphasizing the significance of stromal HIF2α. Taken together, these findings indicate that stromal HIF2α detaches the luminal epithelium surrounding the embryo and activates an embryonic survival signal, which finally enables blastocyst invasion into the stroma.

In accordance with invasion capacity of the embryo, intensity of phosphorylated AKT staining was stronger in the control trophoblast compared with the *Hif2a*-uKO trophoblast (Figure 8E). FOXO1 is a transcriptional factor regulated by the PI3K-AKT pathway (47). FOXO1 is phosphorylated by activated AKT and is translocated from the nucleus to the cytosol (47). Nuclear accumulation of FOXO1 was observed in the embryos attached to uteri of *Hif2a*-uKO mice, although it was stained inside the cytosol in the invaded embryo of control mice (Supplemental Figure 11). These findings indicate that direct contact between the embryo and uterine stroma is required for activation of the PI3K-AKT–FOXO1 pathway as an embryonic survival signal to avoid programmed embryonic death. VEGF, adrenomedullin (ADM), and LOX, which can activate the PI3K-AKT pathway and are regulated by HIF (48–50), are expressed in the uterine stroma and involved in the process of embryo implantation (15, 51–54). We found that mRNA expression of VEGF and ADM as well as LOX at the stroma of implantation sites collected by LCM technique was significantly decreased in *Hif2a*-uKO mice (Fig-
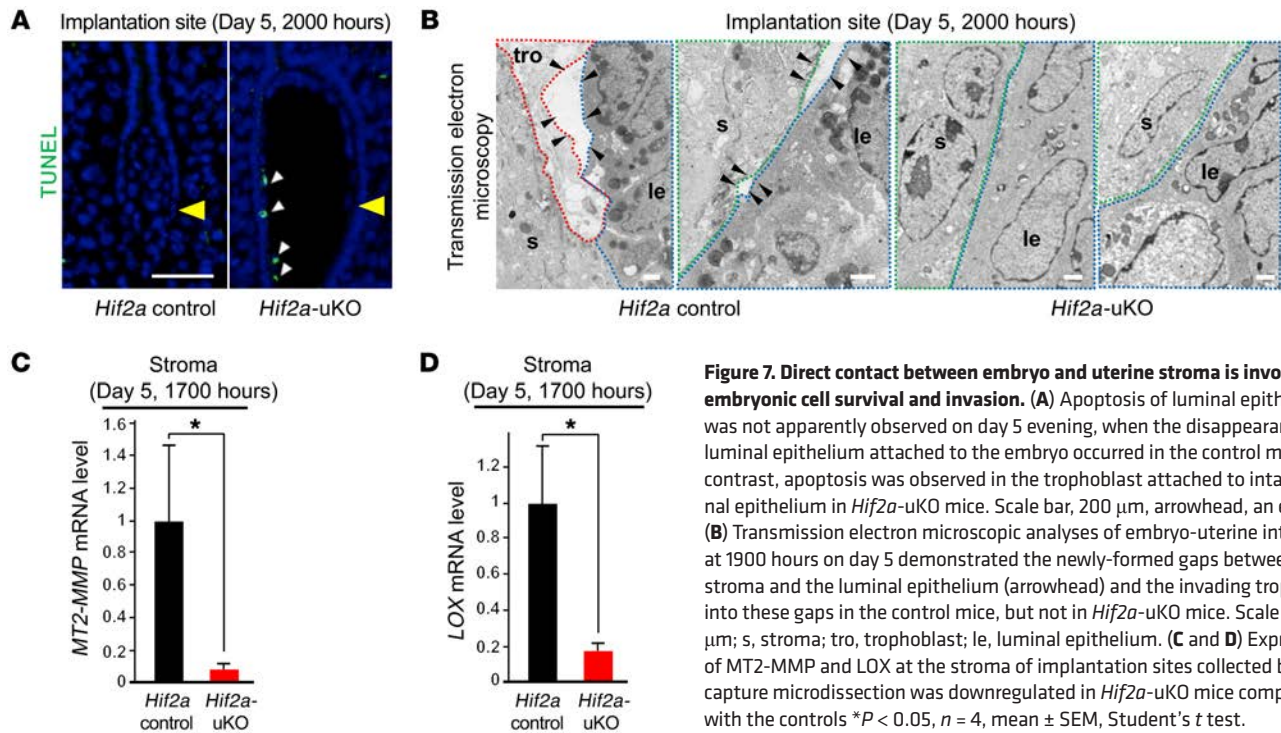
Figure 7. Direct contact between embryo and uterine stroma is involved in embryonic cell survival and invasion. (**A**) Apoptosis of luminal epithelium was not apparently observed on day 5 evening, when the disappearance of luminal epithelium attached to the embryo occurred in the control mice. In contrast, apoptosis was observed in the trophoblast attached to intact luminal epithelium in *Hif2a*-uKO mice. Scale bar, 200 μm, arrowhead, an embryo. (**B**) Transmission electron microscopic analyses of embryo-uterine interface at 1900 hours on day 5 demonstrated the newly-formed gaps between the stroma and the luminal epithelium (arrowhead) and the invading trophoblast into these gaps in the control mice, but not in *Hif2a*-uKO mice. Scale bar, 1 μm; s, stroma; tro, trophoblast; le, luminal epithelium. (**C** and **D**) Expression of MT2-MMP and LOX at the stroma of implantation sites collected by laser capture microdissection was downregulated in *Hif2a*-uKO mice compared with the controls *$P < 0.05$, $n = 4$, mean ± SEM, Student's t test.

ure 7D and Figure 8, F and G), suggesting that HIF2α-regulated stromal VEGF, ADM, and LOX activate the trophoblast cell survival pathway in normal conditions.

Discussion

In the present study, we found that mice with deletion of uterine *Hif2a* showed infertility because of pregnancy failure. Deficiency of uterine *Hif2a* downregulated the expression of decidual luteotrophin, which supports decidual growth through ovarian P_4 production, but P_4 administration did not recover implantation failure and rescued only decidualization. Mice with uterine deficiency of *Hif2a* displaced the implanting embryo in the aberrant position because of decreased LIF expression, but LIF supplementation normalized only the position of embryo attachment and did not recover implantation. These findings indicate that uterine HIF2α contributes to successful implantation regardless of decidualization and the position of embryo attachment. More importantly, TEM revealed that the luminal epithelium attached to the embryo spontaneously detached from the stroma and that the embryo can directly contact the uterine stroma in control mice. Persistent alignment of the luminal epithelium surrounding the embryo with the inactivated embryonic survival signal blocked embryo invasion into the uterine stroma in *Hif2a*-uKO mice (Figure 9). Direct contact between the embryo and the uterine stroma might be involved in embryonic cell survival and invasion in *Hif2a*-uKO mice (Figure 9).

Since the surface of the endometrium is distant from uterine blood vessels, it is possible that oxygen concentration in the luminal epithelium and the stroma near embryos is relatively low compared with the inner endometrium and the myometrium (55). Therefore, it is estimated that the luminal epithelium before implantation is in a hypoxic state and that angiogenesis prominently occurs after

implantation. After angiogenesis in implantation sites, oxygen concentration dynamically rises in the uterus. Previous studies have investigated the role of hypoxia in placental formation (56). On the other hand, few studies have focused on the role of hypoxia in the uterus during implantation. *Hif1a* and *Hif2a* were shown to be strongly expressed in the mouse uterus during embryo implantation in a previous report (15), and HIFα is functionally critical for successful embryo implantation in our study. Physiological uterine hypoxia during implantation may contribute to embryo implantation through HIF, although factors other than hypoxia, such as embryonic stimuli, may be associated with the induction of HIF.

P_4 signaling in the uterus is essential throughout pregnancy, and decidual luteotrophin activates the corpus luteum to maintain luteal function. Luteotrophin is one example of molecular interactions from the uterus to the ovary in rodents. In humans, chorionic gonadotrophin supports luteal function instead of decidual factors, suggesting that maintenance of luteal function by positive feedback of implantation-derived factors may be common machinery for successful pregnancy in mammals. The current study showed that luteal support cannot rescue implantation failure in mice with uterine deletion of *Hif2a*. These data are in accordance with the clinical fact that many patients do not become pregnant through IVF-ET treatment, even after sufficient luteal support. Dysregulation of HIF may be involved in recurrent implantation failure in humans.

Decreased LIF expression and aberrant position of the implantation site were observed in *Hif2a*-uKO mice during embryo attachment. Since a previous report has demonstrated that HIF2α, not HIF1α, transcriptionally induces LIF expression in human colon cancer cell lines (37), it is possible that uterine HIF2α induces LIF via transcriptional regulation in mice. In mouse embryonic stem cells, hypoxia-induced HIF1α directly suppresses expression of the
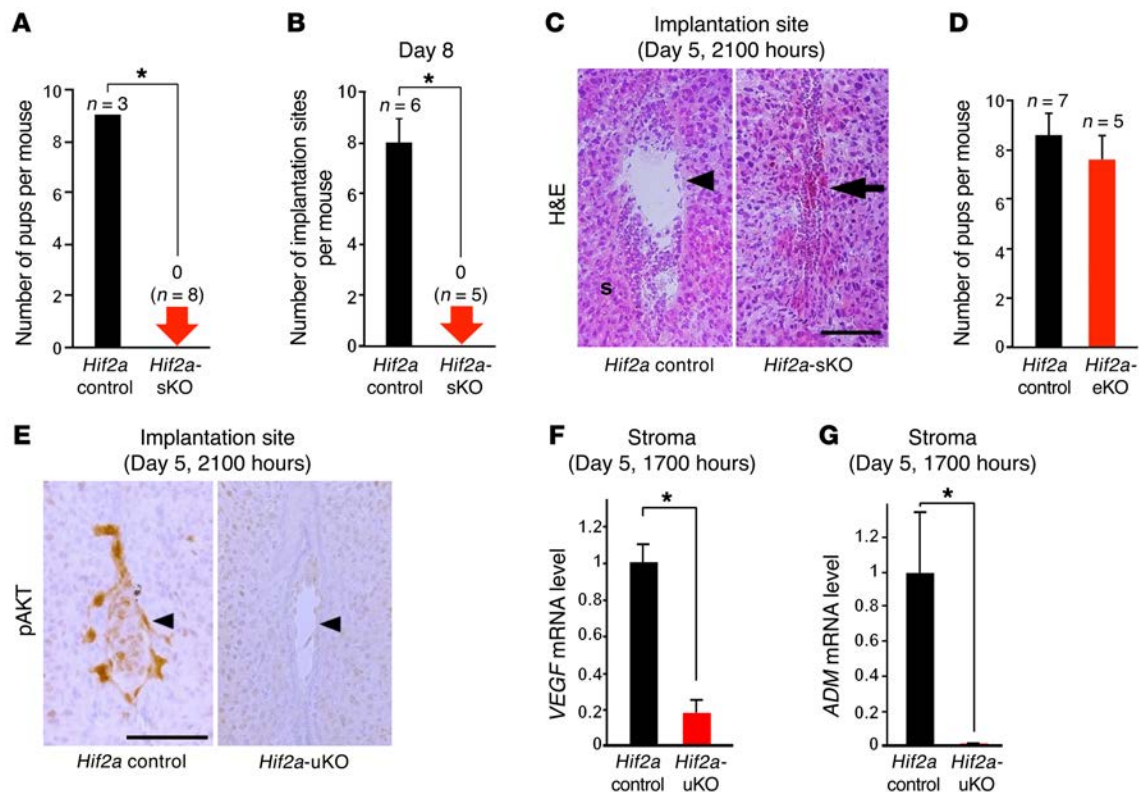
Figure 8. Stromal *Hif2a* is critical for embryo invasion and PI3K-AKT pathway is activated in the implanting embryos. (**A**–**C**) Infertility phenotype with both impaired embryo invasion and persistent presence of luminal epithelium was observed in *Hif2a*-sKO mice. In **A** and **B**, *$P < 0.05$, mean ± SEM, Student's *t* test. In **C**, scale bar, 200 μm; arrowhead, an embryo; s, stroma; arrow, a destroyed embryo with blood cell infiltration. (**D**) *Hif2a*-eKO mice demonstrated normal fertility. $P > 0.05$, mean ± SEM, Student's *t* test. (**E**) Intensity of phosphorylated AKT staining was strong in the control trophoblast compared with *Hif2a*-uKO one. (**F** and **G**) Expression of VEGF and ADM at the stroma of implantation sites collected by laser capture microdissection was decreased in *Hif2a*-uKO mice. *$P < 0.05$, mean ± SEM, Student's *t* test.

LIF receptor through transcriptional regulation and inactivates LIF-STAT3 signaling (36). These findings indicate that HIF1α and HIF2α regulate LIF-STAT3 signaling in different and complex detail. As for the uterus, HIF2α may dominantly activate LIF-STAT3 signaling.

Disappearance of the luminal epithelium might be an important process in embryo invasion. In addition to apoptosis, entosis and phagocytosis of the luminal epithelium by the trophoblast after attachment have been reported (57, 58). In control mice, apoptotic cells in the luminal epithelium at the implantation site are rarely observed; therefore, apoptosis as the cause behind the disappearance of the luminal epithelium can be ruled out. Similarly, entosis of the luminal epithelium was not observed in either *Hif2a*-uKO or the control mice. Our observation demonstrated that EMT from the luminal epithelium to the stroma did not occur during implantation in mice. We discovered intermittent gaps between the luminal epithelium and the stroma that lead to the detachment of the luminal epithelium, which might be a critical process for embryo invasion; these processes are impaired in *Hif2a*-uKO mice.

In concurrence with the detachment of the luminal epithelium from the stroma just before embryo invasion, the trophoblast enters the gap. Previous literature suggested the possibility that uterine stromal cells actively disrupt the epithelial basement membrane (59). The stroma produces several soluble factors, such as VEGF and ADM, to activate the PI3K-AKT–FOXO1 pathway as

an embryonic survival signal and to promote trophoblast invasion into the stroma. MT2-MMP activates MMP2, breaks the extracellular matrix of basement membrane, and regulates epithelial E-cadherin distribution (40–42, 44). LOX debilitates the extracellular matrix of the basement membrane (45, 46). Therefore, LOX and MT2-MMP may cooperatively support remodeling of the basement membrane between the uterine stroma and the luminal epithelium. Since it remains unclear how the luminal epithelium detaches from the stroma and how embryonic activation occurs following invasion, further investigation is needed.

Dynamic molecular changes following embryo attachment are very complicated, and uterine HIF plays various roles in pregnancy. This study revealed that uterine HIF2α is involved in a series of implantation processes, embryo attachment, decidualization, and especially, embryo invasion. The mechanism of embryo invasion has been scarcely reported, and we believe our results provide new evidence that stromal HIF2α controls embryo invasion. The association between human implantation failure and HIF function needs to be clarified in future studies.

Methods

Mice. WT mice (C57BL/6J and ICR, Japan SLC), *Hif1a*-floxed mice (16, 60), *Hif2a*-floxed mice (60, 61) (Jackson Laboratories), *Ltf*-Cre mice (21), *Amhr2*-Cre mice (19), *Pgr*-Cre mice (18), and *Rosa26* Cre-reporter knock-
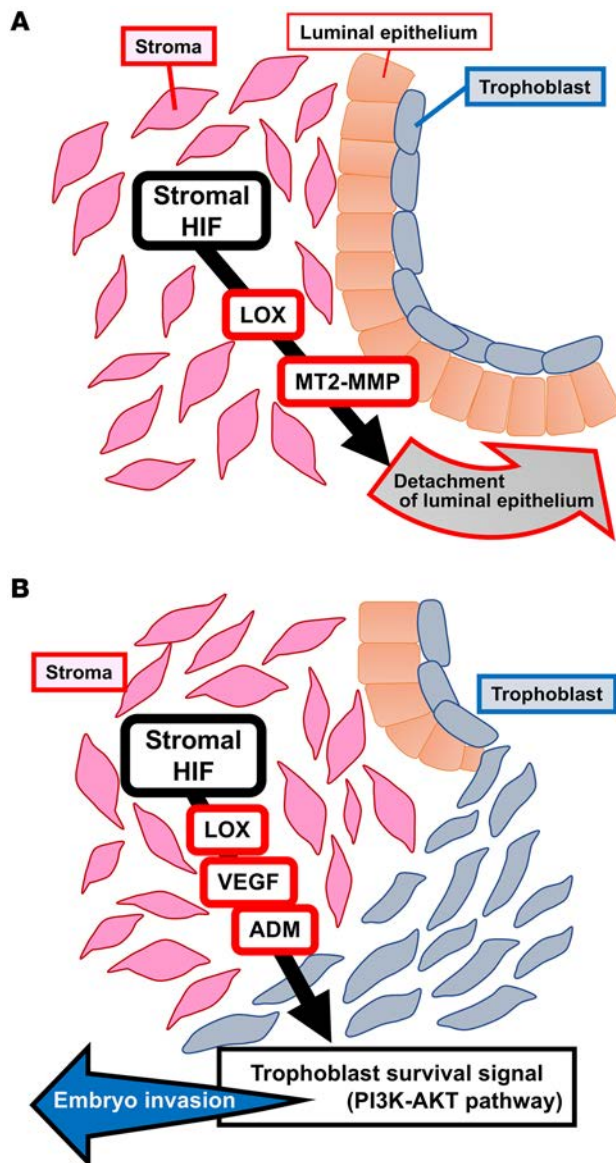
Figure 9. Potential pathways that contribute to embryo implantation through HIF. (**A**) Stromal HIF releases luminal epithelium from stroma through LOX and MT2-MMP, which permits direct contact between stroma and trophoblast. (**B**) Stromal HIF activates PI3K-AKT pathway as a trophoblast survival signal pathway through the induction of LOX, VEGF, and ADM, which promotes embryo invasion.

exhibit green emission before Cre-mediated recombination and red emission after the recombination. For epithelial cell lineage tracing in the uterus, we generated *R26GRR/Ltf*-Cre mice, which have red fluorescence in the uterine epithelium–derived cells (63).

Analysis of pregnancy events. For evaluation of pregnancy phenotypes, 2- to 5-month-old female mice of each line were mated with fertile males, and day 1 of pregnancy was defined as the day when we recognized vaginal plug. Ovulation, fertilization, preimplantation embryo development, and implantation were assessed as described (64). To treat *Hif2a*-uKO mice with exogenous P_4 and recombinant LIF protein, daily subcutaneous injections of P_4 (2 mg/mouse/day) from day 2 of pregnancy and intraperitoneal injection of recombinant LIF (20 μg/mouse) at 0900 hours on day 4 of pregnancy were performed, respectively. Recombinant LIF was produced using LIF expression vector as previously described (65, 66). The LIF expression vector was provided by Eiichi Hondo (Nagoya University, Japan).

Ovarian transplantation. Ovarian transplantation was performed as described (67). Female mice were anesthetized, the ovarian fat pad with the ovary was exteriorized, the bursa opened, and ovaries removed. The excised ovaries were held briefly in M2 medium and grafted back into the bursal cavity of recipient mice. More than 3 weeks after transplantation, the mice with ovary transplantation were mated with fertile WT males.

H&E staining and immunostaining. Frozen sections (12 μm), or formalin-fixed paraffin-embedded sections (6 μm) were subjected to H&E staining and immunohistochemistry. For immunostaining, antibodies against Ki67 (SP6, Thermo Fisher Scientific), and phosphorylated STAT3 (pSTAT3; EP2147Y, Abcam), COX2 (AA570-598, Cayman Chemical), E-cadherin (24E10, Cell Signaling Technology), phosphorylated AKT (pAKT; D9E, Cell Signaling Technology), and FOXO1 (C29H4, Cell Signaling Technology) were used.

Fluorescence assay. Frozen sections (12 μm) were subjected to immunofluorescence. Alexa Fluor 488–conjugated anti-rat immunoglobulin G and Alexa Fluor 555–conjugated anti-rabbit immunoglobulin G were used for protein detection, and nuclear staining was performed with 4, 6-diamidino-2-phenylindole using a fluorescence microscope (DM5000B and HyD, Leica Microsystems GmbH).

Measurement of serum P_4 and E_2 levels. Blood samples from mice were collected on the indicated days of pregnancy. Serum was separated by centrifugation (850*g* for 15 minutes) and stored at –80°C until analysis. Serum P_4 levels were measured by Progesterone EIA kit (Cayman Chemical), and E_2 levels were measured by Estradiol ELISA kit (CalBiotech).

In situ hybridization. Sense or antisense DIG-labeled cRNA probes for *Prl3c1*, *MT2-MMP*, and *LOX* were generated using appropriate polymerases from respective cDNAs as previously described (68). Specific RNA probes were prepared by DIG Labeling Kit (Roche Diagnostics GmbH) and paraffin sections (6 μm) were incubated with the probes and colored using NBT/BCIP solution (Roche Diagnostics GmbH) counterstained by methyl green solution (Wako Pure Chemical Industries).

in mice (*R26GRR* mice) (62) were used in this study. *R26GRR* mice were provide by Ken-ichi Yagami (University of Tsukuba, Tsukuba, Japan) and RIKEN BRC (Tsukuba, Japan). *Ltf*-Cre mice were provided by Sudhansu K. Dey (Cincinnati Children's Hospital Medical Center, Cincinnati, OH, USA). *Amhr2*-Cre mice were provided by Richard Behringer (The University of Texas MD Anderson Cancer Center, Houston, TX, USA). *Pgr*-Cre mice were provided by Francesco J. DeMayo (National Institute of Environmental Health Sciences, Research Triangle Park, NC, USA). *Ltf*, *Amhr2*, and *Pgr* are expressed in the luminal epithelium, the stroma/myometrium, and all the layers of uterus, respectively. Therefore, *Ltf*-Cre, *Amhr2*-Cre, and *Pgr*-Cre mice have the specific expression of Cre recombinase in the uterine epithelium, the stroma, and whole uterus, respectively (63). Mice with deletion of *Hif1a* or *Hif2a* in whole uterus (*Hif1a*-uKO mice and *Hif2a*-uKO mice, respectively) were generated by crossing *Pgr*-Cre with *Hif1a*- or *Hif2a*-floxed mice. Mice with deletion of *Hif2a* in the uterine epithelium or in the stroma (*Hif2a*-eKO mice and *Hif2a*-sKO mice, respectively) were generated by crossing *Hif2a*-floxed mice with *Ltf*-Cre or *Amhr2*-Cre mice. Cre-negative homozygous littermates for the conditional alleles were used as controls. *R26GRR* mice

Laser capture microdissection. LCM was performed as previously described (7). Frozen sections (20 μm) were mounted on polyethylene naphthalate slides (Leica Microsystems), fixed in cold acetone, stained in 0.05% toluidine blue, and dehydrated in ethanol. The target regions in the sections were microdissected with a LMD7000 system (Leica Microsystems). The luminal epithelium and stroma close to a crypt at the antimesometrial pole were dissected out from the uteri by LCM.

RT-quantitative PCR (qPCR). For conventional RNA analyses, total RNA extraction from frozen whole tissues was performed as previously described (7). As for LCM samples, the extracted RNA was amplified using an Ovation PicoSL WTA system V2 (NuGEN Technology), and qPCR was performed as previously described (7). A housekeeping gene (β-actin [Actb]) was used as an internal standard for normalizing the relative mRNA expression. Sequences of qPCR primers are listed in Supplemental Table 1.

TUNEL assay. In situ detection of apoptosis was performed using the In Situ Cell Death Detection Kit (Roche) following the manufacturer's instructions. The signal was detected using a confocal laser scanning microscope (LSM700, Carl Zeiss Microscopy GmbH).

Transmission electron microscopy. Uterine tissues were fixed with a buffered mix of 2.5% glutaraldehyde and 1.6% paraformaldehyde in phosphate buffer (0.1 M, pH 7.4) for 17 hours, and postfixed with 0.1 M cacodylate buffer and 1% osmium tetroxide for 30 minutes, dehydrated, replaced with propylene oxide, embedded in epoxy resin, and hardened at 60°C for 24 hours. The tissues were sectioned using a diamond knife at a thickness of 60–70 nm, mounted onto single slot copper grids with a support film, stained with lead citrate and uranyl acetate, and imaged at 80 kV in a transmission electron microscope (JEM-1011, JEOL).

Statistics. Statistical analyses were performed using a 2-tailed Student's *t* test and Fisher's exact probability test. A value of *P* < 0.05 was considered statistically significant.

Study approval. All mice used in this investigation were housed in the University of Tokyo Animal Care Facility according to the institutional guidelines for the use of laboratory animals. All the animal experiments in the present study were reviewed and approved by the animal experiment committee of the University of Tokyo (Tokyo, Japan).

Author contributions

Acknowledgments

Address correspondence to: Yasushi Hirota, Department of Obstetrics and Gynecology, Graduate School of Medicine, The University of Tokyo, 7-3-1 Hongo, Bunkyo-ku, Tokyo 113-8655, Japan. Phone: 81.3.3815.5411; Email: yhirota-tky@umin.ac.jp.

1. Inhorn MC, Patrizio P. Infertility around the globe: new thinking on gender, reproductive technologies and global movements in the 21st century. *Hum Reprod Update*. 2015;21(4):411–426.

2. Dey SK, et al. Molecular cues to implantation. *Endocr Rev*. 2004;25(3):341–373.

3. Cha J, Sun X, Dey SK. Mechanisms of implantation: strategies for successful pregnancy. *Nat Med*. 2012;18(12):1754–1767.

4. Egashira M, Hirota Y. Uterine receptivity and embryo-uterine interactions in embryo implantation: lessons from mice. *Reprod Med Biol*. 2013;12(4):127–132.

5. Matsumoto H, Fukui E, Yoshizawa M. Molecular and cellular events involved in the completion of blastocyst implantation. *Reprod Med Biol*. 2016;15(2):53–58.

6. Tranguch S, Wang H, Daikoku T, Xie H, Smith DF, Dey SK. FKBP52 deficiency-conferred uterine progesterone resistance is genetic background and pregnancy stage specific. *J Clin Invest*. 2007;117(7):1824–1834.

7. Haraguchi H, et al. MicroRNA-200a locally attenuates progesterone signaling in the cervix, preventing embryo implantation. *Mol Endocrinol*. 2014;28(7):1108–1117.

8. Das SK, et al. Heparin-binding EGF-like growth factor gene is induced in the mouse uterus temporally by the blastocyst solely at the site of its apposition: a possible ligand for interaction with blastocyst EGF-receptor in implantation. *Development*. 1994;120(5):1071–1083.

9. Chen JR, Cheng JG, Shatzer T, Sewell L, Hernandez L, Stewart CL. Leukemia inhibitory factor can substitute for nidatory estrogen and is essential to inducing a receptive uterus for implantation but is not essential for subsequent embryogenesis. *Endocrinology*. 2000;141(12):4365–4372.

10. Song H, Lim H, Das SK, Paria BC, Dey SK. Dysregulation of EGF family of growth factors and COX-2 in the uterus during the preattachment and attachment reactions of the blastocyst with the luminal epithelium correlates with implantation failure in LIF-deficient mice. *Mol Endocrinol*. 2000;14(8):1147–1161.

11. Cheng JG, Chen JR, Hernandez L, Alvord WG, Stewart CL. Dual control of LIF expression and LIF receptor function regulate Stat3 activation at the onset of uterine receptivity and embryo implantation. *Proc Natl Acad Sci U S A*. 2001;98(15):8680–8685.

12. Dengler VL, Galbraith M, Espinosa JM. Transcriptional regulation by hypoxia inducible factors. *Crit Rev Biochem Mol Biol*. 2014;49(1):1–15.

13. Schödel J, Oikonomopoulos S, Ragoussis J, Pugh CW, Ratcliffe PJ, Mole DR. High-resolution genome-wide mapping of HIF-binding sites by ChIP-seq. *Blood*. 2011;117(23):e207–e217.

14. Majmundar AJ, Wong WJ, Simon MC. Hypoxia-inducible factors and the response to hypoxic stress. *Mol Cell*. 2010;40(2):294–309.

15. Daikoku T, et al. Expression of hypoxia-inducible factors in the peri-implantation mouse uterus is regulated in a cell-specific and ovarian steroid hormone-dependent manner. Evidence for differential function of HIFs during early pregnancy. *J Biol Chem*. 2003;278(9):7683–7691.

16. Ryan HE, Lo J, Johnson RS. HIF-1 alpha is required for solid tumor formation and embryonic vascularization. *EMBO J*. 1998;17(11):3005–3015.

17. Tian H, Hammer RE, Matsumoto AM, Russell

DW, McKnight SL. The hypoxia-responsive transcription factor EPAS1 is essential for catecholamine homeostasis and protection against heart failure during embryonic development. *Genes Dev*. 1998;12(21):3320–3324.

18. Soyal SM, et al. Cre-mediated recombination in cell lineages that express the progesterone receptor. *Genesis*. 2005;41(2):58–66.

19. Jamin SP, Arango NA, Mishina Y, Hanks MC, Behringer RR. Requirement of Bmpr1a for Müllerian duct regression during male sexual development. *Nat Genet*. 2002;32(3):408–410.

20. Daikoku T, Jackson L, Besnard V, Whitsett J, Ellenson LH, Dey SK. Cell-specific conditional deletion of Pten in the uterus results in differential phenotypes. *Gynecol Oncol*. 2011;122(2):424–429.

21. Daikoku T, Ogawa Y, Terakawa J, Ogawa A, DeFalco T, Dey SK. Lactoferrin-iCre: a new mouse line to study uterine epithelial gene function. *Endocrinology*. 2014;155(7):2718–2724.

22. Herz Z, Khan I, Jayatilak PG, Gibori G. Evidence for the secretion of decidual luteotropin: a prolactin-like hormone produced by rat decidual cells. *Endocrinology*. 1986;118(6):2203–2209.

23. Bao L, et al. Decidual prolactin silences the expression of genes detrimental to pregnancy. *Endocrinology*. 2007;148(5):2326–2334.

24. Jayatilak PG, Glaser LA, Basuray R, Kelly PA, Gibori G. Identification and partial characterization of a prolactin-like hormone produced by rat decidual tissue. *Proc Natl Acad Sci U S A*. 1985;82(1):217–221.

25. Cha J, et al. Combinatory approaches prevent preterm birth profoundly exacerbated by gene-environment interactions. *J Clin Invest*. 2013;123(9):4063–4075.

26. Binart N, et al. Rescue of preimplantatory egg development and embryo implantation in prolactin receptor-deficient mice after progesterone administration. *Endocrinology*. 2000;141(7):2691–2697.

27. Reese J, et al. Implantation and decidualization defects in prolactin receptor (PRLR)-deficient mice are mediated by ovarian but not uterine PRLR. *Endocrinology*. 2000;141(5):1872–1881.

28. Alam SM, Konno T, Sahgal N, Lu L, Soares MJ. Decidual cells produce a heparin-binding prolactin family cytokine with putative intrauterine regulatory actions. *J Biol Chem*. 2008;283(27):18957–18968.

29. Hiraoka Y, et al. PLP-I: a novel prolactin-like gene in rodents. *Biochim Biophys Acta*. 1999;1447(2-3):291–297.

30. Toft DJ, Linzer DI. Prolactin (PRL)-like protein J, a novel member of the PRL/growth hormone family, is exclusively expressed in maternal decidua. *Endocrinology*. 1999;140(11):5095–5101.

31. Ishibashi K, Imai M. Identification of four new members of the rat prolactin/growth hormone gene family. *Biochim Biophys Res Commun*. 1999;262(3):575–578.

32. Paria BC, et al. Cellular and molecular responses of the uterus to embryo implantation can be elicited by locally applied growth factors. *Proc Natl Acad Sci U S A*. 2001;98(3):1047–1052.

33. Lee KY, et al. Bmp2 is critical for the murine uterine decidual response. *Mol Cell Biol*.

2007;27(15):5468–5478.

34. Lim H, et al. Multiple female reproductive failures in cyclooxygenase 2-deficient mice. *Cell*. 1997;91(2):197–208.

35. Stewart CL, et al. Blastocyst implantation depends on maternal expression of leukaemia inhibitory factor. *Nature*. 1992;359(6390):76–79.

36. Jeong CH, et al. Hypoxia-inducible factor-1 alpha inhibits self-renewal of mouse embryonic stem cells in Vitro via negative regulation of the leukemia inhibitory factor-STAT3 pathway. *J Biol Chem*. 2007;282(18):13672–13679.

37. Wu L, et al. HIF-2α mediates hypoxia-induced LIF expression in human colorectal cancer cells. *Oncotarget*. 2015;6(6):4406–4417.

38. Zhu S, et al. Transcriptional upregulation of MT2-MMP in response to hypoxia is promoted by HIF-1α in cancer cells. *Mol Carcinog*. 2011;50(10):770–780.

39. Erler JT, et al. Lysyl oxidase is essential for hypoxia-induced metastasis. *Nature*. 2006;440(7088):1222–1226.

40. Sato H, Seiki M. Membrane-type matrix metalloproteinases (MT-MMPs) in tumor metastasis. *J Biochem*. 1996;119(2):209–215.

41. Morrison CJ, Overall CM. TIMP independence of matrix metalloproteinase (MMP)-2 activation by membrane type 2 (MT2)-MMP is determined by contributions of both the MT2-MMP catalytic and hemopexin C domains. *J Biol Chem*. 2006;281(36):26528–26539.

42. Hotary K, Li XY, Allen E, Stevens SL, Weiss SJ. A cancer cell metalloprotease triad regulates the basement membrane transmigration program. *Genes Dev*. 2006;20(19):2673–2686.

43. Ota I, Li XY, Hu Y, Weiss SJ. Induction of a MT1-MMP and MT2-MMP-dependent basement membrane transmigration program in cancer cells by Snail1. *Proc Natl Acad Sci U S A*. 2009;106(48):20318–20323.

44. Gómez-Escudero J, et al. E-cadherin cleavage by MT2-MMP regulates apical junctional signaling and epithelial homeostasis in the intestine. *J Cell Sci*. 2017;130(23):4013–4027.

45. Cox TR, Gartland A, Erler JT. Lysyl oxidase, a targetable secreted molecule involved in cancer metastasis. *Cancer Res*. 2016;76(2):188–192.

46. Erler JT, et al. Hypoxia-induced lysyl oxidase is a critical mediator of bone marrow cell recruitment to form the premetastatic niche. *Cancer Cell*. 2009;15(1):35–44.

47. Gilley J, Coffer PJ, Ham J. FOXO transcription factors directly activate bim gene expression and promote apoptosis in sympathetic neurons. *J Cell Biol*. 2003;162(4):613–622.

48. Jiang BH, Liu LZ. PI3K/PTEN signaling in tumorigenesis and angiogenesis. *Biochim Biophys Acta*. 2008;1784(1):150–158.

49. Nagaya N, Mori H, Murakami S, Kangawa K, Kitamura S. Adrenomedullin: angiogenesis and gene therapy. *Am J Physiol Regul Integr Comp Physiol*. 2005;288(6):R1432–R1437.

50. Pez F, et al. The HIF-1-inducible lysyl oxidase activates HIF-1 via the Akt pathway in a positive regulation loop and synergizes with HIF-1 in promoting tumor cell growth. *Cancer Res*. 2011;71(5):1647–1657.

51. Chakraborty I, Das SK, Dey SK. Differential expression of vascular endothelial growth factor and its receptor mRNAs in the mouse uterus around the time of implantation. *J Endocrinol*. 1995;147(2):339–352.

52. Li M, Yee D, Magnuson TR, Smithies O, Caron KM. Reduced maternal expression of adrenomedullin disrupts fertility, placentation, and fetal growth in mice. *J Clin Invest*. 2006;116(10):2653–2662.

53. Li M, Wu Y, Caron KM. Haploinsufficiency for adrenomedullin reduces pinopodes and diminishes uterine receptivity in mice. *Biol Reprod*. 2008;79(6):1169–1175.

54. Li SY, et al. Molecular characterization of lysyl oxidase-mediated extracellular matrix remodeling during mouse decidualization. *FEBS Lett*. 2017;591(10):1394–1407.

55. Rodesch F, Simon P, Donner C, Jauniaux E. Oxygen measurements in endometrial and trophoblastic tissues during early pregnancy. *Obstet Gynecol*. 1992;80(2):283–285.

56. Aplin JD. Hypoxia and human placental development. *J Clin Invest*. 2000;105(5):559–560.

57. Li Y, Sun X, Dey SK. Entosis allows timely elimination of the luminal epithelial barrier for embryo implantation. *Cell Rep*. 2015;11(3):358–365.

58. Aplin JD, Ruane PT. Embryo-epithelium interactions during implantation at a glance. *J Cell Sci*. 2017;130(1):15–22.

59. Schlafke S, Enders AC. Cellular basis of interaction between trophoblast and uterus at implantation. *Biol Reprod*. 1975;12(1):41–65.

60. Semba H, et al. HIF-1α-PDK1 axis-induced active glycolysis plays an essential role in macrophage migratory capacity. *Nat Commun*. 2016;7:11635.

61. Gruber M, Hu CJ, Johnson RS, Brown EJ, Keith B, Simon MC. Acute postnatal ablation of Hif-2-alpha results in anemia. *Proc Natl Acad Sci U S A*. 2007;104(7):2301–2306.

62. Hasegawa Y, et al. Novel ROSA26 Cre-reporter knock-in C57BL/6N mice exhibiting green emission before and red emission after Cre-mediated recombination. *Exp Anim*. 2013;62(4):295–304.

63. Hiraoka T, et al. STAT3 accelerates uterine epithelial regeneration in a mouse model of decellularized uterine matrix transplantation. *JCI Insight*. 2016;1(8):e87591.

64. Hirota Y, Daikoku T, Tranguch S, Xie H, Bradshaw HB, Dey SK. Uterine-specific p53 deficiency confers premature uterine senescence and promotes preterm birth in mice. *J Clin Invest*. 2010;120(3):803–815.

65. Terakawa J, et al. Embryo implantation is blocked by intraperitoneal injection with anti-LIF antibody in mice. *J Reprod Dev*. 2011;57(6):700–707.

66. Kobayashi R, et al. The contribution of leukemia inhibitory factor (LIF) for embryo implantation differs among strains of mice. *Immunobiology*. 2014;219(7):512–521.

67. Shaw JM, Trounson AO. Ovarian tissue transplantation and cryopreservation. Application to maintenance and recovery of transgenic and inbred mouse lines. *Methods Mol Biol*. 2002;180:229–251.

68. Hirota Y, et al. The presence of midkine and its possible implication in human ovarian follicles. *Am J Reprod Immunol*. 2007;58(4):367–373.

SOURCE
DATA

TRANSPARENT
PROCESS

Article

The first murine zygotic transcription is promiscuous and uncoupled from splicing and 3′ processing

Ken-ichiro Abe[1,†], Ryoma Yamamoto[1,†], Vedran Franke[2,†], Minjun Cao[1], Yutaka Suzuki[3,4], Masataka G Suzuki[1], Kristian Vlahovicek[2,5,****], Petr Svoboda[6,*], Richard M Schultz[7,**] & Fugaku Aoki[1,***]

Abstract

Initiation of zygotic transcription in mammals is poorly understood. In mice, zygotic transcription is first detected shortly after pronucleus formation in 1-cell embryos, but the identity of the transcribed loci and mechanisms regulating their expression are not known. Using total RNA-Seq, we have found that transcription in 1-cell embryos is highly promiscuous, such that intergenic regions are extensively expressed and thousands of genes are transcribed at comparably low levels. Striking is that transcription can occur in the absence of defined core-promoter elements. Furthermore, accumulation of translatable zygotic mRNAs is minimal in 1-cell embryos because of inefficient splicing and 3′ processing of nascent transcripts. These findings provide novel insights into regulation of gene expression in 1-cell mouse embryos that may confer a protective mechanism against precocious gene expression that is the product of a relaxed chromatin structure present in 1-cell embryos. The results also suggest that the first zygotic transcription itself is an active component of chromatin remodeling in 1-cell embryos.

Introduction

The oocyte-to-embryo transition (OET) entails a dramatic reprogramming of gene expression and conversion of a differentiated transcriptionally quiescent oocyte to totipotent blastomeres (De La Fuente & Eppig, 2001; Abe *et al*, 2010). The timing of zygotic genome activation (ZGA) is species dependent. Genome activation in mice is the earliest for mammals studied to date; the first wave of transcription (also referred to as the minor ZGA wave) starts at the mid-1-cell stage shortly after pronucleus formation, as evidenced by BrdU incorporation (Bouniol *et al*, 1995; Aoki *et al*, 1997) and expression of sperm-borne transgenes (Matsumoto *et al*, 1994). Although repetitive elements, for example, B2-containing sequences (Vasseur *et al*, 1985) and MuERV-L (Kigami *et al*, 2003), are expressed in 1-cell mouse embryos, transcription of single-copy genes is poorly understood, as is their function, which is not necessary for cleavage to the 2-cell stage (Warner & Versteegh, 1974).

Studies using plasmid-borne reporter genes have provided insights regarding mechanisms that govern transcription in 1-cell embryos. These studies demonstrated that reporter gene expression in 1-cell embryos does not require an enhancer for efficient expression, whereas an enhancer is required for efficient expression in 2-cell embryos (Wiekowski *et al*, 1991; Majumder *et al*, 1993). Thus, 1-cell embryos are transcriptionally permissive, but development to the 2-cell stage is accompanied by formation of a transcriptionally repressive state (DePamphilis, 1993) and genome-wide accumulation of repressive histone modification marks (Santos *et al*, 2005). This developmental change in transcriptional regulation involves DNA replication at the 2-cell stage because an enhancer is not required for efficient transcription when 2-cell embryos were treated with aphidicolin, which inhibits DNA replication (Wiekowski *et al*,

1 Department of Integrated Biosciences, Graduate School of Frontier Sciences, The University of Tokyo, Kashiwa, Japan
2 Bioinformatics Group, Division of Biology, Faculty of Science, Zagreb University, Zagreb, Croatia
3 Department of Medical Genome Science, Graduate School of Frontier Sciences, The University of Tokyo, Kashiwa, Japan
4 The University of Tokyo, Tokyo, Japan
5 Department of Informatics, University of Oslo, Oslo, Norway
6 Institute of Molecular Genetics, Academy of Sciences of the Czech Republic, Prague, Czech Republic
7 Department of Biology, University of Pennsylvania, Philadelphia, PA, USA
   *Corresponding author. Tel: +420 241063147; E-mail: svobodap@img.cas.cz
   **Corresponding author. Tel: +1 215 898 7869; E-mail: rschultz@sas.upenn.edu
   ***Corresponding author. Tel: +81 471 36 3695; Fax: +81 471 36 3698; E-mail: aokif@k.u-tokyo.ac.jp
   †These authors contributed equally to this work
   ****Corresponding author for computational biology

1991; Majumder *et al*, 1993; Henery *et al*, 1995; Forlani *et al*, 1998). The transcriptionally repressive state likely stems from chromatin structure because increasing histone acetylation in 2-cell embryos by treating the embryos with butyrate, an inhibitor of histone deacetylase, relieves the requirement for an enhancer for efficient expression of the reporter gene (Majumder *et al*, 1993; Wiekowski *et al*, 1993). Similar conclusions were reached using expression of the 2-cell transiently expressed endogenous *Eif1a* gene (Davis *et al*, 1996).

Microarray profiling identified zygotic mRNA expression at the 2-cell (major ZGA wave) but not the 1-cell stage (Hamatani *et al*, 2004; Wang *et al*, 2004; Zeng & Schultz, 2005). This finding suggests that mRNAs are either not expressed or microarray profiling is not sensitive enough to detect mRNAs produced during minor ZGA. More recent high-throughput sequencing (HTS) experiments identified hundreds of different mRNAs with increased abundance in 1-cell embryos (Park *et al*, 2013; Xue *et al*, 2013; Deng *et al*, 2014). However, due to increased RNA adenylation in 1-cell embryos (Piko & Clegg, 1982), poly(A) RNA sequencing results are difficult to interpret as they might reflect polyadenylation changes and not 1-cell transcription *per se* (Xue *et al*, 2013; Deng *et al*, 2014). The most comprehensive study regarding transcription in 1-cell embryos to date used SOLiD sequencing after ribosomal RNA depletion and identified ~600 genes upregulated > 1.5-fold between the oocyte and 1-cell embryo (Park *et al*, 2013).

In this study, we employed total RNA sequencing to identify sequences transcribed in 1-cell embryos and to gain understanding about mechanisms that govern their expression. We show that pervasive transcription occurs in intergenic regions including many transposons whose transcription continues far into their genomic flanks; transcription can occur independently of defined core-promoter elements; over four thousand genes are transcribed in 1-cell embryos with ~5% being transcribed transiently; the majority of genes transcribed in 1-cell embryos are also transcribed in 2-cell embryos when the major wave of genome activation occurs; and mRNAs transcribed at the 1-cell stage are mostly nonfunctional because their 3′ end processing and splicing are highly inefficient.

Results

Global analysis of the first wave of transcription

To explore the first wave of zygotic transcription, we characterized total RNA in metaphase II-arrested eggs (MII eggs) and embryos by HTS. We sequenced total RNA rather than selecting poly(A)-containing RNA (poly(A) RNA) because extensive RNA polyadenylation that occurs post-fertilization would be difficult to distinguish from *bona fide* zygotic mRNA synthesis (Piko & Clegg, 1982; Oh *et al*, 2000; Meijer *et al*, 2007). In addition, the RNA was not amplified to further minimize any deviation from the initial distribution of mRNAs. We isolated RNA from two sets of MII eggs and 1-cell embryos and one set of 2-cell and 4-cell embryos, morulae, and blastocysts. We also prepared RNA from 1-cell embryos in which transcription was inhibited by 5,6-dichlorobenzimidazole riboside (DRB), an inhibitor of RNA polymerase II activity (Sehgal *et al*, 1976), and 2-cell embryos treated with the DNA replication inhibitor aphidicolin (Bucknall *et al*, 1973) (Supplementary Table S1). Libraries from two sets of MII eggs and 1-cell embryos were

subjected to 35-nt single-end sequencing (35SE); one set from each stage was subjected to 76-nt paired-end (76PE) sequencing with depths of $33–58 \times 10^6$ (Supplementary Table S1). Analysis of the sequencing results showed a high degree of reproducibility among the duplicate sets as well as for biological replicates (Supplementary Fig S1A). Comparison of our 76PE Illumina data and 50SE SOLiD data obtained by sequencing of total RNA depleted of ribosomal RNA from identical stages (Park *et al*, 2013) showed a high concordance of the signal distribution along chromosomes ($r^2 = ~0.8$, Supplementary Fig S1B) and a good similarity of transcriptome changes between different stages ($r^2 = ~0.6$, Supplementary Fig S1C), confirming the overall reproducibility of our data.

The relative abundance of rRNA, repetitive sequences, annotated mRNAs, and unique sequences in the individual libraries were consistent with previous measurements (Fig 1A and Supplementary Fig S1D) (Piko & Clegg, 1982). For example, the fraction of mRNA in MII eggs and early cleavage-stage embryos is greater than that in somatic cells—for example, mRNA makes 2.5% of total RNA mass in HeLa cells (Jackson *et al*, 2000)—and the decline in the relative abundance of mRNA between the MII egg and 2-cell embryo correlates with the known degradation of maternal mRNA during this developmental period (Bachvarova & De Leon, 1980; Piko & Clegg, 1982). The fraction of mRNA was somewhat higher than previously reported (Piko & Clegg, 1982), which likely reflects that total RNA for HTS was size-selected for RNAs > 200 nt, causing a higher incidence of mRNAs in sequenced libraries. The small increase in the representation of rRNA and repeat-derived sequences at the expense of mRNA-derived reads in 1-cell embryos (Fig 1A) could be a consequence of ongoing maternal mRNA degradation in 1-cell embryos and/or new transcription of rRNA and retrotransposons. The frequency of 5′ external transcribed spacer (ETS)-derived reads from the 45S rRNA precursor, an indirect proxy of rRNA transcription, did not suggest robust rRNA transcription in 1-cell embryos because the amount of 5′ ETS-derived reads in MII eggs was actually greater than that in 1-cell embryos (Supplementary Fig S2A). However, in agreement with rDNA transcription initiating during the 2-cell stage (Zatsepina *et al*, 2003), we observed a ~fivefold increase in the number of 5′ ETS-derived reads between the 1-cell and 2-cell stages and a further more dramatic increase between 2-cell and 4-cell stages (Supplementary Fig S2B).

Unsupervised clustering of the samples based on reads mapping to exon sequences showed that the 1-cell embryo mRNA transcriptome was very similar to that of MII eggs and that DRB treatment had little apparent effect on the transcriptome (Fig 1B). These results are consistent with previous transcriptome studies (Hamatani *et al*, 2004; Wang *et al*, 2004; Zeng & Schultz, 2005) and are further supported by quantification of reads mapping to exons in MII eggs, 1-cell, and 1-cell + DRB samples (Fig 1C and 1D) lending confidence that new insights obtained from our HTS approach are warranted and not an experimental artifact.

The most notable change in the 1-cell RNA population relative to that of MII eggs was a widespread occurrence of individual, rarely overlapping, DRB-sensitive reads whose density rarely exceeded a few reads per locus (~0.1 counts per million (CPM), hence referred to as low CPM reads hereafter). In a display of a larger genomic region, low CPM reads appeared as an unevenly distributed 'grass in a forest' (Fig 2 and Supplementary Fig S3). Low CPM reads appeared more frequently within gene-rich regions but were readily found in
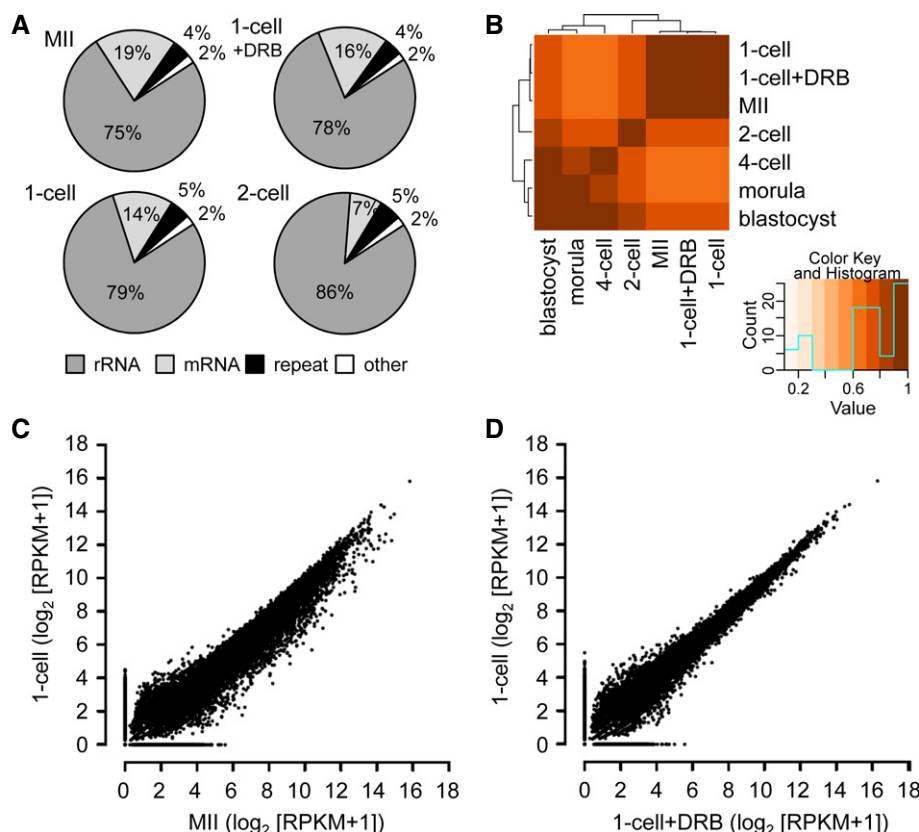
Figure 1.　General features of sequenced total RNA during ZGA.

A　Composition of selected libraries produced from total RNA. Shown is the proportion of reads matching rRNA-derived transcripts (rRNA), transcripts produced from repeats identified by RepeatMasker (repeat), annotated mRNAs (mRNA), and other sequences (other).

B　Hierarchical clustering of 76-nt paired-end datasets from different stages of preimplantation development performed on Spearman correlations between $\log_2$ of RPKM values for transcripts.

C, D　Comparison of MII and 1-cell transcriptomes (C) and 1-cell and 1-cell + DRB transcriptomes (D). The graph was made by plotting expression values for mRNAs ($\log_2[RPKM + 1]$) from 76PE sequencing data. Each point represents one transcript whose position indicates its abundance value in indicated stages. RPKM values were increased by adding 1 in order to obtain $\log_2$ values above zero.

intergenic regions (Fig 2A and Supplementary Fig S3A). Although low CPM reads were also observed at later embryonic stages, their appearance was not as uniform and striking as in 1-cell embryos.

Because the presence of low CPM reads became readily apparent when sequences present in MII eggs were masked (Fig 2B), we examined the annotated proximal end of the Y chromosome (~3 Mb) (Fig 2C). Transcripts detected from this region must be of zygotic origin, and thus, low CPM reads would not be obscured by maternal mRNAs. Indeed, Y-chromosome-derived, DRB-sensitive low CPM reads were readily observed in the 76PE dataset (Fig 2C), and low CPM reads were also found in 50SE data (Park *et al*, 2013) (Supplementary Fig S3B). Given that the low CPM reads originated from genes as well as intergenic regions, we explored these two transcript categories separately.

Widespread intergenic transcription in 1-cell embryos

The occurrence of low CPM reads in intergenic regions was first confirmed by quantitative analysis. We divided intergenic regions across the entire genome into 1-kb segments and determined the number of segments to which at least a single read was uniquely

mapped. The number of 1-kb loci harboring uniquely mapped reads was threefold higher in 1-cell embryos than in MII eggs (Fig 3A). This number decreased gradually with development and reached levels similar to those of MII eggs at the morula stage (Fig 3A), while the number of loci harboring uniquely mapped reads in DRB-treated 1-cell embryos remained similar to that in MII eggs. Furthermore, aphidicolin treatment of 2-cell embryos to inhibit the DNA replication restored the number of loci to the level observed in 1-cell embryos. These results suggest the presence of a transcriptionally permissive state in 1-cell embryos might be governed by the same mechanisms that regulate expression of plasmid-borne reporter genes during this period of development and the 2-cell stage (Wiekowski *et al*, 1991; Majumder *et al*, 1993).

Intergenic transcripts yielding low CPM reads could be either short (i.e., one read or pair of reads would represent one short transcription unit) or they could be fragments of rare long transcripts (i.e., one transcript would yield multiple sequenced fragments, most of which would be far from the actual transcription start site). Two observations suggest some intergenic low CPM reads were derived from fragmented long transcripts. First, when the sequenced libraries were combined to achieve greater depth, low CPM reads
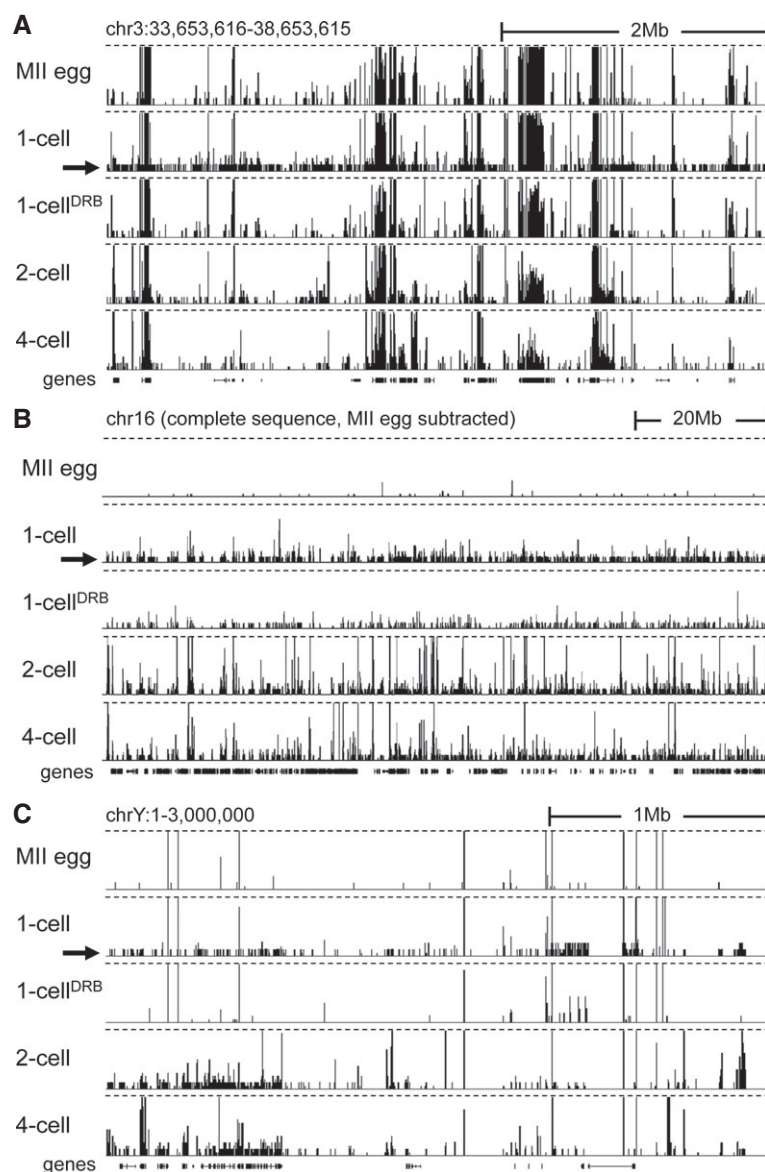
Figure 2. Global view of the minor wave of ZGA.

A Transcription at the 1-cell stage manifests as increased number of low CPM reads scattered across the genome. Shown are HTS data [a customized screenshot from the UCSC Genome browser (Karolchik *et al*, 2012)] from different stages mapped into a 5-Mb region of the genome with a variable gene density. The vertical scale was trimmed at 0.5 CPM; trimming is indicated by horizontal dashed lines. Note the appearance of low-density reads in 1-cell embryos (indicated by the black arrow), which are not observed in unfertilized oocytes and 1-cell embryos treated with DRB. Low CPM reads also appear in intergenic regions.

B Masking maternally transcribed regions reveals chromosome-wide presence of low CPM reads in 1-cell embryos. A UCSC browser screenshot of the chromosome 16 shows 76PE raw data mapped to the genome upon masking reads derived from oocytes. The vertical scale was trimmed at 20 reads; trimming is indicated by horizontal dashed lines. A small number of reads detected in MII eggs comes from repetitive sequences, which otherwise do not yield signal because of multi-mapping restrictions.

C Zygotic transcription from the Y chromosome initiates at the 1-cell stage. Shown are HTS data from different stages mapped into the ~3-Mb annotated region of the chromosome Y. The vertical scale was trimmed at 0.5 CPM; trimming is indicated by horizontal dashed lines. The residual signal on the chromosome Y in MII eggs and 1-cell embryos treated with DRB is an artifact caused by common retrotransposon-derived sequences (mainly MT-derived).

representing discrete short transcriptional units did not overlap but rather were more densely populated over a larger area (Supplementary Fig S3A). Second, numerous transcribed intergenic regions at the 1-cell stage correlated with downstream regions of several different retrotransposons whose transcription at the 2-cell stage apparently invaded their neighborhood.

Repetitive sequences represent a source of potential promoters for intergenic transcription. Accordingly, we analyzed repetitive element-derived reads and found that the 1-cell stage contained the highest frequency of retrotransposon-derived reads among all the samples (Fig 3B). The increase in retrotransposon-derived read abundance between MII and 1-cell stage was DRB-sensitive and
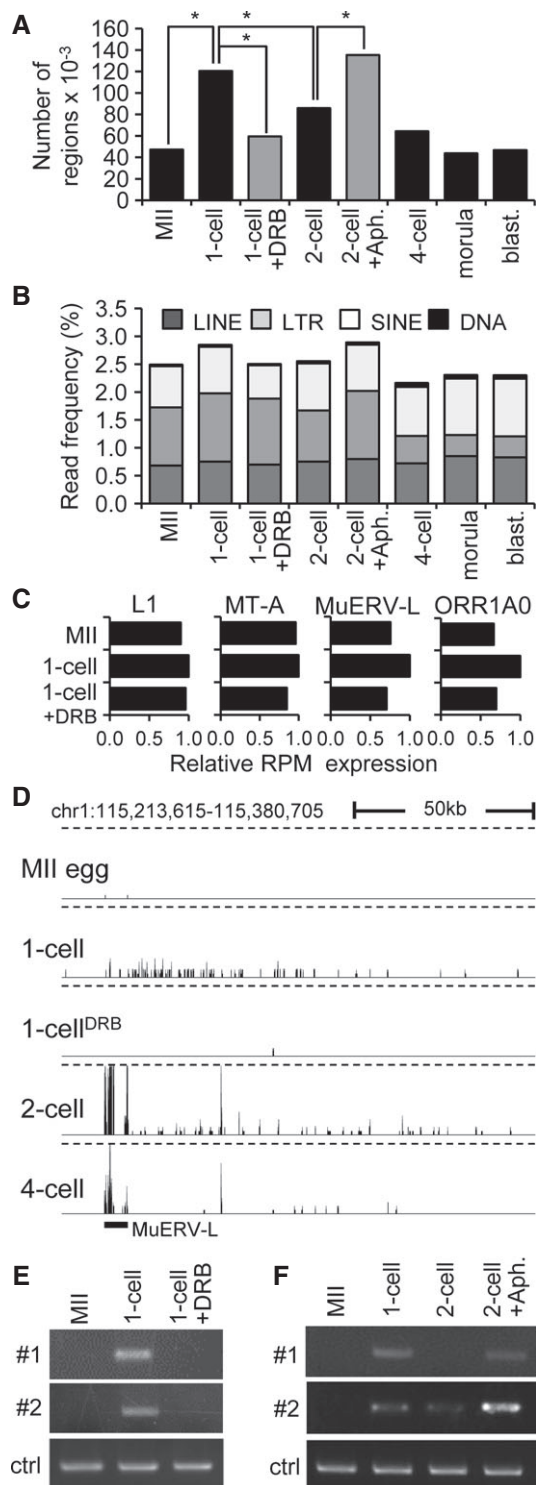
Figure 3. Analysis of genome-wide intergenic transcription in 1-cell embryos.

A Quantitative analysis of transcription from intergenic regions in oocytes and preimplantation embryos. Intergenic regions were divided into 1-kb segments across the whole genome, and the number of segments to which at least a single read was uniquely mapped was determined. Results suggest that treatment of 1-cell embryos with DRB reduced the number of segments yielding intergenic transcripts. In contrast, treatment of 2-cell embryos with aphidicolin (Aph.) prevented reduction of the number of segments yielding intergenic transcripts. Bars representing samples treated with DRB and aphidicolin are gray to distinguish results from treated embryos and from the normal course of preimplantation development. An asterisk indicates a significant difference by chi-square test ($P < 0.05$).

B Frequency of reads derived from mobile elements. Association of reads with a particular class of mobile DNA in each sample was determined by RepeatMasker and is displayed as a percentage of those reads in each library.

C Relative changes of expression of four specific retrotransposons. Relative expression for each retrotransposon was calculated from RPKMs where expression in 1-cell embryos was set to one.

D MuERV-L retrotransposons asymmetrically neighbor higher frequency of low CPM reads in large intergenic regions. Shown is an example of MuERV-L located in an intergenic region, which is not maternally expressed and becomes highly transcribed during zygotic genome activation at the 2-cell stage. A part of its transcription apparently invades almost 150 kb of its genomic flank, whereas the same region downstream of the MuERV-L yields higher frequency of low CPM reads in 1-cell stage in DRB-dependent manner. This pattern is most apparent for MuERV (see also Supplementary Fig S4B), but MT2 and ORR1AO insertions can also produce a similar asymmetric pattern (data not shown). The vertical scale was trimmed at 0.5 CPM; trimming is indicated by horizontal dashed lines.

E, F Validation of intergenic transcription at the 1-cell stage. Two intergenic regions harboring low CPM reads on chromosome 2 in 1-cell embryos were analyzed by RT–PCR. Both loci are annotated in Supplementary Fig S4C. Shown in (E) is RT–PCR analysis of intergenic transcription of two loci (shown in detail in Supplementary Fig S4C) in MII eggs and 1-cell embryos treated with and without DRB. ctrl = RT–PCR of a spiked α-rabbit globin mRNA demonstrating consistent RT–PCR efficiency across samples. Shown in (F) is the effect of inhibiting the second round of DNA replication in intergenic transcription at the 2-cell stage as examined by RT–PCR. Two-cell embryos were treated with aphidicolin (Aph.) 15 h after insemination to inhibit the second round of DNA replication. ctrl = RT–PCR of a spiked rabbit α-globin mRNA demonstrating consistent RT–PCR efficiency across samples. Experiments were performed three times with reproducible results; a representative result is shown (E, F).

Source data are available online for this figure.

The best example of a retrotransposon-supplied promoter producing long intergenic transcripts was the type L mouse endogenous retrovirus (MuERV-L). Transcription of MuERV-L is detected in 1-cell embryos and is very high in 2-cell embryos (Kigami *et al*, 2003; Svoboda *et al*, 2004), and was confirmed by our HTS data (Supplementary Fig S4B). Strikingly, a genomic flank on one side of MuERV-L appeared transcribed up to 200 kb downstream of the element (Fig 3D and Supplementary Fig S4B). In 1-cell embryos, we did not observe high read density over the retrotransposon but saw low CPM reads within the same area as in 2-cell embryos (Fig 3D, Supplementary Fig S4B and C). This feature of MuERV-L elements seemed a general feature that yielded a prominent pattern that became apparent when sequencing data from larger genomic regions were displayed (Supplementary Fig S4B).

To confirm intergenic transcription in 1-cell embryos, we selected two intergenic regions for which reads were uniquely

involved all major classes of retrotransposons (LINE, LTR, and SINE). Consistent with the development of a DNA replication-dependent transcriptionally repressive environment in 2-cell embryos, aphidicolin treatment resulted in higher frequency of retrotransposon-derived reads (Fig 3B). When examined individually, different retrotransposons showed diverse patterns of expression and various levels of transcription at the 1-cell stage (Fig 3C and Supplementary Fig S4A).

mapped in 1-cell embryos but not MII eggs and examined their expression by RT–PCR. One of these intergenic regions was not MuERV-associated (locus #1), whereas the other was downstream of an MuERV-L element (locus #2) (Supplementary Fig S4C). We first confirmed that transcription of these intergenic regions occurred only in 1-cell embryos but not in MII eggs or 1-cell embryos treated with DRB (Fig 3E). We also observed that their expression decreased by the 2-cell stage but remained high when DNA replication was inhibited (Fig 3F).

Taken together, these results suggest that a transcriptionally permissive state fosters promiscuous expression from intergenic regions in 1-cell embryos and includes retrotransposon transcription. Subsequently, promiscuous expression at the 2-cell stage is inhibited in DNA replication-dependent manner.

Core-promoter element-independent transcription in 1-cell embryos

To identify sequence features controlling 1-cell transcription, we constructed pGL3 luciferase vectors containing the promoter region of the *Zp3* or *Tktl1* gene (pGL3-*Zp3* or pGL3-*Tktl1*, respectively),

which are expressed in growing oocytes or embryos at the 1- and 2-cell stages, respectively (Hamamoto *et al*, 2014). These constructs, in principle, allow to test whether transcription in 1-cell embryos can initiate at 'maternal' (active only in the oocyte) and/or at 'zygotic' (active in preimplantation embryos) promoters. As a negative control, we used the original pGL3 luciferase vector lacking the gene promoter (pGL3-Basic). Growing oocytes microinjected with pGL3-*Zp3* showed a significant level of luciferase activity as expected, whereas 1-cell embryos did not (Fig 4A). Surprisingly, the pGL3-Basic vector supported luciferase activity in 1-cell embryos but not in oocytes at a level comparable to that of pGL3-*Zp3* in oocytes (Fig 4A). A corresponding observation was made when the transcriptional activity of pGL3-*Tktl1* and pGL3-Basic was examined in 1- and 2-cell embryos (Fig 4B).

Figure 4. Transcription from a microinjected plasmid lacking an annotated promoter.

A Transcriptional activity in pGL3-Basic vector lacking a promoter in oocytes and 1-cell embryos. pGL3 vector with the *Zp3* or no promoter sequence (pGL3-*Zp3* or pGL3-Basic vector, respectively) was injected into the nuclei of growing oocytes or the male pronucleus of 1-cell embryos. After 8 h, luciferase activity was measured. Data are expressed as mean ± SEM (*n* = 3) and were analyzed using Student's *t*-test. Asterisks indicate significant differences (*P* < 0.05).

B Transcriptional activity in pGL3-Basic vector lacking a promoter in 1-cell and 2-cell embryos. The analysis was performed similarly as in (A), except a pGL3 vector with the *Tktl1* promoter (pGL3-*Tktl1*) replaced pGL3-*Zp3* and the experiment was performed in 1-cell and 2-cell embryos. Data are expressed as mean ± SEM (*n* = 3) and were analyzed using Student's *t*-test. Asterisks indicate significant differences (*P* < 0.05).

C Determination of the transcriptional start sites (TSSs) of the pGL3-Basic vector by 5′ RACE. The 5′ RACE technique generated two major DNA fragments of ~900 and 500 bp. Black arrowheads indicate the 500- and 900-bp positions after gel electrophoresis; white arrowheads show the major products of 5′ RACE (TSS#1 and TSS#2).

D Schematic depiction of results from sequencing of seven and eight randomly selected RACE-derived cDNA clones of TSS#1 and TSS#2, respectively, which indicated two and five TSSs for TSS#1 (TSS#1-1 and TSS#1-2) and TSS#2 (TSS#2-1, TSS#2-2, TSS#2-3, TSS#2-4, and TSS#2-5), respectively, in the pGL3-Basic vector. Black lines represent the regions of pGL3-Basic vector corresponding to the results of DNA sequencing. Gray bars represent those of pGL3-Basic vector that were not found in the results of DNA sequencing. TPS represents the transcriptional pause site, a polyadenylation signal site. MCS represents the multi-cloning site.

E Analysis of promoter activity in the upstream regions of identified TSSs in the pGL3-Basic vector. The 76-bp regions upstream of the TSSs shown in (D) were inserted into the pEluc vector; virtually no luciferase activity is produced in 1-cell embryos microinjected with the pEluc vector (Hamamoto *et al*, 2014). The vectors were injected into the male pronucleus of 1-cell embryos, and luciferase activity was measured after 8 h. The experiments were performed three times. The data are presented as mean ± SEM and were analyzed using Student's *t*-test. Asterisks indicate significant differences between the sample without injection (no injection) and the other samples (*P* < 0.05).

F GC content in the pGL3-Basic vector. The percentage GC content was determined using a 30-bp sliding window analysis with a 1-bp shift.

Source data are available online for this figure.
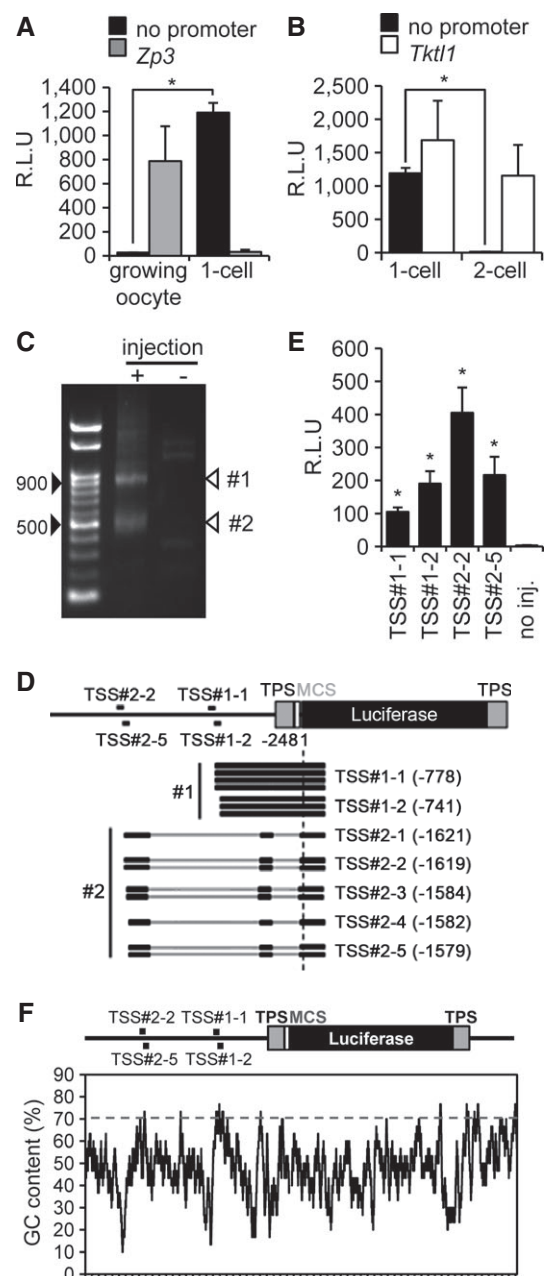
These results suggested that the pGL3-Basic vector contains a cryptic promoter sequence upstream of the luciferase-coding region to support transcription in 1-cell embryos. To locate the corresponding transcriptional start site (TSS) in the pGL3-Basic vector, we performed 5′ RACE. We found two major amplicons ~900 and 500 bp long [designated as products #1 and #2, respectively (Fig 4C)]. These amplicons were cloned, and randomly selected clones were sequenced. cDNA fragments of several sizes were present in the two 5′ RACE products (Fig 4D). Product #1 contained 935- and 898-bp cDNA fragments, indicating that the TSSs corresponding to these products were located 778 and 741 bp upstream of the *Luc*-coding region and were designated TSS#1-1 and TSS#1-2, respectively (Fig 4D). Product #2 included 499-, 497-, 462-, 460-, and 457-bp cDNA fragments. Transcripts corresponding to these cDNAs were spliced, and their TSSs were located 1,621, 1,619, 1,584, 1,582, and 1,579 bp upstream of the *Luc*-coding region and designated TSS#2-1, TSS#2-2, TSS#2-3, TSS#2-4, and TSS#2-5, respectively. Interestingly, product #1 sequences retained an intron, which was spliced out in product #2 (Fig 4D).

We also noted that these TSSs were located upstream of the transcriptional pause site (TPS) (Enriquez-Harris *et al*, 1991), which harbors the consensus sequence of the polyadenylation signal located upstream of the *Luc*-coding region that reduces luciferase activity derived from background transcription (Fig 4D), suggesting that transcription starting from these TSSs was not efficiently terminated by the TPS. Therefore, it was formally possible that transcription initiated at TSS#1 or TSS#2 in the growing oocytes and 2-cell embryos, as well as in 1-cell embryos, but was terminated at the TPS in the oocytes and 2-cell embryos, which resulted in the absence of luciferase activity in these cells. To test this hypothesis, we conducted RT–PCR to detect transcription initiated from TSS#1 and TSS#2. DNA fragments were amplified from 1-cell embryos but not oocytes or 2-cell embryos (Supplementary Fig S5A), indicating that transcription starting from these TSSs occurred only in 1-cell embryos.

To identify the promoter sequences employed by 1-cell embryos, we inserted the 76-bp regions upstream of four TSSs TSS#1-1, TSS#1-2, TSS#2-2, and TSS#2-5, into the p*Eluc* vector (Toyobo, Tokyo), which contains tandem polyadenylation signals and completely terminated transcription upstream of the *Luc*-coding region; there is virtually no luciferase activity in 1-cell embryos microinjected with p*Eluc* vector (Hamamoto *et al*, 2014). Interestingly, reporter gene assays of all 76-bp regions upstream of TSS#1-1, TSS#1-2, TSS#2-2, and TSS#2-5 yielded significant luciferase activities (Fig 4E) despite no known proximal or core-promoter elements, that is, upstream promoter elements (GC-box) and core-promoter elements (TATA-box, B recognition element (BRE), initiator (Inr), and downstream promoter element (DPE)), were common to all four 76-bp regions upstream or downstream of these TSSs (Supplementary Fig S5B).

In mammals, the promoter regions of many genes have a high G/C content and lack a classical TATA-box (Sandelin *et al*, 2007; Fenouil *et al*, 2012). Thus, we searched for G/C-rich regions 76 bp upstream of the aforementioned four TSSs. Using a 30-bp sliding window analysis with a 1-bp shift, we found that all four 76-bp upstream regions contained 30-bp sequences whose G/C contents were > 70% (Fig 4F). This finding suggests that these regions are involved in transcriptional regulation independent of known

core-promoter elements in 1-cell embryos. In addition, the presence of several closely located TSSs suggests that cryptic initiation of transcription can occur without a specific promoter element in 1-cell embryos. Taken together, the plasmid-borne reporter gene analysis suggested that transcription in 1-cell embryos can initiate from sites lacking well-characterized core-promoter elements.

Analysis of genes transcribed in 1-cell embryos

Genes transcribed in 1-cell embryos fall into two categories: those that have transcripts also detected in MII eggs and those that are not detected in MII eggs (or their abundance is very low). For the former class, it was difficult to determine whether the gene was transcribed in 1-cell embryos because the maternally derived transcript would represent the bulk of the transcripts present in the 1-cell embryo. Thus, we first focused on the second category. To select expressed mRNAs, we used empirically determined criteria for reads per kilobase per million (RPKM) ≤ 0.04 and RPKM ≥ 0.12 in MII eggs and 1-cell embryos, respectively, combined with a minimal fourfold increase between MII and 1-cell and a fourfold reduction following DRB treatment. In addition, to minimize false positives stemming from processed pseudogenes and reads mapping to short transcripts, we selected only spliced mRNAs > 500 nt long. Using these criteria, we selected 96 candidate genes transcribed in 1-cell embryos (Supplementary Table S2). Illustrative examples are found in Fig 5A, and RT–PCR confirmation of their expression is shown in Fig 5B.

Interestingly, inspection of each of the 96 candidate genes revealed a frequent occurrence of intron-derived reads in 1-cell embryos. In fact, their density was virtually the same as that observed over exons (Fig 5A) suggesting that our HTS primarily detects nascent transcripts. We decided therefore to use intron-derived reads to estimate the number of genes transcribed in 1-cell embryos for which the maternal transcript was still present and thereby prevented detection of exon-derived reads. To select these genes, we used the same criteria for intron-based selection as for mRNA selection. Using these criteria, we identified 4,039 genes transcribed in 1-cell embryos in DRB-dependent manner (Fig 5C and Supplementary Table S3). Inspection of individual genes confirmed the presence of widespread synthesis of nascent transcripts and showed that exon-based filtering (Supplementary Table S2) also missed many genes whose maternal transcripts were very low but whose expression values for exons fell below the cutoff (Fig 5D). RT–PCR analysis of several selected genes confirmed their transcription in 1-cell embryos (Fig 5E).

Microarray data from a panel of ~40 mouse tissues (Su *et al*, 2004) revealed variable expression patterns of genes transcribed in 1-cell embryos (Supplementary Fig S6A). Expression of more than a half of the genes was ubiquitous, whereas a minority exhibited high tissue specificity (Supplementary Fig S6A). The chromosomal distribution of the 4,039 coding genes suggested that no chromosome was preferentially transcribed (data not shown). Of note is that at least 268 of the 4,039 genes appeared transiently expressed at the 1-cell stage because transcripts were not detected in 4-cell embryos, morulae, and blastocysts, and their RPKM intron values were higher in 1-cell than in 2-cell embryos (Supplementary Table S3). Transcription of these genes could reflect that within the promiscuous first wave of transcription, there is embedded transcription of a
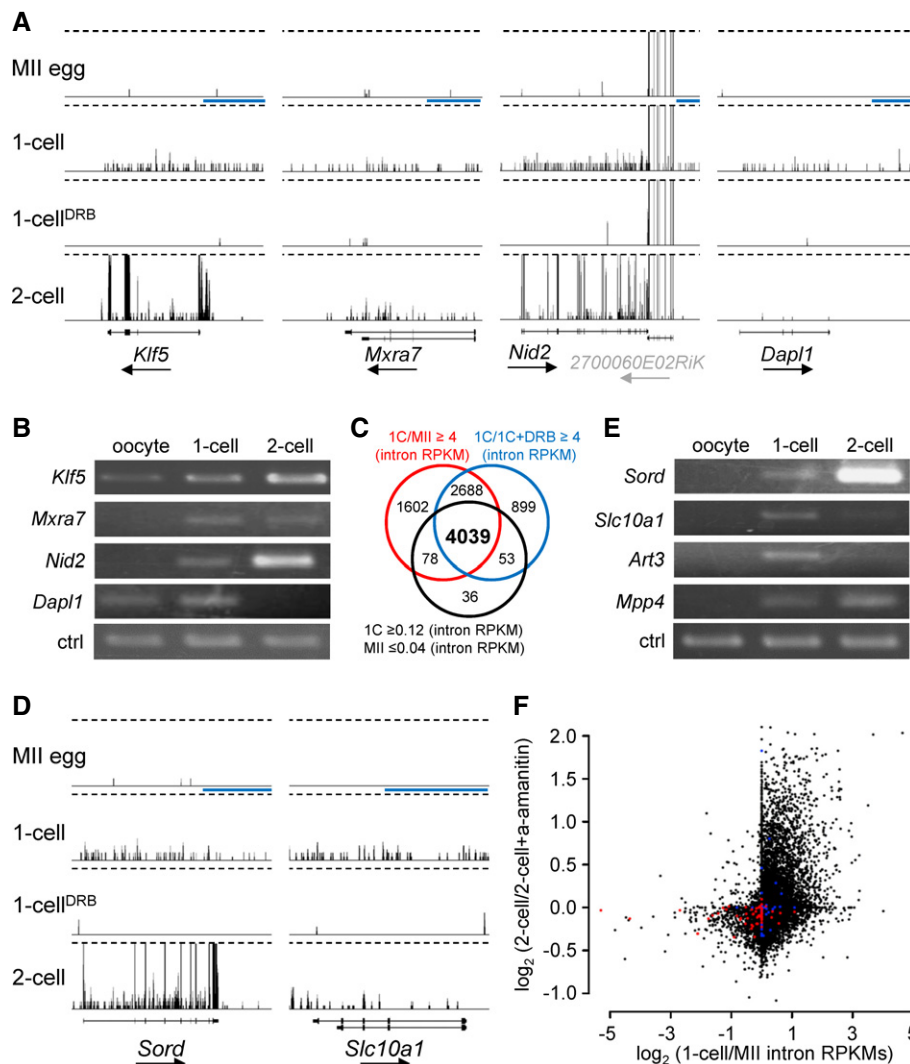
357

Figure 5. Transcription of protein coding genes at 1-cell stage.

A Examples of four genes exhibiting DRB-dependent 1-cell transcription, which were selected using mRNA (exon) RPKM-based filtering. Shown are 76PE HTS data from four different stages visualized in a customized UCSC browser. All sets are shown at the same scale 0–0.5CPM. Dashed lines indicate trimming at 0.5CPM. The horizontal blue scale bar = 10 kb. The black arrow under each gene name indicates transcription orientation. A simplified exon–intron structure of each gene is shown above the gene name.

B RT–PCR analysis of the four genes from (A). ctrl = RT–PCR of a spiked α-rabbit globin mRNA demonstrating consistent RT–PCR efficiency across samples.

C Intron RPKM-based filtering conditions for selecting genes transcribed in 1-cell embryos. The Venn diagram shows an overlap between gene populations where (i) RPKMs of introns in 1-cell embryos were more than fourfold greater than those in MII eggs oocytes (red circle), (ii) RPKMs of introns in 1-cell embryos were more than fourfold greater than those in 1-cell embryos treated with DRB, and (iii) the numbers of reads mapped to introns for a gene were ≥ 0.12 RPKM in 1-cell embryos and ≤ 0.04 in MII eggs.

D Examples of two genes identified among the 4,039 genes depicted in (C). Figure design is the same as in (A).

E RT–PCR analysis of expression of four genes found among the 4,039 genes identified by filtering conditions described in (C). Ctrl amplicon is the same as in (B).

F Relationship between the minor and major wave of ZGA. Each point represents one transcript (gene). The *y*-axis depicts α-amanitin sensitivity in 2-cell embryos [log₂-fold change inferred from microarray profiling (Zeng & Schultz, 2005)]. The *x*-axis depicts 1-cell/MII intron RPKM ratio. Red points represent the 100 most expressed oocyte-specific genes, and blue points represent the 100 most expressed testis-specific genes [tissue specificity and level of expression were inferred from BioGPS source data (Su *et al*, 2004)].

subset of genes constituting a part of a 1-cell-specific transcription program (Supplementary Fig S6B).

To examine whether transcription in 1-cell embryos represents expression of genes that are expressed during the major wave of zygotic transcription in 2-cell embryos, we superimposed intronic RPKM results onto relative changes observed in 2-cell embryos

treated with α-amanitin (Zeng & Schultz, 2005). This analysis unmasked a remarkably strong relationship between 1-cell transcribed genes and genes whose expression is α-amanitin sensitive in 2-cell embryos (Fig 5F). Interestingly, inspection of HTS profiles of genes highly sensitive to α-amanitin showed that *Psat1*, *Rps19*, and many others, which did not pass our selection criteria and were not

included in the list of 4,039 genes, nevertheless appeared transcribed in 1-cell embryos (Supplementary Fig S6C). This finding suggested that our filtering was conservative and that transcription in 1-cell embryos occurs in more than 4,000 genes; that is, transcription is broad-based in 1-cell embryos and occurs across the entire genome. Nevertheless, a certain degree of selectivity exists for transcription in 1-cell embryos because analysis of 100 genes highly expressed on MII eggs indicated that most were not transcribed in 1-cell embryos (Fig 5F). A similar result was found for testis-specific genes (Fig 5F).

Deficient mRNA processing in 1-cell embryos

As described above, a substantial fraction of RNA sequence reads of genes transcribed in 1-cell embryos contained introns and sequences well beyond where transcription should have terminated. For example, the reads for *Klf5* were evenly mapped to introns and exons in 1-cell embryos and beyond the polyA signal (Fig 6A), although the reads in MII eggs and 1-cell embryos were mapped only to exons of *Zp3*, an oocyte-specific gene (Philpott *et al*, 1987) (Fig 6A). Similar mapping patterns of the reads to introns and beyond polyA signals were identified for many genes (Fig 5A and D). These results suggest transcripts from genes transcribed in 1-cell embryos are not processed properly, that is, neither spliced nor terminated correctly.

To estimate the efficiency of 3′ end processing, we compared read frequencies upstream and downstream of polyA sites where the nearest exon was > 10 kb further downstream from the polyA site. Results of this analysis suggested a high incidence of read-through the termination signal in 1-cell embryos that decreased with development (Fig 6B). To estimate the efficiency of splicing, we analyzed the relative ratio of exon and intron-derived frequencies among genes transcribed in 1-cell embryos (Fig 6C) and exon–exon/exon–intron localization of paired-end reads (Fig 6D). Compared to embryos at the 2-cell stage and beyond, 1-cell embryos showed in a DRB-dependent manner a high proportion of intron-derived reads as

Figure 6. Inefficient processing of protein coding transcripts at the 1-cell stage.

A   Example of a gene transcribed at 1-cell stage. Shown are reads from 1-cell- and 2-cell-derived paired-end-sequenced libraries mapping to the *Klf5* gene region. Their distribution indicates inefficient splicing and 3′ end processing in 1-cell embryos. In contrast to the 2-cell embryo, the 1-cell embryo does not show any enrichment of exon-derived reads (exons are depicted as black rectangles) and no apparent transcriptional termination at the 3′ end. A detailed analysis of all reads mapping to the *Klf5* gene identified a single read derived from a spliced *Klf5* transcript. Below is shown profile of *Zp3*, an abundantly expressed oocyte-specific gene with very well defined exon–intron boundaries, which are retained also at the 1-cell stage. The vertical scale was trimmed at 0.5 CPM; trimming is indicated by horizontal dashed lines. The blue scale bars represent 10 kb.

B   Transcription termination analysis. Lines represent median ratios of read counts per kb (RPK) of reads downstream of transcription termination site to exons for gene sets transcribed in 1-cell embryos and subsequent stages but not in MII eggs. Downstream regions for genes with at least one RPK in exons are divided into 1-kb slices, and reads in each slice are counted and divided by the RPK value of the respective exon (point 1, 100%). The 1-cell stage shows higher downstream to exon read ratio indicating the extension of transcription past the polyA site.

C   Violin plot distributions of intron/exon read count ratios per cell stage for genes not transcribed in MII eggs. Intron and exon read counts were normalized to 1 kb length (RPK) and divided to obtain the read ratio for each region transcribed at the 1-cell stage or later. The 1-cell stage shows a shift toward higher intron/exon ratios indicating that a larger proportion of transcripts contain unspliced intronic regions, compared to the later stages. The MII stage is displayed as control and contains no values.

D   Comparison of unspliced/spliced read pair ratios per cell stage. Read counts where one end maps to intron/exon junction or entirely in intron and the other end maps to the adjacent exon were labeled as 'unspliced'. The 'spliced' pairs were selected so that the one end maps either to the splice site and covers two adjacent exons or with each end mapping to separate, adjacent exons. The ratios of unspliced/spliced pair counts normalized to 1-kb length were calculated for all transcribed regions in 1,786 transcripts not expressed at MII and expressed at later stages. The 1-cell stage shows a clear dominance of unspliced reads over the spliced ones, indicating the increased incidence of intron retention in sequenced transcripts.
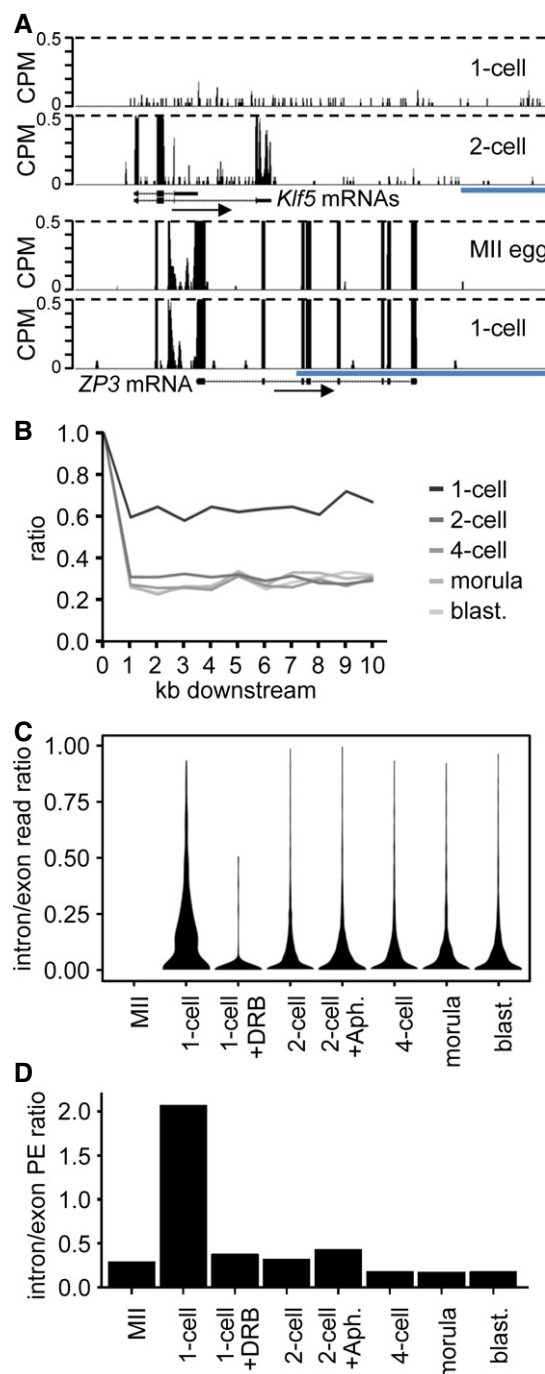
evidenced by the markedly wider violin plot above 0.10 in Fig 6C and a higher ratio of unspliced RNA fragments relatively to spliced ones (Fig 6D). These latter results strongly suggest that nascent transcripts in 1-cell embryos are very poorly spliced.

To confirm the presence of unspliced transcripts in 1-cell embryos, we conducted RT–PCR using primer sets for the *Klf5*, *Nid2*, and *Mxra7* genes. The primer sets were designed within a single exon (primer set PCR A) or across the splicing junction (primer set PCR B) (Fig 7A). All three PCR B products were detected in the 1-cell embryos. Although the amount of product derived from PCR A was higher in 2-cell embryos than in 1-cell embryos, the amount of product obtained from PCR B was markedly higher in 1-cell embryos, suggesting a deficiency in mRNA splicing (Fig 7A). To ascertain whether the deficiency in splicing was restricted to the 1-cell stage, we microinjected a *ftz* pre-mRNA, which was composed of two exons sandwiching an intron, into the nucleus of growing oocytes, and 1- and 2-cell embryos and examined whether the pre-mRNA was spliced into mature mRNA (Fig 7B). The mature mRNA was readily detected in oocytes and 2-cell embryos but not in 1-cell embryos.

The male pronucleus (PN) supports a higher level of transcription than the female PN (Henery *et al*, 1995; Aoki *et al*, 1997). Thus, it was formally possible that splicing occurs in the female PN but was not detected. To address this issue, we generated parthenogenetic embryos and examined the occurrence of unspliced *Klf5*, *Nid2*, *Mxra7*, and *Sord* transcripts. We readily detected unspliced transcripts in the parthenogenotes (Supplementary Fig S7A), suggesting that inefficient splicing was not specific to male pronuclei. Importantly, 50SE data (Park *et al*, 2013) also detected unspliced *Klf5*, *Nid2*, *Mxra7*, and *Sord* transcripts (Supplementary Fig S7B), corroborating reduced efficiency of posttranscriptional processing (Supplementary Fig S8). Of note is that 50SE data from 1-cell parthenogenotes also supported reduced posttranscriptional processing in female PN (Supplementary Fig S8B and C).

Finally, we examined the distribution of SC-35 in oocytes, 1-cell embryos, and later embryonic stages. SC-35 is a component of nuclear speckles, which are associated with storage of splicing factors required for pre-mRNA splicing (Huang & Spector, 1992; Kim *et al*, 2011). Interestingly, whereas male and female pronuclei yielded comparable signal, they both lacked nuclear speckles. In contrast, nuclear speckles were clearly observed in growing oocytes, and 2-cell and 4-cell embryos (Fig 7C). These results suggest that the splicing machinery might not be fully formed or functions inefficiently in 1-cell embryos.

Discussion

Despite variable timing, ZGA in vertebrates occurs in a similar manner in which an initial minor ZGA wave is followed by a major
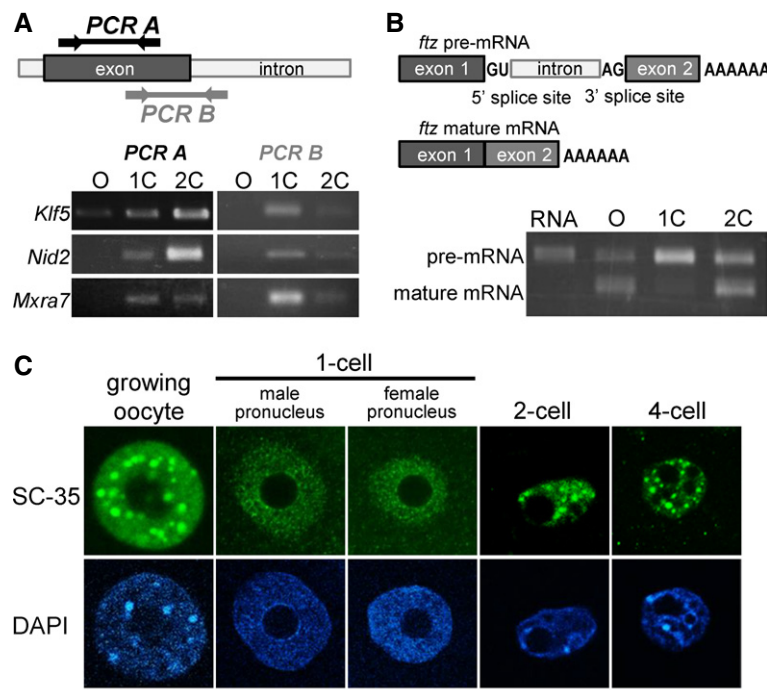

Figure 7. Inefficient splicing in 1-cell embryos.

A RT–PCR analysis of unspliced introns. Upper portion shows the locations for which primer pairs were designed. Lower portion depicts results of an RT–PCR analysis using the primer pairs described in the upper diagram.

B Upper diagrams show the structures of pre- and mature *ftz* mRNAs. Synthesized *ftz* pre-mRNA was microinjected into growing oocytes, and 1- and 2-cell-stage embryos. Lower portion shows the results of RT–PCR using primer pairs for exons 1 (forward) and 2 (reverse).

C Immunofluorescence with an anti-SC-35 antibody of the nuclei of growing oocytes, and 1-, 2-, and 4-cell-stage embryos. The position of the nucleus, detected with DAPI, is shown in the lower portion of the figure. Scale bar, 20 μm.

second wave. Although the major burst of zygotic expression is well characterized in mice (Schultz, 2002; Zeng & Schultz, 2005), *Xenopus* (Paranjpe *et al*, 2013), and zebrafish (Haberle *et al*, 2014), little is known about the identity of the first transcripts expressed during the initial wave, except for zebrafish (Heyn *et al*, 2014).

In mice, the first cleavage separates the earliest transcription from the major wave of transcription and reprogramming of gene expression, which takes place in 2-cell embryos. The transcription in 1-cell embryos, however, still remains poorly understood two decades since its discovery (Matsumoto *et al*, 1994). Here, we provide genome-wide characterization of the initial transcription wave during mammalian ZGA. We used HTS to explore the dynamics of total RNA composition during oocyte-to-embryo transition, focusing primarily on the 1-cell transcriptome. By using total RNA, we obtained a comprehensive and well-mapped dataset that provides information beyond the poly(A) RNA fraction, whose analysis is prone to artifacts. For example, 14 minor ZGA genes identified in mouse and human embryos using poly(A) RNA HTS (Xue *et al*, 2013) are maternally expressed and not upregulated in either Park *et al* (2013) or in our dataset (data not shown).

We find that transcription in 1-cell embryos has unique features consistent with genome-wide, promiscuous, and low-level transcriptional activation uncoupled from efficient production of functional mRNAs. This transcription manifests as low CPM reads, whose analysis is limited by their amount. The following lines of evidence argue that these low-abundance reads are not an experimental artifact but originate from transcripts synthesized in 1-cell embryos and reflect genome-wide transcription during the minor transcription wave: (i) The low CPM reads are reproducible and their presence is strongly reduced following DRB treatment. (ii) The distribution of these reads is not random; they are partially associated with genes and specific repetitive elements. (iii) By increasing depth of the data (by combining HTS data from the same stage), gaps were filled between clustered low CPM reads rather than generating distinct peaks or equalizing low CPM read distribution across the genome. (iv) The presence of newly synthesized RNAs from intergenic and gene regions was detected by RT–PCR. (v) Comparable results were obtained when examining a previously published 50SE SOLiD HTS MII, 1-cell and 2-cell data, which provide better sequencing depth (~1 × 10^8 total mapped reads after rRNA subtraction from 1-cell embryos vs. ~2 × 10^7 total non-rRNA reads from 1-cell embryos in our dataset) (Park *et al*, 2013). Remarkably, the 50SE dataset offers only a partially improved coverage of novel transcripts in 1-cell samples and does not permit either reliable annotation of transcription start sites in 1-cell embryos or for assembly of minor ZGA transcript sequences. Thus, reliable annotation and assembly of intergenic transcripts appearing during minor ZGA will likely require a sequencing depth larger than in current datasets and paired-end sequencing.

Three types of promoters seem to function in 1-cell embryos: promoters of protein coding genes, promoters of various retrotransposons, and cryptic promoters lacking a defined promoter structure. Although HTS data do not allow reliable determination of TSS positions and minimal promoter features required for transcription in 1-cell embryos, transcription factors available in the zygote likely provide some degree of selectivity. These transcription factors would explain why many genes expressed during the major ZGA wave are transcribed in 1-cell embryos whereas highly expressed

maternal and testis-specific genes are poorly transcribed (Fig 5F). We speculate that spurious transcription from oocyte-specific promoters is absent in 1-cell embryos because oocyte-specific transcription factors are no longer present and their absence would facilitate reprogramming of gene expression during OET. According to this model, spurious transcription is sufficient for luciferase expression from a promoterless vector in 1-cell embryos, whereas insertion of the *Zp3* promoter would have a suppressive effect.

The dynamic chromatin structure at 1-cell embryos is likely a key factor underlying the transcriptionally permissive state. A more relaxed chromatin structure in 1-cell embryos than at later developmental stages offers an explanation that transcription in 1-cell embryos does not require defined core-promoter elements as well as the genome-wide opportunistic transcription occurring in genes, retrotransposons, and intergenic regions. Such a developmental change likely underlies the lack of a requirement for an enhancer for expression in 1-cell embryos and why enhancers stimulate transcription starting at the 2-cell stage, a requirement that is relieved by histone hyperacetylation (Wiekowski *et al*, 1991, 1993; Majumder *et al*, 1993; Schultz, 1993); transcription factors require enhancers to access promoters in repressive chromatin and core-promoter elements are essential for stable transcription in eukaryotic cells (Smale & Kadonaga, 2003). Consistent with these findings is that genomic DNA is more sensitive to DNase I at the 1-cell than the 2-cell stage (Cho *et al*, 2002), suggesting that chromatin in 1-cell embryos is less compact, that is, less mature, than at later developmental stages. Also, consistent with such a developmental change in chromatin structure is that histone mobility is much higher in 1-cell embryos than in 2-cell embryos (Aoki, unpublished results). Such promiscuous transcription in 1-cell embryos, however, also presents a threat to genome integrity and an obstacle to establish a specific gene expression pattern required for continued development. Inefficient posttranscriptional processing in 1-cell embryos may therefore confer a protective mechanism against a promiscuous expression. Noteworthy is that a recent report suggests that the earliest transcribed zygotic genes in the zebrafish are intron poor (Heyn *et al*, 2014). In light of our result, it is possible to speculate that functionally relevant intron-poor genes might be actually selected for because they would have a higher chance to produce functional transcript than genes with multiple introns.

That 1-cell transcription may not produce translated/translatable transcripts has been previously suggested, but processing of nascent endogenous transcripts from 1-cell embryos was never examined in depth. For example, protein synthesis from a paternally provided gene is observed only at the 2-cell stage (Matsumoto *et al*, 1994), and mRNAs from endogenous genes were first detected by microarrays at the 2-cell stage (Zeng & Schultz, 2005). Transcripts with intronic sequences have also been detected in bovine preimplantation embryos during the course of genome activation (Graf *et al*, 2014). We find that the 1-cell HTS library contains an unusually high proportion of sequences derived from intronic sequences as well as a high occurrence of unspliced RNAs. Inefficient splicing is not restricted to the male PN as parthogenetic zygotes also fail to splice efficiently nascent transcripts.

One-cell embryos do splice nascent transcripts, albeit poorly, as evidenced by occasional reads mapping across exon–exon junctions in genes present in MII eggs. In addition, the spliced transcripts are produced from microinjected plasmid reporters (Fig 4D and Zeng &

361

Schultz, 2005). Although the splice sites in Fig 4D are, in fact, cryptic (which would still support the notion of aberrant posttranscriptional processing), the physiological relevance of splicing observed upon microinjection of thousands of copies of extrachromosomal DNA is unclear. Furthermore, splicing was not the only posttranscriptional process that was impaired in 1-cell embryos. We also find that transcription readily passes through polyadenylation sites without accumulation of properly terminated transcripts. A combination of reduced efficiency of splicing and polyadenylation (as well as activation of cryptic splice sites) could provide a robust barrier that minimizes the risk of retrotransposition and aberrant gene expression at a time when the embryo is most susceptible to such risk.

ftz pre-mRNA microinjection into oocytes and 1-cell and 2-cell embryos (Fig 7B) provides strong evidence that splicing of nascent transcripts in 1-cell embryos is inefficient, but the molecular basis for inefficient splicing is unclear. The observed absence of SC-35-containing nuclear speckles, which retain pre-mRNA splicing factors (Spector & Lamond, 2011), could either be a cause or consequence of dysfunctional splicing. Inefficient splicing could also be a consequence of the chromatin composition in 1-cell embryos. Exons contain biased chromatin signatures (Spies *et al*, 2009). As our understanding of the relationship between splicing and chromatin structure evolves (reviewed in Bentley, 2014; de Almeida & Carmo-Fonseca, 2014), genome-wide acquisition of splicing linked to chromatin remodeling in early embryos offers an interesting model for further testing.

Finally, our results provide novel insights into the question of importance of 1-cell transcription. Inhibiting transcription starting at the 1-cell stage with α-amanitin does not prevent cleavage to the 2-cell stage but does inhibit cleavage to the 4-cell stage (Warner & Versteegh, 1974). Unfortunately, the irreversible nature of α-amanitin inhibition does not allow to demonstrate importance of transcription in 1-cell embryos *per se*. Interestingly, when 1-cell embryos are cultured in the presence of DRB until the early 2-cell stage and then transferred to DRB-free medium, development arrests at the 2-cell stage (Aoki, unpublished observations). These findings imply that transcription in 1-cell embryos is essential for the development. Thus, it is possible that, despite inefficient posttranscriptional processing, some 1-cell transcripts are functional—either producing proteins or functioning as untranslated long noncoding RNAs. Noncoding RNAs, some of which do not require splicing (Hutchinson *et al*, 2007), can play essential roles in various cellular processes, including regulation of chromatin structure in early embryos (Casanova *et al*, 2013). Finally, it is important to consider that transcription *per se* (and not its products) in 1-cell embryos is important for proper maturation of chromatin. Numerous examples have been shown where the polymerase II complex changes chromatin structure, from nucleosome repositioning, replacement histone deposition, to changes of histone modifications, which include acetylation (reviewed in Butler & Dent, 2012; Das & Tyler, 2013; Weber & Henikoff, 2014). In this model, transcription and chromatin during the minor ZGA form a feedback loop where open chromatin promotes genome-wide pioneering transcription uncoupled from posttranscriptional processing. Pioneering transcription in turn facilitates chromatin remodeling that leads to a properly established chromatin structure and functional posttranscriptional processing during the major ZGA in 2-cell embryos.

Materials and Methods

Collection and culture of oocytes and embryos

Growing oocytes were obtained from 12- to 14-day-old B6D2F1 mice (SLC Japan). The ovaries were transferred to HEPES-buffered KSOM and punctured with a 30-gauge needle. Liberated oocytes with attached follicle cells were harvested, and the follicle cells were gently removed using a narrow-bore glass pipette. The oocytes were then transferred into α-minimal essential medium (α-MEM; Life Technologies, Inc., Grand Island, NY, USA) containing 5% fetal bovine serum and 10 ng/ml epidermal growth factor (both from Sigma-Aldrich).

Metaphase II-arrested eggs (MII eggs) were obtained from super-ovulated 3-week-old C57BL6/J and B6D2F1 female mice (SLC Japan, Shizuoka) that were first injected intraperitoneally with 5 IU of equine chorionic gonadotropin (eCG; ASKA Pharmaceutical Co., Tokyo, Japan) followed 48 h later with 5 IU of human chorionic gonadotropin (hCG; ASKA Pharmaceutical). MII eggs were collected from the ampullae of oviducts 15 h post-hCG injection and transferred to human tubal fluid medium (Lawitts & Biggers, 1993) supplemented with 10 mg/ml BSA (Sigma-Aldrich, Saint Louis, MO, USA). The eggs derived from C57BL6/J and B6D2F1 mice were inseminated with spermatozoa obtained from the caudal epididymis of adult C57BL6/J and ICR mice (SLC Japan), respectively. The spermatozoa were incubated for 2 h in TYH medium (Toyoda *et al*, 1971) and human tubal fluid medium supplemented with 10 mg/ml BSA for the eggs from C57BL6/J and B6D2F1 female mice, respectively, in an atmosphere of 5% CO_2/95% air at 38°C prior to use for insemination. Four to six hours after insemination, the eggs were washed and cultured in potassium simplex optimized medium (Quinn & Begley, 1984). The 1-, 2-, and 4-cell-, and morula- and blastocyst-stage embryos were collected at 13, 32, 48, 72, and 96 h after insemination, respectively.

For DRB and aphidicolin treatment, 1-cell embryos were transferred into KSOM containing 120 μM DRB (Sigma-Aldrich) or 3 μg/ml aphidicolin (Sigma-Aldrich) at 4 (before initiation of transcription (Aoki *et al*, 1997)) or 16 h post-insemination (embryos enter M phase at 16 h after insemination), respectively.

RNA extraction, preparation of the RNA-Seq library, and HTS

Total RNA was extracted from 3,000, 3,000, 4,500, 2,800, 1,400, and 700 MII eggs, 1-, 2-, and 4-cell embryos, morulae, and blastocysts obtained from C57BL6/J mice, respectively, using Isogen (Nippon Gene, Tokyo, Japan), according to the manufacturer's instructions. In the second trials for MII eggs and 1-cell embryos, similar numbers of cells used for the first trials were used for RNA extraction. RNA quality analysis and size-selection (> 200 nt) were performed on the Bioanalyzer RNA Pico Chip (Agilent Technologies, Santa Clara, CA, USA). RNA-Seq libraries were constructed using the mRNA-Seq Sample Preparation Kit (Illumina, San Diego, CA, USA) without selection of polyadenylated RNA. Briefly, size-selected total RNA was fragmented to 40–900-nt fragments in fragmentation buffer at 94°C for 5 min, reverse-transcribed with random primers, and ligated with adaptors. cDNA templates were amplified by PCR in the conditions as follows: the initial heat treatment at 98°C for 30 s followed by 15 cycles of 98°C for 10 s, 65°C for 30 s, 72°C for

30 s, and final treatment of 72°C for 5 min. RNA-Seq libraries were subjected to sequencing using Genome Analyzer IIx (Illumina), and 35-nt single-end and 76-nt paired-end sequencing reads were mapped on the mouse genome. The data were deposited into the ArrayExpress database under reference #E-MTAB-2950. Additional details concerning read mapping and bioinformatics analyses can be found in Supplementary Experimental Procedures.

Reverse transcription and polymerase chain reaction

Total RNA was isolated from 100 MII eggs and embryos using Isogen (Nippon Gene) and treated with RQ1 RNase-Free DNase (Promega, Madison, WI, USA) according to the manufacturer's instructions. As an external control, 50 pg rabbit globin mRNA was added prior to total RNA isolation. The isolated total RNA was subjected to reverse transcription using a PrimeScript RT–PCR kit (Takara Bio Inc., Otsu, Japan) according to the manufacturer's instructions. PCR was performed in a thermal cycler (iCycler; Bio-Rad, Berkeley, CA, Japan) using Ex Taq DNA polymerase (Takara) with 35–38 cycles of 95°C for 30 s, 57–60°C for 30 s, and 72°C for 60 s. After the electrophoresis on an agarose gel, the PCR products were stained with ethidium bromide. The primers and PCR conditions are shown in Supplementary Table S4.

Synthesis and microinjection of *ftz* pre-mRNA

To prepare truncated *ftz* pre-mRNAs, pGEM pre-*ftz* (donated by Mutsuhito Ohno in Kyoto University) was amplified by PCR using a forward primer containing the T7 promoter sequence and a reverse primer containing polyA (40 nt) (Supplementary Table S4). Pre-mRNAs were synthesized using *in vitro* transcription with the mMASSAGE mMACHINE T7 kit (Life Technologies) according to the manufacturer's instructions.

Microinjection was performed on an inverted microscope (ECLIPSE TE300; Nicon Corporation, Tokyo, Japan) using a micro-injector (IM300; Narishige Co., Ltd, Tokyo, Japan). Synthesized RNA diluted in nuclease-free water was placed on ice until microinjection. Growing oocytes and embryos obtained from B6D2F1 mice were transferred to HEPES-buffered KSOM, and then, the synthesized RNA was injected into the nuclei in growing oocytes, the nuclei in single blastomeres of 2-cell-stage embryos 29 h after insemination and the male PN in 1-cell-stage embryos 10 h after insemination using narrow glass capillaries (GC100 TF-10; Harvard Apparatus Ltd., Kent). The concentration and volume of injected RNA are 200 ng/μl and 5 pl, respectively. After 1 h of culture in α-MEM (oocytes) and KSOM (embryos), the oocytes and embryos were collected in Isogen for reverse transcription and polymerase chain reaction.

Luciferase assay

A total of 10 pl of 200 ng/μl plasmid DNA was injected into the nuclei of growing oocytes, male PN in 1-cell embryos from B6D2F1 mice 7–9 h after insemination, and the nuclei in single blastomeres of 2-cell-stage embryos were injected 25–27 h after insemination. After 8 h of culture in α-MEM (oocytes) and KSOM (embryos), the oocytes and embryos were collected in 25 μl of phosphate-buffered saline (PBS; Takara Bio Inc.) containing 1 mg/ml BSA (0.1% BSA/

PBS) for luciferase assays. Luciferase activity was measured using the ONE-Glo Luciferase Assay System (Promega) and Emerald Luc Luciferase Assay Reagent (Toyobo) for the pGL3-vector and p*Eluc*-test vector, respectively, according to the manufacturer's instructions. A total of 30 oocytes or embryos were used in each assay.

Immunostaining

Growing oocytes and embryos were fixed with 4.0% paraformaldehyde (Wako, Osaka, Japan) in PBS for 15 min. After washing three times with PBS/0.1% BSA, the cells were permeabilized with 0.5% Triton X-100 (Wako) in PBS for 15 min and then incubated overnight at 4°C with an anti-SC 35 antibody (Cat#S4045, Sigma-Aldrich) diluted 1/100 in PBS/0.1% BSA. The cells were washed and incubated with Alexa488-conjugated anti-mouse IgG secondary antibody (Invitrogen, Carlsbad, CA, USA) for 1 h at room temperature. After washing, they were mounted in Vectashield (Vector Laboratories, Burlingame, CA, USA) containing 4′,6-diamidino-2-phenylindole (DAPI; Dojindo Laboratories, Kumamoto) for DNA staining. Confocal digital images were collected using a confocal laser scanning microscope (LSM 5 EXCITER; Carl Zeiss MicroImaging GmbH, Oberkochen).

Author contributions

FA designed the experiments. KA, RY, MC, and YS conducted the experiments. KA, RY, VF, MGS, KV, PS, RMS, and FA analyzed the data. VF and KV contributed to the statistical analysis. KA, PS, RMS, and FA wrote the manuscript.

Conflict of interest

The authors declare that they have no conflict of interest.

References

Abe K-I, Inoue A, Suzuki MG, Aoki F (2010) Global gene silencing is caused by the dissociation of RNA polymerase II from DNA in mouse oocytes. *J Reprod Dev* 56: 502–507

de Almeida SF, Carmo-Fonseca M (2014) Reciprocal regulatory links between cotranscriptional splicing and chromatin. *Semin Cell Dev Biol* 32: 2–10

363

Aoki F, Worrad DM, Schultz RM (1997) Regulation of transcriptional activity during the first and second cell cycles in the preimplantation mouse embryo. *Dev Biol* 181: 296–307

Bachvarova R, De Leon V (1980) Polyadenylated RNA of mouse ova and loss of maternal RNA in early development. *Dev Biol* 74: 1–8

Bentley DL (2014) Coupling mRNA processing with transcription in time and space. *Nat Rev Genet* 15: 163–175

Bouniol C, Nguyen E, Debey P (1995) Endogenous transcription occurs at the 1-cell stage in the mouse embryo. *Exp Cell Res* 218: 57–62

Bucknall RA, Moores H, Simms R, Hesp B (1973) Antiviral effects of aphidicolin, a new antibiotic produced by Cephalosporium aphidicola. *Antimicrob Agents Chemother* 4: 294–298

Butler JS, Dent SY (2012) Chromatin 'resetting' during transcription elongation: a central role for methylated H3K36. *Nat Struct Mol Biol* 19: 863–864

Casanova M, Pasternak M, El Marjou F, Le Baccon P, Probst AV, Almouzni G (2013) Heterochromatin reorganization during early mouse development requires a single-stranded noncoding transcript. *Cell Rep* 4: 1156–1167

Cho T, Sakai S, Nagata M, Aoki F (2002) Involvement of chromatin structure in the regulation of mouse zygotic gene activation. *Anim Sci J* 73: 113–122

Das C, Tyler JK (2013) Histone exchange and histone modifications during transcription and aging. *Biochim Biophys Acta* 1819: 332–342

Davis W, De Sousa PA, Schultz RM (1996) Transient expression of translation initiation factor eIF-4C during the 2-cell stage of the preimplantation mouse embryo: identification by mRNA differential display and the role of DNA replication in zygotic gene activation. *Dev Biol* 174: 190–201

De La Fuente R, Eppig JJ (2001) Transcriptional activity of the mouse oocyte genome: companion granulosa cells modulate transcription and chromatin remodeling. *Dev Biol* 229: 224–236

Deng Q, Ramskold D, Reinius B, Sandberg R (2014) Single-cell RNA-seq reveals dynamic, random monoallelic gene expression in mammalian cells. *Science* 343: 193–196

DePamphilis ML (1993) Origins of DNA replication in metazoan chromosomes. *J Biol Chem* 268: 1–4

Enriquez-Harris P, Levitt N, Briggs D, Proudfoot NJ (1991) A pause site for RNA polymerase II is associated with termination of transcription. *EMBO J* 10: 1833–1842

Fenouil R, Cauchy P, Koch F, Descostes N, Cabeza JZ, Innocenti C, Ferrier P, Spicuglia S, Gut M, Gut I, Andrau J-C (2012) CpG islands and GC content dictate nucleosome depletion in a transcription-independent manner at mammalian promoters. *Genome Res* 22: 2399–2408

Forlani S, Bonnerot C, Capgras S, Nicolas JF (1998) Relief of a repressed gene expression state in the mouse 1-cell embryo requires DNA replication. *Development* 125: 3153–3166

Graf A, Krebs S, Zakhartchenko V, Schwalb B, Blum H, Wolf E (2014) Fine mapping of genome activation in bovine embryos by RNA sequencing. *Proc Natl Acad Sci U S A* 111: 4139–4144

Haberle V, Li N, Hadzhiev Y, Plessy C, Previti C, Nepal C, Gehrig J, Dong X, Akalin A, Suzuki AM, van IJcken WF, Armant O, Ferg M, Strahle U, Carninci P, Muller F, Lenhard B (2014) Two independent transcription initiation codes overlap on vertebrate core promoters. *Nature* 507: 381–385

Hamamoto G, Suzuki T, Suzuki MG, Aoki F (2014) Regulation of transketolase like 1 gene expression in the murine one-cell stage embryos. *PLoS ONE* 9: e82087

Hamatani T, Carter MG, Sharov AA, Ko MSH (2004) Dynamics of global gene expression changes during mouse preimplantation development. *Dev Cell* 6: 117–131

Henery CC, Miranda M, Wiekowski M, Wilmut I, DePamphilis ML (1995) Repression of gene expression at the beginning of mouse development. *Dev Biol* 169: 448–460

Heyn P, Kircher M, Dahl A, Kelso J, Tomancak P, Kalinka AT, Neugebauer KM (2014) The earliest transcribed zygotic genes are short, newly evolved, and different across species. *Cell Rep* 6: 285–292

Huang S, Spector DL (1992) U1 and U2 small nuclear RNAs are present in nuclear speckles. *Proc Natl Acad Sci U S A* 89: 305–308

Hutchinson JN, Ensminger AW, Clemson CM, Lynch CR, Lawrence JB, Chess A (2007) A screen for nuclear transcripts identifies two linked noncoding RNAs associated with SC35 splicing domains. *BMC Genom* 8: 39

Jackson DA, Pombo A, Iborra F (2000) The balance sheet for transcription: an analysis of nuclear RNA metabolism in mammalian cells. *FASEB J* 14: 242–254

Karolchik D, Hinrichs AS, Kent WJ (2012) The UCSC Genome Browser. *Curr Protoc Bioinformatics* Chapter 1: Unit 1 4

Kigami D, Minami N, Takayama H, Imai H (2003) MuERV-L is one of the earliest transcribed genes in mouse one-cell embryos. *Biol Reprod* 68: 651–654

Kim Y-D, Lee J-Y, Oh K-M, Araki M, Araki K, Yamamura K-I, Jun C-D (2011) NSrp70 is a novel nuclear speckle-related protein that modulates alternative pre-mRNA splicing in vivo. *Nucleic Acids Res* 39: 4300–4314

Lawitts JA, Biggers JD (1993) Culture of preimplantation embryos. *Methods Enzymol* 225: 153–164

Majumder S, Miranda M, DePamphilis ML (1993) Analysis of gene expression in mouse preimplantation embryos demonstrates that the primary role of enhancers is to relieve repression of promoters. *EMBO J* 12: 1131–1140

Matsumoto K, Anzai M, Nakagata N, Takahashi A, Takahashi Y, Miyata K (1994) Onset of paternal gene activation in early mouse embryos fertilized with transgenic mouse sperm. *Mol Reprod Dev* 39: 136–140

Meijer HA, Bushell M, Hill K, Gant TW, Willis AE, Jones P, de Moor CH (2007) A novel method for poly(A) fractionation reveals a large population of mRNAs with a short poly(A) tail in mammalian cells. *Nucleic Acids Res* 35: e132

Oh B, Hwang S, McLaughlin J, Solter D, Knowles BB (2000) Timely translation during the mouse oocyte-to-embryo transition. *Development* 127: 3795–3803

Paranjpe SS, Jacobi UG, van Heeringen SJ, Veenstra GJ (2013) A genome-wide survey of maternal and embryonic transcripts during *Xenopus tropicalis* development. *BMC Genom* 14: 762

Park S-J, Komata M, Inoue F, Yamada K, Nakai K, Ohsugi M, Shirahige K (2013) Inferring the choreography of parental genomes during fertilization from ultralarge-scale whole-transcriptome analysis. *Genes Dev* 27: 2736–2748

Philpott CC, Ringuette MJ, Dean J (1987) Oocyte-specific expression and developmental regulation of ZP3, the sperm receptor of the mouse zona pellucida. *Dev Biol* 121: 568–575

Piko L, Clegg KB (1982) Quantitative changes in total RNA, total poly(A), and ribosomes in early mouse embryos. *Dev Biol* 89: 362–378

Quinn P, Begley AJ (1984) Effect of human seminal plasma and mouse accessory gland extracts on mouse fertilization in vitro. *Aust J Biol Sci* 37: 147–152

Sandelin A, Carninci P, Lenhard B, Ponjavic J, Hayashizaki Y, Hume DA (2007) Mammalian RNA polymerase II core promoters: insights from genome-wide studies. *Nat Rev Genet* 8: 424–436

Santos F, Peters AH, Otte AP, Reik W, Dean W (2005) Dynamic chromatin modifications characterise the first cell cycle in mouse embryos. *Dev Biol* 280: 225–236

Schultz RM (1993) Regulation of zygotic gene activation in the mouse. *BioEssays* 15: 531–538

Schultz RM (2002) The molecular foundations of the maternal to zygotic transition in the preimplantation embryo. *Hum Reprod Update* 8: 323–331

Sehgal PB, Darnell JE Jr, Tamm I (1976) The inhibition by DRB (5,6-dichloro-1-beta-D-ribofuranosylbenzimidazole) of hnRNA and mRNA production in HeLa cells. *Cell* 9: 473–480

Smale ST, Kadonaga JT (2003) The RNA polymerase II core promoter. *Annu Rev Biochem* 72: 449–479

Spector DL, Lamond AI (2011) Nuclear speckles. *Cold Spring Harb Perspect Biol* 3: a000646

Spies N, Nielsen CB, Padgett RA, Burge CB (2009) Biased chromatin signatures around polyadenylation sites and exons. *Mol Cell* 36: 245–254

Su AI, Wiltshire T, Batalov S, Lapp H, Ching KA, Block D, Zhang J, Soden R, Hayakawa M, Kreiman G, Cooke MP, Walker JR, Hogenesch JB (2004) A gene atlas of the mouse and human protein-encoding transcriptomes. *Proc Natl Acad Sci U S A* 101: 6062–6067

Svoboda P, Stein P, Anger M, Bernstein E, Hannon GJ, Schultz RM (2004) RNAi and expression of retrotransposons MuERV-L and IAP in preimplantation mouse embryos. *Dev Biol* 269: 276–285

Toyoda Y, Yokoyama M, Hosi T (1971) Studies on the fertilization of mouse eggs in vitro: I. in vitro fertilization of eggs by fresh epididymal sperm. *Jpn J Anim Reprod* 16: 147–151

Vasseur M, Condamine H, Duprey P (1985) RNAs containing B2 repeated sequences are transcribed in the early stages of mouse embryogenesis. *EMBO J* 4: 1749–1753

Wang QT, Piotrowska K, Ciemerych MA, Milenkovic L, Scott MP, Davis RW, Zernicka-Goetz M (2004) A genome-wide study of gene activity reveals developmental signaling pathways in the preimplantation mouse embryo. *Dev Cell* 6: 133–144

Warner CM, Versteegh LR (1974) In vivo and in vitro effect of alpha-amanitin on preimplantation mouse embryo RNA polymerase. *Nature* 248: 678–680

Weber CM, Henikoff S (2014) Histone variants: dynamic punctuation in transcription. *Genes Dev* 28: 672–682

Wiekowski M, Miranda M, DePamphilis ML (1991) Regulation of gene expression in preimplantation mouse embryos: effects of the zygotic clock and the first mitosis on promoter and enhancer activities. *Dev Biol* 147: 403–414

Wiekowski M, Miranda M, DePamphilis ML (1993) Requirements for promoter activity in mouse oocytes and embryos distinguish paternal pronuclei from maternal and zygotic nuclei. *Dev Biol* 159: 366–378

Xue Z, Huang K, Cai C, Cai L, Jiang C-Y, Feng Y, Liu Z, Zeng Q, Cheng L, Sun YE, Liu J-Y, Horvath S, Fan G (2013) Genetic programs in human and mouse early embryos revealed by single-cell RNA sequencing. *Nature* 500: 593–597

Zatsepina O, Baly C, Chebrout M, Debey P (2003) The step-wise assembly of a functional nucleolus in preimplantation mouse embryos involves the cajal (coiled) body. *Dev Biol* 253: 66–83

Zeng F, Schultz RM (2005) RNA transcript profiling during zygotic gene activation in the preimplantation mouse embryo. *Dev Biol* 283: 40–57

PCGF6-PRC1 suppresses premature differentiation of mouse embryonic stem cells by regulating germ cell-related genes

Mitsuhiro Endoh[1,2,3,4,5]*, Takaho A Endo[6], Jun Shinga[7], Katsuhiko Hayashi[8], Anca Farcas[9], Kit-Wan Ma[1], Shinsuke Ito[1,2], Jafar Sharif[1,2], Tamie Endoh[1,3,5], Naoko Onaga[1], Manabu Nakayama[10], Tomoyuki Ishikura[1], Osamu Masui[1], Benedikt M Kessler[11], Toshio Suda[3,4], Osamu Ohara[6,10], Akihiko Okuda[12], Robert Klose[9], Haruhiko Koseki[1,2]*

[1]Laboratory for Developmental Genetics, RIKEN Center for Integrative Medical Sciences, Yokohama, Japan; [2]Core Research for Evolutional Science and Technology, Yokohama, Japan; [3]Centre for Translational Medicine,Cancer Science Institute of Singapore, National University of Singapore, Singapore, Singapore; [4]International Research Center for Medical Sciences, Kumamoto University, Kumamoto, Japan; [5]Research Institute for Radiation Biology and Medicine, Hiroshima University, Hiroshima, Japan; [6]Laboratory for Integrative Genomics, RIKEN Center for Integrative Medical Sciences, Yokohama, Japan; [7]Laboratory for Immunotherapy, RIKEN Center for Integrative Medical Sciences, Yokohama, Japan; [8]Department of Developmental Stem Cell Biology, Faculty of Medical Sciences, Kyushu University, Fukuoka, Japan; [9]Department of Biochemistry, Oxford University, Oxford, United Kingdom; [10]Chromosome Engineering Team, Department of Technology Development, Kazusa DNA Research Institute, Kisarazu, Japan; [11]Mass Spectrometry Laboratory, Target Discovery Institute, Nuffield Department of Medicine, University of Oxford, Oxford, United Kingdom; [12]Division of Developmental Biology, Research Center for Genomic Medicine, Saitama Medical University, Saitama, Japan

*For correspondence: csime@nus.edu.sg (ME); haruhiko.koseki@riken.jp (HK)

Abstract The ring finger protein PCGF6 (polycomb group ring finger 6) interacts with RING1A/B and E2F6 associated factors to form a non-canonical PRC1 (polycomb repressive complex 1) known as PCGF6-PRC1. Here, we demonstrate that PCGF6-PRC1 plays a role in repressing a subset of PRC1 target genes by recruiting RING1B and mediating downstream mono-ubiquitination of histone H2A. PCGF6-PRC1 bound loci are highly enriched for promoters of germ cell-related genes in mouse embryonic stem cells (ESCs). Conditional ablation of *Pcgf6* in ESCs leads to robust de-repression of such germ cell-related genes, in turn affecting cell growth and viability. We also find a role for PCGF6 in pre- and peri-implantation mouse embryonic development. We further show that a heterodimer of the transcription factors MAX and MGA recruits PCGF6 to target loci. PCGF6 thus links sequence specific target recognition by the MAX/MGA complex to PRC1-dependent transcriptional silencing of germ cell-specific genes in pluripotent stem cells.
DOI: 10.7554/eLife.21064.001

366

Introduction

Polycomb group (PcG) proteins are evolutionarily conserved epigenetic repressors of developmental genes. PcG-mediated gene silencing involves at least two distinct enzymatic activities directed to histone tails: the first mediates Histone H2A mono-ubiquitination at K119 (H2AK119ub1) by the polycomb repressive complexes 1 (PRC1), while the second mediates H3 tri-methylation at K27 (H3K27me3) by the polycomb repressive complex 2 (PRC2) (*Cao et al., 2002*; *Czermin et al., 2002*; *Kuzmichev et al., 2002*; *Müller et al., 2002*; *Shao et al., 1999*; *Wang et al., 2004*). According to the canonical view, H3K27me3 deposition by the EZH1/2 (enhancer of zeste homologs 1 and 2) histone methyltransferases leads to binding of the H3K27me3-reader protein CBX2 (chromobox protein homolog 2), in turn facilitating sequential recruitment of canonical PRC1 (cPRC1) (*Bernstein et al., 2006*; *Cao et al., 2002*; *Czermin et al., 2002*; *Fischle et al., 2003*; *Kuzmichev et al., 2002*). Conversely, H2AK119ub1 deposition by the non-canonical PRC1 (ncPRC1) promotes downstream recruitment of PRC2 and H3K27me3 (*Blackledge et al., 2014*; *Cooper et al., 2014*). Myriad other accessory molecules interact with both PRC1 and PRC2, conferring robustness and reversibility to PcG-mediated gene repression (*Li et al., 2011*).

The molecular complexity underlying PcG-mediated gene silencing could be partly explained by the diversity of the PCGF factors (from PCGF1 to PCGF6) that directly associate with RING1A/B proteins. For example, canonical PRC1 (cPRC1) may include PCGF2 (also known as MEL18: melanoma nuclear protein 18) or PCGF4 (also known as Bmi1: B cell-specific Moloney murine leukemia virus integration site 1). These cPRC1 complexes can be further classified into specific sub-complexes according to their association with CBX (CBX2/4/6/7/8) or PHC (PHC1/2/3: polyhomeotic homologs 1, 2 and 3) (*Gao et al., 2012*; *Vandamme et al., 2011*). CBX proteins contribute to recognition of H3K27me3, and therefore mediate recruitment of cPRC1 into target loci; while PHC proteins mediate gene compaction through polymerization of the SAM (sterile alpha motif) domain to facilitate transcriptional silencing (*Isono et al., 2013*).

Non-canonical PRC1 (ncPRC1) associates with PCGF1, PCGF3, PCGF5 or PCGF6 and RYBP (RING1 and YY1-binding protein) or YAF2 (YY1 Associated Factor 2), but does not interact with CBX2/4/6/7/8 or PHC1/2/3 (*Gao et al., 2012*). In addition to the core subunits RING1A/B and PCGF1, ncPRC1-containing PCGF1 (PCGF1-PRC1) also incorporates KDM2B [Lysine (K)-Specific Demethylase 2B], BCOR (BCL6 Corepressor), BCORL1 (BCL6 Corepressor-Like 1), RYBP, YAF2 and SKP1 (S-Phase Kinase-Associated Protein 1) (*Farcas et al., 2012*; *Gearhart et al., 2006*). Non-canonical PRC1 complexes are functionally linked with their canonical counterparts (cPRC1), and most of their target genes overlap with each other (*Blackledge et al., 2015*). These overlapping genes often possess unmethylated CpG islands (CGI) in their promoters, and these are preferentially bound by the CXXC (two cysteines separated by two other residues) domain of KDM2B via recognition of unmethylated CpG dinucleotides (*Farcas et al., 2012*; *He et al., 2013*; *Wu et al., 2013*). KDM2B binding to target genes allows direct recruitment of PCGF1-PRC1, followed by binding of PRC2 through recognition of H2AK119ub1 (*Blackledge et al., 2014*; *Cooper et al., 2014*). As PRC2 further recruits cPRC1, non-canonical PCGF1-PRC1 can therefore activate the PRC2-cPRC1 axis to ensure robust transcriptional silencing of developmental genes that harbor unmethylated CGIs.

Another PCGF homolog, PCGF6, was first identified in a multimeric protein complex associated with the E2F6 transcription factor (*Ogawa et al., 2002*). This complex was annotated as PCGF6-PRC1, and was shown to form stable complexes with several other well-known epigenetic factors such as RING1A/B, PCGF6, L3MBTL2 [lethal(3)malignant brain tumor-like 2], RYBP, YAF2, G9A (also known as EHMT2: euchromatic histone-lysine N-methyltransferase 2), GLP (G9a-like protein 1, also known as EHMT1), and CBX1/3 (*Gao et al., 2012*; *Hauri et al., 2016*; *Kloet et al., 2016*; *Ogawa et al., 2002*; *Qin et al., 2012*; *Trojer et al., 2011*). Interestingly, PCGF6-PRC1 also interacts with sequence-specific DNA binding proteins such as E2F6, MAX, MGA and TFDP1 (transcription factor Dp-1) (*Gao et al., 2012*; *Hauri et al., 2016*; *Kloet et al., 2016*; *Ogawa et al., 2002*; *Qin et al., 2012*; *Trojer et al., 2011*). This suggests that such DNA binding proteins could play a role in sequence specific recruitment of PCGF6-PRC1 to target loci; however, this notion has not been experimentally validated.

In this study, we therefore purified the PCGF6-PRC1 complex and examined the contribution of PCGF6 to ESC maintenance and embryonic development. We demonstrate that PCGF6 mediates repression of target genes by recruiting RING1B and facilitating H2AK119ub1. Taking advantage of

a *Pcgf6* conditional allele, we show that PCGF6 and RING1B common targets are enriched for meiosis- and germ cell-related genes in ESCs, and that such genes are robustly de-repressed in the absence of PCGF6 (*Pcgf6*-KO). Importantly, silencing of germ cell-related genes by PCGF6 likely plays a role in proliferation and growth of ESCs. We further demonstrate that PCGF6 is involved in pre- and peri-implantation mouse development. Indeed, loss of *Pcgf6* leads to pleiotropic defects in vivo, including aberrant axial development and impaired placenta formation. We also reveal a unique recruitment mechanism amongst PRC1 complexes whereby PCGF6-PRC1 utilizes its MGA and MAX components as a heterodimeric DNA binding module to directly recognize and repress expression of germ cell- and meiosis-related genes to support ESC maintenance and embryonic development.

Results

PCGF6 forms complexes with PRC1 components

Previous proteomic approaches have repeatedly identified PCGF6 as a component of multimeric protein complexes designated as PCGF6-PRC1 that included MAX, MGA, E2F6, TFDP1, RING1B, RING1A, CBX3, RYBP, L3MBTL2, YAF2 and WDR5 in human cell lines (*Gao et al., 2012*; *Hauri et al., 2016*; *Ogawa et al., 2002*; *Trojer et al., 2011*). To address the composition of PCGF6 complexes in mouse ESCs, we stably expressed an epitope-tagged form of PCGF6 in mouse ESCs and affinity purified it from nuclear extracts, then used LC-MS/MS analysis to identify associated proteins. We observed strong association of PCGF6 with MGA, RING1B, RING1A, CBX3, CBX1, RYBP, L3MBTL2, YAF2 and TFDP1 (*Figure 1A,B*), indicating that the mouse ESC PCGF6 complex is similar to those purified from human cells (*Gao et al., 2012*; *Hauri et al., 2016*; *Kloet et al., 2016*; *Ogawa et al., 2002*; *Trojer et al., 2011*). We however did not detect considerable amounts of MAX in the PCGF6 complexes in mouse ESCs.

We went on to confirm these results by immunoprecipitation followed by immunoblotting (IP-IB). For this purpose, we stably expressed FLAG-tagged PCGF6 in *Pcgf6*-deficient (*Pcgf6*-KO) ESCs (*Figure 1—figure supplement 1A,B*) or FLAG-RING1B in wildtype (WT) ESCs (*Figure 1C*). We observed exogenous FLAG-PCGF6 expressed at the similar level of endogenous PCGF6. We then tested the interaction of these tagged proteins with endogenous RING1B, RYBP, L3MBTL2 and MAX (*Figure 1C*). We indeed found considerable association of MAX with both FLAG-PCGF6 and FLAG-RING1B as well as the other three proteins. We further observed PCGF1 or PCGF2 was not co-IPed with FLAG-PCGF6 while both of them associated with FLAG-RING1B. We finally confirmed EZH2 or SET1 were not co-IPed with either FLAG-PCGF6 or FLAG-RING1B. These results suggested that PCGF6 would be primarily involved in non-canonical PRC1 (ncPRC1), particularly PCGF6-PRC1, in mouse ESCs.

PCGF6 shares target genes with RING1B

The catalytic activity of both canonical PRC1 (cPRC1) and ncPRC1 is mediated by RING1A and RING1B (*Buchwald et al., 2006*; *Gearhart et al., 2006*; *Trojer et al., 2011*; *Wang et al., 2004*). Consistent with this model, it has been shown that genetic ablation of *Ring1A/B* leads to widespread disruption of PRC1-dependent gene repression (*de Napoles et al., 2004*; *Endoh et al., 2008*; *Leeb and Wutz, 2007*; *Wang et al., 2004*). To determine whether PCGF6 plays a role in gene repression in association with RING1B, we examined the overlap between PCGF6- and RING1B-bound sites by PCGF6 ChIP-seq (chromatin immunoprecipitation followed by deep sequencing), by using a FLAG-PCGF6 expressing *Pcgf6*-KO ESCs. Our results considerably overlapped with those reported recently (*Figure 1—figure supplement 1C*) (*Yang et al., 2016*). This analysis revealed that PCGF6 bound to the transcriptional start sites (TSSs) of a group of genes associated with germ cell specific functions, such as *Tex19.1* (testis-expressed protein 19A) and *Tdrkh* (Tudor and KH domain containing) (*Figure 1D*). Indeed, these genes were also marked by RING1B, indicating that PCGF6 and RING1B share common targets.

Intriguingly, cPRC1 targets, such as the *Hoxd* (homeobox protein Hox-D) gene cluster, were not bound by PCGF6 (*Figure 1D*), indicating that PCGF6 might associate with a subset of RING1B-bound genes that are not marked by cPRC1. A detailed examination of ChIP-seq datasets revealed that 1218, 2959 and 4946 genes in ESCs were bound by PCGF6, RING1B, and H3K27me3, respectively (*Figure 1E*). As expected, PCGF6-bound genes partially but significantly overlapped with both
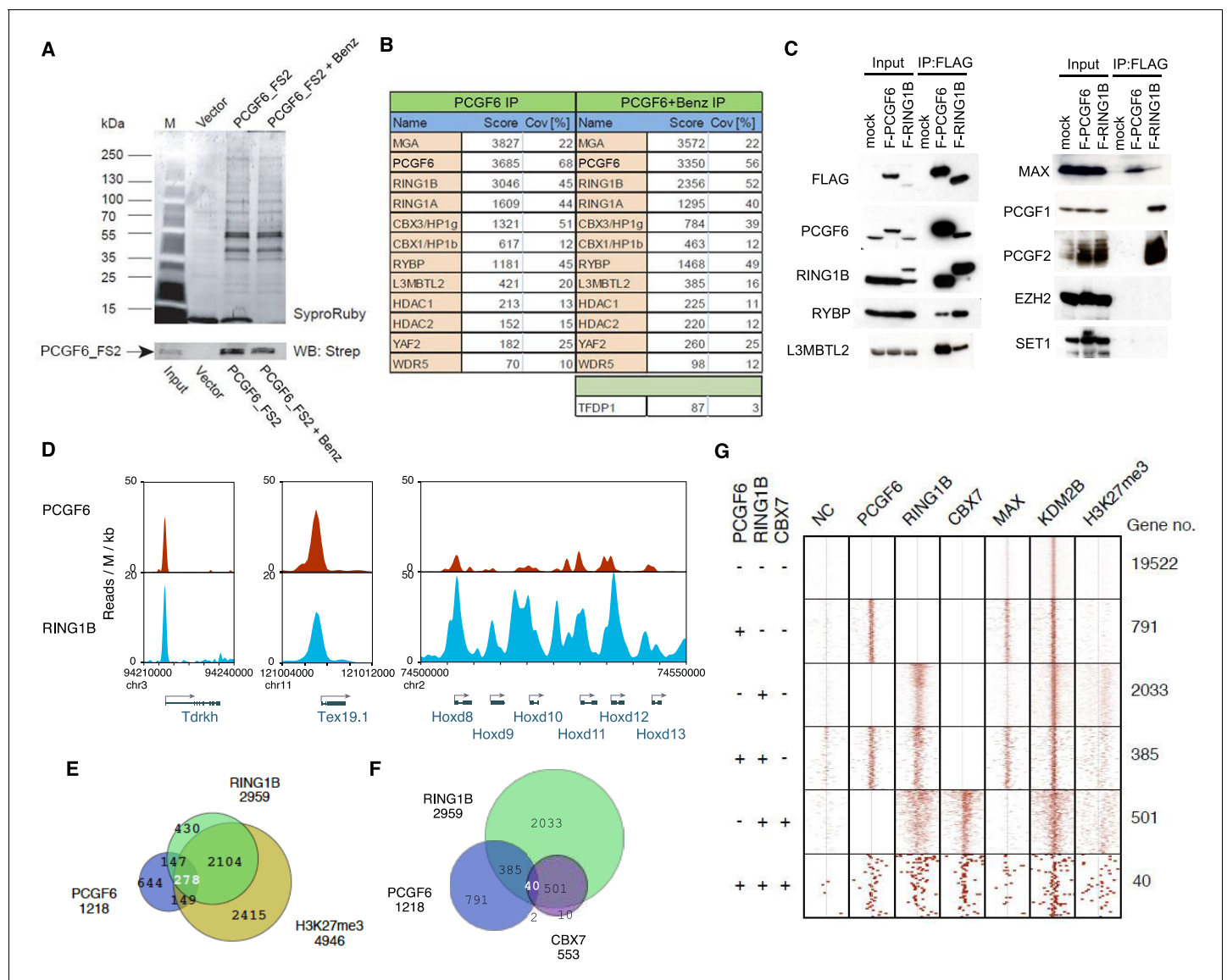
Figure 1. Biochemical properties of PCGF6-PRC1 and its target genes in ESCs. (**A**) Affinity purification of PCGF6-containing complexes in ESCs. To purify PCGF6 and associated proteins, a mouse ESC cell line stably expressing Flag-2xStrepII (FS2)-tagged PCGF6 was generated. Nuclear extract was isolated from this cell-line, PCGF6 was affinity purified, and the purified proteins were subjected to mass spectrometry. Purified PCGF6 fractions were resolved by gradient SDS-PAGE and visualized by SyproRuby staining. The purifications were performed in the absence and presence of benzonase (Benz) to exclude DNA-mediated interactions and a cell line containing only the empty vector was used as control for non-specific binding to the affinity matrix. The elutates were probed by western blot for streptavidin (Strep). (**B**) Identification of proteins that form stable complexes with PCGF6 in ESCs. Elutions from the PCGF6 affinity purification were directly analyzed by tryptic digestion followed by peptide identification by LC-MS/MS. The Mascot scores and peptide coverage are shown for the respective affinity purifications. (**C**) Confirmation of PCGF6-containing complexes by immunoprecipitation-immunoblot (IP-IB) analysis. Whole-cell extracts (WCE) from ESCs expressing FLAG-tagged PCGF6 or RINGB were subjected to IP using anti-FLAG antibody. The WCE and immunoprecipitates were separated on SDS-PAGE and analyzed by IB with the indicated antibodies. (**D**) Screenshot views for the distribution of PCGF6 (red) and RING1B (blue) at target genes in ESCs determined by ChIP-seq. The chromosomal positions are indicated on the x-axis. The transcription start sites (TSSs) are denoted by arrows. (**E**) Venn diagram representation for the overlap of PCGF6, RING1B and H3K27me3 target genes in ESCs identified by ChIP-seq. The number of genes bound by PCGF6, RING1B and H3K27me3 and included in each fraction are indicated. (**F**) Venn diagram representing the overlap of PCGF6, RING1B and CBX7 target genes. Published ChIP-seq data for CBX7 was obtained from NCBI GEO (accession number GSM1041373). (**G**) A heat map view for distribution of PCGF6, RING1B, CBX7, MAX, KDM2B and H3K27me3 in ±4 kb genomic regions around transcription start sites (TSS). Genes are classified based on their occupancy by PCGF6, RING1B and CBX7 in ESCs. The signal from a negative control (NC: FLAG-ChIP in mock transfected ESCs) was also shown.

DOI: 10.7554/eLife.21064.002

The following source data and figure supplement are available for figure 1:

Figure 1 continued on next page

RING1B and H3K27me3 target genes (*Figure 1E,F*). These observations were further validated by ChIP-qPCR analysis (*Figure 1—figure supplement 1D*).

PCGF6 binds in close proximity to the TSS of genes and prefers short-CGIs

To clarify whether PCGF6 marked loci represented cPRC1 or ncPRC1 target genes, we compared the list of PCGF6- and CBX7 (Chromobox Homolog 7)-bound genes. As CBX7 is a key component of cPRC1 (*Bernstein et al., 2006*; *Morey et al., 2013*), exclusion of PCGF6-bound sites from CBX7-bound sites would indicate an ncPRC1-centric role for PCGF6, while an overlap would indicate the opposite. CBX7-bound genes were mostly co-occupied by RING1B, as expected (*Figure 1F*). PCGF6 target sites, however, exhibited only a limited overlap with CBX7, supporting the model in which PCGF6 is predominantly involved in ncPRC1.

To gain insight into the binding profile of PCGF6 at target genes, we plotted PCGF6, RING1B, CBX7, MAX, KDM2B and H3K27me3 ChIP-seq reads in a ±4 kb region surrounding TSS (*Figure 1G*). This analysis revealed that PCGF6 bound in close proximity to TSS, unlike RING1B, CBX7 and H3K27me3, all of which exhibited a broader distribution (*Figure 1G*). We observed considerable association of MAX at PCGF6 targets irrespective of RING1B binding. In contrast, H3K27me3 deposition at PCGF6 targets was mainly seen at RING1B-bound genes. We also noted that PCGF6 target genes harbor CGIs that tend to be slightly shorter and more methylated than CBX7 targets (*Figure 1—figure supplement 1E*). Consistently, PCGF6 targets were bound by KDM2B. KDM2B loss induced a subtle increase of RING1B binding at PCGF6 targets while RING1B binding at CBX7 targets was marginally decreased (*Figure 1—figure supplement 1F*). Moreover, PCGF6-bound genes were up-regulated to a much lesser extent than CBX7-bound genes in *Kdm2b*-KO ESCs (*Figure 1—figure supplement 1G*). These results suggest that the CGI recognition by KDM2B has distinct roles for PCGF6-PRC1 recruitment from that reported for cPRC1 (*Farcas et al., 2012*).

PCGF6 represses RING1B-bound genes

We next wondered whether PCGF6 binding was functionally required for transcriptional repression. To test this, we performed RNA-seq and found that more than 250 genes were considerably up-regulated in *Pcgf6*-KO ESCs (*Figure 2—figure supplement 1A*). Importantly, these genes were a subset of the genes up-regulated in the *Ring1A* and *Ring1B* double knockout (*Ring1A/B*-dKO) ESCs (*Figure 2—figure supplement 1A*). To gain insight into the association of PCGF6 and RING1B for gene regulation, we divided RING1B- or PCGF6-bound genes into three categories (PCGF6+RING1B+, PCGF6-RING1B+ and PCGF6+RING1B-) and examined their expression in WT ESCs using FPKM (fragments per kilobase of exon per million mapped sequence reads) values (*Figure 2—figure supplement 1B*). This analysis showed that the PCGF6+RING1B+ genes were barely transcribed in WT ESCs; likewise, the PCGF6-RING1B+ genes were marginally expressed. In contrast, the PCGF6+RING1B- group that harbors CGIs was robustly expressed. We went on to examine changes of respective gene expression levels in each category in the absence of *Pcgf6* (*Pcgf6*-KO) (*Figure 2A*, left). We found both PCGF6+RING1B+ and PCGF6-RING1B+ genes were significantly up-regulated while expression levels of PCGF6+RING1B- or PCGF6-RING1B- genes were barely altered in *Pcgf6*-KO ESCs (*Figure 2A*, left). We however also found that expression levels of highly up-regulated genes (more than 5-times; indicated by red lines in *Figure 2A*) in the PCGF6+RING1B+ category were considerably higher than those in the PCGF6-RING1B+ category in *Pcgf6*-KO ESCs. Those categories were also up-regulated in *Ring1A/B*-dKO ESCs (*Figure 2A*, right), suggesting a functional link between PCGF6 and RING1A/B for down-regulation of such genes. We further confirmed these changes in expression levels of selected PCGF6+RING1B+ and PCGF6-RING1B+ genes by RT-qPCR in *Pcgf6*-KO and *Ring1A/B*-dKO ESCs (*Figure 2—figure supplement 1B,C*). Together, PCGF6 is
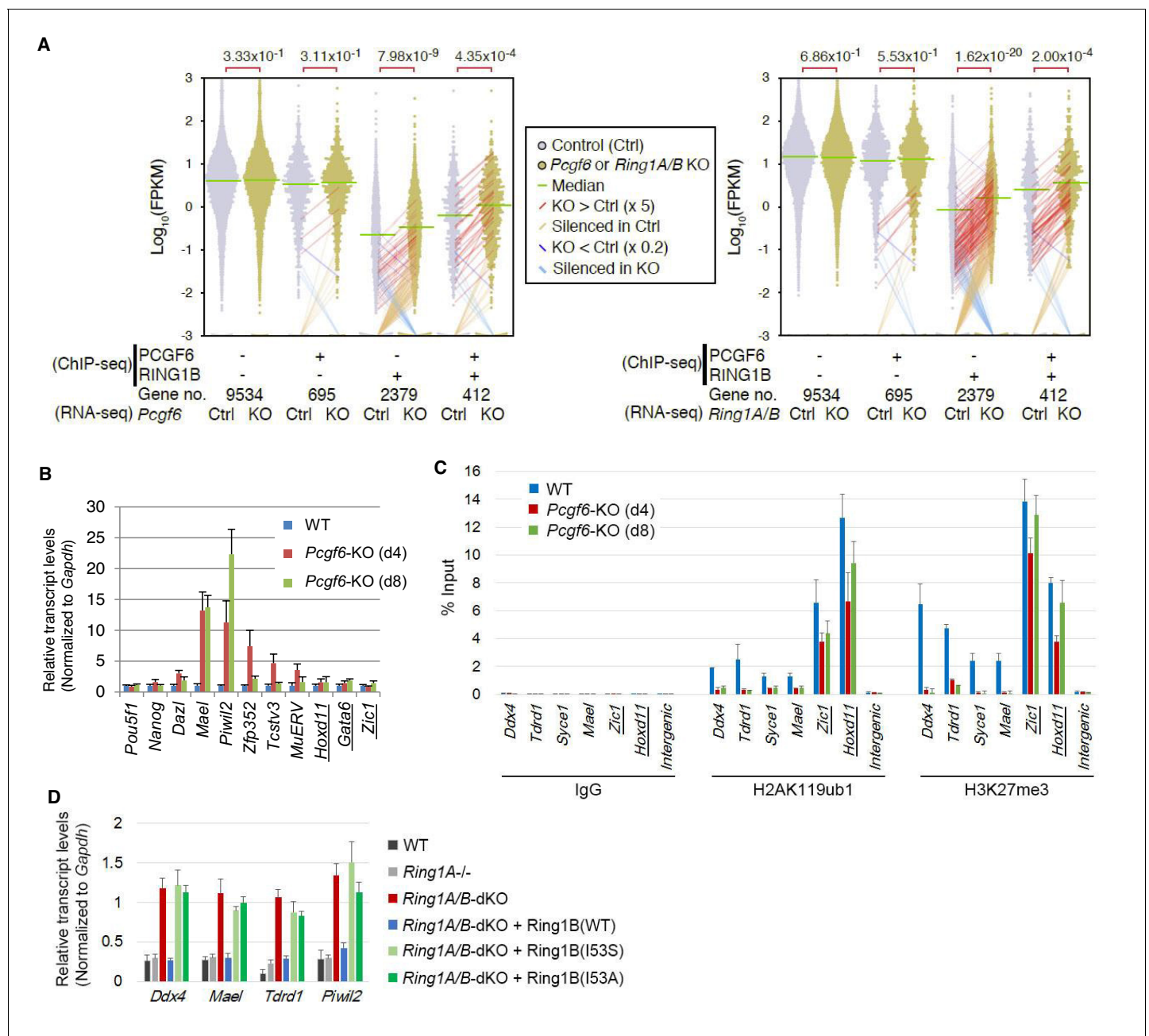
370

Figure 2. RING1B-dependent repression of target genes by PCGF6-PRC1. (**A**) Dot plot representation for gene expression changes in *Pcgf6*-KO (left) and *Ring1A/B*-dKO (right) ESCs. Expression levels of respective genes (FPKM: determined by RNA-seq) in each group (classified by ChIP-seq) in control (Ctrl) and respective knockouts (KO) are shown by grey and yellow dots, respectively. The median of FPKM in each group is indicated by a green horizontal line. Genes whose expression (FPKM) changed more than 5-fold were indicated by red (up-regulated in KO) or blue (down-regulated in KO) lines. Genes silenced in Ctrl but active in KO are indicated by orange lines, while genes vice versa are indicated by light blue lines. The number of genes included in each subset is shown at the bottom. *p*-values for the difference of expression changes between Ctrl and KO were calculated by the Student's *t*-test and are indicated above each graph. (**B**) RT-qPCR-based validation for expression changes of selected genes in *Pcgf6*-KO ESCs. Expression levels of genes required for pluripotency, or bound by PCGF6-PRC1 or canonical PRC1 (underlined) in *Pcgf6*$^{fl/fl}$;*Rosa26::CreERT2*$^{tg/+}$ ESCs before (WT) or after OHT treatment (day 4 and 8). Expression levels were normalized to a *Gapdh* control and are depicted as fold change relative to OHT-untreated (WT) ESCs. Error bars represent standard deviation determined from at least three independent experiments. (**C**) Changes in local H2AK119ub1 and H3K27me3 deposition at selected PCGF6-PRC1 target genes in *Pcgf6*-KO ESCs. Local levels of H2AK119ub1 and H3K27me3 at promoter regions of genes bound by PCGF6-PRC1 or canonical PRC1 (underlined) in *Pcgf6*$^{fl/fl}$;*Rosa26::CreERT2*$^{tg/+}$ ESCs before (WT) or after (day 4 and 8) OHT treatment were determined by ChIP-qPCR analysis. The relative amount of ChIPed DNA is depicted as a percentage of input DNA. Error bars represent standard deviation determined from at least three independent experiments. (**D**) Requirement of RING1B catalytic activity for repression of

Figure 2 continued on next page

Figure 2 continued

genes bound by PCGF6-PRC1. Expression levels of the indicated genes in mock-transfected *Ring1A$^{-/-}$;Ring1B$^{fl/fl}$;Rosa26::CreERT2$^{tg/+}$* ESCs before (*Ring1A$^{-/-}$*) and 2 day after OHT treatment (*Ring1A/B*-dKO) and in those stably expressing wild type (WT) or catalytically-dead (I53S, I53A) Ring1B. Expression levels were normalized to a *Gapdh* control and are depicted as fold change relative to OHT-untreated mock-transfected parental ESCs (*Ring1A$^{-/-}$*). Those in wild-type ESCs (WT) are also shown. Error bars represent standard deviation determined from at least three independent experiments.

The following figure supplement is available for figure 2:

Figure supplement 1. Repression of target genes by PCGF6-PRC1.

suggested to contribute to RING1B-mediated repression of target genes primarily in the PCGF6+RING1B+ category but also in RING1B targets not bound by PCGF6 to a lesser extent. We thus suggest PCGF6+RING1B+ category as a primary target for PCGF6-PRC1-mediated gene repression.

PCGF6 represses germ cell-related genes via RING1B catalytic activity

To gain insight into the physiological role of PCGF6-PRC1-mediated gene regulation in ESCs, we performed gene ontology (GO) analyses, which revealed that PCGF6-PRC1 target genes are enriched in meiosis- and germ cell-related genes as suggested previously (*Zdzieblo et al., 2014*), unlike the cPRC1 target genes that are predominantly enriched in developmental genes (*Figure 2—figure supplement 1D*). These results suggest a potential role of PCGF6-PRC1 for suppression of the meiotic program or germ cell differentiation program, or both, in ESCs.

The RING1A/B proteins play a key role for transcriptional repression by mediating H2AK119ub1 (*Endoh et al., 2012*; *Wang et al., 2004*). We therefore investigated whether PCGF6-PRC1-mediated gene regulation involves H2AK119ub1. Indeed, ChIP-qPCR analyses revealed considerable enrichment of H2AK119ub1 at PCGF6-PRC1 target genes (*Figure 2C*). Furthermore, this H2AK119ub1 enrichment was dramatically diminished in the absence of *Pcgf6*, revealing a role for PCGF6 in mediating H2AK119ub1 deposition (*Figure 2C*). In contrast, H2AK119ub1 enrichment at *Zic1* and *Hoxd11,* cPRC1 targets, was marginally affected in *Pcgf6*-KO ESCs, further supporting our model that PCGF6 is not primarily involved in cPRC1-dependent repression (*Figure 2C*, middle).

To gain insight into the functional involvement of PCGF6-mediated H2AK119ub1 in repression of the target genes, we next examined the effect of loss of RING1B catalytic activity on expression of these genes (*Figure 2D*). Previous reports have demonstrated that mutations of RING1B residue I53 (i.e., I53S or I53A), abrogated its E3 ligase activity by disrupting its interactions with the E2 ubiquitin-conjugating enzyme UBCH5C (also known as UBE2D3: Ubiquitin-conjugating enzyme E2 D3) (*Ben-Saadon et al., 2006*; *Buchwald et al., 2006*; *Endoh et al., 2012*; *Eskeland et al., 2010*). Rescuing the *Ring1A/B*-dKO cells with the I53 mutants failed to maintain transcriptional repression, demonstrating that repression of PCGF6 target genes depends on the catalytic activity of RING1B and likely also downstream H2AK119ub1 deposition (*Figure 2D*).

Since our previous report demonstrated that H2AK119ub1 plays a critical role for recruitment of PRC2 and downstream H3K27me3 deposition (*Blackledge et al., 2014*), we thus investigated H3K27me3 deposition at the representative PCGF6 bound genes, and indeed found a significant H3K27me3 enrichment at these targets (*Figure 2—figure supplement 1E*). As expected, the H3K27me3 level was markedly reduced in the absence of the key PRC2 component EED (embryonic ectoderm development), confirming that H3K27me3 deposition in these genes is mediated by the PRC2 complex (*Figure 2—figure supplement 1E*). We indeed found a considerable reduction in H3K27me3 level at these PCGF6-PRC1 targets in *Pcgf6*-KO ESCs, but only marginally at cPRC1 targets, suggesting a potential role for PCGF6-mediated H2AK119ub1 to recruit PRC2 (*Figure 2C*). However, consistent with a previous report (*Riising et al., 2014*), PRC2-mediated mechanisms exhibited only limited impact on the repression of PCGF6-PRC1 targets (*Figure 2—figure supplement 1F*).

PCGF6 recruits RING1B to target genes and facilitates downstream H2AK119ub1 and H3K27me3 deposition

Previous studies have reported that PCGF6 interacts with RING1B through its RING finger domain (*Akasaka et al., 2002*). Given that PCGF6 loss led to a marked reduction in H2AK119ub1 deposition specifically at PCGF6-PRC1 target genes (*Figure 2C*), we wondered whether PCGF6 is directly involved in recruitment of RING1B and its catalytic activity. To test this model, we expressed a PCGF6 protein fused to the TET repressor (PCGF6/TETR), and ectopically tethered this fusion protein to a pre-integrated TetO array in ESCs (*Figure 3A*), taking advantage of an experimental system that we have previously described (*Blackledge et al., 2014*). ChIP-qPCR analysis showed binding of the PCGF6/TETR fusion protein at the TetO array. Importantly, this was accompanied by considerable enrichment of RING1B, MAX and H2AK119ub1, indicating that PCGF6 recruits PCGF6-PRC1 (*Figure 3A*). We also observed association of EZH2 and H3K27me3 with the TetO array, likely mediated by the upstream H2AK119ub1 as reported previously (*Blackledge et al., 2014*).

To confirm these in vitro findings in vivo, we performed RING1B ChIP-seq in WT and *Pcgf6*-KO ESCs. This experiment demonstrated that RING1B binding to PCGF6-PRC1 target genes such as *Tex19.1*, *Tdrkh*, *Syce1* (synaptonemal complex central element protein 1) and *Mael* (maelstrom spermatogenic transposon silencer) was indeed considerably depleted in the absence of *Pcgf6* (*Figure 3B*). In contrast, RING1B binding to cPRC1 target sites, such as the *Hoxb* cluster, was unaffected.

To determine the role of PCGF6 in RING1B recruitment at ncPRC1 targets in a comprehensive manner, we divided RING1B-bound genes into four categories (*Figure 3C*). The first category consisted of genes bound by RING1B but not PCGF6 or CBX7 (PCGF6-CBX7-RING1B+). Genes in the second category were bound by both PCGF6 and RING1B, but not CBX7 (PCGF6+CBX7-RING1B+); and therefore represented the core targets of the non-canonical PCGF6-PRC1 complex. The third category consisted of the cPRC1 target genes, which were bound by CBX7 and RING1B, but not PCGF6 (PCGF6-CBX7+RING1B+). Finally, the fourth category was marked by all three factors (PCGF6+CBX7+RING1B+). We observed considerable reduction of RING1B binding to the core PCGF6-PRC1 target genes (PCGF6+CBX7-RING1B+) in *Pcgf6*-KO (green dot plots in *Figure 3C*, left; green lines in *Figure 3C*, right). In contrast, cPRC1 target genes (PCGF6-CBX7+RING1B+) were not affected. Consistent with these observations, genetic ablation of *Pcgf2* (*Mel18*) and *Pcgf4* (*Bmi1*), both of which are essential components of the cPRC1 complex, led to reduction of RING1B binding of only cPRC1 target genes (PCGF6-CBX7+RING1B+) (blue dot plots in *Figure 3C*, left; blue lines in *Figure 3C*, right). These observations were further confirmed by ChIP-qPCR for selected target genes (*Figure 3—figure supplement 1A*). Taken together, these findings indicate that PCGF6 preferentially recruits RING1B to PCGF6-PRC1 targets, but not to cPRC1 targets.

To determine whether PCGF6-dependent RING1B recruitment involved direct physical interactions between these two proteins, we tested a PCGF6 mutant with an amino acid substitution (H155Y) in a conserved residue critical for interaction with RING1B (*Buchwald et al., 2006*). We expressed the mutant in *Pcgf6*-KO ESCs, and noted that it indeed failed to interact with RING1B, while retaining the ability to associate with L3MBTL2 and MAX (*Figure 3—figure supplement 1B*). ChIP-qPCR analysis showed that although the mutant PCGF6 could bind the indicated target genes, it failed to recruit RING1B (*Figure 3D*) and, as a result, H2AK119ub1 and H3K27me3 marks were also not established in the target genes. Consistent with this interpretation, the mutant PCGF6 failed to repress PCGF6-PRC1 targets genes (*Figure 3—figure supplement 1C*).

Based on these observations, we concluded that PCGF6 contributes to the assembly and recruitment of the PCGF6-PRC1 complex by direct physical interactions with RING1B, which likely plays a critical role to mediate the repression. Previous and these studies, however, suggest potential involvement of other mechanisms, such as L3MBTL2, G9A/GLP and CBX1/3 for the repression by PCGF6-PRC1 (*Maeda et al., 2013*; *Qin et al., 2012*; *Trojer et al., 2011*). Indeed, we noted that PCGF6 was dispensable for L3MBTL2 binding of gene promoters (*Figure 3E*). As L3MBTL2 has been reported as a recruiter of ncPRC1 (*Qin et al., 2012*; *Trojer et al., 2011*), this observation suggests that PCGF6 and L3MBTL2 may function in parallel to recruit ncPRC1 complexes. We went on to examine contribution of H3K9me2, which is mediated by G9A/GLP, for PCGF6-PRC1-target repression (*Figure 3—figure supplement 1D*). Unlike *L3mbtl2*-KO ESCs (*Qin et al., 2012*), we did not observe considerable changes in H3K9me2 levels in *Pcgf6*-KO. Together, we suggest that the
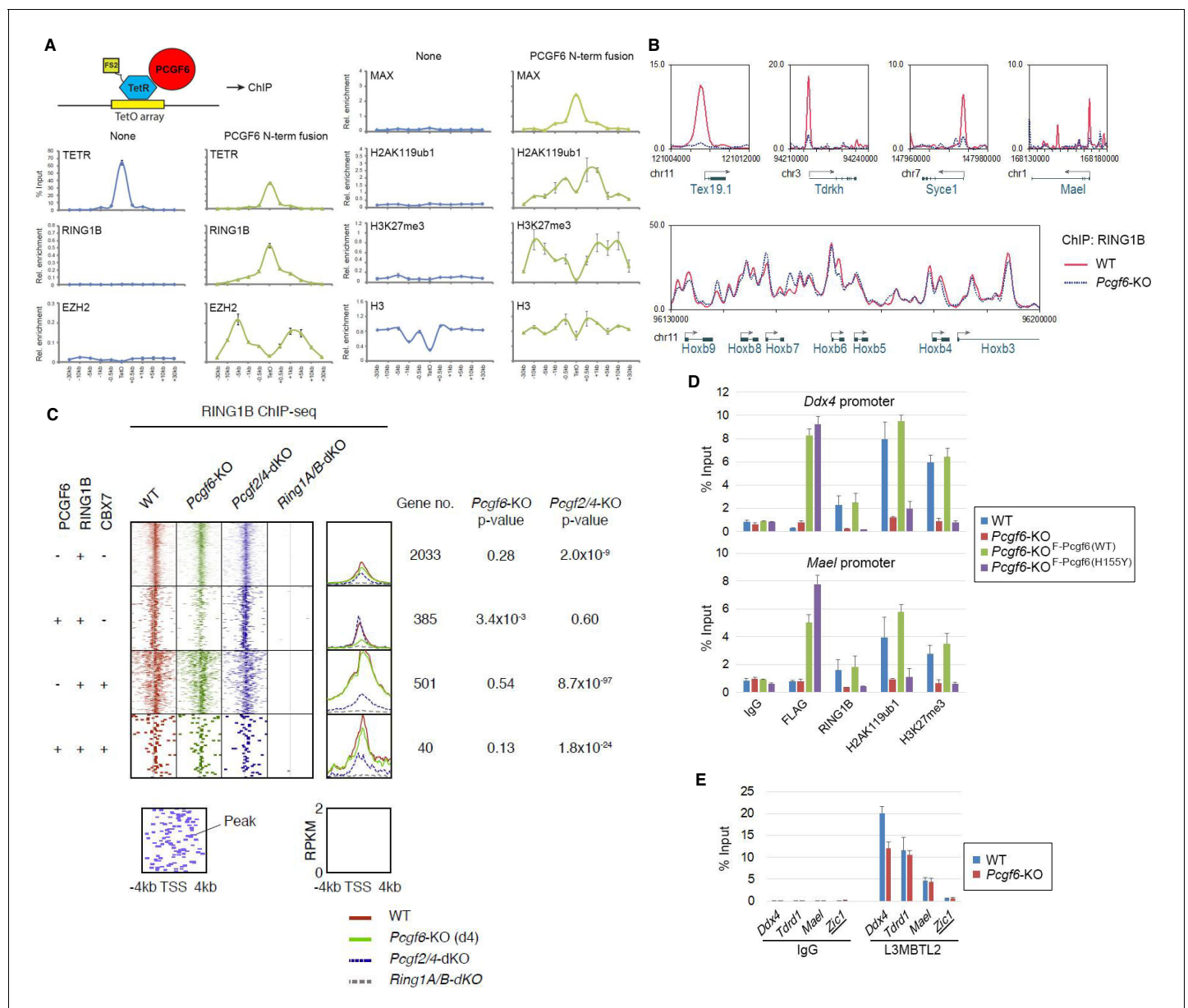
Figure 3. The role of PCGF6 in recruiting PCGF6-PRC1 to its target genes. (**A**) Forced tethering of PCGF6 to a TetO array induced activation of PCGF6-PRC1 recruitment. A schematic illustrating the de novo targeting of the TetR-PCGF6 fusion protein to the TetO sequences (left). ChIP analysis for TetR, RING1B, EZH2, MAX, H2AK119ub1, H3K27me3 and H3 across the TetO-containing locus in ESCs revealed TetR-PCGF6-mediated local activation of the PCGF6-PRC1 pathway (bottom). ChIP experiments were performed at least in biological duplicate with error bars showing SEM. (**B**) Screenshot views of the RING1B distribution at selected target genes in wild type (WT) and *Pcgf6*-KO ESCs. RING1B distribution in *Pcgf6*^{fl/fl};*Rosa26::CreERT2*^{tg/+} ESCs before (WT; red) or 4 days after OHT treatment (*Pcgf6*-KO; blue) revealed by ChIP-seq is shown. The chromosome numbers and locations are indicated on the x-axis. The transcription start sites (TSSs) are denoted by arrows. (**C**) A heat map view of RING1B distribution in ±4 kb genomic regions around TSS in wild type (WT; brown), *Pcgf6*-KO (green), *Mel18/Bmi1*-dKO (blue) and *Ring1A/B*-dKO (gray) ESCs. RING1B-bound genes are further subclassified by binding of PCGF6 and CBX7 (left). Average distribution and p-value for its change in respective KO are also shown (right). (**D**) PCGF6-mediated RING1B recruitment to its target via a direct molecular interaction. Local levels of Flag-tagged PCGF6, RING1B, H2AK119ub1 and H3K27me3 at *Ddx4* and *Mael* promoters in mock-transfected *Pcgf6*^{fl/fl};*Rosa26::CreERT2*^{tg/+} ESCs before (WT) and after OHT treatment (*Pcgf6*-KO) and in ESCs stably expressing WT [*Pcgf6*-KO_F-Pcgf6(WT)] or H155Y Pcgf6 [*Pcgf6*-KO_F-Pcgf6(HY)] constructs were determined by ChIP-qPCR. The relative amount of ChIPed DNA is depicted as a percentage of input DNA. Error bars represent standard deviation determined from at least three independent experiments. (**E**) PCGF6 is dispensable for local L3MBTL2 binding to target genes. Local levels of L3MBTL2 at the promoter regions of the indicated genes in *Pcgf6*^{fl/fl};*Rosa26::CreERT2*^{tg/+} ESCs before (WT) or 4 days after OHT treatment (*Pcgf6*-KO) were determined by ChIP-qPCR. Underlined genes are canonical PRC1 targets.

DOI: 10.7554/eLife.21064.007

Figure 3 continued on next page

374

Figure 3 continued

The following figure supplement is available for figure 3:

Figure supplement 1. The role of PCGF6 in recruiting PCGF6-PRC1 to its target genes.
DOI: 10.7554/eLife.21064.008

L3MBTL2/G9A axis is marginally involved in PCGF6-mediated repression. We further investigated the role of CBX1/3 for the regulation of PCGF6-PRC1 targets by using tamoxifen-inducible *Cbx1* and *Cbx3* double knockout (*Cbx1/3*-dKO) ESCs (*Figure 3—figure supplement 1E*). We did not observe a significant change in the expression levels of PCGF6+CBX7-RING1B+ in *Cbx1/3*-dKO ESCs, suggesting that CBX1/3 have, if any, a marginal role for the repression of PCGF6-PRC1 targets in ESCs (*Figure 3—figure supplement 1F*).

The MAX/MGA heterodimer is required for recruitment of PCGF6-PRC1 to target genes

The above results establish a role for PCGF6 in the recruitment of RING1B, however, the mechanism by which PCGF6-PRC1 is targeted to such loci is not understood. According to the canonical model, H3K27me3 facilitates PRC1 binding via direct recruitment of CBX proteins (*Bernstein et al., 2006*; *Cao et al., 2002*; *Czermin et al., 2002*; *Fischle et al., 2003*; *Kuzmichev et al., 2002*); we therefore examined whether H3K27me3 plays a role in PCGF6 recruitment (*Figure 4—figure supplement 1A, B*). For this purpose, we stably expressed a FLAG-tagged PCGF6 in WT or *Eed*-KO ESCs (deficient for H3K27me3), and compared PCGF6-binding levels at target genes. We did not observe any significant differences in FLAG-PCGF6 binding between WT and *Eed*-KO cells (*Figure 4—figure supplement 1B*), suggesting that H3K27me3 is dispensable for locus-specific recruitment of PCGF6-PRC1. Consistently, H2AK119ub1 levels at genes bound by PCGF6 were not affected in the *Eed*-KO (*Figure 4—figure supplement 1C*). In contrast, PCGF2, a component of cPRC1, barely associates with PCGF6 targets irrespective of H3K27me3 status, while it strongly associates with cPRC1 targets such as *Zic1* and *Hoxb3* in an EED-dependent manner (*Figure 4—figure supplement 1C*). These findings suggests that the H3K27me3-dependent pathway to recruit cPRC1 is barely active at PCGF6-PRC1 targets.

To determine the molecular mechanism that mediates recruitment of PCGF6-PRC1 to target loci, we surveyed the DNA sequences of PCGF6-bound promoters to extract potential transcription factor binding motifs. We observed enrichment of the E-box motif CACGTG, a DNA sequence that is recognized by the bHLH-containing transcription factors including MAX (*Blackwood and Eisenman, 1991*), within these promoters (*Figure 4—figure supplement 1D*). Importantly, this motif was not enriched in RING1B- or CBX7-bound genes (*Figure 4—figure supplement 1D*), suggesting that the E-box motif is a feature of PCGF6-PRC1 targets. Consistent with this notion, we observed considerable overlap between PCGF6-bound and MAX-bound genes, while the overlap between PCGF6-bound and MYC-bound genes was much less (*Figure 4A*). Interestingly, MGA, a transcription factor that also forms a heterodimer with MAX and binds the CACGTG E-box motif (*Hurlin et al., 1999*), is included in the PCGF6 complex determined by us (*Figure 1B*) and others (*Gao et al., 2012*; *Hauri et al., 2016*; *Kloet et al., 2016*; *Ogawa et al., 2002*; *Qin et al., 2012*; *Trojer et al., 2011*). Therefore, we hypothesized that MAX/MGA heterodimer could play a role in PCGF6-PRC1 recruitment.

To examine this possibility, we depleted MAX or MGA by siRNA-mediated knockdown (KD) in FLAG-PCGF6 expressing ESCs. The *Max* or *Mga* mRNA levels were reduced to less than 20% of control by their respective siRNAs (*Figure 4—figure supplement 1E*, top). Western blot analysis revealed that MAX protein was undetectable in the *Max*-KD ESCs, while the expression of FLAG-PCGF6 and RING1B was unchanged (*Figure 4—figure supplement 1E*, bottom). To determine the impact of MAX or MGA depletion, we performed RNA-seq in *Max*-KD or *Mga*-KD ESCs. Interestingly, genes that were bound by MAX, PCGF6 and RING1B (MAX+PCGF6+RING1B+) showed significant up-regulation in *Max*-KD or *Mga*-KD ESCs (*Figure 4B*). We performed locus-specific RT-qPCR assays in the *Ddx4* [DEAD (Asp-Glu-Ala-Asp) box polypeptide 4], *Tdrd1* (Tudor domain containing 1), *Stag3* (stromal antigen 3) and *Mael* loci, and confirmed our RNA-seq results (*Figure 4—figure supplement 1F*).
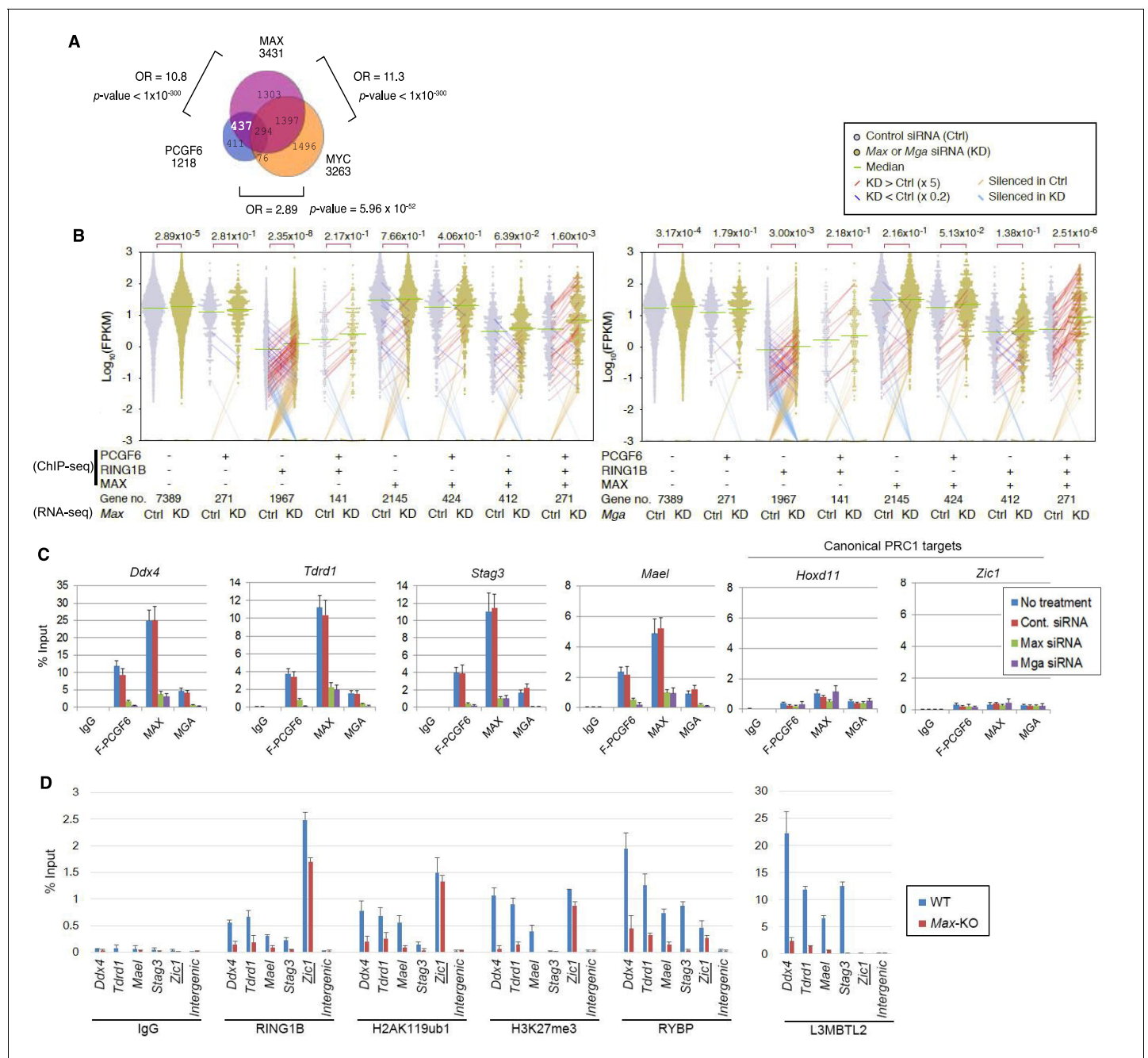
Figure 4. The role of MAX/MGA in recruiting PCGF6-PRC1 to its target genes. (**A**) Considerable overlap of genes bound by PCGF6 and MAX. Venn diagram depicts the overlap of PCGF6, MAX and MYC target genes in ESCs. Published ChIP-seq data for MAX and MYC were obtained from NCBI GEO (accession number GSM1171650 and GSM1171648, respectively). Odds ratio (OR) and *p*-values for the overlap between respective groups are indicated. Numbers represent the number of genes bound by each protein or included in each fraction seen in the Venn diagram. (**B**) Dot plot representation for gene expression changes in *Max*-KD (left) and *Mga*-KD (right) ESCs. Expression levels of respective genes (FPKM: determined by RNA-seq) in each group (classified by ChIP-seq) in control (Ctrl) and respective knockdowns (KD) are shown by grey and yellow dots, respectively. The same codes as described in *Figure 2A* are used. (**C**) Changes in binding of FLAG-tagged PCGF6, MAX and MGA at the selected targets induced by knockdown of *Max* or *Mga*. Local levels of FLAG-tagged PCGF6, MAX and MGA at the respective promoter regions in untreated ESCs or ESCs treated with either control siRNA, *Max* siRNA or *Mga* siRNA were determined by ChIP-qPCR. The relative amount of ChIPed DNA is depicted as a percentage of input DNA. Error bars represent standard deviation determined from at least three independent experiments. (**D**) Changes in local deposition of RING1B, H2AK119ub1, H3K27me3, RYBP and L3MBTL2 at the indicated targets in *Max*-KO ESCs. Underlined genes are canonical PRC1 targets. Their deposition in *Max* conditional KO ESCs before (WT) or after doxycycline treatment (*Max*-KO) was determined by ChIP-qPCR. The relative amount of

Figure 4 continued on next page

Figure 4 continued

ChIPed DNA is depicted as a percentage of input DNA. Error bars represent standard deviation determined from at least three independent experiments.

The following figure supplements are available for figure 4:

Figure supplement 1. The role of MAX/MGA in recruiting PCGF6-PRC1 to its target genes.

Figure supplement 2. Sequence recognition by MAX/MGA is critical for recruiting PCGF6-PRC1 to its target genes.

In contrast, genes bound by PCGF6 and RING1B, but not MAX (MAX-PCGF6+RING1B+), were barely up-regulated (*Figure 4B*). Intriguingly, we observed significant up-regulation of genes bound only by RING1B (MAX-PCGF6-RING1B+). We however also noted that the expression level of up-regulated genes in this category was considerably lower compared to MAX+PCGF6+RING1B+ genes (*Figure 4B*). We thus suggest MAX and MGA primarily contribute to the repression of MAX+PCGF6+RING1B+ genes. GO analysis revealed that genes bound by PCGF6, RING1B and MAX but not by MYC (PCGF6+RING1B+MAX+MYC-), were significantly enriched in germ cell- and meiosis-related functions (*Figure 4—figure supplement 1G*), further supporting our model that PCGF6-PRC1 functions as a dedicated repressor of genes associated with germ cells and meiosis.

We investigated whether binding of PCGF6-PRC1 to gene promoters required MAX and its cofactor MGA. Indeed, ChIP-qPCR in the *Max*-KD or *Mga*-KD ESCs revealed that PCGF6 binding to target loci depends on MAX and MGA (*Figure 4C*). Importantly, MAX and MGA bind these targets in mutually dependent manner (*Figure 4C*). This suggests that MAX and MGA may form a dimer to bind to their targets. We further used a previously reported *Max*-KO ES cell line to test MAX-dependent recruitment of PCGF6-PRC1 (*Hishida et al., 2011*). RING1B and RYBP, which form stoichiometric complexes with PCGF6 (*Figure 1B*), did not bind to PCGF6-PRC1 target loci in the *Max*-KO ESCs (*Figure 4D*). Likewise, local H2AK119ub1 and H3K27me3 levels were considerably decreased, and binding of L3MBTL2, another key regulator of ncPRC1, into PCGF6-PRC1 target genes was also depleted in the *Max*-KO ESCs (*Figure 4D*). In contrast, enrichment of RING1B, H2AK119ub1, H3K27me3 and RYBP at *Zic1*, a cPRC1 target, did not show considerable changes in the *Max*-KO ESCs. These results suggest that recruitment of both PCGF6 and L3MBTL2 requires MAX. We finally checked whether the decreased binding of PCGF6 is not due to secondary effects of transcriptional activation upon MAX depletion. We have selected genes bound by MAX and PCGF6, which were not up-regulated in *Max*-KO ESCs, and confirmed MAX-dependent binding of PCGF6 at these targets (*Figure 4—figure supplement 1H*). Collectively, these findings indicate that the MAX/MGA heterodimer recruits PCGF6-PRC1 to its targets.

Interactions between MAX and PCGF6 play a role in ESC maintenance

A role for MAX in maintaining ESC proliferation and self-renewal ability has been reported in a previous study (*Hishida et al., 2011*). We also observed that conditional deletion of *Max* (*Max*-KO) led to slower ESC proliferation and cell differentiation (*Figure 4—figure supplement 2A*, right). Rescuing the induced *Max*-KO cells with an exogenous WT MAX restored cell proliferation and blocked spontaneous differentiation, as expected. In contrast, mutant MAX proteins harboring defects in the basic region of the bHLH (basic helix-loop-helix) domain [hereafter referred to as MAX(VD) or MAX(Δb)] (*Figure 4—figure supplement 2A*, left), failed to do so (*Figure 5A*, right). These findings indicate that DNA motif recognition by MAX plays a role in maintaining ESCs, at least partly by recruiting the PCGF6-PRC1 complex.

Mechanistically, co-IP analyses showed that a FLAG-tagged MAX protein physically interacts with HA-PCGF6, RING1B and L3MBTL2. The mutant MAX proteins also retained the ability to associate and form stable complexes with HA-PCGF6, RING1B and L3MBTL2 (*Figure 4—figure supplement 2B*). As expected, ChIP-qPCR revealed that the FLAG-tagged MAX could restore binding of the HA-tagged PCGF6 into target loci in *Max*-KO ESCs (*Figure 4—figure supplement 2C,D*), whereas the mutant MAX proteins failed to bind targets and recruit HA-tagged PCGF6. These observations demonstrate a role of the MAX/MGA heterodimer in recruiting PCGF6-PRC1 by direct DNA motif
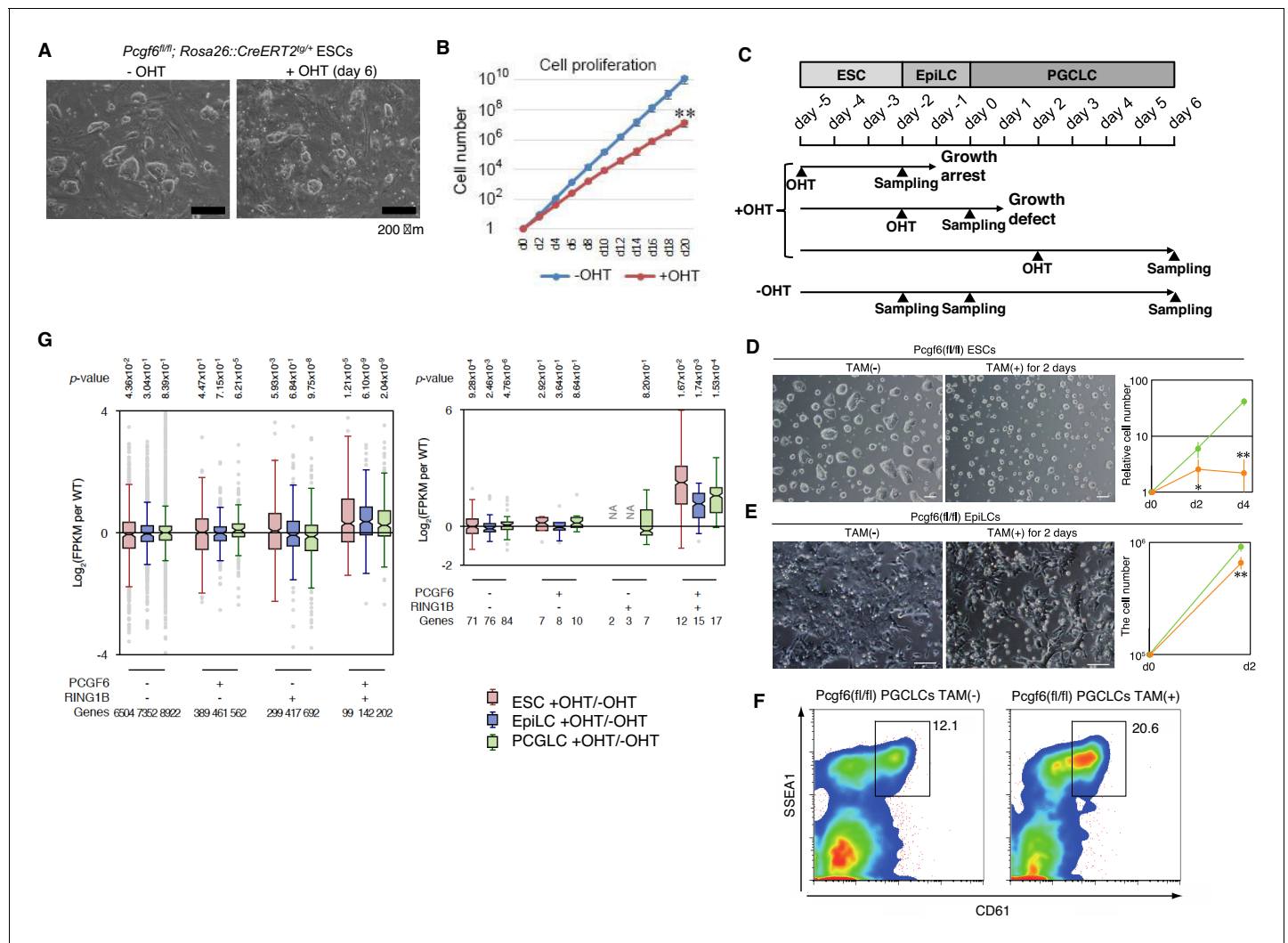
Figure 5. A role for PCGF6 in maintaining ESCs in an undifferentiated state. (**A**) Colony morphology of *Pcgf6*-KO ESCs in the presence of fetal bovine serum (FBS) and 3i. Phase-contrast views of OHT-untreated and –treated (day six) *Pcgf6^fl/fl^;Rosa26::CreERT2^tg/+^* ESCs are shown. Scale bars indicate 200 μm. (**B**) Decreased growth rate of *Pcgf6*-KO ESCs. Proliferation of OHT-untreated or -treated *Pcgf6^fl/fl^;Rosa26::CreERT2^tg/+^* ESCs in the presence of FBS and 3i is shown. (**C**) A schematic representation of the in vitro differentiation scheme for *Pcgf6^fl/fl^;Rosa26::CreERT2^tg/+^* ESCs towards EpiLCs and PGCLCs is shown. OHT was added to deplete *Pcgf6* at the indicated time points (closed arrowheads with 'OHT'). Cells used for RNA-seq analysis were collected at the time points indicated as 'Sampling'. (**D**) PCGF6 is indispensable to maintain proliferation of ESCs in serum-free condition. Phase contrast views of *Pcgf6*-KO [TAM(+); at two days after OHT treatment] and the control [TAM(−)] (left). Growth rates of OHT-treated (yellow) and – untreated (green) cells (right). (**E**) PCGF6 is indispensable to maintain proliferation of epiLCs. Phase contrast views of *Pcgf6*-KO [TAM(+); at 2 days after OHT treatment] and the control [TAM(−)] (left). Growth rates of OHT-treated (yellow) and –untreated (green) cells (right). (**F**) PCGF6 is dispensable for differentiation of post-epiLCs towards PGCLC. OHT-treatment considerably expanded the SSEA1+CD61+ fraction. (**G**) Gene expression changes upon induced deletion of *Pcgf6*. *Pcgf6^fl/fl^;Rosa26::CreERT2^tg/+^* ESCs (red), EpiLCs (blue), and PGCLCs (green) induced upon depletion of *Pcgf6* by OHT treatment for each subset of total genes (left) or meiosis-related genes (right) classified by the presence (+) or absence (−) of PCGF6- and RING1B-binding in ESCs. The average, deviation and distribution of the expression changes for the respective subsets of genes determined by RNA-seq analysis are shown. The box plots represent the median (horizontal line), interquartile range (box), range (whiskers), and outliers (circles). The number of genes included in each subset is shown at the bottom. *p*-values for average gene expression change in each subset upon Pcgf6 depletion were calculated by the Student's *t*-test and are indicated at the top.

DOI: 10.7554/eLife.21064.012

recognition for maintenance of ESCs. To further examine this model, we expressed MAX/TETR, and ectopically tethered this fusion protein to a pre-integrated TetO array in ESCs (*Figure 4—figure supplement 2E*). ChIP-qPCR analysis showed binding of the MAX/TETR fusion protein at the TetO array, which was accompanied by mild enrichment of HA-tagged PCGF6, H2AK119ub1 and

H3K27me3 (*Figure 4—figure supplement 2E*), but barely RING1B (data not shown). These data again support MAX-dependent recruitment of PCGF6-PRC1. The limited effect of MAX/TETR to recruit PCGF6 could be due to a potential dimerization of MAX with other partners than MGA in this experimental setup.

PCGF6-PRC1 is required for maintenance of ESCs and epiLCs in an undifferentiated state

Given that MAX and PCGF6 interact with each other, and that genetic ablation of *Max* causes reduced cell growth and germ cell-directed differentiation of ESCs (*Hishida et al., 2011*; *Suzuki et al., 2016*), we wondered whether knocking out *Pcgf6* would also lead to similar pheno-types. Indeed, the growth rate of *Pcgf6*-KO ESCs was significantly slower than the WT in the pres-ence of three inhibitors (3i: SU5402 for FGFR, PD184352 for ERK, and CHIR99021 for GSK3) and fetal bovine serum as suggested previously (*Zdzieblo et al., 2014*) (*Figure 5A,B*). The growth of *Pcgf6*-KO ESCs was further halted under serum-free condition (*Figure 5D*). Unlike the *Max*-KO, how-ever, *Pcgf6*-KO ESCs maintained an ESC-like morphology. These findings support the notion that PCGF6-PRC1 has a role in ESC proliferation, but may not be essential to maintain ES cell morphology.

Genetic ablation of *Pcgf6* leads to ectopic expression of meiosis-related and germ cell-related genes in ESCs. We therefore examined the impact of *Pcgf6* deletion in primordial germ cell-like cells (PGCLCs), which already express such germ cell-related genes. We induced the PGCLCs via epi-blast-like cells (epiLCs), using an in vitro culture system that we have previously developed (*Hayashi et al., 2011*). In particular, we cultured the ESCs in 2i-containing (MAPK inhibitor and GSK3 inhibitor) media without feeders for 3 days (from day −5 to day −2 in *Figure 5C*), and induced epiLC by adding Activin A and bFGF into the media for 2 days (from day −2 to day 0). We further differentiated the epiLCs into the germ cell-lineage by adding BMPs, SCF, LIF, and EGF for 6 days (from day 0 to day 6). Genetic ablation of *Pcgf6* at day −5 induced growth arrest and cell death of ESCs (*Figure 5D*); while ablation of *Pcgf6* at day −2 caused significant growth defects in epiLCs (*Figure 5E*), revealing a stage-specific role of PCGF6 for growth and survival of ESCs and epiLCs. In contrast, OHT-treatment at day +2 (post-epiLC stage) did not induce growth arrest or cell death and, surprisingly, even accelerated differentiation and proliferation (*Figure 5F*).

The disparate effects of *Pcgf6* ablation in ESCs, epiLCs and PGCLCs raised the question of whether the PCGF6 targets in these cell types are different. We therefore performed RNA-seq before and after knocking out *Pcgf6* in ESCs, epiLCs and PGCLCs (*Figure 5G*). We observed that the same group of genes (the PCGF6+RING1B+ category in ESCs) were de-repressed in ESCs, epiLCs and PGCLCs in the absence of *Pcgf6*. Furthermore, the extent of derepression of PCGF6 tar-get genes was also similar among these three cell types. We observed similar trends for meiosis- and germ cell-related genes (*Figure 6G*, right). Thus, these results indicate that the different pheno-typic impacts of *Pcgf6* ablation in ESCs, epiLCs and PGCLCs are not due to up-regulation of differ-ent sets of genes, but rather suggest that PCGF6-PRC1-mediated gene silencing is essential to maintain ESC and epiLC, but not PGCLC. PCGF6, therefore, plays a role in maintaining pluripotency, likely by suppressing germ cell potential in ESCs.

A role of PCGF6 for pre- and peri-implantation embryonic development

As PCGF6 plays a role in pluripotency and suppression of germ cell-specific genes in ESCs, we won-dered whether PCGF6 possessed similar functions in vivo during mouse embryogenesis. Consis-tently, *Pcgf6* is expressed in broad range of tissues and cell types and even abundantly in testis, ESCs and pre-implantation embryos (*Figure 6—figure supplement 1A,B*). To examine this possibil-ity, we used a constitutive mutant *Pcgf6* allele (*Figure 6A,B,C*). We found that *Pcgf6*-KO (−/−) mice were viable and fertile, but were not born at the normal Mendelian ratio (*Figure 6D*). Lethality among *Pcgf6*$^{-/-}$ homozygous embryos could be observed as early as the blastocyst stage [3.5 days post coitum (dpc)]. Furthermore, embryonic death in the *Pcgf6*$^{-/-}$ line could be continuously detected during post-implantation development. Consistently, we found that about one third of the surviving *Pcgf6*$^{-/-}$ embryos at 10.5 dpc exhibited growth retardation (*Figure 6E*).

To determine the impact of P*cgf6* ablation during the pre-implantation stage, we examined WT and *Pcgf6*$^{-/-}$ ICMs (inner cell mass). We mated homozygous or heterozygous males with
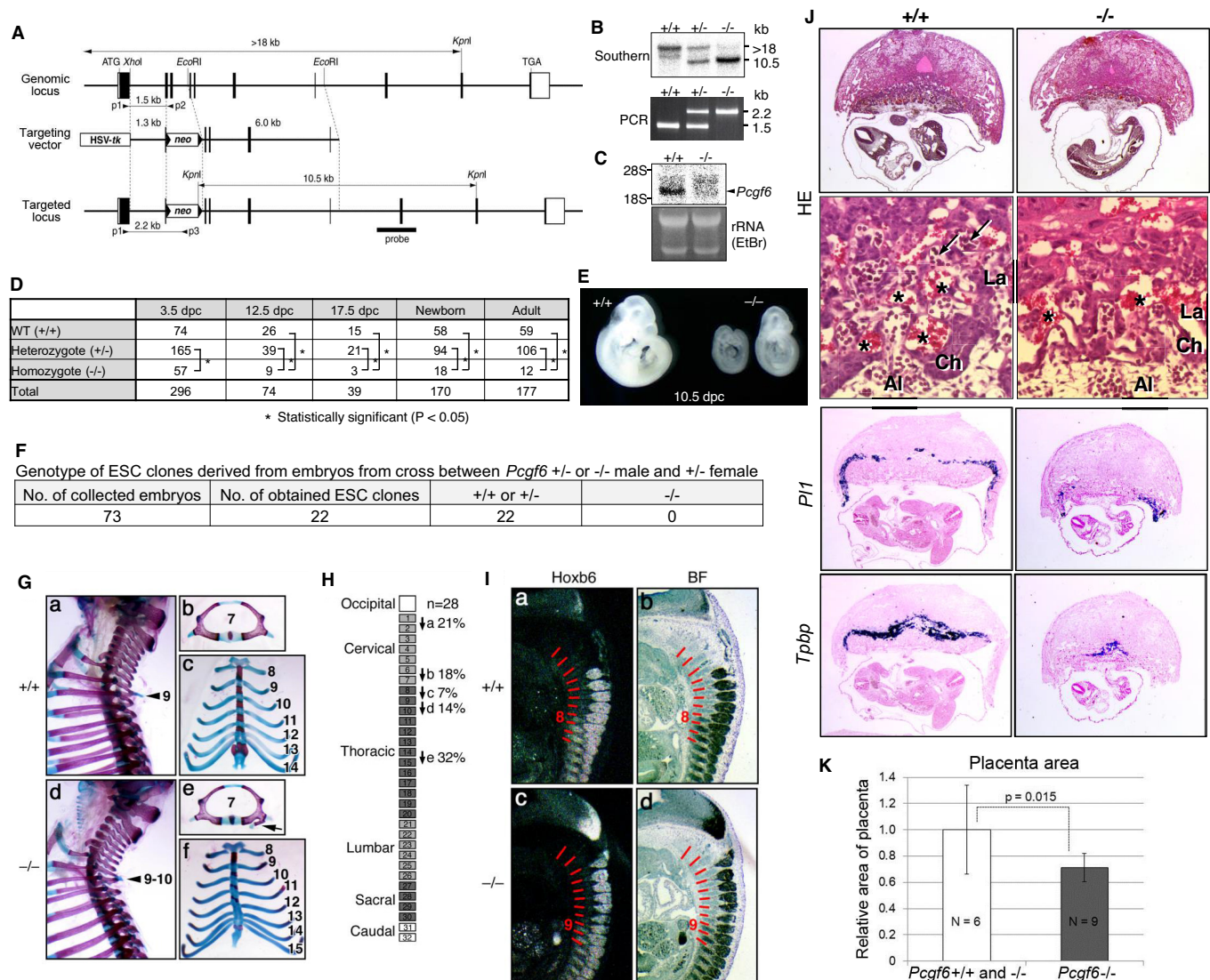
Figure 6. Pleiotropic effects of PCGF6 loss during development. (A) Schematic representation of the *Pcgf6* locus, the targeting vector, and the constitutive mutant allele. To disrupt *Pcgf6*, most of the exon 2 and the entire exon 3 which code for the RING finger domain were replaced with neo. The neo and HSV-tk cassettes were used for positive and negative selection, respectively. The positions of the restriction sites (*Xho*I, *EcoR*I and *Kpn*I), external probe and PCR primers, and sizes of diagnostic fragments are indicated. Coding regions and untranslated regions of *Pcgf6* are indicated by closed and open boxes, respectively. (B) Southern (top) and PCR (bottom) analyses for genotyping. For Southern blotting, genomic DNA was digested by *Kpn*I and probed with the 3' probe, as indicated in A. For PCR, a mixture of three primers (p1, p2 and p3 in A) was used. (C) Northern analysis of *Pcgf6* mRNA expression in wild type (+/+) and homozygous (−/−) adult kidney (top). Ethidium bromide (EtBr) staining of the same gel is shown below. (D) Genotype distribution of progeny of *Pcgf6* heterozygous intercrosses. *p-value<0.05 (χ^2 test), indicating a < 5% probability of conforming to the Mendelian law, which predicts a 1:2:1 ratio between +/+:+/−: −/−. (E) Delayed and/or abnormal development of *Pcgf6*-KO (−/−) embryos at 10.5 dpc. Wild-type (+/+) embryos are shown as controls. (F) Genotype distribution of ESC lines derived from embryos from intercrosses between *Pcgf6*+/+ or −/− male and +/− female is shown. Genotypes of 22 ESC lines were determined using genomic PCR. (G) Skeletal alterations in *Pcgf6*−/− newborn mice. (a, d) Lateral views of the cervical and thoracic regions revealed the prominent spinous process on the 9–10 in *Pcgf6*−/− (d, indicated by an arrow) but on the nine in the wild type (a, indicated by an arrow). (b, e) Overviews of the seventh vertebrae identified association of an anterior tubercle on seven in *Pcgf6*−/−, which appears on six in the wild type (e, indicated by an arrow). (c, f) Ventral views of rib cages identified an ectopic sternal rib in *Pcgf6*−/− (f, labeled 15). (H) Schematic representation summarizing the axial alterations in *Pcgf6*−/− newborn mice. Each arrow represents the following morphological changes in the vertebrae; (a) 1←2: association of the anterior arch of the atlas with the atlas; (b) 6←7: the anterior tubercle(s) on 7, which are normally on 6; (c) 8←9: fusion of rib(s) on 9 to 8; (d) 9←10: the prominent spinous process on 10, which is normally on 9; (e) 14←15: fusion of ribs on 15 to the sternum. (I) Changes in *Hoxb6* expression in *Pcgf6*-KO mice. *Hoxb6* expression in 11.5-dpc wild-type (a) and *Pcgf6*−/− (c) embryos. Segment boundaries are indicated by red lines and segment numbers of anterior expression domains of *Hoxb6* are shown. Bright field views are shown in (b, d).
Figure 6 continued on next page

Figure 6 continued

(J) HE sections of 11.5 dpc wild type (+/+) and *Pcgf6*-deficient (−/−) placentae. Al: allantois, Ch: chorion, La: labyrinth layer, asterisks: enucleated erythrocytes from the mother, arrows: fetus-derived nucleated erythrocytes. Note that fetus-derived nucleated erythrocytes are observed in well-developed labyrinth layer in Wild-type mice but not in *Pcgf6*-KO mice. Expression of trophoblast lineage-restricted markers was analyzed by RNA in situ hybridization. *Pl1* identifies trophoblast giant cells. *Tpbp* identifies spongiotrophoblasts. (K) Quantification of placental area from 10.5 dpc HE sections of wild type (+/+), *Pcgf6* heterozygote (+/−) and *Pcgf6*-deficient (−/−) embryos.

DOI: 10.7554/eLife.21064.013

The following source data and figure supplement are available for figure 6:

Source data 1. HE sections of placentae of wild type (+/+) and *Pcgf6*-KO (−/−) embryos used for analysis shown in *Figure 6K*.

DOI: 10.7554/eLife.21064.014

Figure supplement 1. Skeletal alterations in *Pcgf6*KI/KI and *Pcgf6*/*Pcgf2* dKO newborn mice.

DOI: 10.7554/eLife.21064.015

heterozygous females, and cultured the blastocysts in ESC inducing conditions until ESC-like colonies appeared. From 73 blastocysts collected, we could establish 22 ESC-like lines. Remarkably, among these 22 lines, not a single one was homozygous $Pcgf6^{-/-}$ (*Figure 6F*). As ESCs could not be established from $Pcgf6^{-/-}$ lines, we surmised that *Pcgf6*-deficient ICMs are functionally different from their WT counterparts. Collectively, these results reveal a role for PCGF6 in both pre- and peri-implantation development.

A role of cPRC1 in the regulation of anterior-posterior (A-P) specification of the axial skeleton is well characterized (*Akasaka et al., 1996*; *Isono et al., 2005*; *Suzuki et al., 2002*). Given the essential role of PCGF6 in the PCGF6-PRC1 complex, we therefore asked whether $Pcgf6^{-/-}$ mice also exhibited defects in A-P specification. Intriguingly, we observed morphological alterations of the vertebrae that represent anterior transformations of the axis in these mice (*Figure 6G,H*). To further confirm the role of PCGF6 for A-P patterning, we then tested the impacts of PCGF6 over-expression and, indeed, observed posterior transformations of the axis (*Figure 6—figure supplement 1C,D*). We further found that skeletal alterations in $Pcgf6^{-/-}$ mice were accompanied by aberrant repression of *Hoxb6* at the eighth pre-vertebra (*Figure 6I*). These suggest that PCGF6 regulates A-P patterning presumably through regulation of *Hox* genes. We then examined whether skeletal defects in $Pcgf6^{-/-}$ involved potential interactions of PCGF6-PRC1 with cPRC1 at *Hox* genes (*Figure 1D*, *Figure 6—figure supplement 1E,F*). We indeed observed that anterior transformations in $Pcgf6^{-/-}$ mice were suppressed by the *Pcgf2* mutation, suggesting mutually counteracting properties of PCGF6 and PCGF2.

In addition to the skeletal phenotypes, we also noted significant reduction of placental size, manifested by hypoplasticity and malformation of the labyrinth layer, in the $Pcgf6^{-/-}$ mice (*Figure 6J,K*). In particular, the number of spongiotrophoblast cells and trophoblast giant cells (TGCs), identified by expression of *Pl1* (placental lactogen-I, also known as *Prl3d1*) and *Tpbpa* (trophoblast specific protein alpha), respectively, was dramatically decreased. These findings demonstrate further roles of PCGF6 in peri-implantation development, including A-P specification and regulation of placental development.

Discussion

PCGF6 constitutes a non-canonical PRC1 in association with RING1B

In the present study, we show that PCGF6 constitutes a non-canonical PRC1 complex, PCGF6-PRC1, that includes the core PRC1 component RING1B. PCGF6 physically interacts with RING1B, and plays a role in recruitment of RING1B to target genes, followed by deposition of H2AK119ub1 and transcriptional silencing. We have previously reported that the PCGF1-associated ncPRC1 (PCGF1-PRC1) recruits PRC2 to target genes (*Blackledge et al., 2014*). Here, we demonstrate that PCGF6-PRC1 also has a similar role, as ectopic targeting of a PCGF6 protein fused to the Tet repressor (PCGF6/TETR) to a pre-integrated TetO array leads to sequential binding of RING1B, H2AK119ub1 deposition and PRC2 recruitment in cis (*Figure 3A*).

PCGF6-PRC1 target genes are different from those of PCGF1-PRC1 and canonical PRC1

Like PCGF1-PRC1, PCGF6-PRC1-mediated targeting of PRC2 also takes place in endogenous genomic loci, in particular at promoters of a certain group of genes that are enriched for germ cell-specific and meiosis-specific functions (*Figure 2—figure supplement 1D*). However, these genes are distinct from those bound by PCGF1-PRC1 and canonical PRC1, which mainly include developmental genes (*Figure 1D–G*). Such developmental genes are evolutionarily conserved targets of PcG complexes, and are characterized by long CpG island (CGI) promoters that are usually not marked by DNA methylation (*Sharif et al., 2013*). The CXXC domain containing protein KDM2B recruits PCGF1-PRC1 into these loci by binding unmethylated CGIs (*Blackledge et al., 2014*). In contrast, PCGF6-PRC1 target loci tend to have slightly shorter and more DNA methylated CGIs (*Figure 1—figure supplement 1E*), where KDM2B seems to play distinct roles from PCGF1-PRC1. Indeed, H3K27me3 depositions at PCGF6-PRC1 targets are less active to recruit cPRC1 though underlying mechanisms await elucidative (*Figure 1G*, *Figure 4—figure supplement 1C*). Thus, our findings reveal that there are at least two major modes of gene silencing by PRC1; the first involves PCGF1-PRC1 and cPRC1 and silences developmental genes, while the second involves PCGF6-PRC1 and silences germ cell-specific and meiosis-specific genes (see the model in *Figure 7A*).

The MAX-MGA heterodimer plays a role in recruiting PCGF6-PRC1 to target loci

By surveying DNA sequences of the PCGF6-PRC1 target genes, we find that they are enriched for the binding motif of the bHLHZ (basic helix-loop-helix, also containing a leucine zipper) transcription factor MAX (*Figure 4—figure supplement 1D*). Previous reports showed that MAX forms a heterodimer with MGA, another E-box binding protein (*Hurlin et al., 1999*). Interestingly, we identified MGA as a PCGF6 interacting factor by mass-spectrometry (*Figure 1A,B*), indicating that MAX and MGA may be directly involved in recruitment of PCGF6-PRC1 into target genes. Consistent with this hypothesis, both MAX and MGA were enriched at PCGF6-PRC1 target genes (*Figures 1G*, *4A and C*); and depletion of MAX or MGA by siRNA caused a reduction of PCGF6 binding to these loci (*Figure 4C*).

The MAX/MGA heterodimer independently recruits PCGF6 and L3MBTL2

Previous studies show that the MAX/MGA heterodimer also plays a role in recruitment of the ncPRC1 component L3MBTL2 (*Suzuki et al., 2016*). Our results demonstrate that MAX/MGA independently associates with PCGF6 or L3MBTL2, as ablation of PCGF6 does not affect binding of L3MBTL2 (*Figures 3E* and *4D*). These findings indicate that MAX/MGA represses target genes through multiple mechanisms that may function in parallel. Consistent with this notion, ESCs deficient for MAX or MGA show a more drastic phenotype than the *Pcgf6*-KO ESCs (*Figure 6A,B,D*) (*Hishida et al., 2011*; *Washkowitz et al., 2015*).

Interestingly, L3MBTL2 associates with the H3K9me2 methyltransferases G9A and GLP (*Ogawa et al., 2002*; *Qin et al., 2012*). As G9A and GLP silence germ cell-specific genes in ESCs (*Maeda et al., 2013*), we speculate that L3MBTL2 contributes to transcriptional repression of these genes in association with G9A and GLP; while the same group of genes are silenced by a parallel pathway involving PCGF6 and RING1B (see the model in *Figure 7B*). The existence of several repressive epigenetic mechanisms that target germ cell-specific genes suggests the importance of preventing aberrant activation of such genes during pre- and peri-implantation embryonic development.

Pleiotropic roles of PCGF6 in pre- and post-implantation embryonic development

Consistent with this idea, genetic ablation of *Pcgf6* leads to growth defects in both ESCs and epiLCs (*Figure 5C, D and E*), stem cells lines that approximate pre- and post-implantation embryonic developmental stages, respectively. Furthermore, constitutive deletion of *Pcgf6* causes impaired development of the placenta, in particular of the spongiotrophoblast layer and trophoblast giant cells (TGCs) (*Figure 6J and K*). Such aberrant phenotypes are also observed in the embryo proper,
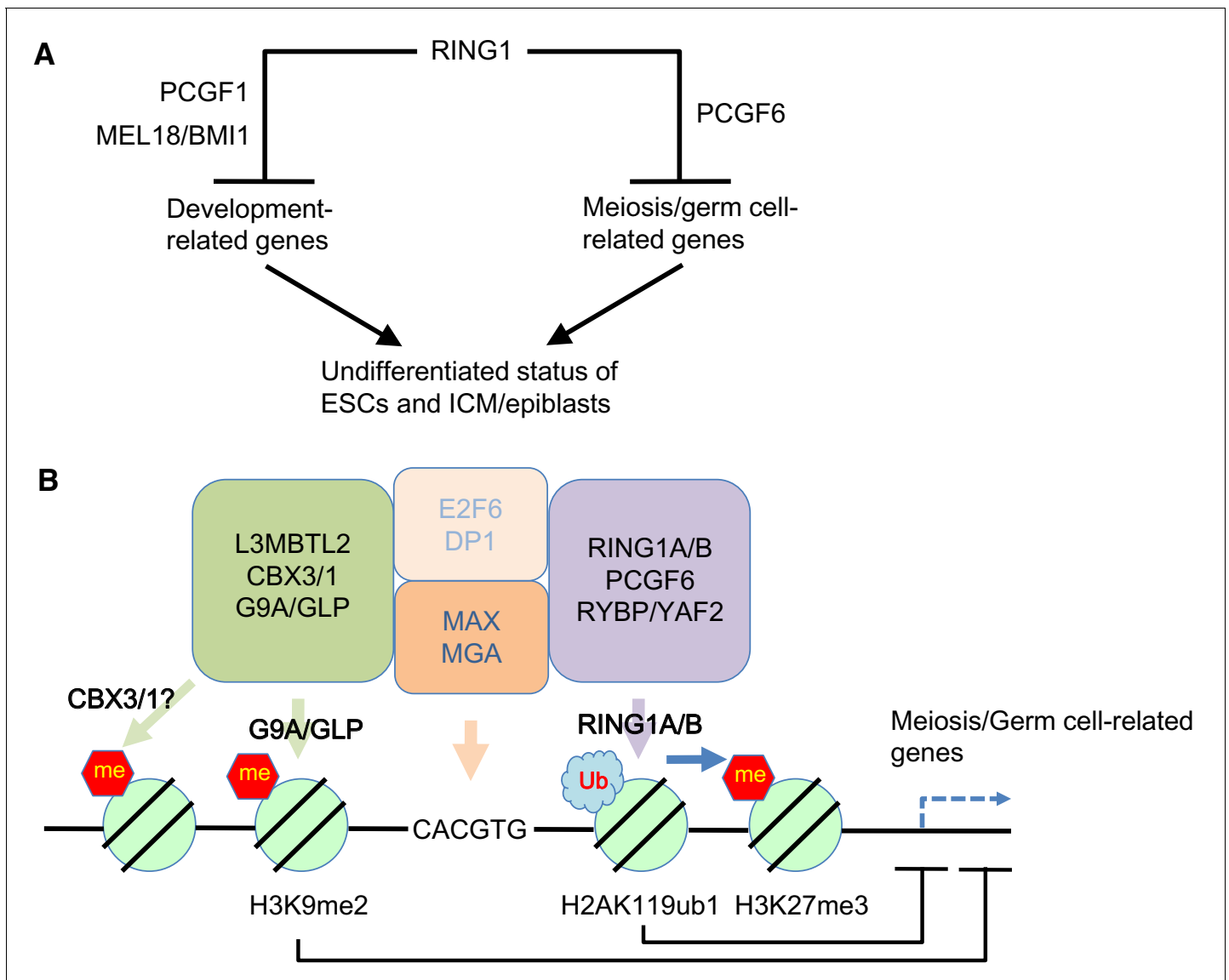
Figure 7. Our model for the role of PCGF6-PRC1. (**A**) Schematic representation for two major modes of gene silencing by PRC1. The first involves PCGF1-PRC1 (PCGF6) and cPRC1 (MEL18/BMI1), which silences developmental genes, and the second involves PCGF6-PRC1 (PCGF6), which silences germ cell-related and meiosis-related genes. (**B**) Schematic representation of PCGF6-PRC1-mediated regulation of germ cell-related and meiosis-related genes in ESCs and pre-/peri-implantation embryos.

DOI: 10.7554/eLife.21064.016

including defects in anterior-posterior (A-P) axis specification and ectopic expression of developmental genes such as *Hoxb6* (*Figure 6G, H and I*).

Concluding remarks

Taken together, we demonstrate a previously unappreciated function of the non-canonical PRC1 component PCGF6 for repression of germ cell-specific genes in ESCs. We further show that transcriptional silencing of such genes requires the function of RING1B and H2AK119ub1, but not PRC2 and H3K27me3. PCGF6-bound genes are enriched for short CGIs, frequently marked by methylated DNA, and are not bound by PCGF1-PRC1. Indeed, developmental genes, which are the main targets of PCGF1-PRC1, are not bound by PCGF6-PRC1, revealing distinct functional roles of these two ncPRC1 complexes. Consistent with this model, PCGF6-PRC1 is recruited to target sites by the MAX/MGA heterodimer, while PCGF1-PRC1 is recruited by the unmethylated CpG binding protein

KDM2B (*Farcas et al., 2012*). Our work thus shows a link between sequence specific DNA binding by the MAX/MGA heterodimer with PRC1-mediated transcriptional silencing of germ cell-specific genes by PCGF6, for regulation of pre- and post-implantation embryonic development.

Materials and methods

Construction of expression vectors

The full length mouse *Pcgf6*, mouse *Pcgf2*, mouse *Ring1B*, and mouse *Max* were PCR-amplified and inserted into a pCAG-IRES-Puro, a pCAG-IRES-BlaS, or a pCAG-IRES-HisD eukaryotic expression vector (Kindly gifts from Dr. Hitoshi Niwa in Kumamoto University) that was modified to express an N-terminal Flag and 2XStrep2 tag, an N-terminal 3xFlag tag, or an N-terminal HA tag. All PCR generated constructs were verified by sequencing. Mutations of the PCGF6 RING-finger domain (H155Y) and the MAX basic domain (L31V and E32D) were introduced into the wild type *Pcgf6* and *Max* constructs, respectively, using the PrimeSTAR Mutagenesis Basal Kit (Takara, Japan).

Antibodies

The RING1B mouse monoclonal antibody has been described previously (*Atsuta et al., 2001*). A rabbit polyclonal antibody against the Flag-2XStrepII sequence was generated as described previously (*Farcas et al., 2012*). Commercially available antibodies were used to detect FLAG-tag (Sigma-Aldrich, St. Louis, MO,, F1804, RRID:AB_262044), HA-tag (Santa Cruz, Dallas, TX, sc-805), RYBP (Millipore, Billerica, MA, AB3637, RRID:AB_631618), L3MBTL2 (Active Motif, Carlsbad, CA, 39569, RRID:AB_2615062), MAX (Santa Cruz, sc-197X, RRID:AB_2281783), MGA (Bethyl, Montgomery, TX, A302-864A, RRID:AB_2615457), PCGF1 (Santa Cruz, E-8: sc-515371), PCGF2 (Santa Cruz, H-115: sc-10744, RRID:AB_2267885), PCGF6 (ORIGENE, Rockville, MD, TA324658), EZH2 (Cell Signaling, Danvers, MA, 4905, RRID:AB_2278249), SUZ12 (Cell Signaling, 3737, RRID:AB_2196850), SET1 (Bethyl, A300-289A, RRID:AB_263413), trimethylated Histone H3 lysine 27 (H3K27me3) (Millipore, 07–449, RRID:AB_310624), dimethylated histone H3 lysine 9 (H3K9me2) (MBL, Japan, MABI0317), H3K27ac (Cell Signaling, 8173, RRID:AB_2616015), monoubiquitinated histone H2A lysine 119 (H2AK119ub1) (Millipore, 05–678, RRID:AB_309899; Cell Signaling, 8240, RRID:AB_10891618), mouse IgM (Millipore, 12–488, RRID:AB_390193), histone H3 (Millipore, 07–690, RRID:AB_417398), and LAMIN B (Santa Cruz, sc-6216, RRID:AB_648156).

Mice and ESC lines

Targeting vectors to knock out *Pcgf6* (*Figure 1—figure supplement 1A*) were introduced into R1 or M1 ESCs. Chimeras were generated by the morula aggregation method. Conditional mutants were mated with *Rosa26::CreERT2* (ERT2-Cre) transgenic mice purchased from Artemis Pharmaceuticals (Germany)(*Seibler et al., 2003*). ESCs were generated from respective blastocyst embryos as described previously (*Endoh et al., 2008*). Male ESCs were used in this study. 4-hydroxy tamoxifen (OHT) at a final concentration of 800 nM was added to culture medium to induce Cre recombinase activity and delete *Pcgf6*. *Cbx1/Cbx3* conditional KO ESCs (*Figure 3—figure supplement 1E*) were generated as described above. *Ring1A*$^{-/-}$; *Ring1B*$^{fl/fl}$; *Rosa26::CreERT2*$^{tg/+}$ ESCs (*Endoh et al., 2008*), *Pcgf2/4*-dKO ESCs (*Elderkin et al., 2007*), *Kdm2b*-KO ESCs (*Blackledge et al., 2014*), and *Max* conditional KO ESCs (*Hishida et al., 2011*) were described previously. For generation of ESC lines stably expressing exogenous cDNAs, 5 μg of the expression constructs were transfected into ESCs using electroporation and stable transfectants were selected using 1.0 μg/mL puromycin as described previously (*Endoh et al., 2012*). Prior to their use in ChIP experiments, ESCs were cultured for two passages under feeder-free conditions. All ESC lines used in this study were tested negative for mycoplasma before use. All animal experiments were carried out according to the in-house guidelines for the care and use of laboratory animals of the RIKEN Center for Integrative Medical Sciences, Yokohama, Japan [Approval number: Kei-27-001(7)]. All gene recombination experiments were carried out according to the in-house guidelines for the genetic recombination experiments of the RIKEN Center for Integrative Medical Sciences (Approval number: Sho-Y2015-018-10).

Max/Mga knockdown

The siRNAs for *Max* and *Mga* were selected according to a previous report (*Maeda et al., 2013*) and purchased from Qiagen (Germany). ES cells were transfected with individual siRNAs using Lipofectamine RNAiMAX reagent (Thermo Fisher Scientific, Waltham, MA) according to the manufacturer's instructions.

PCGF6 protein complex purification

To purify PCGF6 and associated proteins, a mouse ESC line stably expressing Flag-2XStrepII-tagged PCGF6 was generated. Nuclear extracts were isolated from this cell line, the PCGF6 complex was affinity purified, and the co-purified proteins were subject to mass spectrometry as described previously (*Farcas et al., 2012*).

Immunoprecipitation (IP) analysis

Cells expressing each of the tagged constructs were suspended in IP buffer [10 mM Tris-HCl (pH8.0), 1 mM EDTA, 140 mM NaCl, 0.4% NP-40, and 0.5 mM PMSF] and sonicated for several seconds. After centrifugation, the supernatant was collected, and then incubated with anti-FLAG antibody (Sigma-Aldrich; M2) for 120 min at 4°C. The immune complexes were captured by incubation with protein A/G magnetic Dynabeads (Invitrogen, Carlsbad, CA) for 60 min at 4°C. The bead-bound proteins were washed with IP buffer, eluted in SDS sample buffer under reducing condition, separated on SDS-PAGE gels, and subjected to western blot analysis. Tandem mass spectrometry (LC–MS/MS) was performed as described previously (*Farcas et al., 2012*). Materials eluted with desthiobiotin were collected and precipitated using chloroform/methanol and re-suspended materials were subjected to in-solution tryptic digestion followed by nano-liquid chromatography-tandem mass spectrometry (nLC-MS/MS) analysis using a nano-Acquity UPLC (Waters, Milford, MA) coupled to an Orbitrap Velos/Elite mass spectrometer (Thermo Fisher Scientific). MS/MS spectra were searched against the UniProt SwissProt Mouse database (16,683 sequences) in Mascot v2.3.01. Protein assignment was based on at least two identified peptides. Mascot scores and peptide coverage are indicated for each protein (*Figure 1B*).

Gene expression analysis

Total RNA was extracted using the RNeasy Mini kit (Qiagen) with the RNase-Free DNase Set (Qiagen) according to the manufacturer's instructions. Genomic DNA-free RNA samples were further purified using the RNeasy kit RNA cleanup protocol. For subsequent RT-PCR analysis, cDNA was synthesized with the SuperScript III First-Strand Synthesis System (Thermo Fisher Scientific). Quantitative real-time PCR was performed by using the Brilliant III SYBR Green QPCR Master Mix (AgilentLaboratories, Santa Clara, CA), using *Gapdh* as housekeeping gene. For RNA-seq studies, RNA integrity was assessed on a BioAnalyzer; all samples had a RNA Integrity Number (RIN) $\geq$9.5 (Agilent Laboratories). Sequencing libraries were generated according to Illumina's instructions and sequenced on the Illumina HiSeq platform as described previously (*Sharif et al., 2016*).

ChIP-qPCR analysis

Chromatin immunoprecipitation (ChIP) was performed as previously described (*Endoh et al., 2012*), with minor modifications. Sonication was performed using a Covaris focused-ultrasonicator (Covaris, Woburn, MA) to produce fragments of approximately 0.5–1 kb. Immunoprecipitation was performed overnight at 4°C with approximately 2–5 µg of antibody and chromatin corresponding to 5×10^6 cells. Antibody bound proteins were isolated on protein A/G magnetic Dynabeads (Invitrogen), washed extensively, eluted, cross-links were reversed, and then the samples were sequentially treated with RNase and proteinase K before being purified using phenol-chloroform extraction. Real-time qPCR was performed using the Brilliant III SYBR Green QPCR Master Mix (Agilent). For H2AK119u1-ChIP using E6C5 (Millipore #05–678), pre-cleared chromatin from $2–3 \times 10^6$ cells was incubated with 40 ul of E6C5 antibody (Millipore #05–678) (overnight, 4°C), and 30 ul of original Protein A dynabead slurry (Invitrogen) was incubated with 3 ug (=3 ul) of rabbit anti-mouse IgM antibody (Millipore #12–488) (overnight, 4°C). Next day, the chromatin-1st antibody complexes were immunoprecipitated with second antibody - preconjugated protein A dynabeads, and subjected to the conventional ChIP experiments as described above.

ChIP-seq analysis

ChIP-seq libraries were prepared according to Illumina's instructions accompanying the NEBNext ChIP-Seq Library set (NEB, Ipswich, MA, #E6200) and quantified by the KAPA Library Quantification Kit (KAPA, Wilmington, MA), and their sizes were confirmed by Bioanalyzer (Agilent). Libraries were sequenced using Illumina (San Diego, CA) HiSeq system as described previously (*Isono et al., 2013*). The peak calling of ChIP-seq data was performed with MACS2 program. Published ChIP-seq data for CBX7, MAX, and MYC were obtained from NCBI GEO (accession numbers GSM1041373, GSM1171650, GSM1171648, respectively). Published ChIP-seq data for RING1B in wild-type and *Kdm2b*-KO ESCs were also obtained from NCBI GEO (Series GSE55698).

Motif analysis

Binding motifs of PCGF6, RING1B, CBX7, MAX and MYC were detected using a computer program DREME included in the motif analysis suite MEME version 4.9.1 (http://meme-suite.org/). Briefly, 500 bp sequences around the centers of ChIP-seq peaks were collected from the mouse genome and enriched motifs were calculated using the above program with default parameters. Graphical representation of the sequence logo, where letter height was determined by Shannon entropy, was generated using our in-house program.

Generation of the de novo targeting system

E14 mouse ES cells containing a single copy of TetO BAC were generated as described previously (*Blackledge et al., 2014*). Mouse Pcgf6 or Max coding sequence was inserted into pCAGFS2TetR to generate a mammalian expression plasmid for N-terminal FLAG STREPx2 (FS2) tagged PCGF6 or MAX, respectively. Either of these plasmids was transfected into the TetO-containing ESCs and stable clones expressing TetR-PCGF6 or TetR-MAX fusion protein were detected in ChIP experiments using an FS2-specific antibody as previously described (*Blackledge et al., 2014*).

Induction of EpiLCs and PGCLCs

PGCLCs were induced from *Pcgf6*$^{fl/fl}$ ES cells through an epiblast-like state as described previously (*Hayashi et al., 2011*; *Hayashi and Saitou, 2013*). Briefly, the ESCs were first cultured in 2i (MEK inhibitor PD0325901 and GSK-3 inhibitor CHIR99021)-containing media without a feeder layer for 3 days (from day −5 to day −2 in *Figure 5C*) and then subjected to EpiLC induction culture by using media containing Activin A and bFGF for 2 days (from day −2 to day 0). Induced EpiLCs were further differentiated into the germ cell-linage by culturing them with BMPs, SCF, LIF, EGF and others for 6 days (from day 0 to day 6). The impact of PCGF6 loss at different stages was tested by adding OHT at day −5, day −2, or day +2 (*Figure 5C*).

Histological and skeletal analysis of *Pcgf6*-KO mice

Skeletal preparations were made from newborn mice and cleared skeletons were analyzed under a stereomicroscope as described previously (*Akasaka et al., 1996*). RNA in situ hybridization was performed as described previously (*Akasaka et al., 1996*).

Data access

Sequencing and microarray data can be accessed via the geo accession GSE84480 (http://www.ncbi.nlm.nih.gov/geo/query/acc.cgi?token=wdmlougulbwbtgr&acc=GSE84480) and GSE87484 (https://www.ncbi.nlm.nih.gov/geo/query/acc.cgi?token=sbebmckgtlyhlat&acc=GSE87484).

Additional information

Funding

Funder	Grant reference number	Author
Ministry of Education, Culture, Sports, Science, and Technology	Grant-in-Aid for Young Scientist (B) (#25871129)	Mitsuhiro Endoh
Ministry of Education, Culture, Sports, Science, and Technology	Grant-in-Aid for Scientific Research (C) (#16K07372)	Mitsuhiro Endoh
Ministry of Education, Culture, Sports, Science and Technology	Grant-in-Aid for Scientific Research on Innovative Areas (#26112516)	Mitsuhiro Endoh
Ministry of Education, Culture, Sports, Science and Technology	Grant-in-Aid for Scientific Research on Innovative Areas (#24116711)	Mitsuhiro Endoh
RIKEN		Haruhiko Koseki
Ministry of Education, Culture, Sports, Science, and Technology		Haruhiko Koseki
Japan Science and Technology Agency	Strategic Basic Research Programs	Haruhiko Koseki

The funders had no role in study design, data collection and interpretation, or the decision to submit the work for publication.

Author contributions

ME, Conceptualization, Resources, Data curation, Funding acquisition, Validation, Investigation, Writing—original draft, Writing—review and editing; TAE, Data curation, Validation, Investigation, Visualization, Writing—original draft, Writing—review and editing; JShi, Resources, Data curation, Investigation, Writing—review and editing; KH, Data curation, Investigation, Writing—original draft; AF, K-WM, TE, TI, BMK, Resources, Investigation; SI, NO, Investigation; JSha, Data curation, Investigation, Writing—original draft, Writing—review and editing; MN, AO, Resources; OM, Data curation, Investigation; TS, Supervision, Writing—review and editing; OO, Supervision; RK, Resources, Supervision, Investigation; HK, Conceptualization, Resources, Data curation, Supervision, Funding acquisition, Investigation, Writing—original draft, Writing—review and editing

Author ORCIDs

Mitsuhiro Endoh, http://orcid.org/0000-0003-0715-1701
Akihiko Okuda, http://orcid.org/0000-0002-5298-5564
Robert Klose, http://orcid.org/0000-0002-8726-7888
Haruhiko Koseki, http://orcid.org/0000-0001-8424-5854

Ethics

Animal experimentation: All animal experiments were carried out according to the in-house guidelines for the care and use of laboratory animals of the RIKEN Center for Integrative Medical Sciences, Yokohama, Japan [Approval number: Kei-27-001(7)].

Additional files

Supplementary files

• Supplementary file 1. The sequences of primers used in quantitative ChIP-PCR and RT-PCR.
DOI: 10.7554/eLife.21064.017

Major datasets

The following datasets were generated:

Author(s)	Year	Dataset title	Dataset URL	Database, license, and accessibility information
Endoh M, Koseki H, Sharif J, Endo TA	2017	PCGF6-PRC1 suppresses premature differentiation of embryonic stem cells by silencing germ cell-related genes [RNA-Seq]	https://www.ncbi.nlm.nih.gov/geo/query/acc.cgi?acc=GSE84480	Publicly available at the NCBI Gene Expression Omnibus (accession no: GSE84480)
Endoh M, Koseki H, Sharif J, Endo TA	2017	PCGF6-PRC1 suppresses premature differentiation of embryonic stem cells by silencing germ cell-related genes [ChIP-Seq]	https://www.ncbi.nlm.nih.gov/geo/query/acc.cgi?acc=GSE87484	Publicly available at the NCBI Gene Expression Omnibus (accession no: GSE87484)

The following previously published datasets were used:

Author(s)	Year	Dataset title	Dataset URL	Database, license, and accessibility information
Croce LD	2013	Cbx7_ChIPSeq	https://www.ncbi.nlm.nih.gov/geo/query/acc.cgi?acc=GSM1041373	Publicly available at the NCBI Gene Expression Omnibus (accession no: GSM1041373)
Neri F	2014	Max_ChIPSeq	http://www.ncbi.nlm.nih.gov/geo/query/acc.cgi?acc=GSM1171650	Publicly available at the NCBI Gene Expression Omnibus (accession no: GSM1171650)
Neri F	2014	BioMyc_ChIPSeq	https://www.ncbi.nlm.nih.gov/geo/query/acc.cgi?acc=GSM1171648	Publicly available at the NCBI Gene Expression Omnibus (accession no: GSM1171648)
Blackledge NP	2014	KDM2Bfl/fl_RING1B_ChIPSeq	https://www.ncbi.nlm.nih.gov/geo/query/acc.cgi?acc=GSE55698	Publicly available at the NCBI Gene Expression Omnibus (accession no: GSE55698)

References

Akasaka T, Kanno M, Balling R, Mieza MA, Taniguchi M, Koseki H. 1996. A role for mel-18, a polycomb group-related vertebrate gene, during theanteroposterior specification of the axial skeleton. *Development* **122**:1513–1522. PMID: 8625838

Akasaka T, Takahashi N, Suzuki M, Koseki H, Bodmer R, Koga H. 2002. MBLR, a new RING finger protein resembling mammalian polycomb gene products, is regulated by cell cycle-dependent phosphorylation. *Genes to Cells* **7**:835–850. doi: 10.1046/j.1365-2443.2002.00565.x, PMID: 12167161

Atsuta T, Fujimura S, Moriya H, Vidal M, Akasaka T, Koseki H. 2001. Production of monoclonal antibodies against mammalian Ring1B proteins. *Hybridoma* **20**:43–46. doi: 10.1089/027245701300060427, PMID: 11289226

Ben-Saadon R, Zaaroor D, Ziv T, Ciechanover A. 2006. The polycomb protein Ring1B generates self atypical mixed ubiquitin chains required for its in vitro histone H2A ligase activity. *Molecular Cell* **24**:701–711. doi: 10.1016/j.molcel.2006.10.022, PMID: 17157253

Bernstein E, Duncan EM, Masui O, Gil J, Heard E, Allis CD. 2006. Mouse polycomb proteins bind differentially to methylated histone H3 and RNA and are enriched in facultative heterochromatin. *Molecular and Cellular Biology* **26**:2560–2569. doi: 10.1128/MCB.26.7.2560-2569.2006, PMID: 16537902

Blackledge NP, Farcas AM, Kondo T, King HW, McGouran JF, Hanssen LL, Ito S, Cooper S, Kondo K, Koseki Y, Ishikura T, Long HK, Sheahan TW, Brockdorff N, Kessler BM, Koseki H, Klose RJ. 2014. Variant PRC1 complex-dependent H2A ubiquitylation drives PRC2 recruitment and polycomb domain formation. *Cell* **157**:1445–1459. doi: 10.1016/j.cell.2014.05.004, PMID: 24856970

Blackledge NP, Rose NR, Klose RJ. 2015. Targeting polycomb systems to regulate gene expression: modifications to a complex story. *Nature Reviews Molecular Cell Biology* **16**:643–649. doi: 10.1038/nrm4067, PMID: 26420232

Blackwood EM, Eisenman RN. 1991. Max: a helix-loop-helix zipper protein that forms a sequence-specific DNA-binding complex with myc. *Science* **251**:1211–1217. doi: 10.1126/science.2006410, PMID: 2006410

Buchwald G, van der Stoop P, Weichenrieder O, Perrakis A, van Lohuizen M, Sixma TK. 2006. Structure and E3-ligase activity of the Ring-Ring complex of polycomb proteins Bmi1 and Ring1b. *The EMBO Journal* **25**:2465–2474. doi: 10.1038/sj.emboj.7601144, PMID: 16710298

Cao R, Wang L, Wang H, Xia L, Erdjument-Bromage H, Tempst P, Jones RS, Zhang Y. 2002. Role of histone H3 lysine 27 methylation in Polycomb-group silencing. *Science* **298**:1039–1043. doi: 10.1126/science.1076997, PMID: 12351676

Cooper S, Dienstbier M, Hassan R, Schermelleh L, Sharif J, Blackledge NP, De Marco V, Elderkin S, Koseki H, Klose R, Heger A, Brockdorff N. 2014. Targeting polycomb to pericentric heterochromatin in embryonic stem cells reveals a role for H2AK119u1 in PRC2 recruitment. *Cell Reports* **7**:1456–1470. doi: 10.1016/j.celrep.2014.04.012, PMID: 24857660

Czermin B, Melfi R, McCabe D, Seitz V, Imhof A, Pirrotta V. 2002. Drosophila enhancer of zeste/ESC complexes have a histone H3 methyltransferase activity that marks chromosomal polycomb sites. *Cell* **111**:185–196. doi: 10.1016/S0092-8674(02)00975-3, PMID: 12408863

de Napoles M, Mermoud JE, Wakao R, Tang YA, Endoh M, Appanah R, Nesterova TB, Silva J, Otte AP, Vidal M, Koseki H, Brockdorff N. 2004. Polycomb group proteins Ring1A/B link ubiquitylation of histone H2A to heritable gene silencing and X inactivation. *Developmental Cell* **7**:663–676. doi: 10.1016/j.devcel.2004.10.005, PMID: 15525528

Elderkin S, Maertens GN, Endoh M, Mallery DL, Morrice N, Koseki H, Peters G, Brockdorff N, Hiom K. 2007. A phosphorylated form of Mel-18 targets the Ring1B histone H2A ubiquitin ligase to chromatin. *Molecular Cell* **28**:107–120. doi: 10.1016/j.molcel.2007.08.009, PMID: 17936708

Endoh M, Endo TA, Endoh T, Fujimura Y, Ohara O, Toyoda T, Otte AP, Okano M, Brockdorff N, Vidal M, Koseki H. 2008. Polycomb group proteins Ring1A/B are functionally linked to the core transcriptional regulatory circuitry to maintain ES cell identity. *Development* **135**:1513–1524. doi: 10.1242/dev.014340, PMID: 18339675

Endoh M, Endo TA, Endoh T, Isono K, Sharif J, Ohara O, Toyoda T, Ito T, Eskeland R, Bickmore WA, Vidal M, Bernstein BE, Koseki H. 2012. Histone H2A mono-ubiquitination is a crucial step to mediate PRC1-dependent repression of developmental genes to maintain ES cell identity. *PLoS Genetics* **8**:e1002774. doi: 10.1371/journal.pgen.1002774, PMID: 22844243

Eskeland R, Leeb M, Grimes GR, Kress C, Boyle S, Sproul D, Gilbert N, Fan Y, Skoultchi AI, Wutz A, Bickmore WA. 2010. Ring1B compacts chromatin structure and represses gene expression independent of histone ubiquitination. *Molecular Cell* **38**:452–464. doi: 10.1016/j.molcel.2010.02.032, PMID: 20471950

Farcas AM, Blackledge NP, Sudbery I, Long HK, McGouran JF, Rose NR, Lee S, Sims D, Cerase A, Sheahan TW, Koseki H, Brockdorff N, Ponting CP, Kessler BM, Klose RJ. 2012. KDM2B links the polycomb repressive complex 1 (PRC1) to recognition of CpG islands. *eLife* **1**:e00205. doi: 10.7554/eLife.00205, PMID: 23256043

Fischle W, Wang Y, Jacobs SA, Kim Y, Allis CD, Khorasanizadeh S. 2003. Molecular basis for the discrimination of repressive methyl-lysine marks in histone H3 by polycomb and HP1 chromodomains. *Genes & Development* **17**:1870–1881. doi: 10.1101/gad.1110503, PMID: 12897054

Gao Z, Zhang J, Bonasio R, Strino F, Sawai A, Parisi F, Kluger Y, Reinberg D. 2012. PCGF homologs, CBX proteins, and RYBP define functionally distinct PRC1 family complexes. *Molecular Cell* **45**:344–356. doi: 10.1016/j.molcel.2012.01.002, PMID: 22325352

Gearhart MD, Corcoran CM, Wamstad JA, Bardwell VJ. 2006. Polycomb group and SCF ubiquitin ligases are found in a novel BCOR complex that is recruited to BCL6 targets. *Molecular and Cellular Biology* **26**:6880–6889. doi: 10.1128/MCB.00630-06, PMID: 16943429

Hauri S, Comoglio F, Seimiya M, Gerstung M, Glatter T, Hansen K, Aebersold R, Paro R, Gstaiger M, Beisel C. 2016. A High-Density map for navigating the human polycomb complexome. *Cell Reports* **17**:583–595. doi: 10.1016/j.celrep.2016.08.096, PMID: 27705803

Hayashi K, Ohta H, Kurimoto K, Aramaki S, Saitou M. 2011. Reconstitution of the mouse germ cell specification pathway in culture by pluripotent stem cells. *Cell* **146**:519–532. doi: 10.1016/j.cell.2011.06.052, PMID: 21820164

Hayashi K, Saitou M. 2013. Stepwise differentiation from naïve state pluripotent stem cells to functional primordial germ cells through an epiblast-like state. *Methods in Molecular Biology* **1074**:175–183. doi: 10.1007/978-1-62703-628-3_13, PMID: 23975813

He J, Shen L, Wan M, Taranova O, Wu H, Zhang Y. 2013. Kdm2b maintains murine embryonic stem cell status by recruiting PRC1 complex to CpG islands of developmental genes. *Nature Cell Biology* **15**:373–384. doi: 10.1038/ncb2702, PMID: 23502314

Hishida T, Nozaki Y, Nakachi Y, Mizuno Y, Okazaki Y, Ema M, Takahashi S, Nishimoto M, Okuda A. 2011. Indefinite self-renewal of ESCs through myc/Max transcriptional complex-independent mechanisms. *Cell Stem Cell* **9**:37–49. doi: 10.1016/j.stem.2011.04.020, PMID: 21726832

Hurlin PJ, Steingrìmsson E, Copeland NG, Jenkins NA, Eisenman RN. 1999. Mga, a dual-specificity transcription factor that interacts with max and contains a T-domain DNA-binding motif. *The EMBO Journal* **18**:7019–7028. doi: 10.1093/emboj/18.24.7019, PMID: 10601024

Isono K, Endo TA, Ku M, Yamada D, Suzuki R, Sharif J, Ishikura T, Toyoda T, Bernstein BE, Koseki H. 2013. SAM domain polymerization links subnuclear clustering of PRC1 to gene silencing. *Developmental Cell* **26**:565–577. doi: 10.1016/j.devcel.2013.08.016, PMID: 24091011

Isono K, Fujimura Y, Shinga J, Yamaki M, O-Wang J, Takihara Y, Murahashi Y, Takada Y, Mizutani-Koseki Y, Koseki H. 2005. Mammalian polyhomeotic homologues Phc2 and Phc1 act in synergy to mediate polycomb repression of hox genes. *Molecular and Cellular Biology* **25**:6694–6706. doi: 10.1128/MCB.25.15.6694-6706.2005, PMID: 16024804

Kloet SL, Makowski MM, Baymaz HI, van Voorthuijsen L, Karemaker ID, Santanach A, Jansen PWTC, Di Croce L, Vermeulen M. 2016. The dynamic interactome and genomic targets of polycomb complexes during stem-cell differentiation. *Nature Structural & Molecular Biology* **23**:682–690. doi: 10.1038/nsmb.3248

Kuzmichev A, Nishioka K, Erdjument-Bromage H, Tempst P, Reinberg D. 2002. Histone methyltransferase activity associated with a human multiprotein complex containing the enhancer of zeste protein. *Genes & Development* **16**:2893–2905. doi: 10.1101/gad.1035902, PMID: 12435631

Leeb M, Wutz A. 2007. Ring1B is crucial for the regulation of developmental control genes and PRC1 proteins but not X inactivation in embryonic cells. *The Journal of Cell Biology* **178**:219–229. doi: 10.1083/jcb. 200612127, PMID: 17620408

Li X, Isono K, Yamada D, Endo TA, Endoh M, Shinga J, Mizutani-Koseki Y, Otte AP, Casanova M, Kitamura H, Kamijo T, Sharif J, Ohara O, Toyada T, Bernstein BE, Brockdorff N, Koseki H. 2011. Mammalian polycomb-like Pcl2/Mtf2 is a novel regulatory component of PRC2 that can differentially modulate polycomb activity both at the hox gene cluster and at Cdkn2a genes. *Molecular and Cellular Biology* **31**:351–364. doi: 10.1128/MCB. 00259-10, PMID: 21059868

Maeda I, Okamura D, Tokitake Y, Ikeda M, Kawaguchi H, Mise N, Abe K, Noce T, Okuda A, Matsui Y. 2013. Max is a repressor of germ cell-related gene expression in mouse embryonic stem cells. *Nature Communications* **4**: 1754. doi: 10.1038/ncomms2780, PMID: 23612295

Morey L, Aloia L, Cozzuto L, Benitah SA, Di Croce L. 2013. RYBP and Cbx7 define specific biological functions of polycomb complexes in mouse embryonic stem cells. *Cell Reports* **3**:60–69. doi: 10.1016/j.celrep.2012.11.026, PMID: 23273917

Müller J, Hart CM, Francis NJ, Vargas ML, Sengupta A, Wild B, Miller EL, O'Connor MB, Kingston RE, Simon JA. 2002. Histone methyltransferase activity of a Drosophila polycomb group repressor complex. *Cell* **111**:197–208. doi: 10.1016/S0092-8674(02)00976-5, PMID: 12408864

Ogawa H, Ishiguro K, Gaubatz S, Livingston DM, Nakatani Y. 2002. A complex with chromatin modifiers that occupies E2F- and Myc-responsive genes in G0 cells. *Science* **296**:1132–1136. doi: 10.1126/science.1069861, PMID: 12004135

Qin J, Whyte WA, Anderssen E, Apostolou E, Chen HH, Akbarian S, Bronson RT, Hochedlinger K, Ramaswamy S, Young RA, Hock H. 2012. The polycomb group protein L3mbtl2 assembles an atypical PRC1-family complex that is essential in pluripotent stem cells and early development. *Cell Stem Cell* **11**:319–332. doi: 10.1016/j. stem.2012.06.002, PMID: 22770845

Riising EM, Comet I, Leblanc B, Wu X, Johansen JV, Helin K. 2014. Gene silencing triggers polycomb repressive complex 2 recruitment to CpG islands genome wide. *Molecular Cell* **55**:347–360. doi: 10.1016/j.molcel.2014. 06.005, PMID: 24999238

Seibler J, Zevnik B, Küter-Luks B, Andreas S, Kern H, Hennek T, Rode A, Heimann C, Faust N, Kauselmann G, Schoor M, Jaenisch R, Rajewsky K, Kühn R, Schwenk F. 2003. Rapid generation of inducible mouse mutants. *Nucleic Acids Research* **31**:e12–12. doi: 10.1093/nar/gng012, PMID: 12582257

Shao Z, Raible F, Mollaaghababa R, Guyon JR, Wu CT, Bender W, Kingston RE. 1999. Stabilization of chromatin structure by PRC1, a polycomb complex. *Cell* **98**:37–46. doi: 10.1016/S0092-8674(00)80604-2, PMID: 10412979

Sharif J, Endo TA, Ito S, Ohara O, Koseki H. 2013. Embracing change to remain the same: conservation of polycomb functions despite divergence of binding motifs among species. *Current Opinion in Cell Biology* **25**: 305–313. doi: 10.1016/j.ceb.2013.02.009, PMID: 23478215

Sharif J, Endo TA, Nakayama M, Karimi MM, Shimada M, Katsuyama K, Goyal P, Brind'Amour J, Sun MA, Sun Z, Ishikura T, Mizutani-Koseki Y, Ohara O, Shinkai Y, Nakanishi M, Xie H, Lorincz MC, Koseki H. 2016. Activation of endogenous retroviruses in Dnmt1(-/-) ESCs involves disruption of SETDB1-Mediated repression by NP95 binding to hemimethylated DNA. *Cell Stem Cell* **19**:81–94. doi: 10.1016/j.stem.2016.03.013, PMID: 27151458

Suzuki A, Hirasaki M, Hishida T, Wu J, Okamura D, Ueda A, Nishimoto M, Nakachi Y, Mizuno Y, Okazaki Y, Matsui Y, Izpisua Belmonte JC, Okuda A. 2016. Loss of MAX results in meiotic entry in mouse embryonic and germline stem cells. *Nature Communications* **7**:11056. doi: 10.1038/ncomms11056, PMID: 27025988

Suzuki M, Mizutani-Koseki Y, Fujimura Y, Miyagishima H, Kaneko T, Takada Y, Akasaka T, Tanzawa H, Takihara Y, Nakano M, Masumoto H, Vidal M, Isono K, Koseki H. 2002. Involvement of the Polycomb-group gene Ring1B in the specification of the anterior-posterior axis in mice. *Development* **129**:4171–4183. PMID: 12183370

Trojer P, Cao AR, Gao Z, Li Y, Zhang J, Xu X, Li G, Losson R, Erdjument-Bromage H, Tempst P, Farnham PJ, Reinberg D. 2011. L3MBTL2 protein acts in concert with PcG protein-mediated monoubiquitination of H2A to establish a repressive chromatin structure. *Molecular Cell* **42**:438–450. doi: 10.1016/j.molcel.2011.04.004, PMID: 21596310

Vandamme J, Völkel P, Rosnoblet C, Le Faou P, Angrand PO. 2011. Interaction proteomics analysis of polycomb proteins defines distinct PRC1 complexes in mammalian cells. *Molecular & Cellular Proteomics* **10**:M110. 002642–002642. doi: 10.1074/mcp.M110.002642, PMID: 21282530

Wang H, Wang L, Erdjument-Bromage H, Vidal M, Tempst P, Jones RS, Zhang Y. 2004. Role of histone H2A ubiquitination in polycomb silencing. *Nature* **431**:873–878. doi: 10.1038/nature02985, PMID: 15386022

Washkowitz AJ, Schall C, Zhang K, Wurst W, Floss T, Mager J, Papaioannou VE. 2015. Mga is essential for the survival of pluripotent cells during peri-implantation development. *Development* **142**:31–40. doi: 10.1242/dev. 111104, PMID: 25516968

Wu X, Johansen JV, Helin K. 2013. Fbxl10/Kdm2b recruits polycomb repressive complex 1 to CpG islands and regulates H2A ubiquitylation. *Molecular Cell* **49**:1134–1146. doi: 10.1016/j.molcel.2013.01.016, PMID: 233 95003

390

Yang CS, Chang KY, Dang J, Rana TM. 2016. Polycomb group protein Pcgf6 acts as a master regulator to maintain embryonic stem cell identity. *Scientific Reports* **6**:26899. doi: 10.1038/srep26899, PMID: 27247273

Zdzieblo D, Li X, Lin Q, Zenke M, Illich DJ, Becker M, Müller AM. 2014. Pcgf6, a polycomb group protein, regulates mesodermal lineage differentiation in murine ESCs and functions in iPS reprogramming. *Stem Cells* **32**:3112–3125. doi: 10.1002/stem.1826, PMID: 25187489

Contents lists available at ScienceDirect

Bioorganic & Medicinal Chemistry

Hydrophobic structure of hairpin ten-ring pyrrole-imidazole polyamides enhances tumor tissue accumulation/retention *in vivo*

Takahiro Inoue [a], Osamu Shimozato [b,*], Nina Matsuo [a], Yusuke Mori [b], Yoshinao Shinozaki [a], Jason Lin [a], Takayoshi Watanabe [a], Atsushi Takatori [a], Nobuko Koshikawa [a], Toshinori Ozaki [b], Hiroki Nagase [a]

[a] *Laboratory of Cancer Genetics, Chiba Cancer Center Research Institute, 666-2 Nitona, Chuo-ku, Chiba 260-8717, Japan*
[b] *Laboratory of DNA Damage Signaling, Chiba Cancer Center Research Institute, 666-2 Nitona, Chuo-ku, Chiba 260-8717, Japan*

ARTICLE INFO

ABSTRACT

To examine the hydrophobic structure of PI polyamides on tumor accumulation *in vivo*, PI polyamide-fluorescein conjugates **1**–**5** with the distinct number of *N*-methylimidazole (Im) units were synthesized. There existed an inverse relationship between the Im unit number of the compounds and their hydrophobicity. Compound **1** with one Im unit and **3** with three Im units accumulated and retained preferentially in tumor tissues compared to **5** with five Im units. These results suggest the importance of a PI polyamide's primary structure, which partly contributes to its hydrophobic property, on its accumulation and/or retention in tumor tissues *in vivo*.

© 2018 Elsevier Ltd. All rights reserved.

1. Introduction

Pyrrole-imidazole (PI) polyamide is a class of compounds consisting of *N*-methylpyrrole (Py) and *N*-methylimidazole (Im) aromatic amides originally derived from natural oligopeptide antibiotics, such as distamycin A. While distamycin A non-covalently binds to the minor groove of adenine (A) and/or thymine (T) -rich DNA sites,[1] PI polyamides possess a similar specificity for nucleotide binding and improved base recognition. Aromatic Im/Py ring pairs bind to the edges of the Watson-Crick pairs in the double-stranded DNA: Im/Py pairs bind to guanine (G) and cytosine (C) base pairs and Py/Im pairs bind CG pairs; Py/Py pairs bind AT as well as TA pairs.[2–4] PI polyamide physically associates with the minor groove of double-stranded DNA without distorting the helical structure, especially in a γ-aminobutyric acid-linked hairpin configuration.[5] This class of molecules affords binding affinities comparable to certain transcription factors.[6] As such, well-designed PI polyamides targeting to promoter and enhancer elements of the genes of interest could interrupt the assembly of transcription factors, such as TFIIIA,[7] AP-1,[8,9] and HIF-1,[10] and thereby repressing its gene expression.

As aberrant gene expressions as a result of genetic and epigenetic abnormalities have been well implicated in various diseases, the use of PI polyamides presents an attractive option for the development of novel drugs against those diseases. Recently, a PI polyamide targeting to the promoter of *TGFB1* successfully ameliorated progressive renal diseases[9] and hypertrophic scars.[11] Another PI polyamide against an androgen receptor element (ARE) was able to repress the ARE-regulated gene transcriptions, e.g. *VEGF* and *TMPRSS2-ERG*, a unique prostate cancer-related oncogenic fusion gene, and thereby suppressing the xenograft tumor growth of human prostate cancer cells.[12,13] Our recent study of a PI polyamide against oncogenic driver mutant genes *KRAS*[G12D/V] demonstrated differential cytotoxicity *in vitro* and repressed tumor growth in mouse xenograft models *in vivo* without severe adverse effects such as body weight loss,[14] highlighting the promising aspect of PI polyamides in drug development.

While the ability for PI polyamides to accumulate in certain tissues has been revealed in several studies, the underlying physiochemical principles remain unclear. Recent studies showed PI polyamides to accumulate into skin xenograft tumors[15,16] and vital organs such as liver, kidney, and lung,[17] but so far there are few explanations for such a phenomenon. Previously, Fukasawa et al. proposed that the plasma level of intravenously administrated PI polyamide increased positively as their molecular weight,[18] and Kamei et al. hypothesized a potential connection between the Py/Im ratio of a polyamide and its plasma level *in vivo*.[19] As results from Best et al. echoed similar sentiments to the hypothesis that the primary structure of a PI polyamide affected a molecule's distribution *in vivo*, we sought to characterize the potential connection here, as few studies have systematically examined the biodistribution of PI polyamides *in vivo*[20] and no general design

roles on how to utilize the pharmacokinetic profiles of PI polyamides to improve its accumulation exist.

In the present study, we have designed a series of hairpin ten-ring PI polyamides with distinct ratios of Py and Im units to infer the possible effect of hydrophobicity, as governed by the number of Im units, on the molecular machinery of their internalization into tumor tissues *in vivo*. While all PI polyamides rapidly accumulated into tumor tissues, PI polyamides with higher Im unit numbers displayed longer retention times in tumor tissues compared to their counterparts with lower Im unit numbers, suggesting that the primary structure of PI polyamide did in fact affect its tissue distribution *in vivo*. Thus, the hydrophobic property of PI polyamide resulting from its chemical compositions might be implicated in its pharmacodynamic properties.

2. Results

2.1. Molecular design and synthesis of PI polyamide-fluorescein conjugates

To examine whether the compositional variation of PI polyamides could affect its hydrophobicity, we designed five PI polyamide-fluorescein conjugates with different compositions of Im units: **1–5** (Fig. 1). Im units were located at only positions 1 through 7 in hairpin configurations to avoid Im/Im pairings as previous studies suggested that such pairing had no preferential affinity for G-C or A-T pairs.[3] According to the previous studies, β-alanine (β) and γ-aminobutyric acid (γ) residues were incorporated in order to allow the polyamides to be flexible and the hairpin-like structure, respectively.[5,21,22] The designed PI polyamide–fluorescein conjugates **1–5** were synthesized via the Fmoc solid-state peptide synthesis procedure followed by a conjugation of fluorescein with PI polyamides at their N-termini as described in Materials and Methods. Purities (>96%) of the resulting PI polyamide–fluorescein conjugates were confirmed by a high performance liquid chromatography (HPLC), and these compounds were used for following experiments (Fig. SI1).

2.2. The number of imidazole units of PI polyamide reflects its hydrophobicity

A molecule's equilibrium partitioning in a biphasic water and *n*-octanol system, as determined by its $\log P_{OW}$, is a common indicator for the hydrophobicity, measureable from their HPLC corresponding retention times.[23] We thereby measured the retention times of compounds **1–5** and reference compounds, such as ethyl acetate, benzonitrile, acetophenone, and indole (Fig. SI2), and likewise deduced the $\log P_{OW}$ values of **1–5** from their recorded retention times (Table 1). Compound **1** with only one Im unit exhibited the highest $\log P_{OW}$ value, while **5** with five Im units showed the lowest the $\log P_{OW}$ value among these compounds. In addition, the $\log P_{OW}$ values of **2–4** were gradually reduced along with the increase in the number of Im units. These results suggested a clear inverse correlation between $\log P_{OW}$ values of compounds **1–5** and their respective number of Im units.

In the meantime, we analyzed the fluorescence of each polyamide as a precaution to confirm that fluorescence of fluorescein moiety did not vary resulting from a function of the chemical structure of the PI polyamide adduct. We saw an increase in the level of fluorescence quantum yield of compounds **1–3** with their Im unit numbers, suggesting that the number of imidazole units and/or the degree of hydrophobicity partly contributed to their fluorescence properties (Table 1). In contrast, we hypothesized that the consecutive placement of multiple Im units in compounds **4** and **5** somehow altered the local secondary structure and spatial
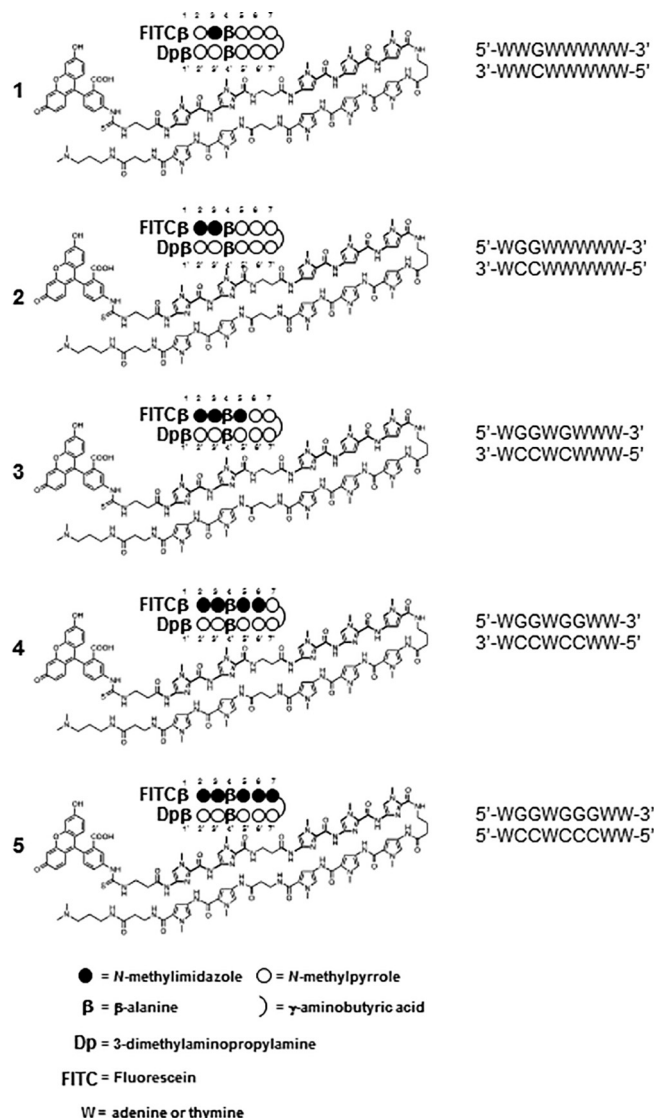

Fig. 1. Chemical structures and graphical schemas of the pyrrole-imidazole polyamide-fluorescein conjugates **1–5** employed in this study. Theoretical target sequences of these compounds are also shown.

Table 1
Partition coefficients ($\log P_{OW}$) and fluorescence quantum yield (ϕ_f) of compounds **1–5**.

Compound	Retention time (min)	$\log P_{OW}$	ϕ_f
1	11.73	1.5	0.022
2	11.4	1.46	0.026
3	10.97	1.42	0.027
4	10.48	1.36	0.01
5	8.86	1.19	0.014

configuration of the polyamide and subsequently decreased their fluorescence (Table 1). All compounds besides **4** displayed similar fluorescence intensity to evaluate the accumulation and retention *in vivo* (Fig. SI3). The reason for compound **4** to exhibit a drop in fluorescence intensity was unclear; while we suspected that the relative symmetric configuration of Im units around the β units somehow contributed to this effect, the investigation was beyond the scope of the current discussion. We thus employed three compounds for further experiments: **1** as a highly hydrophobic compound, **3** as a moderately hydrophobic compound, and **5** as a relatively hydrophilic compound.

2.3. A mode of internalization of PI polyamide-fluorescein conjugates into tumor-derived cells

We next examined the incorporation of PI polyamide-fluorescein conjugates by tumor-derived cells *in vitro* by fluorescent microscopy. Human colon cancer LS180 and SW480 cells were treated with **1**, **3**, **5**, FITC or DMSO. Cell nuclei were stained with 4′,6-diamidino-2-phenylindole (DAPI). Consistent with previous studies,[8,20,24] **1**, **3**, and **5** strongly co-localized in cell nuclei regardless of the distinct hydrophobicity (Fig. 2a and b). Fluorescein was undetectable in the cells (Fig. 2a and b).

We further investigated how PI polyamide-fluorescein conjugates is incorporated by cells. LS180 and SW480 cells were treated with various concentrations of compounds and measured fluorescence intensity by a fluorescence spectrometer. As seen in Fig. 2c and d, **1** was internalized into LS180 and SW480 cells in a dose-dependent manner, although the dose-dependencies of **3** and **5** were not as clear as in **1**. As in certain cases active transport systems are more highly sensitive to temperature than passive transport systems,[25] we examined the incorporation of compounds **1** and **5** by cells cultured under cold incubation that could suppresses certain active transport systems. As shown in Fig. SI4, cold incubation inhibited the internalization of compound **5** but not **1**. These data suggested that hydrophobic PI polyamides were likely incorporated by tumor-derived cells through not only passive diffusion but also certain possible transport mechanisms.

2.4. Accumulation of hydrophobic PI polyamides into tumor in vivo

To test whether the hydrophobicity of compounds **1**, **3**, and **5** could affect its tumor-oriented distribution *in vivo*, we intravenously injected **1**, **3**, **5**, alongside unconjugated fluorescein or dimethyl sulfoxide (DMSO) as controls, into nude mice bearing LS180-derived tumors. The superficial fluorescence of these mice was monitored for 72 h post-administration by quantitative *in vivo* imaging; the mean fluorescence intensity (MFI) in tumor and in non-tumor area was summarized in Fig. 3. In the tumor area, **1** showed an increase in the level of MFI with a peak at 3 h post-administration that sustained over 72 h (Fig. 3a and f). Compound **3** also had an elevated MFI in tumors with a peak at 6 h post-administration, and nearly half of its maximum level was still detectable at 72 h post-administration (Fig. 3b and g); the MFI of **5** in the tumors reached its maximal level at 3 h post-administration and it became undetectable at 48 h post-administration (Fig. 3c and h). In contrast, we could not detect fluorescence in the tumor tissues of subjects injected with unconjugated fluorescein, despite that it did appear to distribute in the entire body with similar kinetics to that of **3** (Fig. 3d and i). This observation affirmed that the fluorescence observed in the tumor tissues of polyamide-injected mice was in fact due to the conjugated fluorescein moiety on the polyamides. Beyond the graft regions, **1** rapidly distributed in the body cavity within 1 h, and its level sharply decreased at 24 h post-administration (Fig. 3a and f), whereas **3** experienced a spike in MFI in non-tumor areas within 5 min but disappeared at 24 h post-administration (Fig. 3b and g). The level of **5** was almost undetectable in the entire body during the experiment (Fig. 3c and h). Similar proportion of distribution of PI polyamide-fluorescein conjugates was seen in another human colon cancer SW480-derived tumor bearing mice (Fig. SI5), collectively suggesting that hydrophobicity of PI polyamide influences tumor-oriented distribution.
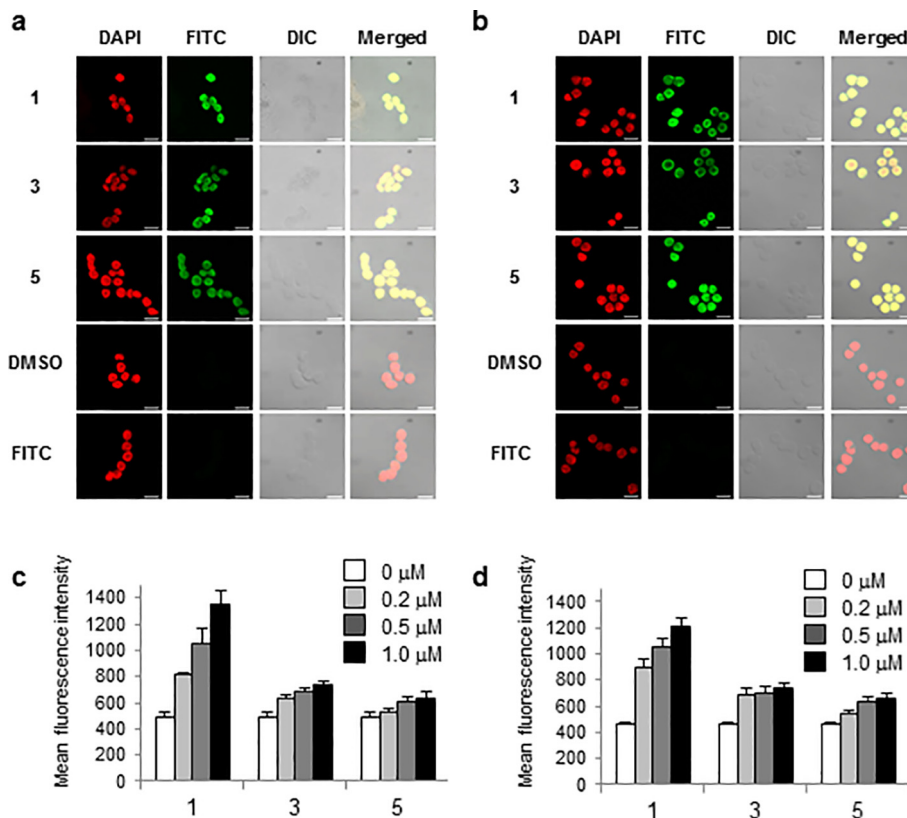

Fig. 2. (a and b) Human colon cancer LS180 (a) and SW480 (b) cells were treated with 1 μM of PI polyamide-fluorescein conjugates **1**, **3**, **5** or FITC, or DMSO (0.1%, v/v) followed by DAPI staining to visualize cellular nuclear. Fluorescence and differential interference contrast (DIC) images were captured under confocal laser microscopy (magnitude: ×630). Merged images of DAPI, FITC and DIC are also shown in the right line. Scale bars indicate 20 μm. (c and d) LS180 (c) and SW480 (d) cells were treated with compound **1**, **3**, or **5** at the indicated doses or left untreated for 24 h at 37 °C. The fluorescence intensities of these cells were determined by fluorospectrometery. Data show mean ± SD of triplicate samples.
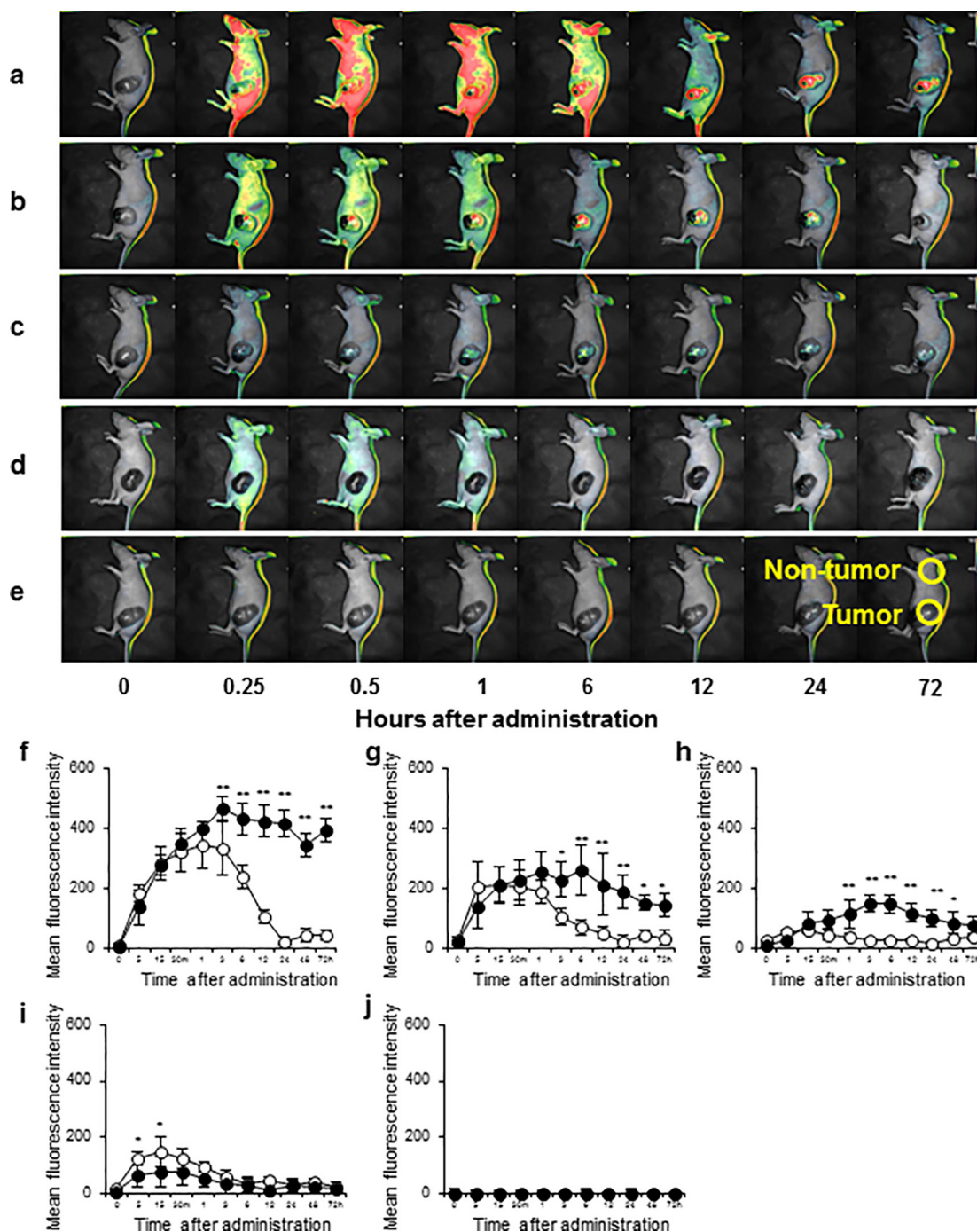
Fig. 3. Human colon cancer LS180 cells were subcutaneously inoculated into flanks of nude mice. Compounds **1** (a), **3** (b), **5** (c), FITC (d), or 1.25% DMSO/PBS (e) was intravenously administrated into the tumor-bearing mice (1 mg/kg) upon approximately 1 cm of growth for *in vivo* fluorescent imaging. The fluorescence images of whole bodies of the treated mice were then taken by an *in vivo* imaging system at the indicated time points post-administration. Circles mark the tumor and the non-tumor areas for measuring fluorescence intensity. The mean fluorescent intensities at the tumor (closed circles) and at the non-tumor area (open circles) of tumor-bearing mice inoculated with compounds **1** (f), **3** (g), **5** (h), FITC (i), and DMSO (j) are shown; error bars indicate SD ($n = 3$, $^{*}p < 0.05$, $^{**}p < 0.01$). Repeated two-way ANOVA was performed to assess the statistical significance of difference of fluorescence intensities between tumor and non-tumor areas ($^{*}p < 0.05$, $^{**}p < 0.01$).

2.5. Long retention of hydrophobic PI polyamides within tumor in vivo

Since the half level of **1** and **3** in the tumor seemingly extended beyond 3 days after their initial injections, we further investigated long-term retention of PI polyamide-fluorescein conjugates in tumor-bearing mice. To this end, we treated the LS180-bearing nude mice with compounds **1**, **3**, and **5** and monitored the resultant fluorescent decay by quantitative *in vivo* imaging until their fluorescein signal disappeared (Fig. 4). The fluorescence of compounds **1**, **3**, and **5** reached their maximal levels around 2 h post-administration and decreased by half around 48 h post-administration. Surprisingly, **1** was still detectable in tumors over 9 days post-administration, while **3** did not; additionally, we found the fluorescence of **5** to extinguish in a time frame as short as 4 days. Notably, **1** was detectable within SW480-derived tumors *in vivo* for up to 22 days (Fig. SI6), indicating that increasing the hydrophobicity of a PIP likely contributed to a longer tumor retention time *in vivo*.
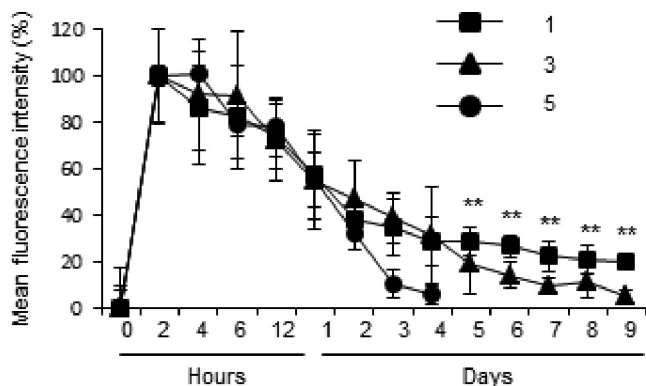
Fig. 4. Human colon cancer LS180 cells were subcutaneously inoculated into flanks of nude mice. All injections were performed intravenously (1 mg/kg) upon approximately 1 cm of growth. Mice with the PI polyamide-fluorescein conjugate **1** (closed squares), **3** (closed triangles) and **5** (closed circles) were monitored at the indicated time points post-administration. The fluorescence intensity at 0 h (before administration) and 2 h was taken for 0% and 100%, respectively. Results show mean ± SD (n = 3). Repeated two-way ANOVA was performed to assess the statistical significance of difference of fluorescence intensities among compounds **1**, **3**, and **5** ($^{**}p < 0.01$).

2.6. Tissue distribution of hydrophobic PI polyamides

The results so-far prompt us to analyze further the distribution of PI polyamide-fluorescein conjugates in tissue sections. PI polyamide-fluorescein conjugates-inoculated animals were resected at 3 days and 9 days post-administration, and the tissue fluorescence distribution was assessed by confocal microscopy. Compounds **1**, **3**, and **5** were mainly detectable in tumors, livers and kidneys at 3 days post-administration, and appeared to co-localize with DAPI, implying that PI polyamide-fluorescein conjugates accumulated in the nucleus *in vivo* (Figs. SI7–SI9). While we did observe some fluorescence in lung, heart, and spleen of mice treated with compounds **3** and **5** (Figs. SI7 and SI8), similar levels in DMSO-treated mice (Figs. 5d and SI10) would suggest that these signals were most likely not an effect of PI polyamide accumulation but instead other unknown factors contributing to the autofluorescence of these organs. We further measured the MFIs in these tissue sections. As shown in Fig. 5a, **1** accumulated preferentially in tumors, and the liver to a smaller extent, and poorly presented in the kidney and spleen on 3 days post-administration. At the same time, **3** was detected in tumors as well as kidneys, but accumulation in the liver was relatively low (Fig. 5b). Compound **5** was largely detected in kidneys compared to tumors and livers (Fig. 5c). Compound **1** remained notably detectable in tumor at 9 days post-administration (Fig. 5a). In contrast, levels of **3** and **5** in tumor tissues largely decreased at 9 days post-administration (Fig. 5b and c), suggesting that the hydrophobic property influences the biodistribution of PI polyamides *in vivo*.

3. Discussion

3.1. Effect of chemical structure of PI polyamide on its hydrophobicity

We herein have synthesized a series of PI polyamides **1–5** with different number of Im units. Given that the presence of an additional nitrogen atom of Im affected its propensity for hydrogen bonding, the degree of hydrophilicity of Im ($\log P_{OW} = -0.06$) is larger than that of Py ($\log P_{OW} = 1.21$).[26,27] In comparison with their $\log P_{OW}$ values, the hydrophobicity of **1** was approximately twice higher than that of **5**. We placed Im units at positions before the γ unit of compounds **1–5** to simplify their chemical structure. In this context, the hydrophilic level of PI polyamide might be correlated with the number of Im units. However, the position of Im unit served a critical role in the specificity of PI polyamide for the recognition of DNA.[28] Furthermore, PI polyamides of the same Im content but different positions have very different physical and cell uptake properties.[20] Therefore, the measurement of $\log P_{OW}$ by using HPLC should be required for better understanding for the relationship between the primary structure and hydrophobicity of PI polyamides.

3.2. Effects of hydrophobic structures of PI polyamides on tumor-oriented accumulation and retention

In the present study, we demonstrated for the first time that the retention time of PI polyamide in tumor tissue was inversely correlated with its Im unit numbers: compound **1** with only one Im unit
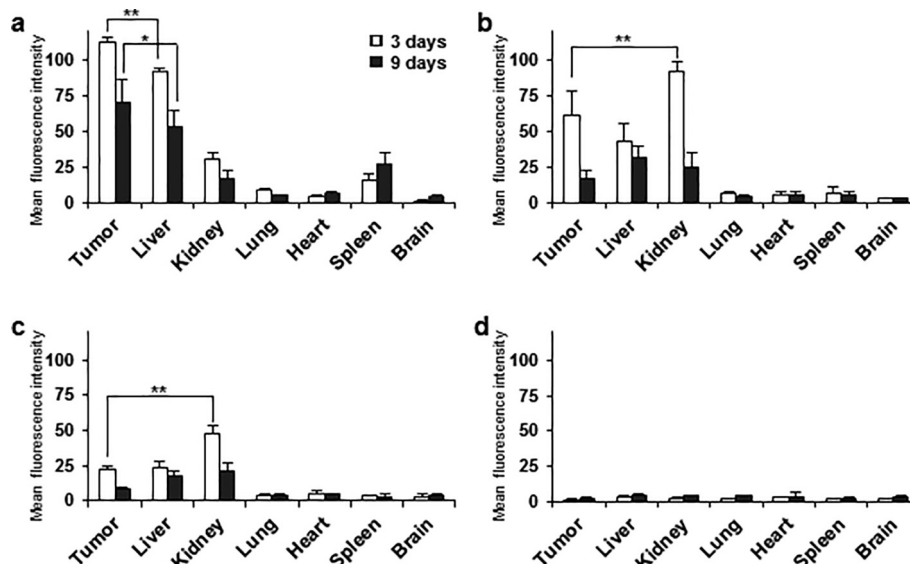

Fig. 5. Tissue sections of tumors and various organs were prepared from LS180-derived tumor-bearing mice with the PI polyamide-fluorescein conjugates **1** (a), **3** (b), **5** (c), or DMSO (d) as a vehicle control at 3 days and 9 days post administration. Their fluorescence was captured under a confocal laser microscope and quantitated their fluorescence intensity. Data shows mean ± SD (n = 3). One-way ANOVA was performed to assess the statistical significance of difference of fluorescence intensities among tissues ($^{*}p < 0.05$, $^{**}p < 0.01$).

was detectable within tumor tissues longer than **3** with three Im units, whereas **5** with five Im units could no longer be found after 3 days. Additionally, **1** retained in tumors over 22 days, a longer retention time compared to previous studies.[15] For this reason, it seems likely that the most hydrophobic **1** is incorporated into tumor tissues much higher than compounds **3** and **5** (Fig. 2). We also have demonstrated for the first time that the mode of internalization of PI polyamide into tumor-derived cells is associated with the Im unit numbers and/or their hydrophobicity: hydrophobic compound might penetrate into cells within tumor tissues through the passive diffusion, whereas certain transport systems could be partly involved in the incorporation of hydrophilic compound. Since certain mechanisms to uptake extracellular substrates were activated in tumor cells via oncogenic signaling pathway,[29] it could be possible that higher activation of endocytosis in tumor cells is responsible for the higher uptake of PI polyamides compared to normal organs. However, further examination to uncover how the tumor cells incorporate PI polyamides remains to be elucidated.

Our *in silico* analysis predicted that compound **1** has the largest numbers of its theoretical target sequences within genomic DNA compared with **3** and **5** (data not shown). As PI polyamide binds to DNA in cellular nuclear, we presumed that excess amounts of fluorescein-free competitors diminish the accumulation of PI polyamide in tumors. We thus synthesized those competitors **6**, **7**, and **8** as shown in Figs. SI11 and SI12 and inoculated them in combination with the relevant compounds **1**, **3**, and **5**, respectively. As shown in Fig. SI13, none of competitors suppressed the accumulation of fluorescein-conjugated PI polyamides, suggesting that the accumulation of PI polyamides in tumors is independent of their sequence-specificity. Furthermore, the hydrophobicity of these competitors would be of particular interest for the interpretation of these findings.

We next hypothesized that the hydrophobic level of PI polyamides is involved in its tumor-oriented delivery. Tumor cells activated tumor-associated angiogenesis upon the deprivation of oxygen and nutrients accompanying the tumor growth, and thereby accelerating growth of tumor tissues.[30] Raskatov et al. demonstrated an increased accumulation of PI polyamides in tumors *in vivo* as a function of tumor vascularization.[31] Tumor vascular system has been considered to be different from blood vessels in normal organs, such as defective vascular architecture and deficiency of lymphatic drainage from tumor tissue.[32] As a result, many kinds of macromolecules like plasma proteins as well as lipids predominantly accumulated and retained in tumor tissues, so-called the enhanced vascular permeability and retention (EPR) effect.[33,34] Our histological examination demonstrated that the hydrophobic PI polyamide **1** in tumor tissue was distributed by the surrounding blood vessels (Fig. SI14). We also observed a large number of deposit-like structures of compound **1** in tissues, such as liver and spleen, obtained from the mice (Fig. SI15). These results might explain why hydrophobic compound **1** exhibits high accumulation and long retention in tumors. In contrast, compounds **3** and **5** might accumulate in tumors, at least in part, by the association with certain plasma proteins and lipids as previously described.[35] However, more detail analysis of the binding affinities of PI polyamides to plasma proteins and the relationship between hydrophobicity of PI polyamides and histological distribution in tumor tissues would need to be clarified.

3.3. A hydrophilicity-mediated distribution and excretion of PI polyamide

Another important finding of the present study was the effect of the hydrophobicity of a PI polyamide's biodistribution *in vivo*. To monitor the plasma level of PI polyamides, we here examined the superficial fluorescence of the compound-treated mice. The kinetics of the superficial fluorescence was similar to that of the

fluorescence intensity in serum (Figs. 3 and SI16). Additionally, cells located in skin tissues hardly incorporated these compounds **1**, **3**, and **5** if their superficial fluorescence reached the highest levels (Fig. SI15). We thereby propose that the superficial fluorescence of PI polyamide-fluorescein conjugate-treated mice serves as a surrogate for measurement of the level of compounds in plasma of experimental animals. Our *in vivo* imaging analysis demonstrated that hydrophilic **5** was rapidly cleared from the body relative to the hydrophobic **1** and **3**, suggesting that the half-life of PI polyamides *in vivo* is associated with its hydrophilicity. Harki et al. described that a hairpin-formed PI polyamide would firstly be transported in the liver and then delivered into bladder rather than gallbladder, implying a possible mode of renal excretion.[36] Consistent with previous studies,[15,31,36] the hydrophobic **1** was preferentially delivered into livers as well as tumors; however, compounds **3** and **5** were incorporated by the cells located in the cortex of kidneys but not in cells of liver, lung, spleen, and skin tissues at 30 min post-administration (Fig. SI15). As the fluorescence intensity of **1**, **3**, and **5** was nearly equal, the likely explanation was that an increase in the hydrophilic level of PI polyamide elevates the rate of its renal excretion as a result of "kidney-homing". Our present results seems to contradict to previous study that higher ratios of Im result in longer retention times in plasma;[19] however, the molecular size of those PI polyamides was smaller than that of the present PI polyamide due to the difference of functional moiety, acetyl moiety or fluorescein moiety. Given that the size of PI polyamides is a critical factor of biological distribution as previously described,[18] we presumed that the biodistribution of acetylated PI polyamides was different from that of fluorescein-conjugated PI polyamides because of size.

Intriguingly, the moderately hydrophobic **3** was observed in both tumors and kidneys, and remained in tumors longer than **5**, suggesting that the hydrophilicity of a PI polyamide contributed to its tumor-homing but not liver-homing property *in vivo*. In support of our hypothesis, Synold et al. also demonstrated that acetylating PI polyamide could potentially increase its hydrophobicity to the extent of altering localization in tissues such as livers, kidneys and lungs and rapidly reducing its plasma concentration.[37] Additionally, several chemical modifications at γ-turn[38] and PEGylation at the carboxyl terminus[39] affected the hydrophobicity of PI polyamide. Thus, an increase in the hydrophilic level of PI polyamide might reduce adverse effect of PI polyamide-based medicine resulting from the modulation of biodistribution *in vivo*, especially the reduction of "liver-homing" property.

4. Conclusion

PI polyamides with different Im unit numbers were synthesized and examined for their differences in tissue distribution within tumor bearing mice. The Im unit numbers of PI polyamides contributed to a polyamide's hydrophobicity in a manner that affected its accumulation and retention in tumor tissues as well as its internalization into tumor-derived cells *in vitro*. Intriguingly, we found that moderately hydrophobic PI polyamides decline the ability of "liver-homing" compared to highly hydrophobic polyamides, suggesting that well-designed PI polyamides potentiate the "tumor-homing" ability and can be utilized as a novel drug delivery system to reduce adverse effects to unintended regions of the body.

5. Materials and methods

5.1. General materials

Human colon cancer-derived cell lines LS180 and SW480 were obtained from American Tissue Culture Collection (Manassas, VA,

USA). PyBOP and NovaPEG Wang resin were acquired from Novabiochem (Gibbstown, NJ, USA); unless otherwise specified, chemicals were obtained from Sigma-Aldrich (St. Louis, MO, USA).

5.2. Chemical synthesis of pyrrole-imidazole (PI) polyamide-fluorescein conjugates

Compounds **1–5** were piecewise synthesized by first generating the polyamide backbone chains (**1**, β -PyIm- β -PyPyPy- γ -PyPyPy- β -PyPy- β; **2**, β -ImIm- β -PyPyPy- γ -PyPyPy- β -PyPy- β; **3**, β - ImIm- β -ImPyPy- γ -PyPyPy- β -PyPy- β; **4**, β -ImIm- β -ImImPy- γ -PyPyPy- β -PyPy- β; **5**, β -ImIm- β -ImImIm- γ -PyPyPy-β-PyPy- β) by stepwise Fmoc solid-phase reaction using a PSSM-8 solid-phase peptide synthesizer (Shimadzu Industry, Kyoto, Japan) at 10 μmol scales of Fmoc- β -alanine NovaPEG Wang resin as previously described.[40] After the synthesis, *N*,*N*-dimethyl-1, 3-propanediamine (Wako, Tokyo, Japan) was mixed with the resin at 65 °C for 2 h for compound cleavage. PI polyamides having the carboxyl-terminal amine was purified by a Prominence high-performance liquid chromatography (HPLC) (Shimadzu Industry, Kyoto, Japan) using a 10 mm × 150 mm Gemini-NX 3u 5-ODS-H reverse-phase column (Phenomenex, Torrance, CA, USA) in 0.1% acetic acid in water with acetonitrile as eluent, at a flow rate of 10 mL/min, and a linear gradient from 0% to 66.7% acetonitrile over 20 min, with ultraviolet detection at 310 nm. Collected polyamide backbones were conjugated with fluorescein as previously described.[20] In brief, the polyamides were dissolved in *N*-methylpyrrolidone with fluorescein-4-Isothiocyanate (FITC; 5 equivalents, Dojindo, Kumamoto, Japan) and *N*,*N*-diisopropylethylamine (10 equivalents, Wako, Tokyo, Japan). After reaction at room temperature for 2 h, the resulting polyamide-fluorescein conjugates were purified by HPLC using a 150 × 4.6 mm Gemini-NX 3u 11A reverse-phase column (Phenomenex) in 0.1% acetic acid in water with acetonitrile as eluent, at a flow rate of 1 mL/min, and a linear gradient from 0% to 66.7% acetonitrile over 20 min, with ultraviolet detection at 310 nm. Mass spectrometric analyses were performed on a Shimadzu LCMS-2020 liquid chromatograph mass spectrometer (LC MS) system (Shimadzu Industry, Kyoto, Japan). **1**: LC–MS *m/z* calculated for $C_{101}H_{111}N_{29}O_{20}S$, $[M+2H]^{2+}$ 1041.92; found 1042.25, $[M+3H]^{3+}$ 694.94; found 695.15. **2**: LC–MS *m/z* calculated for $C_{100}H_{110}N_{30}O_{20}S$, $[M+2H]^{2+}$ 1042.41; found 1042.90, $[M+3H]^{3+}$ 695.27; found 695.55. **3**: LC–MS *m/z* calculated for $C_{99}H_{109}N_{31}O_{20}S$, $[M+2H]^{2+}$ 1042.91; found 1043.40, $[M+3H]^{3+}$ 695.61; found 695.95. **4**: LC–MS *m/z* calculated for $C_{98}H_{108}N_{32}O_{20}S$, $[M+2H]^{2+}$ 1043.41; found 1043.85, $[M+3H]^{3+}$ 695.94; found 696.25. **5**: LC–MS *m/z* calculated for $C_{97}H_{107}N_{33}O_{20}S$, $[M+2H]^{2+}$ 1043.91; found 1044.30, $[M+3H]^{3+}$ 696.27; found 696.55. The corresponding HPLC chromatograms and LC–MS spectra are shown in Fig. SI1.

5.3. Estimation of logP_OW value

The logP_{OW} values were estimated by using reverse-phase HPLC as previously described.[41] In brief, retention times of compounds were measured by using a Prominence HPLC system (Shimadzu Industry, Kyoto, Japan) using a 150 × 4.6 mm Gemini-NX 3u 11A reverse-phase column (Phenomenex, Torrance, CA, USA) with performed in an isocratic condition (0.1% acetic acid: acetonitrile = 4:1) at a flow rate of 1 mL/minute. A standard curve was constructed by plots of the logP_{OW} values versus retention times of reference substrates, such as ethyl acetate,[42] benzonitrile,[42] acetophenone[42] and indole,[43] and then logP_{OW} values of PI polyamides were estimated by their retention times.

5.4. Fluorescence quantum yield

Fluorescence spectra were measured by an FP-8600 spectrometer (JASCO, Tokyo, Japan) and corrected with correlation functions for excitation and mission optics obtained by use of an SID-844 calibration detector (JASCO, Tokyo, Japan). Absorption spectra were recorded by a UV-2400PC spectrometer (Shimadzu Industry, Kyoto, Japan).

Fluorescence quantum yield (φ_f) was estimated by the relative method using a formula, in which, φ, F, A, and n are the quantum yield, the integrated fluorescence intensity, the absorbance at excitation wavelength, and the refractive index of solvent used, respectively, and subscript x and s stand for sample of interest and standard sample, respectively. Fluorescein in 1 mM NaOH/EtOH was used as standard sample ($\varphi_f = 0.92$).[44]

$$\varnothing_f = \varnothing_s \times \left(\frac{F_x/A_x}{F_s/A_s}\right) \times \left(\frac{n_x^2}{n_s^2}\right)$$

5.5. In vitro experiments

Human colon cancer-derived LS180 and SW480 cells were maintained with minimum essential medium (MEM, Gibco Life technology, Carlsbad, CA, USA) and Dulbecco's modified eagle medium (DMEM, Wako, Osaka, Japan) supplemented with 10% heat-inactivated fetal bovine serum (FBS; Invitrogen, Carlsbad, CA, USA) and 50 μg/ml penicillin/streptomycin (Sigma-Aldrich, St. Louis, MO, USA) in a humidified atmosphere with 5% CO_2 at 37 °C.

For *in vitro* PI polyamide incorporation analysis, human colon cancer cells (1×10^5 cells) were grown on glass coverslips and treated with 1 μM of each compound for 2 h. Cells were then washed twice with ice-cold PBS and fixed with 100% methanol for 20 min at −20 °C. Coverslips were mounted with VECTASHIELD Mounting Hard Set Medium with DAPI (Invitrogen, Carlsbad, CA, USA). Fluorescence images were observed under a DMI 4000B confocal laser microscope (Leica Microsystems, Wetzlar, Germany).

For *in vitro* fluorospectrometric analysis, human colon cancer cells (1×10^4 cells) were treated with compounds **1**, **3**, and **5** at the indicated doses for 24 h. Cells were washed twice in PBS. Fluorescence intensity was determined by an ARVO X-3 fluorescence spectrometer (Perkin Elmer, Franklin Lakes, NJ, USA).

5.6. Animal experiments

5.6.1. Ethics statement

Procedures involving animals outlined in the following section satisfied guidelines described in the Proper Conduct of Animal Experiments as defined by the Science Council of Japan. Approval from the Animal Care and Use Committee on the Ethics of the Chiba Cancer Center Institute was obtained prior to experimentation. All experimental steps were carefully performed to ensure the subjects endured minimal suffering.

5.6.2. Xenograft tumor model

Human colon cancer-derived LS180 (3×10^6 cells/mouse) were maintained as described above and subcutaneously inoculated into left flanks of 5- to 8-weeks female BALB/c nude mice (Oriental Yeast, Tokyo, Japan). Compounds **1**, **3**, **5**, or FITC (1 mg/kg), or DMSO/PBS (1.25%, v/v) was intravenously administrated into the tumor-bearing mice when the long diameter of xenograft tumors reached about 1 cm. Fluorescence images of the whole mice were captured at the indicated time points post-administration and the fluorescence intensity of tumor and non-tumor areas were analyzed on a Lumazone imaging system (Roper Bioscience, Tucson, AZ, USA).

For detection of compounds **1**, **3**, and **5** in tissues, the mice were sacrificed at 3 days or 9 days after administration for resection of the following tissues: tumor, liver, kidney, heart, lung, spleen, and brain were resected. Frozen sections were prepared and observed under a DMI 4000B confocal laser microscope (Leica Microsystems, Wetzlar, Germany). Mean fluorescence intensity of tissue sections obtained from the PI polyamide-treated mice (n = 3) was determined by using a WinROOF version 7.0 software (Mitani Corporation, Tokyo, Japan).

5.7. Statistical analysis

Results were presented as mean ± SD of three independent experiments. Data were compared using the unpaired *t*-test, one-way ANOVA, and repeated-measure two-way ANOVA by Ekuseru-Tokei 2010 software (Social Survey Research Information Co., Ltd., Tokyo, Japan) and *p*-value <0.05 was considered to be significant.

Acknowledgments

A. Supplementary data

Supplementary data (additional chromatograms of LC MS and retention times of compounds, fluorescence intensity of compounds, *in vitro* analysis of PI polyamide incorporation by tumor cells and plasma level of these compounds, *in vivo* imaging analysis of tumor-bearing mice treated with compounds and histological analysis of tumor-bearing mice treated with compounds) associated with this article can be found, in the online version, at https://doi.org/10.1016/j.bmc.2018.03.029.

References

1. Pelton JG, Wemmer DE. *Proc Natl Acad Sci USA*. 1989;86:5723–5727.
2. Mrksich M, Wade WS, Dwyer TJ, et al. *Proc Natl Acad Sci USA*. 1992;89:7586–7590.
3. White S, Baird EE, Dervan PB. *Chem Biol*. 1997;4:569–578.
4. Kielkopf CL, Baird EE, Dervan PB, Rees DC. *Nat Struct Biol*. 1998;5:104–109.
5. Mrksich M, Parks ME, Dervan PB. *J Am Chem Soc*. 1994;116:7983–7988.
6. Trauger JW, Baird EE, Dervan PB. *Nature*. 1996;382:559–561.
7. Gottesfeld JM, Neely L, Trauger JW, Baird EE, Dervan PB. *Nature*. 1997;387:202–205.
8. Wang X, Nagase H, Watanabe T, et al. *Cancer Sci*. 2010;101:759–766.
9. Matsuda H, Fukuda N, Ueno T, et al. *Kidney Int*. 2011;79:46–56.
10. Kageyama Y, Sugiyama H, Ayame H, et al. *Acta Oncol*. 2006;45:317–324.
11. Washio H, Fukuda N, Matsuda H, et al. *J Invest Dermatol*. 2011;131:1987–1995.
12. Hargrove AE, Martinez TF, Hare AA, et al. *PLoS ONE*. 2015;10:e0143161.
13. Nickols NG, Dervan PB. *Proc Natl Acad Sci USA*. 2007;104:10418–10423.
14. Hiraoka K, Inoue T, Taylor RD, et al. *Nat Commun*. 2015;6:6706.
15. Raskatov JA, Puckett JW, Dervan PB. *Bioorg Med Chem*. 2014;22:4371–4375.
16. Morita K, Suzuki K, Maeda S, et al. *J Clin Invest*. 2017.
17. Matsuda H, Fukuda N, Ueno T, et al. *J Am Soc Nephrol*. 2006;17:422–432.
18. Fukasawa A, Aoyama T, Nagashima T, et al. *Biopharm Drug Dispos*. 2009;30:81–89.
19. Kamei T, Aoyama T, Tanaka C, et al. *J Biomed Biotechnol*. 2012;2012:715928.
20. Best TP, Edelson BS, Nickols NG, Dervan PB. *Proc Natl Acad Sci USA*. 2003;100:12063–12068.
21. Trauger JW, Baird EE, Mrksich M, Dervan PB. *J Am Chem Soc*. 1996;118:6160–6166.
22. Watanabe T, Shinohara K, Shinozaki Y, et al. *Adv Tech Biol Med*. 2016;4.
23. Valko K. *J Chromatogr A*. 2004;1037:299–310.
24. Nishijima S, Shinohara K, Bando T, et al. *Bioorg Med Chem*. 2010;18:978–983.
25. Iacopetta BJ, Morgan EH. *J Biol Chem*. 1983;258:9108–9115.
26. Abraham MH, Treiner C, Roses M, Rafols C, Ishihama Y. *J Chromatogr A*. 1996;752:243–249.
27. Yang B, Liu H, Chen J, Guan M, Qiu H. *J Chromatogr A*. 2016;1468:79–85.
28. Hsu CF, Phillips JW, Trauger JW, et al. *Tetrahedron*. 2007;63:6146–6151.
29. Nakase I, Kobayashi NB, Takatani-Nakase T, Yoshida T. *Sci Rep*. 2015;5:10300.
30. Raica M, Cimpean AM, Ribatti D. *Eur J Cancer*. 2009;45:1924–1934.
31. Raskatov JA, Szablowski JO, Dervan PB. *J Med Chem*. 2014;57:8471–8476.
32. Hashizume H, Baluk P, Morikawa S, et al. *Am J Pathol*. 2000;156:1363–1380.
33. Matsumura Y, Maeda H. *Cancer Res*. 1986;46:6387–6392.
34. Maeda H, Nakamura H, Fang J. *Adv Drug Deliv Rev*. 2013;65:71–79.
35. Chenoweth DM, Harki DA, Phillips JW, Dose C, Dervan PB. *J Am Chem Soc*. 2009;131:7182–7188.
36. Harki DA, Satyamurthy N, Stout DB, Phelps ME, Dervan PB. *Proc Natl Acad Sci USA*. 2008;105:13039–13044.
37. Synold TW, Xi B, Wu J, et al. *Cancer Chemother Pharmacol*. 2012;70:617–625.
38. Hargrove AE, Raskatov JA, Meier JL, Montgomery DC, Dervan PB. *J Med Chem*. 2012;55:5425–5432.
39. Takagaki T, Bando T, Kitano M, et al. *Bioorg Med Chem*. 2011;19:5896–5902.
40. Bando T, Sugiyama H. *Acc Chem Res*. 2006;39:935–944.
41. Valko K, Du CM, Bevan CD, Reynolds DP, Abraham MH. *J Pharm Sci*. 2000;89:1085–1096.
42. Iwase K, Komatsu K, Hirono S, Nakagawa S, Moriguchi I. *Chem Pharm Bull*. 1985;33:2114–2121.
43. Valkó K, Bevan C, Reynolds D. *Anal Chem*. 1997;69:2022–2029.
44. Sun W-C, Gee KR, Klaubert DH, Haugland RP. *J Org Chem*. 1997;62:6469–6475.

Use of the CRISPR-Cas9 system for genome editing in cultured *Drosophila* ovarian somatic cells

Hirotsugu Ishizu, Tetsutaro Sumiyoshi, Mikiko C. Siomi *

Department of Biological Sciences, Graduate School of Science, The University of Tokyo, 2-11-16 Yayoi, Bunkyo-ku, Tokyo 113-0032, Japan

ABSTRACT

The CRISPR-Cas9 system can be used for genome engineering in many organisms. PIWI-interacting RNAs (piRNAs) play a crucial role in repressing transposons to maintain genome integrity in *Drosophila* ovaries, and cultured ovarian somatic cells (OSCs) are widely used to elucidate the molecular mechanisms underlying the piRNA pathway. However, the germline-specific piRNA amplification system known as the ping-pong machinery does not occur in OSCs, making them unsuitable for elucidating the underlying mechanisms. Mutations in the *lethal (3) malignant brain tumor* gene (*l(3)mbt*) have been shown to cause ectopic expression of germline genes, including ping-pong factors. We therefore performed genome editing of *Drosophila* OSCs using the CRISPR-Cas9 system to achieve *l(3)mbt* knockout, resulting in successful induction of the piRNA amplification machinery. Here, we describe the detailed procedures for generating knockout and knockin OSC cells.

© 2017 Published by Elsevier Inc.

1. Introduction

The CRISPR-Cas9 system was derived from a bacterial defense system against invading viral pathogens, based on the principles of Watson–Crick base pairing, and provides a platform for high-efficiency genome engineering in many organisms [1–5]. The Cas9 nuclease from the type II CRISPR system of *Streptococcus pyogenes* has recently been used successfully for targeted genome editing in a variety of experimental models [6,7]. Cas9 nuclease can be guided to its DNA target by a single-guide RNA (sgRNA), which is a synthetic fusion between the CRISPR RNA and *trans*-activating crRNA [1–3]. Cas9 and its associated sgRNA introduce double-stranded breaks (DSBs) at specific locations in the genome, which are repaired via non-homologous end joining (NHEJ) or homologous recombination [8]. NHEJ repair results in insertion or deletion (indel) mutations at the cut site, which can cause loss of function if the DSB occurs in a coding gene. Homology-directed repair (HDR) is an alternative DNA repair pathway with a typically lower frequency than NHEJ, which can generate precise genetic modifications at a target site in the presence of the corresponding homologous template [9]. HDR can also be used to generate cell lines expressing an endogenous protein tagged with a small peptide, such as FLAG or enhanced green fluorescent protein (EGFP). We recently applied the CRISPR-Cas9 system to cultured ovarian somatic cells (OSCs) to establish OSC derivatives that accommodate the PIWI-interacting RNA (piRNA) amplification machinery termed the ping-pong cycle [10]. In normal, OSCs are devoid of the piRNA amplification machinery [11,12].

piRNAs are small non-coding RNAs (ncRNAs) enriched in the germline in a variety of animals, ranging from sponges, planarians and nematodes to mammals, including humans [13–16]. piRNAs bind PIWI proteins stoichiometrically to form piRNA-induced silencing complexes (piRISCs), which then repress transposons to maintain the integrity of the germline genome [17]. In the absence of piRISC function, the germline genome is damaged by translocation of transposons, leading to impaired germline development and infertility. piRNAs are therefore indispensable for the succession of animal species.

A current model of the piRNA pathway in the fruit fly *Drosophila melanogaster* suggests that piRNAs arise primarily from long ncRNAs transcribed from piRNA clusters, which are interspersed intergenic regions filled with transposon remnants [18]. The primary piRNAs in nurse cells, but not in somatic follicle cells, are subsequently amplified through the ping-pong cycle, where the endonuclease (Slicer) activity of piRISCs proactively consumes transposon transcripts as piRNA precursors to produce secondary piRNAs [18,19]. piRNA amplification and transposon silencing are thus considered to be a coupled event. The ping-pong cycle is a post-transcriptional event involving cytoplasmic PIWI proteins. Specific PIWI proteins, such as Piwi in *Drosophila* and MIWI2 in mice, are transported to the nucleus upon association with piRNAs, where piRISC represses transposons at the transcriptional level [20,21]. The underlying mechanism of nuclear piRISC-driven silencing has

been suggested to mirror that of Ago1-mediated transcriptional silencing in fission yeast [22]. However, the detailed mechanisms responsible for the nuclear event in animals remains unknown.

Various piRNA factors have been identified by genetic screening, mainly in *Drosophila* and mouse models [23–26]. However, the molecular functions of individual factors and the ways in which they interact, physically and/or functionally, to optimize the pathway remain to be determined. piRNAs and piRNA factors are constrained to ovaries and testes, which are not ideal materials for biochemical analyses, and cultured cell lines accommodating the piRNA machinery are therefore required. We previously established *Drosophila* OSCs, which have provided an elegant model for investigating the mechanisms underlying the piRNA pathway, particularly primary piRNA biogenesis and piRISC-mediated transcriptional silencing [11,27]. However, OSCs are not suitable for analyzing the ping-pong cycle because, like somatic follicle cells in the ovaries, OSCs lack the necessary machinery and do not operate the ping-pong cycle.

Mutations in the transcriptional repressor gene *lethal (3) malignant brain tumor* (*l(3)mbt*) result in germline traits in the *Drosophila* brain, including ectopic expression of the ping-pong factors *vasa* and *aubergine* (*aub*), one of the *piwi* members [28]. Based on this earlier finding, we speculated that depletion of *l(3)mbt* in OSCs would activate the piRNA amplification machinery by upregulating the expression of ping-pong factors. Indeed, CRISPR-Cas9-mediated *l(3)mbt* knockout in OSCs led to ectopic expression of genes required for the ping-pong cycle [10]. Traits of secondary piRNAs generated through the ping-pong cycle were also detected in the newly established cells, termed Δmbt-OSCs. Perinuclear foci resembling nuage, known to be the ping-pong centre and thus undetectable in normal OSCs, were also present in Δmbt-OSCs but disappeared following depletion of the core component Vasa by RNA interference, as reported in ovaries [29,30]. Establishment of Δmbt-OSCs will thus aid studies to further our understanding of the mechanisms underlying the ping-pong cycle.

Based on these previous studies, we report a detailed procedure for CRISPR-Cas9-mediated genome editing to produce OSC derivatives with deleted function(s) of specific gene(s) such as *l(3)mbt* (Fig. 1). We also report an additional procedure for producing knockin OSCs using the CRISPR-Cas9 system.

2. Materials and methods

2.1. Production of Cas9 and sgRNA expression vectors

The CRISPR-Cas9 system requires both Cas9 nuclease and gene-specific sgRNA to achieve DSBs at its target site. To select cells

expressing Cas9 at a high level, the *cas9* gene was fused with a T2A-linked blasticidin-resistance gene (Fig. 1). The expression vector pBS-Hsp70-Cas9 (Addgene plasmid #46294) was linearized by inverse polymerase chain reaction (PCR) using primers hybridizing to regions both upstream and downstream of the stop codon. The resulting PCR fragment was ligated with the T2A-linked blasticidin-resistance gene synthesized by gBlocks® Gene Fragments (Integrated DNA Technologies) using a NEB HiFi assembly kit, according to the manufacturer's instructions.

sgRNAs show considerable variation in indel-induction efficiency. We therefore recommend designing and preparing multiple sgRNAs for each target gene. Two sgRNAs can then be introduced into cells simultaneously to increase the efficiency of generating knockout mutants. This may result in the removal of a genomic region between the two sgRNA target sites, resulting in the production of a large-deletion mutant of the target gene. To avoid off-targeting problems of sgRNAs, we used the online sgRNA design tool flyCRISPR Target Finder (http://tools.flycrispr.molbio.wisc.edu/targetFinder/) [10].

The U6 RNA polymerase III promoter is widely used to express sgRNA *in vivo*. This promoter requires a guanine (G) to initiate transcription, and an extra G is therefore added at the 5′ of the sgRNA, even though the 20-nt sgRNA sequence is not designed to begin with a G [5,31]. For constructing sgRNA expression, a single-stranded DNA oligo encoding the sgRNA is annealed with its complementary oligo, and then resultant double-stranded DNA oligo is phosphorylated and ligated with BbsI-digested pU6-BbsI-chiRNA (Addgene plasmid #45946), as described previously [5] (Fig. 2A). The oligonucleotides used in this work are listed in Supplemental Table 1.

2.2. Production of HDR donor vector

To generate a cell line stably expressing an endogenous protein tagged with a 3 × FLAG peptide (or other peptide such as HA) at the N- (or C-) terminal end of the protein, the sgRNA target site should be designed to be closely proximal to the start codon (distance limit of about 50 nucleotides (nt)), or the stop codon in the case of C-terminal tagging (Fig. 2B).

To insert a 3 × FLAG tag into an endogenous protein of interest, vectors individually expressing Cas9 and sgRNA should be co-introduced into cells along with an HDR vector containing a sequence encoding a 3 × FLAG peptide flanked by homologous arms at both ends, corresponding to sequences immediately upstream (5′) and downstream (3′) of the CRISPR-Cas9 target site (Fig. 2B). The recommended length of the homologous arms is 500–800 nt. The HDR vector is constructed by individually
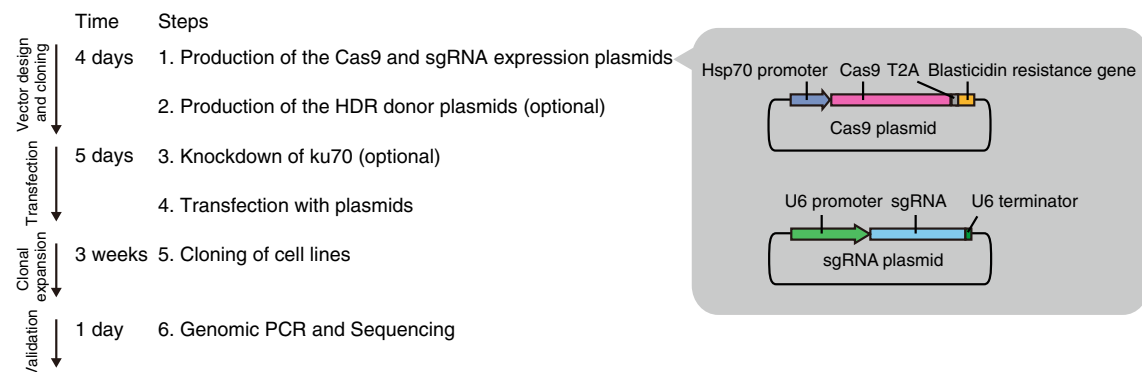

Fig. 1. Flow of mutant generation in OSCs using the CRISPR-Cas9 system. The Cas9 plasmid is designed to express the *SpCas9* and blasticidin-resistance genes simultaneously. Untransfected OSCs can thus be eliminated from culture by blasticidin treatment, thus facilitating cloning of OSC derivatives. A short DNA fragment encoding sgRNA is inserted in the pU6-BbsI-chiRNA plasmid under the U6 promoter. For more detail, see Fig. 2. Cas9 and sgRNA are co-expressed in OSCs, which induce NHEJ-mediated indel mutations at the target loci. To tag a small peptide onto an endogenous protein, an HDR donor plasmid should be co-introduced into OSCs. Knockdown of the NHEJ component *ku70* may enhance the knockin efficiency. Validation is performed by genomic PCR and sequencing of the product.
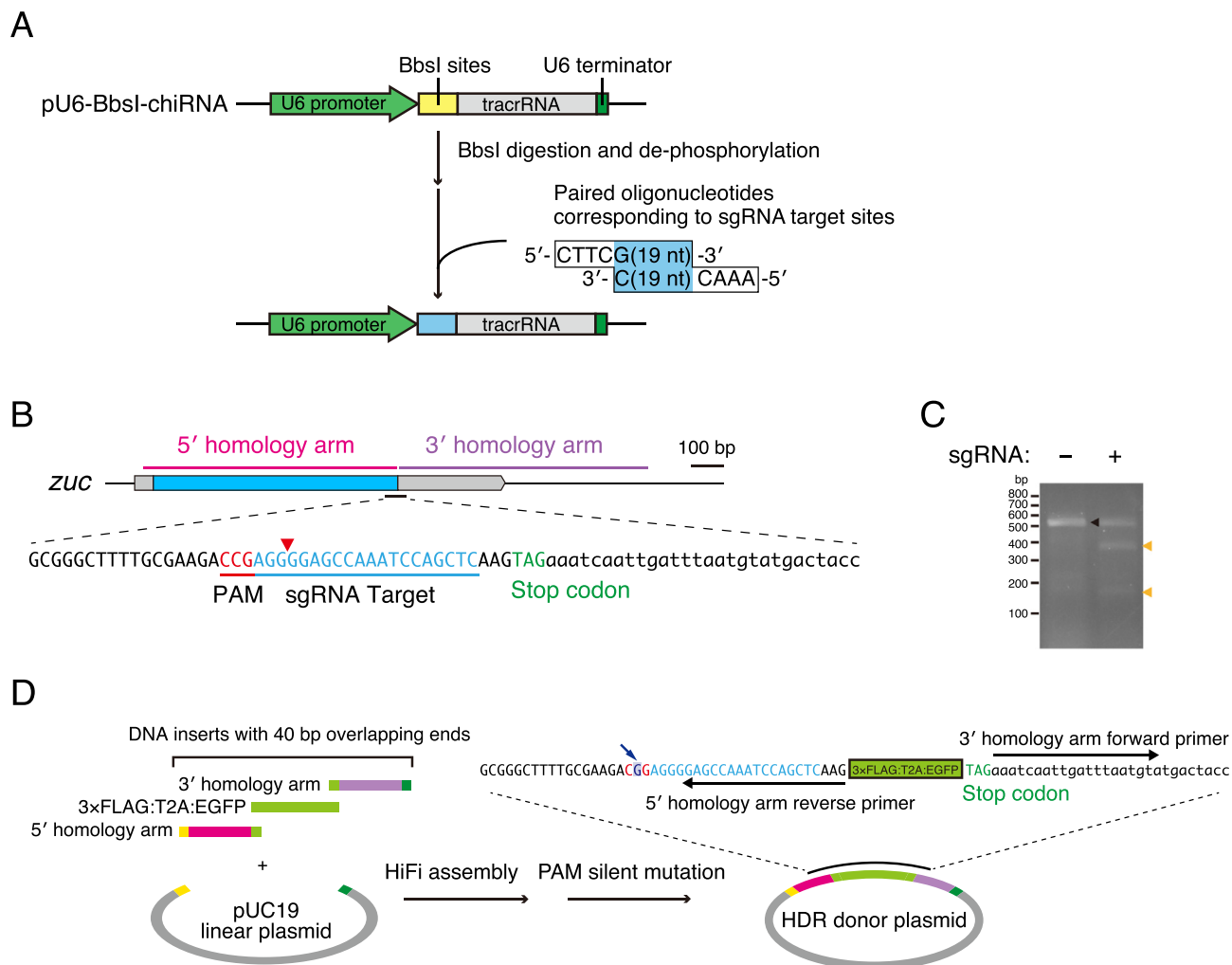
Fig. 2. Construction of sgRNA and HDR donor plasmids. (A) Flow of sgRNA plasmid construction. A short DNA fragment (20 nt) encoding sgRNA designed to have 4-nt overhangs at both 5′ and 3′ ends is inserted into pU6-BbsI-chiRNA at its BbsI site. The sgRNA encoding sequence should start with a G for efficient U6-driven expression. (B) Schematic structure of the *zuc* gene. Sequence of the sgRNA target site (blue letters) proximal to the stop codon (green) and its flanking regions is shown. The PAM sequence is shown in red. The predicted Cas9 cleavage site is indicated by a red triangle. The regions corresponding to 5′ and 3′ homology arms are marked on the top. (C) Mutation induced by the CRISPR-Cas9 system was detected using a Guide-it Mutation Detection Kit. Black triangle indicates the PCR product amplified using the wild-type control genome (sgRNA: −). After CRISPR-Cas9 treatment (sgRNA: +), two shorter DNA fragments were detected (orange triangles), indicating successful genome editing. (D) Flow of HDR donor plasmid construction for tagging a 3 × FLAG peptide at the C-terminal end of Zuc. PCR-amplified 5′ and 3′ homology arms and a synthesized 3 × FLAG:T2A:EGFP fragment are assembled into a linearized pUC19 vector using HiFi assembly reaction. The regions of each homology arm are depicted in (B). PAM silent mutation indicated by blue arrow (on top) was introduced by site-directed mutagenesis. The primer sequences used in this section are listed in Supplemental Table 1. (For interpretation of the references to colour in this figure legend, the reader is referred to the web version of this article.)

amplifying DNA sequences corresponding to the 5′ and 3′ homologous arms by PCR using genomic DNA as a template. To locate a 3 × FLAG tag at the N-terminus of the protein, a reverse primer annealing to the 3′ end of the 5′ arm, and a forward primer annealing to the 5′ end of the 3′ arm are designed to be next to the start codon. To locate a 3 × FLAG tag at the C-terminus, the reverse and forward primers are designed to be next to the stop codon (Fig. 2D). Two additional primers to induce homologous recombination are designed to anneal to the regions 500–800 nt from the start or stop codon, using Primer3 (http://bioinfo.ut.ee/primer3-0.4.0/). Homology tails for HiFi DNA assembly are added in the second PCR step.

Two additional sequences encoding a self-cleaving T2A peptide and an EGFP can also be inserted into the HDR vector, making it easier to screen clonal cell lines with an integrated 3 × FLAG tag. In this work, two gBlocks® Gene Fragments (Integrated DNA Technologies) containing a EGFP, T2A peptide, and 3 × FLAG were synthesized to produce an EGFP:T2A:3 × FLAG or 3 × FLAG:T2A:EGFP fragment for tagging the N- or C-terminal end of the protein,

respectively. This fusion fragment and two PCR products corresponding to the two homology arms were ligated with a linearized pUC19 vector using a HiFi DNA assembly kit. To avoid the donor DNA template being cleaved by Cas9 *in vivo*, a silent mutation should be introduced into the PAM site in the homology arm using a site directed mutagenesis kit. Notably, *S. pyogenes* Cas9 (SpCas9) also recognizes "NAG" as the PAM sequence, albeit less efficiently than "NGG" [32,33], and mutating the PAM site to "NAG" should thus be avoided. An example of the generation of a HDR donor vector of zucchini (*zuc*) is shown in Fig. 2D.

1. Extract genomic DNA from OSCs (or the cells used in your study) using QuickExtract solution (Epicentre), according to the manufacturer's instructions. Adjust the final concentration of the extracted DNA to 100 ng/µl with ddH$_2$O.
2. To amplify the 5′ and 3′ homology arms, add 0.2 µl of Q5 High-Fidelity DNA Polymerase to a reaction mixture containing 4 µl of 5 × Q5 Reaction Buffer, 2 µl of 2 mM dNTPs, 1 µl of 10 µM forward primer, 1 µl of 10 µM reverse primer,

1 μl of 100 ng/μl DNA template, and 10.8 μl of ddH₂O to make a final volume of 20 μl. PCR is then performed under the following conditions: 98 °C 30 s, followed by 30 cycles of 98 °C 10 s, 55 °C 30 s, and 72 °C 30 s.

3. Run the PCR products on a 2% (wt/vol) agarose gel and purify the corresponding bands using a gel extraction kit (Nippon Genetics), following the manufacturer's instructions. Elute the PCR products in 20 μl ddH₂O or TE buffer.

4. Check the DNA concentration using a Nanodrop spectrophotometer or similar machine and adjust to a final concentration of 5 ng/μl with ddH₂O.

5. Set up the PCR reactions for amplifying each homology arm using Q5 High-Fidelity DNA Polymerase in 20 μl total volume (4 μl 5 × Q5 Reaction Buffer, 2 μl 2 mM dNTPs, 1 μl 10 μM 2nd PCR forward primer, 1 μl 10 μM 2nd PCR reverse primer, 1 μl 5 ng/μl DNA template, 10 μl ddH₂O, and 0.2 μl Q5 DNA Polymerase).

6. Perform PCR with the following conditions: 98 °C 30 s, 15 cycles of 98 °C 10 s, 55 °C 30 s, and 72 °C 30 s, followed by 4 °C hold.

7. Run 20 μl of the PCR products on a 2% (wt/vol) agarose gel to detect single-band products. Purify the PCR products using a gel extraction kit, following the manufacturer's instructions and elute in 20 μl ddH₂O or TE buffer.

8. Quantify the concentration of the products using a Nanodrop spectrophotometer.

9. Carry out the HiFi DNA assembly reaction to produce the HDR donor vector using 50 ng of linearized pUC19 backbone (Clontech) and an equimolar amount of each insert in 20 μl total volume, incubate at 50 °C for 1 h, and transform the plasmid into DH5-alpha competent cells.

10. Verify the sequence of the donor vector by sequencing from both ends of the integration site using M13 forward (GTAAAACGACGGCCAGT) and reverse primers (CAGGAAACAGCTATGAC).

11. Digest 2 μg of the plasmid with the restriction enzyme used to cut the vector backbone (e.g. ScaI, Fig. 2D) for at least 1 h, and then purify the linearized plasmid using a DNA purification kit (Nippon Genetics), following the manufacturer's instructions.

2.3. OSC culture and preparation of fly extract

OSCs are cultured in Shields and Sang M3 insect medium containing 10% fetal bovine serum, 10 μg/ml insulin, 0.6 mg/ml glutathione, and 10% fly extract (see below) at 26 °C, in Nunclon™ Delta Surface petri dishes for adherent cells (Thermo Fisher) [34]. Cells are typically split every 2–3 days at a ratio of 1:10. For passaging, cells are washed with phosphate-buffered saline (PBS) and treated with 0.05% trypsin/EDTA for 1 min at 37 °C, followed by addition of culture medium to inactivate the trypsin. Cells are loosened by pipetting, and transferred to new dishes containing fresh culture medium. The quality of the fly extract is critical for the successful maintenance of OSCs and is prepared as follows:

1. Collect 10 g of anesthetized Oregon R adult *Drosophila* in a 50-ml centrifuge tube (10*g* of flies normally yields 50 ml of fly extract). Prepare 50 ml of M3 medium containing 10% fetal bovine serum (M3/FBS) and keep on ice.

2. Add 40 ml of 70% ethanol to the tube containing the flies and shake gently for 5 min at room temperature.

3. Drain off the 70% ethanol by passing the contents of the tube through a metal mesh (500 μm, 75 × 20 mm) and wash the flies several times with PBS. The flies can be stored at this stage at −80 °C for future use.

4. Transfer the flies to an electric food mill (Tescom, TML161 or similar), add 30 ml of ice-cold M3/FBS medium (3 ml/g of flies), and grind the flies for 10 s. Alternatively, the flies can be homogenized using a pestle on ice.

5. Transfer the fly homogenate into a fresh 50-ml tube, place the tube on ice, and add 20 ml of ice-cold M3/FBS medium.

6. Centrifuge the homogenate at 4840×g at 4 °C for 10 min and transfer the supernatant into a fresh 50-ml tube.

7. Transfer the supernatant into a Hybri-bag (Cosmo Bio, SE-S-1001-EX) and seal using a heat sealer.

8. Incubate the bag containing the supernatant at 60 °C in a water bath for 5 min, and then chill on ice for 5 min.

9. Transfer the supernatant into a fresh 50-ml tube and centrifuge at 10,000×g at 4 °C for 3 min.

10. Transfer the supernatant into a fresh 50-ml tube and centrifuge at 10,000×g at 4 °C for 15 min, and then transfer the supernatant into another fresh 50-ml tube.

11. Filter-sterilize the supernatant through a 0.45 μm filter and store the fly extract at −20 °C. We recommend dividing the supernatant into 10-ml and 40-ml aliquots before storing at −20 °C.

12. To make the complete medium for OSCs, thaw the fly extract on ice and add it to a concentration of 10% in Shields and Sang M3 insect medium containing 10% fetal bovine serum, 10 μg/ml insulin, and 0.6 mg/ml glutathione. Filter the medium using a 0.22-μm filter and keep at 4 °C until use.

2.4. Transfection of OSCs with Cas9 and sgRNA vectors

Several transfection approaches, including lipofection and electroporation, achieve efficient transfection of OSCs with plasmids [34]. We use ScreenFect A (Wako Pure Chemical Industries), which show low cytotoxicity and low costs. Previous reports suggested that suppression of key molecules in NHEJ such as KU70, KU80, and DNA ligase IV, could increase the efficiency of HDR-mediated knockin in various organisms [35,36]. We therefore knocked down KU70 prior to OSC transfection with Cas9, sgRNA, and donor vectors to enhance HDR efficiency. Effective gene knockdown in OSCs can be achieved by introducing siRNA duplexes using an Amaxa SF Cell Line 96-well Nucleofector Kit (Lonza).

2.4.1. ku70 knockdown in OSCs by siRNA transfection

1. Harvest OSCs by treating with trypsin as described above, and count the cell numbers.

2. Transfer 2 × 10⁶ cells per transfection to a centrifugation tube and spin at 90×g at room temperature for 10 min.

3. Discard the supernatant and resuspend the cell pellet in 20 μl Nucleofector Solution SF per 2 × 10⁶ cells.

4. Mix 20 μl of cell suspension with 40 pmol siRNA targeting *ku70* (see Supplemental Table 1 for the siRNA sequence). The volume of siRNA solution should be ≤1 μl.

5. Transfer the mixture into a well of a 96-well Nucleocuvette plate and then start the program DG-150 to achieve siRNA transfection.

6. After treatment, incubate the Nucleocuvette plate for 10 min at room temperature.

7. Resuspend the transfected cells in 80 μl of culture medium (see 2.3.12) per well by gentle pipetting, and place in a 3.5-cm dish containing 2 ml of culture medium.

8. Incubate the cells for 24 h in a humidified 26 °C incubator (Approximately 50% cell confluency is desired at this stage).

2.4.2. OSC transfection with plasmids

1. At 24 h prior to transfection, plate 2×10^6 OSCs in a 3.5-cm dish containing 2 ml of culture medium. By the following day (i.e., the day of transfection), the cell confluency should be about 50%. These conditions are required for optimal transfection.
2. Dilute 4 µl of ScreenFect A in ScreenFect A Dilution Buffer to a final volume of 120 µl, mix well by pipetting, and incubate for 2–5 min at room temperature.
3. To perform NHEJ-mediated knockout in OSCs, add 600 ng of Cas9 vector and 600 ng of sgRNA vector (see 2.1) (or 300 ng of each of two sgRNA vectors) in ScreenFect A Dilution Buffer to a final volume of 120 µl (the total amount of DNA added to 120 µl of ScreenFect A Dilution Buffer should be ≤1.2 µg), and mix by pipetting. To perform HDR-mediated knockin in OSCs, add 600 ng of pCas9 vector, 300 ng of sgRNA vector (or 150 ng of each of two sgRNA vectors), and 300 ng of linearized donor vector in ScreenFect A Dilution Buffer to a final volume of 120 µl, and mix by pipetting.
4. Combine the reagent mixture prepared in 2.4.2.2 and the plasmid mixture prepared in 2.4.2.3 above, mix well by pipetting, and incubate for 20 min at room temperature.
5. Drop the mixture slowly onto the OSCs in the dish.
6. Incubate the cells for 48 h at 26 °C before passaging for blasticidin selection or harvesting for mutation detection (see Sections 2.5 and 2.6).

2.5. Mutation detection assay

The induction of indel mutations by the CRISPR-Cas9 system can be confirmed using heteroduplex double-stranded DNA-specific nucleases such as CEL-1 and T7E1 [37]. We assess CRISPR-Cas9-mediated cleavage activities in OSCs using a Guide-it™ Mutation Detection Kit (Clontech). Two PCR (forward and reverse) primers annealing to each side of the Cas9/sgRNA target site, respectively, should be designed using Primer3 (see 2.2 above) and prepared. The ideal length of the DNA fragments amplified by PCR is 400–800 bp.

1. Extract genomic DNA from OSCs treated with the CRISPR-Cas9 system using QuickExtract solution (Epicentre), according to the manufacturer's instructions. Adjust the final DNA concentration to 100 ng/µl with ddH₂O. Genomic DNA extracted from non-transfected OSCs should be used as a negative control.
2. Set up the PCR reaction by adding 10 µl of 5 × Q5 Reaction Buffer, 5 µl of 2 mM dNTPs, 2.5 µl of 10 µM forward primer, 2.5 µl of 10 µM reverse primer, 1 µl of DNA template (100 ng/µl), 28.5 µl of ddH₂O, and 0.5 µl of Q5 High-Fidelity DNA Polymerase to a PCR tube. The primer sequences are listed in Supplemental Table 1.
3. Carry out the PCR under the following conditions: 98 °C 30 s, followed by 30 cycles of 98 °C 10 s, 55 °C 30 s, and 72 °C 30 s.
4. Run 5 µl of the reaction mixture on a 2% (wt/vol) agarose gel to check the products and estimate the concentrations. If non-specific amplification is observed, the PCR conditions may need to be optimized, possibly including redesigning the primers. The DNA concentration of the PCR products should be >20 ng/µl.
5. Add 15 µl of the PCR products to a fresh PCR tube, heat at 95 °C for 5 min, and cool slowly to 85 °C at −2 °C/s, followed by further cooling to 25 °C at −0.1 °C/s.
6. Add 1 µl of Guide-it Resolvase (Clontech) and incubate at 37 °C for 15 min.
7. Analyze the resulting products by 2% (wt/vol) agarose gel electrophoresis (Fig. 2C).

2.6. Cloning of cell lines after the CRISPR-Cas9 treatment

The Cas9 vector contains a blasticidin-resistance gene, and the genome-edited cell lines can therefore be selected by adding blasticidin to the culture medium. We use blasticidin 50 µg/ml, at which concentration all untransfected OSCs should be dead after 1 week of drug exposure. In addition to drug-selection of transfected cells, monoclonal stable cell lines may be isolated by limiting dilution; however, OSCs may need a certain number of neighboring cells to grow appropriately, making it difficult to obtain pure clones by single-cell dilution using 96-well plates. We isolate monoclones by seeding selected cells sparsely in a 6-cm dish and allowing them to expand and form discernible colonies for 1–2 weeks. Cell clumps and debris can be removed using a cell strainer prior to seeding. The individual colonies are then transferred to 24-well plates using a Gilson pipette with a sterile 10 µl tip. An untransfected-cell sample should be included as a negative control for selection. An example of the generation of HDR-mediated knockin at the *zuc* locus is shown in Fig. 3. We isolated 15 clones in this experiment. Variation by genomic PCR and sequencing confirmed that 8 out of 15 (53%) of clones were bi-allelic knockin and 4 out of 15 (27%) of clones were mono-allelic knockin.

1. At 48 h post-transfection, change the blasticidin-containing medium to a final concentration of 50 µg/ml, and incubate at 26 °C for 48 h.
2. Remove the medium, wash the cells once in PBS, add 0.5 ml 0.05% trypsin/EDTA, and incubate for 2 min at 37 °C.
3. Add 0.5 ml of medium to inactivate the trypsin, and dissociate the cells by pipetting.
4. Pass the cell suspension through a 40-µm Flowmi™ Cell Strainer to eliminate clumps and debris, and then count the living cells using trypan blue staining.
5. Seed the cells at a density of 5×10^5 cells per 6-cm dish in 4 ml of medium containing blasticidin, and incubate for 24 h.
6. Repeat steps 2.7.2–2.7.4, and then seed the cells at a density of 5000–10,000 cells per 6-cm dish in 4 ml of medium containing blasticidin, and incubate for 48–72 h.
7. Remove the medium, add 4 ml of fresh, blasticidin-free medium, and culture the cells for 7–10 days to form colonies (Fig. 3A), changing the medium every 2–3 days. At least 20 colonies should have grown per dish.
8. To pick the colonies, prepare 24-well dishes with 500 µl medium in each well. Under a microscope, carefully scrape a colony off using a sterile tip of a P2 Gilson pipette, and then transfer the colony suspension to a well in a 24-well dish. Repeat the procedure for the other colonies and incubate for 48–72 h.
9. Remove the medium and wash the cells once in PBS. Add 0.2 ml of 0.05% trypsin/EDTA and incubate for 2 min at 37 °C.
10. Add 0.5 ml of medium to inactivate the trypsin, and dissociate the cells by pipetting. Transfer the cell suspension to another well of a 24-well plate and incubate for 48–72 h.
11. Once the clones have expanded to high confluency, they can be passaged to a 6-well plate and maintained as described in Section 2.3. After expansion, assay each cell line via PCR or western blotting in order to validate the genome edit (Fig. 3B–D).

3. Troubleshooting

1. Cell viability is low after blasticidin selection: the transfection efficiency may be low. Check cell confluency and DNA quality. The optimal confluency at the time of transfection is around
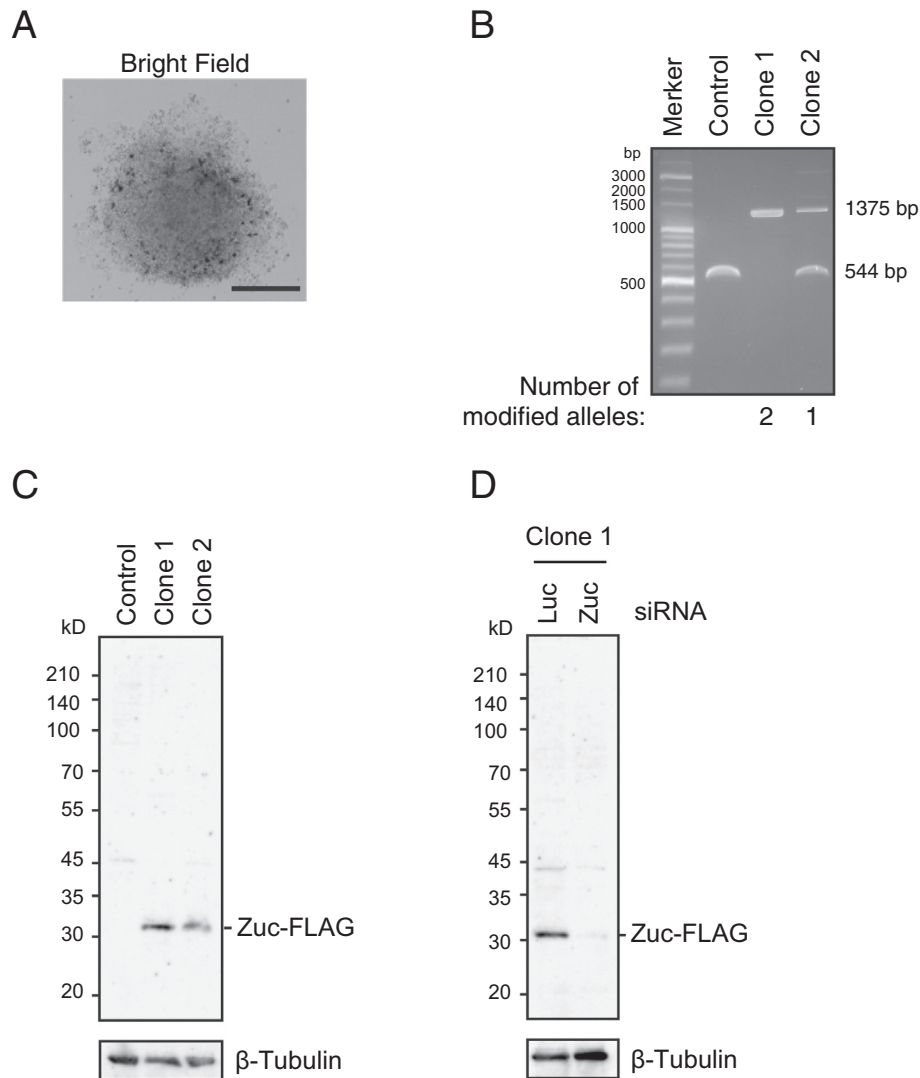
Fig. 3. Cloning and evaluation of genome-edited OSC clone. (A) Bright-field microscope image of cell colony. Scale bar, 200 μm. (B) Genomic PCR product confirmed insertion of a 3 × FLAG peptide at the C-terminal end of Zuc. Clone 1 and 2 are biallelic modification and monoallelic modification, respectively. (C) Western blotting showed expression of Zuc-FLAG. (D) Western blot analysis of clone 1 after transfection with siRNA targeting luciferase or *zuc*. Correct integration of FLAG tag was confirmed by significant reduction of signal after *zuc* knockdown. Western blotting was performed as described previously [10] with monoclonal anti-FLAG (anti-DDDDK, MLB) and anti-β-Tubulin (E7, DSHB).

50%; higher cell densities cause lower transfection efficiencies. Repurify DNA or prepare new DNA for transfection.

2. Number of colonies is low: confirm the number of living cells by trypan blue staining before seeding, and if necessary increase the number of cells per dish. The transient expression of the blasticidin-resistance gene in this method means that prolonged treatment with blasticidin may severely reduce the number of colonies.

3. Too many colonies obtained: cells were not dissociated well and/or diluted correctly. Dissociate into single cells and filter through a cell strainer to remove clumps and debris before seeding.

4. No HDR-mediated knockin mutants obtained: ensure the efficacy of the sgRNA by mutation detection assay (Section 2.5). Redesign the HDR donor template, e.g., increase the size of the homology arms, and ensure that a silent mutation was introduced at the PAM site.

4. Concluding remarks/perspective

Although the concept is already widely accepted, we confirmed the CRISPR-Cas9 system as a powerful, convenient, and rapid tool for genome-editing, even in *Drosophila*-ovary-derived OSCs as used in our piRNA research. Using the CRISPR-Cas9 system enabled us to obtain mutant OSCs, such as Δmbt-OSCs, in less than 1 month. The nuage, perinuclear structure where piRNA biogenesis occurs was detected in Δmbt-OSCs but undetected in parental OSCs, demonstrating the suitability of Δmbt-OSCs, but not OSCs, for investigating the requirements of nuage formation. The detailed procedures reported in this study, from plasmid construction to transfection conditions and cloning of genome-edited cells, were effective in OSCs but have not yet been tried in other cultured cells. However, we suggest that the same procedure may be suitable for use in other cells, possibly with some modifications. The CRISPR-Cas9 system continues to be constantly modified to improve its efficiency and reduce off-target activity, the latter by the use of Cas9 nickase [38]. Attempts have also been made to apply the system for other purposes, such as the artificial alteration of chromatin formation, and CRISPR interference was recently performed by expressing a catalytically dead Cas9 fused with a Krüppel-associated box domain, which represses transcription [39]. We are currently engaged in applying these new

CRISPR-Cas9-based techniques in OSCs to increase their potential for revealing new discoveries in piRNA studies.

Acknowledgements

Appendix A

Reagent

Name	Manufacturer
Agarose	Nippon Gene, Cat# 312-01193
BbsI	NEB, Cat# R0539S
Blasticidin	ThermoFisher Scientific, Cat# R21001
DH5α Competent Cells	ThermoFisher Scientific, Cat# 18258012
DNA Oligonucleotides	ThermoFisher Scientific
dNTPs	Roche, Cat# 11969064001
FBS	Atlas Biologicals, Cat# EF-0500-A
gBlock Gene Fragments	Integrated DNA Technologies
Gel/PCR Extraction Kit	Nippon Genetics, Cat# FG-91202
Guide-it Mutation Detection Kit	Clontech, Cat# 631448
Insulin	Wako Pure Chemical Industries, Cat# 099-06473
L-Glutathione	Sigma, Cat# G6013-10G
Monoclonal ANTI-FLAG M2 antibody	Sigma, Cat# F3165-1MG
HiFi DNA Assembly Master Mix	NEB, Cat# E2621S
Cell Culture/Petri Dishes (35 mm)	ThermoFisher Scientific, Cat# 153066
Cell Culture/Petri Dishes (60 mm)	ThermoFisher Scientific, Cat# 150288
OSC	Our lab
pBS-Hsp70-Cas9	Addgene #46294
pU6-BbsI-chiRNA	Addgene #45946
pUC19 Linearized Vector	Clontech, Cat# 639648 (The pUC19 Linearized Vector is provided as a part of In-Fusion Cloning Kits.)
Q5 High-Fidelity DNA Polymerase	NEB, Cat# M0491S
QuickExtract DNA Extraction Solution	Epicentre, Cat# QE0905T
ScaI-HF	NEB, cat# R3122S
ScreenFect A	Wako Pure Chemical Industries, Cat# 297-73204
SF Cell Line 96-well Nucleofector Kit	Lonza, Cat# V4SC-2096
Shields and Sang M3 Insect Medium	Sigma, Cat# S3652-1L
siRNA	Sigma
Trypsin/EDTA (0.05%)	ThermoFisher Scientific, Cat# 25300062

Appendix B. Supplementary data

Supplementary data associated with this article can be found, in the online version, at http://dx.doi.org/10.1016/j.ymeth.2017.05.021.

References

[1] M. Jinek, K. Chylinski, I. Fonfara, M. Hauer, J.A. Doudna, E. Charpentier, Science 337 (2012) 816–821.
[2] L. Cong, F.A. Ran, D. Cox, S. Lin, R. Barretto, N. Habib, P.D. Hsu, X. Wu, W. Jiang, L.A. Marraffini, F. Zhang, Science 339 (2013) 819–823.
[3] P. Mali, L. Yang, K.M. Esvelt, J. Aach, M. Guell, J.E. DiCarlo, J.E. Norville, G.M. Church, Science 339 (2013) 823–826.
[4] M. Jinek, A. East, A. Cheng, S. Lin, E. Ma, J. Doudna, Elife 2 (2013) e00471.
[5] F.A. Ran, P.D. Hsu, J. Wright, V. Agarwala, D.A. Scott, F. Zhang, Nat. Protoc. 8 (11) (2013) 2281–2308.
[6] P.D. Hsu, E.S. Lander, F. Zhang, Cell 157 (2014) 1262–1278.
[7] J.D. Sander, J.K. Joung, Nat. Biotechnol. 32 (2014) 347–355.
[8] M. Bibikova, M. Golic, K.G. Golic, D. Carroll, Genetics 161 (2002) 1169–1175.
[9] M.R. Capecchi, Science 244 (1989) 1288–1292.
[10] T. Sumiyoshi, K. Sato, H. Yamamoto, Y.W. Iwasaki, H. Siomi, M.C. Siomi, Genes Dev. 30 (2016) 1617–1622.
[11] K. Saito, S. Inagaki, T. Mituyama, Y. Kawamura, Y. Ono, E. Sakota, H. Kotani, K. Asai, H. Siomi, M.C. Siomi, Nature 461 (2009) 1296–1299.
[12] M.C. Siomi, K. Sato, D. Pezic, A.A. Aravin, Nat. Rev. Mol. Cell Biol. 12 (2011) 246–258.
[13] A.A. Aravin, G.J. Hannon, J.J. Brennecke, Science 318 (2007) 761–764.
[14] M. Ghildiyal, P.D. Zamore, Nat. Rev. Genet. 10 (2009) 94–108.
[15] C. Juliano, J. Wang, H. Lin, Annu. Rev. Genet. 45 (2011) 447–469.
[16] Y.W. Iwasaki, M.C. Siomi, H. Siomi, Annu. Rev. Biochem. 84 (2015) 405–433.
[17] C.D. Malone, G.J. Hannon, Cell 136 (2009) 656–668.
[18] J.J. Brennecke, A.A. Aravin, A. Stark, M. Dus, M. Kellis, R. Sachidanandam, G.J. Hannon, Cell 128 (2007) 1089–1103.
[19] L.S. Gunawardane, K. Saito, K.M. Nishida, K. Miyoshi, Y. Kawamura, T. Nagami, H. Siomi, M.C. Siomi, Science 315 (2007) 1587–1590.
[20] S. Kuramochi-Miyagawa, T. Watanabe, K. Gotoh, Y. Totoki, A. Toyoda, M. Ikawa, N. Asada, K. Kojima, Y. Yamaguchi, T.W. Ijiri, K. Hata, E. Li, Y. Matsuda, T. Kimura, M. Okabe, Y. Sakaki, H. Sasaki, T. Nakano, Genes Dev. 22 (2008) 908–917.
[21] A.A. Aravin, R. Sachidanandam, D. Bourc'his, C. Schaefer, D. Pezic, K.F. Toth, T. Bestor, G.J. Hannon, Mol. Cell 31 (2008) 785–799.
[22] D. Moazed, Nature 457 (2009) 413–420.
[23] K. Saito, H. Ishizu, M. Komai, H. Kotani, Y. Kawamura, K.M. Nishida, H. Siomi, M.C. Siomi, Genes Dev. 24 (2010) 2493–2498.
[24] F. Muerdter, P.M. Guzzardo, J. Gillis, Y. Luo, Y. Yu, C. Chen, R. Fekete, G.J. Hannon, Mol. Cell 50 (2013) 736–748.
[25] B. Czech, J.B. Preall, J. McGinn, G.J. Hannon, Mol. Cell 50 (2013) 749–761.
[26] D. Handler, K. Meixner, M. Pizka, K. Lauss, C. Schmied, F.S. Gruber, J.J. Brennecke, Mol. Cell 50 (2013) 762–777.
[27] Y. Niki, T. Yamaguchi, A.P. Mahowald, Proc. Natl. Acad. Sci. U.S.A. 103 (2006) 16325–16330.
[28] A. Janic, L. Mendizabal, S. Llamazares, D. Rossell, C. Gonzalez, Science 330 (2010) 1824–1827.
[29] A.K.A. Lim, T.T. Kai, Proc. Natl. Acad. Sci. U.S.A. 104 (2007) 6714–6719.
[30] C.D. Malone, J.J. Brennecke, M. Dus, A. Stark, W.R. McCombie, R. Sachidanandam, G.J. Hannon, Cell 137 (2009) 522–535.
[31] S.J. Gratz, F.P. Ukken, C.D. Rubinstein, G. Thiede, L.K. Donohue, A.M. Cummings, K.M. O'Connor-Giles, Genetics 196 (2014) 961–971.
[32] W. Jiang, D. Bikard, D. Cox, F. Zhang, L.A. Marraffini, Nat. Biotechnol. 31 (2013) 233–239.
[33] P.D. Hsu, D.A. Scott, J.A. Weinstein, F.A. Ran, S. Konermann, V. Agarwala, Y. Li, E.J. Fine, X. Wu, O. Shalem, T.J. Cradick, L.A. Marraffini, G. Bao, F. Zhang, Nat. Biotechnol. 31 (2013) 827–832.
[34] K. Saito, Methods Mol. Biol. 1093 (2014) 25–33.
[35] S. Ma, J. Chang, X. Wang, Y. Liu, J. Zhang, W. Lu, J. Gao, R. Shi, P. Zhao, Q. Xia, Sci. Rep. 4 (2014) 4489.
[36] V.T. Chu, T. Weber, B. Wefers, W. Wurst, S. Sander, K. Rajewsky, R. Kühn, Nat. Biotechnol. 33 (2015) 543–548.
[37] L. Vouillot, A. Thélie, N. Pollet G3 (5) (2015) 407–415.
[38] B. Shen, W. Zhang, J. Zhang, J. Zhou, J. Wang, L. Chen, L. Wang, A. Hodgkins, V. Iyer, X. Huang, W.C. Skarnes, Nat. Methods 11 (2014) 399–402.
[39] L.A. Gilbert, M.H. Larson, L. Morsut, Z. Liu, G.A. Brar, S.E. Torres, N. Stern-Ginossar, O. Brandman, E.H. Whitehead, J.A. Doudna, W.A. Lim, J.S. Weissman, L.S. Qi, Cell 154 (2013) 442–451.

TRANSPARENT
PROCESS

THE
EMBO
JOURNAL

Article

In vitro expansion of mouse primordial germ cell-like cells recapitulates an epigenetic blank slate

Hiroshi Ohta[1,2,*,†] (iD), Kazuki Kurimoto[1,2,†], Ikuhiro Okamoto[1,2], Tomonori Nakamura[1,2], Yukihiro Yabuta[1,2], Hidetaka Miyauchi[1], Takuya Yamamoto[3,4,5], Yukiko Okuno[6], Masatoshi Hagiwara[7], Kenjiro Shirane[8,9], Hiroyuki Sasaki[8] & Mitinori Saitou[1,2,3,4,**] (iD)

Abstract

The expansion of primordial germ cells (PGCs), the precursors for the oocytes and spermatozoa, is a key challenge in reproductive biology/medicine. Using a chemical screening exploiting PGC-like cells (PGCLCs) induced from mouse embryonic stem cells (ESCs), we here identify key signaling pathways critical for PGCLC proliferation. We show that the combinatorial application of Forskolin and Rolipram, which stimulate cAMP signaling via different mechanisms, expands PGCLCs up to ~50-fold in culture. The expanded PGCLCs maintain robust capacity for spermatogenesis, rescuing the fertility of infertile mice. Strikingly, during expansion, PGCLCs comprehensively erase their DNA methylome, including parental imprints, in a manner that precisely recapitulates genome-wide DNA demethylation in gonadal germ cells, while essentially maintaining their identity as sexually uncommitted PGCs, apparently through appropriate histone modifications. By establishing a paradigm for PGCLC expansion, our system reconstitutes the epigenetic "blank slate" of the germ line, an immediate precursory state for sexually dimorphic differentiation.

Introduction

Primordial germ cells (PGCs) are the founding population of the germ cell lineage that ensures reproduction, heredity, and evolution of a given species. In mice, PGCs originate from the epiblast at around embryonic day (E) 6.25 (Ginsburg *et al*, 1990; Lawson *et al*, 1999; Saitou *et al*, 2002; Ohinata *et al*, 2005), expand their numbers during their migration and in embryonic gonads (from ~30 to 40 at E7.25 to ~25,000 at E13.5: ~600- to 800-fold) (Tam & Snow, 1981; Kagiwada *et al*, 2013), and initiate entry into either spermatogenic or oogenic pathways in response to signals from embryonic gonads from around E11.5 [reviewed in (McLaren, 2003; Spiller & Bowles, 2015)]. Notably, PGCs undergo epigenetic reprogramming, including genome-wide DNA demethylation and histone-modification changes (Seki *et al*, 2005, 2007; Popp *et al*, 2010; Seisenberger *et al*, 2012; Kagiwada *et al*, 2013), effectively erasing the epigenetic memory of a previous generation to create an epigenetic blank slate, upon which either an androgenetic or gynogenetic epigenome for the next generation is established thereafter [reviewed in (Saitou *et al*, 2012; Lee *et al*, 2014)].

On the other hand, PGCs have been known to be refractory to propagation *in vitro* (Buehr, 1997; De Felici *et al*, 2004), which has been a major impediment for their analysis and for their application to reproductive technologies or medicine. It has been reported that mouse pluripotent stem cells (PSCs) are induced into epiblast-like cells (EpiLCs) and in turn into PGC-like cells (PGCLCs), which contribute to proper spermatogenesis and oogenesis and to fertile offspring, upon transplantation or aggregation with gonadal somatic cells followed by an appropriate culture (Hayashi *et al*, 2011, 2012; Hikabe *et al*, 2016; Ishikura *et al*, 2016). Accordingly, mPGCLCs, and more recently, human PGCLCs induced from human PSCs (Irie

1 Department of Anatomy and Cell Biology, Graduate School of Medicine, Kyoto University, Yoshida-Konoe-cho, Sakyo-ku, Kyoto, Japan
2 JST, ERATO, Yoshida-Konoe-cho, Sakyo-ku, Kyoto, Japan
3 Center for iPS Cell Research and Application, Kyoto University, 53 Kawahara-cho, Shogoin, Sakyo-ku, Kyoto, Japan
4 Institute for Integrated Cell-Material Sciences, Kyoto University, Yoshida-Ushinomiya-cho, Sakyo-ku, Kyoto, Japan
5 AMED-CREST, AMED, Chiyoda-ku, Tokyo, Japan
6 Medical Research Support Center, Graduate School of Medicine, Kyoto University, Yoshida-Konoe-cho, Sakyo-ku, Kyoto, Japan
7 Department of Anatomy and Developmental Biology, Graduate School of Medicine, Kyoto University, Yoshida-Konoe-cho, Kyoto, Japan
8 Division of Epigenomics and Development, Medical Institute of Bioregulation, Epigenome Network Research Center, Kyushu University, 3-1-1 Maidashi, Higashi-ku, Fukuoka, Japan
9 Graduate School of Medical Sciences, Kyushu University, 3-1-1 Maidashi, Higashi-ku, Fukuoka, Japan
   *Corresponding author. Tel: +81 75 753 4337; Fax: +81 75 751 7286; E-mail: ohta@anat2.med.kyoto-u.ac.jp
   **Corresponding author. Tel: +81 75 753 4335; Fax: +81 75 751 7286; E-mail: saitou@anat2.med.kyoto-u.ac.jp
   †These authors contributed equally to this work.

et al, 2015; Sasaki *et al*, 2015), have provided relatively abundant experimental materials and have been instructive for analyzing the mechanisms of PGC specification and epigenetic reprogramming upon PGC specification [reviewed in (Saitou & Miyauchi, 2016)]. On the other hand, the induction of PGCLCs, which acquire a property similar to migrating PGCs, is a transient process, and without the aggregation of gonadal somatic cells, PGCLCs have also been refractory to further proliferation or maturation. Thus, establishing a strategy for expanding PGCs/PGCLCs under a defined condition is a key challenge that will open a wide range of novel applications in reproductive biology and medicine. Taking advantage of a relatively large number of PGCLCs induced from PSCs, we here set out to perform a screening to identify chemicals that stimulate the proliferation of mouse PGCLCs.

Results

Screening for chemicals that expand PGCLCs

We first derived several novel male lines of mouse embryonic stem cells (ESCs) bearing the *Blimp1-mVenus* and *Stella-ECFP* (hereafter we designate *Blimp1-mVenus* as BV and *Stella-ECFP* as SC) transgenes (Ohinata *et al*, 2008) and evaluated their efficiencies for PGCLC induction and proliferation. All the ESC lines were induced into EpiLCs by activin A (ActA) and basic fibroblast growth factor (bFGF), and then into BV/BVSC-positive (+) PGCLCs by bone morphogenetic protein 4 (BMP4), leukemia inhibitory factor (LIF), stem cell factor (SCF), and epidermal growth factor (EGF). As shown in Appendix Fig S1A–C, BV (+) PGCLCs increased their numbers in the floating aggregates until day (d) 6 or 8 of induction and waned thereafter, which is consistent with our previous reports (Hayashi *et al*, 2011). Among the lines we evaluated, the BVSC BDF1-2 exhibited the most robust induction and proliferation in the floating aggregates (Appendix Fig S1A–C), and we decided to use this line for the subsequent screening.

We decided to plate d4 PGCLCs, which appear to be in the growing phase in the floating aggregates (Appendix Fig S1A–C), on 96-well plates with m220 feeders, which express a membrane-bound form of SCF known to support the survival of PGCs (Dolci *et al*, 1991; Majumdar *et al*, 1994), and to screen chemicals that enhance BV (+) PGCLC proliferation using a cell analyzer (Fig 1A). We reasoned that BV positivity distinguishes PGCLC proliferation from PGCLC dedifferentiation into embryonic germ cells (EGCs) (Matsui *et al*, 1992), since ESCs/EGCs express no/low *Blimp1*/BV (Durcova-Hills *et al*, 2008; Ohinata *et al*, 2008; Hayashi *et al*, 2011). Since m220 cells were highly vulnerable to mitomycin C (MMC) treatment that was required for their preparation as feeders, we cloned and used a subline of m220 that was resistant to the MMC treatment (Appendix Fig S2A–C). Under the chosen conditions and with the use of LIF, a classical factor known to stimulate PGC proliferation (Matsui *et al*, 1991), the proliferation of PGCLCs was monitored successfully after 7 days of culture as a corresponding increase in BV fluorescence by a cell analyzer (Appendix Fig S2D and E). We confirmed that under this simple positive control condition, there was little to no dedifferentiation of PGCLCs into EGCs.

We therefore embarked on screening of a total of ~2,000 chemical compounds that target a diverse set of intracellular signaling

molecules/pathways for their ability to expand BV (+) d4 PGCLCs after a 7-day culture (Fig EV1A–C). Consequently, at a concentration of 10 μM, we identified 63 chemicals that expanded the BV (+) cells significantly compared to the negative control culture, with the fold differences in BV fluorescence between d1 and d7 of culture being more than 3 SDs (standard deviations) of the mean values for the negative controls (Fig 1B and C, Table EV1). Notably, among the top 25 hit compounds, five (20%) were selective inhibitors for phospho-di-esterase 4 (PDE4) [ibudilast, S-(+)-Rolipram, Rolipram, GSK256066, cilomilast], three (12%) were agonists for retinoic acid (RA) signaling (acitretin, TTNPB, retinoic acid), and one was Forskolin (Fig 1D). PDE4 catalyzes the hydrolysis of cyclic AMPs (cAMPs) to AMP and, therefore, the inhibitors of PDE4 increase the intracellular cAMP levels (Pierre *et al*, 2009; Keravis & Lugnier, 2012). Forskolin is a potent activator of adenylate cyclase and therefore also elevates the intracellular cAMP levels (Pierre *et al*, 2009). RA signaling and Forskolin are known to stimulate PGC proliferation (De Felici *et al*, 1993; Koshimizu *et al*, 1995). Selective inhibitors for other PDEs or non-selective inhibitors for PDEs did not show positive effects on PGCLC proliferation (Fig EV1D). Figure 1C shows the proliferation of BV (+) cells in the presence of a PDE4 inhibitor, GSK256066, at d7 of culture, revealing the formation of multiple colonies with a unique, flat morphology (see below). We performed a similar screening using some of the same chemical libraries with a concentration of 1 μM, which resulted in the identification of the same classes of compounds (selective inhibitors for PDE4, agonists for RA signaling, and Forskolin) as potent stimulators for PGCLC proliferation (Fig EV1E and F).

We also identified 426 and 178 chemicals from 10 and 1 μM screenings, respectively, that had a negative impact on the proliferation or survival of BV (+) cells (the fold reductions in BV fluorescence between d1 and d7 of culture were more than 3 SDs of the mean values of the negative controls: Figs 1B and E, and EV1E and G, Datasets EV1 and EV2). Such chemicals include inhibitors of key signal transduction pathways, including those known to have a positive influence on PGC proliferation/survival, such as the pathways for receptor tyrosine kinase (RTK) signaling, phosphatidylinositol-3 kinase (PI3K) signaling, mammalian target of rapamycin (mTOR) signaling, Janus kinase (JAK) signaling, and AKT signaling [reviewed in (Saitou & Yamaji, 2012)], as well as inhibitors for cell cycle/cell division and for DNA replication/repair. Collectively, these findings strongly indicate that our screening successfully identified chemicals that influence key pathways relevant for PGC proliferation/survival.

Synergistic effect of Rolipram and Forskolin on PGCLC expansion

We decided to focus on the effects of one of the PDE4 inhibitors, Rolipram, in subsequent studies, since PDE4 inhibitors were the most enriched chemicals among the hit compounds (Fig 1D, Table EV1) and Rolipram has been reproducibly used in diverse experiments as an efficient PDE4 inhibitor (Keravis & Lugnier, 2012). We evaluated the effects of Rolipram, Forskolin, and their combined use (both increase intracellular cAMP concentration by different mechanisms) (Pierre *et al*, 2009), on the proliferation of d4 PGCLCs induced from the BVSC BDF1-2 ESCs in GMEM/10% KSR/ 2.5% FCS in the presence of SCF on m220 feeders. We decided not to include LIF in this culture, since it might enhance the possibility of the dedifferentiation of PGCLCs into EGCs when applied with
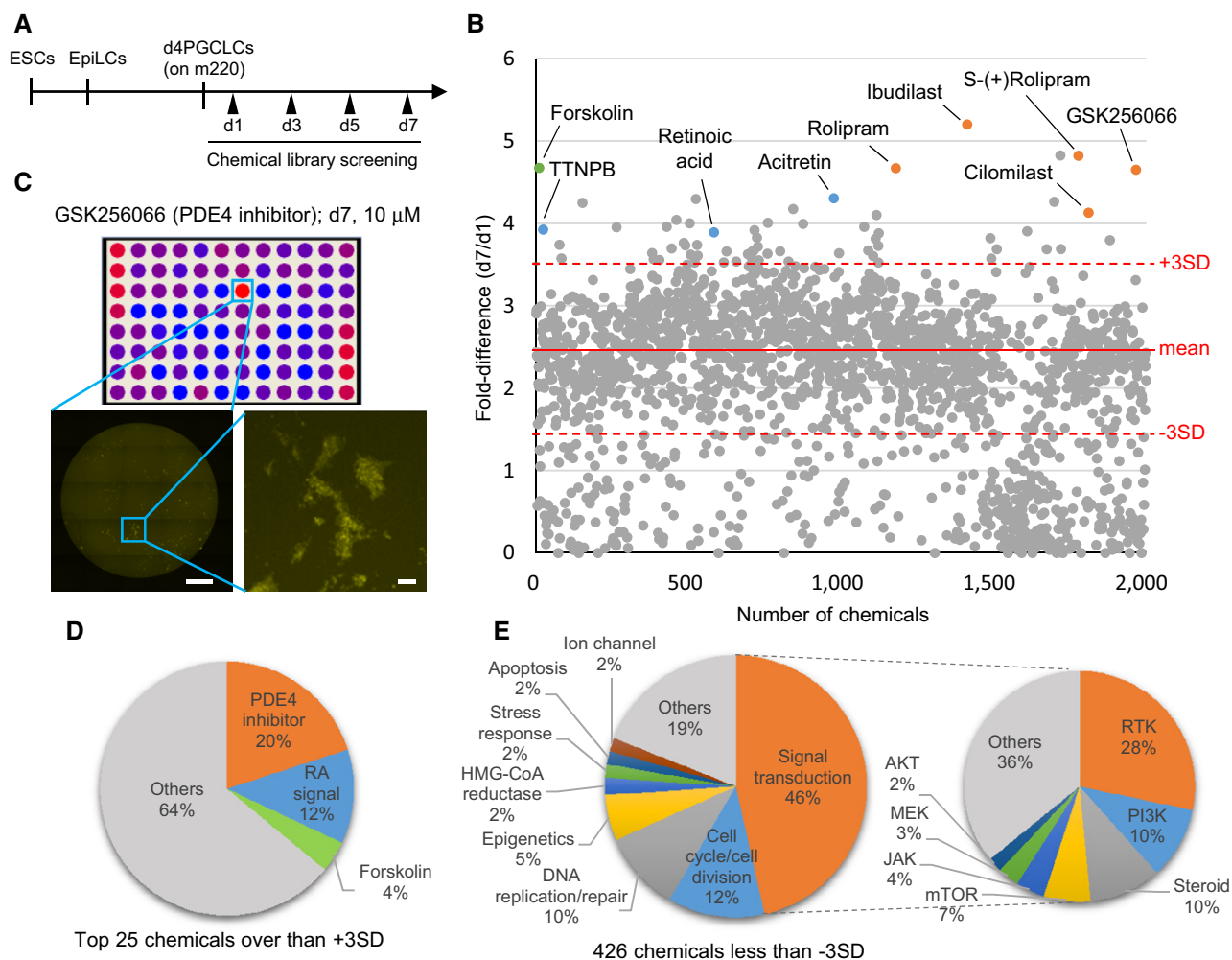
Figure 1. Identification of chemicals stimulating PGCLC proliferation.

A   Experimental procedure for chemical library screening using PGCLCs.

B   Scatter-plot representation of the results of chemical library screening (10 μM). The fold differences in *Blimp1-mVenus* (BV) signals for each compound as detected by a cell analyzer (d7/d1) were plotted. The average value (red line) and 3 SDs (standard deviations: red dotted lines) for the negative controls are indicated. Results for the PDE4 inhibitors, RAR agonists, and Forskolin are shown in orange, blue, and green, respectively.

C   Stimulation of PGCLC proliferation by a representative PDE4 inhibitor (GSK256066, 10 μM). A heatmap image of a 96-well plate at d7 of a screening (top) with a well containing GSK256066 (blue square) magnified for BV fluorescence images (bottom, left, and right). Scale bars: (left) 1 mm; (right) 100 μm.

D   A pie chart classifying the categories of the top 25 compounds (> +3 SDs) in the screening (10 μM).

E   Pie charts classifying the categories of the 426 compounds having a negative effect on PGCLC proliferation/survival (< −3 SD) in the screening (10 μM).

other stimulators of PGC proliferation (Matsui *et al*, 1992). We found that the effect of Rolipram alone (10 μM) was relatively mild and similar to that of Forskolin alone (10 μM) (Fig 2A). However, when Rolipram and Forskolin were applied in combination, they effectively stimulated the proliferation of d4 PGCLCs: With both Rolipram and Forskolin at 10 μM (FR10), d4 PGCLCs exhibited a robust and steady growth at least until d7 of culture (d4c7) and increased their numbers more than 20-fold, corresponding to 4 to 5 doublings (Fig 2A–C). Importantly, the expanded cells formed flat colonies, continued to express BVSC robustly, and exhibited characteristics of motile cells with prominent filopodia and lamellipodia (Fig 2B and D), suggesting that they maintain a property of migrating PGCs after expansion by FR10.

To determine whether Forskolin and Rolipram indeed elevate cAMP concentrations in PGCLCs, we measured the increase of

cAMP concentrations in PGCLCs in response to Forskolin, Rolipram, or both (Materials and Methods). As shown in Fig 2E, Forskolin and Rolipram independently increased the cAMP concentrations in PGCLCs by ~4 nM/1×10^4 d4 PGCLCs. More remarkably, we found that simultaneous addition of Forskolin and Rolipram (FR10) elevated the cAMP concentrations in PGCLCs by more than ~40 nM/1×10^4 d4 PGCLCs.

The FR10 was effective in expanding PGCLCs induced from other male as well as female ESC lines, with an average expansion rate of ~20-fold at d7 of culture: In some cases, it expanded PGCLCs nearly 50-fold, corresponding to 5–6 doublings (Fig 2C). The FR10 was also effective in expanding PGCs at E9.5, but to a somewhat limited extent (up to ~eightfold expansion, Fig 2C), which might have been due to the difference in survivability under the present condition between E9.5 PGCs directly isolated from embryos and d4 PGCLCs
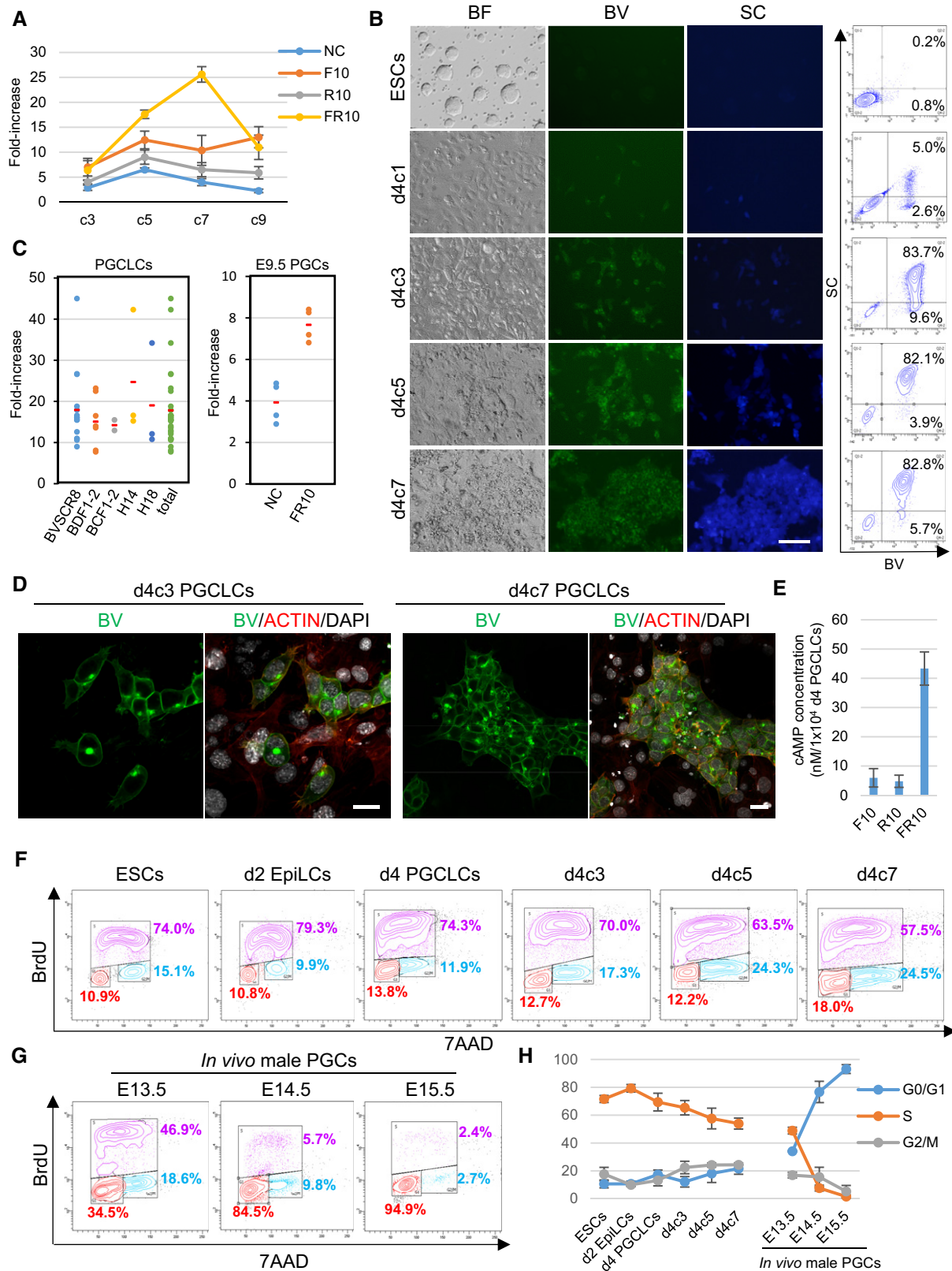
Figure 2.

induced from PSCs *in vitro*. The cell-cycle analysis revealed that a majority of cultured PGCLCs (> ~60%) were in the S phase, with a slight decrease and an apparent corresponding increase in the S and

G2/M phase at d7 of culture, respectively (Fig 2F and H). This is in stark contrast to the cell-cycle property of male germ cells in embryonic gonads, which ceased to proliferate and became arrested in the

410

◀

Figure 2. Establishment of a culture system for PGCLC expansion.

A   Effects of Forskolin and Rolipram on PGCLC proliferation. d4 PGCLCs were cultured in the basal medium (GMEM with 10% KSR, 2.5% FCS, and 100 ng/ml SCF) on m220-5 feeders (NC; negative control) and the effects of 10 μM of Forskolin (F10), Rolipram (R10), and both Forskolin and Rolipram (FR10) on PGCLC proliferation were examined. The numbers of PGCLCs were counted on days 3 (c3), 5 (c5), 7 (c7), and 9 (c9) of culture. Average fold increases of the number of PGCLCs at each time point relative to the number of PGCLCs plated are shown with their SDs (*n* = 3).

B   A representative culture of d4 PGCLCs with FR10. Photographs [images for bright field (BF), *Blimp1-mVenus* (BV), and *Stella-ECFP* (SC)] and the BVSC FACS plots (all live and single cells in culture) were taken for ESCs and on days 1 (d4c1), 3 (d4c3), 5 (d4c5), and 7 (d4c7) of culture. Scale bar, 100 μm.

C   (Left) Expansion by FR10 of PGCLCs induced from male (BVSC R8, BDF1-2, BCF1-2) and female (H14, H18) ESC lines. Fold increases in the numbers of PGCLCs at d4c7 relative to the number of PGCLCs initially plated are plotted for each experiment for each ESC line. The average values are indicated as red bars. (Right) Expansion by FR10 of E9.5 PGCs, as measured in the left panel.

D   Cultured PGCLCs (BV: green) stained with phalloidin (red). Scale bars, 20 μm.

E   The effects of FR10 on the elevation of intracellular cAMP concentrations in d4 PGCLCs. The average values with SDs from three independent experiments are shown.

F–H   Cell-cycle status of cultured PGCLCs (F) and male embryonic germ cells (G). Representative plots for the cell-cycle status by FACS analysis of the indicated cell types are shown. The vertical axis represents BrdU incorporation and the horizontal axis represents DNA content (7AAD). Cells in S, G2/M, and G1 phase are shown in purple, blue, and red, respectively, along with the percentage of each population. The average values with SDs from three independent experiments are shown in (H).

G0/G1 phase after E13.5 (Fig 2G and H) (Western *et al*, 2008). These findings demonstrate that Rolipram and Forskolin act synergistically to progress the cell cycles of PGCLCs, most likely via the robust activation of cAMP signaling.

Robust capacity for spermatogenesis of PGCLCs expanded in culture

We next went on to evaluate whether PGCLCs expanded by FR10 in culture maintain their function as PGCs/PGCLCs. For this purpose, we transplanted d4c7 and d4 PGCLCs induced from the BVSC BDF1-2, BCF1-2, or R8 (on a largely C57BL/6) ESCs (Appendix Fig S3A) into the testes of neonatal *W/Wᵛ* mice lacking endogenous germ cells. We found that the testes transplanted with d4c7 PGCLCs, as well as those transplanted with d4 PGCLCs, induced from the BVSC BDF1-2 or BCF1-2 ESCs, exhibited a significant enlargement in size after 7 months of transplantation (Figs 3A and EV2A), contained numerous seminiferous tubules with evidence of spermatogenesis, and indeed bore abundant spermatozoa (Figs 3B–F and EV2B). Remarkably, the restoration of the spermatogenesis by both d4c7 and d4 PGCLCs from the BVSC BDF1-2 or BCF1-2 ESCs became pronounced enough that the spermatozoa were transported into the epididymis, and such spermatozoa acquired a robust motility to be used for *in vitro* fertilization (IVF) to generate apparently normal offspring (Figs 3G–K and EV2B). Accordingly, the recipient males for d4c7 as well as d4 PGCLCs from the BVSC BDF1-2 or BCF1-2 ESCs were able to produce offspring with substantial litter sizes by natural mating and the resultant offspring exhibited apparently normal growth (Figs 3L–N and EV2B–D).

In contrast, the testes transplanted with d4c7 or d4 PGCLCs from the BVSC R8 ESCs exhibited only a mild increase in size (Fig EV2A) and contained fewer seminiferous tubules with spermatogenesis, and the resultant spermatozoa did not reach the epididymis. We were nonetheless able to obtain apparently normal offspring with intracytoplasmic injection (ICSI) of the resultant spermatozoa, as we reported previously (Hayashi *et al*, 2011). Importantly, as in the case of d4/d6 PGCLCs or PGCs (Ohta *et al*, 2004), none of the d4c7 PGCLCs induced from any of the ESC lines were able to colonize adult testes (Fig EV2E and F). We did not find teratoma formation in any of the transplants. Collectively, these findings demonstrate that the PGCLCs expanded by FR10 in culture faithfully maintain their original functional property and that PGCLCs with a hybrid genetic background are powerful enough to reconstitute the

spermatogenesis of infertile mice so that the recipient mice produce offspring with natural mating.

Transcriptomic properties of PGCLCs during expansion culture

We next went on to determine the detailed transcriptional properties of PGCLCs during their expansion in culture. First, immunofluorescence (IF) analyses revealed that, compared to male germ cells at E13.5, d4c7 PGCLCs, while expressing higher levels of OCT4, exhibited much lower levels of DDX4 and DAZL, key translational regulators that PGCs progressively up-regulate after their colonization of embryonic gonads (Fujiwara *et al*, 1994; Cooke *et al*, 1996) (note that some d4c7 PGCLCs appeared to fully express DAZL) (Fig 4A). Second, we determined the transcriptomes of cultured PGCLCs [d4c3, d4c5, and d4c7 PGCLCs induced from the BVSC R8 ESCs (Appendix Fig S3B)] by an RNA sequencing (RNA-seq) methodology (Nakamura *et al*, 2015, 2016) and compared them with those of ESCs, EpiLCs, d4/6 PGCLCs, and germ cells *in vivo* [PGCs at E9.5, E10.5, and E11.5; male/female germ cells at E12.5 and E13.5 (Kagiwada *et al*, 2013)] (Table EV2). The expression levels of key genes associated with germ cell development in these cell types are shown in Fig EV3. Remarkably, principal component analysis (PCA) clustered cultured PGCLCs closely with d4/6 PGCLCs and then with PGCs at E9.5, E10.5, and E11.5, but distantly with male/female germ cells at E12.5 and E13.5 (Fig 4B), indicating that PGCLCs grossly maintain their transcriptome during their expansion culture. On the other hand, unsupervised hierarchical clustering (UHC) and PCA among PGCLCs revealed a progressive transition of the properties of PGCLCs from d4 to d6, and then to d4c3, d4c5, and d4c7 PGCLCs (Appendix Fig S4A–C). Thus, during expansion culture, PGCLCs appear to undergo a directional transcriptional change, the initial phase of which also manifests in the floating aggregates.

We identified differentially expressed genes (DEGs) between d4c7 and d6 PGCLCs, and between male/female germ cells at E13.5 and d6 PGCLCs. d4c7 PGCLCs up/down-regulated 478 and 409 genes, respectively (Appendix Fig S4D), and the up-regulated genes were enriched with those bearing gene ontology (GO) functional terms such as "intracellular signaling cascade" and "pattern specification process", whereas the down-regulated genes were enriched with those for various metabolic/biosynthetic processes (Appendix Fig S4E). Consistent with the PCA, the DEGs between male/female germ cells at E13.5 and d6 PGCLCs were much larger in number (Fig 4C and D): male/female germ cells at E13.5 up/down-regulated 2,381
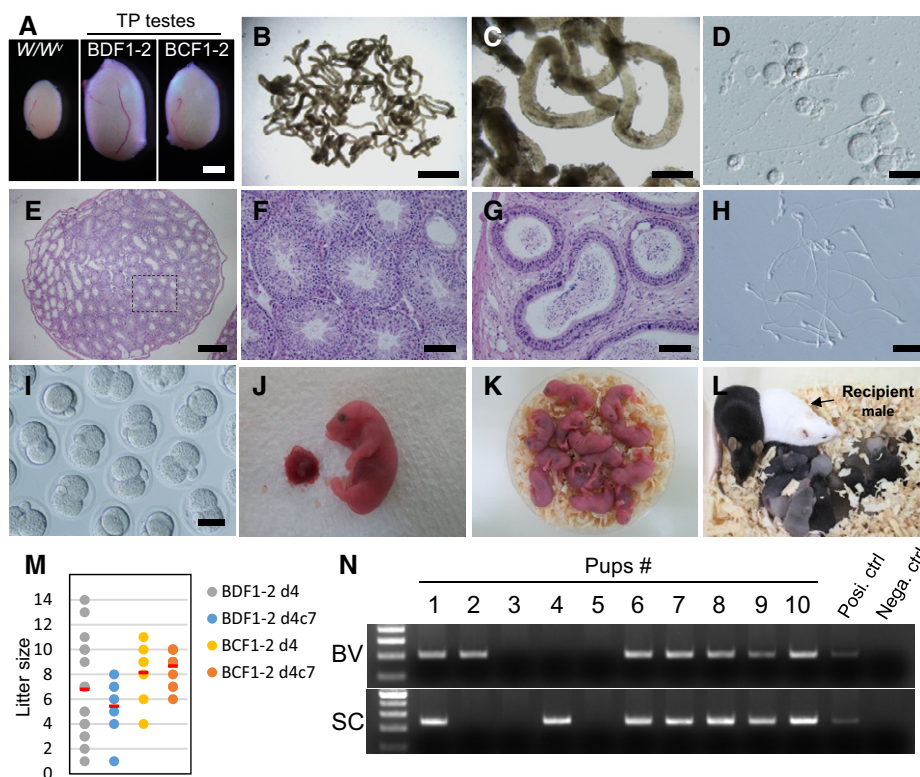
411

Figure 3. Robust spermatogenesis by cultured PGCLCs.

A   *W/W^v* testes (left, untransplanted) 7 months after transplantation of d4c7 PGCLCs induced from BDF1-2 (center) or BCF1-2 (right) ESC lines.

B–D   The seminiferous tubules showing spermatogenesis (B, C) transplanted with d4c7 PGCLCs (BDF1-2), and the resultant spermatozoa (D).

E–G   Hematoxylin and eosin (HE) staining of the sections of a transplanted testis (E, F) and cauda epididymis (G).

H–K   *In vitro* fertilization (IVF) using the sperm (H) retrieved from the cauda epididymis of the recipient mice. The resultant two-cell embryos (I) and the offspring (J, K) with normal placenta (J) are shown.

L–N   Fertility of recipient *W/W^v* mice transplanted with d4c7 PGCLCs (BDF1-2). The fertility of recipient *W/W^v* mice was confirmed by natural mating (L). (M) Litter sizes of recipient *W/W^v* mice transplanted with d4 or d4c7 PGCLCs. The average values are indicated as red bars. (N) Genotype of the offspring from d4c7 PGCLCs for BV and SC transgenes.

Data information: Scale bars: (A) 1 mm; (B) 2 mm; (C, E) 0.5 mm; (D) 20 μm; (F, G, I) 100 μm; (H) 25 μm.

and 1,705 genes, respectively, and these DEGs exhibited enrichments of GO terms reflecting key developmental progressions during germ cell development (Appendix Fig S5A and B) (Dataset EV3). For example, the genes specifically up-regulated in males were enriched with those for "transcription" (*Foxo1, Utf1, Pou6f1*) and "chromatin organization" (*Ezh1, Prmt5, Kdm2a*), the genes specifically up-regulated in females were enriched with those for "regulation of transcription" (*Gata2, Msx1, Cdx2*) and "gamete generation" (*Figla, Nr6a1, Rec8*), and notably, the genes commonly up-regulated in both males and females were enriched with those for "meiosis" (*Spo11, Mael, Sycp1*), "chromosome organization" (*Ehmt1, Suv39h1, Smarc-c1*), and "methylation" (*Piwil4, Satb1, Mll3*), and accordingly, for the so-called "germline genes" that have previously been identified as genes involved in germline functions such as meiosis and transposon repression and repressed in somatic cells primarily by DNA methylation (Weber *et al*, 2007; Borgel *et al*, 2010).

Consistent with UHC and PCA among PGCLCs, the DEGs between d4c7 and d6 PGCLCs acquired such states progressively during the culture (Fig 4E), and notably, they also exhibited progressive up/down-regulation during germ cell development *in vivo* (Fig 4E): They comprised a minor part of—and a majority of

them were included in—the DEGs between male/female germ cells at E13.5 and d6 PGCLCs (Fig 4C and D). Importantly, they did not exhibit a bias for sex-specific regulation (Fig 4C and D). To gain more quantitative insight into the relationship between the DEGs between d4c7 PGCLCs and d6 PGCLCs and those between male/female germ cells at E13.5 and d6 PGCLCs, we plotted expression-level differences between male/female germ cells at E13.5 and d4c7 PGCLCs against those between male/female germ cells at E13.5 and d6 PGCLCs (Fig 4F, Appendix Fig S5C). This analysis revealed that among the 306 genes commonly up-regulated in male/female germ cells at E13.5 and d4c7 PGCLCs compared to d6 PGCLCs, 104 genes were only partially activated (E13.5−d4c7 > 2 folds) and 197 genes were fully activated (−2 folds < E13.5−d4c7 < 2 folds) in d4c7 PGCLCs (Fig 4F). The former included genes such as *Ddx4, Dazl, Brdt, Asz1, Dmrt1, Stra8, Sycp3, Syce1,* and *Smc1b*, and were enriched with the "germline genes", whereas the latter included genes such as *Piwil2, Rpl10 l, Rpl36,* and the Rhox genes (Fig 4F). On the other hand, among the 252 genes commonly down-regulated in male/female germ cells at E13.5 and d4c7 PGCLCs compared to d6 PGCLCs, 68 genes were only partially down-regulated (E13.5−d4c7 < −2 folds) and 180 genes were fully down-regulated
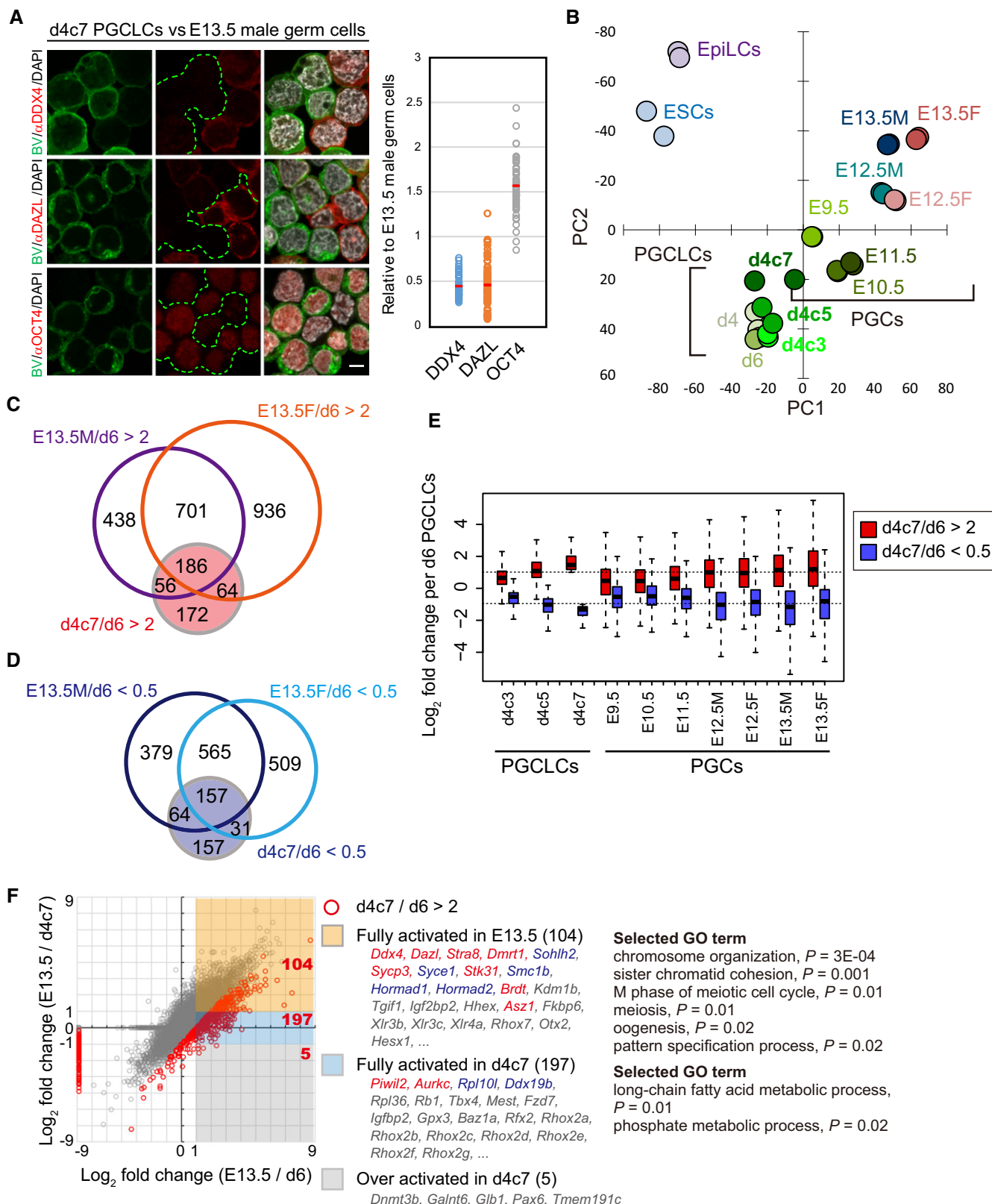
Figure 4.

(2 folds < E13.5−d4c7 < −2 folds) in d4c7 PGCLCs (Appendix Fig S5C). These findings demonstrate that, during expansion, PGCLCs, while essentially maintaining the characteristics of migrating PGCs, gradually acquire a part of the program for germ cell maturation that manifests in embryonic gonads prior to overt sex differentiation.

◄

Figure 4. Transcriptome of cultured PGCLCs.

A   Immunofluorescence (IF) analysis of the levels of DDX4 (top), DAZL (middle), and OCT4 (bottom) in d4c7 PGCLCs [*Blimp1-mVenus* (BV)-positive] compared to E13.5 male germ cells. The d4c7 PGCLCs are delineated by green dotted lines in the middle column. The ratios of the levels in d4c7 PGCLCs to the average levels in E13.5 male germ cells measured by densitometry [DDX4 ($n = 48$), DAZL ($n = 77$), OCT4 ($n = 61$)] are shown on the right (the averages were shown by red bars). Scale bar, 5 μm.

B   PCA of the transcriptome of the indicated cells.

C, D   Venn diagram showing the overlap of genes up (C)/down (D)-regulated in d4c7 PGCLC and E13.5 male/female germ cells, compared to d6 PGCLCs. The numbers of genes in each category are indicated.

E   Box plots [the median (horizontal line), 25th and 75th percentiles (box), and 5th and 95th percentiles (error bars)] of the expression-level differences compared to d6 PGCLCs ($\log_2$ fold differences) of DEGs between d6 and d4c7 PGCLCs during PGCLC cultures or germ cell development (E9.5–E13.5). The color coding is as indicated.

F   Scatter-plot representation of the $\log_2$ expression-level changes in E13.5 germ cells (the larger values in males or females) compared to d6 (x-axis) and d4c7 (y-axis) PGCLCs. Genes up-regulated in d4c7 compared to d6 PGCLCs are indicated with red open circles ("d4c7/d6 > 2"), and if $x > 1$ (i.e., up-regulated in E13.5 germ cells compared to d6 PGCLCs), they are classified according to the fold difference between E13.5 germ cells and d4c7 PGCLCs; "fully activated in E13.5" (up-regulated in E13.5 germ cells, yellow); "fully activated in d4c7" (within twofold difference, cyan); and "over activated in d4c7" (down-regulated in E13.5 germ cells, gray). Representative genes and selected GO terms are indicated. Previously reported "germline genes" (Weber *et al*, 2007; Borgel *et al*, 2010; Kurimoto *et al*, 2015) or other relevant genes are colored red or blue, respectively.

Epigenetic properties of PGCLCs during expansion culture

To explore the mechanism underpinning the characteristics of cultured PGCLCs, we next went on to determine their epigenetic profiles. First, we performed IF analyses, which revealed that, compared to EpiLCs, d4c7 PGCLCs exhibited much lower levels of 5-methylcytone (5mC) (Fig 5A). Consistent with the results of the transcriptome analyses (Fig EV3), compared to EpiLCs, d4c7 PGCLCs expressed a similar level of DNMT1, but much lower levels of DNMT3A/3B and UHRF1 (Fig 5B). Furthermore, compared to EpiLCs, they exhibited higher and lower levels of histone H3 lysine 27 tri-methylation [H3K27me3: representing repression by polycomb complex 2 (PRC2)] and H3K9 di-methylation [H3K9me2: representing repression by G9A/GLP], respectively (Fig 5A). Thus, the epigenetic properties of d4c7 PGCLCs appeared to be grossly similar to those of d6 PGCLCs (Hayashi *et al*, 2011; Kurimoto *et al*, 2015), except that d4c7 PGCLCs appeared to bear much lower 5mC levels than d6 PGCLCs.

We therefore next quantified the genome-wide levels and distributions of DNA methylation in d4c3 and d4c7 PGCLCs (induced from the BVSC R8 ESCs) (Appendix Fig S3) by whole-genome bisulfite sequencing (WGBS) (Table EV3) and of H3K4me3 (representing promoter activity), H3K27 acetylation (ac) (representing active enhancers), and H3K27me3 in d4c7 PGCLCs (induced from the BVSC R8 or BDF1-2 ESCs) by chromatin immunoprecipitation followed by massively parallel sequencing (ChIP-seq) (Table EV4), and analyzed these data in comparison with those of key cell types during PGCLC induction (ESCs, EpiLCs, and d2, d4, and d6 PGCLCs), which we reported recently (Kurimoto *et al*, 2015; Shirane *et al*, 2016). Since bisulfite sequencing does not discriminate 5mC and 5-hydroxymethylcytone (5hmC) (Hayatsu & Shiragami, 1979), and since the 5hmC level during PGCLC induction is almost negligible (Shirane *et al*, 2016), we hereafter designate 5mC and 5hmC collectively as 5mC. Figure 5C shows WGBS and ChIP-seq track transitions around the *Prdm14* locus and the *Hoxb* cluster. Consistent with the IF analyses, remarkably, the 5mCs were almost fully erased in both loci during the PGCLC culture, whereas both active (H3K4me3 and H3K27ac) and repressive (H3K27me3) histone modifications exhibited relatively similar distributions between d6 and d4c7 PGCLCs (Fig 5C), suggesting that the PGCLC expansion is a process to progressively erase 5mCs, while maintaining the histone modifications.

Comprehensive DNA methylation erasure in cultured PGCLCs

Next, we performed more detailed analyses on the 5mC-level dynamics during the PGCLC culture. We focused on the 5mCs in CpG contexts, since CpH (where H = A, C, or T) methylation is limited during PGCLC induction (Shirane *et al*, 2016) and has not been found to exhibit any clear biological role in mammalian cells (Schubeler, 2015). As a key parameter for the genome-wide DNA methylation state, we determined the average 5mC levels of the total unique sequence regions (unique regions: 2-kb sliding windows with 1-kb overlap). We separately determined the 5mC levels of promoters (high, intermediate, and low CpG-density promoters: HCPs, ICPs, and LCPs, respectively) (Weber *et al*, 2007), the consensus sequences of repetitive elements [long interspersed nuclear element 1 (LINE1); intracisternal A particles (IAPs); endogenous retrovirus sequences (ERVs) other than IAPs; and major and minor satellites], and imprint control regions (ICRs) of imprinted genes (Dataset EV4). We also determined the 5mC levels of non-promoter CpG islands (CGIs), exons, introns, intergenic regions, cell type-specific enhancers (Kurimoto *et al*, 2015), and the CGIs of "germline genes" (Weber *et al*, 2007; Borgel *et al*, 2010; Kurimoto *et al*, 2015) (Dataset EV4).

As we reported recently, PGCLCs exhibit a progressive dilution of the 5mCs established in EpiLCs, which bear a DNA methylome highly similar to that of the epiblast, and consequently, d6 PGCLCs acquire an average 5mC level of ~37%, a state considered to be similar to that in migrating PGCs at ~E9.0–9.5 (Seisenberger *et al*, 2012; Kobayashi *et al*, 2013; Shirane *et al*, 2016) (Fig 6A). Strikingly, in agreement with the analyses of *Prdm14* and *Hoxb* loci, in the cultured PGCLCs, there was a progressive dilution of the 5mC level of the d4/d6 cells in essentially all genomic regions, with differing kinetics for unique regions, repeats, and distinct regulatory elements, and as a result, there was an average 5mC level of only ~6% in the d4c7 cells (Figs 6A and EV4, Appendix Fig S6), a level equivalent to that in E13.5 germ cells, which bear the lowest 5mC level throughout the germline cycle (Seisenberger *et al*, 2012; Kobayashi *et al*, 2013). Importantly, the 5mC distribution patterns in essentially all genomic elements, including the repeats, the promoters of demethylation-resistant "germline genes", and the ICRs of imprinted genes, were remarkably similar between d4c3 PGCLCs and E10.5 PGCs, and between d4c7 PGCLCs and E13.5 germ cells (Fig 6B), whereas those between d4c3 PGCLCs and ESCs cultured with two kinase inhibitors (2i) (Habibi *et al*, 2013; Shirane
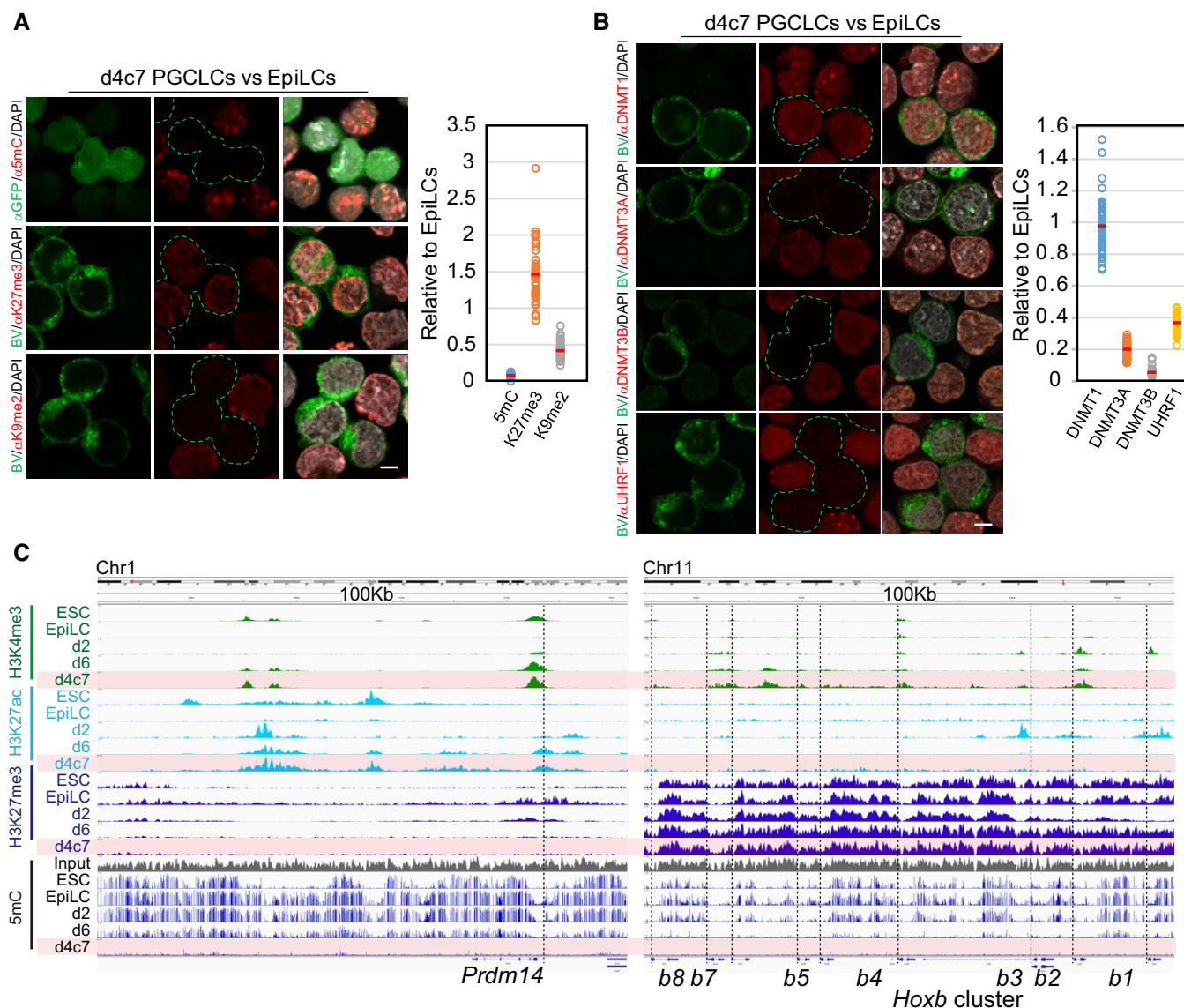
Figure 5. Key epigenetic properties of cultured PGCLCs.

A   IF analysis of the levels of 5mC (top), H3K27me3 (middle), and H3K9me2 (bottom) in d4c7 PGCLCs [*Blimp1-mVenus* (BV)-positive] compared to EpiLCs. The d4c7 PGCLCs are delineated by green dotted lines in the middle column. The relative levels in d4c7 PGCLCs compared to the average in EpiLCs measured by densitometry [5mC ($n = 49$), H3K27me3 ($n = 44$), H3K9me2 ($n = 46$)] are shown on the right (the averages were shown by red bars). Scale bar, 5 μm.

B   IF analysis of the levels of DNMT1, DNMT3A, DNMT3B, and UHRF1 in d4c7 PGCLCs (BV-positive) compared to EpiLCs. The d4c7 PGCLCs are delineated by green dotted lines in the middle column. The relative levels in d4c7 PGCLCs compared to the average in EpiLCs measured by densitometry [DNMT1 ($n = 57$), DNMT3A ($n = 56$), DNMT3B ($n = 51$), UHRF1 ($n = 55$)] are shown on the right (the averages are indicated by red bars). Scale bar, 5 μm.

C   ChIP-seq (H3K4me3, H3K27ac, and H3K27me3) and 5mC-level tracks in 100-kb regions around the *Prdm14* (left) and *Hoxb* cluster (right) in the indicated cell types. The d4c7 PGCLCs are shaded in pink. Transcription start sites (TSSs) are indicated with dotted lines.

et al, 2016), which exhibited similar 5mC levels, were divergent (Appendix Fig S7), suggesting that DNA demethylation in cultured PGCLCs involves similar, if not identical, mechanism as that in PGCs *in vivo*, but not that evoked by 2i *in vitro*. We analyzed the "escapees" that evade the DNA demethylation (5mC > 20%) (Seisenberger *et al*, 2012) and found that the escapees were also largely overlapped between d4c7 PGCLCs and E13.5 germ cells (Appendix Fig S8), and a majority of them were in the vicinity of IAPs (Appendix Fig S8). Thus, the induction of PGCLCs and their

culture with FR10 on m220 feeders reconstituted DNA methylation reprogramming in PGCs in a comprehensive fashion. Nonetheless, as we demonstrated above, the cultured PGCLCs basically maintained the transcriptional state of migrating PGCs (Fig 4B).

We therefore examined the impact of promoter demethylation on transcriptional activation in d4c7 PGCLCs. Reflecting the global DNA demethylation in cultured PGCLCs, as many as 7,737 promoters were demethylated between d6 and d4c7 PGCLCs (5mC > 20% in d6 and < 20% in d4c7) (Fig 6C). Among the 478 genes
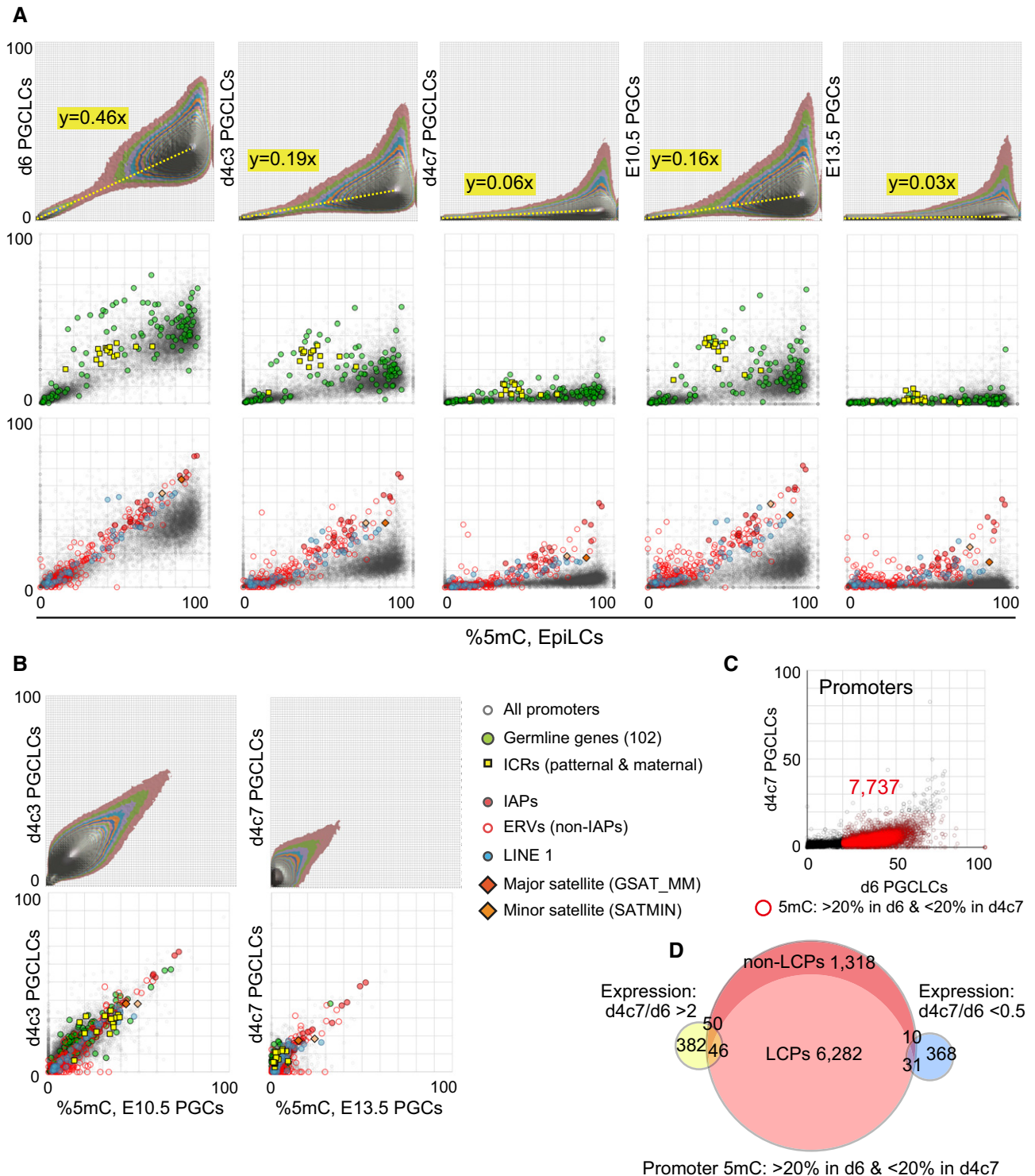
Figure 6. DNA methylation erasure in cultured PGCLCs.

A Scatter-plot comparisons of 5mC levels in d6, d4c3, d4c7 PGCLCs, and E10.5 and E13.5 male germ cells against those in EpiLCs. The 5mC levels of 2-kb unique genomic regions (contour plot, top), ICRs and "germline genes" (*n* = 102) (middle), and repeat consensus sequences (bottom) are shown, and the latter two are shown along with the 5mC levels of promoters. Contour lines are drawn with an interval of 100 regions, the yellow dotted line connects the origin and the peak, and the slopes are shown. The color coding is as indicated.

B Scatter-plot comparisons of 5mC levels between E10.5 male PGCs and d4c3 PGCLCs and between E13.5 male germ cells and d4c7 PGCLCs. The color coding is as in (A).

C Definition of promoters demethylated between d6 and d4c7 PGCLCs; 5mC > 20% in d6 and < 20% in d4c7 (red open circles, *n* = 7,737).

D Venn diagram showing overlap among promoter DNA demethylation and differentially expressed genes between d6 and d4c7 PGCLCs. The promoters demethylated between d6 and d4c7 PGCLCs are classified in LCPs and non-LCPs. The numbers of genes in each category are indicated.

up-regulated in d4c7 PGCLCs compared to d6 PGCLCs, 96 genes were promoter-demethylated, 27 were among the 104 partially up-regulated genes (E13.5−d4c7 > 2 folds) (*Ddx4*, *Dazl*, *Brdt*, *Asz1*, *Dmrt1*, *Stra8*, *Sycp3*, *Syce1*, *Smc1b*, etc.), and 34 were among the fully up-regulated 197 genes (−2 folds < E13.5−d4c7 < 2 folds) (*Piwil2*, *Rpl10l*, *Rpl36*, the Rhox genes, etc.) (Fig 6D, Appendix Fig S9A). The proportions of the promoter-demethylated genes among the partially/fully up-regulated genes were higher than those of the promoter-demethylated genes among the partially/fully down-regulated genes (Fig 6D, Appendix Fig S9A and B). We conclude that promoter demethylation itself contributes partially to the activation of only a limited number of specific genes in cultured PGCLCs.

Compensatory up-regulation of H3K27me3 in demethylated promoters in cultured PGCLCs

We next analyzed the dynamics of the H3K4me3, H3K27ac, and H3K27me3 distributions during the PGCLC induction and expansion. As in the cases of the key cell types during the PGCLC induction, high levels of H3K4me3 were associated predominantly with HCPs in d4c7 PGCLCs (Fig EV5A and B), the H3K4me3 levels around the transcription start sites (TSSs) were positively correlated with the expression levels of the associated genes (Fig EV5C), and reflecting a transcriptomic similarity between d6 and d4c7 PGCLCs, H3K4me3 profiles across the genome were similar between d6 and d4c7 PGCLCs (Fig EV5D) (Dataset EV5). Importantly, the distributions of H3K27ac, which represent enhancer usage and exhibit highly dynamic alterations across different cell types (Calo & Wysocka, 2013) and during the PGCLC induction (Kurimoto *et al*, 2015), were also similar between d6 and d4c7 PGCLCs (Fig 7A and B) (Dataset EV6), indicating that not only the gene expression itself but also the regulation of gene expression is grossly preserved during the PGCLC culture. Nonetheless, we identified H3K27ac peaks (< 15 kb from the TSSs and gene bodies) specific to either d6 or d4c7 PGCLCs, which would represent potential regulatory differences between d6 and d4c7 PGCLCs (Fig EV5E and F).

The distribution patterns of H3K27me3 also appeared to be grossly similar between d6 and d4c7 PGCLCs (Fig 7C and D). Importantly, however, we noted that the promoters with substantial demethylation between d6 and d4c7 PGCLCs (5mC > 20% in d6 and < 20% in d4c7, 7737 promoters), but not those showing no 5mC-level changes, exhibited a general trend for higher enrichment levels of H3K27me3 in d4c7 PGCLCs than in d6 PGCLCs (Fig 7C and D). We also noted that such promoters did not show overall changes of H3K27me3 enrichment levels between EpiLCs and d6 PGCLCs, even though they also exhibited substantial demethylation between EpiLCs and d6 PGCLCs (Fig EV5G and H). These findings indicate that extensive and nearly complete promoter demethylation in cultured PGCLCs is at least in part compensated by concomitant up-regulation of H3K27me3 enrichment levels, which would contribute to the maintenance of a transcriptional state of migrating PGCs in cultured PGCLCs. Examples of genes exhibiting such trends are shown in Appendix Fig S10.

We evaluated the bivalent promoters with both activating H3K4me3 and repressing H3K27me3, which may represent a state poised for activation upon appropriate developmental cues (Voigt *et al*, 2013) (for the definition of bivalency, see Materials and Methods). Consistent with our previous report (Kurimoto *et al*, 2015), the numbers of the bivalent genes were largest in EpiLCs among the key

cultured cell types, and d6 and d4c7 PGCLCs exhibited similar numbers of bivalent genes (Fig 7E). The overlap of the bivalent genes between d6 and d4c7 PGCLCs, however, was relatively moderate [~519/1,058 (~49%)] (Appendix Fig S11A), which was in part due to an inherent technical difficulty in precisely comparing the combinatorial levels of two histone modifications in two different samples. Nonetheless, the bivalent genes in d4c7 PGCLCs exhibited higher enrichments in GO terms such as "pattern specification process" and "embryonic morphogenesis" compared to those in d6 PGCLCs (Fig 7F, Appendix Fig S11A); for instance, d4c7 PGCLCs acquired elevated H3K4me3 levels around the Hoxc cluster, even though the cluster was repressed by high levels of H3K27me3 (Appendix Fig S11B). We conclude that d4c7 PGCLCs bear an epigenome highly poised for developmental regulators, with extremely low levels of genome-wide 5mC and H3K9me2 levels (Figs 5A and 6) (Kurimoto *et al*, 2015), representing an epigenetic "blank slate".

X chromosome dynamics in cultured female PGCLCs

Female ESCs bear two active X chromosomes (XaXa) and show lower genome-wide 5mC levels compared to male ESCs (Zvetkova *et al*, 2005; Shirane *et al*, 2016). A majority of female EpiLCs bear XaXa, and upon floating aggregate formation, they undergo X inactivation, with female mPGCLCs exhibiting one Xa and one inactive X chromosome (XaXi) (Hayashi *et al*, 2012; Shirane *et al*, 2016). We next evaluated the X chromosome dynamics during female PGCLC expansion in culture. Since female ESCs are vulnerable to losing one X chromosome to become XO (Robertson *et al*, 1983; Zvetkova *et al*, 2005), we first examined the extent of the maintenance of two X chromosomes during PGCLC induction and expansion from two lines of female ESCs, BVSC H14 and H18 (129sv/C57BL/6 background) by DNA fluorescence *in situ* hybridization (FISH) analysis of an X-linked gene, *Huwe1*. As shown in Fig 8A, the two Xs were relatively well maintained during the ESCs-to-EpiLC differentiation, but upon induction of PGCLCs, one X tended to be lost (XO: ~60 and ~40% for H14 and H18 d4 PGCLCs, respectively), and the XX/XO ratios were well preserved during the expansion of PGCLCs in culture (XO: ~60 and ~40% for H14 and H18 d4c7 PGCLCs, respectively).

We then examined the Xa/Xi state of PGCLCs during their expansion by evaluating the H3K27me3 positivity on the X chromosomes. As shown in Fig 8B, ~95% of female mouse embryonic feeders (MEFs) had two Xs and ~90% of such cells exhibited a single H3K27me3 spot on one X, indicating their XaXi state. We found that ~50% of the XX d4 PGCLCs exhibited the XaXi state, whereas ~30% of the XX d4 PGCLCs did not show an H3K27me3 spot on the X chromosomes (Fig 8B). Remarkably, only a minority (< 5%) of XX d4c3 and d4c7 PGCLCs exhibited the XaXi state and ~70% of them exhibited no H3K27me3 spot on the X chromosomes (Fig 8B), indicating that one Xi was re-activated or in the process of re-activation during the expansion culture of PGCLCs, which is in good agreement with the notion that d4c7 PGCLCs acquire an epigenetic "blank slate".

Discussion

We have shown here that Rolipram and Forskolin, which elevate intracellular cAMP concentrations via a synergistic mechanism,
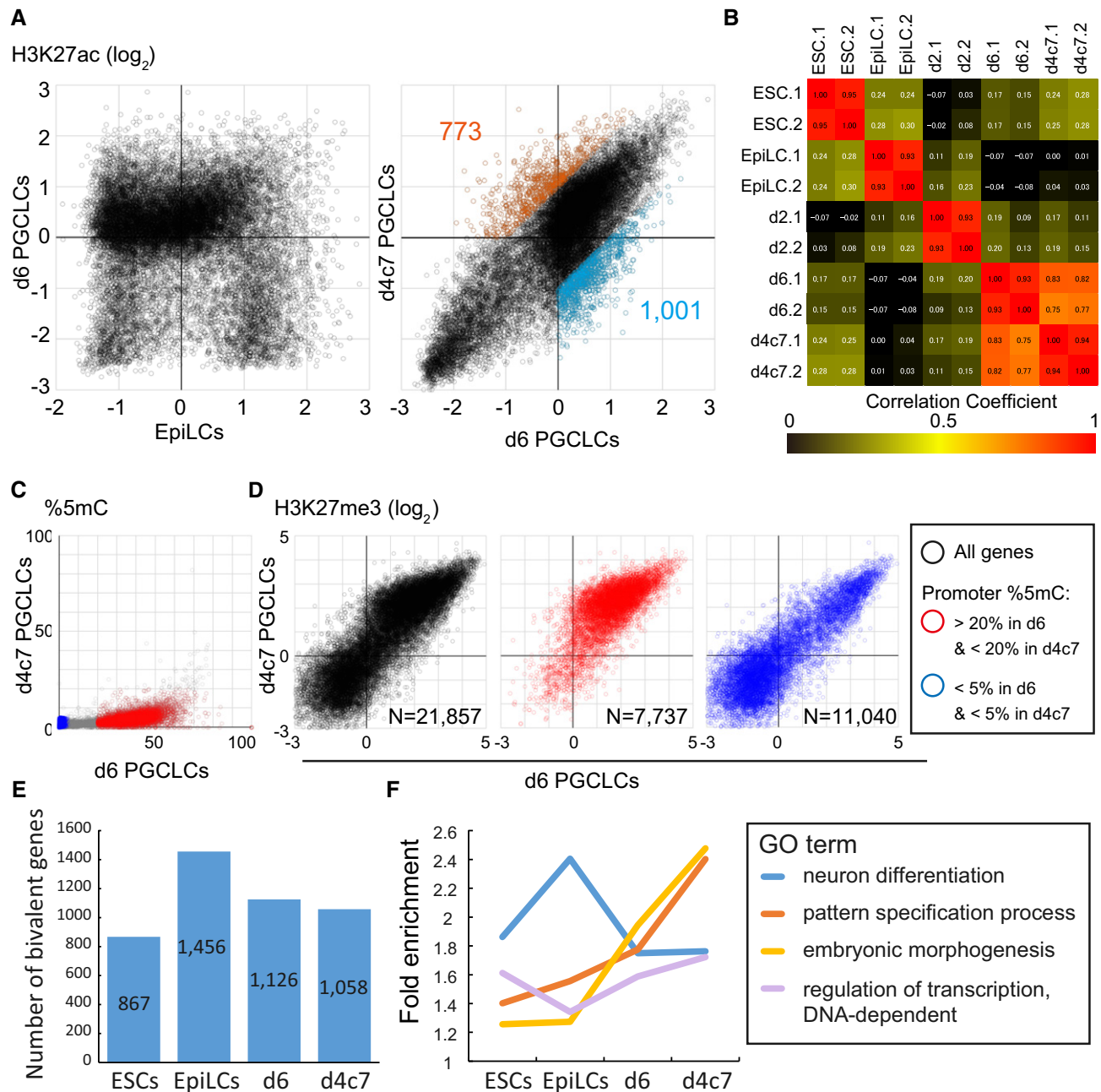
417

Figure 7. Histone-modification dynamics in cultured PGCLCs.

A   Scatter-plot comparisons of log$_2$ H3K27ac levels between EpiLCs and d6 PGCLCs (left), and between d6 and d4c7 PGCLCs (right). The d4c7- and d6-biased H3K27ac peaks are shown in orange and cyan, respectively.

B   Heat-map representation of correlation coefficients of H3K27ac levels in the indicated pairwise comparisons. The color coding is as indicated.

C   Definitions of promoters demethylated/unmethylated only in d4c7 PGCLCs (5mC > 20% in d6 and < 20% in d4c7, red open circles) and in both d6 and d4c7 PGCLCs (5mC < 5% in d6 and d4c7, blue open circles).

D   Scatter-plot comparisons of log$_2$ H3K27me3 levels between d6 and d4c7 PGCLCs around the TSSs of all genes (left, black), genes with promoters demethylated only in d4c7 PGCLCs (middle, red), and genes with promoters demethylated/unmethylated in both d6 and d4c7 PGCLCs (right, blue).

E   Numbers of bivalent genes in ESCs, EpiLCs, and d6 and d4c7 PGCLCs.

F   Transition of the indicated GO term enrichments during PGCLC induction and expansion.

expand PGCLCs up to ~50-fold in the presence of SCF on the m220 feeders (Fig 2), and the expanded PGCLCs robustly contribute to spermatogenesis (Fig 3). Thus, cAMP signaling and

SCF-KIT signaling are the key to PGCLC/PGC proliferation. On the other hand, we have not been successful in extending the PGCLC expansion culture for more than 7 days: Under the current
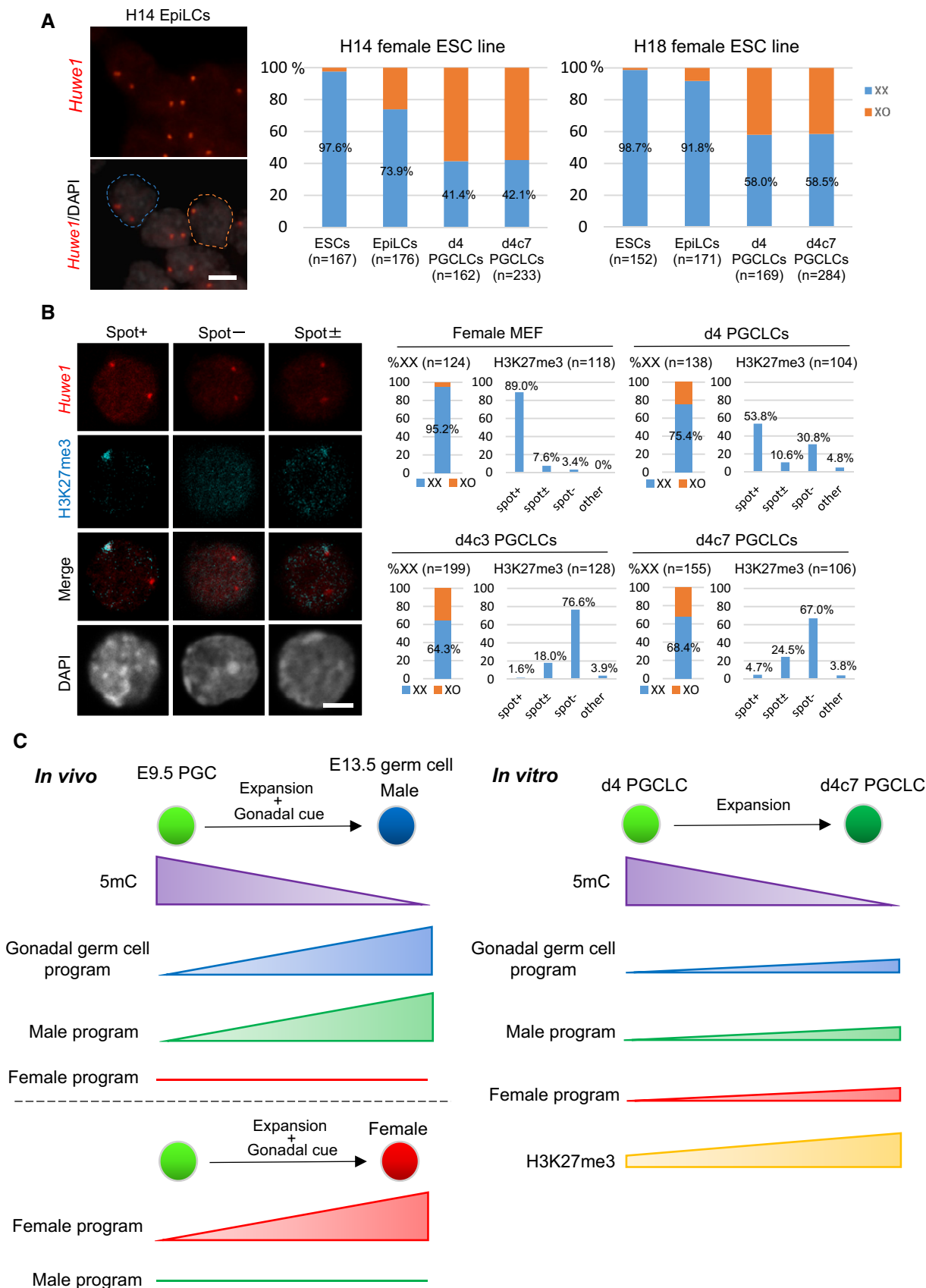
Figure 8.

Figure 8.   X chromosome re-activation in cultured female PGCLCs.

A   Loss of one X chromosome in female PGCLCs during PGCLC induction. (Left) Representative images of female EpiLCs stained for *Huwe1* by DNA FISH. XX and XO EpiLCs are delineated by blue and orange dotted circles, respectively. (Right) Numbers of X chromosomes during PGCLC induction/expansion from two female ESC lines (H14 and H18). Scale bar, 25 μm.

B   Evaluation of X chromosome re-activation in cultured female PGCLCs by double staining for *Huwe1* and H3K27me3. (Left) Representative images for DNA FISH of *Huwe1* and immunofluorescence of H3K27me3. X chromosome re-activation was evaluated in cells retaining two X chromosomes. (Right) Analyses of the *Huwe1* and H3K27me3 signals in female MEFs and d4/d4c3/d4c7 PGCLCs. Scale bar, 5 μm.

C   A model for epigenetic regulation during PGCLC induction/expansion. (Left) *In vivo*, from E9.5 to E13.5, both male and female germ cells propagate substantially (~>100-fold expansion) (Tam & Snow, 1981; Kagiwada *et al*, 2013) and comprehensively erase their DNA methylome. Meanwhile, from around E11.5, they receive signals from gonadal somatic cells, fully acquire "germline" genes, and initiate male or female differentiation [reviewed in (Spiller & Bowles, 2015)]. (Right) During the expansion culture from d4 to d4c7 PGCLCs (~20-fold expansion), PGCLCs comprehensively erase their DNA methylome as PGCs/germ cells *in vivo*. However, due to the lack of cues corresponding to the signals from gonadal somatic cells, PGCLCs essentially preserve their initial transcriptional properties, at least in part through a compensatory up-regulation of H3K27me3 levels around key genes, and thus acquire "germline genes", and male/female properties only moderately. See Dataset EV7 for the summary of expression, 5mC, H3K4me3, and H3K27me3 levels of genes analyzed in this study.

condition, cultured PGCLCs ceased to proliferate and began to decline after ~d9, and they were not maintained upon passaging. In this regard, it would be interesting to examine the effect of other chemicals/signaling pathways identified by our screen on further proliferation of PGCLCs. Rolipram and Forskolin also propagated E9.5 PGCs, but to a limited extent (up to ~eightfold expansion, Fig 2C). Thus, a condition to extend the PGCLC/PGC expansion culture as well as the mechanisms by which cAMP SCF-KIT signaling and SCF-KIT signaling activate the cycling of PGCLCs/PGCs warrant future exploration.

A striking finding was that, upon proliferation, PGCLCs progressively erase their 5mCs apparently at a constant speed and in a manner highly parallel to that in PGCs for all genomic elements, including unique regions, repeats, and distinct regulatory elements such as the ICR of the imprint genes and the promoters of "germline genes" (Fig 6). Consequently, d4c7 PGCLCs establish a DNA methylome essentially identical to that in male/female germ cells at E13.5 (Fig 6). This was clearly a specific event in PGCLCs, since ESCs cultured with FR10, despite their robust propagation, did not show such demethylation (Appendix Fig S12). These observations provide strong evidence in support of two key concepts. First, the dilution of the 5mC patterns established in the epiblast, most likely through a replication-coupled passive mechanism, is the principle for DNA methylation erasure in PGCs. This concept is also supported by the fact that knockout mice of TET1, a primary candidate for the mediation of active DNA demethylation, undergo normal genome-wide DNA demethylation in PGCs (Yamaguchi *et al*, 2012), and by other studies supporting a replication-coupled passive demethylation in PGCs (Seisenberger *et al*, 2012; Kagiwada *et al*, 2013; Arand *et al*, 2015). Second, for the genome-wide DNA methylation erasure to occur, cues from embryonic gonads are essentially dispensable. Thus, it is likely that genome-wide DNA demethylation and sexual differentiation of germ cells that manifests in embryonic gonads by E13.5 are genetically separable events (Fig 8C).

It has previously been reported that an erasure of global H3K27me3 patterns in PGCs, possibly through genome-wide histone replacement, accompanies genome-wide DNA demethylation in PGCs at around E11.5 (Hajkova *et al*, 2008; Mansour *et al*, 2012). After careful examination, however, we did not observe such erasure of H3K27me3 in PGCs in a previous study (Kagiwada *et al*, 2013), and we did not observe it in PGCLCs in this study. To the contrary, PGCLCs grossly maintained their

histone-modification patterns during their expansion, with up-regulation of H3K27me3 enrichment levels around demethylated promoters, and this would be expected to contribute to the relative stability of their transcriptome during expansion (Figs 4 and 7). Thus, PGCLCs expanded in culture free from gonadal cues for sex differentiation can be considered a recapitulation of a unique epigenetic "blank slate" with essentially no DNA methylation and with abundant bivalency. In good agreement with this conclusion, we have shown that cultured female PGCLCs, although sometimes losing a single X, appear to re-activate an Xi that is inactivated upon floating aggregate formation of EpiLCs (Hayashi *et al*, 2012; Shirane *et al*, 2016). Thus, female PGCLC induction and expansion culture will serve as a unique system to analyze the mechanism for X re-activation.

The expansion of PGCs in culture has been difficult and has met with only limited success, which has been a major barrier in promoting PGC biology. The capacity to faithfully expand PGCLCs up to ~50-fold in culture would be instructive for addressing key questions in PGC biology, including the mechanism of the regulation of genome function during epigenetic reprogramming, the mechanism for male versus female differentiation of germ cells, and accordingly, the mechanism for meiotic entry in female germ cells. Moreover, after further modifications/improvements, our strategy could be applied to PGCs/PGCLCs in other mammalian species, including humans, opening the possibility of expanding and maturing human PGCLCs for their further differentiation in culture.

Materials and Methods

Mice

All the animal experiments were performed under the ethical guidelines of Kyoto University. The BVSC (Acc. No. BV, CDB0460T; SC, CDB0465T: http://www.cdb.riken.jp/arg/TG%20mutant%20mice%20list.html) and *Stella-EGFP* transgenic mice were established as reported previously (Payer *et al*, 2006; Seki *et al*, 2007; Ohinata *et al*, 2008) and maintained on a largely C57BL/6 background. The WBB6F1-*W/W^v^*, C57BL/6, DBA/2, C3H, BDF1, and ICR mice were purchased from SLC (Shizuoka, Japan). Noon of the day when a copulation plug was identified was designated as embryonic day (E) 0.5. All mice were housed in a specific pathogen-free animal facility under a 14-h light/10-h dark cycle.

Derivation and culture of ESCs

The BVSC R8, H14, and H18 were reported previously (Hayashi et al, 2011, 2012). The female BVSC mice (largely C57BL/6 background) were mated with male DBA/2 or C3H mice to obtain BDF1 or BCF1 embryos. The blastocysts were placed and cultured in a well of a 96-well plate in N2B27 medium with 2i (PD0325901, 0.4 μM: Stemgent, San Diego, CA; CHIR99021, 3 μM: Stemgent) and LIF (1,000 U/ml; Merck Millipore) on mouse embryonic feeders (MEFs) (Ying et al, 2008; Hayashi et al, 2011). The expanded colonies were passaged by dissociating with TrypLE (Thermo Fisher Scientific). Until passage 2, the ESCs were maintained on MEFs. Thereafter, male ESCs were cultured and maintained feeder-free on a dish coated with poly-L-ornithine (0.01%; Sigma) and laminin (10 ng/ml; BD Biosciences).

Induction of EpiLCs and PGCLCs

Induction of EpiLCs and PGCLCs was performed as reported previously (Hayashi et al, 2011). Briefly, the EpiLCs were induced by plating 1×10^5 ESCs on a well of a 12-well plate coated with human plasma fibronectin (16.7 mg/ml) in N2B27 medium containing activin A (20 ng/ml), bFGF (12 ng/ml), and KSR (1%). The PGCLCs were induced from d2 EpiLCs under a floating condition in a well of a low-cell-binding U-bottom 96-well plate (Thermo Scientific) in serum-free medium [GK15; GMEM (Thermo Fisher Scientific) with 15% KSR, 0.1 mM NEAA, 1 mM sodium pyruvate, 0.1 mM 2-mercaptoethanol, 100 U/ml penicillin, 0.1 mg/ml streptomycin, and 2 mM L-glutamine] in the presence of the cytokines BMP4 (500 ng/ml; R&D Systems), LIF (1,000 U/ml; Merck Millipore), SCF (100 ng/ml; R&D Systems), and EGF (50 ng/ml; R&D Systems). To prepare large numbers of PGCLCs for the chemical library screening, PGCLCs were induced in AggreWell400 (STEMCELL Technologies) using the same medium.

Fluorescence-activated cell sorting

The sample preparations from cell aggregates were performed as described previously (Hayashi et al, 2011). FACS was performed with a FACSAriaIII (BD) cell sorter. BV and SC fluorescence were detected with the FITC and AmCyan Horizon V500 channel, respectively. Data were analyzed with FACSDiva (BD) software.

Establishment of m220 sublines

The m220 cell line (Majumdar et al, 1994) were cultured in a gelatin-coated plate in DMEM with 10% FCS. Since m220 cells were highly vulnerable to mitomycin C (MMC) treatment, we established sublines of m220 resistant to MMC. Briefly, single m220 cells were plated on wells of 96-well plates (6 plates) by FACS. One week after the plating, cell growth was observed in approximately half of the wells. After passaging the cells to one well of each of the two 96-well plates, one plate was frozen as a replica and the other plate was treated with MMC (4 μg/ml, 2 h). At 10 days after MMC treatment, MMC resistance was evaluated by microscopic observation. In total, 242 m220 sublines were established and seven sublines showed high MMC resistance. The m220-5 subline was primarily used for experiments.

Detection of BV (+) PGCLCs by a cell analyzer

d4 PGCLCs were plated on m220-5 feeders in a 96-well plate by FACS, and BV fluorescence was monitored by a cell analyzer (Cellavista; SynenTec). The fluorescence photos for BV were taken by a Cellavista cell analyzer with the following settings: 10× objectives; exposure time: 140 μsec; gain: 4×; binning: 4 × 4; excitation: 500/24 nm; and emission: 542/27 nm. The BV fluorescence was detected by using the following algorithm/attribute parameters: sensitivity: 10; region merging: 200; min. granule intensity: 50; well edge distance: 200; contrast: 1; size: 3,000; intensity: 255; roughness: 500; granularity: 100; granule intensity: 255; granule count: 10,000; longishness: 100; and compactness: 1. The values of "cell nuclei" were used for the detection of BV fluorescence.

Chemical library screening for PGCLC proliferation

We screened the chemical libraries listed in Fig EV1C at concentrations of 10 and 1 μM. We used 96-well plates with MMC-treated m220-5 cells. In each 96-well plate, negative (DMSO only) and positive (LIF) controls were allocated to both sides and the compounds were added to 80 wells (Fig EV1B). Two hundred BV (+) d4 PGCLCs induced from BDF1-2 ESCs were plated in a well of 96-well plates and BV fluorescence was measured on culture day 1 (c1), c3, c5, and c7 by a Cellavista cell analyzer. The values of "cell nuclei" were used for the detection of BV fluorescence. Because the proliferation rates of d4 PGCLCs differed slightly among the experiments, the values from different experiments were adjusted based on the average values of negative controls obtained from the first experiment. For each compound, the fold difference of the BV fluorescence between c1 and c7 was calculated and the compounds with fold difference values > 3 SDs of the mean values of the negative controls were identified as those enhancing the proliferation of PGCLCs.

Expansion culture of d4 PGCLCs and E9.5 PGCs

m220-5 cells were cultured for three passages with 10 μM of both Forskolin and Rolipram to permit adaptation to these compounds prior to MMC treatment (1–2 μg/ml, 2 h), since the MMC-treated m220-5 feeders were vulnerable to Forskolin and Rolipram. d4 PGCLCs or E9.5 PGCs (BDF1×*Stella–EGFP*) were sorted by FACS and plated on m220-5 cells in GMEM containing 10% KSR, 0.1 mM NEAA, 1 mM sodium pyruvate, 0.1 mM 2-mercaptoethanol, 100 U/ml penicillin, 0.1 mg/ml streptomycin, 2 mM L-glutamine, 2.5% FCS, 100 ng/ml SCF, 10 μM Forskolin, and 10 μM Rolipram. Half of the culture medium was changed every 2 days.

Immunofluorescence

The following antibodies were used at the indicated dilutions: rabbit anti-MVH (1/250; Abcam ab13840); rabbit anti-DAZL (1/250; Abcam ab34139); mouse anti-OCT4 (1/250; BD 611203); mouse anti-5mC (1/500; Abcam ab10805); rabbit anti-H3K27me3 (1/500; Millipore 07-449); rabbit anti-H3K9me2 (1/500; Millipore 07-441); rabbit anti-DNMT1 (1/100; Santa Cruz Biotechnology sc-20701); mouse anti-DNMT3A (1/200; Abcam ab13888); mouse anti-DNMT3B (1/200; Novus Biologicals NB100-56514); rabbit anti-UHRF1 (1/100; Santa Cruz Biotechnology sc-98817); and chicken

anti-GFP (1/500; Abcam ab13970). The following secondary antibodies from Thermo Fisher Scientific were used at a 1/500 dilution: Alexa Fluor 568 goat anti-rabbit IgG; Alexa Fluor 568 goat anti-mouse IgG; and Alexa Fluor 488 goat anti-chicken IgG. For staining F-actin, Alexa Fluor 568-conjugated phalloidin (1/40, Thermo Fisher Scientific A12380) was used.

The protocol for immunofluorescence staining was described previously (Hayashi *et al*, 2011; Nakaki *et al*, 2013). For the MVH, DAZL, and OCT4 staining, d4c7 PGCLCs (BDF1-2) were sorted by FACS, mixed with E13.5 male PGCs at a ratio of 1:1 and spread onto MAS-coated glass slides with Cyto Spin 4 (Thermo Fisher Scientific). The E13.5 male germ cells (ICR) were sorted using SSEA1 antibody conjugated with Alexa Fluor 647 by FACS. For the 5mC, H3K27me3 and H3K9me2 staining, d4c7 PGCLCs (BDF1-2) were sorted by FACS, mixed with d2 EpiLCs at a ratio of 1:1 and spread onto MAS-coated glass slides with Cyto Spin 4 (Thermo Fisher Scientific). Images were captured with a confocal microscope (Zeiss, LSM780) and the signal intensities were analyzed by ImageJ (NIH).

Measurement of cAMP concentration

The intracellular cAMP concentration was measured using a cAMP-Glo Max assay kit (Promega) according to the manufacturer's instructions. The standard curve using purified cAMP was generated by calculating the Δ relative light units (RLU [0 nM] – RLU [X nM]). For each sample, 1×10^4 d4 PGCLCs were pretreated with Forskolin and/or Rolipram for 30 min at RT, and the Δ RLU (RLU [untreated sample] – RLU [treated sample]) was calculated. The increase in intracellular cAMP levels by the chemical treatment was inferred from the cAMP standard curve. Three biological replicates were analyzed for each sample.

Cell-cycle analysis

The cell-cycle statuses of ESCs, EpiLCs, d4, d4c3, d4c5, and d4c7 PGCLCs (BDF1-2) and male germ cells at E13.5, E14.5, and E15.5 were examined as reported previously (Kagiwada *et al*, 2013). To label cultured cells, cells were incubated with BrdU (10 μM) for 30 min. To label germ cells, female mice (ICR) were mated with *Stella–EGFP* males, pregnant females were intraperitoneally injected with 1 mg of BrdU, and embryos were collected after 30 min. The cultured cells or male gonads were dispersed into single cells by TrypLE treatment. For the detection of BrdU incorporation, we used an APC-BrdU Flow Kit (BD Biosciences) according to the manufacturer's instructions. The stained samples were analyzed using BD FACSAriaIII (BD) with FACSDiva (BD) software with PGCLCs and male germ cells identified by BV or *Stella-EGFP* fluorescence, respectively. Three biological replicates were analyzed for each sample.

Transplantation of PGCLCs into the testis of *W/Wᵛ* mice

After PGCLCs were purified by FACS, 1×10^4 to 1×10^5 cells per testis were injected into the testes of randomly selected neonate (7 days post-partum) or adult *W/Wᵛ* mice as previously described (Chuma *et al*, 2005). Anti-mouse CD4 antibody (50 mg per dose, clone GK1.5; Biolegend) was injected intraperitoneally on day 0, 2, or 4 for immunosuppression when necessary (Kanatsu-Shinohara

et al, 2003). For the assessment of fertility, the recipients at 10 weeks after transplantation were mated with BDF1 females. The genotyping of offspring for BVSC transgenes was performed as reported previously (Ohinata *et al*, 2008). For HE staining, the testes or epididymis was fixed with Bouin's solution, embedded in paraffin, and sectioned.

In vitro fertilization

Sperm were retrieved from the cauda epididymis and pre-incubated in HTF medium (Kyudo Co., Ltd.) at 37°C for 1 hr. Oocytes were recovered from super-ovulated BDF1 females by injecting PMSG and hCG, and fertilized with the sperm in HTF medium. The resultant two-cell embryos were transferred into the oviducts of pseudo-pregnant ICR females at 0.5 days post-coitum (dpc). Pups were delivered by cesarean section at 18.5 dpc.

LacZ staining

The seminiferous tubules were fixed with 2% paraformaldehyde and 0.2% glutaraldehyde in PBS at 4°C for 1 h. After washing three times with PBS, the seminiferous tubules were incubated in X-gal solution (0.1% X-gal, 0.1% Triton X-100, 1 mM $MgCl_2$, 3 mM $K_4[Fe(CN)_6]$, and 3 mM $K_3[Fe(CN)_6]$ in PBS) at 37°C for 2–3 h.

DNA FISH and immunofluorescence–DNA FISH on PGCLCs

The ESCs, EpiLCs, and female MEFs were dissociated with TrypLE, and d4, d4c3, and d4c7 PGCLCs were purified with FACS. The cell samples were transferred onto a poly-L-lysine (Sigma)-coated glass coverslip in a drop of PBS and allowed to adhere to the coverslip by aspirating the excess medium prior to fixation. For DNA FISH, cell samples on coverslips were fixed for 10 min in 3% paraformaldehyde (PFA) (pH 7.4), permeabilized on ice for 3 min in 0.5% Triton X-100/PBS, and stored in 70% ethanol at −20°C. After dehydrating through an ethanol series, they were denatured in 70% formamide/2× SSC (pH 7.4) for 30 min at 80°C and dehydrated again through an ice-cold ethanol series. They were then hybridized with fluorescent BAC probes (RP24-157H12) for *Huwe1* at 37°C overnight. Coverslips were counterstained with DAPI (1 μg/ml) and mounted in Vectashield (Vector Laboratories).

Immunofluorescence followed by DNA FISH was carried out as described previously (Chaumeil *et al*, 2004, 2008). The cell samples on coverslips were fixed for 10 min in 3% PFA (pH 7.4) at room temperature. Permeabilization of cells was performed on ice in 0.5% Triton X-100/PBS for 3 min. After rinsing in PBS, the preparation was blocked in 1% BSA (Sigma)/PBS for 30 min, incubated with anti-H3K27me3 (1/200; Millipore) overnight at 4°C and then washed in PBS three times and incubated with an Alexa Fluor 488 anti-rabbit secondary antibody (1/500; Thermo Fisher Scientific) for 30 min at room temperature. After washing in PBS, preparations were post-fixed in 4% PFA for 10 min at room temperature and rinsed in PBS. Preparations were incubated in 0.7% Triton X-100, 0.1 M HCl for 10 min on ice. They were then washed twice in 2× SSC for 10 min at RT. Finally, the preparations were denatured in 70% formamide/2× SSC (pH 7.4) for 30 min at 80°C, dipped in ice-cold 2× SSC, and hybridized with fluorescent BAC probes for *Huwe1* as described above.

RNA sequencing (RNA-seq)

Total RNAs were purified from ESCs, EpiLCs, and BVSC (+) d4, d6, d4c3, d4c5, and d4c7 PGCLCs (two biological replicates for each) using an RNAeasy Micro Kit (Qiagen). 10 ng RNAs (equivalent to 1,000 cells) were subjected to the previously described cDNA amplification method (Kurimoto *et al*, 2006), and their 3′ termini were then subjected to deep sequencing on a SOLiD5500xl system as described previously (Nakamura *et al*, 2015). 1 ng RNAs from E10.5 PGCs and E12.5 and E13.5 male/female germ cells, and amplified cDNA from E9.5 PGCs (two biological replicates for each) prepared in the previous study (Kagiwada *et al*, 2013) were also subjected to the RNA-seq.

Chromatin immunoprecipitation sequencing (ChIP-seq)

ChIP-seq was performed as described previously (Kurimoto *et al*, 2015). Briefly, 1×10^5~1×10^6 BV (+) d4c7 PGCLCs were purified with FACS, and fixed with 1% formalin (Sigma) for 10 min at room temperature followed by quenching with 150 mM glycine. The fixed cells were washed with PBS, dissolved in lysis buffer containing 1% SDS, and sonicated using a Bioruptor UCD250 for 10 cycles of 30 s at high power. Solubilized chromatin fraction was incubated with mouse monoclonal antibodies for histone H3K4me3, H3K27ac, or H3K27me3 (Hayashi-Takanaka *et al*, 2011) in complex with M280 Dynabeads Sheep anti-mouse IgG (Life Technologies) at 4°C overnight with rotation (two biological replicates for each). Chromatins were eluted in a buffer containing 1% SDS and 10 mM DTT after washing. The eluents were reverse-crosslinked at 65°C overnight, treated with 4 μg proteinase K at 45°C for 1 h, and purified with a Qiaquick PCR purification column (Qiagen). The ChIP-ed and input DNAs were then sheared to an average size of about 150 bp by ultrasonication (Covaris, Woburn, MA), and subjected to library preparation methods for deep sequencing on a SOLiD5500xl system as previously described (Kurimoto *et al*, 2015).

Whole-genome bisulfite sequencing (WGBS)

WGBS was performed as described previously (Shirane *et al*, 2016). Briefly, purified BV-positive d4c3 and d4c7 PGCLCs (two biological replicates for each) were lysed with 10 mM Tris–Cl (pH 8.0) containing 150 mM NaCl, 10 mM EDTA, 0.5% SDS, and 1 mg/mL proteinase K at 55°C overnight with shaking. The lysate was incubated with 1.32 μg/ml RNase A at 37°C for 1 h, and extracted once with TE-saturated phenol, twice with phenol–chloroform, and once with chloroform. Genomic DNA was precipitated with an equal volume of isopropanol, washed twice with 70% ethanol, air-dried, and then dissolved in 10 mM Tris–Cl (pH 8.0). The purified genomic DNA (50 ng) was spiked with 0.5 ng unmethylated lambda phage DNA (Promega) and subjected to bisulfite conversion and library construction using the post-bisulfite adaptor tagging (PBAT) method (Miura *et al*, 2012) for deep sequencing on an Illumina HiSeq 1500/2500 system as described previously (Shirane *et al*, 2016).

Data analysis for RNA-seq

The RNA-seq read data were mapped on the mouse mm10 genome and annotated to reference genes with extended transcription terminal sites as described previously (Nakamura *et al*, 2015), using cutadapt v1.3 (Martin, 2011), tophat v1.4.1/bowtie v1.0.1 (Kim *et al*, 2013), and cufflinks v2.2.0 (Trapnell *et al*, 2012). Expression levels were normalized to reads per million-mapped reads (RPM). Significant expression levels were defined as $\log_2$ (RPM+1) > 3. Genes were considered as differentially expressed if the fold changes of expression levels were > 2 [i.e. if the difference of $\log_2$ (RPM+1) was > 1]. Genes significantly expressed in at least one sample and differentially expressed in at least one pairwise comparison (10,437 genes) were used in principal component analysis (PCA) and unsupervised hierarchical clustering (UHC). Gene ontology (GO) (Ashburner *et al*, 2000) of differentially expressed genes was analyzed using the DAVID program (Huang da *et al*, 2009).

Data analysis for ChIP-seq

Read data of ESCs, EpiLCs, d6 PGCLCs (Kurimoto *et al*, 2015), and d4c7 PGCLCs were mapped on the mouse mm10 genome and analyzed as described previously (Kurimoto *et al*, 2015) using bowtie v1.1.2 (Langmead *et al*, 2009), picard-tools v2.1.0 (http://broadinstitute.github.io/picard/), IGVtools v2.3.52 (Robinson *et al*, 2011), samtools v1.3 (Li *et al*, 2009), and MACS v2.1.0 (Zhang *et al*, 2008). Read patterns were visualized by IGV (Robinson *et al*, 2011).

H3K4me3 peaks with *P*-values < 10^{-5} detected in proximity (within 1 kb) were combined as a single peak, and the read densities of the peaks within 500 bp from the center were normalized by those of Input (the larger of those within 500 bp and within 5 kb) (IP/Input levels). H3K4me3 peaks with the greatest IP/Input levels among those located within 2 kb from TSSs were considered TSS-associated peaks. The IP/Input levels of TSS-associated H3K4me3 peaks were further normalized to that associated with a gene with the 95th percentile of the significant expression levels, and defined as the H3K4me3 levels.

H3K27ac peaks with *P*-values < 10^{-20} detected in proximity (within 1 kb) were combined as a single peak. The read densities of the peaks within 500 bp from the center were normalized to the average of the $\log_2$ IP/Input levels, and defined as the H3K27ac levels. The H3K27ac peaks were considered biased to d6- or d4c7, if the fold changes of the H3K27ac levels were > 2.

The read densities of H3K27me3 for the regions around TSSs (within 1 kb) and for the TSS-associated H3K4me3 peaks were normalized by Input, and were further normalized to the average IP/Input levels of H3K27me3 around the TSSs of the genes with expression levels of $\log_2$ (RPM+1) > 2.5 and smaller than 3.5, to define H3K27me3 levels.

Data analysis for WGBS

Adaptor trimming, mapping on the mouse mm10 genome, and analyses of WGBS data were performed as described previously (Shirane *et al*, 2016) using the programs Trim Galore! v0.4.1 (http://www.bioinformatics.babraham.ac.uk/projects/trim_galore/), cutadapt v1.9.1, and Bismark v0.15.0 (Krueger & Andrews, 2011), bowtie v1.1.2 and R. The bisulfite conversion rate was estimated as > 99.5% using the lambda phage genome as a positive control.

Promoters were defined as regions 0.9 kb upstream and 0.4 kb downstream from the transcription start sites and classified into three categories depending on their GC content and CpG density as described previously (HCPs, ICPs, and LCPs) (Borgel *et al*, 2010). Promoters with at least 5 CpGs were used for methylation analysis. Coordinates of the ICRs that were defined in E12.5 embryos were obtained from a previous publication (Tomizawa *et al*, 2011). For the methylation analysis of repetitive elements, the processed reads were mapped to the repetitive consensus sequences (Shirane *et al*, 2016) and CpG sites that covered at least four reads were used. The uniquely mapped regions overlapped with repeats were defined using RepeatMasker (Smit, AFA, Hubley, R & Green, P. Repeat-Masker Open-4.0. 2013-2015 http://www.repeatmasker.org). For analysis of the uniquely mapped whole-genomic regions, the 5mC levels in 2-kb sliding windows with 1-kb overlap were calculated.

For the methylation analysis of uniquely mapped regions, CpG sites that covered less than four reads and more than 200 reads were excluded; thus, the minimum sequence depth to call the methylated/unmethylated cytosine was 4. For the methylation analysis of repetitive elements, the processed reads were mapped to the repetitive consensus sequences (RepBase19.0.4) and CpG sites that covered at least five reads were used.

The sequencing and mapping statistics for RNA-seq, ChIP-seq, and WGBS are shown in Dataset EV1, Tables EV3 and EV4, respectively, and summarized in Dataset EV7.

Accession numbers

The accession number for the RNA-seq data of d4c3/d4c5/d4c7 PGCLCs and E9.5/E12.5 germ cells is GSE87644 (the GEO database). The RNA-seq data of ESCs/EpiLCs/d4/d6 PGCLCs [BVSC (+)] (GSE67259) and of E10.5/E11.5/E13.5 germ cells (GSE74094) were downloaded from the GEO database.

The accession number for the ChIP-seq data of H3K4me3, H3K27ac, and H3K27me3 for d4c7 PGCLCs is GSE87645 (the GEO database). The ChIP-seq data of H3K4me3, H3K27ac, and H3K27me3 for ESCs/EpiLCs/d2/d4/d6 PGCLCs (GSE60204) were downloaded from the GEO database.

The accession number for the WGBS-seq data of d4c3/d4c7 PGCLCs is DRA005166 (the DDBJ database). The WGBS-seq data of ESCs/EpiLCs/d2/d4/d6 PGCLCs (DRA003471) and E10.5/E13.5 PGCs (DRA000607) were downloaded from the DDBJ database.

Expanded View for this article is available online.

References

Arand J, Wossidlo M, Lepikhov K, Peat JR, Reik W, Walter J (2015) Selective impairment of methylation maintenance is the major cause of DNA methylation reprogramming in the early embryo. *Epigenetics Chromatin* 8: 1

Ashburner M, Ball CA, Blake JA, Botstein D, Butler H, Cherry JM, Davis AP, Dolinski K, Dwight SS, Eppig JT, Harris MA, Hill DP, Issel-Tarver L, Kasarskis A, Lewis S, Matese JC, Richardson JE, Ringwald M, Rubin GM, Sherlock G (2000) Gene ontology: tool for the unification of biology. The Gene Ontology Consortium. *Nat Genet* 25: 25−29

Borgel J, Guibert S, Li Y, Chiba H, Schubeler D, Sasaki H, Forne T, Weber M (2010) Targets and dynamics of promoter DNA methylation during early mouse development. *Nat Genet* 42: 1093−1100

Buehr M (1997) The primordial germ cells of mammals: some current perspectives. *Exp Cell Res* 232: 194−207

Calo E, Wysocka J (2013) Modification of enhancer chromatin: what, how, and why? *Mol Cell* 49: 825−837

Chaumeil J, Okamoto I, Heard E (2004) X-chromosome inactivation in mouse embryonic stem cells: analysis of histone modifications and transcriptional activity using immunofluorescence and FISH. *Methods Enzymol* 376: 405−419

Chaumeil J, Augui S, Chow JC, Heard E (2008) Combined immunofluorescence, RNA fluorescent *in situ* hybridization, and DNA fluorescent *in situ* hybridization to study chromatin changes, transcriptional activity, nuclear organization, and X-chromosome inactivation. *Methods Mol Biol* 463: 297−308

Chuma S, Kanatsu-Shinohara M, Inoue K, Ogonuki N, Miki H, Toyokuni S, Hosokawa M, Nakatsuji N, Ogura A, Shinohara T (2005) Spermatogenesis from epiblast and primordial germ cells following transplantation into postnatal mouse testis. *Development* 132: 117−122

Cooke HJ, Lee M, Kerr S, Ruggiu M (1996) A murine homologue of the human DAZ gene is autosomal and expressed only in male and female gonads. *Hum Mol Genet* 5: 513−516

De Felici M, Dolci S, Pesce M (1993) Proliferation of mouse primordial germ cells *in vitro*: a key role for cAMP. *Dev Biol* 157: 277−280

De Felici M, Scaldaferri ML, Lobascio M, Iona S, Nazzicone V, Klinger FG, Farini D (2004) Experimental approaches to the study of primordial germ cell lineage and proliferation. *Hum Reprod Update* 10: 197−206

Dolci S, Williams DE, Ernst MK, Resnick JL, Brannan CI, Lock LF, Lyman SD, Boswell HS, Donovan PJ (1991) Requirement for mast cell growth factor for primordial germ cell survival in culture. *Nature* 352: 809−811

Durcova-Hills G, Tang F, Doody G, Tooze R, Surani MA (2008) Reprogramming primordial germ cells into pluripotent stem cells. *PLoS ONE* 3: e3531

Fujiwara Y, Komiya T, Kawabata H, Sato M, Fujimoto H, Furusawa M, Noce T (1994) Isolation of a DEAD-family protein gene that encodes a murine

homolog of *Drosophila* vasa and its specific expression in germ cell lineage. *Proc Natl Acad Sci USA* 91: 12258–12262

Ginsburg M, Snow MH, McLaren A (1990) Primordial germ cells in the mouse embryo during gastrulation. *Development* 110: 521–528

Habibi E, Brinkman AB, Arand J, Kroeze LI, Kerstens HH, Matarese F, Lepikhov K, Gut M, Brun-Heath I, Hubner NC, Benedetti R, Altucci L, Jansen JH, Walter J, Gut IG, Marks H, Stunnenberg HG (2013) Whole-genome bisulfite sequencing of two distinct interconvertible DNA methylomes of mouse embryonic stem cells. *Cell Stem Cell* 13: 360–369

Hajkova P, Ancelin K, Waldmann T, Lacoste N, Lange UC, Cesari F, Lee C, Almouzni G, Schneider R, Surani MA (2008) Chromatin dynamics during epigenetic reprogramming in the mouse germ line. *Nature* 452: 877–881

Hayashi K, Ohta H, Kurimoto K, Aramaki S, Saitou M (2011) Reconstitution of the mouse germ cell specification pathway in culture by pluripotent stem cells. *Cell* 146: 519–532

Hayashi K, Ogushi S, Kurimoto K, Shimamoto S, Ohta H, Saitou M (2012) Offspring from oocytes derived from *in vitro* primordial germ cell-like cells in mice. *Science* 338: 971–975

Hayashi-Takanaka Y, Yamagata K, Wakayama T, Stasevich TJ, Kainuma T, Tsurimoto T, Tachibana M, Shinkai Y, Kurumizaka H, Nozaki N, Kimura H (2011) Tracking epigenetic histone modifications in single cells using Fab-based live endogenous modification labeling. *Nucleic Acids Res* 39: 6475–6488

Hayatsu H, Shiragami M (1979) Reaction of bisulfite with the 5-hydroxymethyl group in pyrimidines and in phage DNAs. *Biochemistry* 18: 632–637

Hikabe O, Hamazaki N, Nagamatsu G, Obata Y, Hirao Y, Hamada N, Shimamoto S, Imamura T, Nakashima K, Saitou M, Hayashi K (2016) Reconstitution *in vitro* of the entire cycle of the mouse female germ line. *Nature* 539: 299–303

Huang da W, Sherman BT, Lempicki RA (2009) Systematic and integrative analysis of large gene lists using DAVID bioinformatics resources. *Nat Protoc* 4: 44–57

Irie N, Weinberger L, Tang WW, Kobayashi T, Viukov S, Manor YS, Dietmann S, Hanna JH, Surani MA (2015) SOX17 is a critical specifier of human primordial germ cell fate. *Cell* 160: 253–268

Ishikura Y, Yabuta Y, Ohta H, Hayashi K, Nakamura T, Okamoto I, Yamamoto T, Kurimoto K, Shirane K, Sasaki H, Saitou M (2016) *In vitro* derivation and propagation of spermatogonial stem cell activity from mouse pluripotent stem cells. *Cell Rep* 17: 2789–2804

Kagiwada S, Kurimoto K, Hirota T, Yamaji M, Saitou M (2013) Replication-coupled passive DNA demethylation for the erasure of genome imprints in mice. *EMBO J* 32: 340–353

Kanatsu-Shinohara M, Ogonuki N, Inoue K, Ogura A, Toyokuni S, Honjo T, Shinohara T (2003) Allogeneic offspring produced by male germ line stem cell transplantation into infertile mouse testis. *Biol Reprod* 68: 167–173

Keravis T, Lugnier C (2012) Cyclic nucleotide phosphodiesterase (PDE) isozymes as targets of the intracellular signalling network: benefits of PDE inhibitors in various diseases and perspectives for future therapeutic developments. *Br J Pharmacol* 165: 1288–1305

Kim D, Pertea G, Trapnell C, Pimentel H, Kelley R, Salzberg SL (2013) TopHat2: accurate alignment of transcriptomes in the presence of insertions, deletions and gene fusions. *Genome Biol* 14: R36

Kobayashi H, Sakurai T, Miura F, Imai M, Mochiduki K, Yanagisawa E, Sakashita A, Wakai T, Suzuki Y, Ito T, Matsui Y, Kono T (2013) High-resolution DNA methylome analysis of primordial germ cells identifies gender-specific reprogramming in mice. *Genome Res* 23: 616–627

Koshimizu U, Watanabe M, Nakatsuji N (1995) Retinoic acid is a potent growth activator of mouse primordial germ cells *in vitro*. *Dev Biol* 168: 683–685

Krueger F, Andrews SR (2011) Bismark: a flexible aligner and methylation caller for Bisulfite-Seq applications. *Bioinformatics* 27: 1571–1572

Kurimoto K, Yabuta Y, Ohinata Y, Ono Y, Uno KD, Yamada RG, Ueda HR, Saitou M (2006) An improved single-cell cDNA amplification method for efficient high-density oligonucleotide microarray analysis. *Nucleic Acids Res* 34: e42

Kurimoto K, Yabuta Y, Hayashi K, Ohta H, Kiyonari H, Mitani T, Moritoki Y, Kohri K, Kimura H, Yamamoto T, Katou Y, Shirahige K, Saitou M (2015) Quantitative dynamics of chromatin remodeling during germ cell specification from mouse embryonic stem cells. *Cell Stem Cell* 16: 517–532

Langmead B, Trapnell C, Pop M, Salzberg SL (2009) Ultrafast and memory-efficient alignment of short DNA sequences to the human genome. *Genome Biol* 10: R25

Lawson KA, Dunn NR, Roelen BA, Zeinstra LM, Davis AM, Wright CV, Korving JP, Hogan BL (1999) Bmp4 is required for the generation of primordial germ cells in the mouse embryo. *Genes Dev* 13: 424–436

Lee HJ, Hore TA, Reik W (2014) Reprogramming the methylome: erasing memory and creating diversity. *Cell Stem Cell* 14: 710–719

Li H, Handsaker B, Wysoker A, Fennell T, Ruan J, Homer N, Marth G, Abecasis G, Durbin R, Genome Project Data Processing S (2009) The sequence alignment/Map format and SAMtools. *Bioinformatics* 25: 2078–2079.

Majumdar MK, Feng L, Medlock E, Toksoz D, Williams DA (1994) Identification and mutation of primary and secondary proteolytic cleavage sites in murine stem cell factor cDNA yields biologically active, cell-associated protein. *J Biol Chem* 269: 1237–1242

Mansour AA, Gafni O, Weinberger L, Zviran A, Ayyash M, Rais Y, Krupalnik V, Zerbib M, Amann-Zalcenstein D, Maza I, Geula S, Viukov S, Holtzman L, Pribluda A, Canaani E, Horn-Saban S, Amit I, Novershtern N, Hanna JH (2012) The H3K27 demethylase Utx regulates somatic and germ cell epigenetic reprogramming. *Nature* 488: 409–413

Martin M (2011) Cutadapt removes adapter sequences from high-throughput sequencing reads. *EMBnet J* 17: 10

Matsui Y, Toksoz D, Nishikawa S, Williams D, Zsebo K, Hogan BL (1991) Effect of Steel factor and leukaemia inhibitory factor on murine primordial germ cells in culture. *Nature* 353: 750–752

Matsui Y, Zsebo K, Hogan BL (1992) Derivation of pluripotential embryonic stem cells from murine primordial germ cells in culture. *Cell* 70: 841–847

McLaren A (2003) Primordial germ cells in the mouse. *Dev Biol* 262: 1–15

Miura F, Enomoto Y, Dairiki R, Ito T (2012) Amplification-free whole-genome bisulfite sequencing by post-bisulfite adaptor tagging. *Nucleic Acids Res* 40: e136

Nakaki F, Hayashi K, Ohta H, Kurimoto K, Yabuta Y, Saitou M (2013) Induction of mouse germ-cell fate by transcription factors *in vitro*. *Nature* 501: 222–226

Nakamura T, Yabuta Y, Okamoto I, Aramaki S, Yokobayashi S, Kurimoto K, Sekiguchi K, Nakagawa M, Yamamoto T, Saitou M (2015) SC3-seq: a method for highly parallel and quantitative measurement of single-cell gene expression. *Nucleic Acids Res* 43: e60

Nakamura T, Okamoto I, Sasaki K, Yabuta Y, Iwatani C, Tsuchiya H, Seita Y, Nakamura S, Yamamoto T, Saitou M (2016) A developmental coordinate of pluripotency among mice, monkeys and humans. *Nature* 537: 57–62

Ohinata Y, Payer B, O'Carroll D, Ancelin K, Ono Y, Sano M, Barton SC, Obukhanych T, Nussenzweig M, Tarakhovsky A, Saitou M, Surani MA (2005) Blimp1 is a critical determinant of the germ cell lineage in mice. *Nature* 436: 207–213

Ohinata Y, Sano M, Shigeta M, Yamanaka K, Saitou M (2008) A comprehensive, non-invasive visualization of primordial germ cell development in mice by the Prdm1-mVenus and Dppa3-ECFP double transgenic reporter. *Reproduction* 136: 503−514

Ohta H, Wakayama T, Nishimune Y (2004) Commitment of fetal male germ cells to spermatogonial stem cells during mouse embryonic development. *Biol Reprod* 70: 1286−1291

Payer B, Chuva de Sousa Lopes SM, Barton SC, Lee C, Saitou M, Surani MA (2006) Generation of stella-GFP transgenic mice: a novel tool to study germ cell development. *Genesis* 44: 75−83

Pierre S, Eschenhagen T, Geisslinger G, Scholich K (2009) Capturing adenylyl cyclases as potential drug targets. *Nat Rev Drug Discov* 8: 321−335

Popp C, Dean W, Feng S, Cokus SJ, Andrews S, Pellegrini M, Jacobsen SE, Reik W (2010) Genome-wide erasure of DNA methylation in mouse primordial germ cells is affected by AID deficiency. *Nature* 463: 1101−1105

Robertson EJ, Evans MJ, Kaufman MH (1983) X-chromosome instability in pluripotential stem cell lines derived from parthenogenetic embryos. *J Embryol Exp Morphol* 74: 297−309

Robinson JT, Thorvaldsdottir H, Winckler W, Guttman M, Lander ES, Getz G, Mesirov JP (2011) Integrative genomics viewer. *Nat Biotechnol* 29: 24−26

Saitou M, Barton SC, Surani MA (2002) A molecular programme for the specification of germ cell fate in mice. *Nature* 418: 293−300

Saitou M, Yamaji M (2012) Primordial germ cells in mice. *Cold Spring Harb Perspect Biol* 4: a008375

Saitou M, Kagiwada S, Kurimoto K (2012) Epigenetic reprogramming in mouse pre-implantation development and primordial germ cells. *Development* 139: 15−31

Saitou M, Miyauchi H (2016) Gametogenesis from pluripotent stem cells. *Cell Stem Cell* 18: 721−735

Sasaki K, Yokobayashi S, Nakamura T, Okamoto I, Yabuta Y, Kurimoto K, Ohta H, Moritoki Y, Iwatani C, Tsuchiya H, Nakamura S, Sekiguchi K, Sakuma T, Yamamoto T, Mori T, Woltjen K, Nakagawa M, Yamamoto T, Takahashi K, Yamanaka S *et al* (2015) Robust *in vitro* induction of human germ cell fate from pluripotent stem cells. *Cell Stem Cell* 17: 178−194

Schubeler D (2015) Function and information content of DNA methylation. *Nature* 517: 321−326

Seisenberger S, Andrews S, Krueger F, Arand J, Walter J, Santos F, Popp C, Thienpont B, Dean W, Reik W (2012) The dynamics of genome-wide DNA methylation reprogramming in mouse primordial germ cells. *Mol Cell* 48: 849−862

Seki Y, Hayashi K, Itoh K, Mizugaki M, Saitou M, Matsui Y (2005) Extensive and orderly reprogramming of genome-wide chromatin modifications associated with specification and early development of germ cells in mice. *Dev Biol* 278: 440−458

Seki Y, Yamaji M, Yabuta Y, Sano M, Shigeta M, Matsui Y, Saga Y, Tachibana M, Shinkai Y, Saitou M (2007) Cellular dynamics associated with the genome-wide epigenetic reprogramming in migrating primordial germ cells in mice. *Development* 134: 2627−2638

Shirane K, Kurimoto K, Yabuta Y, Yamaji M, Satoh J, Ito S, Watanabe A, Hayashi K, Saitou M, Sasaki H (2016) Global landscape and regulatory principles of DNA methylation reprogramming for germ cell specification by mouse pluripotent stem cells. *Dev Cell* 39: 87−103

Spiller CM, Bowles J (2015) Sex determination in mammalian germ cells. *Asian J Androl* 17: 427−432

Tam PP, Snow MH (1981) Proliferation and migration of primordial germ cells during compensatory growth in mouse embryos. *J Embryol Exp Morphol* 64: 133−147

Tomizawa S, Kobayashi H, Watanabe T, Andrews S, Hata K, Kelsey G, Sasaki H (2011) Dynamic stage-specific changes in imprinted differentially methylated regions during early mammalian development and prevalence of non-CpG methylation in oocytes. *Development* 138: 811−820

Trapnell C, Roberts A, Goff L, Pertea G, Kim D, Kelley DR, Pimentel H, Salzberg SL, Rinn JL, Pachter L (2012) Differential gene and transcript expression analysis of RNA-seq experiments with TopHat and Cufflinks. *Nat Protoc* 7: 562−578

Voigt P, Tee WW, Reinberg D (2013) A double take on bivalent promoters. *Genes Dev* 27: 1318−1338

Weber M, Hellmann I, Stadler MB, Ramos L, Paabo S, Rebhan M, Schubeler D (2007) Distribution, silencing potential and evolutionary impact of promoter DNA methylation in the human genome. *Nat Genet* 39: 457−466

Western PS, Miles DC, van den Bergen JA, Burton M, Sinclair AH (2008) Dynamic regulation of mitotic arrest in fetal male germ cells. *Stem Cells* 26: 339−347

Yamaguchi S, Hong K, Liu R, Shen L, Inoue A, Diep D, Zhang K, Zhang Y (2012) Tet1 controls meiosis by regulating meiotic gene expression. *Nature* 492: 443−447

Ying QL, Wray J, Nichols J, Batlle-Morera L, Doble B, Woodgett J, Cohen P, Smith A (2008) The ground state of embryonic stem cell self-renewal. *Nature* 453: 519−523

Zhang Y, Liu T, Meyer CA, Eeckhoute J, Johnson DS, Bernstein BE, Nusbaum C, Myers RM, Brown M, Li W, Liu XS (2008) Model-based analysis of ChIP-Seq (MACS). *Genome Biol* 9: R137

Zvetkova I, Apedaile A, Ramsahoye B, Mermoud JE, Crompton LA, John R, Feil R, Brockdorff N (2005) Global hypomethylation of the genome in XX embryonic stem cells. *Nat Genet* 37: 1274−1279

CrossMark

Zscan4 is expressed specifically during late meiotic prophase in both spermatogenesis and oogenesis

Kei-ichiro Ishiguro[1,4] · Manuela Monti[2] · Tomohiko Akiyama[1] · Hiromi Kimura[1] ·
Nana Chikazawa-Nohtomi[1] · Miki Sakota[1] · Saeko Sato[1] · Carlo Alberto Redi[2,3] ·
Shigeru B. H. Ko[1] · Minoru S. H. Ko[1]

© The Author(s) 2016. This article is published with open access at Springerlink.com

Abstract Mouse zinc finger and SCAN domain containing 4 (Zscan4) proteins, which are encoded by multiple copies of *Zscan4* genes, are expressed specifically in preimplantation embryos in vivo and embryonic stem (ES) cells in vitro. However, the expression patterns of mouse Zscan4 in vivo have been largely elusive. Here, we show that Zscan4 proteins are expressed in adult ovaries and testes. In ovaries, Zscan4 proteins were detected in germinal vesicle (GV) stage oocytes in antral follicles, indicating that *Zscan4* genes are activated during the diplotene/dictyate stage in meiotic prophase I. Remarkably, Zscan4 showed different spatial localization patterns between two distinct GV oocytes, which can be distinguished by global chromatin organization—surrounded nucleolus (SN) and non-surrounded nucleolus (NSN). These spatiotemporal differences in Zscan4 localizations correlated with the transition of RNA polymerase II-mediated transcriptional status during GV oocyte maturation. In testes, Zscan4 proteins were detected in spermatocytes at late pachytene/diplotene stages and in Sertoli cells. These results suggest that

Zscan4 may play critical roles during late meiotic prophase in both males and females.

Keywords GV oocyte · SN and NSN oocyte · Ovary · Testis · ES cell · Preimplantation embryo

Introduction

In the mouse genome, nine copies of zinc finger and SCAN domain containing 4 (*Zscan4*) genes are encoded in the *Zscan4* locus: six members of *Zscan4* genes (*Zscan4a*, *Zscan4b*, *Zscan4c*, *Zscan4d*, *Zscan4e*, and *Zscan4f*) and three pseudogenes (*Zscan4-ps1*, *Zscan4-ps2*, and *Zscan4-ps3*) (Falco et al. 2007). Because it is difficult to distinguish between the copies of the *Zscan4* genes and since there is only a single copy of *ZSCAN4* in the human genome (Falco et al. 2007), the mouse Zscan4 genes are collectively called *Zscan4* (Falco et al. 2007; Zalzman et al. 2010; Amano et al. 2013). The mouse *Zscan4* genes were originally identified for their unique expression during zygotic genome activation (ZGA) in late two-cell stage embryos, but they are also expressed in mouse embryonic stem (ES) cells (Falco et al. 2007; Akiyama et al. 2015).

In mouse ES cells, the transcription of *Zscan4* is transient and reversible, resulting in a small population (1–5%) of Zscan4+ cells in culture at a given time point (Zalzman et al. 2010). A burst of *Zscan4* transcription is accompanied by unique biological events, including transient expression of other ZGA-specific genes (Akiyama et al. 2015), rapid derepression and rerepression of heterochromatin regions (Akiyama et al. 2015), rapid telomere extension (Zalzman et al. 2010), and blockage of global translation (Hung et al. 2013). Moreover, Zscan4 has been shown to enhance the efficiency of generating mouse induced pluripotent stem (iPS)

✉ Minoru S. H. Ko
ko.minoru@keio.jp

1   Department of Systems Medicine, Keio University School of Medicine, 35 Shinanomachi, Shinjuku, Tokyo 160-8582, Japan

2   Research Center for Regenerative Medicine, Fondazione IRCCS Policlinico San Matteo, viale Golgi 19, 27100 Pavia, Italy

3   Dipartimento di Biologia e Biotecnologie L. Spallanzani, University of Pavia, via A. Ferrata 9, 27100 Pavia, Italy

4   Present address: Institute of Molecular Embryology and Genetics, Kumamoto University, 2-2-1 Honjo, Chuo-ku, Kumamoto 860-0811, Japan

🌳 Springer

cells and their quality (Hirata et al. 2012; Jiang et al. 2013). These data suggest that Zscan4 plays critical biological roles in ES cells.

Our previous studies by in situ hybridization and transcriptome analyses showed that *Zscan4* messenger RNA (mRNA) is expressed in mouse preimplantation embryos with the peak at the late two-cell stage, although its protein level is yet to be analyzed (Falco et al. 2007; Zalzman et al. 2010). In accordance with those observations, it was demonstrated that knockdown of *Zscan4* by siRNA leads to delayed progression from the two-cell to four-cell stage and consequently implantation failure (Falco et al. 2007). Thus, *Zscan4* is expressed transiently in preimplantation embryos in vivo, as has been shown in ES cells in vitro. However, a precise expression pattern of *Zscan4* in vivo has been largely elusive, which could be due to the transient nature of expression in a small subset of cell lineages.

In this study, we examined the expression of Zscan4 protein in mouse tissues in vivo. Our cytological analysis demonstrated that Zscan4 protein is expressed in adult reproductive organs—ovary and testis—in addition to preimplantation embryos. Intriguingly, our data suggest that the spatiotemporal expression pattern of Zscan4 protein correlates with the transition of chromatin reorganization and accompanying RNA polymerase II-mediated transcriptional status during oocyte maturation. Moreover, we found that Zscan4 protein is expressed during late meiotic prophase I in adult ovaries and testes. Thus, our current observations will shed light on further approaches to study critical biological functions of Zscan4 in both male and female reproductive cell lineages in vivo.

Materials and Methods

ES cell culture The derivative cells from MC1 (Zalzman et al. 2010; Akiyama et al. 2015) or TA1 mouse ES cells (F1 hybrid of C57BL/6J × 129S6/SvEvTac) (Amano et al. 2013) were used. *Emerald* green fluorescent protein (GFP) knock-in (Z4EmKI) ES cells were described in the accompanied paper (Ishiguro et al. 2016). ES cell lines were maintained on gelatin-coated, feeder-free plates in complete ES medium (Zalzman et al. 2010).

Animal experiments Animal experiments were approved by the Institutional Animal Care and Use Committee (approval nos. 12702-0, 24-010-11).

FACS The fluorescent intensity analysis and sorting of Emerald of Z4c-Em ES cells were performed using a BD FACSAria II. The cells were sorted according to the fluorescent intensity of Emerald and collected into mouse ES cell culture medium at 4°C.

Production of antibodies Polyclonal antibodies against mouse Zscan4 (a.a.1-506) were produced by inserting its complementary DNA (cDNA) fragment in-frame with pET19b (Merck Millipore , Tokyo Japan) in *E. coli* strain BL21-CodonPlus(DE3). His-tagged recombinant proteins were solubilized in a denaturing buffer (6 M HCl-Guanidine, 20 mM Tris-HCl [pH 7.5]) from the inclusion body and purified by Ni-NTA (QIAGEN, Tokyo Japan) under denaturing conditions. After dialyzing against PBS, the purified protein was used to immunize rats and rabbits. The antibodies were affinity purified from the immunized crude serum with immobilized antigen on CNBr-activated Sepharose (GE Healthcare, Tokyo Japan).

Antibodies The following antibodies were used: mouse anti-GFP (Santa Cruz, Tokyo Japan : sc-9996), rabbit anti-GFP (Abcam, Tokyo Japan : ab6556), rabbit anti-RNA polymerase II CTD repeat (phospho S5) (Abcam: ab5131), rabbit anti-RNA polymerase II CTD repeat (phospho S2) (Abcam: ab5095), mouse anti-KAP1 (Abcam: ab22553), mouse anti-SYCP3 (Ishiguro et al. 2011), and human anti-centromere antigen (Inova Diagnostics, San Diego CA).

Histological analysis Ovaries from 4- to 8-wk-old mice and testes from 13-18 dpc embryos and 8-wk-old mice were embedded in Tissue-Tek O.C.T. compound (Sakura Finetek, Tokyo Japan) and frozen in liquid nitrogen. Cryosections were prepared on the MAS-coated slides (Matsunami, Osaka Japan) at 8 μm thickness and then air dried and fixed in 4% paraformaldehyde in PBS at pH 7.4.

Immunofluorescence staining ES cells were grown on a cover glass and fixed in 4% paraformaldehyde (PFA) for 5 min at room temperature and permeabilized in 0.1% TritonX100 in PBS for 10 min. The cells were blocked for 10 min in PBS, 3% BSA, and incubated at room temperature with the primary antibodies in a blocking solution. After three washes in PBS, the cells were incubated for 1 h at room temperature with Alexa-dye-conjugated secondary antibodies (1:1000; Invitrogen) in a blocking solution. DNA was counterstained with Vectashield mounting medium containing 4′,6-diamidino-2-phenylindole (DAPI) (Vector Laboratory, Burlingame CA).

GV, metaphase I (MI), and metaphase II (MII) oocytes and preimplantation embryos were fixed in 4% PFA/PBS for 30 min at room temperature, washed with PBS, and permeabilized with PBS +0.1% Triton X-100. After a brief wash in PBS, they were blocked in 5% BSA/PBS for 30 min at room temperature and then immunostained with first antibodies diluted 1:500 in blocking solution at 4°C overnight. Samples were then briefly washed in PBS and incubated with Alexa-dye-conjugated second antibodies diluted 1:1000 in blocking solution for 1 h at room temperature. Samples were then mounted on slides with Vectashield with DAPI (Vector Laboratories). The same protocol has been used for Zscan4

immunofluorescence on serial sections of adult ovaries and testes with the exclusion of the permeabilization step.

Imaging Immunostaining images were captured with DeltaVision and processed with DeltaVision SoftWoRx software (GE Healthcare) or confocal microscope FluoView Fv10i (Olympus, Tokyo Japan) and processed with FluoView Software. All images shown were Z-stacked. GFP fluorescence and bright field images were captured with OLYMPUS IX73 fluorescence microscope and processed with CellSens standard program.

The intensity profile of Zscan4 signal in both surrounded nucleolus (SN) and non-surrounded nucleolus (NSN) oocytes has been obtained by selecting the region of interest (nucleolus) using the 2D tool of the cited software (Monti and Redi 2016). Each oocyte has been analyzed with Image J to count the corrected total cell fluorescence (CTCF). Briefly, each oocyte belonging to the three groups analyzed (SN spotty, SN diffuse, and NSN) has been selected and the area, integrated density and mean gray value, measured. In the meantime, a region next to each oocyte with no fluorescence has been measured as a background. The CTCF has been obtained using the following formula: Integrated density − (area of selected cell × mean fluorescence of backgrounds).

In vitro germinal vesicle oocyte culture and maturation Ovaries collected from 6- to 8-wk-old female mice were used after 46 h of treatment with 5 IU of pregnant mare serum gonadotropin (PMSG, Sigma, Tokyo Japan). GV oocytes were isolated by puncturing the follicles in KSOM (Merck Millipore , Tokyo Japan) containing 250 μM 3-isobutyl-1-metylxanthine (IBMX, Sigma). To induce resumption of meiosis, the oocytes were cultured in KSOM at 37°C after withdrawing IBMX. Oocytes that had not undergone GV breakdown (GVBD) by 90 min were removed from the experiment.

For in vitro maturation of GV oocytes, 4- to 6-wk-old females were used after 46 h of treatment with 5 IU of PSMG. Briefly, antral oocytes were collected by puncturing the antral follicles, washed in M2 medium, and stained with the fluorochrome Hoechst 33342 to distinguish chromatin organization in the NSN and SN types, as fully described elsewhere (Monti and Redi 2016). After sorting, SN and NSN oocytes were cultured in M2 medium at 37°C and 5% CO_2 overnight. Subsequent MII-SN and MII-NSN oocytes were fixed in PFA 4% for 30 min at room temperature and washed with PBS, blocked with 3% BSA/PBS containing 0.1% Triton X-100 for 1 h at room temperature, and then immunostained as described above.

Collection and in vitro culture of preimplantation embryo Female mice were injected with 5 U of pregnant mare serum gonadotropin (PMSG; Merck Millipore , Tokyo Japan) and 48 h later with 5 U of hCG (Calbiochem), and then crossed with a male mouse. Embryos were flushed out of the mouse oviducts and cultured in a drop of KSOM (Millipore).

Reverse transcription polymerase chain reaction Total RNA was isolated from tissues, isolated oocytes, and ES cells using TRIzol (Thermo Fisher, Yokohama Japan). cDNA was generated from total RNA using Superscript III (Invitrogen) followed by PCR amplification using Ex-Taq polymerase (Takara, Shiga Japan) and template cDNA. Sequences of primers used to generate RT-PCR products from cDNA are as follows:

SYCE1-787F: 5′-cacgagcagctgcagcagaggtgc-3′.
SYCE1-990R: 5′-ttaggtcctgcttgatgggcgctc-3′.
Sycp3-368F: 5′-gctgacatcaacaaagctcttcttg-3′.
Sycp3-605R: 5′-gttgttgtcgaaaaagattagatag-3′.
MuERVL-F: 5′-CCATCCCTGTCATTGCTCA-3′.
MuERVL-R: 5′-CCTTTTCCACCCCTTGATT-3′.
GAPDH-F: 5′-ttcaccaccatggagaaggc-3′.
GAPDH-R: 5′-ggcatggactgtggtcatga-3′.
Zscan4F: 5′-cagatgccagtagacaccac-3′.
Zscan4R: 5′-gtagatgttccttgacttgc-3′.
Meikin-F: 5′-agatggacagcttgttgtcgagta-3′.
Meikin-R: 5′-ctcagcaaatacaacctcagaagc-3′.
GFP-F: 5′-ACGTAAACGGCCACAAGTTC-3′.
GFP-R: 5′-AAGTCGTGCTGCTTCATGTG-3′.

Results

Mouse *Zscan4* mRNA is expressed in the adult testis and ovary It has been shown that *Zscan4* genes are expressed in mouse late two-cell stage preimplantation embryos and only in 1–5% of ES cells at a given time point (Falco et al. 2007; Zalzman et al. 2010). Because *Zscan4* expression in vivo has been largely elusive, we examined its expression pattern in mouse tissues by RT-PCR (Fig. 1A). Expression of *Zscan4* mRNA was detected in the adult ovary and testis, although the levels in these tissues were modest compared to a positive control— Emerald-positive (Em+) MC1 ES cells in which the *Emerald GFP* transgene is expressed under *Zscan4c* promoter (Zalzman et al. 2010). Notably, *Zscan4* mRNA was detected in adult but not embryonic ovary, suggesting that *Zscan4* is expressed in oocytes at later than the diplotene/dictyate stage of meiotic prophase I or in a specific cell type associated with folliculogenesis. Because the RT-PCR in this study cannot distinguish individual *Zscan4* genes and pseudogenes (*Zscan4a*, *b*, *c*, *d*, *e*, *f*, *ps1*, *ps2*, *ps3*), the observed expression level represents total transcripts potentially contributed from individual *Zscan4* loci in the testis and ovary, as has been shown in ES cells (Akiyama et al. 2015). The activation of the endogenous *Zscan4* locus was further validated by the demonstration
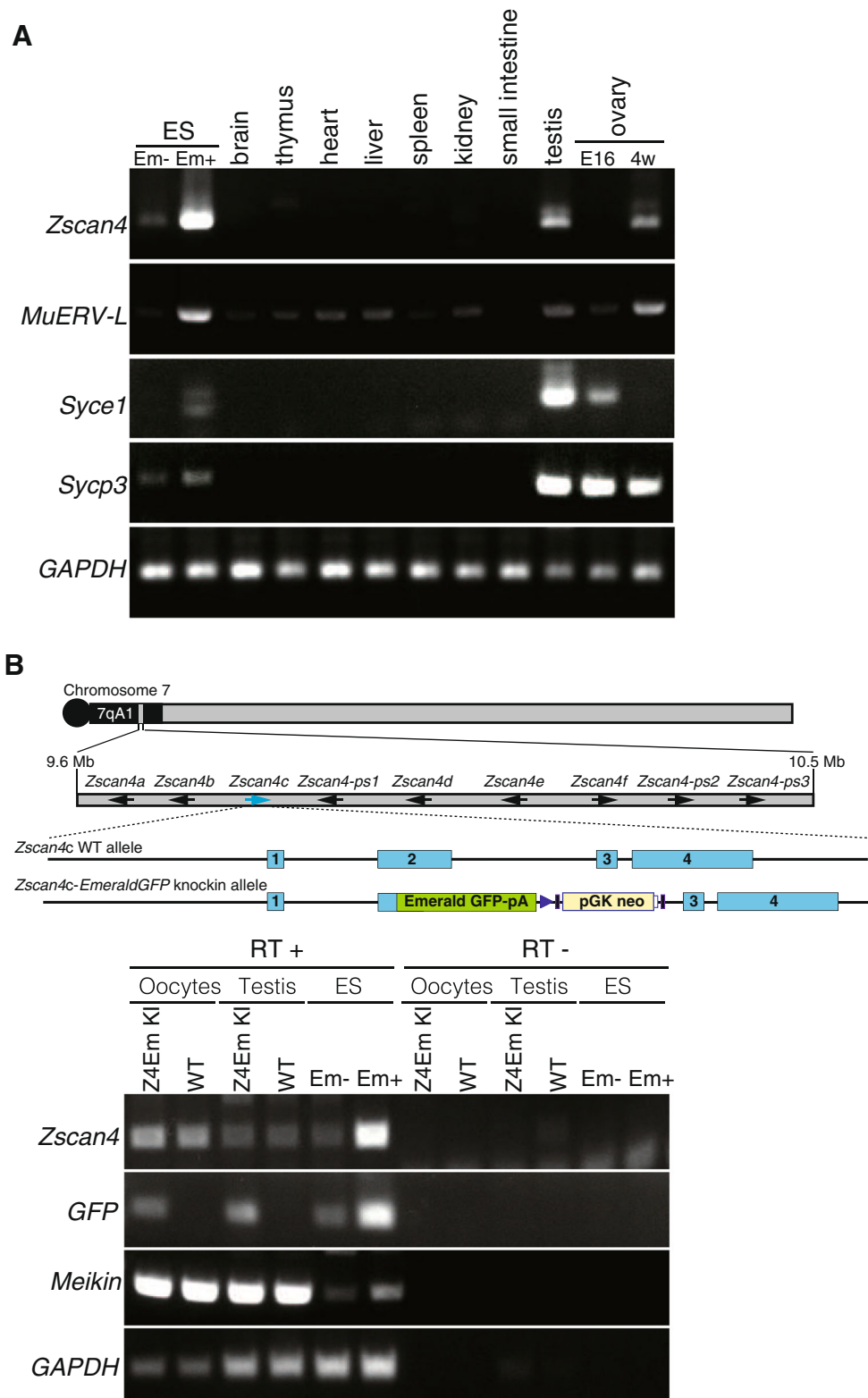
Figure 1. *Zscan4* mRNA expression in the testis and ovary. (*A*) Tissue specificity of mRNA expression for the indicated genes was analyzed by RT-PCR. *E16* fetal ovary at embryonic day 16; *4w* 4-wk ovary; *Em−* and *Em+* Emerald GFP negative and positive populations of mouse MC1 ES cells enriched by FACS, respectively; *Syce1* and *Sycp3*: meiosis specific markers. *MuERV-L* retrotransposon supposed to be highly expressed in Em+ ES cell. (*B*) Expression of endogenous *Zscan4* and exogenous *Emerald GFP*, which is knocked-in at the *Zscan4c* locus, was analyzed by RT-PCR. RNA was extracted from the isolated oocytes and testis in *Emerald GFP* knock-in (Z4EmKI) and wild-type mice and from Z4EmKI ES cells. Schematic Z4EmKI locus is shown (*upper*). *Em−* and *Em+* Emerald negative and positive enriched populations of Z4EmKI ES cells, respectively. *Meikin* meiosis I specific marker (Kim et al. 2015). *RT−* control PCR without reverse transcription.

of the expression of *Emerald* in oocytes and testes isolated from *Emerald*-knock-in (Z4EmKI) mice, in which *Emerald* was inserted into the endogenous *Zscan4c* locus (see accompanied manuscript, Ishiguro et al.) (Fig. 1*B*).

Presence of Zscan4 proteins in germinal vesicle oocytes and preimplantation embryos The aforementioned results led us to examine Zscan4 protein expression in mouse tissues. To this end, we generated new polyclonal antibodies against the full length (506 a.a.) of the Zscan4 protein (see accompanied manuscript), because our previous anti-Zscan4 antibody, which was raised against the most C-terminal-peptide (14 a.a.) epitope of Zscan4c (Zalzman et al. 2010), might have missed detection of truncated forms: Zscan4a, Zscan4b, and Zscan4e proteins.

Immunostaining of adult ovary sections showed background-level signals in ovarian somatic cells and primordial, primary, secondary, and preantral oocytes (Fig. 2). By contrast, Zscan4 protein was detected in the nuclei of oocytes residing in the antral follicles (Fig. 2). These results were consistent with the *Zscan4* mRNA expression in oocytes isolated from the adult ovary (Fig. 1*B*) but not the embryonic ovary (Fig. 1*A*), suggesting that Zscan4 starts to be expressed in or after diplotene/dictyate stages but not before these stages.

To examine Zscan4 protein expression in more detail, we used isolated GV oocytes and embryos at the subsequent stages. Interestingly, GV oocytes showed two types of Zscan4 immunostaining patterns: spotty signals around the nucleolus and a more diffuse signal dispersed through the nucleus (Fig. 3*A*). This finding will be further elaborated in the section below. After germinal
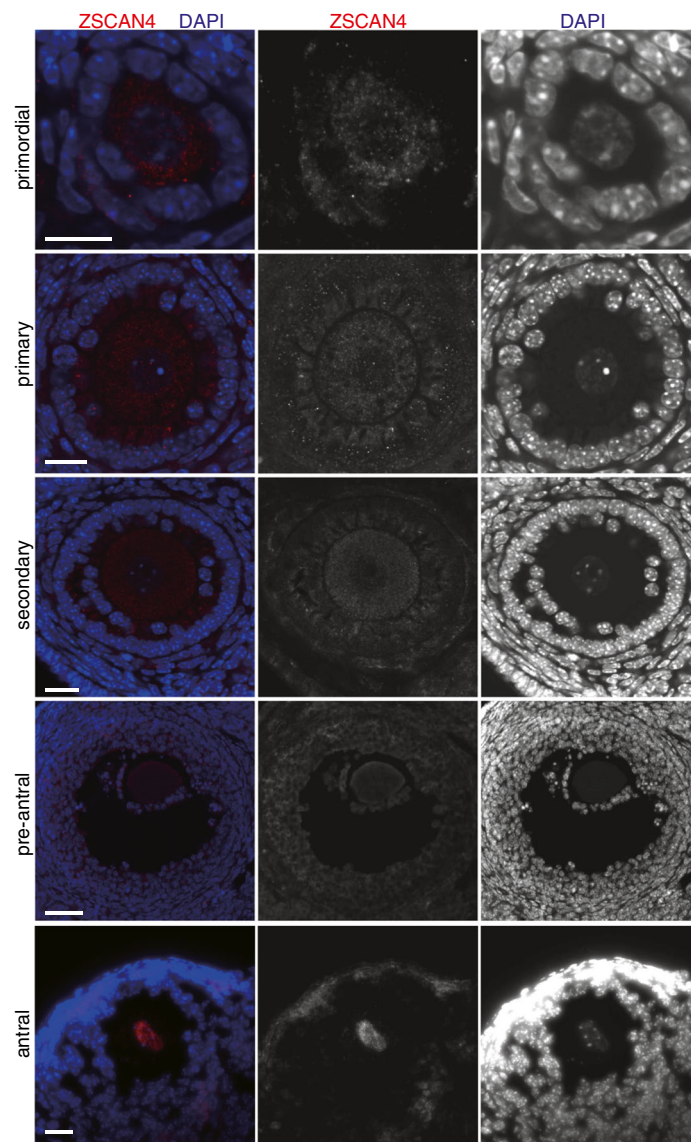
Figure 2. Zscan4 protein is expressed in oocytes of antral follicles. Ovary sections were immunostained as indicated, showing Z-stack sections of Zscan4 immunofluorescence of primordial, primary, secondary, preantral, and antral follicles. *Scale bars*, 20 μm.
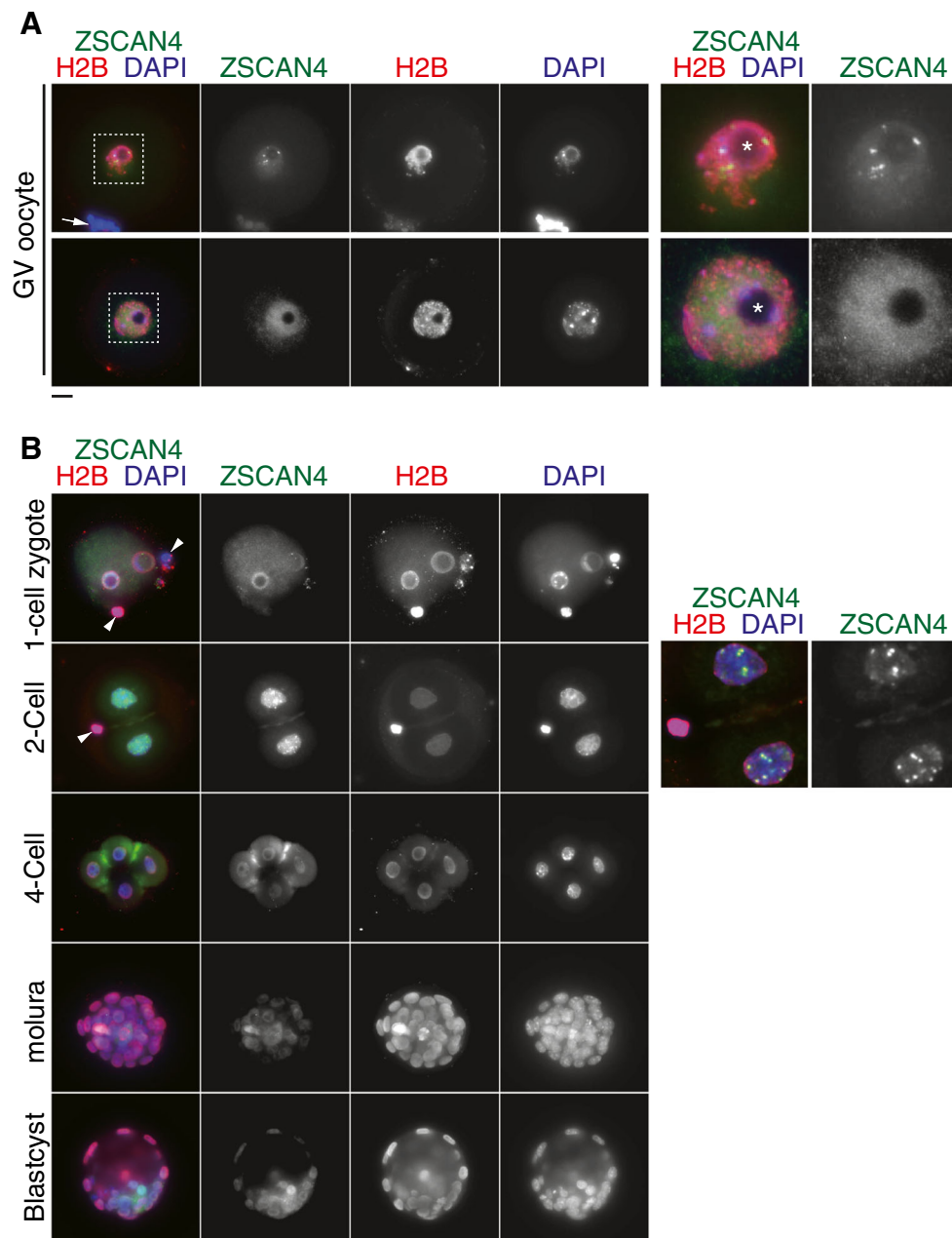
Figure 3. Zscan4 protein is expressed in GV oocytes and preimplantation embryos. (*A*) GV oocytes were immunostained as indicated. Two types of immunostaining patterns in GV oocytes are shown. The *upper example* shows the spotty immunostaining pattern of Zscan4, some of which surround a nucleolus. The *lower example* shows the faint diffusive immunostaining pattern of Zscan4. *Enlarged images* of the nuclei are shown on the *right*. *Arrow* indicates cumulus granulosa cells associated with zona pellucida of GV oocyte. *Asterisk* indicates nucleolus. (*B*) Preimplantation embryos at different developmental stages were immunostained as indicated. Enlarged deconvolution images of partial Z projection for two cells are shown on the *right*, emphasizing intense Zscan4 foci. *Arrowhead* indicates polar body in two cells. *Scale bars*, 20 μm.

vesicle break down (GVBD) followed by resumption of meiosis I, Zscan4 seemed to disappear from the chromosome, though a trace of the protein may remain (Supplementary Fig. 1A). After fertilization at the one-cell stage, weak immunostaining signals were observed in the periphery of pronuclei, which were overlapped with histone 2B (H2B) staining. Because Zscan4 mRNAs were not detected at this stage, the trace amount of Zscan4 proteins may be brought in from gametes. At the two-cell stage, Zscan4 proteins robustly culminated with some intense spots in the nuclei (Fig. 3B), consistent with a sharp increase of *Zscan4* mRNAs detected by in situ hybridization and transcriptome studies (Hamatani et al. 2004; Falco et al. 2007; Macfarlan et al. 2012). After the two-cell stage, Zscan4 protein levels decreased precipitously. Taken together, Zscan4 proteins were produced and present in GV oocytes (diplotene/dictyate meiotic stages) and two-cell embryos.
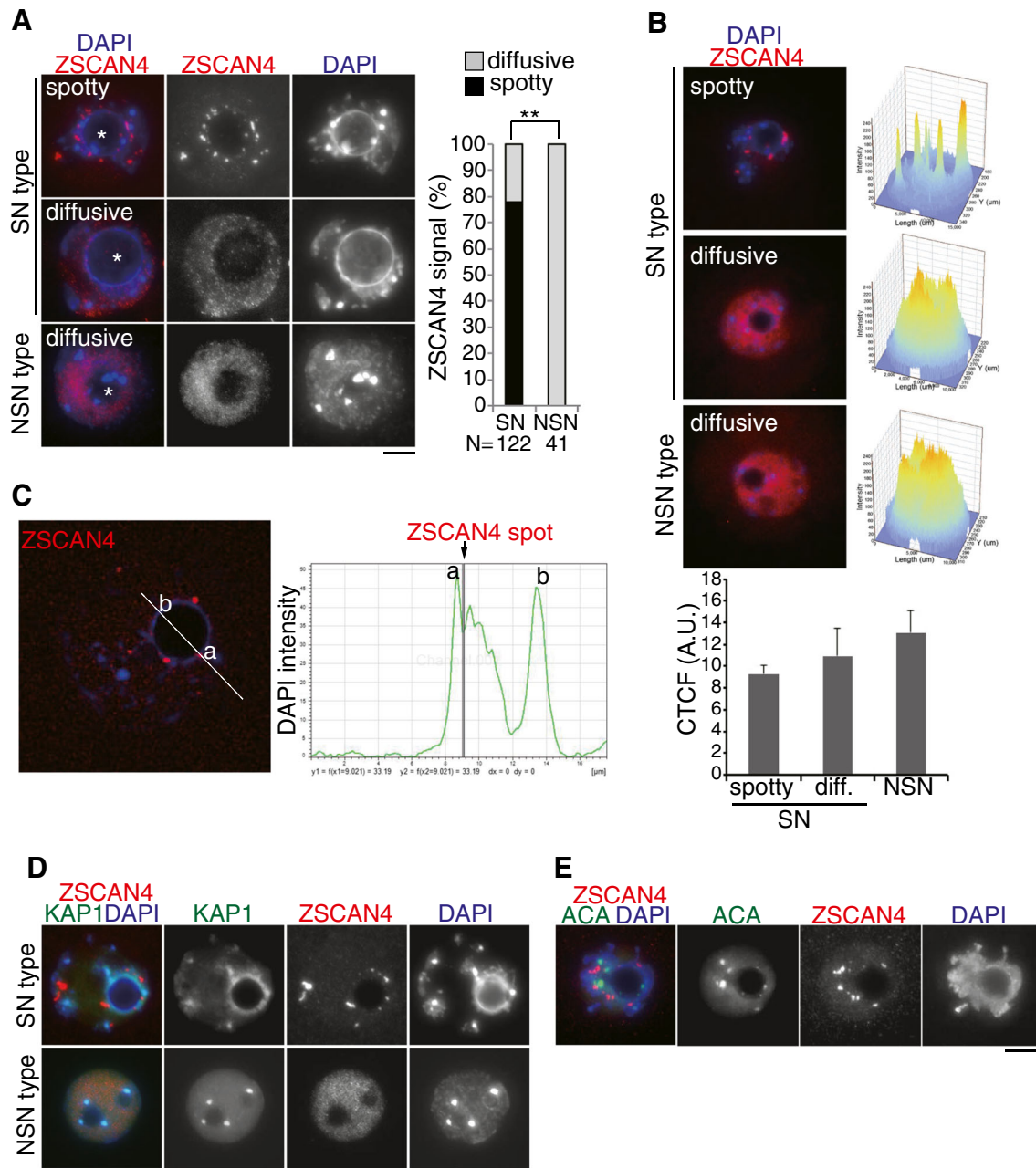
Figure 4. Zscan4 localization in SN- and NSN-type GV oocytes. (*A*) GV oocytes, classified as SN type and NSN type by heterochromatin morphology relative to nucleolus (shown by asterisk), were immunostained as indicated. The spatial localization pattern of Zscan4 was classified as spotty (limited number of foci) and diffusive (dispersed in nuclei). The immunostaining pattern of Zscan4 is quantified in the *right graph*. The number of analyzed GV oocytes (pooled from four independent experiments) is indicated. **$P < 0.001$ (Pearson's chi-square test). (*B*) Intensity profile of Zscan4 immunostaining signal obtained with the FluoView Software from representative GV oocytes with a SN spotty (*top*, $n = 21$), SN diffuse (*middle*, $n = 11$), and NSN (*bottom*, $n = 23$). The value of pixel intensity on *Z*-axis is equal to 200 for the spotty signal (SN spotty) and to 180 (SN diffuse, NSN) for the oocytes with diffuse signal as inferable from the picture. Corrected total cell fluorescence (CTCF, arbitrary units) is shown in the *bottom graph* with SEM. *C* Zscan4 and DAPI signals were scanned across a nucleolus in SN-type GV oocyte (*dashed line*). Signal intensity of DAPI (*green*) and Zscan4 (*gray bar*) is shown on the bottom. *D* SN-type and NSN-type GV oocytes were immunostained for KAP1: a heterochromatic protein which is potentially associated with Zscan4. *E* SN-type GV oocyte was immunostained for anti-centromere antigen (ACA). *Scale bars*, 10 μm.

Two distinct patterns of Zscan4 localizations in germinal vesicle oocytes As mentioned above, detection of two types of Zscan4 immunostaining patterns in isolated GV oocytes (Fig. 3A) prompted us to examine this finding in more detail. We first noticed that these two immunostaining patterns correlated well with two distinct DAPI-staining patterns: a ring of

DAPI-positive heterochromatin around the nucleolus (surrounded nucleolus [SN]) or a more diffuse DAPI signal around the nucleolus (non-surrounded nucleolus [NSN]) (Debey et al. 1993; Zuccotti et al. 1995), which are known to correlate with competency of resuming meiosis I and developmental potential of embryos (Inoue et al. 2008; Monti et al. 2013). Indeed, 78% of SN-type GV oocytes showed a spotty Zscan4 signal, whereas the remaining 22% showed a dispersed Zscan4 pattern. Consistency of the spotty Zscan4 immunostaining pattern was confirmed by overlapped immunostaining with two additional anti-Zscan4 antibodies raised in rat and rabbit (Supplementary Fig. 2). Also, the intensity profile measurement of the immunostaining signals in GV oocytes with NSN- and SN-Zscan4 diffuse pattern versus SN-Zscan4 spotty pattern clearly indicated a comparable level of immunostaining signals among the samples (Fig. 4B), suggesting that the distribution, but not the quantity, of Zscan4 proteins are different in these GV oocytes.

More detailed profiling of signal intensity for Zscan4 immunostaining and DAPI staining across a nucleolus indicated that Zscan4 foci resided at a DAPI-dense region rather than the inner side of the nucleolus in SN-type GV oocytes (Fig. 4C). This notion was further supported by the 3D reconstruction of immunostaining images (Supplementary Movies 1, 2). In mice, most constitutive heterochromatin domains are associated with pericentromeric regions and organized into chromocenters (Saksouk et al. 2015). Previously, we have shown the involvement of Zscan4 in heterochromatin regulation in mouse ES cells (Akiyama et al. 2015). Especially, mass spectrometry analyses of protein complexes associated with exogenous FLAG-tagged Zscan4 (Akiyama et al. 2015) and endogenous Zscan4 (see accompanied manuscript) revealed Zscan4's association with transcriptional repressors, KDM1A/ LSD1, KAP1/TIF1β, and HDAC1. Therefore, we asked whether in SN-type GV oocytes Zscan4 accumulates to heterochromatin regions by co-immunostaining with KAP1 or centromeric protein (Fig. 4D, E) (Supplementary Movie 3). Although Zscan4 foci did not seem to be overlapped with centromeric or pericentromeric regions, they closely coincided with KAP1-stained heterochromatin regions surrounding a nucleolus in SN-type GV oocytes. Thus, it is possible that Zscan4 preferentially localizes to specific sites in the heterochromatin region in SN-type GV oocytes.

Zscan4 localization patterns correlate with transcription status in germinal vesicle oocytes It has been shown that large-scale changes in nuclear organization are associated with modification of histone and chromatin-bound proteins (De La Fuente 2006). A previous study on Br-UTP incorporation in GV oocytes demonstrated that overall transcription level is high in NSN-type GV oocytes, whereas it is repressed in SN-type GV oocytes (Bouniol-Baly et al. 1999; De La

Fuente and Eppig 2001; Miyara et al. 2003). Hence, we asked whether the Zscan4 immunostaining pattern observed in SN- and NSN-type oocytes is associated with transcriptional status by assessing phosphorylation of Ser2 in RNA polymerase II CTD repeat, Pol2(S2P), a marker for active transcriptional elongation of RNA polymerase II (Hsin and Manley 2012; Phatnani and Greenleaf 2006) (Fig. 5A; Supplementary Movie 4). Remarkably, all of the NSN-type GV oocytes showed intense Pol2(S2P) immunostaining with multiple foci throughout the nucleus, indicating that RNA polymerase II-mediated transcriptional elongation is active in NSN-type GV oocytes. By contrast, Pol2(S2P) immunostaining was largely diminished in SN-type GV oocytes with spotty Zscan4 localization. Notably, SN-type GV oocytes with dispersed Zscan4
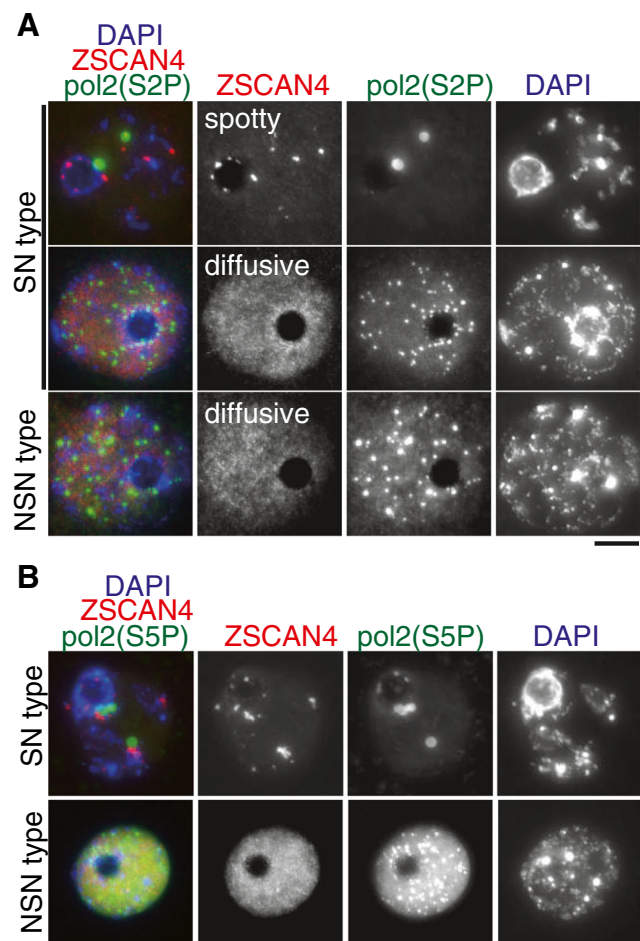

Figure 5. Localization patterns of Zscan4 correlate with Pol II-mediated transcription activity in GV oocytes. (A) SN- and NSN-type GV oocytes were immunostained for *Pol2(S2P)*: RNA polymerase II CTD repeat (phospholylated Ser2), a marker for active transcriptional elongation. Weak Pol2(S2P) in Zscan4-spotty SN-type oocytes (top, n = 27/27), intense Pol2(S2P) in Zscan4-diffusive SN-type oocytes (middle, n = 2/2), intense Pol2(S2P) in Zscan4-diffusive NSN-type oocytes (bottom, n = 3/3). (B) SN- and NSN-type GV oocytes were immunostained for *Pol2(S5P)*: RNA polymerase II CTD repeat (phospholylated Ser5), a marker for active transcriptional initiation.

Figure 6. Zscan4 protein is expressed in late prophase spermatocytes and Sertoli cell. (*A*) Seminiferous tubule sections were immunostained as indicated. Stage X-XI tubule is shown (*upper*). Higher magnitude image is shown (*lower*). *Lep* leptotene, *late P.* late pachytene, *Dip* diplotene, *e St.* elongated spermatid, *Ser.* Sertoli cell. (*B*) Zscan4 immunostaining of spermatocytes at different stages of meiotic prophase and Sertoli cells are shown. *Scale bars*, 5 μm.
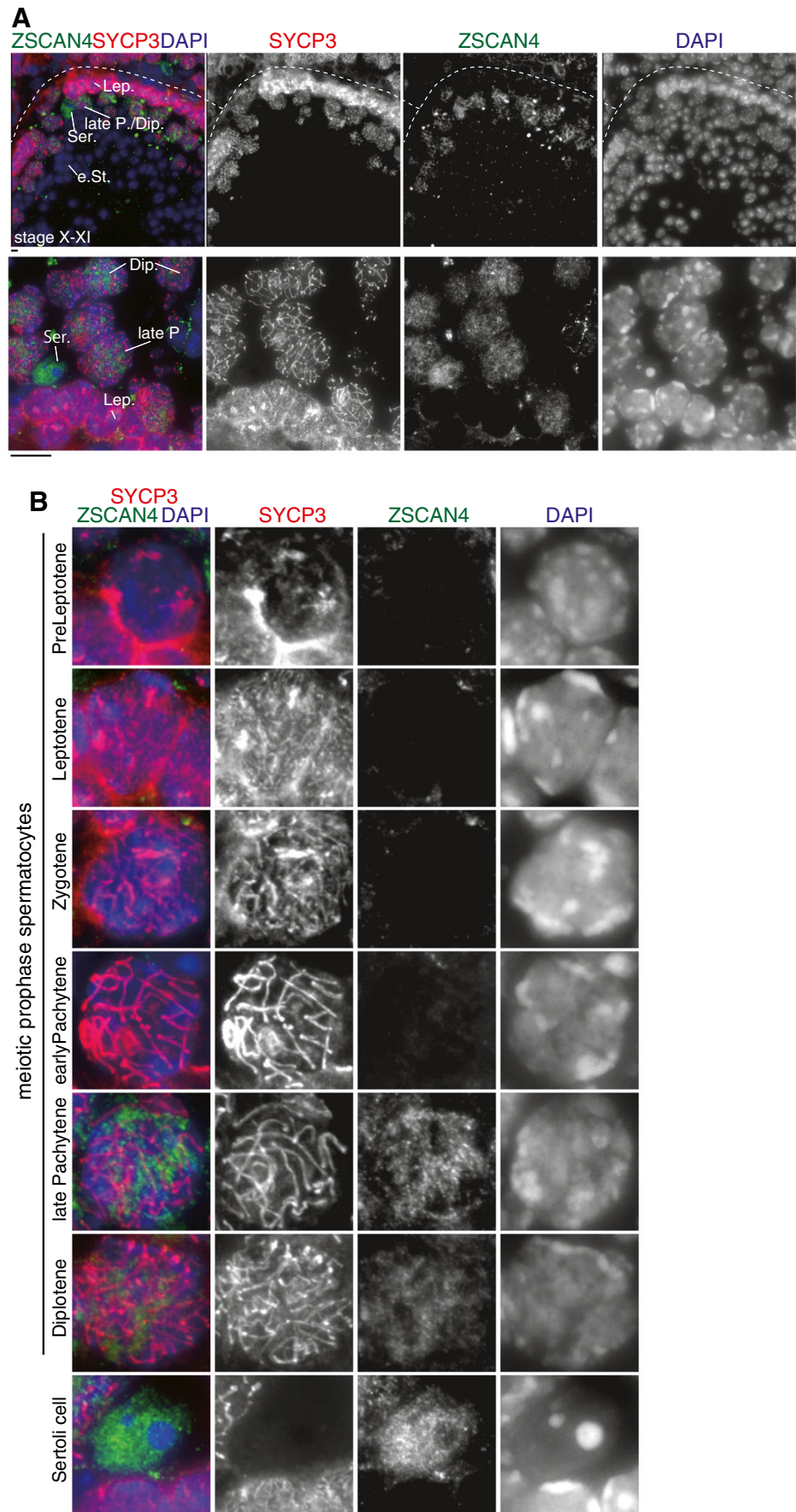
localization showed an intense Pol2(S2P) immunostaining pattern similar to NSN-type. Essentially, the same phenomena were observed in the immunostaining pattern of phosphorylation of Ser5 in RNA polymerase II CTD repeat Pol2(S5P), a marker for active transcriptional initiation (Phatnani and Greenleaf 2006) (Hsin and Manley 2012) (Fig. 5B). Taken together, these results indicate that Zscan4 localization patterns are more precisely correlated with the transcriptional status of GV oocytes than DAPI-staining patterns, i.e., NSN or SN. Essentially, all GV oocytes with a spotty Zscan4 localization pattern are transcriptionally silent, whereas GV oocytes with a diffuse Zscan4 localization pattern are transcriptionally active. On the other hand, some of the SN-type GV oocytes— when Zscan4 shows a diffusive localization pattern—are transcriptionally active, despite the previous belief that the SN-type GV oocytes are transcriptionally silent.

Zscan4 is expressed in late prophase spermatocytes and Sertoli cells Because our RT-PCR suggests that *Zscan4* mRNA is modestly expressed in the adult testis (Fig. 1), we asked whether Zscan4 is expressed in any cell population in the testis at a protein level. Intriguingly, we noticed that Zscan4 was faintly but consistently immunostained in a subset of spermatocytes at particular stages of seminiferous tubule sections (Fig. 6A). It is worth noting that Zscan4 was highly detectable only in late pachytene or diplotene spermatocytes within the stage X-XI seminiferous tubules, but not in spermatocytes at other stages, spermatogonia, or spermatids (Fig. 6B). Contrary to this observation, embryonic testis sections did not show any detectable levels of Zscan4 immunostaining (Supplementary Fig. 3). These results suggest that Zscan4 is expressed in a very restricted timing—late pachytene or diplotene—during male meiosis, which is reminiscent of the restricted expression in late meiotic prophase in oocytes (Fig. 3).

Interestingly, significant levels of Zscan4 immunostaining were also detected in Sertoli cells, in which the signal was more intense compared to late pachytene/diplotene spermatocytes. It is known that Sertoli cells respond to retinoic acid (RA) and cyclically change their functions in a coordinated manner with spermatogenesis (Sugimoto et al. 2012); (Hasegawa and Saga 2012). Because the *Zscan4* locus can be activated in response to RA stimuli in mouse ES cells (Sharova et al. 2007; Sharova et al. 2016) (also, see accompanied manuscript), the expression of Zscan4 in Sertoli cells may be related to the periodic seminiferous cycle in response to RA.

Discussion

In this study, we have shown for the first time that Zscan4 is expressed at a protein level not only in preimplantation embryos but also in specific stages of the post-natal ovary and testis. Notably, in both ovary and testis, Zscan4 is detectable in oocytes and spermatocytes during late meiotic prophase. Because meiotic prophase is equivalent to a prolonged G2 phase in mitotic cell cycle (Eichenlaub-Ritter 2012), the aforementioned data are reminiscent of the observation that Zscan4 is transiently activated at the G2 phase in ES cells (Storm et al. 2014); (Nakai-Futatsugi and Niwa 2016) and in the late two-cell stage (Falco et al. 2007). Although the precise roles of Zscan4 during meiosis are yet to be clarified, the implication for these results is that Zscan4 may play an important role in germ cell lineages as observed in ES cells (Zalzman et al. 2010; Amano et al. 2013; Akiyama et al. 2015).

Previously, we have shown that a burst of *Zscan4* transcription is accompanied by rapid derepression and rerepression of heterochromatin regions in mouse ES cells (Akiyama et al. 2015). Given that heterochromatic regions are reorganized into limited spots of clusters in mouse Zscan4-positive ESCs (Akiyama et al. 2015), our data suggest that similar mechanisms may play a role in heterochromatin organization in Zscan4-positive cell populations in reproductive organs. It is worth noting that Zscan4 is immunopositive in Sertoli cells, where heterochromatic regions are organized into an unusually large chromocenter (Fig. 6B), reminiscent of the heterochromatin clustering in Zscan4-positive ESCs. Crucially, we demonstrated that distinct spatial localization patterns of Zscan4 in SN- and NSN-type GV oocytes are accompanied by the global heterochromatin organization around the nucleolus (Fig. 3A), as shown that 3D genome architecture plays a crucial role in a panoply of cell functions (Krijger et al. 2016). Thus, it is plausible that Zscan4-positive status is associated with global heterochromatin organization in those cell types, though a possible causal relationship between Zscan4 expression and chromatin architecture awaits further investigation.

It has been elusive how SN rather than NSN oocytes shows higher developmental potential (Inoue et al. 2008; Monti et al. 2013), despite the fact that both of them can be ovulated after the hormonal peak. We have shown that two distinct patterns of Zscan4 immunostaining more precisely correlate with RNA polymerase II transcription status in GV oocytes (Fig. 5). Notably, we found that a minor fraction of SN-type GV oocytes shows a diffusive pattern of Zscan4 immunostaining (Fig. 5A). It remains to clarify whether this minor fraction of GV oocytes represents intermediate status from NSN to SN transition (Mattson and Albertini 1990; De La Fuente 2006) or an intrinsic difference in the quality of cytoplasmic constitution (Monti et al. 2013).

Although multiple copies of highly identical *Zscan4* loci technically hamper genetic engineering of the endogenous locus, our recent success in generating a modified allele of *Zscan4* locus prompts us to pursue further genetic analysis. Thus, conditional disruption of either one or all of *Zscan4* loci will shed light on the further elucidation of Zscan4 functions in reproductive cell lineages in vivo.

Conclusion

In ovaries, Zscan4 proteins were detected in germinal vesicle (GV) stage oocytes. Zscan4 showed different spatial localization patterns between SN and NSN oocytes, which correlated with RNA polymerase II-mediated transcriptional status. In testes, Zscan4 proteins were detected in spermatocytes at late pachytene/diplotene stages and in Sertoli cells. These results suggest that Zscan4 may play critical roles not only in preimplantation embryos but also in germ cell lineages in both males and females.

References

Akiyama T, Xin L, Oda M, Sharov AA, Amano M, Piao Y, Cadet JS, Dudekula DB, Qian Y, Wang W, et al. (2015) Transient bursts of Zscan4 expression are accompanied by the rapid derepression of heterochromatin in mouse embryonic stem cells. DNA Res

Amano T, Hirata T, Falco G, Monti M, Sharova LV, Amano M, Sheer S, Hoang HG, Piao Y, Stagg CA, et al. (2013) Zscan4 restores the developmental potency of embryonic stem cells. Nat Commun 4:1966

Bouniol-Baly C, Hamraoui L, Guibert J, Beaujean N, Szollosi MS, Debey P (1999) Differential transcriptional activity associated with chromatin configuration in fully grown mouse germinal vesicle oocytes. Biol Reprod 60:580–587

De La Fuente R (2006) Chromatin modifications in the germinal vesicle (GV) of mammalian oocytes. Dev Biol 292:1–12

De La Fuente R, Eppig JJ (2001) Transcriptional activity of the mouse oocyte genome: companion granulosa cells modulate transcription and chromatin remodeling. Dev Biol 229:224–236

Debey P, Szollosi MS, Szollosi D, Vautier D, Girousse A, Besombes D (1993) Competent mouse oocytes isolated from antral follicles exhibit different chromatin organization and follow different maturation dynamics. Mol Reprod Dev 36:59–74

Eichenlaub-Ritter U (2012) Oocyte ageing and its cellular basis. Int J Dev Biol 56:841–852

Falco G, Lee SL, Stanghellini I, Bassey UC, Hamatani T, Ko MS (2007) Zscan4: a novel gene expressed exclusively in late 2-cell embryos and embryonic stem cells. Dev Biol 307:539–550

Hamatani T, Carter MG, Sharov AA, Ko MS (2004) Dynamics of global gene expression changes during mouse preimplantation development. Dev Cell 6:117–131

Hasegawa K, Saga Y (2012) Retinoic acid signaling in Sertoli cells regulates organization of the blood-testis barrier through cyclical changes in gene expression. Development 139:4347–4355

Hirata T, Amano T, Nakatake Y, Amano M, Piao Y, Hoang HG, Ko MS (2012) Zscan4 transiently reactivates early embryonic genes during the generation of induced pluripotent stem cells. Sci Rep 2:208

Hsin JP, Manley JL (2012) The RNA polymerase II CTD coordinates transcription and RNA processing. Genes Dev 26:2119–2137

Hung SS, Wong RC, Sharov AA, Nakatake Y, Yu H, Ko MS (2013) Repression of global protein synthesis by Eif1a-like genes that are expressed specifically in the two-cell embryos and the transient Zscan4-positive state of embryonic stem cells. DNA Res 20:391–402

Inoue A, Nakajima R, Nagata M, Aoki F (2008) Contribution of the oocyte nucleus and cytoplasm to the determination of meiotic and developmental competence in mice. Hum Reprod 23:1377–1384

Ishiguro K, Kim J, Fujiyama-Nakamura S, Kato S, Watanabe Y (2011) A new meiosis-specific cohesin complex implicated in the cohesin code for homologous pairing. EMBO Rep 12:267–275

Ishiguro et al. (2016) Expression analysis of the endogenous Zscan4 locus and its coding proteins in mouse ES cells and preimplantation embryos. doi:10.1007/s11626-016-0097-yIVAN-D-16-00245.1

Jiang J, Lv W, Ye X, Wang L, Zhang M, Yang H, Okuka M, Zhou C, Zhang X, Liu L, et al. (2013) Zscan4 promotes genomic stability during reprogramming and dramatically improves the quality of iPS cells as demonstrated by tetraploid complementation. Cell Res 23:92–106

Kim J, Ishiguro K, Nambu A, Akiyoshi B, Yokobayashi S, Kagami A, Ishiguro T, Pendas AM, Takeda N, Sakakibara Y, et al. (2015) Meikin is a conserved regulator of meiosis-I-specific kinetochore function. Nature 517:466–471

Krijger PH, Di Stefano B, de Wit E, Limone F, van Oevelen C, de Laat W, Graf T (2016) Cell-of-origin-specific 3D genome structure acquired during somatic cell reprogramming. Cell Stem Cell 18:597–610

Macfarlan TS, Gifford WD, Driscoll S, Lettieri K, Rowe HM, Bonanomi D, Firth A, Singer O, Trono D, Pfaff SL (2012) Embryonic stem cell potency fluctuates with endogenous retrovirus activity. Nature 487:57–63

Mattson BA, Albertini DF (1990) Oogenesis: chromatin and microtubule dynamics during meiotic prophase. Mol Reprod Dev 25:374–383

Miyara F, Migne C, Dumont-Hassan M, Le Meur A, Cohen-Bacrie P, Aubriot FX, Glissant A, Nathan C, Douard S, Stanovici A, et al. (2003) Chromatin configuration and transcriptional control in human and mouse oocytes. Mol Reprod Dev 64:458–470

Monti M, Redi CA (2016) Isolation and characterization of mouse antral oocytes based on nucleolar chromatin organization. J Vis Exp. doi:10.3791/53616

Monti M, Zanoni M, Calligaro A, Ko MS, Mauri P, Redi CA (2013) Developmental arrest and mouse antral not-surrounded nucleolus oocytes. Biol Reprod 88:2

Nakai-Futatsugi Y, Niwa H (2016) Zscan4 is activated after telomere shortening in mouse embryonic stem cells. Stem Cell Reports 6:483–495

Phatnani HP, Greenleaf AL (2006) Phosphorylation and functions of the RNA polymerase II CTD. Genes Dev 20:2922–2936

Saksouk N, Simboeck E, Dejardin J (2015) Constitutive heterochromatin formation and transcription in mammals. Epigenetics Chromatin 8:3

Sharova LV, Sharov AA, Piao Y, Shaik N, Sullivan T, Stewart CL, Hogan BL, Ko MS (2007) Global gene expression profiling reveals similarities and differences among mouse pluripotent stem cells of different origins and strains. Dev Biol 307:446–459

Sharova LV, Sharov AA, Piao Y, Stagg CA, Amano T, Qian Y, Dudekula D, Schlessinger D, and Ko MS (2016) Emergence of undifferentiated colonies from mouse embryonic stem cells undergoing differentiation by retinoic acid treatment. In Vitro Cell Dev Biol Anim.

Storm MP, Kumpfmueller B, Bone HK, Buchholz M, Sanchez Ripoll Y, Chaudhuri JB, Niwa H, Tosh D, Welham MJ (2014) Zscan4 is regulated by PI3-kinase and DNA-damaging agents and directly interacts with the transcriptional repressors LSD1 and CtBP2 in mouse embryonic stem cells. PLoS One 9:e89821

Sugimoto R, Nabeshima Y, Yoshida S (2012) Retinoic acid metabolism links the periodical differentiation of germ cells with the cycle of Sertoli cells in mouse seminiferous epithelium. Mech Dev 128:610–624

Zalzman M, Falco G, Sharova LV, Nishiyama A, Thomas M, Lee SL, Stagg CA, Hoang HG, Yang HT, Indig FE, et al. (2010) Zscan4 regulates telomere elongation and genomic stability in ES cells. Nature 464:858–863

Zuccotti M, Piccinelli A, Giorgi Rossi P, Garagna S, Redi CA (1995) Chromatin organization during mouse oocyte growth. Mol Reprod Dev 41:479–485

Contents lists available at ScienceDirect

Biochemical and Biophysical Research Communications

journal homepage: www.elsevier.com/locate/ybbrc

Structural and functional analyses of nucleosome complexes with mouse histone variants TH2a and TH2b, involved in reprogramming

Sivaraman Padavattan [a], Toshie Shinagawa [b], Kazuya Hasegawa [c], Takashi Kumasaka [c], Shunsuke Ishii [b], Thirumananseri Kumarevel [a, d, *]

[a] RIKEN SPring-8 Center, Harima Institute, 1-1-1 Kouto, Sayo, Hyogo 679-5148, Japan
[b] Laboratory of Molecular Genetics, CREST Research Project of JST (Japan Science and Technology Agency), RIKEN Tsukuba Institute, 3-1-1 Koyadai, Tsukuba, Ibaraki 305-0074, Japan
[c] Japan Synchrotron Radiation Research Institute (SPring-8), 1-1-1 Kouto, Sayo-cho, Sayo-kun, Hyogo 679-5198, Japan
[d] Structural Biology Laboratory, RIKEN Yokohama Institute, 1-7-22 Suehiro-cho, Tsurumi, Yokohama, Kanagawa 230-0045, Japan

ARTICLE INFO

ABSTRACT

Histone variants TH2a and TH2b are highly expressed in testes, oocytes and zygotes. Our recent analysis suggested that these histone variants enhance the induced generation of pluripotent stem cells (iPSCs) when co-expressed along with four transcription factors, Oct3/4, Sox2, Klf4 and c-Myc (OSKM), and are associated with an open chromatin structure [1]. In the present study, we report the crystal structures of nucleosomes (NCPs) with the mouse histone variants, TH2a and TH2b. The structures revealed two significant changes, as compared to the canonical counterparts: fewer histone-DNA contacts and changes in dimer–dimer interactions between TH2a-TH2a′ (L1-loop). In vivo studies with domain swapping and point mutants of the variants revealed that the residues in the histone tails and the TH2a-L1 loop are important for reprogramming. Taken together, our work indicates that the NCP variants with structural modifications and flexible tails are most likely important for enhanced reprogramming of functions.

© 2015 Elsevier Inc. All rights reserved.

1. Introduction

During spermatogenesis, chromatin restructuring occurs by the exchange of somatic histones with testis-specific histone variants [2–4]. TH2a and TH2b were originally identified as testis-specific histone variants [5–8] and they share a promoter, suggestive of a common function [9]. Our recent study showed that both variants are also expressed in oocytes and fertilized eggs, and their expression levels decreased as the embryos differentiated into blastocysts. The TH2a/TH2b variants induce an open chromatin structure, and are enriched, and uniformly distributed both on the X chromosomes and autosomes [1].

Chromatin decondensation is a hallmark of reprogramming [10,11]. Somatic cells can be experimentally reprogrammed back to pluripotency by nuclear transfer into oocytes [12], fusion with embryonic stem (ES) cells [13] or artificially overexpressing four

transcription factors, Oct3/4, Sox2, Klf4 and c-Myc (OSKM) [14]. Our recent study revealed that the histone variants TH2a and TH2b, when co-expressed with OSKM, enhanced the generation of iPSCs by nine-fold. However, either TH2a or TH2b expressed together with canonical H2a/H2b had no effect on reprogramming [1]. Nucleoplasmin (Npm) is an abundant oocyte protein that plays an important role in chromatin decondensation during fertilization [15], and its activity is modulated through phosphorylation [16]. When phosphorylation mimics of nucleoplasmin (P-Npm) and TH2a/TH2b were coexpressed, they enhanced the OSKM-induced iPSC generation by 18-fold. Moreover, iPSCs were generated using only Klf4 and Oct3/4 coexpressed with TH2a/TH2b and P-Npm [1].

Histone variants and chemical modifications of histones and DNA generate diversity in chromatin structure and function [4,17]. In this study, we have determined the nucleosome structures with the mouse testis-specific histone variants TH2a and TH2b, to identify the structural differences as compared to their canonical counterparts. The in vivo studies with domain swapping and point mutants of the histone variants revealed the regions and the key residues important for the reprogramming function.

---

2. Materials and methods

2.1. Histone expression and purification

The mouse testis-specific histone variants, TH2a and TH2b, and the canonical human histones, H2a, H2b, H3.1 and H4, were over-expressed in *Escherichia coli* and purified according to the previously published protocols [18,19]. The domain-swapped and point mutant histone variant proteins were purified in a similar manner.

2.2. Nucleosome preparation and crystallization

The 146-bp DNA and the NCPs were prepared as described previously [19,20]. The octamers were separated from the excess dimers by gel-filtration chromatography in a buffer containing 2 M NaCl. The nucleosomes were reconstituted by salt dialysis and purified from the excess DNA by ion exchange chromatography (Mono-Q 5/5 column, GE Healthcare). Nucleosomes were concentrated to 3.5–4 mg/mL and crystallized by the hanging drop method under the following conditions: 20 mM potassium cacodylate, pH 6.0, 60–70 mM KCl and 70–90 mM $MnCl_2$. The crystals were cryo-protected with the mother liquor, containing with 24% 2-methyl-2,4-pentanediol (MPD) and 6% trehalose.

2.3. Data collection and structure determination

Diffraction data were collected using the synchrotron radiation source at the Beamline BL41XU Station of SPring-8, Japan. The NCP crystals belonged to the orthorhombic space group $P2_12_12_1$, with one molecule per asymmetric unit. The structures were solved by the molecular replacement method, with the PDB entry 1AOI as a search model [21], using the Phaser program. The refinement was performed with Refmac [22] and CNS [23], and model building was accomplished with Coot [24] and Quanta (Accelrys, San Diego, CA, USA). The data collection parameters and refinement statistics are provided in Table S1. All of the structure figures were produced using PyMOL. The atomic coordinates of the GCH, GCHV1, GCHV2 and canonical NCPs have been deposited, with the RCSB ID codes 3X1T, 3X1U, 3X1V and 3X1S, respectively.

2.4. Domain swapping, point mutations, iPSC generation and FACS analysis

The details of the procedures related to domain swapping, point mutations, iPSC generation and FACS analysis are explained in Supplementary Materials and Methods section.

3. Results and discussion

3.1. Nucleosome structures with mouse TH2a and TH2b variants

The histone variants TH2a and TH2b are abundantly expressed during spermatogenesis [2,3], as well as in oocytes and fertilized eggs [1]. Knockout studies in mice revealed that female homozygous $TH2a^{-/-}TH2b^{-/-}$ oocytes have reduced capacity for embryogenesis, and both variants contribute to paternal genome activation [1]. TH2a and TH2b share 87% and 85% sequence identities with the mouse canonical H2a and H2b, respectively (Fig. 1A). Most of the non-conserved residues in the variants are localized at the N- and C-terminal histone tail regions and within the TH2a-L1 loop.

We have determined the structures of three nucleosome core particles (NCPs) with mouse TH2a and TH2b variants: GCH (TH2a-TH2b-H3-H4)$_2$, and the cross variants GCHV1 (TH2a-H2b-H3-H4)$_2$ and GCHV2 (H2a-TH2b-H3-H4)$_2$, with 146-bp palindromic DNA derived from human α-satellite DNA, by the molecular

replacement method (Fig. 1B). (Note: we used the human canonical histones H2a, H2b, H3 and H4, along with the mouse TH2a and TH2b for the nucleosome preparation. The Human and Mouse canonical histones H2a and H2b are having almost 99% sequence identity; H3 and H4 are having 100% identity between the species). In addition, we determined the structure of the human canonical nucleosome, for comparison. The data collection and refinement statistics are summarized in Table 1. Unlike the testis-specific H3T variant [25], the TH2a and TH2b variants form stable octamers under high salt concentrations. The superposition of the GCH, GCHV1, and GCHV2 nucleosomes with the canonical-NCP gave root mean square deviations (r.m.s.d.) of 0.3 Å, 0.5 Å and 0.37 Å, respectively. Intriguingly, closer inspections of the variant NCPs (GCH, GCHV1, and GCHV2) revealed two changes: fewer histone-DNA contacts and significant changes in the L1-L1′ loop interactions between the TH2a-TH2a′ dimers. Recently, chromatin structure containing the human histone H2B variant TSH2B was reported and the overall structural composition is similar to our GCHV1 [26].

3.2. Histone-DNA interactions

The NCP containing the TH2a and TH2b variants had fewer histone dimer-DNA contacts, as compared to its canonical counterpart, due to the altered side-chain conformations of the DNA-interacting residues. In the canonical-NCP, the H2a/H2a′-Arg21 side-chain forms strong H-bonding interactions with DNA at ±31-bp from the entry/exit sites, and also forms H-bonds with the H2a/H2a′-Lys16 main chain CO, thereby holding the H2a N-terminal tail (Fig. 2). Intriguingly in GCH-NCP, the TH2a/TH2a′-Arg21 side chain conformation is altered, resulting in the loss of interactions with DNA and the TH2a/TH2a′-Lys16 residue, and the formation of the two new H-bonds with the TH2b C-terminal end. In the cross variant GCHV2-NCP, the H2a/H2a′-Arg21 side-chain forms H-bonds with the TH2b C-terminus, and weakly associates with DNA and the H2a/H2a′-Lys16 residue. In GCHV1-NCP, the side-chain density of Arg21 was undetectable, presumably due to the high b-factors around the region when compared to other structures.

Single molecule studies revealed that the histone-DNA interactions are unevenly distributed within the nucleosomes. The nucleosome dyad has the strongest interactions, and these are followed by two regions localized approximately ±33-bp from the nucleosome entry/exit sites [27]. Interestingly, the DNA contacts lost at ±31-bp from the entry/exit sites in our variant NCPs might have effects on the nucleosomal stability and function. Histone variants generate diversity in chromatin structures and functions by altering the properties of the nucleosomes [17]. Biochemical analysis suggests that hTSH2B induces the octamer instability compared to H2B [28]. Further studies using mutant mice lacking the expression of TH2B suggest that it not only compensates expression of H2B during spermatogenesis but also it affects the epigenetic reprogramming through histone-DNA or histone−histone interactions [29]. Very recent data clearly indicated that lacking both the TH2A and TH2B variants affects in spermatogenesis by disturbing cohesion release and histone replacement [30]. In the *sin* mutant, the mutated residues encircling the nucleosome dyad, where H3−H4 pair with each other, affect the nucleosome stability, and thereby enhance the octamer mobility with respect to the DNA [31]. The H3 homologue CENP-A has been shown to affect the binding of a 13-bp DNA fragment at the NCP entry/exit sites [32]. The human testis-specific H3T affects nucleosome stability, due to the weaker association of the (H3T-H4)$_2$ tetramer with the H2a-H2b dimer, without affecting the interaction with DNA [25].
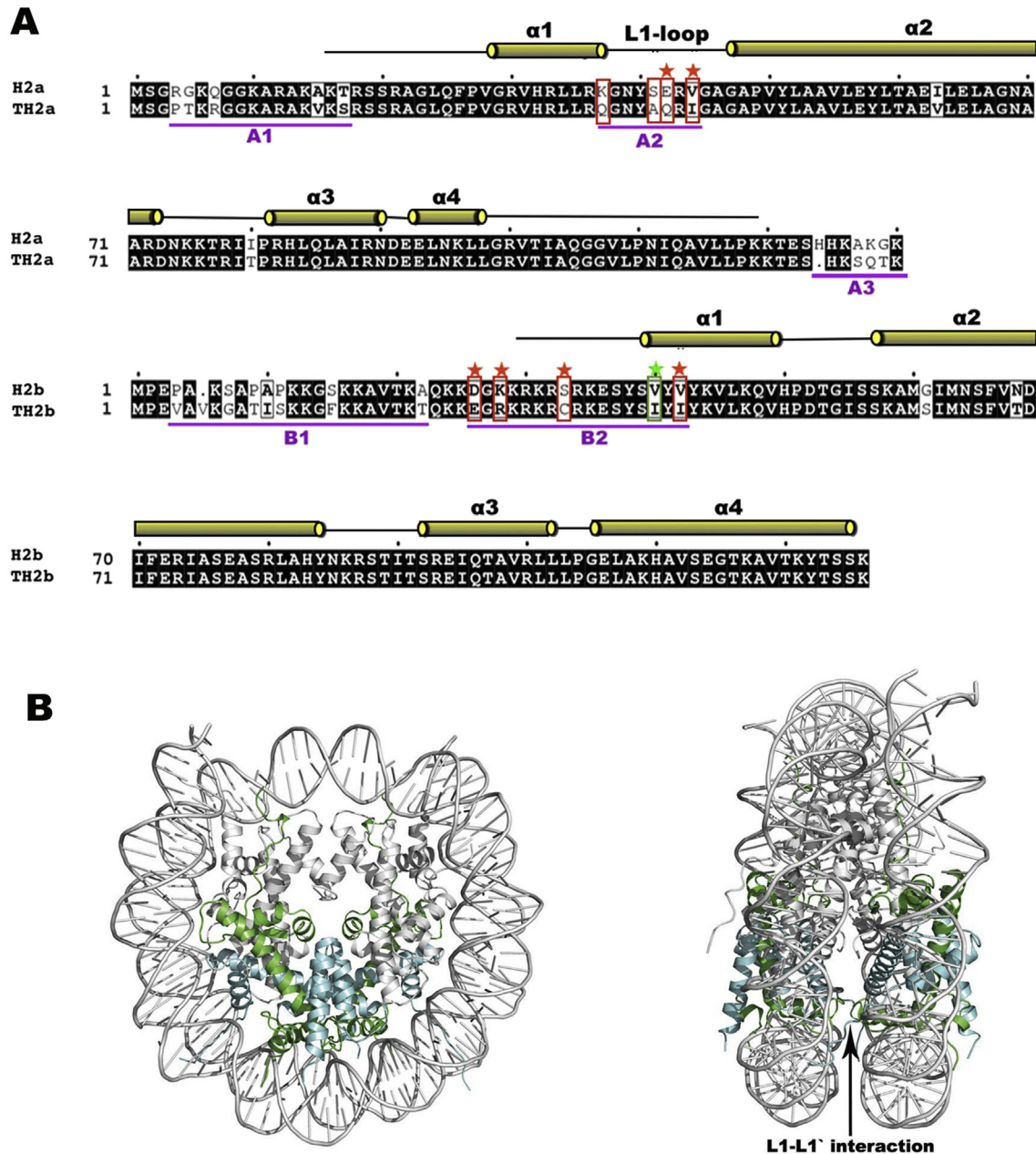
Fig. 1. Sequence alignment and nucleosome structure. A) The sequences of the histone variants, TH2a and TH2b, were aligned with those of the mouse canonical H2a and H2b. Schematic representations of secondary structures are shown above the alignment, and the TH2a L1-loop is labeled. The residues underlined in magenta were domain-swapped with the corresponding canonical sequences, and are labeled A1, A2 and A3 for TH2a, and B1 and B2 for TH2b. The residues enclosed in red boxes within the TH2a (A2) and TH2b (B2) domains were substituted by point mutations with the corresponding canonical residues. The residues marked with red stars down-regulate iPSC generation. The residue in the green box with a star up-regulates iPSC generation by two-fold. B) Crystal structure of the nucleosome complex GCH-NCP (TH2a-TH2b-H3-H4), with TH2a (cyan) and TH2b (green) highlighted. The left figure is rotated by 90° along the Y-axis, and the TH2a-TH2a′ interaction between the L1-L1′ loops is marked by an arrow. (For interpretation of the references to colour in this figure legend, the reader is referred to the web version of this article.)

3.3. L1-L1′ loop interactions

In nucleosomes, the L1-loop connecting the H2a α1-α2 helixes is the only site of contact between the H2a-H2b dimers, and it mediates the interactions between H2a-H2a′ [21]. The L1-loop region is a major site of sequence variation within a histone fold [33] among the H2a variants, and it has been suggested to play a role in the cooperative incorporation of a second dimer during NCP assembly [34].

In the canonical NCP the L1-L1′ loop interface interactions are stabilized by the H2b-His83 residues, which are located on both

sides of the L1-L1′ interfaces and form H-bond contacts (Fig. 3A–D). In GCH-NCP, the L1-L1′ interface lacks H-bond contacts. Intriguingly, the side-chain dihedral angle for TH2b-His84, in both dimers with well-defined electron density, changed its conformation as compared to the canonical H2b. This change affects the interactions between the His84 side-chain and the L1-L1′ interface, and shifts the position of TH2a-Asn39 towards the space generated by the TH2b-His84 residue. In the cross variant GCHV1-NCP, the H2b-His83 side-chain adopts a conformation similar to that in GCH, and thus has lost the contact with the interface. Also, it is noteworthy to mention that we did not observe any structural changes

Table 1
Data collection and refinement statistics.

Data collection	GCH	GCHV1	GCHV2	Canonical
Wavelength	1.00	1.00	1.00	1.00
Space group	$P2_12_12_1$	$P2_12_12_1$	$P2_12_12_1$	$P2_12_12_1$
Cell dimensions				
a, b, c (Å)	105.77,109.59, 181.59	104.43,109.18,175.00	99.32, 108.47,168.67	105.38, 109.36,175.57
α, β, γ (°)	90, 90, 90	90, 90, 90	90, 90, 90	90, 90, 90
Resolution (Å)	2.80 (2.90-2.80)	3.25 (3.31-3.25)	2.90 (3.00-2.90)	2.80 (2.90-2.80)
Reflections (unique)	51,865 (5066)	32,890 (1638)	38,723 (3737)	46,322 (3349)
I/sigma I	19 (2.04)	24.5 (2.65)	13.26 (2.05)	21 (1.76)
Completeness (%)	99.6 (99.1)	99.9 (100)	96.8 (95.3)	91.9 (67.9)
Redundancy	8.1 (7.1)	13.8 (14.0)	11.4 (10.1)	9.8 (8.3)
Rmerge	0.128 (0.72)	0.138 (0.78)	0.184 (0.74)	0.097 (0.73)
Refinement				
Rwork/Rfree	0.203/0.266	0.199/0.270	0.191/0.258	0.190/0.258
Number of atoms				
Protein	6201	6157	6417	5956
DNA	5980	5980	5972	5980
Water	107	30	–	57
B–factors (Å^2)				
Protein	44.7	83.8	27.9	61.5
DNA	100.6	142	63	121.6
R.m.s deviations				
Bond lengths (Å)	0.008	0.009	0.009	0.009
Bond angles (°)	1.419	1.423	1.565	1.436
Ramachandran plot				
Favored (%)	99	96.95	98.68	97.82
Allowed (%)	1.6	2.92	1.32	2.04
Outliers (%)	0.4	0.13	–	0.14
PDB Code	3X1T	3X1U	3X1V	3X1S

around the residue Asn84 (Ser85 in TSH2B) of TH2B in GCH or GHV2 nucleosome structures, when compared to TSH2B [26]. In GCHV2-NCP, the L1-L1′ interface has three H-bonds and resembles the canonical-NCP. Thus, the overall L1-L1′ loop interactions in the canonical and GCHV2-NCPs are tightly connected, as compared to those in GCH and GCHV1, and the following changes could be due to the Ile substitution of Val44 in the TH2a L1-loop.

In comparison to the NCPs described above, the other H2a variant NCPs have markedly different L1-L1′ loop conformations and interactions (Fig. 4). In H2a.Z-NCP, the L1-L1′ loop interaction between H2a.Z-H2a.Z′ is extensive, and the path of the α1-helix and parts of the loop connecting the α1 and α2-helixes differ from those of the canonical structure [35]. In the macroH2a-NCP, the L1-L1′ interface is less flexible and has more hydrophobic interactions. The Lys40 side chain is sandwiched between Tyr41 and Pro39′ and *vice versa* [34]. It is interesting to note that the H2b-His79 residue in both the H2a.Z- and macroH2a-NCPs does not interact with the L1-L1′ interface, and adopts a similar conformation to GCH.

3.4. TH2a/TH2b domain swapping and iPSC generation

Histone tails are epigenetically modified and regulate distinct transcriptional states and nuclear events [36], and are essential for the formation of highly ordered structures [37]. The mouse TH2a/TH2b variants enhance OSKM-induced reprogramming. However, neither each individual TH2a/TH2b variant nor the canonical H2a-H2b has the capacity for enhancing iPSC generation [1]. The above studies clearly suggested that the functional residues in the flexible N- and C-terminal tails and the coexistence of TH2a-TH2b have determining roles in reprogramming. Moreover, the structural studies with these variants revealed changes in the L1-L1′interface and fewer histone-DNA interactions within the nucleosome. To understand the significance of the histone tails and the structural changes of the nucleosome in iPSC generation, we performed domain swapping of variants with mouse canonical histones, as depicted in Fig. 1A. Three domain swaps for TH2a, corresponding to the N-terminal region (A1), the L1-loop (A2) and the C-terminus (A3), and two domain swaps (B1 and B2) for the N-terminus of TH2b were constructed. All five domain-swapping constructs were analyzed for their roles in iPSC generation.

The domain-swapped variants, along with the appropriate counterpart plus KOSM and P-Npm, were expressed in mouse embryonic fibroblasts (MEFs), which also express the GFP marker from the promoter of the ES cell-specific gene *Nanog*. The iPSC generation was analyzed by FACS (Supplementary Figure S1, A). The results clearly showed that all five domains are indeed important for iPSC generation. The swapped TH2a-L1 loop caused reduced iPSC generation, clearly signifying the importance of the structural changes at the L1-L1′interface. A closer view of the other four domains (A1, A3, B1 and B2) in the histone tail regions revealed changes in the positions of the functional residues. For example, the canonical H2b-Ser14 residue is phosphorylated by caspase-3-activated mammalian sterile twenty (Mst1) kinase, which plays an important role in regulating apoptotic chromosome condensation [38]. In TH2b, phenylalanine is located at the equivalent position, and is highly conserved among eukaryotic organisms (Supplementary Figure S1, B,C). Similarly, the H2a-Arg4 residue is deaminated by peptidylarginine deaminase 4 (PAD4), which represses gene transcription [39] and is replaced with Pro in TH2a. The N-terminal tail of H2b is known to be involved in chromatin condensation [40]. Also both of the H2A and H2B N-terminals are required for binding to the nuclear chaperones (Karyopherins family) to be imported into the nucleosome assembly machineries and the N-terminal deletion of H2B reduced its incorporation at all sites by approximately half due to the reduced protein stability though the overall function of H2B is intact in chromatin assembly [41,42], and these may be one probable reason why the N-terminal mutants of both the variants failed to reproduce the iPSC generation. Together, these results suggested that the variants of histone tails might establish alternative epigenetic marks as compared to the canonical counterparts, and they may affect the overall chromatin structure as well as iPSC reprogramming.
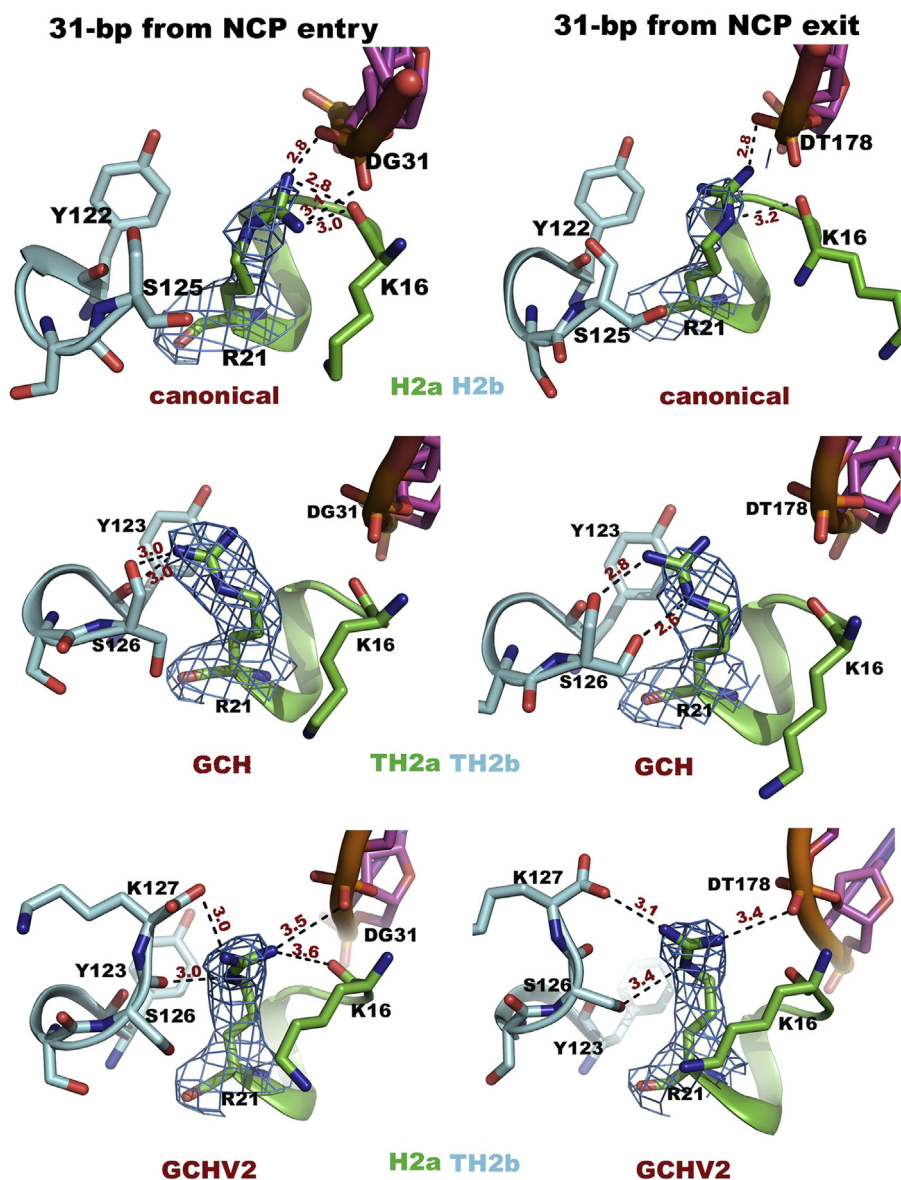
Fig. 2. Histone-DNA interactions. The Arg21/Arg21′ residues in TH2a/H2a from three nucleosome structures (GCH, GCHV2 and canonical-NCP) with 2Fo-Fc electron density maps contoured at 1.0σ are shown in a blue mesh, and their interactions with neighboring residues are depicted by dashed black lines with distances in red. (For interpretation of the references to colour in this figure legend, the reader is referred to the web version of this article.)

3.5. Point mutations in the TH2a (A2) and TH2b (B2) domains

The domain swapping studies clearly suggested that the histone tails and the structural changes in the dimer–dimer interactions between TH2a-TH2a′ (L1-loop) are important for iPSC generation. Among the five domains, only the TH2a-(A2) and TH2b-(B2) domains are structured within the NCP. To determine the importance of each non-conserved residue in the TH2a-(A2) and TH2b-(B2) domains, the residues shown in Fig. 1A were mutated to the corresponding canonical residues, and analyzed for their effects on reprogramming through a FACS analysis.

Intriguingly, two single amino acid substitutions in the TH2a-L1 loop, Gln42 to Glu and Ile44 to Val, each clearly affected the iPSC generation. The numbers of GFP$^+$ cells with these mutants were significantly reduced (Supplementary Figure S1, D), while the Gln37 to Lys and Ala41 to Ser substitutions did not have a major effect. The crystal structure revealed that the L1-L1′ loop

interaction in the NCP consists of both variants (GCH), and only with TH2a (GCHV1) lacks a H-bond, as compared to the H-bonding interaction seen with the canonical and GCHV2-NCPs. This clearly suggested that the replacement of Val44 with the bulky Ile residue in the TH2a L1-loop affects the interface interactions (Supplementary Figure S2, A).

The TH2b-(B2) domain has five non-conserved residues, and the point mutations of Glu27 to Asp, Arg29 to Lys, Cys34 to Ser and Ile43 to Val significantly reduced iPSC generation. Intriguingly, the TH2b-Ile41 to Val mutation up-regulated the iPSC generation by two-fold (Supplementary Figure S1, C-D). Furthermore, only the Ile41 and Ile43 residues had well-defined side chain densities and are strongly conserved among higher eukaryotic organisms (Supplementary Figure S1, C). In GCH-NCP, the TH2b-Ile43 residue is surrounded by a hydrophobic pocket and does not contact the DNA. By contrast, TH2b-Ile41 makes a hydrophobic contact with the DNA at ±25-bp from the
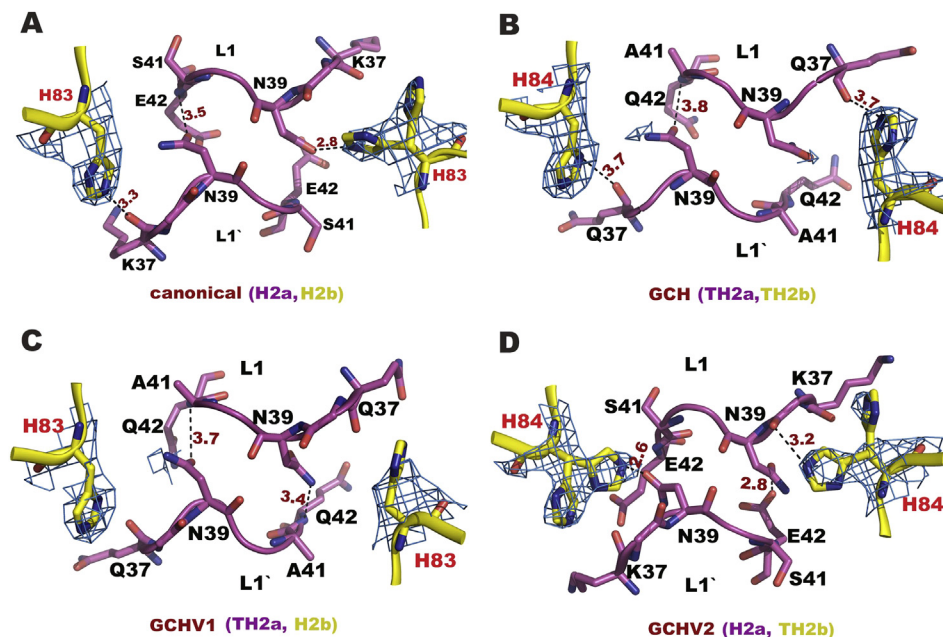
Fig. 3. Close-up views of the L1-L1′ loop interactions within NCPs. A) H2a-H2a′ with H2b (Canonical-NCP). B) TH2a-TH2a′ with TH2b (GCH-NCP), C) TH2a-TH2a′ with H2b (GCHV1-NCP) and D) H2a-H2a′ with TH2b (GCHV2-NCP). The TH2b/H2b-His84/83 residues from both dimers are shown with 2Fo-Fc electron density maps contoured at 1.0σ. The interactions are depicted by dashed black lines.
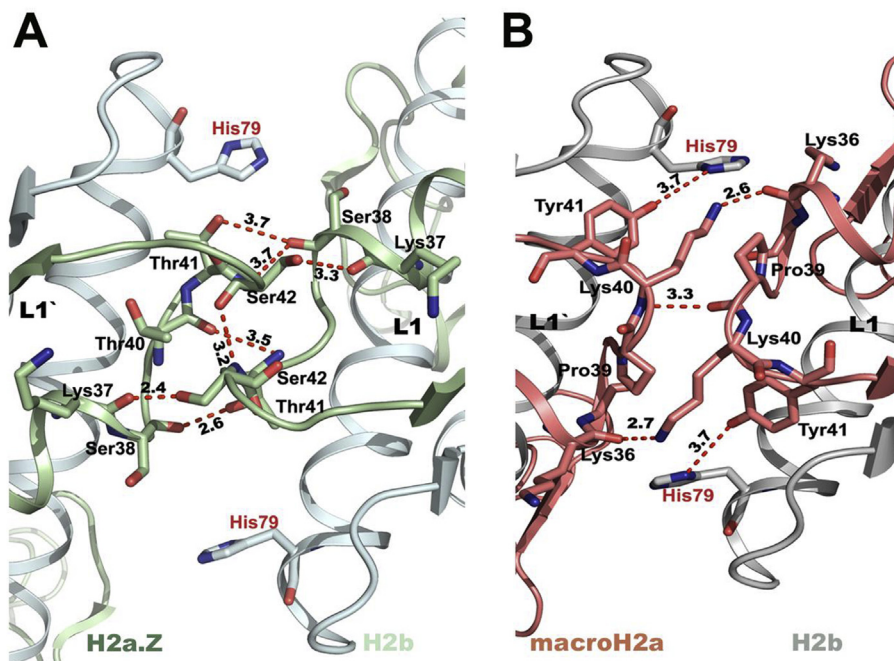

Fig. 4. L1-L1′ loop interactions in H2a variant complexes. A) The H2a.Z-H2a.Z′ interaction (PDB ID: 1F66). B) The macroH2a-macroH2a′ interaction (PDB ID: 1U35). Hydrogen bonds are depicted by dashed red lines and the H2b-His79 residues are marked in red. (For interpretation of the references to colour in this figure legend, the reader is referred to the web version of this article.)

nucleosome entry/exit sites, at a distance of 3.8 Å, and its replacement with Val might affect the above-mentioned interaction (Supplementary Figure S2, B). This loss of interactions will further weaken the strongest histone-DNA interacting region within the NCP, along with the TH2a-Arg21 residue, which might result in the two-fold increase in iPSC generation. It is also interesting to note that both the Glu42 in TH2a and Arg29 in TH2b are critical for iPSC generation in mouse (Supplementary

Figure S1), however they are not coserved with other species like human and rat (Supplementary Figure S1) suggesting that these functional residues might be species-specific. Altogether, the above analyses clearly suggested that the loss of the histone dimer-DNA contacts around ±31-bp from the nucleosome entry/exit sites and the modifications in the L1-L1′ interface interactions between TH2a-TH2a′ might have significant impacts on iPSC generation.

Acknowledgments

Appendix A. Supplementary data

Supplementary data related to this article can be found at http://dx.doi.org/10.1016/j.bbrc.2015.07.070.

References

[1] T. Shinagawa, T. Takagi, D. Tsukamoto, C. Tomaru, L.M. Huynh, P. Sivaraman, T. Kumarevel, K. Inoue, R. Nakato, Y. Katou, T. Sado, S. Takahashi, A. Ogura, K. Shirahige, S. Ishii, Histone variants enriched in oocytes enhance reprogramming to induced pluripotent stem cells, Cell Stem Cell 14 (2014) 217—227.

[2] L.A. Banaszynski, C.D. Allis, P.W. Lewis, Histone variants in metazoan development, Dev. Cell 19 (2010) 662—674.

[3] J. Govin, E. Escoffier, S. Rousseaux, L. Kuhn, M. Ferro, J. Thevenon, R. Catena, I. Davidson, J. Garin, S. Khochbin, C. Caron, Pericentric heterochromatin reprogramming by new histone variants during mouse spermiogenesis, J. cell Biol. 176 (2007) 283—294.

[4] A.K. Shaytan, D. Landsman, A.R. Panchenko, Nucleosome adaptability conferred by sequence and structural variations in histone H2A-H2B dimers, Curr. Opin. Struct. Biol. 32C (2015) 48—57.

[5] Y.C. Choi, C.B. Chae, DNA hypomethylation and germ cell-specific expression of testis-specific H2B histone gene, J. Biol. Chem. 266 (1991) 20504—20511.

[6] I.W. Hwang, K. Lim, C.B. Chae, Characterization of the S-phase-specific transcription regulatory elements in a DNA replication-independent testis-specific H2B (TH2B) histone gene, Mol. Cell. Biol. 10 (1990) 585—592.

[7] R.E. Branson, S.R. Grimes Jr., G. Yonuschot, J.L. Irvin, The histones of rat testis, Archives Biochem. Biophysics 168 (1975) 403—412.

[8] A. Shires, M.P. Carpenter, R. Chalkley, New histones found in mature mammalian testes, Proc. Natl. Acad. Sci. U. S. A. 72 (1975) 2714—2718.

[9] N.E. Huh, I.W. Hwang, K. Lim, K.H. You, C.B. Chae, Presence of a bi-directional S phase-specific transcription regulatory element in the promoter shared by testis-specific TH2A and TH2B histone genes, Nucleic Acids Res. 19 (1991) 93—98.

[10] J. Jullien, V. Pasque, R.P. Halley-Stott, K. Miyamoto, J.B. Gurdon, Mechanisms of nuclear reprogramming by eggs and oocytes: a deterministic process?, Nature reviews, Mol. Cell Biol. 12 (2011) 453—459.

[11] S. Yamanaka, H.M. Blau, Nuclear reprogramming to a pluripotent state by three approaches, Nature 465 (2010) 704—712.

[12] J.B. Gurdon, T.R. Elsdale, M. Fischberg, Sexually mature individuals of Xenopus laevis from the transplantation of single somatic nuclei, Nature 182 (1958) 64—65.

[13] C.A. Cowan, J. Atienza, D.A. Melton, K. Eggan, Nuclear reprogramming of somatic cells after fusion with human embryonic stem cells, Science 309 (2005) 1369—1373.

[14] K. Takahashi, S. Yamanaka, Induction of pluripotent stem cells from mouse embryonic and adult fibroblast cultures by defined factors, Cell 126 (2006) 663—676.

[15] A. Philpott, G.H. Leno, R.A. Laskey, Sperm decondensation in Xenopus egg cytoplasm is mediated by nucleoplasmin, Cell 65 (1991) 569—578.

[16] S. Banuelos, M.J. Omaetxebarria, I. Ramos, M.R. Larsen, I. Arregi, O.N. Jensen, J.M. Arizmendi, A. Prado, A. Muga, Phosphorylation of both nucleoplasmin domains is required for activation of its chromatin decondensation activity, J. Biol. Chem. 282 (2007) 21213—21221.

[17] R.T. Kamakaka, S. Biggins, Histone variants: deviants? Genes & Dev. 19 (2005) 295—310.

[18] Y. Tanaka, M. Tawaramoto-Sasanuma, S. Kawaguchi, T. Ohta, K. Yoda, H. Kurumizaka, S. Yokoyama, Expression and purification of recombinant human histones, Methods 33 (2004) 3—11.

[19] K. Luger, T.J. Rechsteiner, T.J. Richmond, Preparation of nucleosome core particle from recombinant histones, Methods Enzym. 304 (1999) 3—19.

[20] P.N. Dyer, R.S. Edayathumangalam, C.L. White, Y. Bao, S. Chakravarthy, U.M. Muthurajan, K. Luger, Reconstitution of nucleosome core particles from recombinant histones and DNA, Methods Enzym. 375 (2004) 23—44.

[21] K. Luger, A.W. Mader, R.K. Richmond, D.F. Sargent, T.J. Richmond, Crystal structure of the nucleosome core particle at 2.8 A resolution, Nature 389 (1997) 251—260.

[22] G.N. Murshudov, A.A. Vagin, E.J. Dodson, Refinement of macromolecular structures by the maximum-likelihood method, Acta crystallographica. Section D, Biol. Crystallogr. 53 (1997) 240—255.

[23] A.T. Brunger, Version 1.2 of the Crystallography and NMR system, Nat. Protoc. 2 (2007) 2728—2733.

[24] P. Emsley, K. Cowtan, Coot: model-building tools for molecular graphics, Acta crystallographica. Section D, Biol. Crystallogr. 60 (2004) 2126—2132.

[25] H. Tachiwana, W. Kagawa, A. Osakabe, K. Kawaguchi, T. Shiga, Y. Hayashi-Takanaka, H. Kimura, H. Kurumizaka, Structural basis of instability of the nucleosome containing a testis-specific histone variant, human H3T, Proc. Natl. Acad. Sci. U. S. A. 107 (2010) 10454—10459.

[26] T. Urahama, N. Horikoshi, A. Osakabe, H. Tachiwana, H. Kurumizaka, Structure of human nucleosome containing the testis-specific histone variant TSH2B, Acta crystallographica. Section F, Struct. Biol. Commun. 70 (2014) 444—449.

[27] M.A. Hall, A. Shundrovsky, L. Bai, R.M. Fulbright, J.T. Lis, M.D. Wang, High-resolution dynamic mapping of histone-DNA interactions in a nucleosome, Nat. Struct. Mol. Biol. 16 (2009) 124—129.

[28] A. Li, A.H. Maffey, W.D. Abbott, N. Conde e Silva, A. Prunell, J. Siino, D. Churikov, A.O. Zalensky, J. Ausio, Characterization of nucleosomes consisting of the human testis/sperm-specific histone H2B variant (hTSH2B), Biochemistry 44 (2005) 2529—2535.

[29] E. Montellier, F. Boussouar, S. Rousseaux, K. Zhang, T. Buchou, F. Fenaille, H. Shiota, A. Debernardi, P. Hery, S. Curtet, M. Jamshidikia, S. Barral, H. Holota, A. Bergon, F. Lopez, P. Guardiola, K. Pernet, J. Imbert, C. Petosa, M. Tan, Y. Zhao, M. Gerard, S. Khochbin, Chromatin-to-nucleoprotamine transition is controlled by the histone H2B variant TH2B, Genes & Dev. 27 (2013) 1680—1692.

[30] T. Shinagawa, L.M. Huynh, T. Takagi, D. Tsukamoto, C. Tomaru, H.G. Kwak, N. Dohmae, J. Noguchi, S. Ishii, Disruption of Th2a and Th2b genes causes defects in spermatogenesis, Development 142 (2015) 1287—1292.

[31] U.M. Muthurajan, Y. Bao, L.J. Forsberg, R.S. Edayathumangalam, P.N. Dyer, C.L. White, K. Luger, Crystal structures of histone Sin mutant nucleosomes reveal altered protein-DNA interactions, EMBO J. 23 (2004) 260—271.

[32] H. Tachiwana, W. Kagawa, T. Shiga, A. Osakabe, Y. Miya, K. Saito, Y. Hayashi-Takanaka, T. Oda, M. Sato, S.Y. Park, H. Kimura, H. Kurumizaka, Crystal structure of the human centromeric nucleosome containing CENP-A, Nature 476 (2011) 232—235.

[33] C. Bonisch, S.B. Hake, Histone H2A variants in nucleosomes and chromatin: more or less stable? Nucleic Acids Res. 40 (2012) 10719—10741.

[34] S. Chakravarthy, S.K. Gundimella, C. Caron, P.Y. Perche, J.R. Pehrson, S. Khochbin, K. Luger, Structural characterization of the histone variant macroH2A, Mol. Cell. Biol. 25 (2005) 7616—7624.

[35] R.K. Suto, M.J. Clarkson, D.J. Tremethick, K. Luger, Crystal structure of a nucleosome core particle containing the variant histone H2A.Z, Nat. Struct. Biol. 7 (2000) 1121—1124.

[36] S.D. Taverna, H. Li, A.J. Ruthenburg, C.D. Allis, D.J. Patel, How chromatin-binding modules interpret histone modifications: lessons from professional pocket pickers, Nat. Struct. Mol. Biol. 14 (2007) 1025—1040.

[37] J. Allan, N. Harborne, D.C. Rau, H. Gould, Participation of core histone "tails" in the stabilization of the chromatin solenoid, J. Cell Biol. 93 (1982) 285—297.

[38] W.L. Cheung, K. Ajiro, K. Samejima, M. Kloc, P. Cheung, C.A. Mizzen, A. Beeser, L.D. Etkin, J. Chernoff, W.C. Earnshaw, C.D. Allis, Apoptotic phosphorylation of histone H2B is mediated by mammalian sterile twenty kinase, Cell 113 (2003) 507—517.

[39] T. Hagiwara, Y. Hidaka, M. Yamada, Deimination of histone H2A and H4 at arginine 3 in HL-60 granulocytes, Biochemistry 44 (2005) 5827—5834.

[40] A.E. de la Barre, D. Angelov, A. Molla, S. Dimitrov, The N-terminus of histone H2B, but not that of histone H3 or its phosphorylation, is essential for chromosome condensation, EMBO J. 20 (2001) 6383—6393.

[41] N. Mosammaparast, K.R. Jackson, Y. Guo, C.J. Brame, J. Shabanowitz, D.F. Hunt, L.F. Pemberton, Nuclear import of histone H2A and H2B is mediated by a network of karyopherins, J. cell Biol. 153 (2001) 251—262.

[42] A. Jamai, R.M. Imoberdorf, M. Strubin, Continuous histone H2B and transcription-dependent histone H3 exchange in yeast cells outside of replication, Mol. Cell 25 (2007) 345—355.

Short Communication

Distinct requirements for the maintenance and establishment of mouse embryonic stem cells

Riyo Konishi[a], Toru Nakano[a,b,c], Shinpei Yamaguchi[b,d,*]

[a] Department of Stem Cell Pathology, Graduate School of Frontier Biosciences, Osaka University, Yamada-oka 2-2 Suita, Osaka 565-0871, Japan
[b] Department of Pathology, Medical School, Osaka University, Yamada-oka 2-2 Suita, Osaka 565-0871, Japan
[c] CREST, Japan Agency for Medical Research and Development (AMED), Japan
[d] PRESTO, Japan Science and Technology Agency (JST), Japan

ARTICLE INFO

ABSTRACT

Mouse embryonic stem cells (ESCs) that maintain a sustainable pluripotent state are derived from the inner cell mass (ICM) of blastocysts, in which pluripotency is lost during differentiation in vivo. It is unclear when and how the ability to maintain pluripotency is acquired during the derivation of ESCs. We analyzed the required culture condition for the maintenance and establishment of ESCs in detail. Even at low concentration of the GSK3β inhibitor and LIF (LowGiL), the expression levels of pluripotency markers and the chimera-producing ability of the cells were comparable with those of ESCs cultured in the presence of both inhibitors and LIF (2iL). However, blastocysts underwent spontaneous differentiation, and ESCs were not established under LowGiL condition. Time-course analysis showed that 2iL condition for three days from the initiation of culture was sufficient for the acquisition of permanent pluripotency. Although X chromosome-linked pluripotent genes were significantly up-regulated during the culture of both male and female blastocysts in 2iL condition, no such up-regulation was observed in LowGiL condition. In conclusion, 2iL-dependent activation of these X-linked genes at the earliest phase of ESC derivation is one of the molecular bases for the acquisition of permanent pluripotency.

1. Introduction

Mouse embryonic stem cells (ESCs), which are derived from the inner cell mass (ICM) of blastocysts, have the ability to differentiate into all three germ layer lineages, including germ cells (Evans and Kaufman, 1981; Martin, 1981; Smith, 2001). Although ESCs were maintained under the culture condition with serum, leukemia inhibitory factor (LIF) without feeder cells, the pluripotent state was shown to be metastable and heterogeneous under this condition (Hayashi et al., 2008; Niwa et al., 2009; Williams et al., 1988). This problem was resolved by the use of a chemically defined culture medium (2iL) that includes LIF and inhibitors of glycogen synthase kinase-3-β (GSK3β) and mitogen-activated protein kinase (MEK) signaling. This culture medium enabled us to maintain ESCs in a naïve and homogeneous pluripotent state (Ying et al., 2008; Nichols and Smith, 2009; Dunn et al., 2014).

Serum-containing media with LIF have been used for quite some time for the establishment of mouse ESCs (Smith et al., 1988; Williams et al., 1988). However, the efficiency of ESC derivation under this condition was noticeably low and only applicable to a few permissive

strains, including 129/Sv and C57BL/6 (Kawase et al., 1994; Czechanski et al., 2014). Recently, 2iL culture condition was found not only improving the efficiency of ESC derivation, but also establishing ESC from multiple non-permissive strains, including BALB/c and Non-obese diabetic (NOD) (Hanna et al., 2009; Nichols et al., 2009; Czechanski et al., 2014). Although 2iL medium has a strong advantage over conventional serum-containing media in terms of efficient ESC derivation, the loss of gamete-derived DNA methylation in female ESCs is problematic (Yagi et al., 2017). Female ESCs derived under 2iL condition failed to support full-term development of tetraploid blastocyst-complemented embryos because of DNA hypomethylation accompanied by a loss of imprinting. The major source of this hypomethylation was likely the MEK inhibitor, since MEK inhibition decreased the DNA methylation level in ESCs in a dose-dependent manner (Shirane et al., 2016; Choi et al., 2017; Yagi et al., 2017). However, even in cultures incubated either with a decreased concentration of the MEK inhibitor or with a Src inhibitor instead of the MEK inhibitor, a gradual loss of DNA methylation occurred globally (Yagi et al., 2017). Therefore, alternative methods for the derivation and maintenance of ESCs are required, especially for epigenetic studies.
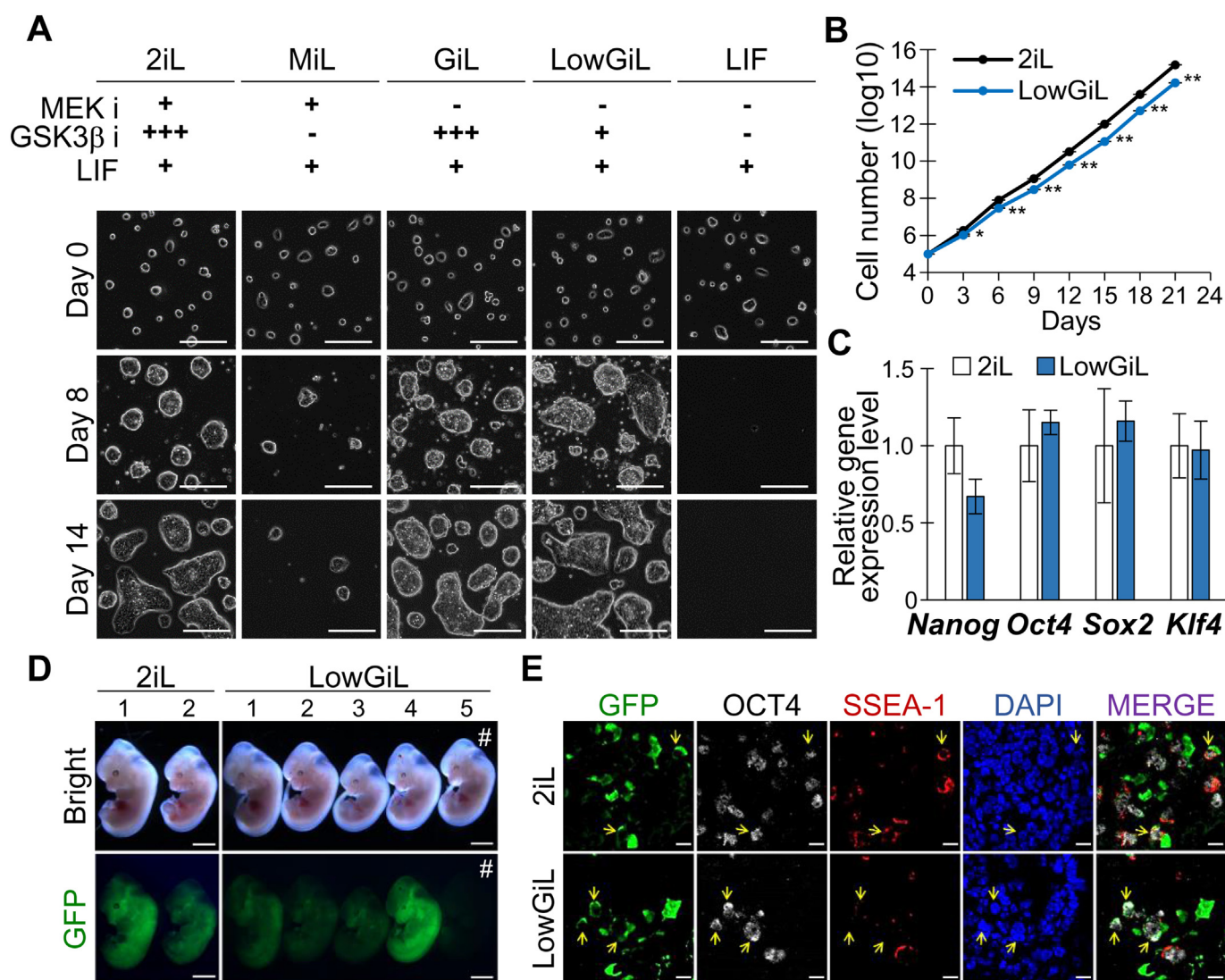
Fig. 1. Maintenance of embryonic stem cells (ESCs) under LowGiL condition. (A): Representative images of ESCs cultured under 2iL, MEK inhibitor + LIF (MiL), GSK3β inhibitor + LIF (GiL), low-concentration GSK3β inhibitor + LIF (LowGiL), and LIF conditions. HyESCs were maintained under 2iL condition without feeder until use. Culture condition was switched to each condition 24 h after the passage (day 0). Scale bar, 200 μm. (B): Growth of ESCs under 2iL and LowGiL conditions. **$P < .01$, *$P < .05$ by *t*-test. *n* = 3. Error bars, SEM. (C): Quantitative reverse transcription PCR (RT-qPCR) analyses of ESCs cultured under 2iL and LowGiL conditions. The relative gene expression level was normalized to *Gapdh*. n = 3. Error bars, SEM. (D): Chimeric embryos generated by the aggregation of wild-type morula and ESCs bearing the CAG-GFP transgene cultured under 2iL or LowGiL conditions. # the embryo with no ESC contribution, serving as the negative control. Scale bar, 2 mm. (E): Immunostaining of the genital ridges from chimeric embryos. Arrows indicate primordial germ cells derived from ESCs. A merge of GFP, OCT4, and SSEA-1 is shown to the right. Scale bar, 10 μm.

In contrast to the permanent pluripotency of ESCs, the pluripotency of the ICM is transient and gradually lost after implantation. The ICM undergoes differentiation into the epiblast and primitive endoderm via distinct FGF signaling-pathways at the peri-implantation stage. FGF4/FGFR1 signaling plays a critical role in epiblast maturation, whereas both FGFR1 and FGFR2 are required for cell-fate decision of primitive endoderm (Kang et al., 2017; Molotkov et al., 2017). The culture of preimplantation embryos with an inhibitor of extracellular signal-related kinase 1/2 (ERK1/2), which functions downstream of FGF4/FGFR signaling, resulted in the suppressed differentiation of the primitive endoderm (Yamanaka et al., 2010; Nichols et al., 2009). Given that the transcriptional profile of naïve ESCs was similar to that of E4.5 early epiblast cells, it is proposed that maturation of the ICM into an early epiblast-like state is a prerequisite for ESC establishment (Boroviak et al., 2014; Boroviak et al., 2015). However, it is unclear when and how the pluripotent state of the ICM becomes permanent during ESC derivation.

In this study, we found that the low concentration of GSK3β inhibitor and LIF (LowGiL) condition without MEK inhibition stably maintained the pluripotency of ESCs. ESCs maintained under LowGiL condition expressed representative pluripotency factors at comparable levels with those in ESCs maintained under 2iL condition, and contributed to all three germ layers in chimeric mouse embryos. On the other hand, pluripotency factors were silenced, and ESCs could not be established from blastocysts under LowGiL condition. Our time-course experiments using blastocysts demonstrated that a pluripotent state could be maintained under LowGiL condition after 3 days of culture under 2iL condition. In particular, our transcriptome analysis demonstrated prominent activation of genes on the X chromosome during this period.

Thus, our study identified a critical period for ESC establishment and provides alternative methods for ESC derivation and maintenance.
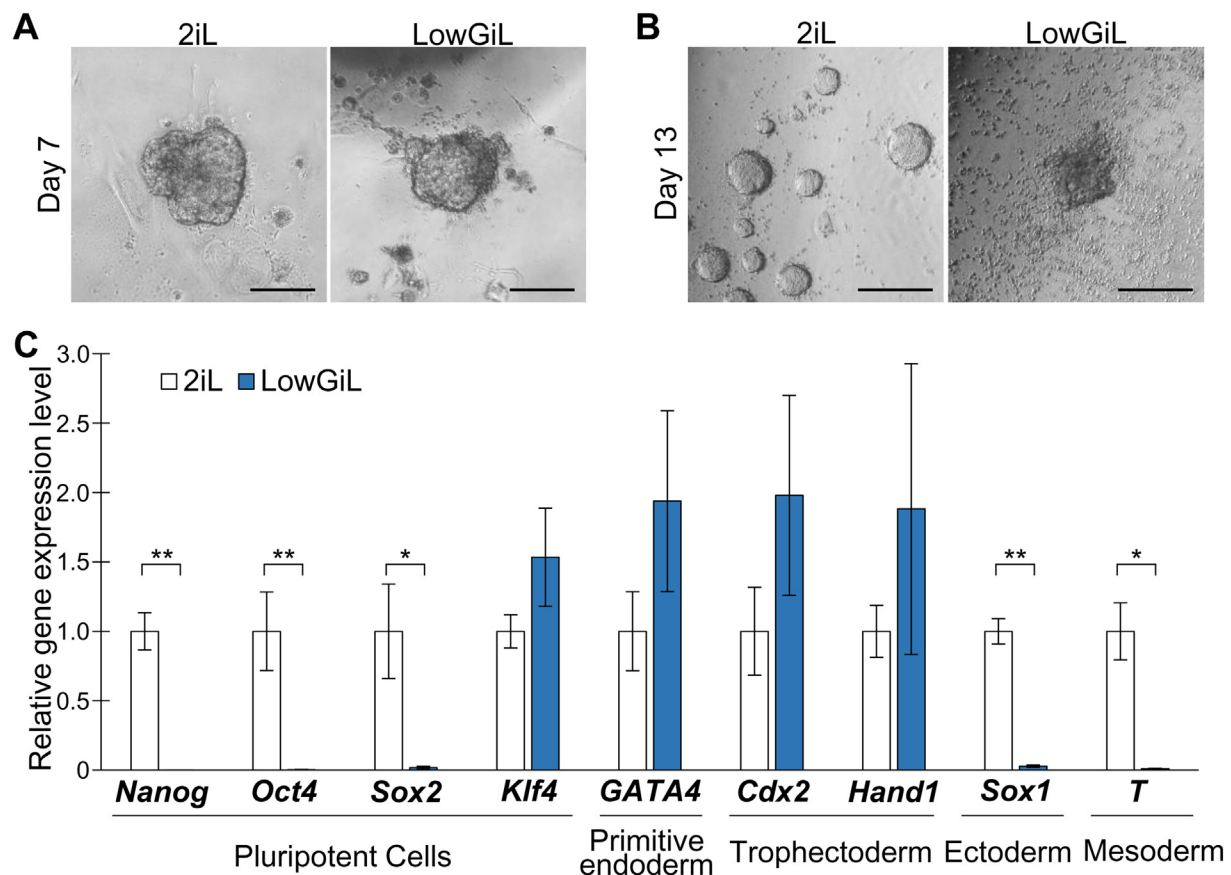
Fig. 2. Establishment of ESCs under LowGiL condition. (A, B): Blastocysts cultured under 2iL and LowGiL conditions for 7 days (A) and 13 days (B). ESCs were established with high efficiency under 2iL condition (10/11, 91%), whereas no ESCs were established under LowGiL condition (0/21, 0%). Scale bar, 200 μm (C): RT-qPCR analysis of blastocyst outgrowth cultured for 7 days under 2iL or LowGiL. Relative gene expression levels were normalized to *Gapdh*. **$P < .01$, *$P < .05$ by *t*-test. n = 3–7. Error bars, SEM.

2. Materials and methods

2.1. Cell culture and proliferation assay

ESCs were basically maintained under 2iL condition using DMEM/F-12, GlutaMAX, $0.5\times$ N-2, $0.5\times$ B-27, 100 U/mL mouse LIF, 3 μM CHIR99021, 1 μM PD0325901, 1 mM L-glutamin, and penicillin/streptomycin with a 0.1% gelatin-coated dish without a feeder layer. The ESC lines used in this study were V6.5 (Rideout 3rd et al., 2000), G4 (George et al., 2007), E14 (Hopper et al., 1987) and, hybrid ESCs (HyESCs) harboring CAG-GFP, which were established in our lab from C57BL/6 × CAST F1 blastocysts. To evaluate the proliferation rate of ESCs, the cells were counted and passaged into 1.0×10^5 six-well plates every 3 days.

2.2. Blastocyst collection and derivation of ESCs

Superovulated B6D2F1 (BDF1) females were mated with BDF1 or B6;B6C3-Tg(CAG/Acr-EGFP)CX-FM139Osb, the transgenic mice expressing GFP ubiquitously from CAG-EGFP on X chromosome (XGFP) males (Isotani et al., 2005). The appearance of the vaginal plug at noon was defined as embryonic day (E) 0.5. E3.5 embryos were collected by flashing of oviduct or uterus with M2 media + 4 mg/mL bovine serum album (BSA). Zona pellucidae were removed using 0.5% pronase. The embryos were individually plated into single wells of 96 well plates coated with matrigel, cultured for the first 3 days under 2iL or LowGiL with 10% of fetal bovine serum (FBS), and then switched to serum-free conditions.

3. Results and discussion

3.1. ESCs can be maintained but not established under LowGiL condition

First, we analyzed the essential conditions for ESC maintenance using various cell lines to elucidate the molecular mechanisms underlying ESC establishment and maintenance. Consistent with previous reports, undifferentiated dome-like colonies and their stable proliferation were observed in ESCs cultured under 2iL condition, while ESCs underwent immediate differentiation and stopped proliferating under LIF-only condition without any inhibitors (Fig. 1A and Supplementary Fig. 1A). When G4, V6.5, and HyESC mouse ESC lines were used, partial differentiation, with a flattened colony morphology, and a reduced proliferation rate were observed in the absence of a GSK3β inhibitor (MiL condition) (Fig. 1A and Supplementary Fig. 1A). In contrast, E14 ESCs were stably maintained under this condition. It is likely that sensitivity to the MiL condition varied among the cell lines; indeed, a previous study reported that the MiL condition stably maintained the pluripotency of ESCs (Dunn et al., 2014). Therefore, MiL is not an appropriate condition for ESC maintenance. Meanwhile, all of the ESC lines evaluated were in a pluripotent state when cultured in the presence of the GSK3β inhibitor and LIF but without the MEK inhibitor (GiL condition) (Fig. 1A and Supplementary Fig. 1A). Even the low concentration of GSK3β inhibitor and LIF (LowGiL condition) produced essentially the same results as did the GiL and 2iL conditions using the same mouse ESC lines. These results show that culture under LowGiL condition is a prerequisite for ESC pluripotency.

ESCs cultured under LowGiL (LowGiL-ESCs) exhibited undifferentiated colonies and grew exponentially for > 1 month. The
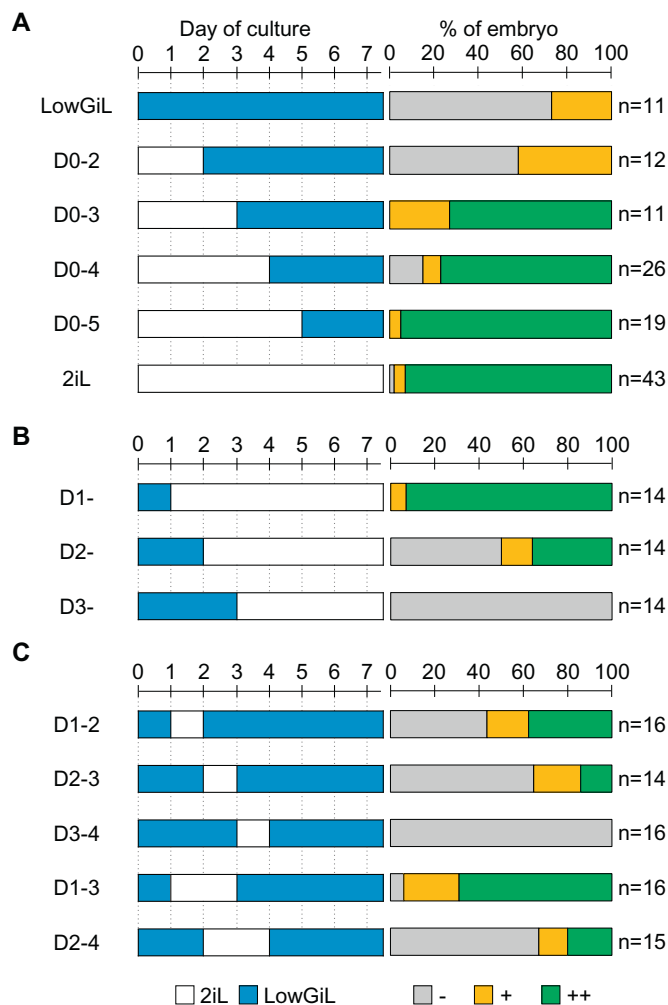
Fig. 3. Time course experiments of ESC establishment. (A–D): The figure shows the experimental design and results of changing the medium from 2iL to LowGiL (A), and from LowGiL to 2iL (B). Culture with 2iL at different periods for 1 or 2 days during ESC establishment (C). Experimental design (left) and ratio of GFP-positive colonies (right) are shown. Embryos were classified according to the number of OCT4-GFP-positive cells at culture day 7 (see Supplementary Fig. 3A–C).

proliferation rates of G4, V6.5 and E14 ESCs under LowGiL condition were comparable to those under 2iL condition. However, HyESC exhibited slightly but significantly lower proliferation rate under the LowGiL than 2iL conditions (Fig. 1B and Supplementary Fig. 1B). The observed differences in sensitivity to LowGiL condition is possibly due to strain differences among the HyESC (F1 from CAST and C57BL/6), G4, V6.5 (F1 from 129/sv and C57BL/6), and E14 (129/Ola) cells. To evaluate whether the pluripotency of HyESCs was affected by LowGiL condition, gene expression and the differentiation potential of the cells were analyzed. Quantitative reverse transcription PCR (RT-qPCR) analysis revealed that the expression levels of *Nanog, Oct4, Sox2, Klf4, and Esrrb* were comparable between LowGiL and 2iL conditions, while *Lin28b, Utf1, Nr0b1* and *Eras* were up-regulated in LowGiL-ESCs (Fig. 1C, Supplementary Fig. 1C). Differentiation potency of LowGiL-ESCs was confirmed by whole body contribution of ESCs in the aggregation chimeric embryos (Fig. 1D). Furthermore, immunohistochemical analysis with specific markers revealed the germ line contribution of each ESC (Fig. 1E). 2iL-ESCs and LowGiL-ESCs exhibited similar contribution rates in chimerism (8/8 [100%] vs. 5/6 [83%]; *P* = .43 by Fisher's exact test) (Supplementary Table 2). Taken together, these results indicate that the pluripotency of ESCs can be

stably maintained with LowGiL.

We investigated whether ESCs could be derived from E3.5 blastocysts under LowGiL condition. We added serum during first 3 days of blastocyst culture, because blastocyst cells hardly expanded in serum-free condition even with the supplementation of 2iL (data not shown). The 2iL condition resulted in very high derivation efficiency (10/11: 91%), but the LowGiL condition established virtually no ESCs (0/21: 0%). Consistent with the previous report, the colony morphology of the blastocyst outgrowth under LowGiL condition was indistinguishable from that under 2iL at day 7 (Boroviak et al., 2014). However, spontaneous differentiation took place under LowGiL condition after the first passage and no dome-like colony appeared even after a few passages (Fig. 2A, B). Blastocysts cultured under LowGiL condition silenced pluripotent factors, such as *Nanog, Oct4*, and *Sox2*, and up-regulated markers of differentiation (Fig. 2C). To identify the key factor of LowGiL condition that causes the failure in ESC establishment, we cultured blastocysts under GiL and Mi + LowGiL conditions. Blastocyst cells cultured in Mi + LowGiL expanded well and maintained OCT4-GFP expression at a comparable level to that cultured in 2iL, while most embryos cultured in GiL lost OCT4-GFP expression as early as day 3 (Supplementary Fig. 2, Supplementary Table 3). These results suggest that the presence of a MEK inhibitor during the early phase of ESC establishment is critical for the acquisition of pluripotency.

3.2. The Critical period for ESC establishment requires 2iL culture condition

To examine this in more detail, we performed a time course analysis regarding the requirement of MEK and GSK3β inhibitors for pluripotency. First, the culture condition was switched from 2iL to LowGiL at different time points, and pluripotency of clones was classified into three categories according to the ratio of OCT4-GFP-positive cells at day 7 (−: 0–25%, +: 25–75%, + +: 75–100%) (Supplementary Fig. 3A and Supplementary Table 4). Clear difference in pluripotency between D0–2 and D0–3 demonstrated that the first 3 days were critical for obtaining permanent pluripotency (Fig. 3A and Supplementary Fig. 3B). Second, the culture condition was changed from LowGiL to 2iL at different time points (Fig. 3B and Supplementary Fig. 3C). When embryos were cultured under LowGiL condition for 24 h and then switched to 2iL condition (D1-), almost all of the embryos were classified as + +. This result is consistent with those of a previous study, showing that 24 h of culture under GiL condition improved ESC derivation from early blastocysts (Boroviak et al., 2014). However, the ratio of + + cells was decreased to < 40% when blastocysts were cultured under LowGiL condition for 2 days (D2-), and none of the colonies maintained OCT4-GFP expression when the LowGiL culture period exceeded 2 days (D3-). These results further support the notion that the initial 3-day culture period was critical for ESC establishment. Based on these results, we examined pluripotency acquisition of E3.5 blastocysts in an experiment with a variable time course (Fig. 3C and Supplementary Fig. 3C). When blastocysts were cultured for 24 h under 2iL condition between days 1 and 2 (D1–2) or days 2 and 3 (D2–3), the percentage of + + cells was < 40% or 20%, respectively. Meanwhile, > 60% of the blastocysts cultured for 48 h under 2iL condition between days 1 and 3 (D1–3) were classified as + +. Next, we cultured blastocysts under Mi + LowGiL between Day 1 and 3, to test whether higher dose of Gi at this period was required for the successful ESC derivation. The ratio of + + clones in Mi + LowGiL:D1–3 were significantly lower than 2iL:D1–3, suggesting that not only Mi but also high dose of Gi at the critical period was important to gain sustainable pluripotent state (Fig. 3C, Supplementary Fig. 3C–E and Supplementary Table 4). It was reported that E4.5 embryos showed more efficient ESC derivation from a single cell than did E3.5 embryos (Boroviak et al., 2014). We evaluated ESC establishment from E4.5 blastocysts under various culture conditions, but E4.5 blastocysts showed similar results to E3.5 blastocysts (Supplementary Fig. 4 and Supplementary Table 4). These results revealed that there was 48 h of critical window for permanent
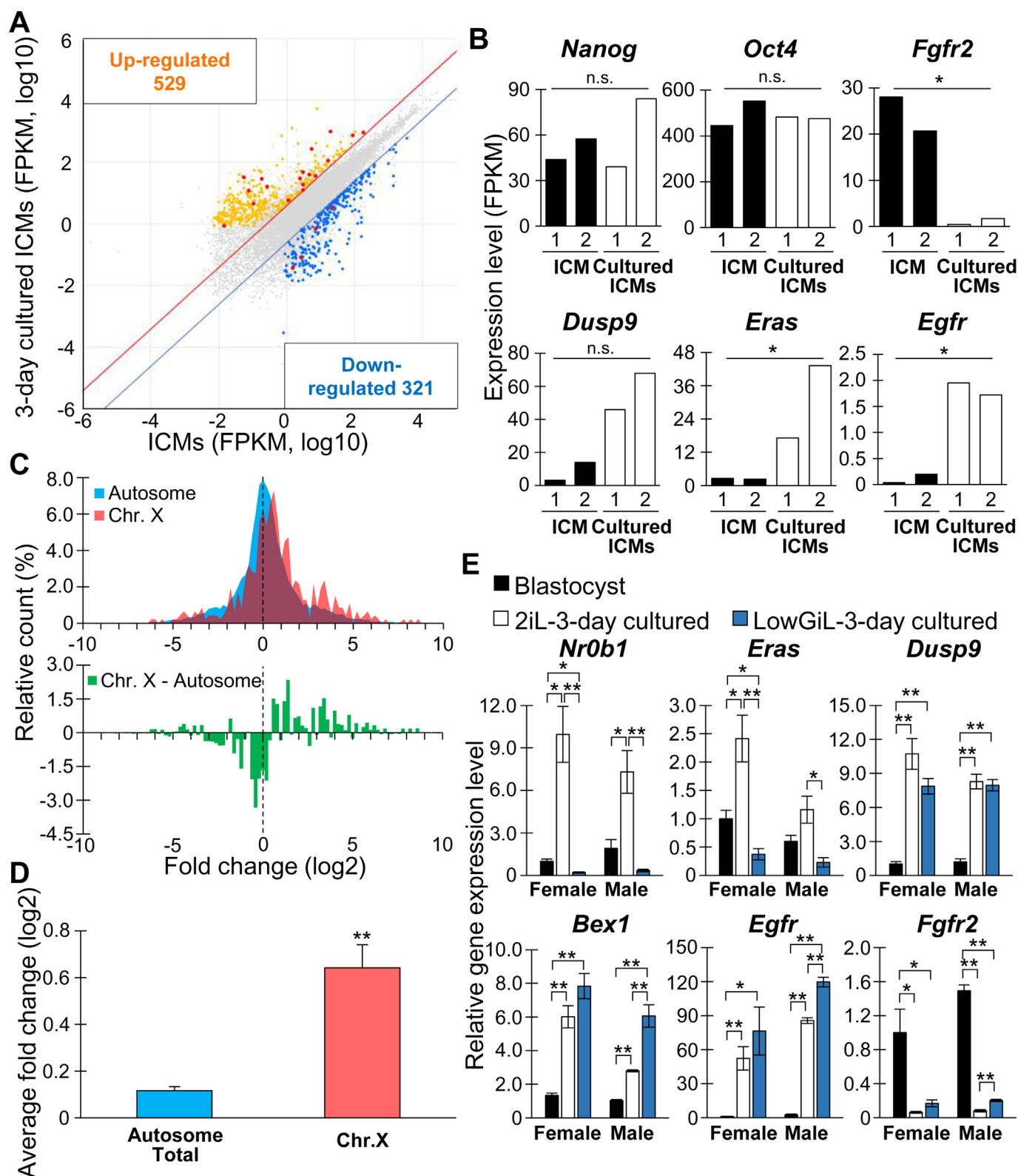
Fig. 4. Changes in gene expression in the inner cell mass (ICM) culture. (A): Scatter plot comparing E3.5 ICM and 3-day-cultured ICM under 2iL condition according to RNA sequencing. The total number of covered and expressed genes was 12,991 (fragments per kilobase of transcript per million fragments mapped [FPKM] > 1.0). Significantly up- and down-regulated genes are shown in yellow and blue, respectively (Fold change > 4.0; $P < .05$). X-linked genes are highlighted in red. (B): Example of differentially expressed genes in cultured ICM versus ICM. The data of two biological replicates were shown. (C): Histogram of fold-change fold change in gene expression on the autosome ($n = 12,518$) and X chromosome ($n = 467$) (top). The result of subtraction of the autosome fold change value from the X chromosome value is shown at the bottom of the histogram. (D): Comparison of the average fold change of autosomal and X-chromosome gene expression between the ICM and 3-day-cultured ICM. Only expressed genes were analyzed (FPKM > 1.0). The Y chromosome is not shown because only six genes were expressed, which was insufficient for statistical analysis. (E): RT-qPCR analysis of blastocysts and blastocyst outgrowth after 3-day culture under 2iL and LowGiL conditions. Relative gene expression levels were normalized to *Gapdh*. ** $P < .01$, * $P < .05$ by t-test. $n = 3$. Error bars, SEM. (For interpretation of the references to colour in this figure legend, the reader is referred to the web version of this article.)

pluripotency under 2iL condition, i.e., between days 1 and 3. Recently, epigenetic and genetic abnormalities of ESCs established under 2iL condition were reported (Choi et al., 2017; Yagi et al., 2017). Our findings would help to minimize the culture period of the ICM in the presence of a MEK inhibitor, which plays a major role in the abnormalities (Choi et al., 2017; Yagi et al., 2017).

3.3. Gene expression changes during the early phase of ESC derivation

Evident differences in GFP expression at day 7, between the D0–2 and D0–3 conditions, suggested that 3-day culture of the ICM cells established a robust transcriptional network for pluripotency, which was maintained even under LowGiL condition (Fig. 3A and Supplementary Fig. 3B). We analyzed the transcriptome of ICMs, before and after the culture under 2iL condition for 3 days, to gain insight into the molecular mechanisms of permanent pluripotency acquisition. In total, 529 and 321 genes were up- and down-regulated by the culture, respectively, among the 23,284 genes covered (Fold change [FC] > 4, $P < .05$) (Fig. 4A and Supplementary Table 5). Up-regulated genes showed enrichment in terms of cell division and chromosome partitioning/cytoskeleton, negative regulation of cell proliferation, while the down-regulated genes showed mild enrichment in terms of amino acid transport, metabolism, and nucleosome assembly (Supplementary Fig. 5). The distribution of the histone H3 lysine 4 trimethylation (H3K4me3) and histone H3 lysine 27 trimethylation (H3K27me3) epigenetic markers changed remarkably during ESC derivation (Liu et al., 2016). Liu et al. (2016) reported that ESCs showed a loss of H3K27 methylation at H3K27me3-marked regions in the ICM. Thus, a global loss of repressive epigenetic marks such as H3K27me3 and DNA methylation is likely the molecular basis for gene activation in the ICM during culture. Although core pluripotent genes such as *Nanog, Oct4, Klf4* and *Sox2* were not significantly changed during the culture, some pluripotent genes, including *Dusp9, Eras,* and *Egfr,* were significantly up-regulated (Fig. 4B and Supplementary Fig. 6) (Heo et al., 2006; Takahashi et al., 2003; Li et al., 2012). Primitive endoderm-related factors, such as *Fgfr2, Gata4, Gata6, Sox7* and *Sox17* were significantly down-regulated during the culture, whereas few of trophectoderm, ectoderm and mesoderm markers were changed (Fig. 4B and Supplementary Fig. 6) (Molotkov et al., 2017). Additionally, *Wnt11, Ctnnb1* (β-catenin), and Notch signal-related genes were significantly up-regulated, supporting the notion that Wnt/β-catenin and Notch signaling are activated during the derivation of ESCs (Supplementary Fig. 6) (Umehara et al., 2007; Lee et al., 2009; Tang et al., 2010).

Significant up-regulation of *Dusp9,* a gene on the X chromosome which is a critical regulator of the ERK pathway (Li et al., 2012), suggests that *Dusp9* is critical for maintaining the pluripotency under MEK inhibitor-free condition. The average up-regulation of X chromosome-linked genes was greater than that of autosome-linked genes (Fig. 4A, C, D). These data suggest reactivation of the inactive X chromosome of female embryos (Okamoto et al., 2004; Minkovsky et al., 2012); to investigate this possibility, we harvested male and female blastocysts separately using X chromosome-linked GFP mice and analyzed the expression of several genes (Isotani et al., 2005). Up-regulation of X chromosome-linked genes, including *Dusp9, Eras, Nr0b1,* and *Bex1,* was observed in both female and male blastocysts, suggesting that a mechanism distinct from X chromosome reactivation regulates the expression of these genes (Fig. 4E) (Kelly et al., 2010). Among them, up-regulation of *Nr0b1* and *Eras* was not observed when blastocysts were cultured under LowGiL condition. These results suggest that X chromosome activation requires more stringent inhibition of the MEK and GSK3β pathways.

We identified the critical period of ESC derivation and found a requirement for strong differentiation inhibition during this period using two inhibitors. Since the FGF/MEK signaling pathway induces primitive endoderm differentiation in the ICM, inhibition of this pathway during the earliest stage of culture is likely to be critical for the maintenance of

pluripotency in the ICM and subsequent successful ESC establishment. A recent study revealed that GATA6-positive primitive endoderm progenitors from E3.25–3.75 blastocysts were eliminated after 4–8 h of culture in the presence of FGF/MEK inhibitors (Bessonnard et al., 2017). In other words, the progenitor of primitive endoderm appeared a little later than the differentiation of pluripotent epiblasts in an FGF/MEK signaling-dependent manner. Consistent with this finding, RNA sequencing revealed that the ICM at E3.5 showed high-level expression of primitive endoderm markers, including *Gata4, Gata6,* and *Sox17,* and that these markers were significantly down-regulated under 2iL condition (Supplementary Fig. 6, Supplementary Table 5). Taken together, the potential of the ICM to differentiate into primitive endoderm was presumably lost under 2iL condition. *Fgfr2* silencing could be the molecular basis for this phenomenon (Fig. 4B). A loss of differentiation potential in primitive endoderm would render FGF/MEK inhibition unnecessary to sustain pluripotency under LowGiL condition.

4. Conclusion

This study revealed that a MEK inhibitor is not necessary for maintenance, but is critical for establishment, of sustainable pluripotent ESCs. We demonstrated that the initial 3 days of blastocyst culture is a critical period for ESC derivation. Transcriptional activation of a subset of genes, especially X chromosome-linked genes, and suppression of primitive endoderm genes were observed when blastocysts were cultured under 2iL condition during this period. This may be one of the molecular bases for permanent pluripotency acquisition occurring during ESC derivation.

Appendix A. Supplementary data

Supplementary data to this article can be found online at https://doi.org/10.1016/j.scr.2018.07.005.

References

Bessonnard, S., Coqueran, S., Vandormael-Pournin, S., Dufour, A., Artus, J., Cohen-Tannoudji, M., 2017. ICM conversion to epiblast by FGF/ERK inhibition is limited in time and requires transcription and protein degradation. Sci. Rep. 7, 12285.

Boroviak, T., Loos, R., Bertone, P., Smith, A., Nichols, J., 2014. The ability of inner-cell-mass cells to self-renew as embryonic stem cells is acquired following epiblast specification. Nat. Cell Biol. 16 (6), 516–528.

Boroviak, T., Loos, R., Lombard, P., Okahara, J., Behr, R., Sasaki, E., Nichols, J., Smith, A., Bertone, P., 2015. Lineage-specific profiling delineates the emergence and progression of naive pluripotency in mammalian embryogenesis. Dev. Cell 35 (3), 366–382.

Choi, J., Huebner, A.J., Clement, K., Walsh, R.M., Savol, A., Lin, K., Gu, H., Di Stefano, B., Brumbaugh, J., Kim, S.Y., Sharif, J., Rose, C.M., Mohammad, A., Odajima, J., Charron, J., Shioda, T., Gnirke, A., Gygi, S., Koseki, H., Sadreyev, R.I., Xiao, A., Meissner, A., Hochedlinger, K., 2017. Prolonged MEK1/2 suppression impairs the developmental potential of embryonic stem cells. Nature 548, 219–223.

Czechanski, A., Byers, C., Greenstein, I., Schrode, N., Donahue, L.R., Hadjantonakis, A.K., Reinholdt, L.G., 2014. Derivation and characterization of mouse embryonic stem cells from permissive and nonpermissive strains. Nat. Protoc. 9 (3), 559–574.

Dunn, S.J., Martello, G., Yordanov, B., Emmott, S., Smith, A.G., 2014. Defining an

essential transcription factor program for naïve pluripotency. Science 344 (6188), 1156–1160.

Evans, M.J., Kaufman, M.H., 1981. Establishment in culture of pluripotential cells from mouse embryos. Nature 292, 154–156.

George, S.H., Gertsenstein, M., Vintersten, K., Korets-Smith, E., Murphy, J., Stevens, M.E., Haigh, J.J., Nagy, A., 2007. Developmental and adult phenotyping directly from mutant embryonic stem cells. Proc. Natl. Acad. Sci. U. S. A. 104 (11), 4455–4460.

Hanna, J., Markoulaki, S., Mitalipova, M., Cheng, A.W., Cassady, J.P., Staerk, J., Carey, B.W., Lengner, C.J., Foreman, R., Love, J., Gao, Q., Kim, J., Jaenisch, R., 2009. Metastable pluripotent states in NOD-mouse-derived ESCs. Cell Stem Cell 4 (6), 513–524.

Hayashi, K., de Sousa Lopes, S.M.C., Tang, F., Lao, K., Surani, M.A., 2008. Dynamic equilibrium and heterogeneity of mouse pluripotent stem cells with distinct functional and epigenetic states. Cell Stem Cell 3 (4), 391–401.

Heo, J.S., Lee, Y.J., Han, H.J., 2006. EGF stimulates proliferation of mouse embryonic stem cells: involvement of Ca2$^+$ influx and p44/42 MAPKs. Am. J. Cell. Physiol. 290 (1), C123–C133.

Hopper, M., Hardy, K., Handyside, A., Hunter, S., Monk, M., 1987. HPRT-deficient (Lesch-Nyhan) mouse embryos derived from germ line colonization by cultured cells. Nature 326 (6110), 292–295.

Isotani, A., Nakanishi, T., Kobayashi, S., Lee, J., Chuma, S., Nakatsuji, N., Ishino, F., Okabe, M., 2005. Genomic imprinting of XX spermatogonia and XX oocytes recovered from XX↔XY chimeric testes. Proc. Natl. Acad. Sci. U. S. A. 102 (11), 4039–4044.

Kang, M., Garg, V., Hadjantonakis, A.K., 2017. Lineage establishment and progression within the inner cell mass of the mouse blastocyst requires FGFR1 and FGFR2. Dev. Cell. 41 (5), 496–510 (e5).

Kawase, E., Suemori, H., Takahashi, N., Okazaki, K., Hashimoto, K., Nakatsuji, N., 1994. Strain difference in establishment of mouse embryonic stem (ES) cell lines. Int. J. Dev. Biol. 38 (2), 385–390.

Kelly, V.R., Xu, B., Kuick, R., Koenig, R.J., Hammer, G.D., 2010. Dax1 Up-Regulates Oct4 Expression in Mouse Embryonic Stem Cells via LRH-1 and SRA. Mol. Endocrinol. 24 (12), 2281–2291.

Lee, S.H., Kim, M.H., Han, H.J., 2009. Arachidonic acid potentiates hypoxia-induced VEGF expression in mouse embryonic stem cells: involvement of Notch, Wnt, and HIF-1α. Am. J. Phys. Cell Physiol. 297 (1), C207–C216.

Li, Z., Fei, T., Zhang, J., Zhu, G., Wang, L., Lu, D., Chi, X., Teng, Y., Hou, N., Yang, X., Zhang, H., Han, J.D., Chen, Y.G., 2012. BMP4 signaling acts via dual-specificity phosphatase 9 to control ERK activity in mouse embryonic stem cells. Cell Stem Cell 10 (2), 171–182.

Liu, X., Wang, C., Liu, W., Li, J., Li, C., Kou, X., Chen, J., Zhao, Y., Gao, H., Wang, H., Zhang, Y., Gao, Y., Gao, S., 2016. Distinct features of H3K4me3 and H3K27me3 chromatin domains in pre-implantation embryos. Nature 537 (7621), 558–562.

Martin, G.R., 1981. Isolation of a pluripotent cell line from early mouse embryos cultured in medium conditioned by teratocarcinoma stem cells. Proc. Natl. Acad. Sci. U. S. A. 78 (12), 7634–7638.

Minkovsky, A., Patel, S., Plath, K., 2012. Pluripotency and the transcriptional inactivation of the female mammalian X chromosome. Stem Cells 30 (1), 48–54.

Molotkov, A., Mazot, P., Brewer, J.R., Cinalli, R.M., Soriano, P., 2017. Distinct requirements for FGFR1 and FGFR2 in primitive endoderm development and exit from pluripotency. Dev. Cell. 41 (5), 511–526 (e4).

Nichols, J., Smith, A., 2009. Naive and Primed Pluripotent States. Cell Stem Cell 4 (6), 487–492.

Nichols, J., Silva, J., Roode, M., Smith, A., 2009. Suppression of Erk signalling promotes ground state pluripotency in the mouse embryo. Development 136 (19), 3215–3222.

Niwa, H., Oqawa, K., Shimosato, D., Adachi, K., 2009. A parallel circuit of LIF signalling pathways maintains pluripotency of mouse ES cells. Nature 460 (7251), 118–122.

Okamoto, I., Otte, A.P., Allis, C.D., Reinberg, D., Heard, E., 2004. Epigenetic dynamics of imprinted X inactivation during early mouse development. Science 303 (5658), 644–649.

Rideout 3rd, W.M., Wakayama, T., Wutz, A., Eggan, K., Jackson-Grusby, L., Dausman, J., Yanagimachi, R., Jaenisch, R., 2000. Generation of mice from wild-type and targeted ES cells by nuclear cloning. Nat. Genet. 24 (2), 109–110.

Shirane, K., Kurimoto, K., Yabuta, Y., Yamaji, M., Satoh, J., Ito, S., Watanabe, A., Hayashi, K., Saitou, M., Sasaki, H., 2016. Global landscape and regulatory principles of DNA methylation reprogramming for germ cell specification by mouse pluripotent stem cells. Dev. Cell 39 (1), 87–103.

Smith, A.G., 2001. Embryo-derived stem cells: of mice and men. Annu. Rev. Cell Dev. Biol. 17, 435–462.

Smith, A.G., Heath, J.K., Donaldson, D.D., Wong, G.G., Moreau, J., Stahl, M., Rogers, D., 1988. Inhibition of pluripotential embryonic stem cell differentiation by purified polypeptides. Nature 336 (6200), 688–690.

Takahashi, K., Mitsui, K., Yamanaka, S., 2003. Role of ERas in promoting tumour-like properties in mouse embryonic stem cells. Nature 423 (6939), 541–545.

Tang, F., Barbacioru, C., Bao, S., Lee, C., Nordman, E., Wang, X., Lao, K., Surani, M.A., 2010. Tracing the derivation of embryonic stem cells from the inner cell mass by single-cell RNA-seq analysis. Cell Stem Cell 6 (5), 468–478.

Umehara, H., Kimura, T., Ohtsuka, S., Nakamura, T., Kitajima, K., Ikawa, M., Okabe, M., Niwa, H., Nakano, T., 2007. Efficient derivation of embryonic stem cells by inhibition of glycogen synthase kinase-3. Stem Cells 25 (11), 2705–2711.

Williams, R.L., Hilton, D.J., Pease, S., Willson, T.A., Stewart, C.L., Gearing, D.P., Wagner, E.F., Metcalf, D., Nicola, N.A., Gough, N.M., 1988. Myeloid leukaemia inhibitory factor maintains the developmental potential of embryonic stem cells. Nature 336 (6200), 684–687.

Yagi, M., Kishigami, S., Tanaka, A., Semi, K., Mizutani, E., Wakayama, S., Wakayama, T., Yamamoto, T., Yamada, Y., 2017. Derivation of ground-state female ES cells maintaining gamete-derived DNA methylation. Nature 548 (7666), 224–227.

Yamanaka, Y., Lanner, F., Rossant, J., 2010. FGF signal-dependent segregation of primitive endoderm and epiblast in the mouse blastocyst. Development 137 (5), 715–724.

Ying, Q.L., Wray, J., Nichols, J., Batlle-Morera, L., Doble, B., Woodgett, J., Cohen, P., Smith, A., 2008. The ground state of embryonic stem cell self-renewal. Nature 453 (7194), 519–523.

RESEARCH ARTICLE

Reprogramming towards totipotency is greatly facilitated by synergistic effects of small molecules

Kei Miyamoto[1,2,*], Yosuke Tajima[3], Koki Yoshida[3], Mami Oikawa[1,2], Rika Azuma[2,4], George E. Allen[1], Tomomi Tsujikawa[3], Tomomasa Tsukaguchi[2], Charles R. Bradshaw[1], Jerome Jullien[1], Kazuo Yamagata[2], Kazuya Matsumoto[2], Masayuki Anzai[4], Hiroshi Imai[3], John B. Gurdon[1] and Masayasu Yamada[3,*]

ABSTRACT

Animal cloning has been achieved in many species by transplanting differentiated cell nuclei to unfertilized oocytes. However, the low efficiencies of cloning have remained an unresolved issue. Here we find that the combination of two small molecules, trichostatin A (TSA) and vitamin C (VC), under culture condition with bovine serum albumin deionized by ion-exchange resins, dramatically improves the cloning efficiency in mice and 15% of cloned embryos develop to term by means of somatic cell nuclear transfer (SCNT). The improvement was not observed by adding the non-treated, rather than deionized, bovine serum. RNA-seq analyses of SCNT embryos at the two-cell stage revealed that the treatment with TSA and VC resulted in the upregulated expression of previously identified reprogramming-resistant genes. Moreover, the expression of early-embryo-specific retroelements was upregulated by the TSA and VC treatment. The enhanced gene expression was relevant to the VC-mediated reduction of histone H3 lysine 9 methylation in SCNT embryos. Our study thus shows a simply applicable method to greatly improve mouse cloning efficiency, and furthers our understanding of how somatic nuclei acquire totipotency.

KEY WORDS: Nuclear transfer, Reprogramming, Epigenetic modification, Mouse

INTRODUCTION

Nuclear reprogramming of a differentiated into undifferentiated embryonic cell state was originally demonstrated by the transfer of somatic cell nuclei into unfertilized eggs using frogs (Gurdon, 1962). Later, successfully cloned animals were reported in many mammalian species using similar strategies (Wakayama et al., 1998; Wilmut et al., 1997). These reprogramming technologies have been greatly accelerated by the finding of induced pluripotent stem (iPS) cells (Takahashi and Yamanaka, 2006). iPS cells are currently regarded as the most convincing source for regenerative medicine

[1]Wellcome Trust/Cancer Research UK Gurdon Institute, University of Cambridge, Tennis Court Road, Cambridge CB2 1QN, UK. [2]Laboratory of Molecular Developmental Biology, Graduate School of Biology-Oriented Science and Technology, Kindai University, Wakayama 649-6493, Japan. [3]Laboratory of Reproductive Biology, Graduate School of Agriculture, Kyoto University, Kyoto 606-8502, Japan. [4]Institute of Advanced Technology, Kindai University, Wakayama 642-0017, Japan.

*Authors for correspondence (masayasu@kais.kyoto-u.ac.jp; kmiyamo@waka.kindai.ac.jp)

K.M., 0000-0003-2912-6777

This is an Open Access article distributed under the terms of the Creative Commons Attribution License (http://creativecommons.org/licenses/by/3.0), which permits unrestricted use, distribution and reproduction in any medium provided that the original work is properly attributed.

while mounting evidence suggests that somatic cell nuclear transfer (SCNT) into enucleated oocytes can result in embryonic stem cells with high quality from the cloned blastocysts (Kim et al., 2010; Ma et al., 2014; Tachibana et al., 2013). Moreover, nuclear transfer techniques offer unique opportunities to revive animals from frozen tissues, potentially including extinct animals (Folch et al., 2009; Wakayama et al., 2008), to produce transgenic animals from somatic cells and to propagate animals with beneficial traits. However, many of these promising attempts have been impeded by the low success rates of SCNT.

Tremendous efforts have been made to improve cloning efficiency. Since failures of epigenetic reprogramming have been often reported in cloned embryos during preimplantation development (Teperek and Miyamoto, 2013), small molecules to alter histone modifications are widely used to facilitate development of SCNT embryos (Ogura et al., 2013). The addition of trichostatin A (TSA), a histone deacetylase inhibitor, to culture medium of SCNT embryos for appropriate duration improves mouse cloning from less than 1% to 6.5% (Kishigami et al., 2006; Rybouchkin et al., 2006). TSA treatment increases levels of histone acetylation and reduces those of repressive histone methylation (Bui et al., 2010), which presumably results in correcting the aberrant expression of transcription factor genes in cloned two-cell embryos (Inoue et al., 2015). Recently, substantial improvements in mouse cloning have been shown by enzymatically removing repressive histone H3 lysine 9 trimethylation (H3K9me3) and up to 11% of SCNT embryos develop to term (Liu et al., 2016; Matoba et al., 2014). This is also true in the case of human somatic cell nuclear transfer (Chung et al., 2015). It is therefore desirable to develop a simple method to lower the level of H3K9me3 in SCNT embryos, for example by supplementation of small molecules to culture medium (Huang et al., 2016) in order to achieve dramatic improvement in animal cloning.

The effect of vitamin C (VC) on the reduction of histone H3K9 methylation and DNA methylation has been well documented in embryonic stem (ES) and iPS cells (Blaschke et al., 2013; Chen et al., 2013; Hore et al., 2016; Walter et al., 2016). VC mediates reduction of Fe^{3+} to Fe^{2+} (Hore et al., 2016), accelerating DNA and histone demethylation through the enhanced activity of Fe^{2+}- and oxoglutarate-dependent enzymes (Monfort and Wutz, 2013). This role of VC as a potent epigenetic modifier, in addition to the well-characterized antioxidant role, allows enhanced reprogramming in iPS cells (Chen et al., 2013; Esteban et al., 2010; Stadtfeld et al., 2012; Wang et al., 2011). Reprogramming after SCNT is also aided by VC supplementation to embryo culture medium in mice (Mallol et al., 2015) and pig (Huang et al., 2011), although improvements in birth rates of cloned mice are modest compared to mRNA injection of histone modifiers (up to 5% versus 11%, respectively). The extent of epigenetic reprogramming and changes in gene expression need

Biology Open

to be determined in VC-treated SCNT embryos. Another important aspect that has not been well explored is whether VC further enhances its effect on reprogramming in collaboration with other factors.

In this report, we examined synergistic effects of TSA and VC, two well-known epigenetic modifiers that can enhance reprogramming. We find that TSA and VC facilitate reprogramming at different times during the one-cell stage and, moreover, synergistically work for the development of SCNT embryos. Interestingly, the effect of TSA and VC is best exerted in our embryo culture condition containing deionized bovine serum albumin (dBSA) (Isaji et al., 2015), resulting in 15% of cloning efficiency. Mechanistically, expression of transcripts that are normally downregulated in cloned embryos is rescued by the sequential treatment of TSA and VC with dBSA. Our improved culture condition allows stable production of cloned mice, thus enabling the SCNT technology to be used for a variety of purposes.

RESULTS
The sequential treatment of trichostatin A and vitamin C boosts cloning efficiency in mice

TSA has been shown to enhance the development of SCNT embryos when it is added to the medium for 10 h or less after egg activation, whereas longer exposure to TSA diminished enhanced embryonic development (Kishigami et al., 2006). We therefore hypothesized that treatment with VC also has a time window when its positive effects are maximized. As a first step, we tested the effect of different concentrations of VC on preimplantation development of mouse SCNT embryos using cumulus cells as donors. VC was supplemented in the embryo culture medium for 24 h after egg activation. Development to the blastocyst stage was significantly improved when 10 µg/ml or more of VC was supplemented (Fig. 1A). We then examined the number of cells at the blastocyst stage. Among the three different concentrations that enhanced development (10, 25 and 50 µg/ml; Fig. 1A), blastocysts treated with 10 µg/ml of VC exhibited a significantly higher number of inner cell mass and trophectoderm cells than control blastocysts (Fig. 1B; $P<0.05$). These results indicate that 10 µg/ml of VC enhances preimplantation development of mouse SCNT embryos. We next examined an appropriate timing of VC treatment for SCNT embryos. It has been reported that 15 h incubation with VC is enough to enhance the development of cloned embryos in pigs (Huang et al., 2011). We further split 15 h of treatment to 8 and 7 h [VC(0-8 h) and VC(8-15 h), respectively]. Interestingly, VC(0-8 h) did not enhance development to the blastocyst stage significantly, while the preimplantation development was improved by VC(8-15 h) (Fig. 1C). As previously reported, significant improvement of embryonic development by TSA was observed when it was added 0-8 h after premature chromosome condensation (Fig. 1C). Together, VC enhances preimplantation development of mouse SCNT embryos and its positive effect is observed when VC is added 8-15 h after egg activation, which represents a different timing from that of TSA treatment.

The optimization experiments of VC treatment for the development of SCNT embryos show that VC works at a different timing to TSA. We therefore hypothesized that the combinational treatment with TSA and VC might further enhance development of SCNT embryos. The sequential treatment with TSA and VC supported highly efficient *in vitro* development to the blastocyst stage [TSA(0-8 h)+VC(8-15 h); Fig. 1C]. Enhanced development was also observed using embryonic fibroblast cells derived from ICR×ICR mice (27% versus 71%; Fig. 1D), demonstrating that the positive effect of TSA and VC is neither limited by mouse strains

nor by cell types. We then evaluated *in vivo* development of SCNT embryos with various controls using cumulus cells as donors (Table 1). VC treatment itself improved the implantation rate when SCNT embryos at the two-cell stage were transferred to surrogates (Table 1). An even higher implantation rate was obtained when TSA was supplemented before VC treatment [TSA(0-8 h)+VC(8-15 h); Table 1]. Importantly, birth rates were dramatically improved by TSA(0-8 h)+VC(8-15 h) treatment compared to all other treatments, including only TSA or VC treatment, and 15% of the transferred cloned embryos developed to live pups (Fig. 1E and Table 1). High birth rates of cloned pups were reproduced by three different operators in two different institutes (Fig. S1A,B). Cloned fetuses obtained by TSA(0-8 h)+VC(8-15 h) treatment showed similar body and placental weight to other treatments (Table 1). These results indicate that TSA and VC synergistically work to markedly improve the cloning efficiency in mice.

The effects of antioxidants and deionized BSA on development of SCNT embryos

VC is known as an effective antioxidation reagent. We therefore asked if other antioxidants similarly enhance the development of mouse SCNT embryos. N-acetyl-L-cysteine (NAC) (Esteban et al., 2010) or vitamin E (Esteban et al., 2010) was added to the culture medium 8-15 h after the commencement of activation, which is the same timing as when VC's positive effect is observed. Although the VC treatment enhanced the development of SCNT embryos, neither NAC nor vitamin E improved the preimplantation development of mouse SCNT embryos (Fig. S2A). These results suggest that VC is not simply replaced by other antioxidants to enhance cloning efficiency. The improved development by VC treatment might not be through its antioxidant effects, although we cannot exclude some contribution of antioxidation to development.

Our culture medium contains deionized bovine serum albumin (dBSA), since commercially available BSA often involves trace amounts of transition metal ions, such as Zn^{2+} and Cu^{2+}, harmful for preimplantation development (Vidal and Hidalgo, 1993). It is also known that VC is reactive to metal ions (Carr and Frei, 1999). We therefore tested if dBSA is crucial for the high developmental potential of TSA- and VC-treated embryos. Development to the blastocyst stage was impaired when BSA was supplemented in the medium and donor cell suspension instead of dBSA (Fig. S2B,C), suggesting that dBSA is also a critical factor for the improved cloning efficiency.

Rescued gene expression in TSA- and VC-treated cloned embryos at the two-cell stage

In order to understand the molecular basis of improved development of TSA- and VC-treated cloned embryos, we performed RNA-seq analyses. SCNT embryos at the two-cell stage (28 h after egg activation), which is right after zygotic genome activation, were used so that an immediate response of TSA(0-8 h)+VC(8-15 h) treatment to gene activation can be judged, and because a previous study identified abnormally expressed genes in SCNT embryos at the same stage (Matoba et al., 2014). Single SCNT embryos incubated in various conditions were subjected to RNA-seq (Fig. 2A). Hierarchical clustering indicated that the transcriptomes of SCNT embryos with TSA(0-8 h)+VC(8-15 h) treatment resembled each other even though nuclear transfer was performed in three independent experiments (Fig. 2B). Interestingly, the treatment with TSA(0-8 h) also resulted in a reproducible transcriptome, but it represented a significantly different pattern from TSA(0-8 h)+VC(8-15 h) (blue box versus red box; Fig. 2B).
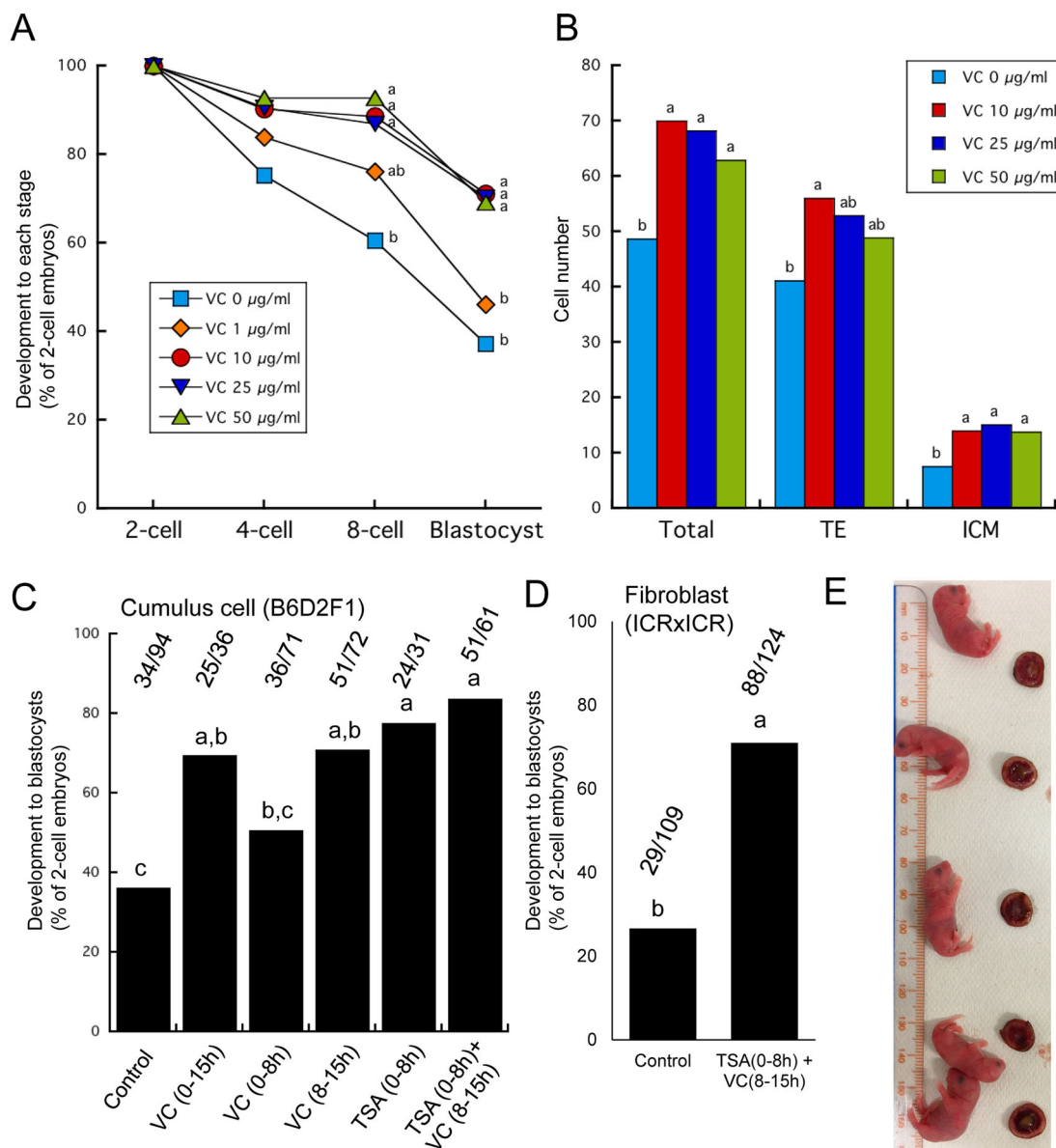
Fig. 1. The effect of epigenetic modifiers, trichostatin A (TSA) and vitamin C (VC), on the development of mouse SCNT embryos. (A) The effect of different concentrations of VC on preimplantation development of the cloned embryos. VC at concentrations of 10 μg/ml and more enhanced development to the blastocyst stage. Different letters within the same stage indicate statistical significance ($P<0.05$, one-way ANOVA with subsequent Tukey's multiple comparison tests). Between 31 and 139 two-cell embryos were used in each treatment (each treatment: n=3-5, control VC 0 μg/ml: n=15). (B) Cell numbers of cloned blastocysts after the treatment with VC at concentrations of 10 μg/ml and more. Different letters within the same part indicate statistical significance ($P<0.05$). Between 12 and 31 blastocysts were examined (n=3-7). (C) Comparison of development to the blastocyst stage of the cloned embryos among VC treatment of different durations, TSA treatment and serial treatment with TSA and VC. Cumulus cells derived from B6D2F1 mouse were used as donor cells. Actual numbers of embryos developed to blastocysts per two-cell embryos are indicated above the corresponding graphs. Different letters indicate statistical significance ($P<0.05$; each treatment: n=3-6, control: n=12). (D) Comparison of development to the blastocyst stage of the cloned embryos using embryonic fibroblasts derived from ICR×ICR mice as donor cells between control non-treated embryos and serially treated embryos with TSA and VC. Actual numbers of embryos developed to blastocysts per two-cell embryos are indicated above the corresponding graphs. Different letters indicate statistical significance ($P<0.05$; n=4,6). (E) Five cloned fetuses and placentae in one foster mother, which were produced by the serial treatment of TSA and VC.

Heat map analysis showed reproducibly upregulated gene expression in SCNT embryos with TSA(0-8 h)+VC(8-15 h) (red box; Fig. S3A), compared to other treatments. Indeed, TSA(0-8 h)+VC(8-15 h)-treated SCNT embryos showed approximately two times more upregulated transcripts than downregulated transcripts when compared to control SCNT embryos (141 upregulated versus 63 downregulated transcripts, FDR<0.05; Fig. S3B and Table S1). GO analysis indicated that different categories of genes were found between up- and down-regulated transcripts (Fig. S3C).

Upregulated transcripts included genes involved in transcriptional regulation and RNA processing (Fig. S3C), representing a similar category to transcripts previously identified as abnormally downregulated in cloned two-cell embryos (Matoba et al., 2014). We then asked if the transcripts upregulated in TSA(0-8 h)+VC(8-15 h) treatment contained the abnormally repressed genes in SCNT embryos (Matoba et al., 2014). Hypergeometric tests indicated that the abnormally downregulated genes were significantly enriched in our upregulated gene list by TSA(0-8 h)+VC(8-15 h) (top venn

Biology Open

Table 1. The effect of trichostatin A (TSA) and/or vitamin C (VC) on full-term development of cloned embryos

Treatments	No. of embryos transferred	% live offspring*	% IP sites**	Average body weight (g) (mean±s.d.)	Average placental weight (g) (mean±s.d.)
NC	178	0 (0)[b]	3 (1.7)[c]	NA	NA
TSA (0-8 h)	124	5 (4.0)[b]	76 (61.3)[a,b]	1.51±0.30	0.25±0.05
VC (8-15 h)	125	0 (0)[b]	56 (44.8)[b]	NA	NA
VC (0-24 h)	84	2 (2.4)[b]	38 (45.2)[b]	1.58±0.18	0.32±0.04
TSA (0-8 h)+VC (8-15 h)	105	16 (15.2)[a]	81 (77.1)[a]	1.43±0.19	0.28±0.07

NC, non-treated control; IP, implantation; NA, not applicable; s.d., standard deviation.
*The proportion of transferred embryos that resulted in live offspring.
**The proportion of transferred embryos that resulted in implantation sites.
[a,b,c]Values with different superscripts within the same column are significantly different as judged by Fisher's exact test ($P<0.05$) (n=4-8).

diagram, $P=9.3×10^{-13}$; Fig. 2C), indicating that TSA+VC treatment at least partially rescues abnormal gene expression in SCNT embryos. Hypergeometric tests were also carried out against histone H3 lysine 9 trimethylation (H3K9me3)-enriched reprogramming-resistant genes identified in the mouse SCNT experiment (Matoba et al., 2014) and human iPS cells (Soufi et al., 2012). Reprogramming-resistant regions found in Matoba et al. (2014) contained 1767 genes, and 26 genes overlapped between those H3K9me3-enriched genes in SCNT embryos and the genes upregulated by TSA+VC ($P=1.1×10^{-6}$; Fig. 2C; Table S2). In contrast, H3K9me3-enriched reprogramming-resistant genes identified in the iPS experiment did not show significant overlap with our gene list ($P=0.44$; Fig. 2C). In conclusion, abnormal gene expression of protein-coding genes, which is often observed in SCNT embryos, is alleviated by serial treatment with TSA and VC after nuclear transfer.

TSA and VC differentially, but cooperatively, contribute to transcriptional activation in SCNT embryos at the two-cell stage

In order to gain insight into the synergistic effects of TSA(0-8 h)+VC(8-15 h), we sought to identify specific effects of TSA(0-8 h)+VC(8-15 h) on gene expression in SCNT embryos at the two-cell stage by comparing to other treatments such as TSA(0-8 h). In contrast to TSA(0-8 h)+VC(8-15 h)-treated SCNT embryos as described above (Table S1), TSA(0-8 h)-treated embryos showed approximately two times more downregulated transcripts than upregulated transcripts when compared to control SCNT embryos (43 upregulated versus 97 downregulated transcripts, FDR<0.05; Table S3); the detection of more downregulated transcripts is in good agreement with the previous study that also identified approximately two times more downregulated transcripts after the TSA treatment (Inoue et al., 2015). Nevertheless, among 43 upregulated transcripts, 13 transcripts were also found in the upregulated gene list in TSA(0-8 h)+VC(8-15 h)-treated embryos (Table S1), suggesting that at least some, but not all, transcripts upregulated by TSA(0-8 h)+VC(8-15 h) are due to the TSA treatment. We then examined the effect of the VC treatment by comparing TSA(0-8 h)-treated embryos to TSA(0-8 h)+VC(8-15 h)-treated ones. TSA(0-8 h)+VC(8-15 h)-treated embryos showed 3.7 times more upregulated transcripts than downregulated transcripts when compared to TSA(0-8 h)-treated embryos (153 upregulated versus 41 downregulated transcripts, FDR<0.05; Table S4). GO analysis showed that genes related to apoptosis were downregulated in TSA(0-8 h)+VC(8-15 h)-treated embryos. Genes related to apoptosis are known to be upregulated in SCNT embryos compared to fertilized embryos (Matoba et al., 2014), and the TSA(0-8 h)+VC(8-15 h) treatment, but not the TSA(0-8 h) treatment, downregulates such detrimental genes for

embryonic development in SCNT embryos. In addition, 35 transcripts out of 153 upregulated transcripts (red highlighted in Table S4) are included in the 141 upregulated transcripts (Table S1), which were identified as differentially expressed genes between TSA(0-8 h)+VC(8-15 h) and control SCNT embryos. Furthermore, 13% of downregulated genes by the TSA (0-8 h) treatment (blue highlighted in Table S3; 13 out of 97 downregulated genes) were upregulated by the TSA(0-8 h)+VC(8-15 h). Taken together, the treatment with VC generally upregulates gene expression, including transcripts that are downregulated by the TSA treatment.

Upregulated expression of the early-embryo-specific retroelement in SCNT embryos treated with TSA and VC

We next asked if treatment with TSA(0-8 h)+VC(8-15 h) affects the expression of retroelements, some of which are highly expressed in mouse embryos at the two-cell stage, including ERVL (Ishiuchi et al., 2015; Macfarlan et al., 2012). ERVL is suppressed in SCNT embryos, compared to IVF embryos (Matoba et al., 2014). Interestingly, the expression of ERVL was upregulated in the SCNT embryos treated with TSA(0-8 h)+VC(8-15 h), compared to the non-treated control SCNT embryos (Fig. 2D). Transcripts from LINE sequences were also upregulated and expression of other retroelements was not greatly affected (Fig. S4). These results suggest that the suppressed expression of the retroelement ERVL in the SCNT embryos is rescued by the TSA(0-8 h)+VC(8-15 h) treatment.

Reduced histone H3K9 methylation is associated with a high developmental potential of TSA- and VC-treated SCNT embryos

We have shown that TSA(0-8 h)+VC(8-15 h) treatment enhances transcription from H3K9me3-enriched reprogramming-resistant genes (Fig. 2C). Moreover, VC has been shown to accelerate epigenetic reprogramming including demethylation of DNA (Zhang et al., 2016) and histone H3K9 (Chen et al., 2013). We therefore examined changes in epigenetic modifications in TSA(0-8 h)+VC (8-15 h)-treated SCNT embryos. The upregulated expression of *Kdm3b*, a H3K9 demethylase, was observed in SCNT embryos after TSA(0-8 h)+VC(8-15 h) treatment (Fig. S5). A reduction in H3K9me3 was also observed at the two-cell stage after TSA(0-8 h)+VC(8-15 h) treatment (Fig. 3A). In addition, 5-hydroxymethylation (5hmC) was increased by TSA(0-8 h)+VC(8-15 h) treatment in SCNT embryos (Fig. S6) suggesting enhanced TET activities and DNA demethylation in SCNT embryos. Together, TSA(0-8 h)+VC (8-15 h) treatment decreases the abnormally high levels of H3K9me3 and DNA methylation in SCNT embryos, which may result in successful activation of reprogramming-resistant genes and the retrotransposons (Fig. 3B).
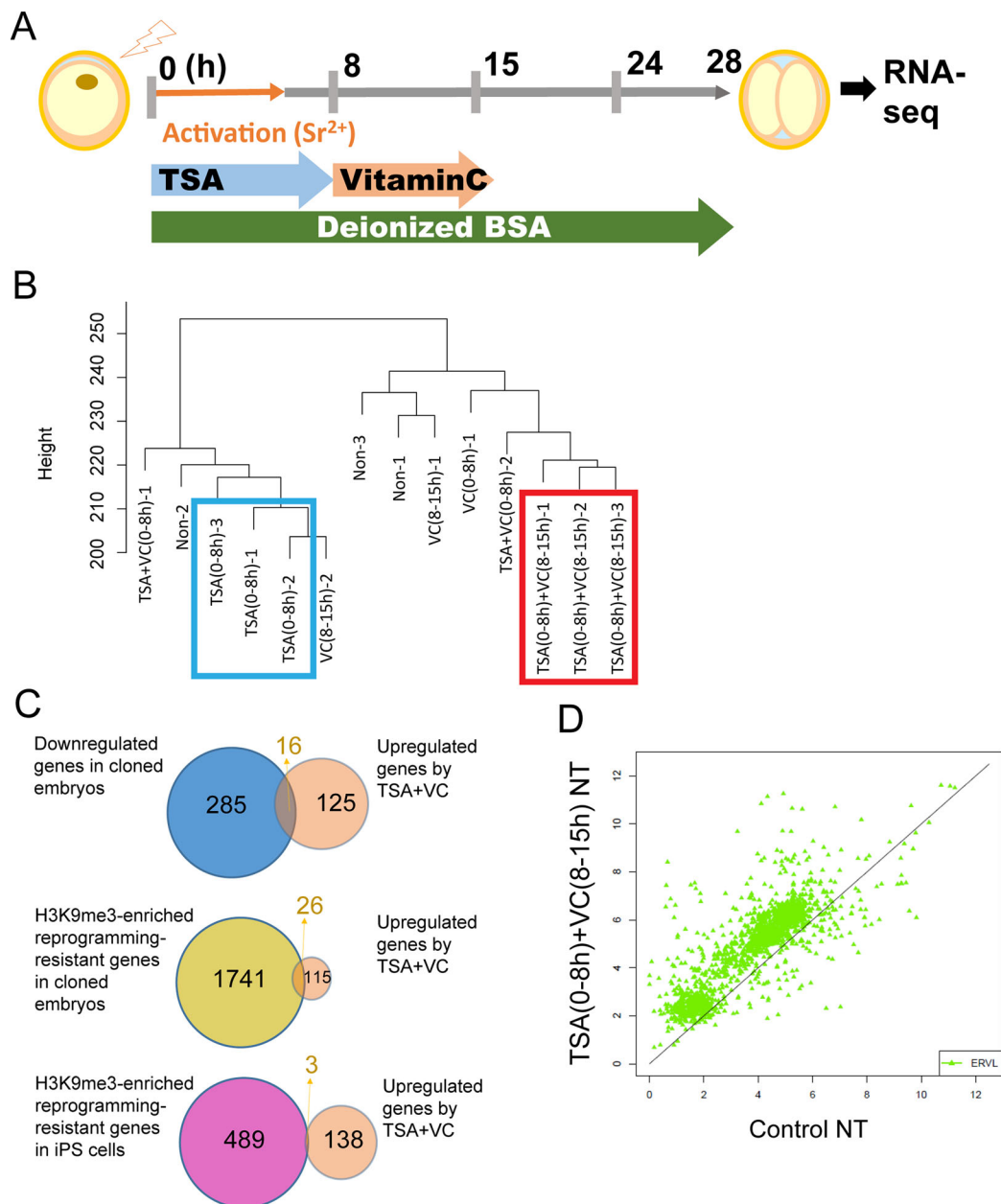
Biology Open

Fig. 2. RNA-seq analyses identify the reproducibly upregulated transcripts and retroelement in SCNT embryos incubated with TSA and VC in the medium containing deionized BSA. (A) An experimental scheme for nuclear transfer with TSA and VC treatment, and subsequent RNA-seq analysis. (B) Hierarchical clustering analysis of the global gene expression profile after SCNT with various different treatments with TSA and/or VC. SCNT embryos incubated with TSA(0-8 h)+VC(8-15 h) are marked by the red square while those with TSA (0-8 h) are with the blue square. (C) Hypergeometric tests were performed among the lists of genes that were upregulated by TSA+VC, downregulated in cloned embryos (Matoba et al., 2014) and identified as reprogramming resistance in cloned embryos (Matoba et al., 2014) and in iPS cells (Soufi et al., 2012). (D) ERVL retroelement was upregulated by the treatment with TSA(0-8 h)+VC(8-15 h) when compared to the control non-treated SCNT embryos.

DISCUSSION

Somatic cell nuclear transfer offers us a unique opportunity to experimentally render differentiated cells totipotent, enabling production of cloned animals from adult somatic cells. However, the adult somatic cells are resistant to this reprogramming and often retain somatic chromatin states even in reconstructed cloned embryos. As a result, SCNT embryos frequently exhibit aberrant histone modifications and gene expression, compared to normally fertilized counterparts. Landmark studies have discovered repeatedly observed abnormalities in SCNT embryos, including ectopic expression of noncoding RNA *Xist* (Inoue et al., 2010),

repression of genes in large organized chromatin K9 modifications (LOCKs) (Fukuda et al., 2010; Inoue et al., 2010), defects in trophoblast cell lineage (Lin et al., 2011) and downregulated expression of genes enriched with H3K9me3 (Matoba et al., 2014). Previous studies have shown that correction of these representative defects greatly improves birth rates of SCNT embryos up to around 15% (Inoue et al., 2010; Lin et al., 2011; Liu et al., 2016; Matoba et al., 2014). The method we presented here also supports a similarly high birth rate of SCNT embryos (15.2%, Table 1). We achieved one of the most efficient mouse clones just by optimizing the culture condition without genetic manipulation, mRNA injection or help
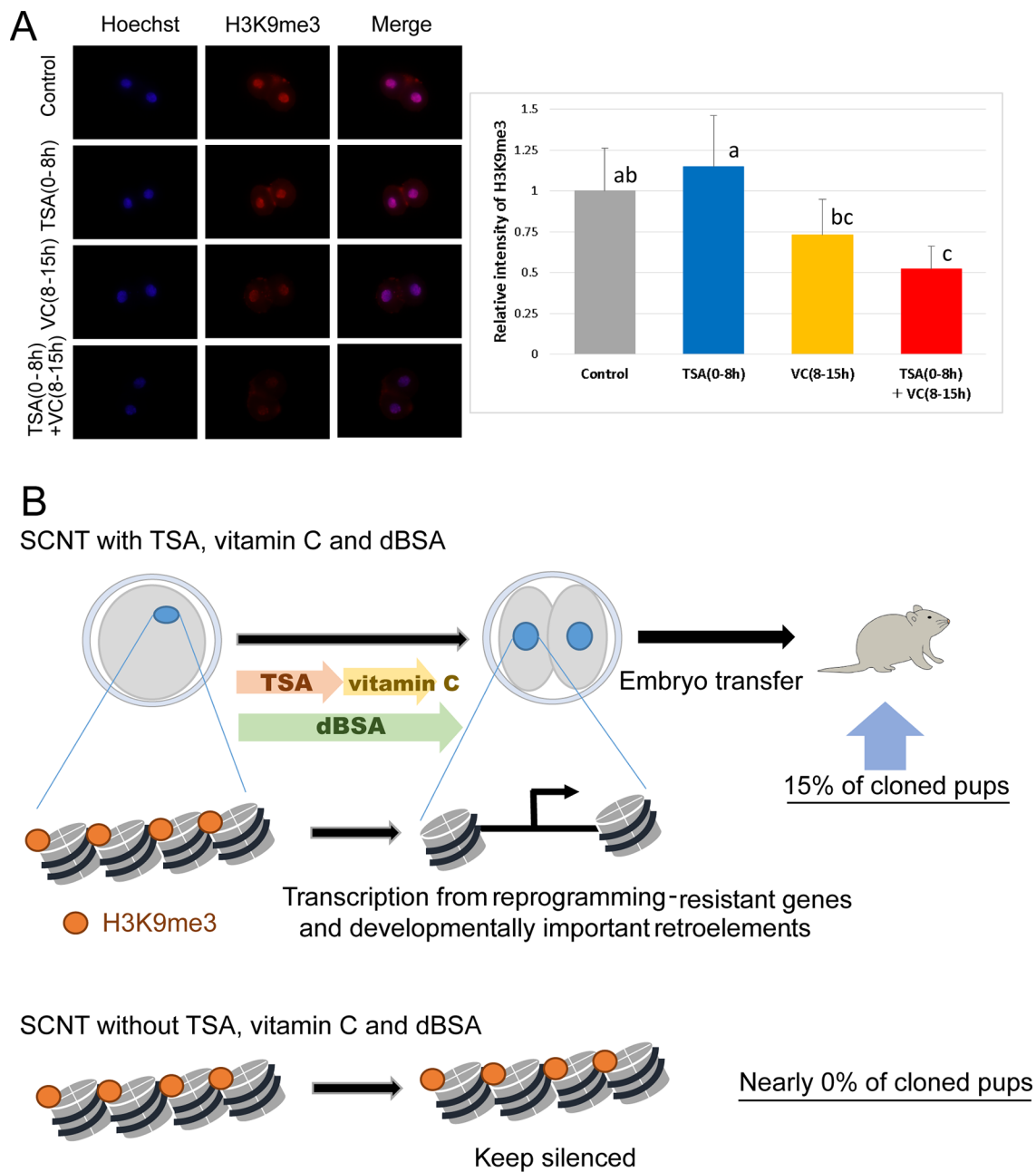
Biology Open

419

Fig. 3. Reduced histone H3K9 trimethylation in SCNT embryos treated with TSA and VC. (A) Immunostaining analysis indicated that SCNT embryos with TSA+VC showed a significantly lower level of H3K9me3 compared to control embryos. Different letters indicate statistical significance ($P<0.05$, one-way ANOVA with subsequent Tukey's multiple comparison tests). Fourteen or fifteen two-cell embryos were examined. Error bars represent means±s.e. ($n=3$). (B) A model shows how the treatment with trichostatin A and vitamin C in the dBSA-containing medium enhances epigenetic reprogramming and results in the enhanced cloning success rate.

of tetraploid complementation. Thus, our simple method will be readily applicable to many laboratories and may be useful for cloning in other species, in which genetic manipulation, RNA injection and tetraploid complementation are not available.

Synergistic effects of histone deacetylase inhibitors with other factors to improve cloning efficiency have been explored because histone deacetylase inhibitors, including TSA, reliably enhance development of cloned embryos (Ogura et al., 2013). Despite numerous attempts, striking additive effects have not been observed (Inoue et al., 2010; Mallol et al., 2015; Matoba et al., 2014), apart from one of the highest mouse cloning rates to term achieved by the TSA treatment and siRNA injection against *Xist* (Matoba et al.,

2011). We here show that sequential treatment of TSA and VC is key to maximizing their influences on reprogramming (Figs 1C and 2B, Table 1). TSA treatment, which begins right after nuclear transfer, increases histone acetylation in pronuclei and accelerates chromatin decondensation and proper organization of constitutive heterochromatin (Bui et al., 2010; Maalouf et al., 2009), suggesting that TSA contributes to initial remodeling of injected somatic nuclei presumably by relaxing chromatin. VC starts to enhance reprogramming 8 h after the commencement of activation, which represents approximately the same timing as the initiation of DNA replication and appearance of DNA repair markers, related to DNA demethylation (Wossidlo et al., 2010). In addition, this timing

458

coincides with Tet3-mediated accumulation of 5hmC (Amouroux et al., 2016). Furthermore, demethylation of H3K9me2 can be induced until 10 h after activation (Wang et al., 2007). These results suggest that dynamic epigenetic reprogramming was induced in SCNT embryos when VC was added in our experiments. It is also noteworthy that the retroelement ERVL is transcribed as early as 8 h after oocyte activation (Kigami et al., 2003). Therefore, the proper erasure of somatic epigenetic memories and establishment of embryonic epigenetic signatures at this stage might be crucial for subsequent gene activation and hence embryonic development. In fact, our RNA-seq analyses revealed that both TSA and VC contribute to rescued gene expression in SCNT embryos at the two-cell stage, although the mechanism of action seems different between those two molecules. TSA induces not only activation of a set of genes but also downregulation of gene expression, while VC generally supports transcriptional activation including those downregulated by the TSA treatment.

The effect of TSA and VC was well-exerted when dBSA was added to mouse embryo culture medium instead of BSA. dBSA has been used as a component of culture media for human bone marrow cells (Leary et al., 1990) and for differentiating human ES cells (Ng et al., 2008). Injection of dBSA into oocyte cytoplasm enhances development of SCNT embryos while addition of dBSA to culture medium does not support better development than control (Isaji et al., 2015). This is in good agreement with our results that only dBSA did not support efficient development (non-treated control in Table 1). Nevertheless, the obvious requirement of dBSA for efficient development was seen when dBSA was used in combination with TSA and VC (Fig. S2), indicating synergistic effects of TSA, VC and dBSA. One possible explanation for this additive effect is that deionization of BSA removes metal ions that are reactive to VC from culture medium, thus increasing the ratio of free VC that can work with intracellular iron ion to increase the activities of Fe^{2+}- and oxoglutarate-dependent enzymes to accelerate demethylation. Further investigation of dBSA may offer opportunities to reveal new mechanistic insight into reprogramming.

A key for efficient reprogramming is to break epigenetic barriers that stabilize somatic cell states. H3K9me3 has been convincingly shown as one of such barriers in SCNT embryos (Liu et al., 2016; Matoba et al., 2014) and in iPS cells (Chen et al., 2013; Soufi et al., 2012; Sridharan et al., 2013). Our study shows that the H3K9me3 barrier can be at least partially removed just by adding TSA and VC to the dBSA-containing medium at the appropriate timing (Figs 2C and 3B). H3K9 demethylation by VC is mediated through the elevated KDM3/4's activity in iPS cells, including KDM3B (Chen et al., 2013). Previous studies showed that the overexpression of Kdm4b, Kdm4d and Kdm5b enhances the development of mouse SCNT embryos (Liu et al., 2016; Matoba et al., 2014), while our TSA(0-8 h)+VC(8-15 h) treatment upregulates Kdm3b expression (Fig. S5). These results suggest that the improved development by the TSA(0-8 h)+VC(8-15 h) treatment might be mediated by a different mechanism from the previously observed effects of histone demethylase overexpression in SCNT embryos. One functional difference between Kdm3b and Kdm4b/4d/5b that has been shown to enhance mouse cloning is that Kdm3b demethylates H3K9me1/2 (Nottke et al., 2009), in good agreement with our observation that the H3K9me2-regualted retrotransposon MuERVL (Maksakova et al., 2013) is upregulated in SCNT embryos (Fig. 2D). Therefore, the improved development by the TSA(0-8 h)+VC(8-15 h) treatment might be not only through reducing H3K9me3, but also by downregulating H3K9me1/2. Moreover, hydroxymethylation

was increased by TSA(0-8 h)+VC(8-15 h) treatment in SCNT embryos (Fig. S6), suggesting enhanced TET activities and DNA demethylation in SCNT embryos. Importantly, incomplete erasure of the somatic type of DNA methylation is also regarded as a major obstacle for successful reprogramming (Mikkelsen et al., 2008). These results demonstrate that TSA+VC treatment in SCNT embryos can overcome epigenetic barriers, resulting in the dramatic improvement of mouse cloning. Although TSA+VC treatment clearly affects epigenetic changes as mentioned above, several lines of evidence demonstrate that the development of SCNT embryos is also influenced by non-epigenetic factors (Miyamoto et al., 2011; Mizutani et al., 2012). For example, abnormal chromosome segregation is a major cause of developmental arrest of cloned embryos (Mizutani et al., 2012), which may in turn result in abnormal gene expression. Inhibition of class IIb HDACs, whose targets include not only histones but also chaperones and tubulin, plays a key role for improved development of cloned embryos (Ono et al., 2010). Furthermore, two-digit cloning rates can be achieved by using latrunculin A, an actin polymerization inhibitor, instead of cytochalasin B (Terashita et al., 2012). It is therefore plausible that the observed positive effects of TSA+VC treatment in the dBSA-containing medium might be accomplished by the combination of epigenetic and non-epigenetic factors, which warrants further investigation into the contribution of non-epigenetic factors. In conclusion, our refined protocol for mouse somatic cell nuclear transfer will ensure the efficient production of cloned mice and will make the SCNT technique widely available for a variety of applications, including preservation of genetic materials and regenerative medicine.

MATERIALS AND METHODS
Animals
B6D2F1 (C57BL/6J×DBA/2N) and ICR mice were obtained from Japan SLC (Hamamatsu, Japan) or CLEA Japan (Tokyo, Japan). This study conformed to the Guide for the Care and Use of Laboratory Animals. All animal experiments were approved and performed under the guidelines of the Animal Research Committee, Kyoto University and Kindai University, Japan.

Collection of oocytes and cumulus cells
Female B6D2F1 mice, aged 8-10 weeks, were superovulated by intraperitoneal injections of 7.5 IU of pregnant mare serum gonadotropin (PMSG; ASKA Animal Health, Tokyo, Japan) followed 48 h later by 7.5 IU of human chorionic gonadotropin (hCG; ASKA Pharmaceutical, Tokyo, Japan). Cumulus–enclosed oocytes at the second meiotic metaphase (MII) stage were collected from the oviducts 15 h after the hCG injection in Hepes-buffered CZB medium (HCZB) (Chatot et al., 1989) and treated with 0.1% hyaluronidase in HCZB at 37°C until dispersion of cumulus cells. Cumulus-free oocytes were then washed and kept in drops of 0.3% dBSA (see below) containing KSOM medium without EDTA (mKSOM), covered with mineral oil, at 37°C in air containing 5% CO_2 until use. Dispersed cumulus cells were removed from the hyaluronidase and placed in 6% dBSA containing HCZB until being used as donor cells for SCNT. For experiments shown in Fig. 1D, mouse embryonic fibroblast cells were derived from day 11.5 mouse embryos (ICR×ICR).

Preparation of deionized bovine serum albumin
Stock solution of dBSA was prepared as described previously (Isaji et al., 2015; Ng et al., 2008). Briefly, BSA (Sigma-Aldrich, cat. code: A3311) was dissolved in distilled water at a concentration of 12%. Approximately 360 mg of mixed ion-exchange resin beads [AG501-X8(D); Bio-Rad] was then added to 10 ml of 12% BSA solution, and the mixture was incubated at room temperature with occasional stirring. When the beads changed color from blue-green to gold, fresh beads were replaced in the BSA solution for a total of three replacements. The supernatant was sterilized with filtration

(0.45 µm, Millipore) and stored at −20°C as 12% stock solution. In mKSOM medium for culturing SCNT embryos, 0.3% BSA was supplemented. For Fig. S2B, BSA purchased from Calbiochem (San Diego, CA, USA, cat. code: 126609) was used to compare with the above mentioned dBSA.

Somatic cell nuclear transfer

SCNT was carried out as described previously (Isaji et al., 2015). Briefly, enucleation of denuded MII oocytes was performed in drops of HCZB containing 5 µg/ml cytochalasin B (Sigma-Aldrich). After enucleation, a donor cell in HCZB with 6% dBSA was placed in the perivitelline space of an enucleated oocyte together with HVJ-E (GenomeONE-CF, Ishihara Sangyo, Osaka, Japan) by tightly attaching the donor cell to the enucleated oocyte, the oocyte was then cultured in mKSOM for 1 h at 37°C in air containing 5% CO_2, during which time it fused with the donor cell. The reconstructed oocytes were activated by the incubation for 6 h in 5 mM $SrCl_2$ and 2 mM EGTA-containing mKSOM supplemented with 5 µg/ml cytochalasin B, referred to as activation medium (Isaji et al., 2015; Kishigami and Wakayama, 2007), at 37°C in air containing 5% CO_2.

Epigenetic modifier and antioxidant treatments of cloned embryos

For epigenetic modifier treatments, trichostatin A (TSA, Sigma-Aldrich, cat. code: T8552) was dissolved in DMSO to prepare 10 µM stock solution and stored at −20°C. Vitamin C (VC, Sigma-Aldrich, cat. code: A5960) was dissolved in distilled water to prepare 1 mg/ml stock solution, filtered, and stored at −20°C. The final concentrations of both epigenetic modifiers were prepared by diluting the stock solution in activation or mKSOM culture media, depending on the experimental procedure (Figs 1 and 2A). The reconstructed oocytes were treated with 50 nM TSA for 8 h from the commencement of activation (COA), with VC at various concentrations (1, 10, 25 and 50 µg/ml) for 24 h after COA, with 10 µg/ml VC for 8 or 15 h after COA, or with 10 µg/ml VC during the period of 8 to 15 h after COA. The best developmental outcome was obtained by incubating the reconstructed oocytes with 50 nM TSA for 8 h after COA followed by treatment of 10 µg/ml VC for 7 h. For antioxidant treatments, N-acetyl-L-cysteine (NAC, Sigma-Aldrich, cat. code: A7250) and vitamin E (VE, Sigma-Aldrich, cat. code: T3634) were used. The reconstructed oocytes were treated with 1 mM NAC or 100 µM VE 8-15 h after COA. The activated oocytes were cultured at 37°C in air containing 5% CO_2 in mKSOM before or after treatments with epigenetic modifiers or antioxidants until reaching the two-cell or blastocyst stages.

Immunofluorescence staining

Cloned embryos at different developmental stages were fixed in 3.7% paraformaldehyde in PBS at 4°C overnight. After permeabilization with 0.5% Triton X-100 in PBS for 40 min at room temperature, samples were blocked in blocking solution (0.05% Tween-20, 1.5% BSA, and 0.5% sodium azide in PBS) for 1 h at room temperature. For 5meC and 5hmeC, the samples were treated with 4 M HCl for 10 min and neutralized with 100 mM Tris-HCl (pH 8.5) for 20 min. The samples were then incubated with primary antibodies at 4°C overnight. The primary antibodies used were rabbit anti-CDX2 (1:100, BioGenex, Fremont, CA, USA, cat. code: CDX2-88), mouse anti-trimethyl histone H3K9 (H3K9me3) (1:100, MBL, Nagoya, Japan, cat. code: MABI0318), mouse anti-5meC (1:200, Active Motif, Carlsbad, CA, USA, cat. code: 61479) and rabbit anti-5hmeC (1:200, Active Motif, cat. code: 39769) antibodies. After washing, the samples were incubated with the secondary antibodies, Alexa Fluor 488-conjugated anti-rabbit IgG antibody (1:500; Thermo Scientific, Waltham, MA, USA) or Alexa Fluor 594-conjugated anti-mouse IgG antibody (1:500; Thermo Scientific) for 1 h at room temperature. After another washing step, the samples were stained with 10 µg/ml Hoechst 33258 for 10 min and mounted on slides in 50% glycerol in PBS.

The fluorescence signals of CDX2, H3K9me3 and Hoechst were observed using a fluorescence microscope (FSX100, Olympus, Tokyo, Japan) using the same contrast, brightness, and exposure settings. Digital images of CDX2, H3K9me3 and Hoechst signals were acquired with the FSX-BSW software (Olympus). Confocal digital images of the fluorescence

signals of 5mC and 5hmC were captured with a confocal laser-scanning microscope (Carl Zeiss, Germany) using the same contrast, brightness, and exposure settings. A semi-quantitative analysis of the fluorescence signals of H3K9me3, 5mC and 5hmC in the nuclei of each group was conducted using Image J. The total intensity of H3K9me3, 5mC and 5hmC in each nucleus was measured from five different random regions and the background value for the cytoplasm was subtracted. This calculated intensity was multiplied by the nuclear volume ($v=4\pi r^3/3$) to yield the total amount of fluorescence for the nucleus (Bui et al., 2010).

Embryo transfer

Pseudopregnant ICR females mated with sterile ICR males were used as embryo recipients. SCNT embryos that had developed to the two-cell stage were transferred to the oviducts of the pseudopregnant females at 0.5 days post-coitus (dpc). Cesarean section and uterine analysis of implantation sites were performed in all recipients at 19.5 dpc. If available, lactating foster mothers were used to raise live pups.

Library preparation

Single embryos after the removal of zona pellucida were subjected to RNA purification using PicoPure RNA extraction kit (Thermo Scientific) according to the vendor's instruction. At the final step of RNA extraction, 9 µl of elution buffer was used to extract RNA from the column. Two µl of RNA out of 9 µl were subjected to Ovation Single Cell RNA-seq System (NuGEN) for making a library for sequencing. Two steps of PCR amplification (14 and 12 cycles) were needed to obtain an adequate amount of DNA for sequencing. The obtained library was quality-checked by TapeStation (Agilent) and quantified using Qubit (Thermo Scientific).

Sequencing data filtering

Single end 50 bp sequencing was carried out using the Illumina Hiseq2000 system. Fastq files from Illumina sequencing were filtered for low quality reads (<Q20), and low quality bases were trimmed from the ends of the reads (<Q20). Adaptors were removed using cutadapt (Martin, 2011). The sequencing reads were then mapped to the mouse genome (mm9) using TopHat and UCSC annotation of exon locations in mm9. This annotation was also used to generate counts of reads covering exonic regions for each gene, and RPKM values were calculated from these by normalizing to total counts and transcript length.

RNA-seq analysis

An unsupervised hierarchical clustering of the RPKM values was performed using hclust in R (using Euclidean distance and Ward agglomeration). To prepare the count data for differential expression analysis, a filter was applied requiring genes to have 1 count per million (CPMs) in all three treatment replicates or in all three controls. Differentially expressed genes were then identified using edgeR. Gene ontology terms showing over-representation of genes that were up- or down-regulated after nuclear transfer were detected using PANTHER (http://www.pantherdb.org/). Hypergeometric tests were performed to compare the overlap between upregulated genes in cloned embryos treated with TSA+VC and other published gene lists (Matoba et al., 2014; Soufi et al., 2012) (GSE59073 and GSE36570). Genes passing CPM filter in the control versus TSA+VC comparison were ordered by fold change. The RPKM values for these genes were z-score normalized across all samples and plotted on a heatmap.

RepeatMasker (http://www.repeatmasker.org/) was used to identify locations of retroelements in the mm9 genome. These were then used to prepare counts, CPMs and RPKMs for each retroelement and differential expression analysis was performed using edgeR (Robinson et al., 2010), all following the procedure detailed above. Scatterplots of RPKM values for TSA(0-8 h)+VC(8-15 h) NT and control NT were generated, splitting the retroelements by subtype.

Statistical analysis

Percentage data were subjected to arcsine transformation before statistical analyses. Data on *in vitro* and *in vivo* embryonic development were analyzed by one-way ANOVA with subsequent Tukey's multiple comparison tests or

Fisher's exact test. Comparison of blastocyst cell numbers and fluorescence intensity were performed by one-way ANOVA with subsequent Tukey's multiple comparison tests. A value of $P \leq 0.05$ was considered significant.

Data availability
RNA-seq data were deposited at NCBI's Gene Expression Omnibus with accession number GSE95053 at http://www.ncbi.nlm.nih.gov/geo/query/acc.cgi?acc/ GSE95053.

Supplementary information
Supplementary information available online at http://bio.biologists.org/lookup/doi/10.1242/bio.023473.supplemental

References
Amouroux, R., Nashun, B., Shirane, K., Nakagawa, S., Hill, P. W. S., D'Souza, Z., Nakayama, M., Matsuda, M., Turp, A., Ndjetehe, E. et al. (2016). De novo DNA methylation drives 5hmC accumulation in mouse zygotes. *Nat. Cell Biol.* **18**, 225-233.

Blaschke, K., Ebata, K. T., Karimi, M. M., Zepeda-Martínez, J. A., Goyal, P., Mahapatra, S., Tam, A., Laird, D. J., Hirst, M., Rao, A. et al. (2013). Vitamin C induces Tet-dependent DNA demethylation and a blastocyst-like state in ES cells. *Nature* **500**, 222-226.

Bui, H.-T., Wakayama, S., Kishigami, S., Park, K.-K., Kim, J.-H., Thuan, N. V. and Wakayama, T. (2010). Effect of trichostatin A on chromatin remodeling, histone modifications, DNA replication, and transcriptional activity in cloned mouse embryos. *Biol. Reprod.* **83**, 454-463.

Carr, A. and Frei, B. (1999). Does vitamin C act as a pro-oxidant under physiological conditions? *FASEB J.* **13**, 1007-1024.

Chatot, C. L., Ziomek, C. A., Bavister, B. D., Lewis, J. L. and Torres, I. (1989). An improved culture medium supports development of random-bred 1-cell mouse embryos in vitro. *J. Reprod. Fertil.* **86**, 679-688.

Chen, J., Liu, H., Liu, J., Qi, J., Wei, B., Yang, J., Liang, H., Chen, Y., Chen, J., Wu, Y. et al. (2013). H3K9 methylation is a barrier during somatic cell reprogramming into iPSCs. *Nat. Genet.* **45**, 34-42.

Chung, Y. G., Matoba, S., Liu, Y., Eum, J. H., Lu, F., Jiang, W., Lee, J. E., Sepilian, V., Cha, K. Y., Lee, D. R. et al. (2015). Histone demethylase expression enhances human somatic cell nuclear transfer efficiency and promotes derivation of pluripotent stem cells. *Cell Stem Cell* **17**, 758-766.

Esteban, M. A., Wang, T., Qin, B., Yang, J., Qin, D., Cai, J., Li, W., Weng, Z., Chen, J., Ni, S. et al. (2010). Vitamin C enhances the generation of mouse and human induced pluripotent stem cells. *Cell Stem Cell* **6**, 71-79.

Folch, J., Cocero, M. J., Chesné, P., Alabart, J. L., Domínguez, V., Cognié, Y., Roche, A., Fernández-Árias, A., Martí, J. I., Sánchez, P. et al. (2009). First birth of an animal from an extinct subspecies (Capra pyrenaica pyrenaica) by cloning. *Theriogenology* **71**, 1026-1034.

Fukuda, A., Cao, F., Morita, S., Yamada, K., Jincho, Y., Tane, S., Sotomaru, Y. and Kono, T. (2010). Identification of inappropriately reprogrammed genes by large-scale transcriptome analysis of individual cloned mouse blastocysts. *PLoS ONE* **5**, e11274.

Gurdon, J. B. (1962). The developmental capacity of nuclei taken from intestinal epithelium cells of feeding tadpoles. *J. Embryol. Exp. Morphol.* **10**, 622-640.

Hore, T. A., von Meyenn, F., Ravichandran, M., Bachman, M., Ficz, G., Oxley, D., Santos, F., Balasubramanian, S., Jurkowski, T. P. and Reik, W. (2016). Retinol and ascorbate drive erasure of epigenetic memory and enhance reprogramming to naive pluripotency by complementary mechanisms. *Proc. Natl. Acad. Sci. USA* **113**, 12202-12207.

Huang, Y., Tang, X., Xie, W., Zhou, Y., Li, D., Zhou, Y., Zhu, J., Yuan, T., Lai, L., Pang, D. et al. (2011). Vitamin C enhances in vitro and in vivo development of porcine somatic cell nuclear transfer embryos. *Biochem. Biophys. Res. Commun.* **411**, 397-401.

Huang, J., Zhang, H., Yao, J., Qin, G., Wang, F., Wang, X., Luo, A., Zheng, Q., Cao, C. and Zhao, J. (2016). BIX-01294 increases pig cloning efficiency by improving epigenetic reprogramming of somatic cell nuclei. *Reproduction* **151**, 39-49.

Inoue, K., Kohda, T., Sugimoto, M., Sado, T., Ogonuki, N., Matoba, S., Shiura, H., Ikeda, R., Mochida, K., Fujii, T. et al. (2010). Impeding Xist expression from the active X chromosome improves mouse somatic cell nuclear transfer. *Science* **330**, 496-499.

Inoue, K., Oikawa, M., Kamimura, S., Ogonuki, N., Nakamura, T., Nakano, T., Abe, K. and Ogura, A. (2015). Trichostatin A specifically improves the aberrant expression of transcription factor genes in embryos produced by somatic cell nuclear transfer. *Sci. Rep.* **5**, 10127.

Isaji, Y., Yoshida, K., Imai, H. and Yamada, M. (2015). An intracytoplasmic injection of deionized bovine serum albumin immediately after somatic cell nuclear transfer enhances full-term development of cloned mouse embryos. *J. Reprod. Dev.* **61**, 503-510.

Ishiuchi, T., Enriquez-Gasca, R., Mizutani, E., Bošković, A., Ziegler-Birling, C., Rodriguez-Terrones, D., Wakayama, T., Vaquerizas, J. M. and Torres-Padilla, M.-E. (2015). Early embryonic-like cells are induced by downregulating replication-dependent chromatin assembly. *Nat. Struct. Mol. Biol.* **22**, 662-671.

Kigami, D., Minami, N., Takayama, H. and Imai, H. (2003). MuERV-L is one of the earliest transcribed genes in mouse one-cell embryos. *Biol. Reprod.* **68**, 651-654.

Kim, K., Doi, A., Wen, B., Ng, K., Zhao, R., Cahan, P., Kim, J., Aryee, M. J., Ji, H., Ehrlich, L. I. R. et al. (2010). Epigenetic memory in induced pluripotent stem cells. *Nature* **467**, 285-290.

Kishigami, S. and Wakayama, T. (2007). Efficient strontium-induced activation of mouse oocytes in standard culture media by chelating calcium. *J. Reprod. Dev.* **53**, 1207-1215.

Kishigami, S., Mizutani, E., Ohta, H., Hikichi, T., Thuan, N. V., Wakayama, S., Bui, H.-T. and Wakayama, T. (2006). Significant improvement of mouse cloning technique by treatment with trichostatin A after somatic nuclear transfer. *Biochem. Biophys. Res. Commun.* **340**, 183-189.

Leary, A. G., Wong, G. G., Clark, S. C., Smith, A. G. and Ogawa, M. (1990). Leukemia inhibitory factor differentiation-inhibiting activity/human interleukin for DA cells augments proliferation of human hematopoietic stem cells. *Blood* **75**, 1960-1964.

Lin, J., Shi, L., Zhang, M., Yang, H., Qin, Y., Zhang, J., Gong, D., Zhang, X., Li, D. and Li, J. (2011). Defects in trophoblast cell lineage account for the impaired in vivo development of cloned embryos generated by somatic nuclear transfer. *Cell Stem Cell* **8**, 371-375.

Liu, W., Liu, X., Wang, C., Gao, Y., Gao, R., Kou, X., Zhao, Y., Li, J., Wu, Y., Xiu, W. et al. (2016). Identification of key factors conquering developmental arrest of somatic cell cloned embryos by combining embryo biopsy and single-cell sequencing. *Cell Discovery* **2**, 16010.

Ma, H., Morey, R., O'Neil, R. C., He, Y., Daughtry, B., Schultz, M. D., Hariharan, M., Nery, J. R., Castanon, R., Sabatini, K. et al. (2014). Abnormalities in human pluripotent cells due to reprogramming mechanisms. *Nature* **511**, 177-183.

Maalouf, W. E., Liu, Z., Brochard, V., Renard, J.-P., Debey, P., Beaujean, N. and Zink, D. (2009). Trichostatin A treatment of cloned mouse embryos improves constitutive heterochromatin remodeling as well as developmental potential to term. *BMC Dev. Biol.* **9**, 11.

Macfarlan, T. S., Gifford, W. D., Driscoll, S., Lettieri, K., Rowe, H. M., Bonanomi, D., Firth, A., Singer, O., Trono, D. and Pfaff, S. L. (2012). Embryonic stem cell potency fluctuates with endogenous retrovirus activity. *Nature* **487**, 57-63.

Maksakova, I. A., Thompson, P. J., Goyal, P., Jones, S. J. M., Singh, P. B., Karimi, M. M. and Lorincz, M. C. (2013). Distinct roles of KAP1, HP1 and G9a/ GLP in silencing of the two-cell-specific retrotransposon MERVL in mouse ES cells. *Epigenet. Chromatin* **6**, 15.

Mallol, A., Santaló, J. and Ibáñez, E. (2015). Improved development of somatic cell cloned mouse embryos by vitamin C and latrunculin A. *PLoS ONE* **10**, e0120033.

Martin, M. (2011). Cutadapt removes adapter sequences from high-throughput sequencing reads. *EMBnet* **17**, 10-12.

Matoba, S., Inoue, K., Kohda, T., Sugimoto, M., Mizutani, E., Ogonuki, N., Nakamura, T., Abe, K., Nakano, T., Ishino, F. et al. (2011). RNAi-mediated knockdown of Xist can rescue the impaired postimplantation development of cloned mouse embryos. *Proc. Natl. Acad. Sci. USA* **108**, 20621-20626.

Matoba, S., Liu, Y., Lu, F., Iwabuchi, K. A., Shen, L., Inoue, A. and Zhang, Y. (2014). Embryonic development following somatic cell nuclear transfer impeded by persisting histone methylation. *Cell* **159**, 884-895.

Mikkelsen, T. S., Hanna, J., Zhang, X., Ku, M., Wernig, M., Schorderet, P., Bernstein, B. E., Jaenisch, R., Lander, E. S. and Meissner, A. (2008). Dissecting direct reprogramming through integrative genomic analysis. *Nature* **454**, 49-55.

Miyamoto, K., Nagai, K., Kitamura, N., Nishikawa, T., Ikegami, H., Binh, N. T., Tsukamoto, S., Matsumoto, M., Tsukiyama, T., Minami, N. et al. (2011). Identification and characterization of an oocyte factor required for development of porcine nuclear transfer embryos. *Proc. Natl. Acad. Sci. USA* **108**, 7040-7045.

Mizutani, E., Yamagata, K., Ono, T., Akagi, S., Geshi, M. and Wakayama, T. (2012). Abnormal chromosome segregation at early cleavage is a major cause of the full-term developmental failure of mouse clones. *Dev. Biol.* **364**, 56-65.

Monfort, A. and Wutz, A. (2013). Breathing-in epigenetic change with vitamin C. *EMBO Rep.* **14**, 337-346.

Ng, E. S., Davis, R., Stanley, E. G. and Elefanty, A. G. (2008). A protocol describing the use of a recombinant protein-based, animal product-free medium (APEL) for human embryonic stem cell differentiation as spin embryoid bodies. *Nat. Protoc.* **3**, 768-776.

Nottke, A., Colaiacovo, M. P. and Shi, Y. (2009). Developmental roles of the histone lysine demethylases. *Development* **136**, 879-889.

Ogura, A., Inoue, K. and Wakayama, T. (2013). Recent advancements in cloning by somatic cell nuclear transfer. *Philos. Trans. R. Soc. Lond. B Biol. Sci.* **368**, 20110329.

Ono, T., Li, C., Mizutani, E., Terashita, Y., Yamagata, K. and Wakayama, T. (2010). Inhibition of class IIb histone deacetylase significantly improves cloning efficiency in mice. *Biol. Reprod.* **83**, 929-937.

Robinson, M.D., McCarthy, D.J. and Smyth, G.K. (2010). edgeR: a Bioconductor package for differential expression analysis of digital gene expression data. *Bioinformatics* **26**, 139-140.

Rybouchkin, A., Kato, Y. and Tsunoda, Y. (2006). Role of histone acetylation in reprogramming of somatic nuclei following nuclear transfer. *Biol. Reprod.* **74**, 1083-1089.

Soufi, A., Donahue, G. and Zaret, K. S. (2012). Facilitators and impediments of the pluripotency reprogramming factors' initial engagement with the genome. *Cell* **151**, 994-1004.

Sridharan, R., Gonzales-Cope, M., Chronis, C., Bonora, G., McKee, R., Huang, C., Patel, S., Lopez, D., Mishra, N., Pellegrini, M. et al. (2013). Proteomic and genomic approaches reveal critical functions of H3K9 methylation and heterochromatin protein-1gamma in reprogramming to pluripotency. *Nat. Cell Biol.* **15**, 872-882.

Stadtfeld, M., Apostolou, E., Ferrari, F., Choi, J., Walsh, R. M., Chen, T., Ooi, S. S., Kim, S. Y., Bestor, T. H., Shioda, T. et al. (2012). Ascorbic acid prevents loss of Dlk1-Dio3 imprinting and facilitates generation of all-iPS cell mice from terminally differentiated B cells. *Nat. Genet.* **44**, 398-405, S391-S392.

Tachibana, M., Amato, P., Sparman, M., Gutierrez, N. M., Tippner-Hedges, R., Ma, H., Kang, E., Fulati, A., Lee, H.-S., Sritanaudomchai, H. et al. (2013). Human embryonic stem cells derived by somatic cell nuclear transfer. *Cell* **153**, 1228-1238.

Takahashi, K. and Yamanaka, S. (2006). Induction of pluripotent stem cells from mouse embryonic and adult fibroblast cultures by defined factors. *Cell* **126**, 663-676.

Teperek, M. and Miyamoto, K. (2013). Nuclear reprogramming of sperm and somatic nuclei in eggs and oocytes. *Reprod. Med. Biol.* **12**, 133-149.

Terashita, Y., Wakayama, S., Yamagata, K., Li, C., Sato, E. and Wakayama, T. (2012). Latrunculin A can improve the birth rate of cloned mice and simplify the nuclear transfer protocol by gently inhibiting actin polymerization. *Biol. Reprod.* **86**, 180.

Vidal, F. and Hidalgo, J. (1993). Effect of zinc and copper on preimplantation mouse embryo development in vitro and metallothionein levels. *Zygote* **1**, 225-229.

Wakayama, T., Perry, A. C. F., Zuccotti, M., Johnson, K. R. and Yanagimachi, R. (1998). Full-term development of mice from enucleated oocytes injected with cumulus cell nuclei. *Nature* **394**, 369-374.

Wakayama, S., Ohta, H., Hikichi, T., Mizutani, E., Iwaki, T., Kanagawa, O. and Wakayama, T. (2008). Production of healthy cloned mice from bodies frozen at −20°C for 16 years. *Proc. Natl. Acad. Sci. USA* **105**, 17318-17322.

Walter, M., Teissandier, A., Perez-Palacios, R. and Bourc'his, D. (2016). An epigenetic switch ensures transposon repression upon dynamic loss of DNA methylation in embryonic stem cells. *Elife* **5**, e11418.

Wang, F., Kou, Z., Zhang, Y. and Gao, S. (2007). Dynamic reprogramming of histone acetylation and methylation in the first cell cycle of cloned mouse embryos. *Biol. Reprod.* **77**, 1007-1016.

Wang, T., Chen, K., Zeng, X., Yang, J., Wu, Y., Shi, X., Qin, B., Zeng, L., Esteban, M. A., Pan, G. et al. (2011). The histone demethylases Jhdm1a/1b enhance somatic cell reprogramming in a vitamin-C-dependent manner. *Cell Stem Cell* **9**, 575-587.

Wilmut, I., Schnieke, A. E., McWhir, J., Kind, A. J. and Campbell, K. H. S. (1997). Viable offspring derived from fetal and adult mammalian cells. *Nature* **385**, 810-813.

Wossidlo, M., Arand, J., Sebastiano, V., Lepikhov, K., Boiani, M., Reinhardt, R., Schöler, H. and Walter, J. (2010). Dynamic link of DNA demethylation, DNA strand breaks and repair in mouse zygotes. *EMBO J.* **29**, 1877-1888.

Zhang, S., Chen, X., Wang, F., An, X., Tang, B., Zhang, X., Sun, L. and Li, Z. (2016). Aberrant DNA methylation reprogramming in bovine SCNT preimplantation embryos. *Sci. Rep.* **6**, 30345.

Large Cytoplasm Is Linked to the Error-Prone Nature of Oocytes

Graphical Abstract

Highlights

- Decreased oocyte cytoplasmic size allows spindles to have better-focused poles

- Decreased oocyte cytoplasmic size enhances spindle checkpoint stringency

- Increased oocyte cytoplasmic size confers the opposite effects

- A large cytoplasmic size is linked to error-prone chromosome segregation in oocytes
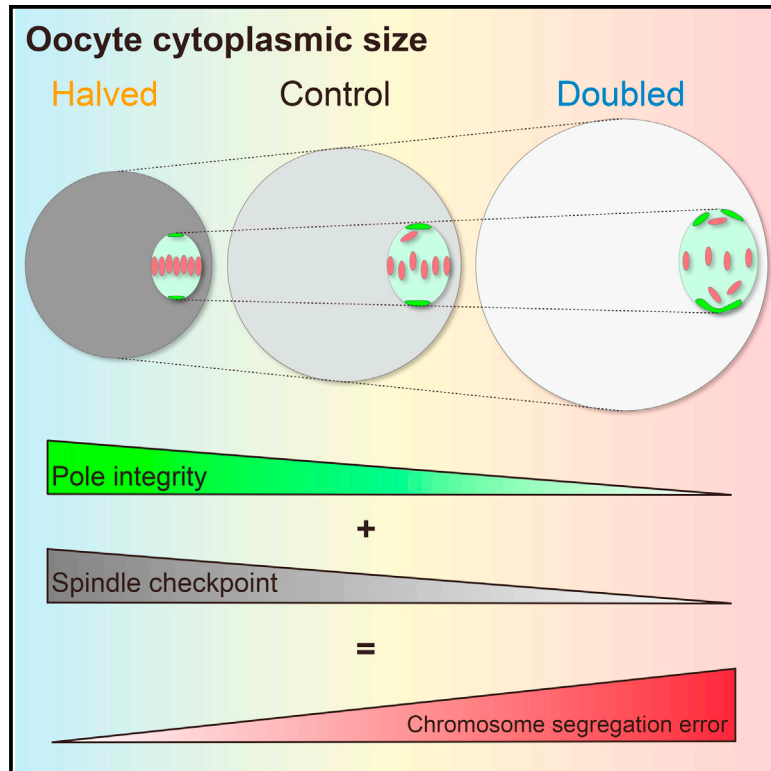
Authors

Hirohisa Kyogoku, Tomoya S. Kitajima

Correspondence

tkitajima@cdb.riken.jp

In Brief

Kyogoku and Kitajima show that cytoplasmic size affects the functionality of the acentrosomal spindle and the stringency of the spindle checkpoint in mouse oocytes, thus providing evidence that the large cytoplasmic size of oocytes is linked to error-prone chromosome segregation during female meiosis, which is a leading cause of aneuploidy.

CellPress

Article

Large Cytoplasm Is Linked to the Error-Prone Nature of Oocytes

Hirohisa Kyogoku[1] and Tomoya S. Kitajima[1,2,*]
[1]Laboratory for Chromosome Segregation, RIKEN Center for Developmental Biology, Kobe 650-0047, Japan
[2]Lead Contact
*Correspondence: tkitajima@cdb.riken.jp
http://dx.doi.org/10.1016/j.devcel.2017.04.009

SUMMARY

Chromosome segregation during meiosis in oocytes is error prone. The uniquely large cytoplasmic size of oocytes, which provides support for embryogenesis after fertilization, might be a predisposing factor for meiotic errors. However, this hypothesis remains unproven. Here, we show that cytoplasmic size affects the functionality of the acentrosomal spindle. Artificially decreasing the cytoplasmic size in mouse oocytes allows the acentrosomal spindle poles to have a better-focused distribution of microtubule-organizing centers and to biorient chromosomes more efficiently, whereas enlargement of the cytoplasmic size has the opposite effects. Moreover, we found that the cytoplasmic size-dependent dilution of nuclear factors, including anaphase inhibitors that are preformed at the nuclear membrane, limits the spindle's capacity to prevent anaphase entry with misaligned chromosomes. The present study defines a large cytoplasmic volume as a cell-intrinsic feature linked to the error-prone nature of oocytes. This may represent a trade-off between meiotic fidelity and post-fertilization developmental competence.

INTRODUCTION

Correct chromosome segregation during cell division is essential for the viability of daughter cells. Most cells thus possess a robust system to ensure error-free chromosome segregation. However, oocytes are a clear exception. Meiotic chromosome segregation in oocytes is highly error prone and, thus, frequently results in the production of aneuploid eggs, which is a leading cause of pregnancy loss and congenital disorders, such as Down syndrome (Jones and Lane, 2013; Nagaoka et al., 2012). The frequency of chromosome segregation errors is much higher in oocytes than in spermatocytes, even in young individuals, and increases with age (Chiang et al., 2012; Jones and Lane, 2013; Nagaoka et al., 2012; Webster and Schuh, 2017). This suggests that not only age-related effects but also oocyte-intrinsic features contribute to the error-prone nature of chromosome segregation. However, which oocyte features are linked to the error-prone nature remains unclear. Moreover, the mechanism by which oocytes, which provide a critical basis for embryogenesis, are prone to errors remains unexplained.

Chromosome biorientation, whereby spindle microtubules attach to the chromosome from opposite spindle poles, is critical for chromosome alignment and thus for correct chromosome segregation. In mouse oocytes, chromosome biorientation is error prone; a stable biorientation with correct attachments is established only after multiple rounds of error corrections (Kitajima et al., 2011). This error-prone chromosome biorientation has been at least partly attributed to the acentrosomal nature of the spindle. Unlike somatic cells, in which centriole-containing centrosomes predefine the two spindle poles and allow biorientation of chromosomes, mammalian oocytes lack centrioles (Bennabi et al., 2016; Dumont and Desai, 2012; Howe and FitzHarris, 2013). In mouse oocytes, acentriolar microtubule-organizing centers (MTOCs) initially form a ball-shaped apolar spindle. The MTOCs then relocate to two opposite poles, thus resulting in spindle bipolarization (Breuer et al., 2010; Clift and Schuh, 2015; Schuh and Ellenberg, 2007). The bipolarized acentrosomal spindle exhibits loosely focused poles with a broad distribution of MTOCs, thereby allowing the microtubules to attach to chromosomes from various directions, thus providing an explanation for the error-prone chromosome biorientation (Breuer et al., 2010; Kitajima et al., 2011; Schuh and Ellenberg, 2007). The spindle with the loosely focused poles in oocytes resembles the somatic spindles with overamplified or fragmented centrosomes observed before the chromosome segregation errors in cancer cells (Breuer et al., 2010; Ganem et al., 2009; Silkworth et al., 2009). These observations contrast with those of mouse embryos at the 8-cell and 16-cell stages, in which the acentrosomal spindles exhibit tightly focused poles (Courtois et al., 2012). Thus, the absence of centrosomes alone does not account for the loosely focused spindle poles during meiosis in oocytes. However, the oocyte-specific features that facilitate the loosening of the acentrosomal spindle poles remain unknown.

The spindle checkpoint, a mechanism that prevents chromosome segregation errors by delaying anaphase onset when kinetochores are not attached to the microtubules (London and Biggins, 2014; Musacchio, 2015), exhibits several unique features in oocytes (Gui and Homer, 2012; Kolano et al., 2012; Lane and Jones, 2014; Lane et al., 2012; Nagaoka et al., 2011; Sebestova et al., 2014). The low stringency of the spindle checkpoint is one factor that contributes to the error-proneness of oocytes. Whereas one unattached kinetochore is sufficient to induce a checkpoint-dependent anaphase delay in normal somatic cells (Rieder et al., 1995), in oocytes this delay is triggered

only when multiple kinetochores are unattached (Gui and Homer, 2012; Kolano et al., 2012; Lane et al., 2012; Nagaoka et al., 2011; Sebestova et al., 2014). This low stringency of the spindle checkpoint may be attributable to the large cytoplasmic volume (Gorbsky, 2015; Jones and Lane, 2013; Verlhac and Terret, 2016), which is one of the most striking features of the oocyte (~80 μm in diameter in mice and ~120 μm in humans). The prevailing view is that a larger cytoplasmic volume dilutes the active checkpoint signal that is generated on kinetochores, thus potentially weakening the checkpoint response (Galli and Morgan, 2016). This hypothesis is consistent with the observation that no spindle checkpoint response is detectable in *Xenopus* oocytes, which have a much larger cytoplasmic volume than do mouse oocytes (Shao et al., 2013). Moreover, when mouse oocytes are bisected, a single chromosome is sufficient to support the checkpoint-dependent anaphase delay (Hoffmann et al., 2011). One recent study has shown that in *Caenorhabditis elegans* embryos, the strength of the spindle checkpoint activated on all kinetochores through the microtubule disruption by nocodazole depends on the kinetochore-to-cytoplasmic ratio (Galli and Morgan, 2016). However, the influence of cytoplasmic volume on the checkpoint response in unperturbed oocytes remains unknown (Gerhold et al., 2016). In unperturbed somatic cells, in which on-kinetochore checkpoint activation is minimal, anaphase inhibitors that are preformed in the nucleus before nuclear envelope breakdown (NEBD) are rate limiting for the checkpoint-mediated anaphase delay (Rodriguez-Bravo et al., 2014). The contribution, if any, of the preformed anaphase inhibitors to the stringency of the spindle checkpoint in oocytes remains unexplored.

In the present study, we show that the uniquely large cytoplasmic volume of oocytes affects the functionality of the spindle through at least two distinct mechanisms. First, the large cytoplasmic volume allows acentrosomal spindle poles to form with a broad MTOC distribution, which is prone to anisotropic deformation and contributes to the error-prone chromosome biorientation. Second, the large cytoplasmic volume dilutes the nuclear factors, including anaphase inhibitors, thus resulting in the failure of the spindle to induce a checkpoint arrest in response to a small number of misaligned chromosomes. These results demonstrate that the large cytoplasmic size is linked to the error-prone nature of oocytes.

RESULTS

The Cytoplasm Scales the Spindle and Controls Anaphase Timing

To investigate the role of the large cytoplasmic volume in meiosis I, we generated mouse oocytes carrying half the normal cytoplasmic volume (halved oocytes) and oocytes carrying twice the normal cytoplasmic volume (doubled oocytes) (Figure 1A). The "halved" oocytes were generated by removing half of the total cytoplasmic volume from an oocyte at the germinal vesicle (GV) stage (prophase of meiosis I) by using a micropipette (Figure S1A and Movie S1). The "doubled" oocytes were generated by the electrofusion of an intact GV oocyte with an enucleated oocytes (Figure S1B and Movie S2). The size measurements of the generated oocytes confirmed the high precision of this technique (Figures S1C and S1D). The induction of meiotic resump-

tion in the halved and doubled oocytes resulted in normal frequencies of entry to and completion of meiosis I (Figure S1E).

Quantitative 3D analysis of the spindle and chromosome dynamics, on the basis of EGFP-MAP4 and H2B-mCherry labels, respectively (Kitajima et al., 2011; Schuh and Ellenberg, 2007), by high-resolution live imaging revealed two major effects of the modified cytoplasmic sizes on meiosis I (Figure 1B and Movie S3). First, the spindle volume was decreased by approximately half in the halved oocytes throughout meiosis I, whereas the spindle volume increased by approximately 2-fold in the doubled oocytes (Figures 1B and 1C). Nevertheless the spindle shape was preserved, because both the length and width of the spindle were similarly affected (Figure S2A). We observed no significant differences in the timing of the establishment of the bipolar spindle shape (Figure S2B) or the density of the microtubules that were labeled with EGFP-MAP4 (Figure S2C). Second, the onset of anaphase was significantly delayed in the halved oocytes and accelerated in the doubled oocytes (Figures 1B and 1D). These results indicate that the cytoplasmic volume affects the scale of the spindle and the timing of anaphase onset.

The Amount of Cytoplasmic Factors Limits the Spindle Size

We considered three possibilities to explain how changes in cytoplasmic size before NEBD affected the spindle scale after NEBD. The pre-NEBD cytoplasm might provide finite amounts of spindle components, thus scaling the spindle through a limiting component mechanism (Levy and Heald, 2012; Marshall, 2015), as observed in in vitro experiments using encapsulated *Xenopus* egg extracts (Good et al., 2013; Hazel et al., 2013). Alternatively, factors liberated from the nucleus through NEBD might negatively control the spindle size in a concentration-dependent manner, in agreement with the hypothesis that the nuclear-to-cytoplasmic ratio is critical for the spindle size (Cui et al., 2005; Novakova et al., 2016). Finally, a cell cortex mechanism that detects the distance to the spindle might control the spindle size, as has been observed in *C. elegans* embryo during anaphase (Hara and Kimura, 2009).

We designed two experiments to determine which of these putative mechanisms is responsible for the proportional changes in the spindle size. First, we induced meiotic resumption in the presence of nocodazole, which prevents microtubule polymerization, and then removed half the cytoplasmic volume from oocytes <40 min after NEBD ("halved after NEBD"). These oocytes, which carried half the amount of cytoplasm-derived factors and the same concentration of nucleus-derived factors as those in control oocytes, were washed and monitored for spindle formation (Figure 2A, Halved after NEBD). In the oocytes halved after NEBD, the spindle size was significantly smaller than that in the controls but was not significantly different from that in oocytes that were halved before NEBD (Figure 2B). Thus, the concentration of the nucleus-derived factors did not significantly influence the spindle scaling. Second, we generated dumbbell-shaped doubled oocytes by interrupting cell rounding after the cell fusion by using the actin stabilizer jasplakinolide (Figure 2C). The spindle, which formed on one side of the dumbbell in the doubled oocytes, was significantly larger than that in the control oocytes but was not significantly different from that in the round doubled oocytes (Figure 2D). This finding suggested that the
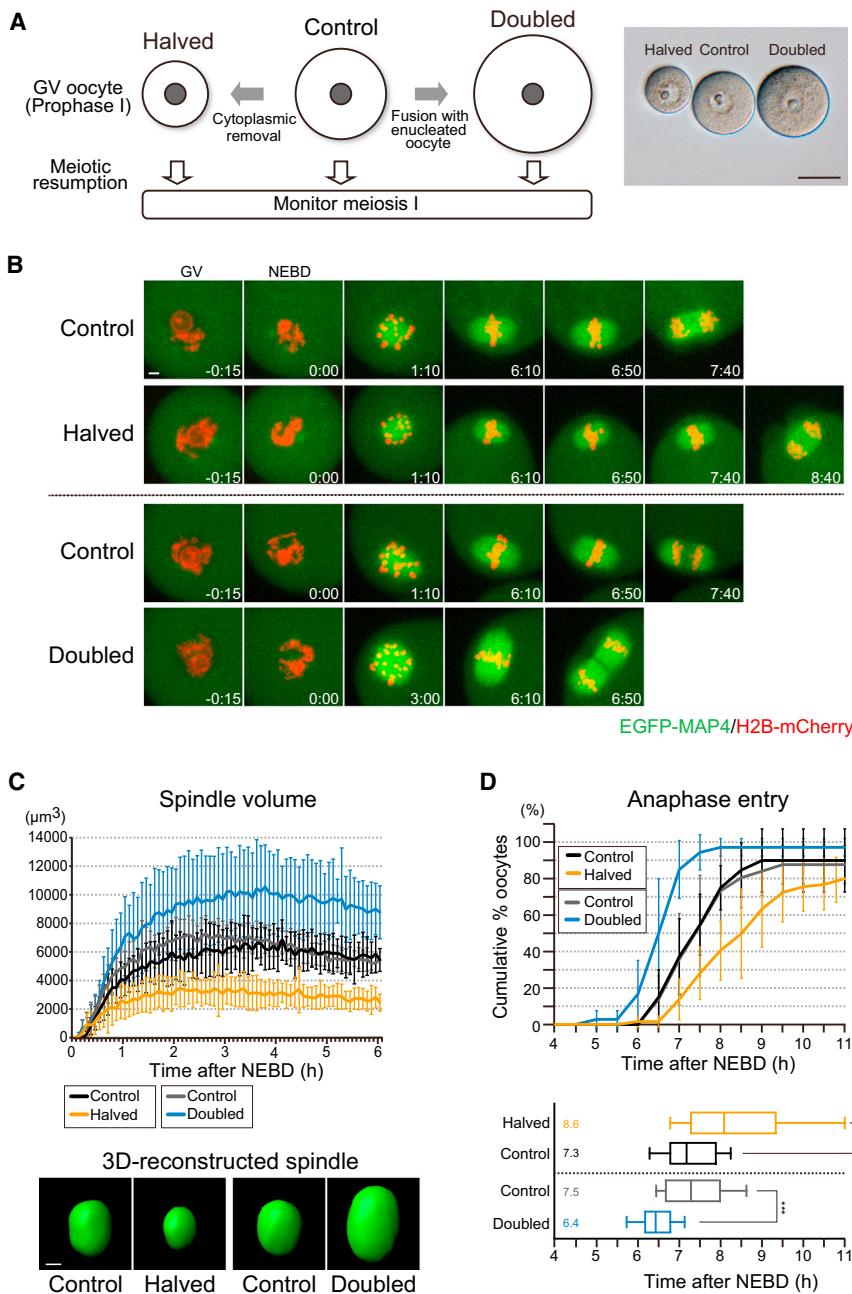
Figure 1. Cytoplasmic Size Controls Spindle Size and Anaphase Timing

(A) Experimental scheme. Image shows the generated oocytes. Scale bar, 100 μm.

(B) Live imaging of meiosis I. Maximum z-projection images of EGFP-MAP4 (microtubules, green) and H2B-mCherry (chromosomes, red). Time after NEBD (hr:min). Scale bar, 5 μm.

(C) Spindle scaling. Spindle volume was determined from 3D-reconstructed images (n = 16, 15, 14, and 16 oocytes). Error bars denote SD. Scale bar, 7 μm.

(D) Cytoplasmic size controls anaphase timing. Line plot shows the cumulative percentage of oocytes that entered anaphase (n = 4 experiments). Error bars denote SD. Box plot shows the time of anaphase onset (n = 53, 35, 42, and 35 oocytes). Boxes show the 25th–75th percentiles and whiskers the 10th–90th percentiles. Two-tailed, unpaired Student's t test was performed. ***p < 0.001.

See also Figures S1 and S2; and Movies S1, S2, and S3.

tigate the local distribution of the MTOCs around the pole, we visualized the polar MTOCs along the spindle axis after a 3D reconstruction and surface rendering (Figure 3A, "Top view"). This view revealed a stochastic distribution of the MTOCs around the pole at the late prometaphase in the control oocytes (Figure 3A, "Top view"). Notably, this MTOC distribution was extended unilaterally and was perpendicular to the spindle axis by late metaphase (Figure 3A, "Top view"). For the quantitative visualization, the top-view images of the polar MTOCs from more than 20 oocytes were aligned and summed to generate an averaged image for each time point (Figure 3B). The averaged top-view images showed that the MTOCs were distributed stochastically around the spindle pole by late prometaphase. By late metaphase, the MTOCs showed an anisotropic, ellipse-like distribution (Figures 3C, S2D, and S2E). This

geometry of the cell cortex does not significantly influence the spindle scaling. Moreover, by exclusion, these results suggested that the amount of cytoplasm-derived factors plays a major role in the spindle scaling observed in our system, in agreement with the spindle scaling through a limiting component mechanism.

Cytoplasmic Size Affects the Distribution of MTOCs at the Acentrosomal Spindle Poles

We then addressed the integrity of the spindles scaled with cytoplasmic size. Live imaging of MTOCs with mNeonGreen-Cep192 confirmed that the MTOCs localized around the spindle poles from late prometaphase to metaphase (Figure 3A ["Side view"] and Movie S4) (Clift and Schuh, 2015). To more thoroughly inves-

finding suggested that the acentrosomal spindle poles composed of MTOCs were prone to anisotropic deformation, even in the control oocytes. In the doubled oocytes, the distribution of the polar MTOCs collapsed into a thread-like arrangement by late metaphase, thus resulting in an extremely broad and anisotropic spindle pole (Figures 3A–3C, S2D, and S2E). In contrast, the polar MTOCs in the halved oocytes maintained an isotropic ring-like arrangement, which was associated with focused spindle poles (Figures 3A–3C, S2D, and S2E). We confirmed these observations in late metaphase by immunostaining (Figure S2F). These results indicated that cytoplasmic size affects the proneness to the anisotropic deformation of the MTOC distribution at the acentrosomal spindle poles (Figure 3A, Diagram).
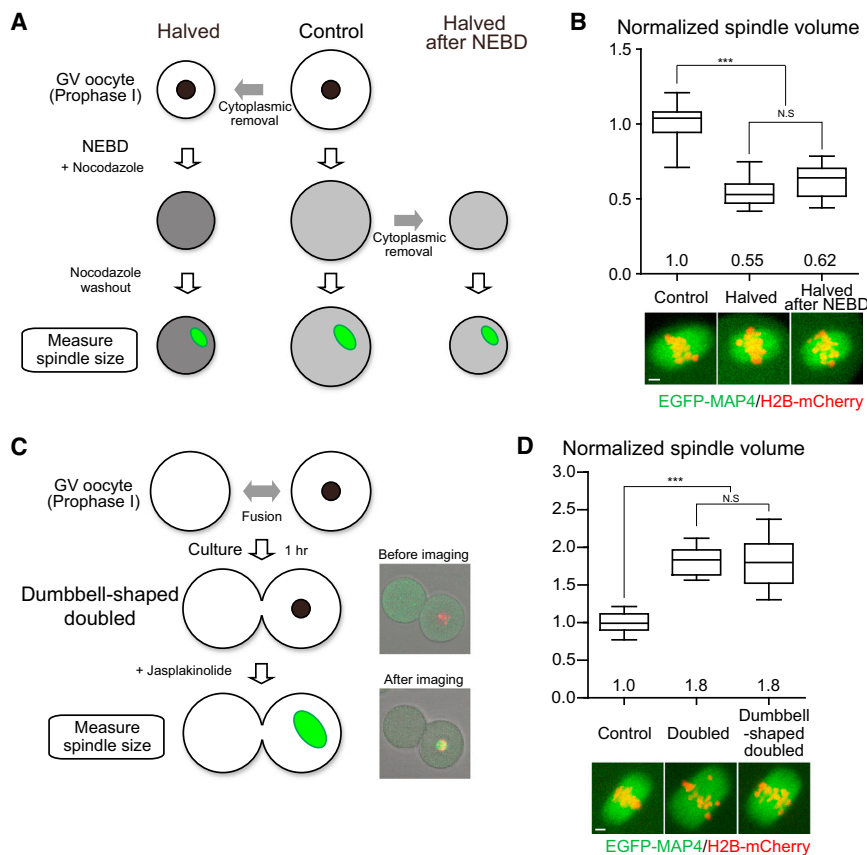
Figure 2. The Amount of Cytoplasmic Factors Controls the Spindle Size

(A) Experimental scheme. The oocytes were halved before or after NEBD. Spindle formation was synchronized through nocodazole washout. The concentration of nucleus-derived factors is doubled in oocytes halved before NEBD, whereas it is intact in oocytes halved after NEBD.

(B) The spindle is half-sized in oocytes halved after NEBD. Spindle volume was determined at late metaphase (n = 17, 12, and 16 oocytes).

(C) Experimental scheme. Oocytes were fused and then meiotic resumption was induced in the presence of 200 nM jasplakinolide to inhibit cell rounding (dumbbell-shaped doubled).

(D) The spindle is double-sized in the dumbbell-shaped doubled oocytes. Spindle volume was determined at late metaphase (n = 44, 23, and 22 oocytes). Control and round-shaped doubled oocytes were treated with 200 nM jasplakinolide at meiotic resumption as was performed in the dumbbell-shaped doubled oocytes.

Boxes show the 25th–75th percentiles and whiskers the 10th–90th percentiles. Two-tailed, unpaired Student's t tests were performed. N.S., not significant. ***p < 0.001. Scale bars, 5 μm.

Cytoplasmic Size Affects the Spindle's Capacity to Align Chromosomes

The observed alterations in the MTOC distribution at the spindle poles suggested an altered spindle functionality. To examine the ability of the spindle to align chromosomes, we determined the fraction of aligned chromosomes on the basis of the spindle equator-chromosome distance, which was normalized to the spindle length in the 3D-reconstructed images of the oocytes expressing mNeonGreen-Cep192 and H2B-mCherry (Figure 4A and Movie S4). This analysis revealed that in the doubled oocytes, the chromosome alignment was significantly delayed compared with that in the control oocytes, whereas it was accelerated in the halved oocytes (Figure 4B). We confirmed these observations at early metaphase by immunostaining (Figure S3A). In agreement with these observations, the overall stability of the kinetochore-microtubule attachments was decreased in the doubled oocytes, whereas it was increased in the halved oocytes (Figures S3B and S3C). Moreover, during metaphase II, the aneuploidy was more frequent in the doubled oocytes compared with that in the control oocytes (Figures S3D and S3E), thus suggesting that chromosomes were missegregated during meiosis I. These cytoplasmic size-dependent effects were likely to be due to the altered functionality of the spindle rather than to the kinetochores, because the amounts of the kinetochore components (Hec1, CENP-C, and CENP-E) and the level of the regulatory phosphorylation (Aurora B/C-dependent phosphorylation of Hec1 at Ser55 and MCAK at Ser92)

(Andrews et al., 2004; Cheeseman et al., 2006; DeLuca et al., 2006; Yoshida et al., 2015) were largely unaffected by cytoplasmic size (Figures S4A–S4F). These results suggest that cytoplasmic size affects the capacity of the spindle to efficiently align chromosomes at the spindle equator.

Cytoplasmic Size-Dependent Effects on the Spindle Poles Contribute to Error-Prone Chromosome Biorientation

To investigate the mechanism underlying the cytoplasmic size-dependent delay in chromosome alignment, we monitored chromosome biorientation by 3D tracking of the kinetochores (Figure 5A and Movie S5) (Kitajima et al., 2011; Sakakibara et al., 2015). From 2.5 to 5.0 hr after NEBD, the majority of the chromosomes established a stable biorientation at the spindle equator (Figures 5A and 5B) as previously reported (Kitajima et al., 2011). During this phase, in the control oocytes a fraction of the chromosomes exhibited a relatively stable association with the spindle poles and a delay in chromosome biorientation (Figures 5B and 5C); 10% (16/160) of the chromosomes remained within 4 μm of the spindle poles for longer than 30 min with no stable biorientation. In the doubled oocytes, the number of such chromosomes was significantly increased (22.5%, 18/80), whereas it was decreased in the halved oocytes (1%, 1/100) (Figures 5B and 5C). A substantial fraction of the chromosomes that remained near the spindle poles in the doubled oocytes exhibited a characteristic transient stretching perpendicularly to the spindle axis within one pole (56%, 10/18) (Figure 5D and Movie S6), as was also observed in a smaller but substantial fraction of the chromosomes that remained near
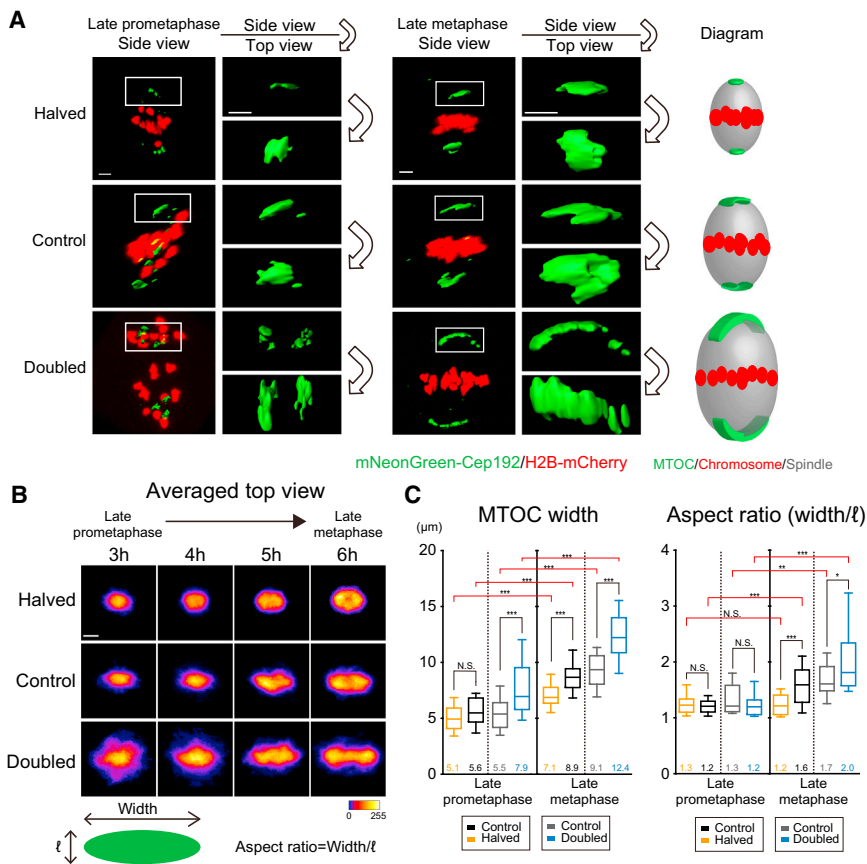
A

Late prometaphase Side view | Side view / Top view | Late metaphase Side view | Side view / Top view | Diagram

Halved

Control

Doubled

mNeonGreen-Cep192/H2B-mCherry   MTOC/Chromosome/Spindle

B

Averaged top view

Late prometaphase → Late metaphase

3h 4h 5h 6h

Halved

Control

Doubled

Width

ℓ

Aspect ratio=Width/ℓ

C

MTOC width

Aspect ratio (width/ℓ)

Figure 3. Cytoplasmic Size-Dependent Deformation of Spindle Poles

(A) MTOC distribution in 3D. Images of mNeonGreen-Cep192 (MTOCs, green) and H2B-mCherry (chromosomes, red) were reconstructed in 3D and surface rendered. In each panel, a side view of the spindle (left) and its pole (right top) and a top view of the pole (right bottom) at late prometaphase (3 hr after NEBD) or late metaphase (6 hr after NEBD) are shown.

(B) Progressive anisotropic deformation of polar MTOCs. Top-view images of polar MTOCs were aligned, averaged, and color-coded (n = 23, 21, and 20 oocytes).

(C) Quantification of MTOC deformation. The width and aspect ratio of the MTOC distribution in top-view images are measured as shown in the diagram in (B) (n = 23, 20, 21, and 20 oocytes). Boxes show the 25th–75th percentiles and whiskers the 10th–90th percentiles. Two-tailed, unpaired Student's t tests were performed. N.S., not significant. *p < 0.05, **p < 0.01, ***p < 0.001.

Scale bars, 5 μm. See also Figure S2 and Movie S4.

the spindle poles in the control oocytes (19%, 3/16). These observations indicated that the individual spindle poles were spatially split into multiple functional units that interacted with chromosomes through incorrectly oriented microtubules, thus contributing to the prolonged presence of the chromosomes near the spindle poles and the erroneous chromosome biorientation. These results suggested that the cytoplasmic size-dependent effects on the spindle poles at least partly contribute to the error-prone chromosome biorientation.

Cytoplasmic Size Affects the Timing of Anaphase Onset through the Spindle Checkpoint by Diluting Nuclear Factors

We then investigated how cytoplasmic size controls the timing of anaphase onset. The onset of anaphase depends on the anaphase-promoting complex/cyclosome (APC/C) (Peters, 2006). To examine the temporal changes in APC/C activity, we monitored the degradation of Securin-EGFP (Herbert et al., 2003; McGuinness et al., 2009). In the control oocytes, during prophase and prometaphase, the level of Securin-EGFP progressively increased (Figures S5A and S5B), thus suggesting that the APC/C-mediated degradation of Securin-EGFP was slower than the production of Securin-EGFP. In the halved oocytes, the kinetics of the increase in the level of Securin-EGFP during these phases was faster than that in the control oocytes but was slower in the doubled oocytes (Figures S5C and S5D). These results suggested that the APC/C activity

during prophase and prometaphase was lower in the halved oocytes and higher in the doubled oocytes.

The spindle checkpoint is a mechanism that inhibits the APC/C (London and Biggins, 2014; Musacchio, 2015). The inhibition of the spindle checkpoint activator Mps1 with the specific inhibitor reversine (Santaguida et al., 2010) revealed that the anaphase delay in the halved oocytes compared with the control oocytes depended on the spindle checkpoint (Figure 6A). We considered two possibilities that might explain how cytoplasmic size controls the timing of anaphase onset through the spindle checkpoint. First, a larger cytoplasmic size dilutes the checkpoint signal generated on kinetochores during prometaphase (Galli and Morgan, 2016), thus possibly affecting the timing of anaphase onset. In this case, the anaphase timing should depend on the kinetochore-to-cytoplasmic ratio after NEBD. A second possibility is that a larger cytoplasmic volume dilutes the concentration of anaphase inhibitors preformed at the nucleus, such as the mitotic checkpoint complex (MCC) generated at nuclear pores (Rodriguez-Bravo et al., 2014), may be critical for determining the timing of anaphase onset. This possibility suggests that the timing of anaphase onset may depend on the nuclear-to-cytoplasmic ratio before NEBD. To distinguish these possibilities, we removed half the cytoplasm from oocytes <40 min after NEBD (Figure 6B, "Halved after NEBD"). In these oocytes, which had an intact nuclear-to-cytoplasmic ratio prior to NEBD and a doubled kinetochore-to-cytoplasmic ratio after NEBD, anaphase onset was not significantly delayed compared with that in the control oocytes (Figure 6C). This result suggested that cytoplasmic size limits the spindle checkpoint-mediated control of anaphase timing through diluting factors that are pregenerated at the nucleus.
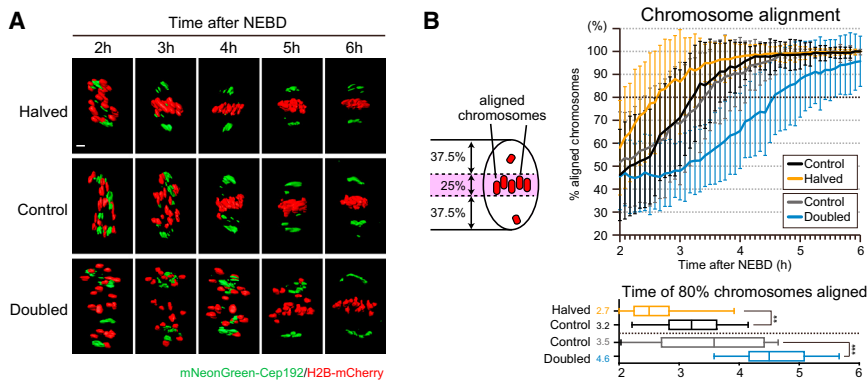
A Time after NEBD

2h 3h 4h 5h 6h

Halved

Control

Doubled

mNeonGreen-Cep192/H2B-mCherry

B

aligned chromosomes

37.5%

25%

37.5%

Chromosome alignment

% aligned chromosomes

Time after NEBD (h)

Control
Halved
Control
Doubled

Time of 80% chromosomes aligned

Halved 2.7
Control 3.2
Control 3.5
Doubled 4.6

Time after NEBD (h)

Figure 4. Cytoplasmic Size Affects the Efficiency of Chromosome Alignment

(A) Images of mNeonGreen-Cep192 (MTOCs, green) and H2B-mCherry (chromosomes, red) were reconstructed in 3D and surface rendered. Views from the side of the spindle are shown. Scale bar, 5 μm.

(B) Cytoplasmic size affects chromosome alignment. Aligned chromosomes were defined as chromosomes with chromosome-equator distances shorter than 12.5% of the metaphase spindle length (Figure S2; halved 21.6 μm, control 26.8 μm, doubled 33.8 μm) in 3D. Error bars denote SD. Box plot shows the time at which 80% of the chromosomes were aligned (n = 22, 27, 21, and 34 oocytes). Boxes show the 25th–75th percentiles and whiskers the 10th–90th percentiles. Two-tailed, unpaired Student's t test was performed. **p < 0.01, ***p < 0.001.

See also Figures S3 and S4.

Anaphase Inhibitors Preformed at the Nucleus Are Diluted by the Cytoplasm after NEBD

In somatic cells, the MCC is pregenerated at nuclear pores and then is enriched on kinetochores after NEBD (Rodriguez-Bravo et al., 2014). The immunostaining of oocytes with an antibody that specifically detects the active form of Mad2 (C-Mad2) (Fava et al., 2011), a component of the MCC (London and Biggins, 2014; Musacchio, 2015), indicated that C-Mad2 was located at the nuclear rim before NEBD in oocytes (Figure 6D), as has been reported in somatic cells (Rodriguez-Bravo et al., 2014). The total amount of C-Mad2 at the nuclear rim was not significantly affected by cytoplasmic size (Figure 6D). After NEBD, however, the amount of kinetochore C-Mad2 was significantly decreased in the doubled oocytes compared with the control oocytes, whereas it was significantly increased in the halved oocytes (Figure 6E). The cytoplasmic size-dependent effects on the level of kinetochore C-Mad2 were not attributable to the altered stability of the kinetochore-microtubule attachments or the altered phosphorylation levels of the kinetochores, because the oocytes with a larger cytoplasm exhibited less stable attachments (Figures S3B and S3D) and intact levels of phosphorylated Hec1 and MCAK (Figures S4E and S4F). Although the level of kinetochore C-Mad2 was globally affected by cytoplasmic size, the misaligned chromosomes exhibited an increased level of C-Mad2 in the kinetochores compared with the aligned chromosomes in the doubled and halved oocytes, which was similar to that in the control oocytes (Figures S6A and S6B) (Chmátal et al., 2015; Lane et al., 2012), thus suggesting that the error correction mechanism in the kinetochore-microtubule attachments (Chmátal et al., 2015) is largely unaffected by cytoplasmic size. These results suggest that the MCC that is pregenerated at the nuclear rim is one of the factors affected by cytoplasmic dilution after NEBD.

The Capacity of the Spindle Checkpoint to Block Anaphase Is Limited by a Large Cytoplasmic Size

The anaphase inhibitors that are preformed at the nucleus not only serve as timers for anaphase onset but also enhance the spindle checkpoint establishment (Rodriguez-Bravo et al., 2014). We tested the possibility that the cytoplasmic size-depen-

dent dilution of nuclear factors might limit the capacity of the spindle checkpoint to block anaphase when activated at kinetochores. We ectopically activated checkpoint signaling on kinetochores by expressing Mad1, a scaffold protein for checkpoint activation, which was fused to the constitutive kinetochore component CENP-C (Figure 6F) (Maldonado and Kapoor, 2011). When Mad1-CENP-C was expressed in the control oocytes, an effective block of anaphase onset was observed (Figure 6G). This block depended on the on-kinetochore checkpoint activation, because the removal of CENP-C from the construct or the introduction of mutations on the functionally critical residues of Mad1 (Kim et al., 2012) dramatically decreased the efficiency of the anaphase block (Figure S6C). When Mad1-CENP-C was expressed in the doubled oocytes, the efficiency of the anaphase block was significantly lower than that observed in the control oocytes expressing Mad1-CENP-C at the same level (Figures 6G and S6D). Furthermore, a low-level expression of Mad1-CENP-C, which was not sufficient to induce an efficient anaphase block in the control oocytes, efficiently blocked anaphase in the halved oocytes (Figures 6H and S6E). Importantly, however, when half the cytoplasmic volume was removed from oocytes <40 min after NEBD ("Halved after NEBD"), the same level of Mad1-CENP-C expression did not induce an efficient anaphase block, a result similar to that observed in the control oocytes (Figures 6H and S6E). Thus, the responsiveness to the on-kinetochore checkpoint activation depends on the nuclear-to-cytoplasmic ratio rather than on the kinetochore-to-cytoplasmic ratio. Together, these results suggest that the capacity of the spindle checkpoint to block anaphase in response to on-kinetochore activation is limited by the cytoplasmic dilution of factors that are preformed in the nucleus.

Cytoplasmic Size Limits the Capacity to Block Anaphase Onset in Response to a Small Number of Misaligned Univalents

We sought to determine whether the cytoplasmic size-dependent effect on the spindle checkpoint response creates a susceptibility to age-related defects. Increasing maternal age decreases chromosome cohesion and induces the premature separation of bivalents into univalents during meiosis I in oocytes
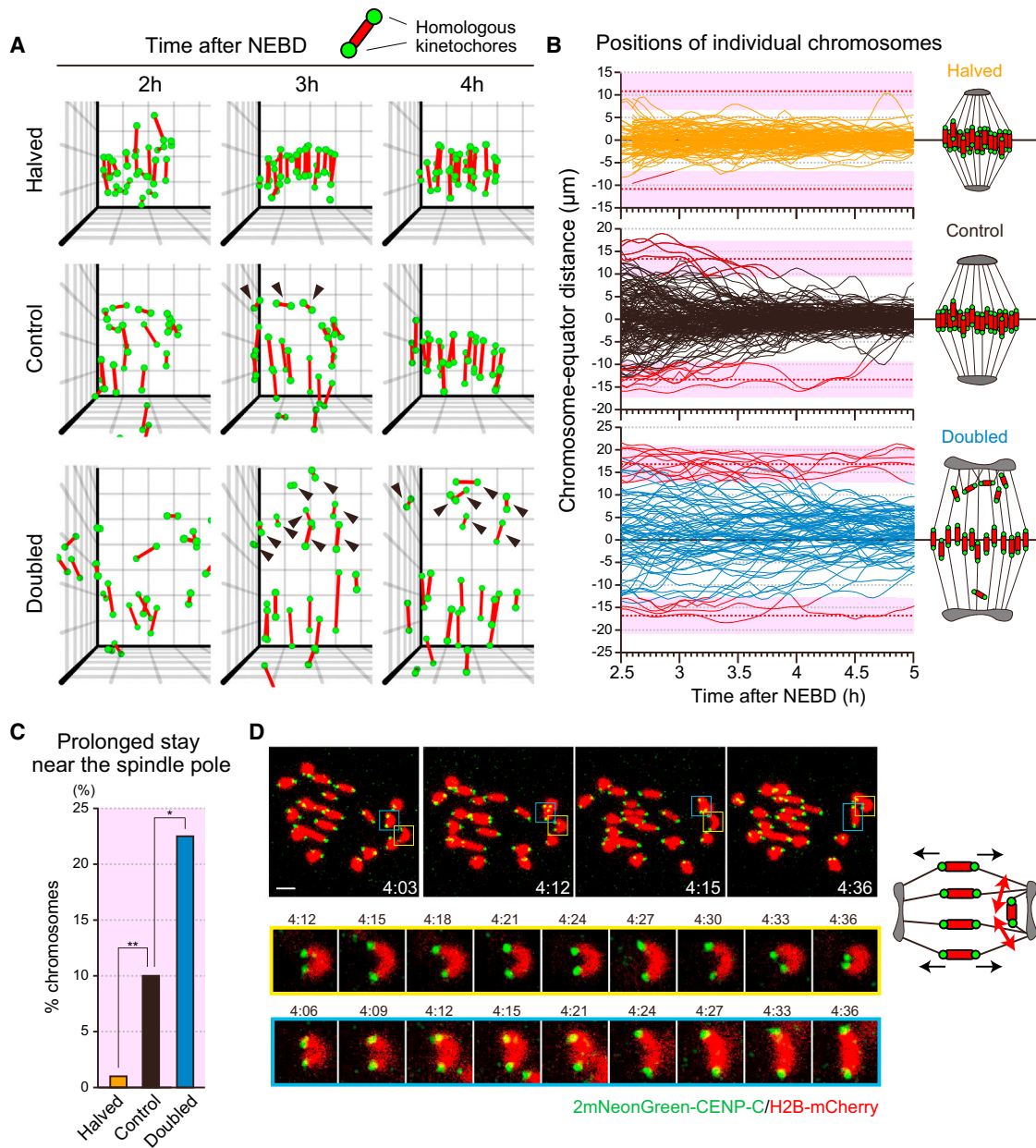
469

Figure 5. Cytoplasmic Size Affects the Efficiency of Chromosome Biorientation

(A) 3D kinetochore tracking. Kinetochore and chromosome positions were determined from images of oocytes expressing 2mNeonGreen-CENP-C and H2B-mCherry. Kinetochore positions are shown in the 3D plot as green spheres. Red bars connect the homologous kinetochores. The view along the spindle equator is shown. Black arrowheads indicate the non-bioriented chromosomes. The unit of the grid is 5 μm.

(B) A fraction of the chromosomes remain near the spindle poles. Dynamics of individual chromosomes along the spindle axis are shown (n = 100, 160, and 80 chromosomes). The positions of the poles of the metaphase spindle are shown as dashed red lines. Pink boxes indicate the positions within 4 μm of the spindle poles. Chromosome tracks that remained within 4 μm of the spindle poles for more than 30 min are indicated by red lines.

(C) Prolonged stay near the spindle poles. Chromosomes that remained within 4 μm of the spindle poles for more than 30 min (indicated by red lines in B) were counted (n = 100, 160, and 80 chromosomes). A chi-square test was performed. *$p < 0.05$, **$p < 0.01$.

(D) Intra-polar chromosome stretching. Maximum z-projection images of doubled oocytes expressing 2mNeonGreen-CENP-C (kinetochores, green) and H2B-mCherry (chromosomes, red). Kinetochore signals are peak enhanced and background subtracted. Chromosomes marked with squares are magnified at the bottom. Note that the chromosomes exhibited a transient stretching perpendicular to the spindle axis as shown in the diagram. Time after NEBD (hr:min). Scale bar, 5 μm.

See also Movies S5 and S6.
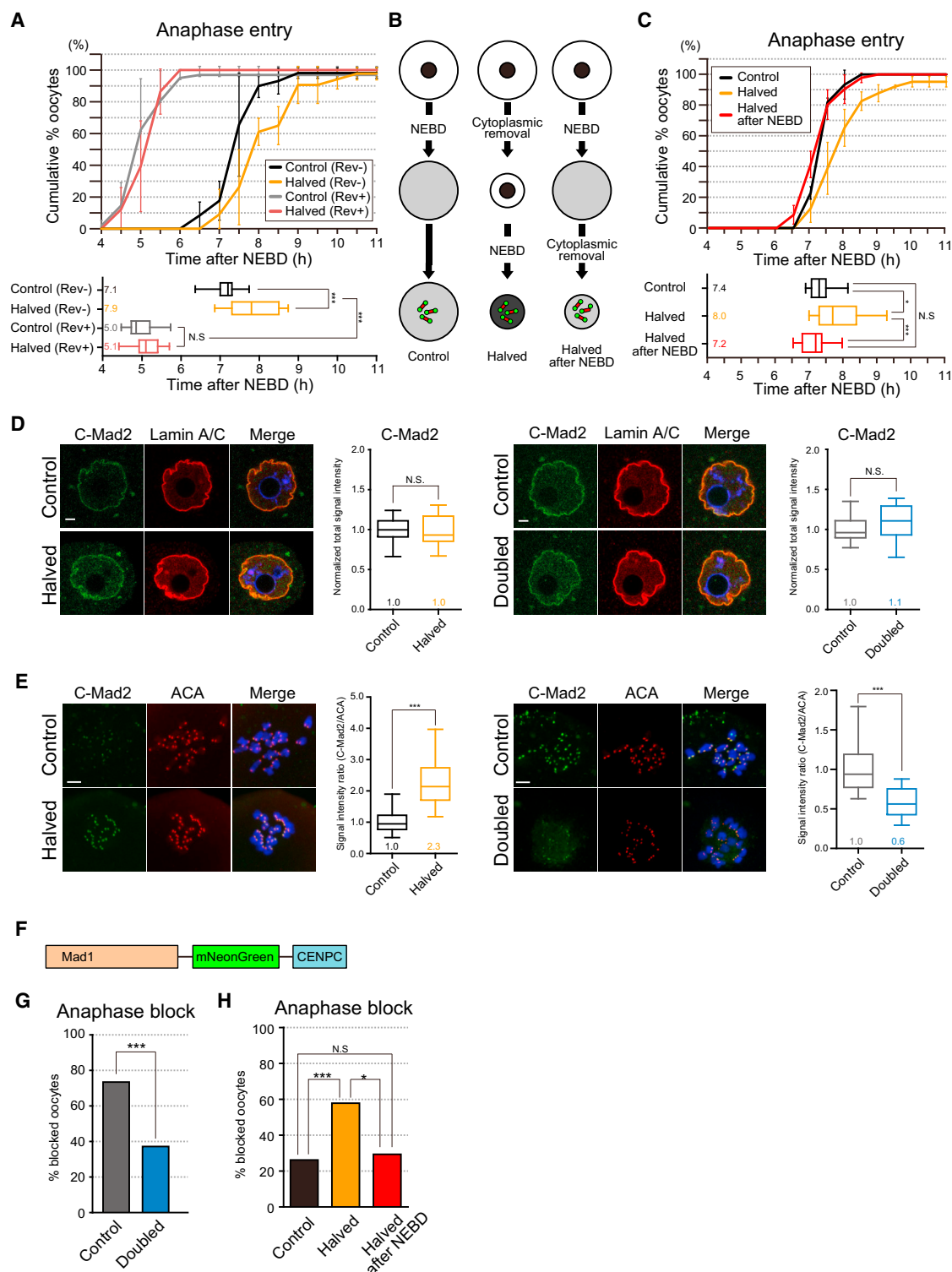
Figure 6. A Large Cytoplasmic Volume Limits the Stringency of the Spindle Checkpoint

(A) Cytoplasmic size-dependent anaphase delay depends on Mps1. Meiotic resumption was induced in oocytes expressing H2B-mCherry in the presence of 1 μM reversine, and cells were monitored for anaphase onset. The cumulative percentage of oocytes that entered anaphase is plotted (n = 4 experiments). Box graph shows the time of anaphase onset (n = 37, 35, 37, and 35 oocytes). Error bars denote SD. Boxes show the 25th–75th percentiles and whiskers the 10th–90th percentiles. Two-tailed, unpaired Student's t tests were performed. N.S., not significant. ***p < 0.001.

(B) Experimental scheme. H2B-mCherry-expressing oocytes were halved before or after NEBD and monitored for anaphase onset. Note that oocytes halved after NEBD carry a double concentration of kinetochores and an intact concentration of nucleus-derived factors.

A

Sycp3 KO with 2 misaligned univalents

2mEGFP-CENP-C/H2B-mCherry

B
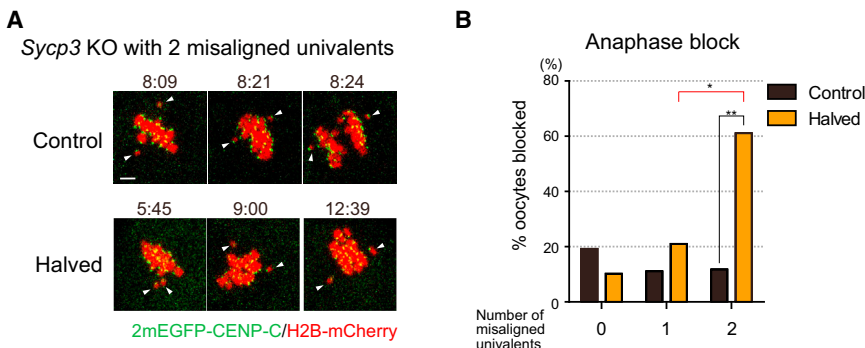
Anaphase block

Figure 7. Cytoplasmic Size Affects the Number of Misaligned Chromosomes Necessary for Anaphase Block

(A) *Sycp3* knockout (KO) oocytes with misaligned univalents. Maximum z-projection images of *Sycp3* knockout oocytes expressing 2mNeonGreen-CENP-C (kinetochores, green) and H2B-mCherry (chromosomes, red). Kinetochore signals are peak enhanced and background subtracted. Arrowheads indicate misaligned univalents. Time after NEBD (hr:min). Scale bar, 5 μm.

(B) Efficient anaphase block with a few misaligned univalents in halved oocytes. The number of misaligned chromosomes was determined by tracking individual kinetochores in 3D throughout metaphase. The percentage of metaphase-arrested oocytes 14 hr after NEBD was determined (n = 26, 39, 18, 19, 17, and 18 oocytes). Chi-square tests were performed. *p < 0.05, **p < 0.01. See also Movie S7.

(Sakakibara et al., 2015; Zielinska et al., 2015). We mimicked this age-related chromosomal defect by genetically introducing univalents into oocytes through knockout of the *Sycp3* gene (Kouznetsova et al., 2007). Univalents are known to undergo the following two distinct dynamics: (1) sister kinetochore biorientation and (2) chromosome misalignment. The former does not activate the spindle checkpoint and results in sister chromatid predivision (Kouznetsova et al., 2007; LeMaire-Adkins et al., 1997; Sakakibara et al., 2015). In contrast, the latter is thought to activate the spindle checkpoint on kinetochores, although it often fails to block anaphase and consequently results in chromosome nondisjunction (Nagaoka et al., 2011; Sakakibara et al., 2015). Using high-resolution live imaging of kinetochores and chromosomes, we monitored the *Sycp3* knockout oocytes carrying univalents that were misaligned throughout metaphase. We found that two misaligned univalents did not significantly block anaphase onset (Figures 7A and 7B; Movie S7) as previously reported (Nagaoka et al., 2011). In the halved *Sycp3* knockout oocytes, however, a significantly increased fraction with two misaligned univalents established an anaphase block, thus preventing the chromosome segregation errors (Figures 7A and 7B; Movie S6). These results suggest that cytoplasmic size increases the number of misaligned chromosomes necessary to block anaphase onset.

DISCUSSION

The efficiency of specialized cellular functions depends on appropriate cell size (Amodeo and Skotheim, 2016; Ginzberg et al., 2015; Levy and Heald, 2012). Fully grown oocytes have extraordinarily large cytoplasmic volumes, thus creating a large space to load maternal proteins and RNAs for embryonic development after fertilization (Alberts et al., 2002). Indeed, the large cytoplasmic size is critical for post-fertilization development; decreasing the cytoplasmic volume significantly decreased the capacity of the oocyte to progress through the early embryonic stages after fertilization (Figure S7). In general, nuclear size correlates with cytoplasmic size, and the nuclear-to-cytoplasmic ratio generally remains constant (Levy and Heald, 2012; Webster et al., 2009). However, the extent of size changes in the nucleus may be constrained by the genome size (Cavalier-Smith, 1982; Gregory, 2005). Indeed, in fully grown mouse oocytes the nuclear-cytoplasmic ratio is ~1:22, which is significantly smaller than that in the 2-cell stage embryo (~1:16).

A cell type-specific balance between the sizes of various intracellular compartments can support specialized cellular functions; however, it may also negatively affect the functions involved in common cellular processes, such as cell division. Our study revealed that the oocytes' uniquely large cytoplasmic volume,

(C) The nucleocytoplasmic ratio controls the timing of anaphase. The cumulative percentage of oocytes that entered anaphase is plotted (n = 4 experiments). Error bars denote SD. Box graph shows the time of anaphase onset (n = 22, 39, and 32 oocytes). Boxes show the 25th–75th percentiles and whiskers the 10th–90th percentiles. Two-tailed, unpaired Student's t tests were performed. N.S., not significant. *p < 0.05, ***p < 0.001.

(D) Immunostaining of C-Mad2 before NEBD. Oocytes were fixed at the GV stage for the staining of C-Mad2 (green), nuclear membrane (Lamin A/C, red), and DNA (Hoechst 33342, blue). Total signal intensity of C-Mad2 at the nuclear rim was measured in 3D. Normalized values are shown (n = 29, 26, 27, and 32 oocytes). Boxes show the 25th–75th percentiles and whiskers the 10th–90th percentiles. Two-tailed, unpaired Student's t test was performed. N.S., not significant. Scale bars, 5 μm.

(E) Immunostaining of kinetochore C-Mad2. Oocytes were fixed 2.5 hr after NEBD for the staining of C-Mad2 (green), kinetochores (ACA, red), and DNA (Hoechst 33342, blue). Image contrast is adjusted based on cytoplasmic signals. Normalized relative signal intensities on kinetochores (n = 28, 36, 30, and 32 oocytes) are shown. Boxes show the 25th–75th percentiles and whiskers the 10th–90th percentiles. Two-tailed, unpaired Student's t test was performed. ***p < 0.001. Scale bars, 5 μm.

(F) Schematic representation of the construct used in (G) and (H).

(G) Checkpoint response to on-kinetochore activation. Oocytes expressing Mad1-mNeonGreen-CENP-C and H2B-mCherry were monitored. Bar graph shows the percentages of metaphase-arrested oocytes 11 hr after NEBD (n = 64, 37 oocytes). Chi-square tests were performed. ***p < 0.001.

(H) Oocytes mildly expressing Mad1-mNeonGreen-CENP-C were monitored. Bar graph shows the percentages of metaphase-arrested oocytes 11 hr after NEBD (n = 42, 38, and 34 oocytes). Chi-square tests were performed. N.S., not significant. *p < 0.05, ***p < 0.001.

See also Figures S5 and S6.

472

which is essential for post-fertilization development, affects the mechanisms responsible for correct chromosome segregation during meiosis before fertilization. Decreasing the cytoplasmic volume was found to accelerate the establishment of stable chromosome biorientation and enhance the stringency of the spindle checkpoint during meiosis. Thus, cytoplasmic size is rate limiting for the efficiency of chromosome biorientation and the stringency of the spindle checkpoint in oocytes.

The large cytoplasmic volume of oocytes limits the efficiency of chromosome biorientation by affecting the capacity of the acentrosomal spindle. The large cytoplasmic volume provides a large amount of spindle components, thus leading to a proportional increase in spindle dimensions. The acentrosomal spindle, which is scaled according to the large cytoplasmic size, exhibits characteristically broad poles. Our results suggest the existence of cytoplasmic molecules that increase the spindle size and broaden the spindle poles in a dose-dependent manner. Future studies will be required to identify such molecules. The MTOC distribution on these broad poles is prone to deformation into anisotropic geometries and separation into multiple functional units, thus contributing to the error-prone chromosome biorientation. It is also possible that other cytoplasmic size-dependent effects on the spindles participate in contributing to the error-prone biorientation. The failure to establish stable chromosome biorientation, owing to the unstable bipolarity of the acentrosomal spindle, has been observed in human oocytes before chromosome segregation errors (Holubcová et al., 2015).

The second effect of a large cytoplasm is a decrease in the stringency of the spindle checkpoint. The large cytoplasm dilutes nuclear factors, thereby increasing the number of unattached kinetochores necessary to instigate checkpoint arrest. The MCC, which is preformed at the nuclear membrane and is critical for determining the checkpoint stringency (Rodriguez-Bravo et al., 2014), is one of the nuclear factors diluted by the cytoplasm. It is possible that the cytoplasmic dilution of checkpoint and MCC components, such as Mad1, Mad2, and BubR1, which were enriched in the nucleus (Figure S6F), may also contribute to lowering the checkpoint stringency. Future studies are needed to determine the critical molecules that limit checkpoint stringency in oocytes. The weakness of the spindle checkpoint contributes to chromosome segregation errors when oocytes carry misaligned chromosomes. Misaligned chromosomes are generated through age-related defects, such as the precocious separation of bivalents into univalents and the decreased function of kinetochores (Chiang et al., 2010; Lister et al., 2010; Sakakibara et al., 2015; Shomper et al., 2014; Zielinska et al., 2015). In human oocytes, chromosome misalignment due to unstable spindle bipolarity also does not block anaphase onset through the spindle checkpoint (Holubcová et al., 2015).

It is unlikely that the differences in cytoplasmic size relative to the nucleus and genome alone can explain the variability in the spindle capacity to biorient chromosomes and the checkpoint stringency in different cell types and organisms. Changes in cytoplasmic size generally occur gradually during differentiation and evolution and are accompanied by global changes in gene transcription, which should compensate for the cytoplasmic size-dependent effects. The changes in cytoplasmic size during post-fertilization embryogenesis, however, may represent an exception to this general rule. During post-fertilization embryo-

genesis, the cell size changes rapidly and dramatically at every cell division, during which transcription is silenced or limited to a specific set of genes in many species, including humans (Ko, 2016). The low level of spindle capacity and checkpoint stringency during meiosis in oocytes may serve as a safeguard against premature chromosome biorientation and excessive checkpoint stringency that may be predisposed by the decrease in cytoplasmic size during post-fertilization divisions.

In summary, this study identified the large cytoplasmic volume of oocytes as a cell-intrinsic feature linked to at least the following two error-prone processes: chromosome biorientation and spindle checkpoint. However, a large cytoplasmic volume also plays a role in supporting embryogenesis. Oocytes may thus have evolved to have a large cytoplasm that provides an optimal balance between chromosome segregation accuracy and support for embryonic development. We hypothesize that the error-prone nature of mammalian oocytes before fertilization is a trade-off of the large oocyte volume, which is important for supporting post-fertilization development.

STAR★METHODS

Detailed methods are provided in the online version of this paper and include the following:

- KEY RESOURCES TABLE
- CONTACT FOR REAGENT AND RESOURCE SHARING
- EXPERIMENTAL MODEL AND SUBJECT DETAILS
  ○ Mice
  ○ Oocyte Collection
  ○ Embryos
- METHOD DETAILS
  ○ Micromanipulation
  ○ Live Cell Imaging
  ○ Immunostaining
- QUANTIFICATION AND STATISTICAL ANALYSIS
  ○ 3D Analysis
  ○ Kinetochore Tracking
  ○ Quantification of Fluorescence Signals
  ○ Statistical Analysis

REFERENCES

Alberts, B., Johnson, A., Lewis, J., Raff, M., and Roberts, K. (2002). Eggs. In Molecular Biology of the Cell, Fourth Edition (Garland Science) https://www.ncbi.nlm.nih.gov/books/NBK26842/.

Amodeo, A.A., and Skotheim, J.M. (2016). Cell-size control. Cold Spring Harb. Perspect. Biol. 8, a019083.

Andrews, P., Ovechkina, Y., Morrice, N., Wagenbach, M., Duncan, K., Wordeman, L., and Swedlow, J. (2004). Aurora B regulates MCAK at the mitotic centromere. Dev. Cell 6, 253–268.

Bennabi, I., Terret, M.-E., and Verlhac, M.-H. (2016). Meiotic spindle assembly and chromosome segregation in oocytes. J. Cell Biol. 215, 611–619.

Breuer, M., Kolano, A., Kwon, M., Li, C.-C., Tsai, T.-F., Pellman, D., Brunet, S., and Verlhac, M.-H. (2010). HURP permits MTOC sorting for robust meiotic spindle bipolarity, similar to extra centrosome clustering in cancer cells. J. Cell Biol. 191, 1251–1260.

Cavalier-Smith, T. (1982). Skeletal DNA and the evolution of genome size. Annu. Rev. Biophys. Bioeng. 11, 273–302.

Cheeseman, I., Chappie, J., Wilson-Kubalek, E., and Desai, A. (2006). The conserved KMN network constitutes the core microtubule-binding site of the kinetochore. Cell 127, 983–997.

Chiang, T., Duncan, F., Schindler, K., Schultz, R., and Lampson, M. (2010). Evidence that weakened centromere cohesion is a leading cause of age-related aneuploidy in oocytes. Curr. Biol. 20, 1522–1528.

Chiang, T., Schultz, R., and Lampson, M. (2012). Meiotic origins of maternal age-related aneuploidy. Biol. Reprod. 86, 1–7.

Chmátal, L., Yang, K., Schultz, R.M., and Lampson, M.A. (2015). Spatial regulation of kinetochore microtubule attachments by destabilization at spindle poles in meiosis I. Curr. Biol. 25, 1835–1841.

Clift, D., and Schuh, M. (2015). A three-step MTOC fragmentation mechanism facilitates bipolar spindle assembly in mouse oocytes. Nat. Commun. 6, 7217.

Courtois, A., Schuh, M., Ellenberg, J., and Hiiragi, T. (2012). The transition from meiotic to mitotic spindle assembly is gradual during early mammalian development. J. Cell Biol. 198, 357–370.

Cui, L.-B., Huang, X.-Y., and Sun, F.-Z. (2005). Nucleocytoplasmic ratio of fully grown germinal vesicle oocytes is essential for mouse meiotic chromosome segregation and alignment, spindle shape and early embryonic development. Hum. Reprod. 20, 2946–2953.

DeLuca, J., Gall, W., Ciferri, C., Cimini, D., Musacchio, A., and Salmon, E.D. (2006). Kinetochore microtubule dynamics and attachment stability are regulated by Hec1. Cell 127, 969–982.

Diaz-Rodríguez, E., Sotillo, R., Schvartzman, J.-M., and Benezra, R. (2008). Hec1 overexpression hyperactivates the mitotic checkpoint and induces tumor formation in vivo. Proc. Natl. Acad. Sci. USA 105, 16719–16724.

Dumont, J., and Desai, A. (2012). Acentrosomal spindle assembly and chromosome segregation during oocyte meiosis. Trends Cell Biol. 22, 241–249.

Fava, L., Kaulich, M., Nigg, E., and Santamaria, A. (2011). Probing the in vivo function of Mad1:C-Mad2 in the spindle assembly checkpoint. EMBO J. 30, 3322–3336.

Galli, M., and Morgan, D. (2016). Cell size determines the strength of the spindle assembly checkpoint during embryonic development. Dev. Cell 36, 344–352.

Ganem, N., Godinho, S., and Pellman, D. (2009). A mechanism linking extra centrosomes to chromosomal instability. Nature 460, 278–282.

Gerhold, A., Labbé, J., and Maddox, P. (2016). Bigger isn't always better: cell size and the spindle assembly checkpoint. Dev. Cell 36, 244–246.

Ginzberg, M., Kafri, R., and Kirschner, M. (2015). On being the right (cell) size. Science 348, 1245075.

Good, M., Vahey, M., Skandarajah, A., Fletcher, D., and Heald, R. (2013). Cytoplasmic volume modulates spindle size during embryogenesis. Science 342, 856–860.

Gorbsky, G.J. (2015). The spindle checkpoint and chromosome segregation in meiosis. FEBS J. 282, 2471–2487.

Gregory, R.T. (2005). Genome size evolution in animals. Evol. Genome 1, 4–87.

Gui, L., and Homer, H. (2012). Spindle assembly checkpoint signalling is uncoupled from chromosomal position in mouse oocytes. Development 139, 1941–1946.

Hara, Y., and Kimura, A. (2009). Cell-size-dependent spindle elongation in the Caenorhabditis elegans early embryo. Curr. Biol. 19, 1549–1554.

Hazel, J., Krutkramelis, K., Mooney, P., Tomschik, M., Gerow, K., Oakey, J., and Gatlin, J.C. (2013). Changes in cytoplasmic volume are sufficient to drive spindle scaling. Science 342, 853–856.

Herbert, M., Levasseur, M., Homer, H., Yallop, K., Murdoch, A., and McDougall, A. (2003). Homologue disjunction in mouse oocytes requires proteolysis of securin and cyclin B1. Nat. Cell Biol. 5, 1023–1025.

Hoffmann, S., Maro, B., Kubiak, J.Z., and Polanski, Z. (2011). A single bivalent efficiently inhibits cyclin B1 degradation and polar body extrusion in mouse oocytes indicating robust SAC during female meiosis I. PLoS One 6, e27143.

Holubcová, Z., Blayney, M., Elder, K., and Schuh, M. (2015). Human oocytes. Error-prone chromosome-mediated spindle assembly favors chromosome segregation defects in human oocytes. Science 348, 1143–1147.

Howe, K., and FitzHarris, G. (2013). Recent insights into spindle function in mammalian oocytes and early embryos. Biol. Reprod. 89, 71.

Ishiguro, K., Kim, J., Fujiyama-Nakamura, S., Kato, S., and Watanabe, Y. (2011). A new meiosis-specific cohesin complex implicated in the cohesin code for homologous pairing. EMBO Rep. 12, 267–275.

Jones, K.T., and Lane, S.I. (2013). Molecular causes of aneuploidy in mammalian eggs. Development 140, 3719–3730.

Kim, S., Sun, H., Tomchick, D.R., Yu, H., and Luo, X. (2012). Structure of human Mad1 C-terminal domain reveals its involvement in kinetochore targeting. Proc. Natl. Acad. Sci. USA 109, 6549–6554.

Kitajima, T., Ohsugi, M., and Ellenberg, J. (2011). Complete kinetochore tracking reveals error-prone homologous chromosome biorientation in mammalian oocytes. Cell 146, 568–581.

Ko, M. (2016). Zygotic genome activation revisited: looking through the expression and function of Zscan4. Curr. Top. Dev. Biol. 120, 103–124.

Kolano, A., Brunet, S., Silk, A., Cleveland, D., and Verlhac, M.-H. (2012). Error-prone mammalian female meiosis from silencing the spindle assembly checkpoint without normal interkinetochore tension. Proc. Natl. Acad. Sci. USA 109, E1858–E1867.

Kouznetsova, A., Lister, L., Nordenskjöld, M., Herbert, M., and Höög, C. (2007). Bi-orientation of achiasmatic chromosomes in meiosis I oocytes contributes to aneuploidy in mice. Nat. Genet. 39, 966–968.

Kárníková, L., Urban, F., Moor, R., and Fulka, J. (1998). Mouse oocyte maturation: the effect of modified nucleocytoplasmic ratio. Reprod. Nutr. Dev. 38, 665–670.

Lane, S., and Jones, K. (2014). Non-canonical function of spindle assembly checkpoint proteins after APC activation reduces aneuploidy in mouse oocytes. Nat. Commun. 5, 3444.

Lane, S.I., Yun, Y., and Jones, K.T. (2012). Timing of anaphase-promoting complex activation in mouse oocytes is predicted by microtubule-kinetochore attachment but not by bivalent alignment or tension. Development 139, 1947–1955.

LeMaire-Adkins, R., Radke, K., and Hunt, P. (1997). Lack of checkpoint control at the metaphase/anaphase transition: a mechanism of meiotic nondisjunction in mammalian females. J. Cell Biol. 139, 1611–1619.

Levy, D., and Heald, R. (2012). Mechanisms of intracellular scaling. Annu. Rev. Cell Dev. Biol. 28, 113–135.

Lister, L., Kouznetsova, A., Hyslop, L., Kalleas, D., Pace, S., Barel, J., Nathan, A., Floros, V., Adelfalk, C., Watanabe, Y., et al. (2010). Age-related meiotic segregation errors in mammalian oocytes are preceded by depletion of cohesin and Sgo2. Curr. Biol. 20, 1511–1521.

Lombillo, V.A., Nislow, C., Yen, T.J., Gelfand, V.I., and McIntosh, J.R. (1995). Antibodies to the kinesin motor domain and CENP-E inhibit microtubule depolymerization-dependent motion of chromosomes in vitro. J. Cell Biol. 128, 107–115.

London, N., and Biggins, S. (2014). Signalling dynamics in the spindle checkpoint response. Nat. Rev. Mol. Cell Biol. 15, 736–747.

Maldonado, M., and Kapoor, T.M. (2011). Constitutive Mad1 targeting to kinetochores uncouples checkpoint signalling from chromosome biorientation. Nat. Cell Biol. 13, 475–482.

Marshall, W. (2015). Subcellular size. Cold Spring Harb. Perspect. Biol. 7, a019059.

McGuinness, B.E., Anger, M., Kouznetsova, A., Gil-Bernabé, A.M., Helmhart, W., Kudo, N.R., Wuensche, A., Taylor, S., Hoog, C., Novak, B., et al. (2009). Regulation of APC/C activity in oocytes by a Bub1-dependent spindle assembly checkpoint. Curr. Biol. 19, 369–380.

Musacchio, A. (2015). The molecular biology of spindle assembly checkpoint signaling dynamics. Curr. Biol. 25, R1002–R1018.

Nagaoka, S., Hodges, C., Albertini, D., and Hunt, P. (2011). Oocyte-specific differences in cell-cycle control create an innate susceptibility to meiotic errors. Curr. Biol. 21, 651–657.

Nagaoka, S., Hassold, T., and Hunt, P. (2012). Human aneuploidy: mechanisms and new insights into an age-old problem. Nat. Rev. Genet. 13, 493–504.

Novakova, L., Kovacovicova, K., Dang-Nguyen, T., Sodek, M., Skultety, M., and Anger, M. (2016). A Balance between nuclear and cytoplasmic volumes controls spindle length. PLoS One 11, e0149535.

Peters, J.-M. (2006). The anaphase promoting complex/cyclosome: a machine designed to destroy. Nat. Rev. Mol. Cell Biol. 7, 644–656.

Rabut, G., and Ellenberg, J. (2004). Automatic real-time three-dimensional cell tracking by fluorescence microscopy. J. Microsc. 216, 131–137.

Rieder, C.L., Cole, R.W., Khodjakov, A., and Sluder, G. (1995). The checkpoint delaying anaphase in response to chromosome monoorientation is mediated by an inhibitory signal produced by unattached kinetochores. J. Cell Biol. 130, 941–948.

Rodriguez-Bravo, V., Maciejowski, J., Corona, J., Buch, H., Collin, P., Kanemaki, M., Shah, J., and Jallepalli, P. (2014). Nuclear pores protect genome integrity by assembling a premitotic and Mad1-dependent anaphase inhibitor. Cell 156, 1017–1031.

Sakakibara, Y., Hashimoto, S., Nakaoka, Y., Kouznetsova, A., Höög, C., and Kitajima, T. (2015). Bivalent separation into univalents precedes age-related meiosis I errors in oocytes. Nat. Commun. 6, 7550.

Santaguida, S., Tighe, A., D'Alise, A., Taylor, S., and Musacchio, A. (2010). Dissecting the role of MPS1 in chromosome biorientation and the spindle checkpoint through the small molecule inhibitor reversine. J. Cell Biol. 190, 73–87.

Sayaka, W., Satoshi, K., Thuan, N., Hiroshi, O., Takafusa, H., Eiji, M., Thuy, B., Masashi, M., and Teruhiko, W. (2008). Effect of volume of oocyte cytoplasm on embryo development after parthenogenetic activation, intracytoplasmic sperm injection, or somatic cell nuclear transfer. Zygote 16, 211–222.

Schindelin, J., Arganda-Carreras, I., Frise, E., Kaynig, V., Longair, M., Pietzsch, T., Preibisch, S., Rueden, C., Saalfeld, S., and Schmid, B. (2012). Fiji: an open-source platform for biological-image analysis. Nat. Methods 9, 676–682.

Schuh, M., and Ellenberg, J. (2007). Self-organization of MTOCs replaces centrosome function during acentrosomal spindle assembly in live mouse oocytes. Cell 130, 484–498.

Sebestova, J., Danylevska, A., Dobrucka, L., Kubelka, M., and Anger, M. (2014). Lack of response to unaligned chromosomes in mammalian female gametes. Cell Cycle 11, 3011–3018.

Shao, H., Li, R., Ma, C., Chen, E., and Liu, J. (2013). Xenopus oocyte meiosis lacks spindle assembly checkpoint control. J. Cell Biol. 201, 191–200.

Shomper, M., Lappa, C., and FitzHarris, G. (2014). Kinetochore microtubule establishment is defective in oocytes from aged mice. Cell Cycle 13, 1171–1179.

Silkworth, W.T., Nardi, I.K., Scholl, L.M., and Cimini, D. (2009). Multipolar spindle pole coalescence is a major source of kinetochore mis-attachment and chromosome mis-segregation in cancer cells. PLoS One 4, e6564.

Takeuchi, T., Ergün, B., Huang, T.H., Rosenwaks, Z., and Palermo, G.D. (1999). A reliable technique of nuclear transplantation for immature mammalian oocytes. Hum. Reprod. 14, 1312–1317.

Verlhac, M.-H., and Terret, M.-E. (2016). Oocyte maturation and development. F1000Res. 5, http://dx.doi.org/10.12688/f1000research.7892.1.

Webster, A., and Schuh, M. (2017). Mechanisms of aneuploidy in human eggs. Trends Cell Biol. 27, 55–68.

Webster, M., Witkin, K., and Cohen-Fix, O. (2009). Sizing up the nucleus: nuclear shape, size and nuclear-envelope assembly. J. Cell Sci. 122, 1477–1486.

Yoshida, S., Kaido, M., and Kitajima, T. (2015). Inherent instability of correct kinetochore-microtubule attachments during meiosis I in oocytes. Dev. Cell 33, 589–602.

Zielinska, A.P., Holubcova, Z., Blayney, M., Elder, K., and Schuh, M. (2015). Sister kinetochore splitting and precocious disintegration of bivalents could explain the maternal age effect. Elife 4, e11389.

475

Report

Testis-Specific Histone Variant *H3t* Gene Is Essential for Entry into Spermatogenesis

Graphical Abstract
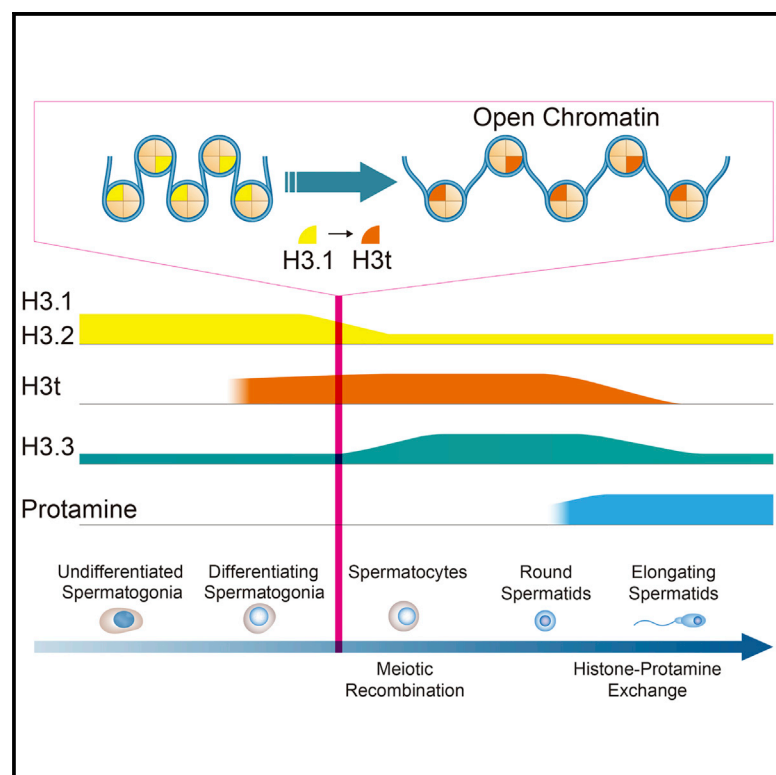
Authors

Jun Ueda, Akihito Harada,
Takashi Urahama, ..., Yasuyuki Ohkawa,
Hitoshi Kurumizaka, Kazuo Yamagata

Correspondence

junueda@isc.chubu.ac.jp (J.U.),
yamagata@waka.kindai.ac.jp (K.Y.)

In Brief

When undifferentiated spermatogonia enter differentiation, they go through meiotic recombination followed by histone-protamine transition, eventually to become highly specialized haploid cells called spermatozoa. Ueda et al. reveal a testis-specific histone variant H3t that enables nucleosomes to form an open chromatin structure and is essential for the initial step of spermatogenesis. *H3t* deficiency leads to azoospermia.

Highlights

- H3t is essential for spermatogenesis, and loss leads to azoospermia

- H3t is expressed in differentiating spermatogonia but lost from spermatozoa

- H3t is required for spermatogonial differentiation and ensures entry into meiosis

- H3t-containing nucleosomes form an open chromatin structure

Accession Numbers

5B1L
5B1M

CellPress

Testis-Specific Histone Variant *H3t* Gene Is Essential for Entry into Spermatogenesis

Jun Ueda,[1,2,10,11,*] Akihito Harada,[3,10] Takashi Urahama,[4,10] Shinichi Machida,[4] Kazumitsu Maehara,[3] Masashi Hada,[5] Yoshinori Makino,[5] Jumpei Nogami,[3] Naoki Horikoshi,[4] Akihisa Osakabe,[4] Hiroyuki Taguchi,[4] Hiroki Tanaka,[4] Hiroaki Tachiwana,[4] Tatsuma Yao,[6,9] Minami Yamada,[1] Takashi Iwamoto,[1] Ayako Isotani,[2] Masahito Ikawa,[2] Taro Tachibana,[7] Yuki Okada,[5] Hiroshi Kimura,[8] Yasuyuki Ohkawa,[3] Hitoshi Kurumizaka,[4] and Kazuo Yamagata[2,9,*]

[1]Center for Education in Laboratory Animal Research, Chubu University, Kasugai, Aichi 487-8501, Japan
[2]Center for Genetic Analysis of Biological Responses, Research Institute for Microbial Diseases, Osaka University, 3-1 Yamadaoka, Suita 565-0871, Japan
[3]Division of Transcriptomics, Medical Institute of Bioregulation, Kyushu University, Fukuoka 812-8582, Japan
[4]Laboratory of Structural Biology, Graduate School of Advanced Science & Engineering, Waseda University, Tokyo 162-8480, Japan
[5]Laboratory of Pathology and Development, Institute of Molecular and Cellular Biosciences, University of Tokyo, Tokyo 113-0032, Japan
[6]Research and Development Center, Fuso Pharmaceutical Industries, Ltd., Osaka 536-8523, Japan
[7]Department of Bioengineering, Graduate School of Engineering, Osaka City University, Osaka 558-8585, Japan
[8]Graduate School of Bioscience and Biotechnology, Tokyo Institute of Technology, 4259 Nagatsuta-cho, Midori-ku, Yokohama 226-8501, Japan
[9]Faculty of Biology-Oriented Science and Technology, Kindai University, Kinokawa, Wakayama 649-6493, Japan
[10]Co-first author
[11]Lead Contact
*Correspondence: junueda@isc.chubu.ac.jp (J.U.), yamagata@waka.kindai.ac.jp (K.Y.)
http://dx.doi.org/10.1016/j.celrep.2016.12.065

SUMMARY

Cellular differentiation is associated with dynamic chromatin remodeling in establishing a cell-type-specific epigenomic landscape. Here, we find that mouse testis-specific and replication-dependent histone H3 variant H3t is essential for very early stages of spermatogenesis. *H3t* gene deficiency leads to azoospermia because of the loss of haploid germ cells. When differentiating spermatogonia emerge in normal spermatogenesis, H3t appears and replaces the canonical H3 proteins. Structural and biochemical analyses reveal that H3t-containing nucleosomes are more flexible than the canonical nucleosomes. Thus, by incorporating H3t into the genome during spermatogonial differentiation, male germ cells are able to enter meiosis and beyond.

INTRODUCTION

When stem cells are committed to enter certain cell lineages, they undergo epigenetic and chromatin remodeling to acquire unique genomic structures that ensure the stability of their fate. The fundamental unit of chromatin is the nucleosome, consisting of ~150 bp DNA and two copies each of histones H2A, H2B, H3, and H4 (Luger et al., 1997). Modifications of histones, especially those of H3, affect the nucleosome structure and consequently play pivotal epigenetic roles in gene regulation (Strahl and Allis, 2000; Goldberg et al., 2007). In addition, the incorporation of nonallelic H3 variants that harbor a few to several amino acid differences into specific genomic loci are thought to play an

important role in changing the chromatin structure and gene regulation during differentiation (Maze et al., 2014; Talbert and Henikoff, 2010). It has been proposed that these might be linked to specific genomic loci, where they act like barcodes with distinct functions (Hake and Allis, 2006). Recently, histone H3 variants of human and mouse have been identified by in silico hybridization screening (Maehara et al., 2015). Some of these variants showed tissue-specific expression, but their significance in cellular and tissue functions remained elusive. Whereas most of the newly identified mouse variants do not have human orthologs and are likely to be derived from H3.3, H3t has a human counterpart, H3T (H3.4) (Witt et al., 1996) and shares a common chaperon recognition motif with H3.1 and H3.2 (Figure 1A), which was then shown to be incorporated into the genome in a replication-coupled manner (Maehara et al., 2015).

RESULTS AND DISCUSSION

H3t Deficiency Leads to Male Infertility in Mice

We first analyzed the expression pattern of H3t in various tissues on the FANTOM5 mouse promoterome database deposited in ZENBU (http://fantom.gsc.riken.jp/zenbu) (Table S1), then confirmed its expression by qRT-PCR amplified with primer sets designed from 5′ cap analysis of gene expression (CAGE) and 3′-sequence (seq) data (Figures S1A and S1B) (Maehara et al., 2015). Consistent with our previous result (Maehara et al., 2015), *H3t* mRNA was specifically expressed in the testis (Figures S1A and S1B; Table S1).

To establish the significance of H3t, we used the CRISPR/Cas9 gene-editing method to generate knockout mice (Mashiko et al., 2013). This gene was located near histone cluster 3 of chromosome 11 and within another gene called *Trim17* (Figure S1C), which made it difficult to disrupt by conventional
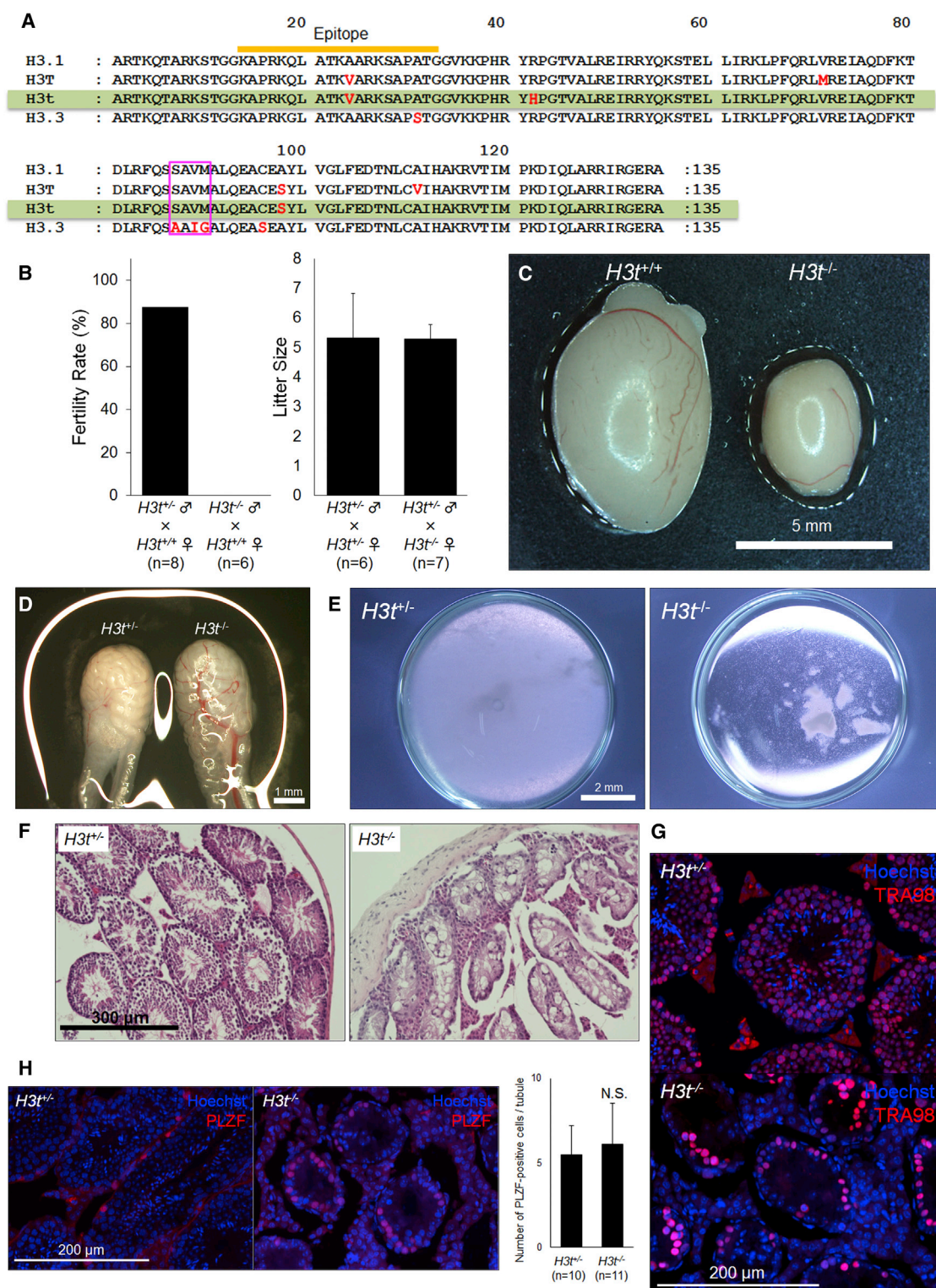
Figure 1. H3t Functions in Spermatogenesis and Is Essential for Male Fertility

(A) Amino acid sequence alignment of histone variants H3.1, H3T, H3t, and H3.3. Amino acids unique to each variant in comparison with H3.1 are highlighted in red. The chaperon recognition motif is boxed in pink, and the epitope used to generate an anti-H3t antibody is indicated (orange bar).

(B) Fertility rate (left) and litter size (right) of *H3t* null mice. *H3t*-homozygous knockout male mice were infertile, whereas the female mice had fertility similar to heterozygous ones.

478

gene-targeting methods. As shown in Figures S1D–S1F, we succeeded in generating an *H3t* null mouse line, which lacked 16 nt including the start codon. Although both male and female knockout mice were viable and healthy, the male mice turned out to be sterile (Figures 1B, S1G, and S1H). In line with this phenotype, *H3t* null mice had strikingly smaller testes compared with wild-type and heterozygous knockout mice (Figures 1C and S1I). Moreover, the caudae epididymides of *H3t* null mice were transparent and lacked spermatozoa (Figures 1D and 1E). There were no indels at the top-scoring potential off-target sites (Figure S1J). Additionally, small testes and infertility were also observed in a different *H3t* knockout founder mouse, generated using the CRISPR/Cas9 method (Figure S1K). These data suggest that these phenotypes were not caused by off-target effects.

In the testis, stem cells are located at the periphery of the seminiferous tubules, and when these cells enter differentiation, they migrate toward the center (Yoshida, 2012). At the onset of differentiation, undifferentiated spermatogonia yield differentiating spermatogonia via reversible, flexible, and stochastic mechanisms (Yoshida, 2012). After premeiotic replication, these differentiating spermatogonia undergo dynamic chromatin remodeling along with meiotic recombination and histone-to-protamine transitions to become highly specialized haploid cells called spermatids (Maze et al., 2014; Talbert and Henikoff, 2010; Bowles and Koopman, 2007).

Next, we analyzed *H3t* null testes in detail to investigate the possible cause of infertility. Intriguingly, although germ cells were retained in these organs, elongating and acrosome-positive spermatids were absent in the *H3t*-deficient testes (Figures 1F, 1G, and S2A), and most of the seminiferous tubules lacked synaptonemal complex protein 3 (SCP3)-positive cells (Figure S2A). These observations suggest that the defect possibly occurs before meiosis. Then we stained seminiferous tubules with stage-specific markers to reveal to what extent germ cells are restored in *H3t* null testes. As shown in Figures 1H and S2B, *H3t* null testes retained promyelocytic leukemia zinc finger (PLZF)-positive undifferentiated spermatogonia comparable with that of control, but the numbers of c-Kit-positive differentiating spermatogonia and γH2A.X histone variant-positive spermatocytes were decreased significantly in the *H3t*-deficient testis. Thus, H3t is likely to function at an early stage of spermatogenesis, probably at the premeiotic differentiation and/or replication stage. From these data, we conclude that *H3t* deficiency leads to azoospermia stemming from spermatogenic failure, but not from other male reproductive tract abnormalities.

To determine the timing of the deficiency more precisely, we investigated earlier stages of spermatogenesis. In testes from 4-week-old mice, the first wave of spermatogenesis was already impaired in the *H3t*-deficient mice (Figures S2C and S2D),

implying that H3t is essential for the initial step of spermatogenesis, and that the loss of germ cells is not caused by aging. Although gonocytes were present in the *H3t* null testes (Figures S2E and S2F), immunostaining for TRA98 (a germ-cell-specific marker) in germ cells started to decline from postnatal day (P) 10 testes, around the time at which spermatocytes emerge and begin to expand (Meikar et al., 2011); this defect became more severe at later stages, and germ cells eventually died via apoptosis (Figures S2G–S2I). These results suggest that H3t is required for spermatogonia (i.e., spermatogenic stem cells) to enter differentiation.

H3t Is Expressed from Differentiating Spermatogonia but Lost from Spermatozoa

To understand the tissue distribution and expression pattern of the H3t protein responsible for the knockout phenotype, we developed an H3t-specific monoclonal antibody targeted against the Val 24 amino acid, which is specific to both H3t and H3T (Figures 1A and S3A–S3E). Consistent with the gene expression data, immunoblotting showed the existence of H3t protein exclusively in the testis among various tissues examined including the ovary (Figures 2A and S3D). However, unlike the H3.3 variant, the H3t protein was absent from mature spermatozoa (Figure 2B), implying that H3t is replaced with the H3.3 variant (van der Heijden et al., 2005; Santenard et al., 2010) and/or protamines during spermatogenesis, so it might not act as a sperm-borne paternal epigenetic memory to offspring (Talbert and Henikoff, 2010). Next, testes from mice showing the first wave of spermatogenesis were examined by immunoblotting. We found that H3t became apparent from P8 to P10, implying that H3t is induced when differentiating spermatogonia emerge, and slightly earlier than the expression of TH2B, a testis-specific histone H2B (Figures 2C, S3F, and S3G) (Shinagawa et al., 2015). Moreover, in testicular sections, canonical H3.1/3.2-type histones were expressed from PLZF-positive undifferentiated spermatogonia (Figure S3H), and these became stronger in c-Kit-positive differentiating spermatogonia, but rapidly lost in spermatocytes and later stages (Figure 2D). In contrast, H3t expression was not observed in PLZF-positive undifferentiated spermatogonia (Figure 2E), but was in c-Kit-positive differentiating spermatogonia. Although *H3t*-deficient germ cells showed defects in an earlier stage, the H3t protein level peaked at the spermatocyte stage, and eventually diminished at the elongating spermatid stage (Figure 2D), indicating that it might also have functions during meiosis and spermiogenesis. Finally, we found that H3t is distributed throughout the genome but is excluded from the X-Y body (Figures 2F and S3I), which is consistent with the replacement of H3.1/3.2-type variants with H3.3 during meiotic sex chromosome inactivation (van der Heijden et al., 2007). Because the X-Y body contains less unsynapsed regions

---

(C–E) Abnormalities of the reproductive tracts of *H3t* null male mice, showing the testis (C), cauda epididymidis (D), and cells dispersed from the cauda epididymidis (E). Note that the cauda epididymidis of *H3*−/− mice was relatively transparent compared with that of *H3t*+/− mice (D), because there were no spermatozoa present in the lumen.

(F) H&E staining of testis sections.

(G) Germ cells were retained in *H3t* null testes. Testes were stained with an anti-TRA98 antibody (a pan-germ cell marker), counterstained with Hoechst 33342.

(H) Undifferentiated spermatogonia were unaffected in *H3t* null testes. Testes were stained with an anti-PLZF antibody, counterstained with Hoechst 33342 (left panel). The number of PLZF-positive cells was counted and indicated as the bar chart (right panel). NS, not significant.
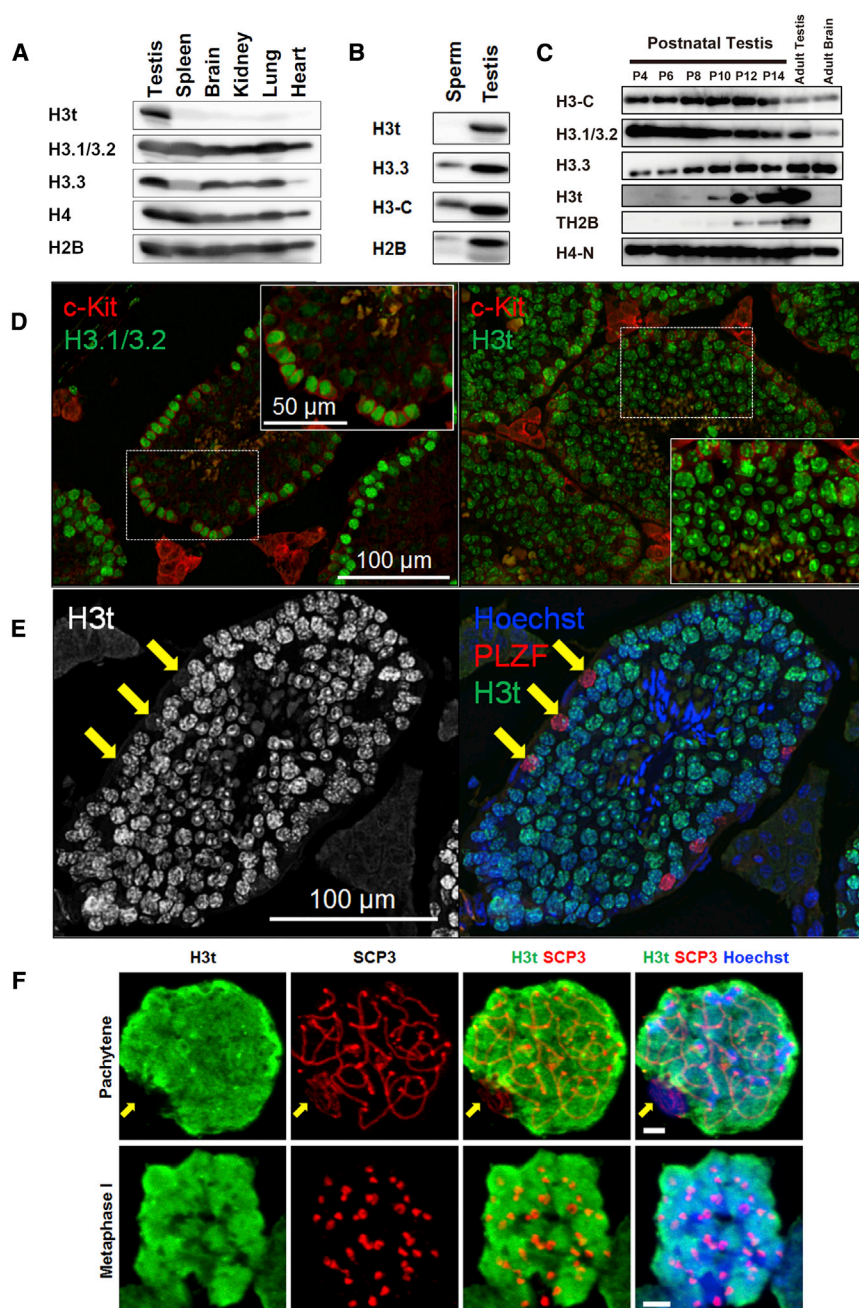
Figure 2. Expression and Functional Timing of H3t Protein Expression in Spermatogenesis

(A–C) Western blot analysis of histone variants in mouse tissues (A), sperm (B), and testes from postnatal mice (P4–P14) (C). H3-C and H4-N represent antibodies against the C-terminal region of H3 and the N-terminal region of H4, respectively, and these recognize all of the H3 and H4 variants.

(D) Immunostaining of testis sections by antibodies against H3.1/3.2 (left) and H3t (right) (green). Both sections were co-stained with an anti-c-Kit antibody (red). Magnified images of boxed areas are shown in each panel.

(E) H3t is expressed from differentiating spermatogonia. Note that H3t is not expressed in PLZF-positive undifferentiated spermatogonia (arrows).

(F) H3t is distributed throughout the genome, but excluded from the X-Y body. Meiotic chromosome spreads were stained with anti-H3t and -SCP3 antibodies. Arrows indicate the X-Y body in pachytene chromosomes. Scale bars, 2 μm.

in vitro, we used a GS cell differentiation system. As expected from the nature of undifferentiated spermatogonia, H3t was absent from undifferentiated wild-type GS cells, but was induced by retinoic acid upon differentiation (Figures 3C, 3D, S3D, and S3J). Confirming that H3t is dispensable for GS cell self-renewal and maintenance of undifferentiated spermatogonia, we successfully established multiple *H3t* null GS cell lines (Figures 3A and 3B). Once the cells were induced to undergo differentiation, "linked-together" morphology appeared in wild-type GS cells, whereas this was hardly observed in *H3t*-deficient cells (Figures 3C–3E) (Dann et al., 2008). This suggests that H3t is also required for GS cell differentiation in vitro. Furthermore, the total H3 protein level in differentiated *H3t*-deficient GS cells was not significantly attenuated compared with wild-type cells (Figure 3D, shown by H3-C), indicating that the differentiation defect observed is not caused by under-dosage of H3 protein level within the nucleus.

compared with autosomes, it is interesting to speculate that H3t is involved in chromosome pairing.

H3t Is Required for Spermatogonial Differentiation and Ensures Entry into Meiosis

Germline stem (GS) cells are known to maintain the characteristics of undifferentiated spermatogonia in media containing glial cell line-derived neurotrophic factor (GDNF), but when treated with retinoic acid they undergo differentiation (Dann et al., 2008; Kanatsu-Shinohara et al., 2004; Bowles and Koopman, 2007). To recapitulate this spermatogonial differentiation defect

The differentiation defect in *H3t*-deficient testes was further validated by mRNA-seq analysis with P10 testes, the stage when germ cells started to show abnormalities (Figure S2G). Although most gene expression was not affected (Figure S4A), the expression levels of genes associated with meiosis as well as other germ-cell-specific histone variants were found to be significantly dysregulated in the *H3t*-deficient testis, and these results were further confirmed in GS cells (Figures 3F–3H and S4B–S4D). Hence, loss of H3t seemed to impair entry into
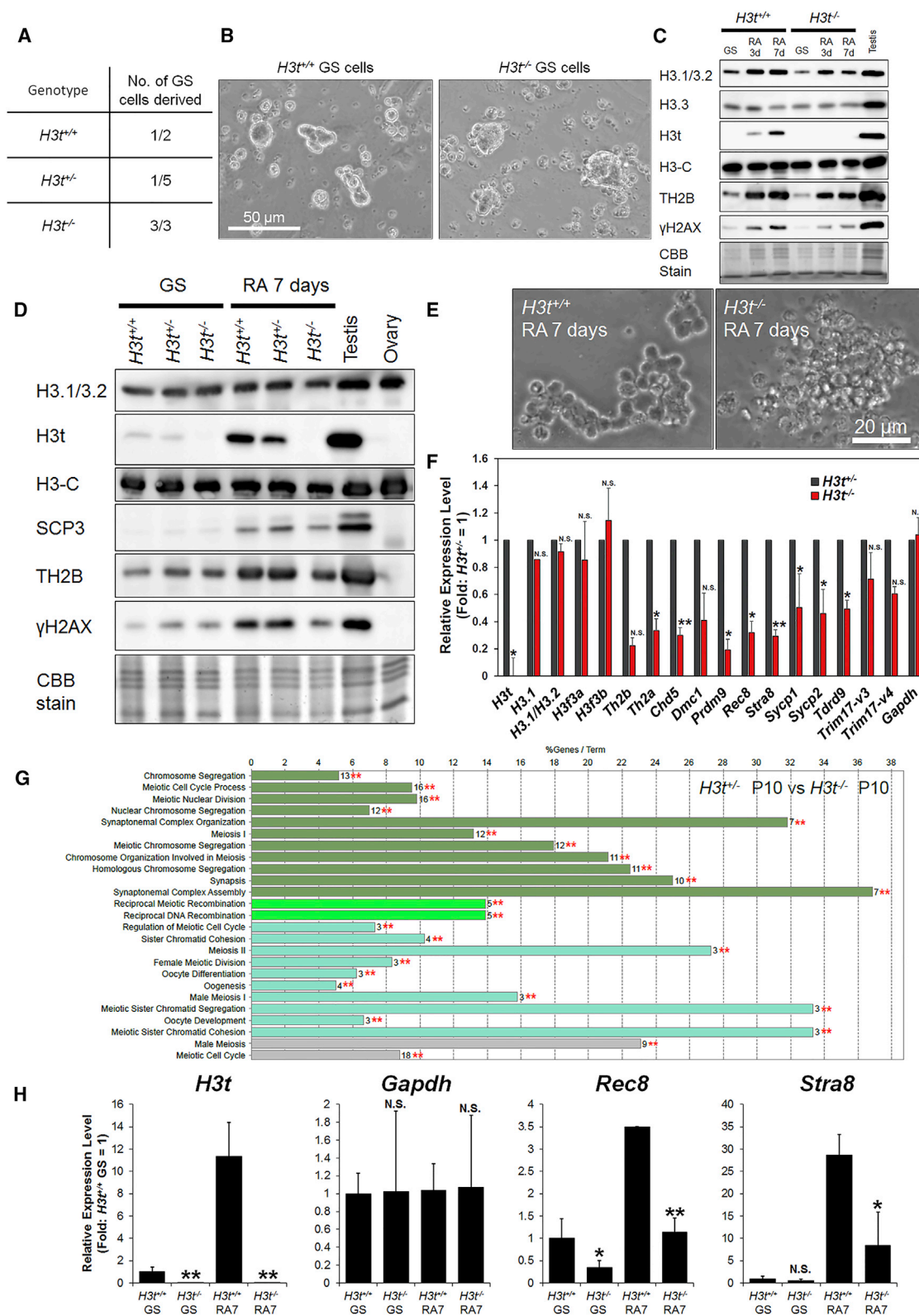
Figure 3. H3t Is Expressed upon Spermatogonial Differentiation and Ensures Entry into Meiosis

(A and B) Derivation of GS cell lines from *H3t* null testes. Note that these lines were established regardless of their genotypes (A), and there was no difference in their morphologies at the light microscopic level (B).

meiosis. Moreover, we noted that *Trim17* was not expressed in neonate testes, but highly expressed in adult testes, and its protein expression level was affected in *H3t* heterozygous knockout adult testes (Figures 3F, S4B, and S4C). These results suggest that, although *H3t* and *Trim17* genes are expressed at different time points, early expressed *H3t* gene seems to have a positive effect on the following *Trim17* gene expression. Taken together with the GS cell data, H3t appears to be induced upon spermatogonial differentiation and possibly replaces canonical H3 proteins, which have been utilized during stem cell replication, ensuring that differentiating spermatogonia can progress into meiosis and beyond.

H3t-Containing Nucleosomes Form Open Chromatin Structure

Our results suggest that the other canonical H3 variants cannot compensate for the functions of H3t in the testis, even though there are only three amino acid differences between H3t and H3.1 (Figure 1A). To gain more insights into its molecular properties, we performed structural and biochemical analyses of the H3t nucleosome. Tachiwana et al. (2010) previously reported that human H3T-containing nucleosomes formed less stable structures than those containing canonical H3.1, by analyzing their crystal structures and biochemical properties. However, the human H3T M71 and V111 residues, which are responsible for instability of the H3T-containing nucleosome, are not conserved in H3t (Figure 1A). Salt and thermal stability assays for the H3t nucleosome revealed that the H3t nucleosome was not substantially unstable compared with the H3.1 nucleosome (Figures S4E and S4F). Therefore, we focused on the H3t-specific H42 residue, which is located near the DNA entry-exit region of the nucleosome. In the H3.1 nucleosome, the basic R42 side chain, corresponding to the H3t H42 residue, forms electrostatic interactions with DNA backbones located at the entry-exit and the nucleosomal dyad regions (Figure 4B, right panel). In contrast, the H42 side chain of H3t is less basic, and this weakens the electrostatic interactions between H3t and DNA around the entry-exit DNA regions of the nucleosome (Figure 4B, left panel). This finding led us to speculate that the DNA around the entry-exit regions in the H3t nucleosome is more flexible than that of the H3.1 nucleosome. To test this possibility, we performed micrococcal nuclease (MNase) and exonuclease III (ExoIII) treatment assays, because these enzymes preferentially degrade DNA that is detached flexibly from histone surfaces. As shown in Figures 4C and 4D, the H3t nucleosome was more sensitive to both MNase and ExoIII, and these were further confirmed by reciprocal amino acid substitutions. That is, the H3.1 R42H nucleosome became sensitive to nuclease digestions, whereas the H3t H42R nucleosome became resistant. Therefore, we conclude that the H42 residue of H3t endows DNA with flexibility at the entry-exit regions of the H3t nucleosome. Last, we tested whether the DNA end flexibility of the H3t nucleosome might result in an open configuration of the chromatin. To this end, we reconstituted polynucleosomes and performed analytical ultracentrifugation assays (Figures S4G–S4J). In good agreement with the above findings, the H3t-containing polynucleosome formed a more open structure than that for H3.1, in the presence and absence of $MgCl_2$ (Figure 4E). Therefore, this unique biochemical property of H3t arising from a single amino acid substitution might give instability between DNA and nucleosomes, and consequently provide an open chromatin structure that is necessary for germ cells to progress into spermatogenesis.

Amino acid sequence implied that H3t is incorporated into chromatin during DNA replication; our results also indicated that H3t is induced upon spermatogonial differentiation, eventually distributed throughout the genome, except for the X-Y body. Because spermatogonia are the only cell types that undergo mitotic replication during spermatogenesis, it is likely that canonical H3 histones are exchanged with H3t while the differentiating spermatogonia are replicating. Consequently, this dynamic exchange of H3 variants might ensure entry into meiosis. Although we did not observe any clear decrease in the total H3 protein in in vitro-differentiated *H3t*-deficient cells (Figure 3D), and no global gene expression alterations were observed in *H3t*-deficient P10 testis (Figure S4A), our present study cannot fully exclude the possibility that the defects observed in vivo might be a mere effect of H3 protein under-dosage. To this end, it will be important to generate knock-in mice, in which H3t is replaced with the H42R point mutant and/or H3.1, and investigate their effects on spermatogenesis. Nevertheless, how the H3t-specific open chromatin structure affects spermatogenesis is of particular interest. Because the phenotype of *H3t*-deficient mice is rather severe compared with known knockout mice of histone modification-related genes (Sasaki and Matsui, 2008), we speculate that H3t, together with other histone variants (Shinagawa et al., 2015; Montellier et al., 2013;

(C) H3t is induced upon GS cell differentiation and protein level increases during this process. GS cells from *H3t*^{+/+} or *H3t*^{−/−} mice were treated with retinoic acid (RA) for indicated days; total proteins were extracted, electrophoresed, and probed with the indicated antibodies.

(D) Expression level of histone variants in GS cells, before and after the induction of differentiation. *H3t*^{+/+}, *H3t*^{+/−}, or *H3t*^{−/−} GS cells were treated with RA for 7 days; total proteins were extracted, electrophoresed, and probed with the indicated antibodies. CBB stain data are indicated as a loading control. Note that there was no drastic reduction in the total H3 protein level in *H3t*^{−/−} GS cells after the induction of differentiation (indicated by H3-C antibody).

(E) Morphologies of GS cells 7 days after the induction of differentiation with RA. The *H3t*^{−/−} GS cells seldom showed "linked-together" morphology.

(F) Meiosis-related genes were less strongly expressed in the testes of *H3t*^{−/−} mice than in *H3t*^{+/−} mice at P10. The expression levels of the indicated mRNAs were analyzed by RT-qPCR. The values in the *H3t*^{+/−} mouse were set to 1 following normalization against the *Eef1a1* expression level. Data represent the mean of three independent experiments ± SD. *$p < 0.05$; **$p < 0.01$. NS, not significant.

(G) Meiosis-related phenotypes were preferentially extracted in gene ontology (GO) analysis. GO pathway terms were specified using downregulated genes in the *H3t*^{−/−} mouse at P10. The bars represent the numbers of genes associated with the terms. The percentages of genes for each GO term are shown on the horizontal axis.

(H) Expression level of meiosis-related genes in GS cells, before and after the induction of differentiation, were analyzed by RT-qPCR. *H3t*^{+/+} or *H3t*^{−/−} GS cells were treated with RA for 7 days. The values in the *H3t*^{+/+} GS cells were set to 1 following normalization against the *Eef1a1* expression level. Data represent the mean of three independent experiments ± SD.
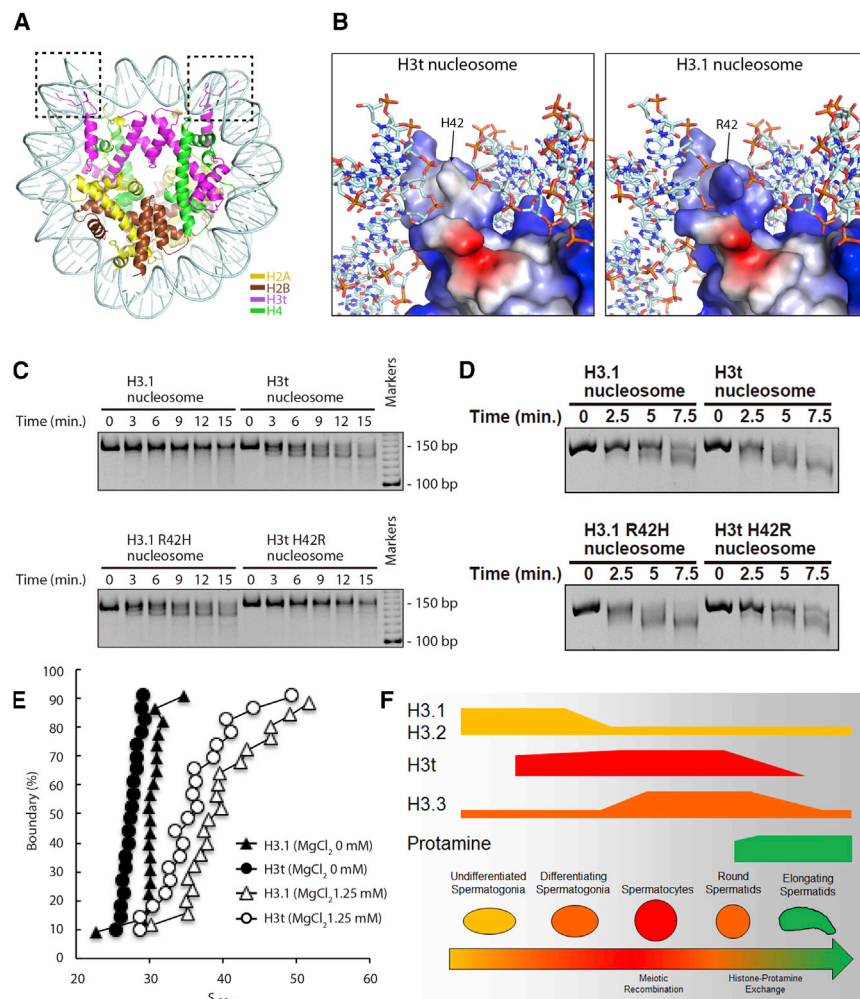
(A) Overall structure of the H3t nucleosome. Dotted squares indicate the enlarged regions around the H3t His42 residue presented in (B). H2A, yellow; H2B, brown; H3t, magenta; H4, green; and DNA, gray.

(B) Close-up view around the H3t His42 region in the H3t nucleosome (left) and the corresponding H3.1 Arg42 region in the H3.1 nucleosome (right). The H3t and H3.1 molecules are shown as an electrostatic surface, and DNAs are shown as a stick representation.

(C) MNase assay. H3t, H3.1, the H3t H42R, and H3.1 R42H nucleosomes were treated with MNase for 0, 3, 6, 9, 12, and 15 min and then deproteinized. The resulting DNA fragments were analyzed by nondenaturing 10% PAGE with ethidium bromide (EtBr) staining. The gel image shown is a representative of three or more independent experiments with similar results.

(D) ExoIII assay. Each nucleosome was treated with ExoIII for 0, 2.5, 5, and 7.5 min and then deproteinized. The resulting DNA fragments were extracted and analyzed by denaturing 14% PAGE with EtBr staining. The gel image shown is a representative of two independent experiments with similar results.

(E) Sedimentation velocity analyses by analytical ultracentrifugation. The experiments with the H3t and H3.1 polynucleosomes are represented as circles and triangles, respectively. Open and filled symbols indicate experiments in the presence and absence of MgCl₂, respectively. The sedimentation coefficient ($S_{20,w}$) distributions were determined by the method of van Holde and Weischet (Demeler and van Holde, 2004).

(F) Schematic diagram of how histone variants and protamines appear to be exchanged during spermatogenesis.

Yuen et al., 2014), lays the structural foundations needed for spermatogenesis-specific events, such as meiotic recombination and histone-protamine exchange (Figure 4F).

In summary, we have demonstrated that a tissue-specific H3 variant has a direct impact on cellular differentiation. We previously found 13 H3 variants in addition to H3t with characteristic tissue distributions (Maehara et al., 2015), and our present study demonstrates the intriguing idea that these variants might also have distinctive roles in tissue formation and cell differentiation. Hence, not only histone modifications, but also a histone variant by itself might dictate the fate of cell lineages during their differentiation.

EXPERIMENTAL PROCEDURES

Animals

All animal care was in accordance with institutional guidelines and was approved by the Institutional Animal Care and Use Committees of both Chubu and Osaka universities.

Statistical Methods

The data are presented as the mean ± SD of three independent experiments. Statistical significance of each pair was calculated with Student's t test, and p values <0.05 were considered statistically significant and are indicated as follows: *p < 0.05; **p < 0.01.

mRNA-Seq and Analysis

Total RNAs were extracted from whole testes of *H3t* homozygous and heterozygous knockout mice at P10. The mRNA-seq libraries were prepared and sequenced according to the Illumina protocol. Differentially expressed genes were extracted using Cufflinks (version 2.2.1, with options "cuffdiff –u –b") with reads mapped onto the mouse genome (mm9) using Tophat (version 2.0.12, with default options). The gene ontology (GO) analysis was performed using ClueGO (Bindea et al., 2009).

ACCESSION NUMBERS

The accession number for the RNA-seq data reported in this paper is DNA Data Bank of Japan: DRA004195. The accession numbers for the atomic coordinates of the H3t and H3.1 nucleosomes reported in this paper are RCSB PDB: 5B1L and 5B1M, respectively.

SUPPLEMENTAL INFORMATION

Supplemental Information includes Supplemental Experimental Procedures, four figures, and three tables and can be found with this article online at http://dx.doi.org/10.1016/j.celrep.2016.12.065.

AUTHOR CONTRIBUTIONS

REFERENCES

Bindea, G., Mlecnik, B., Hackl, H., Charoentong, P., Tosolini, M., Kirilovsky, A., Fridman, W.H., Pagès, F., Trajanoski, Z., and Galon, J. (2009). ClueGO: a Cytoscape plug-in to decipher functionally grouped gene ontology and pathway annotation networks. Bioinformatics 25, 1091–1093.

Bowles, J., and Koopman, P. (2007). Retinoic acid, meiosis and germ cell fate in mammals. Development 134, 3401–3411.

Dann, C.T., Alvarado, A.L., Molyneux, L.A., Denard, B.S., Garbers, D.L., and Porteus, M.H. (2008). Spermatogonial stem cell self-renewal requires OCT4, a factor downregulated during retinoic acid-induced differentiation. Stem Cells 26, 2928–2937.

Demeler, B., and van Holde, K.E. (2004). Sedimentation velocity analysis of highly heterogeneous systems. Anal. Biochem. 335, 279–288.

Goldberg, A.D., Allis, C.D., and Bernstein, E. (2007). Epigenetics: a landscape takes shape. Cell 128, 635–638.

Hake, S.B., and Allis, C.D. (2006). Histone H3 variants and their potential role in indexing mammalian genomes: the "H3 barcode hypothesis". Proc. Natl. Acad. Sci. USA 103, 6428–6435.

Kanatsu-Shinohara, M., Inoue, K., Lee, J., Yoshimoto, M., Ogonuki, N., Miki, H., Baba, S., Kato, T., Kazuki, Y., Toyokuni, S., et al. (2004). Generation of pluripotent stem cells from neonatal mouse testis. Cell 119, 1001–1012.

Luger, K., Mäder, A.W., Richmond, R.K., Sargent, D.F., and Richmond, T.J. (1997). Crystal structure of the nucleosome core particle at 2.8 A resolution. Nature 389, 251–260.

Maehara, K., Harada, A., Sato, Y., Matsumoto, M., Nakayama, K.I., Kimura, H., and Ohkawa, Y. (2015). Tissue-specific expression of histone H3 variants diversified after species separation. Epigenetics Chromatin 8, 35.

Mashiko, D., Fujihara, Y., Satouh, Y., Miyata, H., Isotani, A., and Ikawa, M. (2013). Generation of mutant mice by pronuclear injection of circular plasmid expressing Cas9 and single guided RNA. Sci. Rep. 3, 3355.

Maze, I., Noh, K.M., Soshnev, A.A., and Allis, C.D. (2014). Every amino acid matters: essential contributions of histone variants to mammalian development and disease. Nat. Rev. Genet. 15, 259–271.

Meikar, O., Da Ros, M., Korhonen, H., and Kotaja, N. (2011). Chromatoid body and small RNAs in male germ cells. Reproduction 142, 195–209.

Montellier, E., Boussouar, F., Rousseaux, S., Zhang, K., Buchou, T., Fenaille, F., Shiota, H., Debernardi, A., Héry, P., Curtet, S., et al. (2013). Chromatin-to-nucleoprotamine transition is controlled by the histone H2B variant TH2B. Genes Dev. 27, 1680–1692.

Santenard, A., Ziegler-Birling, C., Koch, M., Tora, L., Bannister, A.J., and Torres-Padilla, M.E. (2010). Heterochromatin formation in the mouse embryo requires critical residues of the histone variant H3.3. Nat. Cell Biol. 12, 853–862.

Sasaki, H., and Matsui, Y. (2008). Epigenetic events in mammalian germ-cell development: reprogramming and beyond. Nat. Rev. Genet. 9, 129–140.

Shinagawa, T., Huynh, L.M., Takagi, T., Tsukamoto, D., Tomaru, C., Kwak, H.G., Dohmae, N., Noguchi, J., and Ishii, S. (2015). Disruption of Th2a and Th2b genes causes defects in spermatogenesis. Development 142, 1287–1292.

Strahl, B.D., and Allis, C.D. (2000). The language of covalent histone modifications. Nature 403, 41–45.

Tachiwana, H., Kagawa, W., Osakabe, A., Kawaguchi, K., Shiga, T., Hayashi-Takanaka, Y., Kimura, H., and Kurumizaka, H. (2010). Structural basis of instability of the nucleosome containing a testis-specific histone variant, human H3T. Proc. Natl. Acad. Sci. USA 107, 10454–10459.

Talbert, P.B., and Henikoff, S. (2010). Histone variants–ancient wrap artists of the epigenome. Nat. Rev. Mol. Cell Biol. 11, 264–275.

van der Heijden, G.W., Dieker, J.W., Derijck, A.A., Muller, S., Berden, J.H., Braat, D.D., van der Vlag, J., and de Boer, P. (2005). Asymmetry in histone H3 variants and lysine methylation between paternal and maternal chromatin of the early mouse zygote. Mech. Dev. 122, 1008–1022.

van der Heijden, G.W., Derijck, A.A., Pósfai, E., Giele, M., Pelczar, P., Ramos, L., Wansink, D.G., van der Vlag, J., Peters, A.H., and de Boer, P. (2007). Chromosome-wide nucleosome replacement and H3.3 incorporation during mammalian meiotic sex chromosome inactivation. Nat. Genet. 39, 251–258.

Witt, O., Albig, W., and Doenecke, D. (1996). Testis-specific expression of a novel human H3 histone gene. Exp. Cell Res. 229, 301–306.

Yoshida, S. (2012). Elucidating the identity and behavior of spermatogenic stem cells in the mouse testis. Reproduction 144, 293–302.

Yuen, B.T., Bush, K.M., Barrilleaux, B.L., Cotterman, R., and Knoepfler, P.S. (2014). Histone H3.3 regulates dynamic chromatin states during spermatogenesis. Development 141, 3483–3494.